Proceedings of the Thirteenth International TOVS Study Conference

INTERNATIONAL ATOVS WORKING GROUP

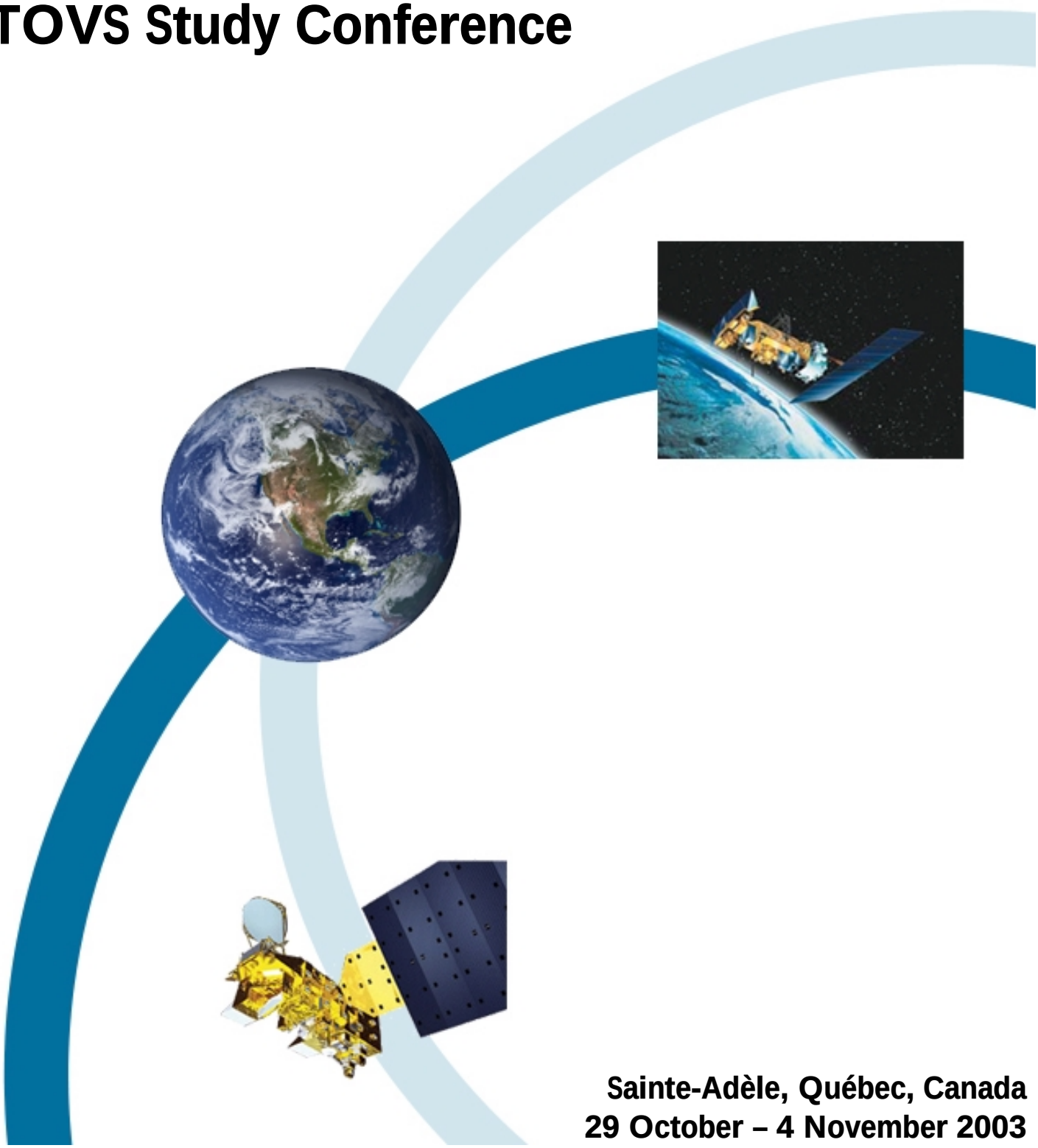

Sainte-Adèle, Québec, Canada
29 October – 4 November 2003

FOREWORD

The International TOVS Working Group (ITWG) is convened as a sub-group of the International Radiation Commission (IRC) of the International Association of Meteorology and Atmospheric Physics (IAMAP). The ITWG continues to organize International TOVS Study Conferences (ITSCs) which have met approximately every 18 months since 1983. Through this forum, operational and research users of TIROS Operational Vertical Sounder (TOVS), Advanced TOVS (ATOVS) and other atmospheric sounding data have exchanged information on data processing methods, derived products, and the impacts of radiances and inferred atmospheric temperature and moisture fields on numerical weather prediction (NWP) and climate studies.

These Technical Proceedings gather together the papers of the scientific presentations and posters from the Thirteenth International TOVS Study Conference (ITSC-XIII) held at the Hotel Le Chantecler in Sainte Adèle, Quebec, Canada from 29 October to 4 November 2003. ITSC-XIII marked the milestone of 25 years of TOVS data starting with the launch of TIROS-N in October 1978. Around one hundred and thirty participants attended the Conference and provided scientific contributions. This was the largest conference to date in terms of number of presentations and posters. In a few cases where a paper has not been submitted by the deadline, the abstract is provided instead. For the first time it was agreed at ITSC-XIII to provide these proceedings on a CD in place of a hard copy Proceedings. This allows the inclusion of more material while reducing printing and distribution costs. The ITWG web site (http://cimss.ssec.wisc.edu/itwg/) also contains electronic versions of the conference papers, presentations and posters. In addition to these Proceedings there is also a Report from the ITSC-XIII meeting also available on the CD, as a hard copy and from the web site. It summarizes the main recommendations and actions from the working groups which met during the meeting. Together, these documents and web pages reflect the conduct of a highly successful meeting in Sainte Adèle. Details of Reports and Proceedings from previous conferences are also available from the web site. If you require a copy of the ITSC-XIII Report and/or CD please contact the working group co-chairs at the co-ordinates below.

ITSC-XIII was sponsored by the Met Office (U.K.), NOAA NESDIS, EUMETSAT, the World Meteorological Organization (WMO), Alcatel, ABB, the Raytheon Company and ITT Industries. The support of these government agencies and private industry companies is gratefully acknowledged. We wish to thank the local organizing committee from Environment Canada, particularly Louis Garand and Clement Chouinard of the Data Assimilation and Satellite Meteorology Division. We also thank and appreciate the contribution of the Environment Canada staff, particularly Maryse Ferland and Danielle O'Shaughnessey, who assisted ably in the organization and conduct of the Conference at Sainte Adèle. We thank the staff of Hotel Le Chantecler for their assistance during the Conference. We also thank Maria Vasys of the University of Wisconsin, who helped with details of the meeting organization, and publication of the Conference Report and Proceedings. Finally, we thank the numerous contributions from Leanne Avila, University of Wisconsin, who assisted in conference planning, on-site meeting organization, and preparation and publication of the Report, this Technical Proceedings and the ITWG Web site.

Roger Saunders
Co-chair ITWG
Met Office (U.K.)
roger.saunders@metoffice.com

Thomas Achtor
Co-chair ITWG
University of Wisconsin-Madison
tom.achtor@ssec.wisc.edu

Table of Contents

Papers from Presentations

Session 4: Radiative Transfer and Surface Modeling

Session 5: Retrieval of Atmospheric Parameters

Author Index

PAPERS FROM ORAL PRESENTATIONS

The assimilation of AMSU-B radiances in the CMC global data assimilation system: Difficulties and impact relative to AMSU-A radiances

C. Chouinard and J. Hallé

Meteorological Service of Canada / Service Météorologique du Canada
Dorval, Québec, Canada

Abstract

The Canadian Meteorological Centre's (CMC) three Dimensional Variational (3D-Var) is an incremental analysis system that is currently used by both our global and regional models with very little modifications. During the last few years, it has undergone a series of upgrades from isobaric to a terrain-following coordinate, and most importantly to the direct assimilation of satellite radiances. The quality control (QC) of observations was also upgraded to a variational quality control whereby the data rejection/acceptance decisions are taken consistently during the minimization problem.

In terms of radiance data, the system currently uses so-called raw level-1b AMSU-A that are quality-controlled (QC), and bias controlled by the data user and not the producer. The QC and thinning algorithms of the radiance data are more complex and system dependent. Because of QC and bias correction algorithms, the impact of satellite data on CMC's analyses and forecasts are now very large and comparable to that of radiosonde data in the SH.

The resolution of NWP forecast/analysis systems is forever increasing and so is the volume of data from various instruments. The volume of satellite data has become quite a challenge even at the level of preparation and QC prior to the analysis step. One aspect of NWP systems which definitely can benefit from this additional data is the moisture analysis. In that context we have started to use the water sensitive radiances from the AMSU-B instruments onboard NOAA-15, NOAA-16, and NOAA-17. As will be shown, the quality of both the temperature and moisture analyses are significantly improved when using these additional radiance data. Preliminary evaluations indicate marked improvements in 5-10 day temperature forecasts and significant improvements in Quantitative Precipitation Forecast (QPF) skill scores in the first 5 days of 10-day forecasts.

Introduction

One of the advantages of variational data assimilation is its ability to assimilate indirect observations such as satellite radiances. With the help of a fast radiative transfer model (RTM), most NWP Centres are now able to directly assimilate radiance data and these have produced significant gains in the quality of operational analyses and forecasts. The quality of measurements from an instrument dictates how much influence this type of data will receive in an analysis system, but when it comes to indirect radiance measurements the quality of the RTM

which maps out the influence of radiance data in physical space, such as temperature and moisture, is also an issue.

The effective sensitivity of a satellite radiance measurement to an atmospheric state variable such as water vapor i.e. the so-called Jacobian is indicative of the impact of the radiance on atmospheric variables. The radiance data from AMSU-A instrument has the advantage of being sensitive almost exclusively to temperature, moreover, its Jacobian is very homogeneous varying very little from Tropical to mid-latitude atmospheric air-masses. On the other hand, the Jacobian of AMSU-B data is primarily sensitive to water vapor, but in drier atmospheres, it is also sensitive to temperature. The Jacobian also varies significantly from Equator to Pole. Because of this dual sensitivity, the assimilation of AMSU-B data is a more delicate problem requiring very accurate temperature and moisture trial fields and prior knowledge of their corresponding background error statistics.

Because of the difficulties inherent to the assimilation of moisture sensitive radiances, their current use at most NWP Centres is limited to the use of a few infrared channels from either the GOES or NOAA/HIRS instruments also onboard the NOAA platforms. NCEP and UKMET have been assimilating AMSU-B data since their availability i.e. NOAA-15 and more recently they have added NOAA-16 and NOAA-17 data. In Canada, we have just started to use AMSU-B in replacement of our current use of statistically derived humidity profiles obtained from the GOES sensors (Garand and Hallé, 1997). In this paper there will be a brief description of the steps involved in the preparation and QC of AMSU-B data prior to assimilation, followed by basic experimental test results, and finally results from their recent implementation in the full 3D-Var global data assimilation system at CMC.

Brief description of the revised 3D-Var analysis system and recent revisions

The basic analysis system used in this study is the one that was described in Gauthier et al. 1999, and more recent improvements have been described in three papers presented at the ITSC-11 and ITSC-12 (Chouinard and Hallé, 2000, Chouinard et al. 2000), and ITSC-13 meetings in Lorne, Australia (Chouinard et al. 2002). It is a global 28 level terrain following co-ordinate analysis/forecast system producing analyses directly on the model's vertical and horizontal grids. The most recent improvements to the system pertain to the preparation, QC, and use of conventional data, and most importantly, the introduction of new sources of satellite data. The combined impact of the new satellite data and the revision of the analysis procedure have contributed to major improvements in the reliability and quality of the CMC forecast/analysis system as described in Chouinard et al. 2002.

The peak sensitivity of some AMSU-B radiances is as high as 200 hPa in Tropical atmospheres and somewhat lower in Extra-Tropical cases. In the previous AMSU-A analysis system, the moisture analysis was limited to 300 hPa because most of the conventional moisture data above that were generally not very reliable. Because the peak sensitivity of some AMSU-B radiances to

moisture is around 200 hPa with tail effects extending up to70 hPa, the moisture analysis top had to be raised so as to retain most of their response. This is graphically illustrated in Fig.1.

Satellite data used in this study

The core satellite data used in this study are the AMSU-A and AMSU-B radiances from the NOAA-15, NOAA-16, and NOAA-17 satellites that are received at CMC via a public FTP link. These data are in level-1b format and originate from an operational NESDIS server in Washington. Further processing of the level-1b radiances is done at CMC using the AAPP software package (http://www.metoffice.com/research/interproj/nwpsaf/atovs/index.html). The main functions of this software package are the navigation and calibration of the level-1b radiance data. Finally, the radiances are coded in BUFR format and stored in a database at CMC.

The AMSU-A instrument has 15 microwave channels with a NADIR resolution of approximately 45km. Because of difficulties in specifying surface emissivities over land and ice, certain channels that are sensitive to skin surface temperature, are not used. Similarly, some stratospheric channels are not used because their peak contribution is above our NWP model top level currently at 10hPa, and consequently, we do not assimilate channels 11 to 14.

The AMSU-B instrument has 5 microwave channels with a higher resolution than the AMSU-A instrument, i.e. 16km (AMSU-B) compared to 45km (AMSU-A). Fig. 2 shows a typical composite coverage map of AMSU-B from the three NOAA satellites in a 6-hour time window. All AMSU-B radiances are sensitive to atmospheric column moisture, temperature, skin surface temperature and, surface emissivity. Over water, all 4 AMSU-B channels are assimilated because the fast surface emissivity model of S. English (FASTEM2) is used. However, over land and over different types of ice surfaces, because the emissivity is not well known, low peaking AMSU-B channels are either restricted or not used.

AMSU-B radiance processing for assimilation

Following the navigation/calibration validation, the AMSU-B data is subject to a passive monitoring check whereby it is systematically compared to simulated radiances over an extended period of a few months. From this comparison a first estimate of systematic and random error is obtained. The random error contains both the noise directly related to the instrument and an added component of noise due to RTM errors. This combined estimate will be used to specify the effective observational error used by the analysis procedure. For more details on the monitoring step, please refer to Chouinard et al. 2002 where this same procedure is described in the context of AMSU-A.

The systematic component of the error, or so-called radiance bias, has to be removed before the data assimilation step. The same procedure developed to remove AMSU-A biases was adapted to the AMSU-B data stream (Chouinard et al., 2002). There was reason to believe that some of the biases in AMSU-B could be related to RTM deficiencies in moisture treatment. However, attempts to relate AMSU-B biases to column-integrated moisture predictors have failed to show improvements over a simpler two-predictor approach. Similarly, attempts to use surface parameters as predictors in the AMSU-B also failed as they did with AMSU-A. Finally, the same type of algorithm is now used for AMSU-A and AMSU-B data, which is the 2 predictor algorithm, namely the geopotential thickness of layer 1000hPa-300hPa and, the geopotential thickness of layer 200hPa-50hPa.

Quality Control

Once the AMSU-B radiance data has been unbiased, it is then subjected to a series of quality control checks before it makes its way to the assimilation. In all, each AMSU-B radiance observation undergoes 14 checks; these are listed in Annex 1. Note that these tests are applied to the bias-corrected radiance rather than the original non-corrected radiance.

Besides checking the radiance itself, we also verify the quality of the complementary information which accompanies each observation, e.g. surface type; scan position, satellite zenith angle, etc. Some tests consist of checking for coding errors. Others check the internal consistency of the report, or the consistency between the type of surface reported and the model surface type, or for gross errors.

Some AMSU-B channels are sensitive to precipitation. These channels are not used since the 3Dvar system does not have a cloud liquid water variable as part of the model state and is incapable of correctly assimilating these radiances. To determine the precipitation contamination for AMSU-B radiances, we make use of a scattering index algorithm developed by Bennartz (1999). As with AMSU-A, some lower-peaking channels are also flagged over high terrain, where the surface contribution is non-negligible. The topography thresholds used are listed in Annex 1. Similarly, in very dry atmospheric conditions mostly in the Polar Regions, we do not assimilate some AMSU-B channels because of a significant surface contribution. These points are easily depicted as the innovation statistics become very large. To eliminate these data, a so-called dryness index was developed. This index is the difference between the observed AMSU-B radiances of channels 3 and 5. By relating the index to areas where innovations were notably larger because of a large surface contribution, a set of threshold values was determined for three of the four AMSU-B channels assimilated. The threshold values of the dryness index are listed in Annex 1.

As for AMSU-A, a Rogue check is performed on the innovations or difference between observed

and simulated radiance *(O –P)*. This is similar to what is referred to as a background check in the context of conventional data. Depending on the channel and its inherent difficulties, innovations greater than 2-4 times the total channel error standard deviation are rejected. The exact multiple of standard deviation used for each channel for the Rogue check are listed in Annex 1.

Rejects are of three different types:

Single: a test rejects each channel individually,

Partial: a test rejects more than one channel, but not all,

Full: a test rejects all channels at an observation point.

Finally, it is also possible for the operational meteorologist to specify the rejection of a complete orbit, in the case of major problems with satellite operations.

Channel selection and horizontal thinning

Following bias correction and quality control, the final data selection process begins. This can be divided into two steps, channel selection and horizontal thinning.

Due to difficulties in specifying surface emissivity and because of uncertainties in the trial field skin surface temperature over land and sea-ice, we make restricted use of lower-peaking channels over these surfaces. Channel selection over water and over land or sea-ice surfaces is summarized in Table 1.

Ocean	**Land or Sea-ice**
AMSU-B 2 to 5	AMSU-B 3 to 5

Table 1. AMSU-B channels selected for assimilation.

In order not to overwhelm the 3D-Var with satellite data and to provide a volume of data compatible with the resolution of the global analysis system grid (240x120), the AMSU-B data are thinned to a separation of about 250km. This separation seems to be optimal at the current system resolution, given the fact that the 3D-Var assumes that observational errors are not correlated horizontally. Effectively at 250 km spacing, the horizontal correlation of the error in the radiance data is negligible.

The thinning process can be summarized as follows:

i) A pre-thinned (75km) AMSU-B data are grouped together in 250km square boxes.

ii) Within a box, a priority scheme determines which pixel will be retained. Priority goes to the pixel which has the lowest percentage of channels rejected; in the case where more than one pixel has the same low percentage; the pixel which is closest to the box center will be chosen.

iii) Radiances measured at the extreme left and right edges of the satellite swath are not used in the analysis because their errors are generally larger. More precisely, fields of view numbered 1-7 and 84-90 are excluded for AMSU-B.

Basic experimental results with AMSU-B radiance data

The first tests with a radiance data pertain to the sensitivity of the channel to atmospheric variables, it is nothing but a verification that the RTM is producing the proper response in the analysis. One observation from each of the channels considered are isolated as well as the atmospheric variables needed for the RTM, and the sensitivity or Jacobian of individual channels are calculated and plotted against each other and compared to other satellite data. The vertical response of the data can then be plotted and inspected to insure that most if not all of the response is within the NWP model vertical domain. Such plots are indicated in the right panel of Fig. 1 and were used to effectively raise the moisture analysis top level. Similarly the sensitivity to surface variables can be looked at and judged whether acceptable for assimilation or not.

The next series of tests pertain to the full 3D-Var system and the evaluation of the response of one channel at one location (not shown), and as shown in Fig. 3, the cumulative contribution of all channels at one location. Again this is to verify that all the operators such as interpolation of the trial field for the RTM are responding as expected, and more specifically to measure the impact of radiances on the temperature and moisture retrievals. Note the difficulty with AMSU-B data in that the response in the Tropics is very large on the moisture retrieval and relatively small on temperature, whereas the response in the Extra-Tropics is large on temperature and relatively small on moisture.

Results from OSE and from the recent implementation of AMSU-B in 3D-Var

In order to evaluate the impact of new data sources, such as AMSU-B in this study, most NWP Centres prepare Observing System Experiments (OSE) with and without these new data to measure their impact in a full forecast/analysis system. It is generally accepted that to get a clear signal, the OSE should cover a period of at least 1 month and preferably two months as was done in this study. We have prepared many such OSEs and present here the latest which produces

acceptable results for both a summer and winter periods.

In Fig. 4, the 2-month averaged verification against the North Hemisphere (NH) radiosonde dataset for the control (operational, blue) and the AMSU-B system (red) are presented. As indicated, the short term 6-h results are very positive particularly on the moisture variables. In Fig. 5, the verification in the Southern Hemisphere (SH) shows a very large positive impact of AMSU-B data on the moisture forecast at 6h, 48h, and somewhat smaller beyond 96h (not shown).

Evaluating against radiosonde data is very valuable because of the high quality of this dataset, however, it does not give a very good evaluation of the system over oceanic areas and other areas such as the SH which are basically void of radiosonde data. NWP Centres also prepare verifications against analyses which has the advantage of evaluating continental and oceanic areas. In Fig. 6, the 500 hPa geopotential anomaly correlation scores for the month of September 2003 are presented. This is 3 months after the June implementation of AMSU-B data in our operational system. As can be seen, the scores of the Canadian model are very competitive with other leading Centres both in the short (day1-4) and the longer term forecasts.

Finally, another measure of performance for verifying the impact of moisture sensitive data such as AMSU-B is by verifying the QPF forecasts issued from the operational (blue) and AMSU-B systems (red). As indicated in Fig. 7, the QPF THREAT scores against the surface synoptic network measurements are significantly improved particularly in the 20mm/24h and above categories with a somewhat more neutral result in the in the less than 20mm/24h categories.

Conclusions

We have successfully implemented the use of moisture sensitive AMSU-B radiances in CMC's 3D-Var data assimilation system. The impact of this additional source of moisture data is very positive on the moisture analyses and, as expected, the precipitation forecasts issued from the new analyses are also improved. The direct impact on moisture fades out with time and beyond 72 hours is not measurable on the moisture forecasts. However, the impact on the other analysis variables such as temperature, geopotential, and wind field, however small initially, becomes increasingly larger in the 4-6 day range contributing to significant improvements in the long term forecasts.

References

Bennartz, R., A. Thoss, A. Dybbroe and D. B. Michelson, 1999: Precipitation Analysis from AMSU, Nowcasting SAF, Swedish Meteorological and Hydrological Institute, Visiting Scientist Report, November 1999.

Chouinard C. and J. Hallé: The impact of TOVS radiances in the CMC 3D-Var analysis system. ITSC-X proceedings, Boulder, Colorado, February 1999, p92-98.

Chouinard C., J. Hallé, and R. Sarrazin: Recent results with TOVS data in the new CMC 3D-Var-analysis system: the combined and separate impact of microwave radiance observations with aircraft wind data. ITSC-XI proceedings, Hungary, Budapest, September 2000, p53-57.

Chouinard C., C. Charette, J. Hallé, P. Gauthier, J. Morneau, and R. Sarrazin: The Canadian 3D-Var analysis scheme on model vertical coordinate. 18th Conference on Weather Analysis and Forecasting, 30 July-2 August 2001, Fort Lauderdale, Florida.

Chouinard C., J. Hallé, C. Charette, and R. Sarrazin: Recent improvements in the use of TOVS satellite radiances in the Unified 3D-Var system of the Canadian Meteorological Centre. ITSC XII proceedings, Lorne, Australia, 27 February-March 5, 2002 (to be published).

Garand L, and J. Hallé: Assimilation of Clear and cloudy-sky Upper -Tropospheric Humidity Estimates Using Goes 8 and Goes 9 Data. *J. Atm. Science*, **14**, pp. 1036-1054.

Gauthier, P., C. Charette, L. Fillion, P. Koclas and S. Laroche, 1999: Implementation of a 3D variational data assimilation system at the Canadian Meteorological Center. Part I: The global analysis, Atmosphere-Ocean, No.2, pp 103-156.

Grody N., F. Weng, and R. Ferraro: Application of AMSU for obtaining hydrological parameters. Microwave and Remote Sensing of the Earth's surface and atmosphere, 2000, pp.339-351.

Annex 1; Quality control tests for AMSU-B channels.

#	Test	Rejected if:	Type of reject
1	topography reject	topography > 2500m for AMSU-B 3, 2000m for AMSU-B 4, 1000m for AMSU-B 5	partial (AMSU-B 3-5)
2	invalid land/sea qualifier	qualifier differs from {0, 1, 2}	full
3	invalid terrain type	terrain type differs from {-1, 0,1}	full
4	invalid field of view number (fov)	fov outside valid range [1,90]	full
5	satellite zenith angle out of range	satellite zenith angle outside valid range [1,60]	full
6	inconsistent field of view and satellite zenith angle	ABS(((fov-45.5)*1.31)-angle) > 1.8	full
7	inconsistent land/sea qualifier and model mask	other than: qualifier=1 (sea observation) and model mask <0.20 (model sea) or qualifier=0 (land observation) and model mask>0.50 (model land)	full
8	inconsistent terrain type and model ice	terrain type=0 (sea ice) and model ice<0.01 (no model ice)	full
9	uncorrected radiance	correction flag is off	single
10	rejected by RTTOV	3Dvar quality control flag is on	single
11	radiance gross check failure	Tb < channel varying Tb min, or Tb > channel varying Tb max.	single
12	Dryness index reject	Dryness index = Tb(AMSUB3) – Tb(AMSUB5) Reject if (dryness index) > 0 for AMSU-B 3, -10 for AMSU-B 4, -20 for AMSU-B 5	partial (AMSU-B 3-5)
13	Bennartz scattering index reject	Bennartz scattering index> 40 over sea-ice, or 15 over sea, or 0 over land.	full
14	innovation rogue check failure	$(y-H(x)) > \alpha * (total\ error)$, where α=2 for AMSU-B 1, =3 for AMSU-B 2 =4 for AMSU-B 3-5	single

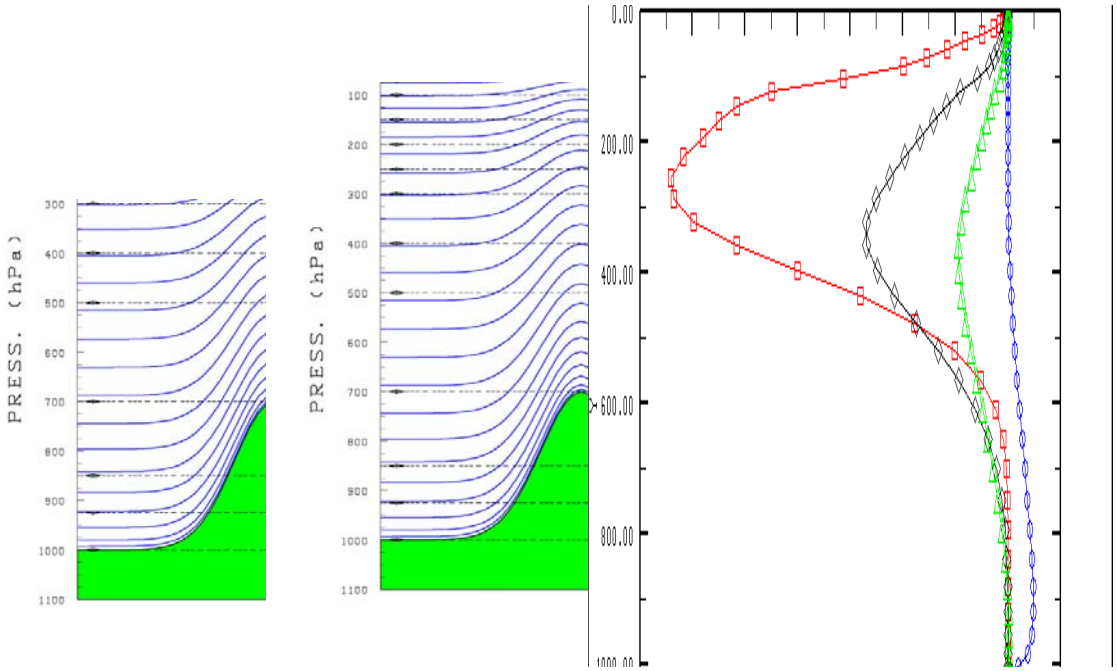

Fig. 1 Schematic view of the model top level of moisture analysis (left panel) prior to AMSU-B in comparison to the current raised top (central panel) to accommodate the sensitivity of AMSU-B radiances (right panel)

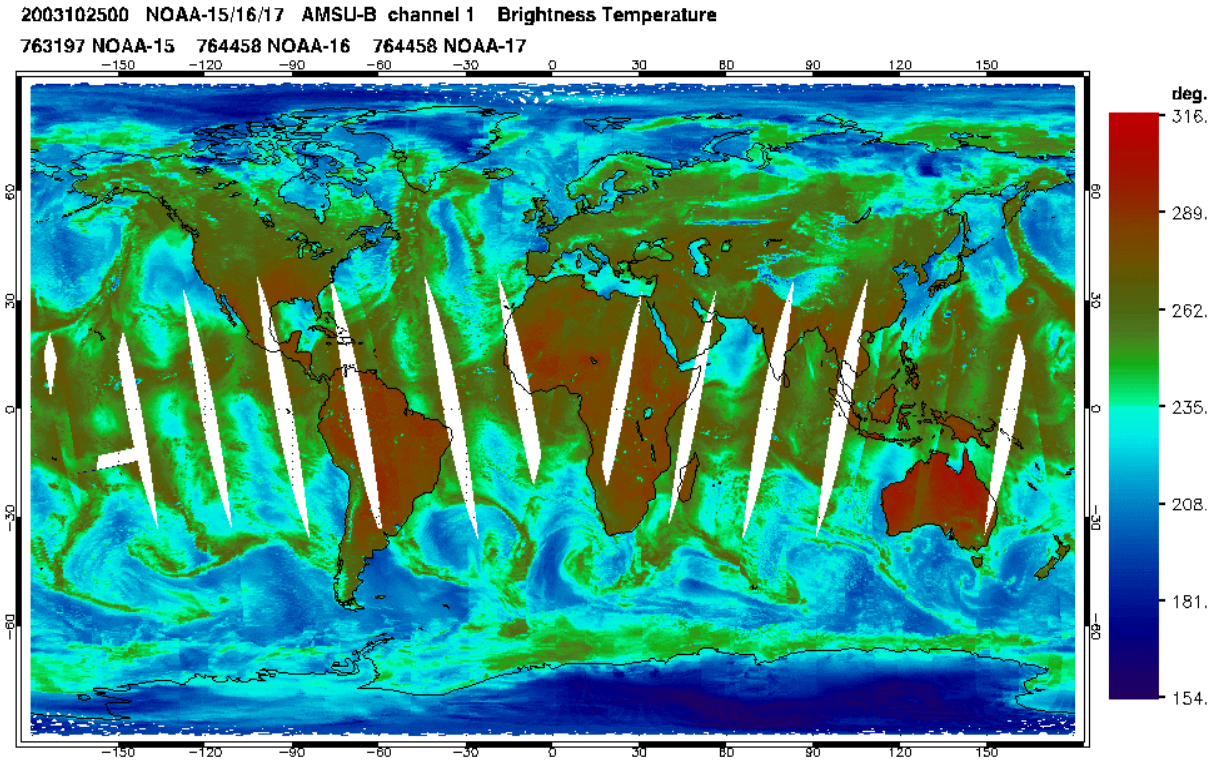

Figure 2. Typical coverage of AMSU-B radiances for a 6-hour time window (16 km footprint**)**

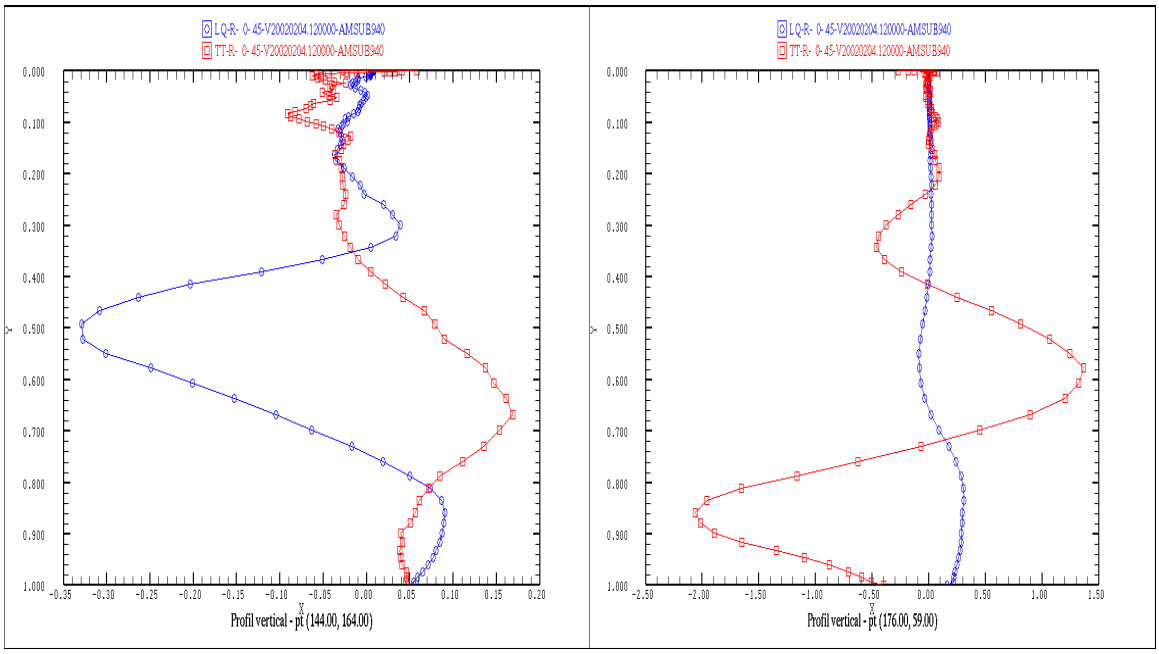

Fig. 3 First analysis tests; impact of the 4 AMSU-B channels at one pixel location. Vertical profile of temperature (red) and lnq moisture variable (blue) analysis increments in the Tropics (left panel) and Extra-Tropics (right panel).

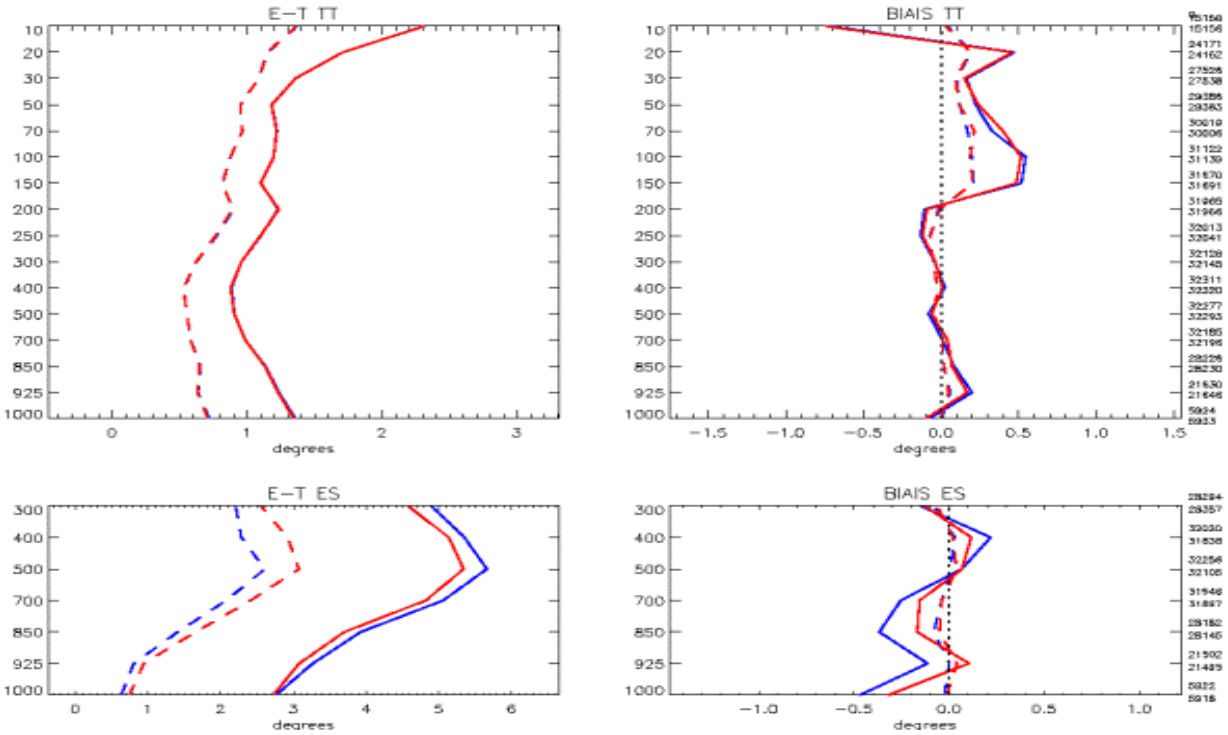

Fig. 4 Verification against NH radiosondes for the August-September 2002 period. Top panels are for temperature and bottom panels for dewpoint depression. Units are degrees.

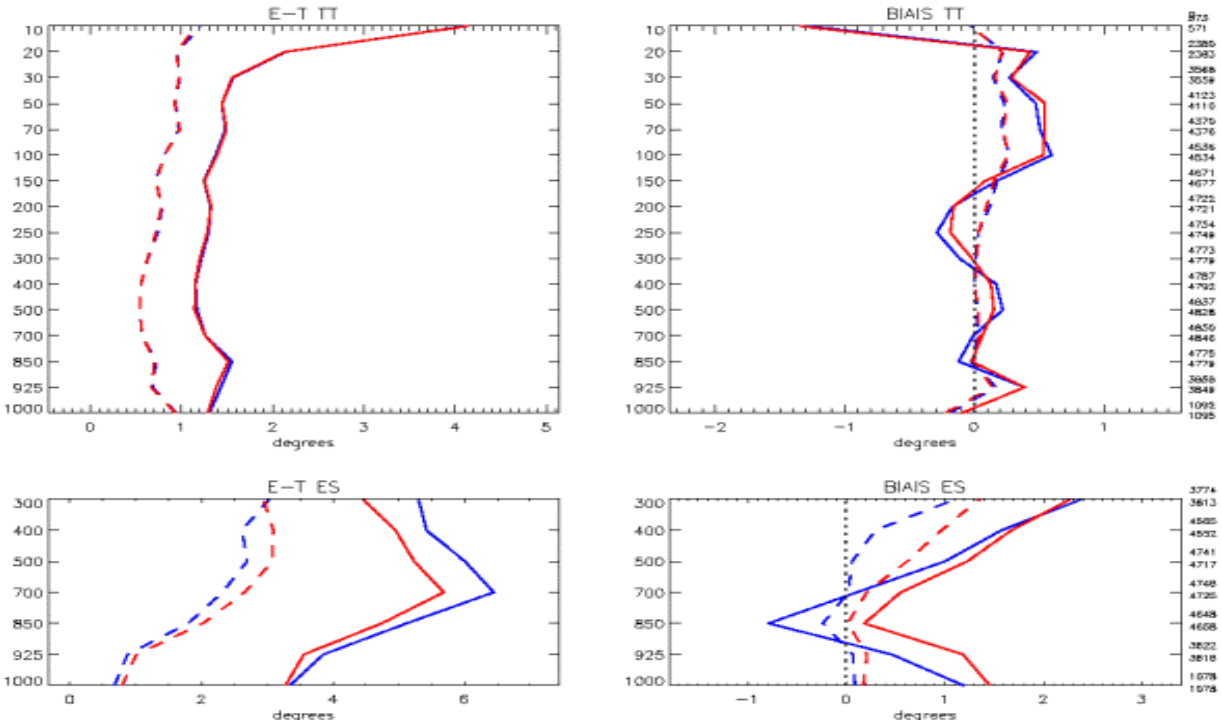

Fig.5 Verification against SH radiosondes for the August-September 2002 period. Top panels are for temperature and bottom panels for dewpoint depression. Units are degrees.

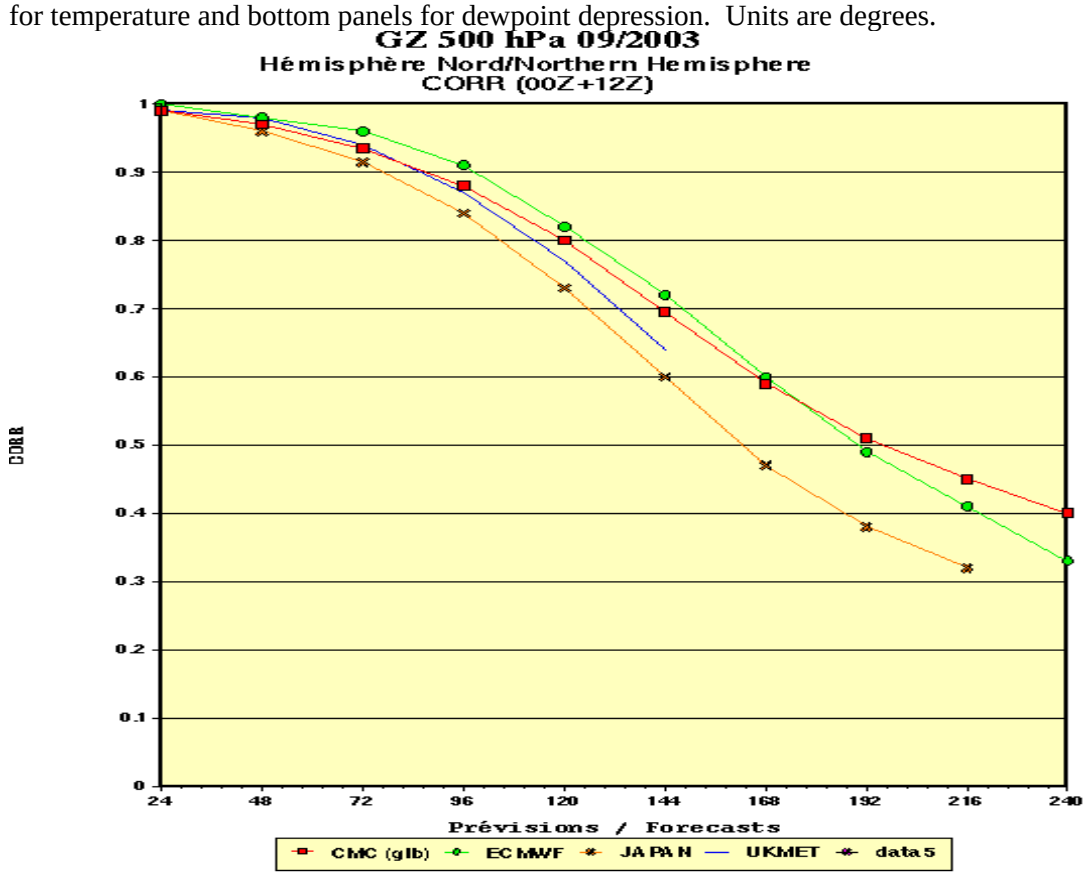

Fig. 6 NH Anomaly correlation scores of the new AMSU-B system (red line) compared to scores from other leading NWP Centres for the month of September 2003.

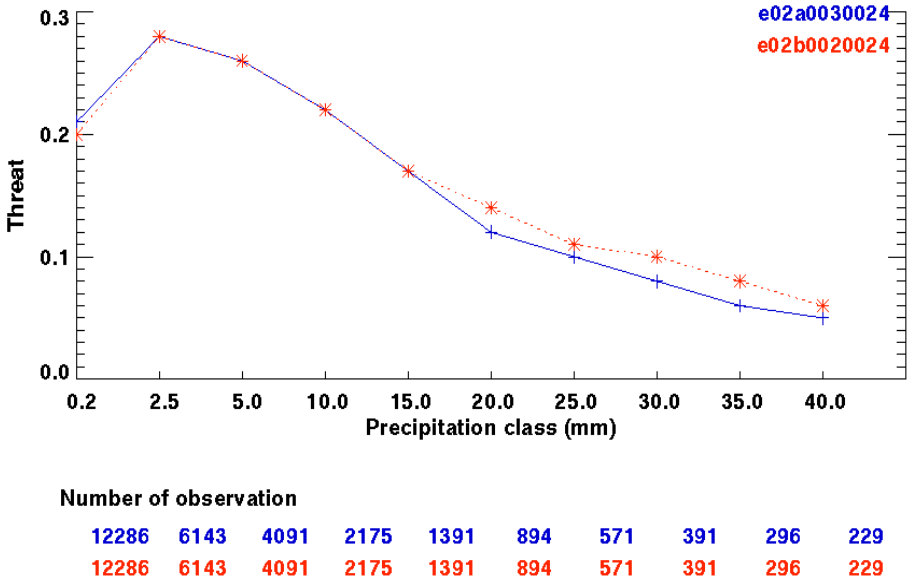

Fig. 7. THREAT scores of the 0-24h QPF forecasts issued from the OPERATIONAL (full blue lines) and the AMSU-B system (red dashed lines) against the NA surface synoptic network measurements. The number of observations in each category and the categories are indicated at the bottom.

Operational use of ATOVS at the Met Office

Stephen English Fiona Hilton, Brett Candy, Keith Whyte, Nigel Atkinson, Andrew Smith, Bill Bell, Una O'Keeffe, Amy Doherty

Met Office, Exeter, United Kingdom,

1. Introduction

The Met Office continues to make effective use of ATOVS radiances in Numerical Weather Prediction (NWP), and this use has been extended significantly in recent years. Whilst data from the HIRS instrument are used only in the global model, extensive use is now made of AMSU-A and AMSU- B in regional and mesoscale NWP. Data is used from three satellites rather than two. In preparation for future developments research has been undertaken in a number of areas. This paper will focus on use of data over land, bias correction and the implementation of RTTOV version 7, as well as briefly discussing the impact of the third ATOVS instrument and preparations for SSMIS. Assimilation of ATOVS in regional and mesoscale NWP is discussed by Candy *et al*. (2003).

The use of ATOVS in global NWP at the Met Office has changed from that described in English *et al*. (2002) only in the addition of NOAA-17 data. The processing system is unchanged. The use of data in regional and mesoscale NWP is described in Candy *et al*. (2003).

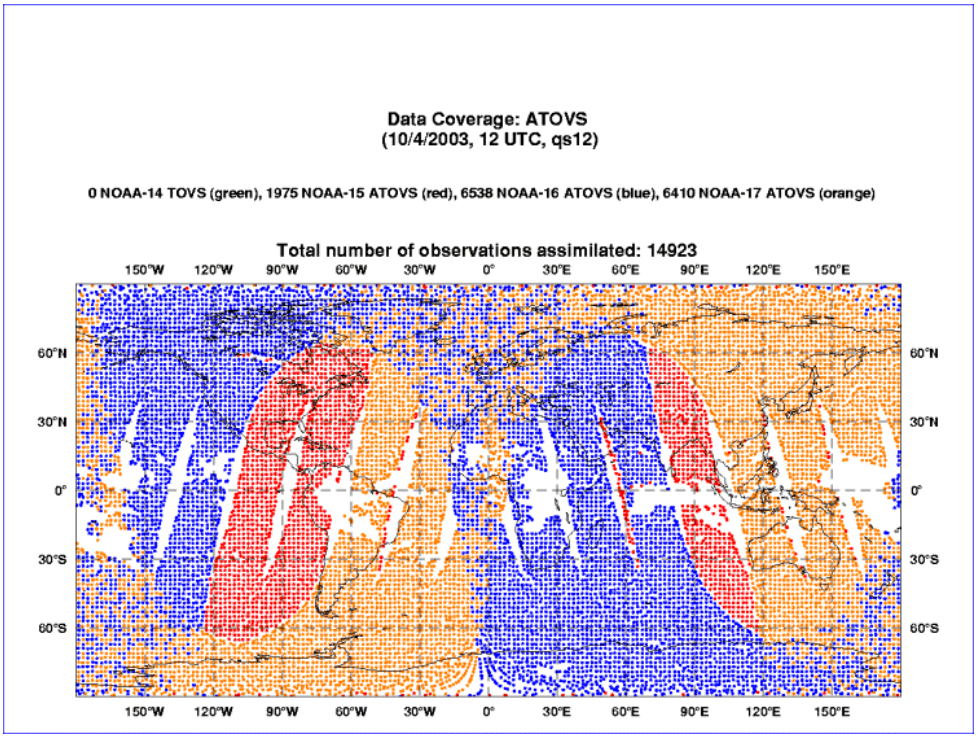

Figure 1: Data coverage for NOAA-15, 16 and 17 level 1D radiances in the Met Office global model stratospheric version for 10 April 2003, 09:00 to 15:00 UTC.

2. Impact of NOAA-17

NOAA-17 ATOVS was introduced operationally on 1st October 2002, just 3 months after launch. This gave complete global coverage in a six hour data assimilation window for the first time (Figure 1). The quality of the data was initially slightly lower than NOAA-15 and NOAA-16 data due to a misalignment of the HIRS. This was corrected in operational Met Office processing in February 2003. The impact of NOAA-17 was nonetheless found to be significantly positive. In the southern hemisphere key fields such as mean sea level pressure and 500 hPa geopotential height have RMS error compared to observations 1-3 % lower. Verification against NOAA-16 radiances at very short range showed RMS errors lower by 1-5% in the troposphere for temperature sounding radiances, but 5-10% lower in the stratosphere and for humidity sounding radiances (Figure 2). The impact of removing NOAA-15 from a three satellite system was found to be roughly twice as large as removing NOAA-17, despite the loss of HIRS and several AMSU channels on NOAA-15. This difference was attributed to the HIRS misalignment error on NOAA-17.

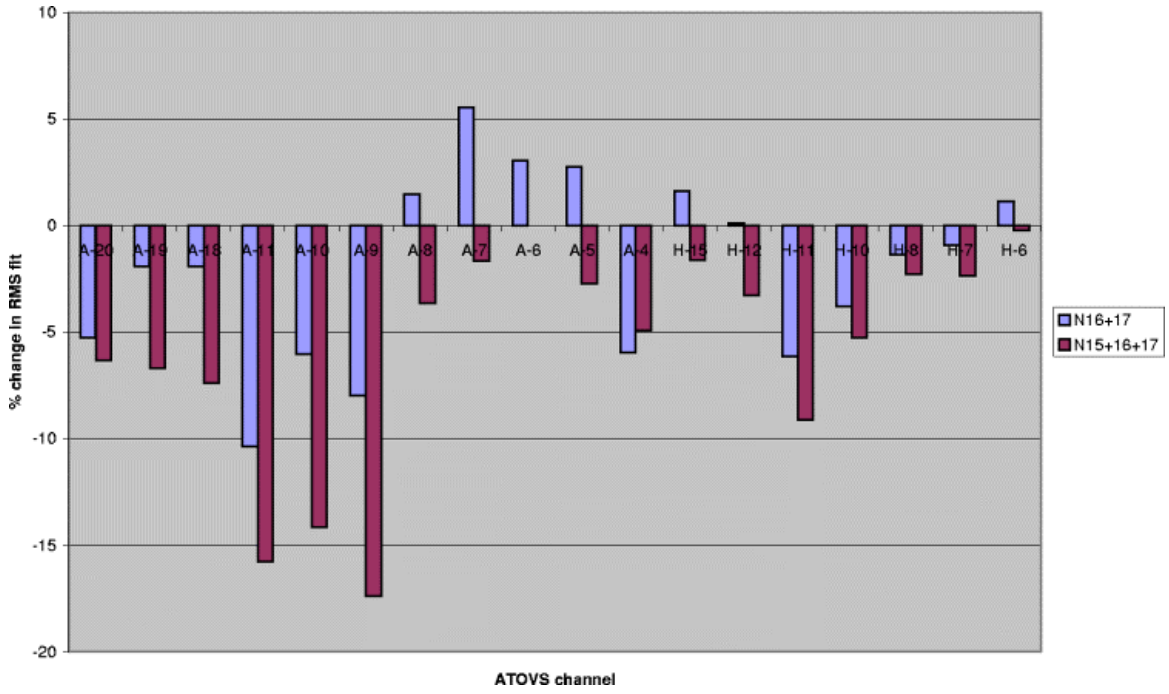

Figure 2: Percentage change in RMS of observed minus background radiances for NOAA-16 for (left to right) AMSU channels 20-18, 11-4 and HIRS channels 15, 12-10, 8, -6 when assimilating NOAA-16 and 17 or NOAA-15, 16 and 17 against a baseline run assimilating NOAA-15 and 16, (15 August – 24 September 2002).

3. Research topics

3.1 Assimilation of ATOVS over land

A system was developed to use emissivities from the atlas of Prigent *et al*. (1997). Despite some initially encouraging results (English, Poulsen and Smith 2000) it was found that the fit of calculated brightness temperatures from the background was not improved compared to using an emissivity of 0.95. Furthermore the model function proposed in English, Poulsen and Smith (2000) was unable to fit the observed brightness temperatures over snow covered surfaces. It is accepted that for many surfaces the variation of emissivity was less than the errors in estimating

the AMSU emissivities from the atlas. The exceptions are the effect of surface water variations, snow cover, ice sheets and deserts. Water fraction from permanent water features (lakes, rivers) can be predicted more accurately from a high resolution surface type atlas. Transient water features are not represented in the emissivity atlas or a surface type atlas. Snow cover and type is also transient in nature (brightness temperature at 89 GHz can vary by over 100 K during the diurnal cycle due to the thawing and re-freezing of the ice crust (Matzler, pers. comm.). This may mean that an emissivity atlas is most helpful over deserts and ice sheets.

3.2 Use of RTTOV version 7

RTTOV-7 offers improved accuracy for several ATOVS channels, especially water vapour channels, compared to previous versions (Saunders *et al*. 2002). More instruments are supported, the model offers new and improved surface emissivity models for both microwave and infrared instruments, the cloud liquid water profile is included and there is a better treatment of ozone. An update to the status of RTTOV is provided in a paper in these proceedings by Saunders *et al.* (2003). However the model was also significantly more expensive to run, mostly because of the increased number of predictors for water vapour and ozone. At the Met Office the replacement of RTTOV-5 by RTTOV-7 was also complicated by a switch from the RTTOV-5 levels (40 levels) to RTTOV-7 levels (43 levels), as RTTOV-7 no longer supports the 40 level scheme..

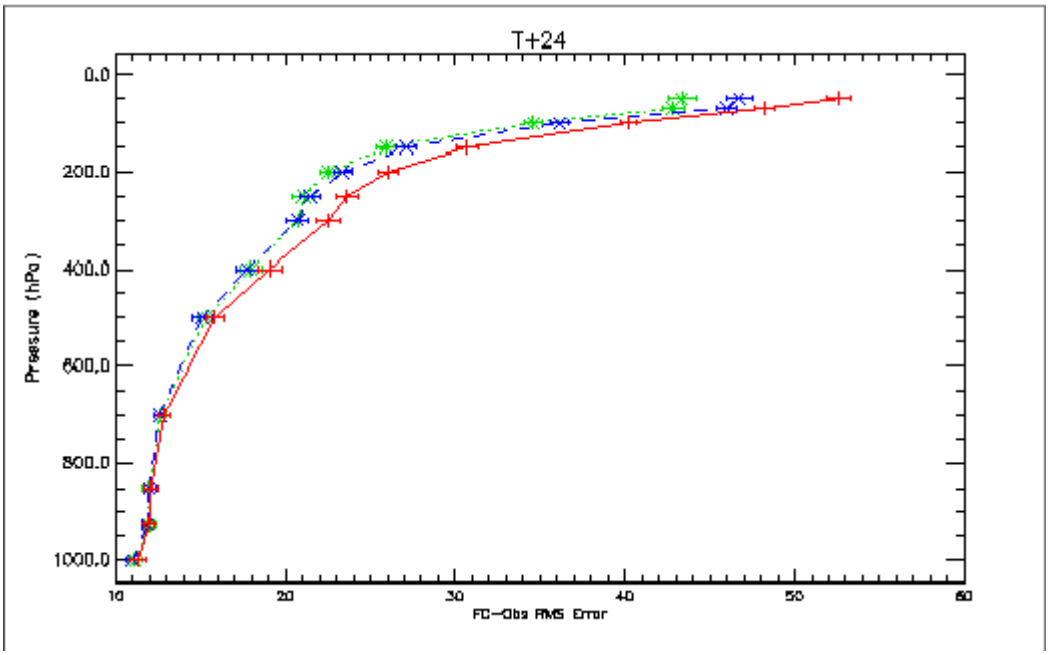

Figure 3: Verification of 500 hPa geopotential height in the region 20 S to 90 S assimilating ATOVS using RTTOV-5 (red line), RTTOV-7 with "passive" bias corrections (blue line) and RTTOV-7 with revised bias corrections (green line).

Trials of RTTOV-7 identified a small bug which was important for data assimilation, but otherwise not apparent, relating to the stratospheric water vapour Jacobians (see Figure 2 of Saunders *et al*. 2003). The trials also showed the importance of retuning bias corrections and any background dependent cloud checks for a new model. When these issues were satisfactorily dealt with RTTOV-7 was able to demonstrate a small positive impact, most notably in the tropics and southern hemisphere. The impact on 500 hPa geopotential height is shown in Figure 3. It was found best to generate initial bias corrections for RTTOV-7 by using RTTOV-5 for assimilation,

but calculating brightness temperatures using RTTOV-7 to generate the bias corrections. In this way RTTOV-7 bias corrections were generated which kept the mean analysis state consistent with that achieved using RTTOV-5. Then the cycle was repeated generating a new set of bias corrections using RTTOV-7 for assimilation with the bias corrections from the "passive" run. This technique allowed the creation of a robust set of bias corrections for use with RTTOV-7

3.3 Model predictor bias correction

Harris and Kelly (2002) showed that use of bias correction predictors based on NWP fields (e.g. 200-50 hPa thickness) had advantages over the use of observation predictors (Eyre 1992). Following Harris and Kelly (2002) a range of possible model predictors was evaluated (layer thicknesses, background BTs, skin temperature, total column water vapour, lapse rate) and trials have been run using two options: Experiment 1) Two mean layer thicknesses (200-50 hPa and 850 to 300 hPa) and calculated BT from background; Experiment 2) Two mean layer thicknesses only. The impact compared to a control using the Eyre (1992) method with AMSU channels 5 and 9 as predictors was neutral in the extra-tropics, but there was a slight increase in tropical moisture. New runs using only two thicknesses gave similar results. However the new scheme also allows use of data where observation based predictors do not work. In particular over Antarctica, Greenland and parts of Africa. Modest positive impact from using these additional observations has been found for geopotential height at medium range (forecast range day four and beyond) at altitudes corresponding to pressures less than 600 hPa.

3.4 Preparation for SSMIS

The Defense Meteorological Satellite Program (DMSP) F16 satellite carrying the first Special Sensor Microwave Imager Sounder (SSMIS) was launched on 18 October 2003. Simulated test data for SSMIS has been provided by NRL/FNMOC and this has been processed successfully. A total water control variable, defined simply as the addition of all moist variables will be used within the 1D-var preprocessing scheme (see Deblonde and English 2003 and English and Weng 2002). Not all SSMIS channel fields of view are collocated. In this sense SSMIS can be considered to comprise four instruments. One with imaging channels like SSM/I, one with temperature sounding channels for the troposphere and stratosphere like AMSU-A and SSM/T, the third with humidity sounding channels like AMSU-B, MHS and SSM/T2 and the last a completely new mesospheric sounder. The AMSU-A, AMSU-B and SSM/I like channels are being processed and will be assimilated on their original grids. The mesospheric sounder, which provides information well above the top of the current Met Office NWP model, is not used. Furthermore use of this latter instrument requires a sophisticated treatment of Zeeman line splitting. SSMIS sounding channels over-sample with short integration times. Therefore individual measurements will be noisy, and some averaging is desirable. After initial implementation of data on the original grid a system will be developed with super-obbing and/or re-mapping.

4. Conclusions

ATOVS radiances continue to be very important for global NWP. Improvements continue to be made to the assimilation, of which the most notable at the Met Office since ITSC-12 was the implementation of NOAA-17 ATOVS. Progress continues to made in others areas with improvements likely to result soon from implementation of a new bias correction scheme, RTTOV-7 and use of ATOVS over existing data voids (e.g. Antarctica). The advent of SSMIS will improve robustness by increasing the number of operational sounding instruments of AMSU quality to four. Evidence at ECMWF (Kelly,

pers. comm.) using Aqua AMSU-A data suggests further benefit can be achieved from a fourth satellite. Work is in hand to use the Aqua data at the Met Office.

References

Candy B.C., English S.J., Renshaw, R.J. Macpherson, B. 2003. Use of AMSU in the UK mesoscale model. *Proceedings of the XIIIth International TOVS Stidy Conference, St. Adele, Canada,* 29 October – 4 November 2003.

Deblonde, G. and English, S.J. 2003 One-dimensional variational retrievals from SSMIS simulated Observations, *In press*. *J. Appl. Meteorol.*

English, S.J., Poulsen, C. and Smith, A.J. 2000. Forward modeling for liquid water cloud and land surface emissivity. *ECWMF/EUMETSAT workshop on use of ATOVS data for NWP assimilation, 2-5 November 1999*, 91-96.

English, S.J., Hilton, F., Jones, D.C., Smith, A.J. and Whyte, K.W, 2002. ATOVS and SSM/I assimilation at the Met Office. *Proceedings of the XIIth International TOVS Stidy Conference, Lorne, Australia,* 28 February – 5 March 2002.

English, S.J. and Weng, F. 2002 Methods for processing cloudy AMSU observations. *Proceedings of the XIIth International TOVS Study Conference, Lorne, Australia.*

Eyre, J.R. 1992. A bias correction scheme for simulated TOVS brightness temperatures *ECMWF Tech. Memo.* **186**.

Harris, B.A. and Kelly,2002: G. A satellite radiance-bias correction scheme for data assimilation. *Q. J. Royal Meteorol. Soc*., **127**, 1127, 1453-1468.

Prigent, C., Rossow, W.B and Matthews, E. 1997. Microwave land surface emissivities estimated from SSM/I observations. *Journal of Geophysical Research (Atmospheres),* **102 (D18)**, 21867-21890.

Saunders, R.W., Matricardi, M., Brunel, P., English, S.J. and Deblonde, G. 2002. RTTOV-7: a satellite radiance simulation for the new millennium. *Proceedings of the XIIth International TOVS Study Conference, Lorne, Australia,* 28 February – 5 March 2002.

Saunders, R.W., English S.J. Rayer P.J., Francis P., Hilton F., Matricardi M., Chevallier F., Brunel P. 2003. Status of RTTOV-7 and plans for RTTOV-8. *Proceedings of the XIIIth International TOVS Stidy Conference, St. Adele, Canada,* 29 October – 4 November 2003.

Use of satellite radiances in the operational ECMWF system

Graeme Kelly

ECMWF, United Kingdom

Currently 70 million satellite radiances are presented to the operational 4D-VAR analysis at ECMWF and about 3.5 million radiances are used in the 4D-VAR minimisation. The paper will summarise the calculations of surface emissivity and the screening for cloud and rain for each sensor. Also the assimilation and forecast impact from the sensors HIRS, AMSUA, AMSUB, and SSMI will also be discussed.

Use of ATOVS raw radiances in the operational assimilation system at Météo-France

Élisabeth Gérard, Florence Rabier, Delphine Lacroix
Météo-France, Toulouse, France
Zahra Sahlaoui
Maroc-Météo, Casablanca, Morocco

Introduction

To set up the technical context, it should be reminded that Météo-France system shares the code with ECMWF and benefits from the developments in satellite data assimilation. Since 22 October 2002 Météo-France has been using ATOVS raw radiances instead of preprocessed radiances in operations. This migration was intended to be conducted in three steps: the assimilation of (1) AMSU A data – which became operational on 22 October 2002 -, then (2) HIRS data – which became operational on 8 December 2003 - and finally (3) AMSU B data – in research mode -. This strategy is motivated by the fact that assimilating infrared data requires a reliable cloud detection technique and assimilating humidity sensitive radiances comes naturally after assimilating temperature sensitive radiances. The experiments were performed on the stretched spectral global model ARPEGE with 43 hybrid coordinate vertical levels from the surface up to about 1 hPa. An horizontal thinning is performed to ensure a minimum distance of about 250 km between raw radiances (as for preprocessed radiances). Bias correction coefficients are computed following Harris and Kelly (2001). A succession of assimilation cycles performed with the data whose impact is to be evaluated will be called “Experiment” and a succession of cycles without these new features will be called “Control”.

Assimilation of AMSU A raw radiances

NESDIS preprocessed data undergo significant preprocessing consisting mainly in instrument collocation and creation of cloud flags. Complicated random and systematic errors are introduced by this process in the data and a direct use of raw radiances can indeed bypass this problem. In doing this, the 1DVar scheme used jointly with the preprocessed data in the assimilation is not used anymore, so that two specific actions have to be performed (Gérard et al. 2002): (1) the lower and upper bounds of the RTTOV-7 radiative transfer model, which requires the vertical temperature profile on 43 pressure levels from 1013.25 hPa up to 0.1 hPa, are controlled by respectively introducing model surface temperature into the control variable and extrapolating the model temperature profile from the top of the atmospheric model (1 hPa) to the top of the radiative transfer model (0.1 hPa) by a regression (Clément Chouinard, personal communication); (2) as the 1DVar cloud flag is not available anymore, rain contaminated data, that hinder from using AMSU A rain sensitive lowest channels, are detected with a test on AMSUA window channel 4 observation departure from first guess. The threshold set to 1.5 K when implementing in operations the assimilation of AMSU A raw radiances has been revisited since then and re-evaluated to

0.7 K for more drastic control of the rain contaminated data (as done at ECMWF**)** and completed by a threshold of 0.1 mm on cloud liquid water path derived from AMSU A channels 1 and 2. Details on the conditions of use of each channel are listed in Table 1, showing special caution for using low peaking channels over land, over sea ice and in cloudy conditions.

Table 1: Conditions of use of AMSU A channels. Each condition is necessary but not sufficient. T_s is the model surface temperature, orog is the model altitude, obs-fg is the observation departure from first guess, ch stands for channel and lat for latitude. Blue ✓ refers to specific sub-conditions.

Conditions of use ✓	**1**	**2**	**3**	**4**	**5**	**6**	**7**	**8**	**9**	**10**	**11**	**12**	**13**	**14**	**15**
3 < scan position < 28					✓	✓	✓	✓	✓	✓	✓	✓			
Open sea (T_s > 271.45 K)					✓	✓	✓	✓	✓	✓	✓	✓			
Sea ice ($T_s \leq$ 271.45 K)							✓	✓	✓	✓	✓	✓			
Land orog < 500/1500 m for channels 5/6					✓	✓	✓	✓	✓	✓	✓	✓			
Clear $\lvert obs\text{-}fg \rvert_{ch\,4} \leq$ 1.5 K					✓	✓	✓	✓	✓	✓	✓	✓			
Cloudy $\lvert obs\text{-}fg \rvert_{ch\,4}$ > 1.5 K |lat| > 30° for channel 8								✓	✓	✓	✓	✓			

The assimilation of AMSU A raw radiances was found to behave better than the assimilation of AMSU A and HIRS preprocessed radiances on a one month pre-operational suite in Aug-Sep 2002, especially in the Southern Hemisphere, in the upper troposphere and in the short forecast range, as illustrated by the 200 hPa geopotential height performance at day 1 in Fig. 1. On a global scale AMSU A raw radiances enable the 200 hPa geopotential height forecast root mean square (rms) error to be reduced by about 1 m in the Northern Hemisphere and about 3 m in the Southern Hemisphere, despite the loss of HIRS data. However the lack of HIRS humidity information was felt, especially in the tropical regions; reintroducing HIRS data in the operational assimilation turned out to be a priority.

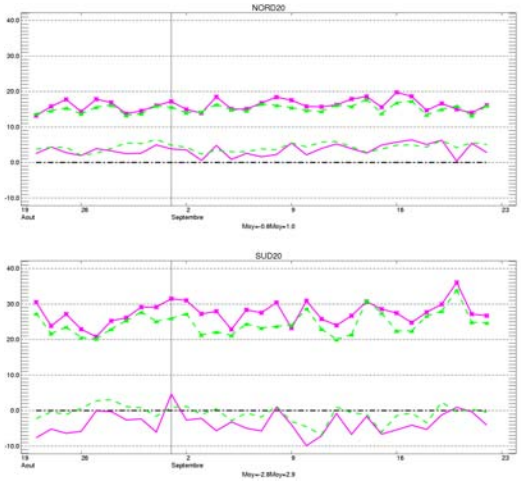

Fig. 1: Time series (22 Aug – 22 Sep 2002) of rms error (curves with symbols) and bias (curves without symbol) for 24 hour forecast of 200 hPa geopotential height when compared to each experiment's own analysis, in the Northern Hemisphere (top) and the Southern Hemisphere (bottom). Control (with preprocessed AMSU A and HIRS data) in pink, Experiment (with AMSUA raw radiances) in green.

Assimilation of HIRS raw radiances

The problem of using HIRS data is to efficiently detect cloud effects in the measured signal. As done for detecting AMSU A rain contaminated data, cloud detection is performed through a test on HIRS observation departure from the first guess in a window channel, i.e. HIRS channel 8 is selected for this task. As done at ECMWF, and with the same thresholds, this test is asymmetric, depends on channel and latitude band. Moreover, as this departure is influenced by surface temperature, sea ice situations are rejected in order not to contaminate this test by erroneous surface temperatures, as shown in Table 2.

Table 2: Conditions of use of HIRS channels. Each condition is necessary but not sufficient. T_s is the model surface temperature, orog is the model altitude, obs-fg is the observation departure from first guess, ch stands for channel and lat for latitude. Blue columns are associated to HIRS water vapour channels. For last row see Text.

Conditions of use ✓	**1**	**2**	**3**	**4**	**5**	**6**	**7**	**8**	**10**	**11**	**12**	**13**	**14**	**15**
3 < scan position < 54				✓	✓	✓	✓			✓	✓		✓	✓
Open sea (T_s > 271.45 K)				✓	✓	✓	✓			✓	✓		✓	✓
Land (orog < 1500 m)											✓			
Clear:														
↳ x(ch,lat) < (obs-fg) $_{ch\ 8}$ ≤ y(ch,lat)				✓	✓	✓	✓			✓	✓		✓	✓
↳ (obs-fg) $_{ch\ 11/12}$ > -3 K										✓	✓			

Research experiments proved to be beneficial to both analysis and forecast performances. However, an unexpected problem showed up in the pre-operational suite which turned out to be unhealthy after a few analysis days, as analysis temperature field was characterised by a succession of large increases and large decreases along the vertical in the upper model levels in the polar regions of the Northern Hemisphere (what is called a “ringing problem”). This problem is probably linked to particular meteorological conditions. The left panel of Fig. 2 illustrates the large temperature decrease at the top of the model, down to about –35 K locally, and about –11 K on average over two weeks in the 60°N-90°N latitude band. These large increments were associated to misused data in undetected cloudy regions, in areas sparsely covered by other observations that might constrain the model backwards, once damage has been done. The guilty observations were found to be water vapour channels 11 and 12 observations, which appeared not to be properly selected: despite the blacklisting and the first guess quality control (see an example of data selection on Fig. 3), some data with largely negative departures from first guess in these channels, i.e. cloud contaminated data, are used in the assimilation, and this bad effect is transported upwards to higher model levels through the background error covariance matrix. Conditions were added on observation departure from first guess in channels 11 and 12, so that any observation characterised by a departure lower than –3 K in these channels is rejected (as indicated in the last row of Table 2 and with red dotted lines on Fig. 3). These conditions appeared to be sufficient to solve the ringing problem, as shown on the right panel of Fig. 2. On average over two weeks in the 60°N-90°N latitude band, temperature analysis differences in absolute value are lower than 0.2 K when the new HIRS blacklist is applied.

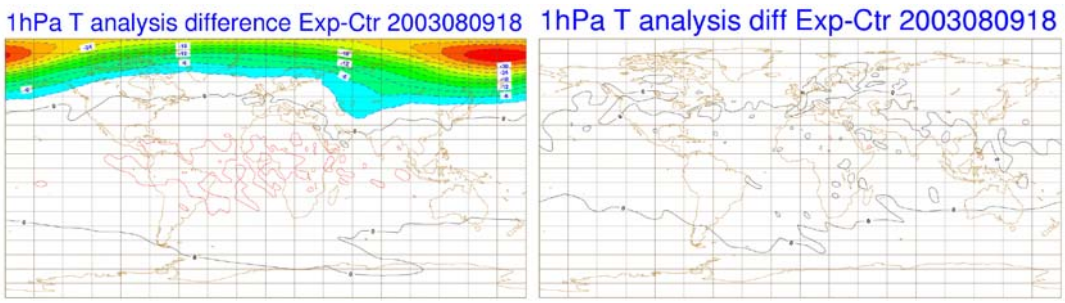

Fig. 2: 1hPa temperature analysis difference between the Experiment (with HIRS data) and the Control (without HIRS data) on 9th Aug 2003 at 18 UTC, 9 days after the beginning of the assimilation period, on the left with the initial blacklist, on the right with the new blacklist (as presented in Table 2). Contour interval is 3 K on both plots.

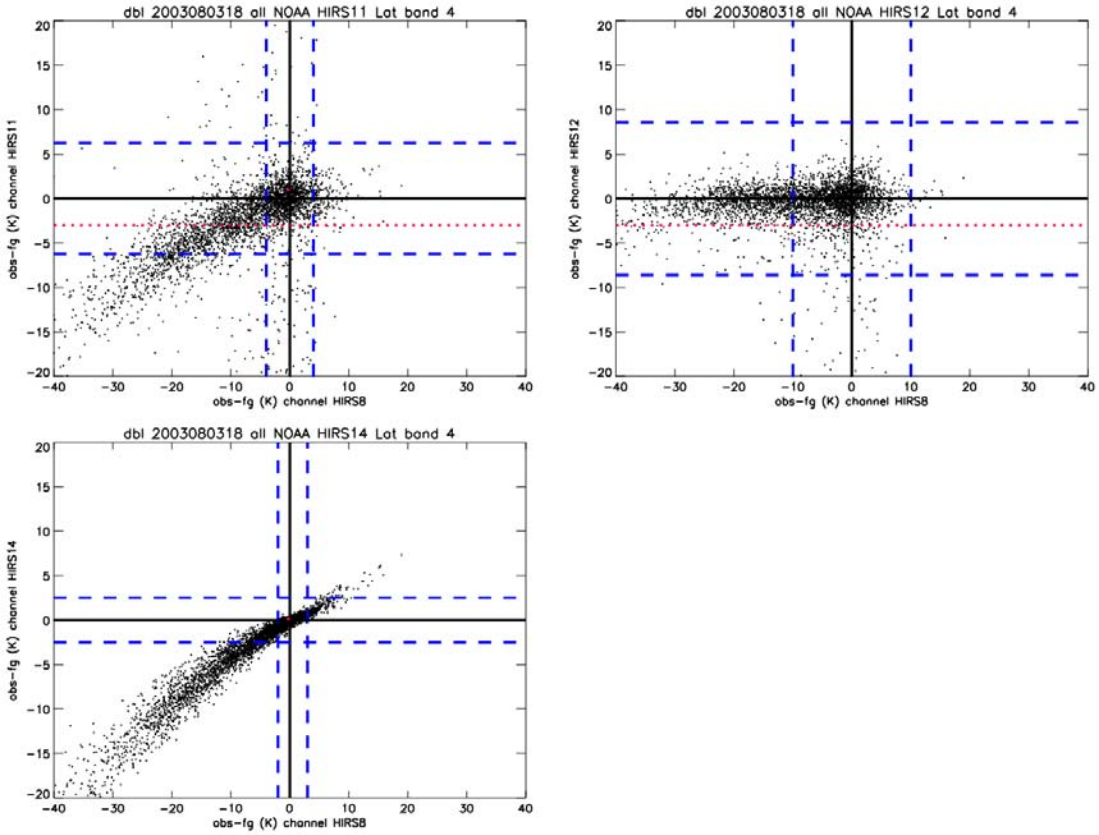

Fig. 3: An example of data selection on quality criteria (no thinning is performed on this particular dataset) for HIRS channels 11 (upper left), 12 (upper right) and 14 (lower left) in the 60°N-90°N latitude band. Thresholds for cloud detection as associated to HIRS channel 8 observation departure from first guess are represented by straight blue lines parallel to the y-axes; first guess quality control thresholds are represented by straight blue lines parallel to the x-axes. Straight red dotted lines represent the additional threshold on channel 11 and 12 observation departures from first guess. A few red isolated dots correspond to data rejected by the CO_2 slicing cloud detection/position method (Kelly, 2003).

Winter (25 Dec 2002 – 11 Jan 2003) and summer (1-17 Aug 2003) experiments were re-run with the new HIRS blacklist. The time series of total column water vapour (TCWV) over the global area are given in Fig. 4 for both periods and statistics on the change in TCWV related to the use of HIRS data are provided for different areas in Table 3. For both periods a global drying of the atmosphere is noticeable, the Experiment analysis has globally 4% (summer) to 6% (winter) less water vapour than the Control analysis; this feature seems to be realistic, as confirmed by the ECMWF analysis (not shown). The biggest relative TCWV decrease is found in the Tropics followed by the Southern Hemisphere. However a slight moistening can also occur in the Northern Hemisphere, over land in winter and over sea in summer.

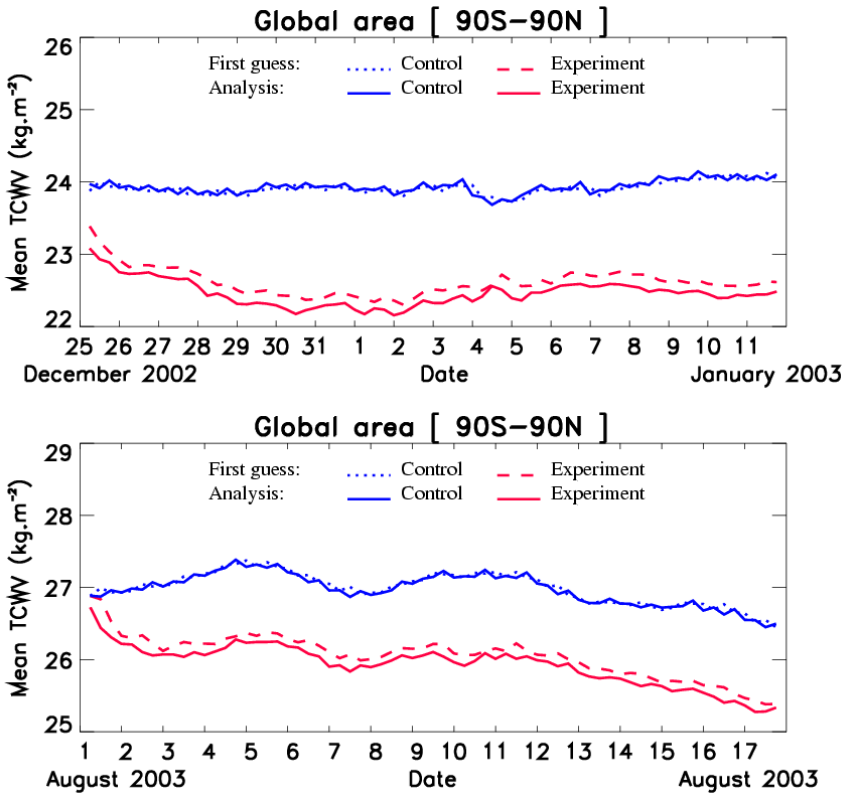

Fig. 4: Time series of total column water vapour (TCWV) globally derived from the first guess and analysis for the Control (without HIRS) and the Experiment (with HIRS) over the winter period (top panel) and the summer period (bottom panel).

Table 3: Relative total column water vapour (TCWV) change obtained in the analysis when using HIRS data, expressed in percent of TCWV obtained without using HIRS data, for the winter (left) and summer (right) periods, for different latitude bands and as a function of the landsea mask.

	WINTER				SUMMER		
%	Global	Sea	Land	%	Global	Sea	Land
Globe	-6.1	-7.4	-0.1	Globe	-3.9	-5.1	-0.3
N. Hem	-3.0	-4.3	0.8	N. Hem	1.1	1.9	-0.1
Tropics	-8.0	-9.6	-0.6	Tropics	-7.1	-8.7	-0.7
S. Hem	-4.7	-3.2	0.5	S. Hem	-3.3	-3.7	0.7

On average over the summer period the relative minimum, that characterizes the vertical profile of specific humidity analysis difference between Experiment and Control, is in the vicinity of 800 hPa as shown in Fig. 5 (top panel),as is the vertical profile of specific humidity increment (analysis minus first guess)in the Experiment (bottom panel). Results for the winter period are similar (not shown). The increments are globally negative throughout the Experiments. The negative TCWV increments should decrease during the Experiments if the assimilation and short-range forecast processes were optimal. However, the constant need to remove moisture at each assimilation cycle (see Fig. 4), especially in the Tropics, reveals that the system produces "undesired" moisture during the following six hours.

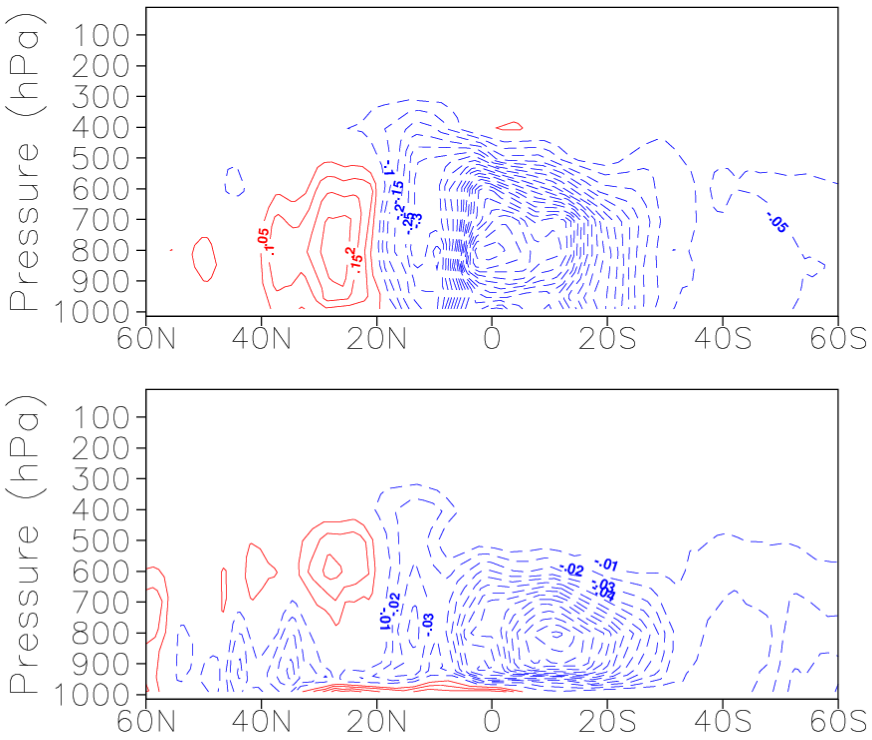

Fig. 5: Zonal mean of specific humidity analysis difference between the Experiment and the Control (top panel) and Experiment increments – analysis minus first guess -(bottom panel), averaged over the summer period and over longitude. The x-axes represent the latitude. The contour interval is 0.05 g.kg^{-1} (top panel) and 0.01 g.kg^{-1} (bottom panel), with solid red contours representing a moistening (positive values) and dashed blue ones a drying (negative values) in the analysis, when compared to Control analysis (top panel) and Experiment first guess (bottom panel).

Despite the disturbed hydrological cycle of the model, HIRS data help to improve the forecast performances, as illustrated by the reduction of rms error of day 2 forecast of geopotential height at 500 hPa to about 1.1 m in the Northern Hemisphere and 1.4 m in the Tropics and Southern Hemisphere during the winter period (Fig. 6). Another illustration of the beneficial effect of HIRS data can be found during the summer period over Europe and North Atlantic Ocean for example (Fig. 7), where medium range forecast performances at day 3 and day 4 are improved (bias and rms error reduction) for geopotential height, wind and relative humidity especially in the mid and upper troposphere.

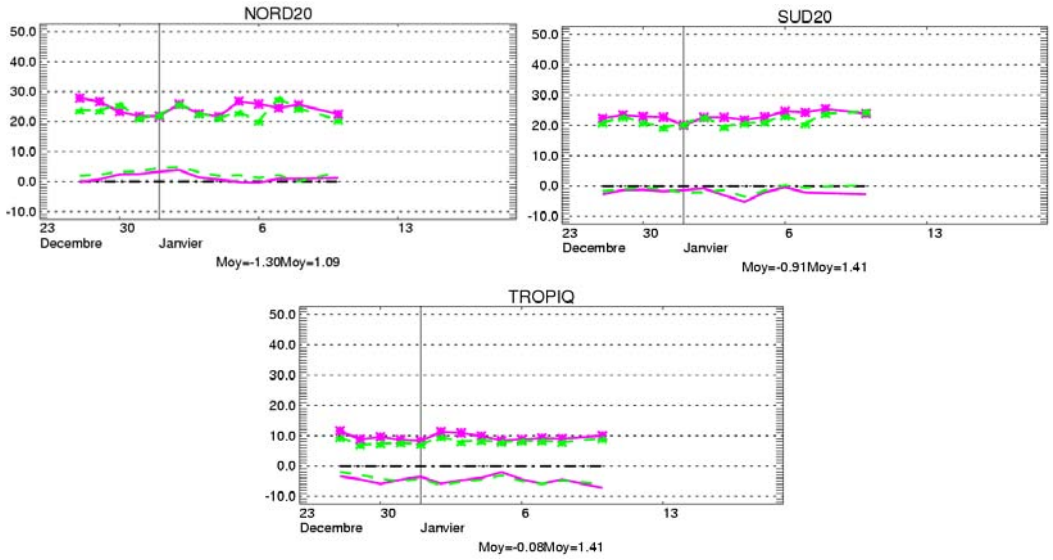

Fig. 6: Time series (winter period) of rms error (curves with symbols) and bias (curves without symbol) for 48 hour forecast of 500 hPa geopotential height when compared to each experiment's own analysis, in the Northern Hemisphere (top left), the Southern Hemisphere (top right) and the Tropics (bottom panel). Control without HIRS data in pink, Experiment with HIRS data in green.

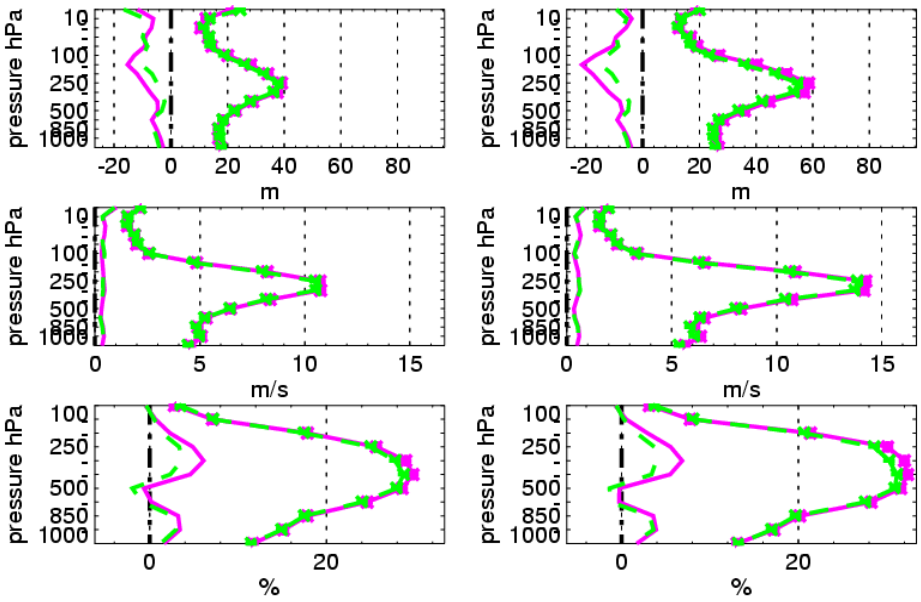

Fig. 7: Profiles of rms error (curves with symbols) and bias (curves without symbol) averaged over the summer period for 72 hour forecast (left panels) and 96 hour forecast (right panels) of geopotential height (top panels), wind (middle panels) and relative humidity (bottom panels). Scores are computed with respect to each experiment's own analysis over Europe and North Atlantic Ocean. Control without HIRS data in pink, Experiment with HIRS data in green.

Assimilation of AMSU B raw radiances

Humidity sensitive microwave channels have the particularity over infrared channels to require less stringent cloud detection. AMSU B has five microwave channels sounding the atmospheric humidity from the lower troposphere to the upper troposphere. However these channels are very sensitive to temperature too. This makes the assimilation of AMSU B data a delicate operation requiring a very good knowledge of the temperature and moisture background error statistics.

Low peaking channels are not used because of uncertainties on the description of the surface properties; only channels 3 to 5 are used, and in the same conditions as at ECMWF, as described in Table 4.

Table 4: Conditions of use of AMSU B channels. Each condition is necessary but not sufficient. T_s is the model surface temperature, obs-fg is the observation departure from first guess, orog stands for altitude and ch for channel. Blue ✓ refers to specific sub-conditions.

Conditions of use ✓	**1**	**2**	**3**	**4**	**5**
9 < scan position < 82			✓	✓	✓
Sea			✓	✓	✓
Land orog < 1000/1500 m for channels 4/5				✓	✓
Ts > 278 K and $\|obs-fg\|_{ch\,2}$ < 5 K			✓	✓	✓

An experiment using AMSU B data (from NOAA16 and NOAA17) on top of AMSUA and HIRS data has been run on a summer period (2-17 Aug 2003). The assimilation of AMSU B data proved on this period to be beneficial to geopotential height forecast, especially in the medium range as it helped to reduce the forecast bias when compared to radiosonde geopotential height by about 5 m at 200 hPa at day 4 in the Northern Hemisphere and about 4 m at 200 hPa at day 3 in the Southern Hemisphere.

As an example of the positive impact of AMSU B data on the forecast performances, Fig. 8 illustrates a comparison of 2 day forecasts at 250 hPa obtained with and without AMSU B data for a perturbation in the North Eastern part of Pacific Ocean. Without AMSU B data the low straddles the ocean and the coast, whereas with AMSU B the low is located over the ocean, at the same place as the Experiment or Control verifying analysis. Moreover the low value in the Experiment forecast (1036.0 dam) is closer to the verifying analysis of the Experiment (1039.6 dam) or Control (1039.7 dam) than the low obtained in the Control forecast (1035.1 dam).

As for temperature and humidity forecast performances, results are more mixed. It is probably too early to draw conclusions from this single 2 week experiment.

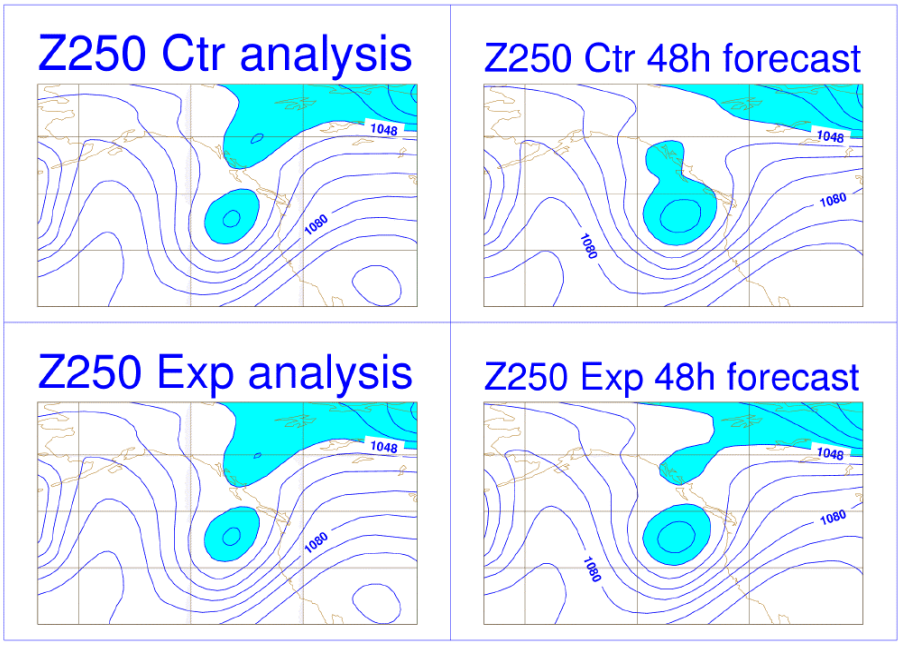

Fig. 8: Maps of 250 hPa altitude (geopotential height divided by gravity constant and by a factor of 10, resulting unit in dam) in the North-East Pacific Ocean. The right panels show the 2 day forecasts verifying 8 Aug 2003 at 00 UTC and the left panels show the verifying analyses. Control (without AMSU B data) charts are on the top, Experiment (with AMSU B data) charts on the bottom. The contour intervals are 8 dam.

Summary and perspectives

The assimilation of each ingredient of ATOVS instrument proved / are expected to be beneficial to the forecast performances of the global model at Météo-France.

(1) Using AMSU A raw radiances instead of AMSU A and HIRS pre-processed radiances improved the short range forecast, particularly in the upper troposphere and in the Southern Hemisphere.

(2) Using HIRS raw radiances in addition to AMSU A raw radiances improves the humidity initial conditions through a global drying of about 4 to 6 %, especially in the Tropics and Southern Hemisphere, and thus reduces the too strong cyclonic activity of the model in the Tropics. Using HIRS data positively affects the geopotential forecast performances below 200 hPa as well as temperature forecast performances, and to a larger extent wind and humidity forecast scores.

(3) Using AMSU B raw radiances in addition to AMSU A and HIRS radiances is expected to improve the medium range forecast performances, but the preliminary results obtained from a single 2 week experiment can not be considered as robust signals.

At the time of the XIIIth TOVS conference, the assimilation of HIRS data was being tested in a pre-operational suite. It became operational on 8 December 2003 with an improved data extraction procedure: instead of a regular sampling of the dataset according to geographical criterion, regular extraction boxes of about 125km×125 km are defined over the globe, in which the HIRS report, which has the largest channel 8 radiance observation value, i.e. the report that has the lowest chance to be cloud contaminated, is selected. This measurement physics-based extraction increases of about 26% the number of HIRS data

used in the assimilation, as the data presented to the assimilation are of better quality and thus less subject to rejection in the first guess quality control.

Experiments with AMSU B data will be run on other periods, with updated bias correction coefficients (as a first approach, bias correction coefficients were computed with respect to the first guess unaware of the existence of AMSU B data, which is the usual preliminary procedure, before any assimilation of new observations).

Optimisation of the use of ATOVS data will then be performed in several directions: revision of data thinning and blacklisting, update of the radiance background error statistics used in the first guess quality control, tuning of the radiance observation error according to the objective method developed at Météo-France (Chapnik et al. 2003).

Another panel of our activities on ATOVS data will be the use of rapidly available EARS (Eumetsat ATOVS Retransmission Service) and Lannion data in the limited area model ALADIN (and later on the mesoscale AROME model to be operational in 2008 at Météo-France), benefiting from the readiness of the 3DVar which will be run in test mode this winter. Impact of those data, of special interest for short cut-off time analysis, will be compared to that of MSG/SEVIRI data (see Montmerle 2003).

References

Chapnik, B., Desroziers, G., Rabier, F. and Talagrand, O. 2003. Estimation of AMSUA radiance error statistics using an optimality criterion. In proceedings of the 13th International TOVS Study Conference (ITSC-XIII), 28 Oct – 4 Nov 2003, Ste Adèle, Canada.

Gérard, É., Rabier, F., Dahoui, M. and Sahlaoui, Z.. 2002. Use of global ATOVS and SSM/I observations at Météo-France. In Proceedings of the 12th International TOVS Study Conference (ITSC-XII), 27 Feb – 5 Mar 2002, The Cumberland, Lorne, Victoria, Australia.

Harris, B. and Kelly, G. 2001. A satellite radiance bias correction scheme for data assimilation. *Quart. J. Roy. Meteor. Soc*., **127**, 1463-1468.

Kelly, G. 2003: Use of satellite radiances in the operational ECMWF system; In proceedings of the 13th International TOVS Study Conference (ITSC-XIII), 28 Oct – 4 Nov 2003, Ste Adèle, Canada.

Montmerle, T. 2003. Impact of the assimilation of MSG/SEVIRI radiances in a mesoscale NWP model. In proceedings of the 13th International TOVS Study Conference (ITSC-XIII), 28 Oct – 4 Nov 2003, Ste Adèle, Canada.

Acknowledgements

We are very grateful to ECMWF for providing the code updates to optimally ingest the ATOVS data within the ARPEGE/IFS collaboration between ECMWF and Météo-France. We also acknowledge the help given by the members of the Satellite Section of ECMWF in providing the blacklist for each instrument of ATOVS and giving an answer to our questions.

Development of a 3D Variational Assimilation System for ATOVS Data in China

Xue Jishan, Zhang Hua, Zhu Guofu, Zhuang Shiyu

Chinses Academy of Meteorological Sciences, Beijing, China

Zhang Wenjian, Liu Zhiquan, Wu Xuebao, Zhang Fenyin.

National Satellite Meteorological Center, Beijing, China

Abstract

A new 3D variational data assimilation system (GRAPES-3Dvar) with the emphasis on effective usage of satellite data has been developed in China. The forward observational operator and its tangent linear and adjoint for satellite radiances are adopted from the software package RTTOV developed by ECMWF. A bias correction scheme for input radiances is also developed. At present only AMSU-A and AMSU-B data over the oceans are used to avoid the influences of inaccurate computation of surface emissivity and erroneous first guess at higher levels. In the experiments of typhoon case studies, the assimilation of ATOVS data results in better analyses of both the inner structure of the typhoon and the large scale environment, and improves the numerical prediction of track and intensity of the typhoon. The assimilation system will be tested in an operational environment.

Introduction

The sparseness of observational data has been thought of the most serious difficulty encountered in improving numerical weather prediction in China. During the summer monsoon seasons, most of the weather systems causing disastrous weather events in China initiated either in the western Pacific or in the Tibetan Plateau where few conventional observations, such as rawinsondes are available. It is hard to increase the observational information by setting up new observing stations in these areas. So the use of satellite observations is of great importance. In comparison with the routine weather forecasts for which satellite images are widely used, the numerical weather models need quantitative use of satellite observations. There are two ways to use the space based sounding data such as TOVS radiances in the numerical weather prediction (NWP). The traditional way is to assimilate the temperature and moisture profiles retrieved from the satellite observations. The new approach is to assimilate the radiances data from the satellite directly. The latter is thought of superior over the former for the consistent treatment of observational and background errors. However, the dependence of the radiances observed from satellite on the atmospheric elements is nonlinear. The radiance data may be assimilated directly only in a frame of variational data assimilation system. In 2001, a research and development project aiming at developing new Global and Regional Assimilation and

Prediction System (GRAPES in short) was launched in China. The variational data assimilation system capable of handling satellite radiances is one of the main components of the project. This paper introduces the progress in the development of new data assimilation system with emphasis on the usage of ATOVS data in numerical weather prediction. The results shown in this paper are preliminary, so the near future workis also discussed.

GRAPES variational data assimilation

The GRAPES data assimilation system is a lat-long grid points system consistent with the GRAPES prediction model. The variables analyzed are wind components (u and v), temperature (or geopotential height at user's option) and specific humidity. Let X_a stand for the field of variables to be analyzed, X_b the background field and Y the observations. The assimilation is in fact to minimize the cost function:

$$J = (X_b - X_a)^T B^{-1}(X_b - X_a) + (H(X_a) - Y)^T O^{-1}(H(X_a) - Y) \qquad (1)$$

where B and O are the covariance matrices of background error and observational error respectively, and H is the observational operator. Special preconditioning based on the square root of the B matrix is introduced to reduce the scale of matrix computation and to accelerate the convergence of iterations in minimizing the cost function. The preconditioning is realized either by a recursive filter for the regional case or by spectral transformation for the global case. It is also assumed that both dynamic and mass fields consist of balanced and imbalanced components, and the background errors of the latter are independent. The flexibility of the observational operator H allows the use of satellite radiances as observational data in the 3DVar.

Assimilation of satellite radiances

In the case of assimilation of satellite radiances, the observational operator is the radiative transfer model which converts the atmospheric temperature and moisture profiles to the radiances received by the satellite. GRAPES 3DVar uses the fast radiation transfer model RTTOV developed by ECMWF. So the operator H in equation (1) becomes:

$$H(X)=\mathrm{RTTOV}(I_v(I_h(X))) \qquad (2)$$

Where I_v and I_h are the operators of vertical and horizontal interpolation from the model grid point to the precise location of the satellite radiances and the vertical levels where RTTOV defines the atmospheric profiles.

The background field is the short term (6-12 hours) prediction of the global model T213 of the National Meteorological Center of China. In this stage, only radiances for those channels not sensitive to the deep clouds, surface states and atmospheric temperature at very high levels (above 10 hpa where serious background errors exist) are assimilated. In the case of ATOVS of NOAA-16 and NOAA-17, the data currently assimilated are AMSU-A channel 5-11 and

AMSU-B 3-5. This channel selection may be rather conservative, so more channels will be tested in the near future.

The relay ***HRPT*** satellite data from NOAA series polar orbiting satellites received in three ground stations are preprocessed with the software package AAPP introduced from EUMETSAT in the National Satellite Meteorological Center and made available for numerical weather prediction. This data set, only covers China and the neighboring area, are used currently for pre-operational trials of the 3DVar system. Raw satellite data with global coverage are expected to be used in the future operational system. The radiances from ATOVS instruments are interpolated to the HIRS sounder's field of view. With high-resolution AVHRR data as well as AMSU data, the cloud detection technique for current ATOVS is improved greatly. When available in the FOV of the HIRS, such information enhances the cloud detection for selecting initial guess and the inversion process.

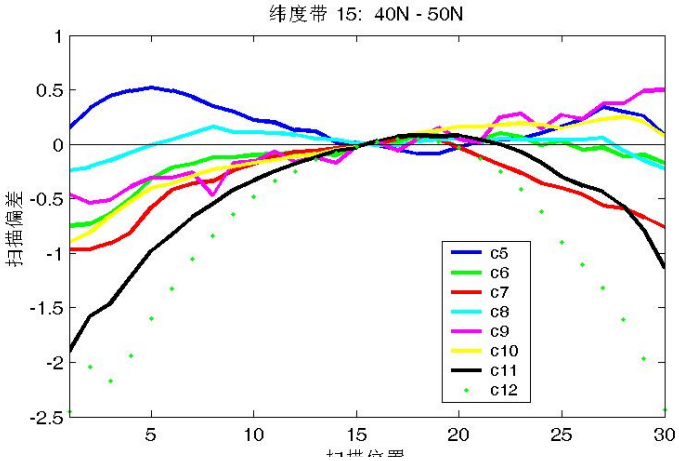

Fig1 Scan bias of NOAA16 AMSU-A CH 5-12 in the zone 40N-50N samples for statistics: Jul.1-10 2003 06/18 UTC (6 hours time window)

Before the data are fed to the 3DVar, two kinds of bias in the observation are corrected following the algorithms proposed by Harris and Kelly (2001). They are the bias depending on scan angles and the bias depending on the categories of air mass. The correction to the scan angle related bias changes with latitudes. The air mass related bias is predicted with linear regression based on the statistics of innovation vectors derived from recent cases. The predictors are the thickness between 1000-300hpa and 200-50hpa, the surface temperatures and the integrated water vapor. Fig 1 shows the scan bias of NOAA16/AMSU-A channel 5-12 in the zone 40-50 deg lat. Fig 2 shows the change of the difference between the observed brightness temperatures and the brightness temperatures derived from the background brought by the bias correction.

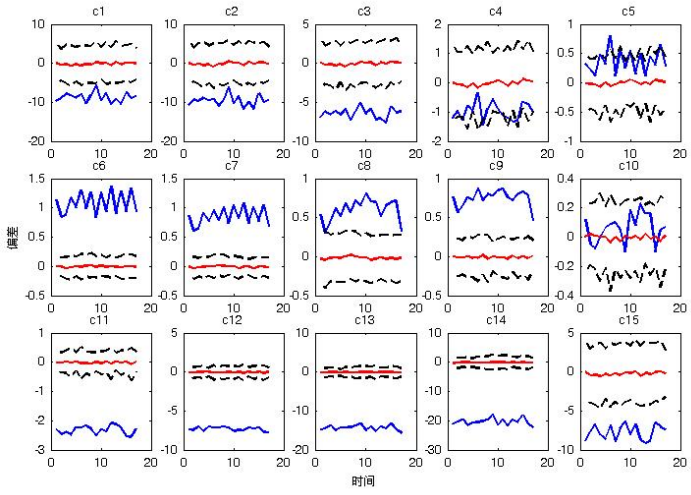

Fig 2 Comparison of brightness temperature (background-obs.) Blue : before correction; Red: after correction; Black : with standard deviation added and substracted

In addition to satellite radiances, conventional rawinsonde observations, cloud motion vectors from geostationary satellites and surface winds from QUIKSCAT are also assimilated by the assimilation system. In order to investigate the impact of ATOVS data on numerical prediction of high impact weather events in China, a series of experiments of assimilation and prediction have been implemented. The results of most cases show positive impacts of ATOVS data on improvement of the analyses and predictions. The most impressive results are the reduction of forecast errors of the tracks of tropical cyclones over the western pacific. A case study is discussed in the next section.

Impact of ATOVS data on typhoon prediction

The case selected here is typhoon Rammasun 2002. The track of this typhoon is shown in Fig 3. As mentioned in section 3, only the ATOVS data received in three ground stations are available for the test. The prediction model used in this impact study is the weather research and forecast model (WRF) developed in the U.S. The first guess is taken from the operational global model T213 of the National Meteorological Center, China. The analysis by the GRAPES-3DVar is processed by the WRF standard initialization scheme to form the initial field of model integration. Three different sets of observational data are used for assimilation. The first set, referred to as the control experiment hereafter, only contains the rawinsondes data available. The second set, the exp1, contains the satellite radiances only. The third set, exp2 hereafter, contains both rawinsondes and satellite radiances. The differences between the predictions with different observational data sets reflect the impact of assimilation of satellite radiances on the forecast. To find the difference of fields of geopotential height on 500hpa level between the above experiments, it is easier to compare the analysis increments, i.e. the difference between analysis and the first guess, for different experiments. The increments are consistent with the coverage of the observational data. When only rawinsondes are used, the analysis is almost the same as the first guess over the western pacific for there are few rawinsondes there. The use of ATOVS data changes the flow characteristics in this region. The positive increment coincident with the subtropical high in the North Western Pacific implies that the high in the analysis is extended more westward and stronger than in the first guess. In many cases, the movement of tropical cyclones over the Western Pacific is dominated by the behavior of the sub-tropical high, so the difference in the position and intensity of the high are very important for the forecast of tropical cyclones.

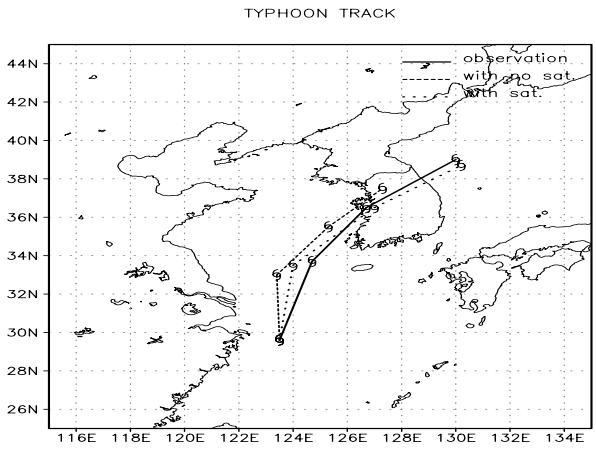

Fig 3 Tracks of typhoon Rammasun 2002 Solid line: observation, dashed line: prediction without ATOVS,

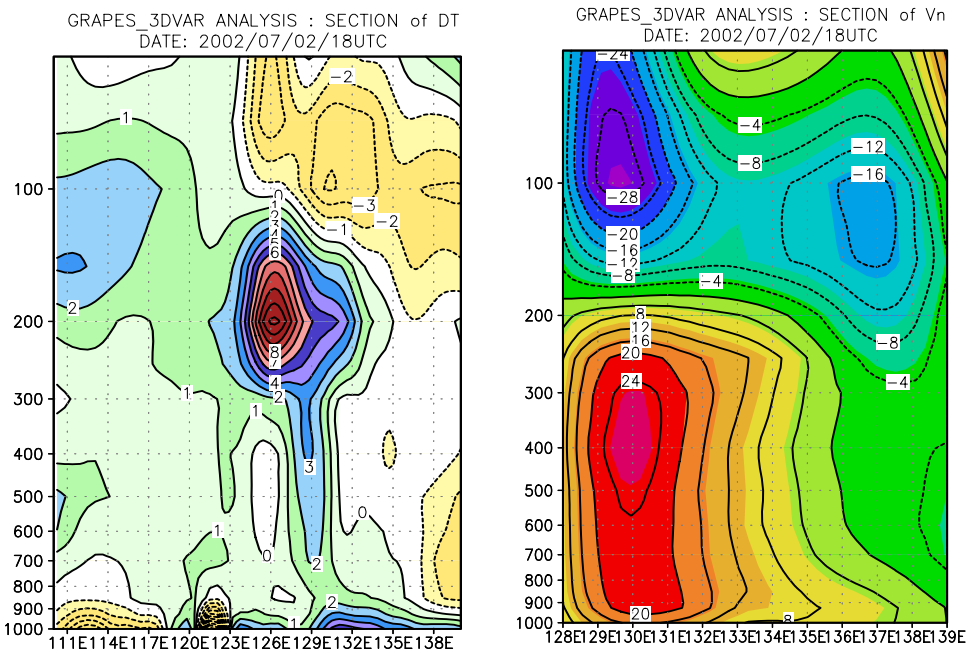

Fig 4 Vertical cross section of analysis with ATOVS along 23 lat Left: temperature anomaly from zonal mean Right: tangential wind

Fig 4 is the vertical cross sections of temperature (anomaly from the zonal mean), and tangential wind component along 23 lat of the analysis with ATOVS data. The warm core near the center and the cyclonic circulation are very well defined. The temperature anomaly and the

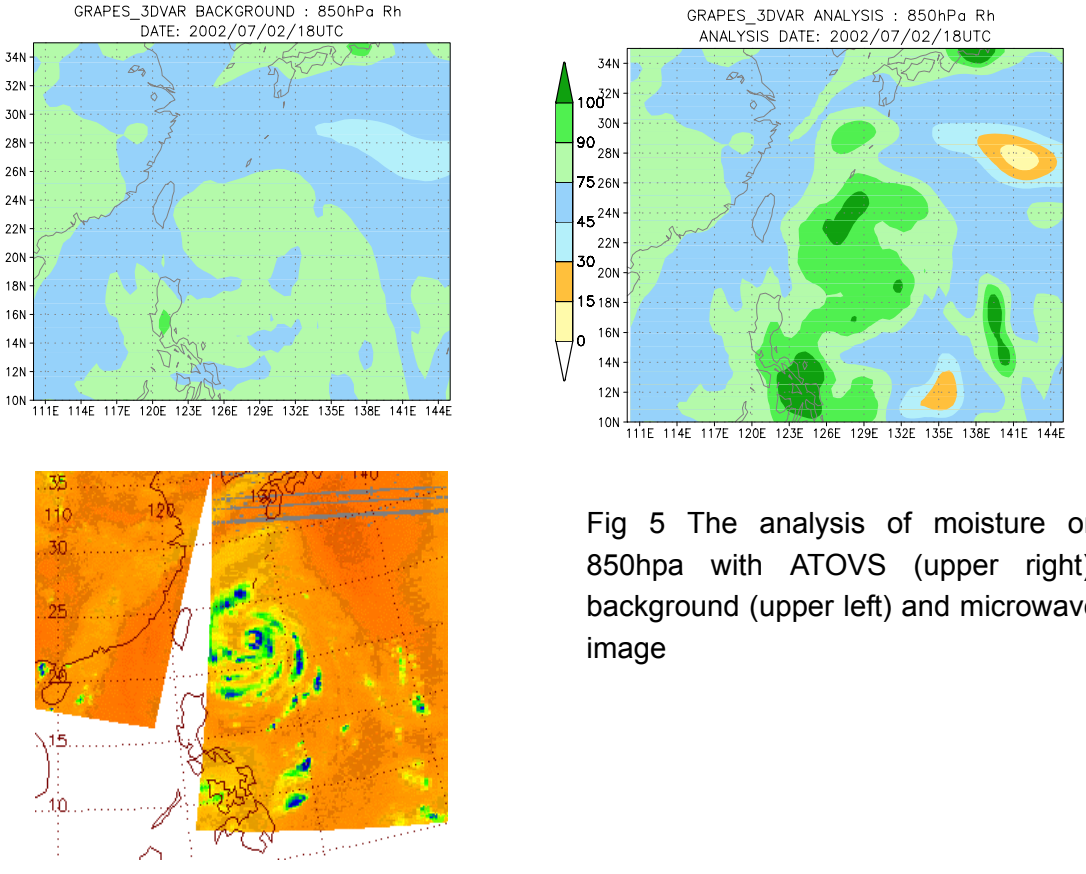

Fig 5 The analysis of moisture on 850hpa with ATOVS (upper right), background (upper left) and microwave image

cyclonic circulation are much weaker in the background fields and similar in the analysis with only conventional rawinsonde data. Fig 5 shows the analyses of moisture with ATOVS data. The background field and the microwave image are also presented in the figure. It is seen from this figure that the assimilation of ATOVS data results in the analysis of moisture much more consistent with the cloud pattern around the typhoon.

Fig 6 shows the comparison of predicted fields of geopotential height on 850hpa level with and without ATOVS data. The analysis used for validation is also presented. It is obvious that the prediction with only conventional rawinsondes incorrectly forecasts the center of typhoon in the central Korea Peninsula. The use of ATOVS data improves the forecast. Fig 3 is the predicted tracks of the center of this typhoon with and without ATOVS data and the track observed. The improvement by using ATOVS data is also seen in this figure.

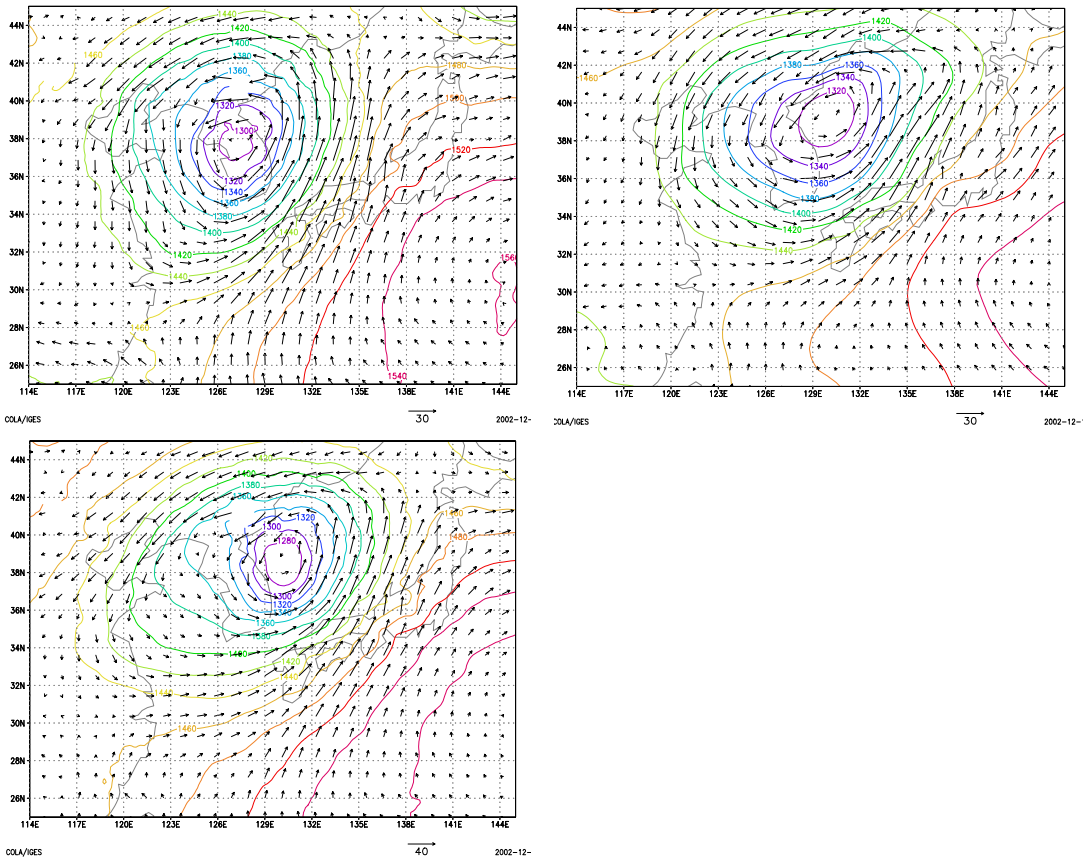

Fig6 Geopotential height on 850hpa. Analysis (upper right), prediction without ATOVS (upper left), prediction with ATOVS (lower).

Discussion

(1) The positive impacts of assimilation of ATOVS data on the typhoon analysis and prediction are found in the real case study of typhoon Rammasun 2002. The use of ATOVS data improves the analyses of the large-scale flow pattern, especially the extension and intensity of the Northwestern Pacific sub-tropic high, as well the moisture fields and inner structure of typhoon. The improvements in the initial fields result in better numerical prediction of typhoon track and intensity.

(2) One of the unrealistic features appearing in the analyzed structure of the typhoon is the relatively low temperature in the mid-low troposphere and weaker tangential wind in the low troposphere which can been seen in fig 5. This may be the result of contamination of radiances by the deep and precipitating clouds near the center of typhoon.

(3) The use of other satellite products may help to further improve the analysis near the center of typhoon. One possibility is to assimilate the wind information from the satellite, such as cloud drift wind from geo-stationary satellites or the surface wind from QUIKSCAT. Some experiments have been done. The results will be reported in other papers.

(4) It has been mentioned that the current channel selection is rather conservative. The use of more channels needs the reduction of errors in the background fields on the upper levels and improvement of the scheme of cloud detection. These issues will be emphasized in the future research.

References

Harris, B.A. and Kelly, G..2001.A satellite radiance bias correction scheme for radiance assimilation. Q.J.R.Meteorol.Soc.,127, 1453-1468

Operational use of the ATOVS radicances in global data assimilation at the JMA

Masahiro Kazumori, Kozo Okamoto, Hiromi Owada
Japan Meteorological Agency, Tokyo, Japan

Introduction

ATOVS radiances have been assimilated operationally in the Japan Meteorological Agency (JMA) global data assimilation system since 28 May 2003. It replaced TOVS/ATOVS retrievals, which had been assimilated in the JMA global data assimilation system since 1982. An Optimum Interpolation (OI) method had been used in the assimilation system. But, since September 2001, 3D-Var method has been operational in the system. The current operational system of ATOVS radiances assimilation at the JMA is composed of two steps. One is the 1D-Var pre-process step (Okamoto, K., Takeuchi Y., Kaido Y., and Kazumori M. 2002) and the other is main 3D-Var-analysis step. Before being supplied to the main 3D-Var analyses, radiance data should be passed the 1D-Var pre-process step. In the 1D-Var, thinning, quality control, channel selection, and bias correction are applied to the radiance data. Level-1D data (Reale 2001) pre-processed by NOAA/NESDIS are used for the assimilation. As a radiative transfer model, RTTOV-6 (Saunders, 1998 and RTTOV-6 SCIENCE AND VALIDATION REPORT, 2000) is used in both 1D-Var and 3D-Var.

Before the operational use of ATOVS radiances, some cycle experiments were performed. These experiments demonstrated dramatic impacts on forecasts and analyses. As these finding, the assimilation of ATOVS radiance became operational. This paper focuses on some upgrades in 1D-Var preprocessor and results of experiments.

1D-Var as a preprocessor

NESDIS 120km ATOVS radiance product (HIRS/3 and AMSU-A), which is pre-processed Level 1D data, is used in JMA. The data undergoes a re-mapping procedure in whitch AMSU-A FOV is interpolated into HIRS/3 FOV by NESDIS and has the cloud flag and the skin temperature. These data are thinned at 250km in equal distance. As for AMSU-B, the data are selected at 180km resolution. This distance is kept constant for all over the world. Beside, clear radiance, closer to analysis time data is preferred in two satellites data overlapped region. Figure 1 shows the change of used data coverage from retrieval assimilation to radiance assimilation.

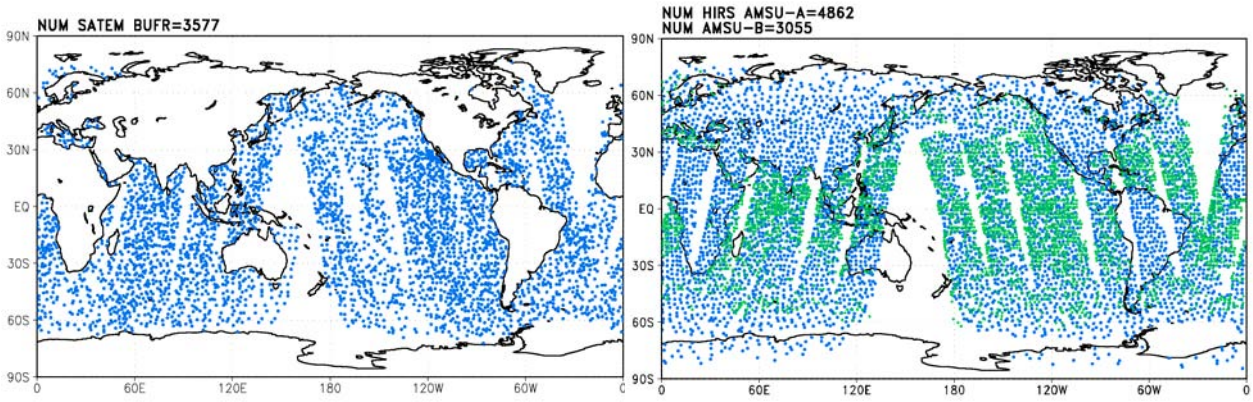

Fig. 1: Coverage in a six-hour data assimilation window of data from ATOVS instruments on NOAA15 and NOAA16 satellites. Left panel is for retrieval assimilation (500 hPa geopotential). Right panel for direct assimilation (Blue:AMSU-A channel6,Green:AMSU-B channel4).

Cloud contaminated data are rejected by cloud cost method based on AAPP procedure (Okamoto et. al. 2002). The surface type (sea, land or coast) is defined by 0.25-degree land mask data set. No coastal data are used. Identification of sea ice affected data is based on SST analysis. The data on the SST less then 274.15K are identified as data on sea ice.

As for channel selection, no lower peaking channel is used, that is AMSU-A channel 4,5 on land. As for AMSU-A channel 6,7, some altitude thresholds are set on land and on sea ice. As for AMSU-A channel 6, over 1500-meter altitude is allowed and over 2500-meter altitude for channel 7. And clear channels of HIRS/3 and AMSU-B and stratosphere channels of HIRS/3 are also selected for the assimilation.

In order to use radiances from ATOVS, biases between the observed radiances and those simulated from a first guess must be corrected. The JMA scheme for ATOVS radiance-bias corrections relied on the model first-guess total column water vapor, the analyzed JMA sea surface temperature, and the calculated brightness temperatures from AMSU-A channels 5,7 and 10 as linear predictors of the bias in all channels that were used. The bias is represented by

$$\mathrm{BIAS}_j(n) = a_{j0} + \sum_{i=1}^{5} a_{ji}(n) X_{ji}(n)$$

a_{j0} are constant, X_{ji} are the predictors, j is channel number and n is scan position index. These coefficients a_{ji} are obtained by satellite and radiosonde collocation for one-year (2002) period. To calculate brightness temperature, profiles of radiosonde observations were used. A first guess was used to complement the profiles at no radiosonde observation level. The each coefficients were made for each scan position. This bias correction scheme contains effects of scan dependence and air mass dependence (Harris and Kelly 2001). Because of moisture bias and temperature bias at upper stratosphere in the JMA global model, this bias correction scheme is not applied to HIRS/3 channel 11,12, AMSU-A channel 12,13,14 and AMSU-B channels 3,4,5. Figure 2 shows an effect of this bias correction. There is complicated scan dependent bias around edge of Level 1D AMSU-A data. But these biases are removed by this scheme.

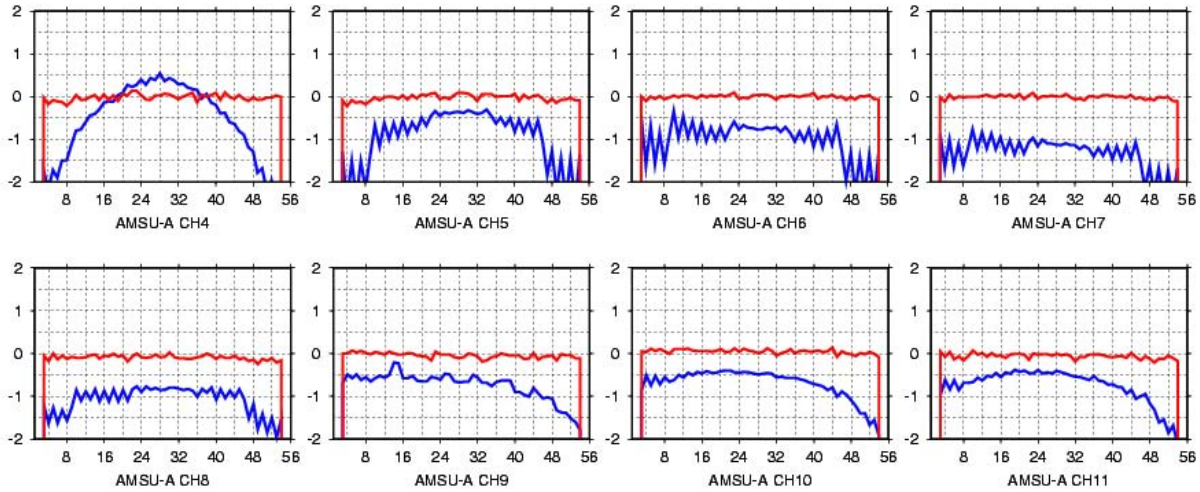

Fig. 2: Uncorrected bias (Blue line) and corrected bias (Red line) by scan position for each channel, NOAA16, AMSU-A, from 27 Jun 2003 to 30 Jun 2003.

Results of experiments

Data assimilation experiments were carried out for two seasons: 27 June 2002 – 9 August 2002, and 27 November 2001 – 9 January 2002. Data configuration of the experiments were:

- Retrieval assimilation(CNTL)
- Direct assimilation without ATOVS retrievals and GMS-5 moisture retrievals (TEST)

In these experiments, JMA GSM (Global Spectral Model) T213L40, 3D-Var assimilation systems were used. NOAA15 (AMSU-A, AMSU-B) and NOAA16 (HIRS/3, AMSU-A and AMSU-B) were used. Moreover new cumulus parameterization scheme of global model was jointly used. The direct assimilation of ATOVS data expanded moisture observation coverage and improved the quality of temperature and humidity analysis. Then, that led to higher performance of the prediction globally.

As for temperature field, a dramatic impact was found in upper stratosphere from 30hPa to 0.4hPa. Figure.3 shows monthly zonal mean temperature for Jul 2002. By using radiances directly, profile of temperature became very smooth. Figure 4 shows a verification of analyzed temperature and first-guess temperature against radiosonde observation. Better fits were found in the troposphere and lower stratosphere.

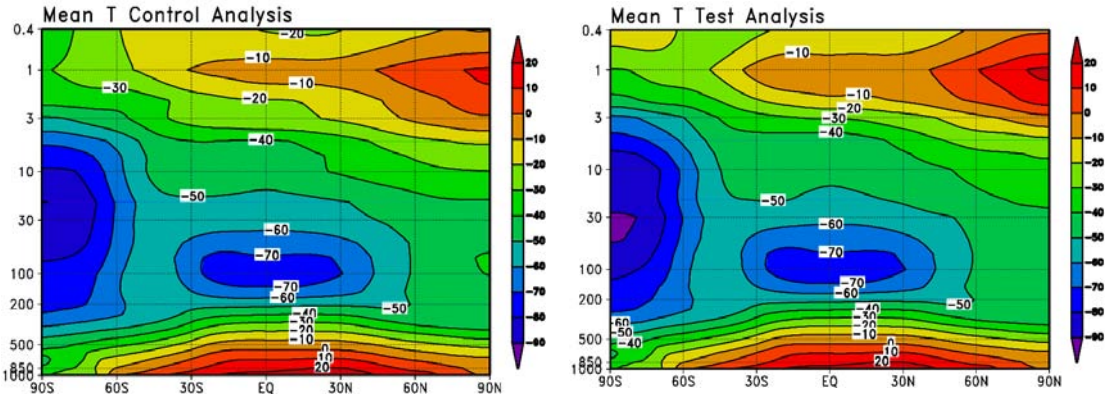

Fig. 3: Zonal mean of temperature in the Experiments averaged over the July 2002 and over longitude. TEST is right panel and CNTL is left panel. The contour interval is 10K.

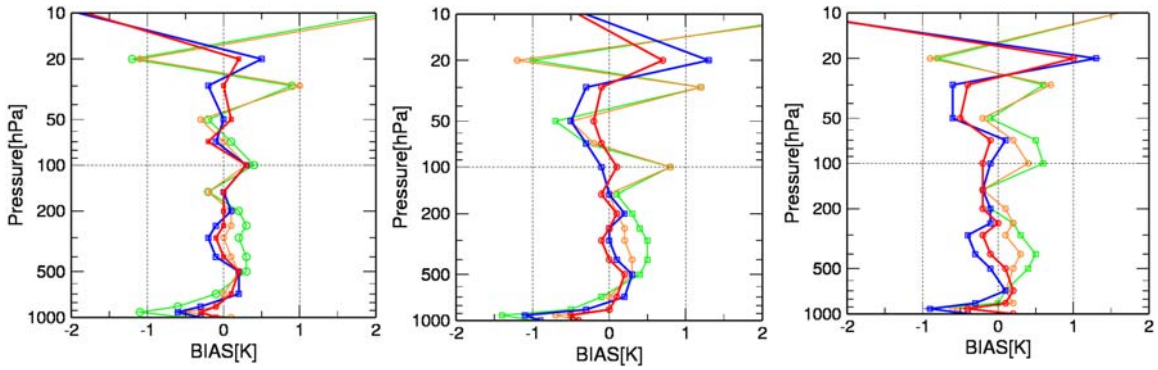

Fig. 4: Mean fit of the background (TEST: blue, CNTL: green) and analysis (TEST: red, CNTL: orange) to radiosonde temperature observations for July 2002. Left panel is Northern hemisphere, middle panel is Tropics, and right panel is Southern hemisphere)

In the TEST case, ATOVS moisture channels, i.e. HIRS/3 channel 10,11,12 and AMSU-B channel 3,4,5 were assimilated instead of GMS-5 retrieved relative humidity. Figure 5 shows a difference between analyzed total precipitable water and SSM/I retrival. The left panel is the difference for CNTL and the right panel for TEST for 15 July 2002. In the TEST case, the difference became small clearly and particularly this trend is large in tropical region. The result means humidity field became

realistic by assimilation of ATOVS moisture channel. Because SSM/I data is not assimilated, that can be considered as independent data.

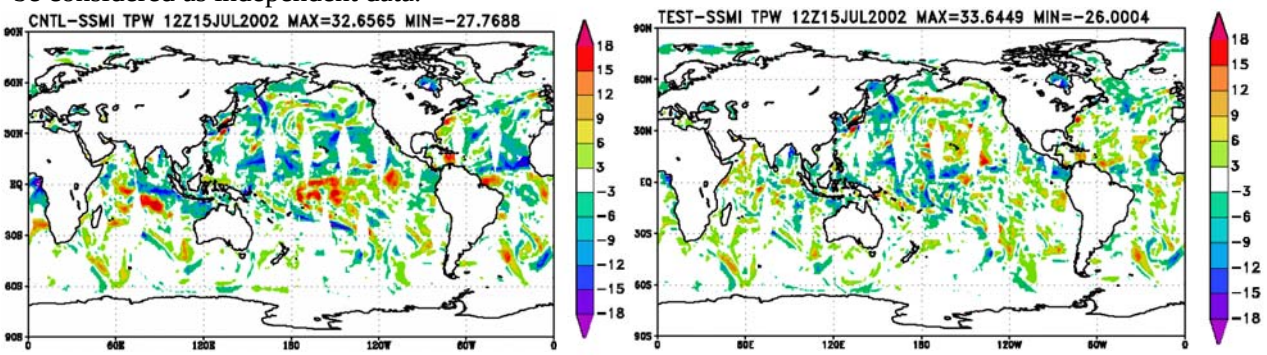

Fig. 5: Difference from analyzed total precipitable water to SSM/I observation for 12UTC 15 July 2003. Left panel is CNTL-SSMI, and right panel is TEST-SSMI. The contour interval is 3mm.

As for forecast impact, the TEST case has demonstrated positive impacts for the geopotential height at 500 hPa (Fig. 6). Particularly, substantial positive impacts were found in the southern hemisphere and in the tropical region. Figure 7 shows a monthly mean difference between RMSE of 24-hour forecasts from TEST and those from CNTL. The negative value means positive impact. Obviously, impact on dynamics in southern hemisphere is larger than other area.

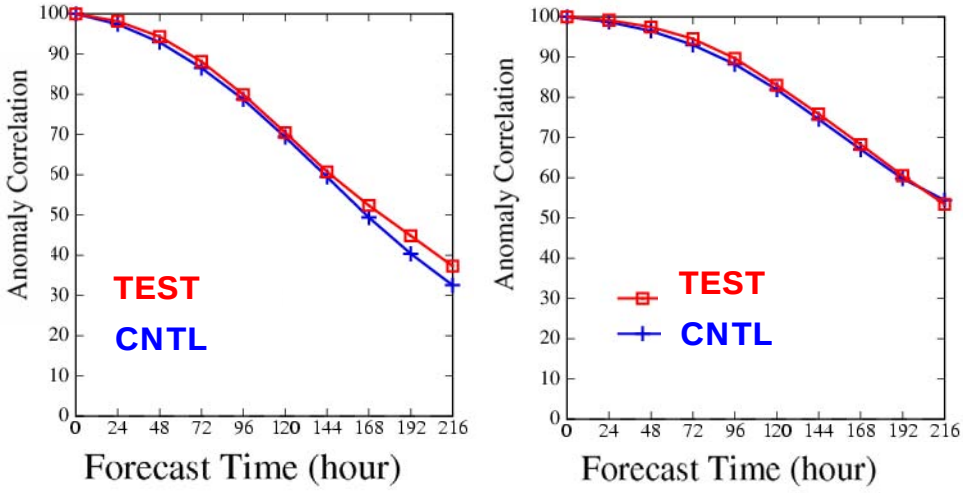

Fig. 6: Mean anomaly correlations for 500hPa geopotential height for the global. Left panel is for July 2002 and right panel is for December 2001. Each score was calculated by averaging 31 cases.

The forecast scores of the temperature at 850 hPa, wind speed at 250 hPa and sea level surface pressure were similarly good. Better predictions of the typhoon track were also found out during pre-operational run in May 2003. Fig. 8(a) is the analyzed field of 500hPa height, Fig. 8(b) is the 24-hour forecast of 500hPa height for TEST (ATOVS radiances assimilation), Fig. 8(c) is difference from Fig. 8(b) minus Fig. 8(a), Fig. 8(d) is the 24-hour forecast of 500hPa height for CNTL (ATOVS retrieval assimilation), Fig. 8(e) is difference from Fig. 8(d) minus Fig. 8(a). Fig. 8(f) is comparison of typhoon track. Red line is TEST, blue line is CNTL, black line is Analyzed track. Dotted circle in Fig. 8 showed the change of forecast for peripheral area of subtropic high pressure (5880-meter contour at 500hPa). Forecast of strength of subtropic high pressure became realistic and typhoon track prediction

was corrected westward. Many good impacts for other typhoon events were also found out.

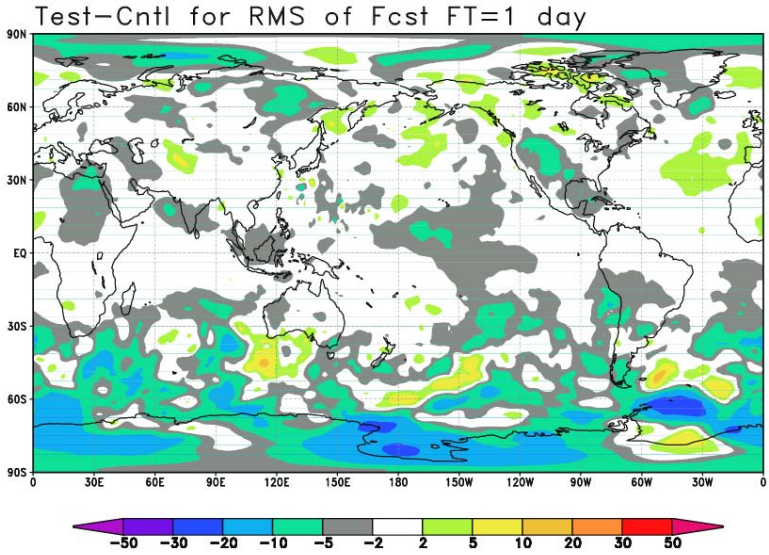

Fig. 7: Monthly mean difference of RMSE from TEST to CNTL at 24-hour forecast. Negative value (Blue color) shows positive impact.

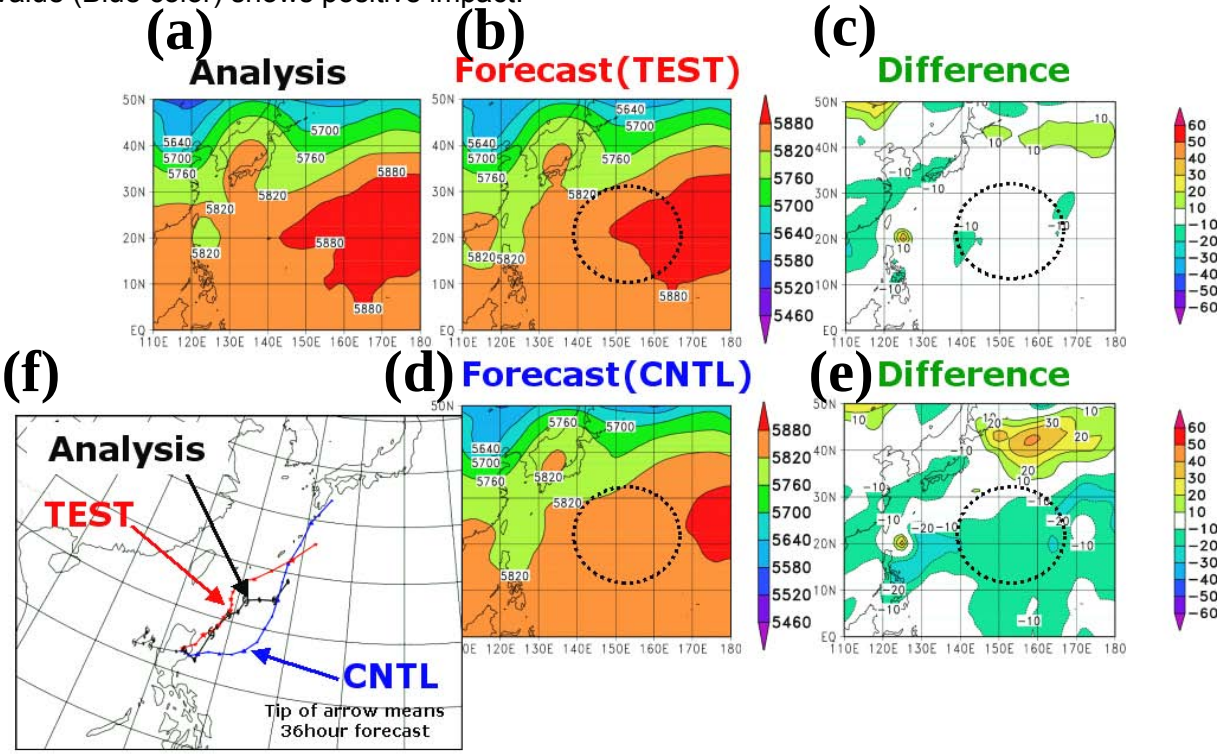

Fig. 8: Typhoon track prediction during pre-operational run. (a):Analyzed field of 500hPa height, (b): 24-hour forecast of 500hPa height for TEST (ATOVS radiances assimilation), (c):Difference from (b) minus (a), (d):24-hour forecast of 500hPa height for CNTL (ATOVS retrieval assimilation), (e): Difference from (d) minus (a). (f): Track of Typhoon. Red:TEST,Blue:CNTL,Black:Analysis.

Summary and Future prospect

JMA has started operational use of ATOVS radiances in the global data assimilation on 28 May 2003. No retrievals from ATOVS radiances and that from GMS-5 have not been used since then. Experiments prior to the operational use have demonstrated dramatic impacts. The temperature

profiles in the upper stratosphere and the global humidity field in the troposphere were improved. The higher accuracy of initial fields of temperature and humidity were confirmed against radiosonde observation and the total precipitable water from SSM/I. As for forecast skills, positive impacts were found for the geopotential height at 500 hPa in the southern hemisphere and in the tropical region. The improvement of short-range forecast was remarkable. And better results on the typhoon track prediction were also found out.

JMA has achieved considerable progress in ATOVS data assimilation, but some un-preferable features are still seen: anomalous change of temperature at some levels in the stratosphere and the excessive concentration of rainfall in 6-hour forecast. To solve these problems, we continue to carry out some experiments and improve the bias correction scheme of ATOVS brightness temperature. Moreover, we are going to assimilate ATOVS Level 1B data to avoid intrinsic errors in level 1D data. And we have a plan to update the radiative transfer model from RTTOV-6 to RTTOV-7. A preparation on Aqua/AIRS data assimilation is underway.

References

Eyre, J. R., 1992: A bias correction scheme for simulated TOVS brightness temperatures. *ECMWF Tech. Memo.*, **186**

Harris, B. A and G. Kelly, 2001: A satellite radiance-bias correction scheme for data assimilation. *Q. J. R. Meteorol Soc.* **127**, 1453-1468

Okamoto, K. Takeuchi Y., Kaido Y., and Kazumori M. 2002. Recent Developments in assimilation of ATOVS at JMA. *Proceedings of 12th International TOVS Study Conference, Lorne, Australia.*

Reale, A. 2001: NOAA operational sounding products from advanced-TOVS Polar Orbiting Environmental Satellites, NOAA Technical Report NESDIS 102, U.S. Dept. of Commerce, Washington D.C.

RTTOV-6 SCIENCE AND VALIDATION REPORT 2000. Available from the NWP SAF web site.

Saunders, R., M. Matricardi and P. Brunel 1998. An improved fast radiative transfer model for assimilation of satellite radiance observations. *Q. J. R. Meteorol. Soc.*, **125**, 1407-1425.

Locally Received and Processed ATOVS Data in the Australian Region LAPS Data Assimilation and Prediction System

C. Tingwell, B. Harris, W. Bourke and J. Paevere

Bureau of Meteorology Research Centre, Bureau of Meteorology Melbourne, Australia

Introduction

The use of 1DVAR retrievals of ATOVS radiances in the Australian Bureau of Meteorology Local Assimilation and Prediction System (LAPS) has produced a modest improvement in forecast skill over that obtained with NESDIS retrievals and represents an important step towards the unification of the data assimilation schemes employed by the Bureau's local NWP system (LAPS) and global system (GASP). The 1DVAR retrieval scheme was implemented in the 29-level operational LAPS system in September 2002, with 1DVAR retrievals used over the sea and below 100 hPa. NESDIS retrievals are used to extend the first guess profiles above the top of the model (50 hPa).

An extended 50-level version of LAPS, with the model top raised to 0.1 hPa and nested within a similarly extended GASP, is being developed to facilitate the assimilation of locally received ATOVS radiances, processed via the AAPP package. The timeliness of local reception and processing should improve the amount of ATOVS data available to the LAPS system which, operationally, employs an early data cut-off. The vertical extension of both models eliminates the need for NESDIS retrievals and promises a fully unified local/global data assimilation system able to handle radiance data, whether received and processed locally or sent from overseas centres via the GTS, equivalently. The results of experiments conducted to date will be presented below.

The LAPS 1DVAR System

In its standard regional configuration, the operational LAPS system covers a domain extending from 65° south to 17° north and from 65° east to 185° east. A tropical version of the system extends further to the north. Gridpoint spacing is .375° and there are 29 sigma levels extending up to a model lid at (nominally) 50 hPa. A number of higher resolution mesoscale implementations of the system are nested within the regional configuration and use the same starting analysis. Operationally, forecasts are run out to +72 hours in the case of the regional system, and +48 hours in the mesoscale systems. LAPS employs a cold-start data assimilation strategy which runs over two 6 hour cycles, beginning 12 hours before the forecast basetime with an analysis based on a GASP first guess, followed by two further analyses based on LAPS 6 hour forecasts. Operational forecast basetimes are 1200 UTC and 0000 UTC. Lateral boundary conditions are supplied from the most recent available GASP forecast (see figure1.) Because of the requirement to deliver a timely forecast product, the operational system employs a +1 hour data cut-off at the forecast base-time.

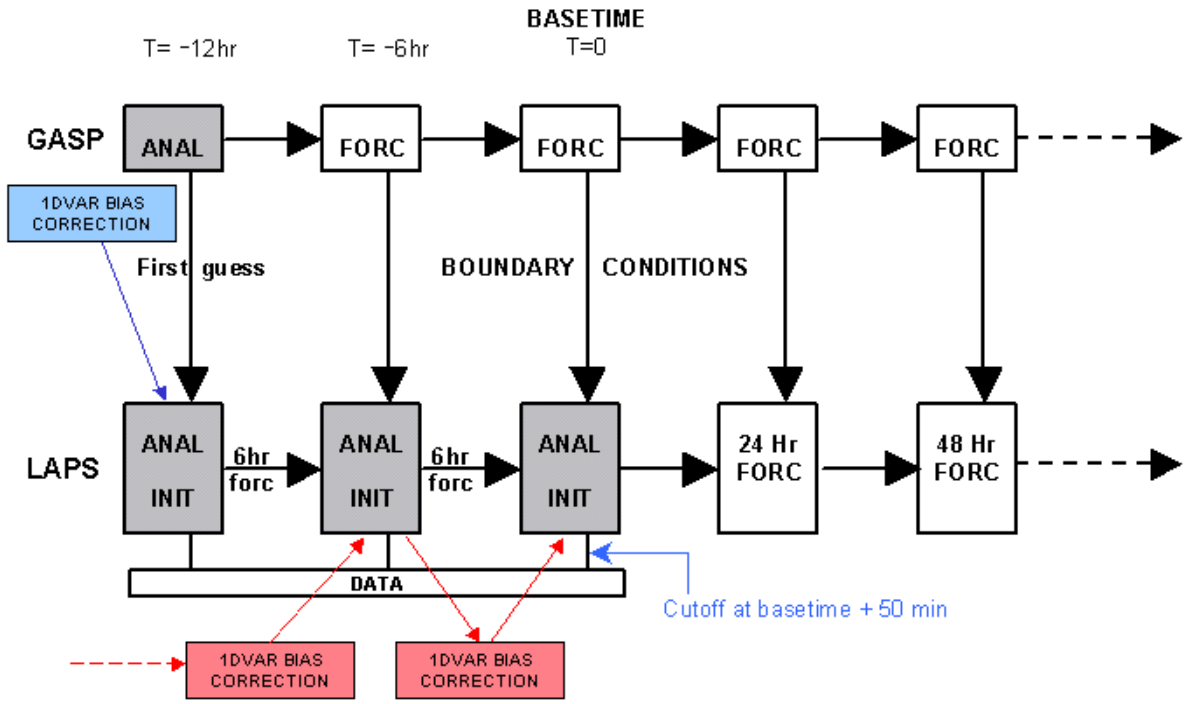

Fig 1: Schematic representation of a LAPS assimilation-forecast cycle

The GASP 1DVAR scheme (Harris and Steinle 1999) was implemented in the LAPS data assimilation cycle with few modifications (Tingwell et al. 2002). The input consists of the NESDIS ATOVS product supplied to the bureau via the GTS. The system computes retrieval error covariance and applies dynamic Purser type scaling (Eyre et al. 1993) to each retrieval which is presented to the OI analysis system in the form of four 1DVAR thickness layers (below 100 hPa) and three precipitable water layers (below 300 hPa). NESDIS thickness layers are used above 100 hPa. NESDIS retrieved temperatures are also used to extend the first-guess profile above the top of the model for use in the forward calculation. Air-mass dependent radiance bias predictors are computed from the first guess (Harris and Kelly 2001). In the LAPS implementation of the scheme, bias predictors generated in the GASP system are employed for the first T - 12 hour retrieval, while the subsequent retrievals, based on LAPS first guesses, employ separate predictors generated by the LAPS system.

Recent Operational Developments The 1DVAR assimilation of ATOVS AMSU-A radiances from NOAA-15 and HIRS and AMSU-A radiances from NOAA-16 was implemented in the operational LAPS suite in September 2002. Pre-implementation trials demonstrated that the system was robust and produced modest positive impact on forecast skill compared to an otherwise identical system that assimilated NESDIS retrieved temperature and moisture profiles (Tingwell et al. 2002). For example, S1 skill scores for 48 hour forecasts of 700 hPa geopotential height typically improved by 0.6 – 0.7 points.

More recently, the 1DVAR system was modified to use the forward model RTTOV 7 (replacing RTTOV 6), thus enabling the assimilation of HIRS and AMSU-A radiances from NOAA-17. This change was implemented operationally in the GASP system in February 2003 and in the LAPS suite in June 2003. Results from one month parallel testing trials showed that in both systems the impact of this change on forecast skill has been neutral.

Current Developments in GASP/LAPS Assimilation

Recent research has focused on the development of a generalized multivariate statistical interpolation scheme (GenSI) which is a major extension of the current operational Optimal Interpolation (OI) based system. This scheme is posed in observation space to allow for more flexibility in the specification of the background error covariances and solves the analysis equation iteratively by a preconditioned conjugate gradient method. It supports both the Australian region and the global domain NWP systems, and allows large volume data selection and the use of extensive data types and improved quality control. It can be readily extended to support 3D radiance assimilation. The software has been implemented to execute both in shared memory and distributed memory computing architectures.

Parallel trials of the GenSI scheme in both LAPS and GASP have demonstrated a marked improvement in the skill of forecasts based on GenSI analyses over those based on OI analyses. Figure 2 shows the average self-verified MSLP S1 skill score, RMS error and bias for a month of LAPS forecasts based on GenSI analyses (red lines) and OI analyses (green lines). The scores were calculated on a standard verification grid covering the most observation-rich part of the LAPS domain. The GenSI based forecasts were nested within boundary conditions which had been generated from GASP forecasts also based on GenSI analyses. There is clear improvement in forecast skill with the GenSI scheme, increasing with longer forecast intervals to a gain of 2.4 S1 points at +72 hours. RMS errors are also improved and similar gains are seen throughout the vertical domain of the model.

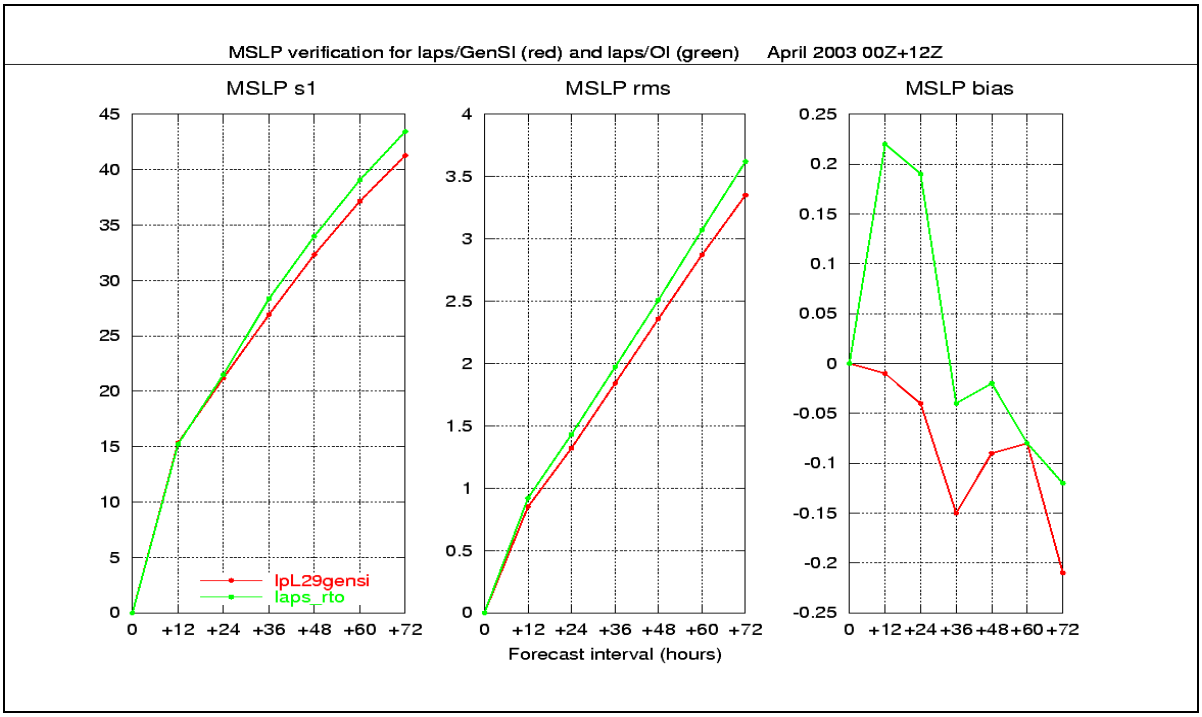

Fig 2: Average MSLP S1 skill score, RMS error and bias for a month of LAPS forecasts based on GenSI analyses (red lines) and OI analyses (green lines). The trial period was April 2003.

A particularly attractive feature of the new scheme is that it provides a single model-independent executable program file which may be used for all configurations of both the global and regional NWP models and thus represents a significant step towards the goal of a fully unified local/global data assimilation system. It is planned to implement GenSI operationally in the first half of 2004.

The Need for Locally Received and Processed ATOVS Radiances

The operational LAPS suite employs an early observational data cut-off (approximately an hour after the forecast base time) to ensure timely generation and dissemination of forecast products. Therefore, timeliness of access to ATOVS data is crucial to the quality of the analyses. Figure 3 shows the NESDIS ATOVS data coverage typically available to the operational LAPS system via the GTS at each of the three analysis times of the cold-start assimilation sequence. For comparison, the data available to the later cut-off GASP system at the corresponding times is shown beneath. We anticipate that the availability of locally received and processed ATOVS level-1D radiance data to the LAPS assimilation system will significantly improve the situation with regard to the final analysis.

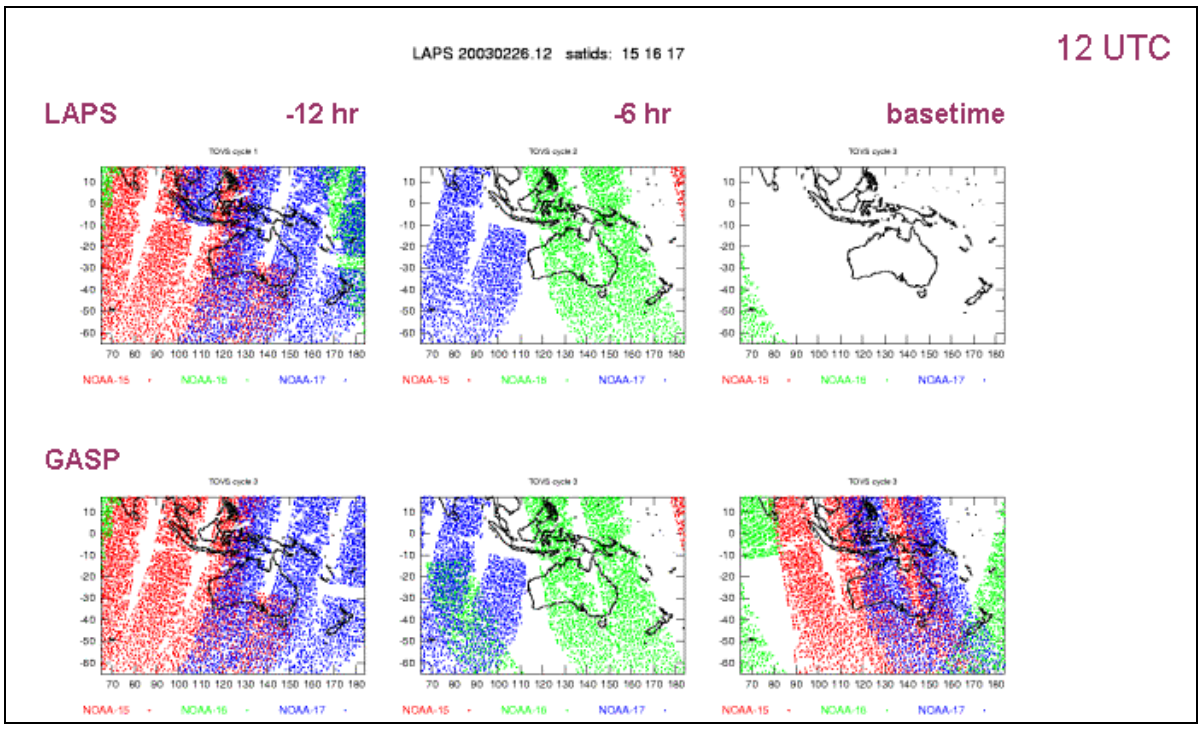

Fig 3: Comparison of ATOVS data coverage in the GASP and LAPS systems for the three analysis times in a LAPS assimilation cycle. Red points represent NOAA-15, green points NOAA-16 and blue points NOAA-17.

To facilitate the assimilation of local radiance data, we have extended the vertical domain and increased the number of vertical levels to 50 in both LAPS and GASP: the new level distribution is plotted in figure 4 alongside the current operational 29 level distributions for both LAPS and GASP. With the 50 level configuration the model lid (nominally 0.1 hPa) is higher than the top level required in the forward model and thus a purely model based first guess may be used in the forward radiance calculation. The need for NESDIS retrieved temperatures to extend the first guess profile is therefore dispensed with and so radiance data unaccompanied by retrieval information (such as locally received radiances) may be assimilated by the 1DVAR system.

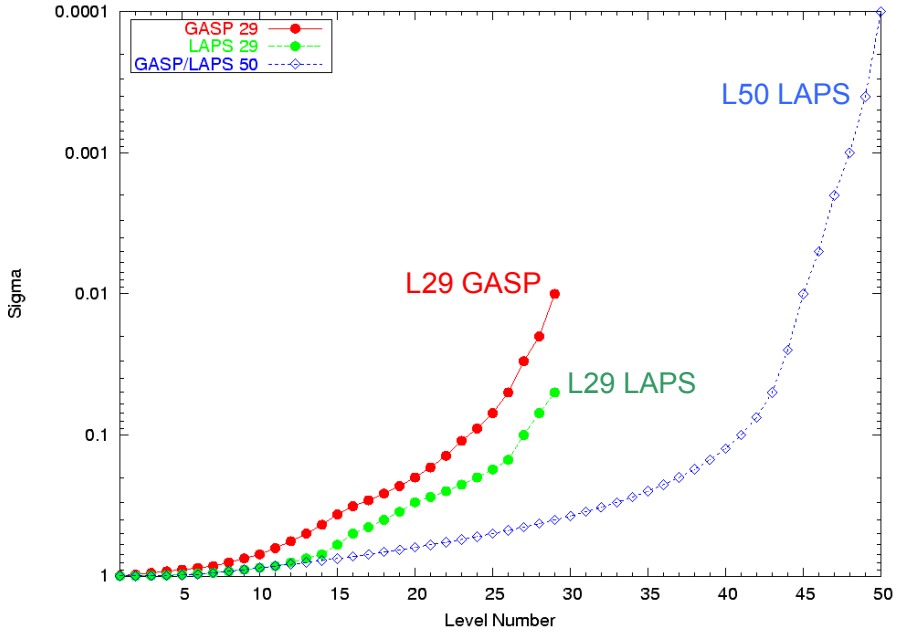

Fig 4: The new 50 level distribution plotted alongside the current operational 29 level distributions for both LAPS and GASP

Trials of 50 Level Systems

We have begun a series of trials of the 50 level configurations of both GASP and LAPS to test the performance and robustness of the models under the new configuration. To date only NESDIS radiance data has been assimilated in these trials. Initial and ongoing trials of the GASP system with the proposed 50 vertical levels and a comparatively low (T79) horizontal resolution (Harris et al. 2002) demonstrated both robust model performance and improved forecast skill with both OI and GenSI analysis schemes. Extension of these trials to the full operational horizontal resolution of T239 required some adjustment of the stratospheric model dynamics – in particular the introduction of Rayleigh friction and an increase in horizontal diffusion – in order to dissipate stratospheric noise. The model time-step was also reduced to avoid occasional CFL violations. With these modifications the T239L50 configuration of GASP, employing GenSI analysis, has run reliably for trial periods of more than one month.

Forecast verification results are shown in figure 5 in which S1 skill score, bias, RMS error and anomaly correlation data are plotted for MSLP and 200 hPa geopotential height. Data for the T239L50 trial are shown as solid lines and that from the corresponding period for the operational T239L29 configuration are shown as broken lines. The verification data shown were calculated for the Australian region and the trial period was April 2003. We note that the impact of the vertical extension to GASP on forecast skill is essentially neutral in the Australian region over the forecast period required to provide boundary conditions for LAPS. Our trials of the 50 level configuration of LAPS have therefore been nested within boundary conditions provided by the T239L50 GenSI GASP system.

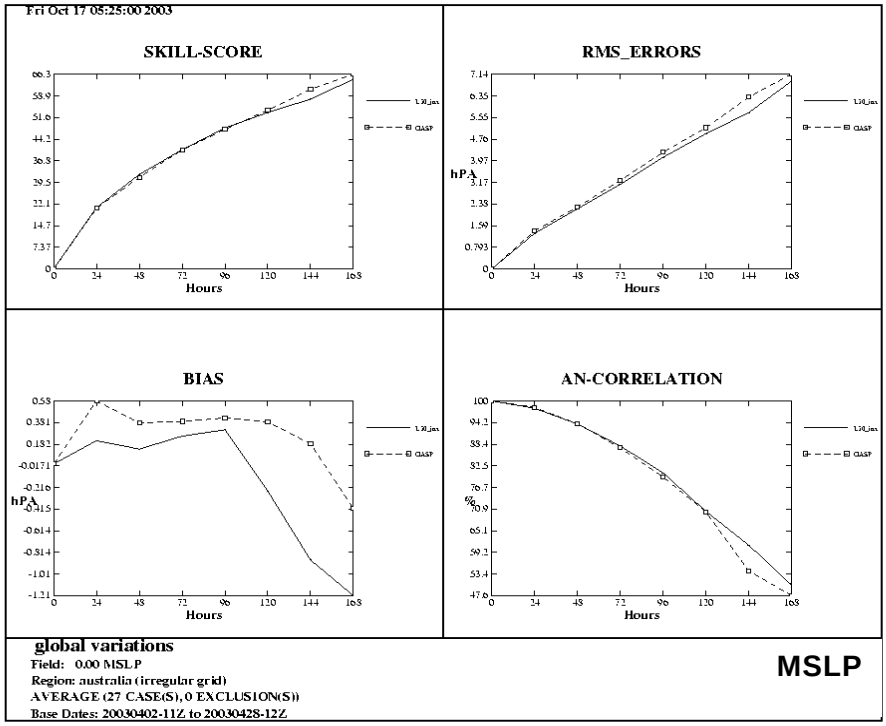

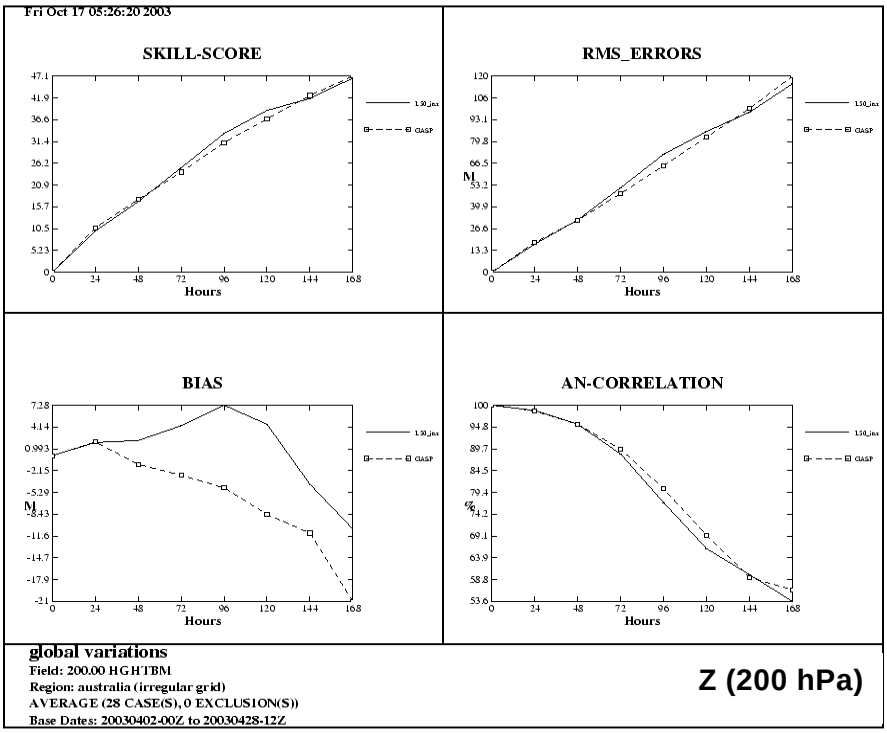

Fig 5: S1 skill score, bias, RMS error and anomaly correlation data, plotted for MSLP and 200 hPa geopotential height. Data from the GASP T239L50 trial are shown as solid lines and that from the corresponding period for the operational T239L29 configuration are shown as broken lines.

Verification results for a preliminary two week trial of the 50 level configuration of the LAPS system are shown in figure 6 (red lines) and compared to results from the operational 29 level configuration of

LAPS calculated for the same period (green lines). Both configurations used GenSI analysis. Shown are S1 skill score, RMS error and bias for MSLP and geopotential height at 500 hPa and 200 hPa, calculated on the standard verification grid. These results indicate modest gains to forecast skill in the upper troposphere with the extension of LAPS to 50 levels.

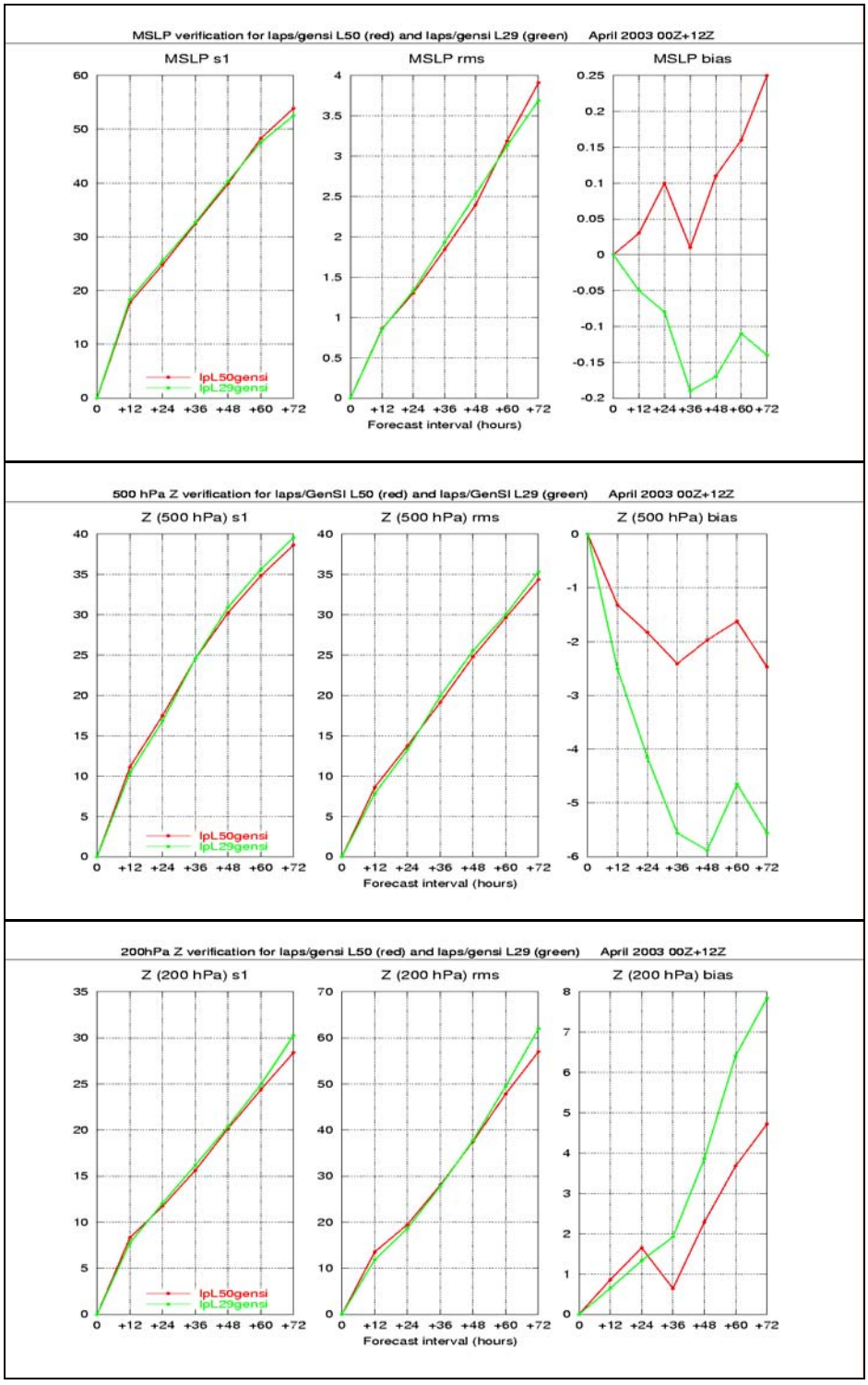

Fig 6: S1 skill score, RMS error and bias for MSLP and geopotential height at 500 hPa and 200 hPa for the 50 level configuration of the LAPS system (red lines) and the 29 level configuration (green lines).

Summary and Future Plans

Preliminary results from tests of the 50 level GASP and LAPS configurations are encouraging, although there may well be further work to do to optimise the stratospheric model dynamics, radiation physics and cloud microphysics. A robust 50 level configuration of GASP and LAPS will then form the basis for testing the 1DVAR assimilation of locally received ATOVS radiances.

The system we envisage for the reception and processing of ATOVS radiance data is shown schematically in figure 7. Current work towards the operational implementation of local reception and processing of radiance data by the Bureau of Meteorology Space Based Observations Section is nearly complete. Data will be processed via AAPP to level 1D, encoded into BUFR format and stored in the Bureau's Real Time Database. It is also planned to receive global ATOVS radiance data from the Met Office, also processed via AAPP to level 1D. These data sources will then provide the input to a fully unified 1DVAR system for GASP and LAPS which will assimilate local and remotely processed ATOVS radiances equivalently, regardless of source.

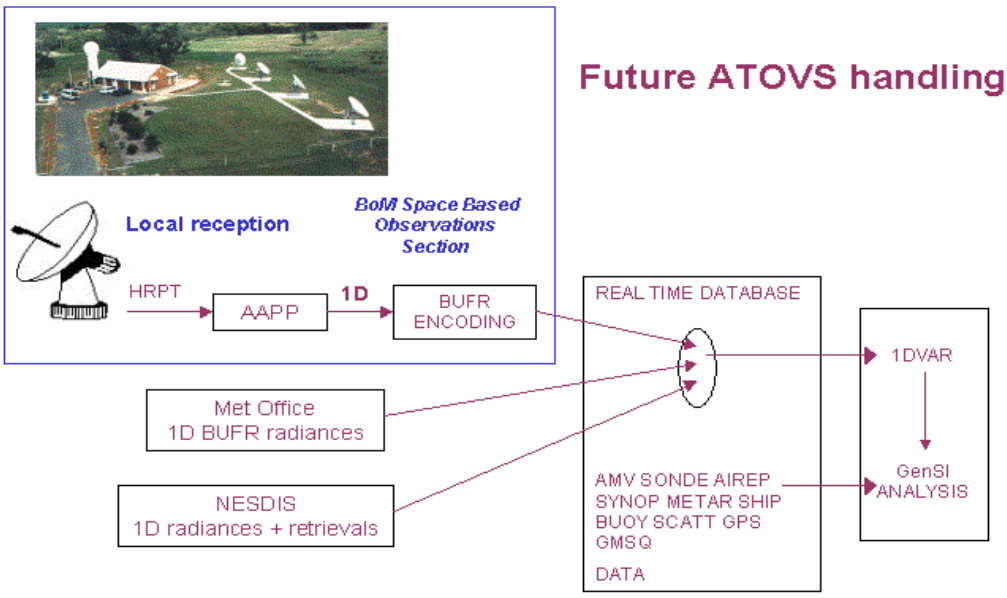

Fig 7: Schematic diagram of the reception and processing of ATOVS radiance data.

NESDIS radiance data will continue to be received and utilised, although its optimal use in combination with data processed via AAPP, and the possible cross-calibration issues that may arise, will require investigation. We also plan to extend the 1DVAR system to assimilate AMSU-B data in the near future. A longer term goal is the production of a unified 3DVAR GASP/LAPS assimilation system.

Acknowledgements

We are grateful to Kamal Puri and Robin Bowen of the BMRC Model Development Group for their help and advice regarding the LAPS system.

References

Eyre J.R., Kelly G.A., McNally A.P., Andersson E., and Persson A. 1993. Assimilation of TOVS radiance information through one-dimensional variational analysis. *Q J R Met Soc*, **119**, 1427-1463.

Harris, B. and Steinle, P. 1999. Variational TOVS radiance assimilation in the GASP model at BMRC. *Technical Proceedings of the Tenth International ATOVS Study Conference*, Boulder, Colorado, January 1999, 241-257.

Harris, B. and Kelly, G. 2001. A satellite radiance bias correction scheme for data assimilation. *Q J R Met Soc*, **127**, 1453-1468.

Harris, B., Bourke, W., Paevere, J. and Steinle, P. 2002. Extending 1Dvar/GASP to 0.1 hPa and the assimilation of 1C AMSU-A . *Technical Proceedings of the 12th International ATOVS Study Conference*, Lorne, Victoria, February 2002.

Tingwell, C., Harris, B. and Bourke, W. 2002. ATOVS 1DVAR retrieval in the Australian region LAPS data assimilation and prediction system. *Technical Proceedings of the 12th International ATOVS Study Conference*, Lorne, Victoria, February 2002.

Enhanced Use of Radiance Data in NCEP Data Assimilation Systems

John C. Derber*, Paul VanDelst[#], XiuJuan Su[&], Xu Li[&], Kozo Okamoto[%] and Russ Treadon*

*NOAA/NWS/NCEP/EMC
[#]CIMSS/UW-Madison @ NOAA/NWS/NCEP/EMC
[&]Science Applications International Corporation
[%]JMA visiting NOAA/NWS/NCEP/EMC
Camp Springs, MD USA

Introduction

There have been significant changes in the use of radiance data at NCEP over the last few years. These changes have included a substantially increased volume of radiance data, an improved radiative transfer system, an improved forecast model (vertical/horizontal resolution, higher model top, improved physics), and improved quality control and bias correction techniques. Within an operational environment, it is necessary to continually maintain and enhance the system to improve the utilization of data. In addition, several new developments to utilize additional sources of radiance data (e.g., AIRS, SSM/IS, and geostationary/polar imagery) are under development. Enhancements in the use of the satellite data along with the current usage of satellite data will be discussed below. Experiments underway at NCEP directed towards the use of AIRS radiances, SSM/I radiances, GOES imager radiances and the use of radiances directly in the SST analysis will be briefly described.

Changes in the use of radiance data at NCEP

The changes to NCEP's use of radiance data can be divided into three main groups: updates to radiative transfer, modification to data selection and quality control, and enhancements to data assimilation and forecast systems. Of course these changes interact with each other within the data assimilation system. None of the changes produced large impacts on the quality of the resultant forecasts and analyses, but each represents a small incremental enhancement of the system. These modifications were implemented into the NCEP operational system on or before 20 Nov. 2003.

The radiative transfer used in the NCEP analysis system uses transmittances calculated using OPTRAN as modified by VanDelst et al.(2002). In addition, the radiative transfer calculations have been updated using new microwave and IR Line-by-Line (LBL) calculations and recalculating the OPTRAN coefficients. The system has been set up to incorporate the water vapour continuum both explicitly and implicitly as part of other calculations. Also, a new high spectral resolution algorithm for estimating the IR surface emissivity over the ocean has been included. This surface emissivity algorithm is described more completely in another ITSC-13 presentation (VanDelst, 2003).

The data selection has been enhanced to allow more control over which observations are selected and to extract more information from the data. In the new system, the data selection is based on a score related to how close the observation is to the center of the selection box, the time difference from the analysis time, and a measure of the likelihood that the data will pass later quality control. This change

in the data selection allowed many more IR and a few more microwave observations to pass the quality control. The IR quality control was also modified (primarily because of the large number of channels available from the AIRS instrument) to base the cloud detection on an estimated cloud percentage and cloud height from the differences in the observed and simulated brightness temperatures. This cloud detection change was discussed in a previous ITOVS meeting (Derber et al., 2002).

General changes to the assimilation system have also been made to enhance the use of all types of data. Previously the atmospheric forecast was assumed to be available either every three hours or just at the analysis time. The surface fields could only be used at the analysis time. Now, the capability to interpolate atmospheric fields and surface fields in time regardless of the frequency of the model output has been included. The analysis is performed twice in the NCEP operational system. There is an early data cut-off (2:45 after the analysis time) from which the aviation and long-range forecast is run. There is also a later data cut-off (6:00 after the analysis time) from which the 6hr forecast is created for use as a background in the next analysis. The analysis from the early cut-off can be used as a guess at the solution (not a background field) for the later analysis. This essentially has the effect of reducing the number of necessary iterations to reach convergence and increasing the number of outer iterations. Note that assuming complete convergence and the same quality control decisions in the outer iteration, the results in the later analysis would be identical whether or not a guess is used. Unfortunately, the option for using a guess field is not currently being exercised in the operation run suite. Finally, considerable effort has been expended to simplify the data handling, streamline the code and fix a few minor bugs.

These changes were all in preparation for major upgrades to the analysis system currently being tested or under development. These upgrades include the inclusion of new types of radiance data (as discussed below) and a new formulation of the background term in grid-space rather than spectral-space. By performing the calculations in grid-space, we will be able to introduce situation dependent background errors and hopefully be able to extract substantially more information from the observations.

Development of new radiance data usage at NCEP

AIRS data

The current trend in infrared satellite systems is to deploy instruments which produce many high spectral resolution channels. The first mega-channel instrument available was the AIRS instrument on the AQUA satellite. For instruments which produced on the order of 20 channels, it was possible to tailor bias correction and quality control decisions for individual channels. For the mega-channel instruments, it has become necessary to develop automated algorithms which can be applied successfully to large numbers of channels without manual intervention. This has been the major difference using AIRS versus HIRS data.

The real-time data stream used by NCEP comes from NASA through NESDIS and has been discussed extensively at ITOVS meetings (Wolf et al., 2002). The 281 channel version of the AIRS data stream is currently being used. Of the 281 channels, 254 were found to be usable. Channels 73-86 were not

used because they peak too high in the atmosphere. (Note specific channel numbers here refer to the original AIRS channel numbers). Channels 1937-2109 were not used since they appear to have non-LTE effects not incorporated in our radiative transfer. Finally, channel 2357 was not used due to large observational-background differences which could not be explained by model forecast errors. In addition, shortwave channels with wavenumbers above 2000 were down weighted and above 2400 removed during the day due to inadequacies in the modeling of reflected solar radiation.

The inclusion of the AIRS data within the NCEP assimilation system was tested in parallel during the Fall of 2003. During this testing, several modifications were introduced into the system including a change in the thinning distance from 150 to 225 km and an increase of the specified observational errors for each channel by .2K to an average of about 1K. These changes were introduced because the AIRS data was producing very large penalties relative to the other data and was slowing the minimization procedure. With the use of the new data selection algorithm, which attempts to choose the clearest field of view available, 38% of the selected radiances passed the quality control and were used in the assimilation. Further updates to the system have since been introduced based on the Fall 2003 experiments, and additional tests of the AIRS data impact are currently underway.

The Fall 2003 experiments showed little impact from the inclusion of the AIRS data. For example, in Figs. 1 and 2, the average fits to the radiosonde temperatures and the daily 5-day Southern Hemisphere forecast skill for the control and AIRS assimilation are shown respectively. Similar results are produced for different observation types and different regions. These figures show the impact was very small. We believe this is primarily due to the presence of clouds where the data potentially would have had the largest impact.

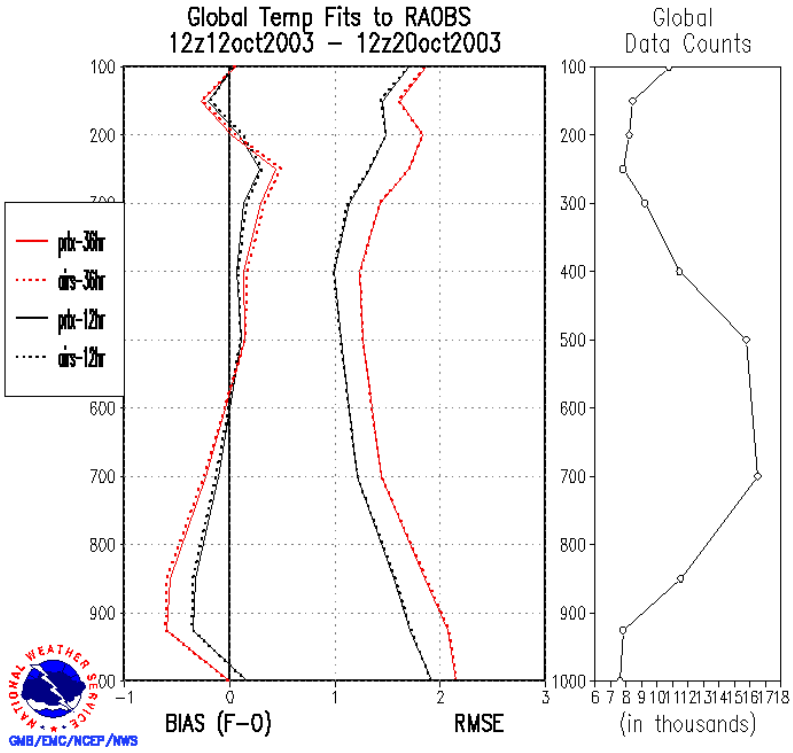

Fig. 1: RMS and bias for fit to radiosonde temperatures with (dashed) and without (solid) using AIRS data. Figure on right gives number of comparisons at each level.

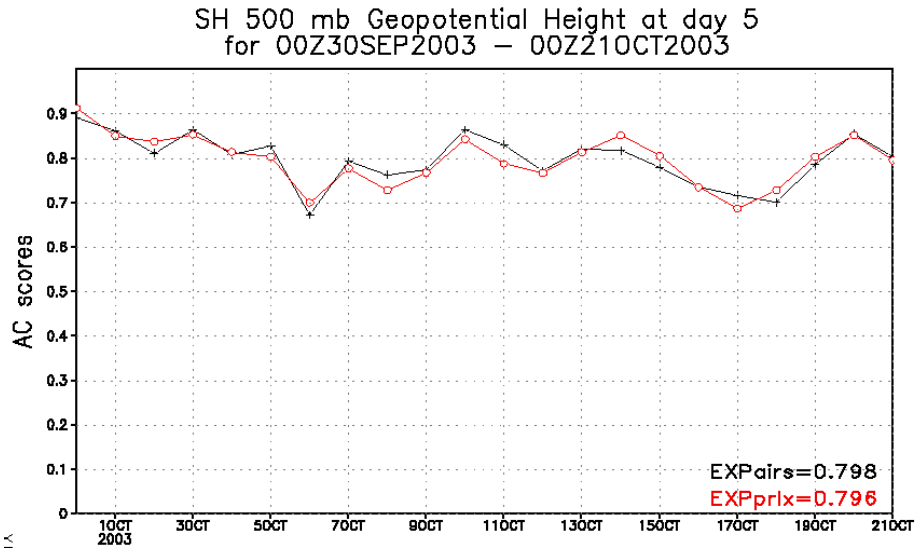

Fig. 2: Southern Hemisphere 500hPa geopotential anomaly correlation with (black) and without (red) AIRS data

GOES Imager data

Experiments are underway to use the GOES imager data in the NCEP global data assimilation system. The inclusion of the GOES imager data is intended to improve the moisture fields. The data is being

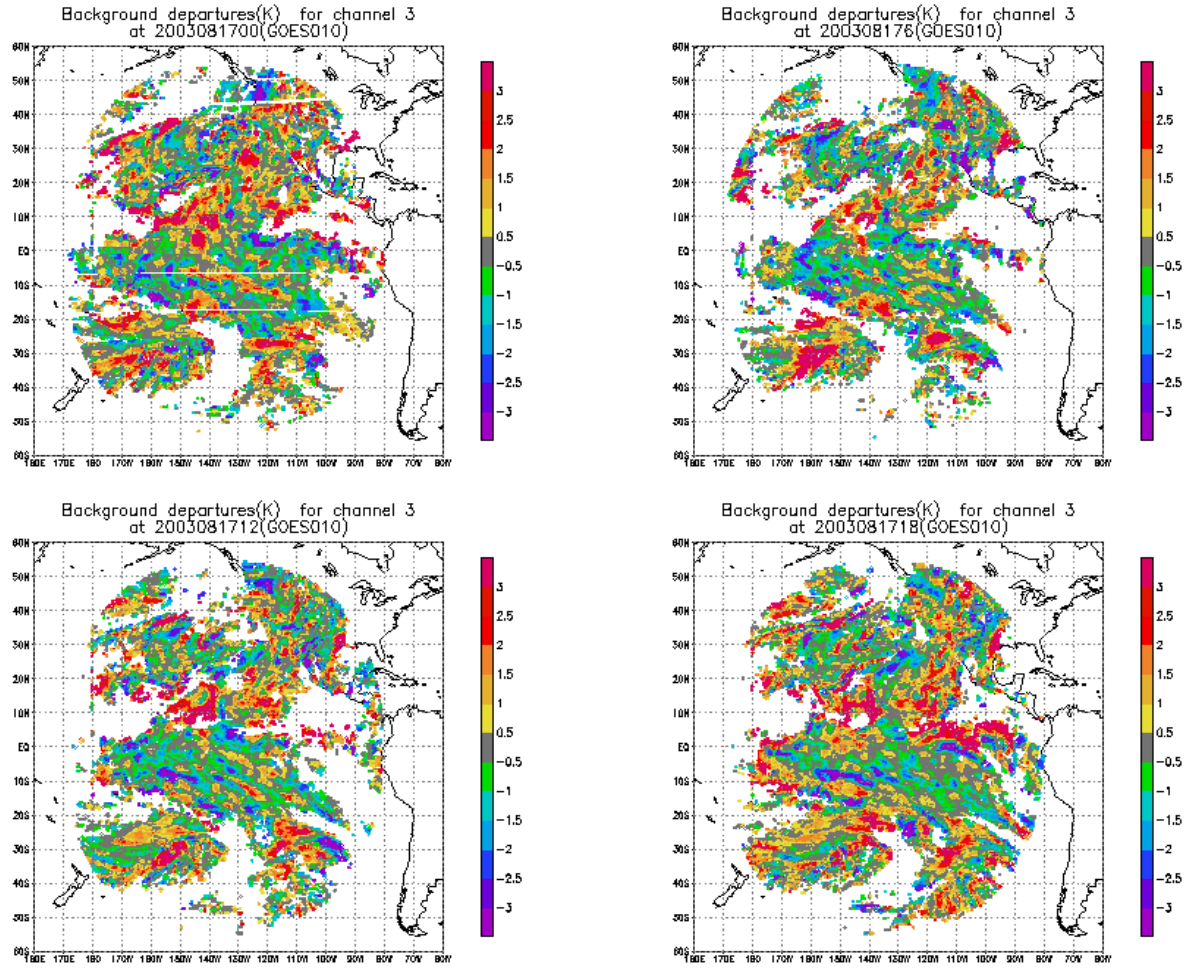

Fig. 3: Brightness temperature difference between observations and simulated observations prior to quality control.

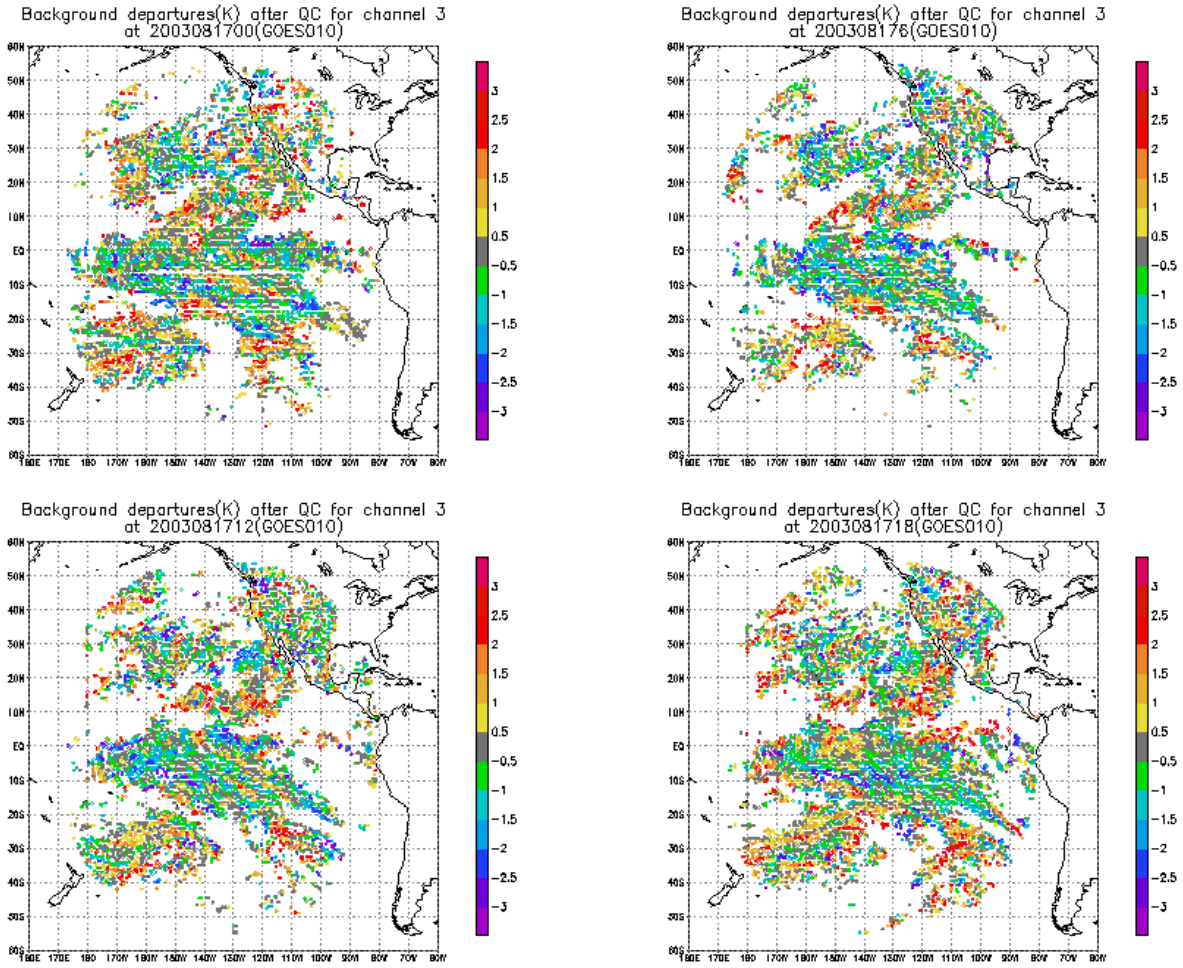

Fig. 4: Brightness temperature differences between observations and simulated observations after quality control

produced by NESDIS and is a 11x17 box average of observations which pass the NESDIS cloud detection quality control procedures. Initially only channel 3 is being used in the assimilation, while window channels 4 and 5 are used in the quality control procedures.

In addition to the standard quality control procedures within our analysis system, three additional quality checks are made to the data. For GOES-12, only box data with greater than a 25% clear sky fraction are being used while for GOES-10 greater than 10% is necessary. Also, the brightness temperature standard deviation within a box is required to be less than 1.5 degrees. Finally, GOES-12 data from 06UTC is not used due to the midnight effect.

In Figs. 3 and 4, the distribution of differences between observations and simulated observations from the background is shown before and after quality control respectively. There is a substantial reduction in the number of observations used by the analysis because of the quality control. However the basic large scale structure remains the same.

Assimilation and forecast experiments have been performed using this data showing a small positive impact on the moisture fields in the analyses and forecasts. Further experiments are currently underway, prior to possible operational implementation.

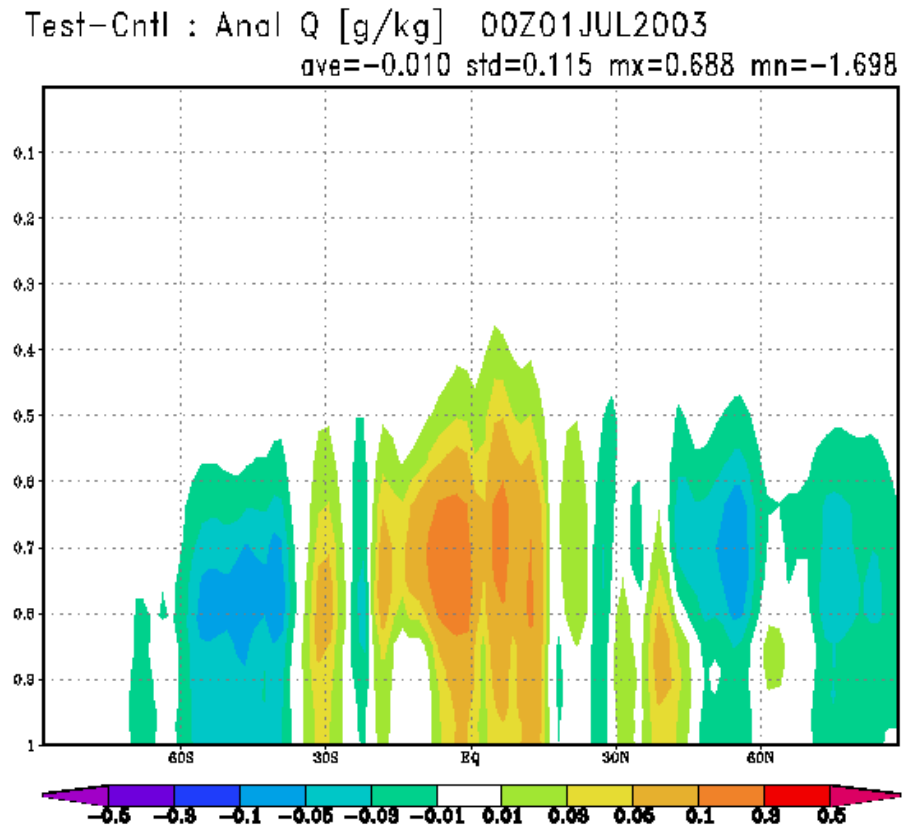

Fig. 5: Specific humidity differences between simulation with and without SSM/I data.

SSM/I data

In order to better use the information in the SSM/I data and to prepare for new conically scanning microwave instruments(e.g., SSM/IS and CMIS), experiments are being performed attempting to directly use the SSM/I observations within NCEP's analysis system. Initially, we are only attempting to use the data over the ocean where the surface emissivity is better known. Again, necessary bias correction and quality control procedures have been developed for this data.

In Fig. 5, the mean differences between the analyses with and without the SSM/I data are shown after several days of assimilation. Note the general increase in moisture in the tropics and decrease in the mid-latitudes. This signal is consistent with known biases in the forecast/analysis system. Experiments continue examining the usefulness of this data.

SST analysis using radiances

The SST plays an important role in atmospheric and oceanographic forecast and analysis systems. While our current operational system using U.S. Navy SST retrievals is able to attain a fairly high degree of accuracy in the SST analysis, future usage will require enhanced accuracy and time resolution. NCEP has begun a project to improve the SST analysis and to allow the use of all types of radiance observations directly in the analysis of the SST. The first step of the project is to examine the impact of using a real atmosphere above the SST field. Since we have a fairly accurate depiction of

the atmosphere above the surface in our atmospheric analyses and short term forecasts, we believe that we can remove a substantial portion of the atmospheric signal in the data (and possibly use the information in the atmospheric analysis) and extract more SST information from the data.

To test this idea, we have produced physical retrievals of SST based on the Community Radiative Transfer Code, the atmosphere from the NCEP's Global Data Assimilation System, the SST analysis from the previous day (as a background SST) and the U.S. Navy Brightness temperatures used to produce their retrievals. In the physical retrieval, 3 quantities are found; the SST increment, atmospheric moisture increment, and atmospheric temperature increment. The atmospheric moisture and temperature are assumed to not vary with height. Since, the AVHRR channels used are window channels and primarily sensitive to the near surface temperature and moisture, this should be a good assumption. However, if sounding channels are used, this assumption will have to be relaxed.

As with other radiance data, it was necessary to develop bias correction and quality control procedures for the AVHRR radiance data. The quality control currently only rejects a few observations since extensive quality control is already performed on the data by the U.S. Navy. Also, there is averaging of fields of view after the quality control which will further smooth out differences and make it less likely to fail the quality control. Since the data is averaged over several fields of view, it is also

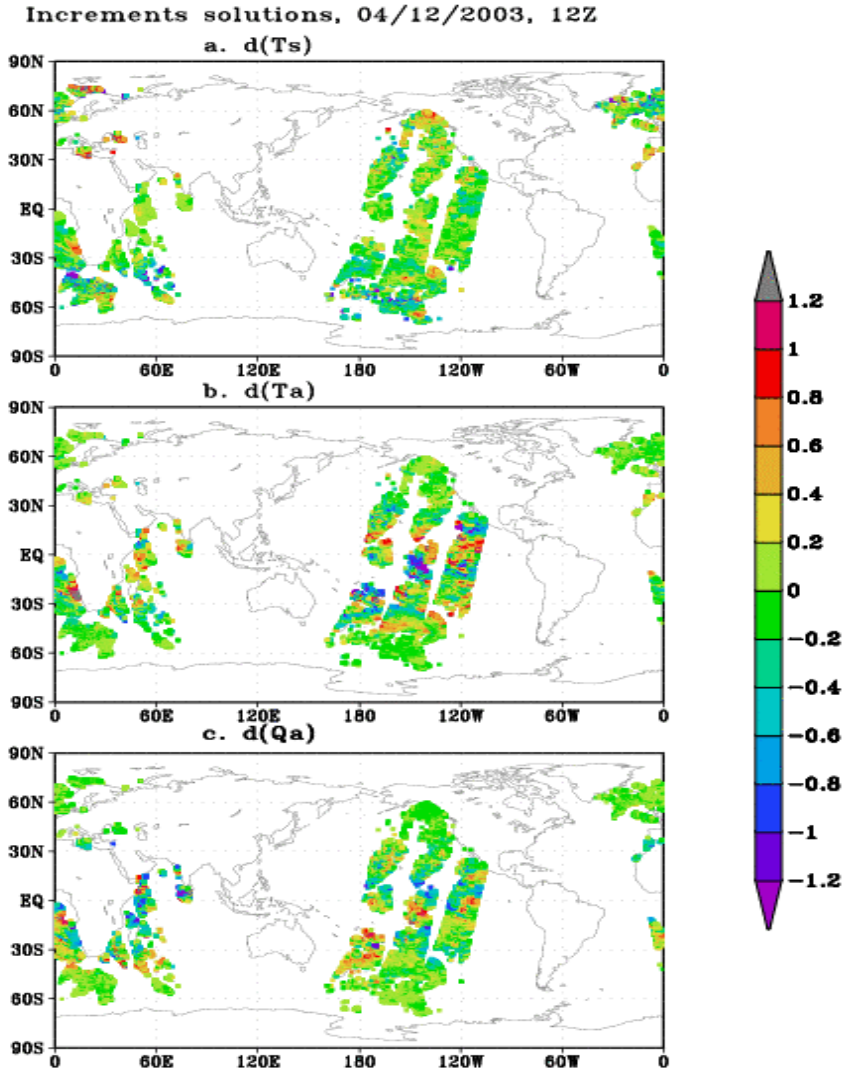

Fig. 6: Physical retrieval of SST (a), atmospheric temperature (b) and atmospheric moisture increments(c).

difficult to perform an angle dependent bias correction. For these reasons, the original observations will be used to attempt to improve the bias correction and quality control procedures.

An example of the SST and atmospheric temperature and moisture retrievals are show in Fig. 6. Note the larger moisture increments and temperature increments in the tropics. This is because of an increased sensitivity to the atmosphere as the amount of moisture increases for channels 4 and 5. The retrievals appear to be relatively insensitive to the background error given the background temperature but are sensitive to the error supplied to the background moisture. Preliminary assimilation experiments show some consistent improvement in the SST analysis from the use of these SST retrievals and a reduction of unrealistic variation between consecutive analyses in the tropics. With the encouraging results from these experiments, the direct inclusion of the radiances in the SST analysis and the meshing of the full 3-D atmospheric analysis with the SST analysis is continuing.

Summary and Future

NCEP has continued to enhance the use of satellite radiance data through improved data assimilation techniques and the incorporation of additional satellite data. Current ongoing new data investigations include AIRS, SSM/I, GOES imager and AVHRR (for use in SST analysis). Of course, there are many new observations from new instruments that will become available over the next five years. However, it is becoming increasingly difficult to get a positive impact from incorporating new satellite data. This limited impact results because many components of the analysis are already well defined by the current observing system, and for other components, the impact is limited by inadequacies in the assimilation system. Thus,successful utilization of all the information in the observing system requires substantial development of the data assimilation systems, not just the inclusion of additional data. NCEP is developing a new unified global/regional data assimilation system which calculates the background error in grid space rather than in spectral space. In this system, we anticipate that local situation dependent background errors can be utilized and substantial improvement in the usage of information in all types of data will result.

References

Derber, J., D. Parrish, R. Treadon, X. Su, P. VanDelst, Y. Tahara,and J. Woollen, 2002 The use of radiance data in the NCEP global and regional data assimilation systems, Proceedings of the Twelfth International TOVS Study Conference, 26 February -5 March, Lorne, Australia, 45-48.

van Delst, P.F.W., Y.Tahara, J.Derber, T.Kleespies, and L.McMillin ,2002: NCEP Radiative Transfer Model Status, Proceedings of the Twelfth International TOVS Study Conference, 26 February -5 March, Lorne, Australia, 282-287.

Van Delst, P.F.W., 2003: NCEP infrared sea surface emissivity model, This volume

Wolf, W. M. Goldberg,. Zhou, Qu and Divarkala, 2002: A fully operational AIRS processing and distribution system, Proceedings of the Twelfth International TOVS Study Conference, 26 February -5 March, Lorne, Australia

Recent improvements in Temperature and Moisture profiles using NOAA satellites AMSU data and their impact on an NWP model over the Indian region.

Devendra Singh,Y.V.Rama Rao, R.C.Bhatia,
S.K.Srivastav,San Prasad and S.K.Mukharjee
India Meteorological Department
Lodhi Road, New Delhi-10003, INDIA
Email: dschahar@hotmail.com

Abstract

The Indian Meteorological Department, New Delhi receives and process NOAA TOVS and ATOVS data in real time. The physical and neural network approaches have been used to retrieve atmospheric temperature and moisture profiles from NOAA-16 &17 satellites AMSU data over the Indian region. The earlier training data set based on global data only for two seasons used in the neural network technique has been replaced by a new training data set based on regional data over land and ocean for all the seasons. The new training data set has improved the temperature and moisture profiles accuracy retrieved using a neural network approach compared to a physical method. The detailed validation and inter comparisons of temperature and moisture profiles have also been carried out with ECMWF analyses over sea and land separately for different seasons for the year 2002-2003. The performance of the neural network technique is found to be superior compared to the physical method.

Recently, temperature and moisture profiles retrieved from NOAA-16 ATOVS data over the Indian region have been used in a regional NWP model for an impact study. The operational NWP system of the Indian Meteorological Department is based on a Limited Area Analysis and Forecasting System (LAFS), which consists of real time processing of data received on the Global Telecommunication System (GTS), objective analysis by 3-D multivariate optimum interpolation (OI) scheme and a multi-layer primitive equation model. Several experiments were performed using temperature and moisture profiles retrieved from NOAA-16 ATOVS data. Using this data several experiments were undertaken to examine the impact of these data sets on some of the important weather systems such as monsoon depression, active monsoon conditions during monsoon 2003. The preliminary studies reveal that these additional data have a positive impact on rainfall prediction of the limited area model. Results of specific cases of impact studies are presented in the paper.

1. Introduction

The Neural Network technique has been used for temperature and moisture profiles using AMSU observations over Indian regions (Singh, et. al., 2002,2003a and 2003b). An evaluation of this method versus a physical inversion approach for retrieval of atmospheric temperature and moisture profiles from Advanced Microwave Sounding Unit (AMSU) measured brightness temperatures is presented in this paper. The evaluation is based on four different seasons of the year 2002-2003 using ECMWF analysis data. The results presented here are only for summer (July, 2002) and winter (January, 2003). Further, comparisons have also been carried out for the temperature and moisture profiles using NOAA-16 and NOAA-17 satellite data over sea and land separately.

The Indian Meteorological Department (IMD) (Prasad et al, 1997) has shown the positive impact of this data in a limited area model. An impact study was also carried out using high resolution (80 km) TOVS temperature-humidity profile data locally derived at IMD, New Delhi (Bhatia et al, 1999). This high-resolution data was able to bring out the impact in the synoptic scale prediction associated with tropical easterly wave activity over the north Indian Ocean. In view of the importance of accurate initial humidity fields in tropical NWP, it is necessary to maximize use of these data from unconventional sources. With this end in view, the present study was taken up to study the impact of ATOVS temperature and moisture profile data on limited area analysis and forecast fields.

2. Data and analysis procedure

Using the limited area analysis and forecast fields as inputs to ATOVS and AVHRR processing package (AAPP), processed temperature and moisture profiles are being retrieved from AMSU data using the ICI (inversion coupled imager) software package developed by CMS, Lannion, MeteoFrance and the IAPP software package developed by the University of Wisconsin, USA. These profiles have also been derived using a Neural Network Technique. In the present study the temperature and moisture profiles retrieved using the ICI package have been used using LAM model guess and IAPP without using LAM model guess. However, work is in progress to feed LAM model guess into IAPP package also. The NOAA-16 & 17 locally processed ATOVS data have an advantage of more data within the short cut-of-time. Daily 2 to 3 passes data approx. 1100 observations in a singe pass covering the land and ocean area are generally available over the Indian region.

3. Accuracy of temperature and moisture profiles

The temperature and moisture profiles have been retrieved using two different retrieval techniques namely Neural Network and Physical inversion using NOAA-16 & 17 AMSU measurements. The bias and rms error of temperature and moisture profiles were computed for the month of July 2002 and January 2003 separately on land and sea over India and it surrounding regions. These errors have been computed against ECMWF analyses. It has been observed that these errors are smaller for Neural Network compared to the physical inversion approach in both seasons over land and sea (Fig-1a, b, c and d). This may be probably due to lack of proper NWP guess in case of physical inversion method. Further, a comparison has been carried out for temperature and moisture profiles using Neural Network technique for NOAA-16 and NOAA-17 satellite data for the month of January 2003. The bias and rms error against ECMWF analysis data indicate that these are comparable for both the satellites (fig-2a, b, c and d).

4. IMD's operational NWP system

IMD operational NWP is based on a limited area analysis and forecasting system (LAFS) that consists of real time processing of data received on Global Telecommunication System (GTS), objective analysis by 3-D multivariate optimum interpolation (OI) scheme and limited area forecast model. The grid point fields for running the model are prepared from the conventional and non-conventional data received through the GTS. The data consists of the surface SYNOP/SHIP, upper air TEMP/PILOT, SATEM, SATOB, AIREP, DRIBU and AMDAR, which are extracted and decoded from the raw GTS data sets. The synthetic observations such as cyclone bogusing data and ATOVS temperature and humidity profile data also included as per requirement. All the data are quality controlled and packed into a special format for objective analysis.

4.1 Analysis procedure and Forecast Model

The objective analysis is carried out by three dimensional multivariate optimum interpolation procedures. The variables analysed are the geopotential, u and v components of wind and specific humidity. Temperature fields are derived from the geopotential fields hydrostatically. Analysis is carried out on 12 sigma surfaces from 1.0 to 0.05 in the vertical and 1^0x1^0 horizontal latitude/longitude grid for limited area horizontal domain of 30^0S to 70^0N ; 0^0 to 150^0E. The generated ATOVS temperature and relative humidity data are included into the regional OI scheme as bogus observations. The observations are generally horizontally consistent over synoptic scales, and very few are rejected by the analysis system. The IMD limited area forecast model is a semi-implicit semi-Lagrangian multilayer primitive equation model based on sigma co-ordinate system and Arakawa C-grid in the horizontal. The present version of the model has a horizontal resolution of 0.75^0x0.75^0 latitude/longitude in horizontal and 16 sigma levels (1.0 to 0.05) in vertical(Prasad et al (1997), Krishnamurti et al (1990). The lateral boundary conditions are obtained from the global forecasts of the National Centre for Medium Range Weather Forecasting (NCMRWF), New Delhi.

5. The impact studies

The impact study was carried out for the active monsoon conditions of 18-22 June 2003, heavy rainfall events of 9 July 2003 and 24-28 July 2003 corresponding to the movement of a monsoon depression across central parts of the country. The specific humidity fields were found to be 12-13 g/kg over the monsoon trough region over central parts of India with a decrease of moisture towards the north. The temperature fields also showed similar features. These features are consistent with the normal meteorological conditions prevailing over this area, which confirms that qualitatively NOAA sounding products are good.

5.1 Active monsoon conditions – 18-22 June 2003

During the period a low pressure area was formed on 19th June over Gangetic West Bengal & adjoining areas with associated cyclonic circulation extending upto mid-tropospheric levels and it persisted over the same area up to 23rd. Another upper air circulation lies over southwest Rajasthan & neighborhood on 19th and persisted on 20th. It moved to northwest Madhya Pradesh and adjoining east Rajasthan on 21st and over west Utter Pradesh & neighborhood on 22nd. Under the influence of these systems heavy rainfall occurred over western and northeast parts and moderate rainfall over central parts of the country. Using the ATOVS data the experiment was conducted for the above period. The mean humidity analysis at 850 hPa for 18 to 22 June 2003 in the Control run (without using pseudo humidity profiles left panel) and Experiment (with humidity data included right panel) is presented in Fig.3. The difference in the control run and experiment are clearly visible and inclusion of pseudo humidity observations has substantially modified the analysis over north and northwest parts of India where high resolution humidity data was available. The mean wind forecast valid for the above days and verification analysis are given in Fig.4 & 5. The forecast experiment wind fields after including the moisture had shown a circulation over west Bengal and adjoining Bay of Bengal that was observed in the verifying analysis. However, the same was not observed in control run. The 5 day accumulated rainfall based on 24 hour forecast by limited area model valid for 19 to 23 June 2003 are presented in Fig.6, control in the left panel and experiment in the right panel. The rainfall prediction after including the profile data has shown 20-30 cm over northern parts of India where as in the control run it was 10-20 cm. The predicted rainfall of 20-30 cm is more close to the observed rainfall over northern parts of India.

5.2 Heavy rainfall event of 9 July 2003

A low pressure area formed on 10th over Haryana and adjoining areas of east Rajasthan & west Utter Pradesh (northern parts of India) on 9th evening with associated cyclonic circulation extending up to mid-tropospheric levels. Under its influence heavy to very heavy rainfall occurred at most places over north and northwest parts of India and moderate rainfall over peninsula and northeast parts of India. In this case the humidity analysis at 850 hPa for 09 July 2003 in the Control run and Experiment is presented in Fig.7. In this case the control run shows humidity of less than 60% over most of the northern parts of India. However, the experiment fields shows 60-80% appears over the area as against a poorly defined pattern in the control run. The day-1 rainfall forecast by limited area model valid for 10 July 2003 presented in Fig.8. A marked improvement is seen in the predicted rainfall pattern over northwest parts of India where the control run was unable to predict the heavy to very heavy rainfall that occurred at most places over northern and northwest India. In the control run most of this area showed 3 to 10 mm rainfall and in experiment it shown from 10 to 40 mm, where as the realized rainfall was 30 to 80 mm with isolated heavy rain fall of 130 mm over Delhi.

5.3 Monsoon Depression over the Bay of Bengal (25-28 July 2003)

A low pressure area formed over northwest Bay of Bengal on 24 July near the southern end of monsoon trough. It intensified into a depression on 25th and further into deep depression by evening and moved in a northwesterly direction and crossed the Orissa coast on 25th morning. After crossing the coast the system retained its intensity for the next two days and moved west northwesterly direction. The system weakened into a depression on 27th and further moved westwards and weakened into low pressure area over northwest India. Under the influence of this system widespread rainfall occurred over Orissa, Jharkhand and Chattishgarh,

central and western parts of India. In this case a marked improvement is seen in the predicted rainfall pattern over central and northern parts of India. In the control run the accumulated rainfall for 25-28 July 2003 predicted heavy to very heavy rainfall belt of 20-30 cm as shown (Fig.9) more north of the actual position in the first few days and more westwards in the subsequent 3 days. However, in the experimental runs the rainfall belt of 5-10 cm lay along the movement of depression with heavy to very heavy rainfall belt of 20-30 cm more concentrated along the coastal areas of Bay of Bengal and north Arabian Sea and adjoining Pakistan. In this case the heavy rainfall over northwest India was not captured in both control and experiment where the humidity profile data over the area was not available during the above period.

6. Conclusions

The training data set based on the regional input for all the seasons has improved the accuracies of temperature and moisture profiles retrieved from AMSU measurements of NOAA satellite series. During actual operations of temperature and humidity retrieval, the scheme uses only the satellite measurements and satellite geometry data, without requiring additional first-guess from modeled profiles. This gives an advantage to many operational sites including those with limited Internet connections.

The study has brought out a distinct positive contribution of the ATOVS derived humidity profile data, used as pseudo observations in the limited area analysis scheme. The forecast model runs to study the impact of the additional humidity data on the rainfall predictions have shown a considerable improvement over northwestern parts of India, as seen from the corresponding observed rainfall. Maximizations of use of such satellite-based observations are expected to considerably improve the initial humidity analysis and subsequent forecasts produced by NWP models.

Acknowledgement

The authors are grateful to the Director General of Meteorology for constant encouragement during the course of this study. The authors are also thankful to Dr. Lydie Lavanant, Meteo-France for providing the ECMWF analysis data.

References

Bhatia, R.C., P.N. Khanna, Kanti Prasad and Y.V. Rama Rao (1999) ‘A preliminary study of the impact of NOAA soundings retrievals on a limited area model (LAM) forecasts, *Proceedings of INTROMET-97*, Vayumandal, Vol.29, No.1-4, pp.147-149.

Devendra Singh, R.C.Bhatia,S.K.Srivastav, Sant Prasad and S.K.Mukharjee ,2002,“Validation of Atmospheric temperature profiles derived using Neural Network approach from AMSU-A measurements onboard NOAA-15 and NOAA-16 satellites and their applications for tropical cyclone analysis ”, Twelfth International TOVS/ATOVS workshop, Lorne , Australia , 27 Feb. – 5 March ,2002.

Devendra Singh, and Birbal Singh, 2003a” Recent improvements in the retrievals of temperature and moisture profiles using NOAA-16 ATOVS data” Journal of Ultra Scientist of Physical Sciences, Vol.15 No.2, 2003.

Devendra Singh, R.C.Bhatia, S.K.Srivastav and Birbal Singh,2003b” An Experiment of the ICI3 Scheme for Retrieving Atmospheric Parameters over Indian region using AMSU data from NOAA-16 satellite”, Mausam,54,1(January 2003),107-110.

Krishnamurti, T.N., Arun Kumar, Yap, K.S., Dastoor, Ashu, P., Davidson, Noel and Sheng, J., 1990: 'Performance of a high resolution mesoscale tropical prediction model, Advances in Geophysics, 32, Academic Press, INC, pp.133-286.

Prasad, K., Rama Rao, Y.V., Sanjib Sen, 1997, 'Tropical cyclone track prediction by a high resolution limited area model using synthetic observations', Mausam, vol.48, No.3, 351-366

Comparison of errors of Temperature profiles using Neural Network and Physical inversion approaches for NOAA-16 satellite AMSU data

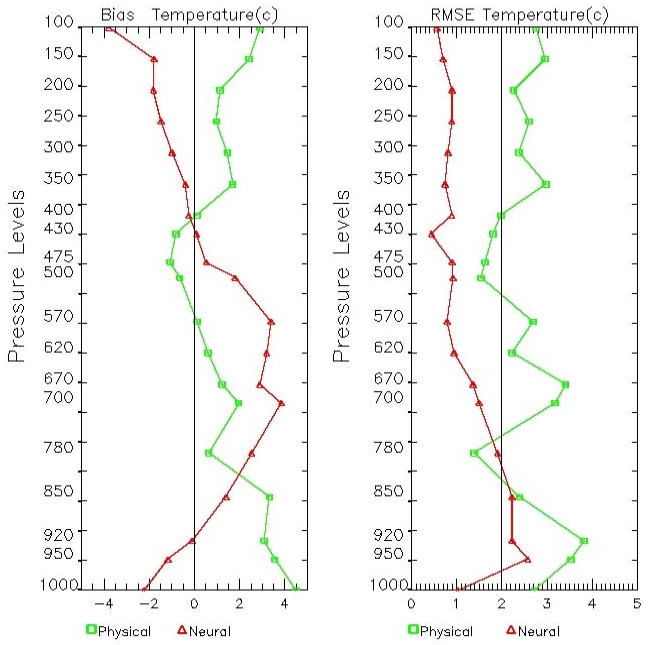

Fig-1 (a) Over Land, July, 2002

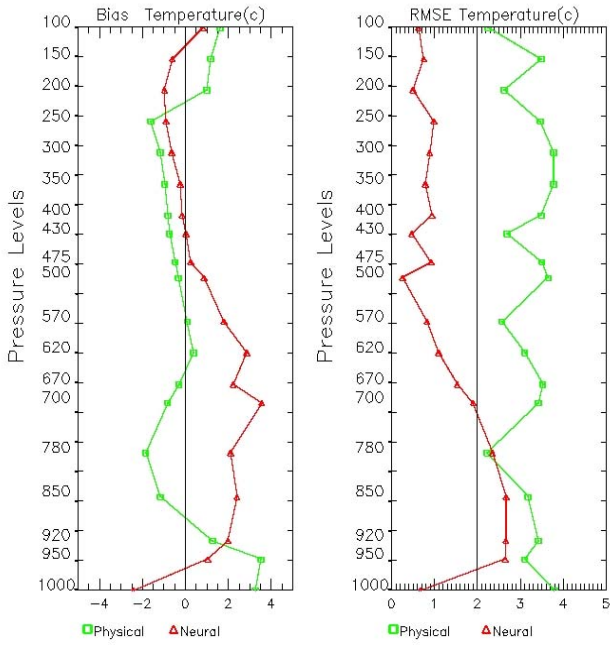

Fig-1 (b) Over Sea, July, 2002

Comparison of errors of Relative humidity profiles using Neural Network and Physical inversion approaches for NOAA-16 satellite AMSU data

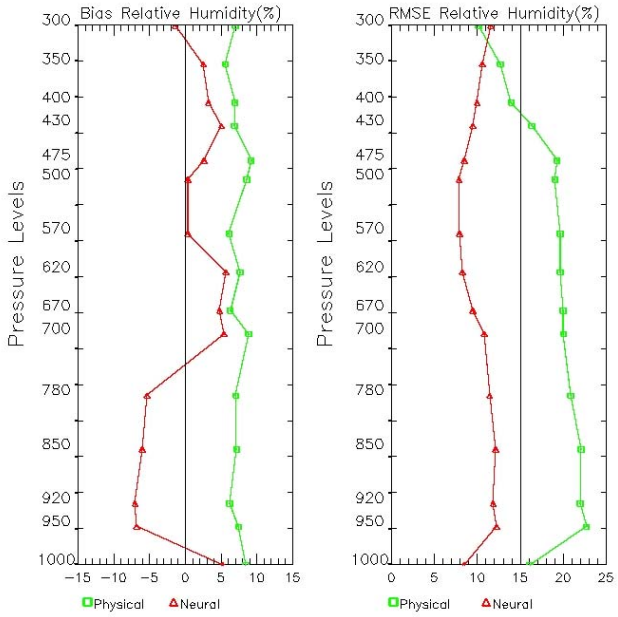

Fig-1 (c) Over Land, July, 2002

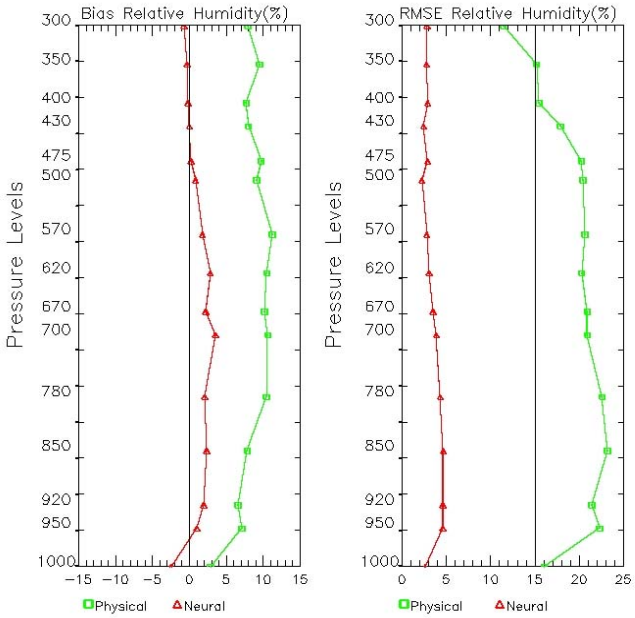

Fig-1 (d) Over Sea, July, 2002

Comparison of errors of Temperature profiles using Neural Network and Physical inversion approaches for NOAA-16 & 17 satellites AMSU data

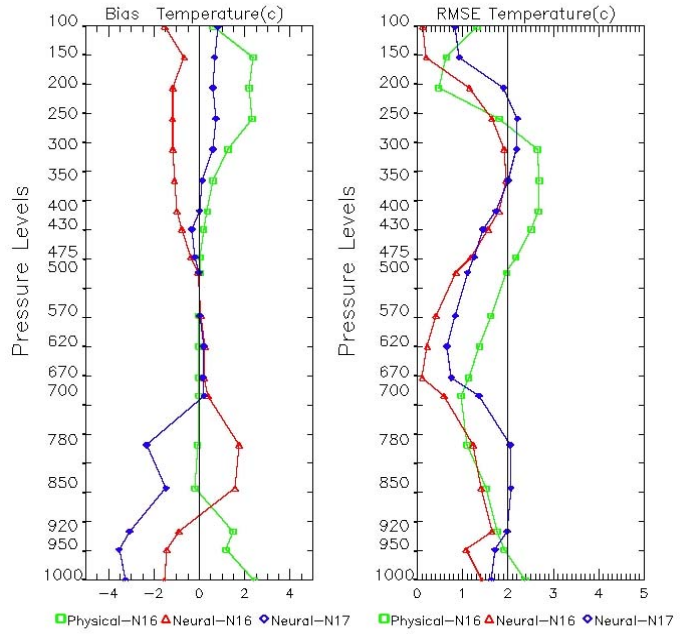

Fig-2 (a) Over Land, January, 2003

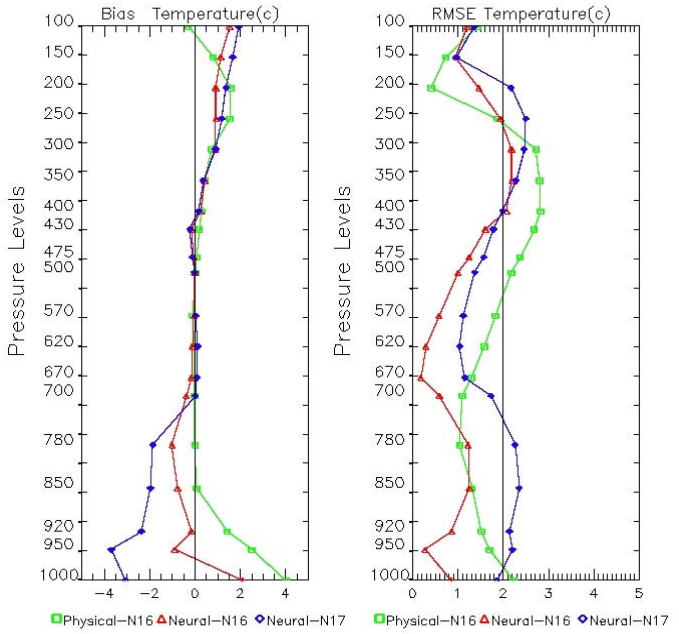

Fig-2 (b) Over Sea, January, 2003

Comparison of errors of Relative humidity profiles using Neural Network and Physical inversion approaches for NOAA-16 & 17 satellites AMSU data

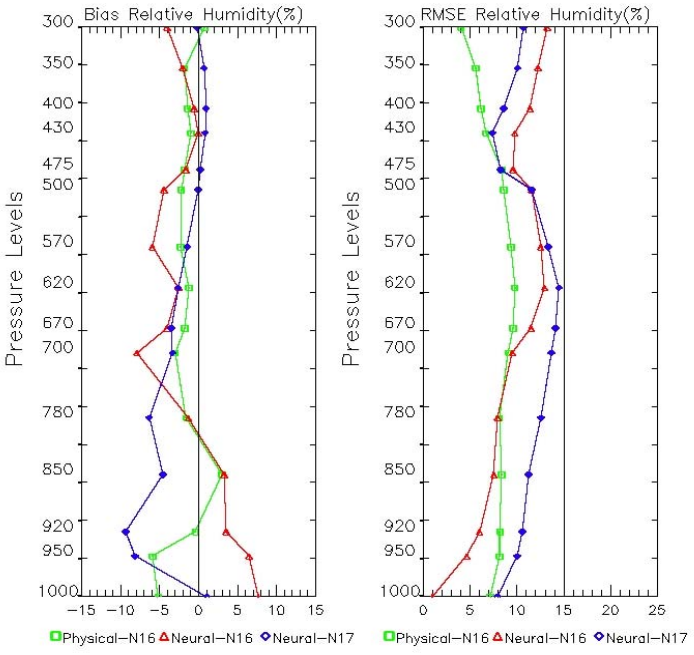

Fig-2 (c) Over Land, January, 2003

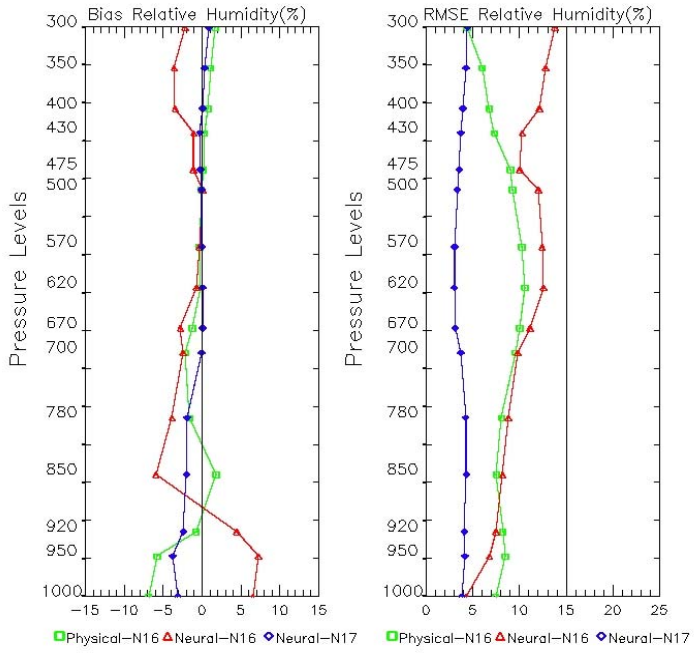

Fig-2 (d) Over Sea, January, 2003

Mean Relative Humidity (%) Analysis for 18-22 June 2003 at 850hPa level. Left: Control Right: Experiment

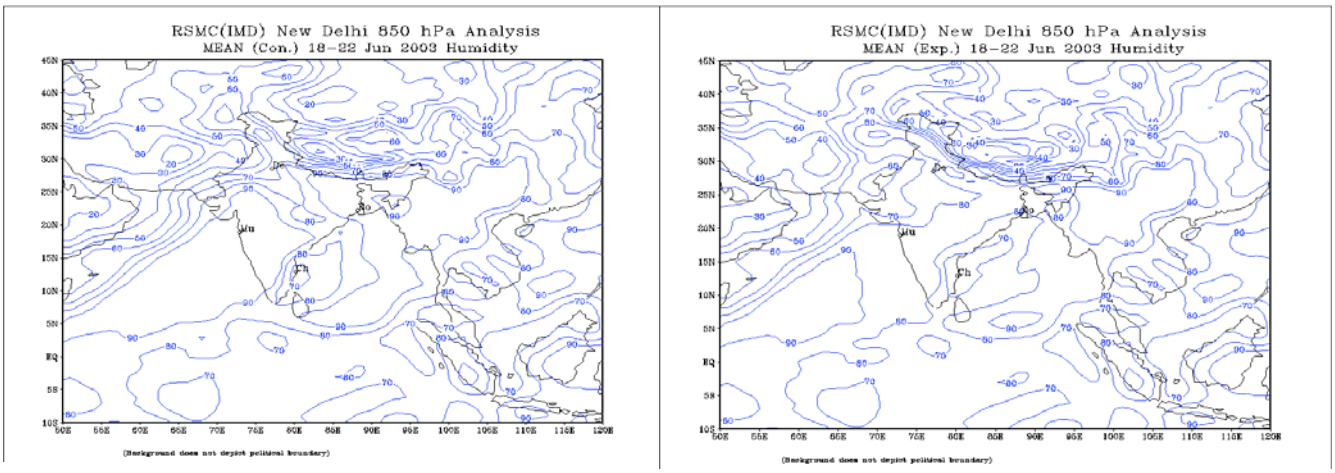

Fig-3

Mean Day-1 forecast wind (kt) for 19-23 June 2003 at 850 hPa level. Left: Control Right: Experiment

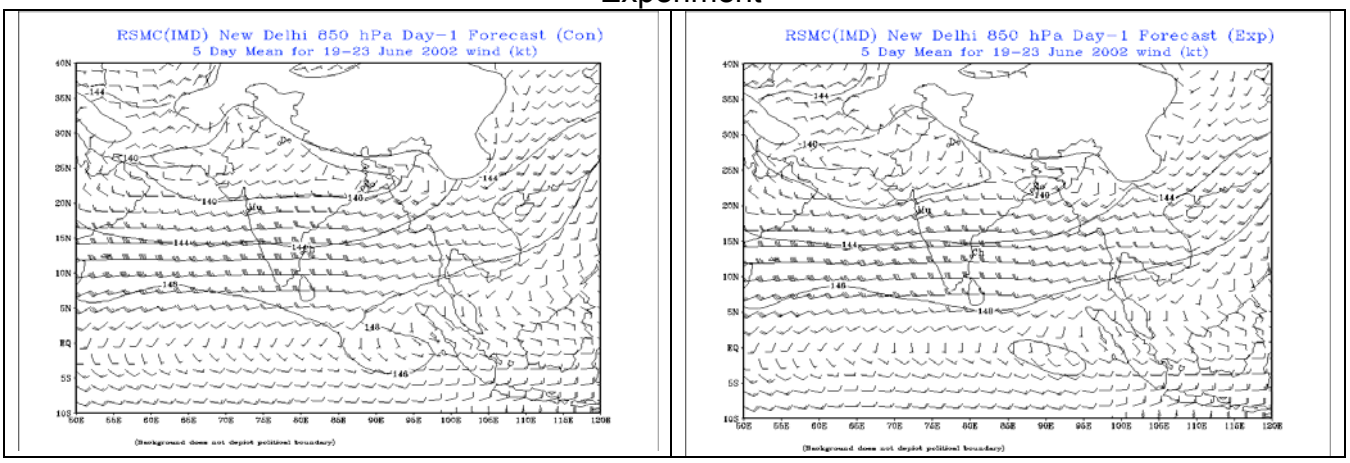

Fig.4

Mean wind (kt) analysis at 850 hPa level. Left: for 18-22 June 2003. Right: for 19-23 June

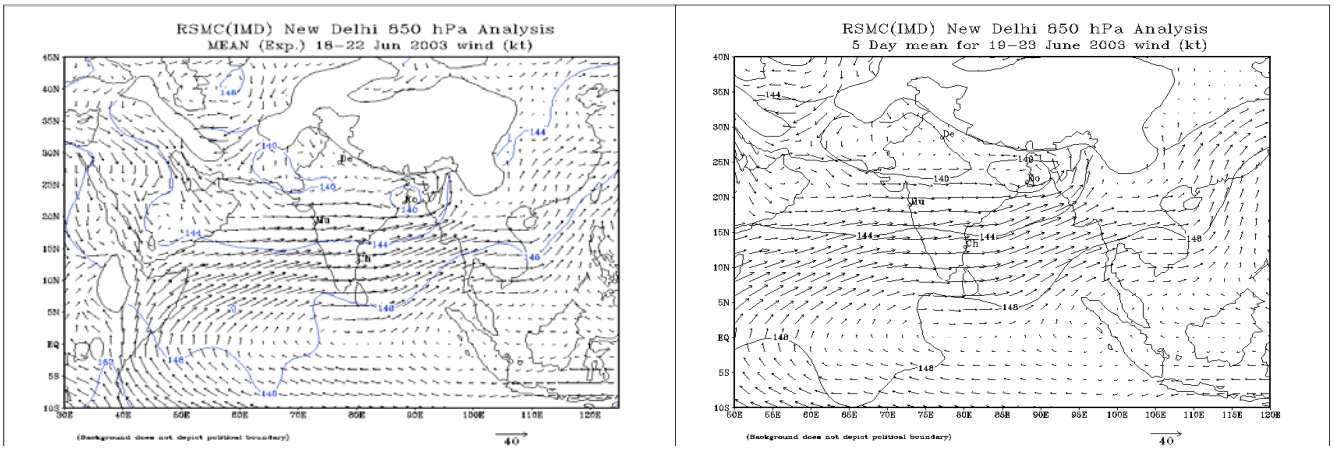

Fig.5

Mean Day-1 forecast rainfall (mm) for 19-23 June 2003. Left: Control Right: Experiment

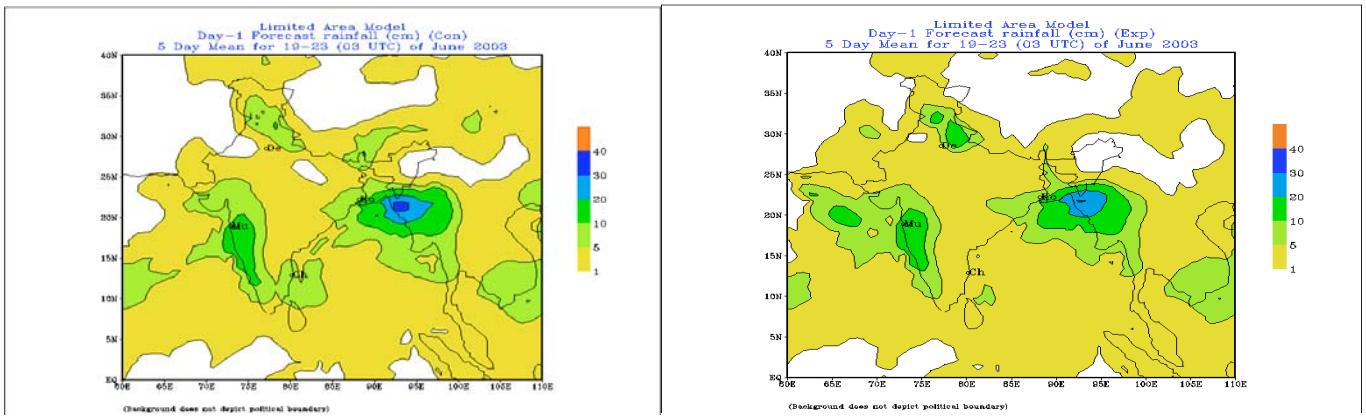

Fig.6

Relative Humidity (%) Analysis for 09 July 2003 at 850 hPa level. Left: Control Right: Experiment

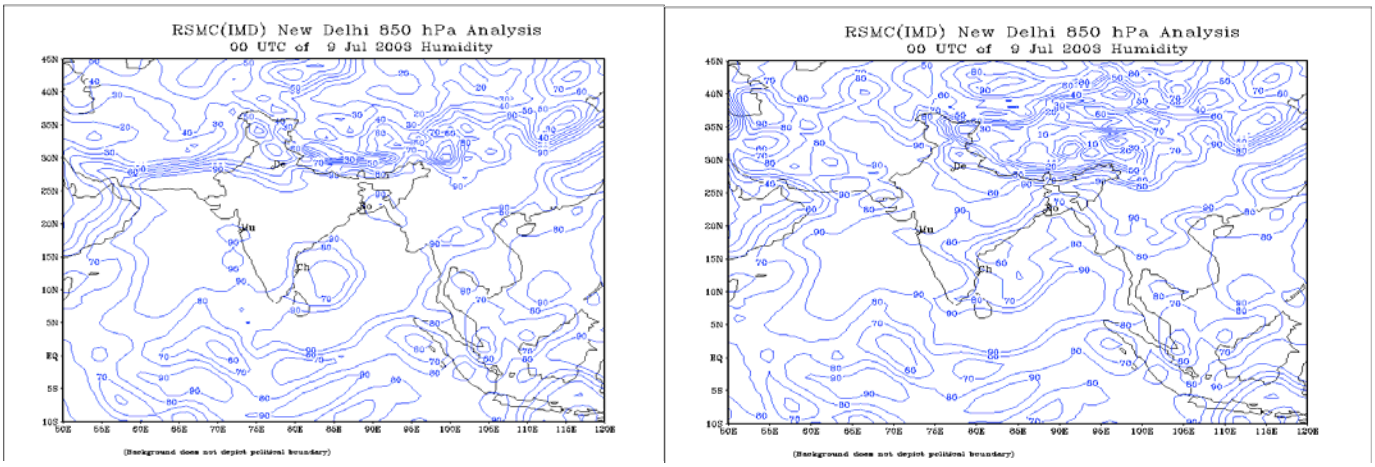

Fig.7

Day-1 forecast rainfall (mm) for 10 July 2003. Left: Control Right: Experiment

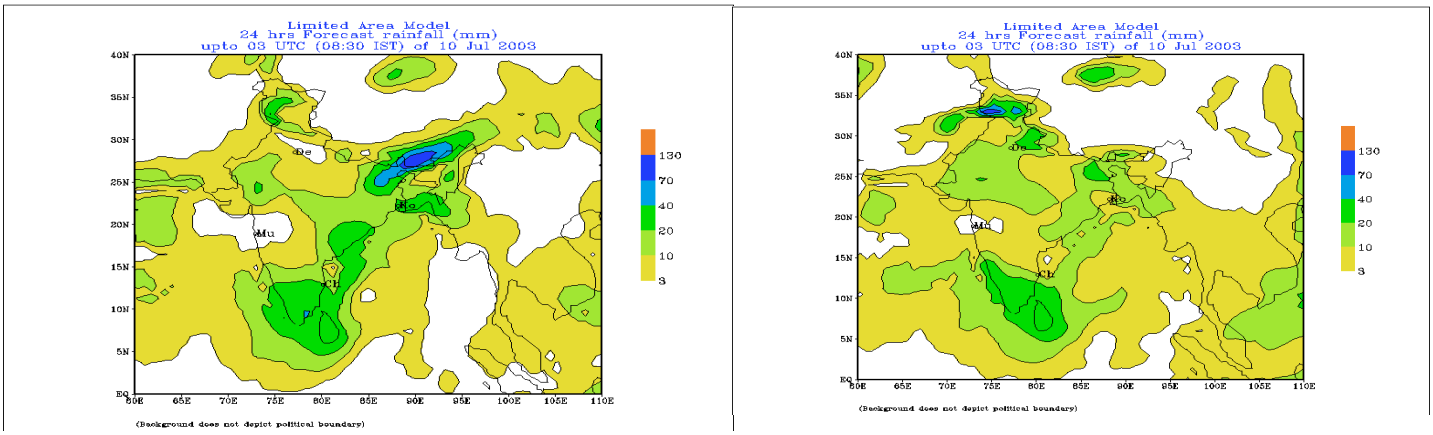

Fig.8

Mean Day-1 forecast rainfall (mm) for 25-28 July 2003. Left: Control Right: Experiment

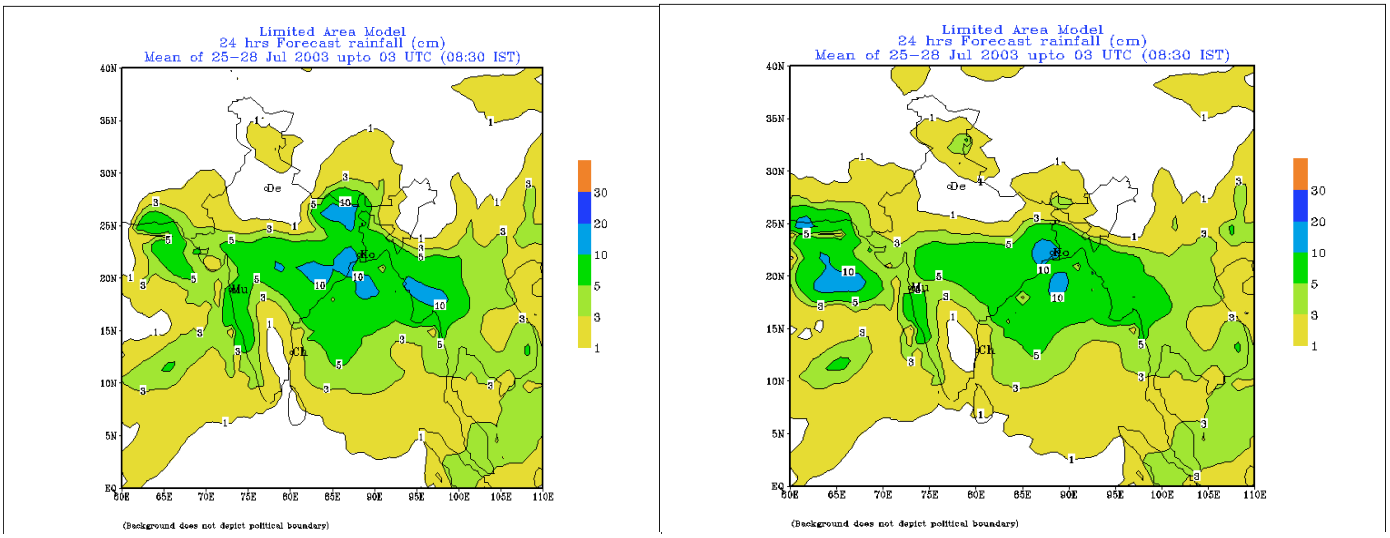

Fig.9

Dynamic Inference of Background Error Correlation between Surface Skin and Air Temperature

Louis Garand, Mark Buehner, and Nicolas Wagneur
Meteorological Service of Canada, Dorval, P. Quebec, Canada

Abstract

One neglected component of the background error covariance matrix used in data assimilation is the correlation between surface skin and air temperature errors. In the process of assimilating radiances which are sensitive to the surface, this correlation becomes important as it allows modification of the background temperature structure in the boundary layer in a more optimum way. In addition, surface data can influence the analysis of skin temperature through this correlation. The skin-air error correlation was inferred dynamically, that is locally and temporally, from ensembles of forecasts valid at the time of analysis. GOES-8 and GOES-10 imager channels were assimilated with and without skin-air error correlation using the MSC operational 3-Dvar analysis system. The impact of the correlation is assessed. Changes in the boundary layer temperature corrections of the order of 0.5 to 1.0 K are not uncommon.

Introduction

NWP centers now assimilate microwave and infrared radiances routinely, providing information on temperature and humidity in the atmosphere. However, most of the information used in NWP has a sensitivity covering the middle or higher troposphere, i.e. the range 200-600 hPa. Information at low levels is lacking, notably over land. Microwave emissivity over land is highly variable as it depends on soil moisture. The emissivity determination is also a problem in the infrared, but much less severe than at microwave frequencies. Due to the higher infrared emissivity, typically above 0.95, the sensitivity of the radiances in the boundary layer (first kilometer) is rather weak, while the sensitivity to surface skin temperature is high.

This paper explores the use of surface sensitive IR channels in NWP. In particular, one statistical parameter of interest is the error correlation between surface skin (hereafter T_s) and air (T_a) temperatures. This correlation is often set to zero for lack of better knowledge. In doing so, the analysis is clearly not optimum. NWP analyses are obtained from increments or changes suggested by the observations to a background estimate, which is typically a 6-h forecast. If the T_s-T_a correlation is high, significant changes to T_s inferred from IR radiances should translate into significant T_a changes in the boundary layer, even if the radiances are weakly sensitive to T_a in that region. In a similar fashion, increments to T_a obtained from surface 2-m observations will allow changes to T_s through the T_s-T_a correlation. Since the numbers of such surface observations is considerable, it is argued that the T_s-T_a correlation is very important in the determination of a T_s analysis. Examples of that impact are presented here.
The determination of the T_s-T_a error correlation represents a challenge. Here, it is determined from an ensemble of 64 6-h forecasts valid at the time of the analysis. The forecasts are taken from a recent

experiment using the ensemble Kalman filter (Houtekamer et al, 2003). The result is a correlation at the desired resolution which varies locally and is valid at the time of the analysis.

Determination of the T_s-T_a error correlation

The T_s-T_a error correlation is obtained from that between T_s and T_a differences with respect to the ensemble mean. In fact only the correlation between T_s and T_a at the lowest predictive level (near 70 m) is calculated. Knowing that value, the correlation between T_s and T_a at other levels is readily obtained from the T_a-T_a inter-level error correlation used in the 3D-var system. Because T_s remains constant and is not perturbed over oceans in forecast ensembles, the correlation can only be derived over land by that method. Fig. 1 shows the correlation maps valid at 06 UTC and 18 UTC June 2, 2002. The resolution, rather coarse at 150 km (240 by 120 points), is the same as that used to compute analysis increments operationally in the global MSC model. The final analysis is obtained by interpolating increments at the resolution of the forecast model, which is about 100 km (400 by 200 points). In general, the T_s-T_a error correlation is high, often exceeding 0.90. It was verified that the lowest correlations tend to occur at night time (i.e. Asia at 18 UTC or America/Greenland at 06 UTC) in regions characterized by surface temperature inversions. In some sectors, the correlation is even negative.

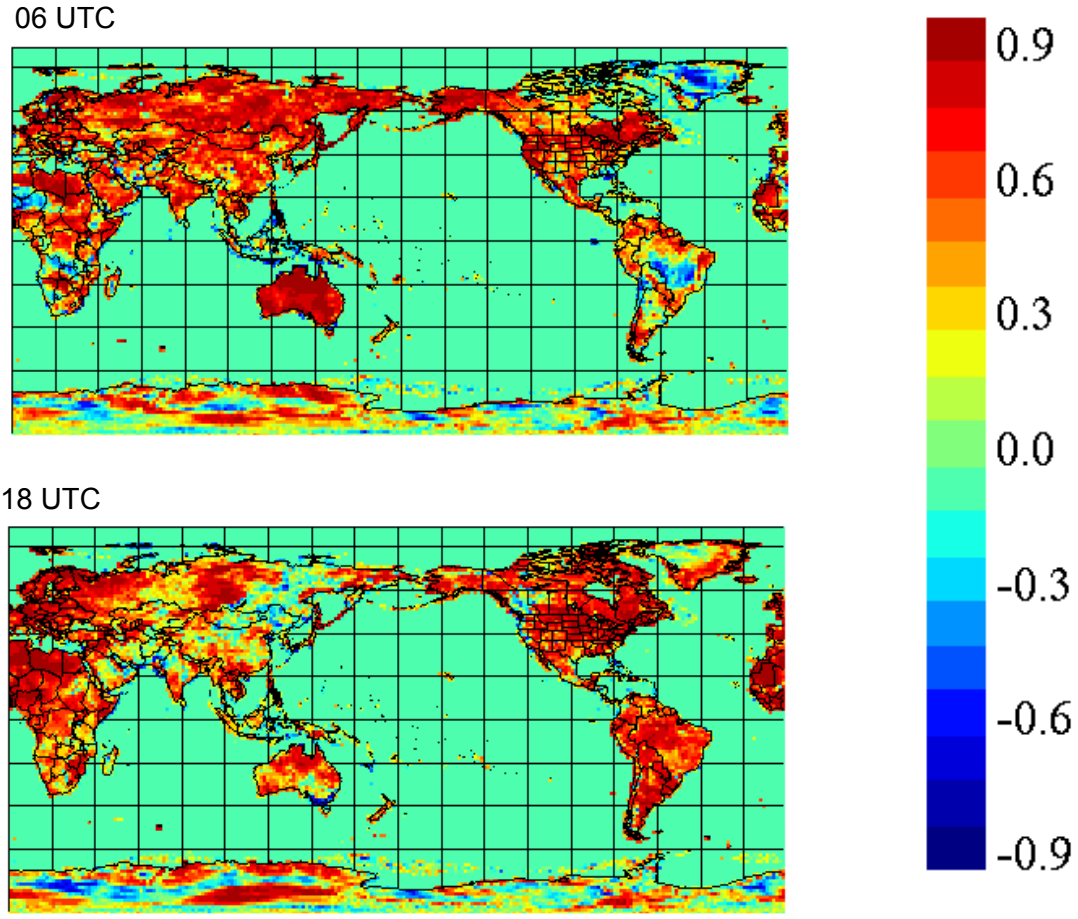

Fig. 1 T_s-T_a error correlation derived from ensemble of 6-h forecasts valid June 2 2002.

Assimilation results

GOES-8 and GOES-10 radiances from Imager 4 (IM4, 11 μ) and IM5 (12 μ) were assimilated in addition to all other data types assimilated operationally. The preparation of the radiance data is described in detail in Garand (2003). This includes the selection of the cloud free pixels, the definition of surface emissivity, and the bias correction procedure. The data cover the Americas and adjacent oceans (10 W-180 W, 60 N to 60 S). Data selected for assimilation are thinned at the resolution of 200 km, which is reasonable for the assimilation of the water vapor channel (IM3, 6.7 μ) but somewhat coarse for the mapping of T_s. Analyses were made with and without T_s-T_a error correlation presented in Fig. 1 for the corresponding two times: 06 and 18 UTC June 2 2002. Fig. 2 shows the resulting T_s analysis increments (by definition the analysis is the first guess plus the increments). The left panels, without correlation, show increments only where satellite data are assimilated. Indeed no other type of data can affect the T_s analysis with the exception of the localized influence of some TOVS microwave radiances. It is noted that increments tend to be negative at night (06 UTC) and positive in daytime (18 UTC). This result is in line with that presented in Garand (2003), i.e. there is clearly a lack of amplitude in the model T_s diurnal cycle. This tendency is largely corroborated in the analyses with correlation (right panels of Fig. 2). Through the T_s-T_a error correlation, surface data are now allowed to contribute to the T_s analysis. Again, the dominant negative increments at night and positive increments during the day give the comforting signal that both surface and satellite data tend to modify the background in the same manner. T_s increments in the range 3-5 K are not uncommon.

The left panel of Fig. 3 shows the T_a increments, with correlation, at 18 UTC. The changes are largely positive and in the typical range 1-3 K. The right panel shows the T_a (70 m) increment difference with-minus-without correlation. These differences can only occur in regions where GOES data are assimilated. This is an important result of this study: the magnitude of the changes is typically of a few tenths of degree, but may locally exceed 1 K. In the vertical, it can be shown that the effect of the correlation remains significant up to a typical height of 1.5 km. This shows that surface channels can contribute significantly to boundary layer profiling.

Validation

Figs. 2-3 showed that the T_s-T_a error correlation operates as expected. However, there is still a need to evaluate the impact of the correlation against independent measurements. Another analysis was done valid at 12 UTC June 2 2002. The numerous radiosonde profiles available at that time were not used in the analysis. Analyzed profiles made with and without correlation were interpolated at the radiosonde sites and compared with the observed profile. Comparisons at sites closest to largest T_a differences (i.e. Fig. 3, right but for 12 UTC) were carried out. The impact was found to be positive at most radiosonde sites. Fig 4-a presents results at Kelowna, British Columbia. The temperature profile with correlation is clearly improved. There is also a modest improvement in moisture. For that station located in the Okanagan valley, the model topography is at 1190 m while the true topography is at 430 m. This represents a problem for data assimilation based on the difference between observed (seeing topography at the scale of the satellite footprint, here near 10 km) and computed radiances. This situation will be alleviated with the next implementation of the global model at 50 km resolution in 2004. Fig. 4-b shows an example of a negative impact at Kuujjwuaq, Quebec (near Ungava Bay). It was found that the radiance causing that change was located about 200 km north of the radiosonde site. Thus the impact arises from the horizontal propagation of the observed negative (cold) increment to the warmer and wetter Kuujjwuaq site. This is a sector of air mass transition. Means to avoid such cases are not trivial, but could be in part minimized by a higher density of observations coupled with higher horizontal resolution in the analysis. An improved local estimate of the background T_s error would also help. The negative impact would have been significantly less if the radiosonde observation had been assimilated.

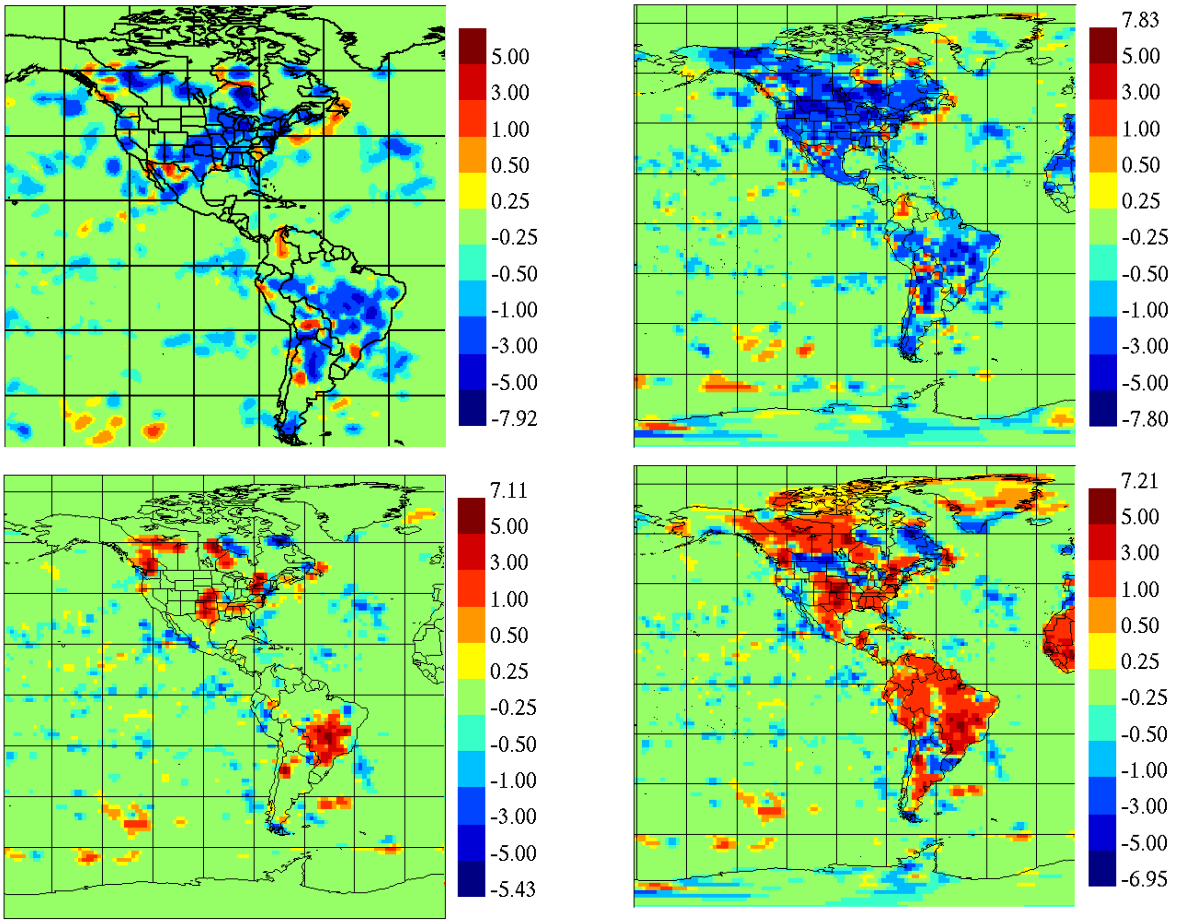

Fig.2 T_s increments at 06 UTC (top) and 18 UTC (bottom) without (left) and with (right) T_s-T_a error correlation.

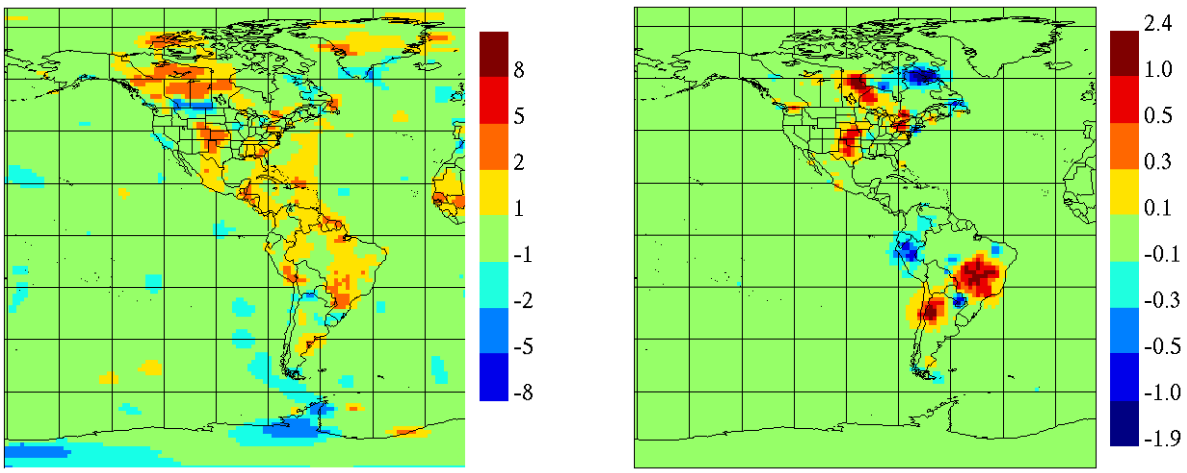

Fig. 3. Left: T_a (70 m) increments with T_s-T_a error correlation at 18 UTC. Right: difference in T_a increments with minus without correlation.

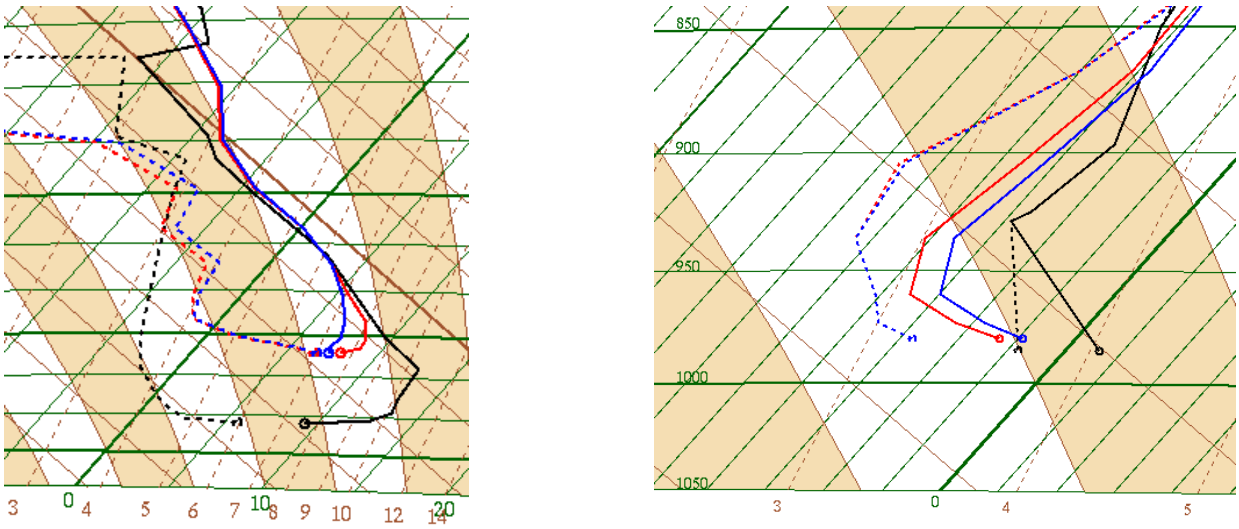

Fig. 4 Temperature (full) and dew point depression (dashed) profiles. Black: radiosonde. Red: with correlation. Blue: without correlation. Left, a) at Kelowna, B.C. Right, b) at Kuujjuaq, Que. Valid 12 UTC June 2, 2002.

Conclusion

Ensemble forecasts are used to infer the T_s-T_a background error correlation as a function of time and location. This methodology may appear at first quite expensive. However ensemble forecasts are developing rapidly at NWP centers and will soon become a routine product. One of the main reasons these ensembles are made is precisely to derive flow dependent background error covariance estimates which can then be used in NWP data assimilation. The T_s-T_a error correlation used here is just one statistical measure which can be derived from the ensembles. At first glance, this product appears realistic. The correlation tends to be generally high, with lower values, as expected, in situations of surface inversions. A remaining problem is to infer the correlation over oceans. There, a reasonable estimate can perhaps be made based on local estimates of static stability.

It was shown that the T_s-T_a background error correlation has a significant impact, in general, on both the analysis of T_s and that of T_a in the boundary layer. The impact is particularly important where infrared radiances sensitive to the surface are assimilated. The study also points to practical problems related to horizontal resolution and horizontal correlation of background errors. It is also possible to incorporate a forward operator relating T_a and T_s with surface values of temperature and humidity needed to compute radiances. This approach is currently under investigation. Even with such an operator, there will still be a need for a good estimate of the T_s-T_a error correlation.

Reference

Garand, L., 2003: Toward an integrated land-ocean surface skin temperature analysis from the variational assimilation of infrared radiances. J. of Applied Meteor., 42, 570-583.

Houtekamer, P., H. Mitchell, G. Pellerin, M. Buehner, M. Charron, L. Spacek, and B. Hansen, 2004: Atmospheric data assimilation with the ensemble Kalman filter: Results with real observations, to appear in Mon. Weather Rev.

First results of the assimilation of AIRS data in Météo-France Numerical Weather Prediction model

Thomas Auligné*, Florence Rabier*, Lydie Lavanant**, Mohamed Dahoui***

** Météo-France, Centre National de Recherche Météorologique,*
42 ave. Coriolis, 31057 Toulouse Cedex 1, France
*** Météo-France, Centre de Météorologie Spatiale,*
BP 147, 22300 Lannion Cedex, France
**** Moroccan Meteorological Service*

Abstract

A subset of channels from AIRS (Atmospheric InfraRed Sounder) aboard AQUA satellite is provided operationally by NOAA/NESDIS to Numerical Weather Prediction (NWP) centers. Studies have been carried out to assimilate this data in the Météo-France NWP suite. They require performance monitoring and bias correction of the observations. The impact of the early assimilation of AIRS on numerical weather forecast is presented.
Infrared radiances are contaminated by clouds in most cases. Therefore, there is a need for a cloud detection scheme. This study focuses on the NESDIS method (Goldberg et al., 2003) that has been validated in a comparison study by Lavanant et al. (2003). In order to take more advantage of the available data, the assimilation of cloudy radiances is investigated, using a radiative transfer model in cloudy conditions (RTTOVCLD). Results from monitoring and 1D-Var assimilation experiments are shown.

Introduction

The Atmospheric InfraRed Sounder (AIRS), launched by NASA in 2002 aboard the AQUA satellite is the first instrument of a new generation called “advanced infrared sounders” (Aumann et al., 2003). 2378 channels are available within the 3.7-15.4 micron range, most of them showing an excellent performance regarding their spectral response and sensitivity. The AQUA polar-orbiting platform provides global coverage of measurements. Thus, an important impact of the assimilation of AIRS data is expected on weather forecast skills.
On the other hand, new challenges are directly linked to this generation of instruments and they need to be solved in order to take full benefit of the data. The first and probably main problem is the dramatic increase of the number of channels (about two orders of magnitude). This results in communication, computing and storage issues. Since NWP centers have a “real-time” constraint for data assimilation, it is currently impossible to assimilate all AIRS channels operationally.
A constant subset of 328 channels is provided by NOAA/NESDIS for AIRS center pixel of every other AMSU field of view (*i.e.* 1 AIRS pixel over 18). Using this product, a first assimilation suite has been implemented to study the impact of AIRS data on weather forecast.
The potential use of cloudy radiances is investigated in a uni-dimensional, non-linear variational algorithm. A diagnostic cloud scheme linking temperature and humidity to cloud variables has been implemented in order to use selected AIRS cloudy radiances to retrieve temperature and humidity profiles.

A conservative assimilation suite

AIRS is providing so many channels that it becomes very difficult to tune the assimilation system for each individual channel. Experiments have shown that mis-using a single channel can degrade dramatically the whole assimilation. Thus it is much easier to degrade the system than to improve it. In this perspective, a conservative suite has been operated that relies on simple tools and should constitute a solid basis for step-by-step developments. An important part of good quality data is currently rejected in the assimilation, decreasing the impact of AIRS on weather forecast, but the main concern in this first experiment is to make sure of the quality of the information introduced in the system.

The NWP system is the French operational model ARPEGE. It is a global spectral model with a linear truncature T358 and 41 vertical levels. The horizontal grid is stretched with a factor C2.4, leading to a resolution from 25km over France to 150km at the antipodes. The assimilation system is a multi-incremental 4D-Var with T107 and T161 truncatures and a stretching factor C1. The assimilation time-window has a range of 6 hours. In this study the latest version of ARPEGE is used ; it includes the assimilation of AMSU-A and HIRS radiances.

To perform the assimilation of AIRS data we follow the general steps needed for the assimilation of a new instrument. Since ARPEGE is very close to IFS model from the European Center for Medium range Weather Forecast, many tunings are identical to the ones chosen by ECMWF. The subset from NOAA/NESDIS includes AIRS pixels with a horizontal sampling of about 90 km; thus no additional thinning is performed. A data quality flag is available in the provided files and is used as a first information for rejection. The screening starts with the calculation of the model-equivalent observation using RTTOV-6M radiative transfer model. Temperature and humidity profiles are needed to 0.1 hPa, so the model is extrapolated above its 1 hPa top.
A gross check is performed on the observations and departures (*i.e.* observation minus model-equivalent observation) for every channel to make sure they stand in reasonable bounds. Then a first-guess check rejects channels whose departures are not compatible with error statistics. These statistics are defined very simply : the background error is set constant for all channels, and the observation errors are defined for wide ranges of the spectrum (0.6 K for upper-temperature channels, 1 K for lower-temperature channels, 2 K for water-vapor channels).
Within the 324 channels provided in the NOAA/NESDIS subset, several are blacklisted (*i.e.* not used in the assimilation). This is the case for channels peaking above or near the model top (1hPa) where the model performance is not sufficient, for channels in the ozone band since ARPEGE only uses climatological ozone information, for channels in the short-wave region that are contaminated by solar reflection during day-time.
Data over land, where surface emissivity is not known precisely enough, are rejected. The edges of the scan, showing significant biases in the radiative transfer calculation, are also are not used.

Infrared radiances are contaminated by clouds; the method chosen in this study consists in selecting pixels that are clear. To achieve this goal, we use the NESDIS cloud detection scheme (Goldberg et al., 2003) based on several tests using AIRS selected channels and the model Sea Surface Temperature (SST). First the brightness temperature for a long-wave window channel (965.43 cm^{-1}) needs to be higher than 270 K. Then the model SST is compared to a predicted SST (from channels 918.65, 965.32, 1228.09, 1236.40 cm^{-1}) and during the night-time to a short-wave window channel (2016.095 cm^{-1}), with thresholds that have been recomputed for ARPEGE performance. This scheme has been compared to other cloud detection schemes and to the MODIS cloud mask collocated with AIRS in a validation study by Lavannant et al. (2003).
During the day-time an additional test has been implemented, rejecting data where AIRS VIS/NIR imager shows more than 10% of cloud inside the AIRS field of view.

After blacklisting, data-quality and cloud-contamination tests, only a small amount of the initial data (about 3 %) is flagged "active" and will go through the rest of the assimilation. An example of the status for window channel 917.31 cm^{-1} is displayed in Fig. 1.
For an initial dataset, a constant bias is calculated for each channel within active data. This flat bias correction is then applied to the corresponding departures during the assimilation. Fig. 2 represents the initial and residual biases for active data within a 6h time-window.

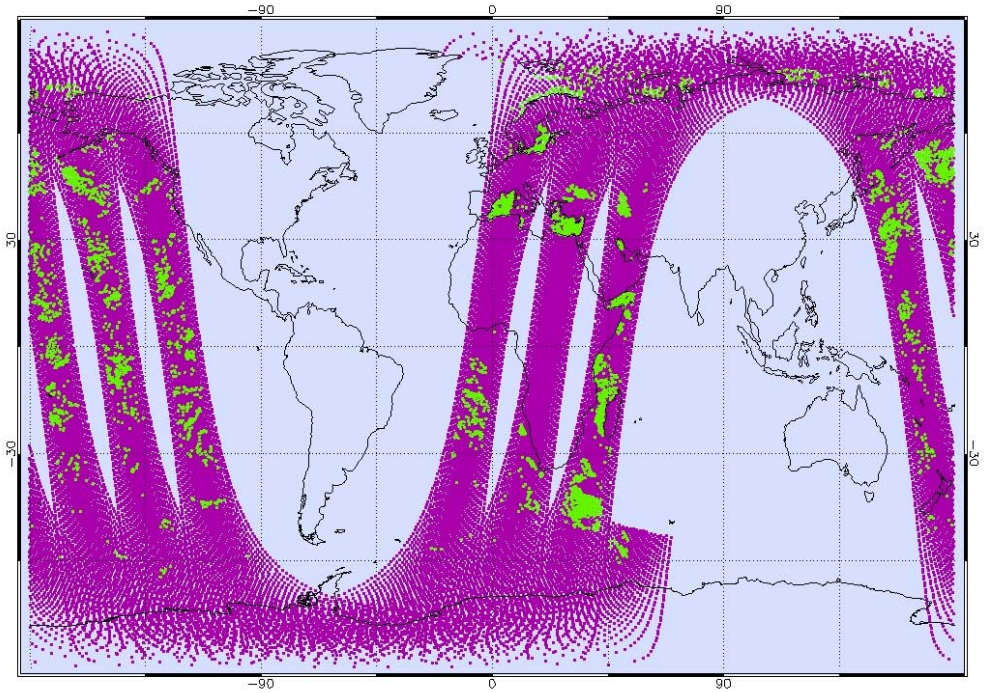

Fig. 1: Status of AIRS window channel 917.31 cm^{-1} after screening. 6h time-window for 2003/08/01 at 00UTC. Green means active ; purple corresponds to rejected data.

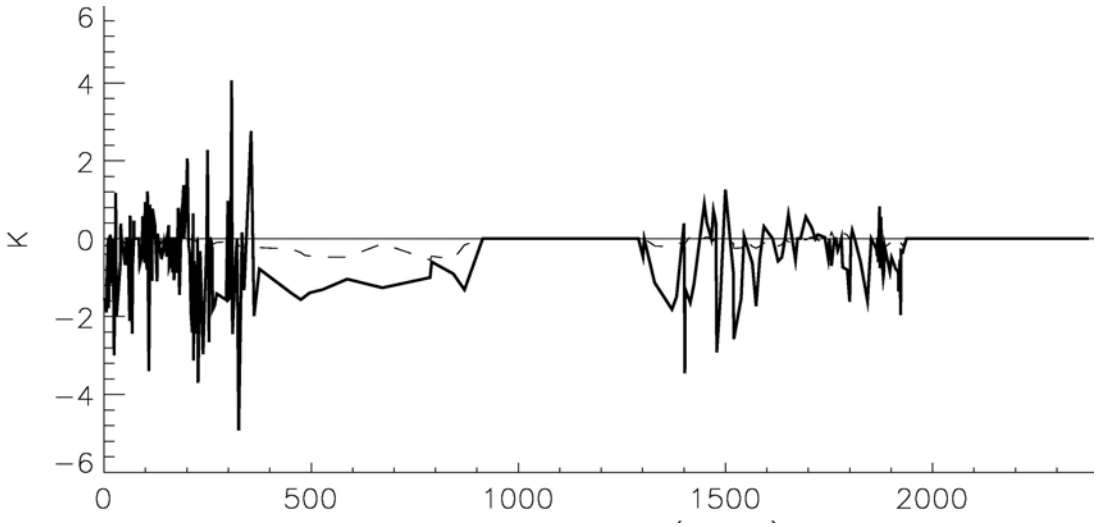

Fig. 2: Observed minus calculated brightness temperatures (in K) averaged for active data within the 6h time-window as a function of AIRS channel number (1→2378). The thick solid line represents the bias before flat bias correction and the dashed line corresponds to the residual bias after bias correction.

Impact of AIRS data on weather forecast

An impact study is performed on the period from the August 1st to August 19th 2003. The "CTRL" experiment is the most recent ARPEGE suite, while the "EXP" experiment is the same suite with the additional assimilation of all the available AIRS data in the 6-hour assimilation time-window. More iterations are allowed in the second 4D-Var minimisation of EXP in order to deal with the overhead of information.

Fig. 3 displays the difference of root mean square errors of CTRL minus EXP with respect to radiosondes. Green lines mean a positive impact of AIRS; red lines correspond to a negative impact. It is first important to notice that the differences between the two experiments are small. Considering the conservative approach followed to introduce AIRS data, where most of the information is rejected, this result is fully understandable.

For geopotential over all domains (Fig.3a), the impact of AIRS is negative above 200 hPa. This can be partially explained by the bias of radiosondes, used here as verification, that increases with the altitude but is not currently corrected. When using ECMWF analysis as verification (not shown), this negative signal is greatly decreased. A slight positive impact for geopotential over the whole troposphere is seen at the latest ranges of forecasts, especially over Europe.

This pattern is also seen for humidity (Fig. 3c) over Europe. Mid-to-high tropospheric humidity is slightly improved with AIRS for 72-96h range forecasts over the southern hemisphere. Temperature (Fig. 3b) is globally neutral, with a small negative impact in most cases at low levels overlooked by a slight positive effect of AIRS for the rest of the troposphere at long range.

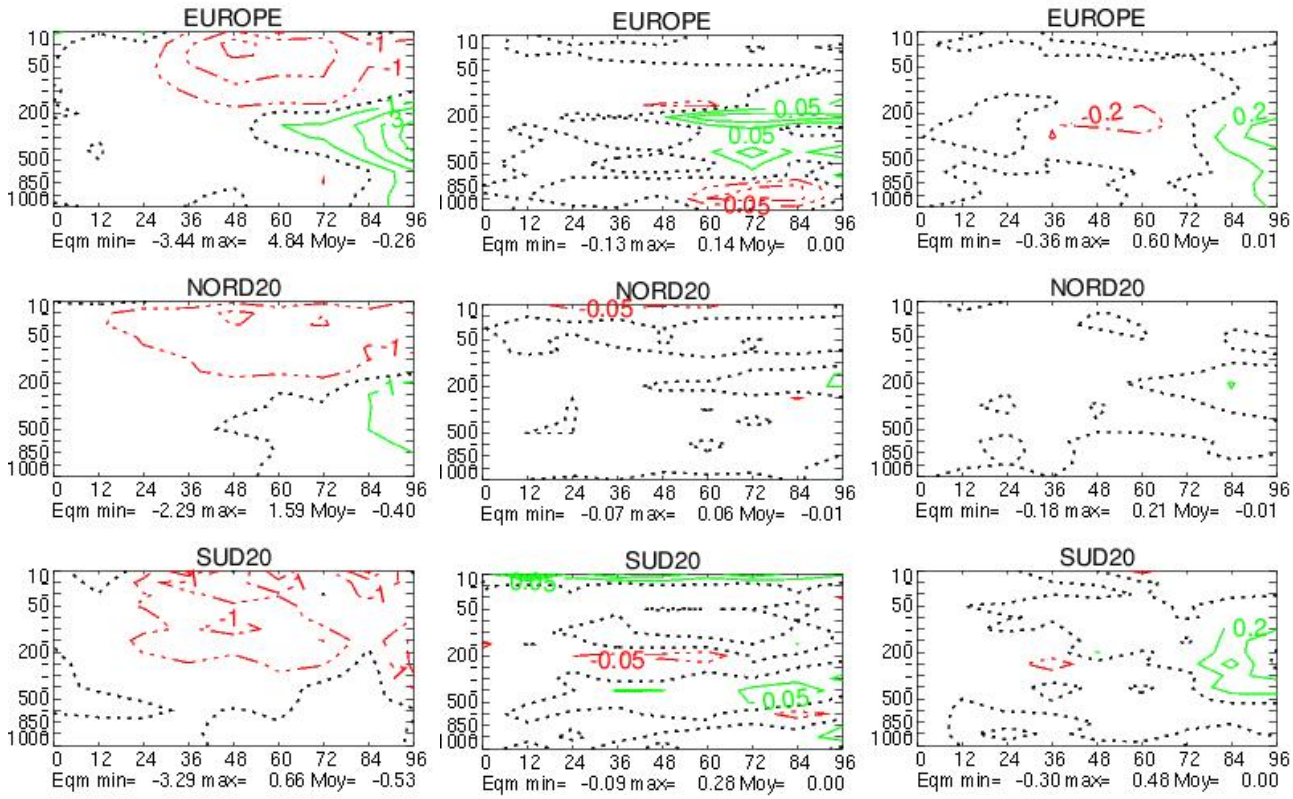

a) b) c)

Fig. 3: Root Mean Square Error (RMSE) of CTRL minus RMSE of EXP with respect to radiosondes for a) geopotential, b) temperature, c) humidity. The X and Y axis define respectively the forecast range and the vertical pressure levels. Positive values are represented in green, negative in red.

1D variational retrieval experiments in cloudy conditions

Developments are on-going at Météo-France for the use of cloudy radiances. For the sake of simplicity, the problem is currently considered uni-dimensional. The approach is based on a non-linear 1D-Var algorithm and the aim is to use selected AIRS cloudy radiances to retrieve temperature and humidity profiles. The observation operator includes RTTOV-7 radiative transfer 0model which contains a cloud-processor module RTTOVCLD (Saunders and Brunel, 2002). A simple diagnostic cloud scheme has been implemented. It reproduces the features from the operational ARPEGE cloud scheme (Gérard, 2001) with a cloud cover evaluation following Xu and Randall (1996). Cloudiness has three origins: large scale (stratiform cloud), subgrid shallow convection and subgrid deep convection over-saturations. For this preliminary study only stratiform and shallow convection clouds are modelled. Indeed, deep convection requires precipitation fluxes from the previous time step. The developed scheme diagnoses the cloud cover, cloud liquid water content and cloud ice water content for the 41 ARPEGE vertical levels. These output parameters are supplied as input, together with control variables T, q and p_s, to RTTOVCLD.

To be in agreement with our simple cloud scheme, we use AIRS cloud information derived from the CO_2-slicing algorithm (Lavanant et al., 2003) to select AIRS FOVs covered by low stratiform clouds (characterized by a cloud top pressure around 800 hPa and a high effective emissivity).

Some retrieval experiments in cloudy conditions (Dahoui et al., 2003) result in improvements on temperature especially at high levels, and in a less pronounced way on humidity (not shown).

During our validation experiments, we noted that the observation operator (cloud scheme + RTTOVCLD) is strongly non-linear for a large number of AIRS CO_2 channels (depending on cloudiness amount). However for some of the tropospheric channels (listed in Table 1) the observation operator is nearly linear in every condition. This result confirms the conclusions from Chevalier et al. (2003). Unfortunately, these channels are far from the influence of low clouds. One can try to perform retrievals in the presence of high and medium-level large-scale clouds.

Table 1: AIRS channels used in 1D-Var retrievals

AIRS Channel	Wavenumber (cm^{-1})	Wavelength (μm)
6	650.81389	15.365376
28	656.12392	15.241023
42	659.55137	15.161821
55	662.76824	15.088230
71	666.77337	14.997599
124	680.41240	14.696969
139	689.77010	14.497584
145	691.39968	14.463414
157	694.68279	14.395059
162	696.06025	14.366572
192	704.44434	14.195586
198	706.14606	14.161376

Conclusion and perspectives

AIRS data has been introduced in Météo-France 4D-Var assimilation system in a conservative manner. The results on weather forecast skills are neutral to slightly positive. They need to be confirmed with more extensive experiments and will be improved by adapting the system to the special requirements of Advanced Infrared Sounders.

Harris and Kelly (2001) bias correction scheme is implemented. It performs a linear regression with fixed predictors derived from the model fields and scan angle with a latitude dependency. A new bias correction scheme based on artificial neural networks is also investigated.

The cloud detection used in this study provides information on a pixel-by-pixel basis. Therefore most of the information AIRS instrument could bring is rejected because of possible cloud contamination. We believe that the assimilation of data from cloudy pixels is one of the major issues for the full exploitation of advanced infrared sounders. A new cloud detection scheme based on a channel-by-channel basis (McNally and Watts, 2001) that can retain information above the cloud top is currently under study.

The first 1D-Var experiments of retrievals in cloudy conditions are encouraging but face the problem of strong non-linearity for most AIRS channels when they are cloud-contaminated. Retrieving cloud top pressure and emissivity for the assimilation of channels that peak near the cloud top could be an alternative and needs to be studied. Finally cloud-cleared radiances presented by Goldberg et al. (2003) show an important potential benefit for NWP and will be addressed in a close future.

Even when regarding clear pixels, assimilating only a constant subset of channels means a significant loss of the available information. On the other hand NWP centers cannot afford to assimilate operationally all channels the "usual" way and this would be pointless because of the strong correlations existing between the channels. Data mining needs to be performed and a good candidate for this operation is Principal Component Analysis as presented by Huang and Antonelli (2001) that furthermore shows special abilities in filtering the instrument noise.

References

Aumann H., Chahine M., Gautier C., Goldberg M., Kalnay E., McMillin L., Revercomb H., Rosenkranz P., Smith W., Staelin D., Strow L., Susskind J., 2003 : AIRS/AMSU/HSB on the AQUA mission: Design, science objectives, data products, and processing systems, *IEEE transaction on geoscience and remote sensing*, **41,** 253-264.

Chevalier F., Lopez P., Tompkins A., Janiskova M. and Moreau E., 2003 : The capability of 4D-Var systems to assimilate cloud-affected satellite infrared radiances. *NWP-SAF document*, NWPSAF-EC-TR-008.

Dahoui M., Auligné T., Lavanant L., Rabier F., 2003 : Use of Modis imager data to help dealing with AIRS cloudy radiances in interesting synoptic situations, *NWP-SAF document*, NWPSAF-MF-VS-003.

Gérard L., 2001 : Physical Parametrizations in ARPEGE-ALADIN operational model. *Météo-France internal documentation*.

Goldberg M., Qu Y., McMillin L., Wolf W., Zhou L. and Divakarla M., 2003 : AIRS Near-Real-Time Products and Algorithms in Support of Operational Numerical Weather Prediction. *IEEE transaction on geoscience and remote sensing*, **41-2,** 379-389.

Harris B. and Kelly G., 2001 : A satellite radiance-bias correction scheme for data assimilation. *Q. J. Roy. Meteor. Soc.*, **127**, 1453-1468.

Huang A. and Antonelli P., 2001 : Application of Principal Component Analysis to high resolution infrared measurement compression and retrieval. *J. Applied Meteorology*, **40**, 365-388.

Lavanant L., Dahoui M., Rabier F., Auligné T., 2003 : Use of MODIS imager to help dealing with AIRS cloudy radiances, *ITSC13 proceedings*.

McNally A. And Watts P., 2003: A cloud detection algorithm for high spectral resolution infrared sounders. *Q. J. Roy. Meteor. Soc.*, in revision.

Saunders R. and Brunel P., 2002 : RTTOV-7 technical report, *NWP-SAF document*, NWPSAF-MO-TR-009.

Xu and Randall, 1996 : A semiempirical cloudiness parametrization for use in climate models. *Journal of Atmospheric Sciences*, **53**, 3084-3101.

The assimilation of AIRS radiance data at ECMWF

A.P. McNally, P.D. Watts, J.A. Smith
European Centre for Medium-range Weather Forecasts
Reading, RG2-9AX, UK

Introduction

The NASA AQUA spacecraft was launched in May 2002 and a subset of radiance data from the AIRS instrument (324 channels from 2378 at 1 sounding location out of 18) have been made available to ECMWF in near-real-time (NRT) since the end of October 2002. Prior to this date a significant amount of technical development was achieved using simulated AIRS data sets routinely provided by NOAA/NESDIS and some early scientific validation was also performed using a pre-released "focus-day" of data (for 24 August 2002). As a result of this preparation the processing (i.e. cloud-screening and monitoring) and assimilation impact experiments were able to commence almost immediately following the arrival of the real AIRS data. This memo documents the progress to date and concludes that we now have a safe "conservative" assimilation system for AIRS which should be considered for a day-1 operational implementation.

Initial evaluation of the AIRS radiance data

Before any assimilation experiments were performed the degree of consistency between AIRS radiances simulated by our radiative transfer model (RTM) and the radiances measured by the instrument had to be evaluated. This not only quantifies the accuracy of the instrument spectral characterization, but also the accuracy of the RTM. Figure 1 shows mean observed minus background radiance departures for data determined as clear (the identification of clear data will be discussed in the next section). It can be seen that the bias indicated by the red line (corresponding to the post-launch spectral response functions) is generally quite small and certainly at a level where it becomes difficult to attribute the source of the bias (i.e. systematic errors in the instrument, RTM or the background fields of temperature and humidity). The largest biases are found in channels with a strong sensitivity to water vapour and the shortwave channels with a sensitivity to solar radiation (not currently modelled by our RTM).

The departure statistics have been found to be very stable in time, but also display very little air-mass dependence. Figure 2 shows zonally averaged biases for channels in the 15 micron band of AIRS ranked vertically from the surface to the top of the atmosphere. On the right hand axis the pressure at which the channel Jacobian reaches a maximum is shown (i.e. its peak sensitivity). For channels sensitive to the mid-troposphere and lower stratosphere there is only a small geographical variation in the bias. Channels peaking near the top of the model display much larger variations with latitude, but these variations are consistent with our knowledge of model systematic temperature errors (from AMSUA and HALOE) and are unlikely to be due to air-mass dependent biases in the AIRS data. Window channels peaking at the surface also show larger systematic variations, but it is impossible to distinguish if these are true biases in the AIRS data or systematic errors in our modelling of the surface emission (i.e. from the model skin temperature and emissivity) or indeed problems detecting cloud over these surfaces. On balance it was concluded that air-mass dependent biases were not significant and that

assimilation experiments could commence with a very simple static (in time) and flat (in space) bias correction applied to the AIRS radiance data. Standard deviations of observed minus background departures (not shown) were found to vary between less than 0.5K for the best channels (dry temperature sounding channels) and 1-2K for the worst channels (i.e. those sensitive to water vapour and temperatures around the surface / stratopause). In most cases the random departure statistics for AIRS were found to be very consistent with values for similar channels on other sensors (e.g. HIRS / AMSUA) that have been observed for many years.

The identification of clear AIRS channels

The cloud detection scheme for AIRS is described in *McNally and Watts 2003* and will not be reproduced here. In summary it is a novel technique for the identification of clear channels at a particular location rather that the more traditional approach of identifying clear locations. Figure 3 shows the location of clear data (shown by red) in 3 different channels for a typical case. The coverage of clear data in the sounding channel sensitive to the upper troposphere / lower stratosphere is only occasionally interrupted by very high cloud, but significantly more data is lost in the channel sensitive to the mid-troposphere. The window channel coverage is sparse and corresponds to the limited number of locations where the atmosphere can be identified as completely clear to the surface. The cloud detection scheme has a number of tuneable parameters which have initially been set to rather stringent values. This possibly results in the wrongful rejection of some clear data, but ensures that errors due to undetected residual cloud contamination in channels flagged clear are very small.

Assimilation configuration for AIRS radiances in 4DVAR

Following a reasonably comprehensive set of experiments carried out over a 1 month initial trial period in October / November 2002 (at a reduced T159 resolution and using a 6hr 4DVAR) we converged upon an initial configuration for the use of the AIRS radiances, the key elements of which are summarized below:

- Input radiance data consists of sampled 1/18 locations and 324/2378 channels

- No assimilation of channels in the O_3 or 4.2 micron band (approximately 100 of the 324 channels)

- Over sea, all channels flagged clear (including window channels) are assimilated

- Over land, only long-wave channels peaking above approximately 400hPa are assimilated

- Soundings are thinned to a horizontal spacing of 120Km preferentially retaining the clearest

- Flat (single global number rather than varying) bias correction used for each channel

- Simple observation error assigned to different blocks of channels (0.6K for dry tropospheric temperature channels away from the surface and stratopause, 1.0K for

stratospheric temperature sounding channels and 2.0K window channels and channels sensitive to water vapour).

The testing that led to this configuration considered a variety of performance measures including the size of analysis increments, the fit to other observations and forecast impact. The configuration selected is by no means optimal, but rather represents a reasonably safe *baseline* system that could be tested as a candidate for day-1 operational implementation. Many of the data excluded from this configuration clearly convey valuable information, but were considered higher risk options until further work on elements such as cloud detection, modelling land surface emission, ozone and solar radiation could be done. The observation errors are similarly set to conservative levels. While these almost certainly overestimate the true observation errors, we currently take no account of inter-channel error correlations and thus some degree of inflation is justified.

Impact experiments using AIRS radiance data

The baseline AIRS configuration described above has been tested at full resolution in 12hr 4DVAR using cycle 25R4 of the IFS between 10 Dec 2002 and 19 March 2003 (a total of 100 cases) and is subsequently referred to as “AIRS”. The control against which the AIRS impact is compared (subsequently referred to as “CTRL”) is generally the operational system, but a research department experiment was used prior to cycle 25R4 being implemented in operations.

Changes to the analysis

Figure 4 shows a difference map (AIRS minus CTRL) of RMS analysis temperature increments at 500hPa (averaged over a ten day period in December 2002). While the contour interval is extremely fine (shading starting at 0.1K) the map shows that there are slightly larger increments over the oceans (where most of the AIRS radiances are used) and a small (but fairly consistent) decrease in increments at radiosonde stations when the AIRS radiances are assimilated (the large increase over central Africa originates from the use of AIRS data over lake Chad that is treated as “sea” in the assimilation). The reduced increments at radiosonde stations is an encouraging diagnostic and shows that the extra work being done by the AIRS data in the analysis improves the agreement with radiosonde data.

Systematic analysis increments in temperature and humidity for the AIRS and CTRL assimilations are shown in figures 5 and 6 respectively as zonally averaged cross-sections (evaluated over the same 10 day period). It can be seen that the mean increments are generally rather small and to first order are very similar in the troposphere and lower stratosphere between the two systems (with the AIRS increments possibly being slightly larger). In the upper stratosphere there are much larger differences in the geographical and vertical distribution of mean increments. As yet these have not be investigated fully, but may reflect the ability of the AIRS channels to resolve finer vertical structures near the stratopause (we hope to use lidar and MIPAS data to examine this issue further). The similarity (in the troposphere) between the mean increments of the AIRS and CTRL is consistent with the small observed minus background radiance biases discussed previously.

Generally the small changes to the analysis illustrated above are not large enough to significantly impact the usual observation fit statistics computed over large areas

(except in the temperature fits above 10hPa where the AIRS slightly improves over the CTRL). However, the fact that the assimilation of AIRS does not change the overall fit to other observations (temperature or wind) is also very encouraging as it suggests that using a very simple "flat" bias correction applied to the AIRS radiances has no detrimental effect.

Forecast impact

Forecasts have been run from the analyses that assimilated AIRS radiances and compared to those from the CTRL system. Figure 7 shows forecast error difference maps (AIRS minus CTRL) for 500hPa height, each system verified using its own analyses and averaged over the first 50 cases of the trial. Blue shading indicates where the AIRS forecasts are better and yellow where they are worse than the CTRL. It can be seen that the assimilation of AIRS has reduced forecast errors at all ranges. The impact is first seen in the short-range (day-3) forecast of the Southern Hemisphere and then in the day-5 forecasts of both hemispheres. The positive signal increases with increased forecast range for the Northern Hemisphere, but becomes marginal beyond day-7 in the Southern Hemisphere (where the situation appears to be more a mixture of good and bad forecasts). No signal is seen in the tropics, but this is due to the choice of forecast variable (i.e. Z500). A positive impact of the AIRS upon the forecasts of tropical temperatures (not shown here). Larger samples (100 cases) of area-averaged mean forecast scores for 500hPa geopotential height have been generated. However, it should be noted that these have been computed using the operational / CTRL analyses for verification, a choice that may slightly penalize the AIRS system. Over 100 cases there is still a very small, but very consistent improvement at all ranges in the Northern Hemisphere (the results of significance testing are contained in tables 1 and 2 show that the improvement is statistically significant at the 1% level for day-5). For the European area (imbedded in the Northern Hemisphere statistics) the positive impact is marginally clearer, but less significant. In the Southern Hemisphere, only a slight improvement is seen at day-3 (significant at the 5% level) and beyond this no improvement is seen over the CTRL (the negative impact at day-10 was not found to be significant < 10%). The verification of temperature forecasts from the 2 systems is generally consistent with the height results in the mid-latitudes, but they additionally show a positive impact of the AIRS in the tropical temperatures at 200hPa . The same statistic for the southern hemisphere shows larger RMS errors when AIRS data are used, but a closer investigation indicates a large systematic difference between the AIRS and CTRL analyses, localized to the edge of the Antarctic continent and not evident at any other level than 200hPa.

Wind forecasts from both systems have been verified and scores at 1000hPa (typical of other levels) display similar signals to the height verifications, although a positive impact due to AIRS in the Southern Hemisphere is slightly more evident. In the statistical significance testing of the forecast impact (shown below) red indicates a positive impact due to AIRS and blue a negative impact. The percentage figure indicates the level at which a *t-test* found the results statistically significant. If no significance better than 10% is found the result is marked with an X

Forecast Range	Northern Hemisphere	Southern Hemisphere	Europe
day-3	5% / 1%	5% / 10%	X / 2%
day-5	0.1% / 1%	10% / X	10% / 5%
day-7	X / X	X / X	X / X

Table 1 Significance testing of 1000hPa (first figure) 500hPa (second figure) height forecast verifications

Forecast Range	Northern Hemisphere	Southern Hemisphere	Europe
day-3	X / 5%	0.1% / 0.1%	10% / 0.5%
day-5	0.1% / 0.1%	2% / 5%	5% / X
day-7	0.1 / 2%	X / X	X / 10%

Table 2 Significance testing of 1000hPa (first figure) 500hPa (second figure) wind forecast verifications

Discussion of results

The assimilation of AIRS radiances with the baseline system described here shows no adverse effects in the analysis (in terms of the fit to other observations) and slightly reduced analysis increments at radiosonde locations. Overall the forecast performance of the baseline AIRS assimilation scheme is encouraging, essentially showing a consistent positive impact in most areas and parameters. However, averaged over the 100 cases the impact is small and warrants some discussion. The assimilation configuration is clearly conservative and a variety of further enhancements (many of which are already being tested) will be described in the next section. However, large improvements over the CTRL may also be limited by the quality of the CTRL system itself. The average level of forecast skill for the CTRL (that currently uses radiances from 3 AMSUA, 2 HIRS, 3 GEOS and 3 SSM/I instruments) is very high and over the period tested was significantly better than forecasts from any other NWP centre. Furthermore, a time series analysis of forecast skill shows that the CTRL system produces very few poor forecasts or "busts". During the 100 day trial **no** day-5 forecasts of 500hPa height scored less that 60% anomaly correlation averaged over either of the hemispheres. Verified over the much smaller European area, still only 6 day-5 forecasts from the CTRL scored worse than 60%. In 4 of these cases the AIRS system improved the forecast by 10% or more (4 AIRS forecasts scored worse than 60% over the period, but the CTRL was never 10% better). Most of the cases where AIRS improves the poor forecasts correlate with when adjoint sensitivity perturbations to the initial conditions (rather than "forced" perturbations) were found to have a large effect. However, the improvements are far less dramatic than those achieved (retrospectively) by the sensitivity perturbations. Usually cloud was found to obscure many of the sensitive locations (resulting in very few tropospheric AIRS radiances being used). In the one case that was relatively clear (24 Feb 2003) it appeared that the some of the analysis increments due to AIRS did correlate with the sensitivity perturbations, but

many did not. Overall it is difficult to argue that the assimilation of AIRS is dramatically fixing bad forecasts on any regular basis. It appears more that the assimilation of AIRS (with the current configuration) is having a small, but relatively consistent positive impact upon the forecast skill.

Work in progress and next steps

On the basis of the results presented here, AIRS radiances were introduced into the ECMWF operational assimilation system on the 7th October 2003.

The areas where we feel the AIRS system can be enhanced in the short-tern relative to the baseline configuration are listed here in no particular order:

Improvements to the cloud detection will remain a priority. We are reasonably confident that the current system is safe, but we know clear data is being discarded. Developments well under way by P Watts and J Smith aim to exploit collocated visible data and cross-spectral checks to allow a more skilful identification of clear channels.

The decision to exclude tropospheric channels over land was made early in the development process and was mainly related to the occurrence of large increments thought to be associated with missed cloud. Since then many improvements have been incorporated to the cloud detection and the use of tropospheric radiances over land will be reviewed.

The issue of bias correction has partially been investigated. While all the results presented here have used a flat bias correction for AIRS radiances, parallel experiments have been performed using the traditional air-mass dependent scheme extended to AIRS. The air-mass dependent correction slightly degrades the fit to radiosonde temperature data at 200hPa and 70hPa relative to the flat correction (suggesting some of the air-mass dependence is systematic model error), but slightly improves the temperature fit at 100hPa. For the 45 cases tested, assimilating AIRS with the air-mass dependent bias correction results in a slightly degraded performance in forecasts of Northern Hemisphere 500hPa height. Thus from the results so far there is no strong incentive to employ an air-mass dependent bias correction for AIRS. G Kelly is currently investigating to what extent the air-mass dependent corrections applied to other sensors (e.g. AMSUA and HIRS) could be relaxed back to a simple flat correction. If this could be achieved without any loss of NWP performance it may assist our parallel efforts to extract CO2 information.

Much of the AIRS information from the short-wave part of the spectrum has not been used. While we are probably far from being able to use short-wave radiances contaminated by solar radiation, significantly more channels than are currently used could be assimilated at night. However, there are some important additional issues related to the accuracy of the RTTOV model around 4 microns (for channels located on the steepest part of the absorption band) and the RTM may need to be upgraded to 101 vertical levels (currently it has only 43) before significant progress can be made.

Finally the observation errors assigned to the AIRS radiances will be reviewed in line with improvements to the cloud detection, bias correction and our general understanding of the characteristics of the AIRS data.

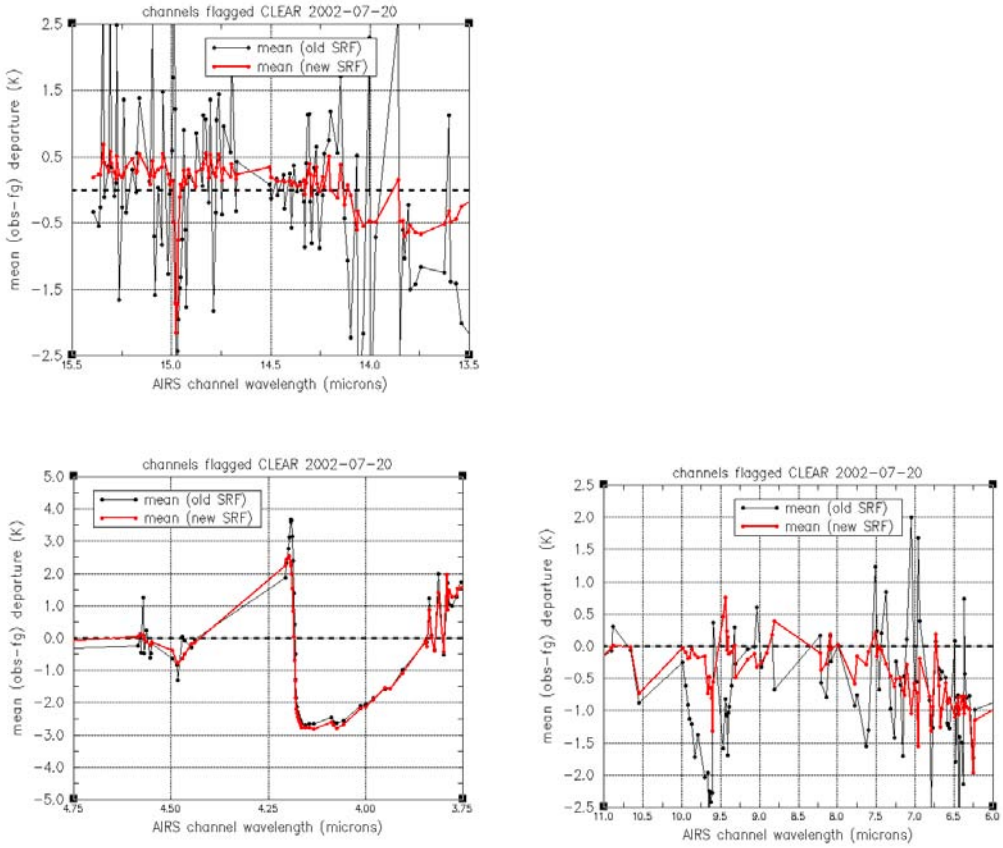

Figure 1 Mean observed minus background radiance biases for clear data. The red line corresponds to the RTM using spectral response functions (SRF) evaluated after launch, the black to pre-launch SRF.

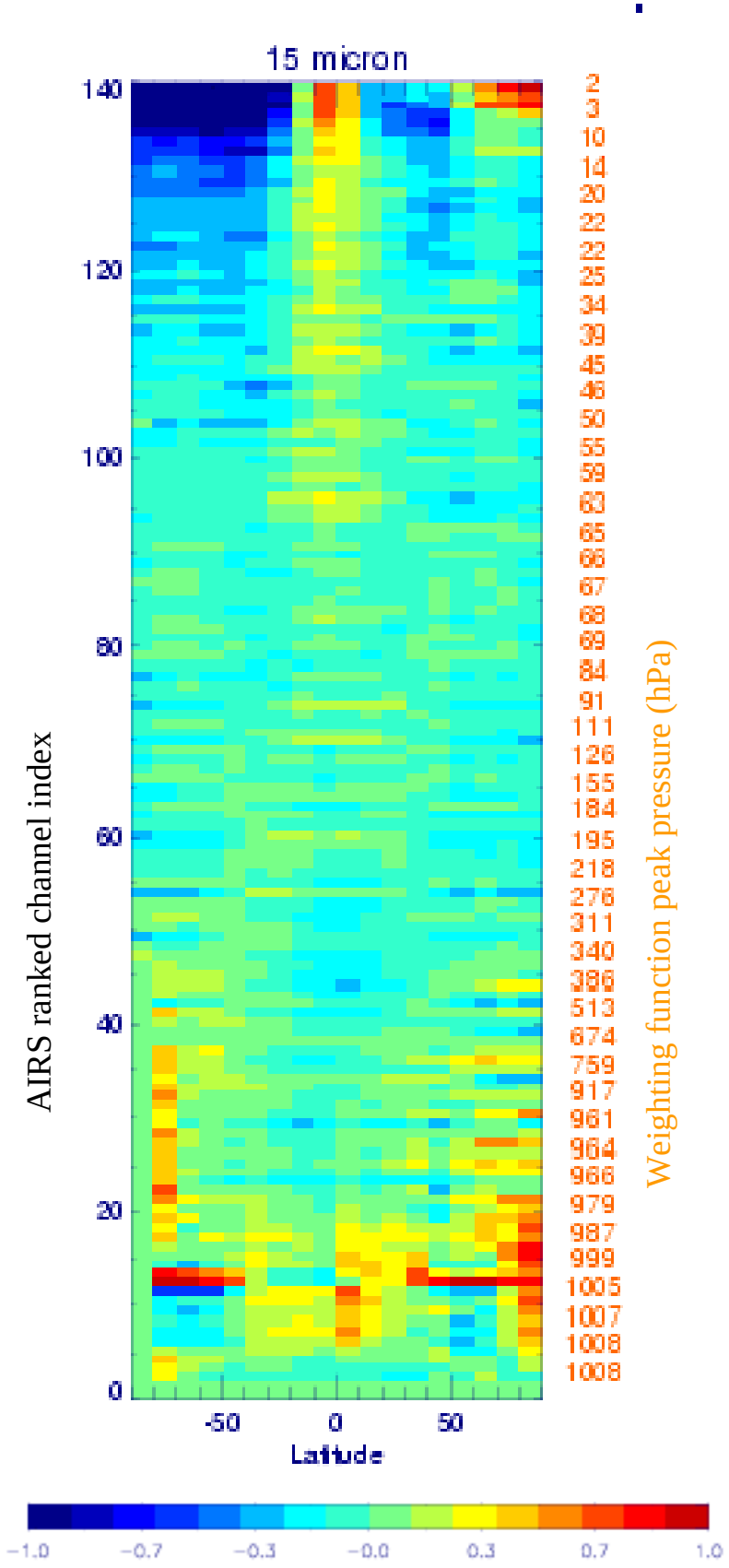

Figure 2 Zonally averaged mean observed minus background radiance departures for the AIRS long-wave channels (15 micron) ranked vertically

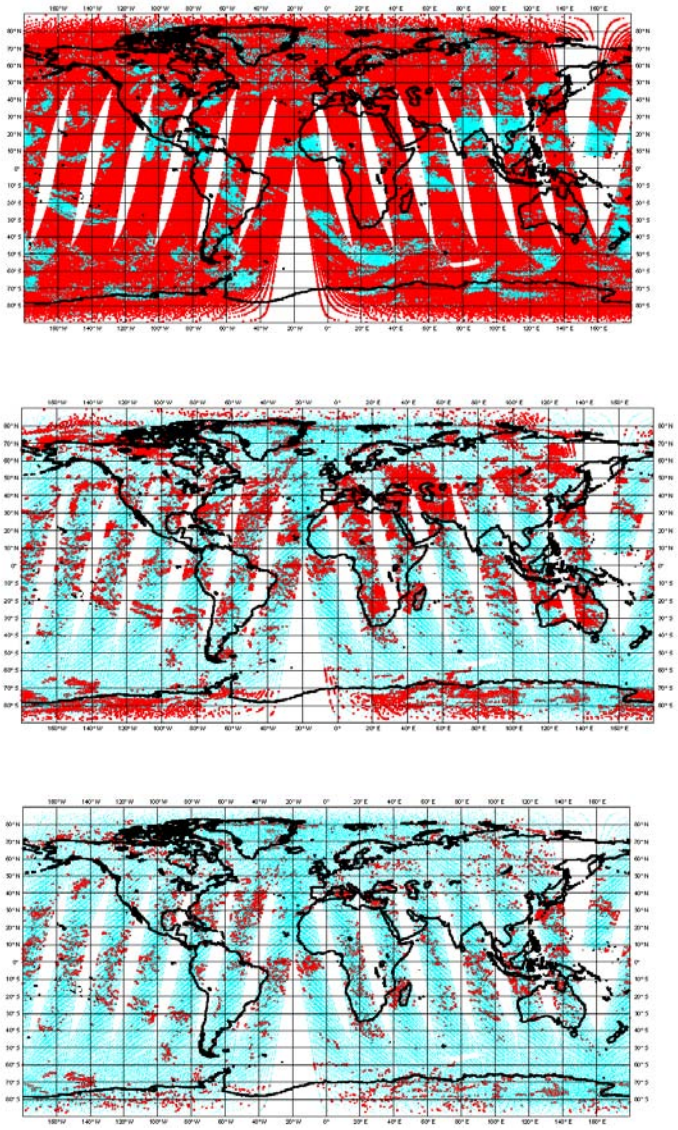

Figure 3 Location of clear data (red symbols) for a lower stratospheric channel at 14.5 microns (top panel), a mid-tropospheric channel at 13.5 microns (centre panel) and a window channel at 11 microns (lower panel)

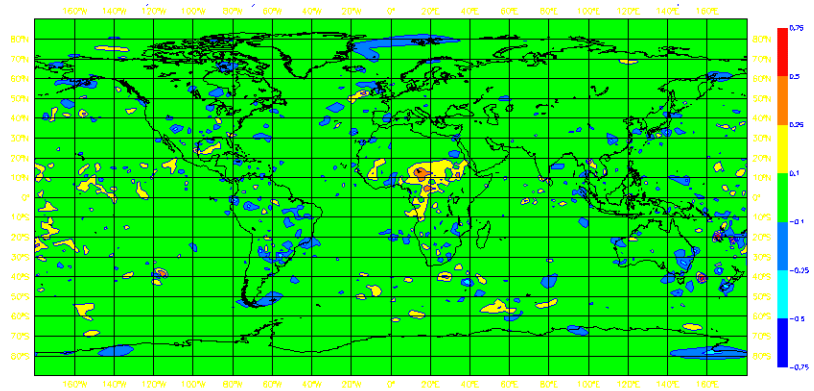

Figure 4 Difference map showing RMS analysis increments of the AIRS system minus those of the CTRL for temperature at 500hPa (averaged over 10 days). Shading starts at 0.1K.

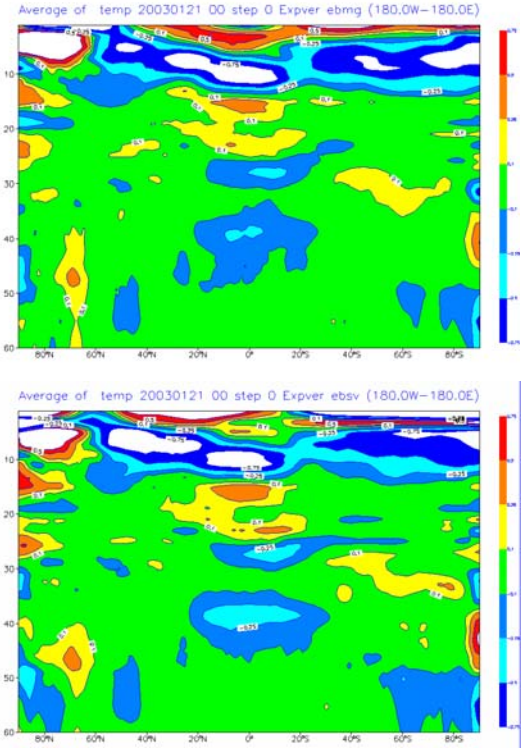

Figure 5 Zonally averaged mean temperature increments (evaluated over 10 days) for the CTRL (top panel) and AIRS (lower panel). Shading starts at 0.1K

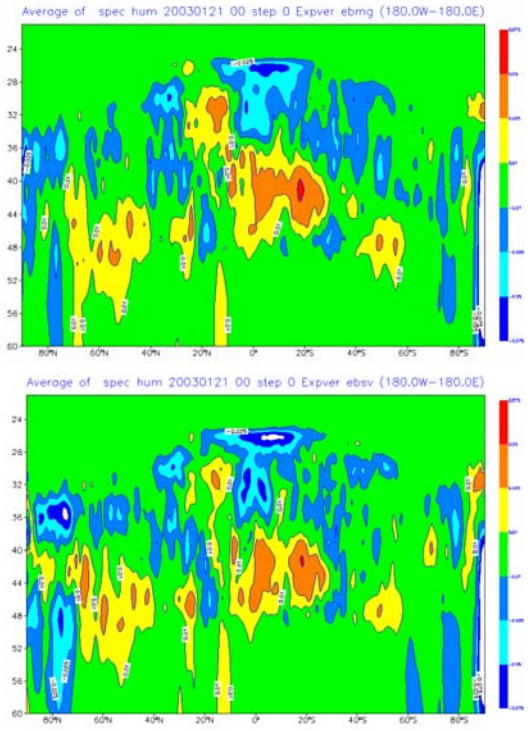

Figure 6 Zonally averaged mean humidity increments (evaluated over 10 days) for the CTRL (top panel) and AIRS (lower panel). Shading starts at 0.01 (delta Q / Q)

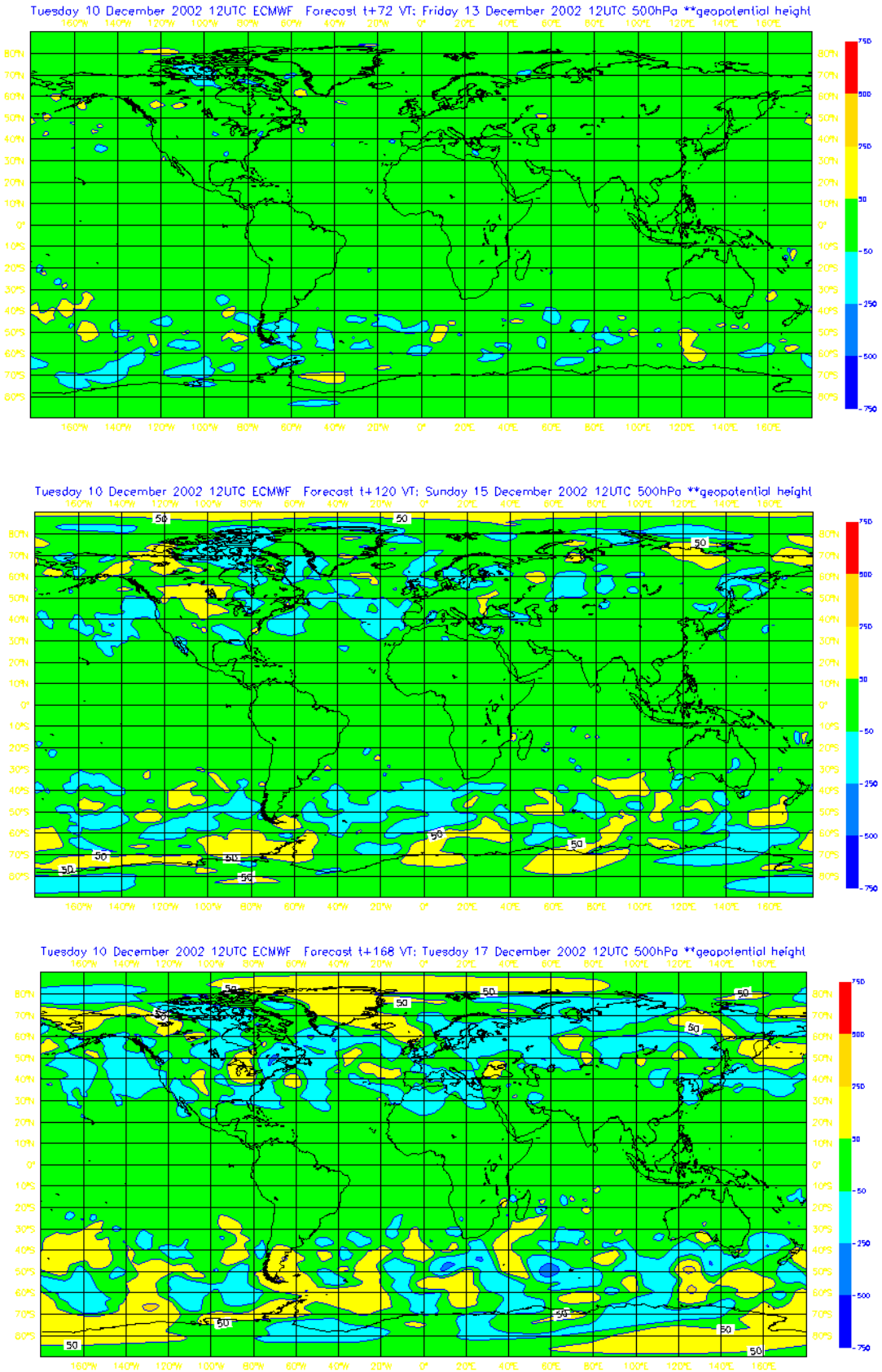

Figure 7 RMS forecast error differences for 500hPa height AIRS minus CTRL

Effect of Predictor Choice on the AIRS Bias Correction at the Met Office

Brett Harris
Bureau of Meterorology Research Centre, Melbourne, Australia

James Cameron, Andrew Collard and Roger Saunders,
Met Office, Exeter, U.K.

Abstract

Based on the Harris and Kelly (2001) bias correction scheme used at ECMWF and the Bureau of Meteorology, a bias correction code was set up at the Met Office to apply to a given set of channels from the AIRS instrument on the AQUA satellite. Using a choice of five bias predictors, scan only and four air-mass predictors based on background fields, various combinations of predictors were applied to a large subset of AIRS channels in order to determine the optimal set of predictors for the subset. For this particular subset, it was found that the optimal predictors were the two air-mass predictors, 850-300 hPa and 200-50hPa thickness.

1. Introduction

The Atmospheric Infrared Sounder (AIRS) is a high resolution spectrometer with 2378 channels in the range of 640 – 2700 cm^{-1} in the infra-red spectrum. The instrument is onboard the NASA AQUA earth observing satellite launched on 4 May 2002. The Met Office receives a subset of brightness temperatures of 324 channels, in near real time from NOAA/NESDIS. It has also developed a cloud detection scheme Takeuchi (2003) as part of a pre-processing scheme. The radiance profiles determined to be 'clear' are then passed to a 1DVAR quality control phase. Those profiles that pass the 1DVAR quality control are then to be passed to the VAR assimilation system.

When any radiance is used in a variational retrieval system, a bias correction needs to be applied, see Eyre(1992). Section 2 details the bias correction scheme used for the AIRS radiances, and is mainly based on the and Harris and Kelly(2001) method which uses background fields as air-mass predictors for the bias correction. Section 3 details the dataset that was used, which was mainly from April 2003, and a small subset from March 2003. The results obtained from using various combinations of bias predictors for both the small subset and the larger subset are presented in Section 4. Section 5 gives a summary of the work performed and some areas of further work.

2. The Bias Correction Scheme

The bias correction scheme, based on Harris and Kelly (2001), uses a constant global scan bias for each channel, and a set of air-mass predictors which may be chosen in advance. Those that were available for selection were

1) **Thick850** 850-300 hPa Thickness.
2) **Thick200** 200-50 hPa Thickness.
3) **T_Skin** Surface Skin Temperature.
4) **Not Used**
5) **BriTemp** Calculated radiance for the given channel.

Predictor 4 was reserved for total column water vapour, but was unavailable in the initial experimental bias correction dataset.

This bias correction method attempts to remove both locally and globally, the bias in observed minus background radiance (O-B), for a large sample of radiance observations. Once the scan bias has been removed, it is straightforward to show mathematically, that the predictors with the highest correlation to (O-B), will be those which are most effective at removing the bias. This is mathematically equivalent to those predictors which reduce the standard deviation in (O-B) by the largest amount.

3. The Datasets

A large dependent sample was used, in this case for the April dataset, to calculate the scan bias and the coefficients of the chosen predictors. Only sea points (not including sea-ice) were used. Also, when calculating the coefficients, the goal of reducing the bias both locally and globally, is achieved by thinning the data so that roughly equal numbers of observations for each air-mass type is used. This is analogous to choosing a uniform spread when performing a one-dimensional line-of-best-fit regression. This ensures that a clump of data does not dominate the regression and cause a bad fit to data from under-represented areas. A slightly smaller dataset was used in the limited March analysis.

	90S-60S	**60S-30S**	**30S-30N**	**30N-60N**	**60N-90N**	**Global**
Total	3935	50468	158164	20222	2073	234862
Thinned	3935	5873	5811	9157	2073	26849

Table 1. The AIRS dataset used for April 2003.

The data is passed through a set of routines adapted from ECMWF and Bureau of Meteorology software which has its own internal quality control.. The scan bias coefficients may be either computed separately or within the regression step for the air-mass coefficients. In both cases the results appeared identical. In all subsequent calculations, the scan bias coefficients were computed within the regression. It is possible to restrict the calculation to scan only, which gave another basis for comparison when attempting to find the best predictor combination.

4. Results

Firstly, something must be said about the numbering conventions used in this paper for AIRS channel numbers. The conventions are the index number 1-324 in the NESDIS dataset, the AIRS channel number 1-2378, and the wavenumber (cm^{-1}). The convention used will be, for example, 77(174)[699.668], where 77 is the index in 1-324, 174 is the index in 1-2378, and 699.668cm^{-1} is the wavenumber.

a) March results using small channel subset.

Initially only five channels were studied. These were chosen on the basis that they corresponded to channels which which had weighting functions which reached to the lower troposphere or the surface. The idea was to investigate the skill of either the T_Skin or the Thick850 predictors.

Index	73	77	85	100	140
Channel	169	174	190	227	914
Wavenumber	698.276	699.668	704.162	714.782	965.842

Table 2. The initial five AIRS channels chosen from March 2003 data.

The bias correction scheme was run for various combinations of predictors ranging from scan only to the full set of (1235) predictors. After the coefficients have been calculated, the bias correction is applied back to the full unthinned dataset. For each of the channels, the global standard deviation for each of the predictor combinations is compared to the standard deviation of the uncorrected bias.

In a simple one dimensional linear regression, the varance of the corrected departures is reduced by a factor of (1-r^2) where r is the correlation of the single predictor with the predictant. Similarly, in a multi-dimensional case, it can be shown that the combination of predictors which gives the greatest reduction in standard deviation has the most skill, and should apart from sampling issues, give the greatest reduction in bias. Figure 1 shows the reduction in standard deviation for the sample channels for various predictor combinations.

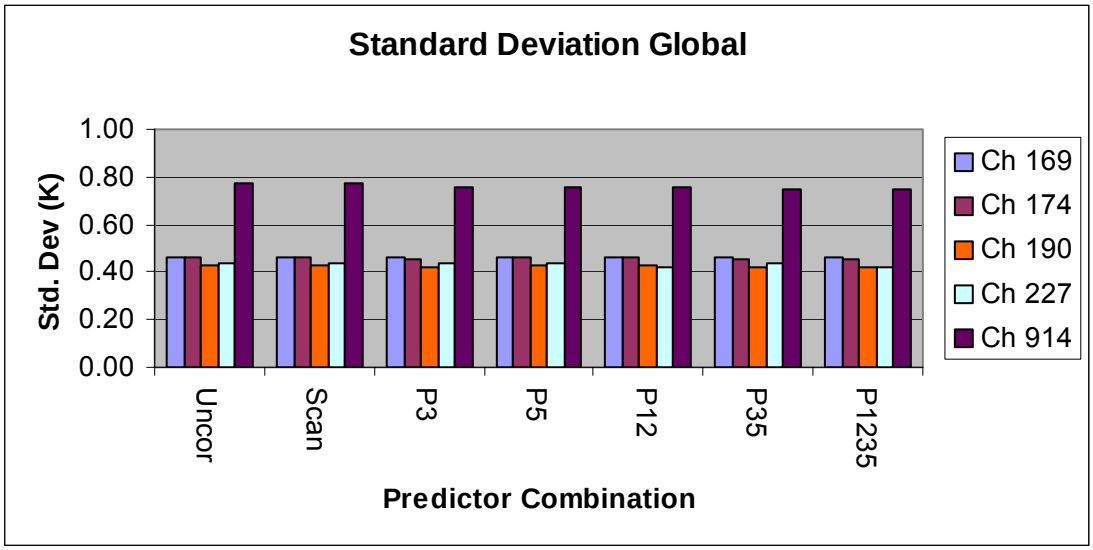

Fig 1 The global standard deviation for the initial five AIRS channels.

It can be seen that scan only has very little skill. More surprisingly, P12 also shows very little skill except for Ch 227. It is possible to compute the correlation between the temperature at various levels and the (O-B) departure. For any temperature level above 900hPa the correlation is very low. This could possibly be due to the skill of the RTTOV-7 forward model. For some channels there is more skill for different predictor combinations. For example, P3 has more skill than P5 for Ch 174. However, the combination P35 has more skill for Ch 914 than each predictor separately. In total, the combination P1235 does best, but the combination P35 appears to encompass most bias, except for Ch 227 where P12 does show some skill. However, this is only an example of global skill, and is skewed towards the tropics as the full unthinned dataset is used.

What is required is a method to determine the local skill of the predictor combination against the uncorrected bias. From the large dataset, the (un)corrected values of (O-B) are computed, and the results analysed using a Cressman analysis technique onto a 160 x 320 grid. The results are then plotted using IDL to produce a latitude-longitude plot of the biases. Using Ch 169, the mean bias was plotted for uncorrected bias, which includes a mean offset in Fig 2(a). The mean offset is absorbed into the scan bias in Fig 2(b). Figure 2(c) shows the reduction in bias if the P12 combination is used for this channel. Predictors P3 and P5 alone, are shown in Fig 2(d) and 2(e) respectively. Finally P35 is shown in Fig 2(f). The combination P1235 was not substantially different to P12 or P35.

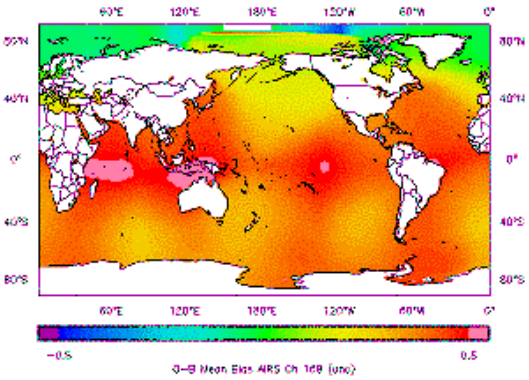

Fig 2(a) Uncorrected bias for Ch 169.

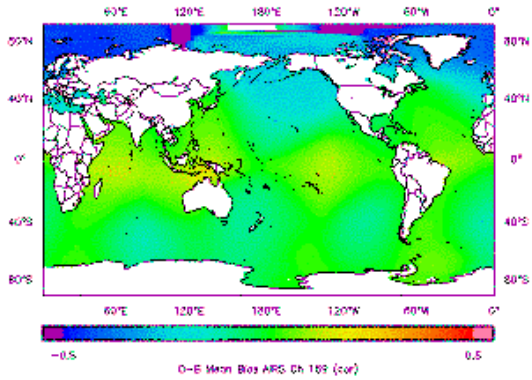

Fig 2(b) Scan bias only for Ch 169.

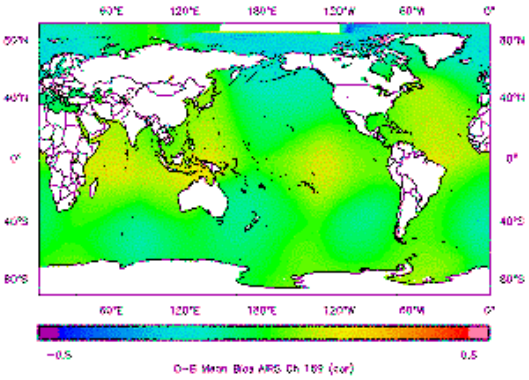

Fig 2(c) Predictors P12 for Ch 169.

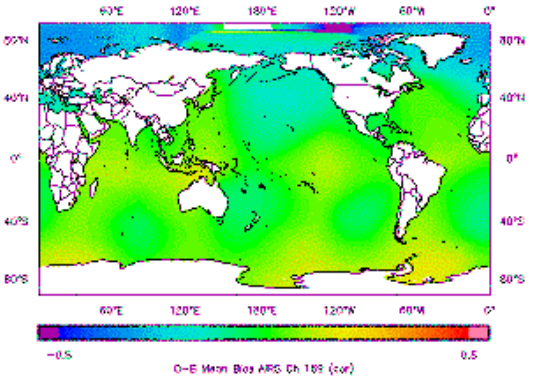

Fig 2(d) Predictor P3 for Ch 169.

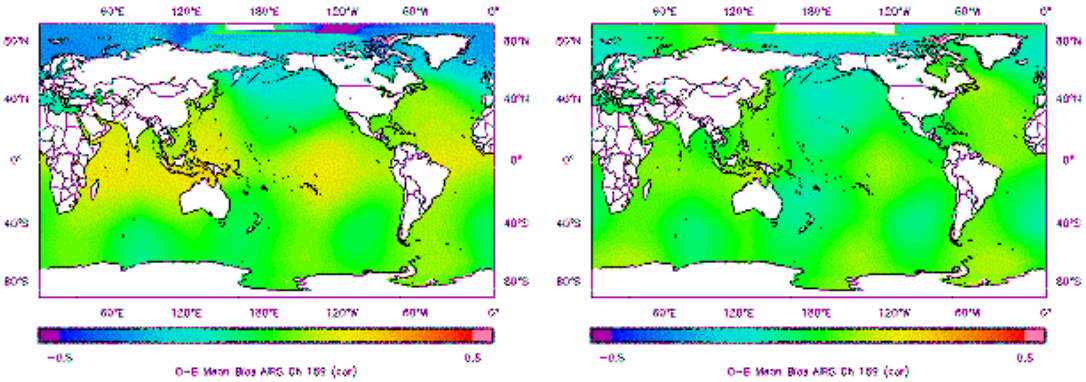

Fig 2(e) Predictor P5 for Ch 169. *Fig 2(f) Predictors P35 for Ch 169.*

For these plots, it is clear that the scan bias alone is insufficient to produce a good reduction in bias over a wide area. It appears P12, P3 or P35 (and P1235) produce a good reduction, but P5 by itself is also insufficient.

A dataset from January/February 2003 was studied in much greater detail. The details of numbers of data from various latitude bands is shown in Table 3 below.

	90S-60S	**60S-30S**	**30S-30N**	**30N-60N**	**60N-90N**	**Global**
Total	4189	48994	133838	15940	624	203585
Thinned	4189	5951	5144	6867	624	22775

Table 3 The dataset used for Jan/Feb 2003.

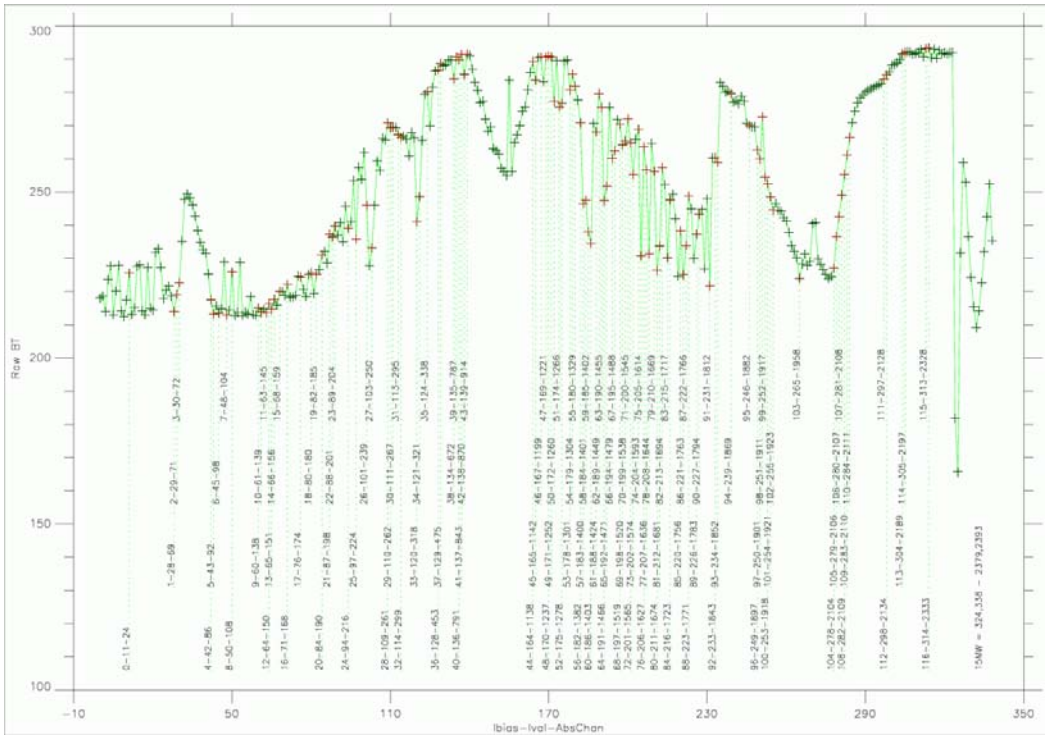

Figure 3 The subset of channels used in Jan/Feb 2003 study.

A much larger subset of channels was chosen for this study, the details of which are are shown in Figure 3.

After the scan bias was applied to the above channels, various combinations of predictors were used, and a statistical technique was used to facilitate the viewing of the mean and standard deviation over latitude bands. The idea was to take an RMS mean of the bias and standard deviation of the unthinned dataset over each latitude band, and to plot the results against channel number.

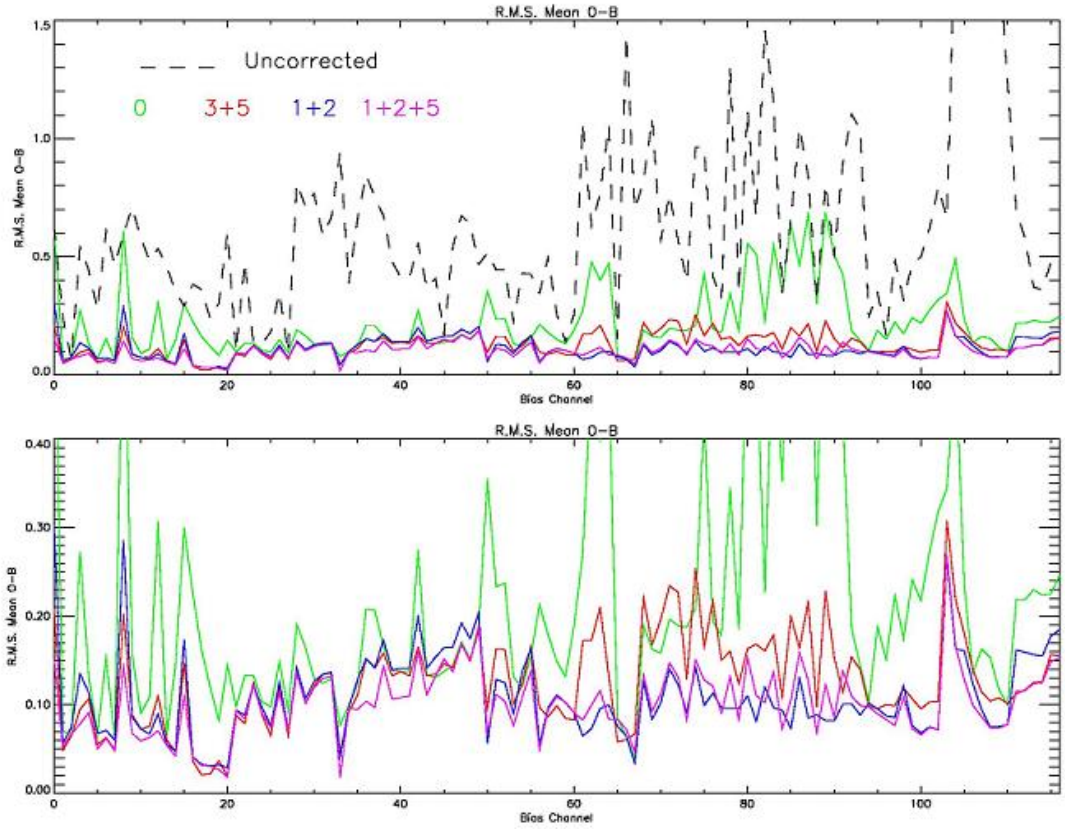

Fig 4 RMS bias by channel number (lower rescaled to exclude uncorrected mean).

Figure 4 shows the RMS bias for a much larger subset of channels. It shows some interesting features not seen in the smaller original subsets. Going to a much larger range of channels, appears to show that the predictor sets P12 and P125 produce the a much better overall reduction in bias then using scan only or using the P35 combination. Also, since the data is expected to be used over land, it is considered desirable to not use the possibly inaccurate skin temperature predictor. Experiments have been performed using the P12 and P125 combinations and can be found in Collard *et. al.* (2003).

5. Conclusions

Of all the combinations of bias predictors used, it is suggested that the combination of the two air-mass predictors (P12) would be the best and simplest combination, after a scan correction has been applied. Of course, many other considerations affect the results, such as the cloud clearing scheme and the interaction with sea-ice. With the datasets given, data assimilation trials are underway to see how

the AIRS data, with this type of bias correction, can impact on forecast performance. (see paper by Collard *et. al.* (2003) for more details in this proceedings).

6. References

Cameron J. The effectiveness of the AIRS bias correction of various air-mass predictor combinations. *Met Office NWP Technical. Report available at:* http://www.metoffice.com/research/nwp/publications/papers/technical_reports/2003/FRTR421/FRTR421.pdf

Collard. A., Saunders R., Cameron J., Harris B, Takeuchi Y. and Horrocks L., Assimilation of data from AIRS for improved numerical weather prediction. *Tech. Proc. XIII ATOVS Study Conference, Montreal, Canada, Oct 29 – Nov 4, 2003.*

Eyre J. A bias correction scheme for simulated TOVS brightness temperatures. *Tech. Memo.* **186**, *ECMWF (1992).*

Harris B. and Kelly G., A satellite radiance bias correction scheme for data assimilation *Quart. J. Roy. Meteorol. Soc.* **127**, *1453 (2001).*

Takeuchi Y. Cloud detection for the Advanced Infrared Radiometer Sounder. *Private communication, JMA (2003).*

Assimilation of data from AIRS for improved numerical weather prediction.

Andrew Collard[1], Roger Saunders[2], James Cameron[2], Brett Harris[3], Yoshiaki Takeuchi[4], Lisa Horrocks[1]

[1]Met Office, Reading, United Kingdom
[2]Met Office, Exeter, United Kingdom
[3]Bureau of Meteorology, Melbourne, Australia
[4]Japan Meteorological Agency, Tokyo, Japan

Abstract

Observations from the Atmospheric Infrared Sounder (AIRS) are assimilated into the Met Office's Numerical Weather Prediction (NWP) model. The processing methodology is described with emphasis on cloud detection and quality control. The impact of the AIRS observations is an improvement in forecast skill of 0.5-1.0% which is a satisfactory result given the conservative nature of this initial implementation. Future improvements that might fully exploit the potential of advanced infrared sounders are discussed.

Introduction

For accurate numerical weather prediction (NWP) it is important that the initial state of the atmosphere is known as accurately as possible. A variety of data sources are currently used to furnish this information, in particular the global radiosonde network and vertical sounding instruments on polar orbiting meteorological satellites. Radiosondes provide measurements of temperature and humidity with high vertical resolution but their spatial coverage can be poor, especially over the oceans and in the Southern Hemisphere. In contrast, satellite soundings provide daily global coverage, but at much lower vertical resolution.

Studies have shown (e.g., Prunet *et al*., 1998; Collard, 1998; Huang *et al*., 1992) that higher vertical resolution (1-2km) than from the ATOVS can be obtained from observations using high spectral resolution advanced infrared sounders which have close to line resolving spectral resolution and many thousands of channels.

Assimilation of Satellite Radiances at the Met Office

Figure 1 illustrates how satellite radiances are assimilated within a variational assimilation framework. In essence, the observed brightness temperatures are compared with simulated observations derived from the NWP model 6 hour forecast fields from the previous assimilation cycle. The differences between the two are used to revise the model fields and the comparison is preformed again. Once convergence is attained, the final revised model fields form the analysis from which the NWP model is run to provide the forecast.

At the Met Office two important parts of this process, the bias correction and quality control, are done in a separate pre-processing stage together with a 1D-var retrieval which is used to infer quantities required to model the observed radiances but which are not available from the NWP forecast fields – particularly skin temperature and the temperature profile above the top of the model. Included in "quality control" is the detection of cloudy fields of view which is discussed further below.

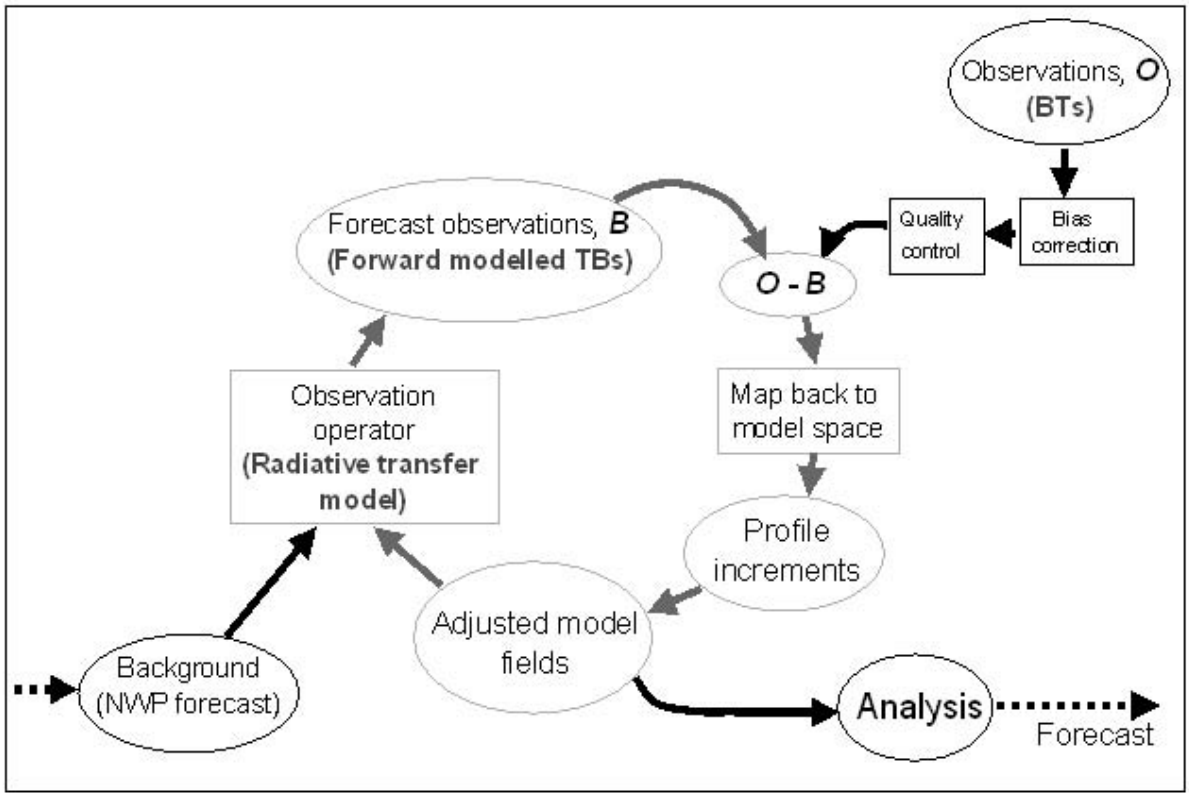

Fig. 1: Schematic illustrating the assimilation of Satellite Radiances.

AIRS Data and Channel Selection

The Atmospheric Infrared Sounder (AIRS) is the first in a new generation of advanced infrared sounders to be launched in the first few years of the 21st century. Although it is an experimental instrument (flying on the EOS-PM – renamed Aqua – satellite), its similarity to future advanced infrared sounders (IASI on MetOp and CrIS on NPOESS) makes it ideal for preparing the operational numerical weather prediction centres for these new instruments.

AIRS is a grating spectrometer with 2378 channels at approximately $1cm^{-1}$ resolution covering the 3-15μm spectral interval (although this coverage is not continuous). It therefore differs from all future advanced infrared sounders which will all be interferometers.

AIRS data are sent to the operational NWP centres from NASA via NOAA/NESDIS (thanks to the efforts of M. Goldberg and W. Wolf). At NOAA/NESDIS the data volume is reduced by around two orders of magnitude, primarily for data transmission reasons. This reduction is done two ways. Firstly, only one in every eighteen fields of view are used – corresponding to the central AIRS field of view in every other co-located AMSU-A field of view. Secondly, a subset of 324 channels are sent that were chosen at NASA/GSFC (Susskind *et al.*, 2003) such that retrievals could be made that could then be used to reconstruct the observed radiances to within the instrumental noise (around 50 of these channels were added later to help with CO_2 retrieval work).

All 324 channels are routinely monitored
(see http://www.metoffice.com/research/nwp/satellite/infrared/sounders/airs/index.html), except for channel 2357 which has been very noisy. In addition all 15 AMSU-A channels from the co-located field of view are also monitored.

After exclusion of those channels that are sensitive to ozone (which we are not considering) and some of the higher peaking CO_2 channels (which not only primarily provide information above the top of our NWP model but some of which require the consideration of non-LTE effects to correctly model

the observations), the total number of channels is further reduced by consideration of the information content (degrees of freedom for signal) for a variety of atmospheres following the method of Rodgers (1996). For assimilation purposes, we therefore consider 71 channels during the day and 86 at night; the difference being due to solar contamination in the shortwave channels during the day that we cannot currently deal with in our radiative transfer models (some extra long wave channels are employed in the daytime though). It is anticipated that more channels may be used in the future once the impact of AIRS is confirmed and the available resources on our new computer (an NEC-SX6) running our new assimilation system (the Met Office will move to 4 Dimensional Variational Assimilation – 4D-var – from 3D-var in 2004) become clear.

Figure 2 shows a typical AIRS spectrum with the 324 channels distributed by NOAA/NESDIS indicated. Also shown are the channels used for assimilation and the channels used in cloud detection (see below).

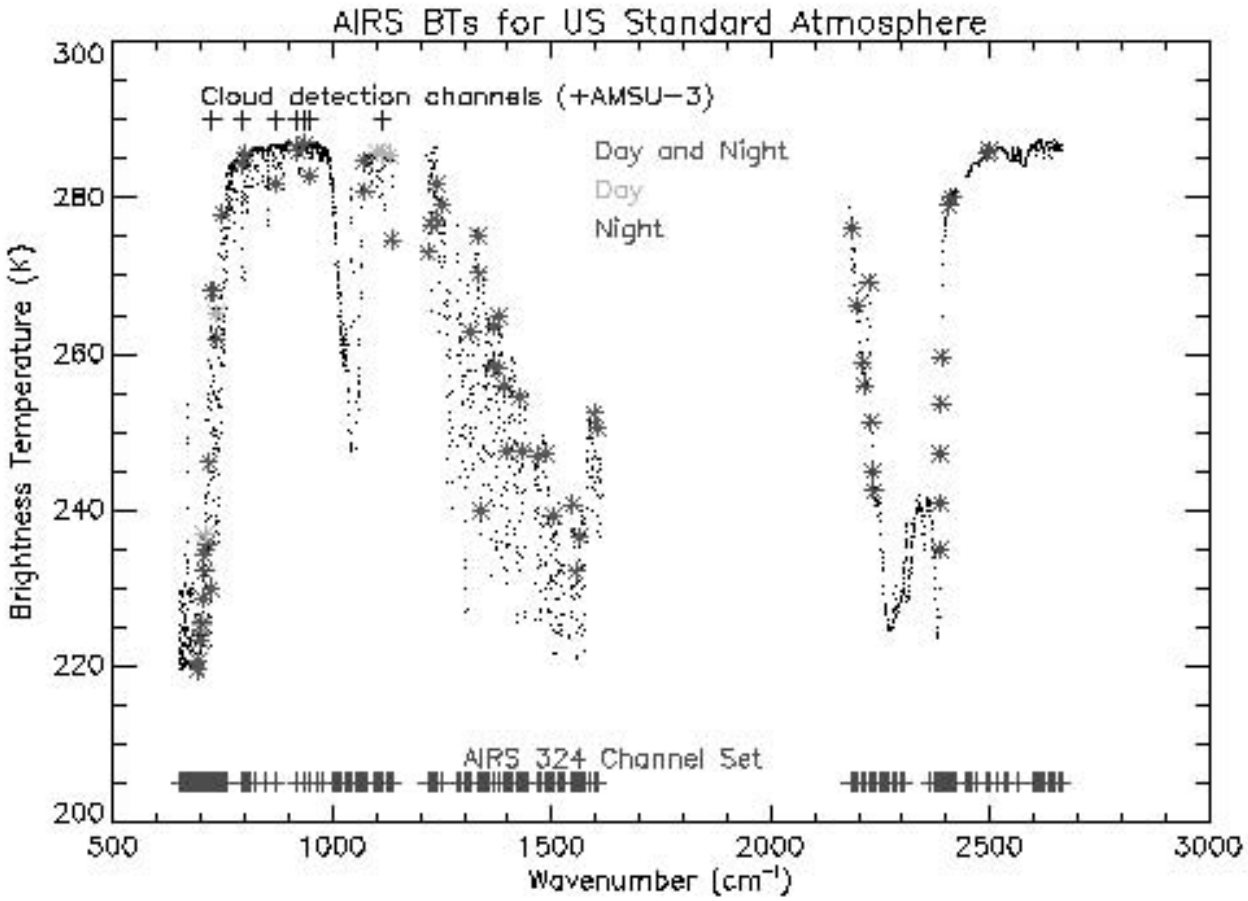

Fig. 2: AIRS Channel selection. The black points are all the AIRS channels, the 324 channels distributed by NOAA/NESDIS are indicated by the red crosses at the bottom. The cyan, red and green stars indicate the channels used for assimilation during the day, night and at all times respectively. Cloud detection channels are indicated by the blue crosses.

Cloud detection and Quality Control

Initial quality control of the observations includes gross checks for reasonable values in all channels that will be used in the later processing. The atmospheric profiles corresponding to the observations are also checked to ensure that they are within the range of acceptable values for the RTTOV radiative transfer model. Bias correction is applied (Harris *et al*., 2004) before the cloud detection stage.

A strategy for the treatment of cloud is essential for the treatment of any infrared system that probes the troposphere. Here we take the conservative approach of only considering those observations where there is no cloud in the field of view. The cloud detection scheme uses the variational cloud detection method of English et al. (1999). This method calculates a cost function which is related to the probability of the field of view being clear given the observations and the calculated clear radiances based on the 6-hour forecast background profiles.

For AIRS, ten channels are used which are distributed through the longwave window region and the 15μm CO_2 band, plus AMSU-A Channel 3 which is the lowest peaking AMSU-A channel for which surface emissivity uncertainties are not a problem for this purpose. The AMSU-A channel is particularly useful as, compared to infrared measurements, it is relatively insensitive to clouds and therefore any inconsistencies between this channel and the infrared channels can be interpreted as an indicator of cloud contamination in the infrared field of view.

Figure 3 shows how the cloud cost function varies with a longwave window channel's observed-background (O-B) difference. The O-B in the window channel is often a strong indicator of a cloud in the field of view, as illustrated by the inset in the figure which shows the full range of observations.

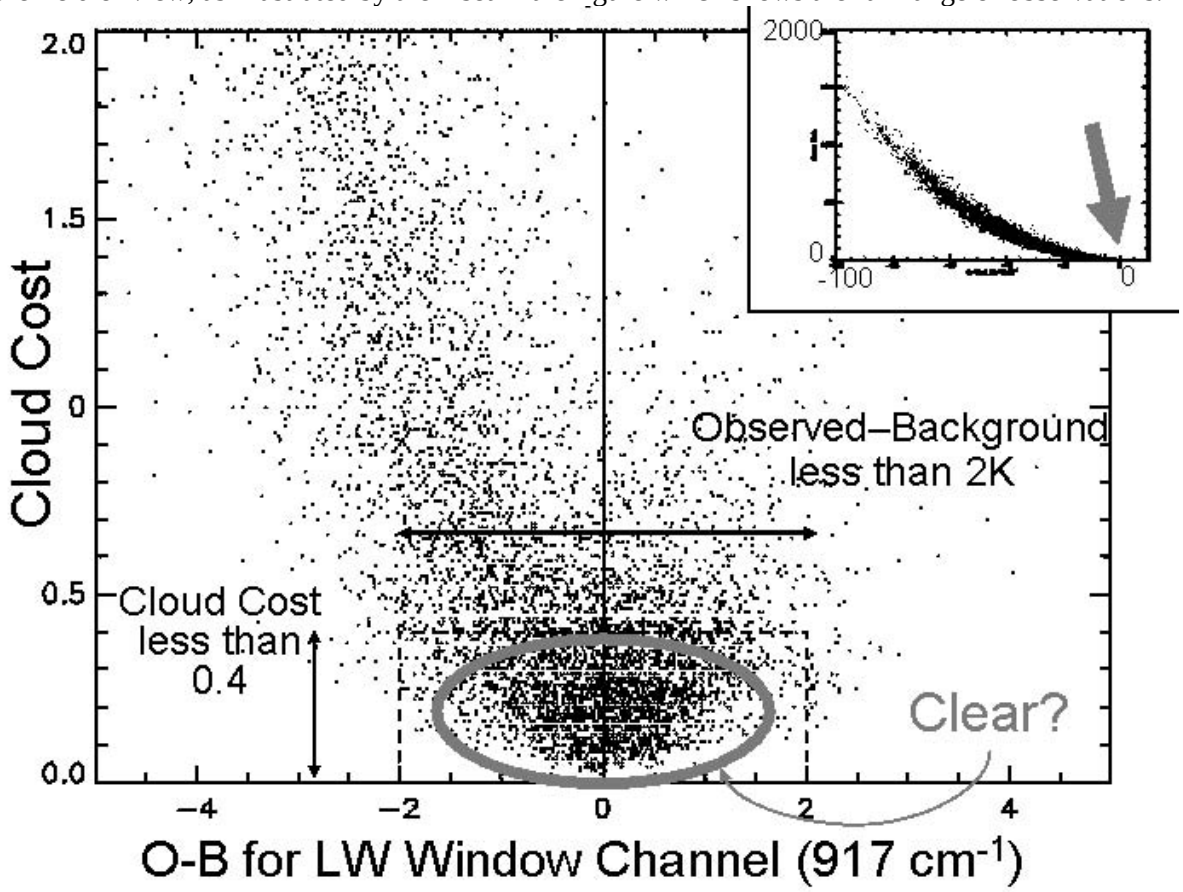

Fig. 3: AIRS Cloud Cost versus the difference between the observed brightness temperatures and those calculated using the model 6hour forecast data for a longwave window channel. Those points where $|O\text{-}B| < 2K$ and the cloud cost < 0.4 are considered clear.

The main panel of this figure shows the cloud costs for cases where any cloud has an impact of only a few Kelvin on the observed brightness temperatures. In this case one can see that there is a clustering of points where the longwave O-B difference is less than 2K and the cloud cost function is less than 0.4K. When one considers the symmetry of the plot and remembers that clouds rarely cause O-B to be positive, it seems reasonable to assume that these points will correspond to observations that may be considered clear.

At this stage, the O-B differences are checked for all channels that are to be used to ensure they lie in the ±20K range, i.e., that there are no channels with gross error when observations and background are compared.

As mentioned above, part of the pre-processing before the observations are presented for assimilation is a 1D-var retrieval in order to determine the temperature profile in the stratosphere and the surface skin temperature neither of which are available from the model in the full assimilation stage. A by-product of this process is that the 1D-var retrieval serves as a final quality control; if the minimisation at the 1D-var does not converge or converges with a high cost function value, the observation may also be problematic at the 3D-var stage and is best rejected (at least in this initial, conservative implementation).

Figure 4 shows a histogram of the final cost functions after the 1D-var minimisation. Theory states that the expected mean value of the cost function (which here is normalised by the number of channels) is 0.5 with a standard deviation of $1/\sqrt{(2\times[\text{Number of Channels}])}$, when all errors are known and Gaussian and the problem is linear. With these caveats, the fact that the 1D-var cost function has a distribution similar to that which theory predicts is very encouraging, as the assumed background, observational and forward model errors are all likely to be different to reality.

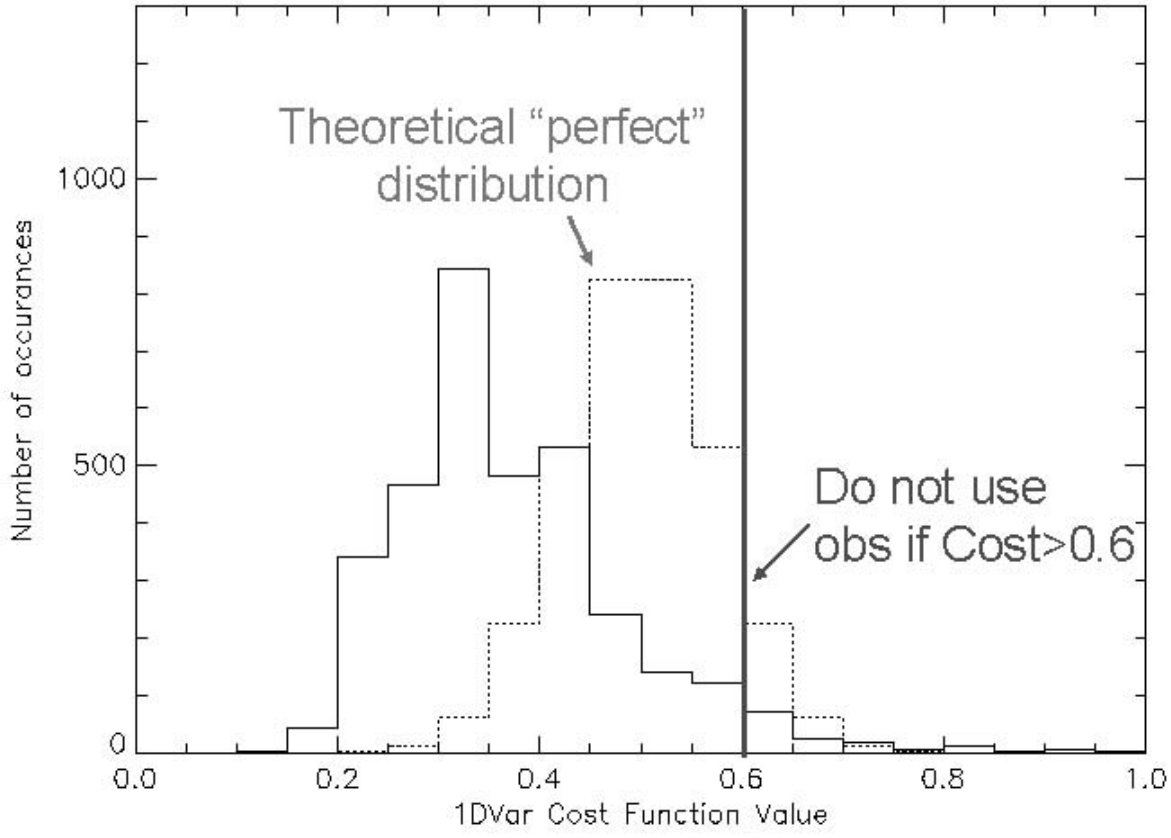

Fig. 4: Histogram of final 1D-var retrieval cost. The dotted line indicates the theoretical curve given perfect knowledge of observational, forward model and background error covariances and a linear problem. Given the uncertainties in these errors, the distribution of 1D-var costs is very encouraging. Also shown is the cut-off employed so as to not assimilate those observations which caused problems in the 1D-var minimisation step (not shown are around ten cases where the cost function is between 1 and 4).

When the 1D-var final cost function is large, this is an indication that the 6 hour forecast and the observations differ significantly. This may be due to a real difference between the forecast and reality,

but it is more likely that there are errors in the observations that preclude closer convergence. Cloud contamination that was missed by the cloud detection scheme is one possibility. Observations with final 1D-var cost function values greater than 0.6 (chosen with reference to the information displayed in Figure 4) are therefore not passed to the assimilation stage. This is the final quality control step apart from the thinning of observations to ensure that observations within 154km of each other are not assimilated to ensure that the assumption of independent observations (i.e., no horizontal error correlation) is valid.

Results of Initial AIRS trials

The results of the initial AIRS trial are summarised in Figure 5 for a four week period in December 2002/January 2003. Here are shown the fields that are used in the evaluation of the "NWP Index" which is the primary figure of merit in the Met Office for evaluating the accuracy of NWP. In almost all fields the impact of the assimilation of AIRS observations is positive (i.e., there is a reduction in RMS error). The overall impacts are an increase in skill of 0.5% when verified versus observations (sondes and surface observations) and 0.7% when verified versus the analysis fields.

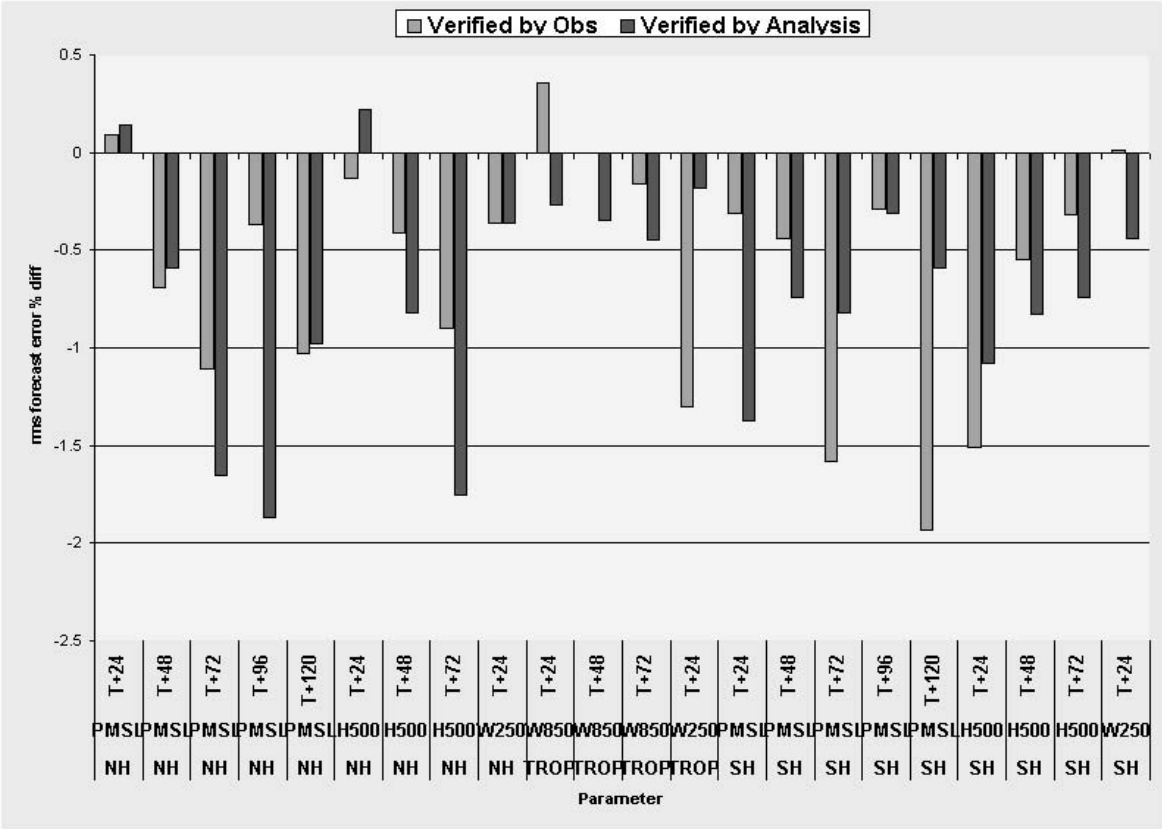

Fig. 5: Preliminary assessment of the Impact of assimilation of AIRS radiances on forecast accuracy (percentage change in RMS error, so negative values are an improvement). The fields considered are the mean sea level pressure (PMSL), the 500hPa height (H500) and the 250hPa winds in the extra-tropics and, in the tropics, the 250hPa and 850 hPa winds.

Discussion

An impact of 0.5-1.0% on the NWP index is very encouraging for an initial trial of the use of these data. In evaluating this impact one must consider that the information supplied from AIRS is in addition to that already supplied from two operational ATOVS instruments, the AMSU components of which have much greater spatial coverage due to their relative insensitivity to cloud.

Given the conservative nature of this initial implementation, there are many possible routes to explore to get a larger impact from AIRS data. These fall broadly into the categories of using more channels, using more observations, better specification of errors, better quality control (including cloud detection) and better bias correction. It is expected that exploration of the first three of these categories will be most fruitful in the years ahead.

The use of a greater number of channels, or the information from them, is important primarily through reducing the signal-to-noise ratio on those atmospheric signals with fine vertical structure. This may be achieved most efficiently through the use of super-channels, reconstructed radiances or even retrievals (most NWP centres have only in the last few years abandoned retrieval assimilation in favour of direct assimilation of radiances). It should be noted that both reconstructed radiances and retrievals both include additional a priori information (most likely climatological) that might adversely effect the analysis for the NWP forecast.

The key to using more observations will be improved treatment of fields of view that contain clouds. The spectral signatures of clouds, temperatures and molecular abundances in a high-resolution infrared spectrum are separable, and there is certainly scope to extract useful information from these observations. Current approaches include the identification of channels that are not sensitive to levels in the atmosphere at and below the cloud top and cloud clearing methods (which make use of auxiliary data to reconstruct the observed radiances that the clear column would produce). More advanced schemes based on variational principles and the explicit treatment of the clouds' optical properties will be explored.

The correct specification of observational and forward model errors is crucial to properly exploit the data in the manner described above. In particular, accurate treatment of inter-channel error correlation will be crucial in preserving the information contained in the subtle variations between channel radiances which are crucial in observing structures with small vertical scales.

Conclusions

Initial results from the assimilation of AIRS radiances show improvements in the main fields considered for NWP evaluation of 0.5-1.0%. This is encouraging given the conservative approach employed, especially considering that the total data volume (i.e., channels × fields of view) is reduced by a factor of ~10000 before the observations are presented to the assimilation system. It is planned to make the assimilation of AIRS data operational in the global NWP model at the Met Office during the spring of 2004.

More aggressive use of these data may produce bigger yields in terms of impact on forecasts, but care must be taken to ensure that the extra data do not degrade the forecasts through, for example, contamination from cloud signals. The efficient use of all the spectral information and the use of more data in cloudy areas are priorities for future improved exploitation of this exciting new type of observation.

References

Collard, A.D. 1998. Notes on IASI Performance. NWP technical report No. 253, Met Office, Bracknell, UK.

English, S.J., Eyre, J.R. and Smith, J.A. 1999. A cloud-detection scheme for use with satellite sounding radiances in the context of data assimilation for numerical weather prediction. Q.J.R. Meteorol. Soc., 125, 2359-2378.

Harris, B, Collard, A., Saunders, R. and Cameron, J., 2004. Effect of air-mass predictor choice on the AIRS bias correction. The Technical Proceedings of the Thirteenth International TOVS Study Conference.

Huang, H.-L., Smith, W.L. and Woolf, H.M. 1992. Vertical resolution and accuracy of atmospheric infrared sounding spectrometers. J. Appl. Meteorol., 31, 265-274.

Prunet, P., Thépaut, J.-N. and Cassé, V. 1998. The information content of clear-sky IASI radiances and their potential for numerical weather prediction. Q.J.R. Meteorol. Soc., 124, 211-241.

Rodgers, C.D. 1996. Information content and optimisation of high spectral resolution measurements. SPIE, 2380, Optical spectroscopic techniques and instrumentation for atmospheric and space research II, Paul B. Hays and Jinxue Wang eds., pp. 136-147.

Susskind, J., Barnet, C.D. and Blaisdell, J.M. 2003. Retrieval of atmospheric and surface parameters from AIRS/AMSU/HSB data in the presence of clouds. IEEE T Geosci Remote, 41 (2), 390-409.

Use of MODIS imager to help dealing with AIRS cloudy radiances

Lydie Lavanant *, Mohamed Dahoui **, Florence Rabier *, Thomas Auligné *****

** Météo-France, Centre de Météorologie Spatiale, BP 147, 22300 Lannion Cedex France*
*** Maroccan Meteorological Service*
**** Météo-France, Centre National de Recherche Météorologique, 42 av. Coriolis, 31057 Toulouse Cedex France*

Summary

The atmospheric Infrared Sounder (AIRS) was launched in May 2002 on board the AQUA platform. This new high spectral resolution instrument provides 2378 channels covering the spectral range between 650 cm^{-1} to 2700 cm^{-1} which allow a good "stand-alone" description of the clouds in the fov by processing an adapting subset of channels.
For the time being, in most operational analysis systems, the assimilation of the satellite radiances is limited to the cloud-free pixels. The assimilation of the AIRS radiances in clear conditions is already defined at Météo-France and is presented in full details in this issue (Auligné and al, 2003). In parallel, developments are on-going for the assimilation of the AIRS cloudy radiances.
This paper focuses on the validation of various cloud-detection schemes applied to AIRS spectra. The clouds are detected and characterized, in height and cover, by using the NESDIS, ECMWF, CO_2-slicing and MLEV schemes. Short description of the four methods is given in this paper. AIRS radiances biases correction is required before any cloud detection and is presented. The resulting AIRS cloud description is then evaluated by using independent information retrieved with the Météo-France cloud mask applied to co-registered MODIS imager data and taken as our reference.
Status on this comparison and on the validation for a ten days period over the North-East Atlantic is presented.

Introduction

The validation of "stand-alone" AIRS cloud–detection schemes was primarily done for a better understanding of the capability of the high spectral resolution for an improved cloud description. The second issue of that work was to determine their remaining limitations compared to the imager capabilities. It was also a way for starting the definition of a more precise cloud detection scheme using the full high spectral resolution for the future METOP/IASI instrument.

As we do not have a direct broadcast system for the AQUA platform at the CMS, we got level1b MODIS, AIRS and AMSU data provided by the NASA/GSFC DAAC web site for only a ten days period from 10 to 20 April 2003 in the North Atlantic. The desarchived 35 granules cover different interesting day and night situations with a variety of cloud types. Only sea situations have been processed. The AIRS data are full resolution spectra and the level1b files contain the localization data for all the instruments which avoids re-doing that complex pre-processing. The first period from 10 to 15 April was used as a training period for the computation all the necessary thresholds and biases coefficients of the models and the validation is done on the second period from 16 to 20 April.

For simulating clear radiances necessary in the ECMWF, CO_2-slicing and MLEV schemes, we used the RTTOV-7 forward model together with the nearest in time and location French ARPEGE NWP atmospheric background. Same biases corrections were applied to the 3 schemes and the same sub-set of channels was used in ECMWF and CO_2-slicing models.

MODIS cloud description

The Moderate Resolution Imaging Spectroradiometer (MODIS) on board the AQUA satellite, is primarily designed for cloud imaging and sea surface temperature. The cloud mask used in this study is an adaptation to MODIS of the NWC SAF package with only MODIS channels similar to SEVIRI channels used (LeGléau and Derrien, 2002). Three output parameters are retrieved; the clear/cloud flag, the cloud type and the cloud top temperature and height.

The cloud mask is based on the fact that the spectral behavior of clouds and earth surfaces are different in window channels. The method chosen is a multispectral technique applied every pixel which is efficient in term of computing time and is relatively easy to adapt. The method was prototyped with AVHRR and GOES imagery and tuned to SEVIRI and MODIS spectral conditions even before data were available. The thresholds are applied to various combinations of channels and depend on the geographical location, on the solar illumination and viewing geometry of the pixel. Thresholds are computed in-line from constant values from experience, from tabulated functions defined off-line through RTTOV simulations, from external data such as NWP forecast fields of land surface temperature and total water vapor content and from climatological atlas of sea surface temperature and albedo. For opaque clouds, the cloud top temperature is obtained through the best fit between simulated and measured 10.8µm brightness temperatures. For high semi-transparent clouds, two methods are used: the CO_2-slicing method which makes use of the fact that the variation of the radiance with height and cloudiness is not the same for a window channel as for a CO_2 sounding channel. An alternative approach called the H_2O/IRW intercept method based on an IR window and a WV channel histogram analysis, is applied when the CO_2-slicing method fails.

Estimations of the accuracy and limits of the cloud mask have extensively been done for AVHRR/HIRS and GOES data during several years, by the NWC SAF team. Validation for MODIS and SEVIRI is in progress. Figures 1 illustrate the efficiency of the cloud mask with the measurement conditions. The left figure shows the comparison of the cloud cover (in octa) automatically derived from GOES-East measurements and visually observed in meteorological stations (SYNOP observations) over continental mid-latitude regions. The right figure shows the accuracy of the cloud top pressure retrieved with HIRS sounding channels, similar to MODIS channels 32 and 34, when compared to coincident lidar observations.

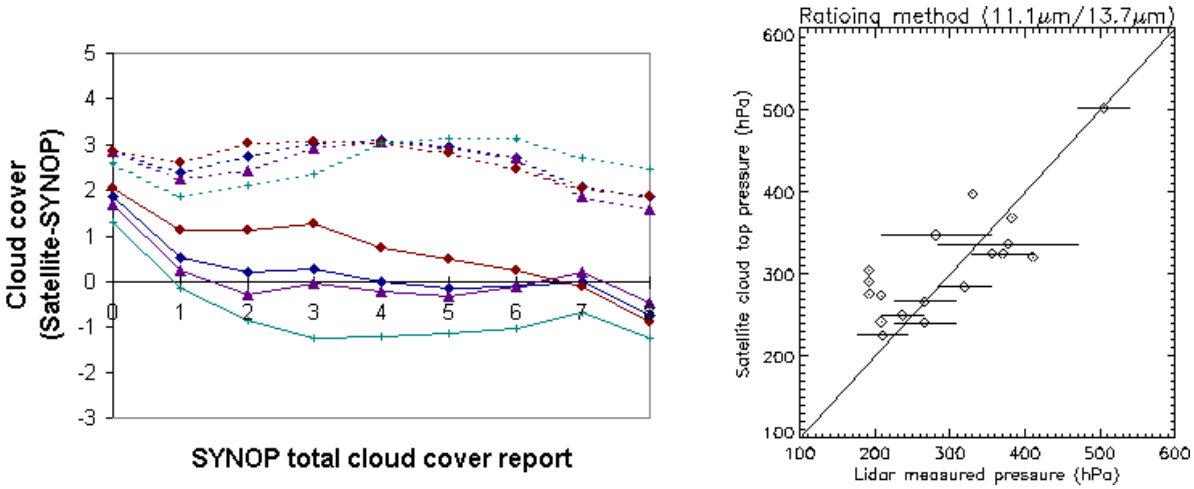

Figures 1. Imager cloud mask accuracy. The left figure shows the comparison of the cloud cover (in octa) from GOES-East data and SYNOP observations in mean and standard deviation for different illumination (day, night, twilight, all) and for continental mid-latitude regions. The right figure concerns the cloud top pressure retrieved with HIRS compared to coincident Lidar measurements (Courtesy NWC SAF team).
For more details see www.meteorologie.eu.org/safnwc

MODIS and AIRS mapping

The processing of the MODIS pixels mapped inside the AIRS fov is an efficient way to detect small amount of clouds because of its high spatial resolution, to determine the number of cloud layers and the complexity of the situation. Also, the imager processing provides accurate cloud top pressures for opaque layers, mainly at medium or low levels. For semi-transparent clouds, the method used for computing the layer temperature is a CO_2-slicing method but with less channels than for AIRS. The two methods are then complementary.

The mapping of MODIS and AIRS is based on their navigation information given in the level1b data and on the scan geometry of the two instruments. An adjustment in line and pixel of the MODIS data in the AIRS fov is done through the minimization of the differences between AIRS brightness temperatures convoluted on MODIS 32 filter and corresponding MODIS observations averaged on the AIRS ellipse. The adjustment depends on the AIRS scan position. Precise ifov adjustment was also tested using the VIS/NIR AIRS imager but for our test dataset the method did not improve the results. Figure 2 shows the statistics of the departure for a four days period corresponding to 20 day and night granules. Figures 3 give an example for one granule of the cloud types inferred with the MODIS cloud mask and for the same granule of the differences between AIRS and MODIS for MODIS channel 32 at the AIRS resolution.

From the MODIS cloud type and temperature characteristics, up to 3 cloud layers are allowed in the AIRS ellipse, each of them with a cloud cover, a cloud classification and a top temperature. A situation is declared clear if less than 5% of MODIS pixels are cloudy in the ellipse.

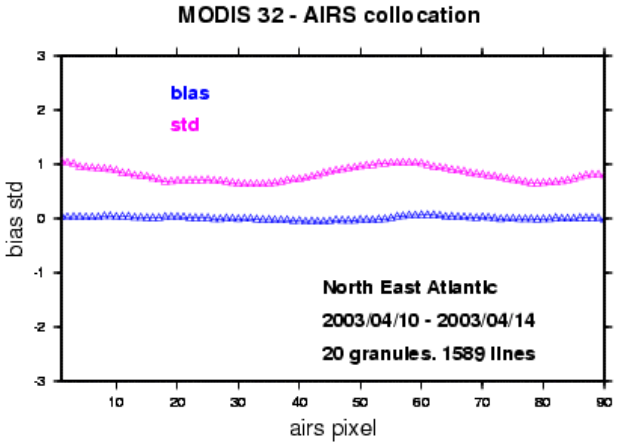

Figure 2: statistics in bias (blue) and standard deviation (in red) function of the AIRS scan position between AIRS and MODIS Tbs for the MODIS filter 32. Day and night data. 20 granules for 4 days

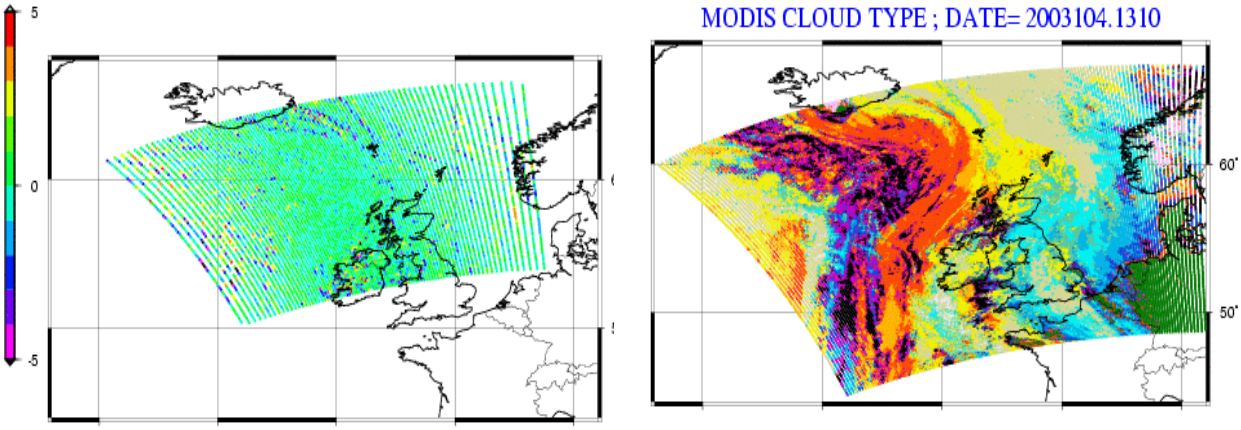

Figures 3: in right example for one granule of the cloud types inferred with MODIS and in left for the same data the differences at the AIRS resolution between AIRS and MODIS for MODIS 32.

AIRS bias correction

The comparison of observed and computed radiances shows the presence of systematic errors arising mainly from errors in the radiative transfer model, instrument measurement/calibration problems or problems in the model fields themselves. The model we used in this study to evaluate the biases of each AIRS channel j in the CO_2 band is based on the collocated AMSU-A observations:

$$A0(j) + \sum_{i=1,8} (Ai(j) * (yi - \overline{yi})) + A9(TWVC - \overline{TWVC}) + A10(Ts - \overline{Ts}) + A11 * \sec$$

Y = AMSU 6, 8,9,10,11,12,13,14
Ts = Surface temperature
Sec= secant of the viewing angle

In our case, for this dataset and this part of the spectrum, the results were slightly better using a correction based on AMSU-A data than with the Harris and Kelly (2001) model usually used in the course of NWP assimilation.
The coefficients were computed on the training period from all AIRS situations declared clear with MODIS mapped in the fov and they were then applied on every AIRS situation of the second time period. The correction is done before the AIRS cloud detection and identically for the ECMWF, CO_2-slicing and MLEV methods. Indeed, the accuracy of the retrieved cloud information highly depends on the correct simulation of the clear radiance Rclr. Figures 4 show, for this second period, the statistics in bias and standard deviation of the departure between RTTOV7 simulated and observed brightness temperatures before (lower figure) and after (upper figure) the bias correction.

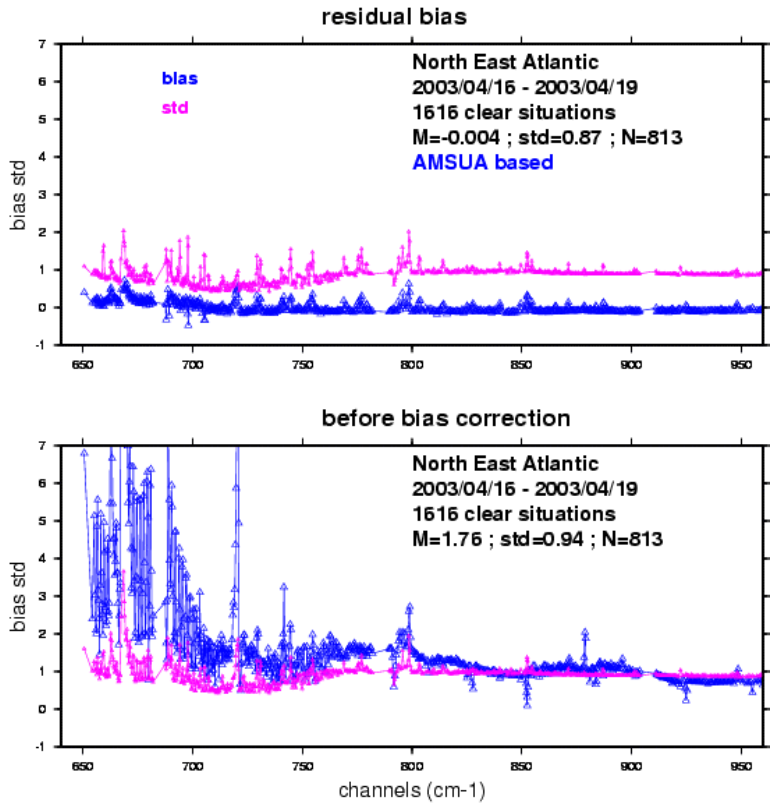

Figure 4: statistics in bias (blue curves) and standard deviation of the departure between RTTOV7 simulated and observed brightness temperatures before (lower figure) and after (upper figure) the bias correction.

NESDIS AIRS cloud detection

The purpose of the NESDIS cloud detection scheme (Goldberg and Zhou, 2002) is the detection of the clear situations, without any cloud characterization in height. It is a very fast model based on an empirical combination of 3 tests applied to AIRS channels and co-registered AMSU-A channels:

1. $AIRS_{sim}$_2112– AIRS_2112 < Thres1 (=2K)
   The simulated AIRS channel 2112 (2391 cm-1) is function of AMSU-A 4, 5, 6 and of the scan and solar zenith angles

and

2. AIRS_2226 (2532cm-1) – AIRS_843 (937.92cm-1) < Thres2 (=10K) (night)
3. Thres3 < SST_{guess} - SST_{sim} < Thres4
   The guess sea surface temperature comes from the nearest French NWP forecast field. The simulated SST is function of the observed AIRS channel numbers 791 (918.747cm^{-1}), 914 (927.122cm^{-1}), 1285 (1228.225cm-1) and 1301 (1236cm-1).

At the time of this study, only pre-launch coefficients were available and slightly different results may be found using the post-launch values.
The NESDIS cloud detection is interested because it does not need to apply a channel bias correction. Also, it is relatively independent of atmospheric prior information, except for sea surface temperature. However, to be accurate, it is important to tune the different thresholds to the concerned time period and geographical location. Figure 5 shows simulated AIRS SST compared to NWP SST for the training dataset. Thresholds of -0.6K and 3.3 K allow the detection of about 99% of the clear situations and more than 95% of the cloudy situations.

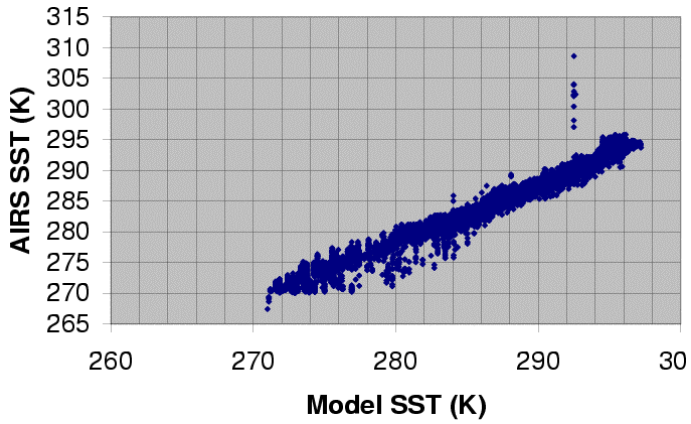

Figure 5: simulated AIRS SST compared to NWP SST for the training dataset.

ECMWF AIRS cloud-free channels selection

The ECMWF scheme (McNally and Watts, 2003) aims to detect channels affected by clouds. Unaffected channels are potentially useful for the NWP assimilation system.
The scheme performs the detection in several steps as follows:

- Simulated AIRS spectra are generated using the nearest NWP forecast profile and the RTTOV7 forward model. Bias correction is applied on each channel.
- Each channel is assigned to the lowest P_k level at which the radiation effect of one opaque cloud layer at P_k, defined as $(|Rclr - Rcld(P_k)|)/Rclr$, is less than 1%. The (measured – simulated) Tbs are then sorted according to the assigned level into five spectral bands at 15, 9, 7, 4.5 and 4.2µm.
- A low pass filter is applied on the ranked information in order to smooth the instrument noise and the cloud emissivity effect.
- Based on the assumption that, when looking downwards, a cloud signal monotonically increases in the channels ranked space, all channels with a (measured – simulated) value less than a threshold are considered as cloud free channels above the cloud layer.

In this study, only the 15µm band was used which concerns 124 channels from the 281 selected channels sent at that time in near-real time by NOAA to European NWP centers. A unique cloud status was given per AIRS fov and not per channel.

CO_2-Slicing Cloud characterization

Calculation of the cloud-top pressure and the effective emissivity is done with the CO_2-slicing method as described by Menzel and Stewart (1983) and Smith and Frey (1990).

$$\frac{(Rclr - Rmeas)_k}{(Rclr - Rmeas)_{ref}} - \frac{Ne_k\,(Rclr - Rcld)_k}{Ne_{ref}\,(Rclr - Rcld)_{ref}} = fpc$$

Rmeas: measured radiance
Rclr: clear radiance computed from a collocated forecast for the same fov
Rcld: black-body radiance at the cloud level n
k= channel in the CO_2 band
ref= reference window channel = 979.1279 cm-1

To summarize the method, the function fpc is computed for each pressure level of the RTTOV7 forward model and the cloud top pressure is the level which minimizes the function. This is done for several channels and the final cloud pressure is the weighted average:

$pcld = \Sigma\,(pcld(k)\ w^2(k)) / \Sigma w^2$

with $W = \delta f_{pc} / \delta \ln p$ the derivative of the cloud pressure function

Then, the effective emissivity is computed for the reference window channel by:

$N\varepsilon = (Rclr - Rmeas)_{ref} / (Rclr - Rcld)_{ref}$

The method assumes that the cloud is a thin layer. A first test determines the situation clear if the departure between clear and cloudy radiances is less than the radiometric noise*sqrt(2) for all the channels. The cloud resulting information is flagged bad if the retrieved cloud emissivity is smaller than 0 or larger than 1.2

We used the CO_2-slicing method for the same 124 selected channels than for the ECMWF scheme from 649.612 cm-1 to 843.913 cm-1. This spectral region provides the best sensitivity to both cloud-top pressure and effective emissivity.

MLEV cloud characterization

The Minimum Local Emissivity Variance scheme (Huang and al, 2003) takes advantages of semi-continuous high spectral resolution spectra. It is a physical method which assumes the slow spectral variation of the cloud emissivity in the CO_2 band. The method simultaneous retrieves the cloud altitude and the effective emissivity spectrum.

For a cloudy or a partially-cloudy fov, the effective cloud emissivity spectrum is given by:

$$N\varepsilon(\nu) = (R_{meas}(\nu) - R_{clr}(\nu)) / (R_{cld}(\nu) - R_{clr}(\nu))$$

The altitude level which ensures the smallest local variation of the effective emissivity is considered as the optimal cloud top pressure solution. For that, we compute the local variances over $\Delta\nu$=5cm-1 local bands:

$$Var_{loc}(\nu) = \Sigma\,[N\varepsilon(\nu) - moy(N\varepsilon(\nu))]^2 \quad \text{in } [\nu - \Delta\nu/2,\ \nu + \Delta\nu/2]$$

The cloud pressure is the one which minimizes the mean value $\Sigma[Var_{loc}(\nu)]$ in the CO_2 spectral band between 650 cm-1 and 850 cm-1.

For this method, we also used RTTOV-7 and the same NWP background as for the previous two methods for simulating the AIRS clear radiances at each level, for each situation and all channels in CO_2 band. However, we did not yet implement a channel sensitivity to pressure of the local variance $\delta Var_{loc}(\nu) / \delta \ln p$ as we did it in the CO_2-slicing method.

Results

The following results correspond to the processing of the second part of the dataset from 16 to 20 April. Dynamic coefficients and thresholds applied in the treatment have been first determined on the training part of the dataset.

	Clear sit. correctly detected		Cloudy sit. correctly classified	
	Day	night	day	night
Number of situations	2799	5470	28510	57719
NESDIS	83.42%	85.52%	87.83%	94.80%
ECMWF	82.67%	88.45%	88.07%	94.36%
CO2-slicing	75.85%	84.11%	89.05%	94.62%
MLEV	76.77%	82.07%	84.33%	91.45%

Table 1: Overall cloud masks efficiency in % of the four schemes for day and night illumination.

For all the granules, we did a systematic visual comparison (not shown here) of the different cloud parameter fields with the corresponding MODIS fields. For all schemes and granules, synoptic cloud patterns are correctly detected. Table1 shows the overall cloud masks efficiency for the different schemes when compared to MODIS. It should be noted that of course the MODIS mask has its own weakness which contributes to the comparison. Nevertheless, the results are very encouraging indicating that the clouds can be efficiently detected with AIRS alone. Results during the night seem systematically better; this could be due to a better accuracy of the background SST used in the four models.

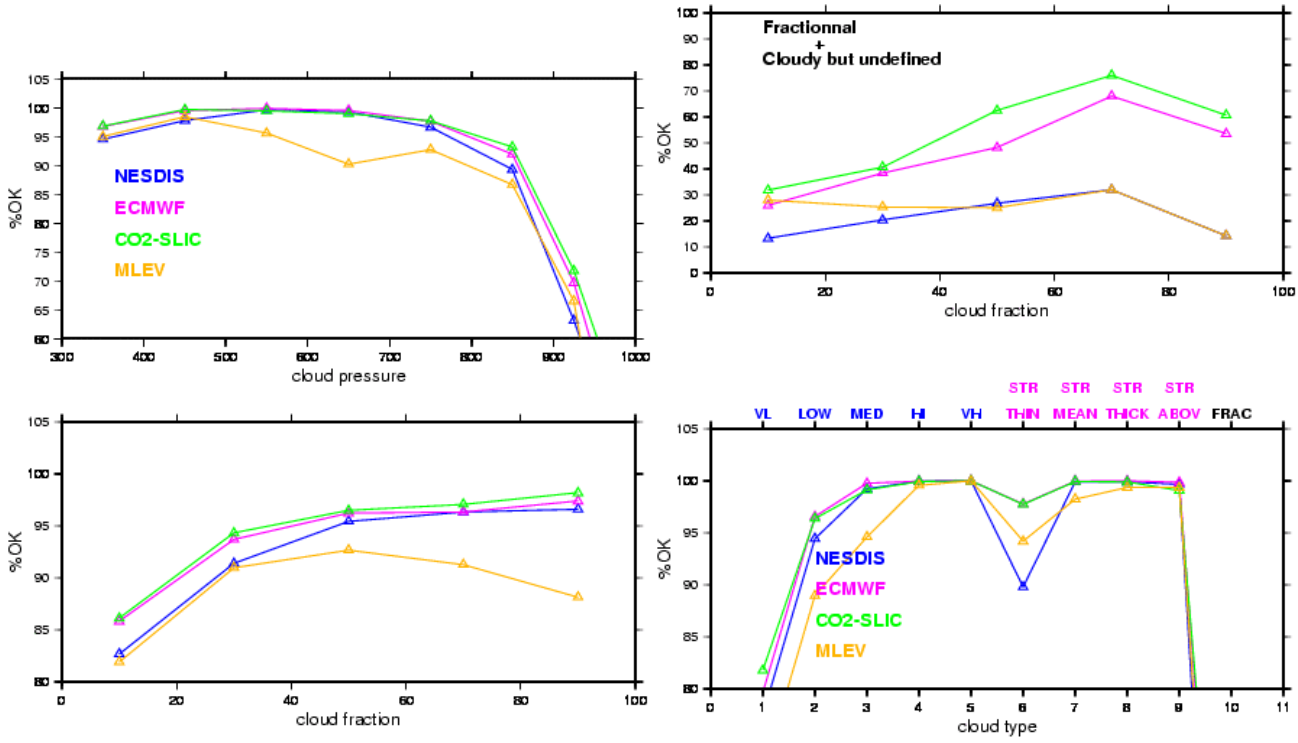

Figures 6: cloud-detection masks efficiency in %, function of the cloud layer cover (lower left figure), of the cloud pressure (upper left) and with the different cloud categories (lower right) given by MODIS. The categories are for opaque clouds Very low, Low, Medium, High, and Very high and for semi-transparent clouds Thin, Mean, Thick optical thickness and clouds above others. A last category defines fractional clouds at the MODIS resolution. The upper right figure is a 'zoom' for the fractional and unclassified clouds by MODIS.

Figures 6 give more details on the cloud-detection masks efficiencies for different characteristics of the cloud layers (cloud cover, pressure and types) inferred with MODIS. For all schemes, small amount of clouds are still difficult to be retrieved. Also some clouds near the surface are missed. From a personal discussion with G. Aumann, the use of the super-window channel at 2616cm-1 (which is not a MODIS channel) should greatly improve the detection of small amounts and low-level clouds. This channel is already used in the NESDIS post-launch detection scheme and we will introduce it in the other methods for future test experiments.
The comparison with the cloud classification shows that thin semi-transparent clouds are difficult to be detected. For these situations, the AIRS footprints are generally completely overcast and the problem is mostly due to the insensitivity of the sounding-based methods to thin optical thickness layers (use of constant and identical thresholds…). The addition of specific threshold cirrus tests from the large imager experience should improve the detection. Also, the description of the atmosphere on more pressure levels could improve the sensitivity of the methods mainly for the MLEV method.
The MLEV scheme appears to be very sensitive to the measurement noise which is important and extremely different between adjacent channels for AIRS on the CO_2 band and an additional treatment to filter the noise through a PCA method has to be added. Detection of mid-tropospheric layers is mainly affected by the noise. Simulations with the METOP/IASI noise characteristics indicate that the method could give results as accurate as the other methods.

Figures 7 show preliminary accuracy estimations of AIRS cloud top pressures inferred with the CO_2-slicing and MLEV, function of the MODIS cloud cover. In case of several cloud layers, the AIRS information is compared to the MODIS highest cloud level. The purpose is to get an incertitude for the selection of unaffected cloud channels above the cloud fields. As said previously, the MODIS cloud top height is also based on a CO_2-slicing method and in the left figure the root mean square of errors is mainly due to the combined incertitude of the same method for two different instruments and to the average with AIRS of the complexity of the situation. Firsts results with the MLEV methods are encouraging: the method seems very sensitive to the top cloud layer in case of multi-layers and more stable with the cloud cover and the cloud height. Not shown here, the comparison with the underlying layers gives worse results. This has to be confirmed with further experiments.

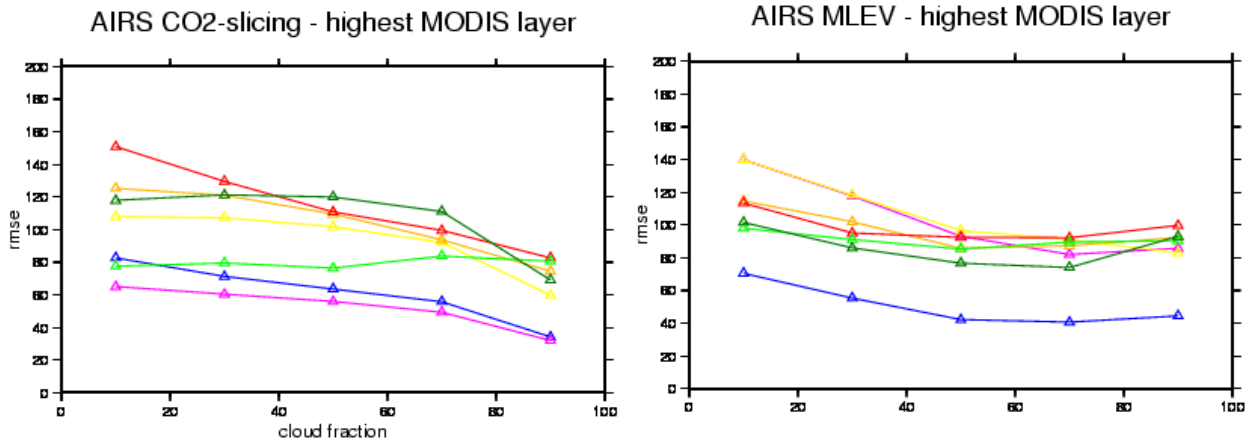

Figures 7: cloud top pressures accuracy for the CO2-slicing and MLEV methods compared to MODIS for different layer levels; <400hPa, 400-500hPa, 500-600hPa, 600-700hPa, 700-800hPa, 800-900hPa, >900hPa.

Conclusion

For all schemes, the synoptic cloud patterns, in cloud detection and height characterization, are correctly detected.

Concerning the cloud detection, for the four schemes, we have a general good agreement with the MODIS cloud mask above 900hPa but the sensitivity to clouds is poor near the surface and for fractional or unclassified clouds.
ECMWF and CO_2-slicing methods are very efficient and give similar results. However, the MODIS description inside the AIRS fov is still useful for the 'difficult' situations, for small amount of clouds, fractional or thin semi-transparent clouds.
The NESDIS model with pre-launch coefficients is less efficient for the thin semi-transparent and fractional categories. However, thresholds depending on location, computing in-line from atlas or forecast, could surely improve the detection. We must note that the NESDIS scheme gives really good information considering that the model is fast, simple and independent of any forecast profile.
In this study, the MLEV method was less efficient than the others, mainly for detecting mid-tropospheric layers and fractional clouds. From simulations, it appears that the method is very sensitive to the measurement noise. We did not try here to filter the AIRS measurement noise, except by only removing all channels with an NeDt, as provided by NOAA, larger than 0.6K but a better treatment is required.

Concerning the cloud top pressure determination, only retrieved in this study with CO_2-slicing and MLEV, for multi layers situations, both methods are better correlated with the highest layer and the MLEV scheme seems more efficient, with a good coherence with MODIS even for small fraction. This of course has to be confirmed on other test cases.

This comparison will be extended to other test cases. This will be the opportunity to improve the MLEV method, by filtering the AIRS measurement noise with a PCA method as described by Huang and Antonelli, 2001, by implementing in the scheme the channel sensitivity to pressure of the local variance. Also, concerning the NESDIS method, we will use the post launch model as described in Goldberg, 2003.

References

Auligné and all. 2003. Firsts results of AIRS assimilation at Météo-France. ITSC-13 proceedings.

Harris, G. Kelly, 2000. A satellite radiance-bias correction scheme for data assimilation. Q. J. Roy. Meteor. Soc., **127**, 1453-1468

Huang, P. Antonelli, 2001. Application pf Principal Component Analysis to high resolution infrared measurement compression and retrieval. J. Applied Meteorology,**40**, 365-388

Huang and al, 2003. Simultaneous retrieval of cloud height and effective emissivity from hyper spectral radiance measurements. OSA/ORS proceedings.

Goldberg, L. Zhou, 2002. AIRS clear detection flag. Presentation material at a meeting

Goldberg and all, 2003. AIRS near real-time products and algorithms in support of operational numerical weather prediction. IEEE transaction on geoscience and remote sensing, 41 no 2, 379-389

LeGléau, M. Derrien, 2001. Use of MODIS to enhance the PGE01-02 of SAFNWC/MSG. EUMETSAT documentation.

LeGléau, M. Derrien, 2002. User manual for the PGE01-02-03 of the SAFNWC/MSG: Scientific part. EUMETSAT documentation.

McNally, P. Watts, 2003. A cloud detection algorithm for high spectral resolution infrared sounders; Q. J. Roy. Meteor. Soc., in revision.

Menzel, W. Smith, T. Stewart. 1983.Improved cloud motion wind vector and altitude assignment using VAS. *J. Appl. Meteor.*, **22**,377-384.

Smith, R. Frey, 1990. On cloud altitude determinations from High Resolution Interferometer Sounder (HIS) observations. *J. Appl. Meteor.*, **29**, 658-662.

Impact of observation density in data assimilation: A study with simulated observations

By Zhiquan Liu [(1)] and Florence Rabier [(2)]

[(1)] National Satellite Meteorological Center, Beijing, China (zqliu@nsmc.cma.gov.cn)
[(2)] Centre National de Recherches Météorologiques, Toulouse, France

Abstract

The potential of high-density observations is studied in a practical context of the 4DVAR assimilation. A series of observing system simulation experiments (OSSEs) are carried out. Observations with both uncorrelated and correlated observation errors are simulated in sensitive areas. The results show that: for the observations with uncorrelated error, increasing the observation density generally improves the analysis and the forecast; for the observations whose error is correlated and by using a sub-optimal scheme (i.e., no modelling of the error correlation), the assimilation system can still extract useful information and one can determine an observation density leading to a minimum error of analysis and forecast. A risk of using horizontal high-density observations is that it could produce unrealistic increments and degrade the analysis on the levels without observations in the case of inappropriate background error correlations.

Introduction

In a 1D study, Liu and Rabier (2002) showed that the optimal density of observations in data assimilation depends mainly on the correlation of observation error. Figure 1 (Liu 2002, p13) shows the analysis error as a function of the observation interval. One can see the results for the 3 cases: (1) for the observations with uncorrelated error, increasing the observation density generally improves the analysis (black-mixed line); (2) for the observations with correlated error and by using an optimal scheme which models the error correlation of observation in the cost function, increasing the observation density beyond a certain threshold will bring little or no improvement of the analysis quality (red-solid line); (3) for the observations with correlated error but by using a sub-optimal scheme which assimilates the correlated data as if they were not, one can find an optimal interval of observations, which reaches a compromise between the risks to have a too low data density and to be affected by the correlated error of observations (blue-dashed line). In this study, one wants to check the results for the cases (1) and (3) in a practical context of the 4DVAR assimilation (the French model "ARPEGE"). As the modelling of the observation error correlation is not coded in ARPEGE, the case (2) is not examined. Two different weather situations poorly predicted by ARPEGE, are studied to examine the impact of various densities of observations on the analysis and the forecast. A series of OSSEs are carried out.

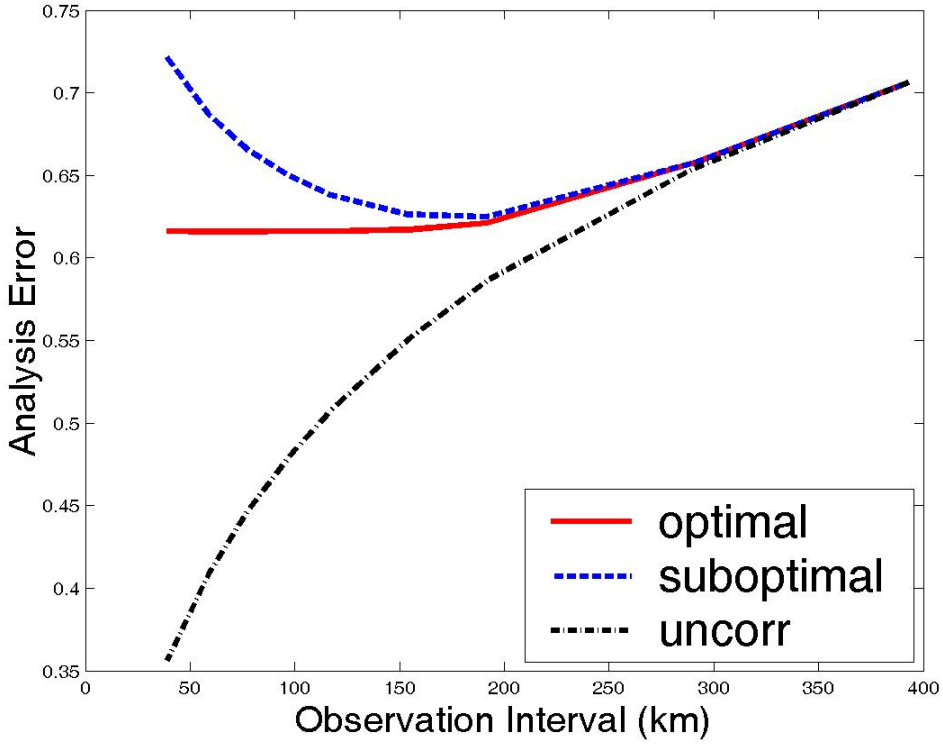

Fig. 1: Variation of the analysis error as a function of the observation interval. The analysis mesh Δx is equal to 100km, the length of the background error correlation r_b=200km. The errors of the background and the observations have the same variance 1. The observation error correlation is of Gaussian type with a correlation length of 100km. The observations and their error covariances for each configuration are extracted from a network of observation with an interval of 20km. From Liu (2002, p13).

Assimilation and forecast system used for OSSEs

The assimilation and forecast system with which the observing-system simulation experiments (OSSEs) are performed is the French ARPEGE (Action de Recherche Petite Echelle et Grande Echelle) model. It is a global spectral model. A specific feature of the model is the use of a stretched grid in the horizontal direction to obtain an increased resolution over a geographical area of interest. The resolution used in the study is taken as the operational configuration in 2001. In the horizontal, it uses a triangular truncation T199. A terrain-following pressure-based hybrid vertical coordinate η with 31 levels is used and the top of the model is about 5hPa. A stretching coefficient 3.5 gives a spectral resolution varying from T696 over France to T57 over New Zealand. The assimilation component of the system includes a multi-incremental 4DVAR assimilation (Veersé and Thépaut, 1998) with a 6h assimilation window for the upper-air and surface pressure fields and an optimal interpolation (OI) analysis for other surface fields. The incremental analysis is performed on a regular unstretched grid in the current implementation. The minimization of the incremental cost function is performed with a successively increased resolution T42, T63 and T95. The configuration of resolution can be denoted in

short by T199C3.5L31/T42-63-95C1.0L31, where “T” represents the spectral truncation, “C” the stretching coefficient and “L” the vertical levels. That corresponds to a distance between the Gaussian mesh points varied from about 20km to 200km for the forecast and 200km for the analysis.

The first case: the Christmas storm in 1999

The first case examined is the storm having hit Europe and in particular France at 18UTC on 27th December 1999. This case is known because of the serious damage and the poor forecasts produced by most of the NWP centers. The trajectory of the 54h forecast started from the pre-operational 4DVAR analysis at 12UTC on 25th December is considered as the true in the OSSEs. This forecast has a low with a central pressure of 968hPa with perfect positioning. The operational forecast at that time (3DVAR) is considered as the background (the central pressure is equal to 975hPa and is poorly positioned). The simulated observations (temperature at all the 31 levels and surface pressure) are in the sensitive area (3066 Gaussian points) and at 48h before the storm. The assimilations of the simulated data with various samplings (0.3, 0.6 and 1.0 spherical degree) are carried out at 18UTC on 25th and followed by a 48h forecast. Two kinds of observation noise models are considered: uncorrelated and horizontally correlated. No vertical correlation is considered. Three models of correlation are considered: the correlation between two points separated by 0.6^{o} reaches 0.6, 0.3 and 0.15 respectively for strong, moderate and weak correlation models.

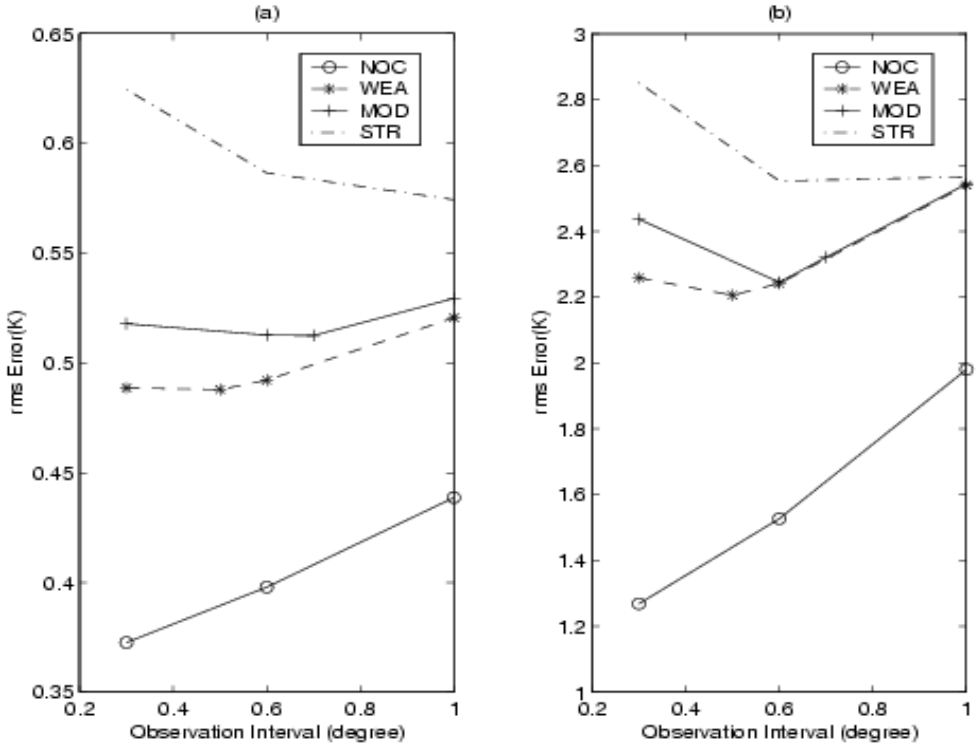

Figure 2: Level-averaged temperature r.m.s. error of (a) the analysis and (b) the 48h forecast for experiments with the weakly correlated (WEA), moderately correlated (MOD), strongly correlated (STR) and uncorrelated (NOC) observation error.

Figure 2 shows the RMS (root-mean-square) of error for the temperature analysis (in the sensitive area) and forecast at 48h (in the targeted area), averaged on all the model levels. The results are the average of 10 OSSEs with different realizations of random error. The assimilation scheme does not take into account the correlation of observation error. One can see that the errors of analysis and forecast increase regularly with the strenthening of the correlation of observation error. Moreover, the variation of the error with the observation interval shows a progressive transition from the uncorrelated case (denoted by "NOC") to the strongly correlated case (denoted by "STR"). For example, the error decreases in a monotonous way with the decrease of the observation interval for the uncorrelated case and increases for the strongly correlated case. A minimum error is located at an intermediate interval in the case of weak correlation (denoted by "WEA") and moderate correlation (denoted by "MOD"). This intermediate interval producing the minimum error of analysis is 0.5° for the case "WEA" and is 0.7° for the case "MOD". For these two optimal intervals, the adjacent observations have the same correlation equal to approximately 0.2 which is close to the value 0.15 found in the 1D study (Liu and Rabier, 2002).

It is noted that the errors of the 48h forecast can be approximately 4-5 times larger than the initial errors of analysis. The difference of the forecast error between various intervals of observation can be of an order of magnitude more significant than that of the analysis error. For example, the reduction of 0.04K of the temperature analysis error for experiment NOC0.6 compared to experiment NOC1.0 leads to a reduction of 0.45K of the forecast error.

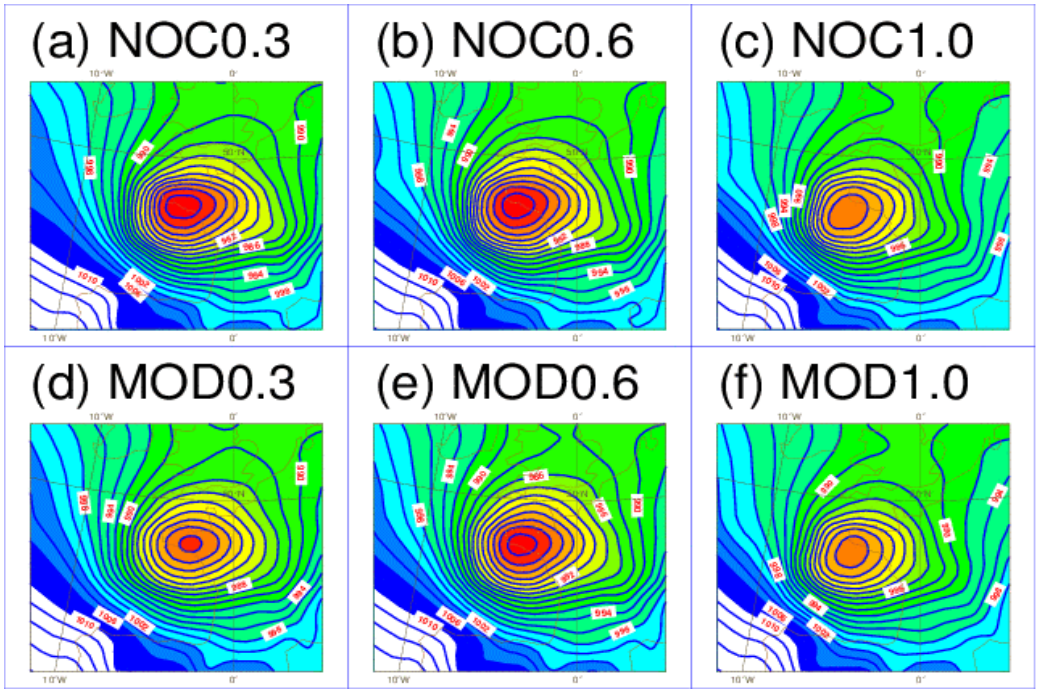

Figure 3: Mean sea level pressure (hPa) of the 48h forecast for 6 experiments: (a) NOC0.3; (b) NOC0.6; (c) NOC1.0; (d) MOD0.3; (e) MOD0.6; (f) MOD1.0.

Figure 3 shows the pressure reduced to the sea level predicted for the 6 experiments. They are consistent with the results in Figure 2. One can see that the three worse forecasts are those of experiment MOD1.0 (3f), NOC1.0 (3c) and MOD0.3 (3d). Their central pressures are respectively 974.6hPa, 974.4hPa and 973.4hPa.

The synoptic case at 00UTC on 25th September 2001

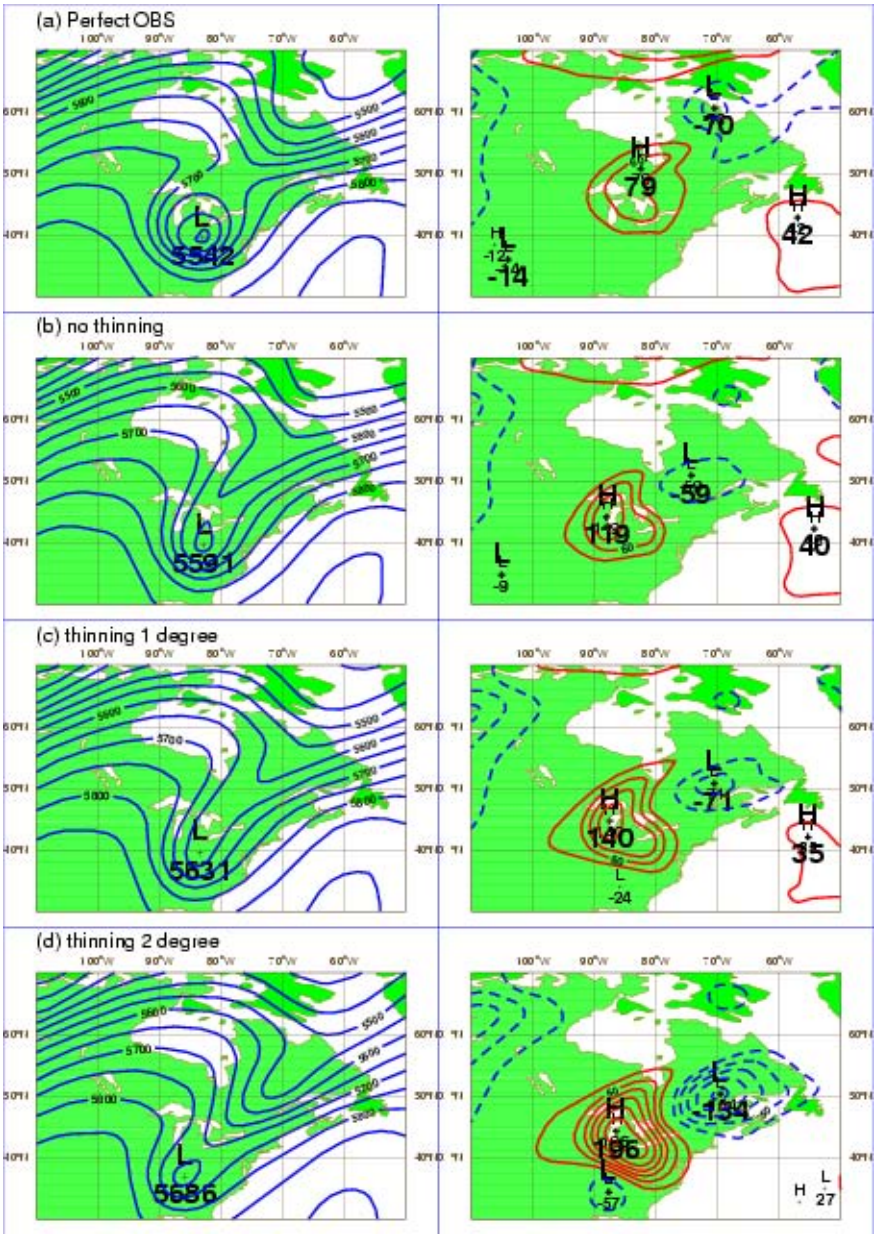

Figure 4: 96h forecast (left panel) and forecast error (right panel) of 500hPa geopotential height (in m) valid at 00UTC on 25th September 2001 for experiments (a). Perfect observations without thinning; (b). Noisy observations without thinning; (c). Noisy observations with a thinning of 1° ; (d). Noisy observations with a thinning of 2° .

The 96h forecast of the ARPEGE from the analysis at 00UTC on 21st September 2001 has an

enormous error (the order of 300m for 500hPa Z) compared to the verified analysis. On the other hand, ECMWF made an almost perfect forecast (thus is used as the true in OSSEs like the first case). The simulated observations with uncorrelated error are radiances of AMSU-A channels 5~12 in the north of North-America at 00UTC on 21st September. Figure 4 shows the 96h forecast of 500hPa Z for 4 experiments. For the 2 cases without thinning, the maximum error is reduced from 300m to 79m and to 119m respectively for the perfect and noisy observations. The forecast is degraded when the number of observations decreases.

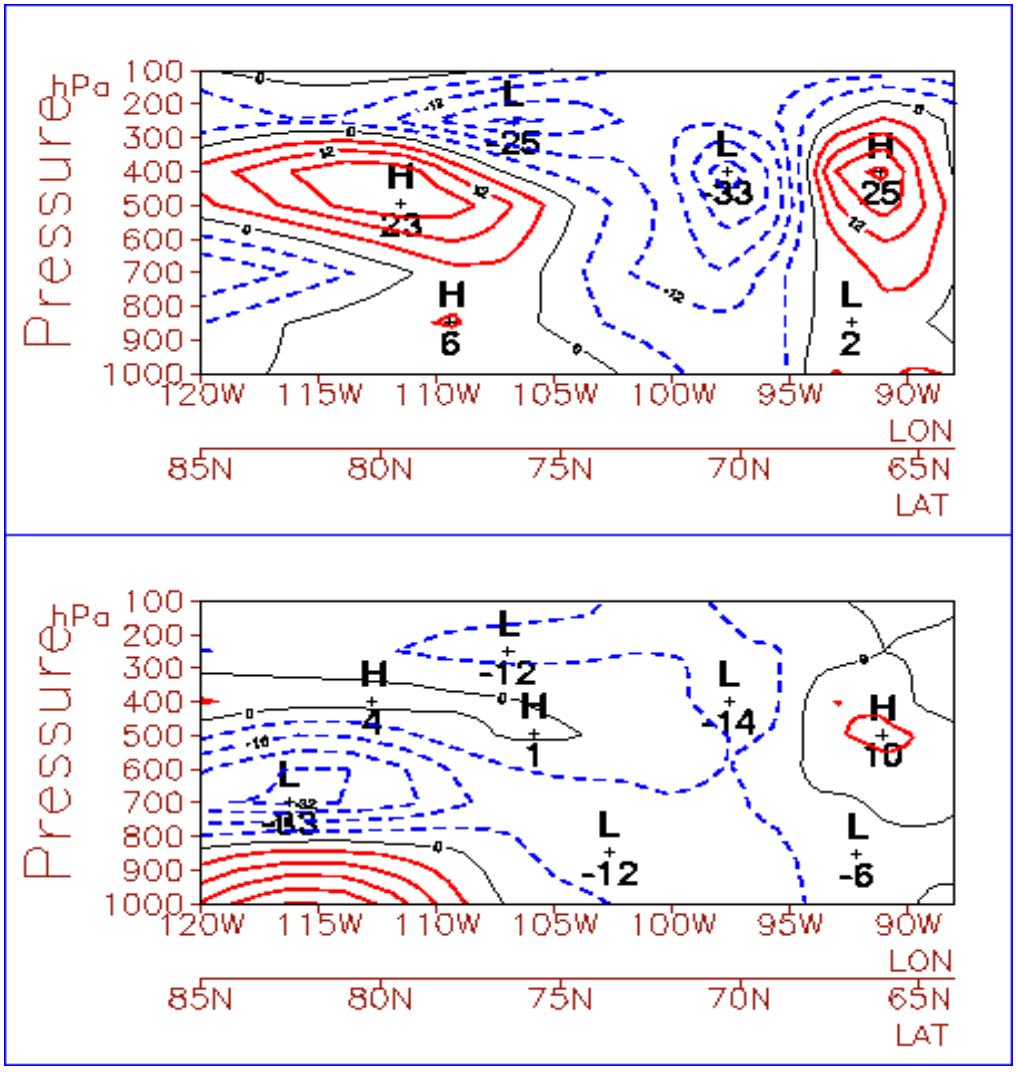

Figure 5: Cross-section of geopotential height (in m). Top panel: for background error; bottom panel: for analysis error with perfect observations.

However, the error on other levels is not always consistent with 500hPa. That can be illustrated by the cross-section in the Figure 5. One can see that the error between 300hPa to 500hPa is considerably reduced but the error at the lower levels is reinforced. We think that this problem comes mainly from the weakness of modelling the background error covariance matrix, which in operational practice is often constant and can propagate the increment in an incorrect way from a place to another

place or from a variable to another variable in certain situations. That represents a risk: employing observations with horizontal high density could accentuate unrealistic increments and degrade the analysis on the levels without observations, although this degradation does not necessarily influence the forecast in the interesting area as shown the Figure 4.

Conclusions and Discussions

This study confirms the results in the 1D study. A correlation of the order 0.2 is suggested for the determination of optimal thinning in the data assimilation. The data with high-density in the sensitive areas are important, particularly for some "tricky" conditions. Inconsistency between horizontal and vertical resolutions introduces certain risks because of imperfections in the background error covariance matrix. The specification of the statistics of observation errors and in particular their correlation, is necessary in order to model them and also to find the optimal thinning of observations. This subject of study constitutes an important work. Some additional results with respect to the statistical diagnostic and tuning of the observation error correlation are not presented here. The interested readers are referred to the recent paper of Liu and Rabier (2003).

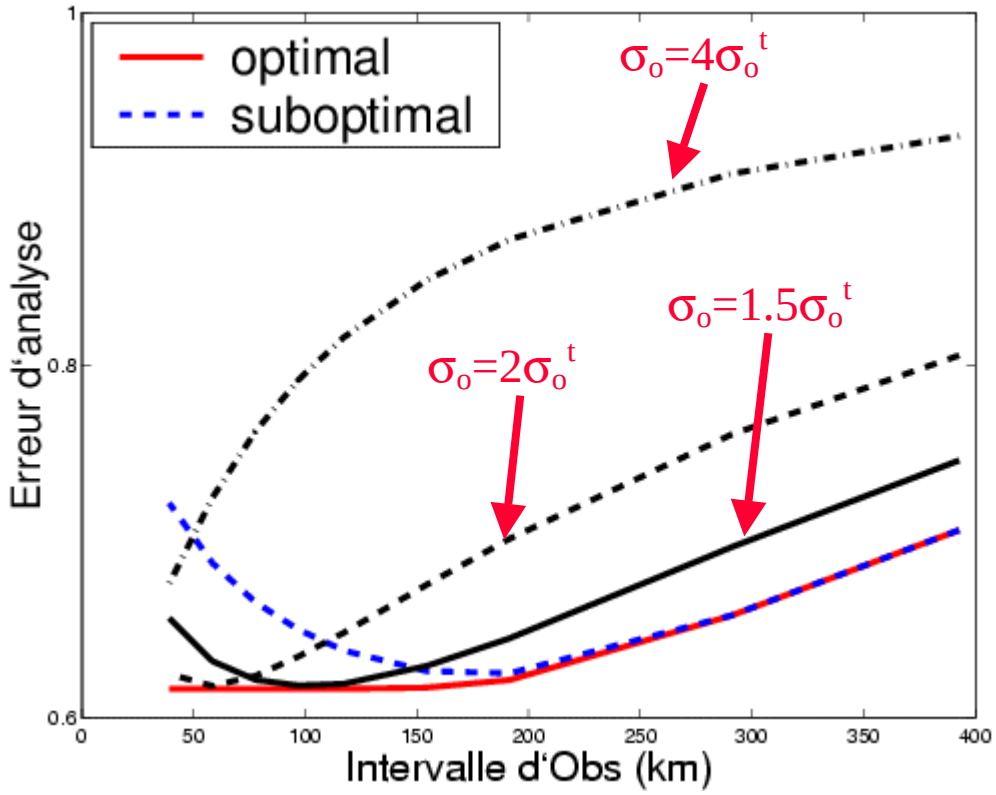

Figure 6: Impact of inflating the observation error. Two color curves are the same as those in the Figure 1, three black curves are the results with different inflating factors (1.5, 2 and 4) for the sub-optimal scheme.

In practice, we have other options to compensate the impact of the observation error correlation in a sub-optimal scheme. For example, inflating the observation error standard deviation σ_o specified

in the assimilation system (i.e., one gives less confidence to these correlated data). This has been applied to the practice but in an empirical way. One can expect that the optimal weight of observation is related to the correlation of observation error. The bigger the error correlation is, the more one should inflate σ_o. The figure 6 illustrates this in the 1D context as shown the figure 1. Two curves in color are the same as those in the figure 1. Three black curves are the results with different inflating factor (1.5, 2 and 4 times) for the sub-optimal scheme. One can sees that the optimal interval decreases when σ_o is inflated (respectively 100km for 1.5 times and 60km for 2 times). We find a correlation of 0.5 and 0.85 for the interval 100km and 60km. Moreover, the analysis error is exactly the same as that for the optimal scheme (red curve). That shows that inflating σ_o is a simple and efficient way to reduce deficiency resulted from the sub-optimality of the assimilation scheme. As expected, the analysis would be worse than that of the optimal scheme if one inflates too much σ_o (that is the case with 4 times inflating). The result in figure 6 implies that the optimal thinning interval depends not only the error correlation value itself but also the observation error standard deviation specified in the assimilation system.

References

Liu, Z.-Q., 2002. Influence of the observation resolution in data assimilation. Thesis of L'Université de Paul Sabatier, Toulouse, France, pp123, available from the author.

Liu, Z.-Q. and Rabier, F., 2002. The interaction between model resolution, observation resolution and observation density in data assimilation: A one-dimensional study. Q. J. R. Meteorol. Soc., 128, 1367-1386.

Liu, Z.-Q. and Rabier, F., 2003. The potential of high-density observations on Numerical Weather Prediction: A study with simulated observations. Q. J. R. Meteorol. Soc., 129, 3013-3035.

Veersé, F. and Thépaut, J.-N., 1998. Multiple-truncation incremental approach for four-dimensional variational data assimilation. Q. J. R. Meteorol. Soc., 124, 1889-1908

Use of AMSU data in the Met Office UK Mesoscale Model

**Brett Candy, Stephen English,
Richard Renshaw & Bruce Macpherson**

The Met Office, Exeter, United Kingdom

1. Introduction

In common with other global NWP centres, assimilation of radiances from the ATOVS instrument package at the Met Office results in a large benefit to global NWP forecasts (English et al., 2000) and has been used operationally since mid-1999 in the Met Office global 3D-Var system. Recently work has been carried out to assess the impact of using radiances from the AMSU A&B instruments in the UK Mesoscale Model (UK Mes). This is a limited area model with a domain covering the British Isles (the region is shown in the right panel of Figure 1) and to date its assimilation scheme has mainly used conventional observations. For the initial implementation of AMSU data in the UK Mes we have used the pre-processing scheme for ATOVS radiances in the global model as closely as possible to avoid duplication and maintenance of computer code. However some departures are necessary and these are described in the following sections.

The assessment of impact in a limited area model can be a difficult exercise, owing to the small domain in which to accumulate statistics and the need to run enough cases to sample the major weather types that occur in the domain. A two-fold approach was taken for this; running case studies on typical weather events and, prior to operational implementation, an extended trial of one months duration. Results from these studies are presented below.

2. AMSU Data

2.1 Data Receipt

ATOVS data in the region around the British Isles are received via a HRPT station located in the west of Scotland. At the Met Office the data is converted to level 1c brightness temperatures for each instrument using the AAPP program[1]. Finally the data is mapped to a common grid (1d level). The HIRS grid is chosen for this, since it is the grid used in the processing of ATOVS data in the global model. The locally received 1d data is routinely monitored against the ATOVS data produced by NESDIS to ensure its quality. For AMSU data the difference between the local and NESDIS data is very small, with channel standard deviations typically less than 0.05K.

2.2 Channel Selection

The current operational implementation of the radiative transfer forward model, RTTOV, in the Met Office 3D-Var system ignores the effects of cloud liquid water and rain droplets on microwave radiances. This simplification can have a big impact on the ability to model certain microwave channels and consequently prior to assimilation a series of tests are required to

[1] For further details see http://www.eumetsat.de/en/area4/aapp or http://www.metoffice.com/research/interproj/nwpsaf/atovs

identify the presence of precipitation and significant cloud water in the field of view. As reported in English et al. (1997) the following tests are used in the AAPP program:

- *Liquid water path test.* This flags observations with a liquid water path in excess of ~100gm^{-2} and in this case AMSU channels[2] 4, 5 and 20 are rejected for assimilation.
- *Rain test.* In this case all AMSU channels with weighting functions peaking in the troposphere are rejected (4 to 8 & AMSU-B).

In addition to this the higher frequency (183 GHz) channels are particularly sensitive to scattering effects caused by ice particles, such as cirrus crystals. A cost function is used to identify scenes containing ice particles with the following form:

$$J = (\mathrm{y} - \mathrm{y}^{\mathrm{b}})^{T} \mathrm{R}^{-1} (\mathrm{y} - \mathrm{y}^{\mathrm{b}})$$

Where y represents the observation vector containing radiances from the three 183 GHz channels, y^{b} represents the background radiance vector computed from a short-range UK Mes forecast field via the RTTOV forward model operator and R represents the error covariance matrix. For scenes in which the computed cost exceeds a given threshold channels 19 and 20 are not used in the assimilation.

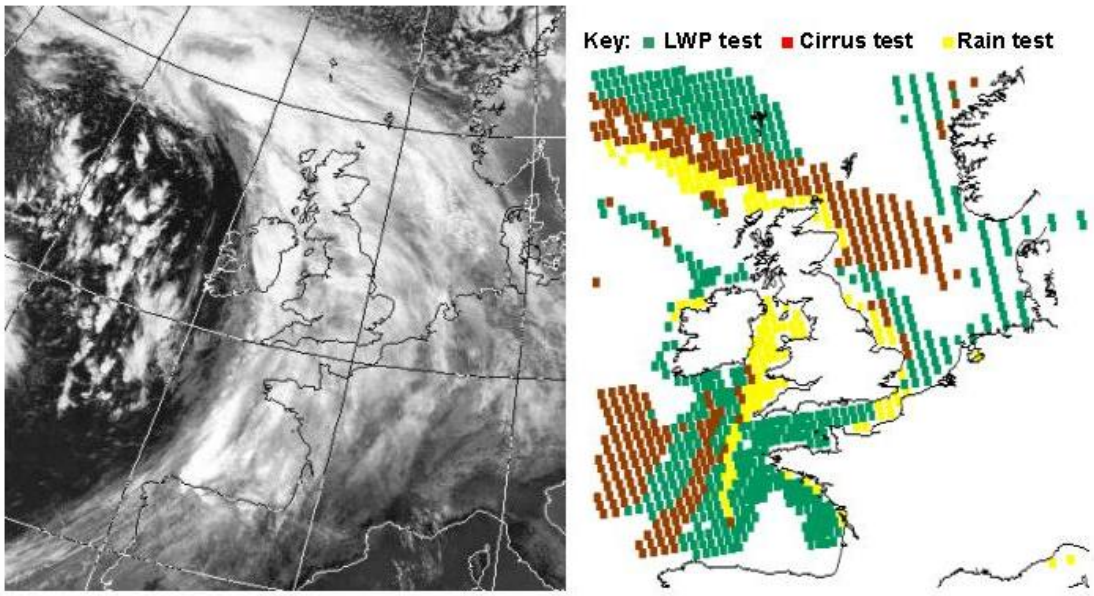

Figure 1: A Case study of an occluded frontal system in the UK Mes area. *Left panel:* Infrared image from the AVHRR instrument (courtesy of the NERC Satellite Receiving Station, University of Dundee, Scotland.). *Right panel:* ATOVS observations failing the screening tests.

Figure 1 shows the classification of data after applying these tests to an overpass. The case is an occluded frontal system in which there is significant precipitation along the cold front lying between northern Spain and Ireland. As expected in a case where most of the region is covered with thick frontal cloud a significant number of observations have been flagged by the screening

[2] Throughout this paper AMSU channels 1 to 15 refer to the AMSU-A instrument, channels 16 to 20 refer to AMSU-B.

tests. Nonetheless there are still regions in which data from all the AMSU channels can be passed to the assimilation scheme, notably in the Bay of Biscay and in the convective region behind the cold front.

In addition to the above screening tests, over land data from the following channels are not assimilated:

- AMSU channels 4 & 5
- AMSU channels 18,19, & 20 (AMSU-B)

This is because the surface emissivity is more variable over land and this will effect both the ability of the radiative transfer model to simulate radiances whose weighting functions peak close to the surface and also the screening tests using window channels, such as the rain test. Work is ongoing at the Met Office to address this issue, with a view to using more data over land.

2.3 Bias Correction

The final step of preprocessing is to bias correct the radiances against the NWP model background. As in the processing of data for the global NWP model, the method of Eyre (1992) is used. AMSU channels 5 and 9 are used as predictors for an airmass dependent bias correction that is applied after scan dependent biases have been removed. A problem in using this procedure for a model such as the UK Mes, that has a small domain, is to accumulate enough reference data sampling representative weather regimes from which to compute the predictor coefficients. One possible solution is to accumulate the reference data over a long time period, say 1 year, but this assumes that the instrument drift is negligible. Since predictor coefficients are already generated for global ATOVS data using the global Met Office model, our solution is to use these values for bias correction in the UK Mes. This assumes that the two models are unbiased with respect to each other, and routine monitoring of the model bias with respect to observations of radiosondes confirms this, at least for the troposphere. Figure 2 demonstrates that the approach is successful for removing the majority of the bias between the AMSU radiances and the UK Mes background.

3. Data Assimilation

The UK Mes uses a 3D Variational scheme (3D-Var) to assimilate observations (Lorenc et al., 2000). AMSU data are assimilated in the form of bias-corrected radiances, in each case ignoring radiances from channels that fail the screening tests (Section 2.2). At the time of writing the current operational configuration uses the following data:

- station reports of pressure, temperature and visibility.
- upper level winds from aircraft.
- satellite atmospheric motion vectors from METEOSAT.
- profiles of winds, temperature and humidity from radiosondes.
- wind profiler data.

In addition, rain rate information from the UK rain radar network is supplied to the forecast model via a latent heat nudging scheme (Jones & Macpherson, 1997). A nudging scheme is also employed to supply moisture information from a cloud product derived from geostationary satellite images and surface reports (Macpherson et al., 1996).

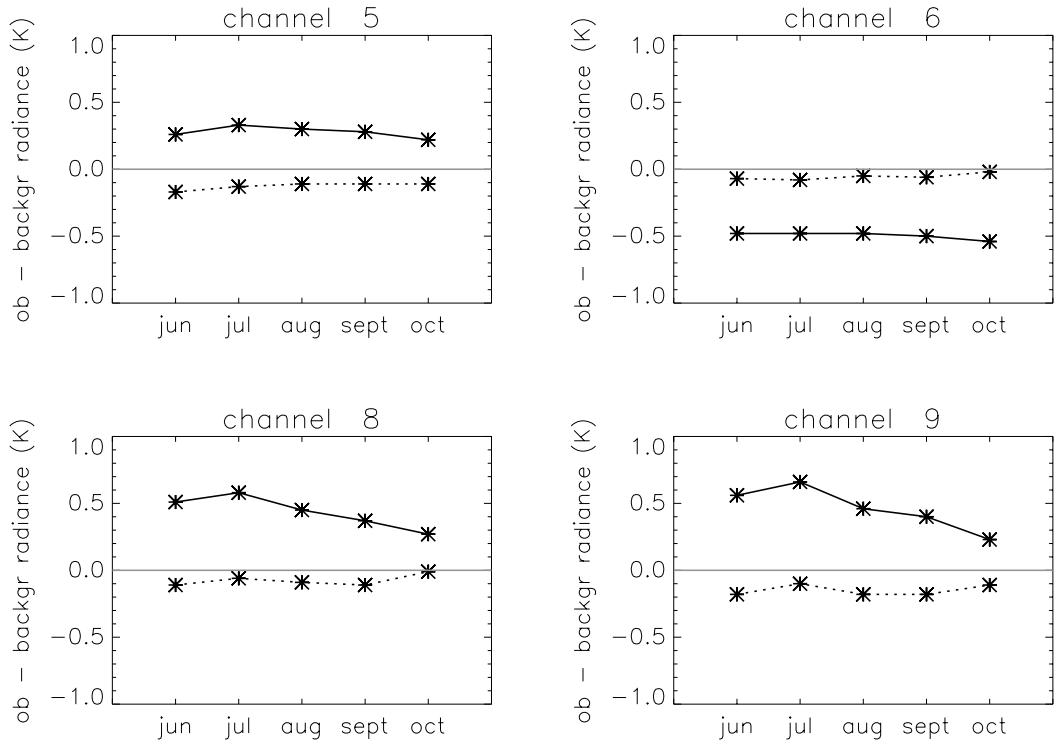

Figure 2: The monthly mean observation minus background difference over the UK Mes domain for several NOAA-17 AMSU channels during 2003. Uncorrected radiances are shown as solid lines and corrected radiances are shown as dashed lines.

4. Forecast Impact Experiments

4.1 Rationale

In a model such as the UK Mes the task of impact assessment for a new observation type can be a difficult exercise, owing to the small model domain. It is important to include enough cases so that a) the accumulated statistics on forecast performance are meaningful and b) a range of representative weather systems are sampled. We have taken a two-fold approach for AMSU data, firstly running a set of case studies that represent typical weather situations over the UK, including one that resulted in a poor operational forecast. Secondly an extended trial of AMSU data was also performed for the duration of one month. The extended trial allows us to measure the impact after the NWP system has adjusted to the presence of AMSU data. This trial was run in near real time in order to use boundary condition information from the operational global NWP model.

4.2 Rerun of a Poor Operational Forecast

On 1st October 2002 duty forecasters reported that a convective event moving across the English Channel from France had been underdeveloped by the model, leading to an underestimation in the strength of the resulting showers. Since the event was triggered in the Bay of Biscay, moisture imformation from AMSU-B could have been useful and to test this we reran the case including AMSU data in addition to the data used operationally. The assimilation/forecast system was run

for 36 hours prior to the rain developing over England and during this time eight overpasses were made over the area of interest by AMSU instruments onboard NOAA-16 and 17. Figure 3 shows the integrated water vapour in the model domain for the operational run and the trial including AMSU radiances. The zone of very humid air in the Bay of Biscay can clearly be seen and it is encouraging that the use of AMSU radiances has helped to moisten it.

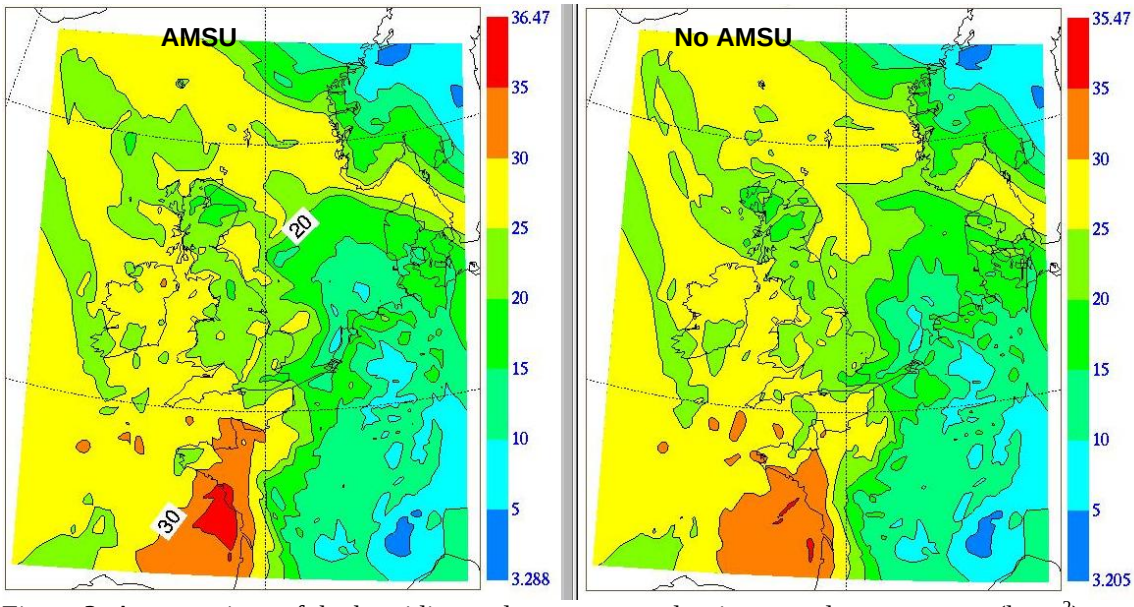

Figure 3: A comparison of the humidity analyses expressed as integrated water vapour (kgm^{-2}). *Left Panel: Model* run including AMSU assimilation. *Right Panel:* Model run without AMSU. Regions shaded in red indicate areas of integrated water vapour in excess of 30 kgm^{-2}

The resulting short-range rain forecast when the convective system is over Southern England is shown in Figure 4. The use of AMSU has increased the extent of the rain band which is encouraging. However the rain band is still underdeveloped when compared to the verifying radar data.

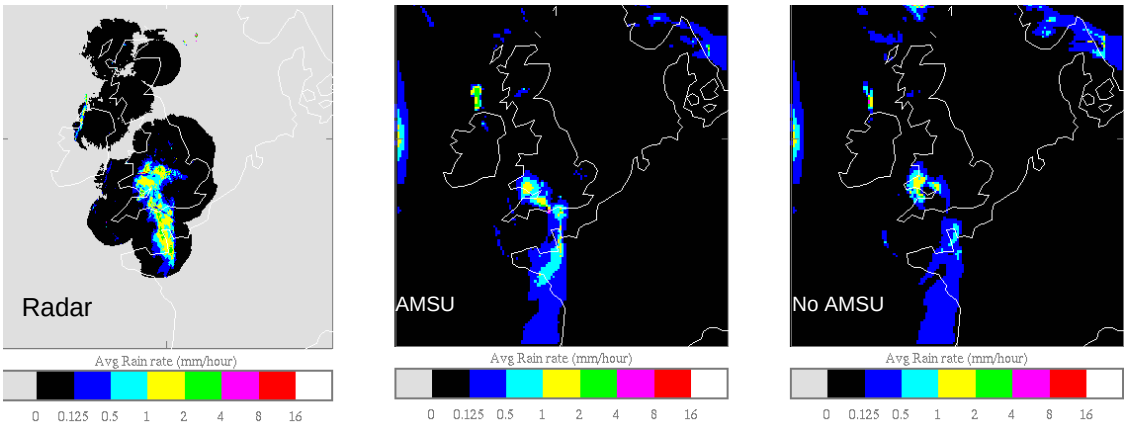

Figure 4: Short-range forcasts of model rain (accumulated between T+5 & T+6 and expressed as an average rain rate) compared to verifying data from the radar network.

4.3 Case Study Set

Twelve cases were chosen which incorporated a range of synoptic situations around the UK (e.g. active front, widespread stratocumulus sheets, etc.). For each case an experiment was run with twelve hours of assimilation including AMSU data, then a 36-hour forecast, and a further 12 hours of assimilation with another 36-hour forecast. Forecasts were then verified using station reports and statistics were produced from all forecasts for the following key meteorological parameters:

- windspeed at 10 m height & temperature at 1.5 m height as skill scores with respect to persistence.
- visibility, cloud cover and 6-hour precipitation accumulation as equitable threat scores (ETS).

The results from the experiment runs are compared to a set of control runs in which AMSU data were not assimilated in Table 1. The impacts are small with four of the parameters being either improved or neutral when AMSU is added.

Parameter	Control ETS / Skill	Trial ETS / Skill	Change
10m wind	0.750	0.750	0.000
1.5m temp	0.700	0.700	0.000
visibility	0.122	0.124	+0.002
cloud cover	0.266	0.263	–0.003
precipitation	0.322	0.323	+0.001

Table 1: Forecast accuracy compared between a set of experiment runs in which AMSU radiances were assimilated and control runs without AMSU data. Statistics were derived using forecasts generated from twelve diverse case studies.

There are several issues concerned with verifying by station reports. These include the sparse nature of their locations and that they are all located on land. Such problems may explain the small improvement to model precipitation forecasts when the moisture channels of AMSU are included. To test this idea the ETS for precipitation was recalculated using radar data as the verification source. Accumulations of precipitation over three hours from the model were compared with accumulations generated from the radar data, using frames such as that displayed in Figure 4. Note that a series of corrections are applied to the radar data to improve its accuracy (Harrison et al., 2000). Figure 5 presents these results as a function of forecast lead time. For the very short-range the precipitation skill of the model has been reduced when AMSU is assimilated, though at T+24 there is an improvement, according to the radar data.

4.4 Extended Trial

Prior to operational implementation an extended trial of one months duration was run. As before verification of the forecast fields was performed against station reports and the results are shown in Table 2. In this case three parameters improved slightly due to the inclusion of AMSU (visibility, surface temperature & cloud cover), whilst two were neutral (precipitation & surface windspeed). Humidity forecast fields were also compared and the mean difference is shown in Figure 6 as a vertical profile. This shows that the principle effect of the radiances is to moisten the

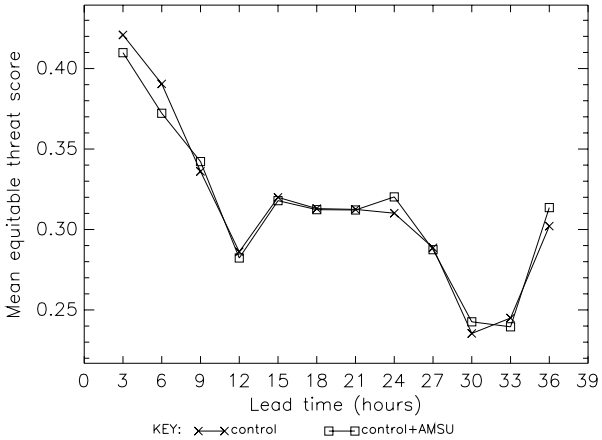

Figure 5: Equitable threat score of three-hour precipitation accumulation computed using radar observations as the verifying data. Rain/no rain threshold was set at an accumulation of 0.5mm.

Parameter	Control ETS / Skill	Trial ETS / Skill	Change
10m wind	0.740	0.740	0.000
1.5m temp	0.590	0.593	+0.003
visibility	0.113	0.117	+0.004
cloud cover	0.414	0.415	+0.001
precipitation	0.364	0.364	0.000

Table 2: Forecast accuracy compared between an extended run in which AMSU radiances were assimilated and a control run without AMSU data. Statistics were derived from data generated over one month.

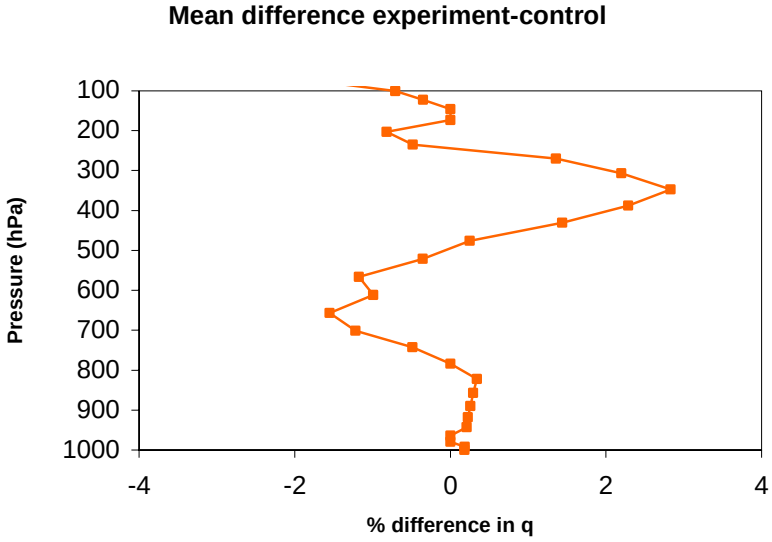

Figure 6: The mean difference (expressed as a percentage change) between the T+3 hour humidity fields for the extended trial. Experiment refers to the run with AMSU radiances.

model above 500 hPa and dry the model below this level. Note that the humidity fields are unchanged below 800 hPa which is consistent with the weighting functions of the 183 GHz channels on AMSU-B. The mean observation minus background difference for radiosonde data, taken from the operational monitoring database for the same period as the trial, shows that generally the radiosonde data have similar biases with respect to the model, namely that the model is too dry aloft and too moist below 400 hPa. This is very encouraging, implying that the radiosondes and radiances are trying to adjust the model in the same direction.

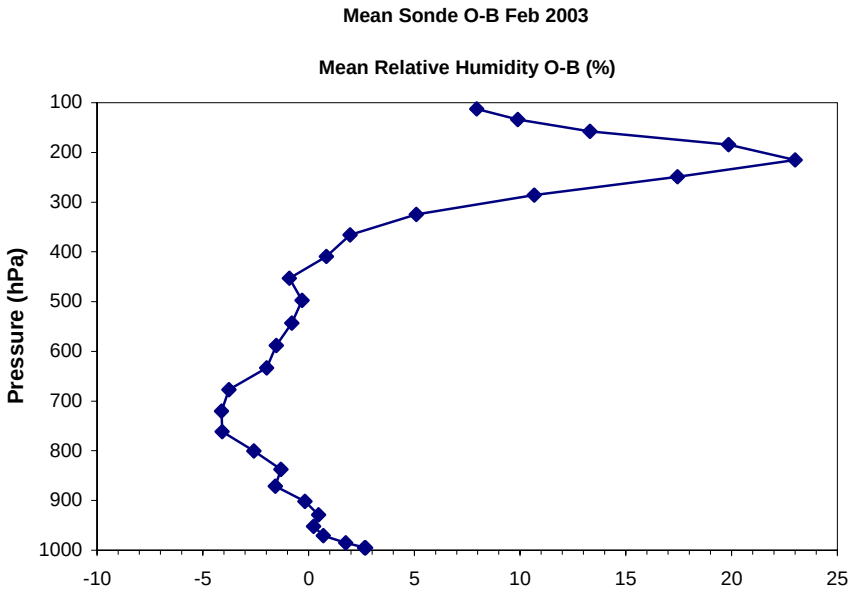

Figure 7: The mean difference between radiosonde observations of relative humidity and the operational UK Mes 3-hour background fields. Data is from 1030 radiosondes for the same period as the extended trial.

5. Conclusions

A series of impact studies have been performed to assess the impact of radiance data from the AMSU instrument in the UK Mes. The observations are pre-processed in a similar manner to those used in the Met Office global model. Generally the impacts on key forecast parameters were either small and positive or neutral. An extended trial of one months duration revealed that the mean analysis increments on the moisture field from the AMSU-B radiances are consistent with the information contained in the radiosonde data. A particularly encouraging result was the improvement of the moisture analysis for a convective event that was poorly handled by the operational model. Based on these results the operational use of AMSU data in the UK Mes commenced in March 2003.

Future work will focus on improving the impact on precipitation forecasts by using more AMSU data in areas of high liquid water path. This could be achieved by retrieving cloud liquid water information in 1D-Var preprocessing and passing it as fixed profiles into the 3D-Var assimilation. Deblonde & English (2003) discuss how cloud liquid water can be implemented in the 1D-Var

framework. Additionally we will investigate the use of channels whose weighting functions are affected by moisture in the boundary layer.

References

Deblonde, G., and English, S. J. 2003. One-Dimensional Variational Retrieval from SSMIS Simulated Observations. *J. Appl. Meteorol.*, 42(10), 1406-1420.

English, S. J., Renshaw, R. J., Dibben, P. C., and J. R. Eyre. 1997. The AAPP module for identifying precipitation, ice cloud, liquid cloud and surface type on the AMSU-A grid. *In Tech. Proc. 9th International TOVS Study Conference; Igls; Austria; 20-26 February 1997; Ed. J. Eyre.* Published by ECMWF, Reading, RG2 9AX, UK, pages 119-130.

English, S. J., Renshaw, R. J., Smith, A. J., Poulsen, C., Whyte, K., Hutchings, J. K., and Jones, D. C. 2000. Current Status In The Assimilation of TOVS and ATOVS Radiances at the UK Met. Office. *In Tech. Proc. 11th International TOVS Study Conference; Budapest; Hungary; 20-26 September 2000; Ed. J. LeMarshall and J. D. Jasper*; Published by BMRC, PO Box 1289K, GPO Melbourne, Vic., 3001, Australia, pages 79-89.

Eyre, J. R. 1992. A bias correction scheme for simulated TOVS brightness temperatures. *ECMWF Tech. Memo.*, 186. Published by ECMWF, Reading, RG2 9AX, UK.

Harrison D. L., Driscol, S. J., and Kitchen, M. 2000. Improving precipitation estimates from weather radar using quality control and correction techniques. *Met. Apps*., 6, 135-144.

Jones, C. D., and Macpherson, B. 1997. A Latent heat nudging scheme for the assimilation of precipitation data into an operational mesoscale model. *Met. Apps*., 4, 269-277.

Lorenc, A. C., Ballard, S. P., Bell R. S., Ingleby, N. B., Andrews, P. L. F., Barker, D. M., Bray, J. R., Clayton, A. M., Dalby, T., Li, D., Payne, T. J., and Saunders, F. W. 2000. The Met Office Global 3-Dimensional Variational Data Assimilation Scheme. *Q. J. Royal Meteorol. Soc.*, 126.

Macpherson, B., Wright, B. J., Hand, W. H., and Maycock, A. J. 1996. The Impact of MOPS Moisture data in the UK Meteorological Office Mesoscale Data Assimilation Scheme. *Mon. Wea. Rev.*, 124, 1746-1766.

Use and impact of satellite data in the NZLAM mesoscale model for the New Zealand region

V. Sherlock, P. Andrews, H. Oliver, A. Korpela and M. Uddstrom

National Institute of Water and Atmospheric Research,
Wellington, New Zealand

Abstract

We describe the current configuration of the New Zealand Limited Area Model (NZLAM) and associated data assimilation system, summarise current data use and present recent work on quantitative verification of NZLAM forecasts. We compare the accuracy of global model forecasts and NZLAM forecasts with initial conditions derived a) from interpolated global analyses and b) using variational data assimilation, and quantify the impact of the use of ATOVS data in the NZLAM variational data assimilation system. Future research directions are described briefly.

Introduction

A combination of intense synoptic flows and mountainous terrain make New Zealand communities susceptible to weather-related hazards – high winds, heavy rainfall, flooding and untimely snowfalls. To forecast such events requires mesoscale modelling of flows and relevant physical processes, and the mesoscale forecast model must have accurate initial conditions. At NIWA we are implementing a limited area model, the New Zealand LAM (NZLAM), with variational data assimilation for forecasting in the 6 – 48 hour range for this purpose (Uddstrom et al., 2002).

In this paper we briefly describe the current configuration of the NZLAM and associated data assimilation system and summarise current data use. We then present recent work on quantitative verification of NZLAM forecasts. We compare the accuracy of global model forecasts and NZLAM forecasts with initial conditions derived a) from interpolated global analyses and b) using variational data assimilation, and quantify the impact of the use of ATOVS data in the NZLAM variational data assimilation system.

NZLAM and data assimilation configurations

The NZLAM is a local implementation of the mesoscale configuration of the Met Office Unified Model version 4.5 (Cullen and Davies, 1991). The NZLAM domain is illustrated in Figure 1. We use a 324×324 grid point rotated latitude-londitude grid, corresponding to a horizontal resolution of 0.11° or $\sim$12 km. The model is discretised on 38 levels in the vertical. Lateral boundary conditions are supplied from a global model configuration of the Unified Model, and are updated hourly. The large area modelled

allows the evolution and interaction of synoptic and mesoscale flows to be resolved explicitly within the domain.

Observations are processed and assimilated using a local implementation of the Met Office variational data assimilation system. Data are currently assimilated using 3D-Var with a 3-hour analysis cycle. We assimilate surface data from land and ship SYNOP stations and BUOYS, upper air data from TEMP and PILOT radiosondes and AMDAR aircraft reports and the satellite data streams discussed in detail below.

We run a cycling forecast-assimilation system, but do not as yet process data in real time. Results presented in this paper are for our February 2000 validation case study period, using observational data supplied by the Met Office.

During the February 2000 case study period the synoptic flows in the New Zealand region were characterised by the predominance of anticyclonic flows over the north central Tasman Sea, and the passage of a number of fronts across the southern region of the domain. A large frontal system traversed the western region of the domain and developed into a cutoff low just west of New Zealand during a 5 day period in mid February.

Satellite data use

TOVS/ATOVS

Radiances from the HIRS, MSU and AMSU instruments on NOAA-14 and NOAA-15 are assimilated directly. The channels assimilated are summarised in Table 1 for the possible scene surface and cloud classifications. Radiances are thinned to one observation per $1^\circ \times 1^\circ$ box, with preference given to clear scenes.

Radiances are corrected for scan-dependent bias, derived from observed – background radiance differences in clear scenes over the whole domain for the case study period. No correction is currently applied for air-mass dependent biases as radiance-based air-mass dependent bias corrections did not give any statistically significant reduction in variance (for the limited time series in question). Similarly, there are insufficient samples to calculate reliable corrections using the method of Harris and Kelly (2001) in the vicinity of radiosondes.

Scan bias corrections derived for the NZLAM domain have been compared with those used operationally at the Met Office in 2000. The two sets of coefficients are in close agreement for the HIRS channels 2–4, MSU channels 3–4 and AMSU channels 6–11 assimilated in the NZLAM. More significant differences (0.2 – 0.5 K) are found for the lower tropospheric sounding channels (HIRS 5, MSU 2 and AMSU 4–5). Large differences (1.0 – 2.0 K) are found in HIRS channels 11–12 (not assimilated at present).

SSM/I

Surface wind speed is retrieved from SSM/I radiances in a 1D-Var observation preprocessing step, and assimilated in 3D-Var. Wind speed retrievals are thinned to one observation per $0.5^\circ \times 0.5^\circ$ box.

Table 1: TOVS/ATOVS channels assimilated for different scene surface and cloud classifications. Conditional channels are used for all scenes except 1: high cloud; 2: high land; 3: microwave rain classifications.

Satellite	Instrument	All scenes	Conditional	Clear, sea
NOAA-14	HIRS	2	3^{1}	4 5
NOAA-14	MSU	3 4	2^{2}	
NOAA-15	AMSU	9 10 11	$6^{1,2,3}$ $7^{2,3}$ $8^{2,3}$	4 5

SSM/I radiances are bias-corrected with the global bias correction coefficients used operationally at the Met Office in 2000. Examination of observed – background statistics for surface windspeed indicates no significant bias in retrieved windspeeds.

GMS atmospheric motion vectors

Atmospheric motion vectors derived by the Japanese Meteorological Agency from GMS-5 radiances, and their corresponding height assignment, are assimilated in the NZLAM. Following the Met Office, winds derived from visible radiances are only used in the lower troposphere over sea, winds derived from infrared window radiances are only used in the upper troposphere, and in the lower troposphere over sea, and winds from infrared radiances in the water vapour ν_2 (6.7 μm) band are only used in the upper troposphere. Observations are thinned based on (standard Met Office) quality control decisions and buddy checks. Detailed study of the monitoring statistics for atmospheric motion vectors is underway.

Objective verification of NZLAM forecasts

As in any modelling activity, validating model predictions and characterising model errors are key to understanding, exploiting and improving model performance.

In NZLAM development we have been particularly interested in comparing NZLAM forecasts from analyses derived using variational data assimilation (NZLAM-VAR) with global model forecasts (from analyses derived using VAR) and with NZLAM forecasts initialised with global analyses interpolated onto the NZLAM grid. These comparisons aim to characterise the accuracy of a cycled mesoscale model with data assimilation, and quantify the benefit of such a model over global model forecasts and mesoscale model forecasts initialised with low resolution fields. For such studies, observations are the only natural choice of reference for verification.

In this work we have run forecasts from 00Z and 12Z UTC out to 48 hours, and verified against TEMP, PILOT, AMDAR, SYNOP (Land and Ship) and BUOY observations at six-hourly intervals. Although we will only discuss radiosonde verifications here we note that the verification results are robust – all the major characteristics of the verification with TEMP and PILOT observations are also borne out in verification with AMDAR observations.

Observational data density is a general issue for quantitative verification, and a particular issue for the New Zealand region and NZLAM domain, where the conventional observing network is sparse.

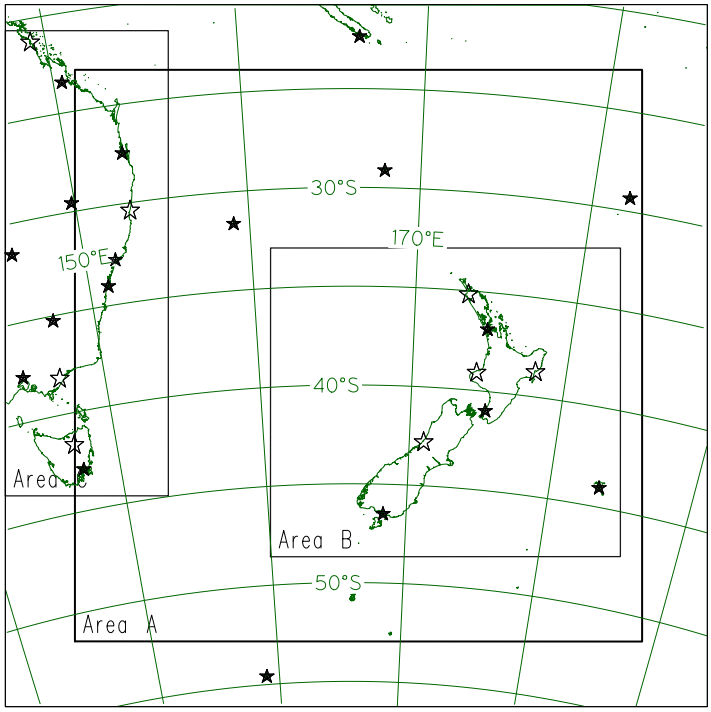

Fig. 1: Illustration of the the New Zealand Limited Area Model domain and verification areas A, B and C. Stars indicate location of the radiosonde stations in the NZLAM domain; open stars indicate stations which only launch PILOT balloons. Radiosondes in area A are used in the current model validation studies. However, all but one the New Zealand sondes are not currently used for verification at 00 and 12 UTC.

Radiosonde stations in the NZLAM domain are illustrated in Figure 1.

Verification is currently performed on area A (defined to exclude sites near the domain boundaries and the interior of the Australian land mass). However, all but one the New Zealand sondes are not currently used for verification at 00 and 12 UTC. This is because the unused sondes were launched at 10 and 22 UTC (i.e. 2 hours earlier than the nominal synoptic observation time) during the case study period and hence excluded by our $\pm$ 1.5 hour verification time window. Consequently, verification statistics predominantly reflect model performance in the North Tasman and the eastern Australian coastal regions. On the order of 200 temperature profiles and 700 wind profiles have gone into the radiosonde verification statistics presented here.

Comparison of global and NZLAM forecasts

Figure 2 illustrates the bias and root-mean-square (RMS) difference between observed and forecast temperatures as a function of pressure for forecasts at the 24 hour range.

In the mid troposphere (700 – 400 hPa), where temperature variability is largely governed by synoptic scale flows and small scale vertical temperature gradients are generally small, the performance of the three models is comparable. However, in the upper troposphere/tropopause region and the planetary

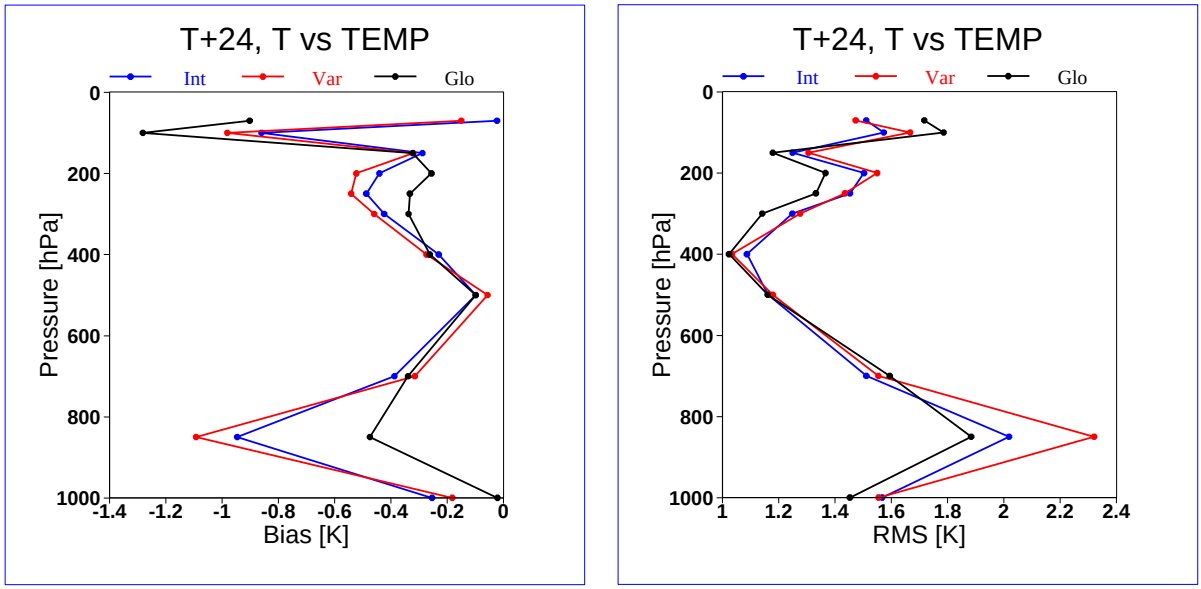

Fig. 2: Bias (lefthand panel) and RMS differences (righthand panel) between forecast and observed temperatures (fc–ob) as a function of pressure for the 24 hour forecast range. Results are illustrated for the global model with initial conditions derived using variational data assimilation (Glo) and for the mesoscale model with initial conditions derived using variational data assimilation (Var) and global analyses interpolated onto the mesoscale grid (Int). Statistics are calculated for the period from 01 to 29 February 2000.

boundary layer, where there are marked small scale vertical temperature gradients, the RMS differences between mesoscale model forecasts and observations are greater than global model RMS differences. Bias makes a significant contribution (a third to a half) to the RMS differences at 850 hPa and in the stratosphere.

It is not unexpected for high resolution model fields to verify worse than low resolution fields: high resolution models will generate sharper features and gradients which will verify worse than smoother, weaker fields if subject to position or timing errors. To characterise model performance we need to identify if and why position and/or timing errors are the source of observed differences, and distinguish these from other sources of model error.

Detailed examination shows that the large differences between NZLAM and global forecasts of the 850 hPa temperature are associated with large differences in modelled low level temperature inversions in the anticyclonic flow regime in the northern central Tasman Sea, over a six day period. These structures will be strongly governed by model physics, and suggest other sources of model error (e.g. modelled convection) may be the source of the observed differences in this instance. In particular, in forecast – observed differences in temperature (negative bias at the 850 hPa inversion layer level) and humidity (positive bias in the planetary boundary layer) and a 1 – 2 K warm bias in the sea surface temperature (SST) assumed in the NZLAM-VAR assimilation experiments (as compared to observed SST's) are all consistent with and overestimation of convective activity in the NZLAM-VAR run. Experiments are

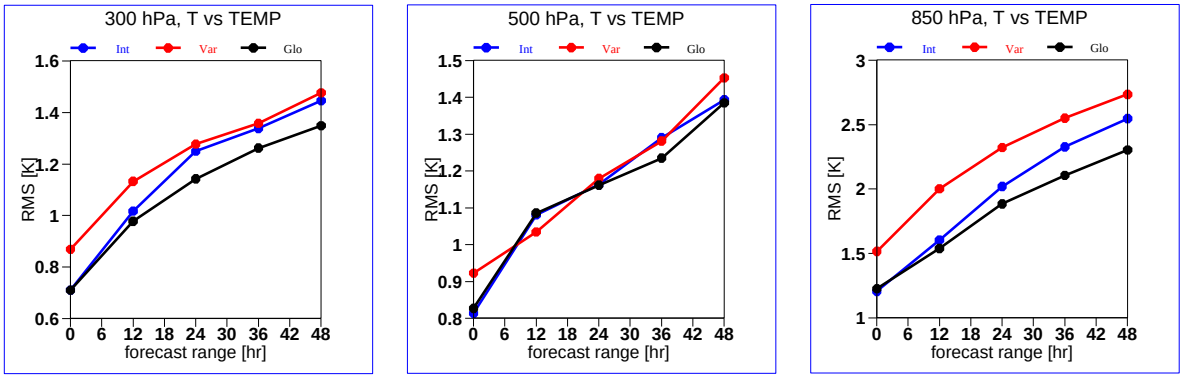

Fig. 3: RMS differences between forecast and observed temperatures as a function of forecast range for three selected pressure levels 300, 500 and 850 hPa.

underway to test this hypothesis.

Figure 3 illustrates the evolution of the RMS differences as a function of forecast range at three characteristic pressure levels, 300, 500 and 850 hPa. At 500 hPa RMS differences increase quasi-linearly with forecast range and the three models are comparable at all forecast ranges. At 300 hPa and 850 hPa the NZLAM-VAR RMS differences are larger than global model RMS differences at all forecast ranges, but the rate of increase of the RMS difference with forecast range is comparable.

RMS differences for forecasts with the NZLAM model initialised using interpolated global analyses rapidly increase from global model RMS levels and tend to NZLAM-VAR RMS levels at longer forecast ranges. We interpret this as a measure of the characteristic time scales for the NZLAM model to generate the stronger small scale structures and gradients we hypothesize are responsible for the larger RMS differences. Again, the validity of this hypothesis is being tested in ongoing studies.

Impact of ATOVS data on forecast accuracy

We have examined the impact of ATOVS data on the accuracy of NZLAM-VAR forecasts from analyses derived using variational data assimilation.

RMS differences between forecast and observed temperatures at the 24 hour forecast range are re-produced in Figure 4. RMS differences for NZLAM-VAR forecasts are compared for experiments where ATOVS data is included and excluded from assimilated data sets. Glodal model RMS statistics are traced for reference.

Assimilation of ATOVS data has a clear, positive impact on the accuracy of forecast temperature throughout the free troposphere (700 – 300 hPa), with improvements in RMS differences of 0.0 – 0.1 K. ATOVS data has little effect in reducing RMS differences at 850 hPa as is to be expected: the vertical resolution of the satellite observations is too low to provide information on the small vertical scales associated with the boundary layer temperature inversion.

The impact of ATOVS data in the upper troposphere/lower stratosphere is not as large as might have been expected. This may be related to strong latitudinal gradients in tropopause height within

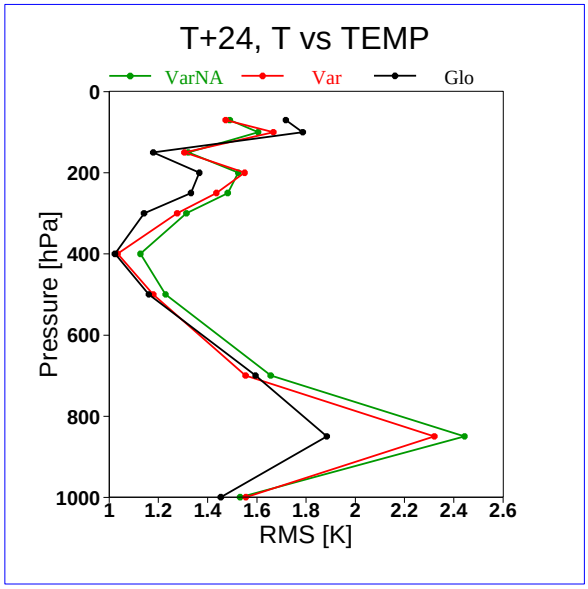

Fig. 4: Comparison of RMS differences between forecast and observed temperatures as a function of pressure for the 24 hour forecast range for the period from 01 to 29 February 2000. Results are illustrated for the global model with initial conditions derived using variational data assimilation including ATOVS (Glo) and for the mesoscale model with initial conditions derived using variational data assimilation with ATOVS data included (Var) and excluded (VarNA) from assimilated data sets.

the NZLAM domain, which may mask the impacts of ATOVS data above and below the tropopause at any given latitude. Alternatively, this may reflect suboptimal use of satellite data in the stratosphere due to errors in modelled stratospheric temperatures (coupled with bias correction and stratospheric extrapolation). Detailed study of these points is planned.

Figure 5 illustrates the evolution of RMS differences as a function of forecast range for 500 hPa temperature and wind, and surface pressure. Assimilation of ATOVS data has a positive impact on 500 hPa temperature RMS differences in the 0 – 36 hour forecast range. A small impact is also found for the 500 hPa RMS vector wind differences and surface pressure differences are reduced at all forecast ranges on assimilation of the ATOVS data.

Taken together, these results suggest that the ATOVS data have a positive impact in constraining the synoptic (quasi-geostrophic) flows.

Conclusions and future work

We have described the implementation of a mesoscale model for the New Zealand region which allows the evolution and interaction of synoptic and mesoscale flows to be resolved explicitly within the model domain.

Preliminary quantitative model validation (and quantitative comparisons of model fields not presented here) suggest that synopotic scale flows are well modelled and constrained by data and lateral boundary conditions.

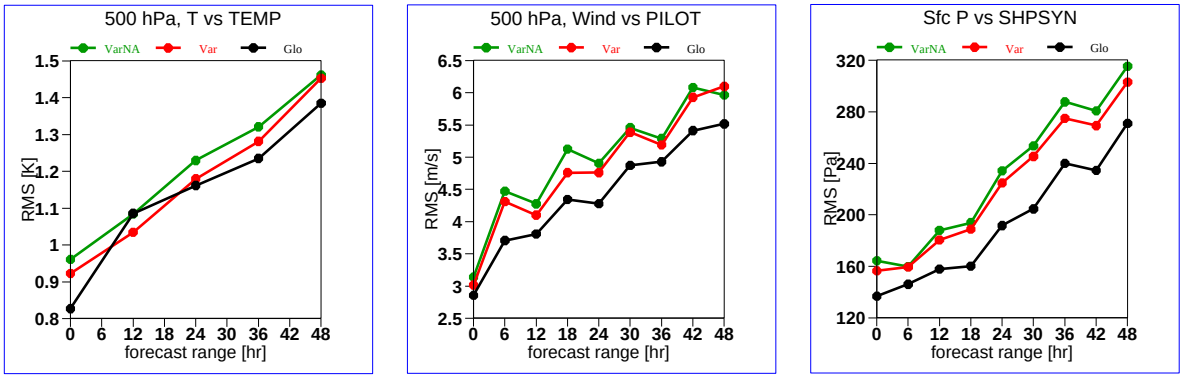

Fig. 5: Comparison of RMS differences between forecast and observed 500 hPa temperatures and vector winds, and surface pressure, as a function of forecast range when ATOVS data are included and excluded from assimilated data sets.

Marked differences in modelled small scale structure are observed, particularly in the planetary boundary layer. Our verification studies suggest these differences are principally governed by model physics and largely unconstrained by currently assimilated data or lateral boundary conditions.

This work is in its infancy, and we envisage numerous extensions to the current validation studies. We intend to extend the case studies in time – an extended (three month) time series, enabling eventual diurnal dependencies and error characteristics on spatial subdomains (Australian and New Zealand land masses) to be examined, and extension to other periods to examine eventual seasonal dependencies. Methods for scale dependent verification and characterisation of position/timing errors are also being explored.

These studies will enable poorly modelled physical processes to be identified, and lead to improvements in both the mesoscale model and the characterisation of it's errors. In turn this will lead to improved data use through improved specification of the background error covariance.

Extensions to our use of satellite data – the use of radiances containing information on tropospheric humidity and the use of satellite-derived sea surface temperatures in specifying surface boundary conditions – are also planned. These data streams could be of particular use in providing additional constraints to the boundary layer dynamics (convective processes) which have been called into question in these preliminary validation studies.

Ultimately we are working towards an operational mesoscale forecasting model, with output serving as input to hazard prediction models (hydrological models, storm surge and wave models) specific to the New Zealand region.

Acknowledgements

We thank the Met Office (UK) for providing the Unified Model and variational data assimilation codes, and for the numerous questions answered during the course of this work. This work was funded under the Foundation for Research Science and Technology contract CO1X0218.

References

Cullen, M. and T. Davies: 1991, A conservative split-explicit integration scheme with fourth order horizontal advection. *Quart. J. Roy. Meteor. Soc.*, **117**, 993–1102.

Harris, B. and G. Kelly: 2001, A satellite radiance bias correction scheme for data assimilation. *Quart. J. Roy. Meteor. Soc.*, **127**, 1453–1468.

Uddstrom, M., P. Andrews, H. Oliver, A. Korpela, and X. Zheng: 2002, The impact of data assimilation on a mesoscale model of the New Zealand region. *Technical Proceedings of the Twelfth International TOVS Study Conference, Lorne, Australia, 27 Feb.-5 Mar. 2002*.

Prospects for All-Weather Microwave Radiance Assimilation

Albin J. Gasiewski[1], Alexander Voronovich[1], Bob L. Weber[2], Boba Stankov[1], Marian Klein[3], Reginald J. Hill[1], and Jain-Wen Bao[1]

[1] NOAA/Environmental Technology Laboratory, 325 Broadway, Boulder, CO, USA
[2] Science and Technology Corporation and NOAA/ETL, Boulder, CO, USA
[3] University of Colorado/NOAA-CIRES, Boulder, CO, USA

Microwave radiometric data from satellite sensors is an extremely valuable source of information for temperature and moisture profiling and radiance assimilation over regions that are either cloud-free or covered by mostly thin non-scattering clouds. However, regions for which assimilation of microwave data would be most valuable include frontal zones where rapidly evolving heavy cloud cover and/or precipitation is present. Although scattering at microwave band above ~50 GHz can be strong in such regions the ability to probe deeply using microwaves can still provide important information on the amount and type of hydrometers and latent heating profiles. Time-resolved observations of cloud and precipitation dynamics can facilitate further inference of moisture and heat fluxes.

Direct radiance assimilation provides an optimal framework by which to utilize such information, however, the use of microwave data in radiance assimilation for all weather conditions remains limited due to several factors, including: 1) the need to rapidly and accurately compute the incremental response functions over heavy clouds and precipitation, and 2) time-sampling limitations of polar-orbiting microwave sensors, 3) microphysical precipitation process model limitations, including lack of appropriate error covariance models, and 4) fast and self-consistent assimilation update techniques. While each of these obstacles is formidable, we discuss in this talk potential solutions currently under study. Specifically, we demonstrate a new discrete-ordinate technique for rapid numerical calculation of the incremental brightness temperature profiles (Jacobian) for a layered scattering atmosphere. Applying this method to simulated data using the MM5 mesoscale atmospheric model of NCAR for Hurricane Bonnie (1998) we illustrate the potential for satellite microwave observations to be used to “lock” the state of a numerical weather model onto observed precipitation dynamics. Both low-Earth orbiting and geosynchronous microwave radiance fields are considered, and ramifications for the prospects of such all-weather assimilation using the proposed Global Precipitation Mission (GPM) and Geosynchronous Microwave (GEM) Sounder/Imager systems are discussed.

NOAA's Satellite and Information Stewardship Program and Plans

Presenter: Mitch Goldberg (for John Bates)

**John Bates, Chief Remote Sensing Applications Division,
National Climatic Data Center, NOAA/NESDIS**

NOAA/NESDIS is implementing a concept of a stewardship umbrella for its new and old satellite data sets and for the processing of satellite data for climate. The elements of this stewardship program include:

1. Careful monitoring of observing system performance for long-term applications
2. Generation of authoritative long-term records through validation of the calibration process, reprocessing, product generation and the blending of *in situ* and satellite measurements
3. Provide state of the environment information for decision makers and place the current state in its historical context
4. Archive and access to fundamental measurements, products and metadata
5. Data rescue for past satellite data sets

This talk will provide an overview of NESDIS progress and plans for stewardship.

Fast passive microwave radiative transfer in precipitating clouds: Towards direct radiance assimliation

Ralf Bennartz *, Thomas Greenwald, Chris O'Dell
University of Wisconsin-Madison

Andrew Heidinger
NOAA/NESDIS

1. Introduction

Passive microwave measurements from space have perhaps the greatest potential for improving global weather analyses because they offer 3D temperature and humidity information in both clear and cloudy conditions and provide information on cloud water mass and 3D precipitation structure. Indeed, assimilation of microwave-derived rainfall and moisture satellite products has shown to significantly improve short-range weather forecasts and the quality of global analyses of moisture and vertical motion (Hou et al. 2001). But direct assimilation of microwave radiance data offers benefits over products derived from radiances. For example, radiance assimilation is not subject to biases from initial guesses and a priori assumptions as are product retrievals, and it allows for better control of background errors in the assimilation environment. As a first step in radiance assimilation in all-weather conditions, observed and global model-produced microwave radiances have been compared in order to evaluate the ability of these models to produce clouds and precipitation (Chevallier and Bauer 2003; Chevallier et al. 2001).

This study, which is supported by the newly formed Joint Center for Satellite Data Assimilation (JCSDA), seeks to develop and test fast radiative transfer modeling systems in preparation for direct assimilation of microwave radiance satellite data (current and future) into NCEP's Global Data Analysis System (GDAS) under all weather conditions, especially precipitating clouds. GDAS currently uses a 3DVAR approach to assimilate SSM/I surface wind speed and precipitation products and radiance data from the Advanced Microwave Sounding Unit (AMSU) but in clear-sky only (Derber and Wu 1998; McNally et al. 2000). Our main goal, therefore, is to extend the capability of GDAS to include microwave radiance data in cloudy and precipitating systems over the oceans. This means incorporating multiple scattering radiative transfer (RT) models since precipitation-size particles scatter microwave radiation primarily at the higher frequencies. Here we give preliminary results of RT calculations at AMSU frequencies using coarser resolution version of the NCEP Global Forecast System (GFS) model output but focusing on clear and nonprecipitating cloudy areas. More complete results for precipitating clouds will be presented at the symposium.

2. Data

2.1 *Global model*

The current version of NCEP's GFS uses a spectral atmospheric model with horizontal resolution at T254 (about 0.5 x 0.5 deg. latitude/longitude) and 64 vertical levels in sigma coordinates. The deep convection scheme is based on Pan and Wu (1994), while shallow convection is parameterized following Tiedtke (1983). The percent area of cloud coverage for a given grid point is not predicted but computed from the relative humidity, saturation specific humidity (q) and a minimum threshold of q using the approach of Xu and Randall (1996). Cloud water and ice are both predicted via a scheme by Zhao and Carr (1997).

GFS degraded products (1^o x 1^o horizontal grid and 26 vertical levels) were used in the analysis since they were readily available online at ftp://ftpprd.ncep. noaa.gov/pub/data/nccf/com/avn/prod. The 12 hr forecast products were selected for the following quantities: temperature, relative humidity, and cloud

Corresponding author address: Ralf Bennartz, Atmospheric and Oceanic Sciences, University of Wisconsin – Madison, 1225 W. Dayton St., Madison, WI, USA, e-mail: Bennartz@aos.wisc.edu

liquid water mixing ratio at all levels; surface temperature, 10 m wind vector, and precipitation rate at the ground. Neither cloud ice mixing ratio nor instantaneous cloud fraction was available.

2.2 *Satellite*

NOAA's AMSU-A/B instrument suite is designed mainly to observe global temperature and humidity at different layers in the atmosphere but it also provides important information on water clouds and precipitation (summarized in Tables 1 and 2). AMSU scans across the direction of motion of the satellite, extending to about $\pm 48^o$ from nadir. It currently flies on the NOAA-15, -16, and -17 satellites.

We utilized the 1^o x 1^o gridded AMSU brightness temperature products available from the NOAA/NESDIS ftp site that are produced separately for each of the three satellites and the ascending and descending nodes. To provide independently determined cloud coverage for the microwave data, AVHRR cloud amount products were obtained using the NOAA operational cloud detection algorithm. These data were also transferred to a 1^o x 1^o grid.

Table 1. AMSU-A characteristics.

Chan	Frequency (GHz)	Sensitivity
1	23.8	Boundary layer (BL) water vapor, surface, precipitation
2	31.4	Water clouds, surface, BL water vapor, precipitation
3	50.3	BL temp, water clouds, precipitation
4	52.8	Lower troposphere temp
5	53.596±0.115	Mid-troposphere temp
6	54.4	Upper troposphere temp
7	54.94	Upper troposphere temp
8	55.50	Lower stratosphere temp
9	f_o=57.290344	Lower stratosphere temp
10	f_o±0.217	Mid-stratosphere temp
11	f_o±0.3222±0.048	Upper stratosphere temp
12	f_o±0.3222±0.022	Upper stratosphere temp
13	f_o±0.3222±0.010	Upper stratosphere/lower mesosphere temp
14	f_o±0.3222±0.0045	Mesosphere temp
15	89.0	BL water vapor, water clouds, surface, precipitation

Table 2. AMSU-B characteristics.

Chan	Frequency (GHz)	Sensitivity
16	89.0±0.9	BL water vapor, water clouds, surface, precipitation
17	150.0±0.9	BL water vapor, water clouds, surface, precipitation
18	183.31±1.00	Upper troposphere water vapor
19	183.31±3.00	Mid-troposphere water vapor
20	183.31±7.00	Lower troposphere water vapor

3. Radiative Transfer Modeling

The RT model tested here to compute brightness temperatures for a given set of model atmospheric and surface parameters is an Eddington two-stream method for plane-parallel conditions (Bauer 2002). The method also incorporates delta scaling to improve accuracy when particles become large compared to incident wavelength (forward scattering becomes greater), such as encountered with large precipitation particles. These methods are accurate to within about 1-2 K under a wide range of conditions when compared to more exact methods (Smith et al. 2002).

Required as input to the two-stream RT model are the effective single-scattering properties of the medium (i.e., extinction, single-scatter albedo, and asymmetry factor) and boundary conditions (i.e., ocean surface emissivity and skin temperature). Single-scattering properties for rain, snow, graupel and hail

were computed from Mie theory at discrete frequencies, temperatures and water contents, assuming an exponential size distribution and ice densities. These calculations were organized in tabular form for interpolation purposes. Because the GFS data products included precipitation rate at the surface only, several crude assumptions were made to vertically distribute the total rate into liquid and ice species. A constant rain rate was assumed from the surface up to cloud base. From there, the fraction of ice (liquid water) precipitation rates was linearly increased (decreased) from 0 to 1 (1 to 0) until a temperature of –20^{o} C was reached, above which only ice existed. Cloud liquid water and ice were similarly partitioned from the freezing level to –20^{o} C. Precipitation rates were converted to water content using an exponential size distribution. Extinction coefficients for gas (water vapor and oxygen) were obtained from OPTRAN (McMillin et al. 1995), which is the gas absorption model used operationally by GDAS, while absorption due to cloud liquid water was computed from Liebe et al. (1992).

As discussed by Chevallier and Bauer (2003), both cloud fraction (which varies vertically) and how clouds are distributed vertically in the volume that comprises a grid point in the model have an impact on computed brightness temperatures. Unfortunately, modeled cloud amount was not available to us, so it was assumed that clouds were completely overcast. Cloud overlap was also not considered. These issues will be addressed in future work.

Finally, ocean surface emissivity was computed from FASTEM-2, a model originally developed by English and Hewison (1998) and further refined and improved by Deblonde and English (2000). The main input variables that FASTEM-2 requires are surface skin temperature, observation zenith angle, frequency, and wind speed at 10 m height.

4. Results

As a consistency check, we first compared clear sky brightness temperatures computed at selected frequencies from the Eddington two-stream model against the existing absorption-only RT model currently in the operational GDAS. Figure 1 shows the 89-GHz brightness temperature field calculated from the two-stream model. Differences between the RT model results were found to be less than 0.1 K (see Fig. 2). However, at one of the frequencies that corresponds to the humidity sounding channel on AMSU-B (channel 18), differences as large as -0.85 K were seen (Fig. 3). It was discovered that these differences were related to the treatment of the thermal source within the model layer. The absorption-only RT model assumes a layer average temperature within the layer, while in the Eddington two-stream model, temperature was allowed to vary linearly throughout the layer. Differences between the RT models are drastically diminished to under –0.0007 K when both use the same thermal source treatment (not shown). Ordinarily this is not an issue if the model vertical grid spacing is sufficiently small. Apparently, the grid spacing is too coarse in the upper troposphere where this channel's weighting function peaks. Use of full resolution GFS data should significantly reduce such differences, however.

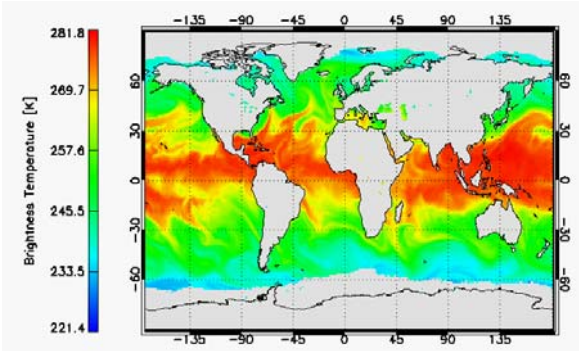

Figure 1: 89 GHz brightness temperature field computed at nadir for clear sky from GFS model output (15 October, 2003 12 hr forecast starting at 06Z) using the Eddington two-stream radiative transfer model.

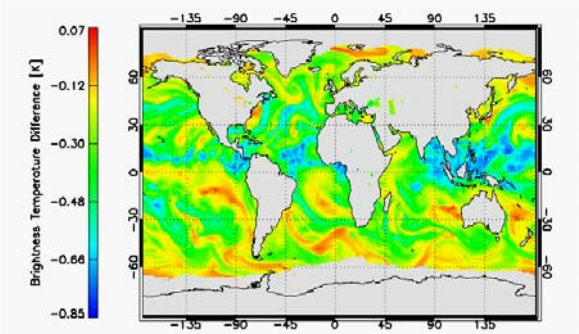

Figure 2: Differences between clear sky 89 GHz brightness temperatures computed from the Eddington model and NCEP's operational absorption-only radiative transfer model for same time as Fig. 1.

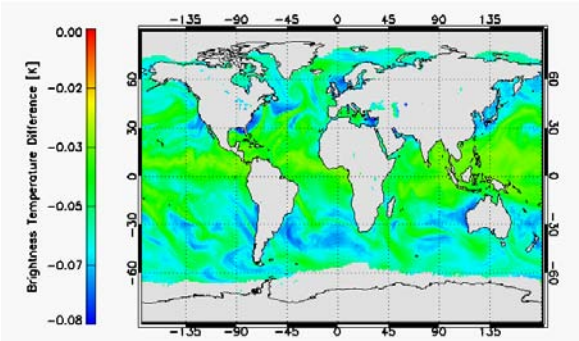

Figure 3: Same as Figure 2 but for AMSU-B channel 18 frequency at a zenith angle of 53°.

Comparisons between simulated and observed brightness temperatures were performed over 4 days (16-19 Oct. 2003) using a time difference of less than 1 hr for the AMSU-A/B window channels (1, 2, 16 and 17) and AMSU-B humidity sounding channels (18-20). Cloud-free regions were defined from the AVHRR-derived products as less than 5% cloudiness, whereas cloudy regions were considered greater than 95% cloudiness.

A qualitative comparison between AVHRR-derived cloud cover, AMSU-B 89 GHz brightness temperature field, and simulated brightness temperature field is given for one time period in Figures 4, 5, and 6 respectively. Outside of convectively active regions of precipitation, many spatial features in the simulated brightness temperature field correspond well with the observed field.

Quantitative comparisons over the 4-day time period for strictly cloud-free regions revealed biases at some frequencies (Fig. 7). Similar biases existed for all three satellites indicating the biases are likely not caused by calibration errors. The large differences at 89 GHz and 150 GHz may be related to uncertainties in characterizing the gaseous absorption, which is more uncertain in spectral window regions; although it may also be due to biases in the GFS model predictions of boundary layer humidity or the surface emissivity model. The noticeable zenith angle dependent bias suggests either a problem with the gas optical path for larger angles or angular deficiencies in the microwave surface emissivity model.

For cloudy nonprecipitating cases, biases are overall smaller and the angle dependent biases are not as prominent although they still remain at the lower frequency channels (Fig. 8). These results suggest that, in general, the GFS model predictions of cloud water mass are reasonable, at least during this time period.

A first calculation of the brightness temperatures at 150 GHz including precipitation is shown in Figure 9. In regions of convective precipitation, scattering by large ice particles plays the major role in causing large depressions in the brightness temperatures at this frequency. Depressions of 30-40 K relative to the background (cloud liquid + gas) are common.

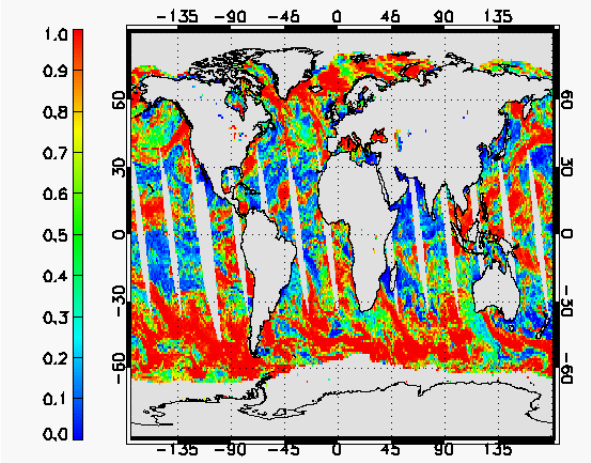

Figure 4: Cloud fraction determined from the NOAA-16 AVHRR for ascending overpasses on 16 October 2003.

5. Conclusions

Preliminary test results of a RT forward modeling system for computing microwave radiances from GSF model parameters compared against AMSU observations has been very encouraging. The system consists of an Eddington two-stream RT model, OPTRAN, FASTEM-2 surface emissivity model, and lookup tables for precipitation scattering properties. Comparisons with NCEP's operational absorption-only RT model under clear skies shows excellent agreement, especially at AMSU water vapor sounding channels. Limited comparisons between brightness temperatures computed from GFS 12 hr forecast fields and AMSU measurements under clear sky conditions showed zenith angle dependent biases for the window frequencies, while comparisons under cloudy cases had the best agreement.

We are currently developing an RT model based on successive orders of scattering; results of which may be presented at the symposium as well.

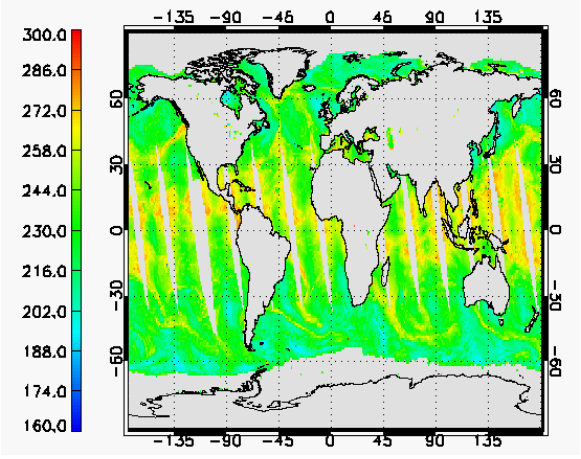

Figure 5: Gridded AMSU-B 150 GHz (channel 17) brightness temperature product for same day as Fig. 4.

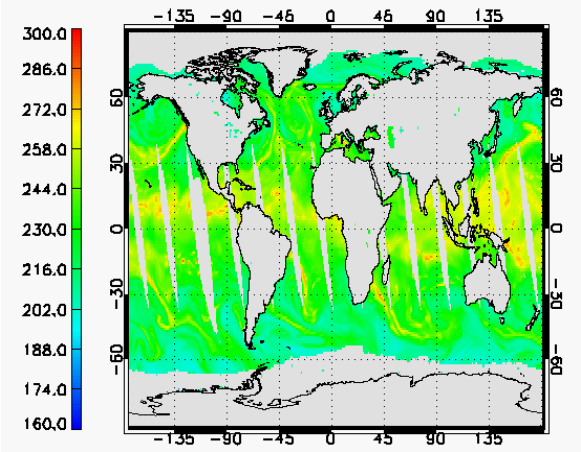

Figure 6: Simulated AMSU-B channel 17 brightness temperatures at nadir conditions and excluding precipitation for 12 hr forecast beginning at 00Z on 16 October 2003.

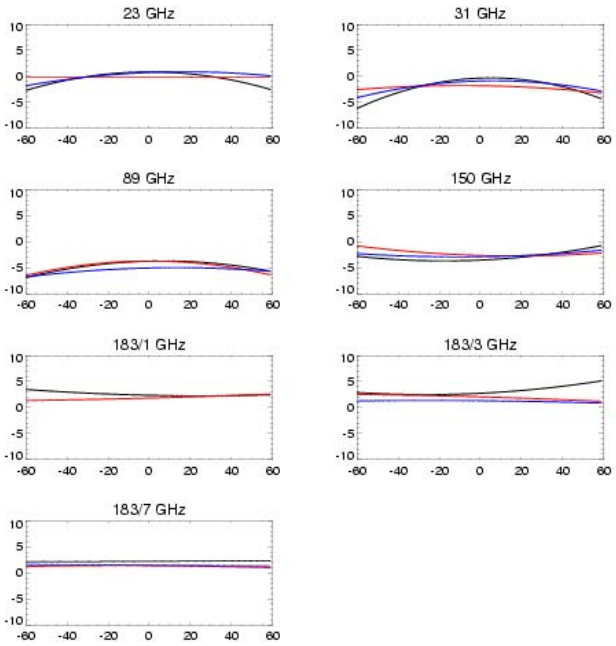

Figure 7: Observed minus simulated brightness temperatures as a function of zenith angle for selected AMSU-A/B channel frequencies under clear sky conditions. Black lines are for NOAA-15, red for NOAA-16, and blue for NOAA-17.

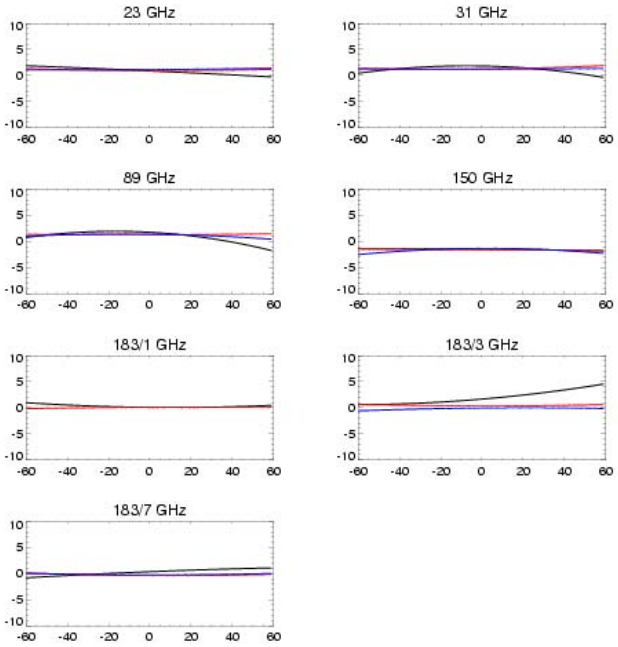

Figure 8: Same as Figure 7 but for cloudy cases.

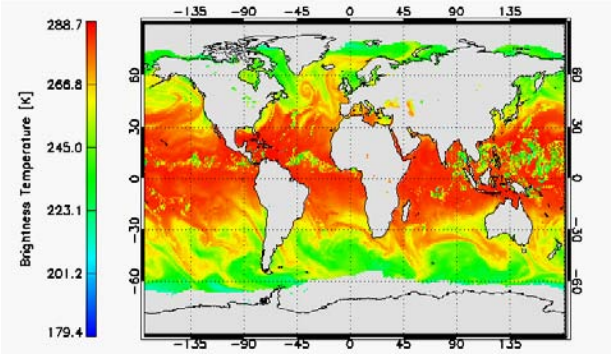

Figure 9: Simulated 150 GHz brightness temperature field that includes precipitation for 15 October, 2003 and 12 hr forecast beginning at 06Z.

6. Acknowledgements

Support was provided by a JCSDA grant through NOAA cooperative agreement NA07EC0676. Thanks go to the UK Met office for use of RTTOV-7. Also greatly appreciated are the contributions of our colleagues, Peter Bauer at ECMWF and Ken Campana at NOAA/NCEP.

7. References

Bauer, P., 2002: Microwave radiative transfer modeling in clouds and precipitation. Part I: Model description. NWP SAF Rep. NWPSAF-EC-TR-006, 27 pp.

Chevallier, F. and P. Bauer, 2003: Model rain and clouds over oceans: Comparison with SSM/I observations, *Mon. Wea. Rev*., **131**, 1240-1255.

Chevallier, F., P. Bauer, G. Kelly, C. Jakob, and T. McNally, 2001: Model clouds over oceans as seen from space: Comparison with HIRS/2 and MSU radiances. *J. Climate*, **14**, 4216-4229.

Deblonde, G., and S. J. English, 2000: Evaluation of the FASTEM-2 microwave oceanic surface emissivity model. *Proc. Int. TOVS Study Conf*., Budapest, Hungary, ITWG/IAMAS, 67-78.

Derber, J. C., and W.-S. Wu, 1998: The use of TOVS cloud-cleared radiances in the NCEP SSI analysis system. *Mon. Wea. Rev*., **126**, 2287-2299.

English, S., and T. J. Hewison, 1998: A fast generic millimetre wave emissivity model. *Proc. SPIE*, 3503, 22-30.

Hou, A. Y., S. Q. Zhang, A. M. da Silva, W. S. Olson, C. D. Kummerow, and J. Simpson, 2001: Improving global analysis and short-range forecast using rainfall and moisture observations derived from TRMM and SSM/I passive microwave sensors. *Bull. Amer. Meteor. Soc*., **82**, 659-679.

Liebe, H. J., P. Rosenkranz, and G. A. Hufford, 1992: Atmospheric 60 GHz oxygen spectrum: New laboratory measurements and line parameters. *J. Quant. Spectros. Radiat. Transfer*, **48**, 629-643.

McNally, A. P., J. C. Derber, W.-S. Wu and B. B. Katz, 2000: The use of TOVS level-1B radiances in the NCEP SSI analysis system. *Quart. J. Roy. Meteor. Soc*., **126**, 689-724.

McMillin, L. M., L. J. Crone, M. D. Goldberg, and T. J. Kleespies, 1995. Atmospheric transmittance of an absorbing gas, 4. OPTRAN: A computationally fast and accurate transmittance model for absorbing gases with fixed and variable mixing ratios at variable viewing angles, *Appl. Opt*., 34, 6269-6274.

Pan, H.-L., and W.-S. Wu, 1995: Implementing a mass flux convection parameterization package for the NMC medium-range forecast model. NMC Office Note, No. 409, 40 pp. [Available from NCEP, 5200 Auth Road, Washington, DC 20233]

Smith, E. A., and others, 2002: Intercomparison of microwave radiative transfer models for precipitating clouds, *IEEE Trans. on Geosc. and Remote Sens.* **40**, 541-549.

Tiedtke, M., 1983: The sensitivity of the time-mean large-scale flow to cumulus convection in the ECMWF model. ECMWF Workshop on Convection in Large-Scale Models, 28 November-1 December 1983, Reading, England, pp. 297-316.

Xu, K. M., and D. A. Randall, 1996: A semiempirical cloudiness parameterization for use in climate models. *J. Atmos. Sci*., **53**, 3084-3102.

Zhao, Q. Y., and F. H. Carr, 1997: A prognostic scheme for operational NWP models. *Mon. Wea. Rev*., **125**, 1931-1953.

Variational Cloud and Rainfall Data Assimilation at ECMWF

Presenter: Tony McNally for Frédéric Chevallier

Frédéric Chevallier, Peter Bauer, Angela Benedetti, Marta Janiskova, Philippe Lopez, Emmanuel Moreau, Adrian M. Tompkins

4D-Var assimilation schemes assume the linearity of their forward model in the vicinity of prior information and consequently do not properly handle variables that have fine temporal and spatial scales compared to the forward model. Hence cloud- and rain- affected satellite radiances are discarded from numerical weather prediction 4D-Var systems despite the critical need of observations within the cloudy regions.

To circumvent that limitation, a '1D-Var+4D-Var' approach has been developed at ECMWF, where 4D-Var assimilates 1D-Var retrievals of temperature and moisture profiles in rain-affected areas. The 1D-Var method is applied either to rain-rate retrievals obtained from satellite observations or directly to satellite brightness temperatures. This paper will present the methodology and will describe the meteorological impact on the forecast system.

Further, we suggest the possibility of assimilating some of the satellite radiances directly in 4D-Var further to achieving improvements in the modelling of clouds: for instance the 6.3 microns channel on-board all the geostationary satellites. The ECMWF 4D-Var system is being modified so as to assimilate such observations and first results may be presented.

Contribution of POLDER to water vapour observation

Michèle Vesperini*, Philippe Dubuisson and Fabrice Ducos***

* Laboratoire d'Optique Atmosphérique - UMR CNRS 8518
Université de Lille 1. 59655 Villeneuve d'Ascq, France.
e-mail: vesperini@loa.univ-lille1.fr

** LOCL - UMR CNRS 8013 ELICO
Université du Littoral Côte d'Opale, 62930 Wimereux, France
Fédération de Recherche CNRS 1818.

I Introduction

Observations of water vapour over land are mainly provided by the radiosonde network with a somewhat sparse distribution over continents of the southern hemisphere. Satellite sensors such as TOVS[1] and SSM/I[2] offer indirect measurements of atmospheric water vapour that may be used with a good accuracy over ocean, but retrivals lack sensitivity and precision over land due to high and variable emissivities. A 2-channel ratio method involving near-infrared measurements was initially developped by (Frouin), and was applied for POLDER-1 (Bouffiès et al., 1997, Vesperini et al., 1999), MODIS (Kaufman and Gao, 1992, Gao and Kaufman, 1998) and MERIS (Bennartz and Fischer, 2001) missions. These methods gave the first opportunity to observe atmospheric column water vapour with a satellite coverage over land, in clear sky conditions. This paper describes the updated algorithm for the POLDER-2 mission (ADEOS-2), starting in April 2003.

II Background of POLDER water vapour retrieval method

POLDER (POLarization and Directionality of Earth Reflectances, Deschamps et al. 1994) is a visible to near-infrared radiometer, providing up to 14 directional reflectance measurements of a given target together with its full polarization characteristics. Its nominal resolution is about 6 km and POLDER geophysical products are computed on an approximately 60km×60km grid. In addition to the innovative directional and polarization capabilities, two channels located beside and in an H_2O gaseous absorption band (respectively 865 and 910 nm) are used to estimate the atmospheric Total Column Water Vapour content (TCWV). Assuming that the surface reflectance does not vary between these two close bands, the 910 to 865 nm reflectance ratio is a function of the atmosphere transmission which is related to the TCWV content. This relation may be parameterized with a polynomial fit. This method is based on absorption so it applies only to situations where direct transmission (from sun to the surface and to the sensor) predominates over scattering by cloud or molecules. This restricts to clear sky over significantly reflecting surfaces such as land and ocean in glitter conditions.

For the first POLDER mission, the coefficients of the polynomial fit were determined from radiative transfer simulations based on HITRAN absorption database (Bouffiès et al, 1997). This needs the reflectances to be calibrated. In-flight calibration of the 865 nm band was performed by transferring the 656 nm band calibration over the spectrally flat sunglint over ocean. The 565 nm band was calibrated following method initially described by Vermote et al. (1992). To perform in-flight calibration of the 910 nm, it is necessary to have humidity observations to refer to over ocean glitter condition to guarantee a white and highly reflective surface. We thus need a data base containing reference humidity data in oceanic areas, together with coincident and colocated POLDER measurements in clear sky and glitter situations for a wide range of atmospheric conditions. In order to get such a data-set as soon as possible after the launch, the

[1] TIROS Operational Vertical Sounder
[2] Special Sensor Microwave Imager

calibration of 910 nm band for the POLDER-1 mission used meteorological analysis of humidity as reference (Hagolle et al., 1999).
Validation of the operational satellite water vapour product was performed by Vesperini et al. (1999) by comparisons with radiosondes and SSM/I TCWV (algorithm of Wentz 1994). These comparisons pointed out two biases in the POLDER water vapour retrievals. First, large POLDER TCWV were overestimated by roughly 10 $kg.m^{-2}$ due to improper calibration of the 910 nm channel. Actually, meteorological analyses may be biased in areas where few observations are available (like ocean). Moreover, over land this bias is mixed with an underestimation of small humidity contents related to the spectral variation of the surface between 865 and 910 nm channels which was on a first attempt assumed to be negligible. The developpement of the new algorithm must settle the determination of the polynomial fit and calibration for the new 910 nm filter and must take into account the spectral variation of the surface reflectance.

III Calibration and Water Vapor parameterization

For the second POLDER mission, it was decided to perform directly the calibration of the TCWV content itself, through the determination of polynomial coefficients, instead of the calibration of the 910 nm reflectance.
A data base including reference humidity data in the form of TCWV, collocated with POLDER level-1 clear sky reflectances is required. Radiosonde/POLDER match ups were first used to develop a method to screen cloudy situations, independantly of level-2 processing, since water vapour calibration has to be performed before level-2 will processed. However, cloud screening does not leave enough matchups to perform calibration. SSMI TWCV observations were thus used as a main reference, the satellite coverage offering much more match-ups than the radiosonde network.

III-a Use of radiosondes

We have selected the level-1 POLDER data for the 3x3 full resolution pixels surrounding each radiosounding from TEMP (fixed stations) and TEMPSHIP (shipstations) messages, available over the globe during the eight-month POLDER-1 mission (between November 1996 and June 1997). 3278 colocations were found over sea, of which 1142 for small islands and 2136 for ships. POLDER data include between 1 and 14 directions for each of the 3x3 pixels. From this initial data set, only the sea and glitter cases were kept. A cloud screening was then performed on this sea-only-and-glitter data set. The cloud detection is based on the fact that unlike liquid-water cloud, glitter targets are highly polarized. A 0.05 threshold on the glitter amplitude was choosen to perform a first cloud screening, which left 219 island and 482 ship cases. Since the glitter amplitude test did not screen out all the cloudy cases, we added a test on the apparent pressure. The apparent pressure of cloud is used for cloud detection in the "Radiation Budget and Cloud" processing line (Vanbauce et al., 1998). The apparent pressure of the target is computed from the oxygen transmission estimated from the 763 to 765 nm reflectance ratio. The cloud detection threshold is calculated as function of geometry and surface pressure. Only the directions within 15^o of the specular reflexion were kept in the final test (Figure 1). The final test leaves only 19 island and 37 ship cases giving a total of 1339 pixel-directions.

III-b Use of SSMI data

To complement the scarse POLDER-radiosonde collocations, further comparisons were made with SSM/I TCWV. The SSM/I instrument (Hollinger et al., 1990) on board the DMSP[3] F10 spacecraft provides TCWV estimates with about 15mn time lag with ADEOS-1. F10 has a shorter lag, revoir figure avec F10. The Wentz algorithm (Wentz, 1997) minimizes iteratively the distance between observed and simulated 19-, 22-, and 37-GHz brightness temperatures in order to find the most probable values of TCWV and other environmental parameters. This algorithm showed very good agreement with in-

[3]Defense Meteorological Satellite Program

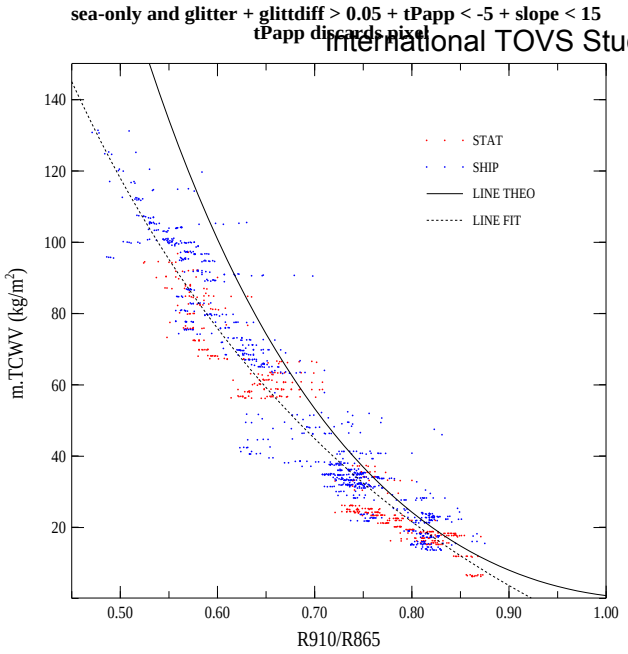

figure 1: Radiosonde TCWV multiplied by airmass m versus POLDER reflectance ratio X=R_{910}/R_{865} for all sea-only-and-glitter cases and after complete cloud screening: glitter amplitude, apparent pressure, reflexion angle

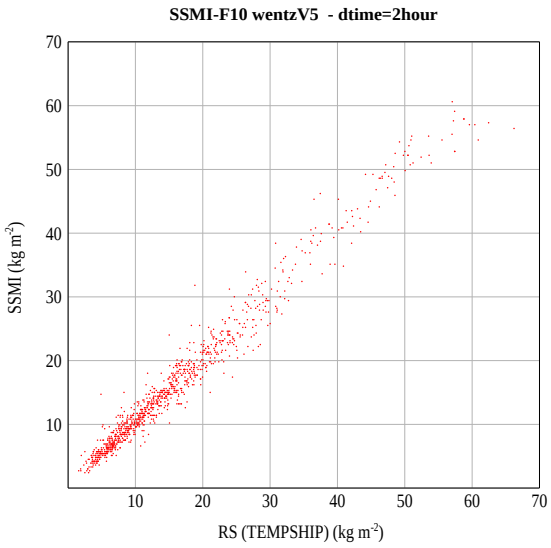

figure 2: SSMI TCWV as function as colocated ship radiosounding (2 hour time lag) between November and June 1997 (kg/m^2)

dependent radiosonde data from both small islands and ships (-0.2 kg/m^2 bias and 3.7 kg/m^2 rms difference) (Deblonde and Wagneur, 1997). The updated version of Wentz processing (full intercomparisons between the DMSP spaceraft series) gives slightly lower values (by 1 to 2 kg/m^2) for TCWV larger than 55 kg/m^2. Figure 2 shows Wentz version 5 estimates, as function of colocated radiosoundings on ship for the POLDER-1 period. It shows a very good correlation (0.99) with 1.00 slope, 0.33 intercept, and 1.55 kg/m^2 RMS error. Level 1 POLDER measurements colocated with SSM/I 0.25 squared gridded TCWV over ocean have been selected for June 1997. Each SSM/I-POLDER-L1 colocation consists in the SSM/I TCWV content and POLDER measurements (all channels) for the 3×3 full resolution pixels closest to the center of the SSM/I pixel. The time lag between POLDER and SSM/I F10 is kept to 15 mn. These colocated data are also filtered to keep cloud-free sunglint directions, with similar test as used for radiosondes match-ups but with more stringent thresholds (refpol>0.2, Tpapp<-100 and, GlitdifP> 0.15).

Figure 3 shows the colocated POLDER / SSMI data after cloud screening together with obtained polynomial $m.U_{WV} = a_2 ln(X^2) + a_1 ln(X)$ fit (a_2=204.55 and a_1=-49.75).

In order to check the algorithm for high and small water vapour contents for which few satellite colocations are available, the polynomial fit is represented with simulated data. Reflectances in the 910 and 865 nm POLDER bands were computed using line-by-line radiative transfert (HITRAN 2000 spectroscopic data base) from atmospheric profiles. Figure 4 shows atmospheric $m.U_{WV}$ as function of computed reflectance ratio together with the polynomial fit obtained with POLDER/SSMI colocations. The agreement is very good even for higher and smaller $m.U_{WV}$ values.

References

Bouffiès, S., F.-M. Bréon, D. Tanré, and P. Dubuisson, 1997: Atmospheric Water Vapor Estimate by a Differential Absorption Technique with the POLDER instrument. *J. Geophys. Res.*, 102, 3831-3841.

Deblonde, G. and N. Wagneur, 1997: Evaluation of global numerical weather prediction analyzes and forecasts using DMSP special sensor microwave imager retrievals. 1. Satellite retrieval algorithm intercomparison study. *J. Geophys. Res.*, 102, 1833-1850.

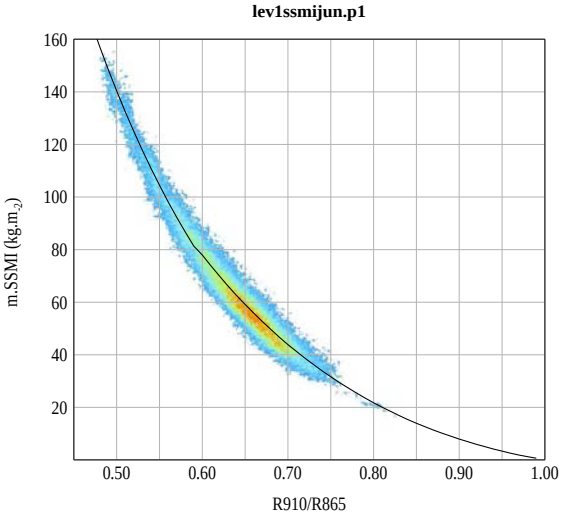

figure 3: SSMI TCWV multiplied by airmass m versus POLDER reflectance ratio X=R_{910}/R_{865} after cloud screening

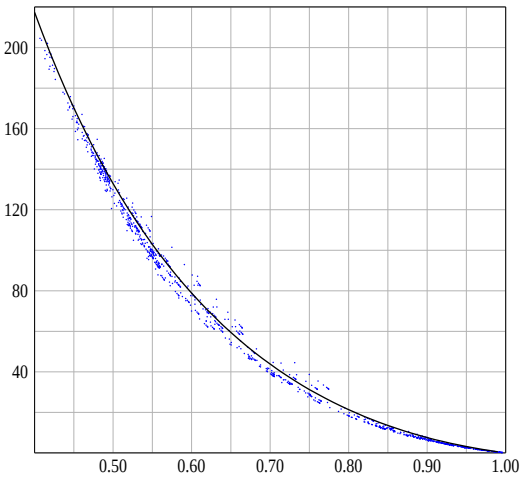

figure 4: profile data base TCWV multiplied by airmass m versus 5A similated HITRAN reflectance ratio X=R_{910}/R_{865} (POLDER channels)

Deschamps, P.Y., F.-M. Bréon, M. Leroy, A. Podaire, A. Bricaud, J.-C. Buriez and G. Sèze, 1994: The POLDER mission: Instrument characteristics and scientific objectives. *IEEE Trans. Geos. Rem. Sens.*, 32, 598-615, 1994.

Bennartz, R. and J. Fischer, 2001: Retrieval of columnar water vapour over land from back-scattered solar radiation using the Medium Resolution Imaging Spectrometer (MERIS). *Remote Sensing of Environment*, 78, 271-280

Hagolle, O., P. Goloub, P.-Y. Deschamps, H. Cosnefroy, X. Briottet, T. Bailleul, J.-M. Nicolas, F. Parol, B. Lafrance and M. Herman, 1999: Results of POLDER In-flight Calibration. *IEEE Trans. on Geosci. Remote Sens.*, 37, 1550-1566.

Hollinger, J.P. , J.L. Pierce, and G.A. Poes, 1990: SSM/I instrument evaluation. *IEEE Trans. Geos. Rem. Sens.*, 28, 781-790.

Vanbauce C., J.C. Buriez, F. Parol, B. Bonnel, G. Sèze and P. Couvert, 1998: Apparent pressure derived from ADEOS-POLDER observations in the oxygen A-band over ocean. *Geophys. Res. Lett.*, 25, 3159-3162.

Vermote, E.F., Santer, R., Deschamps, P.Y. and Herman, M., 1992: In-flight calibration of large field of view sensors at short wavelengths using Rayleigh scattering *Int. J. of Remote Sens.*, 13, 3409-3429.

Vesperini, M., Bréon, F.-M., and D. Tanré, 1999: Atmospheric Water Vapor content from spaceborne POLDER measurements. *IEEE Trans. on Geosci. Remote Sens.*, 37, 1613-1619.

Wentz, F.J., 1994: User's manual SSM/I -2 Geophysical tapes, *RSS Tech. Rep. 070194, Remote Sensing Syst., Santa Rosa, Calif.*

Wentz F. J., 1997: A well-calibrated ocean algorithm for SSM/I. J. Geophys. Res., Vol. 102, No. C4, 8703-8718.

Acknowledgements

Our work is funded by the Centre National d'Etudes Spatiales (CNES) and the Conseil Régional du Nord-Pas-de-Calais. This paper makes use of measurements acquired by CNES/POLDER onboard NASDA/ADEOS. Radiosonde and ECMWF analyses data were obtained through Météo France and SSM/I data from ssmi.com.

Assimilation of AMSU-A Microwave Radiances with an Ensemble Kalman Filter (EnKF)

Herschel L. Mitchell, P. L. Houtekamer, Gérard Pellerin, Mark Buehner and Bjarne Hansen

Service Météorologique du Canada / Meteorological Service of Canada,
Dorval, Québec, Canada

Introduction

The ensemble Kalman filter (EnKF) is a 4D data assimilation method that uses a Monte-Carlo ensemble of short-range forecasts to estimate the covariances of the forecast error (Evensen 1994; Burgers et al. 1998; Houtekamer and Mitchell 1998). It is a close approximation to the standard Kalman filter. The approximation becomes more accurate as the ensemble size increases.

The EnKF is conceptually simple. It does not depend strongly on the validity of hypotheses about the linearity of the model dynamics and requires neither a tangent linear model nor its adjoint. In addition, it parallelizes well.

Like most modern data assimilation methods, the EnKF directly assimilates observed radiance data. This aspect of the EnKF, and in particular the assimilation of AMSU-A microwave radiances, is the focus of this presentation.

First, the EnKF and the experimental environment are briefly described. Then we focus on how the EnKF assimilates the AMSU-A microwave radiances and show some results indicating their impact with the EnKF (including a comparison with similar results from a 3D-Var system). The present text ends with some concluding remarks and a brief outline of our future plans in this area.

The EnKF

For ensemble member i, the EnKF equations can be written as

$$\Psi_i^a = \Psi_i^f + \mathrm{K}(\mathrm{o}_i - H(\Psi_i^f)) \tag{1}$$

$$\Psi_i^f(t+1) = M(\Psi_i^a) + q_i \tag{2}$$

where

Ψ^a : analysis field,

Ψ^f : first-guess (forecast) field,

o_i : vector of (perturbed) observations,

H : interpolation operator (may be nonlinear),

K : gain matrix,

t+1 : the next analysis time,

M : full (nonlinear) forecast model,

q_i : representation of model error.

The gain matrix, K, determines how much weight is given to the innovation, $\mathrm{o}_i - H(\Psi_i^f)$, vis-a-vis the forecast (or first-guess) field, Ψ^f. As in the standard Kalman filter, the gain matrix is defined as

$$\mathrm{K} = \mathrm{P}^f \mathrm{H}^T (\mathrm{H}\mathrm{P}^f \mathrm{H}^T + \mathrm{R})^{-1}, \tag{3}$$

where R is the observational error covariance matrix.

Unlike the standard Kalman filter, the EnKF uses a random ensemble to estimate error covariances, i.e.,

$$\mathrm{P}^f H^T \equiv \frac{1}{N-1} \sum_{i=1}^{N} [\Psi_i^f - \overline{\Psi^f}][H(\Psi_i^f) - \overline{H(\Psi^f)}]^T \tag{4}$$

$$H\mathrm{P}^f H^T \equiv \frac{1}{N-1} \sum_{i=1}^{N} [H(\Psi_i^f) - \overline{H(\Psi^f)}][H(\Psi_i^f) - \overline{H(\Psi^f)}]^T. \tag{5}$$

Note that since H is applied to each background field individually (rather than to the covariance matrix P^f), it is possible to use nonlinear operators. For example, H can be a radiative transfer model if radiance observations are available.

Localization

Correlations associated with remote observations tend to be small and difficult to estimate using small ensembles. To filter covariances at long distances, we use a Schur product (i.e., an elementwise product of two matrices), as described in Houtekamer and Mitchell (2001). That is, instead of directly using covariances calculated from the ensemble, we filter any such covariances using

$$\mathrm{P}^f(r_i, r_j) = \rho(r, L) \circ \mathrm{P}^f_{ensemble}(r_i, r_j), \tag{6}$$

where ρ is a correlation function with compact support and $\circ$ denotes the Schur product. This leads to a positive definite matrix P^f (Gaspari and Cohn 1999). Here r is the distance between points r_i and r_j and L is the distance beyond which the correlation function, ρ, is zero. Our rationale is that as ensemble sizes increase in the future (for

example, with increases in the available computational power), it will be possible to increase L and thereby relax the localization.

In fact, the EnKF never computes the covariance matrix P^f; to calculate the gain matrix, K, only $\mathrm{P}^f H^T$ and $H\mathrm{P}^f H^T$ are required. By applying covariance localization separately in the horizontal and in the vertical, we are effectively using the following modified definition of the gain matrix

$$\mathrm{K} = [\rho_V \circ \rho_H \circ (\mathrm{P}^f H^{\mathrm{T}})][\rho_V \circ \rho_H \circ (H\mathrm{P}^f H^{\mathrm{T}}) + \mathrm{R}]^{-1}. \tag{7}$$

Here ρ_H and ρ_V are the correlation functions used for horizontal and vertical localization, respectively, and $\mathrm{P}^f H^T$ and $H\mathrm{P}^f H^T$ are computed from the ensemble using eqs. (4) and (5), respectively. Actually, rather than using a single ensemble, we use a configuration consisting of a pair of ensembles, as proposed in Houtekamer and Mitchell (1998). Having two ensembles allows the Kalman gain used for the assimilation of data into one ensemble to be computed from the other ensemble.

Currently, the vertical localization forces covariances to zero in 2 units of ln (pressure). Thus, for example, the covariances associated with a 1000-hPa observation fall to zero at 135 hPa, while those associated with a 10-hPa observation fall to zero at 74 hPa.

The Experimental Environment

The EnKF used here has been developed in a series of studies in increasingly realistic environments starting with the 3-level quasigeostrophic model used by Houtekamer and Mitchell (1998) and Mitchell and Houtekamer (2000). For the past few years, we have been using the Canadian Global Environmental Multiscale (GEM) primitive equation model (Côté et al. 1998): initially, a dry 21-level version to assimilate simulated observations (Mitchell et al. 2002) and, more recently, a 28-level version that includes a complete set of physical parameterizations to assimilate real observations (Houtekamer et al. 2003).

Our approach with the EnKF has been to use those observations accepted by the Canadian operational global 3D-Var. As discussed in Houtekamer et al. (2003), this facilitates comparisons with the operational system and allows the EnKF to make use of the operational: (i) "background check" and QCVAR, (ii) TOVS monitoring and bias correction, and (iii) horizontal thinning of TOVS observations.

Currently, of the observations assimilated by the 3D-Var, the EnKF assimilates the following:

- from radiosondes: $u, v, T, q, p_{surface}$;
- from aircraft: u, v, T;
- from satellites: cloud track winds u, v, and AMSU-A microwave radiances;
- surface observations: $T, p_{surface}$.

The EnKF uses the same observational error statistics as the operational 3D-Var. This, too, facilitates comparisons with the operational system.

Assimilation of AMSU-A Microwave Radiances

For the calculation of simulated radiances from a model state vector, the EnKF (like the Canadian operational 3D-Var procedure) uses the RTTOV radiative transfer model. RTTOV-6 (Saunders et al. 1999, Saunders 2000) was used for the experiments presented here, although we have subsequently converted to RTTOV-7. Our implementation of RTTOV is very much based on its use in the operational 3D-Var (Chouinard et al. 2002). Since it uses eqs. (1), (4), (5), and (7) to assimilate observations, the EnKF requires neither the tangent linear nor the adjoint of the radiative transfer model.

Using only observations accepted by the operational 3D-Var, the EnKF assimilates AMSU-A channels 3–10 over open ocean and from three to five of these channels over land and ice depending on the height of the topography, as described by Chouinard et al. (2002). In addition, the AMSU-A observations used operationally are thinned to a horizontal resolution of $\sim$ 250 km.

The results shown below are from data assimilation cycles over a 2-week period in May - June 2002. During this period, AMSU-A observations were available from two polar orbiters, NOAA-15 and NOAA-16. Due to the horizontal thinning of the AMSU-A observations, approximately 3000 profiles were available for assimilation every 6 h from each of these two satellites.

Results from Two Experiments

The first experiment is a TOVS/NOTOVS experiment. Results are evaluated by verifying 6-h forecasts against radiosonde observations. The evaluation is performed over a 5-day period, after a 5-day spin-up. In this experiment, the horizontal grid is 144 $\times$ 72, the EnKF uses a total of 96 ensemble members, and the correlation function used for localization in the horizontal falls to zero at 2300 km.

Results show a neutral to modest improvement in the Northern Hemisphere (not shown). A more substantial positive impact of the AMSU-A observations is observed in the tropics and in the Southern Hemisphere. The Southern Hemisphere results are presented in Fig. 1. It can be seen that assimilation of the AMSU-A profiles results in generally smaller biases and standard deviations (std dev) for all five variables.

The second experiment is a 3D-Var/EnKF comparison. Both methods have been used to assimilate exactly the same set of observations, using the same observational error statistics. The same forecast model (resolution, physical parameterizations, etc.) has been used for both methods. For this experiment, the horizontal grid is 240 $\times$ 120;

the EnKF uses a total of 128 ensemble members; and the correlation function used for horizontal localization in the EnKF falls to zero at 2800 km. Houtekamer et al. (2003) present verifications of 6-h forecasts and analyses against radiosonde observations for this experiment. Here we examine verifications against the AMSU-A data.

Figs. 2 and 3 show O - P and O - A statistics for each AMSU-A radiance channel for the 3D-Var and EnKF assimilation cycles, respectively. A comparison of corresponding panels from the two figures indicates that the current version of the EnKF yields larger std dev values than the 3D-Var, especially for channels 3, 9, and 10. The EnKF also produces larger biases than the 3D-Var system, perhaps because the AMSU-A data is bias corrected using the latter system. The results, while encouraging, indicate that there is considerable room for improvement with respect to the EnKF assimilation of the AMSU-A data.

Conclusions

An EnKF has been developed for atmospheric data assimilation. It is to be used as the data assimilation component of the Canadian operational medium-range Ensemble Prediction System. Results with real observations indicate that the EnKF can be used to assimilate AMSU-A microwave radiances.

Work is continuing aimed at improving the assimilation of the AMSU-A microwave radiances in the EnKF. Among the aspects that we intend to examine are: the effect of the vertical/horizontal localization; the necessity for EnKF-specific (a) QC, (b) monitoring, and (c) bias correction procedures; the desirability of adjusting the observational error specification, including the possible inclusion of observational error correlations. We also intend to assimilate other types of radiance data, e.g., AMSU-B, with the EnKF.

Acknowledgments: The development of a new data assimilation algorithm is a complex project. We are grateful to our many colleagues at Direction de la recherche en météorologie and the Canadian Meteorological Centre for their help, suggestions, and encouragement. We thank Clément Chouinard and Jacques Hallé for their help and advice regarding the assimilation of the AMSU-A radiances. We also thank Chantal Côté for generating Figs. 2 and 3.

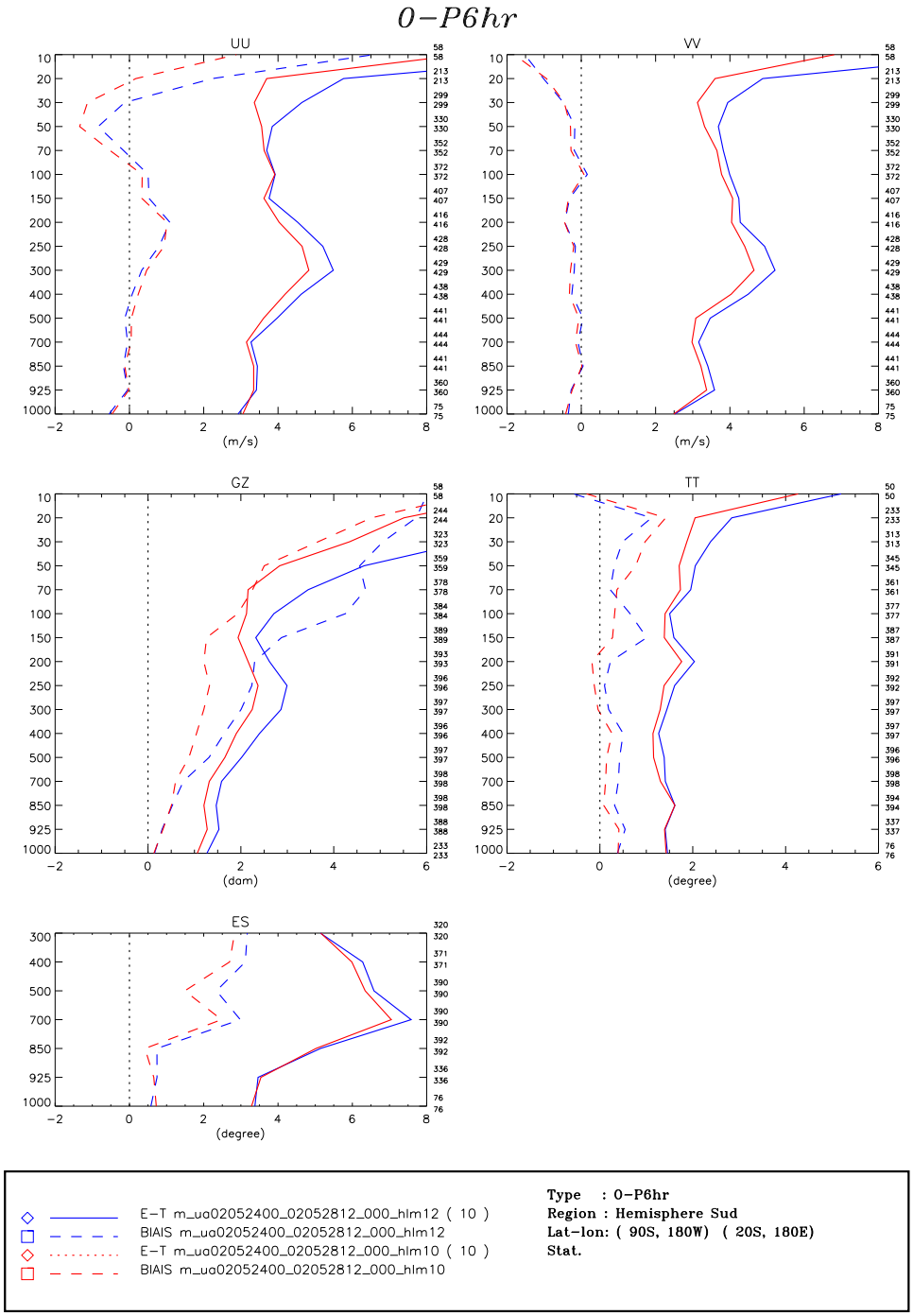

Figure 1: Verification scores for the ensemble mean for the first experiment. The mean value, i.e., bias, (dashed) and std dev (solid) of the observed minus interpolated 6-h forecasts are shown for the assimilation cycle with AMSU-A data (in red) and without AMSU-A data (in blue) for the region south of 20° South.

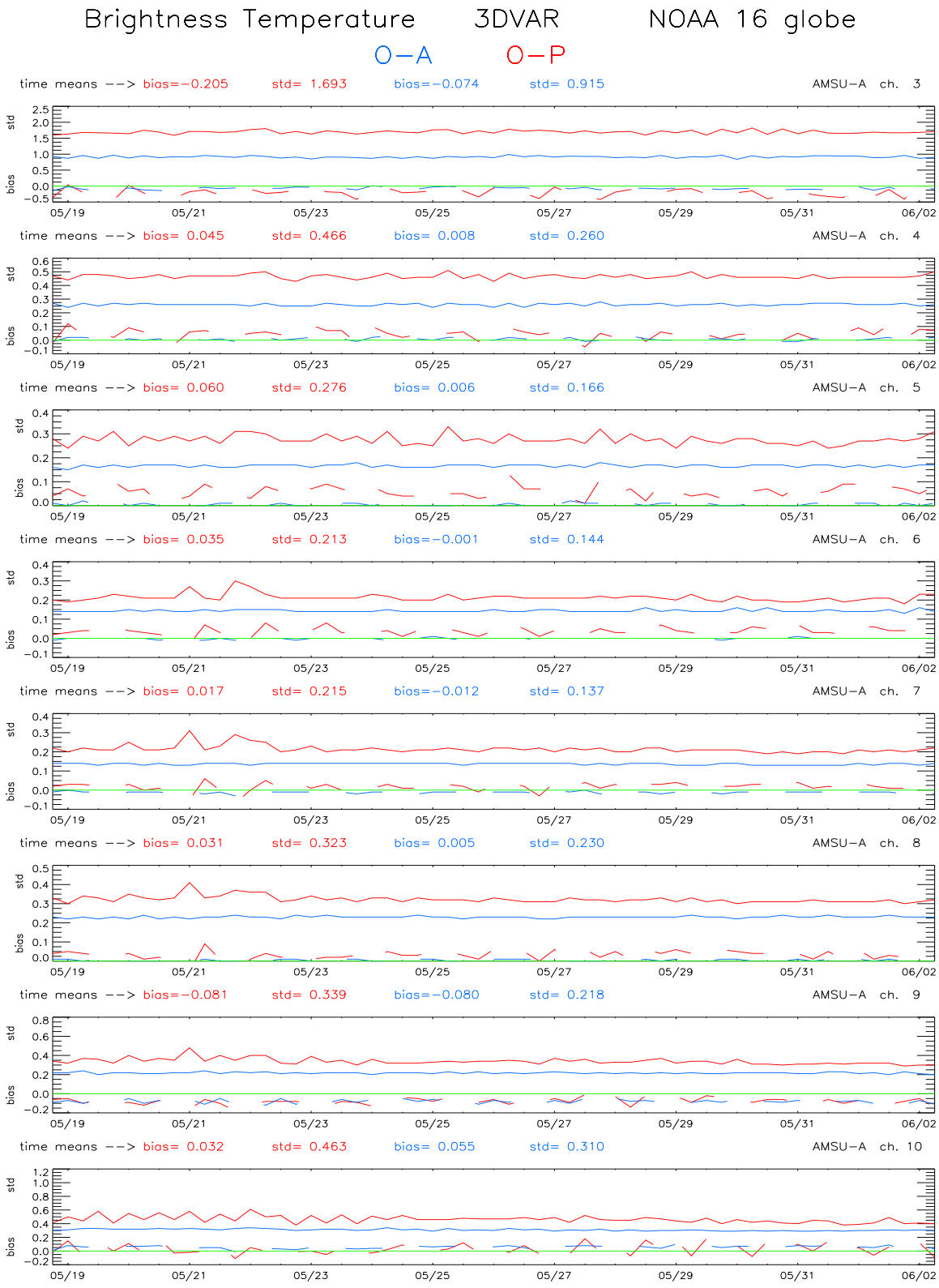

Figure 2: Observed minus analysis (O - A, blue) and observed minus 6-h forecast (O - P, red) for AMSU-A channels 3–10 for the 3D-Var assimilation cycle.

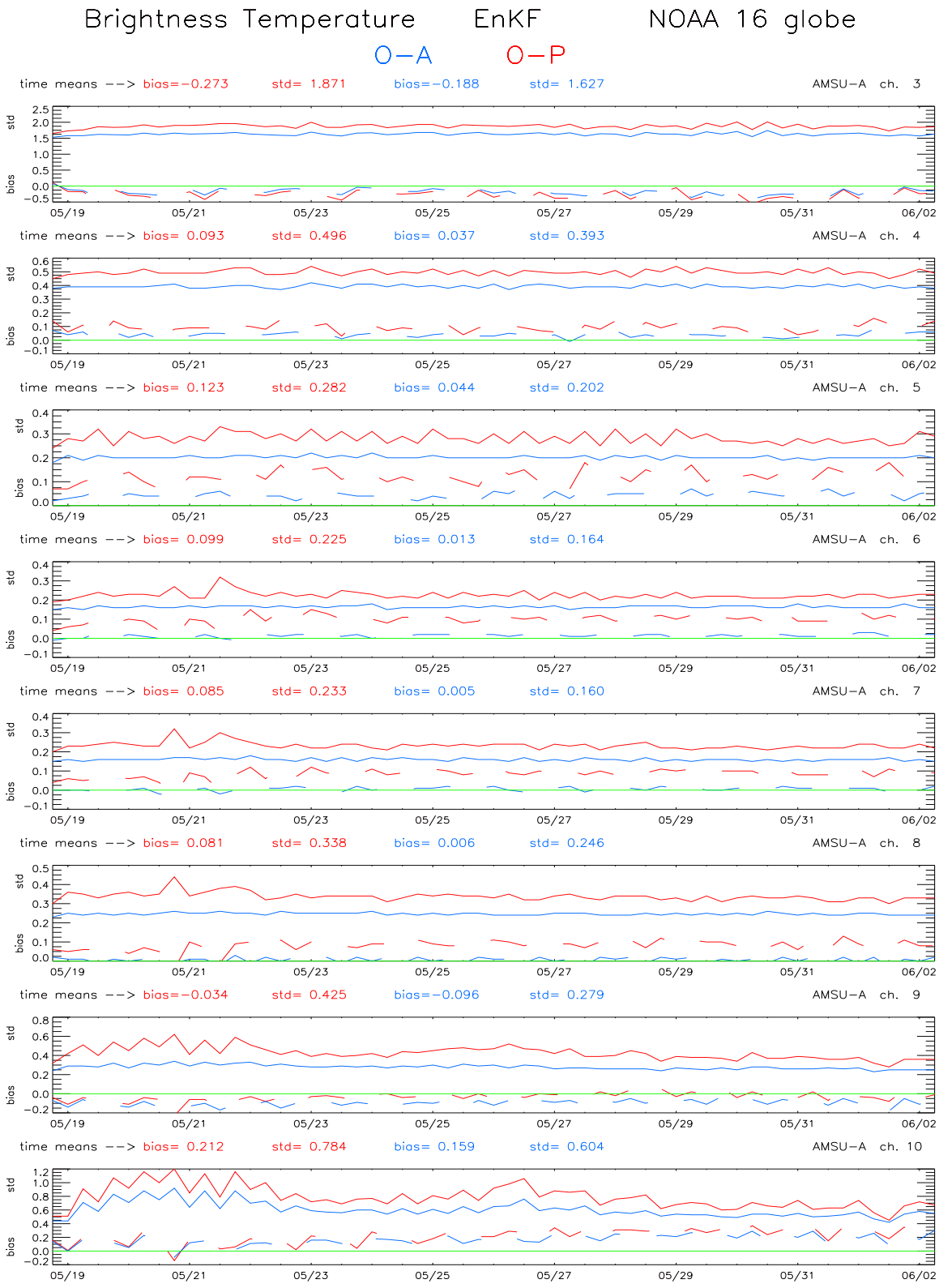

Figure 3: As in Fig. 2, but for the ensemble mean of the EnKF assimilation cycle.

References

Burgers, G., P.J. van Leeuwen, and G. Evensen, 1998: Analysis scheme in the ensemble Kalman filter. *Mon. Wea. Rev.*, **126**, 1719–1724.

Chouinard, C., J. Hallé, C. Charette, and R. Sarrazin, 2002: Recent improvements in the use of TOVS satellite radiances in the unified 3D-Var system of the Canadian Meteorological Centre. Proc. 12th Int'l ATOVS Study Conf., Lorne, Australia, 7 pp.

Côté, J., S. Gravel, A. Méthot, A. Patoine, M. Roch and A. Staniforth, 1998: The operational CMC-MRB Global Environmental Multiscale (GEM) model. Part I: Design considerations and formulation. *Mon. Wea. Rev.*, **126**, 1373–1395.

Evensen, G., 1994: Sequential data assimilation with a nonlinear quasi-geostrophic model using Monte Carlo methods to forecast error statistics. *J. Geophys. Res.*, **99**(C5), 10143–10162.

Gaspari, G., and S.E. Cohn, 1999: Construction of correlation functions in two and three dimensions. *Quart. J. Roy. Meteor. Soc.*, **125**, 723–757.

Houtekamer, P.L., and H.L. Mitchell, 1998: Data assimilation using an ensemble Kalman filter technique. *Mon. Wea. Rev.*, **126**, 796–811.

Houtekamer, P.L., and H.L. Mitchell, 2001: A sequential ensemble Kalman filter for atmospheric data assimilation. *Mon. Wea. Rev.*, **129**, 123–137.

Houtekamer, P.L., H.L. Mitchell, G. Pellerin, M. Buehner, M. Charron, L. Spacek and B. Hansen, 2003: Atmospheric data assimilation with the ensemble Kalman filter: Results with real observations. *Mon. Wea. Rev.* Submitted.

Mitchell, H.L., and P.L. Houtekamer, 2000: An adaptive ensemble Kalman filter. *Mon. Wea. Rev.*, **128**, 416–433.

Mitchell, H.L., P.L. Houtekamer, and G. Pellerin, 2002: Ensemble size, balance, and model-error representation in an ensemble Kalman filter. *Mon. Wea. Rev.*, **130**, 2791–2808.

Saunders, R.W., 2000: RTTOV-6: Science and validation report. 31 pp. [Available from EUMETSAT Satellite Application Facility on NWP, The Met Office, London Road, Bracknell, Berkshire RG12 2SZ, England.]

Saunders, R.W., M. Matricardi, and P. Brunel, 1999: An improved fast radiative transfer model for assimilation of satellite radiance observations. *Quart. J. Roy. Meteor. Soc.*, **125**, 1407–1425.

A Research of Four-dimension Variational Data Assimilation with ATOVS Clear Data

Ma Gang
National Satellite Meteorological Center, Beijing 100081
Wang yunfeng
LASG, Institue of Atmospheric Physics, Chinese Academy of Sciences, Beijing ,100029
Fang Zongyi
National Satellite Meteorological Center, Beijing 100081

1. Introduction

Satellite vertical sounding data, which represent the three-dimensional distribution of the atmospheric state at the time, are based on infrared and microwave observations from meteorological satellites. Nowadays more and more deduced atmospheric parameters from satellite vertical sounding data and other satellite data are used in numerical weather forecasting. In order to use as many of these data that are high spatial resolution, a four-dimension data assimilation scheme is developed to introduce them into a numerical weather prediction model. The quality of the model's initial field is therefore improved. Then the model physical parameters such as wind and water vapor become more rational.

With the use of 4-DVAR, which is based on an adjoint equation, various observations have been introduced into the numerical model. In this paper, a MM5 numerical model is the dynamic restriction and HIRS cloud-clear radiances from NOAA satellite are taken as the forcing of observations. So the known atmospheric rules that are described in the model and the efficient information that is contained in multi-time observations could be used in the prediction. Because the observations which are not in the same form as numerical model variables, in our scheme a fast transfer model, RTTOV5, is used to convert the model variables, such as air temperature and water vapor profiles, into HIRS cloud-clear radiances. If the adjoint of RTTOV5 is performed while the adjoint of MM5 is integrated, the radiances data from satellite can be assimilated into the numerical model directly. It is a virtue of 4-DVAR that the assimilation of observations is performed at the location of observation station. So while each viewing point of a satellite sounder could be processed as an observation station, possible big errors due to the interpolation from regular grids to the station should be turned away. Therefore, the initialization to the assimilated fields are not necessary, for the initial fields have been restricted by the numerical model, which means the variables have been consistent when the adjoint model is integrated.

2. Theory and Model

Because we are using HIRS data from N0AA satellites, the orbit time of the satellites over East Asia varies everyday. Thus it is quite different from the regular time of radiosonde observations. So some errors will be possible if the time of assimilation is fixed. However in 4D-VAR, all orbit times in the assimilation window can get its corresponding output from MM5 and the transform is performed by a fast forward model.

Thus atmospheric state profiles to radiances from satellite can be carried out correctly. The cost function in the 4D-VAR can be represented as:

$$J(x) = J_b + J_s$$

$$J_b = \frac{1}{2}(X - X_b)^T B^{-1}(X - X_b)$$

$$J_s = \sum_i \sum_{ich} [F_i(x_{ich}) - y_{i,ich}^{obs}]^T (O+F)^{-1} [F_i(x_{ich}) - y_{i,ich}^{obs}]$$

where the vectors $X = (u, v, p', t, q)$ are all control variables at initial time, u and v are horizontal wind speed, w is vertical speed, p′is the pressure perturbation, T is air temperature and q is the water vapor. During the assimilation, elements in X are adjusted until the end of iteration. And X_b, which is based on an estimation of error covariance B, is obtained from MM5's analysis. J_b is the background and J_s is the forcing from satellite HIRS data. I is the total NOAA16 orbit number contained in the 2 hours assimilation window, ich is the whole number of HIRS channels that are used in the data assimilation. In general, the error covariance-B of background fields only consists of a diagnostic factor and its values are the difference of the model forecast at the initial time and the time of the 6th hours' integration. This can be represented as: $B = \sqrt{|X_1 - X_2|}/2$ where X_1 and X_2 are the control variables from model prediction at the two times. In the satellite HIRS forcing term, the matrix-(O+F) is the summation of the error covariance of the forward model and HIRS data. Usually the biases from simulated radiances to HIRS observations are transacted to get an approximate matrix (O+F+P). If errors from initial profiles are ignored, the matrix could be predigested to (O+F). In fact, the weighting of satellite forcing is set to be 1, while the values of satellite forcing at the first time and prior statistic biases are considered, an experimental error covariance matrix (O+F) is available. In order to decrease computation, the number of HIRS channels which are involved in the data assimilation is selected. Errors of these channels are independent, for the pressure layers of the channels do not overlap. Thus the matrix (O+F) can be treated as a diagonal matrix.

In 4D-VAR, y_0^0 is set to be value of the first iteration, then the MM5 forward model starts its integration from t_0 to t_N which is the end of the assimilation window. While the model is performed, y_n^0 the atmospheric state vector from MM5, is outputed every 6 hours. When there are satellite observations, radiances of the HIRS channels designed to be involved in the assimilation are calculated by RTTOV5 to get the value of satellite forcing. The adjoint of MM5 starts performing at t_N after the execution of the MM5 forward model. The initial perturbation value of the conjugation function: $\delta^* y(t_N) = W_N(y_N^0 - \hat{y}_N)$ is the initial field of the adjoint model. The basic states of the adjoint model are available from y_n^0 and the gradients of satellite forcing are obtained from the adjoint of RTTOV5 in which the initial values of the adjoint are set to be bias from the simulated radiances to the satellite observations: $W_N(y_n^0 - \hat{y}_n)$. Then, a finite memory semi-Newton algorithm is used to get a new initial field y_0^1 for the MM5 forward model along an optimal convergence direction of cost function. Using iteration of the semi-Newton algorithm, various y_0^k are obtained until the optimal with a more

satisfying precision. Finally $(y_0)_p$ is set to be the initial field of the MM5 forward model to check the possible improvement in the forecast atmospheric state field and precipitation due to the introduction of satellite data in the numerical model.

3. The Experiments and Results

Prior to the assimilation, though the gradients of the forward model and the adjoint of RTTOV5 MM5 have been tested, it is still essential to test the gradients of the 4D-VAR after the coupling of these two models while the potential transmission mistakes between them are considered. While $\psi(\alpha)$ is set as single precision, its value varies with α can be represented as:

α0 =0.0000000E+00

++<α_00=9.9999990E-05>++

I=1 α= 0.10000E-04 F(A)= 0.1002861300E+01

I=2 α= 0.10000E-05 F(A)= 0.9989470500E+00

I=3 α= 0.10000E-06 F(A)= 0.1019896300E+01

I=4 α= 0.10000E-07 F(A)= 0.9372019800E+00

I=5 α= 0.10000E-08 F(A)= 0.5512952800E+00

To check the impact on meso-scale weather prediction by the atmospheric vertical sounding data from satellite, HIRS data from NOAA16 are introduced into a MM5 4D-VAR system to simulate a rainstorm that developed from 21 to 25 July 2002. Both data of background fields and the initial fields from the MM5 forward model are attained from analyzed fields of T106. 100hPa is set as the top of MM5. Since the top of MM5 is far lower than the top of RTTOV5 (0.1 hPa), some climate profiles are used from 100hPa to 0.1 hPa. A cubic spline interpolation is used to get air temperature and water vapor on pressure levels of RTTOV5 from these variables on the pressure levels of MM5. Then an experiential quality control is designed to remove satellite data with large bias to the simulated radiances and a cloud mask method is also used to make sure that all satellite data are located in cloud-clear areas. The length of the assimilation window is 2-hours, so two orbits of NOAA16 are involved in the window from 12 UTC to 14 UTC on July 21. Some preliminary tests show that data from all HIRS channels cannot confirm the best prediction if all these data are introduced into the 4D-VAR. Therefore it is essential to select part of the channels to use in the data assimilation. According to the pressure level of the weighting function of every HIRS channel, some channels could be independent to each other. If channels, such as O_3 channel and short wave window channels (channel 17-19) are ignored, data from 9 HIRS channels are used in the data assimilation while these independent channels are considered.

The center of the test domain is set as 25°N, 120°E. Total grids are 61*61, grid spacing is 45km (figure 1). The primary precipitation from 21 to 22 July 2002 is distributed from 30°N, 112°E to 30°N, 120°E. Because of the cloud cover, HIRS data in one orbit of NOAA16 are used in the data assimilation, only one of the two precipitation centers (one located at 29°N, 114°E, and the other is at 24°N, 109°E) is included in the

orbit area. After 24-hours integration of the MM5 forward model, the simulated precipitation center is at 30°N, 114°E, compared to the total precipitation at 30°N, 117°E of 20.0 mm in the control test, the assimilated total precipitation of 33.1m which is 50% more than the prior value. And the total precipitation and the location of west center are not different in the two tests.

The test shows that assimilation of HIRS data from satellite can get certain improvement to numerical model prediction. Due to the impact of cloud, meso-scale forecasting in cloud area could not get any change. Because only microwave sounding data from satellite can be used in cloud areas, the assimilation of these data could potentially make an improvement to predictions in cloud areas.

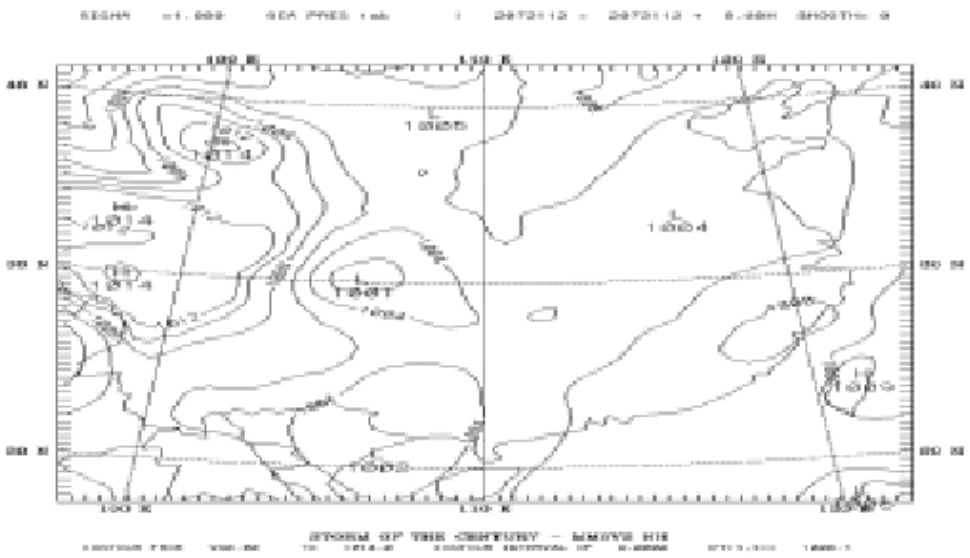

Figure 1. Test terrain of the MM5.

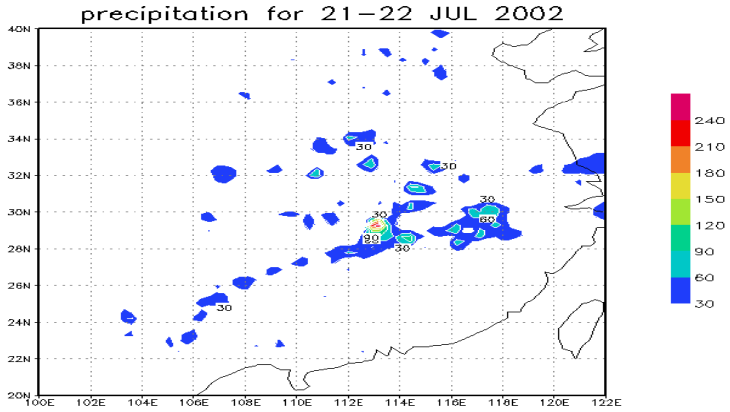

Figure 2. The observed precipitation from 21-22 July.

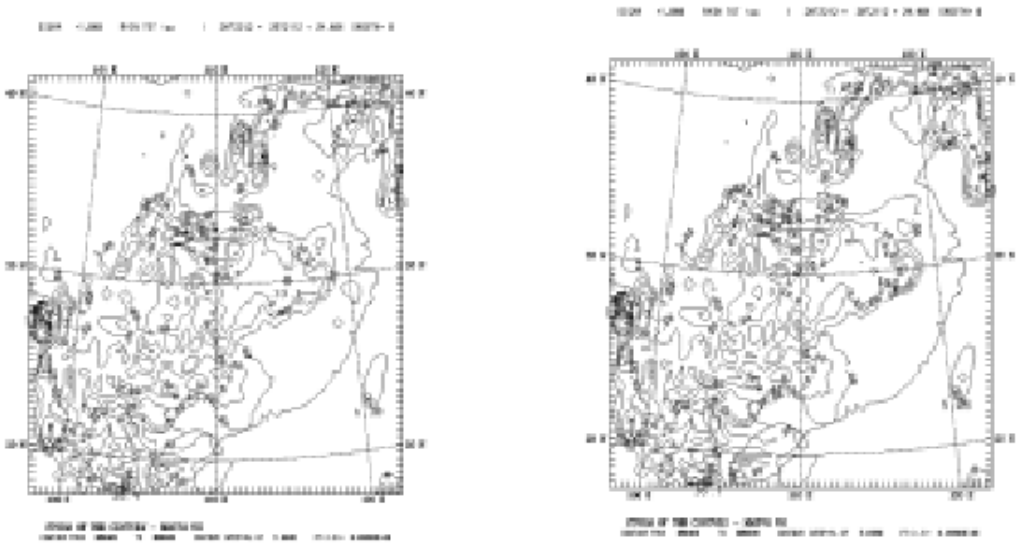

Figure 3. Total 24-hours' precipitation in control test (right) and assimilation test with satellite data (left).

Impact of the assimilation of MSG/SEVIRI radiances in a mesoscale NWP model

by Thibaut Montmerle *
Météo-France/CNRM: 42, av. G. Coriolis 31057 Toulouse, France

Summary

The SEVIRI radiometer onboard MSG provides a complete set of radiance observations in the visible and the infrared spectrum every 15 min with an approximate spatial resolution of 5 km over Europe. Those measurements therefore seems to be particularly well adapted for the weather prediction at convective-scale, since they allow continuous access to information about the variation rates of temperature and humidity fields in space and time.
In order to quantify the impact of the assimilation of SEVIRI radiances in the analysis of those meteorological quantities, the regional NWP model ALADIN and its 3D-Var assimilation system have been used. SEVIRI data from the 12^{th} February 2003 case have been bias corrected, thinned and screened before the assimilation itself. Data from channels 3.9 μ and 9.7 μ have been blacklisted because of strong biases due to cloud contamination and/or calibration problem. Furthermore, a cloud detection scheme has been used in order to keep information above cloud top. The impact of the assimilation of the remained radiances leads to a reduction of the error in the humidity field in mid to high troposphere and to the humidification/drying of areas that allows a better prediction of mid to high level cloud cover. No impact have been observed in the analysis of the temperature field.

1 Introduction

The context of this work is the AROME project, which is Météo-France's future Numerical Weather Prediction (NWP) system at regional scale. This non-hydrostatic model, which is planned to run operationally around 2008, will cover the French territory with a 2.5 km horizontal resolution and will perform 1 to 2 hours data assimilation cycles using a 3D-Var algorithm. In this context of regional weather forecasting, the high horizontal and temporal resolutions of measurements performed by geostationary satellites are an asset compared to polar satellites, despite their weaker spectral and vertical resolutions. The purpose of this paper is to investigate the impact of the assimilation of SEVIRI IR observations in this context.
Since the AROME model still is in research phase, the study presented herein shows preliminary results of the assimilation of radiances observed by SEVIRI the 12^{th} of February 2003 in the 3D-Var assimilation system of the ALADIN model (Radnòti *et al.*, 1996). This spectral hydrostatic model, which is the LAM version of the global model ARPEGE/ IFS, covers the western Europe with a 10 km horizontal resolution. Its initial state and large scale conditions in the boundaries of its retrieval domain are given by ARPEGE outputs.

2 Experimental framework

ALADIN's 3D-Var can be used in research mode to assimilate the same types of observations than ARPEGE/IFS, that are among others radiosondes, ground station measurements, horizontal

*corresponding author's address: montmerle@cnrm.mete- o.fr

wind retrieved by geostationary satellites and radiances observed by the microwave radiometer AMSU-A onboard NOAA-16 and NOAA-17. The formalism of the variational analysis follows closely the work in ARPEGE/IFS (Courtier *et al.*, 1994).
To assimilate SEVIRI brightness temperature (T_b hereafter), this assimilation system has been modified in the following way: the analysis x^a represents the atmospheric state which is the best fit between the background x^b (usually taken as a 6 hour forecast) and the available observed radiances stored in the y vector. The cost function is written under an incremental formulation:

$$\begin{aligned} J(x) &= \tfrac{1}{2}\delta x^T \mathbf{B}^{-1}\delta x \\ &+\tfrac{1}{2}(\mathbf{H}\delta x - d)^T \mathbf{R}^{-1}(\mathbf{H}\delta x - d) \end{aligned}$$

Where δx is the increment defined by the difference between x^a and x^b; $\mathbf{B}$ is the background covariance error matrix computed using the "lagged NMC" method (Siroká *et al.*, 2002). This method is base on the computation of the$\mathbf{B}$ matrix from a pair of forecast valid at the same time, the short term run using the same lateral and initial conditions than the long term run. This allows to reduce the large scale variance and to get sharper analysis increments more adapted for mesoscale assimilation; $\mathbf{R}$ is the observation covariance error matrix; d the innovation vector that represents the departure between the observations and the background model state interpolated in the observation space:

$$d = y - H(x^b)$$

H being the observation operator that allows to write model variable in the observation space. The latter operator can be strongly non linear and contains i) the fast radiative transfer model RTTOV-6 (Saunders *et al.*, 1999), which allows to retrieve T_b from surface pressure and temperature and from vertical profiles of temperature, humidity and ozone, ii) a horizontal interpolation operator permitting to move the control variable profiles on observation locations, iii) a vertical interpolation and extrapolation operators allowing to position these profiles on RTTOV vertical levels. $\mathbf{H}$ is the tangent linear operator of H in the vicinity of the background state x^b. The variational problem is solved by calculating iteratively the cost function and its gradient:

$$\nabla_{\delta x} J = (\mathbf{B}^{-1} + \mathbf{H}^T\mathbf{R}^{-1}\mathbf{H})\delta x - \mathbf{H}^T\mathbf{R}^{-1}d$$

Convergence is obtained after $||\nabla_{\delta x} J||$ reaches a fixed minima.

3 Data preprocessing

The data used in this study comes from the 12^{th} February 2003, which corresponds to the first complete broadcasted SEVIRI image. At 13h30 UTC, these images are displaying a typical winter situation over western Europe characterized by an intense easterly moving low located south of Greenland, by an associated frontal rainband and by strongly anticyclonic conditions over eastern Europe that advects cold air westward, which produces stratus over Belgium and Germany.

3.1 Bias correction

The systematic error of the satellite data can be computed by looking at the innovation vector, as explained in (Harris and Kelly, 2001). This error arises mainly from errors in instrument calibration, radiative transfer model or from biases in model fields. To minimize the effect of the latter, only radiances near radiosondes are taking into account, since it is assumed that the

model is relatively unbiased at these locations. Contrary to polar satellites, bias due to scan angles are negligible for geostationary platform, since these angles are small in this case.

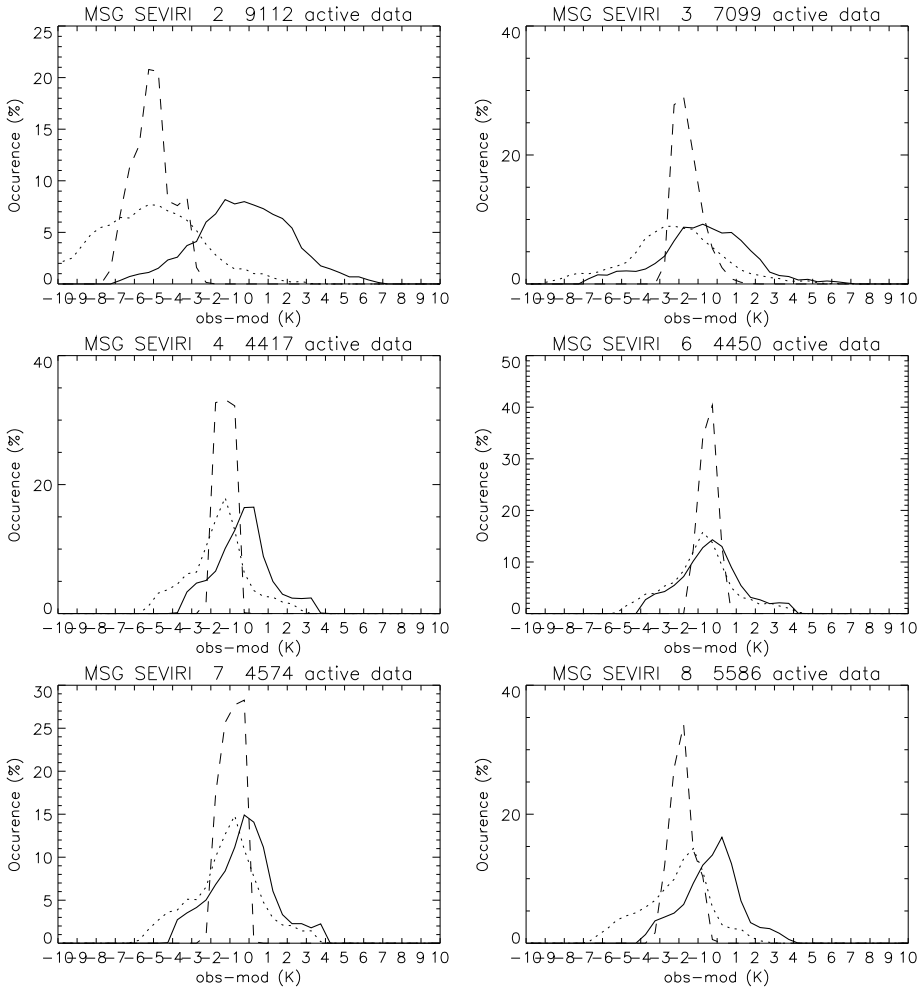

Figure 1: Histograms of T_b for the non-corrected background (dotted line), the applied bias correction (dashed line) and the corrected background (solid line) for the channels WV 6.2 μ (channel 2), WV 7.3 μ (3), IR 8.7 μ (4), IR 10.8 μ (6), IR 12.0 μ (7) and IR 13.4 μ (8)

The air-mass biases are computed for each channel using a multiple linear regression algorithm applied on four predictors that are 1000-300 hPa and 200-50 hPa thickness, model surface skin temperature and total precipitable water. The Fig. 1 shows the result of the bias computation for the six channels WV 6.2 μ, WV 7.3 μ, IR 8.7 μ, IR 10.8 μ, IR 12.0 μ and IR 13.4 μ. IR channels 3.9 μ and IR 9.7 μ have been blacklisted because of strong biases due to cloud contamination and/or calibration problem. For the resulting channels, some cases present strong initial bias (more than 5 K for WV 6.2 μ) which seems to confirm calibration problem for the studied situation. However, the innovation vector post-bias correction is well centered on zero, which indicates a good bias correction. To be really efficient, this method should be applied on several assimilation steps to take into account more data in the computation of the linear regression parameter and to perform monitoring. This point is part of the perspective of this work.

3.2 Screening

Once the bias correction has been completed, further successive operations on data are applied:

- **Cloud detection scheme:** the ECMWF clo- ud detection scheme devoted to the assimilation of AIRS radiances (Watts and McNally, 2002) has been adapted for SEVIRI radiances in order to detect channels that are non affected by cloud contamination. As a matter of fact, those channels are potentially useful by the assimilation system. This method allows to determine for each channel the level at which the presence of a single layer opaque cloud causes a 1 % change in the clear air radiance diagnosed from the model fields. For SEVIRI, it allows in most of cases to keep more data from the two WV channels since their weighting functions have a maximum above 600 hPa.

- **Quality control:** this check rejects data whose (obs-guess) value exceeds the sum of the background and the observation variances (σ_b and σ_o respectively) time an empirical constant α:

$$((y - H(x^b))/\sigma_b)^2 \quad > \alpha(1 + \sigma_o^2/\sigma_b^2)$$

  The uncertainty of the humidity estimation in the troposphere leads to take a larger α for WV channels.

- **Thinning:** To keep the observations relatively uncorrelated, only one pixel over five has been taken into account in the process, which corresponds broadly to one observation every 30 km over Europe. Since the horizontal range of the analysis increment is around 100 km, this choice seems reasonable.

4 Impact of the assimilation of SEVIRI radiances

Results of the assimilation at 12 UTC of the observations out coming the screening process in ALADIN's 3D-Var is summarized on Fig. 2. This figure shows statistics on T_b for each SEVIRI channels separately. The distance between the two curves indicates how the addition of SEVIRI T_b could modify the background fields during the assimilation. A large reduction of RMS error can be seen for the two WV channels, which indicates that a large part of the information carried out by these channels have been taken into account in the analysis. Results are less notable for the 4 resulting IR channels, but their assimilation still is useful. For every channels, the bias are also smaller in the analysis. The cloud detection scheme leads to consider more WV observations (channels 2 and 3) and in a less obvious way T_b observed by the CO_2 absorption band channel (channel 8 at 13.4 μ).

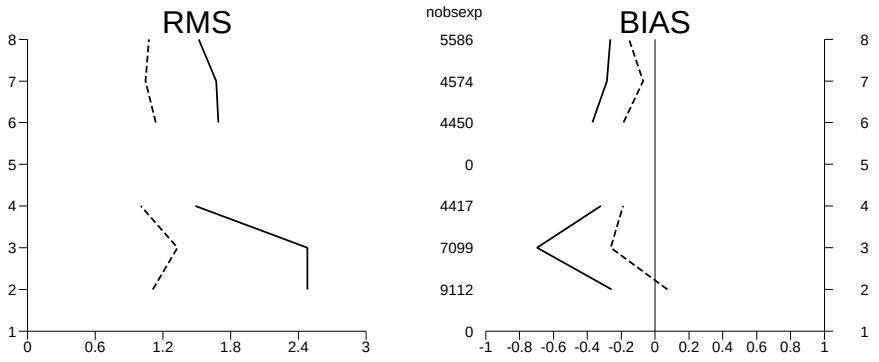

Figure 2: RMS error and bias for obs-guess (solid line) and obs-analysis (dashed line) after the assimilation of SEVIRI radiances. The ordinate axis represent the number of channel and the number of selected data after the screening

To quantify the impact of the assimilation of SEVIRI radiances on the analysis of temperature and humidity, comparisons have been undertaken between radiosondes measurements and values given by the background and the analysis interpolated at the launching sites. Fig. 3 displays such comparisons for 18 radiosondes performed in clear air conditions at the time of the assimilation over western Europe. A notable impact can be seen on the analysis of humidity in mid to high troposphere, with a 10 to 20 % error reduction compared to background values. On the other hand, the impact on temperature analysis is negligible. This can be due to the rather poor spectral resolution of SEVIRI channels, but also to the actual structure of the **B** matrix that leads sometimes to unrealistic information propagation along the vertical axis.

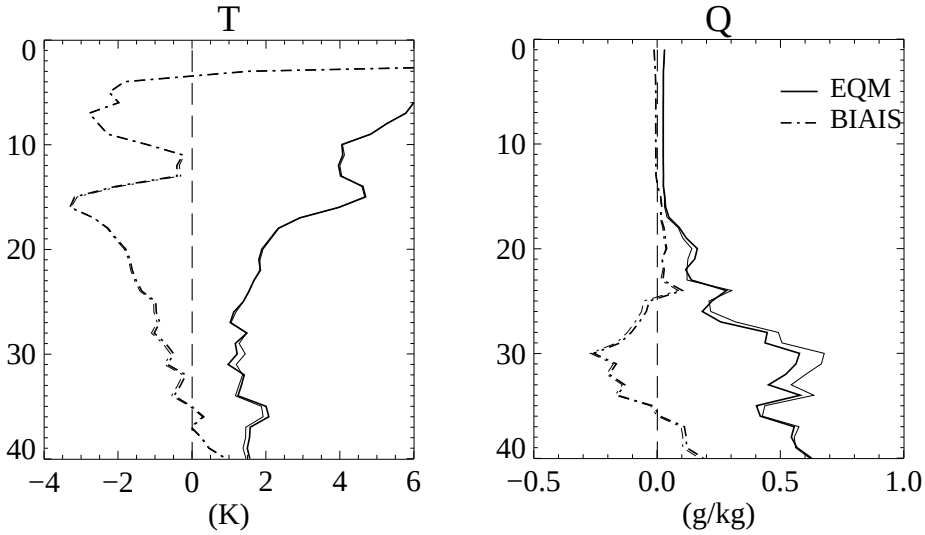

Figure 3: Mean standard deviation and bias profiles (solid end dashed lines respectively) of the difference between 18 radiosondes and the background (thin line) and the analysis (bold line) for the temperature (left column) and the humidity (right column)

5 Impact on short term forecast of cloud cover

During the previous sections, it has been shown that, after the assimilation of SEVIRI radiances (which corresponds to SEV experiment), the analysis increments generate humidification or drying of the mid to high troposphere in better agreement with in-situ measurements. The maximum values of those increments are from the same order of magnitude than those obtained after the assimilation of radiosondes (around 0.6 g/kg for the humidity field) (not shown). The impact on forecasts should therefore be seen on cloud cover fields, diagnosed from relative humidity and precipitations generated by the convection scheme. Comparisons of this quantities with NOAS experiment and Meteosat-7 images is displayed on Fig. 4 (NOAS corresponds to the prediction performed without any data assimilation).

In the SEV experiment, the most noticeable effect is that the atmosphere has been humidified upstream the frontal rain band and south east of Spain mostly around 750 hPa (not shown). After 24 hours forecast, this has permitted respectively to shift the frontal rain band eastward and to get a larger extent to the north of the large convective system located in south west Mediterranean see. The high level cloud cover is also more developed above the northern see. These features seem to be in better agreement with Meteosat WV image than NOAS.

6 Conclusion

SEVIRI data from the 12^{th} February 2003 case have been assimilated in the 3D-Var system of the regional LAM model ALADIN. These data have been firstly preprocessed: channel 3.9 and 9.7 μ have been blacklisted; a pixel-by-pixel air-mass dependent bias correction have been applied; a cloud detection sche- me has been adapted to take into account potential information above cloud top; a quality control check based on the examination of the innovation vector have been performed; data have been thinned. The impact of the assimilation of the resulting observations shows a reduction of the background error in mid to high troposphere for the humidity, mainly due to the information given by the two WV channels. No significant impact on the analysis of temperature has been noticed. The analysis increments lead to humidification or drying of certain areas with the same order of magnitude than increments obtained after radiosonde assimilation. 24 hours prediction shows mid and high level cloud cover in better agreement with observations.
To confirm those encouraging results, other cases have to be examined. Cycled assimilation with different frequencies (from 1 hour to 15 min) are currently under progress in order to study the potential contribution of SEVIRI's high temporal resolution vs. the high spectral resolution of AIRS-like radiometer. To maximize the impact of the assimilation of such observations at regional scale, some work has also to be done on the **B** matrix in order to take into account meteorological phenomena at that scale (such as low level inversion, position of a front...).

Acknowledgement: This work has been done thanks to a Alcatel Space financing.

References

Courtier, P., E. Andersson, W. Heckley, J. Pailleux, D. Vasiljevic, M. Hamrud, A. Hollingsworth, F. Rabier, and M. Fisher (1994). The ecmwf implementation of 3d-var. 1: Formulation. *Quart. J. Roy. Meteor. Soc. 120*, 1367–1387.

Harris, B. A. and G. Kelly (2001). A satellite radiance-bias correction scheme for data assimilation. *Quart. J. Roy. Meteor. Soc. 127*, 1453–1468.

Radnòti, G., R. Ajjaji, R. Bubnová, M. Caian, E. Cordoneanu, K. Von der Emde, J. Gril, J. Hoffman, A. Horányi, S. Issara, V. Ivanovici, M. Janoušek, A. Joly, P. Lemoigne, and S. Malardel (1996). The spectral limited area model ARPEGE-ALADIN. In *PWPRR Report*, Volume n.7, pp. 111–118. World Met. Org.

Saunders, R., M. Matricardi, and P. Brunel (1999). An improved fast radiative model for assimilation of satellite radiance observation. *Quart. J. Roy. Meteor. Soc. 125*, 1407–1425.

Siroká, M., C. Fisher, V. Cass, R. Brozkov, and J.-F. Geleyn (2002). The definition of mesoscale selective forecast error covariances for a limited area variational analysis. *Meteor. Atmos. Phys.*, 1–18.

Watts, P. and T. McNally (2002). A cloud detection approach for airs radiance assimilation. In *12th International TOVS study conference*, Australia.

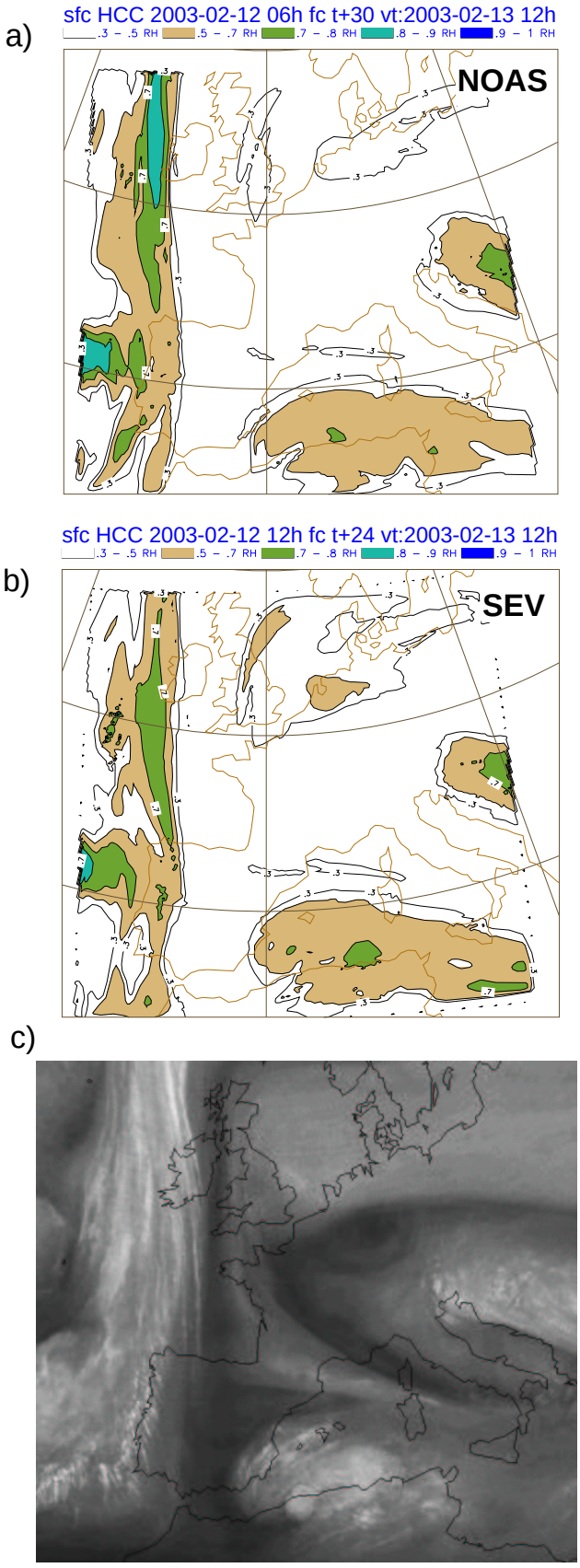

Figure 4: Horizontal cross section of 24 hours forecast of high level cloud cover for (a) NOAS and (b) SEV experiments; (c) corresponding Meteosat WV channel observation

Impact of the ATOVS data on the Mesoscale ALADIN/HU Model

Roger Randriamampianina and Regina Szoták

Hungarian Meteorological Service
1024, Budapest, Kitaibel Pál u. 1
Hungary
e-mail: roger@met.hu

Abstract

At the Hungarian Meteorological Service for the last few years we have been investigating the three-dimensional variational (3D-Var) data assimilation technique in the limited area model ALADIN (ALADIN/HU). Our main objective is to change the so-called dynamical adaptation (initial file from the global model ARPEGE) that is recently in operational use, to a 6-hour data assimilation cycle. Another important task is to use as many observations as possible.

Data from radiosonde and surface observations are already prepared for data assimilation. At present, we are investigating the use of data from aircraft (AMDAR) and satellite (ATOVS) observations. The impact of ATOVS data is studied in two resolutions (80 and 120km). In the ALADIN 3D-Var, the specific humidity is assimilated together with vorticity, divergence, temperature and surface pressure (in multivariate formulation). According to the preliminary results, it is better to assimilate the specific humidity separately (univariate formulation) from all other control variables.

We got promising results when assimilating ATOVS data at 80 and 120 km resolutions.

Introduction

In 2001 a complex study was performed to compare the quality of locally pre-processed ATOVS radiances (level 1d) from CMS (Centre de la Météorologie Spatiale, Météo France) in Lannion with those from NOAA/NESDIS[1] (Randriamampianina and Rabier, 2001). According to the results of this study, the quality of the locally pre-processed ATOVS data is better than the quality of NESDIS data. Moreover, the positive impact of the locally pre-processed ATOVS data on the forecast of the ARPEGE model over Europe (Lannion reception area) was more significant than that of NESDIS.

These encouraging results were one of the reasons to choose the ATOVS data as potential observation to complete the observational database at the Hungarian Meteorological Service (HMS). In 2002 the implementation of the locally pre-processed ATOVS data was performed. Hence, a new concept of data pre-processing was worked out followed by the implementation of a bias correction program to estimate the systematic errors of the local ATOVS data. More information about the pre-processing and the implementation of ATOVS data into the ALADIN three-dimensional variational (3D-Var) data assimilation at the Hungarian Meteorological Service (HMS) is described in Randriamampianina (2003).

This report presents the first results of the study on the impact of ATOVS data on the analyses and forecasts of the ALADIN model. Section 2 gives a brief description of the characteristics of the ALADIN/HU model. Section 3 introduces the pre-processing of ATOVS data. A description of the performed experiments for the impact study is given in Section 4. Section 5 presents the results of the impact study, followed by some selected cases in Section 6. In Section 7 we draw some conclusions and discuss further tasks.

Main characteristics of the ALADIN/HU model and its assimilation system

The hydrostatic version of the ALADIN model was used in this study. The horizontal resolution of the ALADIN/HU is 6.5 km. ALADIN/HU has 37 vertical levels from surface up to 5 hPa. We use the 3D-Var technique as an assimilation system. An important advantage of the variational technique is that the cost function for the observation part is computed in the observation space. Consequently, for

[1] NOAA/NESDIS- National Oceanic and Atmospheric Administration/National Environmental Satellite Data and Information Service

assimilation of radiances, we have to be able to determine them from the model parameters. For this purpose we need a radiative transfer code. In ARPEGE/ALADIN we use the RTTOV code (Saunders et al., 1999), which uses 43 vertical levels. Above the top of the model, an extrapolation of the profile is performed using a regression algorithm (Rabier et al., 2001). Below the top of the model, profiles are interpolated to RTTOV pressure levels. Assimilation systems require good estimation of the background error covariance - the so-called "B" matrix. The B matrix was computed using the "standard NMC method" (Parrish and Derber, 1992). A 6 hour assimilation cycling was chosen, consequently the 3D-Var is running 4 times a day at 00, 06, 12 and 18 UTC. We perform a 48 hour forecast one time a day from 00 UTC.

Data pre-processing

We receive the ATOVS data through an HRPT antenna. The AMSU-A, level 1C, data are pre-processed by the AAPP (ATOVS and AVHRR Pre-processing Package) package.

Choice of Satellite

Because of its technical specification, our antenna is able to receive data from only two satellites at the same time. Data from NOAA-15 are available over the ALADIN/HU domain at about 06 and 18 UTC, while data from NOAA-16 are available around 00 and 12 UTC. The orbit of the NOAA-17 is between the orbits of the other two satellites a bit closer to that of NOAA-16. We know that NOAA-15 has problems not only with the AVHRR instruments but also with some microwave channels (AMSU-A-11 and AMSU-A-14). Nevertheless, NOAA-15 and NOAA-16 were chosen for the impact study to guarantee the maximum amount of observation at each assimilation time.

Extraction of ATOVS data

Satellite data observed and pre-processed in the interval of ±3 hours from the assimilation time are treated. The maximum number of the orbits found at one assimilation time varies up to 3 (see Fig. 1).

Bias correction

The systematic error of the satellite data can be shown by comparing the observed radiances with the computed (simulated) ones. The systematic error arises mainly from errors in the radiative transfer model, instrument calibration problems or biases in the model fields. The bias correction coefficients for data from NOAA15 and NOAA16 were computed for the study period according to Harris and Kelly (2001). Note, that the bias coefficients were computed for different latitude bands. Fig. 2 demonstrates the bias, computed for the same latitude band for NOAA-15 and NOAA-16.

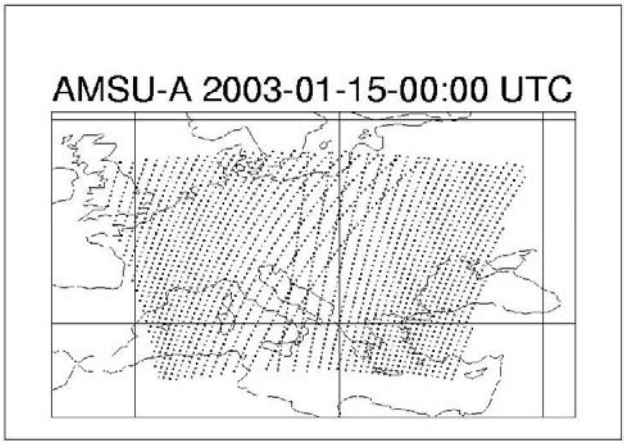

Figure 1: Satellite data over the ALADIN-HU domain (central + inner zone).

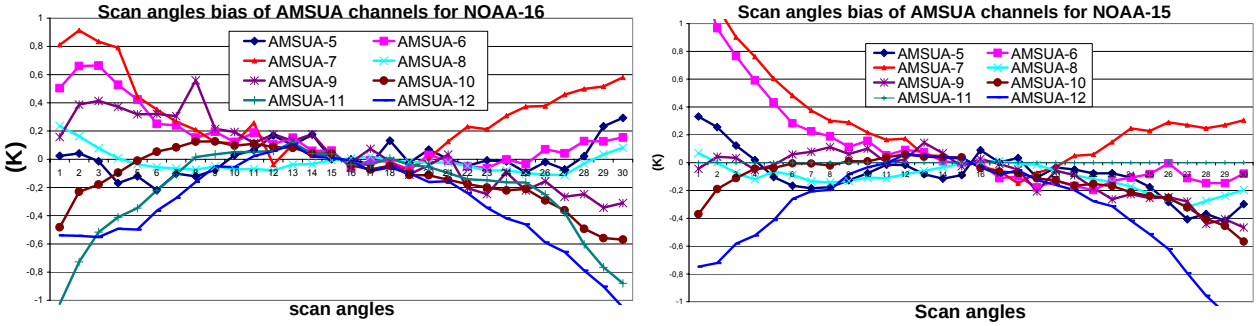

Figure 2: Bias (in degree Kelvin) specific to the scan angles varies with latitude band. Figures present cases, when the biases were computed for the same latitude band.

Channel selection

Analysing the bias of the brightness temperature, specific for each AMSU-A channel, inside all possible latitude bands, we decided to keep the same number of channels as they were used in the ARPEGE model (see Table 1.).

Table 1.:The use of AMSU-A channels

Channel number	1	2	3	4	5	6	7	8	9	10	11	12	13	14	15
Over Land					x	x	x	x	x	x	x	x			
Over Sea					x	x	x	x	x	x	x	x			
Over Sea ice							x	x	x	x	x	x			
Cloudy pixel								x	x	x	x	x			

Note, that over land channels 5 and 6 are used when the model orography is less than 500m and 1500m, respectively

Our study is interesting from the point of view of using AMSU-A data over land (see Table 1.), because the percentage of land over the ALADIN-HU domain is more than 70%.

Observation statistics and assimilation of radiances

It is necessary to check the efficiency of the statistics (observation error) used to handle the observation in case of new data and, in our case, "new model configuration" (more examples can be seen in Randriamampianina and Rabier, 2001). The observation (AMSU-A radiances) minus guess (computed radiances) were compared with the observation minus analysis for this purpose (see Fig. 3). These graphs show statistics computed from a few days (2003.02.20-2003.02.25) cycling. The distance between the two curves indicates how the addition of the AMSU-A data could modify the first-guess fields during the assimilation. The larger the distance, the bigger the impact of the observation (so, of the AMSU-A) on the analysis. These results are comparable to those computed in Randriamampianina and Rabier (2001). Thus, we decided to keep the original values of the theoretical standard deviation at this stage as it is used in ARPEGE.

Experiments design

In the experiments, two thinning techniques (80 and 120 km resolutions) were investigated. The impact of ATOVS data was studied for a two-week period (from 2003.03.20 to 2003.03.06). Surface (SYNOP) and radiosonde (TEMP) observations were used in the control run. The impact was evaluated comparing the control run with runs with TEMP, SYNOP and ATOVS data. Examining the first results, we found that the impact of ATOVS data on analysis and forecasts depended on the way the control variables (vorticity, divergence, temperature and surface pressure and the specific humidity) were handled. In particular, the assimilation of the specific humidity in univariate form or with all control variables using the multivariate formulation was focused on.

The following experiments were carried out:

T8000 - TEMP, SYNOP and AMSU-A data were assimilated. The AMSU-A data were thinned at 80km resolution. The multivariate formulation was used for all control variables.

T1200 - TEMP, SYNOP and AMSU-A data were assimilated. The AMSU-A data were thinned at 120km resolution. The multivariate formulation was used for all control variables.

Aladt - TEMP and SYNOP were assimilated - control run. It is our 3D-Var cycling running in parallel suite. The multivariate formulation was used for all control variables.

Touhu - TEMP, SYNOP and AMSU-A data were assimilated. The AMSU-A data were thinned at 80km resolution. The specific humidity was assimilated as a univariate control variable, while the other control variables were assimilated using multivariate formulation.

12uhu - TEMP, SYNOP and AMSU-A data were assimilated. The AMSU-A data were thinned at 120km resolution. The specific humidity was assimilated as a univariate control variable, while the other control variables were assimilated using multivariate formulation.

Aluhu - TEMP and SYNOP were assimilated - the control run. The specific humidity was assimilated as a univariate control variable, while the other control variables were assimilated using multivariate formulation.

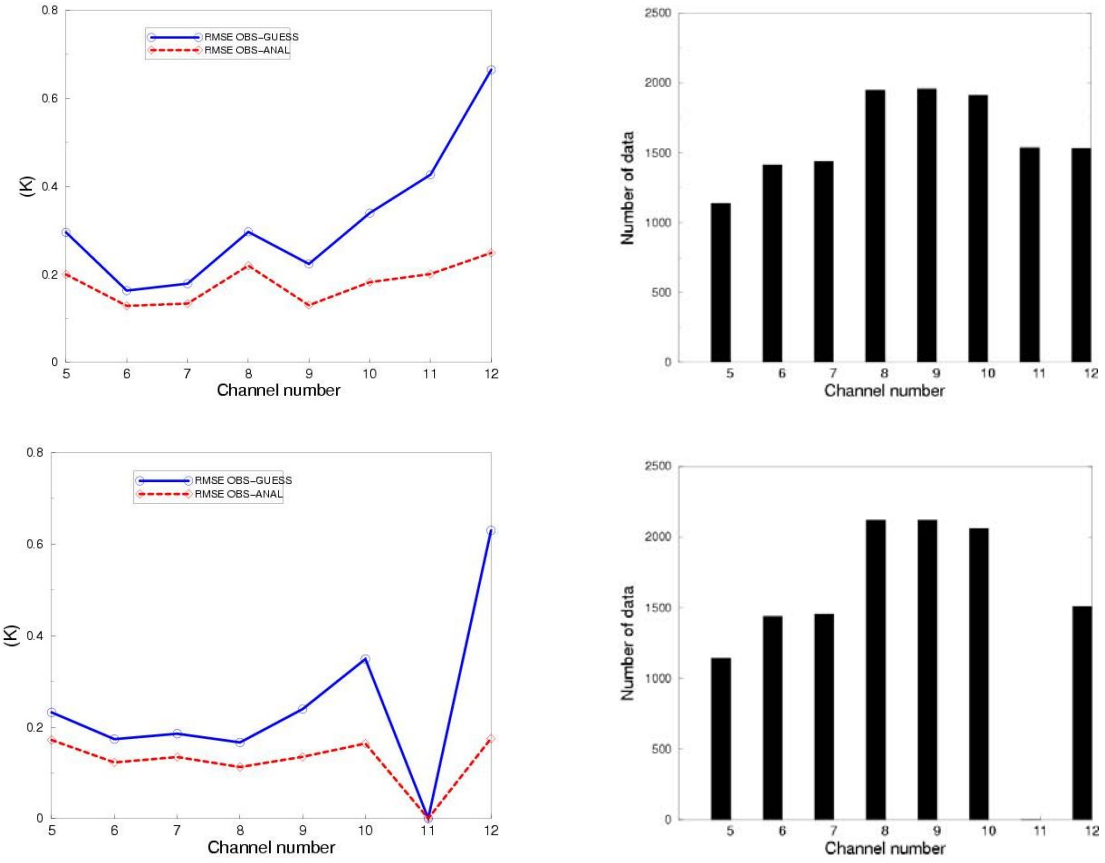

Figure 3: Example of statistics of observation minus guess (solid line) and observation minus analysis (dashed line) for AMSU-A at 00 UTC (upper graphs) and 06 UTC (lower graphs) for a five-day cycling (from 2003.02.20 to 2003.0225) (left hand side). On the right one can find the number of data used in the computation of the statistics.

Objective verification

The bias and the root mean square error (RMSE) were computed from the differences between the analysis/forecasts and the observations (SYNOP and TEMP) and also with the long cut-off analyses of the global model ARPEGE.

Most important results

Using multivariate formulation

- We found that AMSU-A data have positive impact on the analyses and forecasts of geopotential height when assimilating them in both 80 and 120 km resolutions. Especially, on lower levels (i.e. below 700 hPa), the impact was positive for all forecast ranges. Positive impact on the short-range (until 12 hour) forecast was observed for all model levels (see Fig. 7)
- A neutral impact on the analysis and forecasts of wind speed was observed.
- A neutral impact of AMSU-A data on the temperature profile was found.
- Regarding the relative humidity fields, clear negative impact was observed.

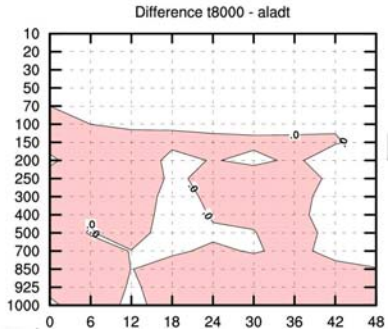

Figure 7: Difference between the root mean square errors for geopotential height: $RMSE_{T8000} - RMSE_{aladt}$. Negative value (coloured) means that the error of run with ATOVS data is less than that of control run, thus the ATOVS data have positive impact. X and Y axes present the forecast ranges (in hour) and the model levels respectively (in hPa)

The "stability" of the negative impact of AMSU-A data on relative humidity fields showed that the source might have come from the way the humidity data had been assimilated. We decided to separate the specific humidity from the multivariate formulation and assimilate it alone (univariate form).

Assimilating the humidity in univariate form

- The impact of AMSU-A data on forecast of geopotential height was somewhat less, but positive compared to the run with multivariate formulation.
- Positive impact on the temperature above 700 hPa was observed from the 24 hour forecast range (see Fig. 8)
- Concerning the impact on relative humidity, improvement could be observed (Fig. 9). It is important to mention that we found big improvement at all model levels when assimilating the humidity data in univariate form, especially for levels around the tropopause (Fig. 10). It can be also observed on the run without ATOVS data (Fig. 10).
- A neutral impact was found for the wind speed.

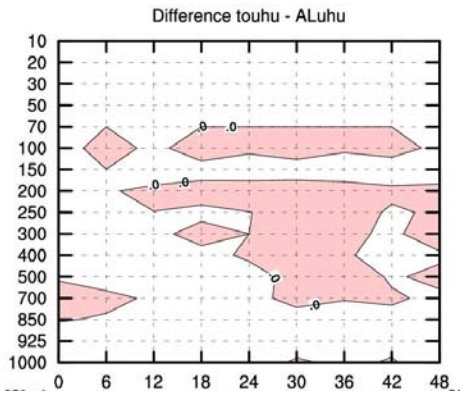

Figure 8: Difference between the root mean square errors of temperature in case of assimilating the humidity data in univariate form: $RMSE_{touhu} - RMSE_{aluhu}$. Negative value (coloured) means that the error of run with ATOVS data is less than that of control run, thus the ATOVS data have positive impact. X and Y axes present the forecast range (in hour) and the model levels respectively (in hPa).

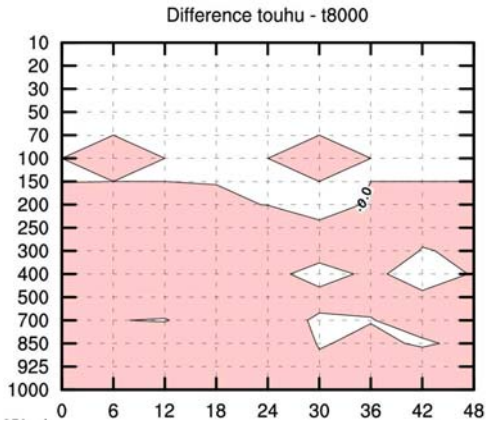

Figure 9: Difference between the root mean square errors of relative humidity: $RMSE_{touhu} - RMSE_{T8000}$. Negative value (coloured) means that the error is reduced when assimilating the specific humidity in univarite form.

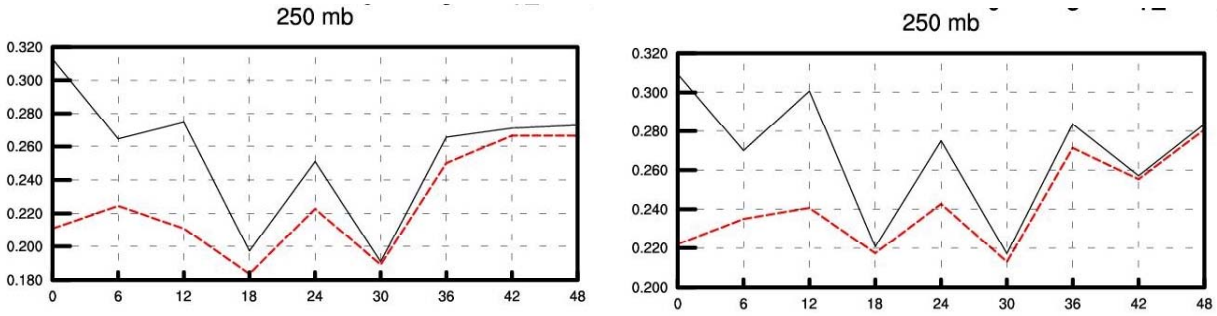

Figure 10: Root mean square forecast errors of relative humidity (in percent) at 250 hPa level against radiosonde observation. Comparison of two 3D-Var runs with ATOVS data assimilated in 80 km resolution (left hand side graph) and runs with TEMP and SYNOP data (right hand side graph). Solid line: when the multivariate formulation was used for all control variables. Dashed line refers to case, when the specific humidity was assimilated in univariate form. X axis presents the forecast ranges in hour.

Influence of resolution

We performed comparisons to evaluate the influence of resolution of ATOVS data on the analysis and forecast. In general, the positive impact of ATOVS data on geopotential and temperature was stronger in case of finer (80 km) resolution of ATOVS data. The 120 km resolution gave "better" impact on relative humidity, wind speed and wind direction when using multivariate formulation. Assimilating the humidity data in univariate form, the finer resolution gave "better" impact on relative humidity (see Fig. 11).

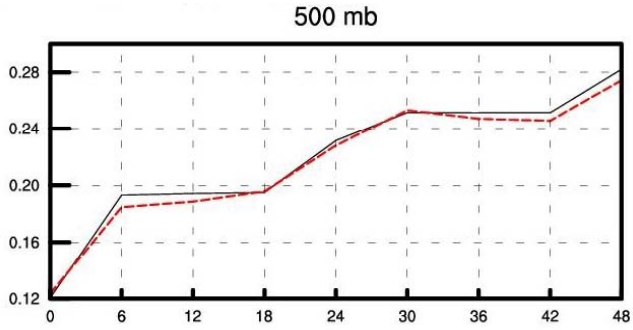

Figure 11: Root mean square forecast errors of relative humidity (in percent) at 500 hPa level against radiosonde observation. Comparison of two 3D-Var runs with ATOVS data when the humidity was assimilated in univariate form. Dashed line: thinning in 80 km (touhu). Solid line: thinning in 120 km (120uhu). X axis presents the forecast ranges in hour.

We concluded, that the positive impact was somewhat stronger in general when ATOVS data were assimilated at finer resolution, especially when the specific humidity was assimilated in univariate form.

Selected cases

As it was shown above, the impact of ATOVS data on the forecast on different parameters was slightly positive or neutral in general. In the following, we chose certain cases within the study period to compare the runs with and without ATOVS data with a special attention on forecast of precipitation.

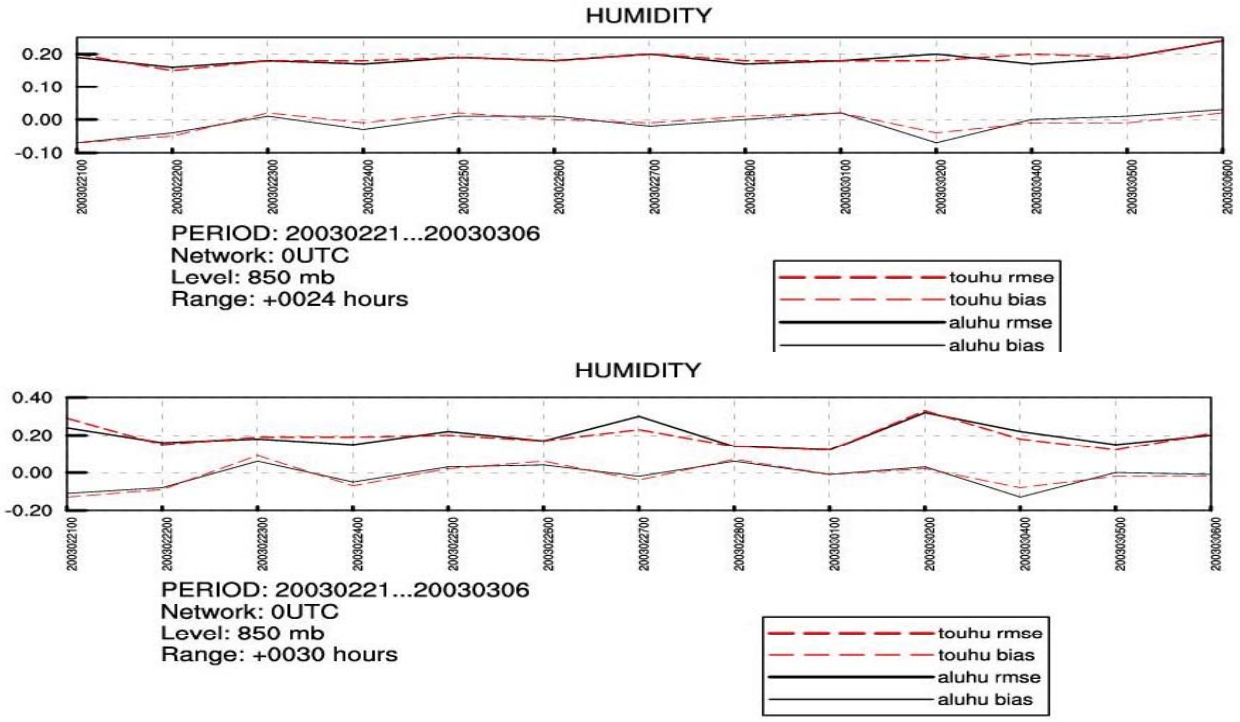

Figure 12: Day-to-day root mean square forecast errors (in percent) (upper curves) and biases (lower curves) of relative humidity at 850 hPa model level. Comparison of 3D-Var run with ATOVS data assimilated in 80 km (touhu, dashed line) with the control one (with TEMP and SYNOP only) (aluhu, solid line) for 24 (upper graphic) and 30 (lower graphic) hour forecast ranges.

Exploring the reasons of negative impact on the forecast of humidity it was ascertained that in some cases no ATOVS data was available at all (e.g. 24 February, see Fig. 12), or the negative impact was characteristic for territories, located rather far from the satellite pass (e.g. 28 February). It indicates that the negative impact may refer to the absence of ATOVS data, so that the ATOVS data did not have the possibility to correct the "bad quality" first-guess fields.

We examined what differences we receive in the spatial distribution of cumulative precipitation depending on the use (here we mean inclusion or exclusion) of ATOVS data in 3D-Var runs. The results of this study are given in Figures 13-15.
Figure 13 shows that from synoptical point of view there is no big difference between the maps, created from results of the runs without (left) and with (right) ATOVS data. The objective verification, however, showed positive impact on 24-hour and neutral impact on 30-hour forecasts (Fig. 12) of ATOVS data on the humidity on this particular day (2 March). Figures 14 illustrates differences in cumulative precipitation between the runs without (left) and with (right) ATOVS data at the Eastern coast of Poland and Western part of Byelorussia. According to the real situation, presented in Figure

15, there was some precipitation over the mentioned area. One can see that the run with ATOVS data could slightly better describe this situation (4 March).

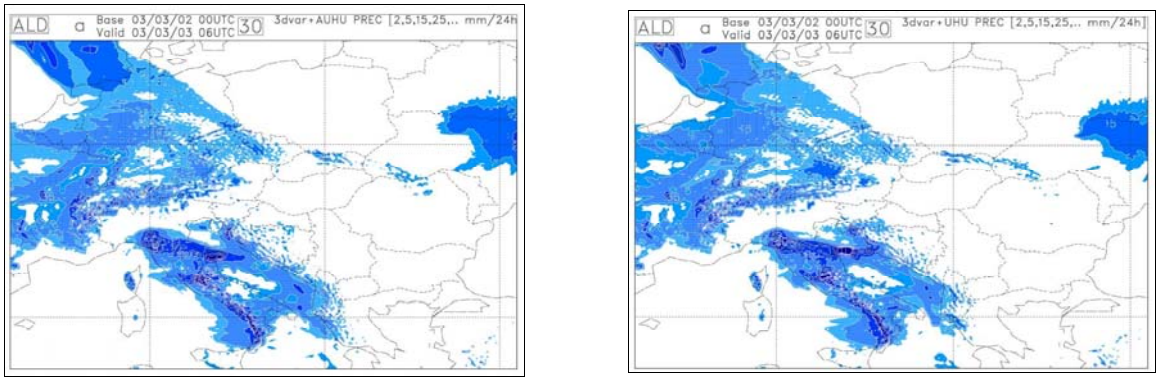

Figure 13: The 24 hour cumulative precipitation (in mm) predicted over the ALADIN/HU domain from 2003.03.02 00 UTC. On the left: control run (with TEMP and SYNOP). On the right: 3D-Var run with ATOVS assimilated in 80 km resolution. In both runs the humidity was assimilated in univariate form. Note that the 24-hour cumulated precipitation is the difference between the cumulative precipitation predicted at 6 and 30 hour forecast ranges.

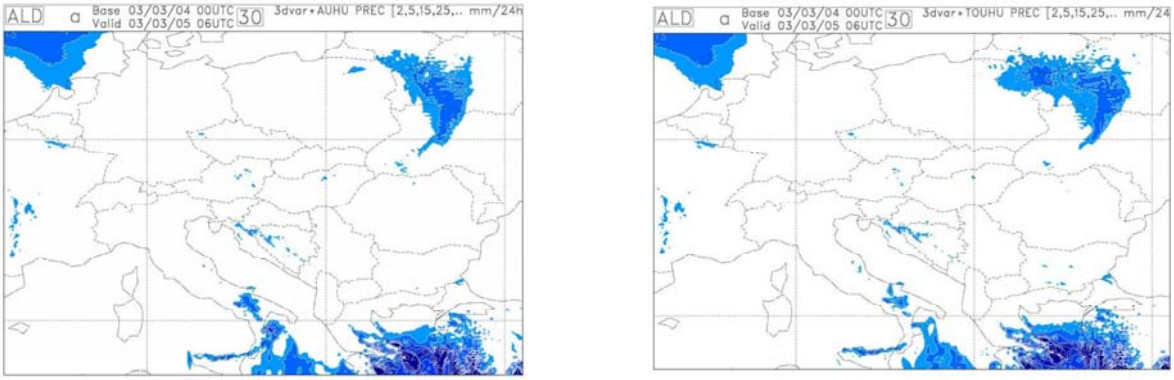

Figure 14: The 24 hour cumulative precipitation (in mm) predicted over the ALADIN/HU domain from 2003.03.04 00 UTC. Upper picture: control run (with TEMP and SYNOP). Lower picture: 3D-Var run with ATOVS assimilated in 80 km resolution. In both runs the humidity was assimilated in univariate form. Note that the 24-hour cumulated precipitation is the difference between the cumulated precipitation predicted at 6 and 30 hour forecast ranges.

We examined also a situation when ATOVS data were available over a very small part of the ALADIN/HU domain (case of Feb. 28). Analysing the 24-hour cumulative precipitation, we found that the run with ATOVS data gave poorer results than the run without ATOVS data for cases, when the rainy territories were located far away from the satellite pass. Moreover (see the 24 h. forecast on Feb. 28 as an example), the impact of ATOVS data was slightly negative.
Detailed analyses of the above mentioned cases provide important additional information for the impact study compared to statistical evaluation. Thus, the indexes of the objective verification sometimes might not be enough for thorough assessment of the impact of satellite data on analysis and forecast.

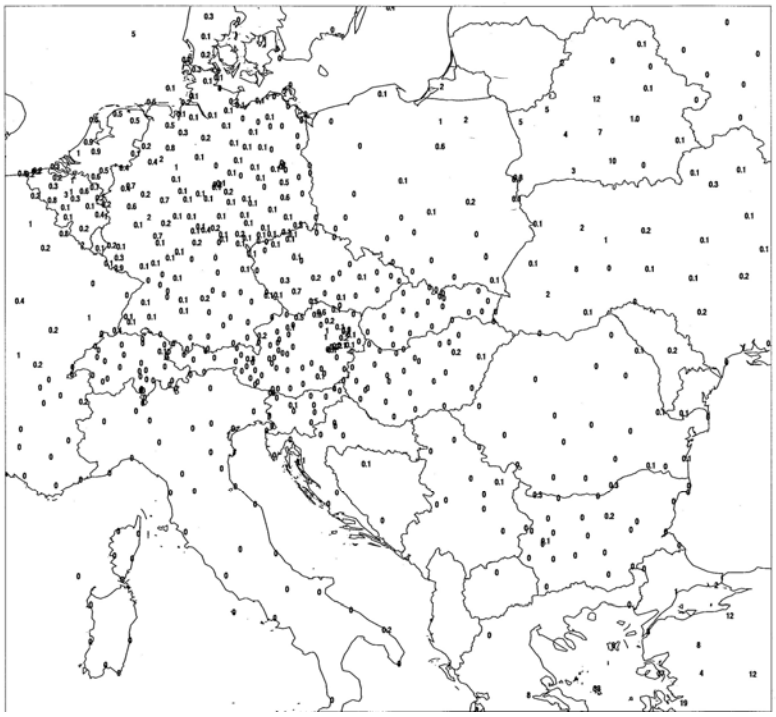

Figure 15: The 24 hour cumulative precipitation (in mm) extracted from SYNOP telegrams for 2003.03.05 06 UTC (upper picture) and the distribution of the ATOVS pixels at 2003.03.04 00 UTC (situation after screening - active observation) (lower picture).

Comparison with the French global model (ARPEGE) long cut-off analyses

We compared the forecasts from runs with and without ATOVS data with the ARPEGE long cut-off analyses at 4 forecast ranges (12, 24, 36 and 48 hours). The objective of this comparison is to have the horizontal distribution of the impact over the ALADIN/HU domain.

Figure 16 indicates that positive impact is dominating all over the ALADIN/HU domain. However, when comparing the average statistics for the 2 cases (Fig. 17), the impact might be slightly positive (36 hour forecast, 500 hPa) or slightly negative (12 hour forecast, 500 hPa) (Fig 17). We found similar results when comparing statistics for other variables.

Summary, further suggestions and experiments

- The assimilation of the ATOVS data into the limited area model ALADIN/HU gave neutral impact in general (the positive and negative impacts were slight) but the positive impact is dominating all over the domain.
- Because of the problems related to the humidity, it is recommended to assimilate the humidity data in univariate form. We changed the assimilation of the humidity from multivariate to univariate in the version of 3d-Var, running actually in parallel suite in Budapest.
- The impact of the ATOVS data on the forecast of temperature was slightly negative in the lower levels. To avoid this, we decided to investigate the use of channels sensitive to the lower atmospheric layers (channels 5, 6 and 7) before performing any further experiments.
- The impact of ATOVS data with finer (80 km) resolution was somewhat "better", than that of 120 km resolution data. It is recommended to perform the further assimilation of ATOVS data in finer resolution.
- Further experiments should be done to clarify what kind of expectations we can have with respect to assimilation of ATOVS data.
- Similar results were obtained when performing the impact study on other 2-week period. It is recommended to perform further experiments to study the changes in the impact of ATOVS data on the forecast in extreme weather conditions.

To sum up, we can state that at the present stage no definite positive impact of ATOVS data on the forecast can be proved in the 3D-Var data assimilation system of the ALADIN model, so it is necessary to continue the experiments.

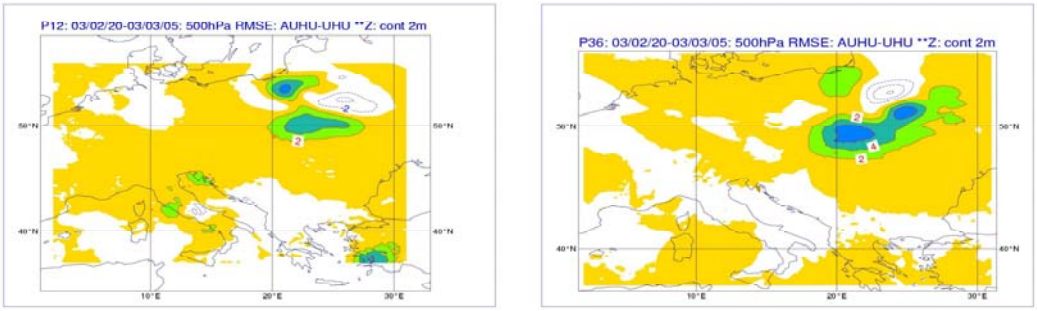

Figure 16: Difference between the root mean square forecast errors ($RMSE_{aluhu} - RMSE_{touhu}$) on geopotential field when comparing the forecasts with the ARPEGE long cut-off analyses. One can see the 12 hour (left-hand side) and 36 hour (right hand-side) forecasts. Coloured areas (positive values) indicate, that run without AMSU-A has bigger error, so the impact of AMSU-A is positive.

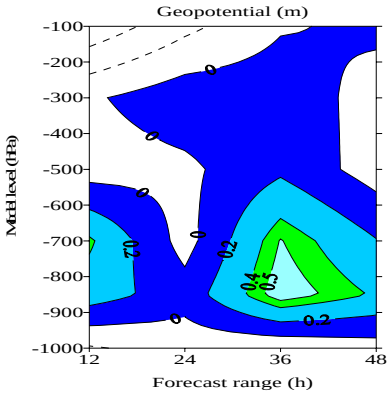

Figure 17: Difference between the root mean square forecast errors ($RMSE_{aluhu} - RMSE_{touhu}$) of geopotential field when comparing the forecasts with the ARPEGE long cut-off analyses. In coloured areas we have positive impact of the AMSU-A data on forecasts

Acknowledgement

We thank Élisabeth Gérard, Philippe Caille, Jean-Marc Audouin for their help in the local implementation and the Hungarian colleagues for the fruitful discussions. The support of Hungarian National Scientific Foundation (**OTKA T031865** and **T032466**) is highly acknowledged.

References

Harris, B. A. and Kelly, G., 2001: A satellite radiance-bias correction scheme for data assimilation, *Q.J.R. Meteorol. Soc*., **127**, 1453-1468

F. Rabier, É. Gérard, Z. Sahlaoui, M. Dahoui, R. Randriamampianina, 2001: Use of ATOVS and SSMI observations at Météo-France. 11th Conference on Satellite Meteorology and Oceanography, Madison, WI, 15-18 October 2001 (preprints). Boston, MA, *American Meteorological Society*, pp367-370.

Roger Randriamampianina and Florence Rabier, 2001: Use of locally received ATOVS radiances in regional NWP. *NWP SAF report, available at HMS and at Météo-France*.

Roger Randriamampianina, 2003: Investigation of the use of local ATOVS data in Budapest, *ALADIN newsletter*, ***23***, *available also on:* http://www.cnrm.meteo.fr/aladin/newsletters/newsletters.html.

Parrish, D. F. and J. C. Derber, 1992: The National Meteorological Centre's spectral statistical interpolation analysis system. *Mon. Wea. Rev.*, **120**, 1747-1763

Saunders, R, M. Matricardi and P. Brunel, 1999: An improved fast radiative transfer model for assimilation of satellite radiance observations. *Q.J.R. meteorol. Soc.*, **125**, 1407-1425

Preparations for NOAA-N

Thomas J. Kleespies
NOAA / NESDIS / ORA
Camp Springs, MD USA

Introduction

NOAA-N is a continuation of the KLM series. However, there are significant differences in instrumentation and processing techniques that affect the users of the data. This paper will describe many of these changes. No discussion will be made here of level two processing, which is well described in Reale (2004).

Spacecraft

NOAA-K/L/M were all launched using Titan-IIs. NOAA-N will use a Delta-2 launch vehicle. This will permit a more precise orbital insertion and eliminate the need for an apogee kick motor. NOAA-N is expected to remain within one hour of the nominal equator crossing for up to eight years. The hydrazine propulsion system has been replaced by a gaseous nitrogen system. This simplifies spacecraft preparation and safety concerns on the launch pad. There are three solid state recorders on NOAA-N, whereas NOAA-M had one, and earlier satellites had none. The projected launch date at the time of this writing is September 15, 2004.

Instruments

There is no change to the AVHRR-3, SBUV-2 or the AMSU-A instruments. The infrared sounder is now a HIRS-4. The field of view has decreased to 10 km from 19 km for the HIRS-3. There is another Platinum Resistance Thermometer (PRT) in the black body. This is directly in the center and will give a better characterization of the temperature gradient as well as providing a better estimate of the black body temperature within the smaller angular field of view. There is also a new temperature sensor near the field stop.

The Microwave Humidity Sounder (MHS) is a new instrument, although it has considerable heritage with the AMSU-B. There are two frequency changes: the AMSU-B 150 and 183.31+-7 GHz channels are now 157 and 190.31 GHz on the MHS. Two of the channels now have horizontal polarization. The internal design is much different. There is greater redundancy in the MHS than in the AMSU-B. For example, the processor and interface electronics are completely redundant, including redundant PRTs.

Processing Changes

The AVHRR visible instrument counts to albedo transformation is now well documented and will be published soon. The non-linear term for the infrared has been increased in precision from six to seven digits. There is a scaling factor change that users must be aware of. There is no provision to account for lunar intrusion in the space look at this time, but this will be re-visited after launch.

There is no change to the HIRS-4 processing due to the change in field of view size. As noted above, there are now five PRTs which are averaged to produce the blackbody temperature. The PRT temperature conversion is now a 5^{th} order polynomial. While the effect of this change is small, it is more accurate. A new algorithm has been proposed to address the problem with the 24 hour average of calibration slope (Cao and Ciren, 2004). When this algorithm is implemented, a new lunar intrusion algorithm will also be implemented. The lunar intrusion detection is based upon Kigawa and Mo (2002). When lunar intrusion is detected, the intercept is computed from the blackbody, and the contaminated slope is removed from the running average of three calibration sequences.

The AMSU-A lunar intrusion is described in Kigawa and Mo (2002). This method calculates a bulk temperature of the moon. Offline testing works very well, with an accuracy of about 0.06K.

The MHS lunar intrusion algorithm is simpler since there are four independent space looks, and the FOV is smaller than that of the AMSU-A. The objective here is simply to find the one or two coldest spacelooks during a lunar intrusion event. The PRT temperature is computed differently from the AMSU-B in that the PRT and three precision resistors, or calibration channels are used.

Level 1B Format Changes

It is planned that all level 1B header records number one will have an identical preamble, which will comprise approximately the first one-hundred bytes. The HIRS header record will have some bytes offset to accommodate this preamble. The level 1B multiple header record option may be implemented on all instruments. The additional header records will contain ancillary dataset names and any metadata needed for reprocessing. With the exception of the MHS, all data record changes are supposed to be transparent to the user who does not need to make use of enhanced features such as lunar intrusion correction. It is intended that all of these changes will be made to all of the KLM level 1B data streams prior to the NOAA-N launch. The new 1B formats are available from ftp://metroweb.nesdis.noaa.gov/pub/noaa-n.
At this site there is a directory for each instrument, which contains the 1B format, the 1B format differences from NOAA-KLM, and sample NOAA-N level 1B data simulated from NOAA-16.

Documentation

The NOAA-KLM User's Guide will be amended to reflect NOAA-N specifics (http://www2.ncdc.noaa.gov/docs/klm/). A separate NOAA-N supplement page will have links to pertinent sections of the revised NOAA-KLM User's Guide. Ms. Kathy Kidwell will remain the editor of the User's Guide for the next few years.

Processing Environment

The primary processor for the 1B data will change from an Amdahl mainframe to an IBM-AIX-RS6000. Thus the native text will change from EBCDIC to ASCII, and the native MVS real numbers will change to IEEE floating point. The result is that the 1B scaled integers will be fed by a higher base precision floating point.

Direct Readout

There are some changes to the HRPT format, which will be reflected in the NOAA-KLM User's Guide. The point of contact for direct readout is now Darrell Robertson, Darrell.Robertson@noaa.gov.

Acknowledgements

The Author wishes to acknowledge the contributions to this paper of Changyong Cao, Kathy Kidwell, Tsan Mo, Dave Morel, Jerry Sullivan, Mike Weinreb and Fred Wu.

References

Cao, C. and P. Ciren, 2004. Operational High Resolution Infrared Radiation Sounder Calibration Algorithms and Their Effects on Calibration Accuracy, Proc 13th Int. TOVS Study Conf., 29 Oct- 4 Nov 2003, St. Adele, Quebec, Canada.

Kigawa, S. and T. Mo, 2002. An Algorithm for Correction of Lunar Contamination in AMSU-A Data. NOAA Tech. Rep. NESDIS 111.

Reale, A., 2004. NESDIS ATOVS Operational Sounding Products, Proc 13th Int. TOVS Study Conf., 29 Oct- 4 Nov 2003, St. Adele, Quebec, Canada.

Operational High Resolution Infrared Radiation Sounder (HIRS) Calibration Algorithms and Their Effects on Calibration Accuracy

Changyong Cao
NOAA/NESDIS/ORA, Camp Springs, Maryland, USA
and
Pubu Ciren
QSS Group Inc., Lanham, Maryland, USA

Introduction

The High Resolution Infrared Radiation Sounder (HIRS) is an operational atmospheric sounding instrument that has been carried on NOAA polar orbiting satellite series for more than two decades. It is a traditional cross-track line scanning radiometer that measures scene radiance in the infrared and visible spectrum. Among the twenty spectral channels, there are twelve long-wave channels (669 to 1529 cm^{-1}), seven shortwave channels (2188 to 2657 cm^{-1}), and one visible channel (0.69 μm), all of which use a single telescope with a rotating filter wheel consisting of twenty individual spectral filters. An elliptical scan mirror is stepped 56 times in increments of 1.8 degrees to provide cross-track scanning. The field of view for HIRS (HIRS/3 series) on NOAA-15,-16, and -17 is 1.4 degrees in the long-wave and 1.3 degrees for the shortwave channels. From an altitude of ~833 km, the HIRS footprint on the ground at nadir is 20.3 km in the shortwave and visible channels, and 18.9 km in the long-wave channels (ITT, 1998). Data from the HIRS instruments are used, in conjunction with other instruments, to estimate the atmosphere's vertical temperature profile, outgoing long-wave radiation (OLR), and upper tropospheric humidity. The data are also used to determine sea surface temperatures, total atmospheric ozone levels, precipitable water, cloud height and coverage, and surface radiance.

Calibration of the HIRS infrared channels consists of independent views of the onboard warm blackbody and cold space. This provides a two-point calibration in which the calibration intercept and slope for each channel can be computed and used to convert instrument output counts to radiance. However, there are several complications in the operational HIRS calibration which affect the calibration accuracy. HIRS calibrates only once every 40 scan-lines, or one calibration cycle in every 256 seconds. As a result, the calibration coefficients between the calibration cycles have to be interpolated to the individual scan-lines. In the more than 20 year history of operational HIRS calibration, several interpolation methods have been used and unfortunately, depending on which method is used, these algorithms can produce HIRS level 1b radiance data with significant differences in scene brightness temperature. Operational HIRS instrument calibration has significant impact on products at all levels. Although the effect on weather applications is relatively small, it is important for long term climate studies where high calibration accuracy is required. In this study, the operational HIRS calibration algorithms are evaluated, and sample test data sets are analyzed to

quantify the effects. A new algorithm is proposed to reduce the calibration biases caused by the previous calibration algorithms.

The Calibration Algorithm for NOAA-KLM/HIRS

Prior to NOAA-15/HIRS, a simple calibration algorithm was used for HIRS/2 series of the instrument. This algorithm (Kidwell, 1998) used the fixed calibration coefficients calculated from the last calibration scans on the first half scans of a super-swath and those calculated from the following calibration scans on the second half of the super-swath. This was a relatively robust algorithm for handling the peculiar calibration cycles of HIRS. Unfortunately, this algorithm may cause a jump in the values of the brightness temperatures (Kidwell, 1998), especially when the calibration coefficients changed from one calibration cycle to the next.

With the launch of NOAA-15 in 1998, a new calibration algorithm (for clarity, it is referred to as HIRS operational calibration algorithm version 3.0) was developed for NOAA-KLM/HIRS and has been used in the operations (Goodrum, et al., 2000). In this algorithm, it is assumed that the HIRS instrument gain never changes appreciably within any 24 hour period. Therefore, it was believed that a 24 hour average slope (inverse of gain) can be used to calibrate all the data during the period. This simplified the calibration, especially if the slopes at an individual calibration cycle became unreliable, such as in the event of moon contamination in the space view. In addition, it was believed that the secondary mirror baffle temperature contributes to the background radiation and thus affects the intercepts for the earth view scan-lines between two calibration cycles. Therefore, it was decided that a correlation between the secondary mirror temperature and the intercept should be computed once every 24 hours and used to correct the intercepts. As a result, the intercepts were determined using the following equation:

$$I'_{(n)} = I'_{l(n)} + I'_{T(n)} \tag{1}$$

Where:

$$I'_{l(n)} = \left(I'_{(k-1)} + n \cdot \frac{I'_{(k)} - I'_{(k-1)}}{40} \right) \tag{2}$$

$$I'_{T(n)} = b_1 \cdot \left((T_{(n)} - T_{(k-1)}) + n \cdot \frac{T_{(k)} - T_{(k-1)}}{40} \right) \tag{3}$$

$I'_{(n)}$ is the intercept for Earth view scan-line n (n=1 to 38), $I'_{l(n)}$ is the linear interpolation of the intercept between the two closest calibration cycles, $I'_{T(n)}$ is the correction to the intercept based on the telescope temperature, $I'_{(k)}$ is the intercept at the calibration cycle k, n is the scan-line number within

the calibration cycle (n=1 to 38), $T_{(k)}$ is the secondary mirror temperature at the calibration cycle k, and $T_{(n)}$ is the secondary mirror temperature at scan-line n.

There are several problems with algorithm 3.0 which can cause calibration errors in the operational calibration of HIRS data. The assumption of a stable instrument gain may not be valid. It is true that during normal operations, the instrument gain of HIRS can be stable during a 24 hour period, because the instrument gain is mainly affected by the background flux reaching the detector from the filter wheel, which is normally stable (ITT, 1996). However, the instrument gain will change in response to the filter wheel temperature change. A typical scenario that happened to NOAA-15/HIRS shows this process:

The HIRS filter wheel normally has a temperature of ~285K which is not controlled. The filter wheel temperature is not measured directly but is inferred from the filter wheel housing temperature, which has an operating temperature range of 273.15K to 333.15K. Although in normal operations, this temperature only varies about ~0.1K per orbit, the temperature can increase due to friction in the filter wheel bearing, which also causes increased jitter and higher than normal filter motor current. This may cause the filter wheel to become out of sync. To alleviate this problem, the filter housing heater is turned on to draw lubricants into the bearing, but unfortunately, it also further increases the filter temperature (by as much as 8 degrees). This temperature increase significantly changes the background flux reaching the detector. Since the HgCdTe detector has a nonlinear response, the increase in the radiation reaching the detector causes the operating response range to shift to a different portion on the non-linear response curve, which has a different gain. When this occurs, the 24 hour average slope, which could be 24 hours old, is outdated. The opposite occurs when the filter temperature drops from the high temperature to a normal temperature. As a result, using this 24 hour average slope causes calibration biases (Cao and Hui, 2003; Brunnel 2002). Since the radiance is for the most part a linear function of the slope, a 1 percent error in the slope translates to 1 percent in radiance, or for the long-wave channels, 1 percent radiance error may cause as much as 1 K error in the observations. In reality, errors on the order of 2-3% have been observed in some channels of HIRS on NOAA-15 during such events.

Although the filter temperature is relatively stable on an orbit by orbit basis, there is no guarantee that it will not fluctuate for any of the HIRS instruments. For example, since 2002, the NOAA-15 HIRS filter temperature fluctuates on the order of a few degrees several times a month. At the time of this writing, NOAA-15 HIRS had just recovered from the typical filter jitter problem that lasted a few days, during which the radiance data could not be used in product generation due to significant calibration biases.

In addition to the problem in the slopes, the method for computing the intercepts deserves further analysis because it affects every scan-line of the data at all times. In equation (2), the linear interpolation of intercepts between calibration cycles ($I'_{l(n)}$) is accurate if the change in the intercepts between these two cycles is linear. However, as it was pointed out by algorithm 3.0, the background

flux may be affected by the telescope temperature change within a calibration cycle (or 256 seconds). It should be noted that the telescope temperature contributes to the background flux as a whole. Although the secondary mirror temperature has the largest fluctuation, its effect alone may not be accurately determined without a thorough thermal analysis of the system. On the other hand, at the front of the telescope, the only temperature sensor available is located near the secondary mirror. Therefore, the secondary mirror temperature is used to represent the thermal environment of the front of the telescope and its relationship to the intercept is rather empirical. Ideally, the correlation between the intercept and the telescope temperature should be determined in a thermal model. Therefore, it is possible that in the future, b_1 in equation (3) will be a variable determined based on various parameters, including instrument component temperatures.

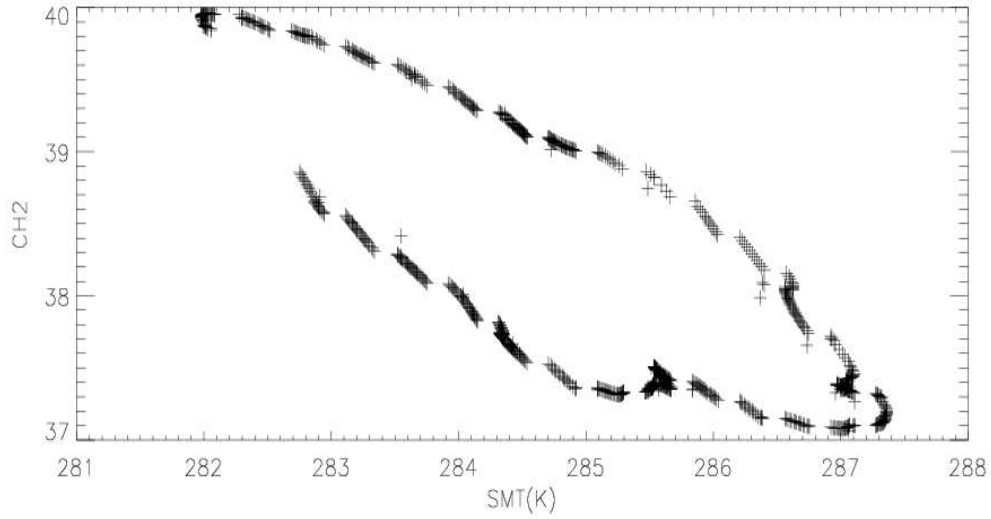

Figure 1. Correlation between secondary mirror temperature (SMT) and channel 2 intercept for one sample orbit

Figure 1 shows the typical correlation between the intercept and secondary mirror temperature for one orbit of NOAA-17 data. It is clear that this correlation is not linear but elliptic in shape. There is a different correlation between day and night time of the orbit, and there is a transition period in the polar regions. Therefore, the linear correlation assumption is not exactly valid, although on the first order, there is a general correlation that is somewhat linear. Another criticism of this analysis is the fact that in computing the intercept it applies a correlation derived from global data to a local problem of secondary mirror temperature fluctuations. The global correlation between the intercept and the secondary mirror temperature is determined by a number of factors at various instrument component temperatures, which is not the case within a superswath, where only the secondary mirror temperature fluctuated. Finally, it is arguable whether the secondary mirror temperature is reliable enough as an indicator of background flux. This is because the secondary mirror assembly has a small thermal inertia and its temperature fluctuates easily. The largest fluctuation occurs in the polar

region, where the sun can directly illuminate the back of the secondary mirror. However, not all of the fluctuations may contribute to the change in the intercept. Because of the problems in the slopes and intercepts described above, a new calibration algorithm (algorithm version 4.0) is developed and described in the next section.

HIRS Calibration Algorithm Version 4.0

The main purpose of the HIRS calibration algorithm version 4.0 was to correct the problem in the calibration slopes in the previous algorithm. In computing the intercepts, a switch is added to make the correction using the telescope temperature optional. Also, the linearly interpolated intercepts is stored in the secondary calibration coefficients field in the level 1b data for comparison purposes. Radiances produced by algorithm 4 and 3 have been compared using NOAA-15, -16, and –17 HIRS data (Cao and Hui, 2003). Additional radiance comparisons with AIRS/AQUA have also been performed (Ciren and Cao, 2003). Algorithm 4.0 is expected to become the operational HIRS calibration algorithm for NOAA-N (Kleespies, 2003). The detailed description of this algorithm is as follows:

The slopes and intercepts at the blackbody scan-lines

For HIRS, the 48 space view samples followed by 56 blackbody view samples establish a calibration cycle, which occurs every 40 scan-lines or 256 seconds. At each calibration cycle, the slopes and intercepts at the blackbody scan-lines or "BB slopes and intercepts" (also referred to as "raw" slopes and intercepts) are computed for the 19 infrared channels and stored with the blackbody view data in the HIRS level 1b file (same as in the previous algorithm). However, due to the increased significance of the individual BB slopes and intercepts in algorithm version 4.0, the following changes must be made.

When screening the space and BB view samples, those that are out of the gross limits for the signed 12 bit counts should be removed, and then the standard deviation of counts computed. If the standard deviation is within the noise level (NEDC = abs{NEDN/slope}, NEDN is the instrument noise specification), all samples passed the screening. Samples deviated from the mean by more than 3 sigma should be removed and the mean recomputed for the next step. On the other hand, if the standard deviation of counts is greater than the noise specification, it must be flagged in the level 1b data. Then use the median value of the samples for further processing.

This method is used for the last 48 samples of both the space and blackbody view in a calibration cycle. As a result, as long as the PRT data are valid, the calibration slopes are always computed unless all counts are out of the gross limits. The quality of the slopes is then evaluated (discussed later).

The method for computing the BB slopes and intercepts at the calibration cycles remains the same as that for algorithm 3.0, with the exception that consideration should be given in software

design to a possible non-linearity correction algorithm in the future. Currently spaces are reserved for the quadratic term in the level 1b data, although it has never been implemented due to uncertainties in the prelaunch non-linearity test results.

Calibration for a normal super-swath

a) Slope

A super-swath is defined as 40 scan-lines of HIRS data that start with a calibration cycle, followed by 38 Earth view scan-lines (figure 2). For a normal super-swath in the middle of an orbit, the calibration slopes for the 38 Earth view scan-lines of the current super-swath is the running average of three values: the BB slopes of calcycle(k), calcycle(k-1), and calcycle(k-2), i.e.,

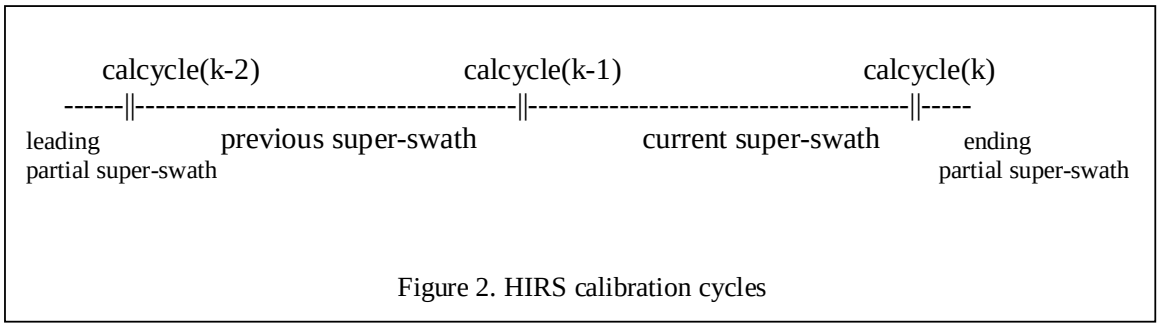

Figure 2. HIRS calibration cycles

$$S'(k\text{-}1{:}k) = [S(k\text{-}2) + S(k\text{-}1) + S(k)]/M \qquad (4)$$

Where:

S'(k-1:k) = the running average of the three slopes, to be used for the 38 Earth view scan-lines in the current super-swath

S(k-2) = the BB slope for the calibration cycle k-2

S(k-1) = the BB slope for the calibration cycle k-1

S(k) = the BB slope for the calibration cycle k

k = calibration cycle number

M = number of qualified BB slopes (see the quality control section) used for averaging (M=1 to 3)

There are several reasons for using a running average for the slopes. First, this will provide fresh slopes that are computed near the time of Earth observations, compared to the 24 hour average slopes in the previous algorithm. Second, using a 3 calibration cycle average reduces fluctuations due to noise. Third, the assumption here is that the slopes at the three calibration cycles do not differ significantly as long as the background flux has not changed significantly during the period. This is a major improvement from the previous algorithm where it was assumed that the slope does not change for any 24 hour period.

b) Intercept

First, the intercepts at the calibration cycles are recomputed using the average slopes derived in the previous step.

$$I'(k) = -S'(k-1:k)*C_{sp} \quad (5)$$

Where: $I'(k)$ = the recomputed intercept for the calibration cycle k

$S'(k-1:k)$ = the average slope for the current super-swath

C_{sp} = space-view count average for the calibration cycle k

Then, the intercept for each of the Earth view scan-lines between two calibration cycles are interpolated using a slightly modified version of equation (1):

$$I'_{(n)} = I'_{l(n)} + \beta * I'_{T(n)} \quad (6)$$

Where $I'_{(n)}$ is the intercept for Earth view scan-line n (n=1 to 38), $I'_{l(n)}$ is the linear interpolation of the intercept between the two calibration cycles, and $I'_{T(n)}$ is the correction to the intercept based on the telescope temperature. β is a switch with values of either 0 or 1. When β =0, $I'_{T(n)}$ is effectively turned off.. The above equation for computing intercepts is essentially unchanged from algorithm 3.0, except that the correction based on telescope temperature can now be turned off.

Calibration for a partial super-swath

A partial super-swath occurs when an orbit of HIRS data does not begin or end with a complete calibration cycle. In both cases, the number of Earth view scan-lines in the super-swath could be any number between 1 and 38. Currently most HIRS orbits have both beginning and ending partial super-swaths. Partial super-swaths also occur when the data stream is broken in the middle of an orbit. Furthermore, when the calibration coefficients cannot be computed for more than one calibration cycle (such as in the rare event of calibration breakdown), the remaining data should be treated as a partial super-swath in data processing.

Since the BB slopes and intercepts are missing on one side of the partial super-swath, it is generally recognized that the calibration coefficients for the partial super-swaths will not be estimated as reliably as those for a normal super-swath. However, it should be noted that the six-minute data overlap between succeeding orbits for the current NOAA polar-orbiting satellites is specifically designed to cover the gaps in the HIRS partial super-swath. Since the calibration cycles are 256 seconds apart, in most cases, users requiring a continuous data stream should be able to safely discard both the beginning and ending partial super-swath, because the discarded data are actually available in the adjacent orbit in a full super-swath. Conceptually, if the HIRS orbits were processed sequentially in time, one could use the last BB calibration coefficients from the previous orbit to interpolate the calibration coefficients for the current beginning partial super-swath. However, not all HIRS orbits are processed sequentially in the operations and the following alternative method should be used:

The calibration slope of a partial super-swath is the average value of the qualified slopes (discussed later) from the nearest two (or at least one) calibration cycles available, either from the

previous orbit, or from within the same orbit. In case none of them is qualified, use the most recent 24 hour average. The calibration intercepts for a partial superswath are computed using the same method as algorithm 3.0. For local receiving stations, b_1 in equation (3) (which is currently derived from 24 hours of global data) may not be appropriate for interpolating the intercepts for the local data. Since the correlation between the telescope temperature and the intercept varies over an orbit, the b_1 values can be better estimated using the local data, separating day and night.

Data storage in the level 1b file

At the calibration cycles, the BB slopes and intercepts for each channel are stored along with the blackbody scan-lines (same as algorithm 3.0). The recomputed slopes and intercepts are stored along with the spaceview scan-lines (which were zeros in algorithm 3.0). For Earth view scan-lines, the recomputed slopes for the current superswath and the interpolated intercepts are stored as primary calibration coefficients. The recomputed slopes are also stored as the secondary coefficients, along with the linear portion of the intercept $I'_{l(n)}$. The 24 hour average slopes and the b_1 coefficients are stored in the level 1b header.

Moon Detection

It is known that the moon may contaminate the space view for several consecutive orbits in a month. When this occurs, it may corrupt the calibration slopes for one calibration cycle (according to modeling). The AMSU moon detection and correction algorithm by Kigawa and Mo (2002) is being implemented in operations. In this algorithm the moon is detected based on ephemeris data, and the space view count is estimated based on the predicted moon temperature. Preliminary studies for HIRS using the same algorithm suggest that this algorithm can be used for HIRS moon detection. However, correction based on predicted moon temperature requires further study due to complex issues involving moon emissivity in the infrared. Therefore, for HIRS calibration algorithm 4.0, the same AMSU moon detection algorithm will be implemented for HIRS. Once the moon is detected in calcycle(k), the slope S(k) becomes invalid and should be removed from equation (4).

When the space view is contaminated by the moon, the intercepts for the calcycle(k) can be computed using the following equation.

$$I'(k) = R_{bb} - C_{bb} * S'(k\text{-}1{:}k) \qquad (7)$$

Where R_{bb}=radiance computed based on the PRT data.

C_{bb} = blackbody view count

Here it is assumed that the instrument gain did not change within the last two calibration cycles, and the PRT measurements of the blackbody temperature is valid. The moon as an infrared calibration source for stability monitoring of HIRS is currently under study and more details will be available later.

Quality control on the calibration coefficients

Regardless whether the moon is detected, the surviving slopes will be checked to ensure that their values are within 2% from their mean value. If not, the one furthest from the mean value is removed and the mean recomputed. This process continues till the condition is satisfied, or alternatively, till only one slope is left.

The mean slopes are then checked against their 24 hour orbit averages. If it deviates from the 24 hour average value by more than 10%, it is considered an anomaly and the 24 hour average value should be used instead (flagged in the level 1b data). If the slope for a channel is anomalous, the intercept is also suspect. Therefore, the intercept in this case should be taken from the last qualified intercept (except in the case of moon contamination as discussed above). If this still fails, the 24 hour average value is used. For a newly launched HIRS instrument, the slope values are not checked until 24 hours of HIRS data have been collected and the normal slopes and intercepts for each channel have been confirmed in off-line analysis.

The main assumption for algorithm version 4.0 is that the calibration slope for each of the 19 IR channels does not change for more than 10% within any consecutive 24 hour period. Historical data suggest that the 24 hour variation in the slopes during normal operations is less than 2%. The slopes are most responsive to the filter wheel temperature change. In the extreme case of NOAA-15/HIRS, a ~6% change in the slope has been observed in some channels when the filter wheel temperature changed a few degrees during a 24 hour period.

The 24 hour file used in the previous algorithm should be expanded to include the following items for future use: Corresponding to the slopes and intercepts, for each calibration cycle, the solar zenith angle and latitude at the nadir, the blackbody temperatures from all the individual PRTs, the temperatures from the secondary and tertiary telescope temperature sensors, the filter wheel housing temperatures, and the baseplate temperature. These parameters may be used in the future for modeling the b_1 values in equation (3). Finally, all anomalies should be flagged in the level 1b data. The details of the bit usage will be decided in the software design process and documented in the user's guide. All related parameters, such as the percent threshold values, will be subjected to changes during the lifetime of the instrument. The threshold values used in the version 4.0 algorithm are based on NOAA-KLM/HIRS data and their validity for future HIRS instruments needs to be determined post-launch.

Concluding Remarks

The operational HIRS calibration algorithms have significant impacts on products at all levels. Since the HIRS does not calibration every scan-line, the calibration coefficients between calibration cycles have to be interpolated based on a number of assumptions. At least two calibration

algorithms using different interpolation methods have been used in the history of the operational HIRS calibration. The HIRS calibration algorithm 4.0 is developed to correct the problems in the previous version of the algorithm, which has caused calibration biases on the order of a few degrees, especially in the long-wave channels. A switch is added for the intercepts to make the correction using the telescope temperature optional. Also, the linearly interpolated intercepts will be stored in the secondary calibration coefficients field in the level 1b data for comparison. Algorithm 4.0 is expected to become the operational HIRS calibration algorithm for NOAA-N.

Acknowledgements

The authors wish to thank Dr. Thomas Kleespies of NOAA/NESDIS/ORA for a critical reading of the manuscript. Also, comments and suggestions from Dr. Michael Weinreb of NOAA/NESDIS/ORA and Mr. Ken Jarva of CSC are greatly appreciated. This study is partially funded by NOAA/NESDIS/OSD.

References

Brunnel, Pascal 2002. ATOVS Navigation and Calibration: Comparison between Local AAPP and Global NESDIS Methods, Conference Proceedings, EUMETSAT STG/SWG.

Cao, Changyong and Hui Xu 2003. Inter-satellite calibration of the High Resolution Infrared Radiation Sounders on NOAA-15, -16, and -17, Proceedings of CalCon2003, Logan, Utah.

Ciren, Pubu, and Changyong Cao 2003. First comparison of radiances measured by AIRS/AQUA and HIRS/NOAA-16/-17, Proceedings of International TOVS Study Conferences, Ste. Adele, Canada, 29 October - 4 November 2003.

Goodrum, Geoffrey, Katherine B. Kidwell, and Wayne Winston 2000. NOAA KLM User's Guide (http://www2.ncdc.noaa.gov/docs/klm), Department of Commerce, Washington DC.

ITT 1996. High Resolution Infrared Radiation Sounder HIRS/4 Technical Description. ITT Aerospace/Communications Division, Fort Wayne, IN.

ITT 1998. High Resolution Infrared Radiation Sounder HIRS/3 Instrument Manual and Alignment/Calibration Handbook & Optical Data, ITT Industries, Fort Wayne, IN.

Kidwell, Katherine B. 1998. NOAA Polar Orbiter Data User's Guide (http://www2.ncdc.noaa.gov/docs /podug/index.htm).

Kigawa, Seiichiro, and Tsan Mo 2002. An Algorithm for Correction of Lunar Contamination in AMSU-A Data, NOAA Technical Report, NESDIS 111, U.S. Department of Commerce.

Kleespies, Thomas J. 2003. Preparations for NOAA-N, Proceedings of International TOVS Study Conferences, Ste. Adele, Canada, 29 October - 4 November 2003.

Status of RTTOV-7 and plans for RTTOV-8

Roger Saunders, Stephen English, Peter Rayer, Peter Francis, Fiona Hilton
Met Office, Exeter, U.K.

Marco Matricardi, Frederic Chevallier
ECMWF, Reading, U.K.

Pascal Brunel,
MétéoFrance, Lannion, France

Introduction

Fast radiative transfer (RT) models are an important tool both for assimilation of satellite radiances in numerical weather prediction (NWP) models and performing physical retrievals. Fast RT models should include both the forward model, which computes satellite radiances for a given profile vector, and its jacobian which, for a given profile, computes the partial derivative of the change in radiance with respect to each of the input profile variables. The latest version of RTTOV, RTTOV-7, was released in March 2002 by the NWP Satellite Application Facility (SAF) and has been distributed to over 54 users worldwide. RTTOV-7 has several improvements over the previous version, RTTOV-6, that are described in the paper by Saunders *et. al.* (2002) and presented at ITSC-12. The main upgrades were: improved water vapour and ozone channel simulation, improved microwave surface emissivity model, support for AIRS, MODIS and SSM/I(S), additional routines for simulating multi-layer cloudy radiances and a new more flexible organisation of the coefficient ingest code. In January 2003 a slightly modified version of RTTOV-7, referred to as RTTOV-71, replaced the March 2002 version which took care of some minor bugs in the original code.

This paper updates the status of RTTOV-7, since ITSC-12, and outlines the scientific and technical upgrades being made for the next version of RTTOV due to be released in Feb 2004. The RTTOV-7 software is available to users on request from the NWP SAF (mailto:rttov.nwpsaf@metoffice.com) on a CDROM or via FTP. The RTTOV-7 documentation can be viewed on the NWP SAF RTTOV web site at http://www.metoffice.com/research/interproj/nwpsaf/rtm/ and will be updated from time to time. Technical documentation about the software can be found in the RTTOV-7 installation and users guide and, at a more detailed level, in the RTTOV-7 technical report. Details of the scientific changes and validation tests are in the RTTOV-7 science and validation report (2002) also available from the web site. Users of the code are invited to submit comments for improvements or report bugs to mailto:rttov.nwpsaf@metoffice.com. An RTTOV email newsgroup exists to share experiences, report bugs and broadcast information on updates to the coefficient files or code. Just send a request to this email to be included on the newsgroup.

Current status of RTTOV-7

The current version of RTTOV-7 is RTTOV-71 released by the NWP-SAF in January 2003. This version corrected all the known bugs in the code updated at:
http://www.metoffice.com/research/interproj/nwpsaf/rtm/rttov7_bugs.html
In addition new coefficient files have been released that were not part of the RTTOV-7 export package. They are:

- NOAA-17 ATOVS & AVHRR
- AQUA MODIS, AMSU-A, HSB, AIRS & AMSR-E
- ADEOS-2 AMSR

These files can be downloaded from the RTTOV-7 web page. A complete list of sensors now supported by RTTOV-7 is given at Table 1. There are plans to include coefficients to simulate

NOAA-18 ATOVS (including MHS), MTSAT imager, METOP-1 ATOVS and IASI, and Windsat. The latter two sensors will be for RTTOV-8 only.

The RTTOV-7 code (or earlier versions) is being used in many NWP centres for radiance assimilation. A survey was made in 2003 to assess, which sensors the users were simulating with the code and the results are presented in Figure 1. Currently ATOVS, SSM/I and SEVIRI are the main sensors being simulated.

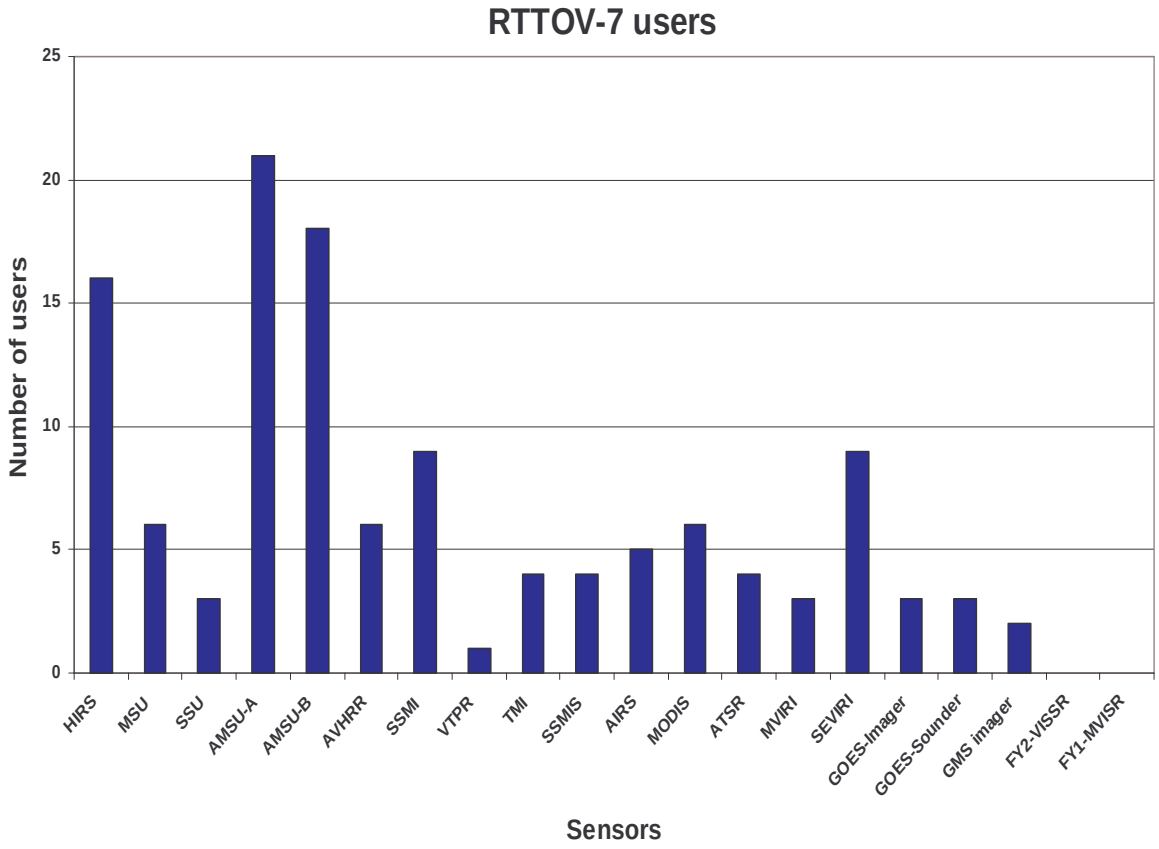

Figure 1 Results of user survey on which sensors are being simulated

One problem has been reported related to the water vapour jacobians in the stratosphere. Unrealistic spikes have been noted for some water vapour profiles in the 5-100hPa level for the AMSU-A channels 5-11. Some examples are shown in Figure 2. This is believed to be due to the low variability in the water vapour transmittances used in the training set causing spurious features in the water vapour transmittances computed from some profiles. As these levels are well above most of the water vapour in the atmosphere the simplest solution is not to allow levels above 115hPa to affect the water vapour profiles in the assimilation/retrieval. Failure to do so can cause problems in the minimisation process.

A significant limitation of the RTTOV model is that the transmittances are only computed on 43 atmospheric levels. This is sufficient for most filter radiometers but for the new advanced sounders it has been shown (Sherlock, 2001) that about 60 levels are required for accurate simulations.

Significant biases exist for very broad spectral channels (e.g. MVIRI 6.7μm, AVHRR 3.7μm) as the Planck function varies significantly across the band. To reduce the mean biases Planck weighted

transmittances have been shown to be an effective way to compute the coefficients from and the results are presented in the poster presented at ITSC-13 by Brunel and Turner (2003).

Platform/Sensor	Sat ids	Channels
NOAA HIRS	6-17	1 to 19
NOAA MSU	6-14	1 to 4
NOAA SSU	6-14	1 to 3
NOAA AMSU-A	15-17	1 to 15
NOAA AMSU-B	15-17	1 to 5
NOAA AVHRR	6-17	3b to 5
DMSP SSMI	8-15	1 to 7
NOAA VTPR	2-5	1 to 8
TRMM TMI	1	1 to 9
DMSP-SSMIS	16	1 to 24*
EOS-AIRS	2	1 to 2378
EOS-MODIS	1-2	1 to 17
EOS-AMSU-A	2	1 to 15
EOS-HSB	2	1 to 4
EOS/ADEOS AMSR	2/2	1 to 14
ESA-(A)ATSR	1-3	1 to 3
METEOSAT	2-7	1 to 2
MSG SEVIRI	1	4 to 11
GOES-Imager	8-12	1 to 4
GOES-Sounder	8,10,11	1 to 18
GMS imager	5	1 to 2
FY2-VISSR	2	1 to 2
FY1-MVISR	3-4	1 to 3

**mesospheric channels 19-21 are not simulated accurately*

Table 1. Platforms and sensors supported by RTTOV-7 as at 1 Nov 2003.

Developments in line-by-line model database

Infrared model

The RTTOV-7 model is based on the same line-by-line (LbL) model transmittances as used for RTTOV-5/6 that were computed using GENLN2 (Edwards, 1992) on 43 pressure levels from 0.1 to 1013hPa with a diverse radiosonde profile set selected from the TIGR v2 dataset. The computations were performed 7 years ago based on HITRAN-96 spectroscopy and the CKD2.1 water vapour continuum. There are now more recent versions of the spectroscopic datasets available and so it was decided to update the dependent set of transmittances this time using HITRAN-2000 and CKD2.4. In addition a new set of 51 diverse profiles has been generated from ECMWF reanalysis fields that allow dynamically consistent profiles of temperature, water vapour and ozone to be generated from the surface to 0.1hPa. These profiles are described in more detail in Chevallier *et. al*. (2000). For the line-by-line model transmittance calculations they were re-interpolated on to the AIRS 101 pressure levels, which were felt to be sufficient for any advanced sounder simulations. For this set of calculations the water vapour continuum absorption was computed separately in preparation for RTTOV-8 that will have the option of separate predictors for the water vapour line and continuum absorption. Also a separate set of CO_2 transmittance profiles were computed to allow the option of retrieving CO_2 using RTTOV-8. The current status (Nov 2003) is that all of the GENLN2 line-by-line model computations have been completed and the convolutions with the instrument filter responses are now underway after the transmittances have been interpolated to the required number of levels. In addition it is also planned to use transmittance calculations from the latest version of

kCARTA (Strow *et. al*,. 1998) as the treatment of CO_2 line mixing has been improved for this model and been validated by comparison with AIRS measurements.

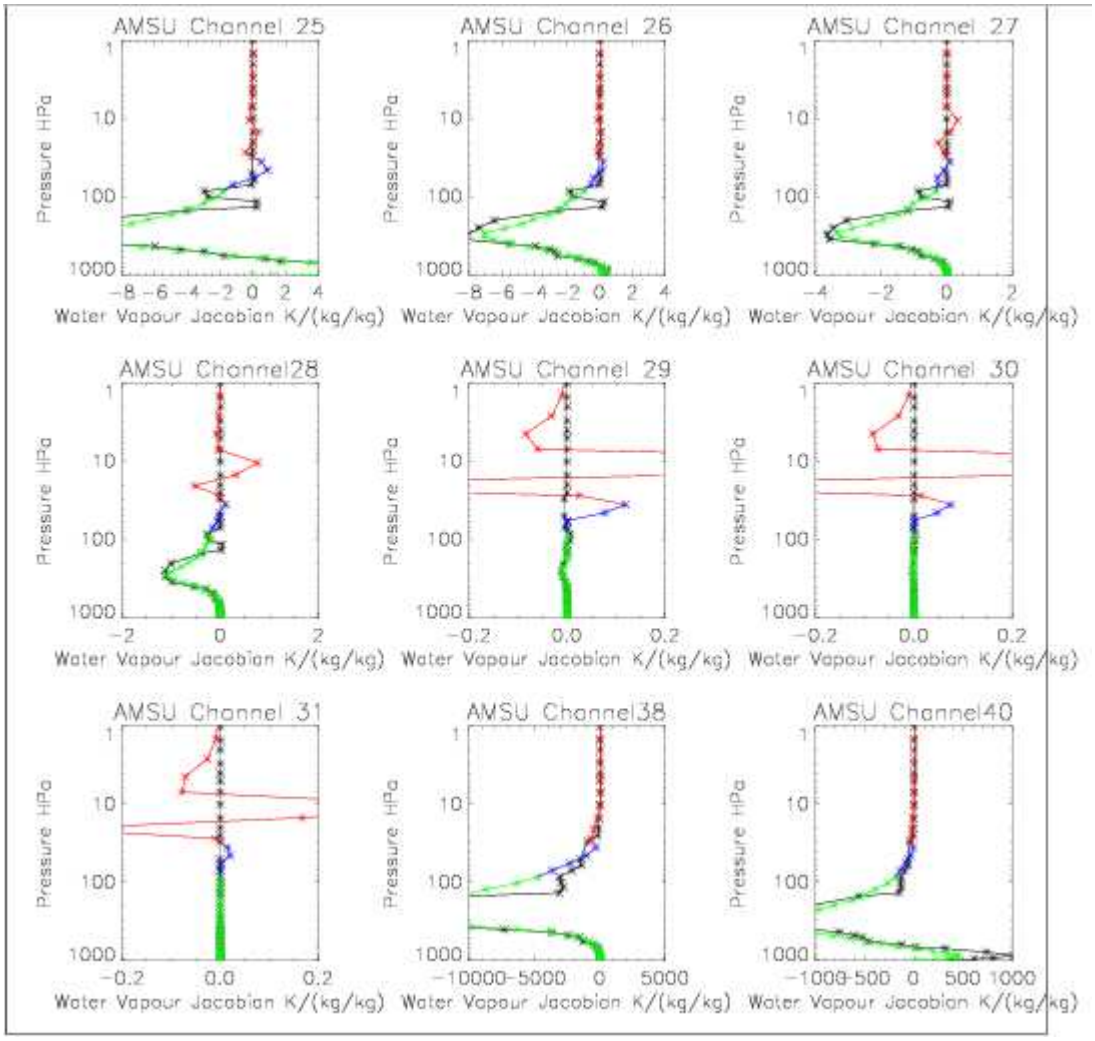

Figure 2. Spikes observed in RTTOV-7 water vapour jacobian. Black denotes RTTOV-5 values and the red, blue and green line denotes the RTTOV-7values.

Microwave model

The Liebe MPM89 model (Liebe *et. al.*, 1989) is still the model used for the microwave water vapour transmittance and MPM92 for the oxygen transmittance calculations. Comparisons have been made with other microwave models (e.g. Garand *et. al.*,2001) but only small differences are seen and so there are no plans to update the microwave transmittances in the short term.

Plans for RTTOV-8

Preparations are now well underway within the NWP-SAF for the next version of RTTOV. The main developments are:

- The code has been completely rewritten using all features of Fortran-90.
- Allow easier use of different number of levels (e.g. ~45 for ATOVS, ~60 for AIRS).
- Revise predictors (number, robustness) and separate water vapour continuum.
- Include CO_2 as an optional variable gas.
- Include scattering code around RTTOV-8 to allow simulation of rain affected microwave radiances.
- Allow simulation of fully polarimetric microwave simulations.
- Improve infrared cloudy radiance simulations.

- Add capability for IASI/CrIS simulations.
- Provide a RTTOV-7 like interface so that if users don't want to change their interface they can recompile the code using the new RTTOV-8 library.

The plan is to release RTTOV-8 to users in early 2004. It will be announced on the web page and on the email group. It will be free of charge for all non-commercial users who sign the licence agreement. For the longer term the NWP SAF is being extended into an initial operational phase and as part of this will be the further development of RTTOV-8 to RTTOV-9 due to be released in early 2007.

Acknowledgements

The RTTOV developments described here were carried out as part of the activities of the SAF for NWP, partially funded by EUMETSAT.

REFERENCES

Brunel, P. and D.S. Turner 2003 On the use of Planck weighted transmittances in RTTOV. *Poster presented at ITSC-XIII Ste Adele, Quebec, Canada, 29 Oct – 4 Nov 2003 (see ITWG web site for details).*

Chevallier, F., A. Chédin, F. Chéruy, and J.-J. Morcrette 2000 TIGR-like atmospheric-profile databases for accurate radiative-flux computation. *Quart. J. Roy. Meteorol. Soc.* **126** *777-785.*

Edwards, D P 1992: GENLN2. A general Line-by-Line Atmospheric Transmittance and Radiance Model *NCAR Technical note NCAR/TN-367+STR (National Center for Atmospheric Research, Boulder, Co., 1992).*

Garand, L., Turner, D.S., Larocque, M., Bates, J., Boukabara, S., Brunel, P., Chevallier, F., Deblonde, G., Engelen, R., Hollingshead, M., Jackson, D., Jedlovec, G., Joiner, J., Kleespies, T., McKague, D.S., McMillin, L., Moncet, J. L., Pardo, J. R., Rayer, P. J., Salathe, E., Saunders, R., Scott, N. A., Van Delst, P., Woolf, R. 2001 Radiance and jacobian intercomparison of radiative transfer models applied to HIRS and AMSU channels. *J. Geophys. Res.,* **106**, *D20. 24017-24031.*

Liebe, H., J.T. Manabe and G. Hufford 1989 Millimeter wave attenuation and delay rates due to fog/cloud conditions. *IEEE Trans. Antennas Propag.,* **37,** *1617-1623.*

RTTOV-7 2002 RTTOV-7 Science and Validation report. *NWP SAF report available from RTTOV web site:* http://www.metoffice.com/research/interproj/nwpsaf/rtm/

Saunders, R.W., S. English, P. Rayer, M. Matricardi, F. Chevallier, P. Brunel, G. Deblonde 2002 RTTOV-7: A Satellite Radiance Simulator for the New Millennium. *Tech. Proc. ITSC-XII Lorne, 27 Feb - 5 Mar 2002.*

Sherlock, V.J. 2001 Vertical discretisation for advanced sounder fast radiative transfer models: grid refinement for RTIASI. *Met Office forecasting research technical report* **336**. *Available at URL:* http://www.metoffice.com/research/interproj/nwpsaf/rtm/papers/vres.pdf

Strow, L.L., H.E. Motteler, R.G. Benson, S.E. Hannon, and S. De Souza-Machado 1998: Fast computation of monochromatic infrared atmospheric transmittances using compressed look-up tables. *J. Quant. Spectrosc. Rad. Transfer* **59** *481-493.*

JCSDA Infrared Sea Surface Emissivity Model

Paul van Delst

Joint Center for Satellite Data Assimilation
Cooperative Institute for Meteorological Satellite Studies
Camp Springs MD, USA

Introduction

The Global Data Assimilation System (GDAS) at NCEP/EMC previously used an infrared sea surface emissivity (IRSSE) model based on Masuda *et al* (1988). This Masuda model doesn't account for the effect of enhanced emission due to reflection from the sea surface (only an issue for larger view angles) and emissivity data was only available at a coarse spectral resolution making application to high resolution instruments, such as AIRS, problematic. The model has been updated to use sea surface emissivities derived via the Wu and Smith (1997) methodology as described in van Delst and Wu (2000). The emissivity spectra are computed assuming the infrared sensors are not polarized and using the data of Hale and Querry (1973) for the refractive index of water, Segelstein (1981) for the extinction coefficient, and Friedman (1969) for the salinity/chlorinity corrections. Instrument spectral response functions (SRFs) are used to reduce the emissivity spectra to instrument resolution. These are the values predicted by the IRSSE model.

The IRSSE Model

A starting point was the sea surface infrared emissivity model, SSIREM, described in Sherlock (1999),

$$\varepsilon(\theta) = c_0 + c_1\hat{\theta}^{N_1} + c_2\hat{\theta}^{N_2} \qquad (1)$$

where $\hat{\theta} = \frac{\theta}{60^\circ}$ is the normalized view angle, and N_1 and N_2 are integers.

The coefficients c_0, c_1, and c_2 for a set of N_1 and N_2 are determined by regression with a maximum residual cutoff of $\Delta\varepsilon = 0.0002$ only for wind speeds of $0ms^{-1}$.

In generating the sensor emissivities, it was noticed that the emissivity variation with wind speed was much larger than the 0.0002 residual tolerance used in SSIREM. This is shown in figure 1 where the wind speed variation of computed emissivity with respect to $0.0ms^{-1}$ for NOAA-17 HIRS channel 8 for view angles 0-65° can be much larger than 0.0002 (note that the HIRS only scans out to 50° – the data at large angles is used for fitting purposes only).

Since the sensor emissivity variation with wind speed was greater than 0.0002, the exponents N_1 and N_2 of the emissivity model were also allowed to vary in the fitting process. For integral values of N_1 and N_2 their variation with wind speed suggested inverse relationships for both (see fig.2). When the exponents were changed to floating point values and the fitting exercise repeated, the result showed a smoother relationship (see fig.3).

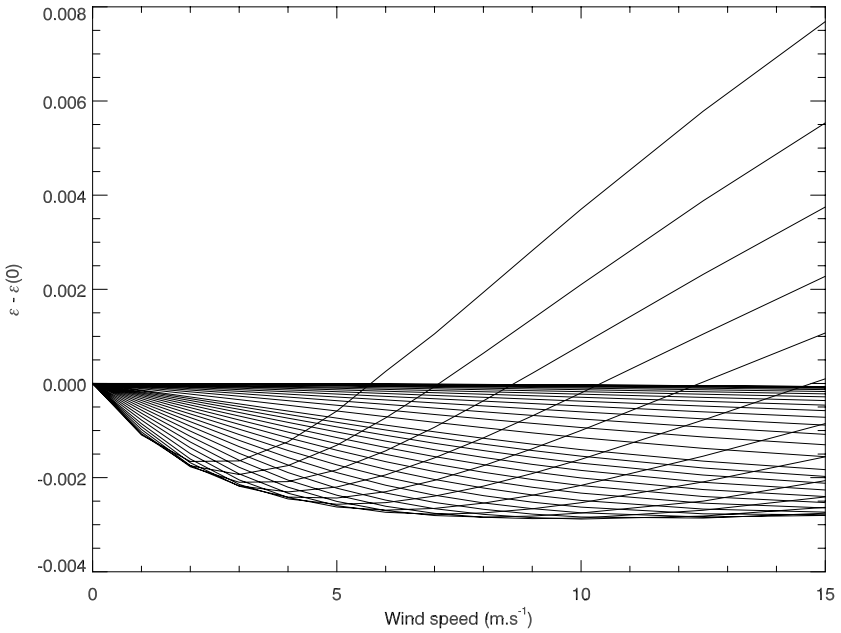

Fig. 1: Wind speed dependence of emissivity for NOAA-17 HIRS channel 8 at view angles 0-65°. (Larger angles used to bound regression fits.)

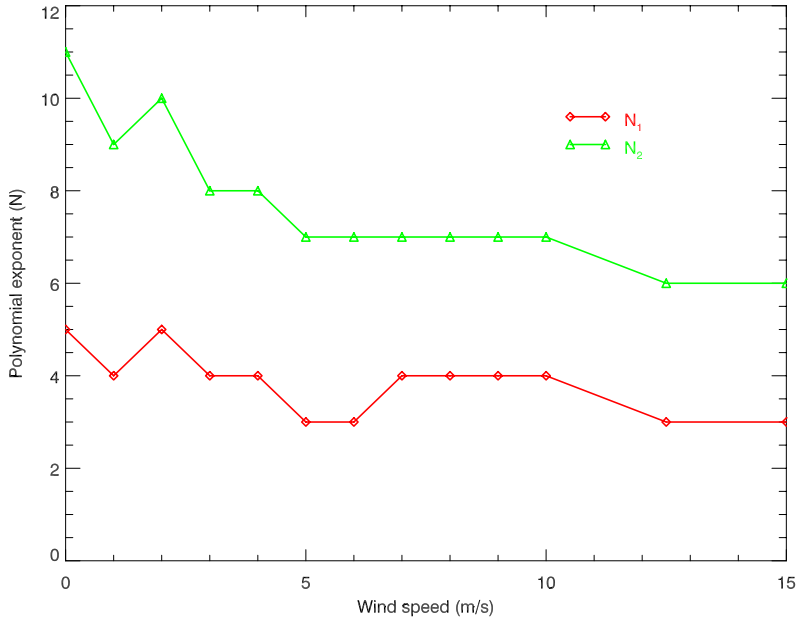

Fig.2: Variation of emissivity fit integral polynomial exponents with wind speed for NOAA-17 HIRS channel 8.

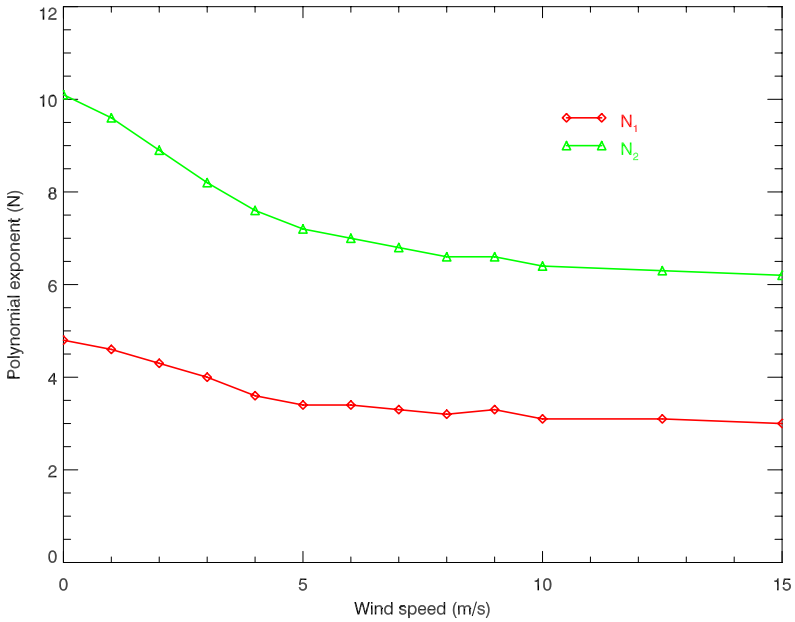

Fig.3: Variation of emissivity fit floating point polynomial exponents with wind speed for NOAA-17 HIRS channel 8.

Based on the smooth variation of the exponents with wind speed shown in figure 3, the emissivity model was changed to,

$$\varepsilon(\theta,v) = c_0(v) + c_1(v)\hat{\theta}^{c_2(v)} + c_3(v)\hat{\theta}^{c_4(v)} \qquad (2)$$

where v is the wind speed in ms^{-1}. In generating the model coefficients, for a series of wind speeds 0-15ms^{-1}, the coefficients c_i were obtained using Levenberg-Marquardt least-squares minimization. Interpolating coefficients for each c_i as a function of wind speed were then determined. In using the model, the c_i are computed for a given wind speed and these computed coefficients are used in equation 2 to calculate the view angle dependent emissivity.

Emissivity Fit Statistics

The emissivity fit RMS residuals for an independent data set are shown for all wind speeds in figure 4 for NOAA-17 HIRS and the Aqua AIRS 281 channel subset. For both instruments, the maximum emissivity fit error was at the 0.00002 level. For instruments that scan out to higher view angles, e.g. GOES instruments, the maximum errors were around 0.0001 at 65°.

To determine the impact of emissivity fit errors on the top-of-atmosphere (TOA) brightness temperatures (T_B), the fitted emissivities were used in radiative transfer calculations. Two tests were run; one determining the impact of emissivity fit errors on the TOA T_B values for all wind speeds, and another to determine the impact when emissivities at only 0.0ms^{-1} are predicted.

The TOA T_B RMS residuals for HIRS and AIRS for all wind speeds are shown in figure 5. The maximum residuals for either instrument never exceeded 0.001K. Figure 6 shows the same RMS residuals, but only for prediction of emissivities at zero wind speed. This shows the expected error if one neglects the wind speed effect on emissivity. The increase in the RMS residuals is about two orders of magnitude which, while a large increase, still results in very small temperatures errors. The maximum errors are about the same magnitudes.

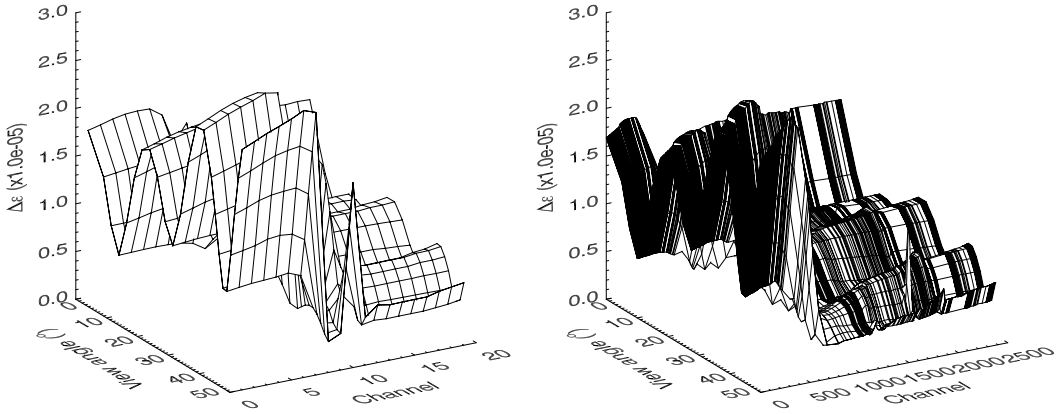

Fig.4: RMS emissivity fit residuals for NOAA-17 HIRS (*left*) and Aqua AIRS 281 channel subset (*right*), all wind speeds 0-15ms^{-1}.

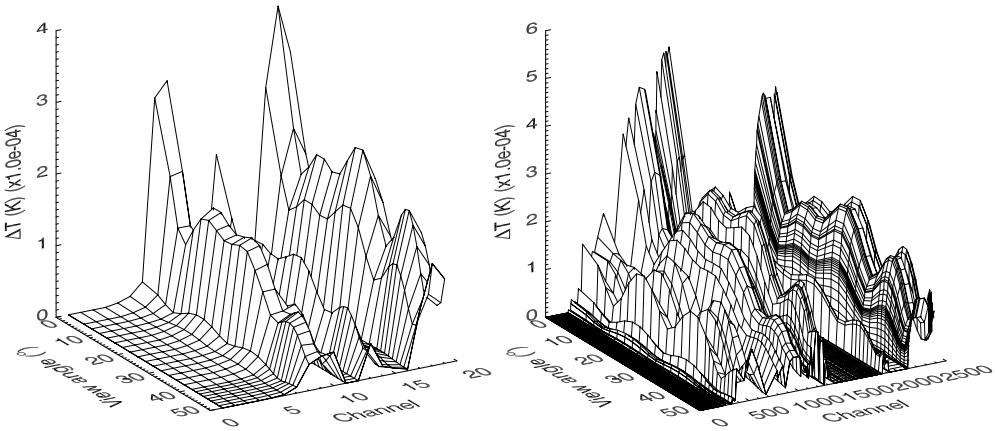

Fig.5: RMS top-of-atmosphere brightness temperature residuals due to emissivity fit for NOAA-17 HIRS (*left*) and Aqua AIRS 281 channel subset (*right*), all wind speeds 0-15ms^{-1}.

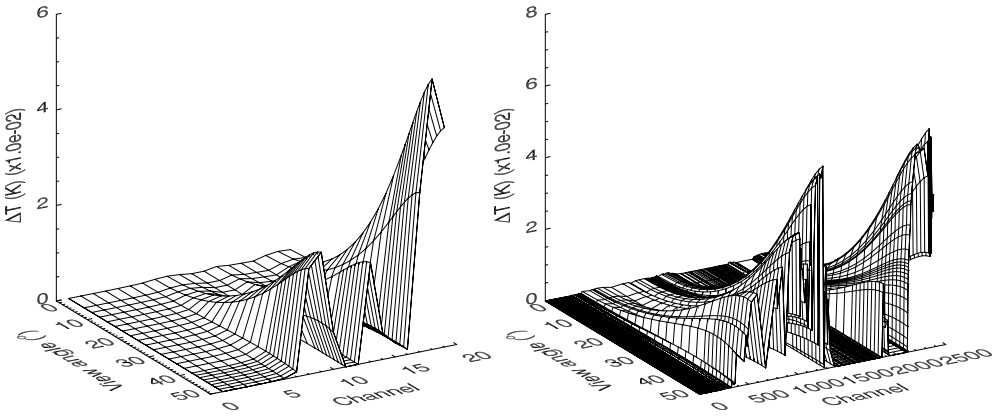

Fig.6: RMS top-of-atmosphere brightness temperature residuals due to emissivity fit for NOAA-17 HIRS (*left*) and Aqua AIRS 281 channel subset (*right*), all wind speeds, but only predicting 0.0ms^{-1} wind speed emissivities.

The wind speed effect is not as negligible for instruments that scan at larger view angles. The RMS and maximum TOA T_B residuals for the GOES-12 sounder, predicting only zero wind speed emissivities, are shown in figure 7. The residuals are much larger for higher view angles,

becoming significant in terms of instrument noise and general atmospheric transmittance modeling errors.

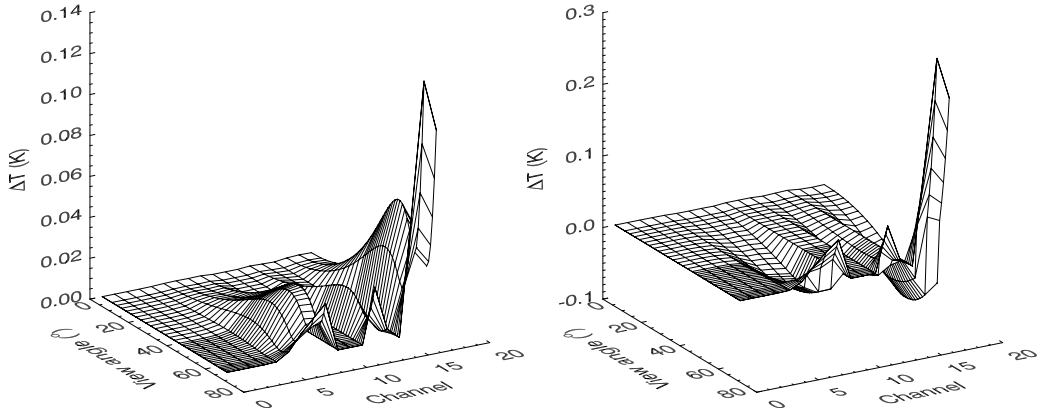

Fig.7: RMS (left) and maximum (right) top-of-atmosphere brightness temperature residuals due to emissivity fit for GOES-12 Sounder, all wind speeds, but only predicting 0.0ms^{-1} wind speed emissivities. Note the larger errors at higher view angle compared to the HIRS and AIRS.

Conclusions

When wind speed is taken into account, the fit residuals are relatively independent of view angle and channel with magnitudes (average, RMS, and maximum) of around 10^{-4} – 10^{-3}K. For those instruments with maximum scan angles <50-55° (e.g. HIRS, AIRS), ignoring the wind speed effect does increases the errors, but to much less than the instrument noise in most cases. When large view angles are used, however, the wind speed dependence of the emissivity must be included to avoid large errors in the result. Given the relative simplicity of the model (see eqn.(2)) and how it was implemented, there is no speed of execution impact in including the wind speed as a predictor.

Acknowledgements

This work was funded under NOAA grant NA07EC0676

References

Friedman, D. 1969. Infrared characteristics of ocean water. *Appl. Opt.*, **8**, 2073-2078

Hale, G.M. and Querry, M.R. 1973. Optical constants of water in the 200nm to 200μm wavelength region. *Appl. Opt.*, **12**, 555-563

Masuda, K., Takashima, T., and Takayama, Y. 1988. Emissivity of pure and sea waters for the model sea surface in the infrared window regions. *Rem. Sens. Env.*, **24**, 313-329

Segelstein, D.J. 1981. The complex refractive index of water. M.S. Thesis, University of Missouri, Kansas City, Missouri.

Sherlock, V.J. 1999. ISEM-6: Infrared surface emissivity model for RTTOV-6. Forecasting Research Technical Report No.299, UK Met. Office, NWP division.

van Delst, P.F.W. and Wu, X. A high resolution infrared sea surface emissivity database for satellite applications. Technical Proceedings of The Eleventh International ATOVS Study Conference, Budapest, Hungary 20-26 September 2000, 407-411

Wu, X. and Smith W.L. 1997. Emissivity of rough sea surface for 8-13μm: modeling and verification. *Appl. Opt.*, **36**, 2609-2619.

A Microwave Snow Emissivity Model

Fuzhong Weng
Joint Center for Satellite Data Assimilation
NOAA/NESDIS/Office of Research and Applications, Camp Springs, Maryland
and
Banghua Yan
Decision Systems Technologies Inc., Rockville, Maryland

Abstract

This paper presents a new microwave snow emissivity model which is empirically derived from satellite retrievals and ground-based measurements. This model produces a variety of snow emissivity spectra at microwave frequencies according to snow types. As part of this model, an algorithm is also developed to classify snow type using the Advanced Microwave Sounding Unit (AMSU) measurements at 23.8, 31.4, 50.3, 89 and 150 GHz. It is shown that the global snow emissivity simulated with this model agrees with that retrieved from satellite measurements.

1. Introduction

Information on land surface emissivity is important for both satellite data assimilation schemes and retrievals of atmospheric parameters from satellite measurements. Recently, a model was developed to simulate the emissivity over various land conditions including snow [Weng et al., 2001] and has been operationally used in the National Centers for Environmental Prediction (NCEP) global forecast system data assimilation system (GDAS). It is found that the discrepancies between simulated and observed brightness temperatures are significant in the polar areas where snow has been probably metamorphosed and vertically stratified [Weng et al., 2001].

Microwave emissivity at the frequencies ranging from 20 to 150 GHz over land can be directly retrieved from satellite measurements [Jones and Vonder Haar, 1997; Prigent et al., 1997; Yan and Weng, 2002]. Statistical information on emissivity such as mean and standard deviation was also generated at the Special Sensor Microwave Imager (SSM/I) frequencies [Yan and Weng, 2002]. It was shown that snow emissivity strongly varies with season and surface types. In this study, we use both satellite retrievals and the ground-based estimations from Mätzler [1994] to derive a new emissivity model.

2. The Nature of Problems

The brightness temperature, T_B, emanating from a scattering-free atmosphere is related to surface emissivity, ε, through

$$T_B = \varepsilon T_s \tau + T_u + (1-\varepsilon) T_d \tau \qquad (1)$$

where T_s is the surface temperature, T_u and T_d are the brightness temperatures associated with upwelling and downwelling radiation, respectively, and τ is the atmospheric transmittance. In the satellite data assimilation scheme, we need to calculate the brightness temperatures at various frequencies with a surface emissivity model. An error in emissivity is directly translated into the error in brightness temperature, viz.

$$\Delta T_B = \tau (T_s - T_d) \Delta\varepsilon \, . \qquad (2)$$

Table 1 displays the errors of brightness temperatures at the Advanced Microwave Sounding Unit (AMSU) frequencies for $\Delta\varepsilon$ of 0.04. Obviously, at a window channel where τ is relatively larger and T_d is smaller, the emissivity uncertainty has a much larger impact on the brightness temperature.

For example, at 150 GHz, ΔT_B is about 7.0 °K when total precipitable water, *TPW*, is 2 mm, T_s is 230 °K and surface pressure, P_s, is 1000 mb. For P_s of 600 mb, ΔT_B increases to about 8.0 °K. At the sounding channels near 50-60 GHz oxygen absorption band, ΔT_B decreases as the frequency approaches to the center of the absorption band. At 52.8 GHz, ΔT_B increases from 0.2 °K to 2.3 °K as P_s decreases from 1000 mb to 600 mb.

Table 1. Errors of brightness temperatures (ΔT_B) in relation to the errors of surface emissivity.

Freq (GHz)	Ts = 230 K and TPW = 0.5 mm						Ts = 230 K and TPW = 2.0 mm					
	Ps = 600 (mb)			Ps = 1000 (mb)			Ps = 600 (mb)			Ps = 1000 (mb)		
	T_d(K)	τ	ΔT_B(K)	T_d(K)	τ	ΔT_B(K)	T_d(K))	τ	ΔT_B(K)	T_d(K)	τ	ΔT_B(K)
50.3	49.30	0.774	5.593	112.5	0.487	2.289	49.8	0.771	5.559	113.6	0.483	2.247
52.8	111.2	0.492	2.337	188.6	0.153	0.253	111.6	0.490	2.322	189.0	0.151	0.248
150	4.4	0.980	8,844	12.5	0.944	8.209	11.4	0.949	8.295	32.3	0.856	6.771
183.3±7	16.6	0.925	7.893	43.5	0.807	6.018	57.9	0.739	5.087	127.8	0.435	1.786
183.3±3	55.3	0.750	5.242	104.1	0.538	2.709	151.6	0.320	1.005	208.1	0.086	0.076
183.3±1	134.6	0.392	1.496	160.1	0.288	0.806	219.8	0.024	0.010	227.2	0.007	0.001

At the sounding channels near the 183.3 GHz water vapor absorption band, ΔT_B strongly varies with *TPW*, P_s and frequency. At 183.3±7 GHz which is the furthest from the band center, ΔT_B increases from 1.8 °K to 6.0 °K as *TPW* decreases from 2.0 mm to 0.5 mm for P_s of 1000 mb. For P_s of 600 mb, ΔT_B is up to 7.9 °K. At 183.3±1 GHz, the impact of surface emissivity on the brightness temperature is the smallest (~ 0.01 °K) for a *TPW* of 2.0 mm. However, for a drier atmosphere, the impact is significantly higher, especially over a region where the surface pressure is lower. For example, ΔT_B at 183.3±1 GHz increases from 0.8°K to 1.5 °K as P_s decreases from 1000 mb to 600 mb for a *TPW* of 0.5 mm. This implies that the uncertainty in surface emissivity over a high-elevation terrain and under a moisture deficient atmosphere will significantly increase the uncertainty in simulating the brightness temperatures at microwave sounding channels.

3. Microwave Snow Emissivity Spectra

3.1 Microwave Emissivity Spectra

In this study, the emissivity is retrieved from satellite and ground-based measurements at various frequencies and is further used to produce the entire spectra over various snow conditions. At microwave frequencies between 4.9 and 94 GHz, eleven snow emissivity spectra over Switzerland were reported by Mätzler (1994). While Mätzler's studies provide the unique information of snow emissivity at lower frequency, there are some deficiencies in the two following aspects: 1) There is no emissivity information at frequencies above 94 GHz, and 2) there are some obvious gaps in two neighborhood emissivity spectra. Thus, satellite retrieved emissivity offers some information complementary to the ground-based estimates.

Using the AMSU measurements at five window channels collocated with radiosonde temperature and water vapor profiles, we calculate snow emissivity between 23.8 and 150 GHz under clear-sky conditions. It is found that several emissivity spectra are frequently observed from these AMSU measurements yet they were not included in Mätzler's data sets. Therefore, these two data sets have been combined to obtain the emissivity spectra at the frequencies ranging from 4.9 to 150 GHz. Since the AMSU measures weighted radiances from vertical and horizontal polarization, Mätzler's data sets are also combined using

$$\varepsilon = \cos^2(\theta)\varepsilon_v + \sin^2(\theta)\varepsilon_h \qquad (3)$$

where θ is the local zenith angle, ε_v and ε_h are the emissivity at vertical and horizontal polarization, respectively. Figure 1 displays sixteen emissivity spectra vs. frequency at the local zenith angle of 50 degree. At 4.9 GHz, the emissivity is least dependent on snow types because of the weakest scattering effects from snow. The largest variability in the emissivity spectra occurs at higher frequencies due primarily to the variability of volumetric scattering within snow.

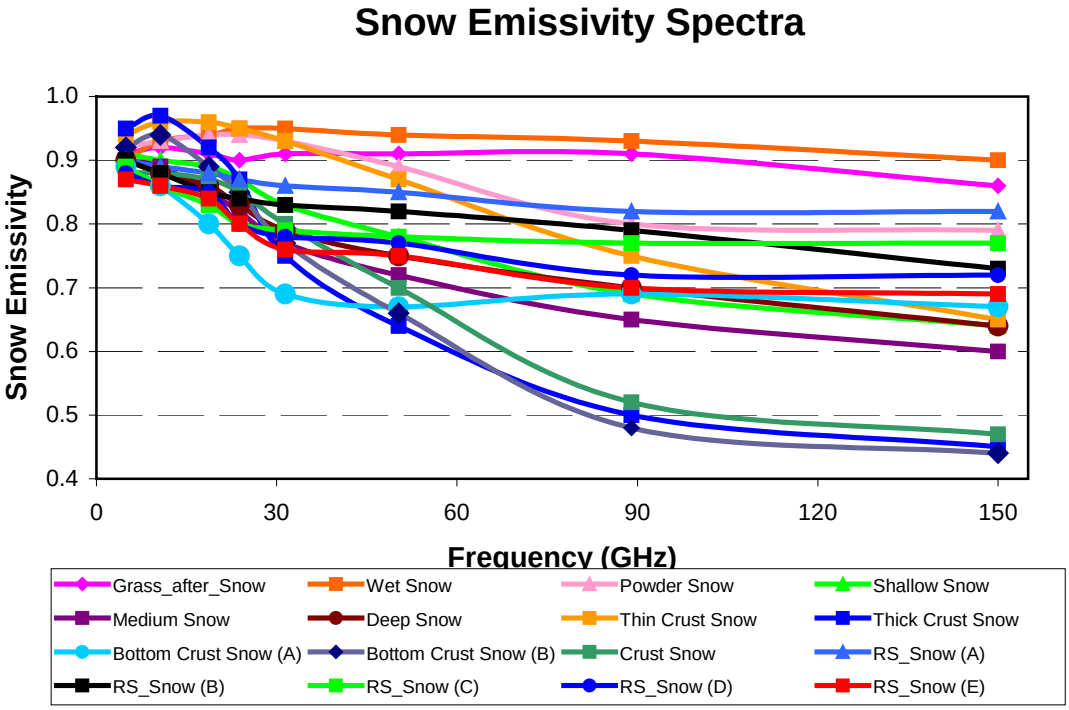

Figure 1. Microwave emissivity as a function of frequency across the range between 4.9 and 150 GHz for sixteen snow surfaces. The type indicated by "RS", radiometric snow, implies a distinct emissivity spectrum but can't be directly associated with a physical snow type. **1.** Wet snow: at least a wet surface layer; **2.** Grass_after_Snow: short grass on a flat ground after snow melts; **3.** RS (A): radiometric type; **4.** Power snow: 24 – 37 cm deep at temperature ranging from –3 to –13 ^{o}C; **5 – 7.** RS (B~D): radiometric types; **8**. Thin crust: wet snow covered by refrozen crust whose thickness is 1-3 cm; **9.** RS: radiometric type; **10.** Bottom crust (A): snow metamorphosed to a thick, hard crust (~ 40 cm) formed at the bottom of the new winter snow; **11.** Shallow: dry winter snow having water equivalent (WE) of 4 – 10 cm and having not undergone melting and metamorphism; **12.** Deep: winter snow having a WE of 25 – 63 cm; **13.** Crust: a layer of refrozen snow (~10 cm) on the top of a wet thin snow (~ 3 cm) with unfrozen ground; **14.** Medium depth: winter snow having a WE of 10 – 25 cm; **15.** Bottom crust (B): aged and refrozen snow on frozen ground (6 to 15 cm), **16.** Thick crust: wet snow covered by a refrozen layer of 4 – 30 cm.

3.2 Identification of Snow Type

To use the emissivity information in Fig. 1, we must first identify the snow type. Using the AMSU five window channel measurements, we develop several discriminators (DI_0 ~DI_5). These

discriminators are used to estimate the intensities of emissivity differences between five pairs of frequencies (e.g. 23.8/31.4, 31.4/ 89.0, 31.4/150.0, 50.3/150.0, 89.0/150.0),

$$DI_0 = a_0 + a_1 T_{B1} + a_2 T_{B1}^2 + a_3 T_{B2} + a_4 T_{B2}^2 + a_5 T_{B3} + a_6 T_{B3}^2, \quad (4a)$$

and

$$DI_j = a_0 + a_1 T_{B2} + \sum_{i=1}^{5} a_{(i+1)} DT_{B1} \ (j = 1 \sim 5), \quad (4b)$$

where

$$DT_{B1} = T_{B1} - T_{B2}, \quad (5a)$$
$$DT_{B2} = T_{B2} - T_{B4}, \quad (5b)$$
$$DT_{B3} = T_{B2} - T_{B5}, \quad (5c)$$
$$DT_{B4} = T_{B3} - T_{B5}, \quad (5d)$$
$$DT_{B5} = T_{B4} - T_{B5}. \quad (5d)$$

and T_{B1}, T_{B2}, T_{B3}, T_{B4}, T_{B5} are brightness temperature at 23.8, 31.4, 50.3, 89, 150 GHz, respectively. Here, coefficients $a_0 \sim a_6$ are listed in Table 2.

Table 2. Coefficients used to compute various discriminators ($DI_0 \sim DI_5$, LI, HI, $DS_1 \sim DS_3$) in snow type classification algorithm.

Indices	**Coefficients**						
	a_0	a_1	a_2	a_3	a_4	a_5	a_6
DI_0	1.72E+00	6.940E-03	2.02E-05	1.22E-02	1.23E-05	2.63E-02	4.88E-05
DI_1	2.67E-02	-1.23E-04	4.39E-03	-2.80E-03	2.92E-03	-8.46E-05	-2.84E-03
DI_2	-5.69E-02	2.07E-04	7.38E-04	1.38E-03	2.45E-03	1.20E-03	-3.46E-03
DI_3	-2.86E-01	1.21E-03	9.00E-04	7.10E-03	-4.21E-03	2.51E-03	6.96E-03
DI_4	-2.34E-01	1.02E-03	-4.02E-03	1.35E-02	-1.18E-02	2.31E-03	1.51E-02
DI_5	-2.26E-01	9.99E-04	1.62E-04	4.01E-03	-5.19E-03	1.31E-03	8.96E-03

Two indices, LI and HI, are also defined to estimate the intensity of surface emission at 31.4 and 150.0 GHz, respectively, viz.

$$LI = DI_0, \quad (6a)$$

$$HI = DI_0 - DI_3. \quad (6b)$$

Three additional indices, DS_1, DS_2 and DS_3 are defined as follows:

$$DS_1 = \sum_{i=1}^{2} DI_i \ , \quad (7a)$$

$$DS_2 = \sum_{i=4}^{5} DI_i \ , \quad (7b)$$

$$DS_3 = \sum_{i=1}^{5} DI_i \ ,. \quad (7c)$$

to describe the emissivity variation within a broader frequency range. For example, smaller DS_1 and DS_2 indicate less variation of snow emissivity within lower and higher frequency range, which are characteristics of fresh or wet or shallow snow. On the other hand, larger DS_1 and DS_2 imply a rapid decrease of emissivity within lower and higher frequency range, which are typical of aged or refrozen or deep snows. In general, higher LI and HI with lower DS_1, DS_2 and DS_3 imply fresh and

shallow snow, whereas a higher LI but a lower HI with higher DS_1, DS_2 and DS_3 identify a deep wet snow covered by a thick layer of refrozen snow (e.g. crust snow). For each snow type, we develop various thresholds for all indices (see Table 3). The brightness temperature at 150 GHz (T_{B5}) itself also helps a further classification of some snow types.

Table 3. Thresholds of various discriminators developed for snow type classification.

Snow Type	**Thresholds**					
	LI	HI	DS_1	DS_2	DS_3	T_{B5}
1	≥0.83	≥0.86	-	≤0.01	≤0.01	≥200.
	≥0.87	≥0.85	-	≤0.06	≤0.10	≥200.
	≥0.87	≥0.83	≤ -0.02	≤0.12	≤0.16	≥204.
	≥0.90	≥0.89	-	-	-	-
	≥0.92	≥0.85	-	-	-	-
2	≥0.84	≥0.83	-	≤0.08	≤0.10	≥195.
	≥0.85	≥0.85	-	≤0.10	-	≥190.
	≥0.86	≥0.81	-	≤0.12	-	≥200.
	≥0.86	≥0.81	≤ 0.00	≤0.12	-	≥189.
	≥0.90	≥0.81	-	-	-	≥195.
3	≥0.80	≥0.76	-	≤0.05	-	≥185.
	≥0.82	≥0.78	-	-	≤0.25	≥180.
	≥0.90	≥0.76	-	-	-	≥180.
4	≥0.89	≥0.73	-	≤0.20	-	-
	≥0.89	≥0.75	-	-	-	-
	≥0.93	≥0.72	-	-	-	-
5	≥0.81	≥0.70	-	≤0.20	-	≥160.
	≥0.83 ≤0.88	≥0.70 ≤0.78	-	-	-	≥160.
6	≥0.75	≥0.76	-	≤0.08	-	≥172.
	≥0.77	≥0.72	-	≤0.12	≤0.15	≥175.
	≥0.78	≥0.74	-	-	≤0.20	≥172.
	≥0.80	≥0.77	-	-	-	≥170.
	≥0.82	-	-	≤0.15	≤0.22	≥170.
	≥0.82	≥0.73	-	-	-	≥170.
7	≥0.75	≥0.70	-	≤0.15	≤0.25	≥167.
	≥0.77	≥0.76	-	-	-	-
	≥0.80	≥0.72	-	-	≤0.30	-
	≥0.77	≥0.73	-	-	≤0.25	-
	≥0.81	≥0.71	-	-	-	-
	≥0.82	≥0.69	-	-	-	-
8	≥0.88	≥0.58	-	-	-	-
9	≥0.73	≥0.67	-	-	-	-
10	≤0.83	≥0.66	-	-	-	-
11	≥0.82	≥0.61	-	-	-	-
12	≥0.77	≥0.58	-	-	-	-
13	≥0.77	≤0.52	-	-	-	-
14	≥0.74	≥0.55	-	-	-	-
15	≥0.74	-	-	-	-	-
16	-	-	-	-	-	-

Figure 2 displays the global snow types classified from NOAA-15 AMSU measurements on February 3, 2002. These snow types are best defined in a radiometric sense due to their distinct emissivity spectra. The snow types having smaller numbers are newly formed (shallow and powder), whereas those with larger numbers indicate aged snow (deep crust). In Northern Greenland and deep Antarctic regions, snow types are higher and probably deep crust. Also, the snow occurring over the western parts of North America and the northern parts of central Europe is newly formed and wet.

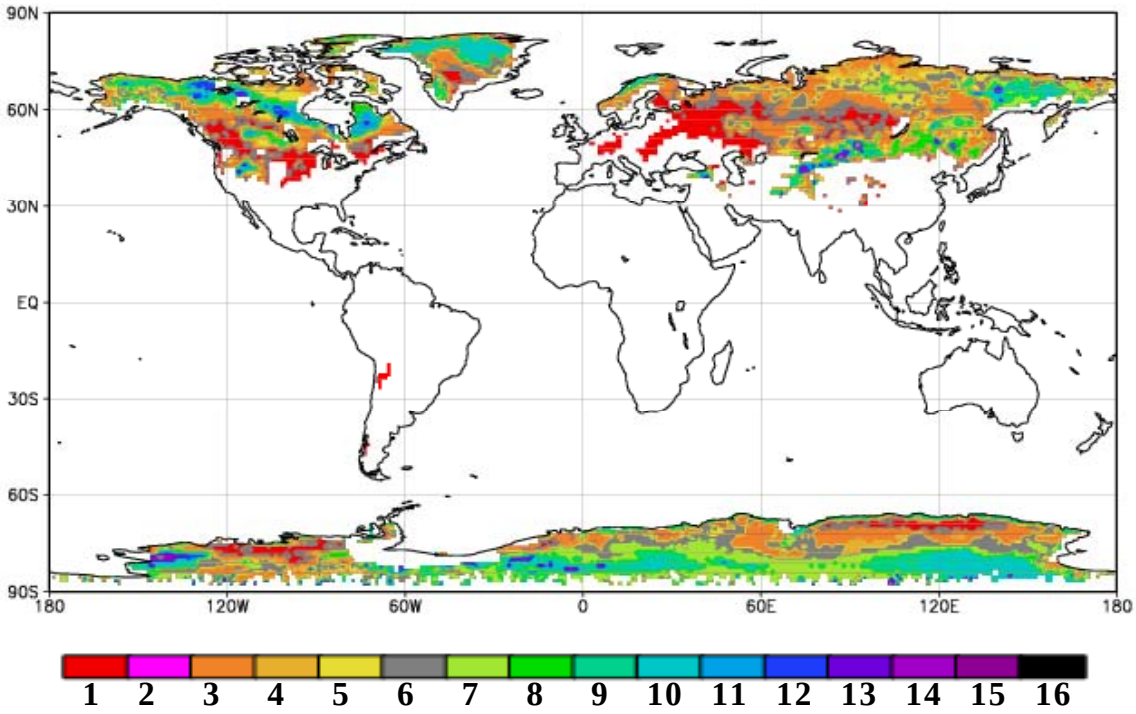

Figure 2. Global distribution of radiometric snow types derived from the AMSU.

4. Simulations of Global Snow Emissivity

Figures 3a and 3b display the emissivity maps at 31.4 GHz and 150 GHz simulated using the emissivity data in Fig. 1 and snow types in Fig. 2. The emissivity at 31.4 GHz is usually larger than 0.9 at mid- to high latitudes. Note that the emissivity at 31.4 GHz is less sensitive to snow type, compared to that at 150 GHz. Also, the emissivity at 150 GHz is lower for higher values of snow types (aged snow). For a snow type of 12 or greater (see Antarctic near 60^{o}W and Northern Alaska), the emissivity at 150 GHz could be as low as 0.6. The larger variability at 150 GHz is due primarily to an increasing volumetric scattering at high frequencies within snow.

Global snow emissivity simulated at a frequency range 5 – 150 GHz agrees well with that retrieved from the AMSU measurements. Figures 3c and 3d display the retrieved snow emissivity at 31.4 and 150 GHz, respectively. The retrievals are calculated using Eq. (1) with GDAS atmospheric temperature and water vapor profiles, and surface temperature. Since all optical parameters in Eq. (1) are computed without taking into account clouds, the emissivity may be overestimated over the areas where clouds and precipitation are present. (Note our analysis shows $\partial\varepsilon/\partial L > 0$, where L is the cloud liquid water path). For example, over the northern central Europe near the Caspian and Black Seas, the retrieved emissivity at 150 GHz is much higher than simulation due to clouds (cloud

image not shown here). Using the AMSU retrieved emissivity under cloud-free conditions, we found the errors of our snow emissivity model are generally less than 4 – 5%, with the smallest ones at higher frequencies (2 –3 %).

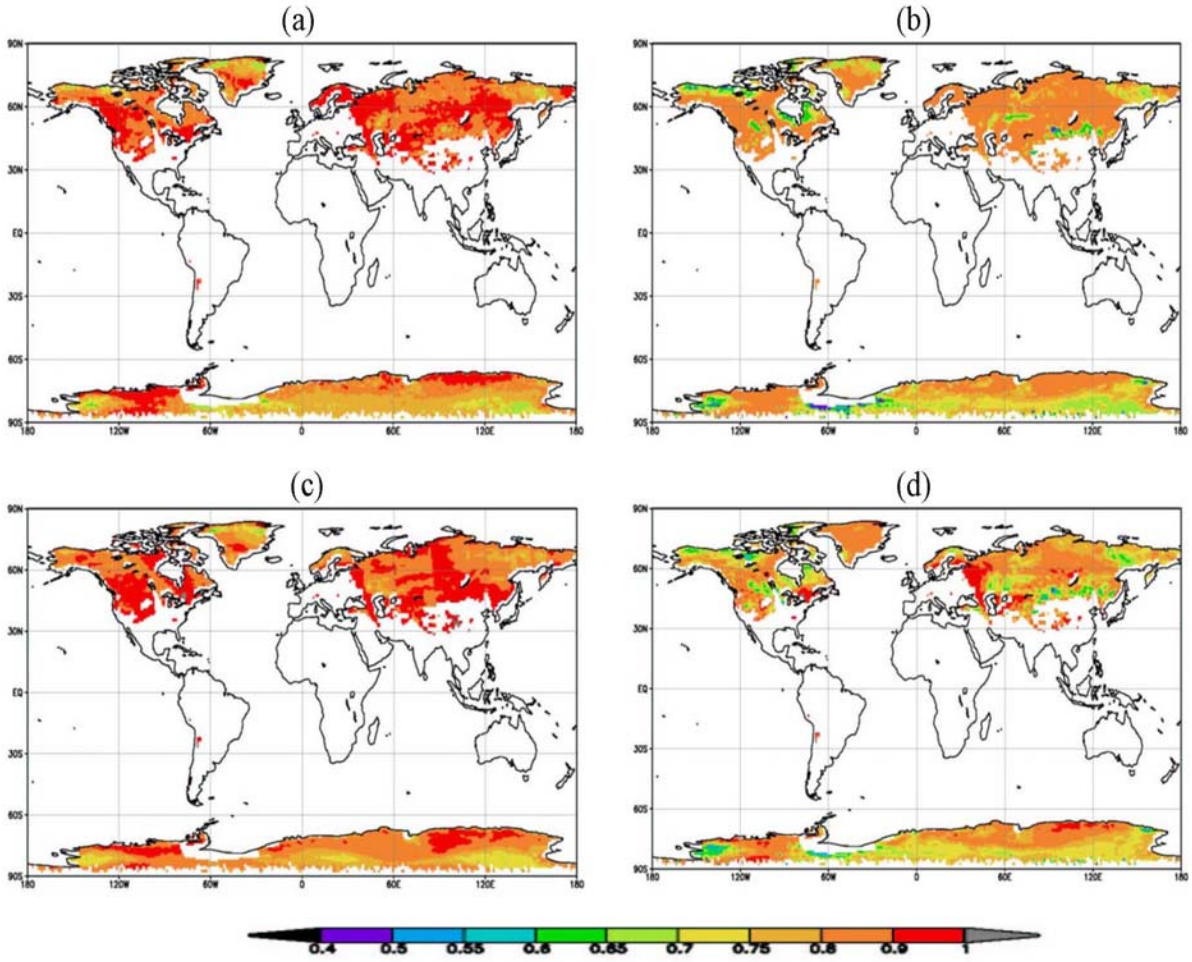

Figure 3. Global distributions of snow emissivity simulated from the model at (a) 31.4 GHz and (b) 150 GHz, compared with AMSU retrievals (c) and (d).

5. A Summary

A new snow emissivity model is developed using the retrievals from satellite and ground-based microwave measurements. The emissivity spectra are classified as sixteen types. An algorithm was developed to identify the snow through a set of discriminators that are defined with five AMSU window channel measurements. Global emissivity maps simulated with this newly developed model exhibit a reasonable distribution, and the errors of simulations are significantly reduced, compared with our earlier developed model.

Acknowledgements: This research is supported by Joint Center for Satellite Data Assimilation directed research program funds.

References

Jones, A. S. and T. H. Vonder Haar, 1997: Retrieval of microwave surface emittance over land using coincident microwave and infrared satellite measurements, *J. Geophys. Res*.,**102**, 13,609-13,626.

Mätzler, C., 1994: Passive microwave signatures of landscapes in winter, *Meteor. Atmos. Phys.*, **54**, 241-260.

Prigent, C., W. B. Rossow and E. Matthews, 1997: Microwave land surface emissvities estimated from SSM/I observations, *J. Geophys. Res*., **102**, 867-890.

Weng, F., B. Yan, and N. C. Grody, 2001: A microwave land emissivity model, *Geophys. Res.,* **106**, 20,115-20,123.

Yan, B. and F. Weng, 2002: A ten-year (1993-2002) time-series of microwave land emissivity, SPIE Third International Asia-Pacific Symposium, Hangzhou, China.

THE 2003 EDITION OF GEISA: A SPECTROSCOPIC DATABASE SYSTEM FORTHE SECOND GENERATION VERTICAL SOUNDERS RADIANCE SIMULATION

http://ara.lmd.polytechnique.fr

N. Jacquinet-Husson, N.A. Scott, K. Garceran, R. Armante, A. Chédin
Laboratoire de Météorologie Dynamique (Atmospheric Radiation Analysis Group)
Ecole Polytechnique- Route Départementale 36
91128, Palaiseau, France

Associated co-authors

A. Barbe, C. Claveau, L. Daumont, M.R. Debacker-Barilly, A. Hamdouni, L. Régalia-Jarlot, Vl.G. Tyuterev. *Groupe de Spectrométrie Moléculaire et Atmosphérique (France)*
K. Chance. *Harvard-Smithsonian Center for Astrophysics (USA)*
S.N. Mikhaïlenko, S.A. Tashkun, A.A. Chursin. *Institute of Atmospheric Optics (Russia)*
L.R. Brown, R.A. Toth. *Jet Propulsion Laboratory (USA)*
J.M. Flaud, I. Kleiner. *Laboratoire de Photophysique Moléculaire (France)*
V. Dana, D; Jacquemart, J.Y. Mandin, J.L. Teffo. *Laboratoire de Physique Moléculaire et Applications (France)*
A. Rublev. *Laboratory for Information Technologies and Mathematical Simulation (Russia)*
L. Schult. *Max Plank Institut für Meteorologie (Germany)*
C. Clerbaux, P.F. Coheur, S. Fally, J. Vander Auwera. *Université Libre de Bruxelles (Belgium)*
A. Goldman. *University of Denver (USA)*
M. Birk, F. Schreier, G. Wagner. *Deutsches Zentrum für Luft und Raumfahrt (Germany)*
D. Newnham, K.M. Smith. *Rutherford Appleton Laboratory (UK)*
V. Nemtchinov, P. Varanasi. *State University of New-York at Stony Brook (USA)*
M.D. Hurley. *Ford Motor Company (USA)*
M. Hess, K. Köpke. *Meteorologisches Institut der Universität München (Germany)*
S. Massie. *National Center for Atmospheric Research (USA)*

Introduction

The performances of the second generation vertical sounders, like AIRS (Atmospheric Infrared Sounder: http://www-airs.jpl.nasa.gov/) in the USA, and IASI (Infrared Atmospheric Sounding Interferometer: http://earth-sciences.cnes.fr/IASI/) in Europe, will be highly dependent on the present-day knowledge of the accuracy of the spectroscopic parameters of the optically active atmospheric gases, since they are essential input in the forward models used to simulate recorded radiance spectra. Consequently, there is an acute need for comprehensive, trustworthy and operational interactive spectroscopic databases to benefit the research in direct and inverse radiative transfer. In this context, since 1974 the ARA (Atmospheric Radiation Analysis) group at LMD (Laboratoire de Météorologie

Dynamique, France) has developed GEISA (Gestion et Etude des Informations Spectroscopiques Atmosphériques: Management and Study of Atmospheric Spectroscopic Information), a computer accessible database system (Chédin et al (1982); Husson et al. (1992;1994). Currently, GEISA is involved in activities related to the assessment of the capabilities of IASI, as described in Jacquinet-Husson et al. (1998).

The GEISA database in its 2003 Edition: an overview

Since its 1997 edition (GEISA-97), the GEISA database, extensively described in Jacquinet-Husson et al. (1999), has been updated twice: partially in 2001 (Jacquinet-Husson et al. 2003) and extensively in 2003 (GEISA-03).
The GEISA-03 system comprises three sub-databases, i.e.:

- **The GEISA-03 sub-database on line transition parameters:**

GEISA-03 sub-database of line transition parameters involves 42 molecules (98 isotopic species) and contains 1,668,371 entries (321,905 supplementary entries since GEISA-97), in the spectral range from 10^{-6} to 22,656 cm^{-1}.
The included molecules are constituents of the atmospheres of Earth (major permanent and trace molecules) and of other Planet (such as: C_2H_4, GeH_4, C_3H_8, C_2N_2, C_4H_2, HC_3N, H_2S, HCOOH and C_3H_4, for the Giant Planets). Among the spectroscopic parameters archived in GEISA, the most important for atmospheric radiative transfer modelling are: the wavenumber (cm^{-1}) of the line associated with a vibro-rotational transition, the intensity of the line (cm $molecule^{-1}$ at 296K), the Lorentzian collision halfwidth (cm^{-1} atm^{-1} at 296 K), the energy of the lower level of the transition (cm^{-1}), the transition quantum identifications for the lower and upper levels of the transition, the temperature dependence coefficient of the halfwidth, the database management identification codes for isotopes and for molecules.

Details for updates

Twenty molecules have been updated in GEISA-03, i.e.:
H_2O: Three spectral regions have been re-investigated. In the 500 to 2850 cm^{-1} region, the line parameters were replaced with a compilation of 10755 water transitions obtained by Toth (1998, 1999, 2000) and Toth et al. (1998). In the 9650-11400 cm^{-1} region, the update comes from of empirical line parameters of $H_2{}^{16}O$ obtained by Brown et al. (2002). In the 13000-26000 cm^{-1} region the new line parameters are from Carleer et al. (1999), Coheur et al. (2002) and Fally et al. (2003).

CO_2: The previous line parameters of the transitions belonging to the four most abundant isotopomers $^{12}C^{16}O_2$, $^{13}C^{16}O_2$, $^{16}O^{12}C\,^{18}O$ and $^{16}O^{12}C\,^{17}O$ in the 442-2797 cm^{-1} spectral region, have been replaced with 48627 new ones covering the 436-2826 cm^{-1} spectral range, issued of the results described in Tashkun et al. (1998, 2001) and Teffo et al. (2002, 2003).

O_3: Updates occur in four spectral regions: In the 600-1232 cm^{-1} spectral region, new and more accurate line parameters for the ν_1 and ν_3 bands of $^{16}O_3$ were derived by Wagner et al. (2002) and Flaud et al. (2003). A complete new study of the 1300-1500 cm^{-1} spectral range, related with the $2\nu_2$, $3\nu_2-\nu_2$, $\nu_1+\nu_3+\nu_3-\nu_2$ and $2\nu_3-\nu_2$ bands of $^{16}O_3$, has been made by Barbe et al. (1998). The 1820-2260 cm^{-1} ($2\nu_3$, $\nu_1+\nu_3$ and $2\nu_1+\nu_3$ interactive bands of $^{16}O^{18}O^{16}O$) and the 2600-2900 cm^{-1} (triad: $\nu_2+2\nu_3$, $\nu_1+\nu_2+\nu_3$ with $2\nu_1+\nu_2$) regions, have been reinvestigated by De Backer-Barilly et al. (2003) and by Mikhaïlenko et al. (2002), respectively.

N_2O: 279 lines in the spectral region 870-1240 cm^{-1}, recently revisited by Daumont et al. (2002), have been substituted in two bands, ν_3-ν_1 and ν_3-$2\nu_2$, the intensities of which were doubtful. In addition, a technical update has removed 118 duplicated lines in the spectral interval 564 cm^{-1} - 629 cm^{-1}.

CH_4 and CH_3D: The CH_4 and CH_3D contents of GEISA have been extensively updated. The spectral range has been extended from 6184.492cm^{-1} to 9199.2846 cm^{-1}, and the number of entries increased from 66883 to 216196 (weaker transitions of $^{12}CH_4$ and new bands of $^{13}CH_4$ and CH_3D included). Full details about the revision in the spectral interval from 0.01 to 6184.492 cm^{-1} can be found in a review paper by Brown et al. (2003). The new CH_4 near infrared data from 4800-5500 cm^{-1} and 6180-10000cm^{-1} are from an empirical list obtained by Brown (2003), from a few selected FTS laboratory spectra.

O_2: The two spectral regions, 7664.726-8064.311 cm^{-1} and 11483.727-15927.806 cm^{-1}, have been updated thanks to new results by Goldman et al. (2003) and by Brown and Plymate (2000), respectively.

NO: A new line list has been produced (Goldman 2003) in the first overtone region of the main isotopic species $^{14}N^{16}O$, i.e. between 3547.318 and 3799.155 cm^{-1}. This calculation has been issued from experimental data from Mandin et al. (1997,1998) and theoretical results from Gillis and Goldman (1982).

NO_2: A new linelist was set up in the spectral region of the $\nu_1+\nu_3$, $\nu_1+2\nu_2$ and $\nu_1+\nu_2+\nu_3-\nu_2$ bands of the $^{14}N^{16}O_2$ main isotopic species. New line parameters come from the works of Mandin et al. (1997), Dana et al. (1997), Devi et al. (1982), May and Webster (1990).

NH_3: The line parameters of the interval 0.058-5294.502 cm^{-1} have been totally replaced by those issued by Kleiner and Brown (2003) and described in Kleiner et al. (2003).

PH_3: New data from Brown and Kleiner (2003), described in Kleiner et al. (2003), have replaced the whole content of the region from 770.877 to 2478.765 cm^{-1}.

OH: Line parameters in the ultraviolet region from 29808.500 to 35877.030 cm^{-1} , from Gillis et al. (2001) have been added to the GEISA archive.

HBR: New line parameters of $H^{79}Br$ and $H^{81}Br$, for the spectral regions of the pure rotation band $X^1\Sigma^+$ (0-0) (16.692-396.474 cm^{-1}) and of the fundamental band (1-0) (2123.812-2790.533 cm^{-1}), have been derived for spectroscopic databases update, as described in Goldman et al. (2003).

HI: The description of the updates in the spectral regions of the $X^1\Sigma^+$ (0-0) (12.842-319.820 cm^{-1}) and of the (0-1) (1950.689-2403.162 cm^{-1}) bands, is given in Goldman et al. (2003).

C_2H_6: In the spectral region 2975.331-2977.926 cm^{-1}, a modified list by Rinsland et al. (1998), for the $^pQ_3$ sub-branch in the ν_7 band, has replaced the previously archived line parameters.

C_2H_2: The updates of the database has concerned three spectral regions: the 13.6- and 5-μm regions, from work performed by Mandin et al. (2000), Jacquemart et al. (2001, 2002), and the 7.5 -μm region, from results by Vander Auwera (2000).

HOCl: A new line list has been created in the spectral interval 1178.673-1320.332 cm^{-1}, corresponding to the ν_2 region, on the basis of the works of Flaud et al. (1998), Flaud (2002) and Vander Auwera et al. (2000).

CH_3Cl: In the spectral region from 1261.562 to 1645.899 cm^{-1} , a list of 8989 transitions of the [ν2, ν5, 2ν3] -vibrational-band triad, prepared by Brown (2002) and based upon the work of Chackerian et al. (1998), has been newly archived, for $CH_3{}^{35}Cl$ and $CH_3{}^{37}Cl$.

COF_2: An update of the 1856.730-2001.348 cm^{-1} region has been made thanks to a list generated by Brown (2001), based on an unpublished analysis of the line positions.

HO_2: Spectroscopic parameters for the ground state have replaced by those generated upon the basis of the work of Chance (1997, 2003)).

A summary of GEISA-03 line transition parameters sub-database content, in terms of number of entries, is given in Table 1. The molecular species formulas are listed in column 1 with, in column 2, their associated identification codes. In columns 3 and 4 are given the number of entries, for each molecular species, in GEISA-97 and in GEISA-03, respectively, with, in column 5, the differences between the numbers of entries in these two editions of the database. Updated molecular species have been coloured in red, if the number of entries has been increased, or in blue, on the contrary. Light green background corresponds to GEISA/IASI-03 specific archive (see related section in the following). It has to be noticed that, in this new edition of GEISA, particular attention has been paid to remove duplicated lines and to harmonize default values for unknown spectroscopic parameters.

- **The GEISA-03 sub-database on absorption cross-sections**

As described in Jacquinet-Husson et al. (1999), besides the line transition parameters data catalog itself, GEISA includes, a second catalog, providing, at various temperatures and pressures, the cross-sections (unit: cm^2 $molecule^{-1}$) of species exhibiting dense spectra , not suitable for a discrete parameterized format. The GEISA-03 archived has been significantly enriched since the GEISA-97 issue. The spectral range has been extended: from 200 cm^{-1} to 2000 cm^{-1} (from 556 cm^{-1} to 1763 cm^{-1}, previously) and the number of molecules has increased, as well, from 23 to 35. The updated already archived species are: CFC11, CFC12, CFC14, HCFC22, HCFC123, HCFC124, HFC125, HFC134a, HCFC141b, HCFC142b, HFC152a, HCFC225ca, HCFC225cb, HFC32, HFC143a, HFC134, N_2O_5, SF_6, $ClONO_2$. No update has occurred for CFC-13, CFC-113, CFC-114, CFC-115. Eleven molecular species are new for GEISA-03 archive, these are:
HFC-143, HCFC-21, C_2F_6, C_2H_2, C_2H_4, C_2H_6, C_3H_8, C_4H_8, HNO_4, SF_5CF_3, HCH-365mfc.

A summary of the GEISA-03 sub-database on absorption cross-sections is given in Table 2. The molecular species names, with their associated identification codes, are listed in columns 1 and 2, respectively. In the three following columns are the experimental conditions associated with the data files, i.e.: the spectral coverage (cm-1), in column 3; the overall temperature range (K), in column 4; the total pressure range (Pa), in column 5. For each file, the number of associated temperature-pressure sets is in column 7 and the related references, in column 8. Reference “GEISA-97” corresponds to non updated molecules. New archived molecular species have been coloured in red. Light green background corresponds to the GEISA/IASI-03 specific archive (see related section in the following).

- **The GEISA-03 sub-database on microphysical and optical properties of atmospheric aerosols**

A common GEISA and GEISA/IASI aerosol sub-database has been recently issued for GEISA/IASI-01 (see Jacquinet-Husson et al. (2003) for details). It gathers the micro-physical and optical properties from published aerosol data catalogs, the overall content of which deals with the archive of complex refractive indices and possibly computed optical related properties, for selected basic aerosol components. Softwares for data management and user-selected aerosol mixtures elaboration are available from the archive. No update of this sub-database has occurred for GEISA-03.

The GEISA/IASI database: 2003 Edition

The GEISA/IASI database derives from GEISA as described in Jacquinet-Husson et al.(1998, 2003). GEISA/IASI is being elaborated with the purpose of assessing the IASI measurements capabilities, within the ISSWG (IASI Sounding Science Working Group), in the frame of CNES (Centre National d'Etudes Spatiales, France)/EUMETSAT (EUropean organization for the exploitation of METeorological SATellites) European Polar System (EPS), by simulating high resolution radiance spectra and/or experimental data. To benefit as soon as possible from improvements in the knowledge of spectroscopic parameters and to ensure the continuous upgrade and maintenance of GEISA/IASI during the fifteen years of life of the IASI instrument, EUMETSAT and CNES have created a GEISA/IASI Database Scientific Committee (GIDSC). EUMETSAT is planning to implement GEISA/IASI into the EPS ground segment.

The GEISA/IASI database, in its 2003 edition (GEISA/IASI-03), is an extraction of GEISA-03 within the IASI or AIRS spectral range (599- 3001 cm^{-1}) with a similar structure, including the three independent sub-databases described above.

GEISA/IASI-03 line transition sub-database contains spectroscopic line parameters stored following the GEISA-03 standard with extended line parameter information (including associated error estimations), for 14 molecules (53 isotopic species) representing 702,550 entries. The GIDSC selected molecules are: H_2O, CO_2, O_3, N_2O, CO, CH_4, O_2, NO, SO_2, NO_2, HNO_3, OCS, C_2H_2, N_2.

It has to be noticed that in GEISA/IASI, CH_3D is considered as an isotope of CH_4. It is considered as an independent molecule in GEISA. Related with the H2O archive in the 10 μm region, alternative line parameters, from Stewart (2003), have been issued has a support study for IASI, and archived in GEISA/IASI-03.

In the GEISA/IASI-03 sub-database on Absorption cross-sections, six molecular species, among the 35 present in GEISA-03, have been selected. These are : CFC-11, CFC-12, CFC-14, CCl_4, N_2O_5 and HCFC-22.

GEISA/IASI-03 is detailed extensively in a paper in preparation, to be submitted at JQSRT.

Table 1: GEISA-03 individual lines sub-database summarized updates and contents

Spectral Range: 10^{-6} – 25232.004100 cm^{-1}

Molécule	ID.	GEISA 97	GEISA 2003	2003 - 1997
H_2O	1	50217	58726	8509
CO_2	2	62816	76826	14010
O_3	3	281607	319248	37641
N_2O	4	26771	26681	-90
CO	5	13515	13515	0
CH_4	6	66883	216196	149313
O_2	7	6292	6290	-2
NO	8	94738	99123	4385
SO_2	9	38853	38853	0
NO2	10	100680	104224	3544
NH_3	11	11152	29082	17930
PH_3	12	4635	11740	7105
HNO_3	13	171504	171504	0
OH	14	41786	42866	1080
HF	15	107	107	0
HCl	16	533	533	0
HBr	17	576	1294	718
HI	18	237	806	569
ClO	19	7230	7230	0
OCS	20	24922	24922	0
H_2CO	21	2702	2701	-1
C_2H_6	22	14981	14981	0
CH3D	23	11524	35518	23994
C_2H_2	24	1668	3115	1447
C_2H_4	25	12978	12978	0
GeH_4	26	824	824	0
HCN	27	2775	2550	-225
C_3H_8	28	9019	8983	-36
C_2N_2	29	2577	2577	0
C_4H_2	30	1405	1405	0
HC_3N	31	2027	2027	0
HOCl	32	15565	17862	2297
N_2	33	117	120	3
CH_3Cl	34	9355	18344	8989
H_2O_2	35	100781	100781	0
H_2S	36	20788	20788	0
HCOOH	37	3388	3388	0
COF_2	38	54866	83750	28884
SF_6	39	11520	11520	0
C_3H_4	40	3390	3390	0
HO_2	41	26963	38804	11841
$ClONO_2$	42	32199	32199	0
Total lines :		**1,346,466**	**1,668,371**	**+321,905**

Table 2: GEISA-03 Cross-Sections Sub-Database

Molecule	Mol ID	Spectral coverage (cm^{-1})	Temperature range (K)	Pressure range (Pa)	Number of TP sets	References
CFC-11	1	210 - 2000	296	93325	1	Hurley(2003); Christidis(1997)
		500 - 1600	297	0	1	MSF/ RAL (2003)
		810 - 1120	190 - 296	1000 - 101325	55	Li & Varanasi (1994) ; Varanasi (2000)
CFC-12	2	850 - 1190	253 - 287	0	3	Clerbaux (1993)
		210 - 2000	296	93325	1	Hurley(2003)
		800 - 1200	190 - 296	1000 - 101392	57	Varanasi & Nemtchinov (1994); Varanasi (2000)
CFC-13	3	765 - 1235	203 - 293	0	3	GEISA97
CFC-14	4	220 - 2000	296	93325	1	Hurley (2003)
		1250 - 1290	180 - 296	1005 - 101458	55	Nemtchinov & Varanasi (2003a)
CFC-113	5	780 - 1232	203 -293	0	6	GEISA97
CFC-114	6	815 - 1285	203 -293	0	6	GEISA97
CFC-115	7	955 - 1260	203 -293	0	6	GEISA97
HFC-32	8	204 - 2000	296	93325	1	Hurley (2003); Pinnock (1995)
		995 - 1475	203 - 297	0 - 100000	17	MSF/ RAL (2003)
HFC-125	9	700 - 1465	287	0	1	Clerbaux (1993)
		495 - 1504	203 -293	0 - 80000	16	Di Lonardo (2000)
		208 - 2000	296	93325	1	Pinnock (1995); Hurley (2003)
HFC-134	10	210 - 2000	296	93325	1	Hurley(2003); Christidis(1997)
		600 - 1700	203 - 297	0 - 100000	9	MSF/ RAL (2003)
HFC-134a	11	815 - 1485	253 - 287	0	3	Clerbaux (1993)
		203 - 2000	296	93325	1	Pinnock (1995); Hurley (2003)
		600 - 1600	203 - 296	0 - 100000	15	MSF/ RAL (2003)
		1035 - 1340	190 - 296	2666 - 101376	33	Nemtchinov & Varanasi (2004)
HFC-143	12	204 - 2000	296	93325	1	Pinnock (1995); Hurley (2003)
HFC-143a	13	694 - 1504	203 - 293	0 - 800000	19	Di Lonardo (2000)
		200 - 2000	296	93325	1	Pinnock (1995); Hurley (2003)
		580 - 1500	203 - 297	0 - 100000	9	MSF/ RAL (2003)
HFC-152a	14	700 - 1600	203 - 293	0 - 80000	16	Vander Auwera (2000)
		840 - 1490	253 - 287	0	3	Clerbaux (1993)
		200 - 2000	296	93325	1	Pinnock (1995); Hurley (2003)
HCFC-21	15	785 - 840	296	133	1	Massie et al. (1985)

Molecule	Mol. ID	Spectral coverage (cm-1)	Temperature range (K)	Pressure range (Pa)	Number of TP sets	References
HCFC-22	16	700 - 1500	203 - 293	0 - 80000	8	Vander Auwera (2003)
		765 - 1380	253 - 287	0	3	Clerbaux (1993)
		208 - 2000	296	93325	1	Pinnock (1995); Hurley (2003)
		760 - 1195	181 - 297	2666 - 101936	51	Varanasi (2001)
HCFC-123	17	740 - 1450	253 - 287	0	3	Clerbaux (1993)
		204 - 2000	296	93325	1	Pinnock (1995); Hurley (2003)
HCFC-124	18	675 - 1425	287	0	1	Clerbaux (1993)
		208 - 2000	296	93325	1	Pinnock (1995); Hurley (2003)
HCFC-141b	19	209 - 2000	296	93325	1	Pinnock (1995); Hurley (2003)
		710 - 1470	253 - 287	0	3	Clerbaux (1993)
HCFC-142b	20	650 - 1475	253-287	0	3	Clerbaux (1993)
		200 - 2000	296	93325	1	Pinnock (1995); Hurley (2003)
HCFC-225ca	21	695 - 1420	253 - 287	0	3	Clerbaux (1993)
		600 - 2000	296	93325	1	Pinnock (1995); Hurley (2003)
HCFC-225cb	22	715 - 1375	253 - 287	0	3	Clerbaux (1993)
		600 - 2000	296	93325	1	Pinnock (1995); Hurley (2003)
N2O5	23	540 - 1380	205 - 293	0	5	Wagner & Birk (2003)
SF6	24	650 - 2000	296	93325	1	Hurley (2003)
		925 - 955	180 - 295	2693 - 101350	29	Varanasi (2001)
ClONO2	25	500 - 1330	190 - 297	0 - 15580	25	Wagner & Birk (2003)
		1265 - 1325	201 - 222	0	3	GEISA97
CCl4	26	750 - 812	208 - 297	1070 - 101272	32	Nemtchinov & Varanasi (2003b)
C2F6	27	1061 - 1285	180 - 296	3320 - 101363	43	Zou & al. (2004)
		210 - 2000	296	93325	1	Highwood (1999);Hurley (2003)
		600 - 2750	203 - 293	0 - 80000	15	MSF/ RAL (2003)
C2H2	28	450 - 2000	296	93325	1	Highwood (1999);Hurley (2003)
C2H4	29	220 - 2000	296	93325	1	Highwood (1999);Hurley (2003)
C2H6	30	220 - 2000	296	93325	1	Highwood (1999);Hurley (2003)
C3H8	31	220 - 2000	296	93325	1	Highwood (1999);Hurley (2003)
C4F8	32	500 - 1600	203 - 297	0 - 65000	19	MSF/ RAL (2003)
HNO4	33	770 - 830	268	93	1	Massie et al. (1985)
SF5CF3	34	600 - 2000	296	93325	1	Hurley (2003)
HCH-365mfc	35	665 - 1480	287	0	1	Clerbaux (1993)

References

Barbe, A., Chichery A., Tyuterev, Vl.G., Tashkun S., Mikhailenko, S. 1998. The $2\nu_2$ and $3\nu_2$- ν_2 bands of ozone. *Spectrochim. Acta A.*, **54**, 1935-45.

Brown, L.R., Plymate, C. 2000. Experimental Line Parameters of the Oxygen A Band at 760 nm. *J. Mol. Spectrosc.,* **199**, 166-79.

Brown, L.R, Toth, R.A, Dulick, M. 2002. Empirical line parameters of $H_2{}^{16}O$ near 0.94μm: positions, intensities and air-broadening coefficients. *J. Mol. Spectrosc*., **212**, 57-82.

Brown, L.R, Benner, D.C., Champion, J.-P., Devi, V.M., Fejard, L., Gamache, R.R., Gabard, T., Hilico, J.C., Lavorel, B., Loëte, M., Mellau, G.C., Nikitin, A., Pine, A.S., Predoi-Cross, A., Rinsland, C.P., Robert, O., Sams, R.L., Smith, M.-A.H., Tashkun, S.A., Tyuterev, Vl.G. 2003. Methane Line Parameters in HITRAN. *J.Q.S.R.T.*, **82**, 219-38.

Brown, L.R. 2001; 2002; 2003. Private communications.

Carleer, M., Jenouvrier, A., Vandaele, A.C, Bernath, P.F., Mérienne, M-F., Colin, R., Zobov, N.F., Polyansky, O.L., Tennyson, J. and Savin, S.A. 1999.The near infrared, visible, and near ultraviolet overtone spectrum of water. *J. Chem. Phys.*; **111(6),** 2444-50.

Chance, K.V., Park, K., Evenson, K.M., Zink, L.R., Stroh, F., Fink, E.H., Ramsay, D.A. 1997. Improved molecular constants for the ground state of HO_2. *J. Mol. Spectrosc.*, **183,** 418.

Chance, K.V. 2003. Private communication.

Chackerian, Jr. C., Brown, L.R., Lacome, N., Tarrago, G. 1998. Methyl chloride ν_5 region line shape parameters and rotational constants for the ν_2, ν_5 and $2\nu_3$ vibrational bands. *J. Mol. Spectrosc.*, **191**, 148-157.

Chédin, A., Husson, N. and Scott, N.A. 1982. Une banque de données pour l'étude des phénomènes de transfert radiatif dans les atmosphères planétaires: la banque GEISA. *Bulletin d'Information du Centre de Données Stellaires (France),* **22**, 121-21.

Clerbaux, C., Colin, R., Simon, P.C., Granier, C. 1993. Infrared Cross Sections and Global Warming Potentials of 10 Alternative Hydrohalocarbons. *J. Geophys. Res.*, **98**, 10491-97.

Coheur, P-F, Fally, S., Carleer, M., Clerbaux, C., Colin, R., Jenouvrier, A., Mérienne, M-F, Hermans, C. and Vandaele, A.C. 2002. New water vapor line parameters in the 26000-13000 cm^{-1}. region. *J.Q.S.R.T.*, **74**, 493-510.

Christidis, N., Hurley, M.D., Pinnock, S., Shine, K.P. and Wallington T.J. 1997. Radiative forcing of climate change by CFC-11 and possible CFC replacements. *J. Geophys. Res.*, **102**, 19597-609.

Dana, V., Mandin, J.-Y., Allout, M.Y., Perrin, A., Régalia, L., Barbe, A., Plateaux, J.-J., Thomas, X. 1997. Broadening parameters of NO_2 lines in the 3.4 micron spectral region. *J.Q.S.R.T.,* **57**, 445-57.

Daumont, L., Claveau, C., Debacker-Barilly, M-R., Hamdouni, A., Régalia-Jarlot, L., Teffo, J-L., Tashkun, S.A. and Perevalov, V.I. 2002. Line intensities of $^{14}N_2{}^{16}O$: the 10 micrometers region revisited. *J.Q.S.R.T.,* **72**, 37-55.

De Backer-Barilly, M-R., Barbe, A., Tyuterev, Vl.G. 2003. Infrared spectrum of $^{16}O^{18}O^{16}O$ in the 5micron range: Positions, intensities, and atmospheric applications. *Atmos. Oceanic Opt. ,***16-3**, 183-8.

Devi, V.M., Fridovich, B., Jones, G.D., Snyder, D.G.S., Das, P.P., Flaud, J.-M., Camy-Peyret, C., Rao, K.N. 1982. Tunable diode laser spectroscopy of NO_2 at 6.2 μm. *J. Mol. Spectrosc*., **93**, 179-95; Devi, V.M., Fridovich, B., Jones, G.D., Snyder, D.G.S., Neuendorffer, A. 1982. Temperature dependence of the widths of N_2-broadened lines of the ν_3 band of $^{14}N^{16}O_2$. *Appl. Opt.*,**21,** 1537-38.

Di Lonardo, G., Masciarelli, G. 2000. Infrared absorption cross-sections and integrated absorption intensities of HFC-125 and HFC-143a. *J.Q.S.R.T.*, **66**, 129-42.

Fally S, Coheur, P-F., Carleer, M., Clerbaux C., Colin R., Jenouvrier A., Mérienne M.F., Hermans, C. and Vandaele, A.C. 2003. Water vapor line broadening and shifting by air in the 26000-13000 cm^{-1} region. *J.Q.S.R.T.*, **82**, 119-32

Flaud, J.-M., Birk, M., Wagner, G., Orphal, J., Klee, S., Lafferty, W.J. 1998. The Far-Infrared Spectrum of HOCl: Line Positions and Intensities. *J. Mol. Spectrosc.,* **191**:362-367.

Flaud, J-M., Wagner, G., Birk, M., Camy-Peyret, C., Claveau, C., De Backer-Barilly, M-R., Barbe A. and Piccolo C. 2003. Ozone absorption around 10 μm. *J. Geophys. Res.,* **108- D9**, 4269, doi:10.1029/2002JD002755.

Flaud, J.-M. 2002. Private communication.

Gillis, J.R. and Goldman, A. Nitric oxide IR line parameters for the upper atmosphere. 1982. *Appl. Opt.* **21**, 1616-27.

Gillis, J.R., Goldman, A., Stark, G., Rinsland, C.P. 2001. Line parameters fort he $A^2\Sigma^+\_X^2\Pi$ bands of OH. *J.Q.S.R.T.*, **68**, 225-30.

Goldman, A., Stephen, T.M., Rothman LS, Giver LP, Mandin JY, Gamache RR, Rinsland CP, Murcray FJ. 2003. The 1μm CO_2 bands and the O_2 (0-1) $X^3\ \Sigma^-_g - a^1\Delta g$ and (1-0) $X^3 \sum {}^-_g - b^1\sum {}^+_g$ bands in the Earth atmosphere. *J.Q.S.R.T.*, **82,** 197-205.

Goldman, A., Coffey, M.T., Hannigan, J.W., Mankin, W.G., Chance, K.V., Rinsland, C.P. 2003. HBr and HI line parameters update for atmospheric spectroscopy databases. *J.Q.S.R.T.*, **82**, 313-17.

Goldman, A. 2003. Private communication.

Highwood, E.J., Shine, K.P., Hurley, M.D., Wallington, T.J. 1999. Estimation of direct radiative transfer forcing due to non-methane hydrocarbons. *Atmos. Environ*. **33**, 159-67.

Hurley, M.D. 2003. Private communication.

Husson, N., Bonnet, B., Scott, N.A. and Chédin, A. 1992. Management and study of spectroscopic information: the GEISA program. *J.Q.S.R.T.*, **48**, 509-18.

Husson, N., Bonnet, B., Chédin, A., Scott, N.A., Chursin, A.A., Golovko, V.F. and Tyuterev, Vl.G. 1994. The GEISA data bank in 1993. A PC/AT compatible computers' new version", *J.Q.S.R.T.*, **52**, 425-38.

Jacquemart, D., Claveau, C., Mandin, J.-Y. and Dana, V. 2001. Line intensities of hot bands in the 13.6 μm spectral region of acetylene $^{12}C_2H_21$. *J.Q.S.R.T.,* **69**, 81-101.

Jacquemart, D., Mandin, J.-Y., Dana, V., Régalia-Jarlot, L., Thomas, X. and Von Der Heyden P. 2002. Multispectrum fitting measurements of line parameters for 5 μm cold bands of acetylene. *J.Q.S.R.T.,* **75**, 397-422.

Jacquinet-Husson, N., Scott, N.A., Chédin, A., Bonnet, B., Barbe, A., Tyuterev, Vl.G., Champion, J.P., Winnewisser, M., Brown, L.R., Gamache, R., Golovko V.F. and Chursin, A.A. 1998. The GEISA system in 1996: Toward an operational tool for the second generation vertical sounders radiance simulation. *J.Q.S.R.T.,* **59**, 511-27.

Jacquinet-Husson, N., Arié, E., Ballard, J., Barbe, A., Brown, L.R., Bonnet, B., Camy-Peyret, C., Champion, J.P., Chédin, A., Chursin, A.A., Clerbaux, C., Duxbury, G., Flaud, J.-M., Fourrié, N., A.Fayt, A., Graner, G., Gamache, R., Goldman, A., Golovko, Vl., Guelachvilli, G., Hartmann, J.-M., Hilico, J.C., Lefèvre, G., Naumenko, O.V., Nemtchinov, V., Newham, D.A., Nikitin, A., Orphal, J., Perrin, A., Reuter, D.C., Rosenmann, L., Rothman, L.S., Scott, N.A., Selby, J., Sinitsa, L.N., Sirota, J.M., Smith, A.M., Smith, K.M., Tyuterev, Vl.G., Tipping, R.H., Urban, S., Varanasi P. and M.Weber, M. 1999. The 1997 spectroscopic GEISA databank. *J.Q.S.R.T.,* **62,** 205-54.

Jacquinet-Husson, N., Scott, N.A., Chédin, A., and Chursin A.A. 2003. The GEISA spectroscopic database system updated for IASI direct radiative transfer modelling. *Atmos. Oceanic Opt.* **,16-3**, 256-61.

Kleiner, I., Tarrago, G., Cottaz, C., Sagui, L., Brown, L.R., Poynter, R.L., Pickett, H.M., Chen, P., Pearson, J.C., Sams, R.L., Blake, G.A., Matsuura, S., Nemtchinov, V., Varanasi, P., Fusina, L., Di Lonardo, G. 2003. NH_3 and PH_3 line parameters: 2000 HITRAN update and new results. *J.Q.S.R.T.*, **82**, 293-312

Kleiner, I. and Brown, L.R. 2003. Private communication.

Li, Z. and Varanasi, P . 1994. Measurement of the absorption cross-sections of CFC-11 at conditions representing various model atmospheres. *J.Q.S.R.T.,* **52**, 137-44.

Mandin, J.-Y., Dana, V., Régalia, L., Barbe, A., Thomas, X. 1997a. Λ-Splittings and Line Intensities in the First Overtone of Nitric Oxide. *J. Mol. Spectrosc.*,**185,** 347-55.

Mandin, J.Y., Dana, V., Perrin, A., Flaud, J.-M., Camy-Peyret, C., Régalia, L., Barbe, A. 1997b. The $\{\nu_1+2\nu_2, \nu_1+\nu_3\}$ bands of $^{14}N^{16}O_2$: line positions and intensities; line intensities in the $\nu_1+\nu_2+\nu_3$ - ν_2 hot band. *J. Mol. Spectrosc.*, **181**, 379-88.

Mandin, J.-Y., Dana, V., Régalia, L., Barbe, A., Von der Heyden, P. 1998. Lambda-Splittings and Line Intensities in the 3 ← 1 Hot Band of $^{14}N^{16}O$: The Spectrum of Nitric Oxide in the First Overtone Region. *J. Mol. Spectrosc.*, **187**, 200-5.

Mandin, J.-Y, Dana, V., and Claveau, C. 2000. Line intensities in the ν_5 band of acetylene $^{12}C_2H_2$. *J.Q.S.R.T.*, **67**, 429-46.

M.S.F./R.A.L: Molecular Spectroscopy Facility/RutherfordAppleton Laboratory. Smith, K.M. 2003. Private communication.

Massie, S.T., Goldman, A., Murcray, D.G., Gille, J.C. 1985. Approximate absorption cross sections of F12, F11, $ClONO_2$, N_2O_5, HNO_3, CCl_4, CF_4, F21, F113, F114, and HNO_4. *Appl. Opt.,* **24,** 3426-27.

May, R.D. and Webster, C.R. 1990. Laboratory measurements of NO_2 line parameters near 1600 cm^{-1} for the interpretation of stratospheric spectra. *Geophys Res Let.,* **17,** 2157-60.

Mikhailenko, S., Barbe, A. and Tyuterev, Vl.G. 2002. Extended analysis of line positions and intensities of ozone bands in the 2900–3200 cm^{-1} region. *J. Mol. Spectrosc.*, **215**, 29-41.

Nemtchinov, V., Varanasi, P. 2003a. Thermal infrared absorption cross-sections of CF_4 for atmospheric applications. *J.Q.S.R.T.*, **82,** 461-71.

Nemtchinov, V., Varanasi, P. 2003b. Thermal Infrared Absorption Cross-sections of CCl_4 needed for Atmospheric Remote-Sensing. *J.Q.S.R.T.,* **82,** 473-81.

Nemtchinov, V., Varanasi, P. 2004. Absorption cross-sections of HFC-134a in the spectral region between 7 and 12 μm, *JQSRT.*, **84**, 285-94.

Pinnock, S., Hurley, M.D., Shine, K.P., Wallington, T.J. and Smyth, T.J. 1995. Radiative forcing of climat by hydrochlorofluorocarbons and hydrofluorocarbons. *J Geophys Res.*, **100,** 23227-38.

Rinsland, C.P., Jones , N.B., Connor, B.J., Logan, J.A., Pougatchev, N.S., Goldman, A., Murcray, F.J., Stephen, T.M., Pine, A.S., Zander, R., Mahieu, E., Demoulin, P. 1998. Northern and southern hemisphere ground-based infrared spectroscopic measurements of tropospheric carbon monoxide and ethane. *J Geophys Res.*, **103:28**, 197-217.

Stewart, B.C (Ed.) 2003. Support study on Water Vapor Spectroscopy for IASI. *Final Report, EUMETSAT Contract EUM/CO/01/939/DK*. 159pp.

Tashkun, S.A., Perevalov, V.I., Teffo, J.-L., Rothman, L.S. and Tyuterev, Vl.G. 1998. Global fitting of $^{12}C^{16}O_2$ vibrational-rotational line positions using the effective Hamiltonian approach. *J.Q.S.R.T.,* **60**, 785-801.

Tashkun, S.A., Perevalov, V.I. and Teffo**,** J-L. 2001. Global fittings of the vibrational-rotational line positions of the $^{16}O^{12}C^{17}O$ and $^{16}O^{12}C^{18}O$ isotopic species of carbon dioxide. *J. Mol. Spectrosc*., **210**, 137-145.

Teffo, J-L., Daumont, L., Claveau, C., Valentin, A., Tashkun S.A. and.Perevalov, V.I. 2002. Infrared spectra of the $^{16}O^{12}C^{17}O$ and $^{16}O^{12}C^{18}O$ species of carbon dioxide: The region 500-1500 cm^{-1}", *J. Mol. Spectrosc*., **213**, 145-152.

Teffo, J-L., Daumont, L., Claveau, C., Valentin, A., Tashkun S.A. and Perevalov, V.I. 2003. Infrared spectra of the $^{16}O^{12}C^{17}O$ and $^{16}O^{12}C^{18}O$ species of carbon dioxide: II The region 1500-3000 cm^{-1}. *J. Mol. Spectrosc*., **219**, 271-281.

Toth RA. 1998. Water vapor measurements between 590 and 2582 cm^{-1}: Line positions and strengths. *J. Mol. Spectrosc*., **190,** 379-96.

Toth, R.A. 1999.Analysis of line positions and strengths of $H_2{}^{16}O$ ground and hot bands connecting to interacting upper states: (020), (100), and (001). *J Mol Spectrosc*., **194**, 28-42. Toth, R.A. 1999. HDO and D_2O low pressure, long path spectra in the 600-3100 cm^{-1} region I. HDO line positions and strengths. *J. Mol. Spectrosc.,* **195,** 73-97.

Toth, R.A. 2000. Air- and N_2-Broadening parameters of water vapor: 604 to 2271 cm^{-1}. *J. Mol. Spectrosc.,* **201,** 218-43.

Toth, R.A, Brown, L.R, Plymate, C. 1998. Self-broadened widths and frequency shifts of water vapor lines between 590 and 2400 cm^{-1}. *J.Q.S.R.T.*, **59**, 529-62.

Vander Auwera, J. 2000. Absolute intensities measurements in the $\nu_4+\nu_5$ band of $^{12}C_2H_2$: Analysis of Herman-Wallis effects and forbidden transitions. *J. Mol. Spectrosc*., **201**, 143-50.

Vander Auwera, J., Kleffmann, J., Flaud, J.-M., Pawelke, G., Burger, H., Hurtmans, D., Petrisse, R. 2000. Absolute ν_2 line intensities of HOCl by simultaneous measurements in the infrared with a tunable diode laser and far-infrared region using a Fourier transform spectrometer. *J. Mol. Spectrosc*., **204**, 36-47.

Vander Auwera, J. 2000. Infrared absorption cross-sections for two substituted ethanes: 1,1-difluoroethane (HFC-152a) and 1,2-dichloroethane. *J.Q.S.R.T.,* **66,** 143-51.

Vander Auwera, J. 2003. Private communication. Ballard, J., Knight, R.J., Newnham, D.A., Vander Auwera, J., Herman, M., Di LOnardo, G., Masciarelli, G., Nicolaisen, F.M., Beukes, J.A., Christensen, L.K., McPheat, R., Duxbury, G., Freckleton, R., Shine, K.P. 2000. An intercomparison of laboratory measurements of absorption cross-sections and integrated absorption intensities for HCHC-22. . *J.Q.S.R.T.*, **66**, 109-28.

Varanasi, P., Nemtchinov, V. 1994. Thermal infrared absorption coefficients of CFC-12 at atmospheric conditions. *J.Q.S.R.T.,* **51**, 679-87.

Varanasi, P. 2000. Private communication.

Varanasi, P. 2001. Private communication. Varanasi, P., Nemtchinov, V., Li, Z., Cherukuri, A. 1994. Spectral Absorption-coefficient Data on HCFC-22 and SF_6 for Remote Sensing Applications. . *J.Q.S.R.T.,* **52**, 323-32.

Wagner, G., Birk, M., Schreier, F., Flaud, J.-M. 2002. Spectroscopic database for ozone in the fundamental spectral regions. *J. Geophys. Res.* **107-D22**, 4626-43.

Wagner, G., Birk, M. 2003. Private Communication. New infrared spectroscopic database for chlorine nitrate. *J.Q.S.R.T.,***82**, 443-60.

Zou, Q., Sun, C., Nemtchinov, V., Varanasi, P. 2004. Thermal infrared cross-sections of C_2F_6 at atmospheric temperatures. *J.Q.S.R.T.,***83**, 215-21.

An Alternate Algorithm to Evaluate the Reflected Downward Flux Term for a Fast Forward Model

D.S. Turner
Meteorological Service of Canada
Downsview, Ontario, Canada

Introduction

In order to assimilate vast amounts of satellite data received daily, fast and efficient radiative transfer models are favoured. Many approximations are used by these models in order to minimize their computational time. An appropriate approximation is one where observed radiances can be simulated by the model with zero bias and little error. Inappropriate approximations are ones where significant non-zero biases are produced. Significant non-zero biases result in observations having little impact on numerical weather prediction schemes unless an empirical bias correction scheme is employed. It is preferable to avoid approximations that produce non-zero biases, or at least find approximations that minimize the magnitude of the bias.

Some approximations only work over a limited range of situations. Within this range the biases are negligible, however once outside this range the biases may become significant. The current approximations of the attenuated reflected downward flux (ARDF) term of the top of the atmosphere (TOA) radiance equation, as seen by a satellite, are examples of limited applicability. Current fast forward models (FFM) approximate the downward flux by the downward radiance evaluated using the TOA transmission function defined by either the satellite zenith angle, model M1, (eg RTTOVS, Saunders et al, 1999) or a constant angle, model M2, (eg MSCFAST, Garand et al, 1999). The latter is more realistic as it precludes an explicit dependency on zenith angle, but is computationally slower as it requires two passes through a transmittance model. Earlier studies with the High-resolution Infrared Radiation Sounder, HIRS, and the Atmospheric Infrared Sounder, AIRS, (Turner, 2001) indicate that the bias of the difference between a line-by-line radiative transfer model (LBL) and these models are satellite zenith angle and surface pressure dependent, and that in many instances have a small bias only for a small range of relatively high emissivities and surface pressures. For example, assuming a target bias of less than .1K the useful range of emissivities in M1 is from 1 to .9 at low altitudes. Consequently this model is inappropriate for some frequencies over land where emissivities may be as low as .6 in sandy soil.

This article proposes an alternate method of approximating the reflected downward flux that attempts to reduce the bias over a wider range of emissivity and surface pressure whilst using less computational time than the two pass method of M2. The method modifies the surface to TOA transmittance function by raising it to the power κ which is a function of the secant of the satellite zenith angle and surface pressure. A comparison of the proposed model, M3, is made with the other two models across the AIRS channels.

Alternate Algorithm

The downward flux is approximated by replacing the angular integration of the transmission function by a transmission function evaluated at a representative zenith angle. The optimum diffusivity factor, the secant of this angle, is usually taken to be 1.66. The diffusivity factor varies with the optical depth (Liu, 1988), thus the assumption of a diffusivity factor that is not related to the atmosphere as in M1, or a constant diffusivity factor regardless of atmosphere, as in M2, invariably leads to errors. Consequently any improvement to the ARDF model should allow for a diffusivity factor that varies with optical depth.

The ARDF term is the product of the upward return transmittance and the downward flux, $<\Im_s(\theta)\, F^{\downarrow}>$, and is approximated by

$$\frac{(1-\varepsilon)}{\pi} <\Im_s(\theta)> \left[\left(\sum_{k=1}^{s} \frac{<\Im_{k-1}(\varphi)> - <\Im_k(\varphi)>}{<\Im_{k-1}(\varphi)> <\Im_k(\varphi)>} <\bar{B}_k> \right) <\Im_s(\varphi)> \right] \qquad (1)$$

where the term enclosed in [] is the approximation to $F^{\downarrow}$, $\Im_k$ is the level k to TOA transmittance, θ is the satellite zenith angle, φ defines the path of the transmittance function approximating the downward flux, B is the Planck function, ε is the surface emissivity (Note: the reflection is assumed to be isotropic) and the subscript **s** denotes the surface, which can be a topographical or cloud top surface. $\Re$, $\Im$ and B are functions of wavenumber and $<f>$ signifies that f has been convoluted with a response function and integrated over wavenumber. The emissivity is considered to be constant over a response function. For models M1 and M2, φ=θ and secφ=1.66 respectively.

Frequently it is easier to consider differences between equivalent brightness temperature, BT, instead of radiance when comparing models. BT(f) signifies that the radiance f has been converted to a brightness temperature. Conversions are made using the band correction coefficient method outlined in Planet (1988).

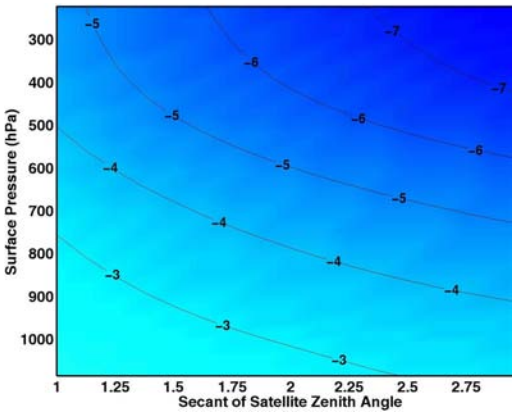

Fig 1: Comparison of the bias (K) across 52 atmospheres between BT($<\Im_s F^{\downarrow}>$) and BT($<\Im_s><F^{\downarrow}>$) for AIRS channel 1018.

Past experience shows that a term <ab> may not necessarily be approximated by <a><b>. There are many such terms in Eqn 1, particularly in the downward flux term. Figure 1 illustrates the mean of the difference between BT($<\Im_s F^{\downarrow}>$) and BT($<\Im_s><F^{\downarrow}>$) ,or bias, across a set of representative atmospheres. Even under this idealistic situation the biases are large. As there are many AIRS channels that exhibit similar behaviour this approximation cannot be relied on. Therefore any scheme to improve the ARDF model should also incorporate a correction to account for the decomposition of $<\Im_s F^{\downarrow}>$ in Eqn 1.

A simple approximation to the ARDF term was found that involves a simple transformation applied to the upward transmittance profile. The method makes the supposition that, on average, for a given surface pressure and zenith angle there exists a value $\varkappa$ which modifies $\Im(\theta)$ such that replacing $\Im(\varphi)$ with

$\Im(\theta)^{\kappa}$ provides a good estimate of the RDF term; ie,

$$\frac{(1-\varepsilon)}{\pi} <\Im_s(\theta)> \left[\left(\sum_{k=1}^{s} \frac{<\Im_{k-1}(\theta)>^{\kappa(p_s,\theta)} - <\Im_k(\theta)>^{\kappa(p_s,\theta)}}{<\Im_{k-1}(\theta)>^{\kappa(p_s,\theta)} <\Im_k(\theta)>^{\kappa(p_s,\theta)}} <\bar{B}_k> \right) <\Im_s(\theta)>^{\kappa(p_s,\theta)} \right] \quad (2)$$

κ is interpreted as a combination of a variable diffusivity factor which depends on the optical depth above the surface and a correction that takes into account the decomposition of $<\Im_s F^{\downarrow}>$.

The evaluation of κ is straightforward. First, the fast mean transmittance and Planck models are constructed. Then for each surface pressure and zenith angle combination a search for the optimal κ that minimizes

$$\left| \langle \Im(\theta,p_s) F^{\downarrow}(p_s) \rangle - \{\Im_s(\theta)\} \left(\sum_{k=1}^{s} \frac{\{\Im_{k-1}(\theta)\}^{\kappa(p_s,\theta)} - \{\Im_k(\theta)\}^{\kappa(p_s,\theta)}}{\{\Im_{k-1}(\theta)\}^{\kappa(p_s,\theta)} \{\Im_k(\theta)\}^{\kappa(p_s,\theta)}} \{\bar{B}_k\} \right) \{\Im_s(\theta)\}^{\kappa(p_s,\theta)} \right| \leq \delta \quad (3)$$

is implemented, where δ is an error criterion (ideally zero). The quantities enclosed by {} are obtained from the FFM. The procedure is repeated for a set of surface pressures and secants for each channel and the results set in a table.

For the creation of the new model, M3, $\{\Im_s(\theta)\}$ is first evaluated, followed by a determination of the relevant $\kappa(p_s,\theta)$ via bi-cubic interpolation within the κ-table, followed by the modification of $\{\Im_k(\theta)\}$ by κ which is used by the ARDF calculation (Eqn 1). It should be noted that since the values of κ are obtained by a minimization involving the fast model under consideration, they may not be directly applicable to a different model. For example, a set of κ derived for RTTOV may not necessarily be optimal for MSCFAST.

Simulations of Radiances

All quantities of the form $<f>$ are calculated with the fast LBL radiative transfer model (FLBL, Turner, 1995) assuming a non-scattering plane parallel atmosphere. These quantities were calculated for 52 diverse ECMWF model atmospheres (Chevallier, 2001) on 48 levels (.005 to 1085 hPa). The calculations were repeated for 17 zenith angles ($\sec\theta$ = 1 to 3. in .125 steps), 21 emissivities (0 to 1. in .05 steps), and 24 surface pressures (223 to 1085 hPa). The wide range of surface pressures accounts for a wide range of topographical surfaces and cloud tops. These calculations are repeated for all 2378 AIRS channels.

Quantities of the form $\{f\}$ are evaluated by a fast model. The basic FFM is that of M1 (RTTOV). M1 uses the same predictors and methodology described in Saunders et al (1999). The regression coefficients of the RTTOV fast transmittance model are generated from the FLBL calculations applied to the atmospheres and conditions described above. Model M2 is a modified version of M1 in which a second pass is made through the fast transmittance model for $\sec\varphi$=1.66. These transmittances are used to evaluate M2's downward flux, $\{F^{\downarrow}\}$. The new model, M3, is also a modified version of M1 in which the surface to space transmittance is modified by κ to form its effective value of $\{F^{\downarrow}\}$. The κ-table is constructed using Eqn 3 with M1 supplying the quantities $\{f\}$. The minimization is applied to 24 surface

pressures (223 to 1085 hPa) and 6 secants (1, 1.25, 1.5, 1.75, 2., 2.25) for each member of the 52 atmospheres. $\kappa(p_s,\theta)$ is the mean value of $\kappa(p_s,\theta)$ across the 52 atmospheres. In general the values of $\kappa(p_s,\theta)$ range between 0 and 2. They tend to decrease towards 0 with increasing optical depth; ie, with increasing surface pressure and increasing $\sec\theta$.

Results

The FLBL, M1, M2 and M3 brightness temperature for each atmosphere are evaluated for 6 secants, 21 emissivities and 24 surface pressures and the bias and standard deviation (stdv) of differences between the FLBL and the FFMs are evaluated. These statistics represent the FFM model error.

On average M3 is a faster algorithm than M2. It takes about 1.25 times more CPU time than M1, whereas M2 takes about 1.6 times longer than M1.

A sample of the comparison between the 3 models for a specific (ε, p_s, θ) as a function of AIRS channels is illustrated in Figs 2 and 3 along with the case where ε=1 (no ARDF). These figures only provide a snap shot of the total range of possibilities considered. Figures 4 through 7 illustrate the full variation of (ε, p_s, θ) for a couple of channels.

In channels where the weighting function peaks well above the surface there is no difference between the models. In all virtually all other channels M1's performance is poor, which is mostly due to the explicit angular dependency in $F^{\downarrow}$.

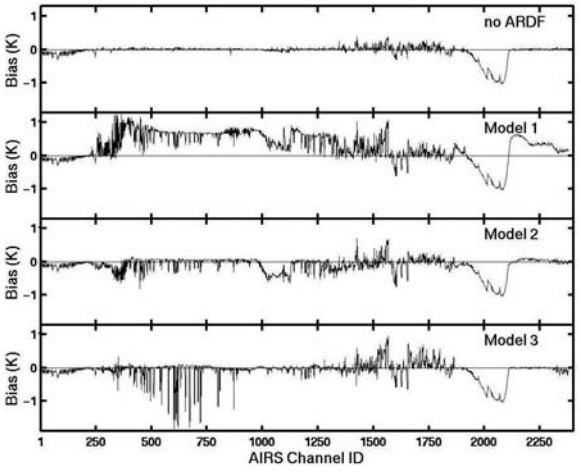

Fig 2: Bias of the differences between the FLBL and the 3 FFMs for ε=.7 and P_s=1013.25 hPa for a nadir view.

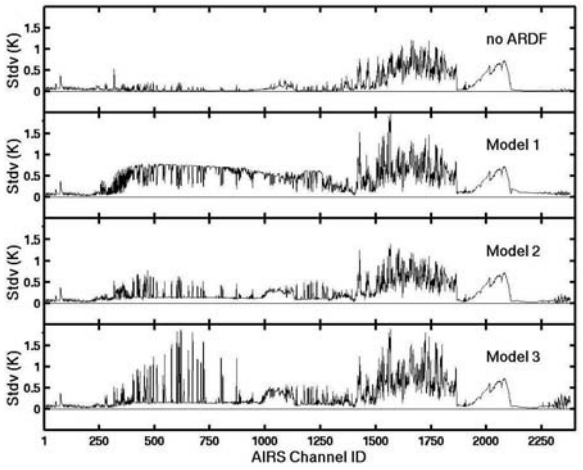

Fig 3: Stdv of the differences between the FLBL and the 3 FFMs for ε=.7 and P_s=1013.25 hPa for a nadir view.

M2 and M3 perform well over a wide range of ε and p_s in many channels, but does poorly in others. Both channels exhibit, at worst, a very small angular dependancy due to the explicit angular dependence of the return path, however the dependency is considerably smaller than that observed in M1. Both extend the range of ε and p_s where the biases are acceptablly small. In some channels M3 performs very well as seen in Fig.4, where the bias is acceptable over the entire range of ε and p_s. In other channels M2 performs better than M3 as in Fig. 6, but only in a few channels does M2 achieve the very low bias across the full spread of ε and p_s as M3 does. In many instances the biases are acceptably low for emissivities greater than .5 and surface pressures greater than 850hPa which is the sufficient for much of the global surface, ocean and land.

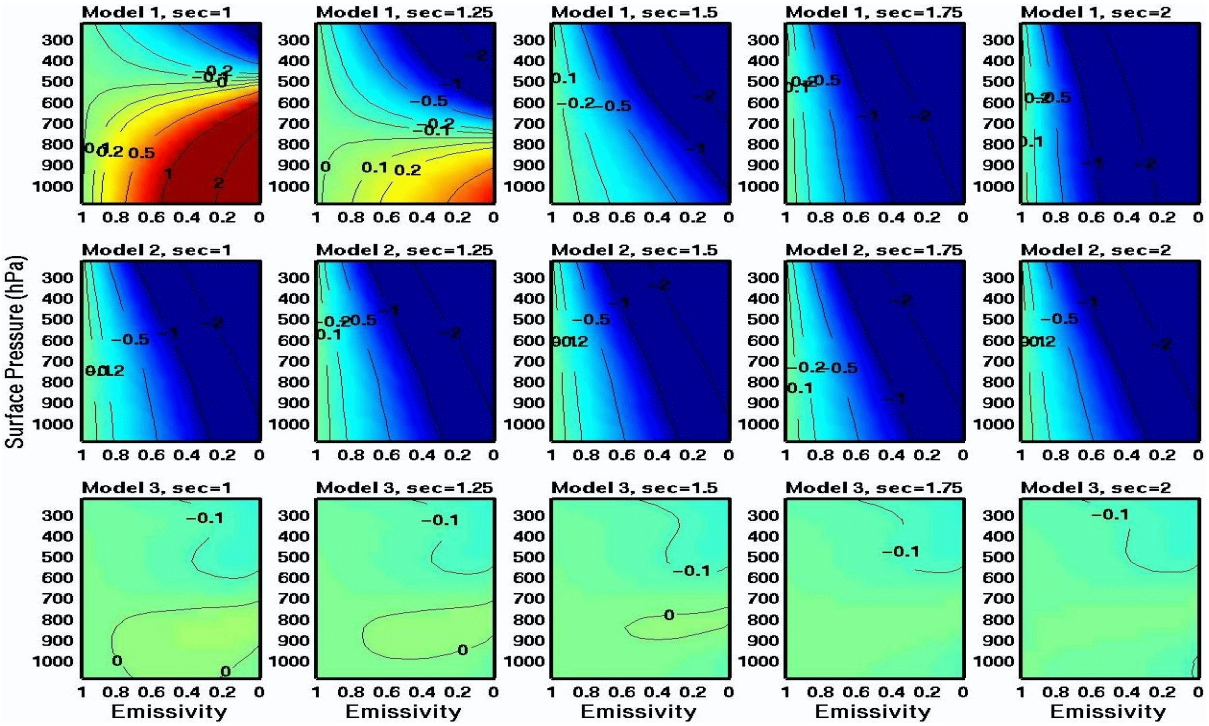

Fig 4: M1, M2 & M3 bias (K) as a function of surface emissivity, surface pressure and zenith angle secant for AIRS channel 1018 (1007.86 (cm^{-1})).

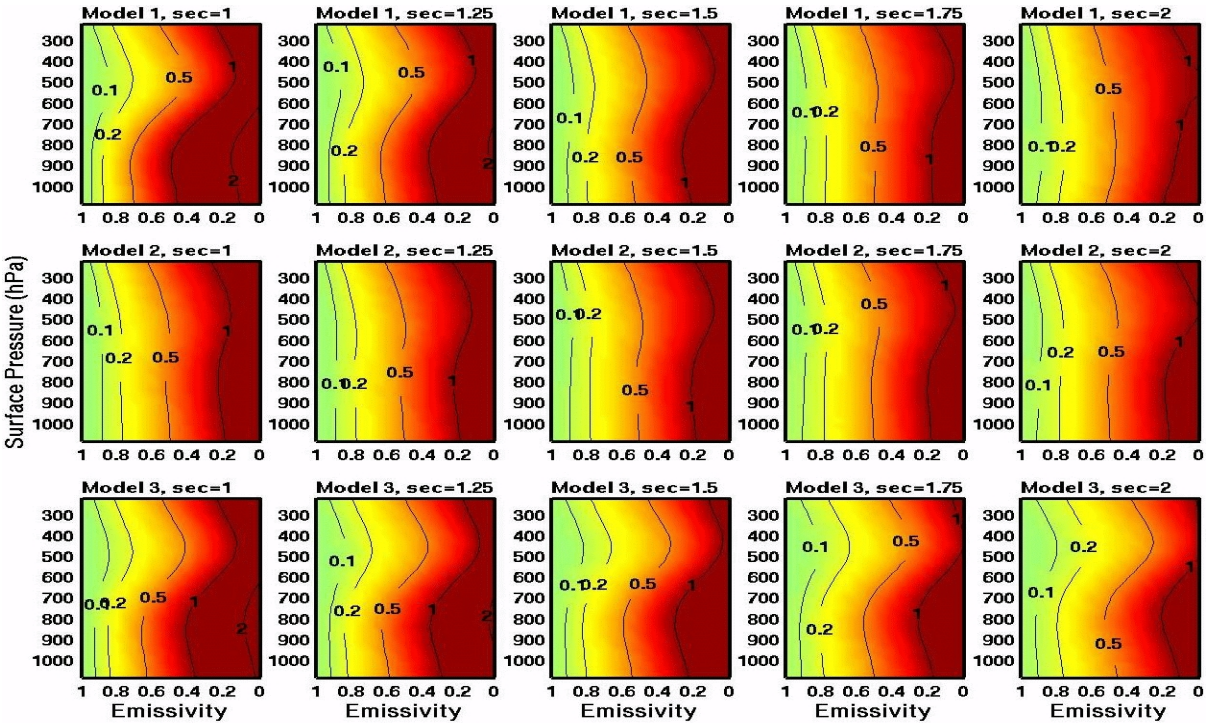

Fig 5: M1, M2 & M3 stdv (K) as a function of surface emissivity, surface pressure and zenith angle secant for AIRS channel 1018 (1007.86 (cm^{-1})).

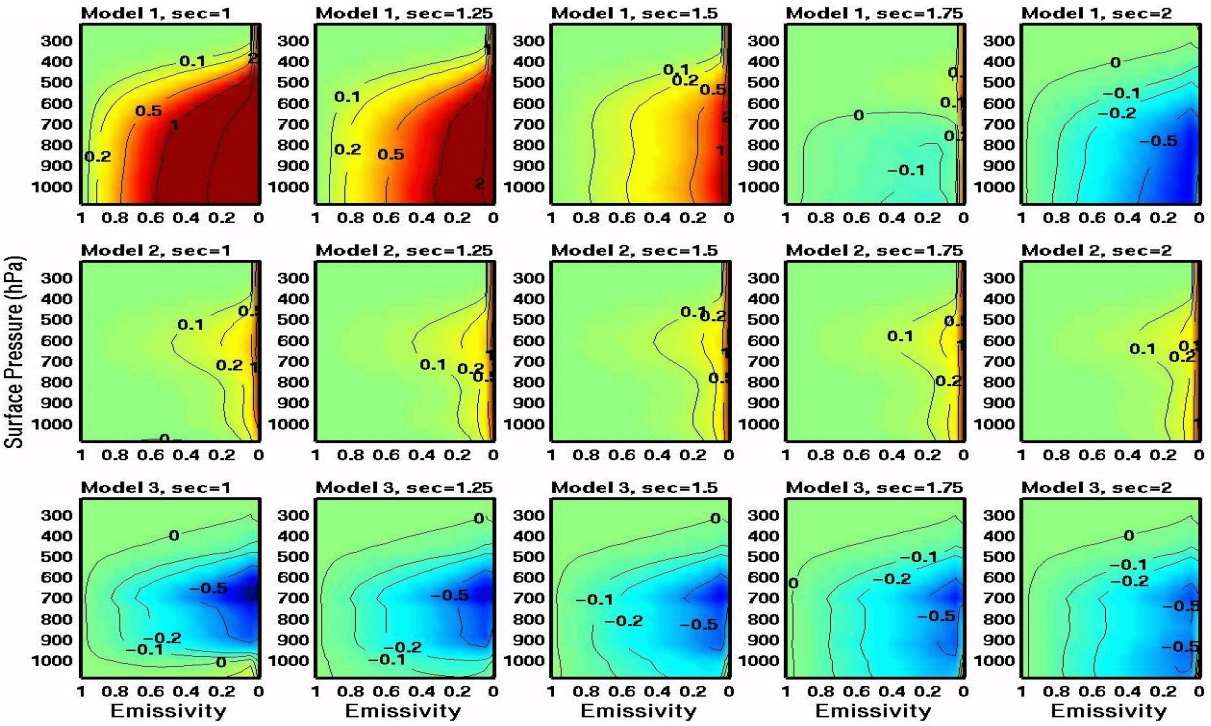

Fig 6: M1, M2 and M3 bias (K) as a function of surface emissivity, surface pressure and zenith angle secant for AIRS channel 610 (851.80 (cm^{-1}))

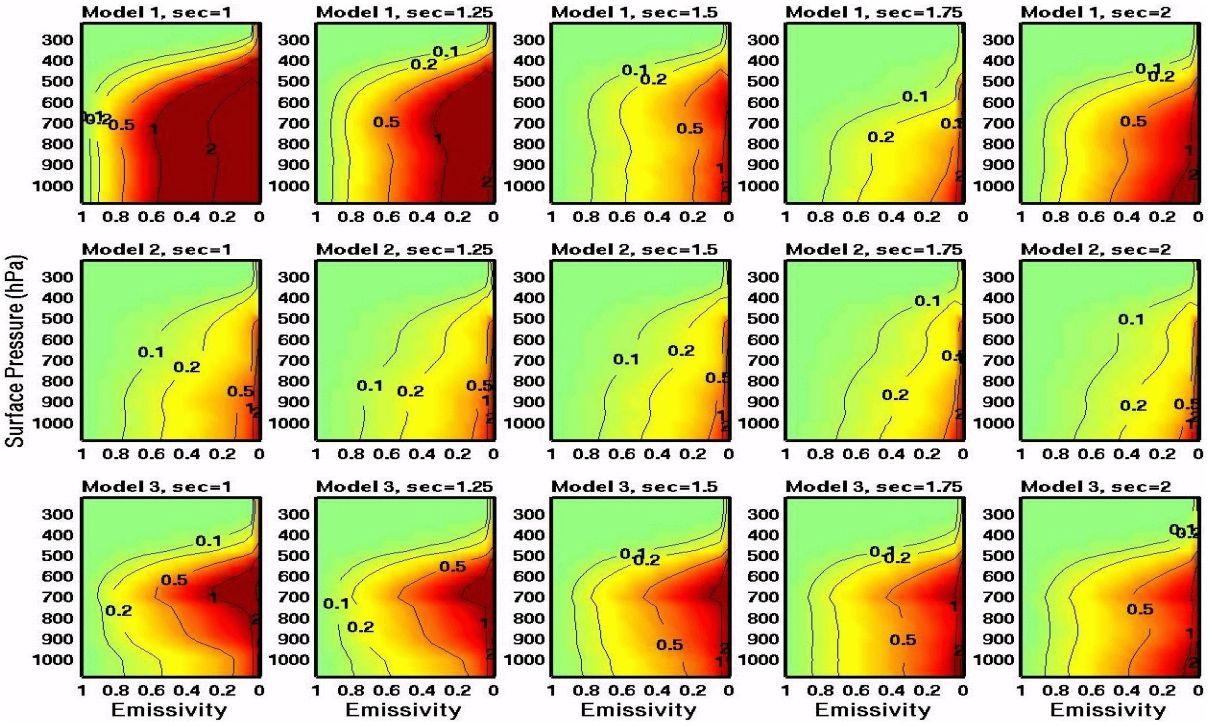

Fig 7: M1, M2 and M3 stdv (K) as a function of surface emissivity, surface pressure and zenith angle secant for AIRS channel 610 (851.80 (cm^{-1})).

The angle dependency of the M1 standard deviations is weaker than the bias. The patterns of stdv for M2 are generally similar to those of the average pattern (over secθ) of M1 and those of the new model are similar to M2 but occasionally better. Generally the stdv increases with decreasing emissivity. Except for the angle dependency, the stdvs are not very different over the three models.

Conclusions

An alternate algorithm has been developed which is more accurate than M1. Under many conditions it is as good as or better than the double pass model M2 and significantly faster in its execution compared with M2. Although demonstrated with the assumption of isotropic reflection, the scheme is actually independent of the angular distribution of the reflected energy, requiring only that the reflectivity be constant over the response function.

Unfortunately the new scheme is not yet consistently as good as the double pass method. Neither M2 nor M3 could be used exclusively over the entire AIRS spectrum without a penalty for many channels.. However, depending on the level of desired accuracy M3 could be used exclusively if the range of ε and p_s is constrained to emissivities and surface pressures greater than about .5 and 850hPa respectively. Exclusive use of M2 is possible under a somewhat more restricted regime. It is also possible that either model could be used exclusively under a carefully chosen subset of channels.

In principle one would expect that M3 would be the better model since it correctly allows for a variable diffusivity factor, however this is not always the case. There are many "spikes" in the bias and stdv

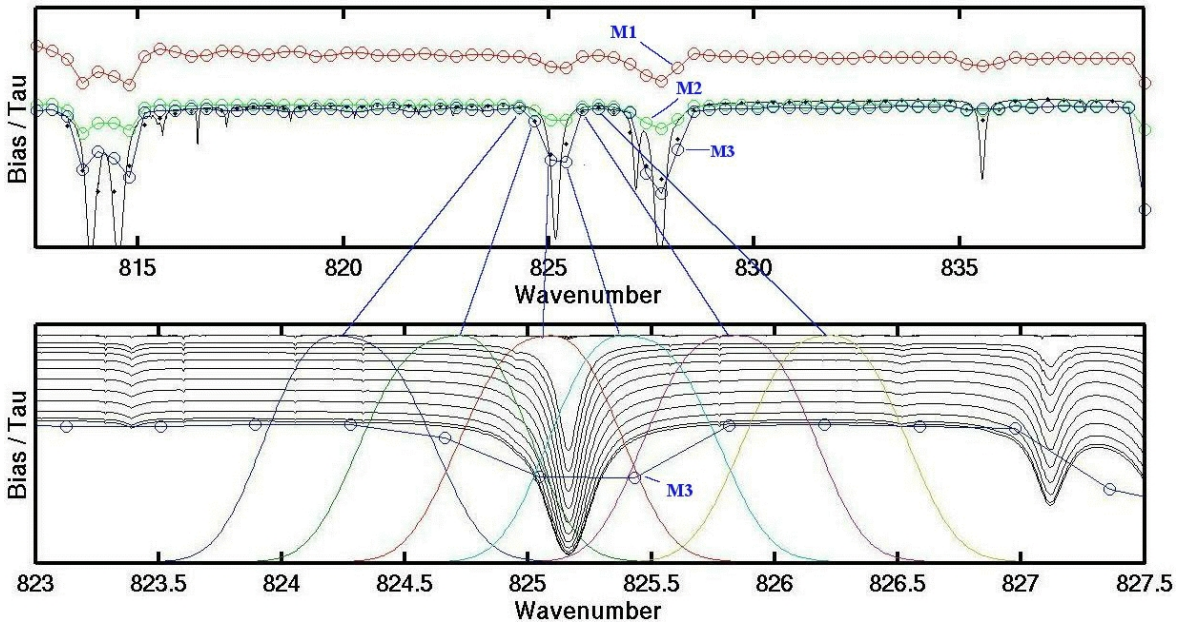

Fig 8: The upper box is an expanded view about channel 539 (825.046(cm^{-1})) of the bias curves of Fig 2. The dark line with no circles is the TOA transmittance spectrum from 1013hPA for a standard atmosphere. The lower box is a further expansion of the spectrum. In addition to some additional TOA transmittance spectra from various pressures, six AIRS response functions are superimposed.

curves of Figs. 2 and 3. It is in these regions where M2 does better than M3. Figure 8 is a high resolution examination of Fig 2 about channel 539. Here it can be seen that the bias of all three models 'spike', M1 improves and the others do not (the stdv also 'spikes' at these locations). When overlayed with a typical TOA transmittance spectra and AIRS response functions it can be seen that these 'spikes' collocate with moderate to strong transmission lines, specifically the near-wing and core regions where the transmission function is highly non-linear. Most of the spikes observed in Fig. 2 are collocated to water vapour lines

More study is required to determine if the spikes can be eliminated. The problem appears to be in the coefficient generation scheme since the bias and stdv have 'spikes' when the ARDF is excluded. Until the problem of the spikes can be resolved the only advantage M3 has over M2 is computational speed, otherwise either model can be used, or specific models for specific AIRS channels.

References

Chevallier, F., Sampled Databases of 60-level Atmospheric Profiles from ECMWF Analyses, SAF programme Research Report No. 4, EUMETSAT/ECMWF, 28pp, 2001.

Garand, L., D.S. Turner, C. Chouinard, and J. Hallé 1999. A physical formulation of atmospheric Transmittances for the massive assimilation of satellite infrared radiances, *J. Appl. Meteorol.* **38**, 541-544.

Liu, Quanhua and Johannes Schmetz, 1988. On the problem of an Analytical Solution to the Diffusivity Factor. *Beitr. Phys. Atmosph.*, **61**, 23-29.

Planet, W.G., Data Extraction and Calibration of TIROS-N/NOAA Radiometers. NOAA Tech. Memo. Ness 107-Rev. 1, U.S. Dept. of Commerce, Washington, D.C. U.S.A., 58pp, 1988

Saunders, R., M. Matricardi and P. Brunel, 1999. An improved fast radiative transfer model for assimilation of satellite radiance observations. *Appl. Opt.* **34**, 8396-8399.

Turner, D.S., 1995. Absorption Coeficient Estimation Using a Two Dimensional Interpolation Procedure, *JSQRT*, **53**(6) 633-637.

Turner, D.S., Revisiting the Attenuated Reflected Downward Flux Term of the Radiative Transfer Equation, in Technical Proceedings of the Twelfth International TOVS Study Conference, Lorne, Victoria, Australia, 27 Feb- 5 Mar 2002

Infrared radiative transfer modeling using the Optimal Spectral Sampling (OSS) method

Jean-Luc Moncet, Gennadi Uymin, Xu Liu and H. Snell

The OSS method is a simple and flexible approach to radiance modeling originally developed for the real-time processing of NPOESS/CrIS data. OSS-based models have been produced for the airborne NAST-I and AIRS instruments as well as for microwave sensors. The monochromatic treatment of the radiative transfer in OSS confers the ability to directly model non-positive ILS (such as interferometric functions) and to accommodate different observer altitudes (for airborne applications). In addition, it greatly simplifies the computation of analytical Jacobians and makes it possible to model scattering effects in an accurate and computationally efficient way. An overview of the theoretical basis and examples of applications of the OSS method will be presented. More details will be given in a companion poster.

Spectral surface emissivity for use in assimilation of IR radiance data over land

Małgorzata Szczech-Gajewska[1], Florence Rabier[2]

[1] *Institute of Meteorology and Water Management*
ul. P. Borowego 14, Kraków, Poland

[2] *Météo-France, 42 av. G. Coriolis*
Toulouse, France

Abstract

The interest of the usage of the very high spectral resolution satellite measurements, as from AIRS or IASI instruments, over land will certainly be growing in the next few years. Preparatory studies have begun with the creation of appropriate "climatological" maps for surface spectral emissivity (SSE), based on new Ecoclimap (Masson et al.2002) vegetation and land cover types and the infrared SSE values from spectral libraries (MODIS, ASTER and JPL) compiled with the ones modelled by Snyder et al. (1998). Separated emissivity maps were created for 18 wavebands in the infrared spectral range and for each month. The final maps were validated with MODIS channel 31 and 32 land surface emissivity products based on the split-window method, and in radiative transfer model RTTOV-7 with HIRS channel 8 and AIRS data.

I. Introduction

The use of very high spectral resolution satellite measurements over land, as given by AIRS or IASI instruments, will certainly increase in the next few years. Preparatory studies have begun with the creation of appropriate "climatological" maps for surface spectral emissivity (SSE). Here I will present maps of these quantities and their validation. Emissivity maps were prepared on the base of the new Ecoclimap (Masson et al.2002) vegetation and land cover types and the infrared SSE values from spectral libraries (MODIS, ASTER and JPL) compiled with the ones modelled by Snyder et al. (1998). New emissivity maps were produced separately for 18 wavebands in the infrared spectral range and for each month. The final maps were validated with MODIS channel 31 and 32 land surface emissivity products based on the split-window method. Further validation of this new SSE was performed by quantifying the impact brought by this new emissivity when computing simulated radiances for IR sounder. It was first carried out with the radiative transfer model RTTOV-7 with High-resolution Infra-Red Sounder (HIRS) channel 8 data. A further step has consisted in the validation with Atmospheric Infrared Sounder (AIRS) measurements. Extensive tests of the SSE with the AIRS data are currently performed.

To retrieve and assimilate the very fine spectral resolution measurements from advanced IR sounders (IASI/AIRS) we need to have the ancillary information (background) which specifies the behaviour of the variables or constitutes some a-priori constraints. In order to estimate the quality of the background information one need to compute the background error covariance, called B matrix. A first estimate of land surface skin temperature (LST) can be taken from model forecast, and surface spectral emissivity (SSE) can be provided by climatological values depending on the land cover type. To calculate the background error covariance for temperature (vertical profile + surface) the Ensemble method was used. For the emissivity the B matrix is calculated for 18 wavebands, separately for each of the different land

cover types. Chosen wavebands fully cover the IASI and AIRS spectral range. The data for emissivity climatological maps (SSE background) were taken from the MODIS spectral library. Additionally, preliminary experiments with emissivity as a control variable in a 1-dimensional variational assimilation model (1D-Var) have been run.

II. Land surface types and emissivity climatological maps

The new classification of surface types was based on the Ecoclimap a complete surface parameter global dataset (Masson, 2003). In general, areas of homogenous vegetation were represented by 215 ecosystems. They were derived by combining existing land cover maps, climate maps, normalised difference vegetation index (NDVI) inferred from observations of the Advanced Very High Resolution Radiometer (AVHRR) instrument and The Food and Agriculture Organisation (FAO) database of soil texture. Most of these ecosystems were a combination of only one of the following 12 vegetation types (so-called pure ecosystems): bare soil, rocks, permanent snow and ice, crops type C3 (omnipresent except tropical and equatorial belts, and where the corn is intensively cultivated), crops type C4 (applied for crops C3 exceptions), irrigated crops, natural herbaceous (temperate), natural herbaceous (tropics), wetland herbaceous or irrigated grass, needleleaf trees, evergreen broadleaf trees, and deciduous broadleaf trees. Those pure ecosystems with addition to urban areas and water gave us full description of 14 simplified global land cover types, for further emissivity assignments. Currently in the climatological files for the ARPEGE model, 5 land cover types exist: high vegetation, low vegetation, bare soil, permanent ice and water. ARPEGE cover types were believe to be representative enough to use them for the characterization of the emissivity background errors.

The Infrared Atmospheric Sounding Interferometer (IASI) range (645-2760cm^{-1}, 8461 channels) got divided into 18 wavebands with respect to their usefulness for the channel selection (informative bands). The wavebands have been chosen narrower and denser in areas with high (>0.5) transmittancy running average over 40 channels. This was done in order to follow the variability of the land cover types spectra and to validate the emissivity climatology created from MODIS emissivity maps (channels 31 and 32). The resulting wavebands are:

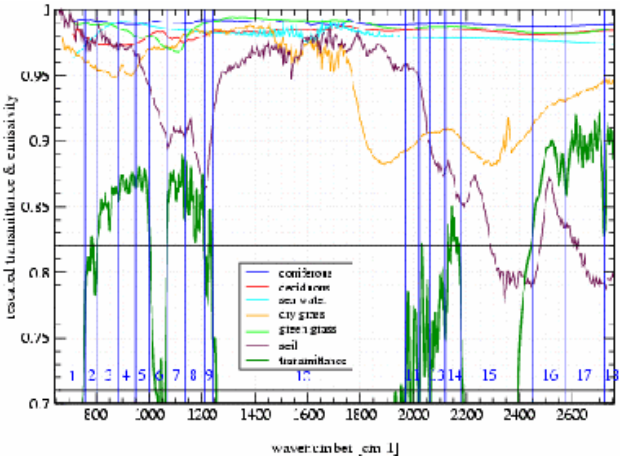

Fig.1: IASI transmittance and emissivity spectra of different land cover types. Transmittance (thick green) is a running average over 40 channels (scaled by 1/3 then shifted by 0.6).

645-760, 760-805, 805-885, 885-950, 950-1000, 1000-1068, 1068-1135, 1135-1210, 1210-1240, 1240-1968, 1968-2020, 2020-2064, 2064-2120, 2120-2180, 2180-2450, 2450-2575, 2575-2720, 2720-2760cm^{-1}. Climatological fields of surface spectral emissivity were created respectively to these wavebands. The creation was based on the global new land cover types and vegetation maps with resolution of 0.5 all over the globe (Masson, 2003) and SSE calculated for each of 14 simplified types from separate emissivity spectra of different natural and man-made materials. Then, the SSE maps were taken as an input for the modified climatological configuration of the ARPEGE model in which emissivity was interpolated to the final model grid.

III. Validation of the SSE maps

The validation of the spectral emissivity climatological maps has been done in a few steps. Firstly we have compared (subjective) SSE maps for wavebands 805-885cm^{-1} and 885-950cm^{-1} with the MODIS emissivity maps for channels 32 and 31 respectively. The next step consisted in testing of the new SSE in the radiative transfer model RTTOV-7 with use of observations of HIRS instrument channel 8, which points to the surface. Finally, tests were performed with real AIRS data in preselected 324 channels (also using RTTOV-7).

MODIS

The Moderate Resolution Imaging Spectroradiometer (MODIS) instrument on board NASA's Terra satellite routinely retrieves land surface products, and SSE among them. The method used for retrieval of emissivity maps which were used for our initial comparison was the 'split-window' technique, using MODIS bands 31 (centered at 900cm^{-1}) and 32 (833cm^{-1}). These data are avaliable at 1 km spatial resolution, and temporally divided into groups: individual swath data, 1-day average and 8-day average. Fig.2 presents an example of comparison of the surface spectral emissivity climatological map in band 4 for the month of August against the MODIS SSE composite of individual swaths for the 20 of August 2000. One can note a good correspondence between these emissivity fields.

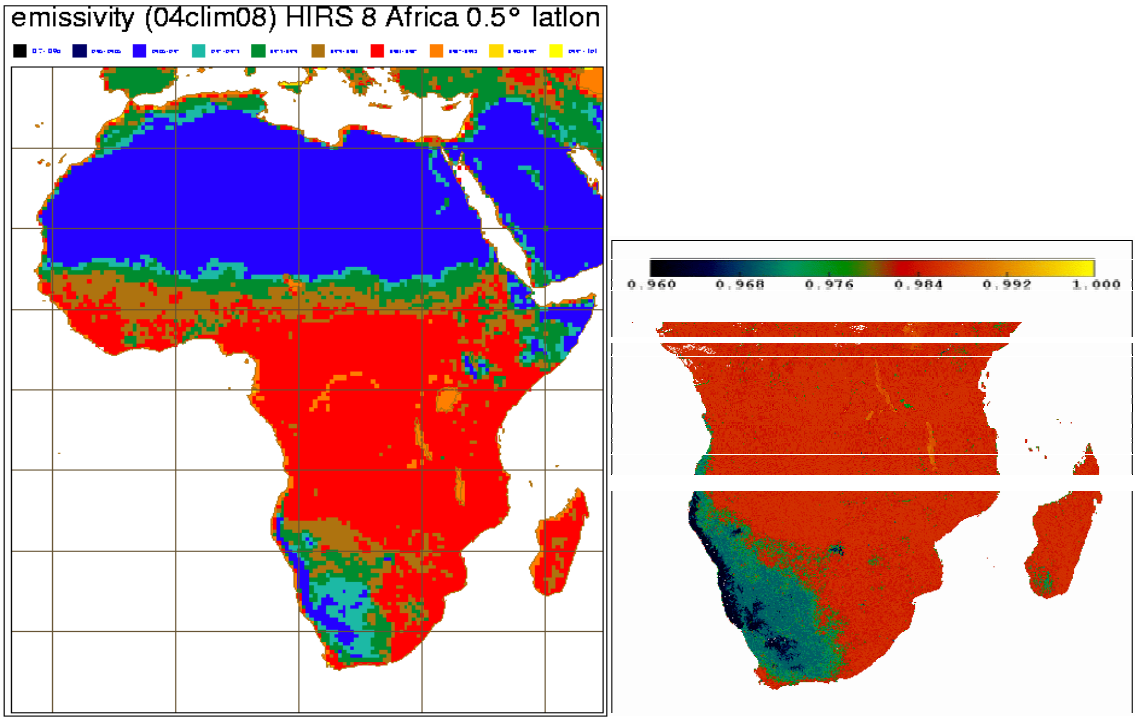

Fig.2: On the left side - climatological map of the SSE for the month of August, and on the right one the SSE composite map retrieved from MODIS band 31 measurements. Both figures have the same colour scale.

Also for other areas of the globe, not presented here, the agreement between both kinds of maps was also high. MODIS data are free of charge and can be accessed from the webpage referenced in bibliography.

HIRS-8

As it was already mentioned, the new SSE was also tested against observations of the HIRS instrument, for channel 8. This channel is centered at 900 cm^{-1} with half-power bandwidth equal to 35 cm^{-1}. It corresponds very well to MODIS band 31, is very sensitive to surface parameters and it can be used to detect cloud contamination. As we work with surface data, there is a strong requirement that the radiances we use were measured in clear sky conditions. Tests have been done on the differences

between measured and the forecasted brightness temperatures (obs-guess) in this channel window. As a forecasted brightness temperature (Tb) we use the brightness temperatures calculated in RTTOV-7 from atmospheric state vector taken from the 6-hour ARPEGE model forecast. This state vector is a vertical atmospheric profile containing the temperature and humidity at 43 pressure levels, surface air and skin temperature, surface pressure and surface spectral emissivity. A cloud test to eliminate the cloudy points we applied on channel 8, assuming that for clear sky conditions the difference between measured and the forecasted Tb lies in between -1 and 2K and is

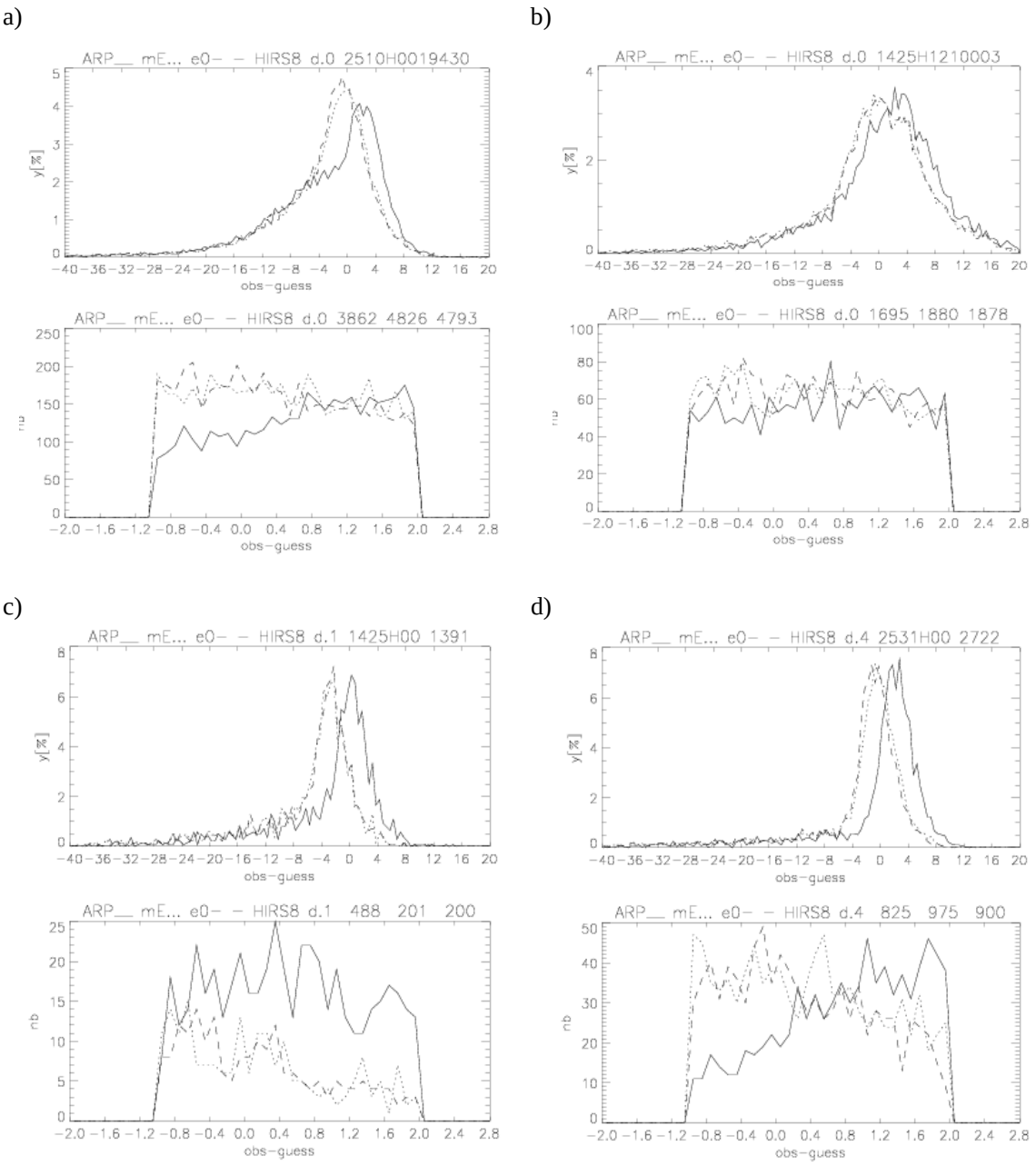

Fig.3: Histograms of obs-guess values for different days and domains. a) and b) are cumulated over the whole globe, c) over Europe and d) over Africa. Temporal ranges are: a) 25-31.12.2002 cycle 00z, b) 14-25.06.3002 cycle 12z, c) as "b" but cycle 00z, d) as "a". Upper graphs shows distribution of obs-gues values for the whole sample, while the bottom ones only show 'not cloudy' points. Solid line corresponds to used ARPEGE emissivity, dotted one to the new SSE, and dashed line represents the results with RTTOV-7 emissivity.

not latitude dependent. To evaluate the quality and usefulness of the new climatology for emissivity, we

compared the values of obs-guess with the RTTOV-7 run for different values of surface emissivity for the same state vector. As a first reference run, the emissivity from ARPEGE was used, i.e. SSE=0.93 for dry land, 0.99 for moist land and partial snow cover and 1.00 for ice-caps and full snow cover. The second one was RTTOV7 run with its own emissivity value, i.e. SSE=0.98 everywhere for land. All the tests were performed on the same sample of initial profiles. On Fig.3 the top graphs represent histograms of the full range of obs-guess values, and the bottom ones - the number of cloud free or small obs-guess points in each sample. The solid line is the ARPEGE reference, the dotted one corresponds to the new SSE, and the dashed one to the RTTOV reference. Note the values written in the titles of the bottom graphs: they are the number of profiles for which obs-guess values pass the 'cloud test' for the three emissivity used. The various panels a) to d) correspond to the various areas and times of day.

The results are not obvious to interpret, they do not show clearly and unambiguously the general improvement of the estimated Tb converted by the radiative transfer model with the use of the new surface emissivity. We compared the number of profiles for which the difference: observed Tb and estimated one in RTTOV, had stayed in the range -1 to 2K ('cloud test'). What we can observe is that for the period of 25.12.2002-10.01.2003 use of new SSE considerably improves the values of simulated brightness temperature in comparison with the ones obtained with the use of the SSE from the ARPEGE model (on fig.3a dotted and solid lines). On the contrary for the period of 14-25.06.2003, especially over Europe, the use of the surface emissivity from the global model gave the best results (fig.3c). One explanation of that could be the unusally hot and dry summer in that region this year. The state of vegetation was not similar to the 'climatological' one. It means that instead of green grass and crops there were dry ones. As one can see on fig.1 the difference between dry and green grass emissivity spectra in band nr.4 (corresponding to HIRS channel 8) was significant. So, as the result SSE=0.93 (as it is in ARPEGE) appeared to be better for that unusual period than the new SSE with values between 0.973 and 0.987. Also there was noticed dependence between low emissivity areas and values of SWI (soil wetness index) taken from the ARPEGE model. For the next tests we want to use SWI additionaly to land cover type in estimation of local emissivity value. Considering Tb calculated with the use of SSE=0.98 (RTTOV default value for land) as a reference, seems that that the new SSE did not improve very much the estimation of brightness temperature. In some cases the difference in the number of 'good' points was negligible (fig.3abc), in others it could reach up to 8 percent (fig.3d).

Table 1. Comparison of the number of 'good points' with use of new SSE against emissivity from RTTOV-7 and ARPEGE, for all periods together for different domains.

	globe	Europe	N Am	S Am	Africa	Austral	Asia	Antarct
RTTOV-$7_{(0.98)}$	2,9%	1,7%	2,2%	-3,10%	10,8%	4,30%	3,7%	0,7%
ARPEGE	16,5%	12,8%	11,6%	-2.4%*	30,3%	50.3%*	12,9%	0,3%

In table 1 are presented results of the comparison tests for all tested periods together, for different domains. The values mean by how many more “good points” were for Tb estimation in radiative transfer model with use of the new SSE. Negative values (as it is for South America) mean that in average (over all tested periods) new SSE was giving worse Tb. The comparisons against ARPEGE emissivity, as for South America as for Australia (*) could be neglected because of low resolution of the ARPEGE model on that areas (it has stretched geometry).

In general one can say that the use of new SSE decreased the difference between measured and the simulated brightness temperatures, or stayed neutral. But there could exist exceptions while some extreme, long term atmospherical conditions appeared. Moreover some additional tests on just clear sky profiles could give more detailed ideas about the new SSE behaviour.

AIRS

For the validation of the new SSE with AIRS measurements, the same strategy was applied, with a different cloud detection and channel selection. The AIRS cloud detection scheme was based on multichannel data, and it has been found to be quite sensitive to small clouds only partially filling the field of view, optically thin cloud and stratiform cloud with a top temperature near identical to the surface (McNally,2003). So, it was more accurate with comparison to the 'cloud test' applied to HIRS 8 data. Additionally the AIRS imager was also used to detect clouds. As a result the validation of the new surface emissivity has started on profiles for purely clear sky conditions.

As the Atmospheric Infrared Sounder is an instrument with very high spectral resolution the use of all 2378 channels is not practical and efficient. So thinning of the data was advised and a subset of 324 channels was prepared by NOAA AIRS Science Team. These channels were grouped into the 18 earlier mentioned bands, but because of some differences in spectral coverage of IASI and AIRS instruments, the wavebands number 11, 12, 13, 14 and 18 were out of AIRS range. Additionally in ARPEGE 1D-VAR satellite radiances assimilation there was no ozone analysis included, so channels from bands 5, 6, 7 and partially 9 were blacklisted from the assimilation process (i.e. they do not enter the analysis). The other problem was caused by 'solar contamination' in the short wavelength part of the spectrum. Channels touched by this problem could be used by night, but then the AIRS imager could not be used to detect clouds. As a consequence we rejected also the wavebands 16, 17 and partially 15. From the remaining bands we also excluded the ones with low transmittancy values (these channels were not seeing the surface), namely number 1, 10 and also 2. Finally only two full bands remained: 3 (four channels) and 4 (four channels), and partially band 9 (one channel) and 15 in the longwave part. Considering the usefulness of the bands we neglected band 9 because of a lack of channels to compare with and to analyse the impact of the SSE. From waveband 15 we kept four longwave channels pointing to the levels closest to the surface.

Summarizing, for SSE validation with the AIRS data and subsequently in 1D-VAR we could use three bands 3, 4 and 15, with 12 channels. As we intend to use the same wavebands for 1D-VAR, the new B matrix has been calculated just for these bands, and very high correlation was found between adjacent bands 3 and 4, and almost zero correlation of these two bands with band number 15. For simplicity reason (diagonal B) we merged wavebands number 3 and 4 as the average emissivity values in those were relatively close. And the result was, that finally we would use 8 channels: four from merged bands 3 and 4, and four from band 15.

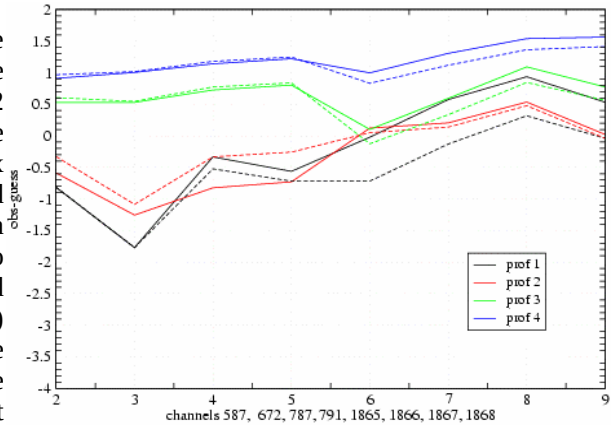

Fig.4: Obs-guess values of Tb for 8 selected channels in 2 bands. Continuous line refers to SSE=0.98 (RTTOV, reference), the same colour but dashed line corresponds to new SSE.

First validation tests were performed for 4 randomly chosen profiles over land. As it can be seen on fig.4 introducing the new SSE values for separated channels in wavebands improved the estimation of the brightness temperatures from the atmospheric state vector especially for band 15. The integer values of x axis from 2 to 9 correspond respectively to AIRS channels: 587, 672, 787, 791 (merged bands 3 and 4) and 1865, 1866, 1867, 1868 (band 15). Further tests will be performed on a larger sample of profiles.

IV. Background error statistics

To retrieve and assimilate the very fine spectral resolution measurements from advanced IR sounders (IASI/AIRS) one need to have the ancillary information (background) which specifies the behaviour of the variables or constitutes some a-priori constraints. In order to estimate the quality of the background information one need to compute the background error covariance, called B matrix. This matrix is one of the most important elements of the data assimilation system - it determines the filtering and the propagation of the observed information. We were estimating the B matrices for temperature profile with LST and for emissivity.

Temperature

As a background (first guess) for the temperature we used the 6h forecast from the ARPEGE model. To estimate the background errors with Ensemble method we projected the ensemble of forecasts onto ARPEGE gridpoint space (truncation T199) and interpolated onto 43 RTTOV7 levels. The final ensemble was composed of 10 independent 3d-var analysis experiments for the month of May

2001. For consecutively numbered members were calculated the differences between the background fields for each 6h cycle, so the statistics were based on 234 background differences. From them we calculated the background error covariances, separately averaged over gridpoints of land, sea and globally. The surface is the 44th level. The correlations for high atmosphere levels haven't looked realistic, the reason for that was the extrapolation from 31 ARPEGE levels to 43 in the radiative transfer (RT) model. In the stratosphere RT has 14 levels and ARPEGE only 3, next 15 RT levels (stratosphere and upper troposphere) correspond to 12 in the forecast model. Just for the lower troposphere (below 500 hPa) an equivalent spanning of levels between ARPEGE and RTTOV7 is satisfactory : 16 model levels refer to 14 of RT.

The global B matrix generally used in radiative transfer model was calculated at ECMWF (J.-N. Thepaut), also using the Ensemble method, but the interpolation to 43 RT levels was from 60 levels in the IFS model, which allow a better description of the high atmosphere. Because none of the B matrices is experimental and we wanted to keep the land surface characteristics and remove "noise" from the top of the atmosphere, we decided to mix both matrices - the present one for land and the ECMWF one. A "transition matrix" for combining them was used.

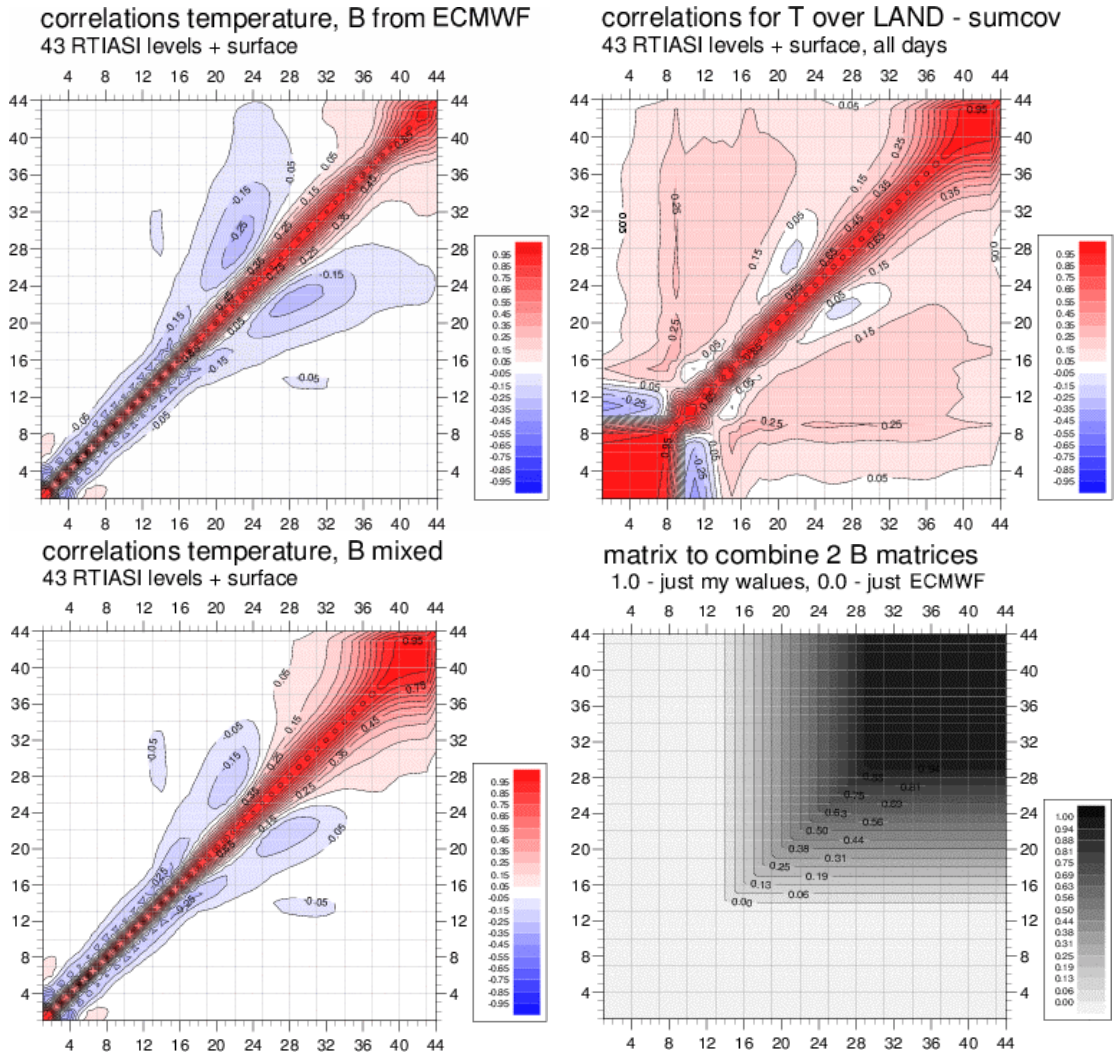

Fig.5: Creation of the final B matrix for land. The ECMWF B matrix was actually the matrix calculated by J-N Thepaut.

For the first 14 RT levels it keeps just the ECMWF covariance, above the 29th level just mine, and in-between a mixture of both matrices, with a linearly growing ratio (with a step of 6.25%). The original matrices, the transition matrix and the final one are shown on Figure 5.

Created in such a way, the matrix is non singular, and 1D-Var tests with this matrix have given positive results.

Emissivity

As it was mentioned before the estimation of the emissivity covariance matrices has been based on 5 ARPEGE land cover types as there has not been enough emissivity spectra samples to built separate background error covariance (B) matrices for each of new 14 types. Emissivity data (laboratory measurements) were taken from the MODIS and ASTER spectral libraries. We obtained from there about 270 samples of different kinds of natural and man made materials. "Sample" means the infrared emissivity spectrum of some plant or material (range: 600-3000cm^{-1}).

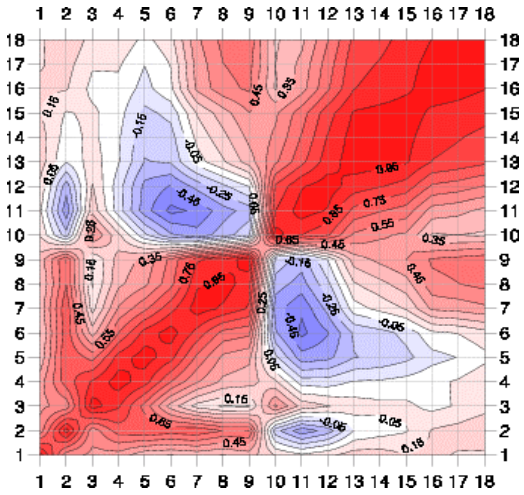

Fig.6: Correlations of SSE for 18 spectral wavebands for bare soil.

First the mean emissivity value per waveband and per sample was estimated, and then we average them for each land cover type. Next, in each waveband we calculated the differences for each land type, and afterwards emissivity covariances for all 18 bands. Calculation of statistics were done for -log(1-SSE). On the fig.6 are shown the correlations for bare soil type as the most representative one. For the bare soil we obtained the biggest number of emissivity samples. The numbers of the samples for other types were much smaller and not really sufficient to make the statistics on them. Although the SSE of high vegetation and ice have shown very strong correlations between all wavebands. It could be caused by the lower variability of their spectra with wavenumber. A different case is for bare soil emissivity and partially for low vegetation. For bare soil, surface spectral emissivity can change from 0.77 to 1.0 in IR IASI range (645-2760cm^{-1}); for low vegetation it can change from 0.88 to 0.98.

IV. 1D-Var

A scheme of 'one-dimentional variational analysis' (1D-VAR) is a method for extracting information from satellite measured radiances for use in the data assimilation system. It is based on the same principles as 3DVAR just applied to the analysis of atmospheric profile in a single location, using a forecast profile and its error covariance as a constraint. Brightness temperatures corresponding to the state vector x are computed using the radiative transfer model RTTOV-7. The used background covariance matrices, B, for temperature and emissivity are those described above, with more details in Szczech-Gajewska (2002).

Works on the non-linear 1D-VAR have begun, but still there no results to present. Up to that moment the introduction of emissivity as a control variable have been applied, but not yet tested.

V. Conclusions

In conclusion, the new emissivity maps based on the Ecoclimap are consistent with MODIS SSE maps retrieved with the 'split-window' method for bands 31 and 32. Usage of the local surface spectral emissivity (the closest point to the position of profile) in radiative transfer model RTTOV-7 with HIRS 8 data have not clearly shown that the estimation of the brightness temperature from atmospheric profile were really improved with comparison to the default SSE value for RTTOV-7, but were usually better than with the emissivity currently used in ARPEGE. In the case of Tb simulated with ARPEGE SSE being the reference, the increase of the number of 'good' points while using the new surface emissivity reaches up to 30% globally (with some exceptions).

Preliminary results for AIRS data showed that we could expect Tb values simulated in RTTOV with new SSE closer to the measured ones. But the validation on more numerous sample of profiles is still required. Finally the work on 1D-VAR must be continued on the inversion of radiances and emissivity retrieval. Tests with background error covariances matrices, especially the one for T, with explicit correlations between Ts and atmospherical T should be performed.

References

Belo Pereira, M. 2002. Improving the assimilation of water in a NWP model. *ALATNET Newsletter 4*

Masson, V. 2003. A Global Database of Land Surface Parameters at 1-km Resolution in Meteorological and Climate Models. accepted to *Journal of Climate*, 2003, vol.16

McNally, A., Smith, J., Watts, P. 2003. Performance of a high spectral resolution cloud detection scheme for AIRS data used at ECMWF. *proceedings of Symposium on Earth Observation and Satellite Meteorology*

Snyder, R. 1998. Classification-based Emissivity for Land Surface Temperature Measurement from Space. *Int. J. Remote Sensing*, vol.19, no.14, 2753-2774

Szczech-Gajewska, M. 2002. Parametrisation of background error statistics for surface parameters (LST, SSE), to be used for future assimilation of advanced IR sounders over land. *ALATNET Newsletter 5*

Laboratory emissivity data were taken (autumn 2001) from:
http://speclib.jpl.nasa.gov/
http://asterweb.jpl.nasa.gov/
http://www.icess.ucsb.edu/modis/EMIS/html/em.html

MODIS hdf files were ordered from:
http://edcimswww.cr.usgs.gov/pub/imswelcome

Atmospheric Spectroscopy with AIRS: Validation of the AIRS Forward Model

L. Larrabee Strow

The high spectral resolution radiances measured with the Atmospheric Infrared Sounder (AIRS) launch on NASA's AQUA platform in May 2002 are providing a unique data set for improving our understanding of atmospheric emission spectra, which will hopefully lead to improved weather and climate products without the need for empirical tuning of these products. We have compared radiances observed with AIRS to radiances computed from ECMWF analysis/forecast products, and computed from a wide range of radiosonde measurements recorded coincident with an AIRS overpass. Our analysis of these results concentrate on clear, night, ocean conditions where the surface emissivity should be well known, and the detection of cloud-free fields-of-view is most accurate. We now have a dataset that includes large numbers of nominally clear observations over many months, allowing accurate statistical analysis, at least for the ECMWF comparisons. Results assessing the accuracy of various formulations for the water vapor continuum will be discussed, both in the atmospheric windows and inside the strong water band centered at 6.7 microns. In addition we will present analysis of the validation of the temperature sounding channels that are influenced by carbon dioxide emission.

Validation of Satellite AIRS LST/LSE Products Using Aircraft Observations

Robert O. Knuteson, Brian J. Osborne, Henry E. Revercomb, and David C. Tobin
University of Wisconsin Space Science and Engineering Center, Madison, WI, USA

William L. Smith, Sr.
NASA Langley Research Center, Hampton, VA, USA

Introduction

Weather satellites have shown positive impact on forecast models for data collected over the world's oceans. However, the use of weather satellite data over land areas has been limited. One of the problems faced by users of broadband infrared measurements is the inability to separate the effect of land surface temperature (LST) from natural variations in land surface emissivity (LSE). A new generation of infrared sounders has been developed for obtaining improved profiles of atmospheric temperature, water vapor, and trace gas concentrations. A characteristic of these advanced sounders is the use of spectrometers with nearly continuous coverage of the 8-14 micron infrared window region with resolving powers of 1000 or greater. These high spectral resolution sounders have the advantage of being able to resolve individual absorption lines of water vapor and carbon dioxide and thereby provide a number of transparent "microwindows" that require a smaller atmospheric correction than broad-band instruments. In addition, it has been recognized that high spectral resolution infrared observations have another important advantage over broad band measurements in that they allow an effective surface temperature to be determined simultaneously with an effective land surface emissivity. A method for emissivity – temperature separation using high spectral resolution infrared observations has been developed at the University of Wisconsin Space Science and Engineering Center (UW-SSEC) in conjunction with NASA Langley Research Center (LaRC). The algorithm has been applied to UW-SSEC's ground-based Surface-Atmospheric Emitted Radiance Interferometer (S-AERI), the UW-SSEC Scanning High-resolution Interferometer Sounder (S-HIS) aircraft instrument, and the NPOESS Atmospheric Sounder Testbed – Interferometer (NAST-I) operated by NASA LaRC. Recently data from the NASA Atmospheric InfraRed Sounder (AIRS) satellite instrument have been compared with measurements from these ground-based and high altitude aircraft over the U.S. Department of Energy Atmospheric Radiation Measurement (ARM) Southern Great Plains (SGP) site in north central Oklahoma, USA. The lessons learned from this analysis have implications for the future operational use of data from the NPOESS CrIS and the METOP IASI sensors.

This paper includes the results of a ground-based survey of the validation site, results of a simulation of top of atmosphere upwelling infrared radiance observations at high spectral resolution, analysis of aircraft observations over the ground site, and comparison with results derived from the AIRS satellite instrument.

ARM Site Survey

The UW-SSEC conducted a ground-based survey of the DOE ARM SGP site in north central Oklahoma (USA) over a period of several years (1996-2003). This survey includes both a characterization of the land cover/land use in the vicinity of the ARM SGP central facility and

detailed measurements of the surface emissivity of selected land types. One of the co-authors developed the methodology shown in Figure 1 for the classification of the land cover (Osborne et al. 2003). The upper panel shows the 8x8 mile grid used in the ground-based survey of land cover while the lower pie chart shows the percentage occurrence of each class. The land cover is a mixture of permanent grassland pasture intermixed with fields of winter wheat and/or bare soil. The density of the wheat grass in each field leads to a change in the vegetation fraction during the growing season (from 0 to 100%). Figure 2 presents the results of the ground-based surface emissivity survey with the UW-SSEC S-AERI instrument (Knuteson et al. 2003). The key result from the emissivity survey is that the wheat field measurements can be represented as a linear combination of measurements of "pure" scene types; vegetation (grass) and bare soil (quartz mineral).

Simulated High Altitude Observations

This paper will follow the theory outlined in Knuteson et al. (2004). The cloud-free radiative transfer equation, neglecting solar radiation and scattering effects, for a downlooking infrared sensor viewing a homogeneous surface is given by the following equation

$$I_\nu = \int_0^Z B_\nu[T(z)]\frac{\partial \tau_\nu(z,Z)}{\partial z}\,dz + \varepsilon_\nu \cdot B_\nu(T_S)\cdot\tau_\nu(0,Z) + (1-\varepsilon_\nu)\cdot\tau_\nu(0,Z)\int_\infty^0 B_\nu[T(z)]\frac{\partial \tau_\nu(z,Z)}{\partial z}\,dz,$$

where I_ν, ε_ν, B_ν, T_s, $\tau_\nu(z_1,z_2)$, Z, and T(z) are observed spectral radiance, spectral emissivity, spectral Planck function, the surface temperature, spectral transmittance at wavenumber ν from altitude z_1 to z_2, sensor altitude, and air temperature at altitude *z*, respectively. The first term of the equation is the emission from the atmosphere above the surface, the second term is the direct emission from the surface that reaches the sensor, and the third term is the downwelling atmospheric emission reflected off the ground under the approximation of a lambertian surface. The emissivity can be formally expressed (below) where R^{OBS} is the observed upwelling radiance,

$$\hat{\varepsilon}_\nu = \frac{[R_\nu^{OBS} - N_\nu^{\uparrow}] - \tau_\nu \overline{N}_\nu^{\downarrow}}{\tau_\nu B_\nu(\hat{T}_S) - \tau_\nu \overline{N}_\nu^{\downarrow}}$$

$$\frac{de_\nu}{e_\nu} = \frac{-B_\nu(T_S)}{B_\nu(T_S) - \overline{N}_\nu^{\downarrow}} \bullet \frac{dB_\nu(T_S)}{B_\nu(T_S)}$$

N^{UP} represents the upwelling emission from the atmosphere only and N^{DN} represents the downwelling flux at the surface. The ^ symbol denotes "effective" quantities as defined in Knuteson et al. (2004). The fractional change in emissivity is shown to vary on and off of spectral emission lines according to the reflected infrared radiance.

Figure 3 shows the result of a simulation of upwelling infrared radiance at 20 km altitude for the spectral resolution of the S-HIS instrument (0.5 cm^{-1} unapodized). The atmospheric pressure, temperature and water vapor are obtained from the combination of a Vaisala RS80H radiosonde, a Radiometrics microwave radiometer, and the CART Raman Lidar (CRL). The magnitude of the reflected contribution to the upwelling radiance is shown for each of three surface emissivity assumptions. Figure 4 illustrates the technique for the determination of the effective surface temperature by the minimization of the spectral variance in the derived surface emissivity spectrum. This "optimum" surface temperature is then used to compute the final derived effective emissivity spectrum. This technique is used for ground-based data where both the up and down welling radiance are measured, but it has also been successfully applied to aircraft and satellite measurements where the atmospheric contributions have been calculated using a line-by-line radiative transfer program.

Scanning-HIS and AIRS Results

Prior to the launch of the Aqua platform with the NASA AIRS instrument, the UW-SSEC conducted several aircraft campaigns to characterize the surface emissivity and surface temperature variations in the vicinity of the ARM SGP central facility at the spatial scales needed for validation of satellite products. Figure 5 illustrates the spatial scale of the Scanning HIS field of view (2 km) compared with that of AIRS (about 15 km). Observations from a NASA ER-2 flight of 31 March 2001 were analyzed by averaging the S-HIS footprints over a spatial dimension similar to that expected from the AIRS instrument. The result of the analysis directly over the ARM SGP central facility shows that the effective emissivity derived from the spatially averaged S-HIS data can be approximately represented as a linear combination of the pure scene types measured in the ground-based survey. A case study over the same validation site has been analyzed with AIRS satellite data collected on 16 November 2002. The broader spatial coverage of the satellite data is illustrated in Figure 6, which shows the observed brightness temperature at 12 μm over north central Oklahoma and southern Kansas. The symbols mark the central facility (diamond) and the boundary facilities (triangles). After application of the "online/offline" technique the distribution of surface temperature and emissivity assumes a very reasonable pattern. The cooler temperatures are associated with the high emissivity vegetation corresponding to the permanent grassland in the southeastern corner of the domain. The warmer (daytime) temperatures correspond to the "wheat belt" where at this time of year more of the bare soil is exposed. The central facility is in the wheat-growing zone but quite near the transition region. Figure 7 highlights some of the emissivity spectra derived from AIRS radiance observations near the ARM SGP central facility.

Conclusions

The high spectral resolution structure of the infrared surface reflection can be used to determine the effective value of Ts for which ε_ν is constant across spectral absorption/emission lines. Using ground-based measurements at the ARM SGP site, area averaged emissivity can be accurately represented using a single parameter (vegetation fraction) and two pure scene types; vegetation (grass) and bare soil (quartz signature). The results of ground-based, aircraft-based, and satellite-based infrared observations are shown to provide a consistent representation of the surface emissivity in the vicinity of the ARM Southern Great Plains site. These research products will be used in the validation of the AIRS "standard" land surface products.

Acknowledgements

This work was supported through the NASA AIRS science team and the U.S. DOE ARM science team projects of H. Revercomb (1990-2003).

References

Knuteson, R. O., F. A. Best, D. H. DeSlover, B. J. Osborne, H. E. Revercomb, W. L. Smith, Sr., 2004: Infrared land surface remote sensing using high spectral resolution aircraft observations, *Adv. Space Res.*, Vol. 33, 2004 (in press).

Knuteson, R. O., R. G. Dedecker, W. F. Feltz, B. J. Osborne, H. E. Revercomb, D. C. Tobin, 2003: Infrared Land Surface Emissivity in the Vicinity of the ARM SGP Central Facility, Proc. of the Thirteenth ARM Science Team Meeting, Broomfield, CO, March 31–April 4, 2003.

Osborne, B. J., R. O. Knuteson, H. E. Revercomb, J. F. Short, and D. C. Tobin, 2003: Ground truth measurements for validation of AIRS land surface temperature and emissivity products at the Southern Great Plains validation site, in Fourier Transform Spectroscopy, OSA Technical Digest (Optical Society of America, Washington DC, 2003), Quebec City, 3–6 February 2003.

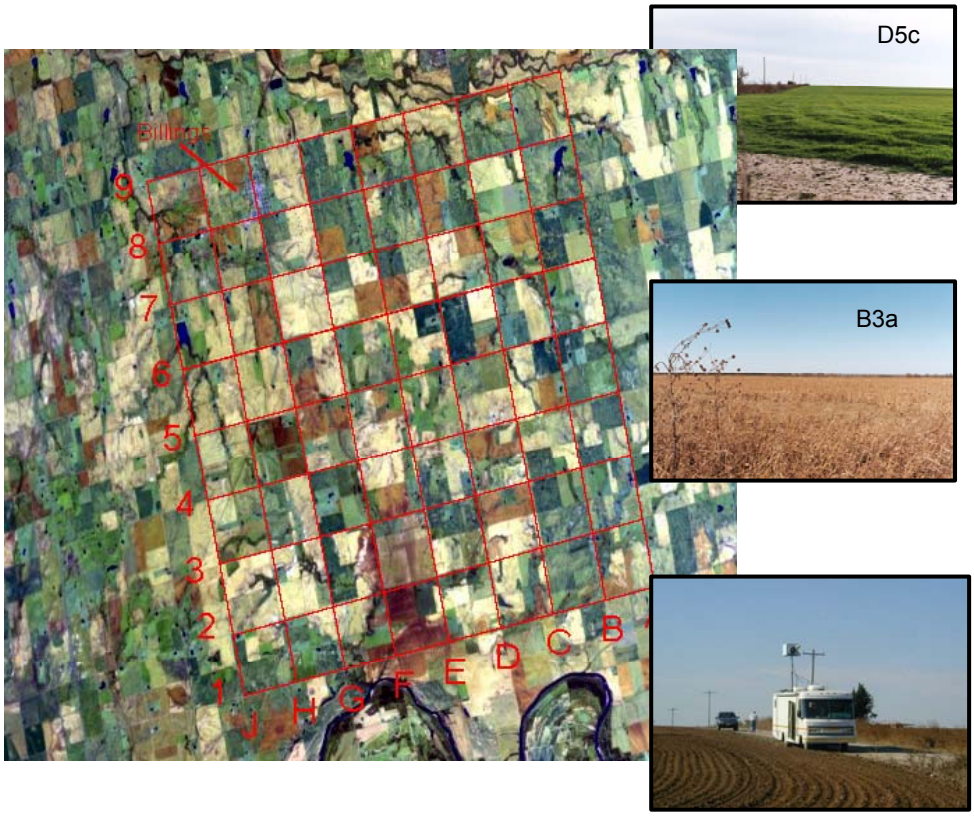

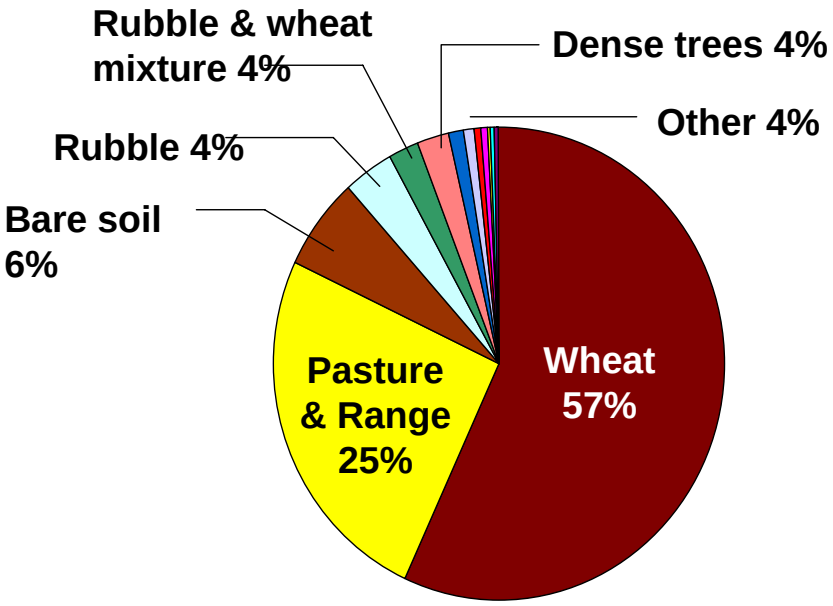

Fig. 1: The upper panel shows the 8x8 mile grid used in the ground-based survey of land cover in the vicinity of the DOE ARM SGP central facility. Land cover surveys were conducted by UW personnel in 2001, 2002, and 2003 at different times of the year. The results of the November 2002 survey are shown in the pie chart. The category "Pasture and Range" is composed of permanent grassland while the "Wheat" category is a mixture of wheat grass and bare soil which changes fraction during the growing season.

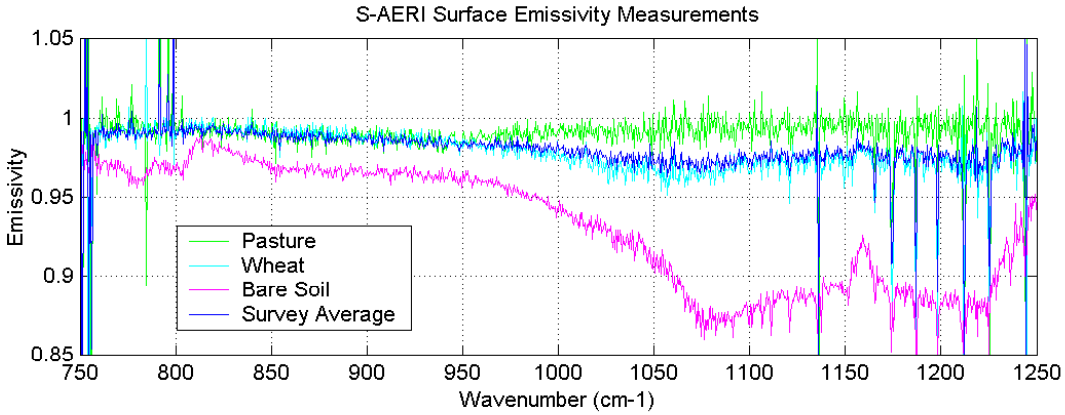

Fig. 2: UW ground-based emissivity survey conducted at the DOE ARM SGP central facility. The upper left photo shows a farm field in the early stages of winter wheat growth (March 2001). Notice the bare soil is visible between the small wheat plants at this time of year. The Scanning AERI, shown in the upper right, was used to measure the emissivities shown in the lower panel. The curve indicated as “wheat” in the plot is the measurement from the field shown above. The importance of this measurement is that the wheat measurement is very similar to the linear combination of “pure” scene types (grassland pasture and bare soil) obtained by the land cover survey. This suggests that the primary variable that determines the spectral contrast in surface emissivity is the fraction of vegetation in the instrument field of view. This result is true at all scales from the half meter scale of the ground-based Scanning AERI, to the 2 km scale of the Scanning HIS aircraft instrument, and the 15 km scale of the AIRS satellite instrument.

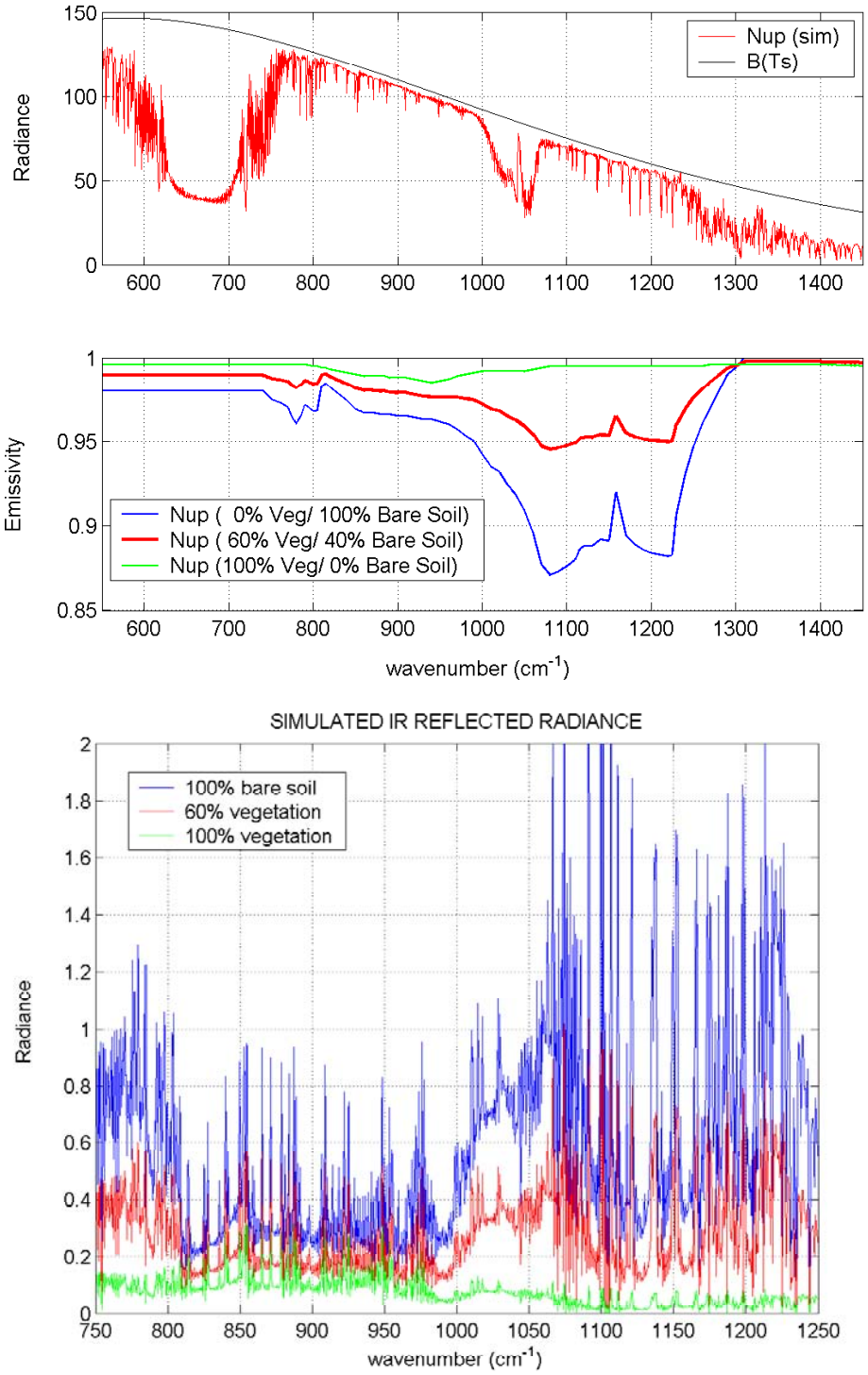

Fig. 3: Simulation of upwelling radiance at high spectral resolution (0.5 cm^{-1}) for an observer at 20 km (upper panel). This simulation uses the emissivity of pure scene types measured in the vicinity of the DOE ARM SGP central facility site and a linear combination suggested by the ground based survey (center panel). The lower panel shows the size of the infrared reflected radiance for each of the three emissivity curves.

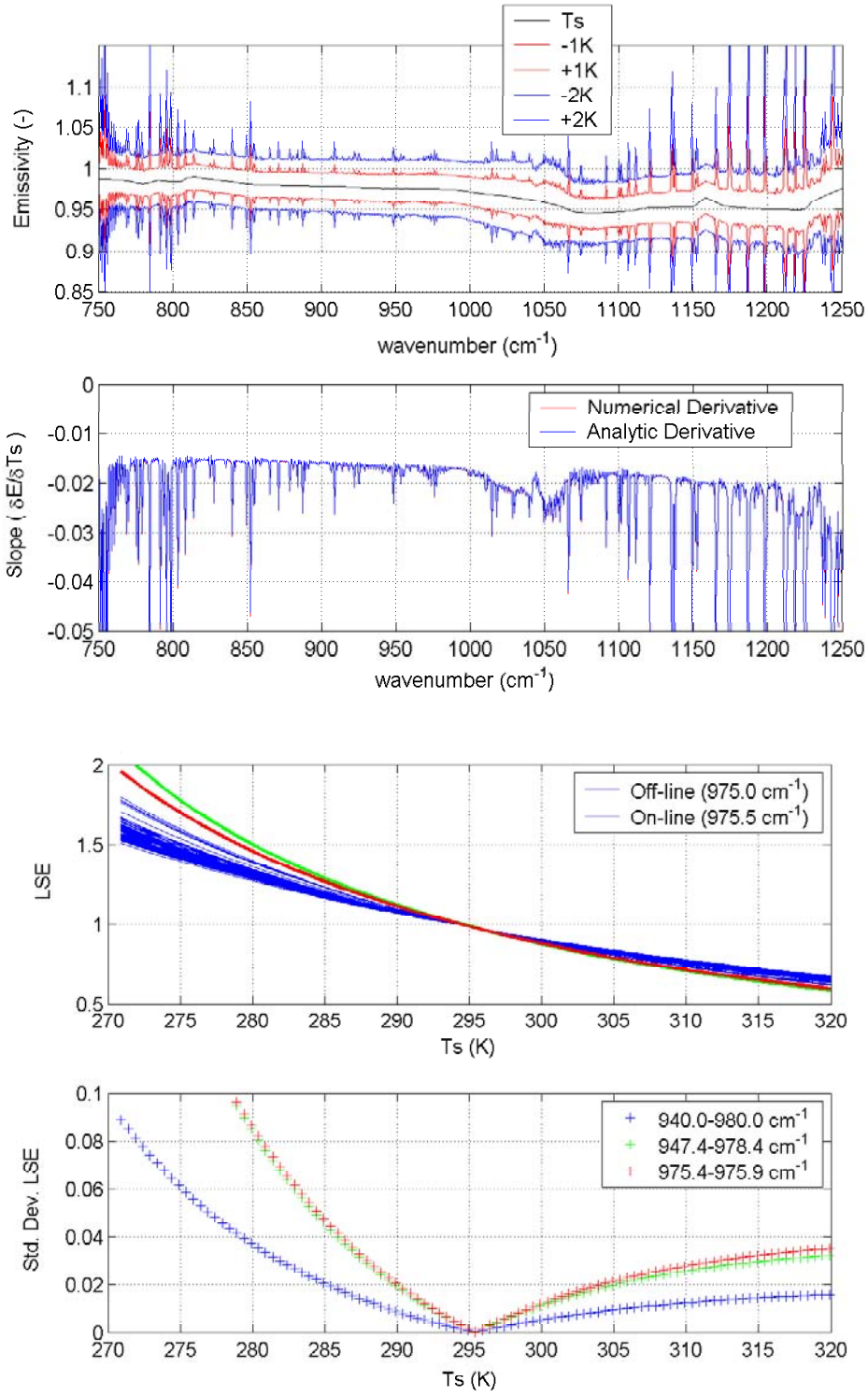

Fig. 4: Simulation of the derived emissivity as a function of land surface temperature. The top panel is the derived emissivity versus wavenumber for a range of surface temperatures. The second panel is the ratio of the change in emissivity for a change in surface temperature. The third panel shows on-line (red & green) versus off-line (blue) channels. The lower curve shows the true surface temperature is the minimum of the wavenumber standard deviation of emissivity as a function of surface temperature.

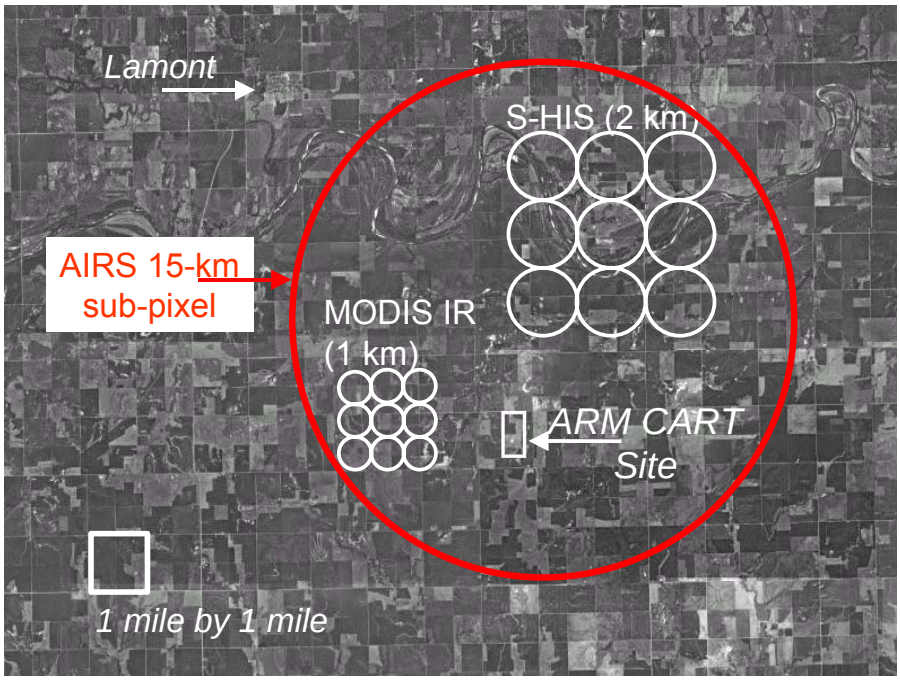

Aerial photo from http://terraserver.homeadvisor.msn.com/

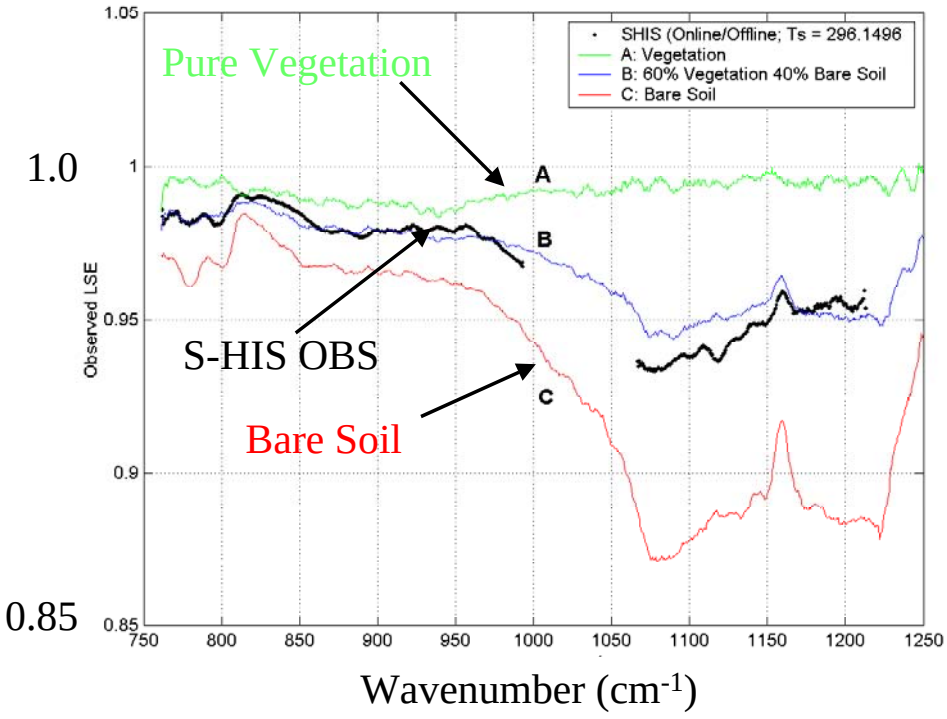

Fig. 5: The upper panel shows the approximate field of view sizes of AIRS, Scanning HIS, and MODIS instruments over an aerial photograph of the vicinity of the DOE ARM SGP central facility site. The lower panel shows that the effective land surface emissivity derived from Scanning HIS observations from 31 March 2001 18:45 UTC (averaged over 15 km) can be approximated by a linear combination of pure scene types (grass and bare soil). The best fit to these observations is 60% vegetation and 40% bare soil.

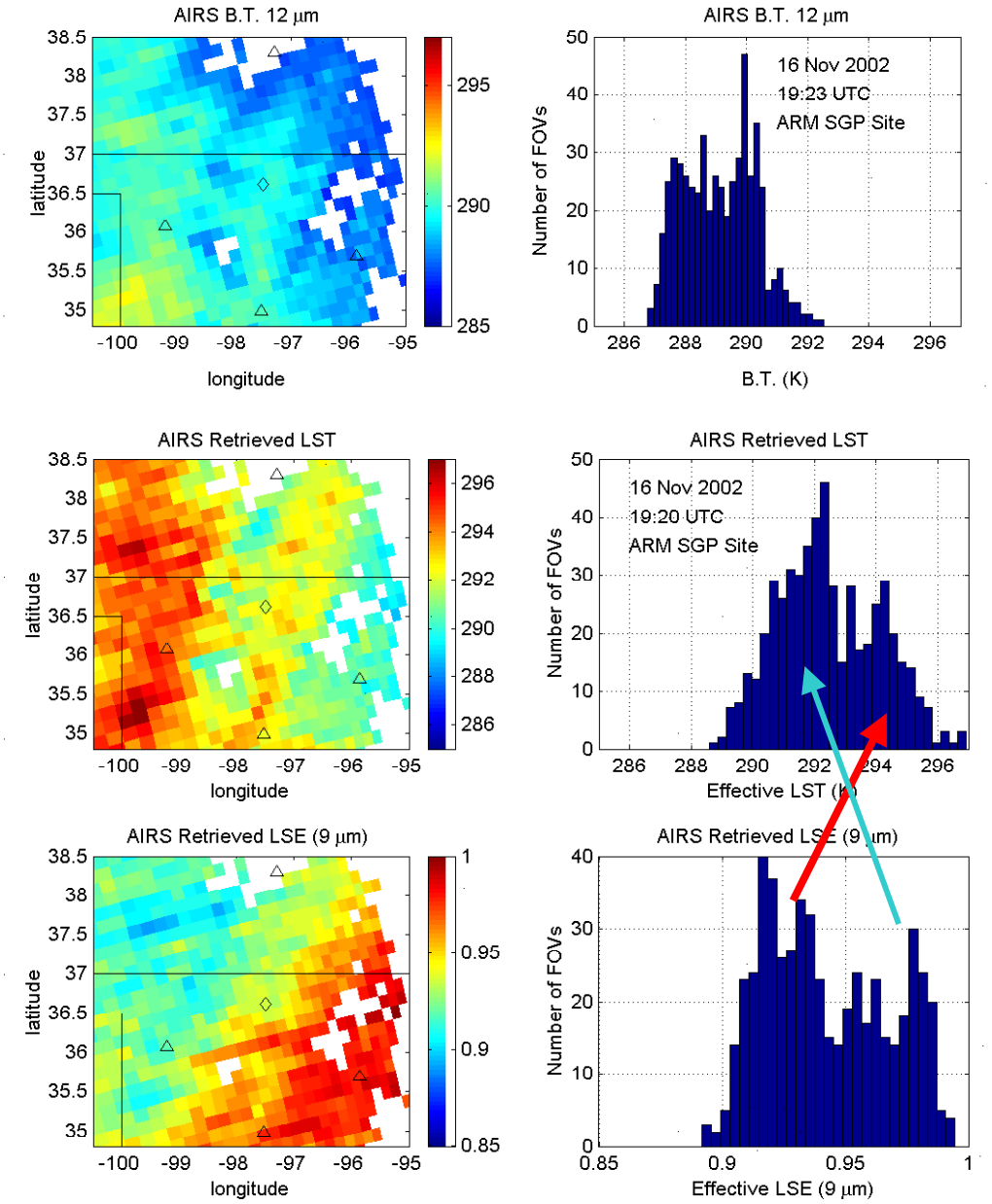

Fig. 6: The observed AIRS brightness temperature at 12 μm over the DOE ARM SGP site in north central Oklahoma, USA (16 Nov 2002 19 UTC) is shown in the upper panels as a brightness temperature map and as the corresponding histogram. The center panels show the land surface emissivity derived from the AIRS observations using the methodology described in the text. Note that the single brightness temperature distribution shifts to warmer temperatures and becomes two distinct distributions. The effective land surface emissivity derived simultaneously with the land surface temperature is shown in the lower panels. Lower emissivity values (at 9 μm) correspond to regions of higher surface temperaure. The results are consistent with the land cover survey which indicates that the central facility (indicated by the diamond symbol) is near the transition between high emissivity grassland (100% vegetation) to the southeast and wheat farming (mixed vegetation) with more low emissivity bare soil exposed.

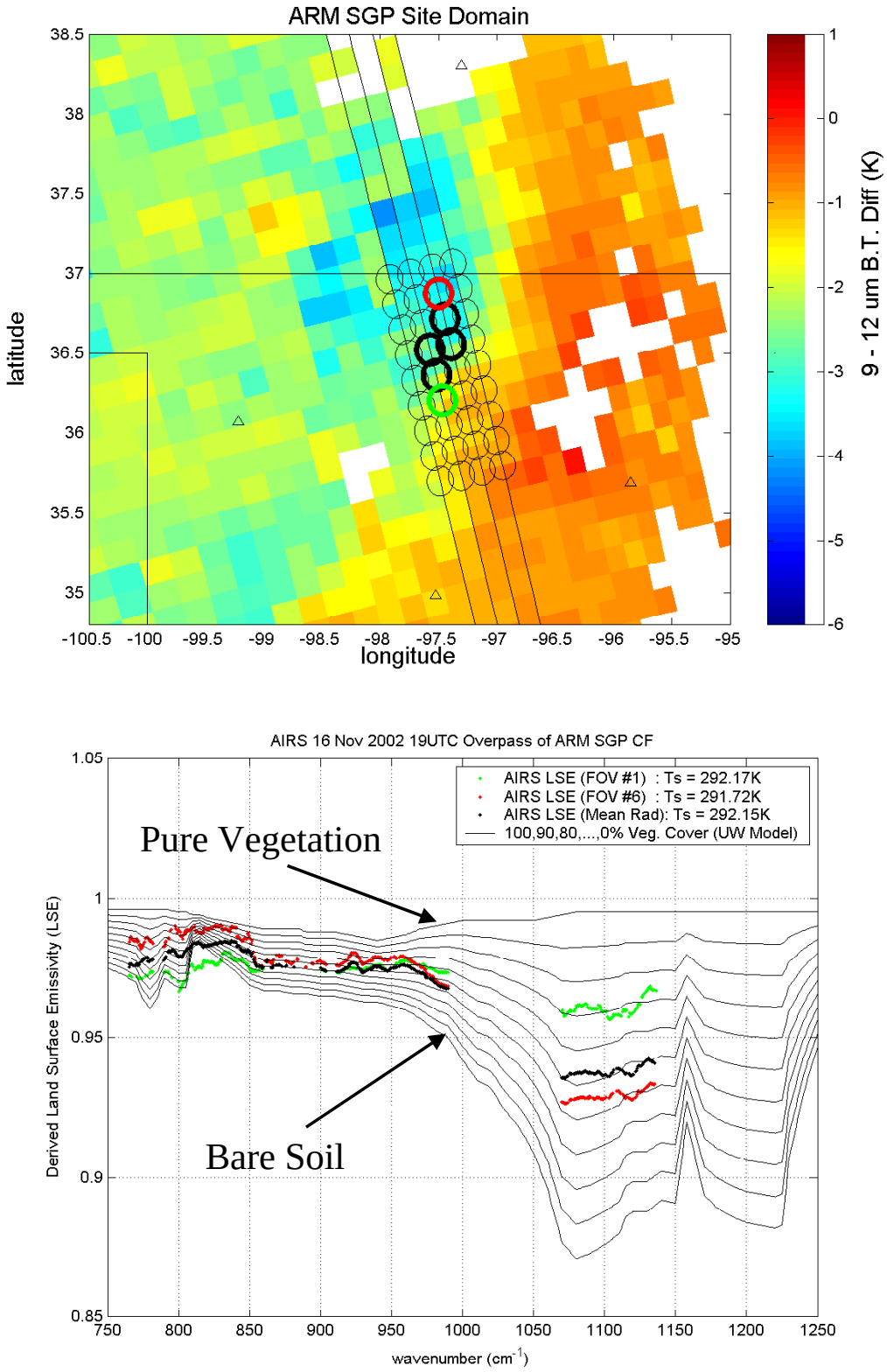

Fig. 7: Highlighted AIRS fields of view in the region near the DOE ARM SGP central facility (upper panel) show considerable variability in the effective emissivity (lower panel) derived from the AIRS radiances (16 Nov 2002 19 UTC). [UW Research Product]

Advances in the Use of Super Channels for Processing High Spectral Resolution Satellite Measurements

Larry McMillin
NOAA/NESDIS/Office of Research and Applications
Camp Springs, MD 20746

ABSTRACT

The AIRS instrument has a large number (2378) of potential channels. For use for observing meteorological parameters, several methods have been proposed and/or used to extract the information efficiently. These include selecting a subset of channels, using eigenvectors, and using "super channels", which are averages of channels which view similar atmospheric features. The super channels are selected using a constraint on the wavelength range to be covered, then selecting all the channels that have similar transmittances to be combined in one "super channel". Super channels have a number of features that make them attractive. They use all the information to reduce the noise and are efficient to use since both rapid transmittance models and equivalent Planck functions can be generated for each super channel. This means that it requires the same effort to calculate the radiance for one super channel as for a single AIRS channel. Super channels and Planck functions have been calculated for the AIRS instrument and a rapid transmittance model has been used to generate coefficients that allow rapid calculations of the corresponding transmittances. The information content of the super channels is evaluated and shown to be equivalent to content of the full channel set.

1. INTRODUCTION

A new generation of operational infrared sounders for observing the earth and its atmosphere at high spectral resolution is being built and will become operational in the next few years. The number of channels (spectral "points") will vary from about 1400 for the Cross-track Infrared Sounder (CrIS) to about 8400 for Infrared Atmospheric Sounding Instrument (IASI). Observations from both instruments are expected to be assimilated operationally into numerical weather models by 2010. Such large numbers of channels can swamp numerical forecast models. In addition, many of the channels are highly correlated and provide redundant information except for the noise. Although some channels could just be eliminated, it is desirable to include the redundant channels in a retrieval to average out the noise. Several ways have been suggested such as the use of eigenvectors. One way that has been suggested is the use of "super channels" (McMillin and Goldberg, 1997), which are averages of highly correlated channels. This approach solves several difficulties associate with other approaches. With "super channels" both a reasonable transmittance function and a reasonable Plank function exist. It is obvious that this approach is useful only if the "super channels" have a corresponding Planck function. Otherwise the Planck calculations have to be done for each individual channel and averaged, and little computation is saved. With the Planck function, one calculates the transmittance for the "super channel" and multiplies it by its corresponding Planck value, just as for a normal channel. This paper presents an approach for accomplishing the use of "super channels" that includes a Planck calculation. Super channel accuracies are better than 0.015K when compared to the "exact" calculation.

2. APPROACH

2a. Selecting the channels

In an earlier paper (McMillin and Goldberg, 1997), we presented an approach in which the channel with the largest variance was selected first. Then the channel whose temperature was most highly correlated with the first was found. If the correlation was greater than a limiting value, the two channels were combined, the combined channel was kept, and the number of channels was reduced by one. This process was repeated until no channels that met the combination criteria were left. One of the features of this approach stems from the fact that channels in the window regions are highly correlated. For example, all the channels that might be used for split window approaches tended to end up in one super channel. This had the undesirable effect of sometimes grouping channels with different weighting function weights together, especially channels that peaked near the surface. The split window is a good example, because it works because the channels are correlated; yet they need to be differenced to calculate the atmospheric attenuation.

Because of this behavior, it was decided to match channels based on the shape of the weighting functions. This allows super channels peaking at different heights to be extracted, even though the temperatures for the channels may be highly correlated. The channels were combined by looking at correlations of the weighting functions at each of the 100 levels used in the AIRS radiative transfer calculation. Channels that were highly correlated were combined to form a super channel. With the first attempt, no limit was placed on the wave number interval. When combinations covering a wide wave number range appeared and were associated with large errors, a limit was placed on the maximum wave number range allowed. The errors were caused by the inability of the Planck approximation to work accurately when the wavenumber range is too large. Limiting the wavenumber range allowed for any given super channel solved the problem and gave the accuracies that were desired. Two hundred wavenumber is a good value to use for a limit.

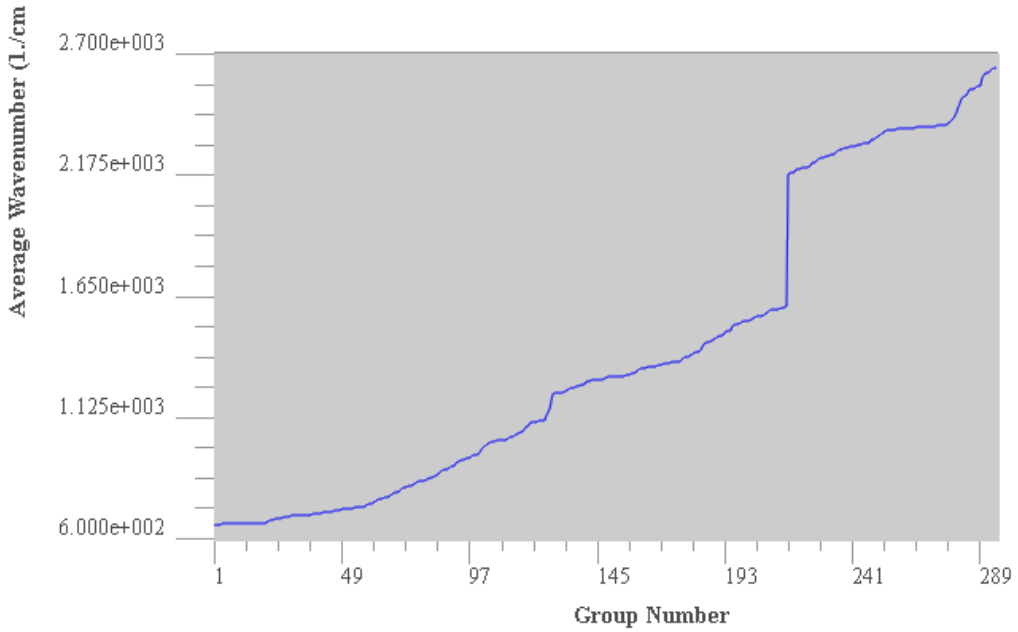

Fig 1. the average wavenumber for the super channel group numbers

Fig. 1 shows the average wavenumber associated with each group. The groups have been ordered according to the wavenumber. The jumps in wavenumber are gaps between the detector arrays that result in gaps in the coverage of the AIRS instrument. These gaps were intentionally placed in spectral regions where the additional information content did not justify the additional cost.

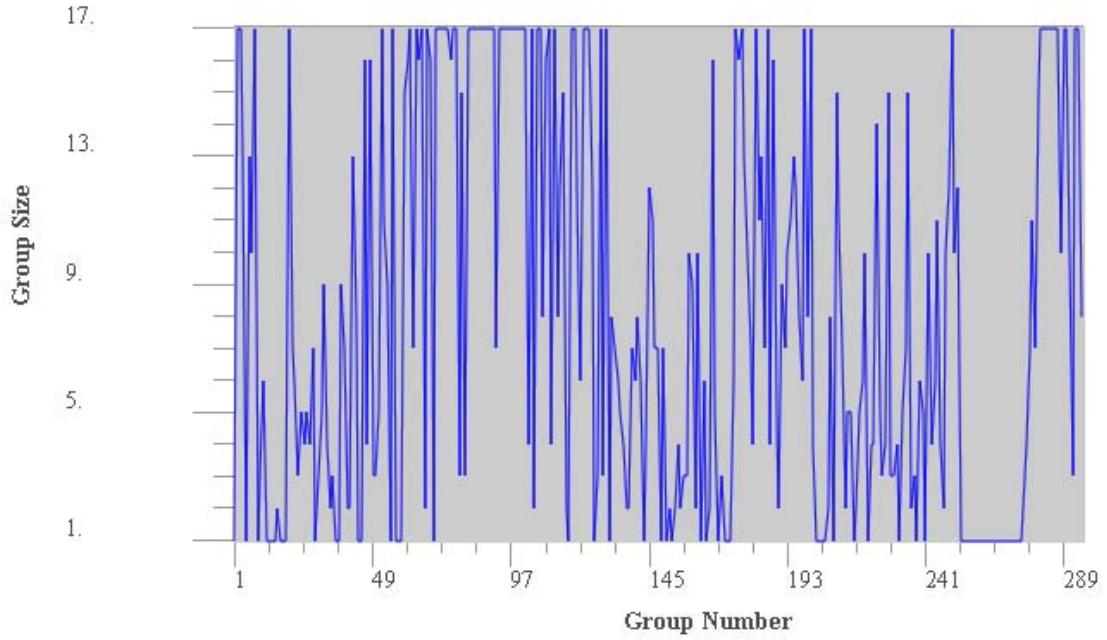

Fig. 2 The group sizes listed as a function of the group number

Fig. 2 shows the group size as a function of the group number. Sizes range from 1 to 17. There are over 60 groups that have 17 sub channels. There are also over 60 channels that are unique and can't be combined with any other channel. If these are not needed for a particular application, eliminating them can reduce the number of groups. Many of these are unique because they are channels with roughly equal absorption by two different gases such as carbon dioxide and water vapor. Finding another channel with the same effects is rare so they don't get combined. At the same time, using such channels is difficult and may not justify the cost of doing the forward calculation. Fig. 3 shows the wavenumber range for the groups. The maximum range is under 130 wavenumbers.

Once the "super" channels are selected, it is necessary to calculate transmittances for the "super" channels. The rapid transmittance techniques, Optical Path TRANsmittance (OPTRAN) routines that we use at the National Environmental Satellite Data and Information Service (NESDIS) provide the means of calculating transmittances. These algorithms have been applied to broadband instruments and are suitable for the rapid transmittance calculations (McMillin et al. 1985). Applying OPTRAN to "super" channels is similar to applying to a broadband instrument such as HIRS. Coefficients can be generated for the transmittances corresponding to the super channels using the existing algorithms.

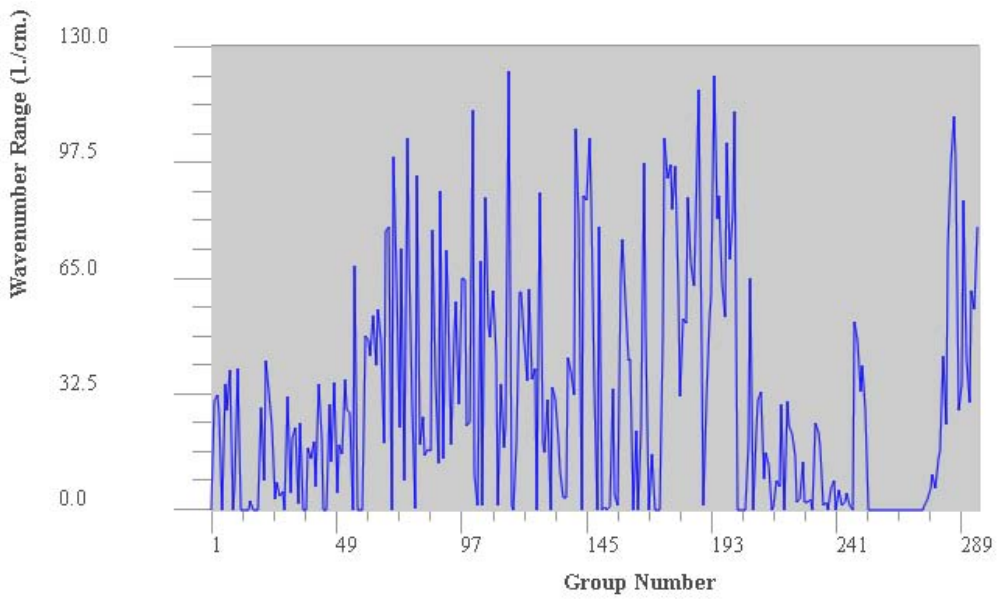

Fig. 3 The wavenumber range as a function of the group number

2b. Calculating the Planck function

A super channel is useful only if a corresponding radiance can be determined. As mentioned earlier, if the individual channels have to be summed up for each profile, no time is saved and the point of making the super channels is lost. We solve this problem by using the band corrections that have been used for TOVS soundings (McMillin et al. 1981), but with an improvement. In the old approach, the Planck function was used to calculate radiances at the wavenumber that represents the centroid of the filter function. We will use $\bar{\nu}$ to denote this wavelength. The temperature used for the calculation was then modified by the expression

$$T^* = a + bT \qquad (1)$$

where T^* denotes the temperature used for radiance calculation, T denotes the true temperature, and a and b are constants. These were derived by the following procedure:

Using a set of profiles, radiances at a spectral resolution that can be considered to be monochromatic were calculated at the frequencies that cover spectral range for a given channel. These were then convoluted with the filter function for that channel to produce the "true radiance." At the same time, the radiance for temperature, T^*, at wavenumber, $\bar{\nu}$, was calculated. This was repeated for temperatures spanning the range covered by the particular channel, typically 200 K -

320 K, and the values of a and b that minimized the maximum brightness temperature error over the range of atmospheric temperatures observed by that particular channel were found using an iterative procedure that changed the values of a and b to increase the accuracy until a specified accuracy was obtained.

In our approach, we treat the wavenumber as an additional variable to be optimized in the minimization. It is usually close to the centroid, but does not match it exactly. Adding another degree of freedom to the optimization increases the wavelength range over which the approximation is valid. We found negligible errors over a range as wide a 500 cm^{-1}. However, for this application the range was reduced to 200 cm^{-1}. This allows us to average over super channels of this width or less and is adequate for super channels for two reasons. Averaging channels from widely spaced spectral regions produces other problems (such as large ranges in surface emissivity) which we wish to avoid, and channels which should be averaged should have similar spectral characteristics. Figures 4 and 5 show the values of a and b that were obtained. For a single AIRS channel, the value of a should be 0 and the value of b should be 1.0. For the larger groups, the value of a gets as large as 1.0 and the value of b gets as small as .9975. It should be noted that the "super" channels used for this study were derived from simulations, but the information content was determined using AIRS data. Ideally, the "super" channels should also be derived using real measurements and this is being done. However we note that doing so should improve the results. Even with this limitation, the current results are accurate enough for many uses.

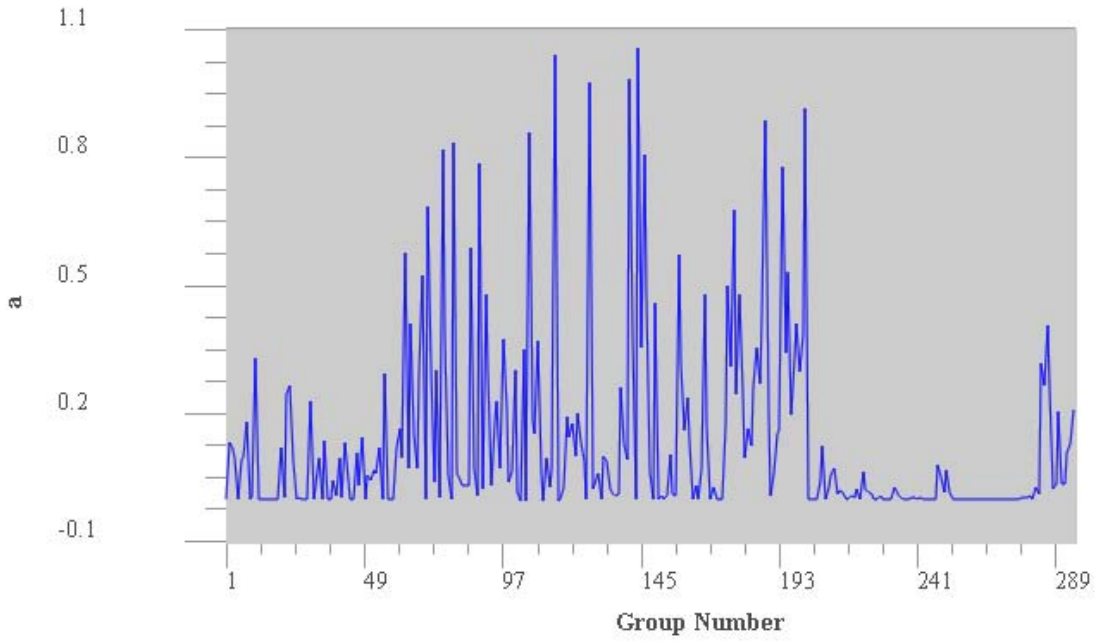

Fig. 4 The value of the a coefficient as a function of the group number.

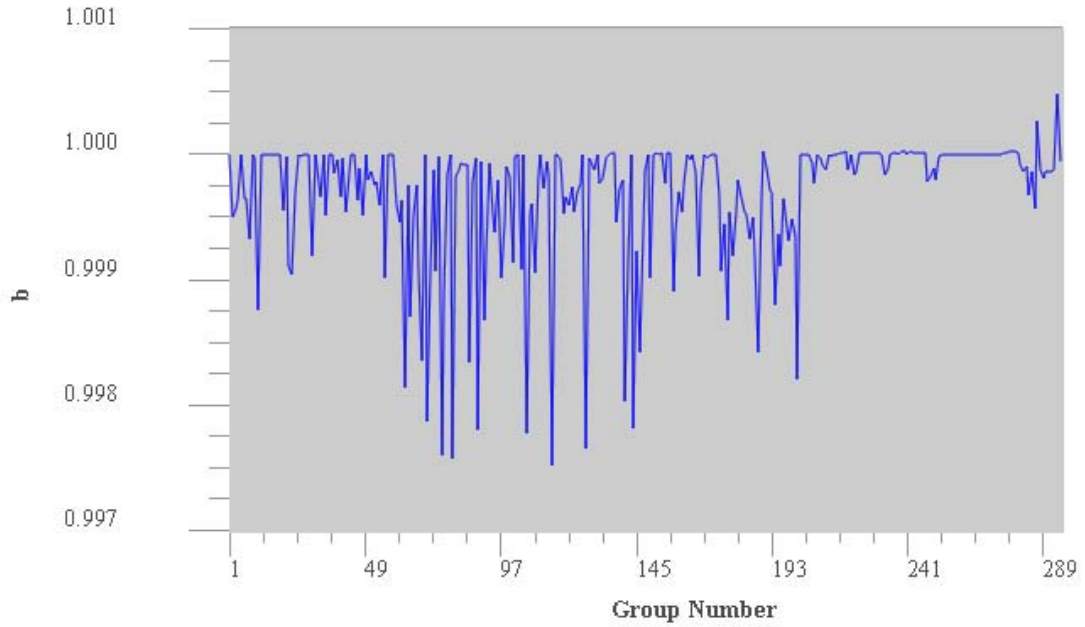

Fig. 5 Value of the b coefficient as a function of the group number.

3. RESULTS

A global set of profiles was used to define the groups. The set was obtained from a set of global operational TIROS operational Vertical Sounder (TOVS) measurements matched with radiosondes. Since these are simulations, the TOVS measurements are not that important, but they did provide a means for supplementing the radiosondes to provide the more complete specification of the atmospheric state that is required for radiative transfer calculations. For example, a surface skin temperature, an ozone profile, and an upper atmospheric temperature were obtained from the retrieval and used to supplement the radiosonde information to obtain complete profiles. Two hundred profiles were used to generate the retrieval coefficients.

The channels that were added together to define the “super channels” were selected by summing the level transmittances over both levels and atmosphere to calculate a channel-by-channel correlation matrix. Then a channel was selected and the remaining channels were scanned to find a channel that matched its characteristics. The limits used were .999 and +/-100 wavenumbers for the lower frequency channels (< 1357.5 cm. $^{-1}$), and .9995 and +/-100 wavenumbers for the higher frequency channels.

This produced a set of 295 “super channels”. The group sizes ranged from 1 to 17. As mentioned earlier Fig. (1) shows the frequencies for the groups, Figs. 2 shows the group sizes, Fig. 3 shows the wavenumber range, Figs. 4 & 5 show the Plank calculation coefficients, and Fig. 6 shows the errors. The actual maximum error observed was 0.0115K, but we will round this to 0.015 K or less.

This is certainly good enough for most uses. Making the selection criteria tighter could reduce the errors. Conversely, relaxing the selection criteria could reduce the number of super channels. In other words, there is a trade between accuracy and number of channels. The selection we made is a reasonable compromise, but not the only one.

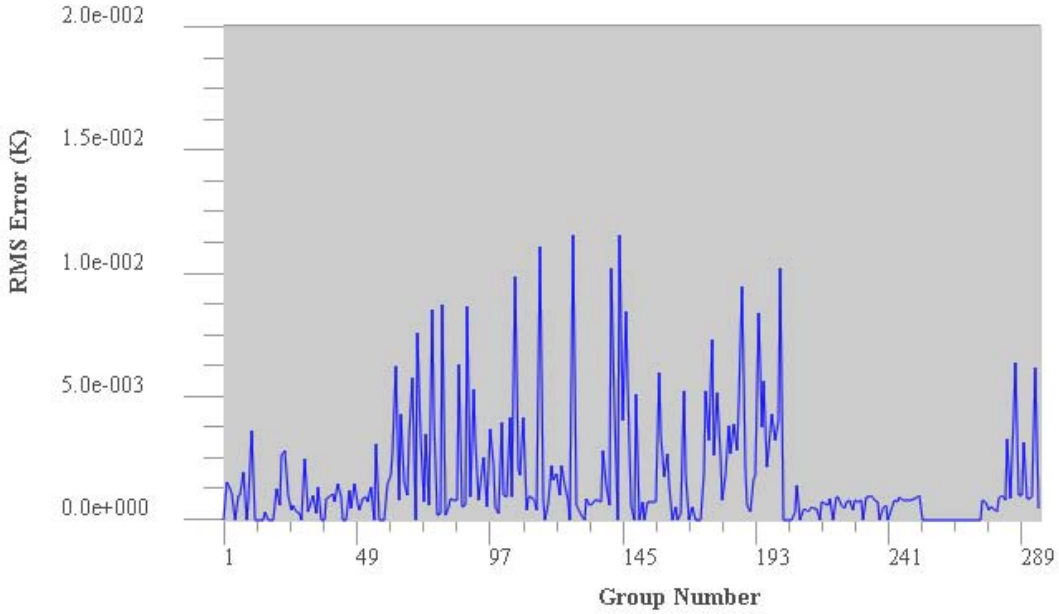

Fig. 6 RMS error for the groups as denoted by group number

4. FORWARD CALCULATION ERROR

As mentioned, a forward transmittance model is required for super channel calculations. Fig. 7 shows the errors in the forward calculation. Dark blue shows the error for dry, green is for water vapor, red is for ozone, and cyan is the total amount. For most channels the error is less than 0.01K. It is larger for selected channels where the error is dominated by ozone, both near the 9.6 ozone absorption band and at isolated lines where the ozone absorption is significant. It should be noted that similar errors have been noted for individual AIRS channels, so this is a transmittance issue, not a super channel one. The number of super channels shown in Fig. 7 is less than the number shown in Fig. 6. This is because Fig. 7 includes only those AIRS channels which do not show a history of noise and are therefore considered to be reliable. This reduced the number of channels in some of the groups and some groups were totally eliminated.

5. INFORMATION CONTENT

There are several possible ways to reduce the volume of data and retain information content. Eigenvectors are one way, but a fast radiative transfer calculation is difficult if not impossible. In any case, it is desirable to know the information content that is lost when reducing the data volume. At this point, it should also be mentioned that the AIRS instrument has some channels that are

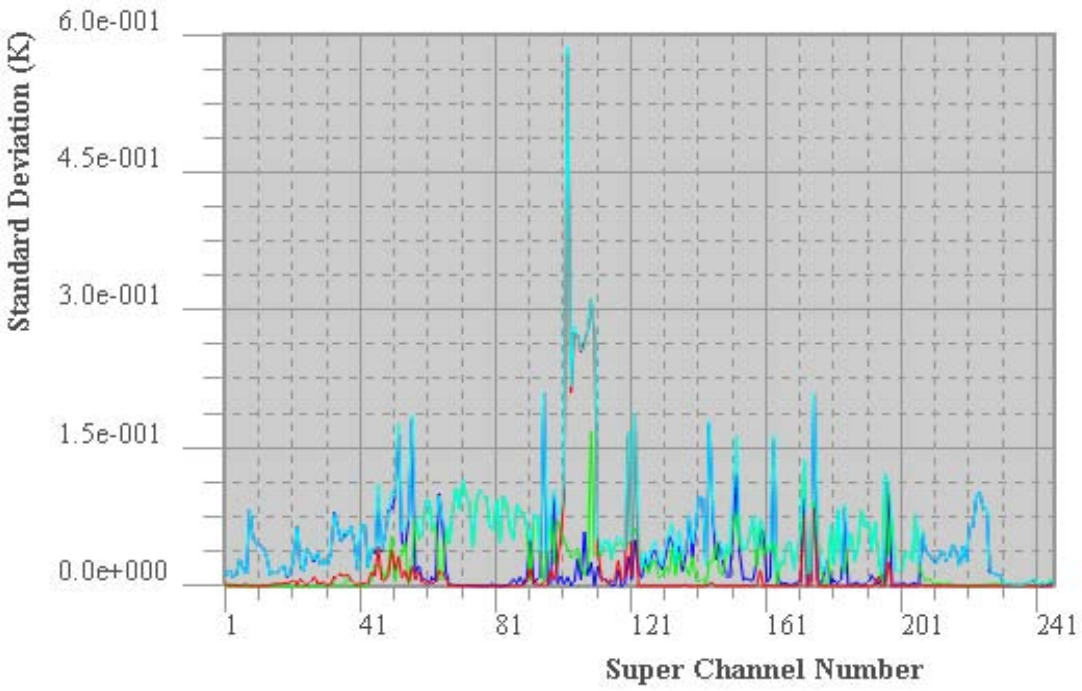

Fig. 7 Radiance errors as a function of the super channel number. Blue shows the dray gas values, red shows the ozone values, green shows the water vapor values, and cyan shows the total.

noisy. With the large number of redundant channels, this is not a major issue, but it needs to be stated that only the "good" channels were used for this analysis. The total variance was calculated as the sum of the diagonal elements of the covariance matrix. This calculation is obvious for the actual case. For the super channels, the variance was calculated by taking the variance for a particular super channel and multiplying it by the number of channels averaged together. The ratio of the variances was then calculated by dividing the value for the super channels by the value for the individual channels. The ratio was 0.9986, which means that the super channel approach captures over 99% of the total variance.

6. EXAMPLES OF SUPER CHANNELS

Figures 8 and 9 show some examples of super channels. Figure 8 shows an example of super channel 1 for an AIRS granule, an area of 135 scan lines by 90 scan positions. This super channel is an average of 13 individual channels. Figure 9 shows the corresponding values for super channel number 9, which consists of a single channel. The reduction in error due to the averaging is obvious.

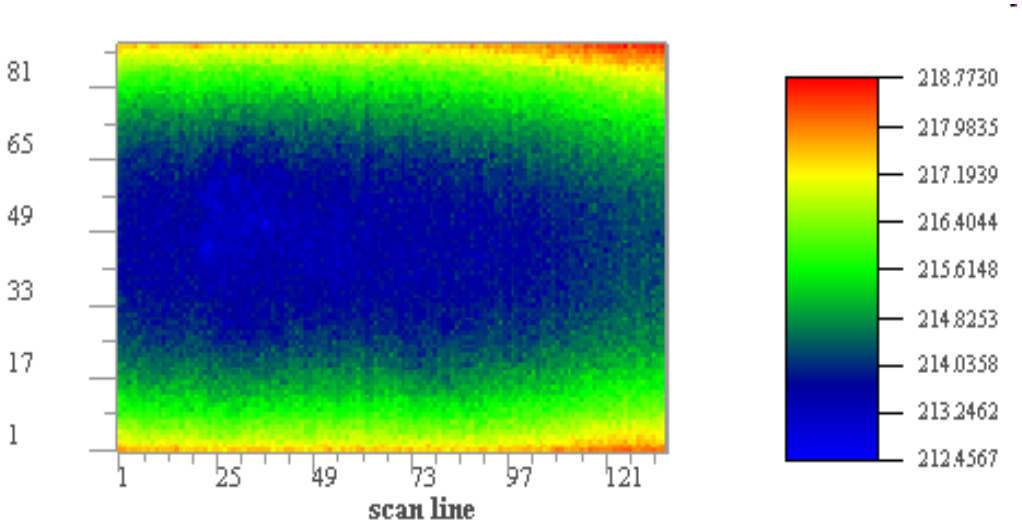

Fig. 8 Temperatures for AIRS super channel 1 which is an average of 13 channels.

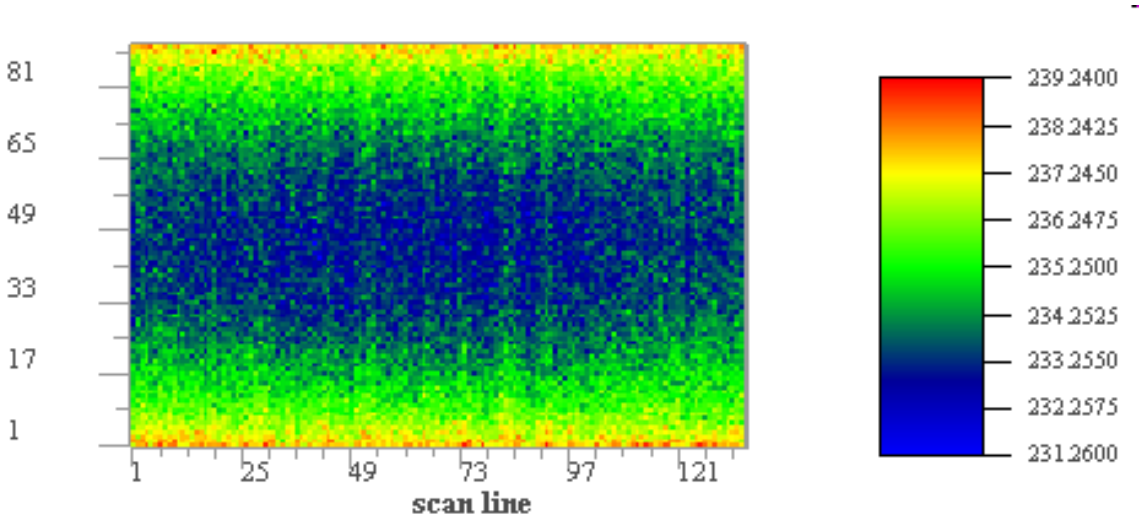

Fig. 9 Temperatures for AIRS super channel 9 which is a single channel.

7. SUMMARY AND CONCLUSIONS

We have combined two approaches, a rapid transmittance and a Planck function approximation to provide a rapid radiance calculation for advanced high-resolution satellites. Together, these

provide the speed and accuracy required for rapid calculations. The number of channel calculations is reduced by a factor of 10 while the error is kept under to 0.015K.

ACKNOWLEDGEMENTS

This work was partly supported by funding from the AIRS project.

REFERENCES

L.M. McMillin and M.D. Goldberg, 1997. "The Use of Super Channels for High Resolution Soundings", *Tech. Proceedings of the Ninth International TOVS Study Conference*, *Igls Austria, 20 - 26 Feb.* Pp 327-330.

L.M. McMillin, L.J. Crone, and T.J. Kleespies, 1985. "Atmospheric transmittance of and absorbing gas. 5. Improvements to the OPTRAN Approach", *Appl. Optics*, **34, 36**. pp 8396-8399.

M.P. Weinreb, H.E. Fleming, L.M. McMillin, & A.C. Neundorffer, 1981. "Transmittances for the TIROS Operational Vertical Sounder", *available from the superintendent of Documents, U.S. government Printing Office, Washington D.C. 20402*.

RTIASI-4: a new version of the ECMWF fast radiative transfer model for the infrared atmospheric sounding interferometer

Marco Matricardi

European Centre for Medium-Range Weather Forecasts
Reading, Berkshire, UK

Abstract

An improved version of RTIASI, the ECMWF fast radiative transfer model for the Infrared Atmospheric Sounding Interferometer, has been developed. In the new version of RTIASI (RTIASI-4) the accuracy of the fast transmittance model has been improved by including 4 more molecules (HNO3, CCl4, CF4 and OCS) in the line-by-line computations and by using the year 2000 release of the HITRAN molecular database. By using a revised set of water vapour training profiles in the stratosphere, the condition of the regression has been improved so that unphysical oscillations observed in the stratospheric water vapour Jacobians have been virtually eliminated. RTIASI-4 features a revised vertical pressure grid that allows the integration of the radiative transfer equation to be performed with significantly increased accuracy. The water vapour transmittance model has been significantly improved by weighting the data prior to performing the regression and by introducing a dedicated transmittance model for the continuum absorption. Minor adjustments to the predictors for water vapour have also been made. A significant improvement to the previous versions of the model is the inclusion of CO, CH_4, N_2O and CO_2 as profile variables. Finally, a solar term has been introduced to evaluate the solar radiance reflected by a land or water surface in a non-scattering atmosphere.

Introduction

Radiances from the Advanced TIROS Operational Vertical Sounder (ATOVS) on the National Oceanic and Atmospheric Administration (NOAA) polar orbiting satellites are used operationally at the European Centre for Medium-Range Weather Forecasts (ECMWF). A potentially useful addition to the current satellite sounders is the Infrared Atmospheric Sounding Interferometer (IASI) (Cayla 1993). In combination with the Advanced Microwave Sounding Unit (AMSU-A), the Microwave Humidity Sounder (MHS), and the Advanced Very High Resolution Radiometer (AVHRR/3), IASI is the core payload of the European Organisation for Exploitation of Meteorological Satellites (EUMETSAT) Meteorological Operational Satellite (METOP-1) (Klaes et al. 2000) and will contribute to the primary mission objective of METOP-1 that is the measurement of meteorological parameters for NWP and climate models.

A prerequisite for exploiting radiances from conventional and high-resolution sounders is the availability of a fast radiative transfer model (usually called the observation operator) to predict a first guess radiance from the model fields (temperature, water vapour, ozone, surface emissivity and perhaps clouds in the future).

As part of the preparations being made at ECMWF to exploit the IASI datasets, RTIASI, the ECMWF fast radiative transfer model for IASI, has been developed (Matricardi and Saunders 1999). The original version of RTIASI has undergone a number of significant upgrades that has led to the release of a number of different versions of the model. The scope of this paper is to illustrate the work undertaken at ECMWF to develop the most recent versions of RTIASI, RTIASI-4.

In RTIASI-4 the number of gases included in the line-by-line (LBL) computations has been increased to include HNO_3, CCL_4, OCS and CF_4 and the database of line-by-line transmittances has been generated using the year 2000 version of the HITRAN molecular database (Rothman et al. 2003).

To reduce the errors that are introduced in the radiative transfer calculations by limiting the number of layers to 43, RTIASI-4 uses a vertical pressure grid with increased number of levels. The new grid is made of 90 levels that extend from 1050 hPa to 0.005 hPa.

The transmittance model for water vapour (line absorption) has been improved by using a single algorithm with the data being weighted prior to performing the regression. For the prediction of the water continuum absorption, a new scheme has been introduced in RTIASI-4 where the water continuum is handled separately from the other gases. The advantage of having a separate fast model for the continuum is that any change in the continuum coefficients can be addressed without the need of generating a new line-by-line database.

A significant improvement to the previous versions of the model is the inclusion in RTIASI-4 of CO, CH_4, N_2O and CO_2 as profile variables. Finally, RTIASI-4 features the inclusion of a solar term to evaluate the solar radiance reflected by a land or wind roughened water surface in a non-scattering atmosphere.

The formulation of the fast radiative transfer model

The basic methods that were applied to develop RTIASI have been documented in Matricardi and Saunders (1999) and Matricardi (2003). In this section only the main components are discussed. Any major change to the model is documented in detail in the next sections.

In RTIASI-4 the atmosphere is divided into 89 layers defined by pressure levels from 0.005 hPa to 1050 hPa and is assumed to be plane-parallel in local thermodynamic equilibrium with no scattering. The model uses the polychromatic form of the radiative transfer equation (i.e. the use of convolved transmittances in the radiative transfer equation is based on the assumption that this is equivalent to the convolution of the monochromatic radiances).

In the RTIASI-4 fast transmittance model the computation of the optical depth for the layer from pressure level j to space along a path at angle θ involves a polynomial with terms that are functions of temperature, absorber amount, pressure, and viewing angle. The effective optical depth at wave number $\tilde{\nu}^*$ ($\tilde{\nu}^*$ is the central wave number of the IASI channel and the circumflex over the symbol denotes convolution) from level j to space can be written as:

$$\hat{\rho}_{j,\tilde{\nu}^*} = 0 \qquad \text{j=1} \tag{1}$$

$$\hat{\rho}_{j,\tilde{\nu}^*} = \hat{\rho}_{j-1,\tilde{\nu}^*} + \sum_{k=1}^{M} a_{j-1,\tilde{\nu}^*,k} X_{k,j-1} \qquad \text{j=2,90} \tag{2}$$

where M is the number of predictors and the functions $X_{k,j}$ constitute the profile-dependent predictors of the fast transmittance model. To compute the expansion coefficients $a_{j,\tilde{\nu}^*,k}$ (sometimes referred to as fast transmittance coefficients), a set of diverse atmospheric profiles (Matricardi and Saunders 1999) is used to compute, for each profile and for several viewing angles, and for various absorbing constituents, accurate LBL transmittances for each level defined in the atmospheric pressure layer grid. The effective optical depths $\hat{\rho}_{j,\tilde{\nu}^*}$ are then used to compute the $a_{j,\tilde{\nu}^*,k}$ coefficients by linear regression of $\hat{\rho}_{j,\tilde{\nu}^*} - \hat{\rho}_{j-1,\tilde{\nu}^*}$ versus the predictor values calculated from the profile variables for each profile at each viewing angle.

In this paper, H_2O, CO_2, O_3, N_2O, CO, CH_4 are allowed to vary, the other gases are held constant and will be referred to as fixed. Gases are considered as fixed if their spatial and temporal concentration variations do not contribute significantly to the observed radiance. In RTIASI-4 we define fixed gases as N_2, O_2, HNO_3, OCS, CCl_4, CF_4, CCl_3F (CFC-11) and CCl_2F_2 (CFC-12). Among the fixed gas species, HNO_3, OCS, CCl_4, and CF_4 were not included in the previous version of the code, RTIASI-2. The inclusion of four more absorbers in the LBL computations is the result of a study where the impact of un-modeled absorbers on IASI radiances was evaluated.

Regression coefficients in RTIASI-4 are generated from a database of LBL transmittances computed using the GENLN2 model (Edwards, 1994). In RTIASI-4 the molecular parameters for the LBL computations are taken from the year 2000 release of the HITRAN database (Rothman et al. 2003).

To reduce the occurrence of unphysical oscillations in the water vapour Jacobians in the region above 100 hPa, in RTIASI-4 the numerical conditioning of the regression in the stratosphere has been improved by replacing the current stratospheric water vapour profiles with a much wider profile set from HALOE (Evans 1997).

Weighting of the input data prior to the regression

The scheme used in RTIASI-2 to model the behaviour of the water vapour layer optical depth involves a split algorithm (Matricardi and Saunders 1999). This can result in discontinuities in the water vapour Jacobians and a relatively poor prediction of the water vapour layer optical depth. To eliminate these discontinuities, a single algorithm for water vapour is used in RTIASI-4 with the data being weighted prior to performing the regression. As noted by Straw et al. (2003), since the radiance coming either from the layers where no attenuation is taking place or from the layers where the transmittance has become very small contributes little to the total radiance, not all the data are of equal importance for the regression. To improve the accuracy of the regression it would be desirable to have the computation of the regression coefficients not to be influenced by data corresponding to optically thick situations. These data

have a negligible impact on the simulated radiances and exhibit a behavior that is more complex to model than the one for the optically thin case. Consequently, in RTIASI-4 input data to the regression are weighted in terms of the effective contribution to the total radiance with the weighting function chosen to be equal to $\hat{\tau}_{l,\tilde{\nu}^*} - \hat{\tau}_{l+1,\tilde{\nu}^*}$ (the contribution from a single layer to the top of the atmosphere radiance is proportional to $\hat{\tau}_{l,\tilde{\nu}^*} - \hat{\tau}_{l+1,\tilde{\nu}^*}$). This will result in smaller weights for situations where either no attenuation is taking place or the transmittance is very small and larger weights for situations where the emission from the layer is more significant.

A new scheme for prediction of water vapour continuum

For water vapour the continuum type absorption is of particular importance. In RTIASI-2 the continuum type absorption for H_2O was included in the LBL computations but no predictors of the type described above were included in the water vapour model. In RTIASI-4 the regression for the water continuum is handled separately from the other gases. The advantage of having a separate fast model for the continuum is that any change in the continuum coefficients can be addressed without the need of generating a new LBL database. A considerable amount of time and disk space can then be saved. It also allows the reduction of the number of predictors used in the water vapour model helping improving the accuracy of the regression since the interaction of some of the predictors can cause numerical instabilities in the results of the regression.

In RTIASI-4 the water continuum transmittance is parameterized using the model described by equations (1) and (2). Regression coefficients are generated using a database of monochromatic transmittances computed using version 2.4 of the CKD continuum model (Clough et al, 1989). The water continuum transmittance can be considered constant over an IASI channel and therefore the convolved transmittance can be replaced by the monochromatic continuum transmittance. The prediction of the continuum optical depths in RTIASI-4 is performed using a total of four predictors: two for the self-continuum absorption and two for the foreign-continuum absorption (Matricardi 2003).

Refinement of the vertical pressure grid

The layering choice made in RTIASI-2 (43 homogeneous layers of fixed pressure levels) limits the accuracy of the radiance computation. This is determined by the temperature gradient across the layer since it is dependent on the evaluation of the Planck function at a mean layer temperature that should be representative of the temperature variation across the layer. In principle the greater the number of layers the higher the accuracy of the radiance computation. On the other hand, the numbers of layers largely control the execution time of the LBL computations and the size of the associated database. There is no need however to go to a disproportionate number of layers since any gain in accuracy that is below the noise level of the instrument is not be detected.

The above considerations have led to a revision of the pressure grid used in RTIASI-4. To arrive at the definition of the new pressure grid, tests were made where the sensitivity of the top of the atmosphere radiance to the refinement of the pressure grid was studied. Computations were made for

several profiles representative of average situations in the atmosphere. Results show that water vapour channels are mostly sensitive to refinement of the grid between 600 and 100 hPa whereas for the channels in the temperature sounding bands most of the radiance difference is generated by the refinement of the grid in the stratopause and lower mesosphere. This has lead to the definition of a new pressure grid made of 90 levels with pressure ranging from 0.005 to 1050 hPa. We carried out trials that show that any gain in accuracy in radiance computation achieved by refining further the 90 levels pressure grid is below the noise level of IASI (Matricardi 2003).

The impact of the choice of layering on LBL radiances is shown in figure 1 where the difference between simulated IASI spectra computed using 43 and 90 vertical pressure levels is plotted for three different atmospheres. Larger differences are observed across the whole 6.3 μm (1594 cm^{-1}) water vapour band and in the centre of the 4.3 μm (2325 cm^{-1}) band with a lesser impact in the 15 μm (660 cm^{-1}) band. It is evident from Fig.1 that differences depend on the atmospheric state and in particular on the vertical gradients of water vapour and temperature in the upper troposphere and lower stratosphere.

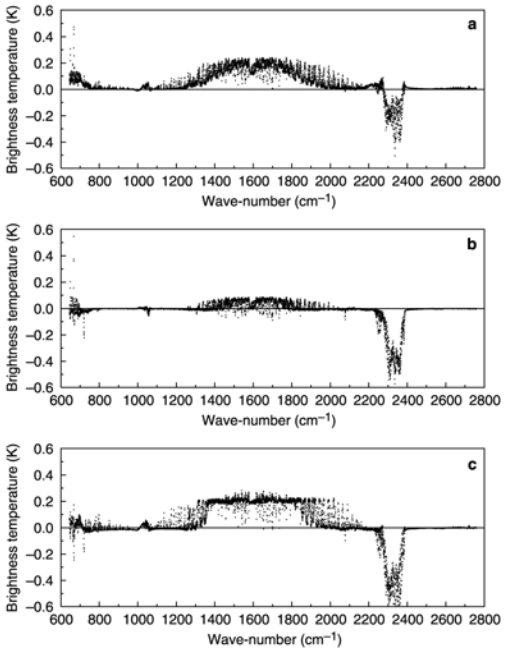

Figure 1: difference between simulated IASI spectra obtained using 43 and 90 vertical pressure levels. Results are shown for (a) Mid-latitude spectrum; (b) Artic spectrum; (c) Tropical spectrum.

Inclusion of trace gases CO_2, N_2O, CO and CH_4 as profile variables in RTIASI

In RTIASI-4, CO_2, N_2O, CO and CH_4 profiles are allowed to vary and are profile variables in the fast model with H_2O and O_3. For each of the gases allowed to vary, the profiles used to compute the database of LBL transmittances are chosen to represent the range of variations in absorber amount found

in the real atmosphere and should be representative of the gas observed behavior. The trace gases profiles used in RTIASI-4 are a blend of profiles from in-situ measurements and profiles generated using chemistry models.

The CO_2 profiles were assembled assuming that the vertical distribution of this gas is constant in the troposphere and decreases by 5 to 10 ppmv between the tropopause and about 22 km altitude (see Bischof et al, 1985). No further change is assumed above this layer. CO_2 profiles were generated on the basis of the season/latitude classification used for the original temperature/humidity 43 profile set.

For the generation of the N_2O profiles we assumed N_2O is well mixed in the troposphere. The N_2O profile set was generated from Cryogenic Limb Array Etalon Spectrometer (CLAES) (Reber et al. 1993) measurements in the stratosphere and from CMDL and AGAGE measurements at the surface (for further information see http://www.cmdl.noaa.gov and http://www.cdiac.ornl.gov/ndps/alegage.html). Profiles from CLAES were joined by parabolae to a constant tropospheric mixing ratio based on measurements obtained at the surface.

The CO profile set was generated assembling profiles based on MOZART 3D model calculations (Brasseur et al., 1998; Cunnold, 2001) and measurements taken during the STRATOZ III and TROPOZ II campaign in the Austral summer, 4-26 June 1984, and in the Austral winter, 9 January to 1 February 1991 (Marenco et al., 1995). Since no stratospheric data were available from these sources, mixing ratios in the troposphere were extrapolated to the stratosphere assuming a lapse rate equal to the one from the corresponding seasonal USAFGL CO profile.

For CH_4, profile concentrations in the troposphere are based on the IMAGES model calculations (Müller and Brasseur, 1995; Clerbaux et al., 1998). The profile set covers the seasonal cycle of the gas. Although the latitudinal gradient was retained, absolute values at all levels were scaled to reflect recent estimates of surface values from measurements made at the stations of the CMDL network. Tropospheric mixing ratios were joined by parabola to stratospheric measurements made by CLAES.

Finally, details of the predictors used for the CO_2, N_2O, CO and CH_4 transmittance model can be found in Matricardi (2003).

Performance of the fast model for simulation of IASI radiances

The accuracy of RTIASI-4 simulations has been assessed by a comparison of the radiances computed by the fast model with the corresponding values from the LBL model. A set of profiles independent of the regression coefficients has been used to allow uncertainties from different type of profiles to be included.

The analysis of the results discussed below concentrates on the error of RTIASI-4 in terms of the bias, standard deviation and rms of the radiance differences between the fast and LBL radiative transfer models.

Radiance errors in equivalent black body brightness temperature were calculated comparing radiances obtained by using the polychromatic form of the radiative transfer equation where transmittances from the fast and LBL models were used respectively. Spectra were computed for 117 independent profiles and six viewing angles from 0^o to 64^o. Results are shown in Fig. 2 where the mean value, standard deviation and rms of the difference between the fast and LBL computed radiances in units of equivalent black body brightness temperature is given for both the RTIASI-4 and RTIASI-2 models.

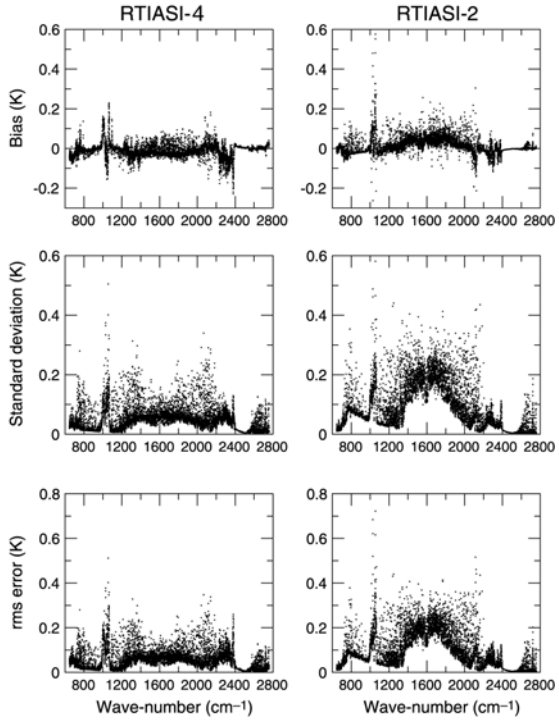

Figure 2:mean value, standard deviation and rms of the difference between fast model and GENLN2 computed brightness temperatures for 117 diverse profiles and 6 viewing angles.

Worst results are obtained for the channels where absorption for either lower atmosphere water vapour or ozone is important. A comparison with the error score for RTIASI-2 readily assesses the much improved accuracy of the RTIASI-4 transmittance model. An almost universal improvement is achieved that is most dramatic in the 1594 cm^{-1} water vapour band and in the 11 μm (900 cm^{-1}) window region mainly as a result of the new water continuum model.

The formulation of the model for the solar term

In RTIASI-4 we have introduced a solar term to evaluate the effect of solar radiance that is transmitted through the atmosphere and then partially reflected back upward through the atmosphere to the receiver. For the case of solar radiance reflected by a land surface, a proper treatment of the solar term would then require the knowledge of the bi-directional reflectance of the considered surface. Given that the bi-directional reflectance is not currently available in RTIASI-4, we treat the reflecting surface as a perfect diffuser following the Lambert law. For a Lambertian surface the bidirectional reflectance is constant and is equal to the surface albedo. If we assume that the atmosphere along the downward and upward path is the same, the solar radiance $\hat{L}_{\hat{\nu}^*}$ that reaches the detector can be written as

$$\hat{L}_{\tilde{\nu}^*} = \frac{1}{\pi} \rho^L \hat{I}^{\oplus}_{\tilde{\nu}^*} \mu_{\oplus} \hat{\tau}_{\tilde{\nu}^*}(\mu_{eff}) \tag{3}$$

where ρ^L is the surface albedo, $\hat{I}^{\oplus}_{\tilde{\nu}^*}$ is the solar irradiance at the top of the atmosphere and $\hat{\tau}_{\tilde{\nu}^*}(\mu_{eff})$ is the surface-to-space transmittance for the path angle μ_{eff} defined as

$$\frac{1}{\mu_{eff}} = \frac{1}{\mu} + \frac{1}{\mu_{\oplus}} \tag{4}$$

This is equivalent to say that the reflected solar radiance depends on a single transmittance whose secant is equal to the sum of the secants of the viewing (μ) and solar zenith angles ($\mu_{\oplus}$).

For the case of solar radiance reflected by a wind roughened water surface, the reflective characteristics of the wind roughened water surface are modeled following the approach by Yoshimori et al. (1995). In this model the probability density P of the wave slope obeys a Gaussian distribution whereas the spectrum of the wave slope is specified by the Joint North Sea Wave Project (JONSWAP) (Hasselmann et al.1973) wave-spectral model. The total variance of the slope is given by

$$\sigma^2_{tot} = \int_0^{\infty} \Psi(\omega)[k(\omega)]^2 d\omega \tag{5}$$

where $k(\omega)$ is the inverse function of the dispersive relation of the full-gravity capillary wave and $\Psi(\omega)$ is the frequency spectrum of the surface wave as specified by the JONSWAP wave model.

In the model by Yoshimori et al. (1995) shadowing (the fact that the slopes on the back sides of the waves and deep in the troughs between waves are hidden from view) is treated explicitly and allows the estimate of the reflected solar radiance for large solar zenith angles.

The solar source function used in RTIASI-4 is based on theoretical radiative transfer calculations for the solar atmosphere made by Kurucz (1992). In the spectral region of interest for IASI, it is strongly dependent on measurements made by the ATMOS instrument on the Space Shuttle.

For the case of solar radiance reflected by a water surface the solar radiance that reaches the detector can be written as

$$\hat{L}_{\tilde{\nu}^*} \cong \hat{I}_{\tilde{\nu}^*}{}^{\oplus} \quad w_{\tilde{\nu}^*}(\mu, \varphi, \mu_{\oplus,} \varphi_{\oplus}) \quad \hat{\tau}_{\tilde{\nu}^*}(\mu_{eff}) \tag{6}$$

Here $w_{\tilde{\nu}^*}(\mu, \varphi, \mu_{\oplus,} \varphi_{\oplus})$ is the effective reflectivity of the wind roughened water surface whereas φ is the azimuth angle of the receiver and $\varphi_{\oplus}$ is the azimuth angle of the sun.

The computation of $\hat{\tau}_{\tilde{\nu}}(\mu_{eff})$ in equations (3) and (6) requires the evaluation of transmittances at large zenith angles. For the fast transmittance model to be able to simulate transmittances for a wider range of zenith angles, we have extended the database of line-by-line transmittances by computing data for an additional number of eight more zenith angles, namely, the angles for which the secant assumes the

following values: 2.58, 3.04, 3.72, 4.83, 6.1, 7.2, 9, 12. This extended range allows evaluating the solar term for zenith angles as large as $\approx 85°$. The additional database of line-by-line transmittances was generated only for the shortwave channels ($\tilde{\nu} \geq 2000\, cm^{-1}$).

Since the larger range of zenith angles increases the difficulty of fitting the line-by-line optical depths, we have developed a dedicated transmittance model for the shortwave. The new model uses a revised and larger number of predictors (Matricardi 2003).

Conclusions

An improved version of RTIASI (RTIASI-4), the ECMWF fast radiative transfer model for IASI, has been developed.

The accuracy of the LBL computations has been improved by including 4 more molecules (HNO3, CCl4, CF_4 and OCS) and by using the year 2000 release of the HITRAN molecular database. By using a revised set of water vapour training profiles in the stratosphere, the condition of the regression has been improved so that unphysical oscillations in the stratospheric water vapour Jacobians have been virtually eliminated. The RTIASI-4 features a revised vertical pressure grid that allows the integration of the radiative transfer equation to be performed with significantly increased accuracy. The water vapour transmittance model has been significantly improved by weighting the data prior to performing the regression and by introducing a dedicated transmittance model for the continuum absorption. RTIASI-4 can now handle variable CO_2, N_2O, CO ,CH_4 and a solar term has been introduced to evaluate the solar radiance reflected by a land or water surface in a non-scattering atmosphere.

Results for RTIASI-4 and the previous version of the code, RTIASI-2, shows the much-improved accuracy achieved by use of the revised transmittance model for water vapour. Errors in the centre of the 1594 cm-1 water vapour band and in the 11 (900 cm-1) window region have been reduced four-fold. For 95% of the channels RTIASI-4 can reproduce LBL radiances better than 0.15 K. Larger errors are observed in the ozone-sounding band and in the spectral regions where absorption from lower atmospheric layers water vapour takes place.

Acknowledgements

We wish to tank T. Clough, AER, for having provided the software to generate the solar irradiance spectrum, D. Cunnold, Georgia Tech, for having assembled the dataset of MOZART CO profiles and C. Clerbaux, Service D'Aeronomie, for having provided the tropospheric profiles for CH_4. Discussions with T. McNally, J.N. Thépaut and P. Watts, all staff at ECMWF, were also valuable during the course of this work. Marco Matricardi is supported by EUMETSAT (contract EUM/CO/01/882/DK and EUM/CO/02/989/PS) through the IASI pre-launch definition studies.

References

Bischof, W., Borchers, R., Fabian, P., and Kruger, B.C., 1985, "Increased concentration and vertical distribution of carbon dioxide in the stratosphere", Nature, 316, pp. 708-710.

Brasseur, G.P., Hauglustaine, S., Walters, S., Rasch, P.J., Müller, J.F., Granier, C., and Tie, X.X., 1998, "MOZART, a global chemical transport model for ozone and related chemical tracers. I. Model description", *J. Geophys. Res*., **103**, pp 28265-28289.

Cayla, F., 1993, "IASI infrared interferometer for operations and research", in High Spectral Resolution Infrared Remote Sensing for Earth's Weather and Climate Studies, *NATO ASI Series 1,* Ed. A. Chedin, M. Chaine and N. Scott.

Clough, S.A., Kneizys, F.X. and Davis, R.W., 1989, "Line shape and the water continuum", *Atmos. Res*., **23**, pp. 229-241.

Clerbaux, C., Chazette, P., Hadji_Lazaro, J., Megie, G., Müller, J.-F. and Clough, S.A., 1998, "Remote sensing of CO, CH4 and O3 using a space-borne nadir-viewing interferometer", *J. Geophys. Res.*, **103**, pp 18999-19013.

Cunnold, D., Georgia Tech, USA (personal communication, 2001)

Edwards, D.P., 1992, "GENLN2. A general line-by-line atmospheric transmittance and radiance model", NCAR Technical note NCAR/TN-367+STR.

Evans, S.J., Imperial College, London, UK (personal communication, 1997)

Klaes, K.D., Buhler, Y., Wilson, H., and Wollenweber, F., 2000, "The EUMETSAT Polar System: mission and products", proceedings of the 2000 EUMETSAT Meteorological Satellite Data User's Conference, Bologna, Italy, 29 May-2 June 2000.

Kurucz, R.L., 1992, "Synthetic infrared spectra", in Infrared Solar Physics, IAU Symphosium 154, edited by D.M. Rabin and J.T. Jefferies, Kluwer, Acad., Norwell, MA.

Hasselman, K., Barnet, T.P., Bouws, E., Carlson, H., Cartwright, D.E., Enke, K., Ewing, J.A., Gienapp, H., Hasselman, P., Kruseman, P., Meerburg, A., Muller, P., Olbers, D.J., Richter, K., Sell, W., and Walden, H., 1973, "*Measurements of Wind Wave Growth and Swell Decay during the Joint North Sea Wave Project (JONSWAP)* (Deutsches Hydrographisches Institut, Hamburg, germany).

Marenco, A., Jonquieres, I., Gouget, H., and Nédélec, P., 1995, " Experimental determination of meridional distribution and long term evolution of tropospheric ozone from large scale airborne campaigna (STRATOZ/TROPOZ) and Pic du Midi data series: Consequences on radiative forcing", *Global Environmental Change*, edited by W.C. Wang and I.S.A. Isaksen, *NATO ASI Ser*., **32**, pp 305-319.

Matricardi, M. and Saunders, R., 1999, “Fast radiative transfer model for simulation of infrared atmospheric sounding interferometer radiances”, *Applied Optics*, **38**, pp. 5679-5691.

Matricardi, M., 2003, “RTIASI-4, a new version of the ECMWF fast radiative transfer model for the infrared atmospheric sounding interferometer”, ECMWF technical memorandum 425.

Mhller, J.-F. and Brasseur, G., 1995, “IMAGES: A three-dimensional chemical transport modelo of the global troposphere”, *J. Geophys. Res*., **100**, pp 16445-16490.

Reber, C.A., Trevathan, C.E., McNeal, R.J., and Luther, M.R., 1993, “The Upper Atmosphere Research Satellite (UARS) Mission”, *J. Geophys. Res*., **98**, D6, pp 10643-10647.

Rothman, L.S., Barbe, A., Chris Benner, D., Brown, L.R., Camy-Peyret, C., Carleer, M.R., Chance, K., Clerbaux, C., Dana, V., Devi, V.M., Fayt, A., Flaud, J.-M., Gamache, R.R., Goldman, A., Jaquemart, D., Jucks, K.W., Lafferty, W.J., Mandin, J.-Y., Massie, S.T., Nemtchinov, V., Newnham, D.A., Perrin, A., Rinsland, Schroeder, J., Smith, K.M., Smith, M.A.H., Tang, K., Toth, R.A., Vander Auwera, J., Varanasi, P.,Yoshino”,2003, “The HITRAN molecular spectroscopic database: edition of 2000 including updates through 2001”, *J. Quant. Spectrosc. Radiat. Transfer*, **82**, pp. 5-44.

Yoshimory, K., Kazuyoshi, I., and Ichioka, Y., 1995, “Optical characteristics of a wind roughened water surface: a two dimensional theory”, Applied Optics, **Vol. 34**, No. 27, pp. 6236-6247.

Comparison of the CMC analysed fields of Integrated Water Vapour with those retrieved from the SSM/I

David Anselmo and Godelieve Deblonde
Meteorological Service of Canada, Dorval, Quebec, Canada

Abstract

On June 19th, 2003 the Canadian Meteorological Centre (CMC) began assimilating Advanced Microwave Sounding Unit-B (AMSU-B) clear-sky brightness temperatures and Geostationary Observing Earth Satellite (GOES) radiances in its 3D-Var global data assimilation system (Chouinard and Hallé 2003). These new satellite data join the AMSU-A level-1b clear-sky brightness temperatures that are already assimilated (channels 3-10 over oceans, 6-10 over land) at CMC since June 7th, 2001 (Chouinard et al. 2002). To prepare for the assimilation of Special Sensor Microwave Imager (SSM/I) brightness temperatures, the CMC analysed integrated water vapor (IWV) fields are evaluated over open oceans by comparing them with SSM/I retrieved IWV. Two comparisons are performed. Firstly, SSM/I IWV fields are compared against analysed fields to measure the impact of assimilating AMSU-A channel 3 (50.3 GHz) which has a non-negligible humidity dependence. Analyses prior to the addition of AMSU-B and GOES data are used for this purpose. Two assimilation cycles are executed: one assimilating AMSU-A channels 3-10 and the other channels 4-10. Secondly, SSM/I IWV is compared with analysed fields of IWV that are derived with and without the additional AMSU-B and GOES data over the same period. Results show that with respect to moisture the impact of assimilating AMSU-A channel 3 is small, but the benefit of assimilating AMSU-B and GOES data is substantial.

Introduction

At the Meteorological Service of Canada recent efforts have aimed to improve the global analyses produced by the Canadian Meteorological Centre's (CMC) operational analysis system by increasing the volume of quality satellite-borne observations that are assimilated. For example, clear-sky brightness temperatures measured by the Advanced TIROS[1] Operational Vertical Sounder (ATOVS) instrument package aboard NOAA's polar orbiting satellites have been introduced to the assimilation cycle over the past 2½ years. Advanced Microwave Sounding Unit-A (AMSU-A) level-1b observations from NOAA 15 and NOAA 16 were added on June 7th, 2001, and from NOAA 17 on December 11th, 2002. AMSU-B data from the three NOAA satellites was added more recently on June 19th, 2003. Also at that time, the assimilation of radiances from the water vapour channel of the GOES-W satellite replaced that of GOES retrievals of dewpoint depression (DPD) that had been included since 1993 (Garand 1993; Garand and Hallé 1997).

Preliminary work is now under way to assimilate Special Sensor Microwave Imager (SSM/I) brightness temperatures in the global cycle. In preparation for the inclusion of this new data source, two sensitivity experiments were conducted using the CMC's 3D-Var assimilation scheme. The aim of the first experiment was to measure the impact of assimilating channel 3 (50.3 GHz) of the AMSU-A instrument, prior to the introduction of the AMSU-B and GOES data. As with the 7 imaging channels of the SSM/I instrument (at frequencies/polarizations of 19.35 V,H, 22.235 V, 37.0 V,H, and 85.5 V,H GHz), channel 3 is sensitive to atmospheric moisture. The objective of the second experiment was to determine how the recent addition of AMSU-B data and the change in the type of GOES data that is assimilated have affected the analysed moisture fields.

Experimental Setup

To evaluate the experiments, retrievals of integrated water vapour (IWV) were employed. These retrievals were derived from open-water, non-precipitating SSM/I observations using a regression algorithm (Alishouse et al. 1990; Petty 1990). SSM/I brightness temperatures from the Defense Meteorological Satellite Program's (DMSP) polar orbiting satellites (DMSP 13, DMSP 14, and

[1] Television Infrared Observation Satellite (TIROS) was the name given to the original polar orbiting satellites in the 1960s, which have since evolved into the NOAA satellite series.

DMSP 15) were applied independently in this exercise, since intercalibration coefficients were not available. For each of the two experiments, there was a CONTROL run and a TEST run. Analysed IWV fields were computed by vertically integrating specific humidity, output by the assimilation cycle in CONTROL or TEST mode, over the 28 CMC global model terrain-following coordinates. These were then interpolated to the SSM/I observation locations for each 6-hr period over the length of the experiment. Mean IWV fields representing the observed values and analysed values were computed on a global 1^o x 1^o grid using a straightforward binning and averaging technique over the period of the experiment. Finally, the mean analysed IWV fields were compared against the mean SSM/I IWV fields to formulate our conclusions. The results shown below are with respect to the DMSP 15 satellite only, although the DMSP 13 and DMSP 14 results are very similar.

Experiment #1

For the first experiment, the CONTROL configuration (labelled CH3) consisted of the assimilation of AMSU-A data from channels 3 through 10 over a 3 week period in March, 2003 (see Table 1 for a summary of the ATOVS channel parameters). In the TEST configuration (labelled NOCH3), AMSU-A data from channels 4 through 10 were assimilated over the same period. In both cases, humidity profiles from GOES-W and GOES-E were also assimilated. To allow for a period of stabilization after the removal of channel 3 in the NOCH3 simulation, only the last two weeks of data were analysed (i.e. March 8^{th} to March 21^{st}). Additionally, statistics were calculated for grid boxes that contained a minimum of 50 SSM/I observations. This represents 9-10% of the observations that would normally occur during a 2 week period within a 1^o x 1^o sized box (no filtering).

Table 1: ATOVS Channel Parameters

ATOVS Channel No.	AMSU-A Channel No.	Frequency (GHz)	Polarization
1	1	23.8	V
2	2	31.4	V
3	3	50.3	V
4	4	52.8	V
5	5	53.596	H
6	6	54.4	H
7	7	54.94	V
8	8	55.5	H
9	9	57.29	H
10	10	57.29	H
11	11	57.29	H
12	12	57.29	H
13	13	57.29	H
14	14	57.29	H
15	15	89.0	V
	AMSU-B Channel No.		
16	1	89.0	H
17	2	150.0	H
18	3	183.31	H
19	4	183.31	H
20	5	183.31	H

Experiment #1 Results

In Figure 1a the difference between the mean observed IWV field and the mean analysed IWV field for CH3 is given. Generally, it can be concluded that the model has underestimated the amount of atmospheric moisture over tropical regions, particularly over the Indian Ocean. A very large surplus of moisture in the analyses is evident over the southern Pacific Ocean, just off the west coast of South America. It has been noted by Deblonde (1999) that this positive bias is attributed to an overestimation of humidity by the GOES DPD retrievals as a consequence of persistent marine stratocumulus clouds. In contrast, the dry bias evident west of South America along the equator is attributed to clear skies. Neither area is handled well by the procedure used to derive vertical humidity profiles from GOES radiances since radiosonde observations required to calibrate the retrievals are

not available. The cloud distribution described above was verified over the period of the experiment by cloud liquid water charts produced by Remote Sensing Systems (RSS) Inc.[2] (not shown).

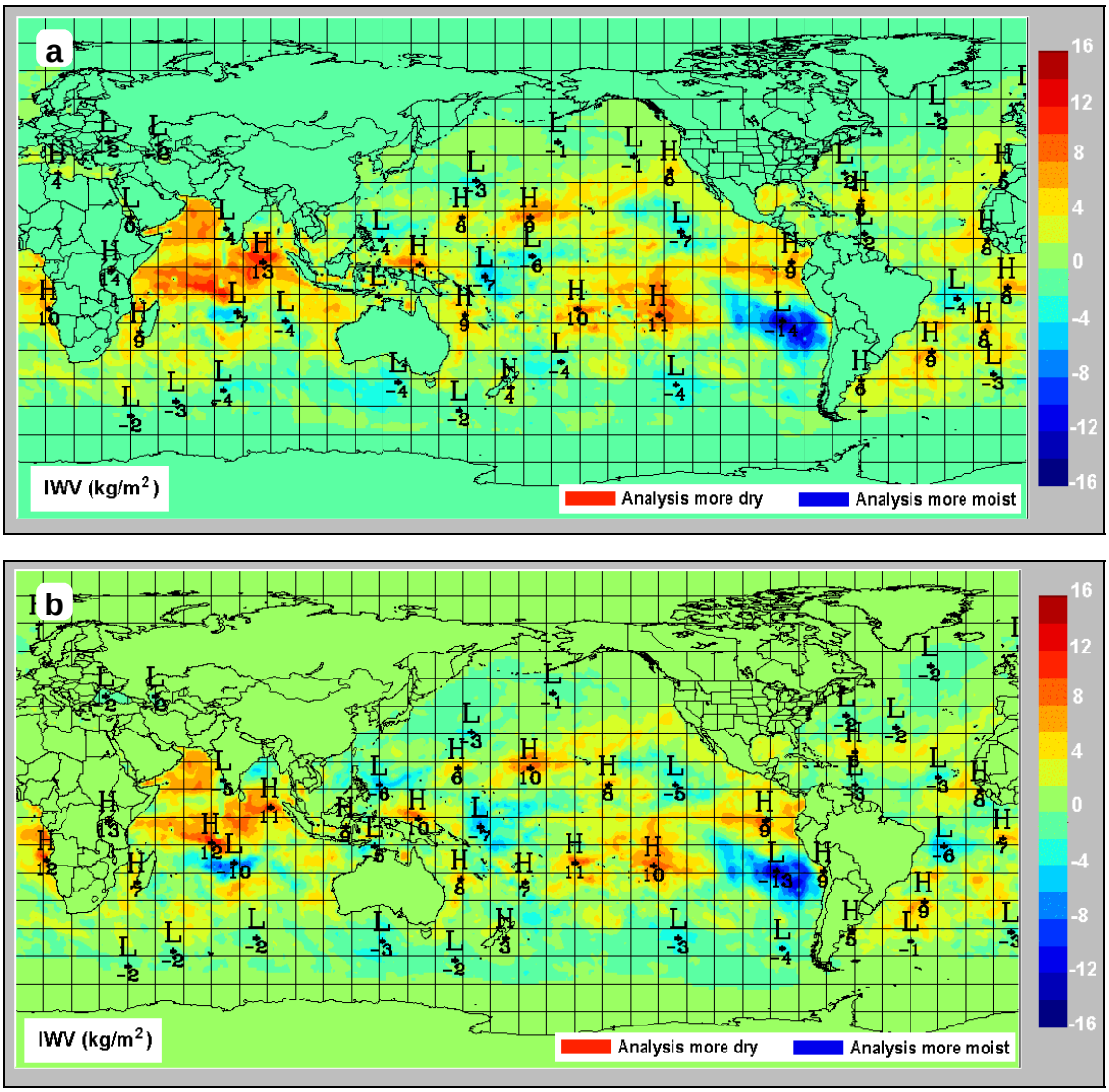

Fig. 1: Observed IWV (kg m^{-2}) minus analysed IWV for CH3 run (a) and for NOCH3 run (b) of Experiment #1.

From the high degree of similarity between Figure 1a and Figure 1b, it is evident that the exclusion of AMSU-A channel 3 from the assimilation process does not result in any obvious positive or negative impact on the analyses, with respect to moisture. As expected, the strong positive anomaly off the west coast of South America is not affected by the absence of channel 3 data in NOCH3.

Statistics for the two runs are summarized in Figure 2. Generally, the analysed IWV field correlates equally well with the observed field, regardless if channel 3 is assimilated or not. However, the biases show an improvement in most regions, except between 20°S to 60°S, when channel 3 observations are excluded. A large reduction in positive bias in the tropics primarily reflects an increase in moisture over the Indian Ocean. The changes to standard deviation are negligible. A plot of the zonally averaged difference in analysed IWV between CH3 and NOCH3 over the entire globe (Figure 3) further demonstrates the moistening that has occurred over tropical and northern mid-latitude regions. As well, drying is observed over a narrow southern middle-latitude band as a result of the removal of AMSU-A channel 3.

[2] available at www.ssmi.com.

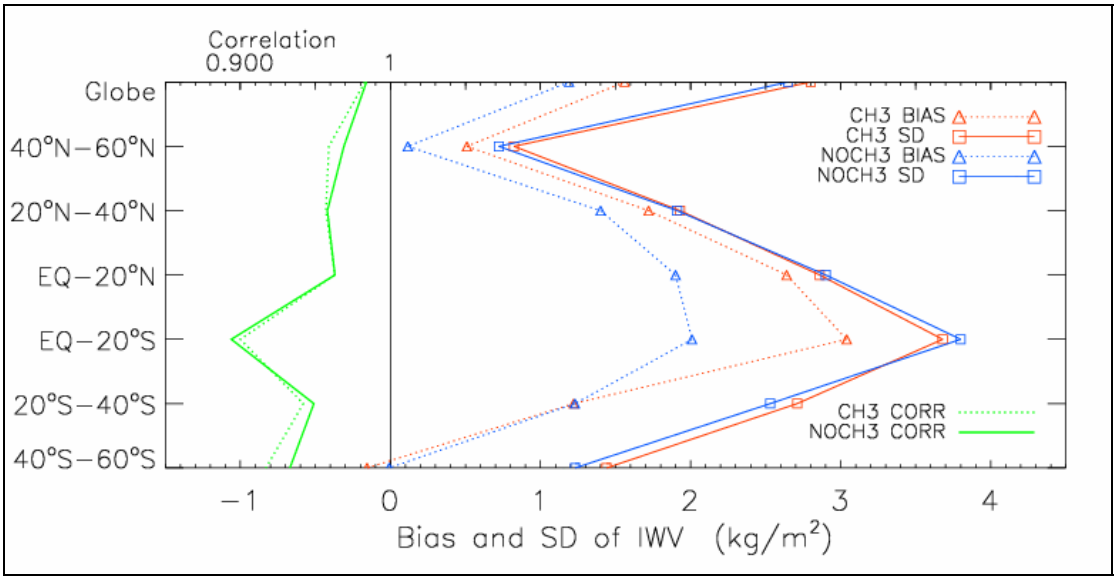

Fig. 2: Bias (dashed blue/red lines), standard deviation (solid blue/red lines), and correlation (green lines) statistics for CH3 and NOCH3 runs of Experiment #1 with respect to DMSP 15 observations. Statistics are computed over 6 latitude bands between 60°S and 60°N, and for the globe (top of chart).

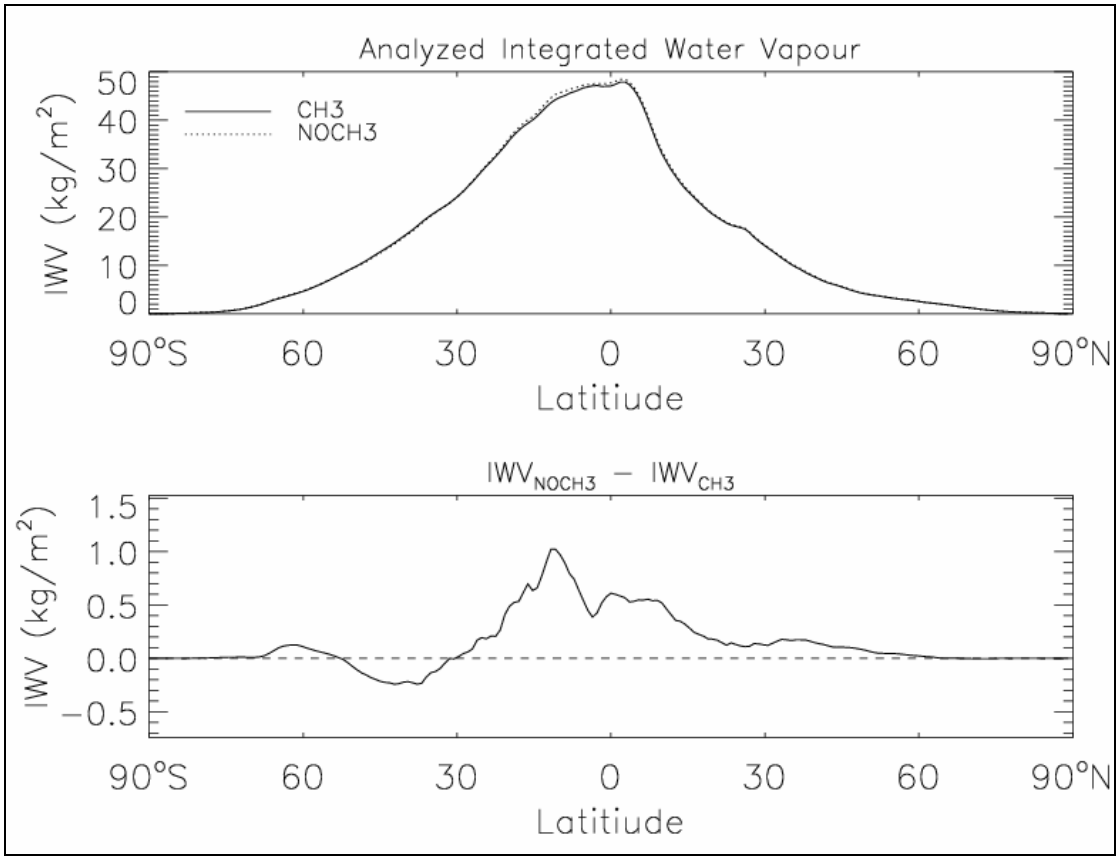

Fig. 3: Zonally averaged analysed IWV (kg m^{-2}) for CH3 and NOCH3 runs of Experiment #1; absolute values (top) and difference field (bottom).

Experiment #2

For the second experiment, the CONTROL simulation (labelled NOAMSUB) assumed the CMC's operational configuration of the assimilation process during the month of May, 2003. In this

arrangement, AMSU-A clear-sky observations (channels 3-10) from NOAA 15, NOAA 16, and NOAA 17 and vertical humidity retrievals from the GOES-W satellite were assimilated (GOES-E data was unavailable for the month of May). The experimental configuration (labelled AMSUB) assumed the CMC's parallel configuration during the same period. In this arrangement, AMSU-A (channels 3-10) and AMSU-B (channels 2-5) clear-sky brightness temperatures from the NOAA 15, NOAA 16, and NOAA 17 polar orbiting satellites were assimilated. As well, direct assimilation of radiance observations from the water vapour channel of GOES-W replaced the assimilation of GOES retrievals of DPD. Statistics were calculated for grid boxes that contained a minimum of 100 SSM/I observations. Again, this represents 9-10% of the observations that would normally occur during a 31 day period within a 1^o x 1^o sized box.

Experiment #2 Results

Similar to Figure 1a, the difference between the mean observed IWV and the mean analysed IWV for NOAMSUB for the month of May shows a model that underestimates the amount of atmospheric moisture in tropical areas and slightly overestimates it over the southern latitude oceans and the northern Pacific ocean (see Figure 4a). However, the large moisture surplus noted off the west coast of South America in Figure 1a is negligible in the May plot. The monthly mean cloud liquid water map produced by RSS for May confirms that there was much less marine stratocumulus in the area over the period. Nonetheless, significant moisture deficits and surpluses in the analyses remain in the NOAMSUB simulation over the northwestern and far eastern Indian Ocean, the far western Pacific Ocean, the northern equatorial Pacific, and much of the Atlantic Ocean. Large differences in moisture over the Atlantic Ocean between the NOAMSUB run and the CH3 run of Experiment #1 are due to the absence of GOES-E data in the former simulation.

The mean difference field produced when AMSU-B data and GOES radiances are assimilated is given in Figure 4b. It is clear that the additional data is providing valuable information to bring the analysed moisture fields much closer to the SSM/I moisture fields. In particular, the amplitudes of the significant dry biased regions have been reduced by a factor of at least two. Two prominent moisture surplus regions previously noted over the equatorial Pacific Ocean have also been brought inline with DMSP 15 observations by the AMSUB simulation.

Computing the difference between the mean analysed IWV fields that were produced by the NOAMSUB and AMSUB runs illustrates the intense, localized changes to the global humidity levels that have occurred (Figure 5). It is interesting that these changes are specifically targeting the most problematic areas identified in the NOAMSUB simulation.

A summary of statistics similar to that produced for Experiment #1 is provided in Figure 6. From this information, it is easy to conclude that the assimilation of the new data has a remarkable positive impact on the analyses. In all regions, the mean AMSUB IWV values correlate much better with SSM/I observations - between 60^oS and 60^oN the correlation has increased from 0.932 to 0.977. A global moistening of the analyses in the AMSUB cycle is evident by comparing the bias statistics. In the zone bounded by 40^oS and 60^oS there is a small deterioration in the analysed humidity as regions where the moisture is already overestimated become more humid. Between 40^oN and 60^oN the additional data has a neutral effect as the bias changes from slightly positive to slightly negative. In the tropical and extratropical areas in between, however, the increase in moisture is beneficial as it reduces a dry bias. In all regions the additional data gives a notable decrease in the standard deviation of IWV with respect to SSM/I observations. The largest gains are made in the tropics, where the standard deviation actually becomes smaller in magnitude than the bias. Hence, there are still improvements to be made, which perhaps could be realised by the assimilation of SSM/I data.

Incidentally, one of the more weakly correlated regions in the NOAMSUB run is the band EQ to 20^oN, which may be due to areas of intense convection associated with the Inter-Tropical Convergence Zone (ITCZ). This hypothesis is supported by Figure 2 which shows that in the March experiment the most weakly correlated band was EQ to 20^oS, where portions of the ITCZ would have resided at a time of the year closer to Southern Hemispheric summer.

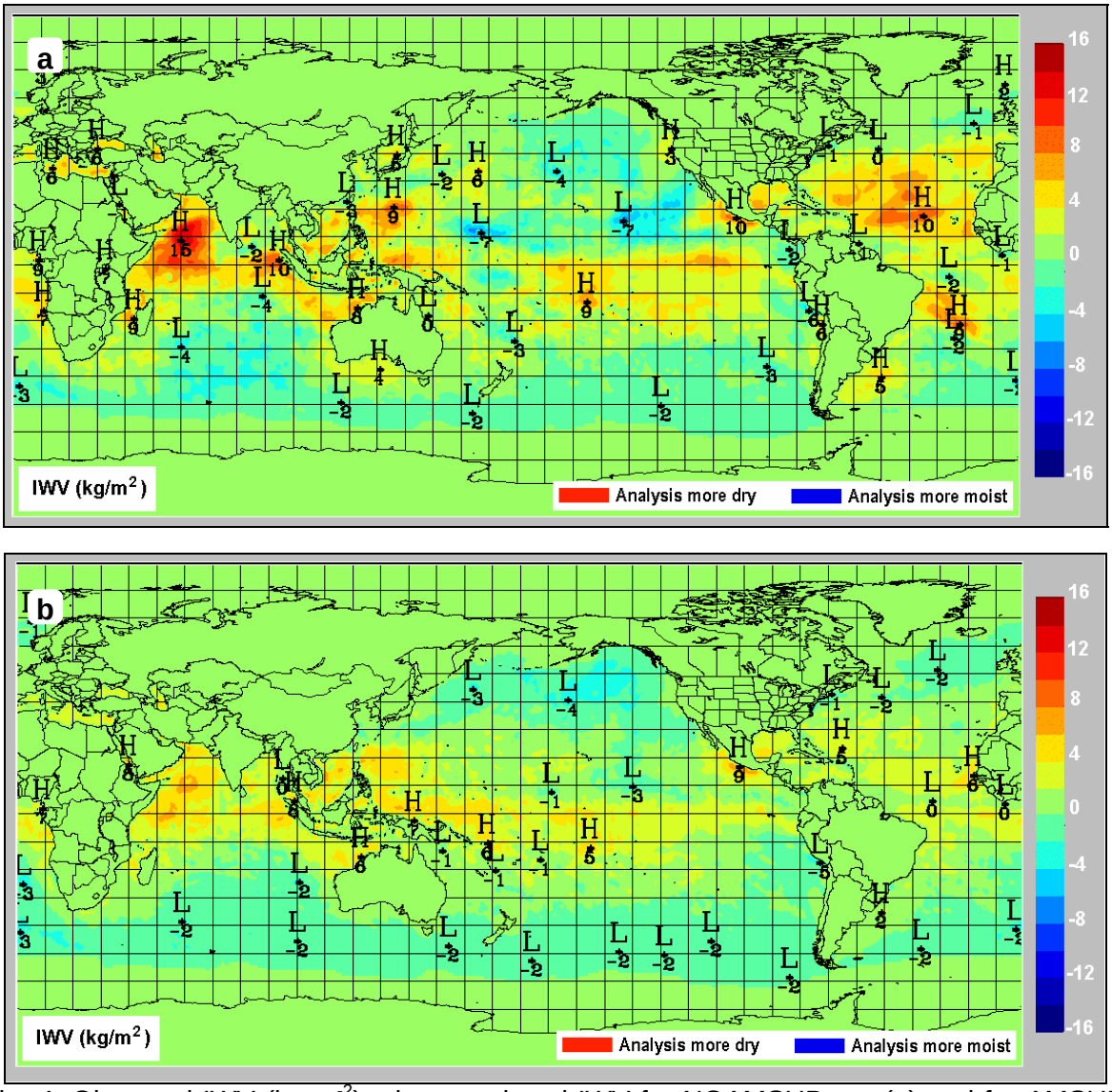

Fig. 4: Observed IWV (kg m^{-2}) minus analysed IWV for NOAMSUB run (a) and for AMSUB run (b) of Experiment #2.

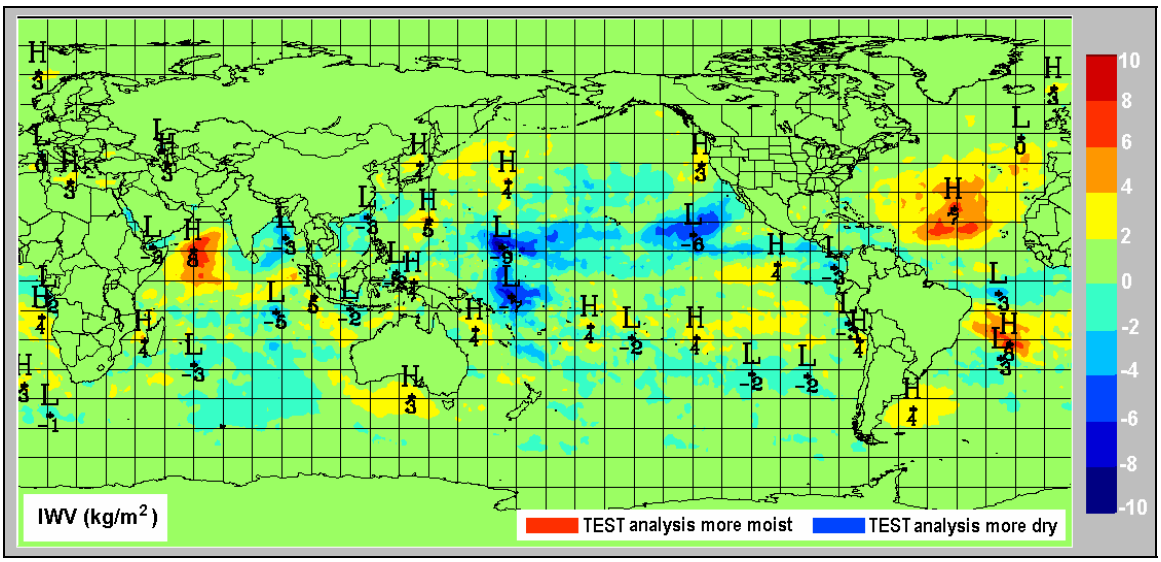

Fig. 5: Analysed IWV (kg m^{-2}) for AMSUB run minus that for NOAMSUB run of Experiment #2.

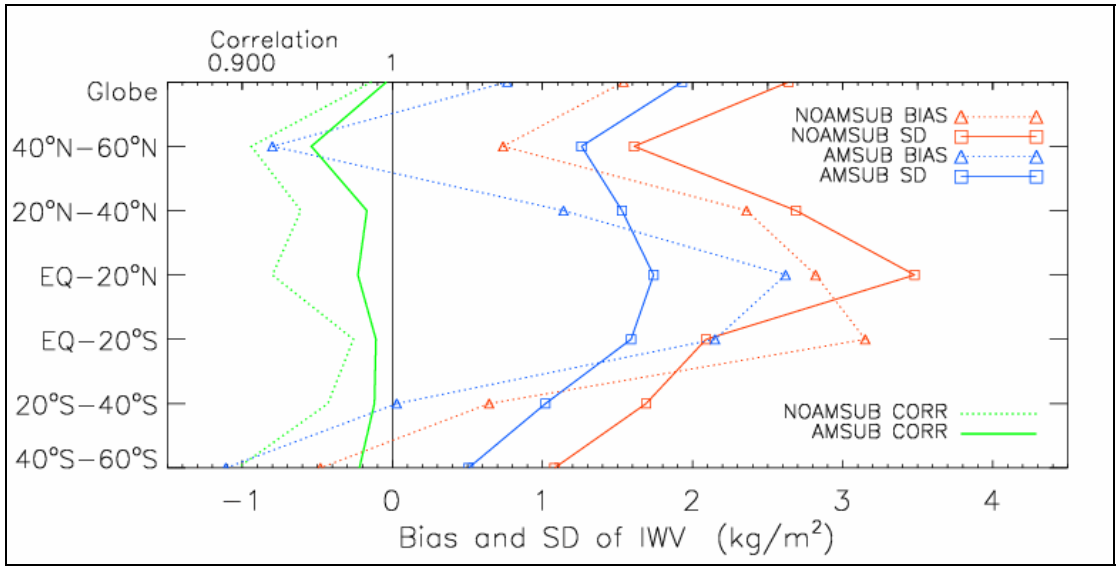

Fig. 6: Same as in Fig.2 except for NOAMSUB and AMSUB runs of Experiment #2.

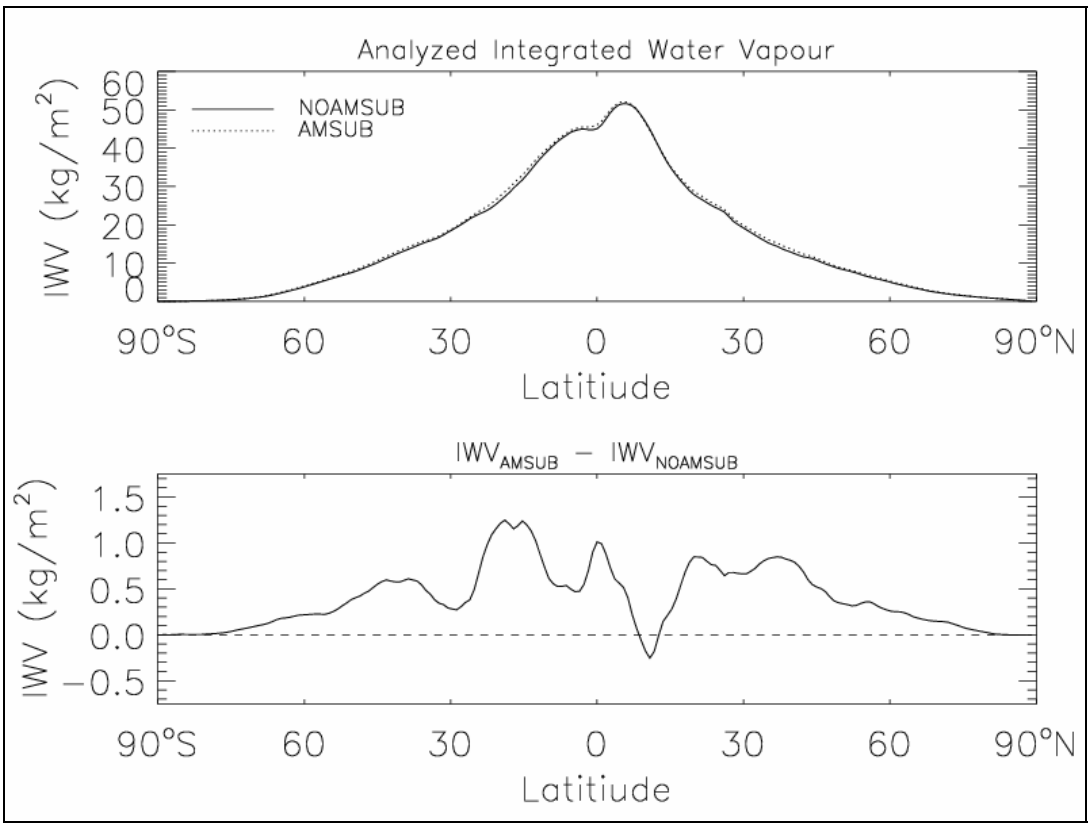

Fig. 7: Same as in Fig. 3 except for NOAMSUB and AMSUB runs of Experiment #2.

Zonally averaged changes to the mean analysed IWV field brought about by the new assimilation setup are illustrated in Figure 7. This chart verifies that the additional data works to increase the amount of moisture in the analyses almost everywhere on the globe. The exception is a small amount of drying which occurs in the subsidence band located just north of the ITCZ. Figure 8 depicts the vertical structure of changes to the mean specific humidity field. From the bottom panel it is evident that the drying near 10-12°N occurs in the lowest 100-200 hPa of the atmosphere. Otherwise, the most significant relative increases in moisture occur between 15°S and 55°S at 850 hPa (max. of 13.0%), and directly over the equator at 500 hPa (11.0%). This is not surprising since the AMSU-B channels peak at higher altitudes in a tropical air mass and at lower altitudes in a cooler, extratropical air mass.

As well, satellite data plays a larger role in the Southern Hemisphere due to more data being assimilated over open waters and fewer land-based observations. Changes to the humidity field between 60° latitude and the poles are considered insignificant due to the lack of absolute moisture in these regions.

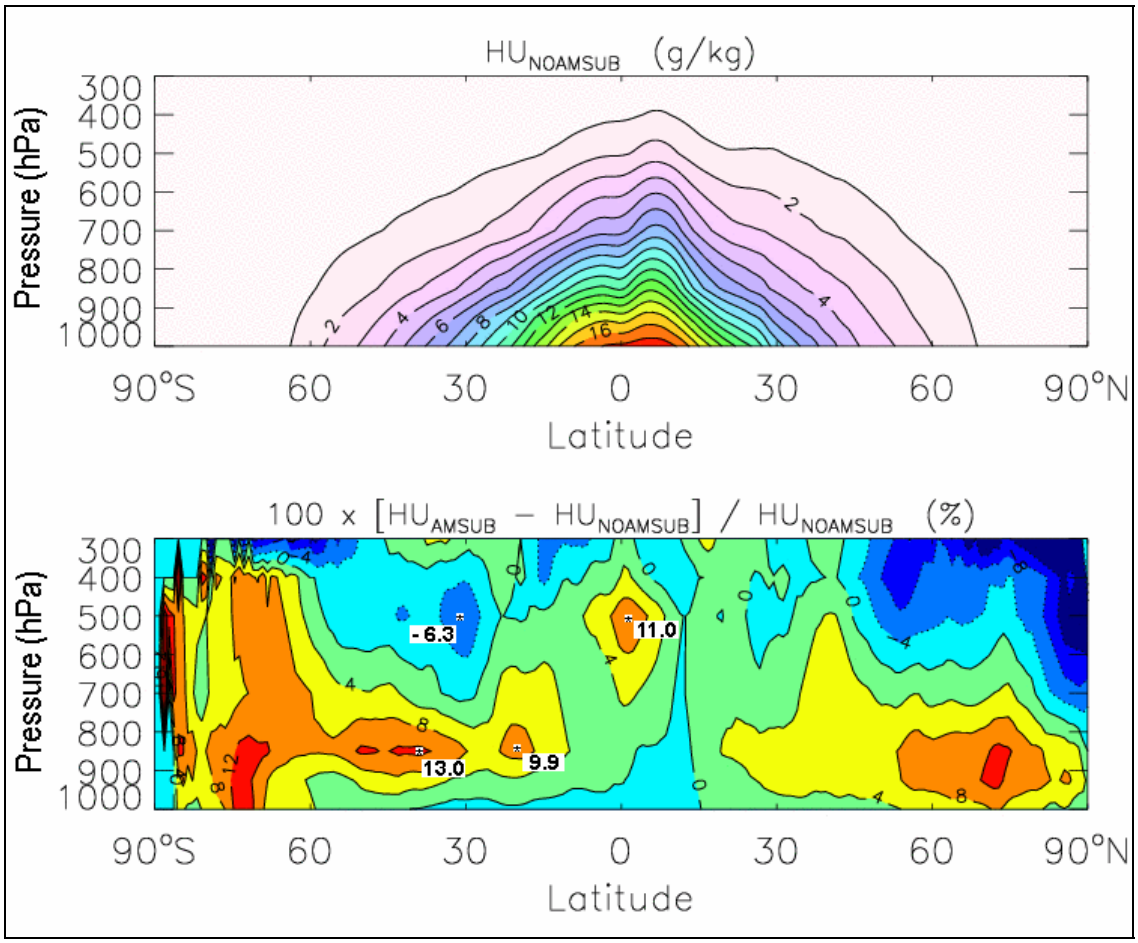

Fig. 8: Zonal averages of the mean analysed specific humidity (g kg^{-1}) for NOAMSUB and AMSUB runs of Experiment #2; absolute value for NOAMSUB (top) and relative change (bottom).

Conclusions

Two assimilation experiments were conducted in an effort to answer the following questions:

1) What is the significance of assimilating AMSU-A channel 3 brightness temperatures (over open oceans) in the production of CMC analyses?
2) How has the addition of AMSU-B brightness temperatures and the replacement of GOES DPD retrievals by GOES water vapour channel radiances affected the analyses?

To address the first question, two assimilation cycles were studied over a three week period in March of 2003. In one simulation, observations from AMSU-A channels 3 through 10 were assimilated. In the second, only observations from AMSU-A channels 4 through 10 included. Mean IWV fields were calculated from the analyses output over the final two weeks of each cycle, and compared against mean IWV fields calculated from SSM/I observations. Differences in the global distribution of moisture indicated that the inclusion of channel 3 radiances produces a less humid atmosphere over the tropics and northern latitudes, and a mildly more humid atmosphere over the southern mid-latitudes. Drying of the atmosphere over much of the globe when channel 3 is included slightly deteriorates the analyses when compared against SSM/I observations. Standard deviation and correlation statistics remain largely unaffected whether channel 3 is assimilated or not. Thus, the

impact with respect to moisture of including channel 3 in CMC's global assimilation cycle is concluded to be small. Note, AMSU-A channel 3 is also sensitive to temperature. However, its effect on analysed temperature fields was not explored in this study.

In response to the second question, operational analyses were extracted from CMC archives for the month of May, 2003. These analyses were produced with the assimilation of AMSU-A channels 3-10 brightness temperatures and GOES DPD retrievals. During the same period, a parallel run was executed at CMC whereby the GOES humidity profiles were removed from the assimilation process, and measurements from AMSU-B channels 2-5 and the GOES water vapour channel were added.

Differences between the monthly mean IWV fields computed from operational (NOAMSUB) and parallel (AMSUB) analyses with that derived using SSM/I observations show a significant improvement in the parallel configuration. More specifically, the inclusion of AMSU-B brightness temperatures results in more humidity being captured in the analyses, which for areas bounded between 40^{o}S and 40^{o}N reduces a prominent dry bias. Between 40^{o}N and 60^{o}N, the dry bias becomes a wet bias, and between 40^{o}S and 60^{o}S a wet bias becomes slightly larger in magnitude. In all regions, but especially the tropics, a notable reduction in standard deviation is observed. The newer moisture fields correlate much more strongly with SSM/I than in the previous design. An analysis of 2-D global plots of mean IWV from NOAMSUB and AMSUB shows that the largest differences with SSM/I are greatly reduced. The effect of assimilating the GOES-W water vapour channel cannot be determined in this study since this channel peaks at higher, less humid altitudes which were not a focus of the plots and statistics shown. The parallel version of the assimilation scheme became operational at CMC on June 19^{th} of 2003.

In the coming months work will be performed to examine the effect of assimilating SSM/I brightness temperatures in the AMSUB configuration of Experiment #2, to see if the moisture fields can be improved even more.

References

Alishouse, J. C., S.A. Snyder, J. Vongsathorn, and R. R. Ferraro, 1990. Determination of oceanic total precipitable water from the SSM/I. IEEE Trans. Geosci. Remote Sens., 28, 811-816.

Chouinard, C., J. Hallé, C. Charette, and R. Sarrazin, 2002. Recent improvements in the use of TOVS satellite radiances in the unified 3D-Var system of the Canadian Meteorological Centre. International TOVS Study Conference-12, Lorne, Australia.

Chouinard, C. and J. Hallé, 2003. The assimilation of AMSU-B radiance data in the Canadian Meteorological Centre global data assimilation system: their difficulties relative to the assimilation of AMSU-A radiances. International TOVS Study Conference-13, St. Adele, Canada.

Deblonde, G. 1999. Variational assimilation of SSM/I total precipitable water retrievals in the CMC analysis system. Mon. Wea. Rev., 127, 1458-1476.

Garand, L. 1993. A pattern recognition technique for retrieving humidity profiles from Meteosat of GOES imagery. J. Appl. Meteor., 32, 1592-1607.

Garand, L. and J. Hallé, 1997. Assimilation of clear- and cloudy-sky upper-tropospheric humidity estimates using GOES-8 and GOES-9 data. J. Atmos. Oceanic Technol., 14, 1036-1054.

Petty, G. W., 1990. On the response of the SSM/I for atmospheric parameter retrievals. Ph. D. thesis, University of Washington, 252 pp.

The AMSU Observation Bias Correction and Its Application Retrieval Scheme, and Typhoon Analysis

Chien-Ben Chou, Kung-Hwa Wang

Central Weather Bureau, Taipei, Taiwan, R.O.C.

Abstract

*Si*nce most of AMSU channels have a beam position-dependent bias, it is crucial to remove such a bias for providing useful profiles of the atmosphere. Measurement errors are estimated from the differences between satellite observations and the simulated satellite observations, which were obtained from a radiative transfer operator with 12-hours forecast of their input. The measurement errors estimated in this way will contain the forecast error of a 12 hour forecast. The NMC method assumes that the statistics of differences between forecasts at different ranges valid at the same time are the representative of forecast error statistics. The differences used in the NMC method have been transferred to brightness temperature in each AMSU channel with the radiation transfer operator. These data can then be used to obtain the value of 12 hours forecast error in brightness temperature for each AMSU channel. Thus, the 12 hour forecast error in each AMSU channels can be removed when the measurement errors are estimated as mentioned above.

In this study, we carefully examine the AMSU beam near Taiwan. A bias correction method, which concerns the beam position-dependent bias and the effect of 12 hours forecast error used on the regression equations, has been built. A data retrieval method based on one-dimensional variational scheme has also been developed. Through the comparison of the retrieved profiles and the background fields, we found that the method worked well near the Taiwan area. Even with quite accurate background fields, the retrieved profiles have shown positive impact to improve the fields. The results show that the improvement made in the retrieval scheme over the background error is about 0.45K in the temperature profiles, above 780 hPa. The study used corrected AMSU data to identify thermal anomalies and estimate tangent winds that successfully analyzed typhoon structure.

Introduction

In the past few years much research has involved variational retrieval schemes. Variational retrieval methods are examined that under a precise background field provide better retrieval results (Eyre, 1989). A variational iteration method was applied in this research. One important issue in variational retrieval is to correct the satellite observation bias and to estimate random errors. Observation bias is estimated from the difference between observed brightness temperature and simulated brightness temperature. Simulated brightness

temperature is calculated based on a forecast model through a RTE model. So the observation bias is included in the numerical forecast model's error. In order to make the data correct for retrieval, a statistical correct scheme is needed.

Variational Methodology

The solution of the variational retrieval scheme is to get the minimum value of the cost function. Then it gets the best atmosphere parameter: x. The cost function is written as follows.

$$J(x) = \left(x - x^b\right)^T C^{-1}\left(x - x^b\right) + \left\{y^m - y(x)\right\}^T E^{-1}\left\{y^m - y(x)\right\} \qquad (1)$$

x^b is background (or initial guess). C is covariance of background error. y^m is observation values. $y(x)$ is simulation values from RTE while atmosphere parameters are x.

The cost function is the sum of the deviation between x and the background and the deviation between the observed value and calculated value under x situation. So we should find a proper x that lets the calculated value correspond to the observation value relevantly. The methodology is using Newtonian iteration method(Eyre 1989).

$$\begin{aligned} x_{n+1} &= x^b + W_n\left\{y^m - y(x_n) - K_n(x^b - x_n)\right\} \\ W_n &= CK_n^T(K_nCK_n^T + E)^{-1} \end{aligned} \qquad (2)$$

When the value $x_{n+1} - x_n$ is smaller than a threshold, then above function converges.

The covariance error of the background field may be obtained by statistical calculation from the error of 12 hour forecast field (Parrish and Derber 1992). Errors of other parameters are set as follows, surface air temperature is 2.34K, surface air humidity is 0.3 ln(g/kg), surface temperature is 1.67K, surface pressure is 3.42hPa, the content of ozone is 40 Dobson, cloud height is 200hPa, cloud fraction is 0.5 and cloud liquid water content is 0.5mm. (Eyre 1990).

Surface emissivity is described as in (Grody 1988)

$$\varepsilon(\nu) = \frac{\varepsilon_\nu + \varepsilon_x(\nu/\nu_0)^k}{1 + (\nu/\nu_0)^k} \qquad (3)$$

During the retrieval procedure the corrected magnitude of background error depends on the ratio of observation error and background error, which is presented by matrix E and matrix C. The calculation of the observation covariance error is a little complicated. The estimated satellite observation error includes instrument error, satellite data procedure error, radiation transfer model error and error of radiation model input parameters. In summary, above items could be classified into two items, that is systematic error and random error. Systematic error is possiblely corrected. Random error is the diagonal elements in matrix E. Because the limb

effect of AMSU is asymmetrical, limb adjustment procedure is also necessary.

AMSU Bias Correct and retrieval result

The merit of variational retrieval can be applied directly to satellite observation data; it may avoid some errors which were caused during preprocessing (Eyre 1989). AMSU limb effects along the viewing angle are due to asymmetry, we must adjust for this. First, we plot the scatter diagrams of AMSU for each channel to each FOV. Before doing the adjustment, the difference between observation data and calculated data are chosen. This data should be estimated for its mean and standard deviation. If any channel differences between observation and calculated are larger than 3 times of the standard deviation, these data are treated as bad data. Channel 7, for four different scan angles, are shown in Fig. 1.

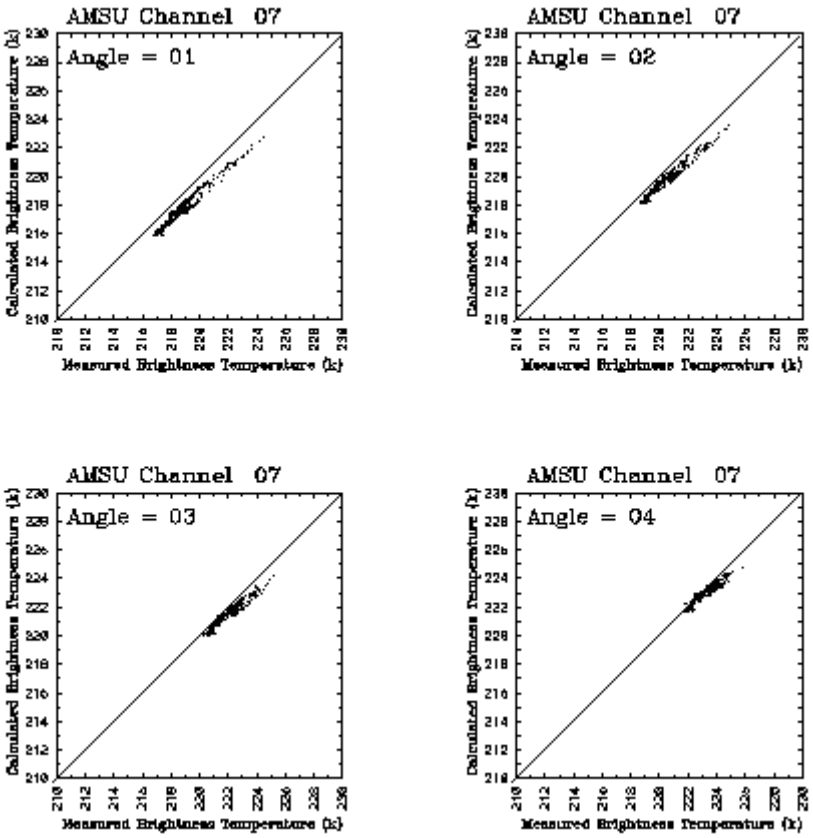

Fig.1: Scattering diagram of AMSU channel 7 for simulated Tb and measured Tb from FOV of 1 to 4. The scan angle biases are a little difference.

After proper data are selected, regression coefficients are calculated for each channel in each viewing angle to correct the observation. Then adjusted brightness $T^* = aT_B + b$ will be found, where T_B is the observed satellite brightness temperature, a is slope and b is intercept.

About 900,000 data were used to get these coefficients. Because estimated observation systematic error and random error are included in the background (forecast) error, the 12 hours forecast statistic error has been transferred to radiance. Then the background error can be removed. AMSU channel 2 is used as a parameter to adjust surface emissivity, this adjustment will be done when calculated Tb are equivalence to observed Tb. In reality it is not a proper procedure, but it is more reasonable when no observations of surface emissivity exist. Real data on 22 June 2002 were tested, and the improvement of vertical temperature is significant, as shown on Fig. 2.

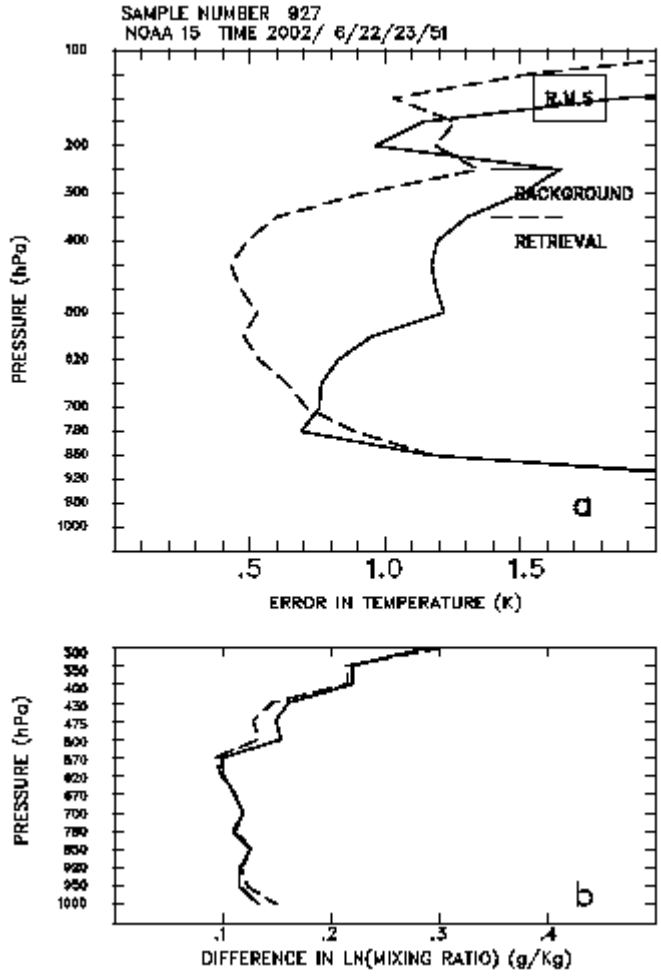

Figure 2. Real data on 22/Jun/2002 23Z. Total 927 corrected satellite observation were retrieved. (a)temperature (b)maxing ratio mean error covariance. Solid line is background error and dash line is error of retrieval.

Limb Adjustment on AMSU

For the asymmetry of AMSU limb bias, statistical methods were considered. We tried to use the algorithm from Goldberg(2001). Because of misinterpretation of the physical

coefficient, some channels of AMSU were not corrected. The results are shown on Fig 3. Surface channel 1,2 are correct, but others channels are failed to be correct. Further investigation is needed.

Typhoon Monitoring - methodology

Understanding the thermal structure of typhoons is helpful to weather forecasting. It has been examined that a relationship exists between temperature anomalies and the maximum wind and central pressure of tropical cyclones.(Kidder 2000) Whether to make a limb correction to each FOV before

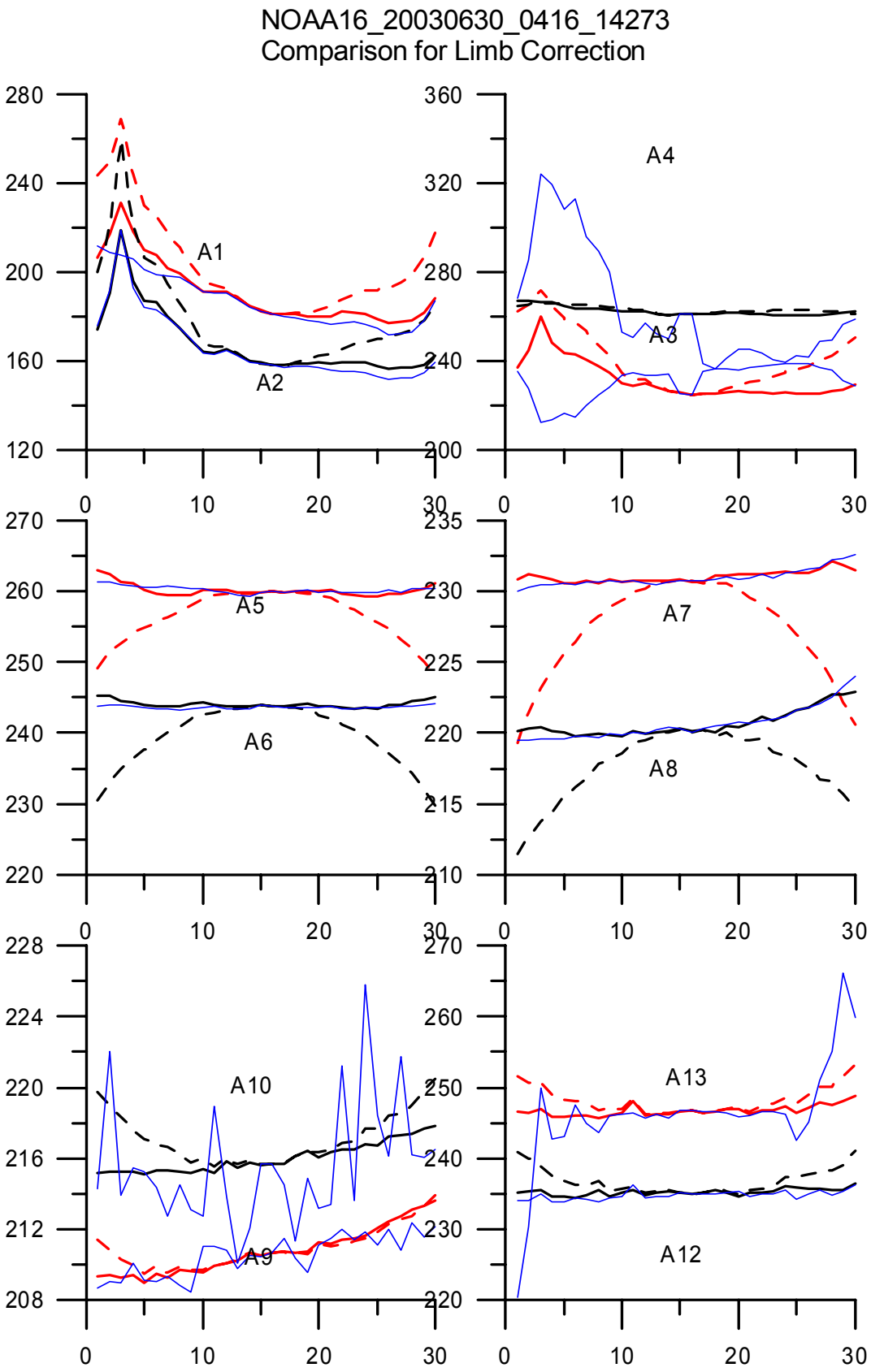

Figure 3. AMSU limb adjustment results for NOAA 16 channel 1-13. Dash line means raw data, red solid line means applied by NESDIS coefficients, blue line means results in this study.

retrieval or make a different set of coefficients for each FOV is a controversial problem. Zhu and Kidder (2002) show that the RMS error is less than 1.75K for the above two schemes. So here, the latter scheme was chosen for further processing.

AMSU has the capability to penetrate cloud, but the AMSU observation still can be interfered by raindrops. It may cause the temperature too cool under 700hPa in retrieval temperature profiles near the typhoon center. So under heavy rainfall situation channel 3-5 are not recommended be use in retrieval. Only channesl 6-11 were used to retrieve temperature profile. When temperature profiles are retrieved from AMSU, the 2 or 3 dimension gradient wind vectors can be estimated using the gradient balance equation. The algorithm to estimate the 2-dimension gradient wind is from the paper of Kidder (2000). In order to study the center of a typhoon, the 250hPa highest temperature anomaly is located. The method used to drive the 3-dimension wind vector has been described in Zhu etal. (2002).

Typhoon Monitoring - result.

The above techniques was applied on the typhoon of 16/Oct/2001 23Z. As shown in Fig 4, AMSU channels 6-11 of NOAA-15 was used for the case study. The anomaly of temperature near the center of the typhoon is obviously identified. Anomaly warming extends from level 250hPa with anomaly of 7K to level 620hPa with a 4K anomaly. The warm core is a little inclined to the north. The gradient wind is changing with the radius of typhoon and pressure variance as shown in Fig 5. Maximum wind speed is located at a radius about 100km. Mean maximum wind speed is about 25m/s. From the pattern of the wind fields, positive vorticity exists in the lower layer of the typhoon. Weak negative vorticity is located on upper layers of the typhoon. The structure of the typhoon is reasonable, given general acknowledge. The core of maximum wind speed inclines to the outside, this is characteristic of a strong typhoon. According to the empirical function (Kidder 2000) , the temperature anomaly is used to estimate the maximum wind speed and radius of maximum wind speed. This typhoon has a maximum temperature anomaly of about 10.5K, so the maximum wind speed should be 46m/s, and radius of maximum wind speed is 125Km. From Fig. 5 mean maximum wind speed is about 25m/s, which is the value of the mean azimuth angle. So the estimated wind speed is reasonable. Others cases were studied and provided a reasonable analysis.

Conclusion

AMSU data is a widely used in NWP and weather analysis. We applied proper adjustment to correct the observation error, allowing AMSU data to be used more precisely. When the observation error is corrected, the 1D variational retrieval test shows that the correcting process is needed.. Temperature anomalies can be obtained from retrieved temperature profiles. Based on these temperature profiles, the 2 and 3dimension wind vectors are

successfully driven. A local typhoon statistical analysis database is necessary for further utilization. Typhoons often make a severe disaster in the northwest Pacific Ocean area. AMSU may provide more precise information on typhoon analysis.

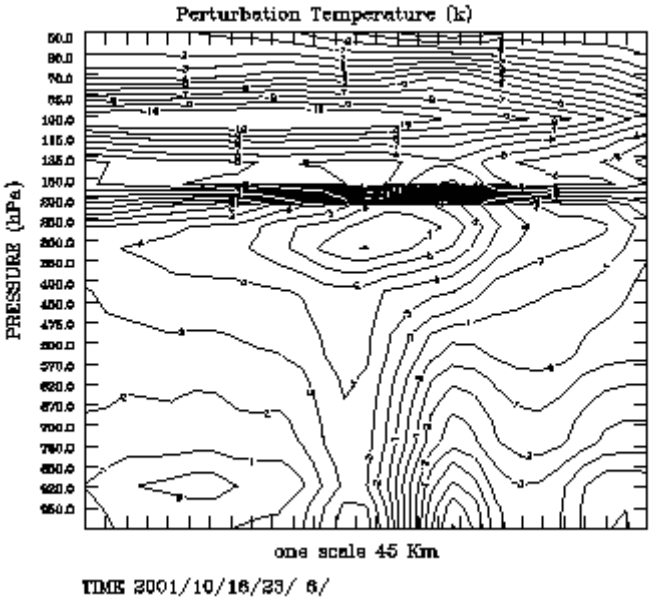

Figure 4. Temperature anomaly analysis profile obtained from south to north (right) on Typhoon HaiYen

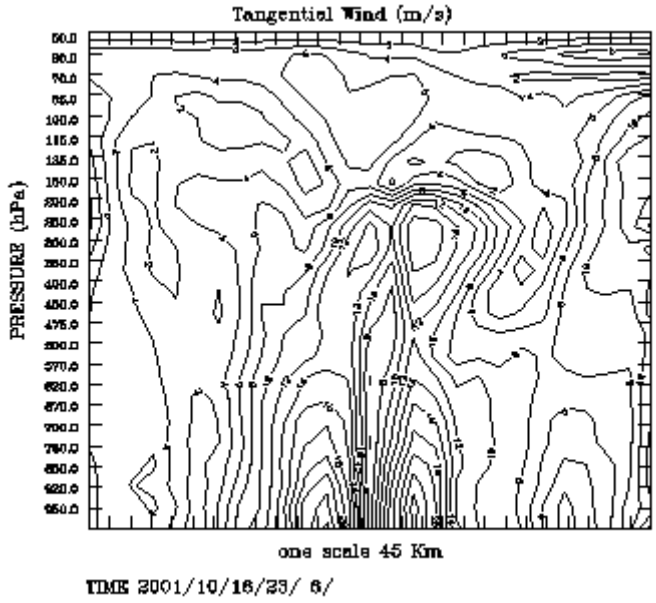

Figure 5. Gradient wind profile (Mean azimuth) on typhoon HaiYen.

The effect of ice particles on AMSU is needed for further study. Precipitation and water vapor content were not considered in this research. That will be the future task.

References

Eyre, J. R., 1989, Inversion of cloudy satellite sounding radiances by nonlinear optimal estimation: Application to TOVS data. *Quart. J. Roy. Meteor. Soc*., **115**, 1027-1037.

Eyre, J.R., 1990, The information content of data from satellite sounding system: A simulation study. *Quart. J. Roy. Meteor. Soc*., **166**, 401-434.

Goldberg, M. D., D. S. Crosby, and L. Zhou, 2001, The Limb Adjustment of AMSU-A Observations: Methodology and Validation, *J. Appl. Appl. Meteor.*, **40**, 70-83.

Grody, N.C., 1988, Surface identification using satellite microwave radiometers, *IEEE Transations on Geoscience and Remote Sensing*, **26**, 850-859.

Kidder, S.Q., and Coauthors, 2000. Satellite Analysis of Tropical Cyclone Using the Advanced Microwave Sounding Unit (AMSU). *Bull. Amer. Meteor. Soc.*, **81**, 1241-1259.

Parrish, D. F. and J.C. Derber, 1992, The national Meteorological Center's spectral statistical interpolation analysis system. *Mon. Wea. Rew*., **120**, 1747-1763.

Zhu, T., D. L. Zhang, and F. Weng, 2002. Impact of Advanced Microwave Sounding Unit Measurements on Hurricane Prediction. *Mon. Wea. Rev*., **130**, 2416-2432

Level 1B Products from the Atmospheric Infrared Sounder (AIRS) on the EOS Aqua Spacecraft

T. Pagano,[a,*] H. Aumann,[a] Ken Overoye[b]

[a]California Institute of Technology, Jet Propulsion Laboratory, Pasadena, California
[b]BAE Systems, Lexington, Massachusetts

Abstract

The Atmospheric Infrared Sounder (AIRS) was launched May 4, 2002 on the EOS Aqua Spacecraft. A discussion is given of the objectives of the AIRS experiment, including requirements on the data products. We summarize the instrument characteristics, including sensitivity, noise, and spectral response, and preflight calibration results leading to the estimate of the calibration accuracy. The Level 1B calibration algorithm is presented as well as the results of in-flight stability and sensitivity measurements.

Keywords: Atmosphere, Sounding, Calibration, Stability

Introduction

The Atmospheric Infrared Sounder (AIRS, shown in Fig. 1) is a hyperspectral infrared sensor on the Earth Observation Satellite (EOS)-Aqua Spacecraft. AIRS is designed to measure atmospheric temperature and water vapor profiles with greater sensitivity and accuracy than prior systems in support of weather forecasting and climate-changes studies. When combined with the Advanced Microwave Sounding Unit (AMSU-A), the AIRS/AMSU system produces the data products with accuracies identified in Table 1. This paper focuses on the AIRS IR Radiance product. The 3% accuracy requirement is met easily as shown here. A description of the project status one year after launch can be found in the literature (Pagano et al., SPIE 2003).

Table 1: AIRS/AMSU Data Products and Accuracies

	RMS Uncertainty
Radiance Products (Level 1B)	
AIRS IR Radiance	3%
AIRS VIS/NIR Radiance	20%
AMSU Radiance	.25 – 1.2 K
Standard Core Products (Level 2)	
Cloud-Clear IR Radiance	1.0 K
Sea Surface Temperature	0.5 K
Land Surface Temperature	1.0 K
Temperature Profile	1 K
Humidity Profile	15%
Total Precipitable Water	5%
Fractional Cloud Cover	5%
Cloud Top Height	0.5 km
Cloud Top Temperature	1.0 K

Fig. 1: The AIRS Instrument Prior to Delivery to the Aqua Spacecraft

*tpagano@jpl.nasa.gov, (818) 393-3917
**This research was carried out at the Jet Propulsion Laboratory, California Institute of Technology, under a contract with the National Aeronautics and Space Administration.

AIRS Instrument

The AIRS instrument, developed by BAE SYSTEMS, incorporates numerous advances in infrared sensing technology to achieve a high level of measurement sensitivity, precision, and accuracy (Morse et al., 1999). This includes a temperature-controlled spectrometer (158K $\pm$ 0.1K) and long-wavelength cutoff HgCdTe infrared detectors cooled by an active-pulse-tube cryogenic cooler. It is this temperature control that is most likely responsible for the observed stability in the instrument. The Focal Plane Assembly (FPA) contains 17 individual line arrays of detectors in a 2 x N element array where N ranges from 94 to 192. The AIRS acquires 2378 spectral samples at resolutions, $\lambda/\Delta\lambda$, ranging from 1086 to 1570, in three bands: 3.74 μm to 4.61 μm, 6.20 μm to 8.22 μm, and 8.8 μm to 15.4 μm. AIRS scans the earth scene up to ±49.5° relative to nadir with a spatial resolution of 13.5 km. Each scan provides a full-aperture view of space and an on-board blackbody calibration source. AIRS also has a visible/near infrared (VIS/NIR) photometer, which contains four spectral bands with a spatial resolution of 2.3 km.

Pre-Flight Instrument Characterization

Accurate characterization of the instrument response is critical to climate observations. Results from the pre-flight calibration are presented in the literature (Pagano et al., 2000). They show very good characterization of the radiometric, spectral, and spatial response of the AIRS. Here we highlight the stability of the results indicating a stable instrument and Level 1B data product.

Radiometric Calibration Equations and L1B

The radiometric transfer equations are derived from the design of the AIRS instrument and the measurement approach as discussed in the literature (Pagano et al., IEEE 2003). These radiometric transfer equations form the basis of the Level 1B calibration for AIRS. The scene radiance is derived from the signal counts as follows:

$$N_{sc,i,j} = \frac{a_o(\theta_j) + a_{1,i}(dn_{i,j} - dn_{sv,i}) + a_2(dn_{i,j} - dn_{sv,i})^2}{1 + p_r p_t \cos 2(\theta_j - \delta)} \tag{1}$$

and

$$a_o(\theta_j) = P_{sm} p_r p_t [\cos 2(\theta_j - \delta) + \cos 2\delta] \tag{2}$$

The second part of the gain and offset correction every scan is to perform a gain correction using the On-Board Calibrator (OBC) blackbody. We discuss calibration of the OBC blackbody below. Once achieved, the gain used in flight in the radiometric transfer equation is obtained using the first radiometric transfer equation solving for the a_1 term while viewing the OBC blackbody.

$$a_{1,i} = \frac{N_{OBC,i}(1 + p_r p_t \cos 2\delta) - a_o(\theta_{OBC}) - a_2(dn_{obc,i} - dn_{sv,i})^2}{(dn_{obc,i} - dn_{sv,i})} \tag{3}$$

Explicitly defining the terms in the radiometric transfer equations, we have:

$N_{sc,i,j}$ = Scene radiance of the i^{th} scan and j^{th} footprint (mW/m^2-sr-cm^{-1})
P_{sm} = Plank radiation function evaluated at the temperature of the scan mirror
$N_{OBC,i}$ = Radiance of the On-Board Calibrator (mW/m^2-sr-cm^{-1})
i = Scan Index
j = Footprint Index (1 to 90)

θ = Scan Angle. θ = 0 is nadir.

$dn_{i,j}$ = Raw Digital Number in the Earth View for the i^{th} scan and j^{th} footprint

$dn_{sv,i}$ = Space view counts offset. This is an algorithmic combination of eight AIRS raw space view digital numbers.

a_o = Radiometric offset. This is nonzero due to polarization and is scan angle dependent.

$a_{1,i}$ = Radiometric gain. This term converts dn to radiance based on the radiometric gain as determined using the OBC blackbody.

a_2 = Nonlinearity Correction

$p_r p_t$ = Polarization Product. This is the product of the polarization factor from the scan mirror and the spectrometer.

δ = Phase of the polarization of the AIRS spectrometer

Radiometric Sensitivity and Noise

Radiometric sensitivity is expressed as the Noise Equivalent Temperature Difference (NEdT) for a scene temperature of 250K. The NEdT for AIRS is measured by interpolating the noise while viewing cold space and the OBC at 308K as published in the literature (Pagano, IEEE 2003). The NEdTs for AIRS are shown in Fig. 2 pre-flight and in-orbit as calculated using equation 5.

Noise characterization is performed by acquiring instrument digital output while viewing a known calibration target temperature. In this test, the AIRS scan mirror is locked at the calibration target for 20 minutes while data are collected. For AIRS, data were acquired while viewing the Space View Blackbody (SVBB), and the Large Area Blackbody (LABB). Fig. 3 shows the noise amplitude (1 sigma) in counts while viewing the space view. Also shown in the figure is the amplitude of the noise that is correlated among all the channels in a module. Correlated noise does exist in some AIRS modules, with M1, M2, M4, and M8 showing the greatest levels. Worst case, these levels are about 2x lower than the nominal noise and are not surprising since all detectors in a readout share common circuitry. These levels are very low since the AIRS noise is very low in the shortwave channels, and the random noise will be higher at non-zero scene radiances.

Calibration Coefficients

Coefficients for these terms were derived from a set of linearity tests that took over 12 hours to complete. During this time, a well-calibrated external blackbody, the LABB, is stepped in temperature, and the

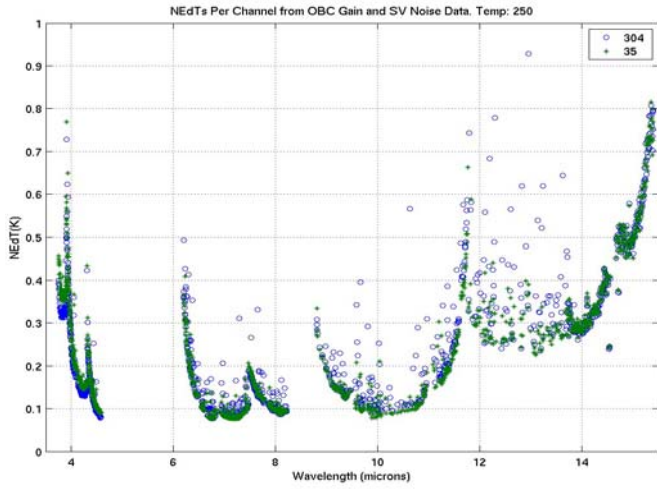

Fig. 2: NEdTs for AIRS at 250K measured pre-launch and in orbit

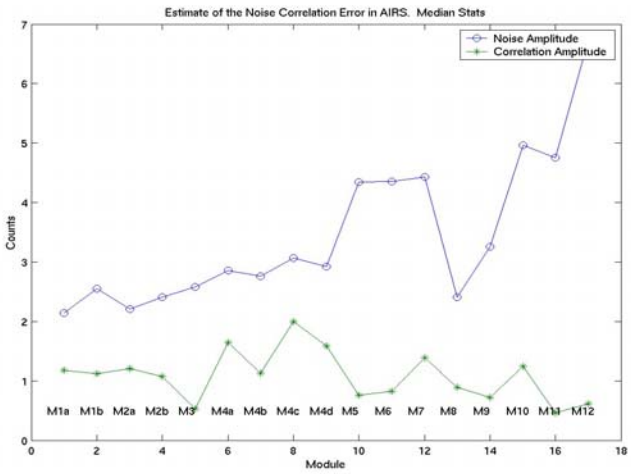

Fig. 3: Amplitudes of the random noise and the correlated noise in the 17 airs modules.

instrument response is recorded. The resulting nonlinearity from two separate measurements is plotted in Fig. 4. We see less than 1.5% nonlinearity with better than 0.2% repeatability of the measurement for tests taken four days apart and at different scan angles.

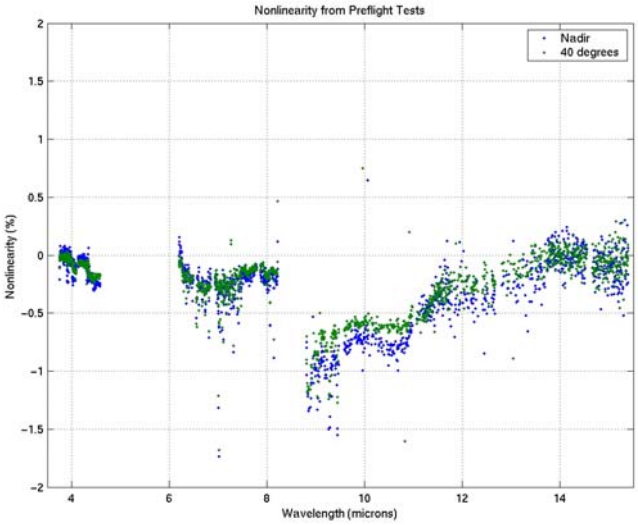

Fig. 4: Instrument stability is evident in the nonlinear term obtained from tests separated by 4 days.

Fig. 5 shows the polarization term, $p_r p_t$, calculated using three different methods. The first uses the offset from the linearity tests and equation 2 to solve for the polarization term. Data from two different tests are shown in the figure. We also plot the polarization obtained from the bottoms-up component model and from the subsystem-level test, which measured the polarization of the spectrometer. The worst-case difference is $\pm$ 0.4K. The Level 1B uses the average of the "component" and "measured" polarization products.

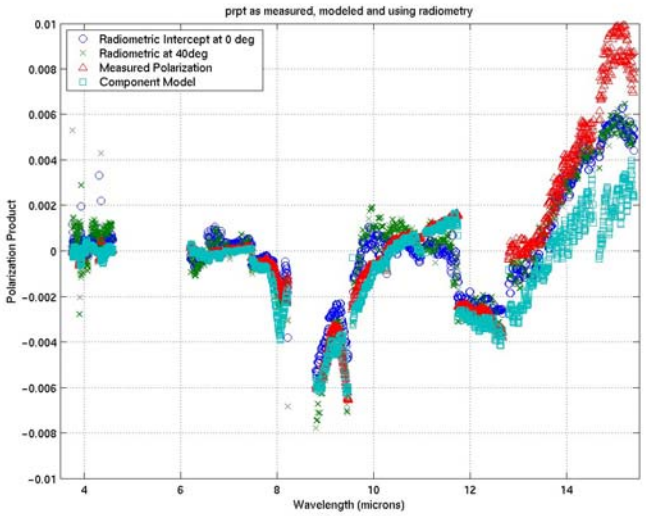

Fig. 5: Product of spectrometer and scanner polarization factors obtained from three methods.

This type of end-to-end testing of the Level 1B calibration prior to flight was very successful for AIRS. The Level 1B radiometric calibration coefficients derived during these tests prior to launch have not been updated one year later in flight since the validation campaign shows good agreement with in-situ, aircraft and spaceborne measurements from other sensors.

Radiometric Uncertainty

We can determine the uncertainty in the radiometry by applying variance analysis on the radiometric transfer equations (1, 2, and 3). This will give us only those errors that are directly attributable to the calibration equation. We can add to this the uncertainty of the AIRS transfer standard, the Large Area Blackbody (LABB), to arrive at an overall measurement uncertainty.

$$\partial N_{SC}^{\,2} = \left(\frac{\partial N_{SC}}{\partial p_r p_t}\Delta p_r p_t\right)^2 + \left(\frac{\partial N_{SC}}{\partial T_{sm}}\Delta T_{sm}\right)^2 + \left(\frac{\partial N_{SC}}{\partial \varepsilon_{sm}}\Delta \varepsilon_{sm}\right)^2 + \left(\frac{\partial N_{SC}}{\partial \varepsilon_{OBC}}\Delta \varepsilon_{OBC}\right)^2 + \left(\frac{\partial N_{SC}}{\partial T_{OBC}}\Delta T_{OBC}\right)^2 + \left(\frac{\partial N_{SC}}{\partial a_2}\Delta a_2\right)^2 + \left(\frac{\partial N_{SC}}{\partial dn}\Delta dn\right)^2 \qquad (4)$$

Rather than solve for the equation analytically, we can apply the variance directly to the radiometric equation and calculate the change in radiance. This was performed in a computer model with the following assumptions for the error terms.

Error Terms

Pol: $p_r p_t$: The first primary error term is the uncertainty in the product of the polarization factors of the scan mirror and spectrometer. We cannot explain the differences in Fig. 5 between the various

approaches, and carry the difference between the radiometric offset term at nadir and the average of the modeled and component offset terms as the radiometric error.

Scan Mirror Temperature and Emissivity: ΔT_{sm}, $\Delta \varepsilon_{sm}$: The AIRS scan mirror temperature is monitored using a non-contacting temperature sensor located at the base of the rotating shaft. The uncertainty in the scan mirror temperature is estimated to be less than 0.5K by design. Models executed by the instrument contractor estimate the uncertainty to be less than 1K. The scan mirror emissivity uncertainty at launch is carried in the polarization term; the degradation effects are not included in this model so the results represent at-launch expectations.

OBC Temperature Uncertainty: ΔT_{OBC}: The temperature of the OBC Blackbody is monitored by four temperature sensors located in and around the OBC. We have seen fluctuations on the order of ±0.05K in the blackbody temperature, but we believe the noise on this circuit to be on the order of ±0.01K. All other biases on this term come out of the emissivity calibration of the OBC.

OBC Gain Correction Term: $\Delta \varepsilon_{OBC}$: A 0.3K offset was applied during the calibration to match the radiances of the OBC and the external LABB. The residuals are contained in the gain correction term, ε_{OBC}. It is possible that the observed gain corrections are due to how we view the OBC and the LABB and are not well understood. We therefore have included all of the gain correction as an error; i.e. $\Delta \varepsilon_2 = 1-\varepsilon_{OBC}$. We obtain this term during the pre-flight testing (Pagano et. al IEEE 2000) during the radiometric calibration while viewing the LABB.

Nonlinearity: Δa_2: The uncertainty in the nonlinear term is taken to be the difference in the values obtained for this term for the nadir and 40 degree tests as shown in Fig. 4.

Non-Random Instrumental Noise: Δdn: This term represents the instrumental noise while viewing the target. By convention, we do not include the random noise terms in the absolute radiometric uncertainty estimate. This is most likely because the retrieval process minimizes the impact of random noise on most products. We present the random noise separately as in Fig. 2. We include here the non-random, correlated instrumental noise component as a full radiometric error. It is not know what effect correlated noise has in the Level 2 retrieval processing; further simulation is planned.

Error Results

Fig. 6 shows the results of predicting the radiometric errors based on the assumptions in the previous section. The major contributors are the correlated noise, the polarization term, and the gain. The correlated noise is the highest of these yet is the most uncertain in its contribution on the radiometry. For all channels, we see the radiometric error to be less than 0.18K. These errors will later be combined with the predicted LABB radiometric accuracy to arrive at an estimate of the AIRS radiometric accuracy.

Overlaid on the prediction is the error resulting from an independent measurement of the LABB. Data from a first day were used derive the radiometric calibration coefficients for AIRS Level 1B calibration algorithms. These were then applied to data acquired four days later to observations of the LABB calibration source. The Level 1B faithfully reproduced the LABB temperature to within 0.1K for most bands as shown in Fig. 3. The error is the difference between the derived temperature of the LABB using the calibration coefficients and the true temperature obtained from the LABB temperature sensors.

Preflight Radiometric Accuracy Estimate

The absolute radiometric accuracy of the AIRS depends on the traceability of the AIRS calibration standard, the LABB, and the Space View Blackbody (SVBB) to National Institute of Standards and Technology (NIST) Standards. The LABB and SVBB have an identical cavity structure (Fig. 7). The first bounce surface is inclined at 45 degrees relative to the incident beam. It is constructed of a specular black

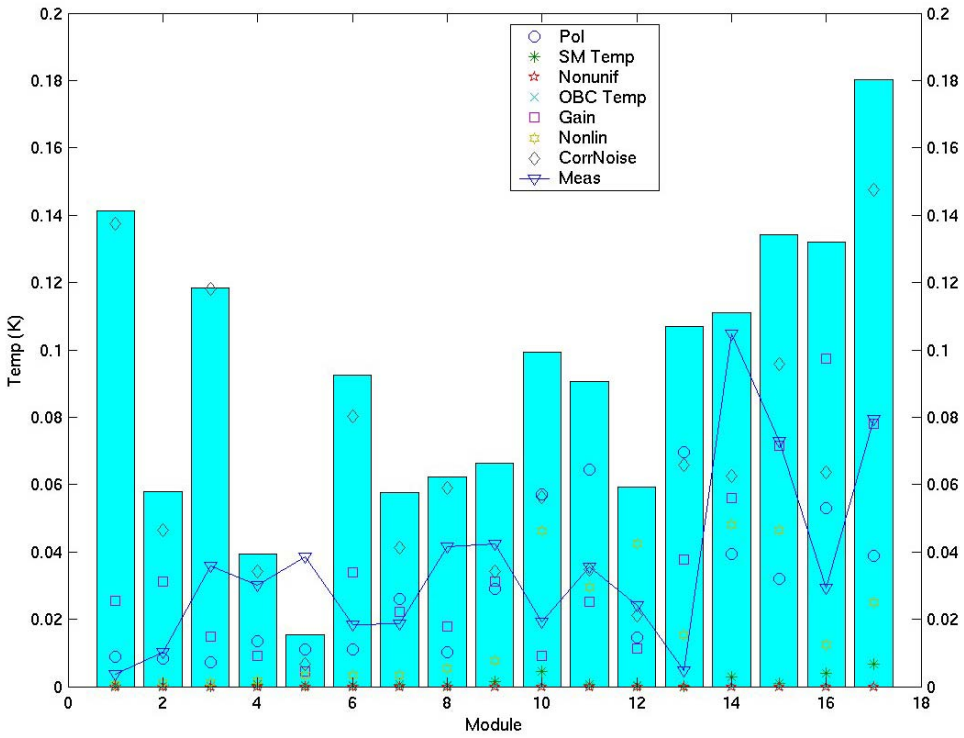

Fig. 6: Modeled radiometric error and measured repeatability pre-launch.

paint with specified reflectance of less than 13.5% for wavelengths below 6 um and less than 17.5% below 15.4 um. The effective emissivity is expected to be 0.9999 for the cavity with a temperature precision of 0.01K, stability of 0.01K. The uncertainty of the first surface is specified to be less than 0.03K with all other surfaces less than 0.1K. With more than 90% contribution from the first surface, we expect the radiometric uncertainty to be better than 0.05K.

Our estimate of the absolute uncertainty of the LABB and SVBB of better than 0.05K combined, with the better than 0.18K radiometric errors gives us a total radiometric uncertainty of better than 0.2K. The radiometric accuracy of the AIRS measurements is better than 0.2K on average. Any single measurement is accurate to the 0.2K root sum squared with the NEdT values at the scene temperature as shown in Fig. 2 for a scene temperature of 250K.

Spectral Response

The Spectral Response calibration is not part of the Level 1B algorithm, but it is discussed briefly here for completeness. Spectral calibration was performed using an interferometer as a spectral calibration source. Signals were acquired on every detector simultaneously for each step of the interferometer mirror. The instrument spectral response was obtained by Fourier Transform of the measured response. Measurements were made at three different temperatures and resulted in no change to the spectral response shape (Pagano et al., 2000). Absolute knowledge of the spectral response centroids prior to flight has been demonstrated to be better than 5 ppm (Gaiser et al., 2003).

In-Flight Accuracy and Stability

Accuracy Comparison with ECMWF

The accuracy of the Level 1 products looks exceptional at this time. Comparison of the AIRS observed (O) radiances (in terms of brightness temperature) to calculations (C) based on the European Center for

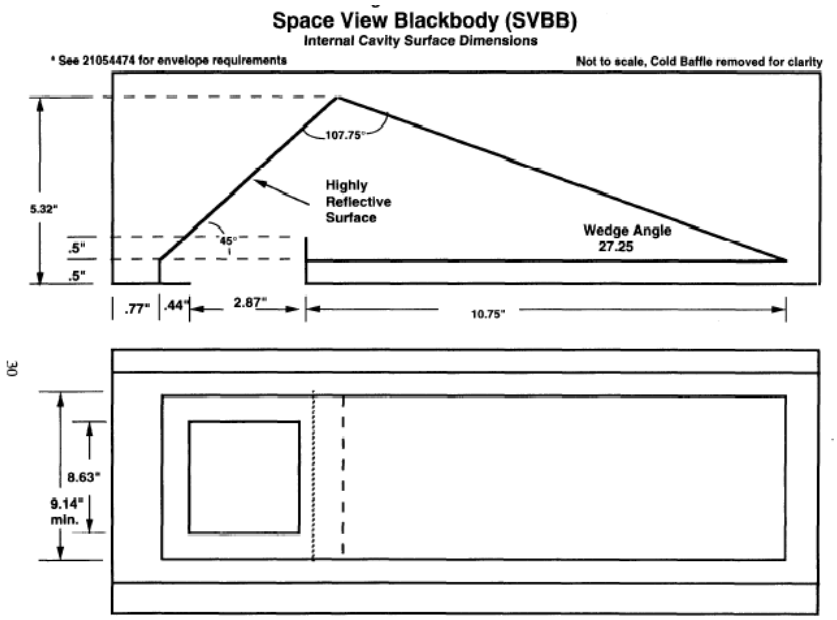

Fig. 7: AIRS SVBB and LABB internal Geometry.

Medium-Range Weather Forecast (ECMWF) using the AIRS Radiative Transfer Algorithm (RTA) have shown (Pagano et. al SPIE 2003) less than ±1.0 K difference for most of the spectrum with no tuning applied. This comparison tells us that the AIRS radiances are very close to truth, but also that the ECMWF forecast models are very good. Comparison with Scanning HIS (Revercomb et. al 2002), MODIS and GOES (Tobin et. al, 2003) also show better than 0.2K agreement.

Stability Comparison with Buoy Network

Comparisons of AIRS channel 2616 cm^{-1} with the Real-Time Global Sea Surface Temperature (RTG SST) (based on buoy measurements) between 1 September 2002, when routine data from AIRS became available, and 31 March 2003 show extremely good AIRS radiometric stability (Aumann et. al SPIE 2003).

Spectral Stability

Spectral centroids of the SRFs are determined in orbit by correlating observed upwelling radiance spectra with pre-calculated, modeled radiance spectra. Results of using this technique to determine the spectral stability of the AIRS have shown (Gaiser et al., 2003) less than 0.2 microns of FPA shift. For AIRS, 1 micron of focal plane shift is 1% of the SRF width. Since the AIRS widths are approximately 1/1000 of the center frequency, the 0.2-micron shift, we observe approximately 2 ppm of the center frequency. This far exceeds our stability requirement of 10 ppm.

Summary and Conclusions

The AIRS instrument allows for a simple and straightforward radiometric calibration. Since the design is solid state, accurate characterization of the spectral response functions pre-flight combined with thermal control results in good knowledge of the spectral frequencies, without continuous on-board calibration correction. The Level 1B calibration algorithms, therefore, only include radiometric terms. The radiometric calibration is straightforward and relatively simple as demonstrated in this paper. The resulting calibration accuracy has been predicted to be better than 0.2K. These predictions agree well with repeatability measurements that show better than 0.1K repeatability. The noise levels are higher than this for many channels and must be considered for any single measurement from the AIRS using

only a single channel. Level 2 algorithms, however, mitigate the noise in the instrument through retrievals that involve use of many channels. A small amount of correlated noise in the AIRS instrument is present at a fraction of less than ½ the random noise. These have been included in the radiometric accuracy estimates, which leave us with better than 0.2K RMS uncertainty.

Independent validation has demonstrated better than 0.2K agreement with other in-situ, spaceborne, and airborne instruments. Stability is better than 0.1K when viewing a single channel at 2616 cm^{-1} over oceans. The AIRS Level 1B product has been very stable and accurate since the instrument was declared operational. This long stable well-calibrated data product will be a useful climate data record for scientists for years to come.

Acknowledgements

The authors would like to thank Steve Gaiser, Steve Broberg, Denis Elliot, Thomas Hearty, Steve Licata, and Rudy Schindler of the AIRS Calibration Team at JPL; Margie Weiler of Swales Aerospace; and Scott Hannon of University of Maryland (Baltimore County).

References

References from Journals

Aumann, H., M. Chahine, D. Barron, Sea Surface Temperature Measurements with AIRS: RTG.SST Comparison. *SPIE Proc.*, 5151-30, August 2003.

Gaiser, S., H. Aumann, D. Gregorich, T. Hearty, In-flight refinement of the radiometric, spectral and spatial calibration of the Atmospheric Infrared Sounder (AIRS), *SPIE Proc.*, 5151-28, Aug. 2003

Morse, P., J. Bates, C. Miller, Development and test of the Atmospheric Infrared Sounder (AIRS) for the NASA Earth Observing System (EOS), *SPIE Proc.*, 3759-27, July 1999

Pagano, T., H. Aumann, D. Hagan, K. Overoye, Pre-Launch and In-flight Radiometric Calibration of the Atmospheric Infrared Sounder (AIRS), *IEEE TGRS*, **41**, No. 2, Feb. 2003, p. 265.

Pagano, T., H. Aumann, L. Strow, Pre-launch Performance Characteristics of the Atmospheric Infrared Sounder (AIRS), SPIE *Proc.*, 4169-41, Sept. 2000.

Pagano, T., M. Chahine, H. Aumann, D. Elliott, E. Manning, V. Realmuto, C. Thompson, B. Lambrigtsen, S. Lee, S. Broberg, E. Olsen, E. Fetzer, L. Strow, AIRS/AMSU/HSB on EOS Aqua: First Year Post Launch Assessment, *SPIE Proc.*, 5151-25, Aug. 2003

Revercomb, H., R. Knuteson, F. Best, D. Tobin, W. Smith, W. Feltz, R. Petersen, D. LaPorte, S. Ellington, M. Werner, R. Dedecker, R. Garcia, N. Cigonovich, H. Howell, K Vinson, S. Ackerman, Applications of high-spectral resolution FTIR observations by the radiometrically accurate ground based AERI and the scanning HIS aircraft instruments, *SPIE Proc*., 4897-03, Oct. 2002.

Tobin, D. C., H. E. Revercomb, S. A. Ackerman, P. Antonelli, M. Gunshor, R. O. Knuteson, C. Moeller, Characterization of Atmospheric Infrared Sounder (AIRS) Earth Scene Radiances in Fourier Transform Spectroscopy, *OSA Technical Digest* (Optical Society of America, Washington DC, 2003), Quebec City, 3-6 Feb. 2003.

References from Websites

"EOS Reference Handbook," Published 1999,
http://eospso.gsfc.nasa.gov/eos_homepage/for_scientists/data_products/refbook1999.php

AIRS Level 2 Status

Evan Fishbein, Thomas Hearty,
Sung-Yung Lee[1], Evan Manning, Edward Olsen
Jet Propulsion Laboratory/California Institute of Technology,
Pasadena, California, USA

Abstract: *The AIRS Team Leader Facility at JPL is developing software to process AIRS data. The software will be run at NASA GSFC DAAC in Greenbelt Maryland. The retrieval algorithm, which generates atmospheric and surface parameters from radiance products, is called the Unified Team Algorithm. Many science team members are responsible for various parts of the retrieval algorithm. They test their software at their home institution and integrate it into the AIRS level 2 software.*

The AIRS project has the goal of temperature retrieval accuracy of 1K in 1 km thick layers in the troposphere. For water vapor profiles, the accuracy goal is 10% relative accuracy in 2 km thick layers in the troposphere. We are also planning to retrieve surface and cloud parameters as well as minor gases like O_3 and CO.

The Atmospheric InfraRed Sounder (AIRS) is a facility instrument on NASA's second EOS satellite called Aqua. The satellite was launched in early May 2002 into 1:30 PM descending sun-synchronous orbit. AIRS is designed to measure atmospheric temperature and water vapor profiles and works with two passive microwave sounders, AMSU-A and HSB. The details of the sounding instrument suite and the science objectives can be found in H. H. Aumann, et al[1].

The AIRS Science Team is responsible for algorithms to process AIRS sounding suite. Table 1 lists science team members and their roles in the retrieval algorithm.

Team Member	Level 2 Role
P Rosenkranz	MW Only retrieval algorithm MW Rapid Transmittance Algorithm
C Gautier	VIS/NIR cloud algorithm
L Strow	AIRS Rapid Transmittance Algorithm
L McMillin	Brightness Temperature Bias Correction Local Angle Correction
M Goldberg	Initial Regression Retrieval Algorithm
J Susskind	Final Physical Retrieval Algorithm and Cloud Clearing Algorithm

Table 1. Roles of AIRS Science Team Members

The AIRS team at JPL combines these algorithms into the "Unified Team Algorithm" and delivers operational software to the Goddard DAAC for use in operational data processing. Figure 1 outlines data and algorithm flow in the Level 2 software. JPL is also responsible for developing other algorithms not supplied by the science team.

[1] The presenter's e-mail address is Sung-Yung.Lee@jpl.nasa.gov

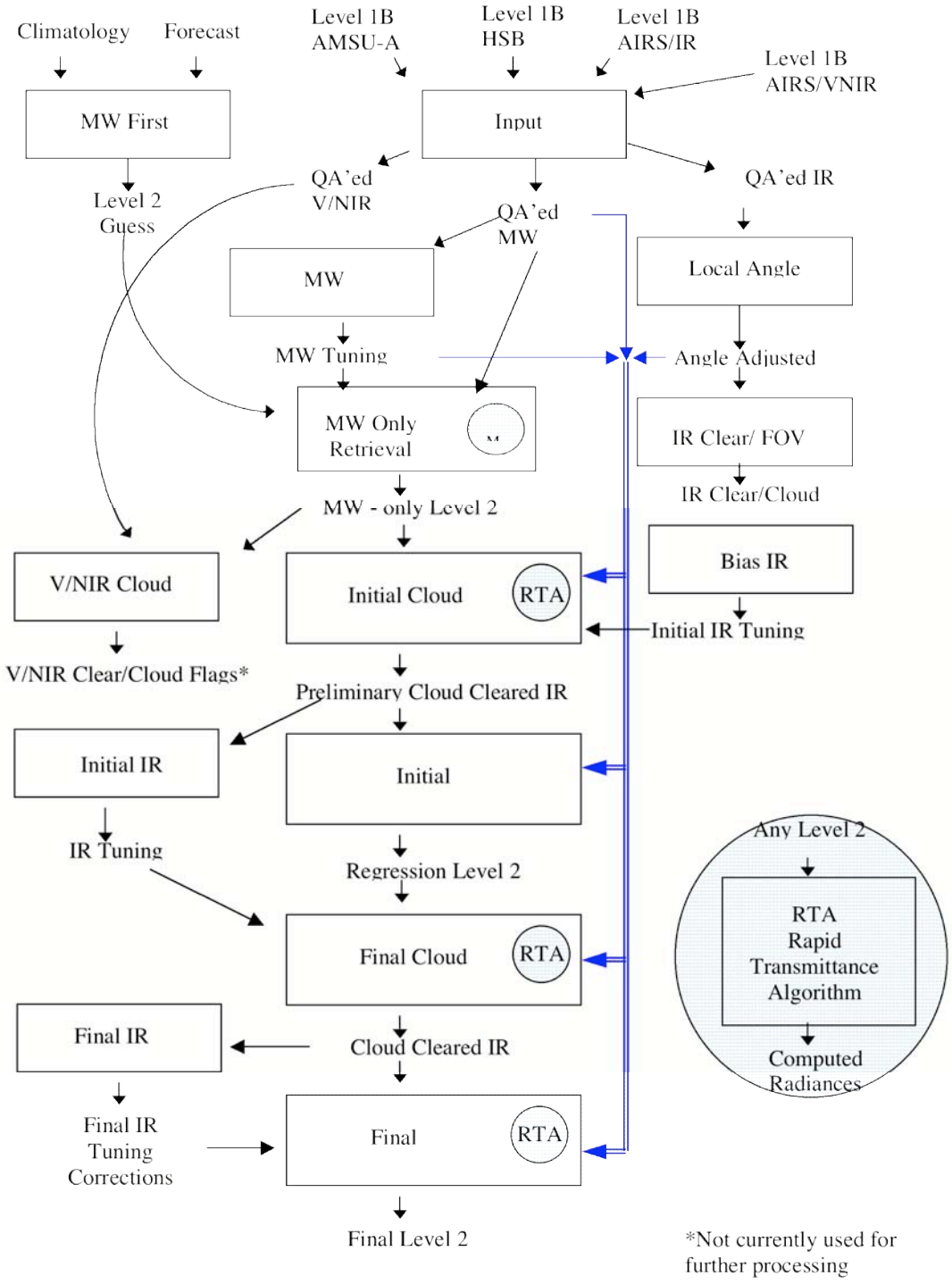

Figure 1. AIRS Level 2 Data Flow

Figures 2 through 6 show a sample AIRS spectrum over tropical ocean, highlighting channels used by the physical retrieval algorithm. The initial regression uses the majority of the AIRS channels. Figure 2 covers the whole AIRS spectral range, while other figures cover interesting spectral regions. In the figures blue asterisks denote channels used in temperature sounding, green asterisks denote water vapor sounding channels, and red asterisks are channels used in surface retrieval. The channels used in ozone, methane and CO retrievals are marked with cyan, magenta and yellow asterisks, respectively.

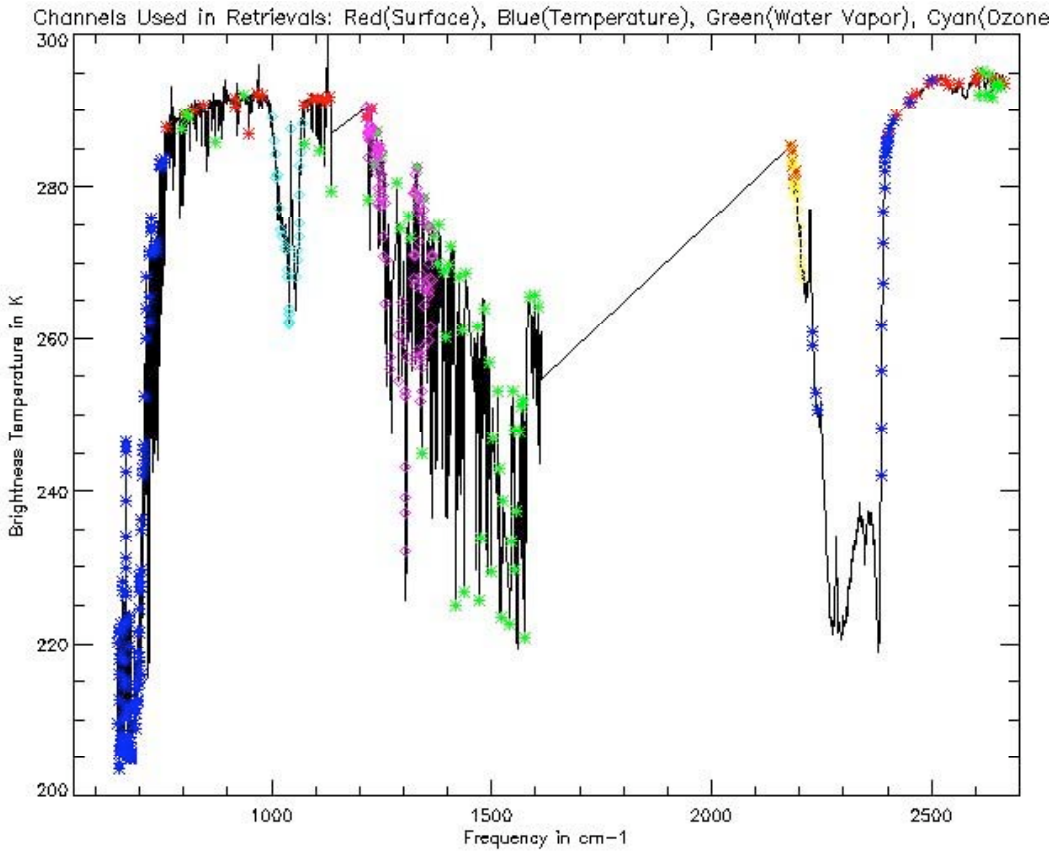

Figure 2. AIRS Spectrum for US Standard Atmosphere

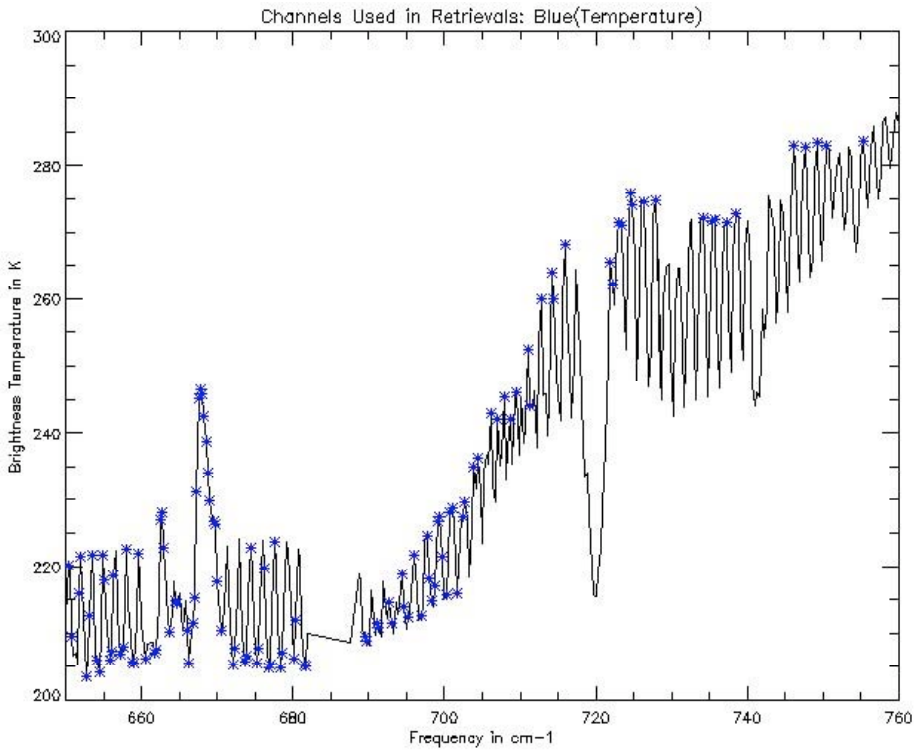

Figure 3. 16 micron CO2 Channels

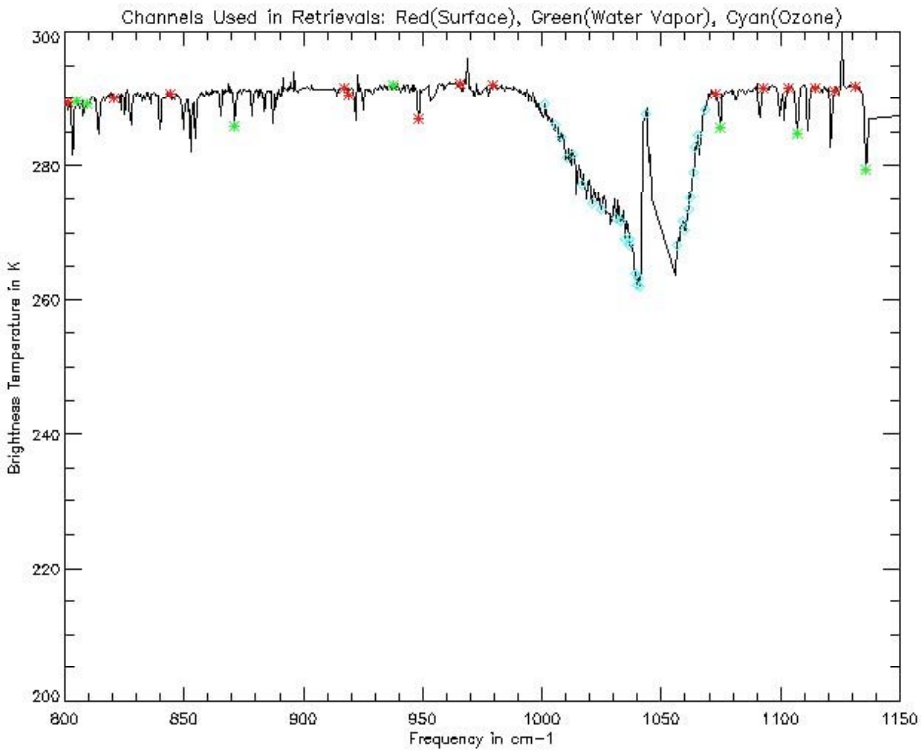

Figure 4. Longwave Window Channels

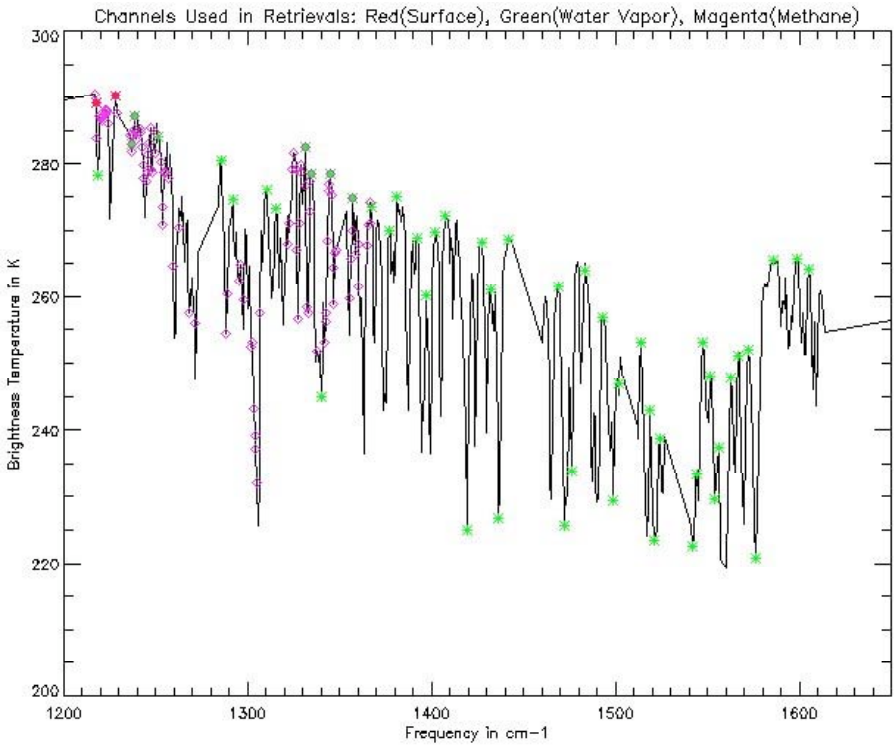

Figure 5. Water Band Channels

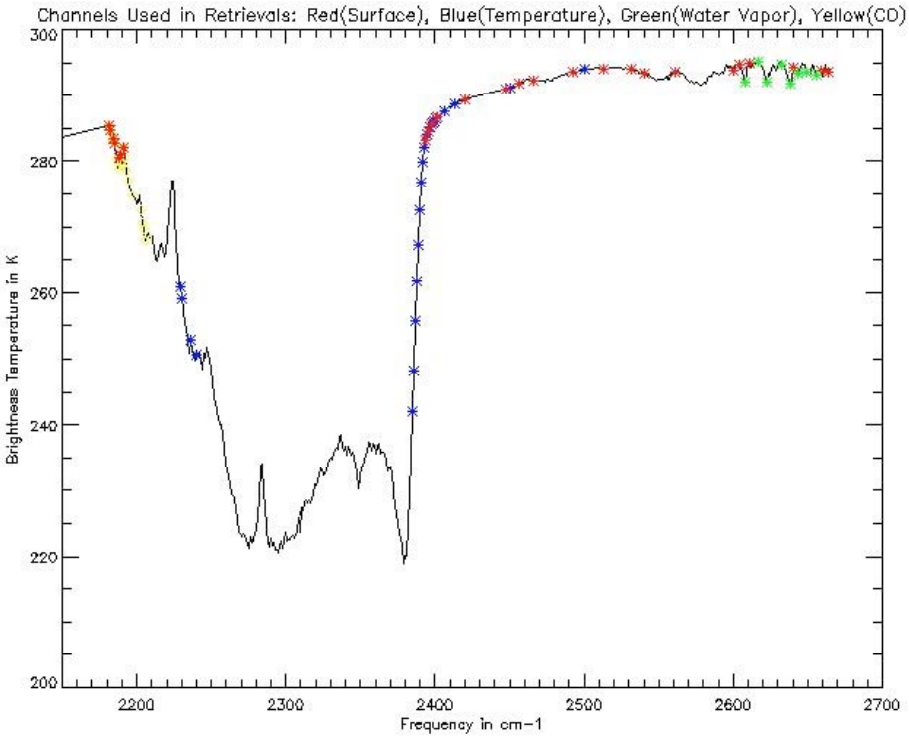

Figure 6. Shortwave Channels

Figure 7 shows the weighting functions of the AIRS channels used in temperature sounding. Most of these channels are in the 14 to 16 micron CO_2 band. Only a few channels in the 4.3 micron CO_2 band are used in the temperature sounding because of non-LTE behavior of the 4.3 micron CO_2 channels. It is worth noting that the highest peak of the weighting functions is near 2 mb, with a significant tail going well above 0.5 mb.

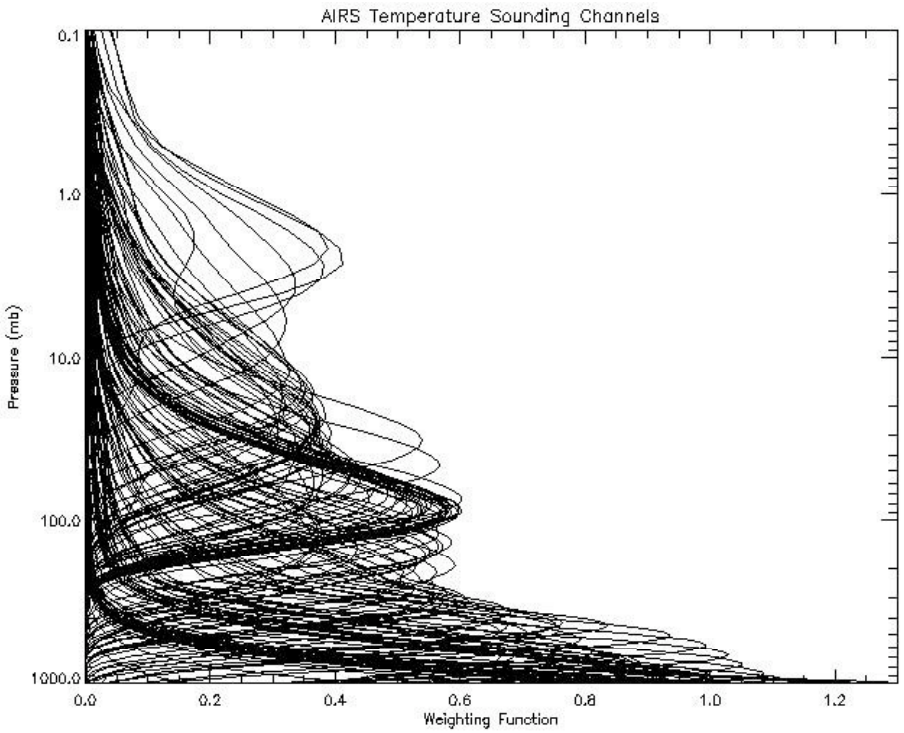

Figure 7. Weighting Functions of Temperature Sounding Channels

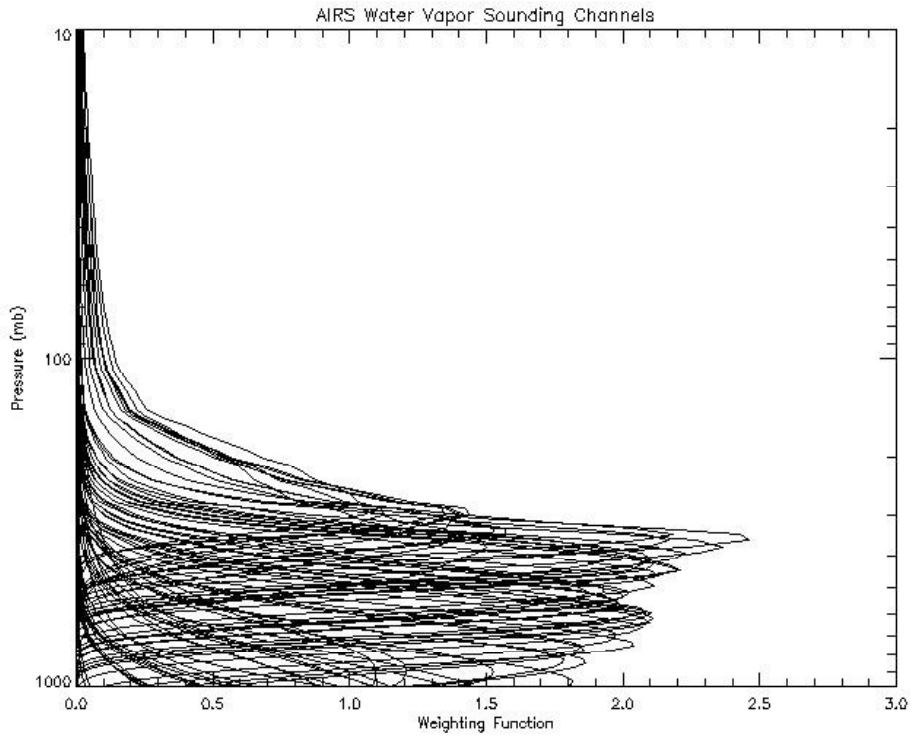

Figure 8. Weighting Functions of Water Vapor Sounding Channels

Figure 8 has the weighting functions of water vapor channels. The highest peak of the weighting functions of these channels is near 300 mb. The significant contributions from above 200 mb give confidence that upper tropospheric water vapor can be retrieved accurately.

The AIRS project has selected “focus days” to study retrieval statistics compared to ECMWF analysis. The focus days are generally chosen every 48 days to have identical orbit patterns. The Aqua spacecraft has a 16-day orbit cycle. Figure 9 shows the biases and the RMS differences of AIRS v3.1.9 retrievals vs. ECMWF analysis for 7 focus days between September 6, 2002 and May 27, 2003. Version 3.1.9 AIRS retrieval software is currently being evaluated in the NOAA NESDIS near-real-time production system. Note that the statistics are very stable without updates to software or tables. The same bias correction is used throughout the year.

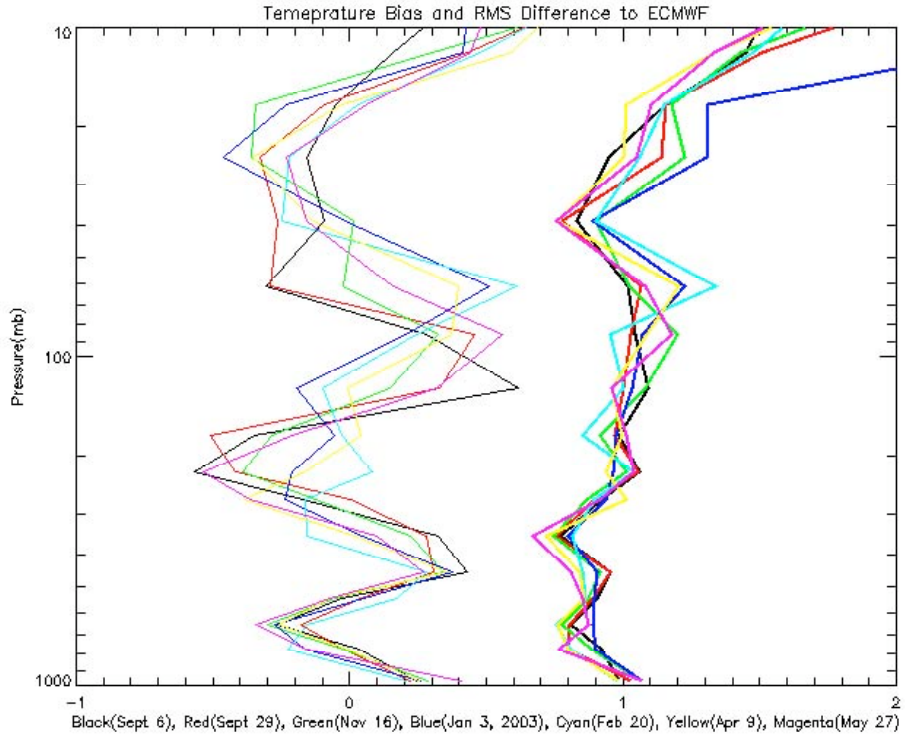

Figure 9. Bias and RMS with respect to ECMWF Analysis

AIRS retrieval software version v3.0.9 was sent to Goddard DAAC, along with a validation report, E. Fetzer[1]. Goddard DAAC has processed level 2 data with this version since August 2003. Level 1B AIRS data has been publicly available since April 2003. Old data since September 2002 will also be processed soon with the latest software and released. All data processed at GDAAC can be accessed through their web page http://daac.gsfc.nasa.gov/atmodyn/airs/ This web page also has a good set of documents for AIRS data users. Any questions regarding AIRS data can be directed to the AIRS Dynamics Data Support Team at the above web site, or to Edward Olsen at the AIRS project, Edward.Olsen@jpl.nasa.gov.

The level 2 processing software produces three sets of output files, described in table 2. In accordance with EOS policy, most AIRS data files are in HDF-EOS swath. One set of files is written for each 6 minutes worth of data, producing 240 granules of data for each day. Detailed description of the files and the parameters in the files can be found in the above GDAAC Atmospheric Dynamics web site. Most of the parameters in these files are at AMSU-A spatial resolution, 45 km at nadir. Some exceptions, including cloud parameters, are produced at AIRS resolution, 15 km at nadir.

File Type	Short Description
Level 2 Standard	Standard, or core, products including T(p), q(p), O_3(p), T_s. Profile data in standard levels that are adopted from WMO levels. Cloud parameters.
Level 2 Support	Research products and other intermediate products. Profiles at 100 fine levels chosen for forward algorithm. Contains data needed to compute radiances accurately.
Cloud Cleared Radiances	Radiances that would have been observed if the FOV was clear. Available only where combined IR/MW algorithm succeeds.

Table 2. AIRS Level-2 File Description

AIRS Level 2 software program also produces browse products, simple grids of selected parameters for use in ordering data from EOSDIS. These daily browse products can be averaged to produce monthly means. The following figures are monthly means for January 2003.

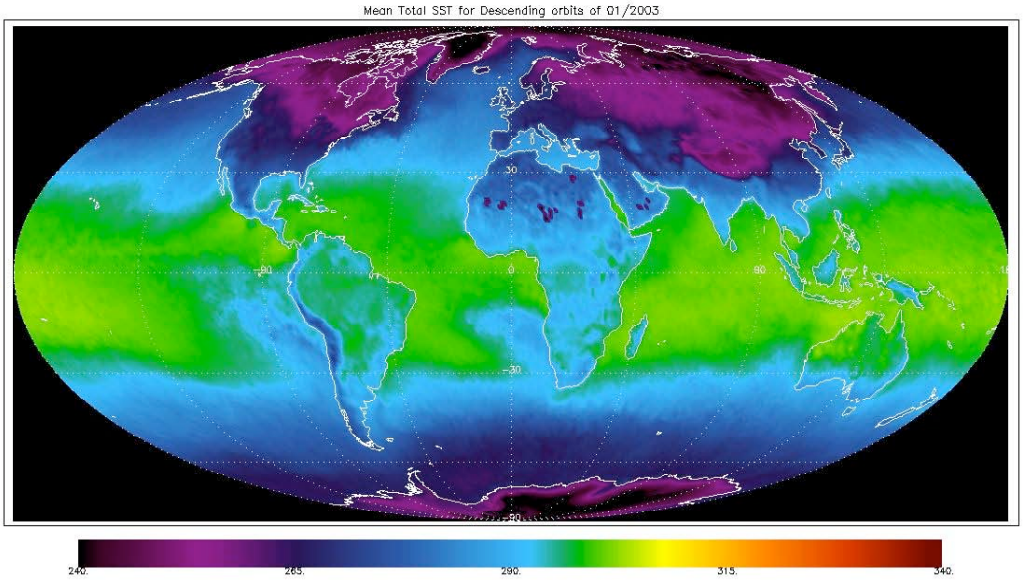

Figure 10. Monthly Mean Skin Temperature Descending Orbits for January 2003

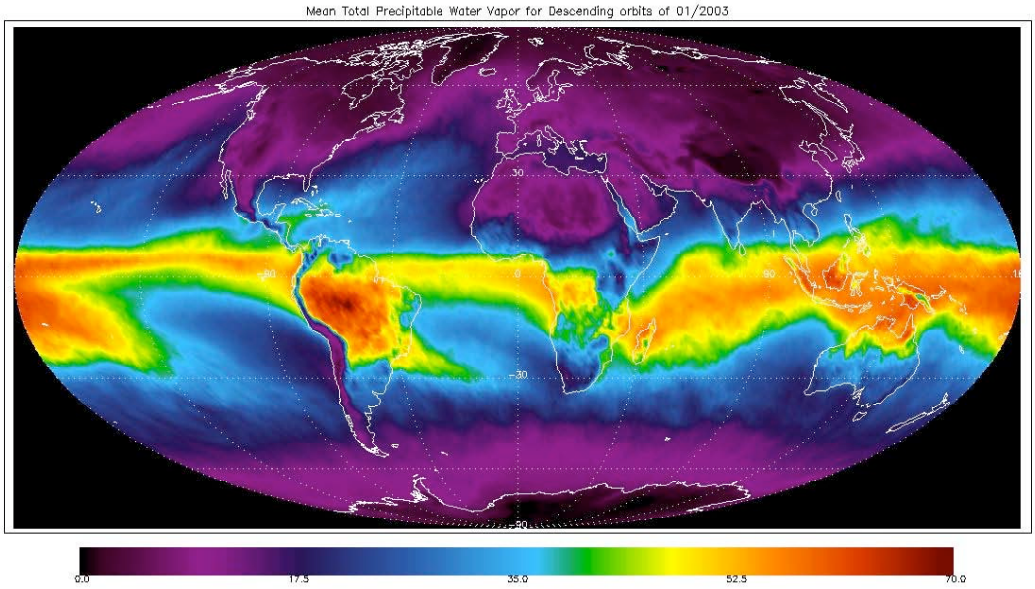

Figure 11. Monthly Mean Total Precipitable Water Vapor Descending Orbits for January 2003

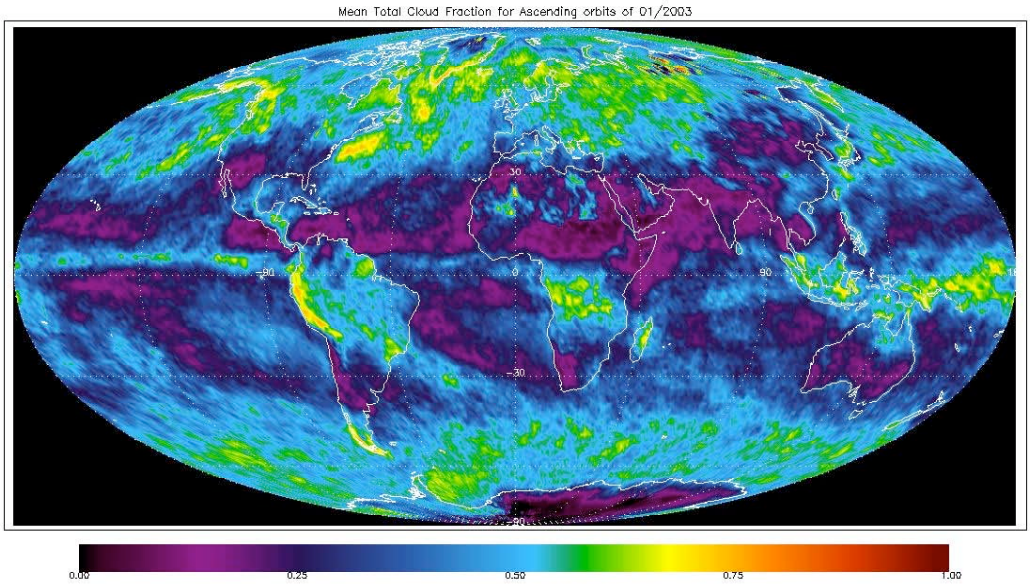

Figure 12. Monthly Mean Effective Cloud Fraction Ascending Orbits for January 2003

References:

H. H. Aumann et al, "AIRS/AMSU/HSB on the Aqua Mission: Design, science objectives, data products, ad processing systems," IEEE Trans. Geosci. Remote Sensing, vol 41, pp 253-264, Feb 2003.

E. Fetzer (editor), "AIRS/AMSU/HSB Validation Report for Version 3.0 Data Release", August 2003. Electronic copy of the report can be found from GDAAC as http://daac.gsfc.nasa.gov/atmodyn/airs/guide/airs_l2/V3.0_Validation_Report.pdf.

Atmospheric Soundings of Temperature, Moisture and Ozone from AIRS

Mitchell D. Goldberg, Christopher D. Barnet, Larry M. McMillin, Walter Wolf, Lihang Zhou and Murty Divakarla

National Oceanic and Atmospheric Administration, National Environmental Satellite, Data, and Information Service, Office of Research and Applications, Camp Springs, Maryland, USA.

Introduction

The NASA EOS AQUA high-spectral resolution Atmospheric InfraRed Sounder (AIRS) and the Advanced Microwave Sounding Unit (AMSU) were successfully launched into a low earth sun-synchronous polar orbit on May 13, 2002 at an altitude of 705 km. Five months later, NESDIS started to distribute spatially and spectrally thinned radiances to Numerical Weather Prediction (NWP) centers. The thinned dataset contains 324 out of 2378 channel radiances for every 18th AIRS fields of view (fovs). (There are 3x3 AIRS 15 km fovs within every AMSU 42 km fov; the 18th fov is the center AIRS fov associated with every other AMSU fov.) Each dataset include observations from a six minute period, hence there are 240 such "granules" per day. The thinned granule dataset also include all AMSU channels. The impact of AIRS at ECMWF was been reported to be "small, positive and persistent" (McNally, private communication) and the data are now used operationally. The impact at NCEP was reported to be slightly positive, and much smaller than the impact from assimilating the first NOAA AMSU sounder data in 1998. One of the first questions that come to mind is how can a technically advanced high-spectral resolution infrared sounder like AIRS with its excellent signal to noise performance and relatively high vertical resolution have such a small impact. The answer may be due to spatial thinning and the current state of science for radiance assimilation, which is to use only cloud-free radiance observations. The percentage of assimilated AIRS channel radiances can range from 100% for channels peaking in the upper stratosphere, above the clouds, to 5% for channels peaking in the lower atmosphere. However, because the 1 km vertical resolving power of AIRS is concentrated in the lower atmosphere, the lower peaking and likely cloud contaminated AIRS channel radiances are the most important. Given the very small areal coverage of AIRS data being assimilated, due to clouds, the small impact of AIRS, especially in the lower troposphere, is to be expected. So how can AIRS have a larger impact? We believe the answer is to use more AIRS data by assimilating cloud-contaminated or cloud-cleared radiances. Another option is to assimilate the AIRS retrievals of atmospheric temperature, moisture and ozone profiles, which will become available in near real-time during 2004. A key reason for distributing AIRS products to NWP centers is to enable the NWP community as well as the product generators to learn how to best produce and utilize high-resolution infrared sounder data prior to the operational CrIS and IASI instruments. So the

disappointment of a small impact should be followed by intensive activities to use more AIRS data. One of the goals for 2004 from the AIRS Science Team is demonstrate the high quality of AIRS cloud-cleared data and deliver it to the NWP community. The yield of successful cloud-cleared fovs is about 50%. The purpose of this paper is to show the large improvement in retrieval accuracy using AIRS, when compared to AMSU , in the presence of clear and partly cloudy fovs, and also for cases that have been cloud-cleared. We hope the outstanding performance of AIRS retrievals shown in this paper will encourage the NWP community to assimilate cloud-cleared radiances. The algorithms for deriving products, including clear detection and cloud-clearing, from AIRS /AMSU can be found in the special AQUA IEEE issue (Goldberg et al. (2003), Susskind et al. (2003)).

Retrieval Accuracy in Clear and Partly Cloudy Conditions

The clear fov detection techniques and how they are applied are described in greater detail in Goldberg et al. (2003). There are three key tests. The first test predicts a single AIRS channel at 2390 cm-1, which peaks near 850 mb, from AMSU channels 4, 5 and 6, the second test computes the spatial variability of the 2390 cm-1 for a 3 x 3 array of AIRS fovs, and the third test, ocean only, compares the AIRS sea surface temperature (SST) retrieval with the NWP model SST. The results shown in this paper will be based on regression, trained using the ECMWF analysis. The regression algorithm is based on principal component analysis (PCA) and details are also given in Goldberg et al. (2003). Eighty five principal component scores (PCS) along with AMSU brightness temperatures are used for linear regression predictors. The first experiment was to generate a set of coefficients for "clear" fovs. The ECMWF data used for training is screened for outliers, because we cannot assume that the model is perfect everywhere. However for many situations the model analysis is rather accurate. The outliers are determined by removing cases with large differences between measured and computed radiances. We also generated coefficients for clear to partly cloudy situations. These cases were determined by simply using test 1. If the difference between the predicted AIRS minus the observed 2390 cm-1 AIRS is larger than 2 K, the fov is determined not to be too cloudy (clear, partly cloudy or low clouds). This accounts for about 60 % of the data. The fovs declared clear are approximately 5% of the data. Figure 1 compares retrieval accuracies from clear-only and partly cloudy situations. The figure also compare AIRS vs AMSU-only retrieval accuracies. The "accuracy" curves shown in this figure is the root mean square (rms) difference between the retrieval and ECMWF analysis for an independent ensemble. The solid curves are the retrieval rms differences for ocean clear only cases, whereas the dashed curves are the rms differences for global non-clear cases. The results demonstrate the large improvement of AIRS over AMSU, as well as the very good performance of AIRS even in the presence of cloud contamination. The coverage for the clear - partly cloudy areas area shown in Figure 2.

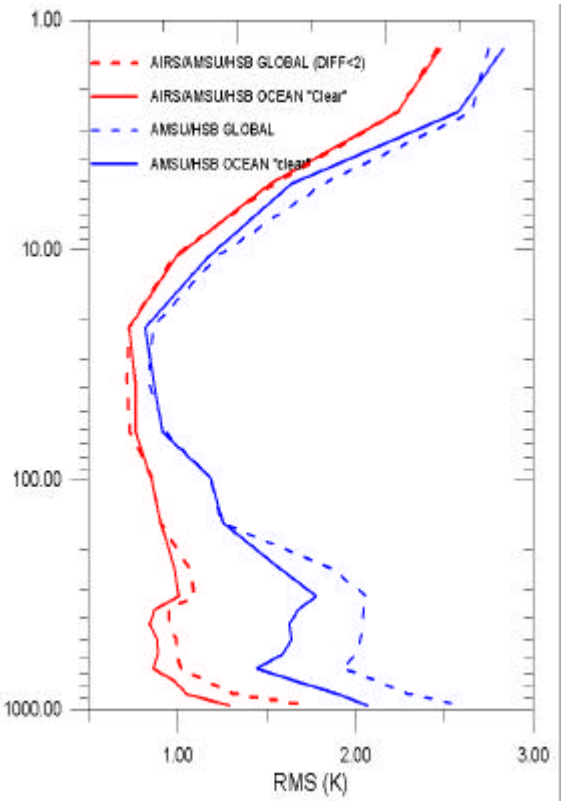

Figure 1 Retrieval RMS Errors

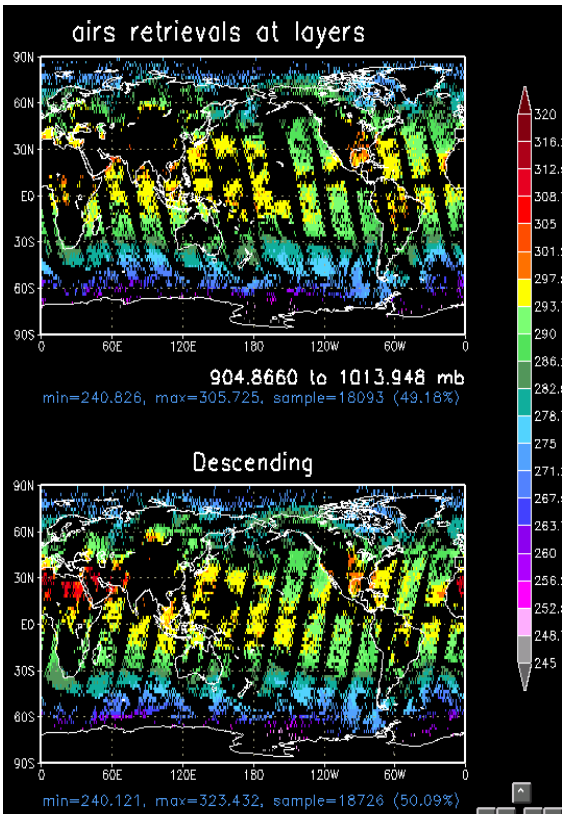

Figure 2: Coverage of partly cloudy regions

Retrieval Accuracy from Cloud-Clearing

The cloud clearing algorithm is described in Susskind et al. (2003). Cloud-clearing begins with an AMSU retrieval of atmospheric temperature, moisture and skin temperature. The retrieval is used as the first guess in the cloud-clearing algorithm. After the AIRS radiances are cloud-cleared, the cloud-cleared radiances are transformed into principal component scores (PCS), and the PCS are used as regression predictors for deriving the AIRS/AMSU temperature, moisture and ozone retrieval . The conversion of radiances to PCS also yields the reconstruction score (RS). The RS provides a measure of how well the radiances can be reconstructed, when compared to the input radiances. A reconstructure score of unity indicates that the reconstruction fit is at the noise level. For cloud-cleared radiances, the score can vary from 0.33 to a number much greater than one. The RS is near 0.33 when the entire 3x3 array of AIRS fovs is clear and the cloud clearing algorithm simply averages the radiances from the 9 fovs. When the score is greater than one, the cloud clearing has amplified the noise with respect to a single fov. Figure 3 shows maps of RS for different ranges of RS. The map on the upper left (RS<0.5) show the areas (~5%) that have been declared clear (i.e. all 3x3 fovs are clear). The map on the upper right show the areas where the cloud-cleared radiance have adjusted noise characteristics that are not larger than the original instrument single fov noise (RS< 1). This area is about 60% of the total. So we

can restrict the use of cloud-cleared radiances to cases with "zero" single fov noise amplication, and still achieve a very good yield. The lower left shows areas where the score is less than 2, and we have observed that the larger RS are near the edge of clouds.

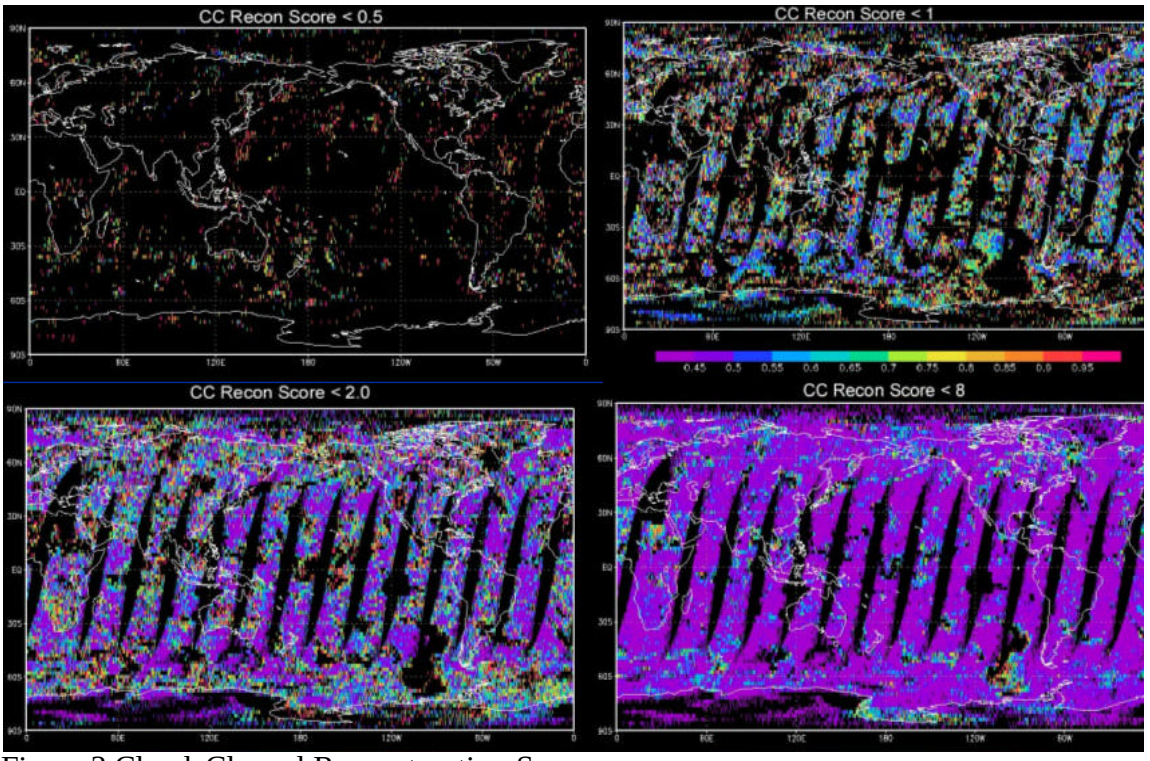

Figure 3 Cloud-Cleared Reconstruction Scores

Regression coefficients were generated from a training set of cloud-cleared radiances collocated with the ECMWF analysis of temperature, moisture and ozone. The ECMWF data are screened by requiring a 2 K agreement between measured and computed radiances for 12 channels: 702.7, 706.7, 711, 712.7, 715.9, 724.8, 746.0, 759.57, 965.4, 1468.83, 1542.35 and 1547.88 cm-1. The training set was derived from three different days (from September 2002, January 2003 and June 2003). Figure 4 shows the a typical training population for a given day. The retrieval accuracy, compared to ECMWF for dependent and independent ensembles are shown in Figure 5. The RMS differences are similar to those obtained from clear fovs, which were shown in Figure 1. We also generated retrieval rms differences based on collocated radiosondes. Figure 6 show the results, along with retrieval rms errors from ATOVS. The AIRS retrieval errors are significantly lower than ATOVS, including the systematic bias. The larger errors for the lower tropospheric temperature are probably due to uncertainties arising from collocation temporal and spatial differences. However, the difference between the ATOVS and AIRS retrieval remains large. Previous simulation studies have found that AIRS generally reduces the retrieval error by about 0.5K, and this appears to be holding for the radiosonde comparison. For moisture, the retrieval errors are significantly smaller than ATOVS. The natural large variability of water vapor combined with uncertainties in radiosonde-observed water vapor will prevent us to yield the 10-15% accuracies often reported in simulated studies.

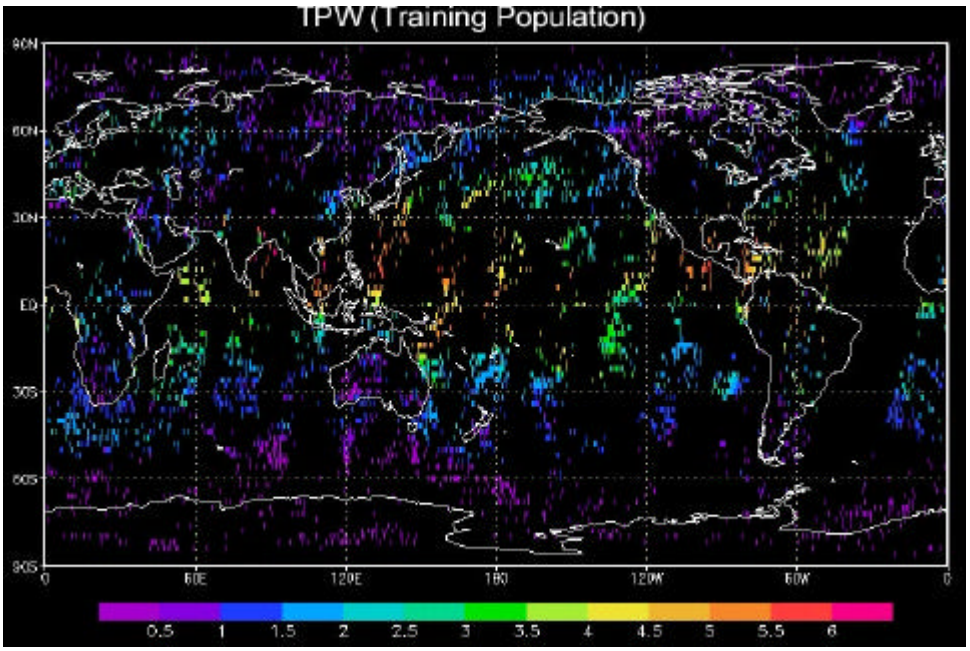

Figure 4. Distribution of collocated AIRS and ECMWF data used in generating regression coeffcients.

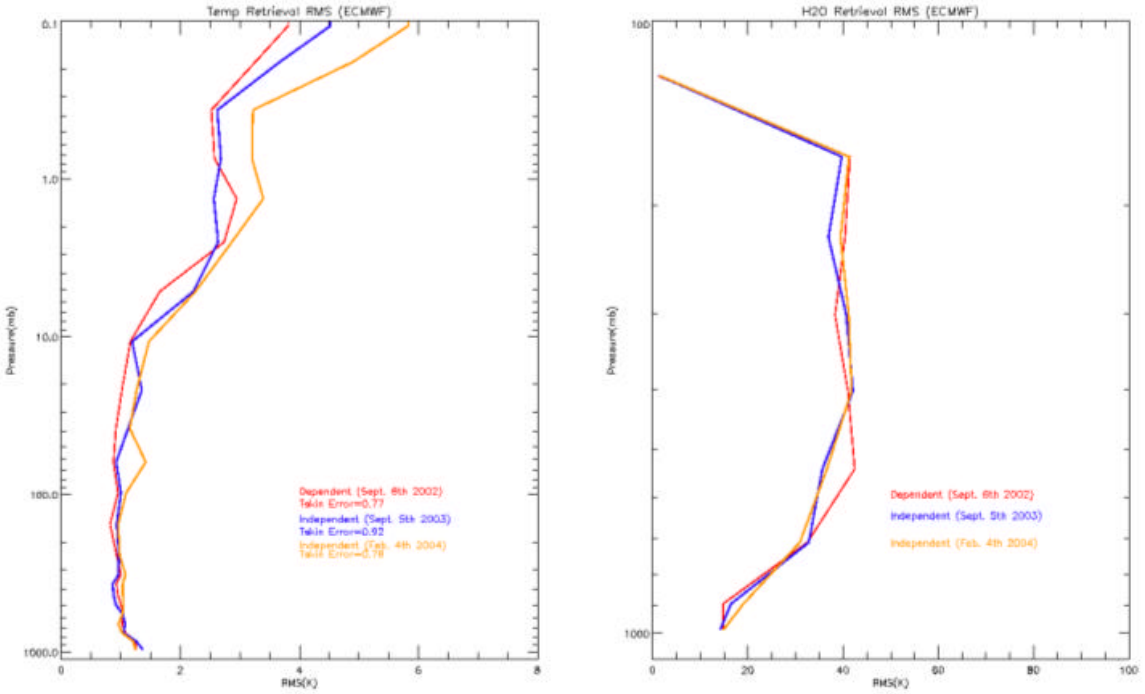

Figure 5 Temperature (K) and Water Vapor (%) RMS difference between AIRS retrieval ans ECMWF

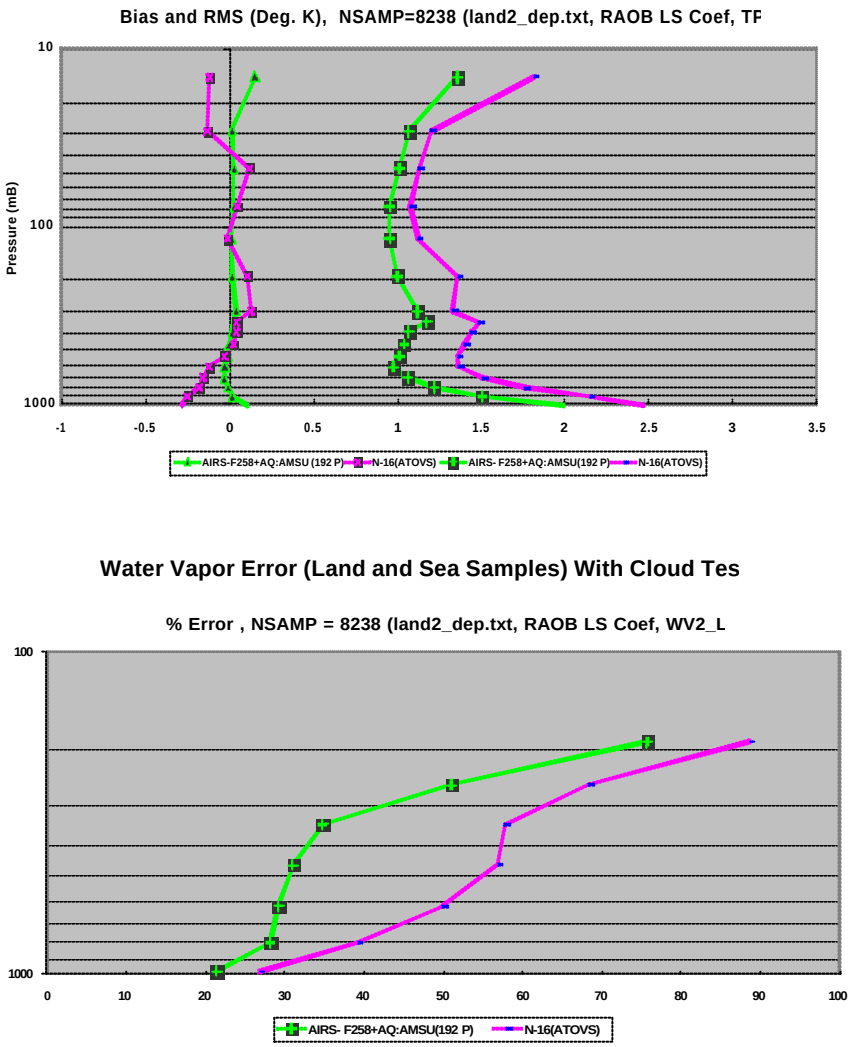

Figure 6 Temperature (K) and Moisture (%) RMS differences between retrieval and collocated radiosonde.

Summary

We have demonstrated very good retrieval performance from AIRS in clear, partial cloudiness and cloud-cleared fovs. The impact in NWP will likely remain small, unless AIRS cloud contaminated or cloud-cleared radiances are assimilated. The challenge for the NWP satellite data assimilation community is to assimilate AIRS data in the presence of clouds, otherwise the full impact of high spectral resolution infrared observations will not be realized. Another option, of course, is to assimilate AIRS retrievals, which are also derived in near real-time.

References

Goldberg, M.D., Y. Qu, L.M. McMillin, W. Wolf, L. Zhou, and M. Divakarla, 2003: AIRS near-real-time products and algorithms in support of operational numerical weather prediction, IEEE Trans. Geosci. Remote Sensing, vol.41, pp 379-389, Feb. 2003

J. Susskind, C. Barnet and J. Blaisdell, Retrieval of atmospheric and surface parameters from AIRS/AMSU/HSB data under cloudy conditions, IEEE Trans. Geosci. Remote Sensing, vol.41, pp 390-410, Feb. 2003

AIRS Real-Time Sounding Profile Retrieval For IMAPP (International MODIS/AIRS Processing Package) Users

Elisabeth Weisz, Hung-Lung Huang, Jun Li, Suzanne Seemann, Eva Borbas, Liam Gumley

Cooperative Institute for Meteorological Satellite Studies, University of Wisconsin-Madison, Madison, Wisconsin, U.S.A

Introduction

The high-spectral-resolution Atmospheric Infrared Sounder (AIRS) was launched onboard the NASA (National Aeronautics and Space Administration) Earth Observing System (EOS)-Aqua platform on May 4, 2002. AIRS is complemented by AMSU (Advanced Microwave Sounding Unit) and HSB (Humidity Sounder Brazil) for the primary purpose to retrieve vertical temperature and humidity profiles. AIRS measures radiation in 2378 channels at a spectral resolution of $\lambda/d\lambda=1200$ in the infrared region from 3.7 to 15.4 μm. AIRS is a scanning instrument with a footprint at nadir of 13.5 km and 90 footprints per scanline. Global coverage is accomplished twice a day. Six minutes of AIRS data, known as a granule, comprises 135 scanlines.

The unprecedented accuracy and global wealth of AIRS sounding products will support climate studies and various research efforts such as weather prediction. Current work at CIMSS includes the development of a real-time Direct Broadcast (DB) processing algorithm to retrieve atmospheric parameters in the troposphere and lower stratosphere as well as surface parameters as part of the International MODIS (Moderate Resolution Imaging Spectroradiometer)/AIRS Processing Package (IMAPP). This paper reviews and discusses the pre-release version of the IMAPP-AIRS retrieval methodology. The algorithm is a statistical eigenvector regression retrieval to obtain a fast and accurate first estimate of the atmospheric state. Evaluation of the results is done by comparison with ECMWF (European Center of Medium-range Weather Forecasts) analysis data, operational AIRS products, radiosonde observations, and retrievals from GOES (Geostationary Operational Environmental Satellite) and MODIS.

Retrieval Methodology

In the regression retrieval the relationship between atmospheric state X and the measurements Y can be simply described by

$$X=CY^T \qquad (1)$$

where C is the matrix of regression coefficients. The least-square regression solution proposes

$$C=XY(Y^TY)^{-1} \qquad (2)$$

The coefficients, derived from a sufficiently large training set of representative atmospheric profiles and surface parameters, are then applied to any real-time measurement spectrum in the retrieval step (1). In practice, one often uses the deviations of the radiances from the sample mean for Y. The current retrieval methodology utilizes an eigenvector regression algorithm (Smith and Woolf 1976, Huang and Antonelli 2001) where regression of compressed radiances against the atmospheric state is performed. The eigenvectors (or principal components) are calculated from the covariance matrix of the training data set of simulated radiances. Performing eigenvector regression with only a few eigenvectors (those with largest eigenvalues) reduces the dimension of the regression problem, as well as the impact of random noise. Investigating retrieval results for different numbers of eigenvectors we found that about 30 eigenvectors seem sufficient for successful retrieval performance. Our current

retrieval products include atmospheric temperature, moisture and ozone profiles, Total Precipitable Water (TPW), total ozone, surface skin temperature and surface emissivity.
The global training data set comprises TIGR3 and NOAA88 profiles supplemented by special desert and polar cases. To characterize surface properties an ecosystem type has been assigned to each pixel to obtain realistic surface pressure, surface skin temperature and surface emissivity. Radiances are calculated for all profiles in the training database using the Stand-Alone Radiative Transfer Algorithm (SARTA, Strow et al. 2003). Furthermore, we classify the training set of radiances on the basis of their Brightness Temperature (BT) in Kelvin (K) at 1000 cm^{-1}. Regression coefficients are computed for each of the six classes identified by the threshold values outlined in Table 1. For the retrieval the observed spectrum is assigned to the appropriate class and the corresponding set of coefficients is used. Note that each class in the training has an overlap of 10 K with its upper and lower neighboring class. This is to ensure that when the retrieval is misclassified the use of non-optimal class retrieval coefficients (likely from an adjacent class) still produces reasonable results. Another classification we performed is based on the scanning angle. Regression coefficients have been calculated for different scanning angles between 0 and 49 degrees. We found that both classification procedures refine the output and optimize retrieval performance.

Table 1: Brightness Temperature (BT) classification scheme (values are given in Kelvin).

Class	Training: BT at 1000 cm^{-1}	Retrieval: BT at 1000 cm^{-1}
1	$BT \leq 260$	$BT \leq 255$
2	$250 < BT \leq 270$	$255 < BT \leq 265$
3	$260 < BT \leq 280$	$265 < BT \leq 275$
4	$270 < BT \leq 290$	$275 < BT \leq 285$
5	$280 < BT \leq 300$	$285 < BT \leq 295$
6	$290 < BT$	$295 < BT$

Results

The retrieval algorithm, as described above, has been applied to global as well as local observational data. Fig. 1 illustrates surface skin temperature and surface emissivity at wavenumber 926 cm^{-1} over the CIMSS (Cooperative Institute for Meteorological Satellite Studies) DB area for October 23, 2003.

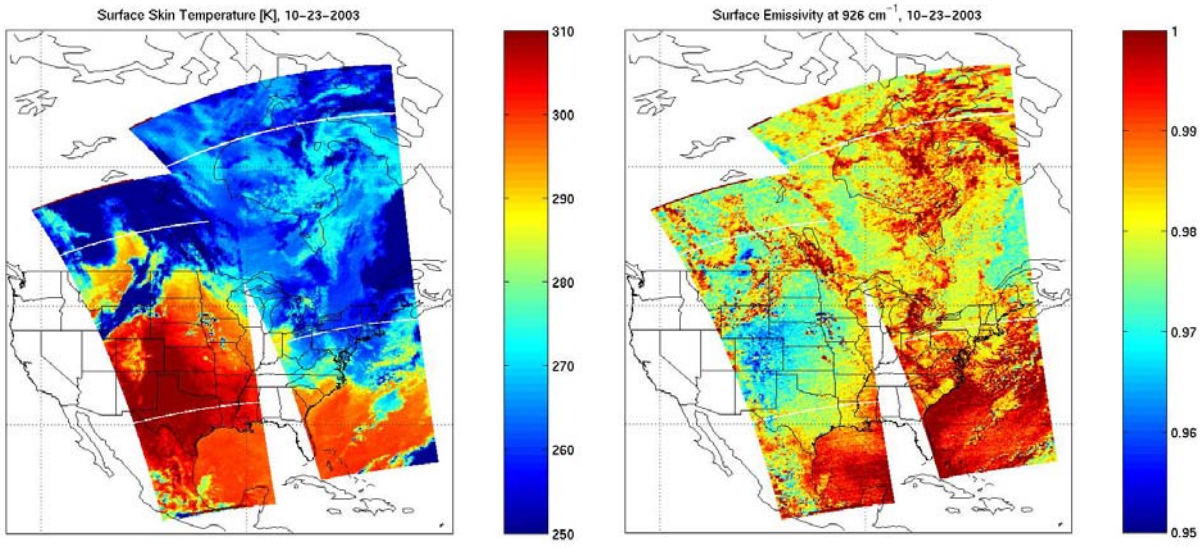

Fig. 1: Real-time DB retrieval of surface skin temperature (left) and surface emissivity at 926 cm^{-1} (right) for 10-23-2003.

Note, the retrieval is shown for all pixels regardless of whether they are cloudy or clear. Since our retrieval algorithm is designed to process clear-sky radiances only, we need a reliable cloud mask to identify clear and cloudy field-of-views. To address this issue we are making use of the 1km-MODIS cloudmask product (Ackerman et al. 1998). Daytime granule 192 on September 2, 2003 has been selected to illustrate clear scene identification. Fig. 2 and Fig. 3 show retrievals of temperature at 850 mbar and TPW, respectively, for all pixels (left panel) as well for clear pixels only (right panel). The retrievals are being compared with the corresponding ECMWF analysis fields. Note that the analysis data has been spatially interpolated to AIRS measurement locations, and the difference in time is approximately one hour. For temperature we find some differences in the fine-scale structure between retrievals and analysis but the spatial average is in good agreement. Differences are more drastic in the case of humidity (not shown) and TPW (Fig. 3), although some features are similarly depicted.

The Root-Mean-Square (RMS) error of the difference between analysis and retrieval for all clear pixels (approximately 4500 in number) is given in Fig. 4 for temperature and humidity profiles at each pressure level as well as for skin temperature and TPW. Largest values occur at and near the surface, partly caused by surface parameters (in particular surface skin temperature and surface emissivity) not being sufficiently and/or incorrectly represented in the training data set. Another reason is the assumption of linearity between measurements and atmospheric state in the regression retrieval problem. An iterative non-linear physical retrieval method will yield significantly smaller errors in the boundary layer. It should be mentioned that the 1-km (for temperature) and 2-km (for humidity) "layer mean RMS" profiles are commonly used by the AIRS science team. Layer mean RMS is significant smaller than the corresponding level RMS for both temperature and humidity retrievals.

Intercomparison with an analysis filed may not be sufficient to characterize the retrieval error. The residual, which is the difference between the observations and the calculated radiances (the latter calculated by the forward model using the retrieved profile as the input), is more indicative of how the retrieved and the model data represent the actual state of the atmosphere. Fig. 5 shows the RMS error, the standard deviation and the mean (or bias) of the residuals of the clear pixels as a function of wavenumber. Results are shown for the retrieved granule (left) and for the analysis (right) in the spectral range from 500 to 1700 cm^{-1}. All three quantities are significant smaller for the retrieval than for the analysis, in particular in the long-wave atmospheric window region where the difference can be as large as 3 K.

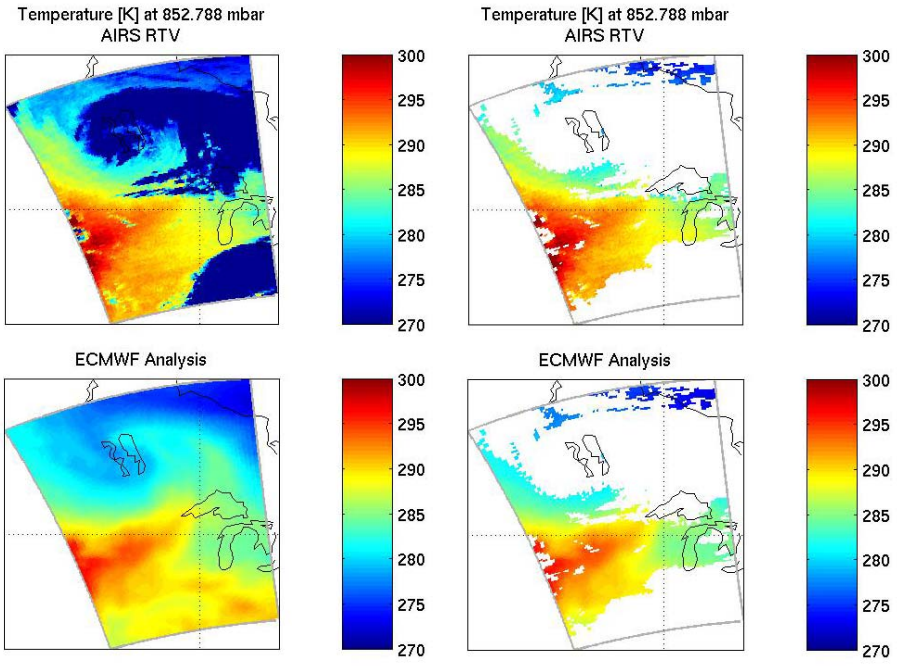

Fig. 2: Retrieved temperature [K] at ~850 mbar (top) for granule 192 (09-02-2003) compared with ECMWF analysis (bottom) with cloud filtering (right) and without (left).

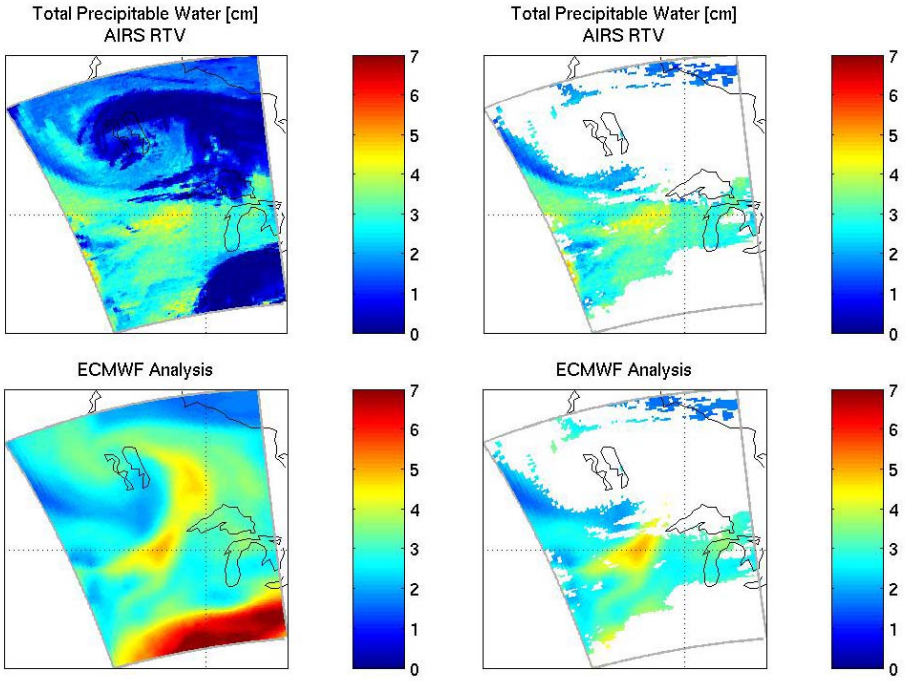

Fig. 3: Retrieved TPW [cm] (top) for granule 192 (09-02-2003) compared with ECMWF analysis (bottom) with cloud filtering (right) and without (left).

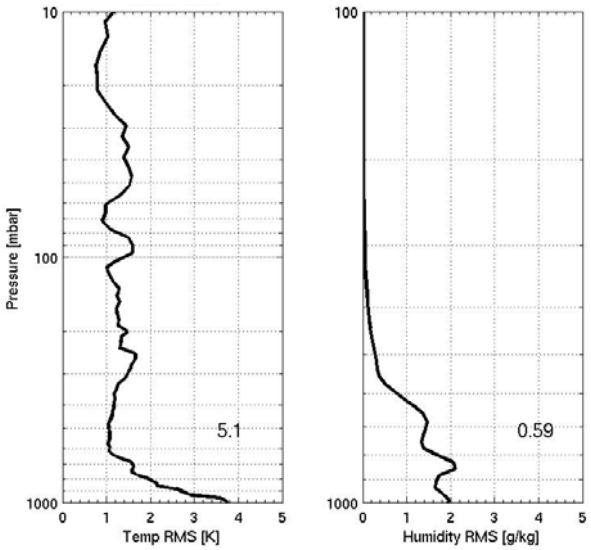

Fig. 4: RMS (at each pressure level) of ECMWF analysis minus retrieval for temperature (left) and humidity (right) shown for clear pixels of granule 192 (09-02-2003). The numbers inside the panels refer to the RMS error of skin temperature [K] and of total precipitable water [cm] respectively. Note the lowest pressure level shown is 10 mbar for temperature and 100 mbar for humidity.

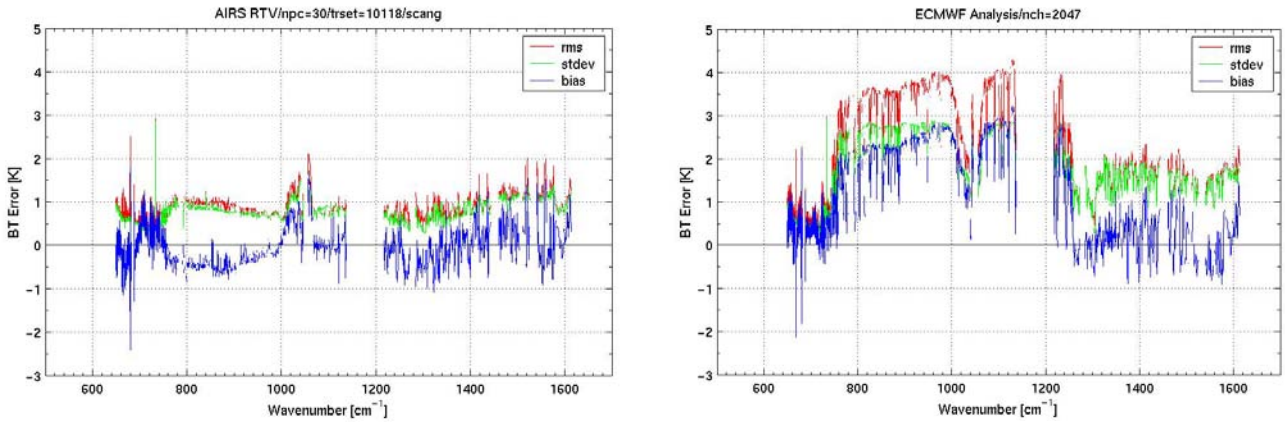

Fig. 5: Root-mean-square error (red), standard deviation (green) and bias (blue) of brightness temperature residuals as a function of wavenumber for the retrieval (left) and the ECMWF analysis (right).

Comparison with MODIS (Seemann et al. 2003) and GOES retrieval (Schmit et al. 2002) is displayed in Fig. 6 for temperature and moisture at 620 mbar for the same granule as above. This figure demonstrates that the IMAPP AIRS retrieval is in good agreement with operational and well-validated retrieval products. It should be mentioned that the different coverage is due to different cloudmasks and different spatial resolution of the measurements.

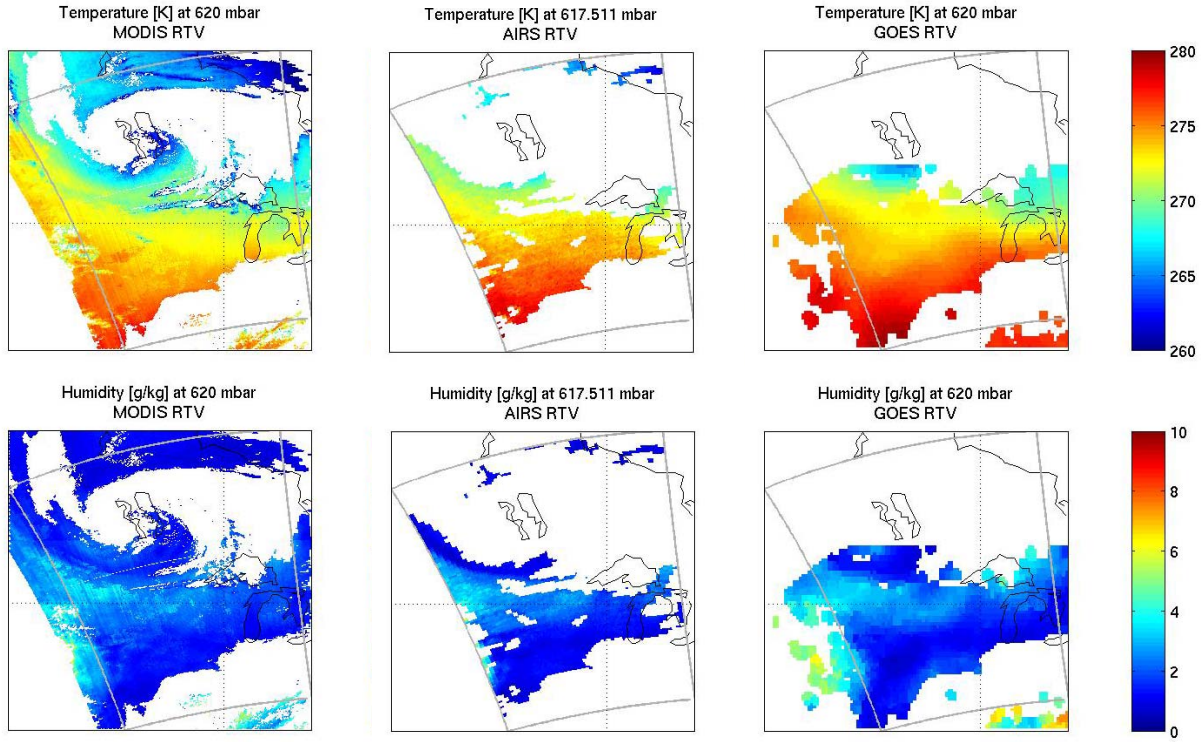

Fig. 6: Retrievals of temperature (top) and moisture (bottom) at 620 mbar for the MODIS (left), AIRS (middle) and GOES (right) instrument.

An ongoing task is to compare the IMAPP AIRS retrieval results with the L2 Standard Retrieval Product (called operational product hereafter) which has been made public available by the AIRS Science Team in September 2003. The operational products are obtained by using cloud-cleared radiances calculated for an AMSU footprint (Susskind et al. 2003). An AMSU footprint encompasses a 3x3 array of AIRS footprints. To be able to compare our retrieval with the operational product we apply our regression coefficients to the operational L2 cloud-cleared radiance product to obtain the

same spatial resolution. We demonstrate this type of evaluation for temperature (daytime granule 7, 09-02-2003) and for humidity (daytime granule 175, 09-02-2003) in Fig.7. Both variables are shown over ocean at ~850 mbar for the operational product (left), IMAPP AIRS retrieval (middle) and the ECMWF analysis (right). Note, only pixels with successful and validated cloud-clearing and retrieval performance are displayed. Operational and IMAPP AIRS retrievals have similar temperature fields, and the verification against the analysis suggests that good regression retrieval estimates are achievable. The main features in the humidity field as depicted in the analysis (Fig. 7, bottom right) are well identified by both retrievals, but the absolute values differ to some extent. For the case shown we find that the IMAPP AIRS regression retrieval (middle panel) is quite successful in describing the moist regions quantitatively. Nevertheless, the differences found in this study make further comparison and investigation necessary.

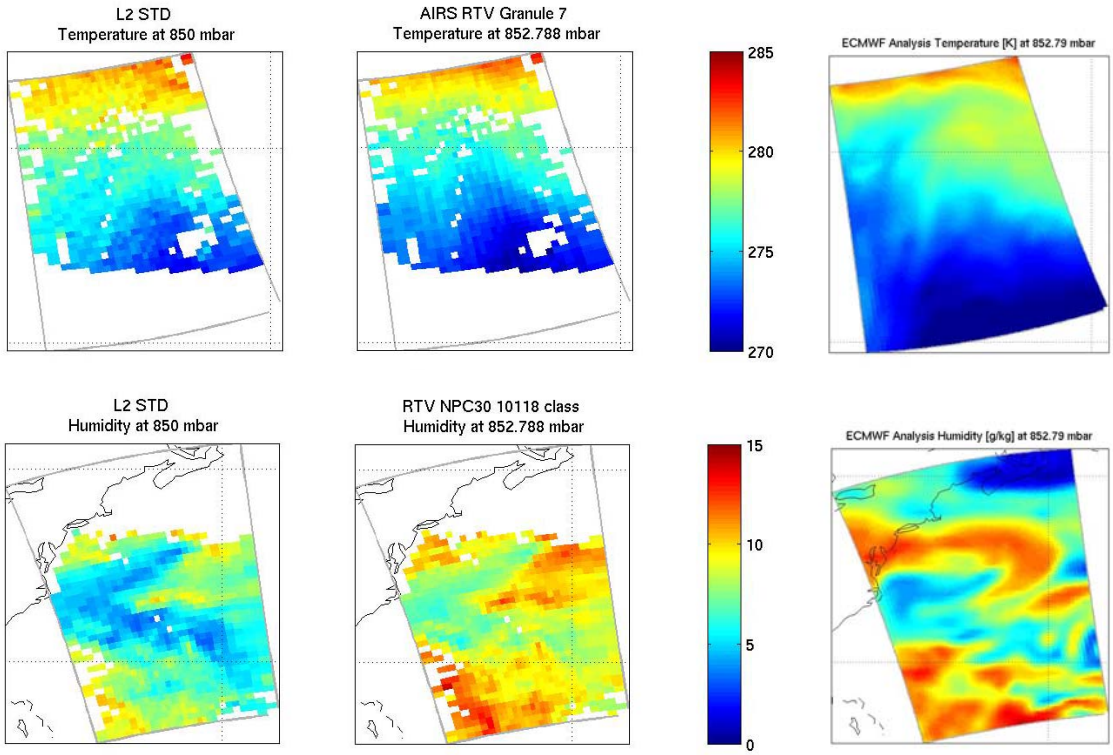

Fig. 7: L2 operational retrieval (left), AIRS IMAPP retrieval (middle) and ECMWF analysis (right) for temperature (top) and humidity (bottom) at 850 mbar.

Radiosonde observations provide an important opportunity to investigate retrieval performance, although temporal and spatial mismatch between radiosonde and satellite measurements have to be kept in mind when comparing the observed radiosonde profile with the retrieved profiles. In Fig. 8 one example of a single-profile retrieval compared with the radiosonde profile is presented. The upper panels display (from left to right) the temperature profiles, the corresponding differences of RAOB minus the retrieved profile profile, humidity profiles and their differences. Retrieved profiles include GOES, operational AIRS and IMAPP AIRS retrieval. The associated brightness temperature residuals are shown in the lower panels. Both retrieval results and residuals are comparable. Current efforts include retrieval validation against a large number of co-located radiosondes to quantify retrieval performance in a statistical sense.

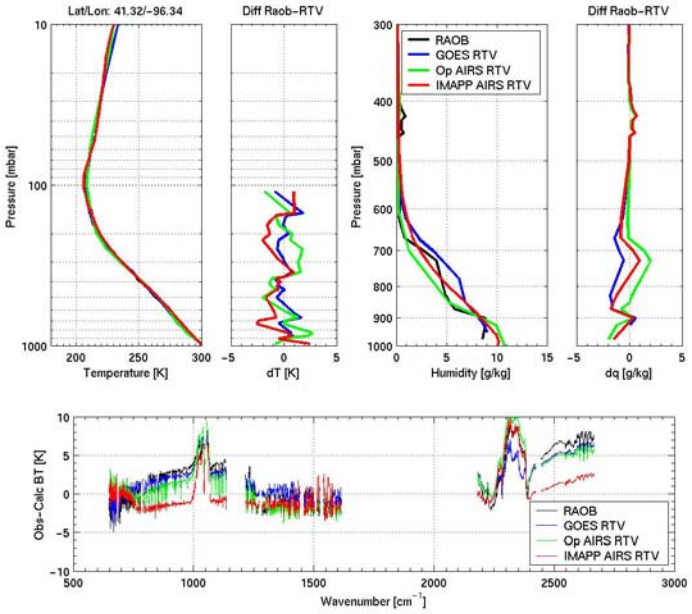

Fig. 8: Top: Profiles of temperature, temperature difference (radiosonde profile minus retrieval), humidity, and humidity difference for radiosonde (black), retrieved profiles of GOES (blue), operational AIRS (green) and IMAPP AIRS (red). Bottom: associated BT residuals in K.

Summary and Conclusions

We have presented algorithm and results of the pre-release version of the IMAPP AIRS regression retrieval. Results obtained so far promise acceptable retrieval performance in real-time. On-going efforts to improve these results include preparation of the training database, investigation of eigenvector compression and noise-filtering techniques. Furthermore, we will continue to validate IMAPP AIRS sounding retrievals against radiosonde observations, analysis fields, operational retrieval products from AIRS and other instruments such as GOES and MODIS.

The main drawback of the regression retrieval method is the assumption of a linear relationship between the measured radiances and the atmospheric state. To address this problem a more sophisticated non-linear physical inversion that includes information about first guess (background), error statistics and weighting functions will be implemented. We expect significant improvements from the physical method in particular for humidity soundings. Nevertheless, the linear regression retrieval will continue to be indispensable in achieving the 1K/1km and 10%/1km requirements for tropospheric temperature and humidity, respectively.

Other future research efforts include the optimal use of AIRS cloud-cleared radiances and improved handling of cloud contamination within the single and multiple field-of-views retrieval. Significant effort will be made related to single field-of-view humidity retrieval to provide regional meso-scale real-time applications for international direct broadcast users.

Acknowledgements

The authors thank the AIRS Science Team at NASA's JPL (Jet Propulsion Laboratory) for their overall support and ECMWF for the use of model analysis fields. We also acknowledge the contributions from various research teams at SSEC (Space Science and Engineering Center) and CIMSS at UW-Madison. This research is supported by NASA grants NAS5-31377 and NAG5-13402.

References

Ackerman, S.A., Strabala, K.I., Menzel, W.P., Frey, R.A., Moeller, C.C., Gumley, L.E. 1998. Discriminating clear sky from clouds with MODIS. *J. Geophys. Research-Atmospheres*,**103**, 32141-32157.

Hung-Lung, H., Antonelli, P. 2001. Application of principal component analysis to high-resolution infrared measurement compression and retrieval. *J. Appl. Met.*, **40**, 365-388.

Seemann, S.W., Li, J., Menzel, W.P., Gumley, L.E. 2003. Operational retrieval of atmospheric temperature, moisture, and ozone from MODIS infrared radiances. *J. Appl. Met.*, **42**, 1072-1091.

Schmit, T.J., Feltz, W.F., Menzel, W.P., Jung, J., Noel, A.P., Heil, J.N., Nelson, J.P., Wade, G.S. 2002. Validation and use of GOES sounder moisture information. *Wea. Forecasting*, **17**, 139-154.

Smith, W.L., Woolf, H.M. 1976. The use of eigenvectors of statistical covariance matrices for interpreting satellite sounding radiometer observations. *J. Atmos. Sci.*, **33**, 1127-1140.

Strow, L.L., Hannon, S.E., De Souza-Machado, S., Motteler, H.E., Tobin, D. 2003. An overview of the AIRS radiative transfer model. *IEEE Trans. Geosci. Remote Sensing*, **41**, 303-313.

Susskind, J., Barnet, C.D., Blaisdell, J.M. 2003. Retrieval of atmospheric and surface parameters from AIRS/AMSU/HSB data in the presence of clouds. *IEEE Trans. Geosci. Remote Sensing*, **41**, 390-409.

Current results from AIRS/AMSU/HSB

Joel Susskind[a], Robert Atlas[a], Christopher Barnet[b], John Blaisdell[c], Lena Iredell[c], Genia Brin[c], Juan Carlos Jusem[c], Fricky Keita[c], Louis Kouvaris[c], Gyula Molnar[b]

[a]NASA Goddard Space Flight Center, Greenbelt, MD, USA 20771
[b]Joint Center for Earth Systems Technology, NASA GSFC, Greenbelt, MD, USA 20771
[c]Science Applications International Corporation, NASA GSFC, Greenbelt, MD, USA 20771

Abstract

AIRS was launched on EOS Aqua on May 4, 2002, together with AMSU A and HSB, to form a next generation polar orbiting infrared and microwave atmospheric sounding system. The primary products of AIRS/AMSU/HSB are twice daily global fields of atmospheric temperature-humidity profiles, ozone profiles, sea/land surface skin temperature, and cloud related parameters including OLR. The sounding goals of AIRS are to produce 1 km tropospheric layer mean temperatures with an rms error of 1K, and layer precipitable water with an rms error of 20%, in cases with up to 80% effective cloud cover. Pre-launch simulation studies indicated that these results should be achievable. Minor modifications have been made to the pre-launch retrieval algorithm as alluded to in this paper. Sample fields of parameters retrieved from AIRS/AMSU/HSB data are presented and temperature profiles are validated as a function of retrieved fractional cloud cover. As in simulation, the degradation of retrieval accuracy with increasing cloud cover is small. Select fields are also compared to those contained in the ECMWF analysis, done without the benefit of AIRS data, to demonstrate information that AIRS can add to that already contained in the ECMWF analysis. Assimilation of AIRS temperature soundings in up to 80% cloud cover for the month of January 2003 into the GSFC FVSSI data assimilation system resulted in improved 5 day forecasts globally, both with regard to anomaly correction coefficients and the prediction of location and intensity of cyclones.

Introduction

AIRS/AMSU/HSB is a state of the art advanced infra-red microwave sounding system that was launched on the EOS Aqua platform in a 1:30 AM/PM sun synchronous orbit on May 4, 2002. An overview of the AIRS instrument is given in Pagano et al[1]. The sounding goals of AIRS are to produce 1 km tropospheric layer mean temperatures with an rms error of 1K, and layer precipitable water with an rms error of 20%, in cases with up to 80% effective cloud cover. Aside from being part of a climate mission, one of the objectives of AIRS is to provide sounding information of sufficient accuracy such that when assimilated into a general circulation model, significant improvement in forecast skill would arise. The pre-launch algorithm to produce level 2 products (geophysical parameters) using AIRS/AMSU/HSB data, and expected results based on simulation studies, are given in Susskind et al.[2] The results of that simulation indicate that the sounding goals of AIRS/AMSU/HSB should be achievable. In that simulation, perfect knowledge of the instrumental spectral response functions and the inherent physics of the radiative transfer equations was assumed. Therefore, if the true state of the atmosphere and underlying surface were known perfectly, one could compute the radiances AIRS, AMSU, and HSB would see exactly up to instrumental noise. Susskind

et al.[2] alluded to the fact that this is not the case but in reality, and additional terms would have to be included in the retrieval algorithm to account for systematic differences (biases) between observed brightness temperatures and those computed knowing the "true" surface and atmospheric state, as well as residual computational errors after that systematic bias is accounted for (computational noise). In this paper, we show results based on the algorithm we were using to analyze AIRS/AMSU/HSB data on June 30, 2003, which we will refer to as Version 3.1. This algorithm is very similar to the pre-launch version, with the major differences attributable to the factors described above. JPL delivered an earlier version of the algorithm, Version 3.0, to the Goddard DAAC, for the earliest near real time processing of AIRS level 2 products starting in August 2003. We have used Version 3.1 to analyze data for the AIRS focus day September 6, 2002, and all of January 2003 for use in a forecast impact experiment. Research to further improve the results of analysis of AIRS/AMSU/HSB data is continuing. JPL plans to deliver an improved version to the DAAC in the Spring of 2004 to be used to process near real time AIRS data from that point forward, as well as reprocess all AIRS data from September 2002, when the instrument became stable.

Overview of the AIRS Team Retrieval Algorithm

The AIRS team retrieval algorithm is basically identical to that described in Susskind et al.[2] The key steps are outlined below: 1) Start with an initial state consistent with the AMSU A and HSB radiances[3]; 2) Derive IR clear column radiances $\hat{R}_i^0$ valid for the 3x3 AIRS Fields of View (FOVs) within an AMSU A Field of Regard (FOR) consistent with the observed radiances and the initial state; 3) Obtain an AIRS regression guess[4] consistent with $\hat{R}_i^0$ using 1504 AIRS channels; 4) Derive $\hat{R}_i^1$ consistent with the AIRS radiances and the regression guess; 5) Derive all surface and atmospheric parameters using $\hat{R}_i^1$ for 415 AIRS channels and all AMSU and HSB radiances; 6) Derive cloud parameters and OLR consistent with the solution and observed R_i; 7) Apply quality control, which rejects a solution if the retrieved cloud fraction is greater than 80% or other tests fail. In the event that a retrieval is rejected, cloud parameters are determined using the initial microwave state and observed AIRS radiances. Figure 1 shows a typical AIRS spectrum and indicates by different colors the AIRS channels used in different retrieval steps which are performed sequentially.

Results Using Version 3.1

Figure 2 shows the number of cases for each retrieved effective fractional cloud, in 0.5% bins, for the whole day September 6, 2002. The effective fractional cloud cover is given by the product of the fraction of the field of view covered by clouds and the cloud emissivity at 11 μm. The average global effective cloudiness was determined to be 38.26%. Also shown is the percent of accepted retrievals as a function of retrieved effective cloud cover. Roughly 93% of the cases with retrieved effective cloud cover 20% were accepted, falling to 63% at 60% effective cloud cover, and to 45% at 80% effective cloud cover. All cases with retrieved effective cloud cover greater than 80% are rejected.[2] The average effective fractional cloudiness for all accepted cases was 27.06%. These results are very similar to what was shown in the simulation study.[2]

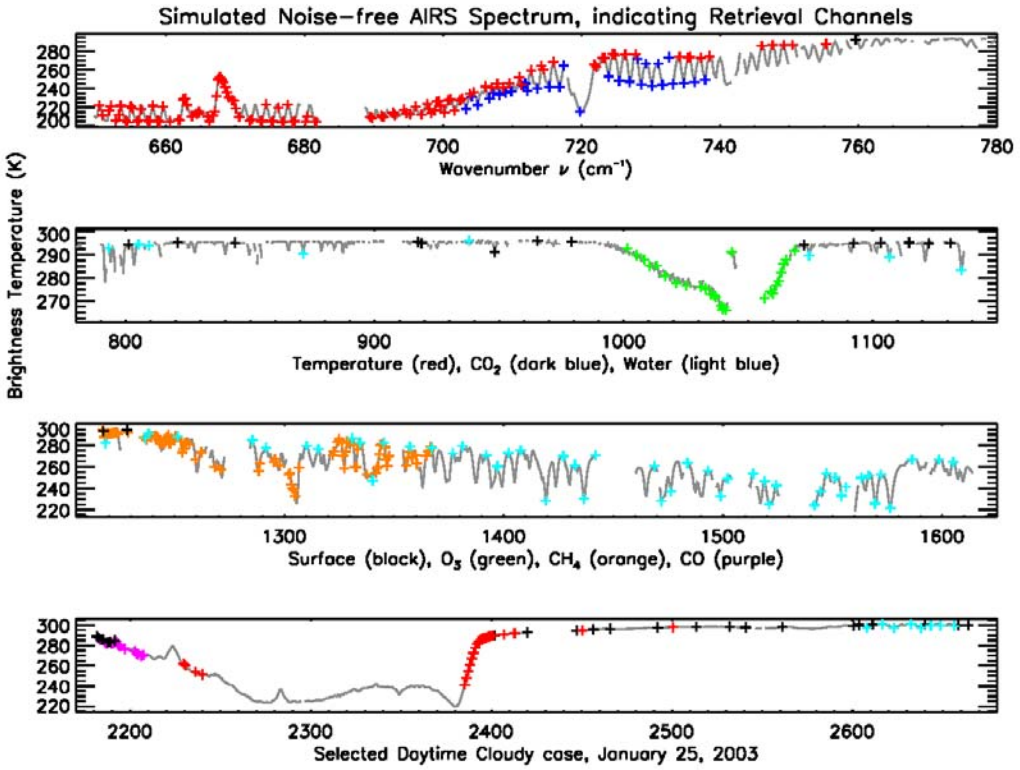

Figure 1

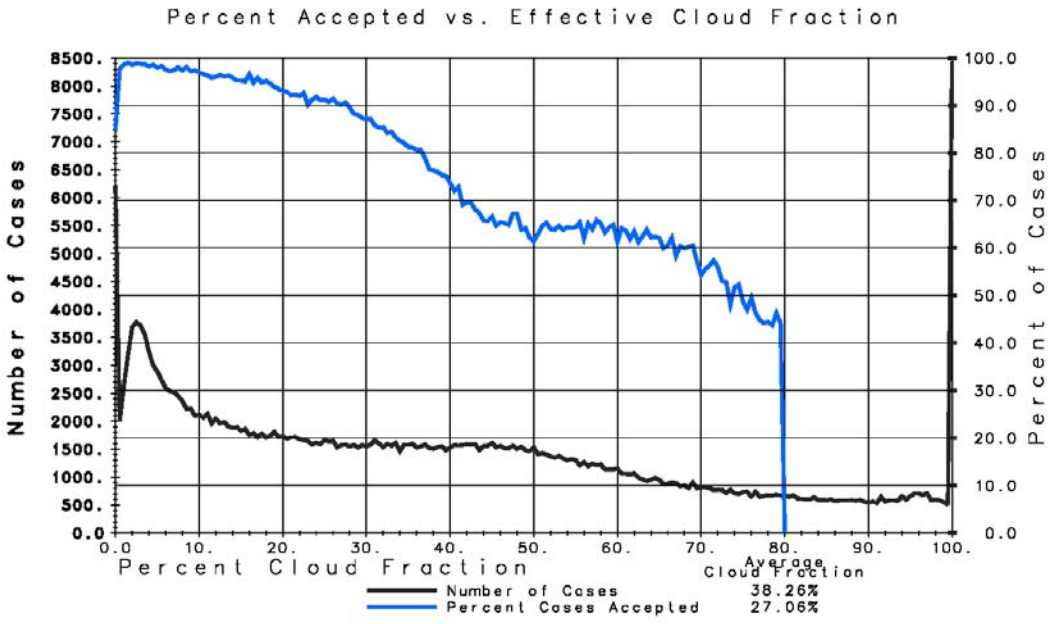

Figure 2

Figure 3 shows the RMS difference between retrieved 1 km layer mean temperatures and the collocated ECMWF forecast for all accepted cases as a function of retrieved effective cloud fraction. Results are shown for each of the lowest 8 km of the atmosphere. Agreement degrades with increasing cloud cover, but only very slowly except in the lowest 1 km of the atmosphere. RMS temperature differences from ECMWF at all levels are somewhat larger than the 1 K goal for retrieval accuracy. Part of this difference can be attributed to the fact that the ECMWF forecast is not perfect. It is also possible that the accuracy of the ECMWF forecast may be somewhat poorer with increasing cloud cover. The increase in RMS temperature differences at 0% cloudiness is somewhat misleading because a large percentage of clear cases occurred over Antarctica on this day.

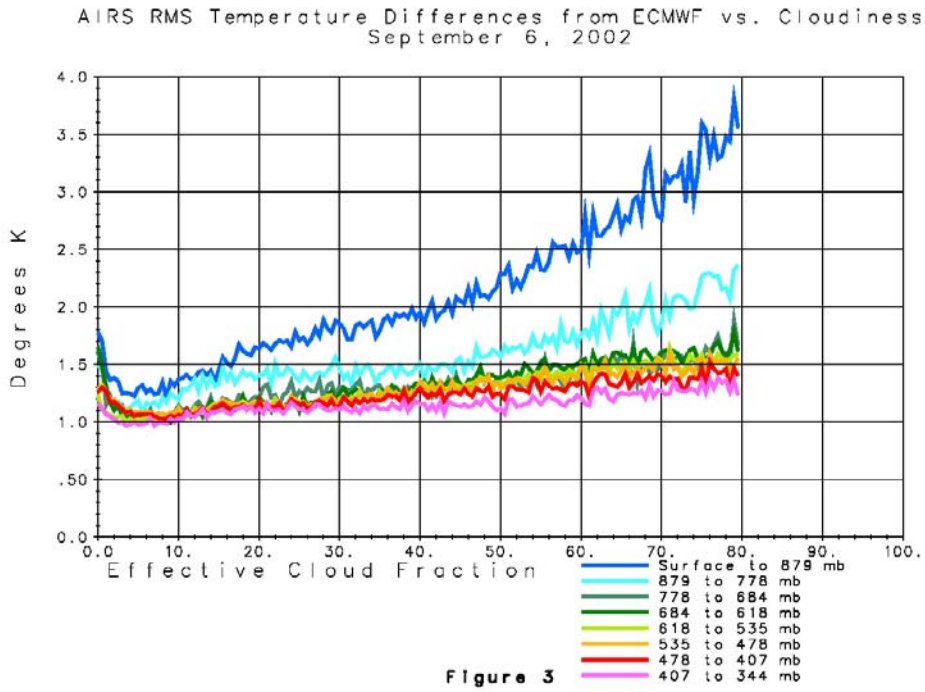

Figure 3

Figures 4a and 4b show RMS differences of temperature and moisture profiles from the “truth” with both simulated and real data. The gray and black curves reflect all accepted cases, and the pink and red curves are cases identified as clear, for simulated and observed radiances respectively. For temperature, 1 km layer mean differences from the truth are shown, and for water vapor, % differences in total integrated water vapor in 1 km layers are shown. In simulation, the truth is known perfectly, while with real data, the 3 hour ECMWF forecast is taken as a proxy for “truth”. For real data, as in simulation, temperature retrievals under cloudy conditions (roughly 66% of all cases are accepted) degrade by only a few tenths of a degree compared to cases identified as clear (roughly 8% of the cases are identified as clear), while water vapor retrievals do not degrade at all. Differences from “truth” are poorer with real data than in simulation. Two major causes of degradation are: 1) perfect physics was assumed in simulation; and 2) the “truth” has errors in real data. The degradation of soundings in the presence of “real clouds”, as compared to soundings in clear cases, appears to be similar to that implied by simulation.

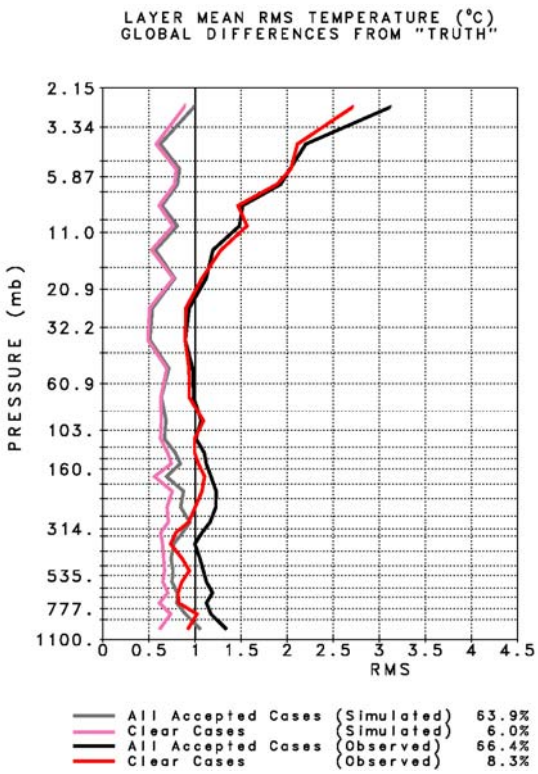

Figure 4a

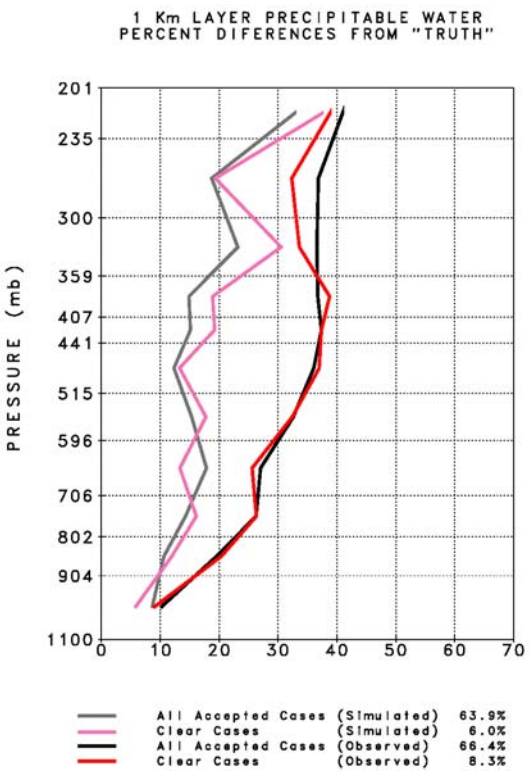

Figure 4b

Figure 5a shows RMS layer mean temperature differences between accepted retrievals, the ECMWF forecast, and collocated radiosonde reports (± 1 hour, ± 100 km) for September 6, 2002. The number of cases included in each of the layers is indicated at the right of the figure. It is interesting to note that the RMS temperature differences between the retrievals and ECMWF are generally smaller in the vicinity of radiosondes than they were globally (see Figure 4a). This is because the ECMWF forecast is more accurate in the vicinity of radiosondes than it is globally. The 3 hour ECMWF forecast agrees with radiosondes to 1 K between roughly 750 mb and 20 mb. Spatial and temporal sampling differences between ECMWF, retrievals, and radiosondes contribute to some extent to the increased differences between both ECMWF and retrievals as compared to radiosondes beneath 750 mb, as spatial and temporal variability of the atmosphere is greatest near the surface. Retrieval accuracy near radiosondes is somewhat poorer than that of the forecast at all levels, especially in the vicinity of 200 mb. This is most likely due to limitations in the current methodology used to account for systematic errors in the radiative transfer used in the calculations and accounting for residual physics errors in the channel noise covariance matrix. We expect further improvement in this area.

Figure 5b shows analogous results for percent differences in 1 km layer mean precipitable water, for which the sounding goal for AIRS is 20%. With regard to water vapor, it is clear that AIRS retrievals are significantly more accurate than the ECMWF forecast above 700 mb. AIRS differences from radiosondes are greater than the 20% goal. Spatial and temporal sampling differences between AIRS and radiosondes may contribute significantly to the apparent water vapor “errors” as water vapor changes rapidly in space and time.

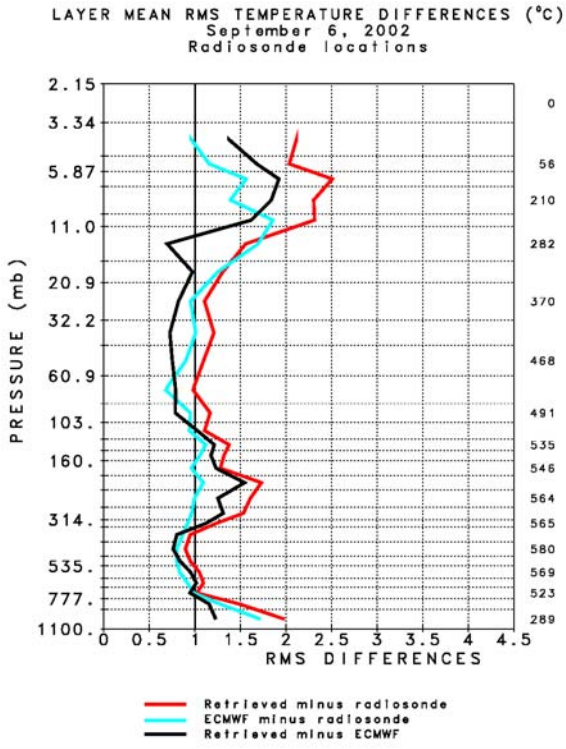

Figure 5a

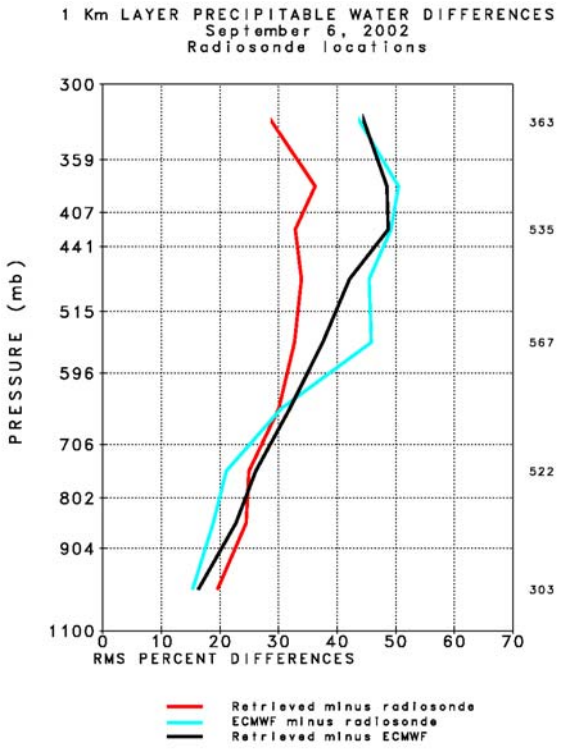

Figure 5b

Figure 6a shows the retrieved effective cloud top pressure and effective cloud fraction for ascending orbits on January 25, 2003. The results are presented in terms of cloud fraction in 5 groups, 0-20%, 20-40%, etc. with darker colors indicating greater cloud cover. These groups are shown in each of 7 colors, indicative of cloud top pressure. The reds and purples indicate the highest clouds, and the yellows and oranges the lowest clouds. Cloud fields are retrieved for all cases in which valid AIRS/AMSU observations exist. Gray means no data was observed. Figure 6b shows the retrieved 500 mb temperature field. Gray indicates regions where either no valid observations existed or the retrieval was rejected, generally in regions of cloud cover 80-100%. Retrieved temperature profile fields are quite coherent, and show no apparent artifacts due to clouds in the field of view. Figures 7c and 7d show retrieved values of total precipitable water vapor above the surface and above 300 mb. Note the high values of upper tropospheric water vapor to the east of extensive cloud bands attributed to cold fronts.

Figure 7a shows the retrieved 700 mb temperature field for ascending orbits on January 25, 2003. Figure 7b shows the collocated ECMWF 3 hour forecast 700 mb temperature field. These fields appear very similar to each other. Their difference is shown in Figure 7c, in which white shows agreement to ± 0.5K, each shade of red shows AIRS warmer than ECMWF in intervals of 1 K (0.5 – 1.5, 1.5 – 2.5, etc.), and each shade of blue shows AIRS colder then ECMWF in intervals of 1 K. The area weighted global mean difference of the two fields is 0.08 K, and the area weighted standard deviation is 1.13 K. Most areas are white or the first shade of red or blue. The largest differences between the two fields occur in the vicinity of 35°S – 55°S, 100°E – 140°E, and show up as a dipole,

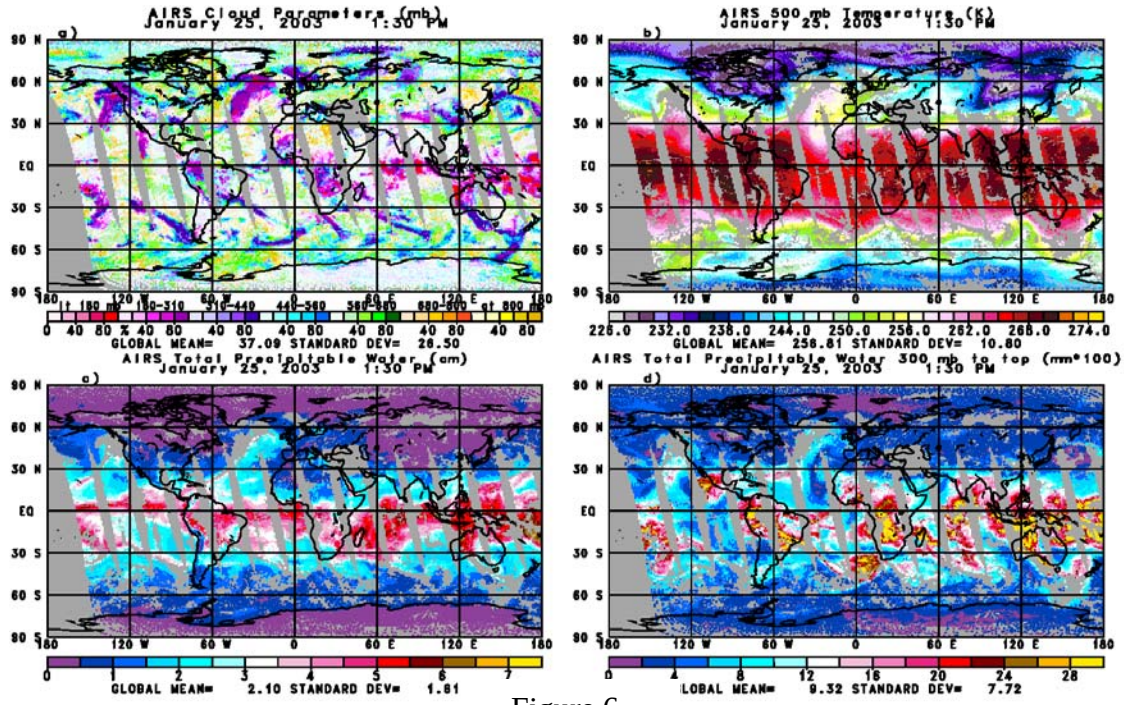

Figure 6

with AIRS warmer to the west of 120°E and colder to the east. Figures 7a and 7b show this to be an area of a cold air mass, extending from the polar region to the mid-latitudes. This cold air mass is coherent in both the retrieved and forecasted fields, but is centered further east in the retrieved field compared to the forecast field, corresponding to a phase error in the 3 hour ECMWF forecast. This is precisely the type of information that satellite data can provide (if accurate enough) to help improve forecast skill. Figure 7d shows the difference between the retrieved and forecast 100 mb temperature fields. At the 100 mb level, a corresponding warm front (not shown) exists in both the retrieved and forecast fields in the area discussed above, with an analogous phase error to that found at 700 mb. Consequently, the retrieved 100 mb field is cooler than ECMWF to the west and warmer to the east in the region discussed above. This out of phase relationship of patterns of differences from ECMWF at 700 mb and 100 mb is indicative of phase errors in the ECMWF forecast, as there is no reason for retrieval errors to be out of phase with each other at 700 mb and 100 mb. This out of phase relationship in spatial patterns of differences between retrieved and forecast temperatures at 700 mb and 100 mb is found in numerous places in Figures 7c and 7d and indicates many areas where the satellite data should improve the ECMWF forecast.

Forecast Impact Experiments

The data assimilation system used in the experiments is FVSSI which represents a combination of the NASA Finite Volume General Circulation Model (FVGCM) with the NCEP operational Spectral Statistical Interpolation (SSI) global analysis scheme implemented at lower than the operational horizontal resolution – T62. The basics of the finite-volume dynamical core formulation are given in DAO's Algorithm Theoretical Basis Document (see http://polar.gsfc.nasa.gov/sci_research/atbd.php), and the FVGCM has been shown to produce very accurate weather forecasts when run at high resolution.[5] The AIRS temperature profiles produced by SRT were presented to the SSI analysis as rawinsonde profiles with observational error specified at 1°K at all vertical levels.

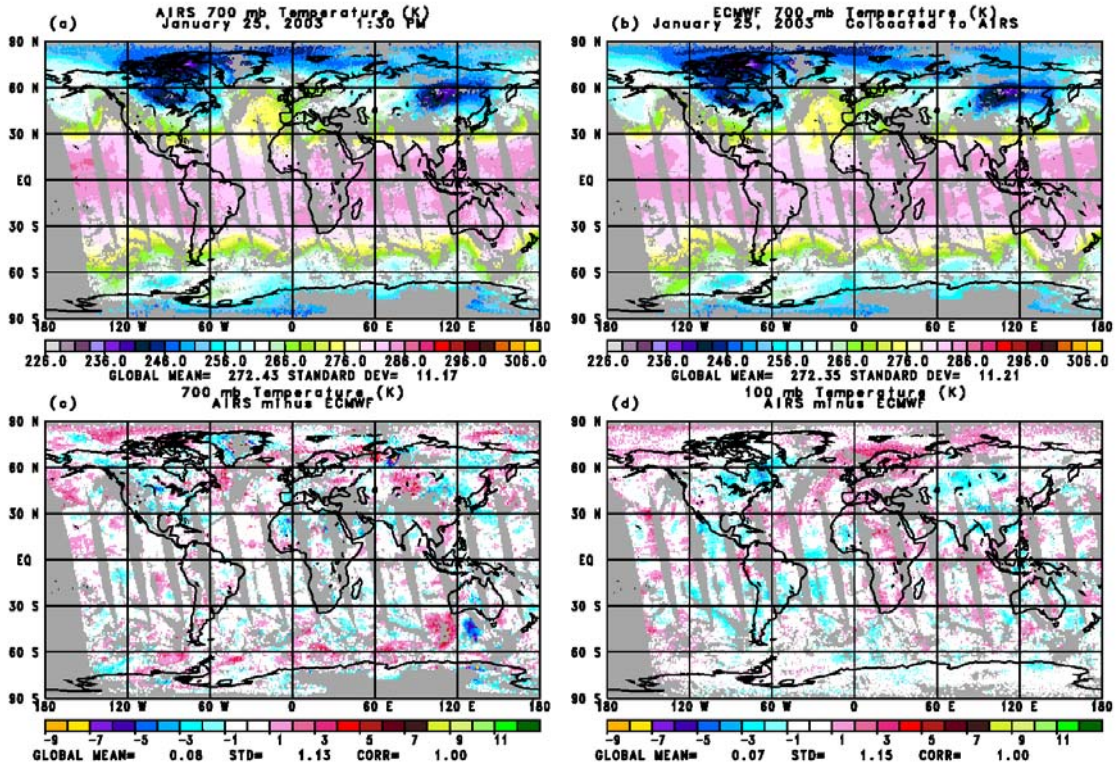

Figure 7

Results are presented for three sets of experiments in which data was assimilated for the period January 1 – January 31, 2003. Five day forecasts were run every two days beginning January 6, 2003 and forecasts every 12 hours were verified against the NCEP analysis, which was taken as "truth". In the first experiment, called "control", all the data used operationally by NCEP was assimilated, but no AIRS data was assimilated. The operational data included all conventional data, TOVS and ATOVS radiances for NOAA-14, 15, and 16, cloud tracked winds, SSM/I total precipitable water and surface wind speed over ocean, QuikScat surface wind speed and direction, and SBUV ozone profiles. In the second and third experiments, called "clear AIRS" and "all AIRS", temperature profiles retrieved from AIRS soundings were assimilated in addition to the data included in the "control" experiment. "Clear ocean" included all accepted temperature retrievals derived from AIRS over ocean and sea ice in cases where the retrieved cloud fraction derived from AIRS was less than or equal to 2%, while the "all ocean" experiment assimilated accepted AIRS temperature soundings over ocean and sea ice for all retrieved cloud fractions.

Figure 8 shows anomaly correction coefficients of forecast sea level pressure verified against the NCEP analysis for both Northern Hemisphere extra-tropics and Southern Hemisphere extra-tropics for both the "control" and "all AIRS" experiments. In the Northern Hemisphere, addition of all AIRS soundings resulted in an improvement in average forecast skill of the order of 1 hour or less, but an improvement in average forecast skill in the Southern Hemisphere on the order of 6 hours results from assimilation of AIRS soundings. Assimilation of AIRS soundings under essentially clear conditions (not shown), resulted in somewhat poorer forecasts than using all AIRS soundings. It should be noted that the

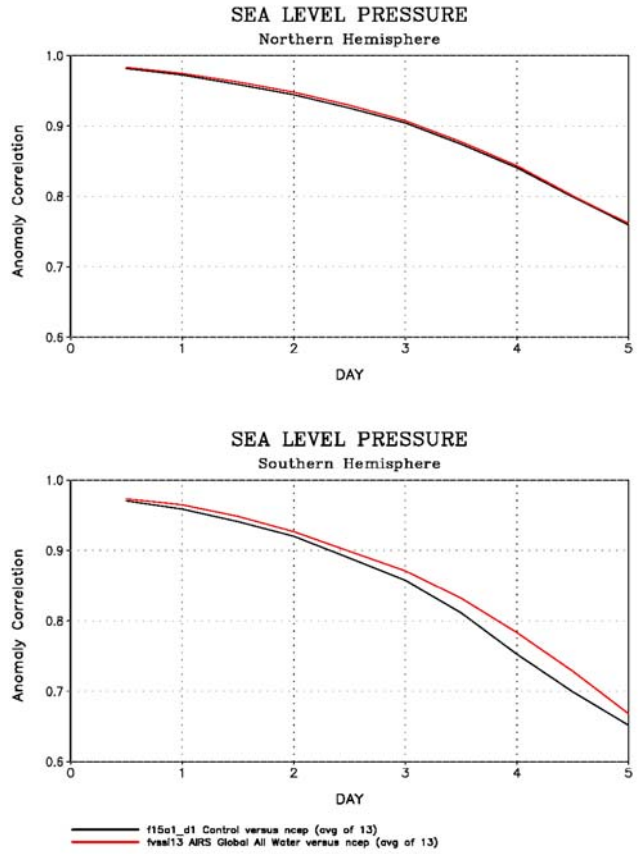

Figure 8

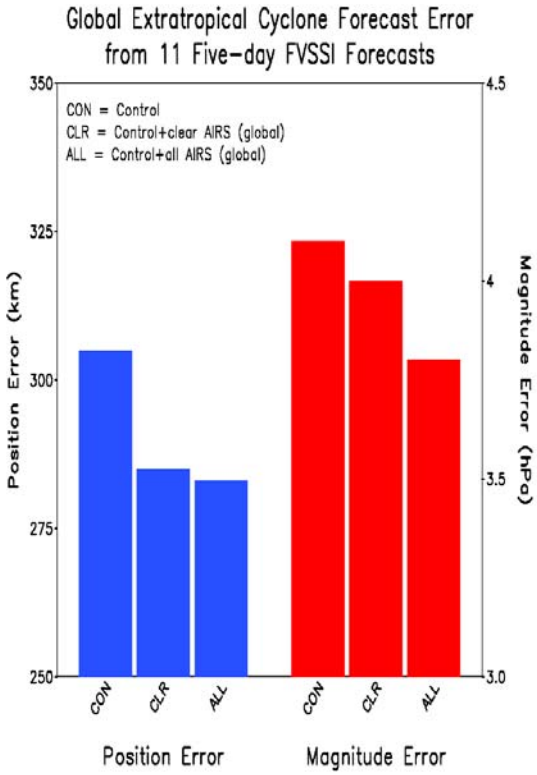

Figure 9

Aqua orbit (1:30 ascending) is almost identical to that of NOAA 16 carrying HIRS3, AMSU A and AMSU B, so AIRS/AMSU/HSB soundings are providing additional information to that contained in the AMSU A/AMSU B radiances on NOAA 16 in the same orbit.

Figure 9 shows the RMS position error (km) and magnitude error (hPa) for 5 day forecasts of extra tropical cyclones in the three experiments. It is apparent that addition of AIRS soundings improved RMS forecast skill for both the position and magnitude of extra-tropical cyclones globally, and addition of AIRS soundings in partially cloudy areas further improved forecast skill as compared to use of soundings only in essentially clear conditions.

Several thousand cyclones verifications are included in these statistics. Addition of AIRS data did not improve forecasted cyclone position and intensity for each cyclone. Some were improved substantially however. Figure 10 shows the impact of AIRS data on the 24 hour forecast of position and intensity of tropical storm Beni, which was centered roughly 4° east of New Caledonia on January 31, 2003 with a central pressure of 990 mb (see Figure 10d). The control forecast (Figure 10a) produced a relatively weak cyclone (1007 mb) displaced considerably to the northwest, while the 24 hour forecast using AIRS data (Figure 10b) was much more accurate in both position and intensity (995 mb). It is significant to note that our forecast using AIRS data was more accurate in both position and intensity than the NCEP operational forecast (Figure 10c) in this case, which, even though it used a higher resolution model and analysis system, did not have the benefit of AIRS data. The results shown indicate the potential of AIRS soundings to improve operational forecast skill. We are working with NCEP to arrange an experiment to add AIRS temperature soundings to an otherwise

equivalent run on the NCEP computing system to see the extent, if any, that operational forecast skill can be improved upon.

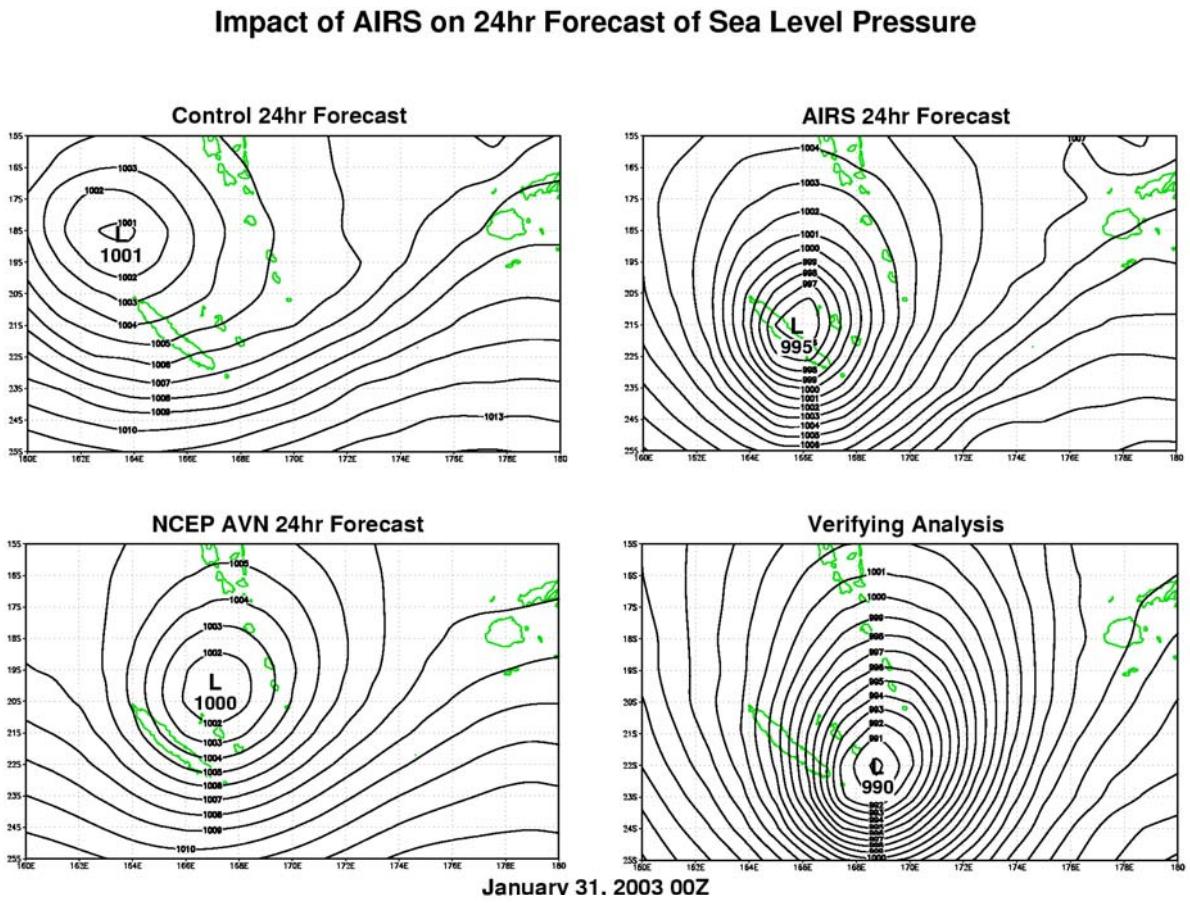

Figure 10

References

Pagano, T. S., H. H. Aumann, D. E. Hagan, and K. Overoye, February 2003. Prelaunch and in-flight radiometric calibration of the Atmospheric Infrared Sounder (AIRS). *IEEE Trans. Geosci. Remote Sensing*, **41**, 265-273.

Susskind, J., C. D. Barnet, and J. M. Blaisdell, February 2003. Retrieval of Atmospheric and Surface Parameters from AIRS/AMSU/HSB Data in the Presence of Clouds. *IEEE Trans. Geosci. Remote Sensing*, **41**, 390-409.

Rosenkranz, P. W., 2000. Retrieval of temperature and moisture profiles from AMSU-A and AMSU-B measurements. In *Proc. IGARSS*.

Goldberg, M. D., Y. Qu, L. M. McMillin, W. Wolff, L. Zhou, and M. Divakaria, February 2003. AIRS near-real-time products and algorithms in support of operational numerical weather prediction. *IEEE Trans. Geosci. Remote Sensing*, **41**, 379-389.

Lin, S.J., R. Atlas, and K. S. Yeh, January-February, 2004. Global weather prediction and high end computing at NASA. *Computing in Science and Engineering*, 29-35.

First global measurement of mid-tropospheric CO_2 from NOAA polar satellites : The tropical zone

A. Chédin, S. Serrar, N.A. Scott, C. Crevoisier, R. Armante

Laboratoire de Météorologie Dynamique, Institut Pierre-Simon Laplace, Ecole Polytechnique, 91128 Palaiseau, France

Abstract

Mid-tropospheric mean atmospheric CO_2 concentration is retrieved from the observations of the NOAA series of polar meteorological satellites, using a non-linear regression inference scheme. For the four years of the present analysis (July 1987 – June 1991), monthly means of the CO_2 concentration retrieved over the tropics (20N-20S) from NOAA-10 show very good agreement with what is presently known. Not only the phase of the seasonal variations (location of the peaks) but also their amplitude and their latitudinal evolution match quite well recent *in situ* observations made by properly equipped commercial airliners measuring in an altitude range similar to the one favoured by the satellite observations. Moreover, the annual trend inferred corresponds to the known increase in the concentration of CO_2 as a result of human activities. Also, the impact of El Nino Southern Oscillation (ENSO) events is clearly seen and confirms analyses of *in situ* or aircraft observations and of model simulations. Forty-eight maps of monthly mean mid-tropospheric CO_2 concentration have been produced at a resolution of 15°x15°. A rough estimate of the method-induced standard deviation of these retrievals is of the order of 3.0 ppmv (less than 1%). The coming analysis of the almost 25 years of archive already accumulated by the NOAA platforms should contribute to better an understanding of the carbon cycle.

Introduction

Knowledge of present carbon sources and sinks, including their spatial distribution and their variability in time is essential for predicting future carbon dioxide atmospheric concentration levels. Because the atmosphere integrates over varying carbon surface sources and sinks, the distribution of CO_2 in the atmosphere and its time evolution can be used to quantify surface fluxes. However, this approach is currently limited by the sparse and uneven distribution of the global flask sampling programs. For example, regional carbon budgets are reconstructed from about 100 points. As a consequence, inferring surface sources and sinks from observed concentrations is still highly problematic (*Rayner et al.* 1999 ; *Schimel et al.* 2000).

Satellite measurements of the distribution of global atmospheric CO_2 would in principle fill this gap in scale (*Rayner and O'Brien* 2001). Measurements that densely sample the atmosphere, in time and in space, would provide a crucial constraint, allowing uncertainty in transport versus other information (on source and sink characteristics) to be separated and reduced.

Recent studies (*Chédin et al.* 2002a-c) have shown that atmospheric concentration variations (seasonal, annual) of major greenhouse gases (CO_2, N_2O, CO) may be retrieved from observations of

the National Oceanic and Atmospheric Administration (NOAA) polar meteorological satellite series, in addition to their main mission of measuring atmospheric temperature and moisture global fields. The method used for these studies was based on the analysis of the differences between the satellite observations and simulations from a radiative transfer model using collocated radiosonde data and fixed gas concentration as the prime input. Its main limit was its dependency upon collocations between satellite observations and radiosonde measurements because of their inability to measure all necessary information (surface temperatures, upper stratospheric temperatures, etc.) and the uneven and, by far, not global distribution of the radiosonde stations.

The method used here, a non-linear regression inverse model based on the Multi-Layer Perceptron (MLP), relies on the only satellite observations, in essence global. It is applied to the platform NOAA-10, providing seasonal cycles and trends for latitude bands of 5° and global monthly maps of mid-tropospheric mean CO_2 concentration, at the spatial resolution of 15° longitude by 15° latitude, for the period July 1987 to June 1991. It may easily be extended to the almost 25 years of archive already accumulated.

Data and method

Details on the data used and on the method are given in *Chédin et al.* (2003a). The approach described in this article was however modified here to prepare processing daytime observations. The modification consists in removing from the predictors of the non-linear regression the HIRS channel 18 measuring at 4.0 μm and potentially contaminated by solar radiation. Results presented here are limited to nighttime observations (around 7.30 pm local time) and to the tropical zone (20N-20S). It is worth pointing out that the tropical zone coincides with the region where the surface flask network is the least efficient and, also, with the region of strong convective vertical mixing which rapidly transmits surface carbon flux variations to that part of the troposphere observed by the satellite.

Results and comparisons with aircraft observations

Four years of NOAA-10 observations (from July 1987 to June 1991, included) have been processed and interpreted in terms of mid-tropospheric CO_2 concentration.

Results are shown either zonally, for latitude bands of 5°, for the purpose of comparison with existing aircraft observations, or globally, at the resolution of 15° latitude by 15° longitude, chosen in such a way that enough items are present in each grid box to give robust statistics. A grid box with less than 300 items, indicating an area where dense cloudiness dominates, is rejected (see *Chédin et al.* 2003a).

Global maps of mid-tropospheric CO_2 concentration

Forty-eight maps of monthly mean mid-tropospheric CO_2 concentration (gross average between 4.5-5.0 to 13 km), covering the period from July 1987 to June 1991, have been produced at the spatial resolution of 15°x15° (1°x1° moving average). The choice of this spatial resolution results from a compromise between two requirements of having a relatively dense spatial coverage (increasing the spatial resolution) and obtaining robust statistics (decreasing the spatial resolution). Figure 1 shows maps of CO_2 concentration for April and June 1988 and the corresponding number of items averaged. There is no evidence of a relationship between CO_2 inferred and the number of data averaged. April is the month where CO_2 shows maximum of variability and where CO_2, accumulated during northern

hemisphere winter, reaches tropical latitudes. One can notice a gradient west-east of CO_2 mean concentration in the northern tropical Pacific in April, and an area of relatively higher CO_2 amount south of India in June. Similar signatures are observed for the same months of the other years considered here. They are likely to be explained by transport mechanisms. Further investigations are necessary to elucidate factors influencing mid-tropspheric CO_2 variations (sources, sinks and transport).

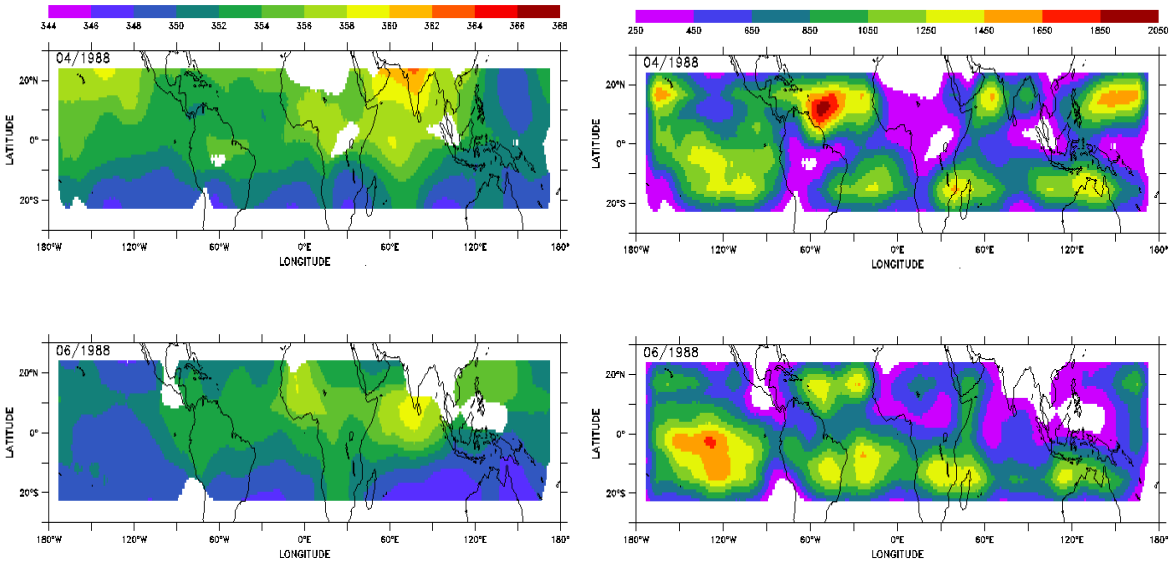

Figure 1 Left: CO_2 monthly mean concentration maps as retrieved from NOAA-10 for 04/88 at the top and 06/88 at the bottom, Right: The corresponding number of items averaged.

Figure 2 shows the time variation of inferred CO_2 mean standard deviation over the tropics. There is evidence of a seasonal variation with maxima in spring (values between 4 and 5 ppm) and minima in summer, early fall (about 3 ppm). These standard deviations may tentatively be seen as resulting from the combination of the standard deviation of the method (σ_M) itself and of the standard deviation of the natural variability (σ_V) of CO_2 (15°x15°, one month). Doing so, σ_M comes to about 3.0 ppmv (less than 1%) and σ_V comes to 1 ppmv in July-September and to less than 3 ppmv in February-April. Such numbers look reasonable. However, this result is more an appreciation of the internal consistency of the method than an estimation of its accuracy.

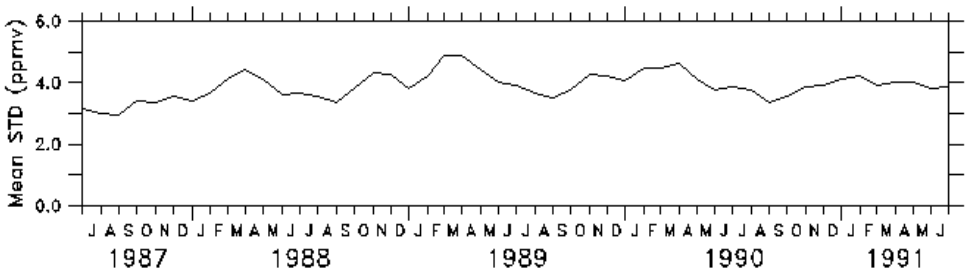

Figure 2: Time variation of mean standard deviation of the inferred CO_2 over the tropics

Seasonal cycle and trend (zonal means)

Our knowledge of the distribution of CO_2 in the mid to high troposphere is quite limited at present. However, two studies (*Matsueda et al.* 2002 ; *Nakazawa et al.* 1991) cover relatively long periods of time and relatively wide domains of latitude. *Matsueda et al.* (2002), hereafter referred to as "MII", report on *in situ* observations made twice a week from commercial airliners. These measurements go from April 1993 to April 1999 and were made within the altitude range 9-13 km and extend in latitude from 30N to 30S, between Japan and Australia. In 1984 and 1985, similar observations made between Tokyo and Anchorage, and between Tokyo and Sydney, were analysed by *Nakazawa et al.* (1991). Figure 8 of MII shows the mean observed seasonal cycle for 12 latitude bands of 5° each, between 30N and 30S. It may be directly compared to our Figure 3 which displays similar cycles, retrieved from NOAA-10 between 20N and 20S. The agreement is relatively good for what concerns both the amplitudes and the phases of the cycles: rapid decay of the amplitude from 20N to the Equator and delay of phase. Similarly, both sources of data show a more complex Southern Hemisphere seasonality, also pointed out by *Nakazawa et al.* (1991), with two concentration peaks: around June-July and November-December for the aircraft observations, and around May and November for the satellite retrievals. This one-month lag may be explained by the fact that the altitude ranges observed are different: from 9 to 13 km for *in situ* observations and from 4.5-5.0 to about 13 km for NOAA-10 (*Nakazawa et al,* 1991-1992). Figure 3 also shows peak-to-peak amplitudes of the average seasonal CO_2 cycles slightly larger than those shown on Fig. 8 of MII, in agreement with the above references.

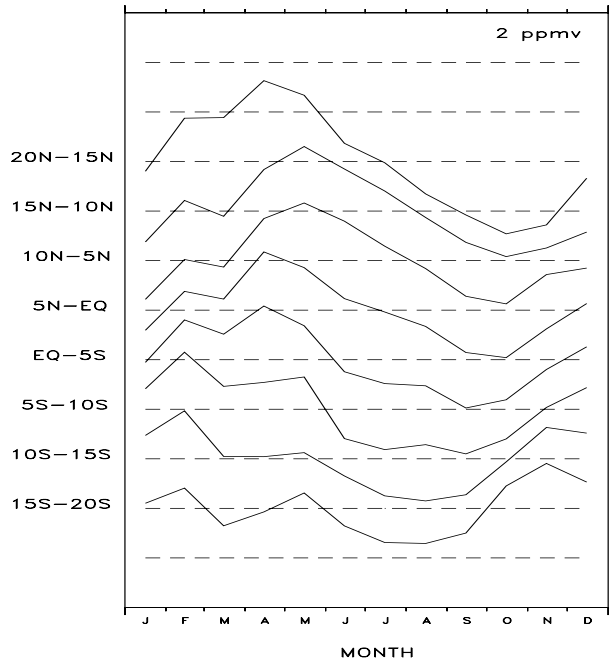

Figure 3: The mean seasonal cycle for 8 latitude bands between 20N and 20S as retrieved from NOAA-10 (July 1987-June 1991) ; mean altitude range covered ~4.5-5.0 to 13 km . Ordinate division length is 2 ppmv.

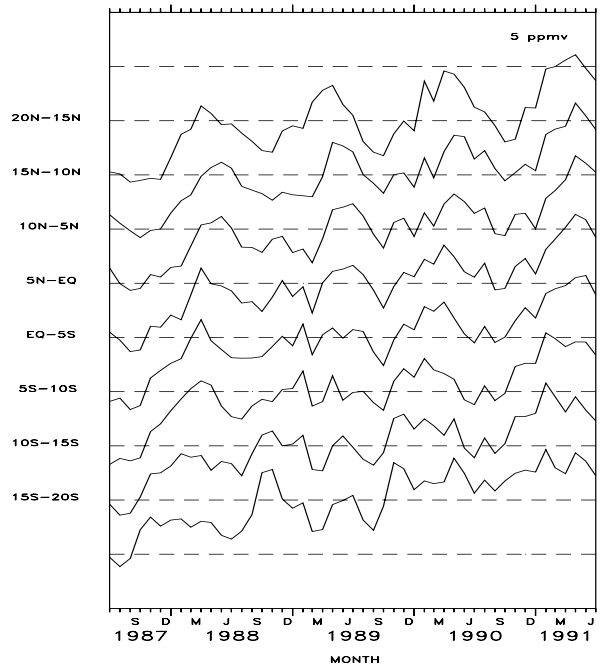

Figure 4: Time variation (monthly means) of the CO_2 concentration for 8 latitude bands between 20N and 20S as retrieved from NOAA-10 for the period July 1987 to June 1991. Ordinate division length is 5 ppmv.

Growth rates

Further analysis of the data of Figure 4 was carried out following a procedure similar to *Matsueda and Inoue* (1996) or to *Duglokencky et al.* (1994) (details are given in *Chédin et al.* (2003a)). Figure 5 summarizes the results of this analysis for the northern tropics (0N-20N; Figure 5a) and for the southern tropics (0S-20S; Figure 5b). The derivative of the long term trend (the dashed line) gives the growth rate.

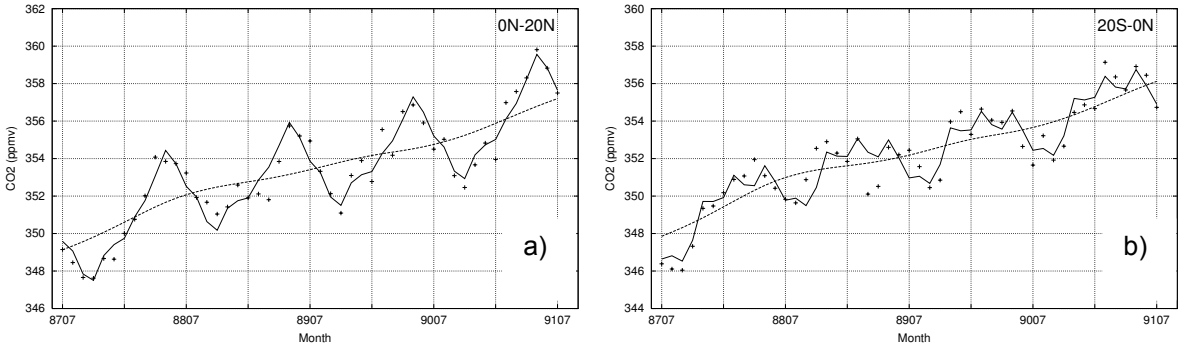

Figure 5: Time variations of CO_2 concentration for the northern tropics (0N-20N; left) and the southern tropics (0S-20S; right) . The crosses represent the individual (monthly mean) data. The dashed line represents the long term trend, and the solid line represents the sum of the trend and the four harmonics used for the fit

Figure 6a shows the mean growth rates for the northern (0-20N) and the southern (0-20S) tropics and emphasizes the previously observed patterns, and, at the same time, draws attention to the relationship between the rate of rise of CO_2 and the ENSO (*Bacastow* 1976 ; *Keeling et al.* 1995 ; *Feely et al.* 1999 ; *Jones et al.* 2001). Figure 6b shows the southern oscillation index (SOI) monthly means from NOAA/ National Centers for Environmental Prediction (NCEP) website (*www.cpc.ncep.noaa.gov/products/*), for the time period considered. The dashed line is the 7-month running mean as in MII. The correlation between the CO_2 growth rate and the SOI is obvious and very similar to the correlation observed by MII, although the time period is different. La Nina events clearly correspond to a decrease of the growth rate and the contrary for El Nino events. Figure 6c, similar to Figure 5 of MII, shows the relationship between the CO_2 monthly mean growth rates and the SOI, the solid line being for the northern tropics and the dashed line for the southern tropics. Each cross represents one month and the time sequence starts from the upper left crosses, the first month being here January 1988. The relationship appears most significant when the SOI values are not too close to zero, which is not surprising, and appears mostly noisy when it is the case. The upper part of the sequence corresponds to the decrease of the growth rate, itself associated with the decline of the 1986-1987 El Nino and the development of the 1988-1989 La Nina, and the lower part to the overall increase of the growth rate, consequence of the decline of the La Nina event and of the arriving El Nino of 1991. The relationship observed by MII presents numerous similarities (see their Figure 5), with almost the same slope. The differences, in particular the bi-modal behavior seen on Figure 6c, contrary to Fig. 5 of MII, may probably be attributed to the differences between the two time periods studied. Altogether, the conclusions obtained here almost completely agree with those of MII.

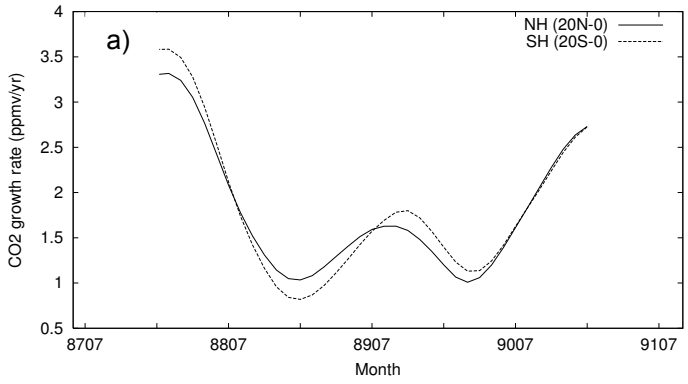

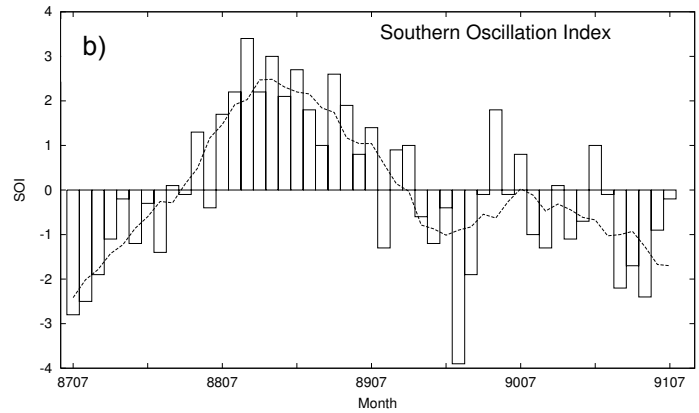

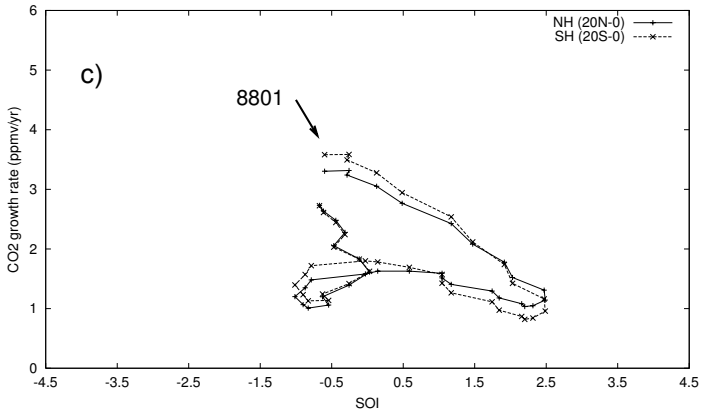

Figure 6 : (a) : time variation of the CO_2 growth rate for the northern tropics (0N-20N), solid line, and for the southern tropics (0S-20S), dashed line, as retrieved from NOAA-10 ; (b) : time variation of the Southern Oscillation Index (SOI) and its 7-month running mean, dashed line ; (c) : relationship between the CO_2 growth rate and the SOI for the northern tropics, plusses, and for the southern tropics, crosses.

Conclusion and perspectives

Recent studies (*Chédin et al.* 2002a-c) have shown that signatures of the atmospheric concentration variations of major greenhouse gases and, in particular, CO_2, may be detected from the observations made by the NOAA polar meteorological satellites, in addition to the main signatures of atmospheric temperature, moisture, surface or cloud characteristics. The CO_2 signatures, which essentially come from the mid to high troposphere, are weak and not easy to interpret in terms of global fields of CO_2 concentration. The method developed in this article, a non linear regression inference scheme based on the Multi-Layer Perceptron (MLP), has proven its ability to retrieve important features of the distribution of CO_2 and of its time evolution. The period covered goes from July 1987 to June 1991 and the observations are from NOAA-10. The area analyzed has been, in a first step, restricted to the tropics (20N-20S) where the lower variability of the atmospheric temperature helps de-correlating its variations from those of CO_2. In almost complete agreement with accurate, mid to high tropospheric *in situ* measurements made by properly equipped commercial aircrafts over a long period of time (see MII), satellite retrievals are able to:

- describe the CO_2 seasonal cycle and its evolution in latitude ;

- describe the time variation of the CO_2 concentration as a function of latitude ;

- quantify the mean rate of rise of CO_2 over the 4-year period (a value of 1.75 ppmv/year is found) and describe the time evolution of the CO_2 growth rate as a function of latitude ;

- confirm the strong correlation between the growth rate and the Southern Oscillation Index (SOI) during a time period marked by the declining 1986-1987 El Nino, the strong 1988-1989 La Nina, and the coming 1991 El Nino ;

- produce monthly mean global maps of mid-tropospheric CO_2 concentration at a resolution of 15° by 15°. Within each such grid-boxes, the standard deviation of the sample of CO_2 retrievals, after having

deduced an estimate of the part attributed to the natural variability of CO_2 over one month, is of the order of 3.0 ppmv, less than 1%.

The main limit of the method developed here is the dependence of the retrievals on the capability of the forward radiative transfer model, used to create the MLP training data set, to accurately match the satellite observations. Any such model has biases that are air mass, and possibly latitude, dependent. Removal of these biases goes through the use of large sets of collocated radiosonde (to feed the forward model) and satellite observations. Problems arise when latitude bands are not enough covered by such "matchups". To refine our knowledge of the forward radiative transfer model systematic biases, great efforts are presently being made to augment the number of collocations using the European Center for Medium Range Weather Forecasting (ECMWF) ERA-40 archive.

The planned analysis of the almost 25 years of archive already accumulated by the NOAA polar platforms should certainly contribute to a better understanding of the carbon cycle through the interpretation of these retrievals in terms of surface carbon fluxes via a carbon flux inversion model, coupling *in situ* and space observations.

These results also strengthen our hope to greatly improve our knowledge of the global distribution of a variety of radiatively active gases with the coming second generation vertical sounders like AIRS or IASI, both characterized by a much higher spectral resolution allowing a more sophisticated retrieval scheme than the one developed here for the present TOVS channels (*Chédin et al*. 2003b) and a still better handling of the cloud detection. The first simulations obtained with a similar retrieval method presented in this paper are extremely encouraging (*Crevoisier et al.*, this issue).

References

Bacastow, R. B., Modulation of atmospheric carbon dioxide by the Southern Oscillation, *Nature*, 261, 116-118, 1976.

Chédin, A., S. Serrar, R. Armante, N. A. Scott, and A. Hollingsworth, Signatures of annual and seasonal variations of CO_2 and other greenhouse gases from NOAA/TOVS observations and model simulations, *J. Climate*, 15, 95-116, 2002a.

Chédin, A., S. Serrar, A. Hollingsworth, R. Armante, and N.A. Scott, Detecting annual and seasonal variations of CO_2, CO and N_2O from a multi-year collocated satellite-radiosonde data-set using the new Rapid Radiance Reconstruction Network (3R-N) model, *In Press in J. Quant. Spectrosc. Radiat. Transfer*, 2002b.

Chédin, A., A. Hollingsworth, N.A. Scott, S. Serrar, C. Crevoisier, and R. Armante, Annual and seasonal variations of atmospheric CO_2, N_2O and CO concentrations retrieved from NOAA/TOVS satellite observations, *Geophys. Res. Letters*, 29, 110-1/4, 2002c.

Chédin, A., S. Serrar, N. A. Scott, C. Crevoisier, R. Armante, First global measurement of midtropospheric CO_2 from NOAA polar satellites : Tropical zone, *J. Geophys. Res.*, 108(D18), 4581, doi:10.1029/2003JD003439, 2003a.

Chédin, A., R. Saunders, A. Hollingsworth, N. A .Scott, M. Matricardi, J. Etcheto, C. Clerbaux, R. Armante, and C. Crevoisier, The feasibility of monitoring CO_2 from high-resolution sounders, *J. Geophys. Res.,* 108(D2), 4064, doi:10.1029/2001JD001443,2003b.

Duglokencky, E. J., K. A. Masarie, P. M. Lang, P. P. Tans, L. P. Steel, and E. G. Nisbet, A dramatic decrease in the growth of atmospheric methane in the northern hemisphere during 1992, *Geophys. Res. Letters,* 21, 45-48, 1994.

Feely R. A. ,R. Wanninkhof, T. Takahashi, and P. Tans, Influence of El Nino on the equatorial Pacific contribution to atmospheric CO_2 accumulation, *Nature*, 398, 597-601, 1999.

GLOBALVIEW-CO_2, Cooperative Atmospheric Data Integration Project- Carbon dioxide. CD-ROM, NOAA/CMDL, Boulder, Colorado. [Also available on Internet via anonymous FTP to ftp.cmdl.noaa.gov, Path: ccg/co2/GLOBALVIEW], 1999.

Jones, C .D., M. Collins, P. M. Cox, and S. A. Spall, The carbon cycle response to ENSO : a coupled climate-carbon cycle model study, *J. Climate*, 14, 4113-4129, 2001.

Keeling, C. D., T. P. Whorf, M. Wahlen, and J. van der Plicht, Interannual extremes in the rate of rise of atmospheric carbon dioxide since 1980, *Nature*, 375, 666-670, 1995.

Matsueda, H., and H. Inoue, Measurements of atmospheric CO_2 and CH_4 using a commercial airliner from 1993 to 1994, *Atm. Environ*., 30,1647-1655, 1996.

Matsueda, H., H. Y. Inoue, and M. Ishii, Aircraft observation of carbon dioxide at 8-13 km altitude over the western Pacific from 1993 to 1999, *Tellus*, 54B, 1-21,2002.

Nakazawa, T., K. Miyashita, S. Aoki, and M. Tanaka, Temporal and spatial variations of upper tropospheric and lower stratospheric carbon dioxide, *Tellus*, 43B, 106-117, 1991.

Nakawaza, T., S. Murayama, K. Miyashita, S. Aoki, and M. Tanaka, Longitudinally different variations of lower tropospheric carbon dioxide concentrations over the North Pacific ocean, *Tellus*, 44B, 161-172,1992.

Rayner, P. J., I. G. Enting, R. J. Francey, and R. Langenfels, Reconstructing the recent carbon cycle from atmospheric CO_2, d13C and O2/N2 observations, *Tellus*, B51, 213-232, 1999.

Rayner, P. J., and D. M. O'Brien, The utility of remotely sensed CO_2 concentration data in surface source inversions, *Geophys. Res. Lett., 28, 175-178, 2001*.

Schimel, D. S., J. Mellilo, H. Tian, and A. D. McGuire, Contribution of increasing CO_2 and climate to carbon storage by ecosystems in the United States, *Science*, 287, 2004-2006, 2000.

Mid-tropospheric CO_2 retrieval in the tropical zone from AIRS observations

Cyril Crevoisier, Alain Chédin, Sylvain Heilliette, Noëlle A. Scott, Soumia Serrar and Raymond Armante

Laboratoire de Météorologie Dynamique / C.N.R.S. / I.P.S.L., Ecole Polytechnique, Palaiseau, France

Abstract

The new 2378 channel high spectral resolution NASA/Aqua/Atmospheric Infrared Sounder (AIRS) launched in May 2002 is used to retrieve mean concentration of atmospheric carbon dioxide (CO_2). A reduced set of AIRS channels, presenting a high sensitivity to variations of the atmospheric CO_2 and reduced sensitivities to variations of other atmospheric components, and well covering the mid-troposphere (from 700 hPa to the tropopause), is first selected using the Optimum Sensitivity Profile (OSP) method. A cloud elimination procedure based on AIRS and Atmospheric Microwave Sounding Unit (AMSU) observations is then performed to detect clear fields of view. The resulting AIRS and AMSU measurements, the latter being not sensitive to CO_2 variations, are used in a neural network inference procedure. This non-linear regression scheme has already proven its efficiency in the retrieval of mid-tropospheric CO_2 from NOAA polar satellites. The first results obtained with AIRS give hope to improve the accuracy of the retrieval. Maps of monthly mean mid-tropospheric CO_2 concentration are obtained for a few months in the tropics [20S;20N]. The retrievals show good agreements with aircraft observations.

Introduction

Progress in both basic earth-system science and in managing the carbon cycle to mitigate climate change requires robust and verifiable understanding of the current behaviour of the system (Schimel et al. 1995, IPCC, 1998). Knowledge of today's carbon sources and sinks, including their spatial distribution and their variability in time, is essential for predicting the future carbon dioxide (CO_2) atmospheric concentration levels. The atmosphere being a superb integrator of spatially and temporally varying surface fluxes (Tans et al. 1990), the distribution of CO_2 atmospheric concentration and its evolution in time and space can be used to quantify surface fluxes. However, this approach is currently limited by the sparse and uneven distribution of the global flask sampling programs. Satellite measurements of the distribution of global atmospheric CO_2 concentration would in principle fill this gap in scale (Rayner and O'Brien 2001). Densely sampling the atmosphere, in time and space, they would provide a crucial constraint on the models.

The feasibility of retrieving CO_2 and other trace-gas concentrations from space has been proven with the National Oceanic and Atmospheric Administration (NOAA) Television Infrared Observation Satellite (TIROS-N) Operational Vertical Sounder (TOVS) radiometers (Chédin et al. 2002, 2003ab). For the first time, 4 years of monthly mean CO_2 concentration has been retrieved from

TOVS observations over the tropics [20S;20N] for the period 1987-1991. A rough estimate of the method-induced standard deviation of these retrievals is of the order of 3 ppmv (0.85 % of the mean CO_2 concentration).

The new high-spectral-resolution Atmospheric Infrared Sounder (AIRS) launched onboard the NASA/Aqua platform in May 2002 is expected to improve the accuracy of trace gas retrievals and will allow to make comparison with TOVS observations in terms of space and time variability of CO_2 atmospheric concentration which potential benefits for global carbon research are invaluable.

Data description

AIRS measures 2378 frequencies at high spectral resolution and covers most of the infrared spectrum. Also flying onboard Aqua, the Advanced Microwave Sounding Unit (AMSU-A) measures 15 microwave frequencies. Since April 2003, LMD downloads AIRS and AMSU data from NESDIS. These data are the restricted set of 324 AIRS channels, the 15 AMSU-A channels, for the 9 AIRS Fields Of View (FOVs) and for every other AMSU FOVs.

AIRS channels sensitive to CO_2 are located into two spectral bands, near 15 µm and 4.3 µm. To avoid huge computation time, and to eliminate the signals that could interfere with CO_2 signal, a set of 43 AIRS channels presenting the best properties to retrieve CO_2 has been selected with the Optimum Sensitivity Profile (OSP) method (Crevoisier et al. 2003). These channels present a high sensitivity to CO_2 variations and low sensitivity to other atmospheric components such as water vapour, ozone (O_3), nitrous oxide (N_2O), carbon monoxide (CO), and surface parameters. They are located in both CO_2 bands and well cover the vertical, with the exception of the tropopause and the boundary layer, as can be seen on Figure 1 which shows the CO_2 Jacobians (partial derivative of the channel brightness temperature to a layer CO_2 concentration) for the 43 OSP channels, as computed by the 4A forward model in its latest version (Scott et al., in preparation; http://ara.lmd.polytechnique.fr/). As a result, AIRS channels are sensitive to CO_2 variations in the range 700 to 100 hPa.

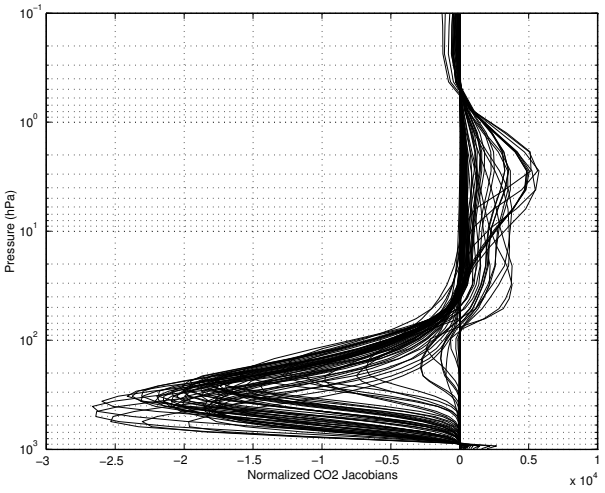

Fig. 1: CO_2 Jacobians of the 43 OSP channels.

Only clear-sky situations are used to retrieve CO_2. Not-clear situations (clouds, aerosols) are detected by numerous tests based on thresholds. Basically, three kinds of tests are used. They are detailed in Table 1. All together, there are 15 differences between brightness temperatures (BT) : (1) 8 differences between BT of AIRS and AMSU channels, the latter being not sensitive to clouds; (2) 5 differences between BT of AIRS channels and their "clear-sky" prediction from AMSU channels 5, 6 and 8 through regressions. The regression coefficients are computed from the TIGR atmospheric database using least-squares. The statistical results show no mean and a standard deviation of about 0.5 K; (3) 2 differences between window channels. The threshold values were obtained from 5 days in February 2003. As a result, in the tropics, over sea, during night, about 82% of the situations are found not-clear.

$\| T_B(213) - T_B(A6) \| < 2.25$ K	$\| T_B(308) - T_B^{reg}(308) \| < 2.5$ K
$\| T_B(1947) - T_B(A6) \| < 2.25$ K	$\| T_B(309) - T_B^{reg}(309) \| < 2.5$ K
$\| T_B(2106) - T_B(A6) \| < 2.25$ K	$\| T_B(2106) - T_B^{reg}(2106) \| < 2.5$ K
$\| T_B(2110) - T_B(A6) \| < 2.25$ K	$\| T_B(2110) - T_B^{reg}(2110) \| < 2.5$ K
$\| T_B(151) - T_B(A8) \| < 2.75$ K	$\| T_B(2112) - T_B^{reg}(2112) \| < 2.5$ K
$\| T_B(2106) - T_B(A8) \| < 2.75$ K	
$\| T_B(2110) - T_B(A5) \| < 2.75$ K	$\| T_B(787) - T_B(2226) \| < 2.75$ K
$\| T_B(2112) - T_B(A5) \| < 2.75$ K	$\| T_B(787) - T_B(2333) \| < 2.75$ K

Table 1: AIRS clear-sky tests. $T_B(213) - T_B(A6)$ stands for AIRS channel 213 brightness temperature minus AMSU channel 6 brightness temperature. $T_B^{reg}(308)$ stands for the prediction from AMSU channels 5, 6 and 8 through regressions of AIRS channel 308 brightness temperature.

As validation, a comparison with the cloud fields retrieved by the Moderate Resolution Imaging Spectroradiometer (MODIS) also flying onboard Aqua has been performed for the month of April 2003 (products available on http://modis-atmos.gsfc.nasa.gov/). A comparison between AIRS clear-sky test results and MODIS cloud-top-pressure product is shown on Figure 2 for April 27th, 2003. According to the MODIS cloud top pressures, all the clouds above 800 hPa are detected. Remaining low clouds are not detected. However, this does not affect the retrieval of CO_2 concentration that is performed above 700 hPa.

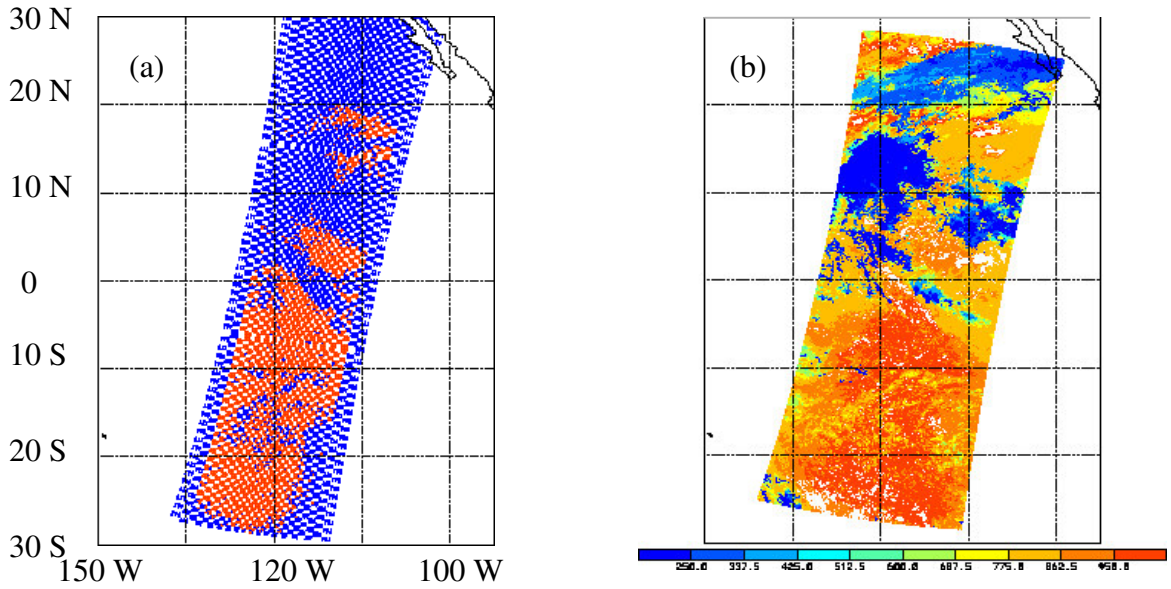

Fig. 2: For 27 April 2003, [30N;30S] and [150W;105W], (a) clear (red) and unclear (blue) situations as given by AIRS clear-sky test ; (b) corresponding MODIS cloud-top-pressure.

A neural network approach

The signal induced on AIRS brightness temperatures by the variations of CO_2 concentration remains weak (a few tenth of Kelvin). Therefore, as done in Chédin et al. (2003), a method based on neural network using Multilayer Perceptron (MLP) has been preferred to a more classical one and is now being described. A detailed description of the method, already used for TOVS observations, can be found in Chédin et al. (2003).

The MLP network (Rumelhart et al. 1986) is a non-linear mapping model composed of parallel processors called "neurons". These processors are organized in distinct layers. The first layer groups the inputs of the network (the predictors). The intermediate layers are called the "hidden layers". The last layer groups the outputs of the network (the predictands). Each neuron is connected

to the neurons of the previous and following layers, a weight being given to this connection. These weights contain the whole information of the network. To optimise the weights, a minimization of a positive-define cost function measuring the mismatch between neural outputs and desired outputs is performed for a set of representative patterns, the so-called "learning set", for which inputs and outputs are known. Use is made of the Error Back-Propagation algorithm (Rumelhart et al. 1986), with stochastic steepest descent. The learning step is made sample by sample, chosen iteratively and stochastically in the learning set.

For this study, the tropical atmospheric situations of the Thermodynamic Initial Guess Retrieval (TIGR) database (Chédin et al. 1985, Chevallier et al. 1998) are used as the training set. Each situation is described by its profiles of temperature, water vapour and ozone. The trace gases are assumed constant along the vertical. CO_2 concentration varies in the range 352-392 ppmv, with a mean value at 372 ppmv. N_2O and CO concentrations are assumed to be equal to 324 ppbv and 100 ppbv respectively. These are the predicted concentration values for the year 2003 (IPCC 2001). Clear-sky AIRS brightness temperatures, transmittances and Jacobians (partial derivative of the channel brightness temperature to a layer physical variable such as temperature, gas concentration for H_2O, O_3, CO_2, N_2O, CO, surface temperature and emissivity) are then computed for all the profiles using the fast line-by-line 4A model. AMSU brightness temperatures are computed using the MW-STRANSAC model. The computation is performed for 15 scan angles between 0° (nadir) and 57° for, so far, a single value of surface pressure (1013 hPa). The present study is limited to the tropics, because of the reduced temperature variability in this region, and to sea cases (single surface pressure). The simultaneous use of the infrared measurements, sensitive to both temperature and CO_2 variations, and the microwave measurements, sensitive only to temperature variations, allows separating the two effects.

According to the above considerations, the chosen neural architecture is the following. The input layer is composed of: (1) 15 AIRS brightness temperatures of tropospheric channels chosen among the OSP selection (173, 175, 180, 185, 193, 213, 218, 250, 1946, 1947, 1948, 2106, 2107, 2108, 2109), (2) 5 AMSU-A brightness temperatures of channels 6, 8, 9, 10 and 11, and (3) 4 differences between AIRS and AMSU brightness temperatures. All together, there are 24 predictors. The output layer of the network is composed of: (1) the difference between the true (associated with inputs) value of CO_2 concentration and the reference one (372 ppmv), and (2) 15 differences between the "true" AIRS brightness temperatures (associated to the true CO_2 concentration value) and the "reference" one (associated to the reference CO_2 concentration value). All together, there are 16 predictands. Our past experience and several trials have led us to chose 80 neurons for the first hidden layer and 50 for the second one.

To take into account the instrument noise, a Gaussian noise defined by the equivalent noise temperature computed at the temperature of each channel is added to the input brightness temperatures at each step of the learning phase.

A total of 10 MLPs have been trained for a single surface pressure (1013 hPa) and 10 scan angles (from nadir to 40° to avoid the edges of the orbits).

The MLPs are trained with simulated data. Therefore, before presenting observations to the network, the eventual brightness temperatures systematic biases between simulations and observations must be taken into account and removed. In the absence of enough radiosonde measurements, this is done by comparing satellite observations with simulations based on our forward model and European Centre for Medium-Range Weather Forecast (ECMWF) analyses. For each channel, the bias is obtained by averaging on the whole period and the whole tropics, the differences between clear-sky AIRS observed brightness temperatures and the brightness temperatures computed from the nearest

(time and space collocation) ECMWF analyses. The biases show no strong latitudinal variations, nor significant time variations.

Results and Discussion

Retrieval of CO_2 mid-tropospheric concentration has been performed for seven months of AIRS observations from April to October 2003, in the tropics [20S;20N], over sea, at night. Daytime observations are not considered to avoid possible contamination by solar radiation: use is made of the AIRS observations at 1:30 am local time. The tropical region is of first interest for carbon study as the flask network is less efficient in this part of the globe. Moreover, the strong convective vertical mixing existing in the tropics transmits surface carbon flux variations to that part of atmosphere seen by AIRS.

Two maps of monthly mean retrieved mid-tropospheric CO_2 concentration are shown on Figure 3 at a resolution of 15° × 15° (0.75° × 0.75° moving average) for the months of April and September 2003. This resolution was chosen to combine a relatively dense spatial coverage with robust statistics. Boxes having not enough situations, because of the removing of not-clear situations, are not considered (blank areas on Figure 3). They mostly follow the regions of deep convection. The resulting number of situations per month and per grid-box is about 2000 in regions where clear-sky is preponderant but can reach 500 in more cloudy areas.

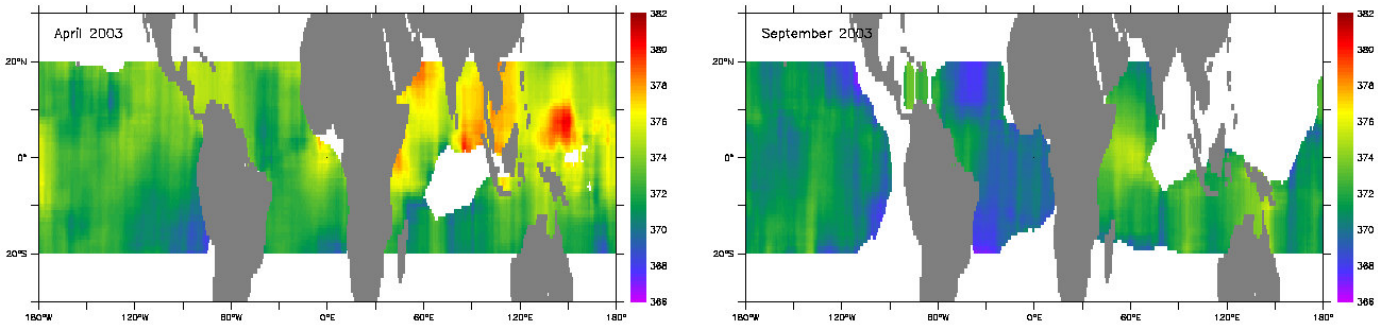

Fig. 3: Monthly mid-tropospheric CO_2 concentration as retrieved from AIRS observations in the tropics for April (left) and September (right) 2003 at a resolution of 15°×15°.

The decrease of CO_2 concentration from April (maximum) to September (minimum), especially in the northern hemisphere, is well seen. For the seven months analysed, the obtained variability of CO_2 concentration matches the known behaviour of the gas. The maximum of variability is found in Spring (April and May). On the contrary, autumnal months (September, October) show a relatively low variability of CO_2. The high concentration found in Asia starts to disappear at the beginning of summer with the increase of photosynthesis activities of the northern biomass. The latitudinal gradient found in April is 6 ppmv from southern to northern tropics and goes down to -1.5 ppmv in September. These values are coherent with several studies made on latitudinal variation of CO_2 (Machida et al. 2003, Vay et al. 1999). From July to September, a maximum of CO_2 concentration is found east of Africa in the equatorial region. This strong signature, already found with TOVS observations in the years 1987-1991, might be due to pollution in Asia going down to this region. Such result is of great importance to validate carbon transport models.

A first way to estimate the dispersion of the retrievals goes through the study of the induced standard deviation (std) of each monthly 15° × 15° box (Chédin et al. 2003). A globally dispersion around 3 ppmv (0.8 % of the mean CO_2 concentration) is observed, the maximum std being found in

the months of April-May (3.2 ppmv), when the natural variability of CO_2 is high, and the minimum std being found in the months of July-September (2.7 ppmv), when the natural variability of CO_2 is low. The observed std may be seen as the combination of the std of the method (σ_M) and of the std of the natural variability (σ_V). Doing so, σ_M comes to 2.5 ppmv (0.8 % of the mean CO_2 concentration) and σ_V comes to 1 ppmv for April and to 2.1 ppmv for July-September. These values look reasonable as the retrievals are only performed over sea and therefore do not take into account the variability of CO_2 over land.

Our knowledge of CO_2 distribution in the middle and high troposphere is reduced, most of the measurements having been made by flasks at the surface. Fortunately, in situ observations made by commercial airliners from April 1993 to March 2003 and partly analysed in Matsueda et al. (2002) have been collected by the World Data Centre for Greenhouse Gases (WDCGG) as part of the Global Atmosphere Watch (GAW) programme. These observations cover the altitude range 9-13 km, between Japan and Australia. The monthly mean CO_2 variations obtained in the northern [0;20N] and southern [20S;0] tropics are shown on Figure 4 in black. The seasonal cycle is clearly seen in the northern tropics whereas the southern hemisphere variation is more complex.

Monthly mean of CO_2 concentration as retrieved from AIRS observations for the whole tropics is shown on the same figure for the period April-October 2003 (red line). The shift between the two plots may be explained by the different geographical regions considered (the regions covered by aircraft observations can present high concentrations as clearly seen on Figure 3, giving a CO_2 signal higher than the one obtained for the whole tropics), and by the bias removal procedure described in Section 2 that is not optimal. Efforts are made to improve the results by using radiosonde measurements instead of analyses for the determination of the empirical corrections.

Apart this difference in the mean value, the AIRS retrieved variation of CO_2 agrees with the aircraft measurements: in the northern tropics, a maximum is found in April, a minimum in September, with a peak-to-peak variations of 3.5 ppmv; in the southern tropics, the signal is more complex but can be directly compared to the one observed by aircrafts in 2002.

Also, the latitudinal variation of the mean AIRS retrieved seasonal cycle as seen in 8 latitude bands of 5° each from 20°N to 20°S shows once more a very good agreement with aircraft observations.

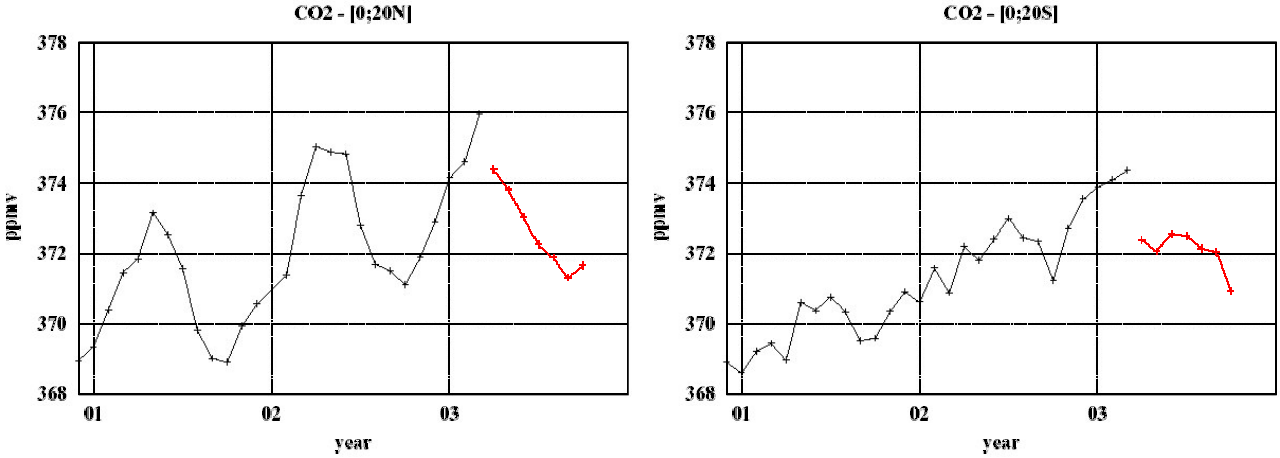

Fig. 4: Monthly mean of CO_2 concentration as retrieved in the northern (left) and southern (right) tropics from AIRS observations (from April to October 2003, in red) and as observed by aircraft (from January 2001 to March 2003, in black).

Conclusion

Mid-tropospheric CO_2 concentration has been retrieved in the tropics, over sea, at night from AIRS observations. The extension of the retrieval to land and daytime cases will allow us to study the effect of diurnal cycle. A comparison with carbon flux inversion models is in progress in cooperation with the Laboratoire des Sciences du Climat et de l'Environnement, Saclay, France, and the Max-Planck Institute for Biogeochemistry, Jena, Germany within the frame of the European COCO project. The first results have shown the extraordinary potential of space observations to better understand the behaviour of CO_2 in the atmosphere.

Acknowledgments

We are very happy to thank Walter Wolf for his constant help while providing us with AIRS data. Calculations were performed at IDRIS, the computer centre of CNRS. This work was supported by the European COCO project.

References

Chédin, A., N. A. Scott, C. Wahiche, and P. Moulinier 1985. The improved initialisation inversion method: A high resolution physical method for temperature retrievals from satellite of the TIROS-N series*, J. Climate Appl. Meteor.,* **24**, 128-143.

Chédin A., A. Hollingsworth., N. A. Scott, S. Serrar, C. Crevoisier, and R. Armante 2002. Annual and seasonal variations of atmospheric CO_2, N_2O and CO concentration retrieved from NOAA/TOVS satellite observations, *Geophys. Res. Letters,* **29***, no. 8*, 110-114.

Chédin A., R. Saunders, A. Hollingsworth, N. A. Scott , M. Matricardi, J. Etcheto, C. Clerbaux, R. Armante, and C. Crevoisier, 2003a. The feasibility of monitoring CO_2 from high resolution infrared sounders*, J. Geophys. Res.,* **108**, 4064.

Chédin A., S. Serrar, N. A. Scott, C. Crevoisier and, R. Armante, 2003b. First global measurement of mid-tropospheric CO_2 from NOAA polar satellites : Tropical zone, *J. Geophys. Res.,* **108***,* **D18**, 4581.

Chevallier, F., F. Chéruy, N. A. Scott, and A. Chédin, 1998. A neural network approach for a fast and accurate computation of a longwave radiative budget, *J. Appl. Meteorol.,* **37**, 1385-1397.

Crevoisier C., A. Chédin, and N. A. Scott, 2003. AIRS channel selection for CO_2 and other trace-gas retrievals, *Q. J .Roy. Meteor. Soc,* **129**, 2719-2740.

Intergovernmental Panel on Climate Change (IPCC), Climate Change 1995: *Contribution of Working Group I to the second Assessment Report of the Intergovernmental Panel on Climate Change*, 572 pp., Cambridge University Press, New York.

Machida, T., K. Kita, Y. Kondo, D. Blake, S. Kawakami; G. Inoue, and T. Ogawa, 2003. Vertical and meridional distributions of the atmospheric CO_2 mixing ratio between northern midlatitudes and southern subtropics*, J. Geophys. Res.,* **108, D3**, 8401.

Matsueda, H., H. Y. Inoue, and M. Ishii; 2002. Aircraft observation of carbon dioxide at 8-13 km altitude over the western Pacific from 1993 to 1999*, Tellus, Ser. B,* **54**, 1-21.

Rayner, P. J., and D. M. O'Brien, 2001. The utility of remotely sensed CO_2 concentration data in surface source inversions*, Geophys. Res. Lett.,* **28**, 175-178.

Rumelhart, D.E., G. E. Hinton, and R. J. Williams, 1986. Learning internal representations by error propagation, in *Parallel Distributed Processing: Explorations in the Macrostructure of*

Cognition, vol. 1, edited by D. E. Rumelhart and McClelland, pp. 318-362, MIT Press, Cambridge, Mass.

Schimel, D.S., J. Mellilo, H. Tian, and A. D. McGuire, 2000. Contribution of increasing CO_2 and climate to carbon storage by ecosystems in the United States, *Science,* **287**, 2004-2006.

Tans, P. P., I. Y. Fung, and T. Takahashi, 1990. Observational constraints on the global atmospheric CO_2 budget, *Science,* **247**, 1431-1438.

Vay, S. A., B. E. Anderson, T. J. Conway, G. W. Sachse, J. E. Collins Jr., D. R. Blake, and D. J. Westberg, 1999. Airborne observations of the tropospheric CO_2 distribution and its controlling factors over the South Pacific Basin, *J. Geophys. Res.,* **104, D5**, 5663-5676.

The Validation of AIRS Retrievals

Eric J. Fetzer*, Edward T. Olsen*, Luke L. Chen*, Denise E. Hagan*, Evan Fishbein*, Larry McMillin †, Jiang Zhou † and W. Wallace McMillan%

*Jet Propulsion Laboratory, California Institute of Technology, Pasadena California, USA
†National Oceanic and Atmospheric Administration / National Environmental Satellite Data and Information Service, Camp Springs, Maryland, USA
% Department of Physics, University of Maryland Baltimore County, Baltimore MD, USA

Abstract

The initial validation of Atmospheric Infrared Sounder (AIRS) experimental retrievals was completed in August 2003 as part of public release of version 3.0 data. The associated analyses are reported at http://daac.gsfc.nasa.gov/atmodyn/airs/, where data may be accessed. Here we describe some of those analyses, with an emphasis on cloud cleared radiances, atmospheric temperature profiles, sea surface temperature, total water vapor and atmospheric water vapor profiles. The results are applicable over ocean in the latitude band ±40 degrees.

Cloud Cleared Radiances

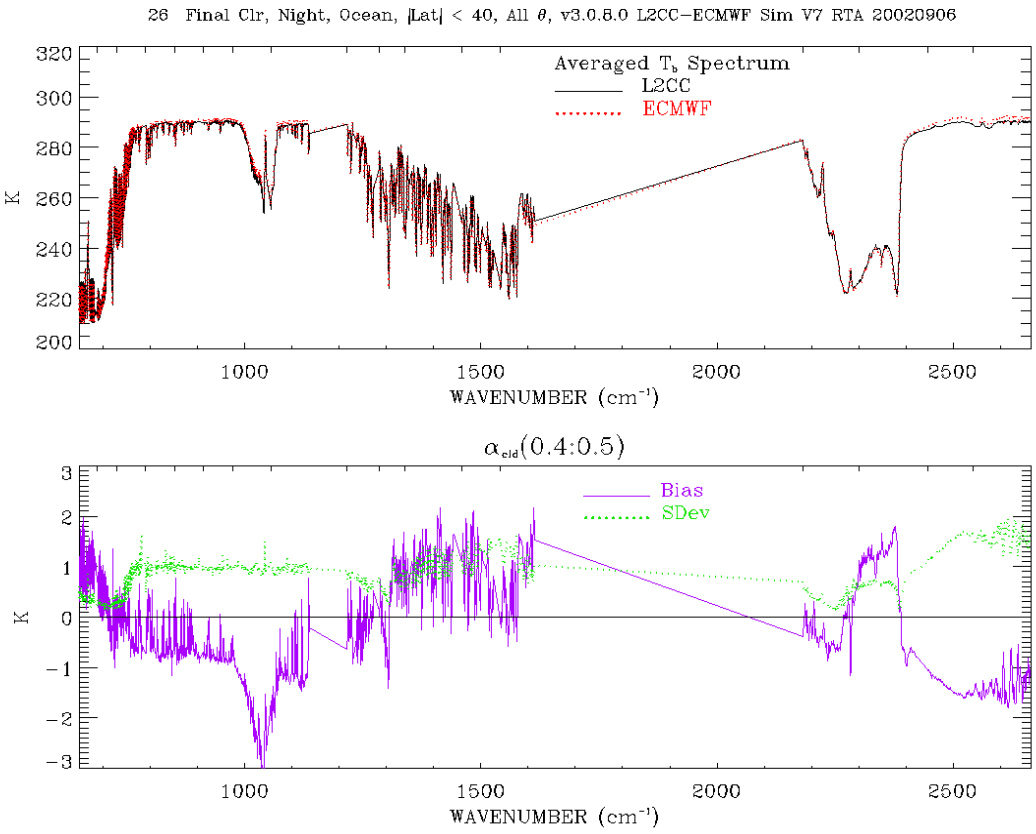

Figure 1. Mean spectra of AIRS cloud-cleared radiances and ECMWF-modeled spectra (upper panel), and statistics of differences for retrieved cloud fraction of 40-50% (lower panel), 6 September 2002.

Cloud cleared radiances were validated by comparison with simulated radiances from the European Center for Medium Range Weather Forecasting (ECMWF) forecasts. Figure 1 shows the mean radiances and difference statistics for retrieved cloud fractions of 40-50% for September 6, 2002. Brightness temperature differences as large as 2 K, especially in the water vapor channels (around 1500 wavenumbers) are apparent. Efforts are ongoing to determine whether the differences are due to AIRS retrievals or to model representation, particularly of water vapor. Errors exceed 3-5 K for retrieved cloud fractions of 60-70%, suggesting a fundamental limit to cloud clearing applicability.

Sea Surface Temperature

Sea surface temperatures (SST) were validated against three data sets: the European Center (ECMWF) analyses, operational buoys, and a ship borne radiometer. Differences with ECMWF are -0.8 K ± 1.0 K. Differences against buoys are -0.8 K ± 1.1 K. Both results are skewed by rejection of retrievals deviating from National Centers for Environmental Prediction (NCEP) forecast SST by more than 3 K. SST comparisons with a ship-borne radiometer are -0.85 ± 1.2 K, and these are not based on rejected retrievals. The time series of differences between AIRS retrieved and radiometer observed SST are shown in Fig. 2.

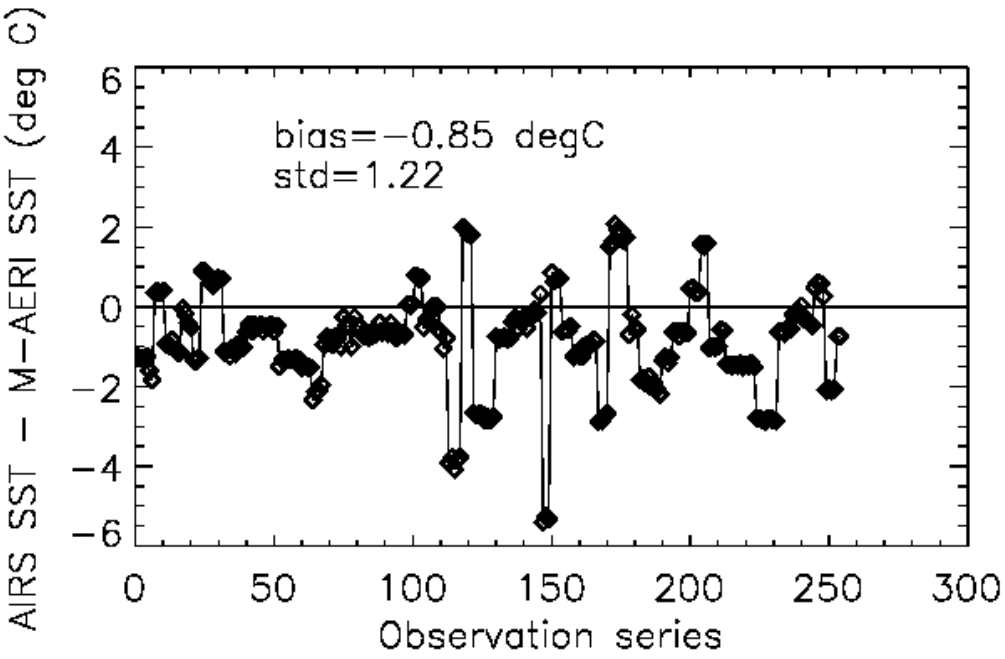

Figure 2. Difference between AIRS retrieved SST and SST observed by the Marine-Atmospheric Emitted Radiance Interferometer onboard the *Explorer of the Seas* cruise ship.

Temperature Profiles

Temperatures were validated against the ECMWF model, and operational and dedicated radiosondes. Figure 2 shows the profile of RMS temperature differences compared with the ECMWF model. Results are similar for operational and dedicated radiosondes. These results are also based on a rejection by a 3 K SST difference with the NCEP forecast SST. Similar values are seen for differences based on cloud fractions of 50% or less, without resorting to comparison with NCEP SST.

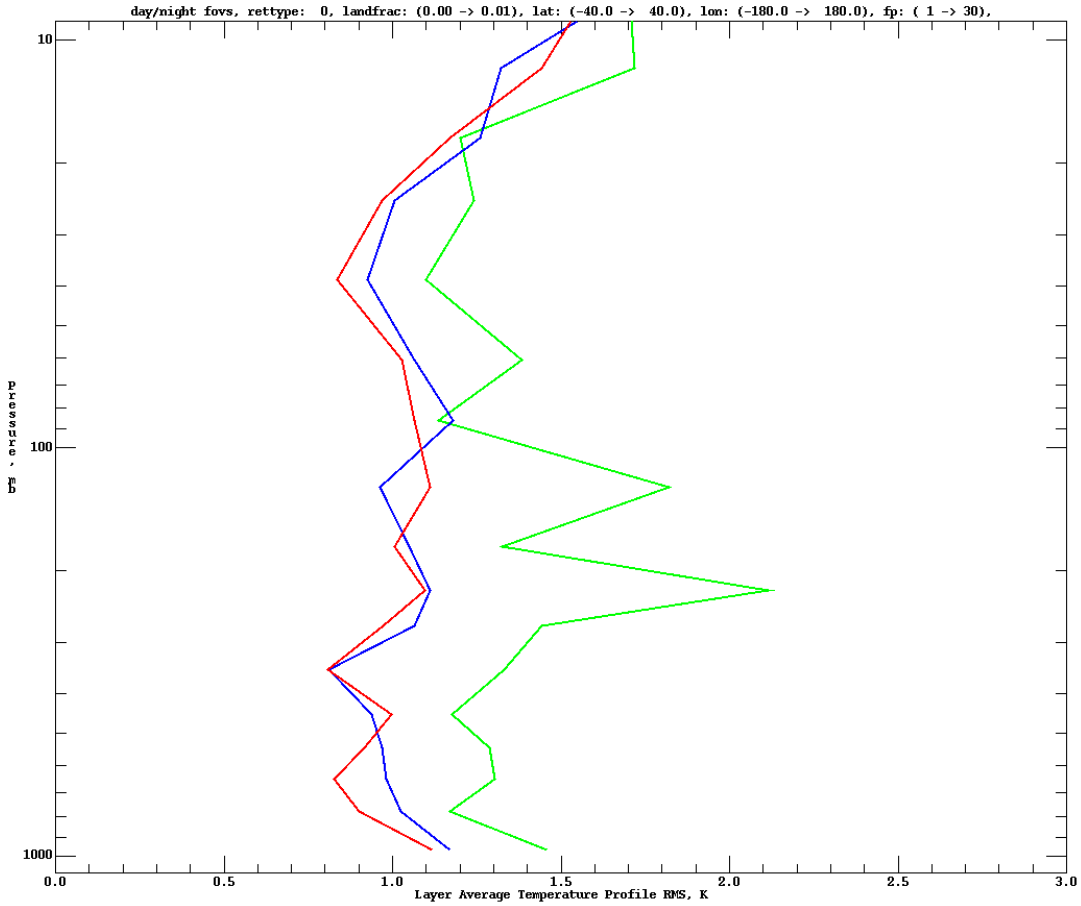

Figure 3. Root-mean-squared differences between AIRS retrieved and ECMWF temperatures in one-kilometer thick layers. Green is microwave-only retrievals, blue is regression retrievals, and red is infrared retrievals.

Total Water Vapor

Total water vapor retrievals were compared against ECMWF, and operational and dedicated radiosondes. These results are summarized in Table 1. Note that the biases are 2% or smaller at every location except Nauru, the location of the Atmospheric Radiation Measurement

Table 1. Differences in total water vapor for several data sets.

Data source	Relative Bias, percent	Relative RMS, percent
ECMWF analyses	0.01	16.2
Operational sondes	1.9	13.7
Dedicated Sondes, Chesapeake Platform	-0.1	10.6
Dedicate Sondes, Nauru (ARM TWP)	-10.0	11.4

Program Tropical Western Pacific (ARM TWP) site. Nauru has some of the highest water vapor loading in the atmosphere, up to 80 mm, and the discrepancy is due to a slight misrepresentation of the water vapor continuum in the forward radiative transfer model contained in the AIRS retrieval software. (Continuum characteristics are very difficult to measure in the laboratory.) This has been corrected in the latest version of the forward model and the retrieval software. A scatterplot of total water vapor from the Chesapeake Light Platform is shown in Figure 4. The Platform is located 15 km off the mouth of Chesapeake Bay, and the sondes were launched during September and October 2003. The large dynamic range is due to a combination of geophysical variability and balloon that burst in the lower atmosphere

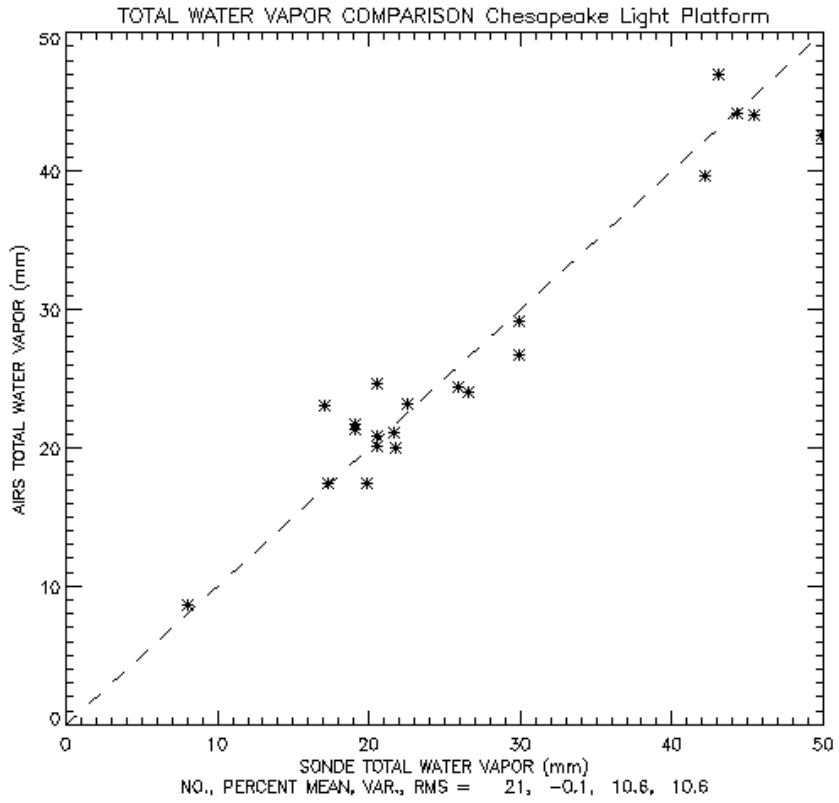

Figure 4. AIRS retrieved total water vapor versus radiosonde observations for dedicated sondes launched from the Chesapeake Light Platform.

Water Vapor Profile

Water vapor profiles were validated against the ECMWF model and operational radiosondes. The emphasis in this initial validation effort was on lower tropospheric water vapor. Table 2 shows the mean and variance of the differences between AIRS retrievals and the three data sources. The 1100 to 700 mb mean and variance are roughly consistent with the results for total water vapor shown above. The cause of the differences at upper levels is being investigated. Candidate mechanisms include model shortcomings, time and space disagreements between AIRS and dedicated sondes, known problems with sondes above 500 mb, and problems with the AIRS retrieval system. Identifying and correcting the latter is an active area of research for the AIRS science and validation teams.

Table 1. Differences in layer averaged water vapor for several data sets.

Layer	ECMWF (%)	Operational Sondes (%)
1100 to 700 mb	-1.8 ± 9.6	3.6 ± 11.0
700 to 500 mb	-1.1 ± 31.2	0.0 ± 26.5
500 to 350 mb*	-12.5 ± 30.0	-3.7 ± 50.5

Validation of Atmospheric InfraRed Sounder (AIRS) Spectral Radiances with the Scanning High-resolution Interferometer Sounder (S-HIS) aircraft instrument

Henry E. Revercomb, David C. Tobin, Robert O. Knuteson, Fred A. Best, William L. Smith*, Paul van Delst, Daniel D. LaPorte, Scott D. Ellington, Mark W.Werner, Ralph G. Dedecker, Ray K. Garcia, Nick N. Ciganovich, H.Benjamin Howell, Steven Dutcher, and Joe K. Taylor

University of Wisconsin-Madison, Space Science and Engineering Center
1225 West Dayton Street, Madison Wisconsin, 53706
* NASA Langley Research Center

ABSTRACT

The ability to accurately validate high spectral resolution IR radiance measurements from space using comparisons with aircraft spectrometer observations has been successfully demonstrated. The demonstration is based on a 21 November 2002 under-flight of the AIRS on the NASA Aqua spacecraft by the S-HIS on the NASA ER-2 high altitude aircraft and resulted in brightness temperature differences approaching 0.1K for most of the spectrum!

Aircraft comparisons of this type provide a mechanism for periodically testing the absolute calibration of spacecraft instruments with instrumentation for which the calibration can be carefully maintained on the ground. This capability is especially valuable for assuring the long-term consistency and accuracy of climate observations, including those from the NASA EOS spacecrafts (Terra, Aqua and Aura) and the new complement of NPOESS operational instruments. The validation role for accurately calibrated aircraft spectrometers also includes application to broadband instruments and linking the calibrations of similar instruments on different spacecraft.

Both the AIRS and the S-HIS calibrations are expected to be very accurate (formal 3-sigma estimates are better than 1 K brightness temperature for a wide range of scene temperatures), because high spectral resolution offers inherent advantages for absolute calibration and because they make use of high emissivity cavity blackbodies as onboard radiometric references. AIRS has the added advantage of a cold space view, and the S-HIS calibration has benefited from the availability of a zenith view from high altitude flights on the Proteus aircraft. The S-HIS has also benefited from calibration techniques developed over many years in conjunction with the original HIS aircraft instrument and with the Atmospheric Emitted Radiance Interferometer (AERI) instruments developed for the DOE ARM Program. The absolute radiometric calibration is traceable to NIST, and in the future, we plan to check the calibration directly by inter-comparison to a NIST-maintained sensor (the TXR radiometer).

It is expected that aircraft flights of the S-HIS and its close cousin the NPOESS Atmospheric Sounder Testbed (NAST) will be used to check the long-term stability of AIRS and the NPOESS operational follow-on sounder, the Cross-track Infrared Sounder (CrIS), over the life of the mission.

1. Introduction

The need for higher accuracy and more refined error characterization of radiance measurements from space (and corresponding geophysical products) to improve both weather forecasting and climate change monitoring has led to a new emphasis on conducting direct tests of in-orbit performance, referred to as "validation". Validation involves collecting higher quality reference data from specially maintained airborne and ground-based facilities that can support refined analyses of a controlled set of well-understood measurements, instead of statistical analyses of data having inconsistent pedigree and unknown error characteristics. This is a positive trend that will help take full advantage of our satellite systems.

The validation activities initiated for the NASA Earth Observing System (EOS) platforms, which are well underway for the Terra and Aqua platforms and will soon be initiated for Aura, are setting the stage for enhanced validation of new observational satellite systems. Extensive plans for validation of the National Polar Orbiting Environmental Satellite System (NPOESS) and future geosynchronous systems are also underway. The Scanning High-resolution Interferometer Sounder (S-HIS) aircraft instrument discussed in this paper is an important validation tool that is currently being used for both EOS and NPOESS. For NPOESS, S-HIS use is coordinated with the NPOESS Airborne Sounder Testbed (NAST) to optimize payload compatibility with joint field campaigns and for critical inter-comparison tests of accuracy.

2. The Scanning High-resolution Interferometer Sounder (S-HIS)

The Scanning HIS is an airborne Michelson Interferometer follow-on to the original University of Wisconsin HIS (Smith, et al., 1989; Revercomb, et al., 1988a) that was flown successfully on the NASA ER2 from 1986 to 1998. The original nadir-only spatial sampling of the HIS has been replaced by cross-track coverage with similar 2-km footprints, while at the same time S-HIS is smaller and much easier to operate (Revercomb, et al., 1996, 1998). In addition to the NASA ER2, it has been successfully flown on the NASA DC8 and on the Scale Composites Proteus, as shown in Figure 1. As illustrated, the Proteus implementation also provides a zenith view to augment calibration information and as a valuable capability for studying upper level water vapor.

Typical S-HIS radiance spectra are shown in Figure 2. The overlapping regions of the three spectral bands are used to constrain the non-linearity correction required for the longwave and midwave bands that use photo-conductive HgCdTe detectors. The shortwave band uses an InSb detector and its expected linearity is confirmed by the lack of telltale out-of-band contributions. As with the original HIS (Revercomb, et al., 1988b, 1989, 1997; Best, et al., 1997), accurate calibration has been a major goal for the S-HIS. Figure 3 shows the 3-sigma radiometric performance expected for S-HIS. Note that for scene temperatures above 220 to 240 K, the 3-sigma absolute calibration accuracy is less than 0.3 K! For carefully calibrated IR spacecraft instruments, the accuracy will be even better for cold scene temperatures, because space provides a well-known cold reference.

The zenith viewing option was first implemented in November 2002. Up and down-looking observations from 14 km altitude are shown in Figure 4. Note the accurate zero determined from the warm and intermediate temperature blackbody spectra shown, even for the non-linear longwave and midwave bands. The zenith view adds an important constraint on the S-HIS non-linearity correction algorithm (Revercomb, 1994).

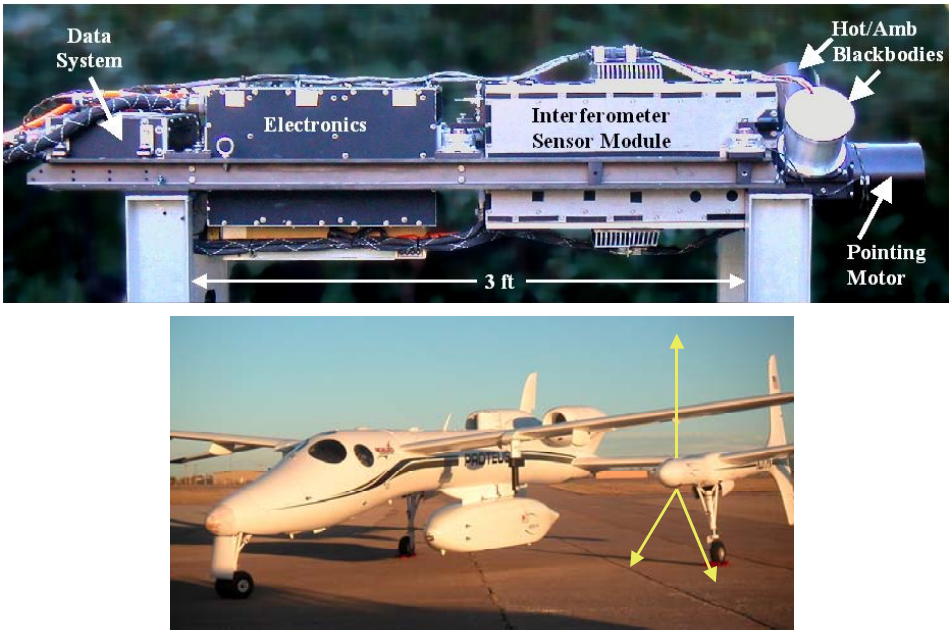

Figure 1. Scanning HIS instrument and illustration of cross-track and zenith viewing from the Proteus aircraft. S-HIS has been configured to fly on the NASA DC8 and ER2 aircraft as well as the Proteus.

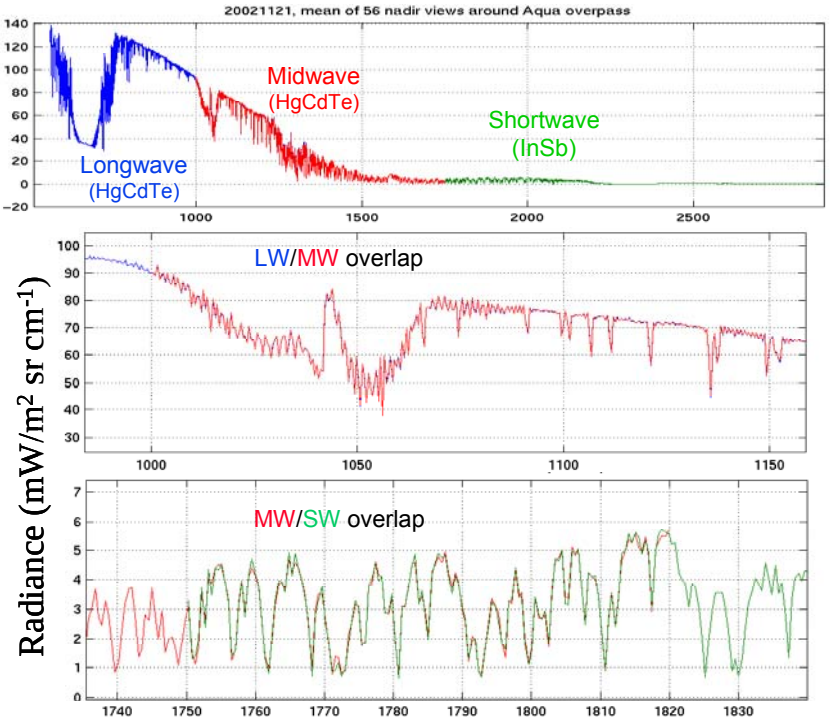

Figure 2. Scanning HIS radiance spectra collected over the Gulf of Mexico on 21 November 2002 from the NASA ER2 at 20 km altitude during the Terra-Aqua Experiment (TX-2002). The three separate spectral bands of S-HIS are illustrated, along with the good agreement between spectra from neighboring bands where they overlap.

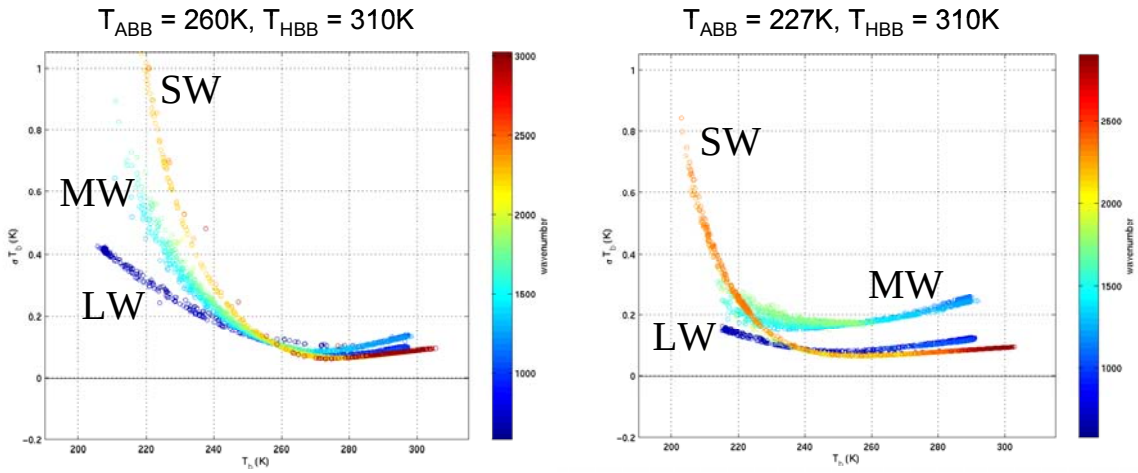

Figure 3. Three-sigma calibration accuracy estimates for Scanning HIS with two different ambient blackbody temperatures. Conditions apply to AIRS vadiation flights on 21 November 2002 on the ER2 over the Gulf of Mexico (left) and 16 November 2002 on Proteus over the DOE Atmospheric Radiation Measurement (ARM) site in Oklahoma. T_{ABB} and T_{HBB} are the ambient and hot blackbody temperatures.

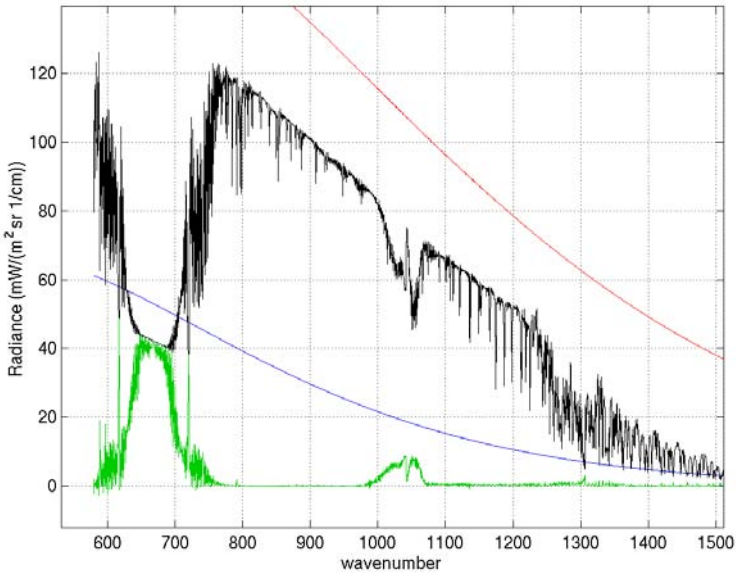

Figure 4. Comparison of zenith (green) and nadir (black) radiance spectra from the Proteus at 14 km over the DOE Atmospheric Radiation Measurement (ARM) program Southern Great Plains site on 16 November 2002. Spectra of the reference blackbodies used for calibration are shown in red and blue.

3. Validation of AIRS with Scanning HIS

The Atmospheric Infrared Sounder (AIRS) on the NASA Aqua spacecraft launched on 20 May 2002 is a cryogenic cross-dispersed grating spectrometer (Aumann et al., 2003). It employs 7 different orders of dispersion to map the spectrum onto 12 detector modules with a total of 15 linear arrays. A single spatial footprint is detected at a time, with the field being focused on the grating to minimize the impact of non-uniform cloudy scenes on spectral calibration.

The differences in spatial and spectral sampling that need to be accounted for in making accurate comparisons of AIRS and S-HIS are illustrated in Figure 5. The technique selected for doing this is to make use of calculations that account for the actual spectral and spatial characteristics of each instrument. The calculated spectra allow the observation-minus-calculation residual for each instrument to be compared, avoiding the first-order effects of these differences. To improve this comparison even further, the residuals are each convolved with the Instrument Line Shape (ILS) of the other. This is equivalent to eliminating grating contributions from optical path differences larger than measured by S-HIS and weakly apodizing S-HIS to match the effect of the AIRS ILS.

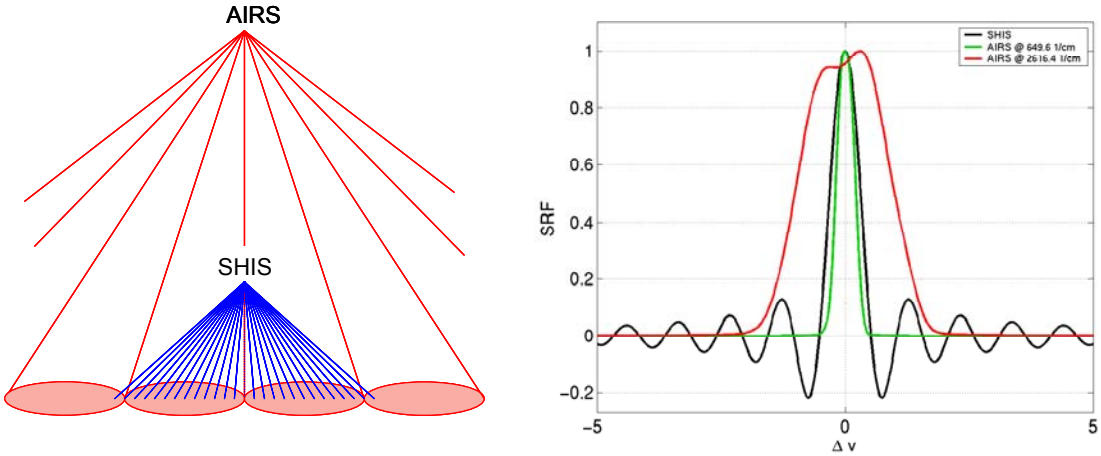

Figure 5. Illustration of the differences between AIRS and S-HIS spatial viewing conditions (left) and spectral Instrument Line Shape (ILS) functions that need to be accounted for in making detailed radiance comparisons.

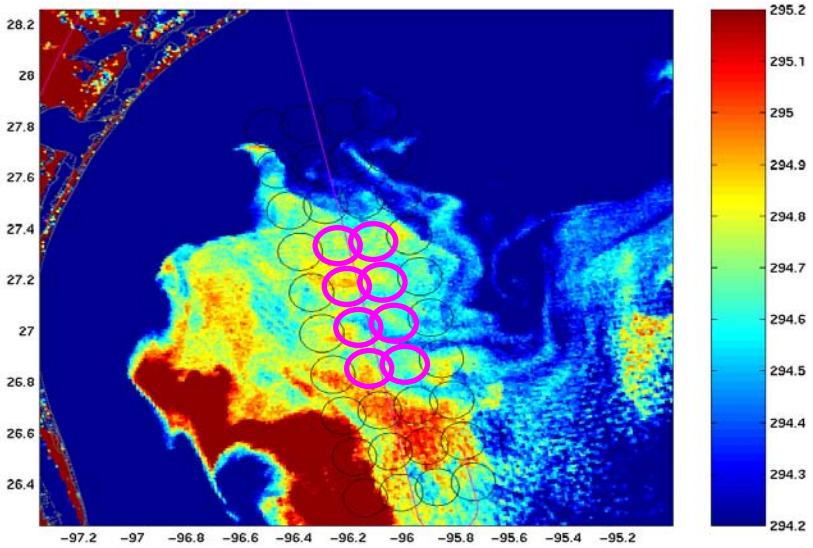

Figure 6. Aqua MODIS 12 micron band image over the Gulf of Mexico on 21 November 2002, illustrating the aircraft sub-track (narrow line) and the 8 near nadir AIRS footprints (~15 km diameter) chosen for comparison based simultaneity and scene uniformity (peak-to-peak brightness temperature variations of about 0.5 °C).

The best conditions for validation of AIRS with Scanning HIS to date were encountered over the Gulf of Mexico on 21 November 2002 as part of the Terra Aqua Experiment (TX 2002). The excellent scene uniformity is illustrated in Figure 6, and the first-order spectral comparison is shown in Figure 7. For this first-order comparison, the spectra from each instrument have been noise filtered using principle component techniques, and averaged over common spatial footprints.

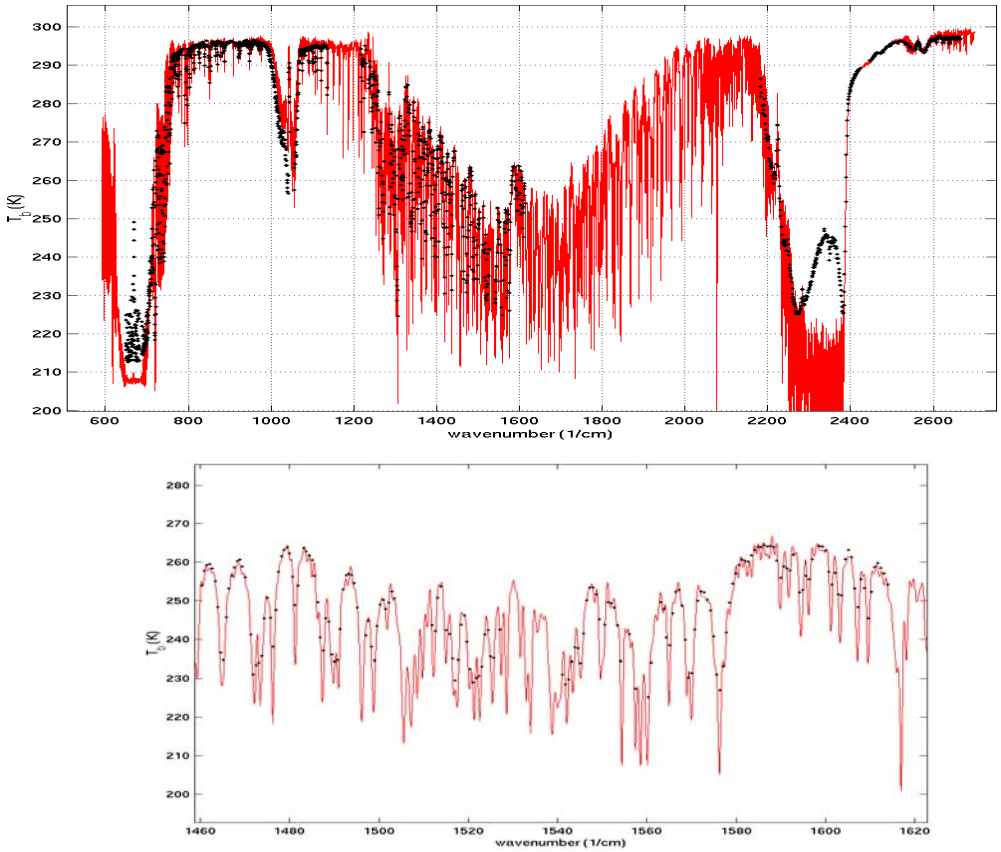

Figure 7. Average of Scanning HIS spectra (red) from inside 8 AIRS footprints (see Figure 6) compared to AIRS spectral channels (black +'s) averaged over the 8 footprints. For this comparison, nothing has been done to account for the different spectral characteristics or altitudes of the two platforms. The portions of the AIRS spectra in the middle of the 15 and 4-micron carbon dioxide bands are sensitive to altitudes above the ER2 altitude of the S-HIS and should not be expected to agree. However, the spectrum from near the middle of the 6.3-micron water vapor band (lower blow-up) is a region where the effective spectral resolutions are comparable, and where the major contributions come from below the ER2. Note the excellent agreement in this region.

The final comparison between S-HIS and AIRS radiances is shown in Figure 8 as the difference of spectrally normalized obs-calc residuals. The excellence of the agreement is demonstrated by the histograms for each module, as discussed in the caption. Note that while the small residual differences are not just for window regions, but extend deeply into the 15-micron carbon dioxide band and also into the 6.3-micron water vapor band. The analysis also identified a spectral scale error in one AIRS module (Figure 9).

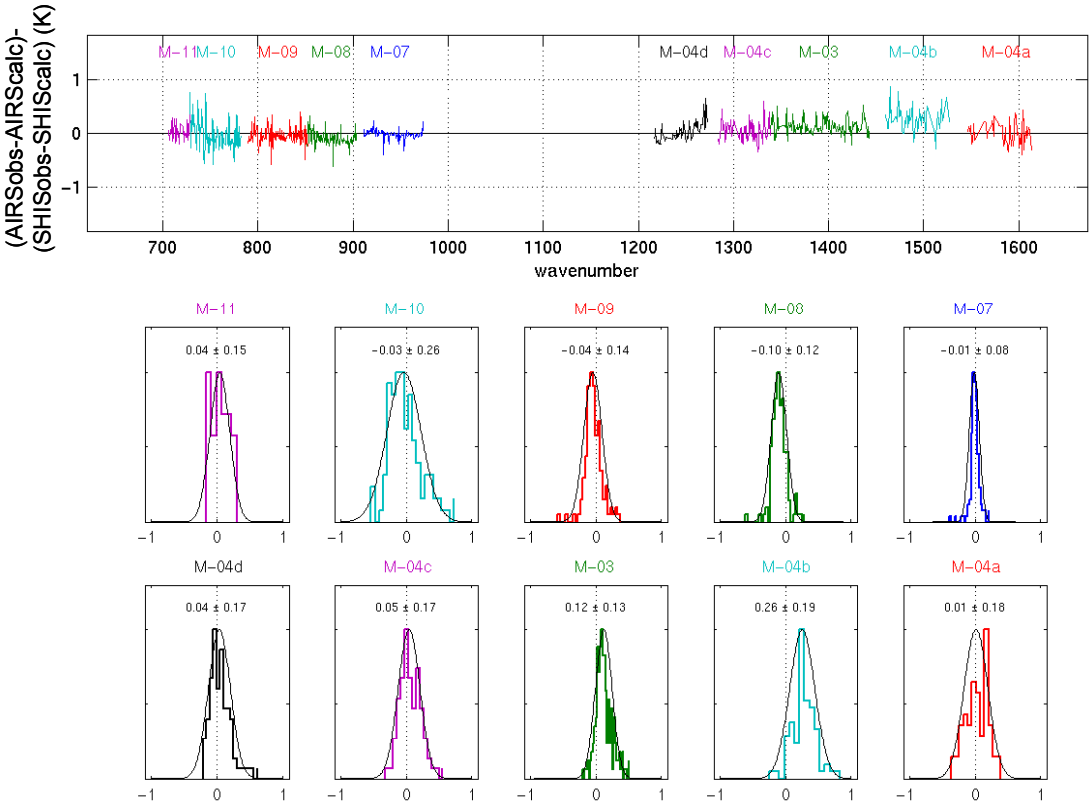

Figure 8. Summary of final AIRS to Scanning HIS comparison with elimination of channels with significant sensitivity above the ER2. The colors distinguish different detector modules of the AIRS instrument (separate linear detector arrays), with corresponding color coded histograms of differences. Note the excellent agreement! The mean agreement over most modules is order 0.1 °C or less (M-04b is the one exception with a mean of 0.26 °C). Also, the standard deviations are with one exception less than 0.2°C.

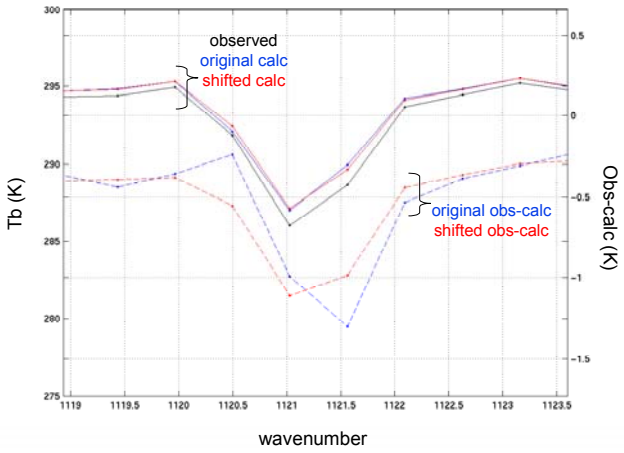

Figure 9. Evidence for very small shift in the spectral calibration of AIRS channels (3% of spectral resolution) from module M-05 discovered with S-HIS. The original shift has now been confirmed with direct comparisons of calculated spectra with AIRS and the spectral response functions adjusted to remove it.

4. Assessment of MODIS Calibration from AIRS

Having validated AIRS with S-HIS, it is useful to consider the implications for other infrared instruments. Since the AIRS provides reasonably high spectral resolution, it can be used to simulate the radiance of lower resolution instruments, such as the EOS MODIS imager, by convolving the AIRS spectrum with the normalized MODIS spectral resolution function for each of the 15 MODIS IR bands. A sample AIRS spectrum is compared to MODIS spectral response functions in Figure 10. Note that there are some gaps in the AIRS spectrum that create significant convolution errors, unless they are accounted for.

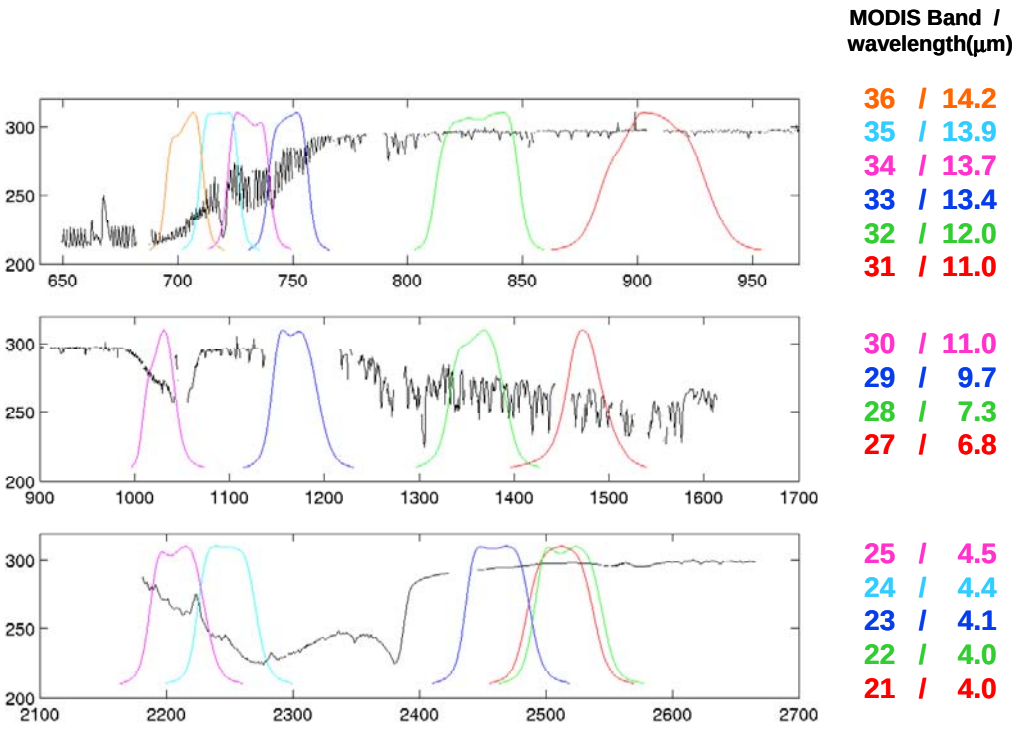

Figure 10. Comparison of AIRS spectrum and MODIS spectral response functions for its overlapping IR bands. It is clear that most MODIS bands can be simulated with AIRS by convolving the AIRS spectra with the MODIS spectral response functions.

The results of comparing co-located AIRS and MODIS for a large selection of global samples, chosen from reasonably uniform AIRS footprints is shown in Figure 11. Note that the numbers of comparisons range from a few 100,000 for window channels and the ozone channel to almost 2 million for the most opaque channel 36. The distributions of AIRS-MODIS differences shown in blue for each band are the final results with corrections for convolution errors determined from a standard atmosphere. The blue bars give an estimate of the convolution errors and are centered at the mean AIRS-MODIS difference. Given the excellent agreement between AIRS and S-HIS, it is expected that the largest part of these differences are issues with MODIS. The most significant differences occur for the most opaque 15-micron CO2 bands (34-36) and for water vapor (27, 28).

Red=without accounting for convolution error
Blue=accounting for convolution error with mean correction from standard atmospheres

p-p Convolution Error (CE) Estimate

Band	Diff	CE	Diff	Std	N
21	0.10	-0.01	0.09	0.23	187487
22	-0.05	-0.00	-0.05	0.10	210762
23	-0.05	0.19	0.14	0.16	244064
24	-0.23	0.00	-0.22	0.24	559547
25	-0.22	0.25	0.03	0.13	453068
27	1.62	-0.57	1.05	0.30	1044122
28	-0.19	0.67	0.48	0.25	1149593
30	0.51	-0.93	-0.41	0.26	172064
31	0.16	-0.13	0.03	0.12	322522
32	0.10	0.00	0.10	0.16	330994
33	-0.21	0.28	0.07	0.21	716940
34	-0.23	-0.11	-0.34	0.15	1089663
35	-0.78	0.21	-0.57	0.28	1318406
36	-0.99	0.12	-0.88	0.43	1980369

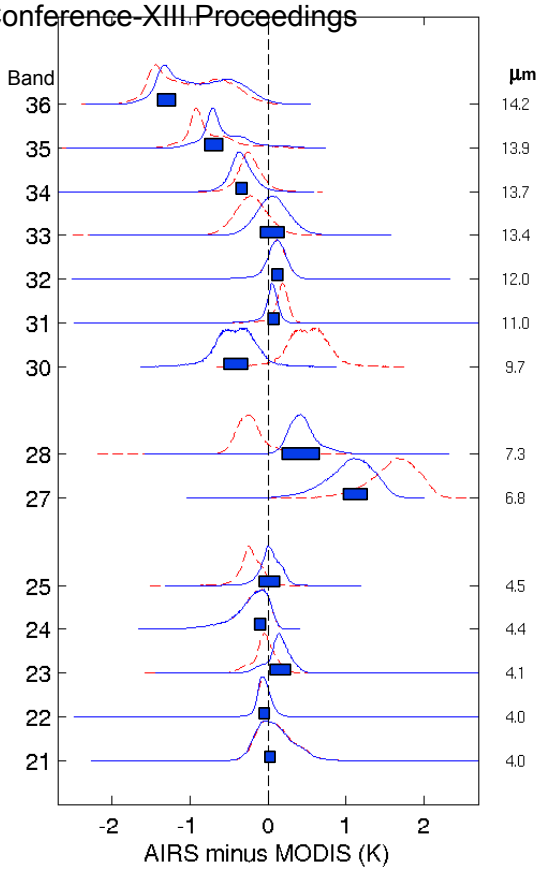

Figure 11. Distributions of brightness-temperature differences between AIRS and MODIS for a large number of samples (N) taken from scenes with reasonably small spatial non-uniformity. An spectral shift in the MODIS spectral response functions could account for most of these differences. It has been demonstrated that a single spectral shift would make the differences small for a wide range of scene brightness temperature conditions.

5. Summary

These initial results of comparing AIRS in orbit on the Aqua platform to aircraft observations from S-HIS illustrate the substantial advantages of high spectral resolution observations for accurate calibration applications.

The basic conclusions are listed below:

1. The calibration uncertainty of advanced high spectral resolution infrared observations are approaching the 0.1 K desired for climate applications,
2. High spectral resolution observations from airborne instruments (S-HIS & NAST) are now proven tools for the detailed validation of satellite based observations,
3. AIRS is providing high quality global radiances for atmospheric sounding & climate applications, and a calibration reference for other IR instruments, and
4. High spectral resolution Aircraft comparisons provide a way to periodically test the absolute calibration of spacecraft instruments with instrumentation that can be carefully re-calibrated with reference standards on the ground, which is especially valuable for assuring the long-term consistency and accuracy of weather and climate observations.

Acknowledgements

We gratefully acknowledge the support of the Integrated Project Office (IPO), contract 50-SPNA-1-00039 and of NASA contract NAS5-31375 for support of S-HIS instrument refinement, field deployment, and data analysis for this work. Integration of S-HIS to the Proteus and early development was supported by the DOE ARM Program.

References

Aumann, H.H., Chahine, M.T., C. Gautier, M.D. Goldberg, E. Kalnay, L.M. McMillan, H. Revercomb, P.W. Rosenkranz, W.L. Smith, D.H. Staelin, L.L. Strow, and J. Susskind, 2003: AIRS/AMSU/HSB on the Aqua Mission: Design, Science Objectives, Data Products, and Processing Systems. IEEE Transactions on Geoscience and Remote Sensing, 41, p 253-264.

Best, F.A.; Revercomb, H.E.; LaPorte, D.D.; Knuteson, R.O., and Smith, W.L, 1997: Accurately calibrated airborne and ground-based Fourier transform spectrometers II: HIS and AERI calibration techniques, traceability, and testing. In: Proceedings of the Council for Optical Radiation measurements (CORM) 1997 Annual Meeting, National Institute of Standards and Technology (NIST), Gaithersburg, MD

Revercomb, H.E., D.D. LaPorte, W.L. Smith, H. Buijs, D.G. Murcray, F.J. Murcray, and L.A. Sromovsky, 1988a: High-Altitude Aircraft Measurements of Upwelling IR Radiance: Prelude to FTIR from Geosynchronous Satellite. Mikrochimica Acta [Wien], II, 439-444.

Revercomb, H.E., H. Buijs, H.B. Howell, D.D. LaPorte, W.L. Smith, and L.A. Sromovsky, 1988b: Radiometric Calibration of IR Fourier Transform Spectrometers: Solution to a Problem with the High Resolution Interferometer Sounder. Applied Optics, 27, 3210-3218.

Revercomb, H.E., H. Buijs, H.B. Howell, R.O. Knuteson, D.D. LaPorte, W.L. Smith, L.A. Sromovsky, and H.W. Woolf, 1989: Radiometric Calibration of IR Interferometers: Experience from the High-resolution Interferometer Sounder (HIS) Aircraft Instrument. RSRM '87:Advances in Remote Sensing Retrieval Methods, A. Deepak, H. Fleming, J. Theon (Eds.). A. Deepak Publishing, Hampton, Virginia

Revercomb, H. E., 1994: Techniques for Avoiding Phase and Non-linearity Errors in Radiometric Calibration: A Review of Experience with the Airborne HIS and Ground-based AERI. Keynote Address, Proceedings of the 5th International Workshop on Atmospheric Science from Space using FTS, p 353-378, Tokyo, Japan, 30 November -2 December.

Revercomb, H. E., W. L. Smith, F. A. Best, J. Giroux, D. D. LaPorte, R. O. Knuteson, M. W. Werner, J. R. Anderson, N. N. Ciganovich, R. W. Cline, S. D. Ellington, R. G. Dedecker, T. P. Dirkx, R. K. Garcia, and H. B. Howell, 1996: Airborne and ground-based Fourier transform spectrometers for meteorology: HIS, AERI and the new AERI-UAV. Proceedings SPIE Optical Instruments for Weather Forecasting, edited by G.W. Kamerman, 2832, 106-117.

Revercomb, H. E., F. Best, D. LaPorte, R. Knuteson, W. Smith, N. Ciganovich, R. Dedecker, T. Dirkx, R. Garcia, R. Herbsleb, J. Short, and H. Howell, 1997: Accurately Calibrated Airborne and Ground-based Fourier Transform Spectrometers I: HIS and AERI Instrument Design, Performance, and Applications for Meteorology and Climate. Council for Optical Radiation Measurements (CORM) 1997 Annual Meeting, National Institute of Standards and Technology (NIST), Gaithersburg, Maryland, 29 April.

Revercomb, H.E., D. C. Tobin, V.P. Walden, J. Anderson, F.A. Best, N.C. Ciganovich, R.G. Dedecker, T. Dirkx, S.C. Ellington, R.K. Garcia, R. Herbsleb, H.B. Howell, R.O. Knuteson, D. LaPorte, D. McRae, and M. Werner, Recent Results from Two New Aircraft-based Instruments: the Scanning High-resolution Interferometer Sounder (S-HIS) and the NPOESS Atmospheric Sounder Testbed-Interferometer (NAST-I), Proceedings of the Eighth International Workshop on Atmospheric Science from Space using Fourier Transform Spectrometry (ASSFTS8), Toulouse, France, 16-18 November, 1998; sponsored by Meteo-France, CNES, CNRS; p 249-254.

Smith, W.L., H.M. Woolf, H.B. Howell, H.-L. Huang, and H.E. Revercomb, 1989: The Simultaneous Retrieval of Atmospheric Temperature and Water Vapor Profiles - Application to Measurements with the High-resolution Interferometer Sounder (HIS). RSRM '87:Advances in Remote Sensing Retrieval Methods, A. Deepak, H. Fleming, J. Theon (Eds.). A. Deepak Publishing, Hampton, Virginia.

Validation Studies Using NAST-Interferometer Field Measurements

Allen M. Larar[a], William L. Smith[a], Daniel K. Zhou[a], and Stephen Mango[b]

[a]NASA Langley Research Center, Hampton, VA 23681
[b]NPOESS Integrated Program Office, Silver Spring, MD 20910

The Integrated Program Office (IPO) developed and supports high-altitude aircraft flights of the National Polar-orbiting Operational Environmental Satellite System (NPOESS) Airborne Sounding Testbed (NAST) as part of risk mitigation activities for future NPOESS sensors. The NAST-Interferometer (NAST-I) is a high spectral and spatial resolution (0.25 cm^{-1} and 0.13 km nadir footprint per km of aircraft altitude, respectively) cross-track scanning (2 km swath width per km of altitude) Fourier Transform Spectrometer (FTS) observing within the 3.7 – 15.5 micron spectral range. NAST-I infrared spectral radiances are used to characterize the atmospheric thermodynamic state and provide information on radiatively active trace gases (e.g. O_3 & CO), clouds, and the terrestrial surface during experimental campaigns. These direct and derived NAST-I data products greatly contribute toward instrument and forward model pre-launch specification optimization and will enhance post-launch calibration/validation activities for the Cross-track Infrared Sounder, CrIS, to fly on NPP and NPOESS (as well as for other advanced atmospheric spaceborne sensors). In this paper we address some of the challenges associated with validating infrared spectral radiances obtained from such high spectral resolution remote sensing systems. This will include comparison of NAST-I infrared spectral radiances measured during recent field experiment campaigns with other radiance measurements as well as radiance calculations performed using Line-by-Line (LBL) and "Fast" forward radiative transfer models based on independent, nearly-coincident observations of atmospheric state.

Validation and Comparison of S-HIS and NAST-I Retrievals for THORPEX 2003

P. Antonelli*, H. E. Revercomb*, R. O. Knuteson*, D. C. Tobin*, S. Dutcher*, W. L. Smith+ and D. Zhou+

*University of Wisconsin, Madison, Wisconsin; +NASA Langley Research Center, Hampton, VA

Abstract

The Scanning High-resolution Infrared Sounder (S-HIS) and the NPOESS Aircraft Sounding Test-bed Interferometer (NAST-I) have flown simultaneously on the same platform during the 2003 THORPEX Observing System Test (PTOST) campaign. Both the instruments are Michelson interferometers and possess very high spectral and spatial resolution. The results of several airborne missions exploited in the past years have shown that the absolute accuracy of the spectral radiances measured with these instruments is excellent. This paper aims to take advantage of the simultaneous observations collected by the two interferometers and by the other instruments such as the Cloud Physics Lidar (CPL), the MODIS Airborne Simulator (MAS) and Dropsondes, involved in the mission, to show: a) the observation capabilities of S-HIS, b) the relative accuracy of the S-HIS derived products with respect to those derived by the other instruments c) the differences in the vertical and horizontal structure of the retrieved temperature fields between S-HIS and NAST-I.

Introduction

The S-HIS participation to the THORPEX program was aimed to answer the following questions: 1) What can be retrieved, in terms of vertical and horizontal resolution, from S-HIS observations? 2) How do the S-HIS observing capabilities compare to those of other instruments involved in the experiment? 3) How do we make the information about the atmospheric state embedded in the Fourier Transform Spectrometers data available to Numerical Weather Prediction (NWP) models? 4) Which impact do the FTS data have on NWP model analysis and forecast?

The work done for PTOST and presented in this paper focuses the first two questions, leaving the third and the fourth one to future work. The paper is divided in two main parts, the first one describes the THORPEX program and its first experiment (PTOST) and the second one describes the results (temperature retrievals) obtained for a specific case study and their validation. A short section dedicated to the conclusions closes the paper.

THORPEX

Overview

THORPEX is a 10 year international research program under the auspices of the World Meteorological Organization/World Weather Research Program (WMO/WWRP) deigned to accelerate improvements in short range (up to 3 days), medium range (3-7 days) and extended range (two week) weather forecast. THORPEX tries to asses the potential to produce significant quantitative and qualitative improvements in forecasts of high impact weather by addressing and examining issues related to predictability and observing system design. The program builds upon ongoing advances within the basic-research and operational-forecasting communities, and aims to enhance the international collaboration between these communities and with users of forecast products. The 2003 Pacific THORPEX Observing System Test (PTOST) is the first in the 10 year series of Pacific and Atlantic observation campaigns in support of the WWRP/USRP THORPEX Program.

Platforms and Instruments

PTOST was conducted from February 18 to March 15, 2003. The campaign focused on the characterization of high-impact weather in the North Pacific north of Hawaii, within the context of the overall objectives of THORPEX. It had objectives regarding tropical cloud characteristics and ocean thermal properties, as well as complimentary satellite validation and aviation weather objectives. The observing platforms and systems used for PTOST/2003 are the NASA ER-2 Aircraft equipped with:

- S-HIS (Infrared) a 0.5 cm^{-1} resolution Fourier transform spectrometer;
- NAST-I (Infrared) a 0.25 cm^{-1} resolution Fourier transform spectrometer;
- CPL (visible), measures backscatter cross-sections of cloud and aerosol particles at 1.064 and 0.532 microns, providing cloud and aerosol backscatter quick-looks, depolarization ration quick looks, optical depth and cloud boundaries;
- MAS (visible, infrared) a 50-channel multi-spectral imager Fast Ozone Photometer - high altitude /in situ/ ozone concentration.

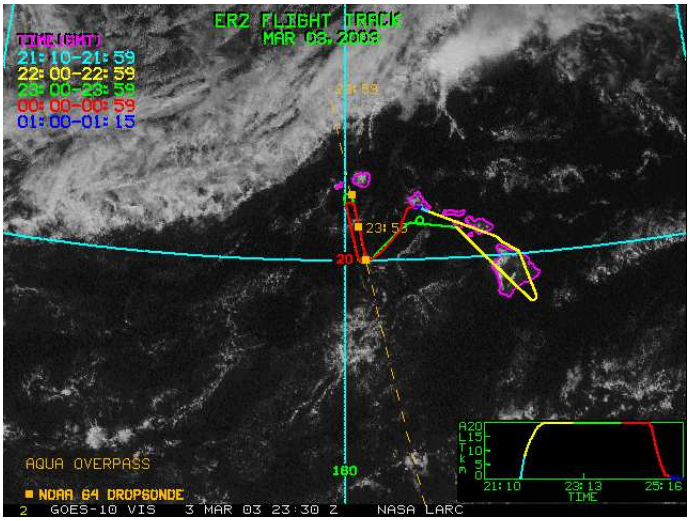

Figure 1: 03 March 2003: ER-2 Flight Track. The yellow squares indicate the locations where dropsondes were released by the G-4.

and the NOAA/G-4 Aircraft, coordinated with the ER-2 and equipped with:

- AVAPS high-density dropsonde system (simultaneous monitoring of 8 dropsondes).
- NOAA Aeromomy Laboratory measurements of ozone and carbon monoxide.
- Flight-level thermodynamic, wind velocity, and turbulence measurements.

The Science Objectives of the PTOST/2003 were: the inter-comparison of forecast skills using NOAA/G-4 dropsonde profiles in observationally sensitive regions versus ER-2 thermodynamic profiles from the S-HIS and NAST-I which are essentially a future sounder simulator (such as GIFTS or HES); the impact of cloud-top temperatures on data assimilation and forecasts given cloud-top heights from the ER2 airborne LIDAR combined with AIRS (Airborne Infra red Sounder), S-HIS, and NAST cloud-top temperature and water vapor phase data.

Case Study

To answer the questions 1 and 2 in the introduction we selected as case study for this paper March 3rd, 2003 (030303). Data were collected between 23:40 and 00:00 UTC of the following day. The ER-2 took off from Honolulu (21:10 UTC) , flew South-East, over Big Island of Hawaii (22:30 UTC), North-West toward Kaua'i and then it completed 2 loops (*race tracks*) South of Kaua'i at 00:00 UTC (see figure 1). Four dropsondes were released along the *race track*, South of Kaua'i, by the G-4, between 23:40 and 00:40 UTC, and one radiosonde was lunched from Lihue at 00:00 UTC.

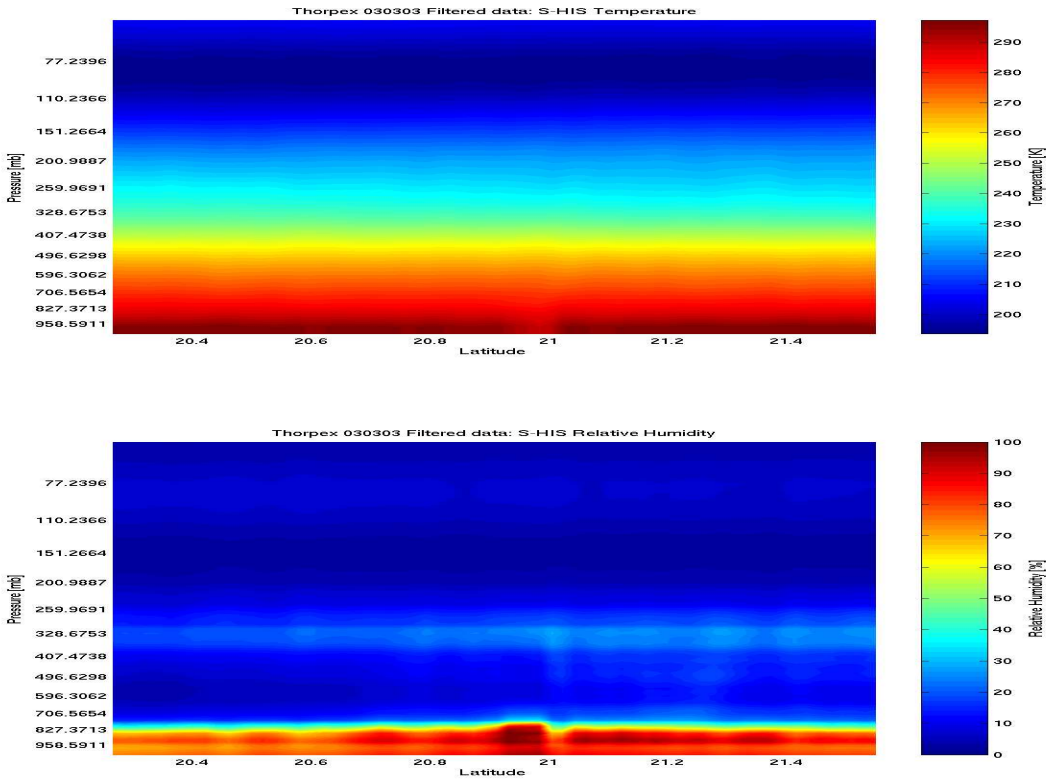

Figure 2: S-HIS VCS for Temperature (top) and Relative Humidity (bottom). The retrieved VCS refer to the flight segment South of Kaua'i between 23:48 and 00:03 UTC.

S-HIS Participation to THORPEX

S-HIS participation to PTOST aimed to provide atmospheric Temperature ($T(p)$) and water vapor Mixing Ratio, or Relative Humidity ($MR(p)$, $RH(p)$) profiles and cloud micro and macro-physical properties. The results showed in this paper focus only on the profiling capabilities of S-HIS. The atmospheric temperature and water vapor fields (figure 2) are retrieved from S-HIS observations using a statistical regression approach used at NASA Langley Research Center [Zhou et al. 2002, Huang and Antonelli 2001] .

Validation

The S-HIS retrieved profiles have been validated against the radiosonde launched at Lihue on March 4th, at 00:00 UTC. Figure 3 shows the comparison between the retrieved profiles and the radiosonde profile for temperature (first plot on the left) , water vapor $MR(p)$ (second plot from the left), and $RH(p)$ (third plot from the left), as functions of pressure. The forth plot shows how S-HIS retrieved profiles and of the radiosonde are relatively close in time (<10 min) and space (< 30 Km). The comparison of the profiles shows good accuracy of the S-HIS retrieval for both

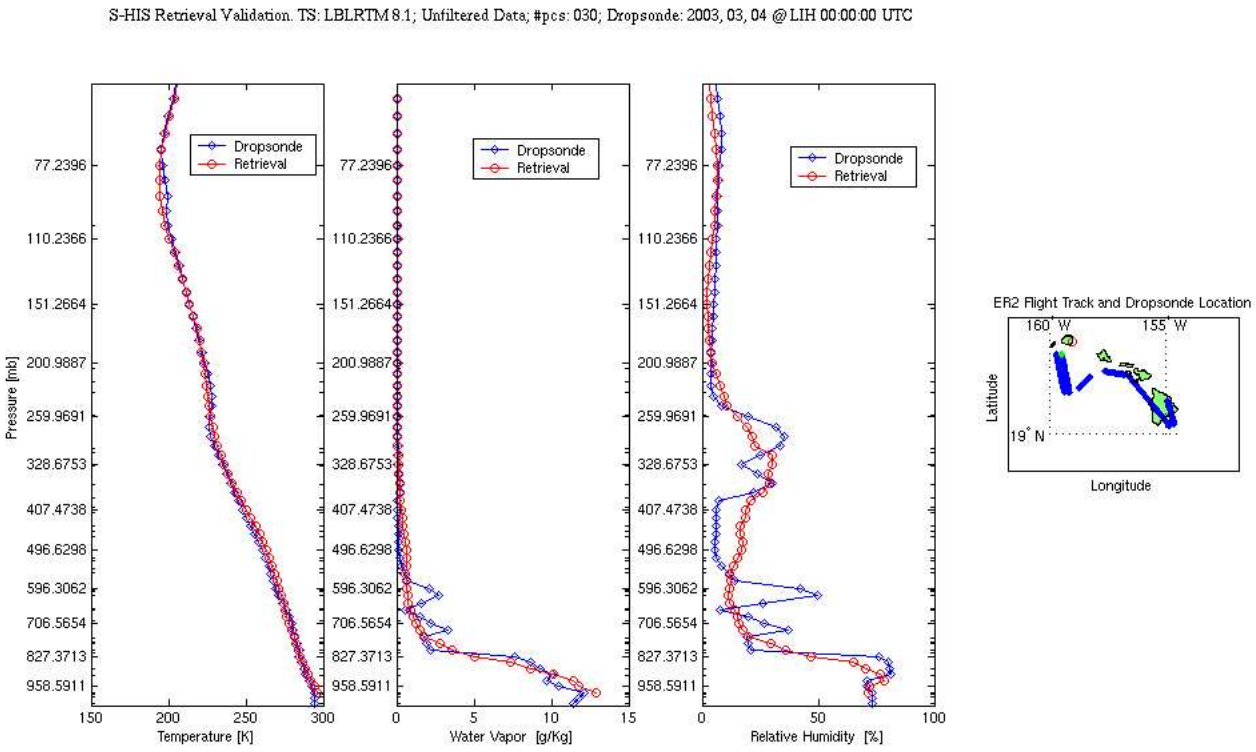

Figure 3: Validation of S-HIS derived temperature and water vapor mixing ratio profiles (red curves). The profiles have been validated against the radiosonde profiles observed at Lihue at 00:00 UTC (blue curves). Starting from the left side the first plot shows the comparison of the temperature vertical profiles. The second and third plots show the comparison between the water vapor mixing ratio and relative humidity vertical profiles. The forth plot shows the location of the S-HIS retrieved profiles and of the radiosonde. The comparison of the profiles shows good accuracy of the S-HIS retrieval for both temperature and water vapor.

temperature and water vapor.

The profiles have been also validated against the dropsondes released by the G-4 South of Kaua'i. The top plot, in figure 4, shows a Vertical Cross Section (VCS) of the temperature deviation field, obtained interpolating spatially the deviation of 3 dropsonde temperature profiles from their mean. The plot shows an horizontal temperature gradient of about 7 K at 250 hPa. The bottom plot, obtained interpolating spatially the deviation of the 3 S-HIS retrieved temperature profiles (closest in space to the dropsonde) from their mean, shows the same vertical structure of the top plot. This comparison clearly shows the capability of S-HIS to provide valuable information about horizontal atmospheric structures at high spatial resolution ($\sim 2.5\ Km$).

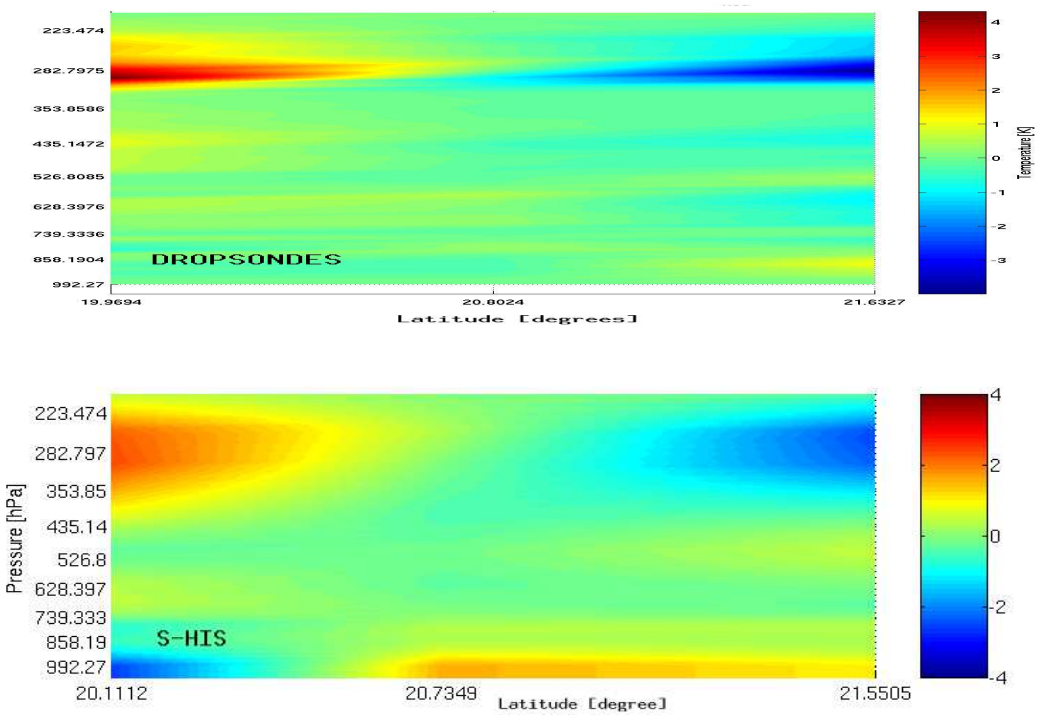

Figure 4: VCS of temperature deviation from the mean. The plots have been obtained interpolating spatially the deviation of 3 dropsonde temperature profiles from their mean (top) and 3 S-HIS retrieved temperature profiles (closest in space to the dropsonde) from their mean (bottom). They both show an horizontal temperature gradient of about 7 K at 250 hPa. The agreement between the images shows the S-HIS capability of accurately *observing* spatial temperature gradients.

Inter-comparison S-HIS, NAST-I

The VCS of the temperature deviation, derived from S-HIS observations, has been also compared to the one derived from NAST-I (courtesy of the NAST-I NASA Langley group). In figure 5 the vertical structures shown in the two cross sections are similar. Both the instruments were able to *observe* the vertical temperature inversion at 12.5 Km of altitude and the strong horizontal temperature gradient ($\sim$ 7 K) at 10 and 15 Km of altitude. But the cross sections still show differences that, considering the similarities between the two instruments, are not expected and have to be further investigated.

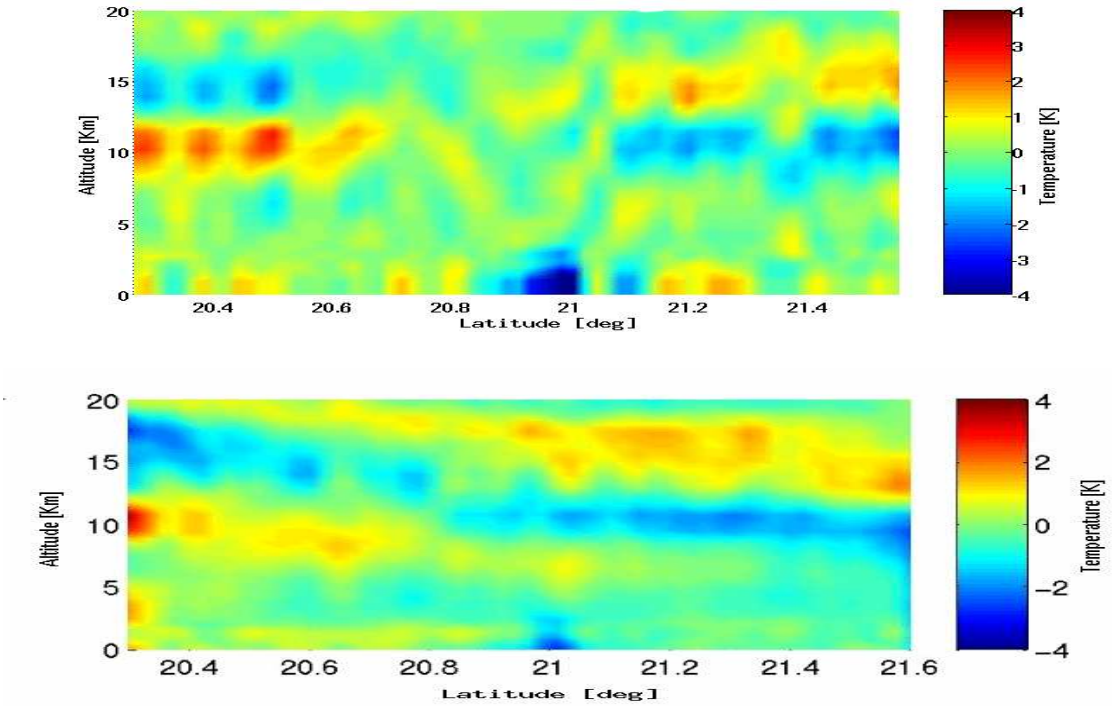

Figure 5: VCS of temperature deviation from the mean. The plots show the VCS as observed by S-HIS (top) and NAST-I (bottom) at full spatial resolution. The comparison of the two cross section shows similarities between the two spatial structures. Both the instruments were able to catch the vertical temperature inversion at 15.5 Km and the horizontal gradient at the same temperature. The plots also show differences that have to be further investigated.

Conclusions

The goal for this paper was to address the issues related to observational capabilities of S-HIS, in terms of vertical and horizontal resolution, and how they compare to the capabilities of other instruments involved in PTOST. With regard to the first question, S-HIS temperature retrievals for the selected case study, have been proved to be in good agreement with radiosonde data (figure 3). They have also been proved to be in good agreement with the profiles measured by the dropsondes released by the G-4. Most importantly S-HIS showed the capability of observing real spatial structures of the atmospheric temperature field that could represent a valuable source of information for NWP models. The S-HIS retrieved temperature field was found to be in good agreement with the NAST-I retrieved field. But the comparison between the temperature retrievals obtained from the two interferometers showed also some differences that were not expected and that should be further investigated.

References

[Revercomb et al. 1996] Revercomb, H.E.; Smith, W.L.; Best, F.E.; LaPorte, D.D.; Knuteson, R.O.; Werner, M.W.: Anderson, J.R.; Ciganovich, N.N.; Ellington, S.D., and Dedecker, R.G.: *Airborne and ground-based Fourier transform spectrometers for meteorology - HIS, AERI and new AERI-UAV*. Optical Instruments for Weather Forecasting, Proceedings of the Conference, Denver, CO, 8-9 August 1996. Bellingham, WA: Society of Photo-Optical Instrumentation Engineers, 1996. (SPIE Proceedings volume 2832). Pp106-117.

[Smith et al., 1999] Smith, W.L.; Larar, A.; Hinton, B.; Howell, H.B.; Revercomb, H.E.; DeSlover, D.H.; Sisko, C.A.; Tobin, D.C.; Cousins, D.; Mooney, D.; Gazarik, M., and Mango, S., 1999: *The NPOESS Airborne Sounder Testbed-Interferometer (NAST-I): The validation of results from a new and revolutionary airborne remote sensing tool*. In: Conference on Atmospheric Radiation: A Symposium with tributes to the works of Verner E. Suomi, 10th, Madison, WI, 28 June-2 July 1999 (preprints). Boston, MA: American Meteorological Society; 1999. Pp548-551.

[Cousin and Gazarick, 1999] Cousins, D. and M.J. Gazarick 1999: *NAST Interferometer Design and Characterization*. Final Report, MIT Lincoln Laboratory Project Report NOAA-26, July 13,1999.

[Revercomb et al., 1988] Revercomb, Henry E.; Buijs, H.; Howell, Hugh B.; LaPorte, D.D.; Smith, William L., and Sromovsky, L.A. 1988: *Radiometric calibration of IR Fourier transform spectrometers: Solution to a problem with the High-Resolution Interferometer Sounder.* Applied Optics 27(15), 1 August 1988, pp3210-3218.

[Zhou et al. 2002] D. K. Zhou, W. L. Smith, J. Li, H.B. Howell, G.W. Cantwell, A.M. Larar, R.O. Knuteson, D.C. Tobin, H.E. Revercomb, and S. A. Mango 2002: *Thermodynamic product retrieval methodology and validation for NAST-I.* Applied Optics Vol. 41, No. 33

[Huang and Antonelli 2001] Hang H-L, P. Antonelli, 2001: *Application of Principal Component Analysis to High-Resolution Infrared Measurements Compression and Retrieval.* Journal of Applied Meteorology, 40, 365-388

Validation of Satellite AIRS Retrievals with Aircraft NAST-I Soundings and Dropsondes – Implications for Future Satellite Sounding Capabilities

W. Smith, D. Zhou, P. Antonelli[†], H. Howell[†], H. Huang[†], R. Knuteson[†], A. Larar, J.Li[†], S. Mango[‡], H. Revercomb[†], L. Strow[#], D. Tobin[†], H. Woolf[†], X. Liu
AtSC, NASA Langley Research Center, Hampton, VA
[†] SSEC, University of Wisconsin–Madison, Madison, WI
[‡] NPOESS Integrated Program Office, Silver Spring, MD
[#]University of Maryland Baltimore Campus, Baltimore, MD

ABSTRACT

The airborne NPOESS Aircraft Sounding Test-bed Interferometer (NAST-I) has flown on numerous flights under the Aqua satellite in order to validate AIRS radiance measurements and profile retrievals. The NAST-I is an excellent AIRS airborne validation tool since it possesses relatively high spectral and spatial resolution as well as relatively low radiance measurement noise, especially after the data are spatially averaged to the footprint size of the AIRS sensor. The results of these airborne missions have shown that the AIRS calibration validates well against airborne interferometer radiance measurements[1]. Here, it is shown that the retrievals obtained using the same retrieval algorithm are in general agreement, although the airborne NAST-I result possesses higher vertical resolution as a consequence of it's higher spectral resolution and lower "effective" radiance noise level. The "effective" radiance noise level is a function of the single spectral sample radiance measurement noise, the number of spectral channels used for the retrieval, and the number of spatial samples averaged to produce the final profile result. For the NAST-I aircraft instrument, the effective radiance noise level is extremely small, particularly after reducing the horizontal linear resolution to that of the satellite AIRS instrument (i.e., ~14 km for AIRS as opposed to ~2 km for NAST-I), and as a result its relatively large spectral range and high spectral resolution (i.e., NAST-I possess nearly four times the number of spectral channels as does the AIRS). It is shown here that spatial averaging of the AIRS data, which decreases the noise level of the radiances used for the retrieval, improves the vertical resolution of the profile results.

1. Introduction

A new era of higher vertical resolution atmospheric temperature and moisture profile retrievals from satellite radiance measurements has begun in an attempt to improve weather and climate monitoring and forecasts. The higher vertical profile resolution is to be achieved by a one to two order of magnitude enhancement of the spectral resolution and coverage, dependent upon spectral location[2, 3]. Improved Instrument Line Shape (ILS) (i.e., spectral position) knowledge, and a lower spectral radiance noise over that characteristic of the current operational sounding spectrometers (Smith, et. al., 1979, 1991) also contribute to the improved vertical resolution. The approach is soon to be implemented using high precision Fourier Transform Spectrometers (FTS) on both European (METOP) and US (NPOESS) operational polar satellites beginning in 2005. Imaging spectrometers are under development for the future generation of operational geostationary spacecraft, the Geostationary Imaging Fourier Transform Spectrometer (GIFTS) being an experimental prototype to be in orbit during the latter part of this decade[4].

The first airborne tests of the high vertical resolution sounding concept began with the advent of the High resolution Interferometer Sounder (HIS) [5,6] flown on NASA's the high altitude ER-2

aircraft from 1985 to 1998. The success of the HIS led to a spaceborne demonstration of concept instrument, the Atmospheric Infrared Sounder (AIRS), a cryogenic cross-dispersed grating spectrometer[7], launched on the NASA Aqua satellite on 20 May 2002. In order to validate the AIRS and the operational instruments to follow, two improved airborne FTS instruments were developed, the Scanning HIS (S-HIS) and the NPOESS Airborne Sounding Testbed-Interferometer (NAST-I)) which are a cross-track scanning Michelson Interferometer follow-on to the original nadir-only viewing HIS. Both the S-HIS and the NAST-I were developed to collect controlled sets of very high quality spectral radiance and retrieved atmospheric profile reference data as needed to validate the spacecraft radiance measurements and derived geophysical products. Beyond Aqua, the airborne FTS validation approach will be applied to the Aura and NPP research satellites and the Meteorological European Terrestrial Operational Polar satellite (METOP) and the National Polar Orbiting Environmental Satellite System (NPOESS) operational satellites.

This paper focuses on the use of the NAST-I for the validation of the Aqua AIRS profile retrieval capability. (The use of S-HIS for the validation of AIRS radiance measurement accuracy has been addressed in these proceedings by Revercomb[2]. In order to conduct an objective assessment, the AIRS and NAST retrievals are produced using exactly the same retrieval algorithm. The forward radiative transfer model used for the AIRS retrievals is the SARTA[8], based on the GENLEN line-by-line model, whereas that used for the NAST retrievals is the OSS model[9], based on LBLRTM. No adjustment of the radiances (i.e., radiance tuning) is made, on the basis of comparisons between observed and calculated radiances, to account for forward radiative transfer model errors. The results show that the retrievals from the NAST-I radiances possess higher vertical resolution than those produce from AIRS radiances. This was expected due to the higher spectral resolution, broader spectral coverage, and thus lower effective noise achieved by NAST-I. Thus, NAST-I is a very good AIRS product validation tool. It is also shown that the vertical resolution of the AIRS retrievals is improved by 3 x 3 footprint averaging of the data which reduces the spectrally random noise level of the radiances used for the retrieval by a factor of 3.

2. The NPOESS Aircraft Sounder Testbed – Interferometer (NAST-I)

The NPOESS Airborne Sounding Testbed-Interferometer (NAST-I) [8,9] was developed to be flown on high altitude aircraft to provide experimental observations needed to finalize the specifications and to test proposed designs and data processing algorithms for the Cross-track Infrared Sounder (CrIS) to fly on the National Polar-orbiting Operational Environmental Satellite System (NPOESS). NAST-I is a Michelson Fourier Transform Spectrometer with high spectral resolution ($0.25 cm^{-1}$) and high spatial resolution (0.13 km linear resolution per km of aircraft flight altitude at nadir). The NAST-I spatially scans cross-track to the aircraft motion +/- 48.2 degrees, thereby providing a 2.3 km ground track swath width per km of aircraft flight altitude. The radiometric noise is about 0.3 K, spectrum-to-spectrum, dependent upon spectral region and scene temperature. The spectral precision is generally better than 0.25 K, spectral point to spectral point, within a given radiance spectrum.

As shown in figure 1, the NAST-I has a spectral range of 3.6 - 16.1 μm, without gaps, and covers the spectral ranges and resolutions of all planned advanced high spectral resolution infrared spectrometers to fly on polar orbiting and geostationary weather satellites, including the EOS-AIRS, METOP-IASI, the NPP/NPOESS-CrIS, and the EO3-GIFTS. Thus, the NAST-I data can be used to simulate the radiometric observations to be achieved from these advanced sounding

instruments. Moreover, the forward radiative transfer models and product retrieval algorithms planned for these satellite systems can be validated prior to launch. Finally the NAST-I can be used for the fundamental purpose of post-launch calibration and validation of products for the advanced satellite sounding systems.

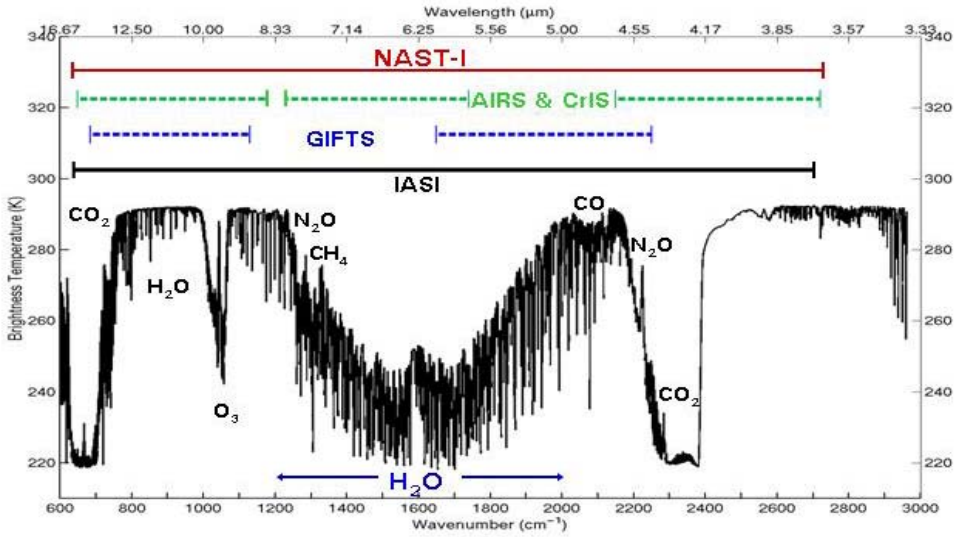

Figure 1: The NAST-I spectral coverage compared to that of advanced satellite sounders.

The NAST-I instrument design is based on reflective optics, KBr beam splitter compensator and separate integral detector/cooler assemblies operating at 65K. A heated and an ambient cold blackbody sources are viewed in each scan to provide absolute radiometric calibration at the level of 0.25 K. Dynamic alignment of the interferometer optics, a pressurized N2 enclosure and wire coil shock mounts are used to minimize the environmental effects of aircraft flight. The instrument processor/controller is based on a Pentium CPU with real time digital signal processing. A ring laser gyro/GPS navigation sensor is used to earth locate the data.

The NAST-I spatially scans the Earth and atmosphere from an aircraft, such as the high-altitude NASA ER-2 research airplane or the Northrop-Grumman Proteus aircraft. From an aircraft altitude of 20 km, 2.6 km spatial resolution is achieved, thereby providing three-dimensional hyper spectral images of radiance and derived geophysical products (figure 2).

The NAST-I aircraft interferometer instrument is capable of spatially mapping atmospheric temperature and moisture with a very high horizontal resolution (~1-3 km, depending on altitude and scan angle). The basic NAST-I product is a two-dimensional "image" of spectral radiance, for any spectral channel within the 3.5 to 16.5 micron range of the instrument (figure 2). The derived products include cloud and surface radiative and physical properties (e.g., spectral emissivity and temperature, cloud-top pressure and optical depth) and a three-dimensional representation of the temperature, water vapor, and the concentration of other radiatively active trace gases (e.g., O_3, CO, CH_4, and N_2O) of the atmosphere. NAST-I provides a vertical resolution of 1–2 kilometers for atmospheric temperature and water vapor, so that distinct layers are observed, the number depending upon aircraft altitude. Thus, as the aircraft passes over the Earth, NAST-I scans an area at the Earth's surface collecting data on the properties of the Earth's surface and atmosphere beneath the aircraft. The wide variety of surface and atmospheric sounding and cloud products support scientific studies as well as provide a means to validate both

forward model and inverse algorithms to be used for future spacecraft high spectral resolution sounding instruments.

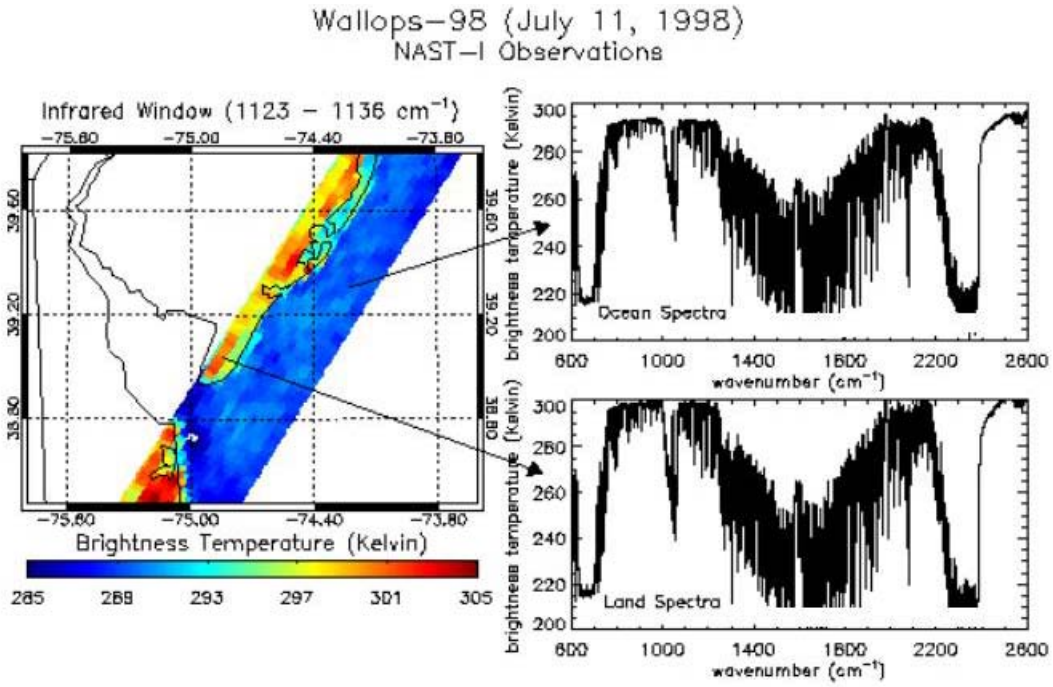

Figure 2: NAST-I Observations along the Atlantic coast of Virginia on July 11,1998.

3. Sounding Retrieval Approach

Temperature and moisture sounding capability of the NAST-I high spectral resolution infrared sounder, has been tested during numerous field programs. The retrieval results are obtained using the eigenvector regression retrieval method as applied to high spectral resolution interferometer data[12, 13]. In this technique, a training sample of historical radiosonde data is used to simulate radiance spectra for the NAST-I instrument. In the simulation, the radiosonde temperature and humidity structure is used to diagnose the cloud top level. For the spectral radiance calculations, each radiosonde, which possesses cloud, is treated as both a clear sky and as an opaque cloud condition profile. The opaque sky condition profile is created by representing the radiosonde temperature and moisture profile below the cloud as isothermal, at cloud top temperature, and saturated. This profile adjustment enables the retrieval system to obtain a clear sky equivalent, from a radiative transfer point of view, temperature and moisture profile regardless of the cloud condition. If the sky is cloud free, then the correct atmospheric profile will be obtained from aircraft level down to the earth's surface. If an opaque cloud exists, the correct atmospheric profiles will be retrieved down to cloud top with an isothermal, at cloud top temperature, and saturated profile being retrieved below the cloud top down to the earth's surface. If a semi-transparent or broken cloud cover exists, then the correct profile will be retrieved down to the cloud top level; below the cloud a temperature profile intermediate to the true profile and the cloud top temperature, and a less than saturated water vapor condition, will be retrieved, the proportion of isothermal and saturation structure being dependent on the cloud opacity and fraction (see figure 3). The surface emissivity spectrum for each radiosonde profile is randomly selected from a set of laboratory measured emissivity spectra for a wide variety of surface types[14]. Trace gas species, such as ozone and carbon monoxide are specified using a statistical

representation based on correlations of these gases with temperature and humidity conditions specified by the radiosonde data[15].

Eigenvectors are computed and regression equations which relate the eigenvector amplitudes to the radiosonde temperature and water vapor values, surface temperature, and the coefficients of an eigenvector representation of the surface emissivity spectra[16], used in the radiance simulation, are derived, assuming a variable number of eigenvectors for the representation of the spectral radiance information. Appropriate random instrumental noise is then added to the simulated radiance data set and retrievals are performed for all cases as a function of the number of eigenvectors. The optimal number of eigenvectors is then selected as that number which minimizes the RMS retrieval error for the historical radiosonde data set. This number generally ranges between 15 and 50, for NAST-I, depending upon the variance associated with the particular data set used (higher natural variance requires a larger number of eigenvectors to represent the information content of the radiance spectra). The regression equations for the optimal set are then applied to real NAST-I radiance measurements, which are corrected for reflected solar radiation contributions. The reflected solar contribution correction is based on a reflected solar spectrum calculated for a model surface and atmospheric condition, similar to that being observed, and the radiances observed in the 4.0 and 9.0-micron window regions of the spectrum[10]. Since all the radiative transfer calculations and eigenvector decomposition analysis are done "off-line" to the actual data processing, the algorithm is extremely fast when applied to real data

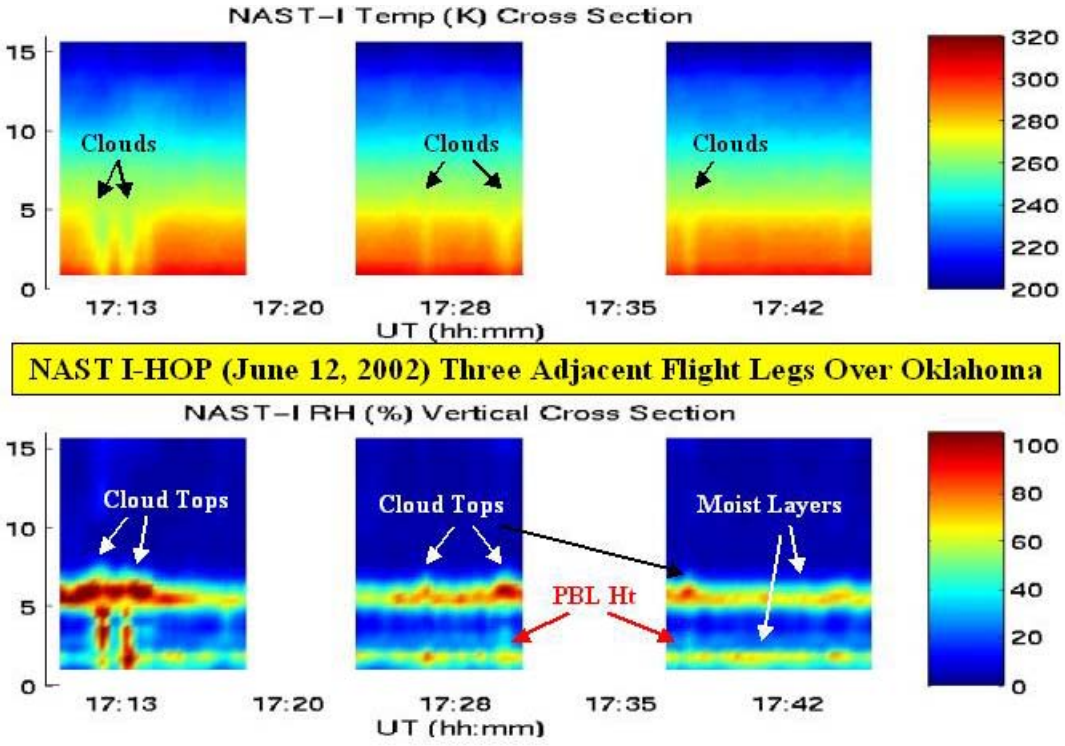

Figure 3: Typical temperature and moisture retrievals observed by NAST-I during the I-HOP field experiment conducted over Kansas and Oklahoma. One can see from that the temperature tends toward the isothermal (top panel) and the moisture saturated (bottom panel) below the cloud, the degree of which depends on the cloud opacity.

4. Validation of AIRS Retrievals with NAST-I Retrievals

The Atmospheric Infrared Sounder (AIRS) on the NASA Aqua spacecraft launched on 20 May 2002 is a cryogenic cross-dispersed grating spectrometer[7]. It employs 7 different orders of dispersion to map the spectrum onto 12 detector modules with a total of 15 linear arrays. The AIRS instrument is the first spaceborne spectrometer designed to meet the 1-K/1-km sounding accuracy objective by measuring the infrared spectrum quasi-continuously from 3.7 to 15.4 microns with high spectral resolution ($\nu/\delta\nu$ = 1200/1). The sensitivity requirements, expressed as Noise Equivalent Differential Temperature (NEdT), referred to a 250-K target-temperature ranges, from 0.1 K in the 4.2-μm lower tropospheric sounding wavelengths to 0.5 K in the 15-μm upper tropospheric and stratospheric sounding spectral region. Spatial coverage and views of cold space and hot calibration targets are provided by a 360-degree rotation of the scan mirror every 2.67 seconds. Table 1, below, summarizes the AIRS measurement characteristics.

Table 1. AIRS Measurement Characteristics

Data Rate	1.27 Mbits per second
Spectral Range	IR: 3.74 – 4.61 μm, 6.20-8.22 μm, 8.80-15.4 μm (2378 spectral channels) VIS/NIR: 0.4 – 1.1 microns
Spectral Resolution ($\nu/\delta\nu$)	1200 (0.5 – 2.25 cm^{-1})
Field of View	IR: 1.1 degree (13.5 km at nadir from 705 km altitude) VIS/NIR: 0.2 degree (2.3 km from 705 km altitude)
Swath Width	99 degree (1650 km from 705 km orbit altitude)
Scan Sampling	IR: 90 x 1 x 1.1 degree VIS/NIR: 720 x 8 x 0.2 degree
Scan Period	2.67 seconds

Figure 4 shows the spectral channels of the NAST-I and the AIRS used for the atmospheric sounding retrievals. There are approximately three times as many NAST channels as there are AIRS channels (i.e., 4425 compared to 1594 spectral channels for NAST-I and AIRS, respectively) used for the retrievals as a result of the higher spectral resolution of the NAST.

Figure 5 shows the Aqua underpass leg of the NASA ER-2 for which sounding comparisons were performed. There were also four dropsondes released from the NOAA Gulfstream 4 (G-4) aircraft along the flight track directly under the Aqua satellite, one each at the Northern and Southern ends, and two in the middle portion of the eastern leg of the flight loop shown. The ER-2 NAST, Aqua AIRS, and G-4 dropsonde observations were all within a few minutes of each other.

Figure 6 shows the footprints of the Aqua AIRS sounding instrument and those of the NAST-I for the data used for the sounding intercomparison. One can see from the images for the window spectral region (870 – 900 cm^{-1}) that there was some low cumulus cloud across the middle of the ER-2 flight leg used for the intercomparison. One can also see the spatial resolution differences between the NAST-I and the Aqua AIRS brightness temperature observations, the NAST-I possessing almost 40 times higher area resolution than the AIRS (nominally, 2.5 vs. 15 km linear resolution). The very high spatial resolution of the NAST-I is important for isolating clear sky observations needed for obtaining accurate soundings to the Earth's surface for validating the lower resolution satellite retrievals.

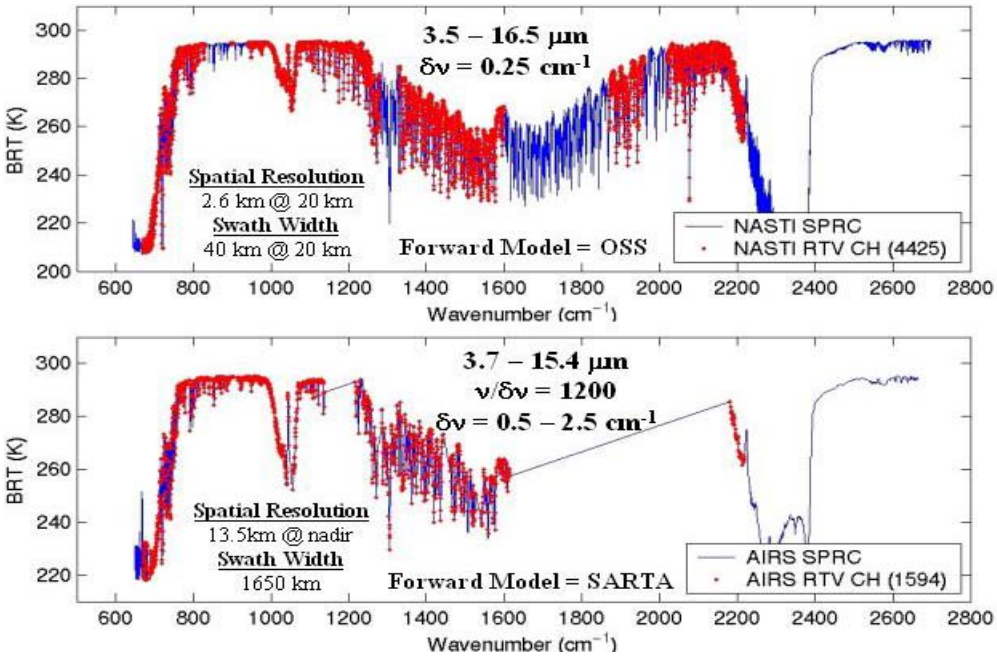

Figure 4: Spectral channels (red dots) used for the sounding retrievals are shown here.

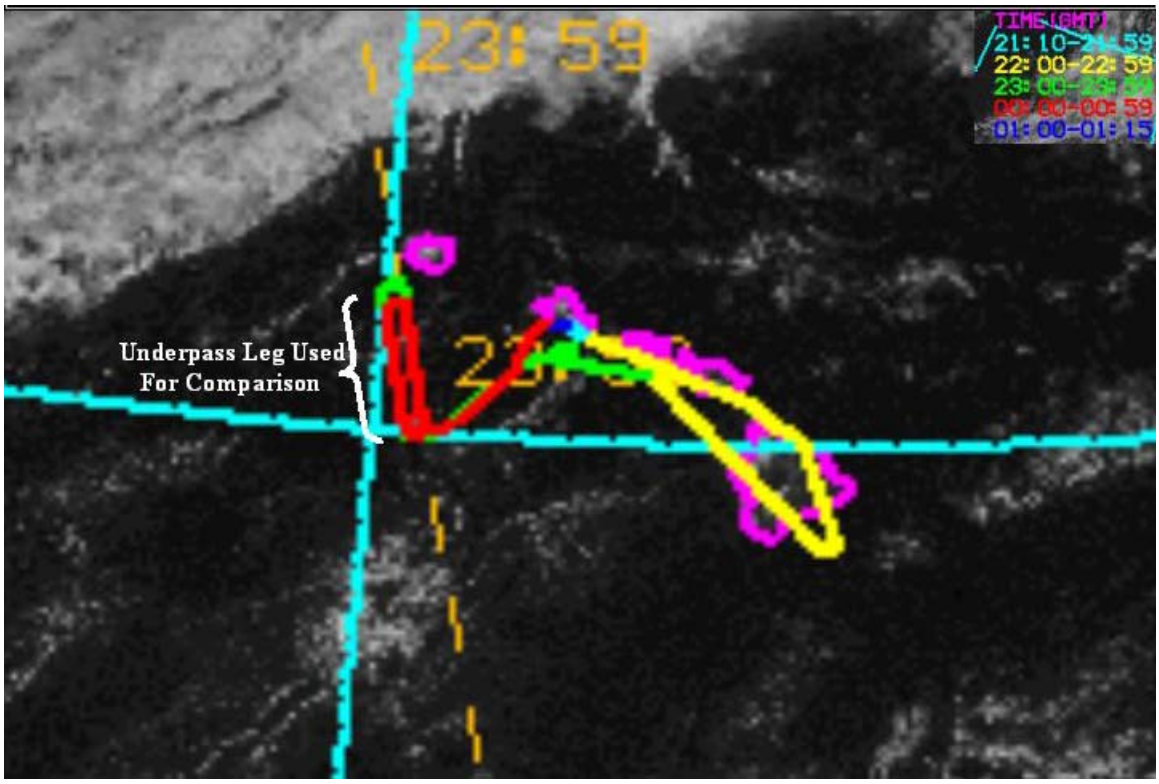

Figure 5. The NASA ER-2 flight tracks on March 3, 2003 in the vicinity of the Hawaiian islands. The flight track used for the comparison of NAST-I and dropsonde soundings with the Aqua AIRS retrievals are shown (the dashed brown line is the Aqua orbital track).

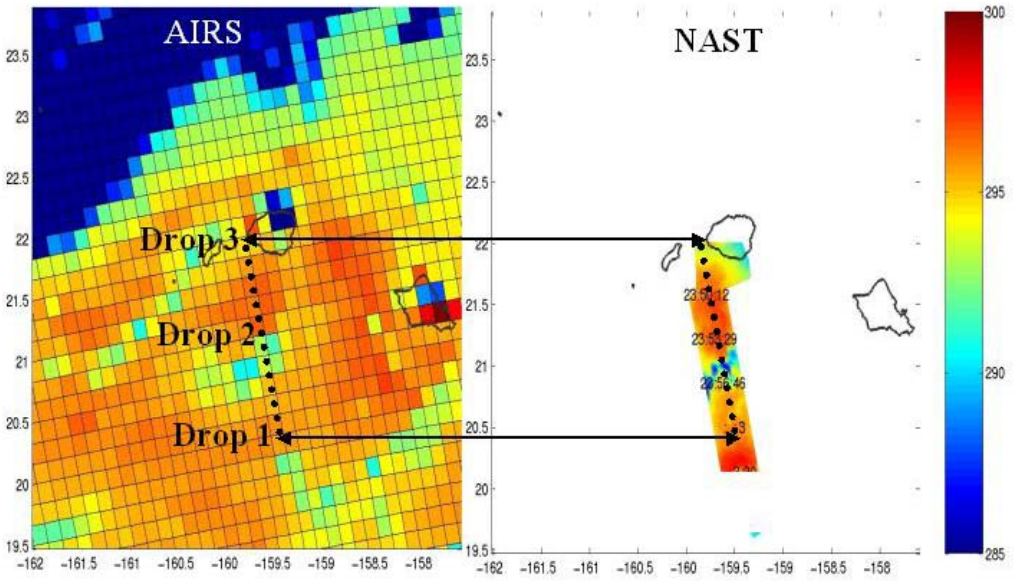

Figure 6. Brightness temperature (870 – 900 cm^{-1}) images showing the footprints of the AIRS and NAST-I radiance data used for sounding intercomparisons shown in figure 7.

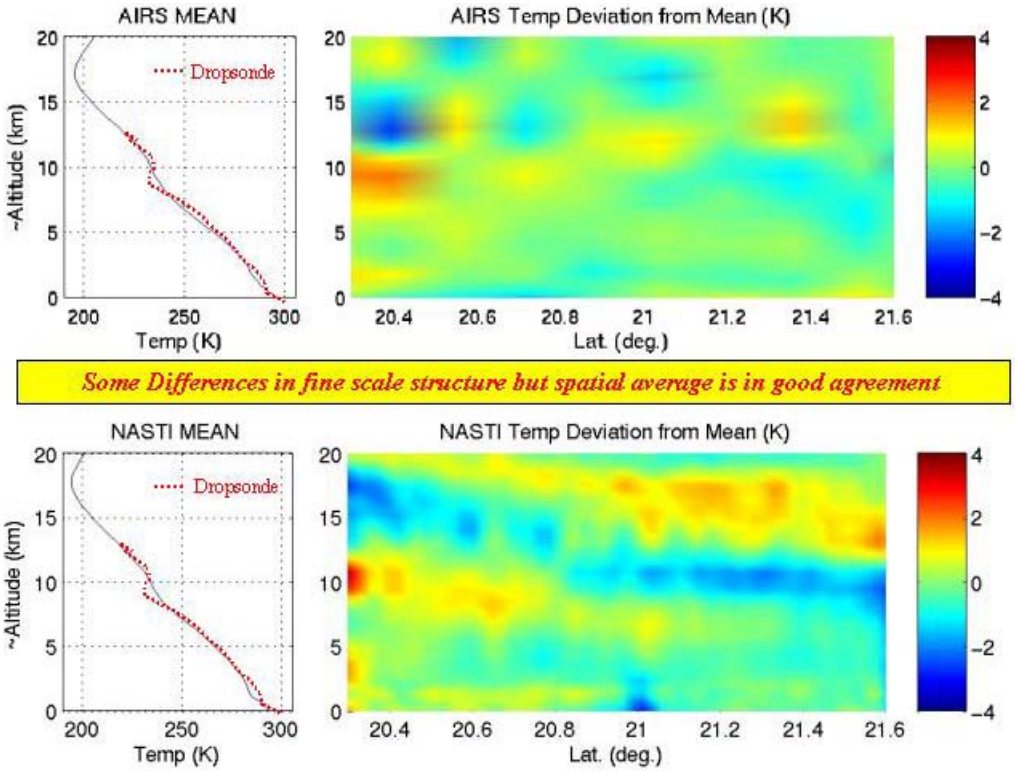

Figure 7. Cross-sections of full spatial resolution AIRS and NAST-I retrievals along the flight tracks shown in figures 5 and 6. The color panels illustrate the temperature anomaly from the mean profiles shown on the left of each cross-section. The average of the dropsonde measurements along the flight tracks are shown by the red dots superimposed on the soundings.

Figure 7 shows the comparison between the temperature profiles obtained from the full spatial resolution Aqua AIRS (~ 15 km) and ER-2 NAST-I (~2.5 km) measurements along the orbital track of the Aqua. The cross-sections are illustrated in terms of the deviation of the profiles from their mean along the track. The mean profiles are shown to the left of each cross-section image. The spatial average of the dropsonde measurements along the track are superimposed upon the AIRS and NAST-I mean profiles to provide validation of the absolute values of the temperature retrieval results. As shown from the cross-sections, there are significant differences in the fine scale spatial structure of the AIRS and NAST-I cross-sections, although the mean profiles are in reasonably good agreement. In this case, the AIRS retrievals look noisy compared to the spatially coherent NAST-I cross-sections.

In order to explain the fine scale spatial resolution differences shown in figure 7, AIRS level measurement noise was artificially added to the NAST-I radiance observations prior to performing the retrieval process. Figure 8 below shows the result. As can be seen, the retrieval cross-section based on the NAST-I, with AIRS level noise introduced, has now lost its spatial coherency; the cross-section appears to be noisy like the AIRS result. Thus, the likely explanation for the difference between the full resolution AIRS and NAST-I vertical resolution is due to the inferior effective radiance noise level of the AIRS data as compared to NAST-I. The effective radiance noise level is a function of the single sample instrument noise and the number of spectral channels used for the retrieval. In this case the NAST-I effective radiance noise is about one third that of the AIRS, since the NAST-I results consists of an average of three adjacent cross-track scan spots and three times as many spectral channels are used for the retrieval.

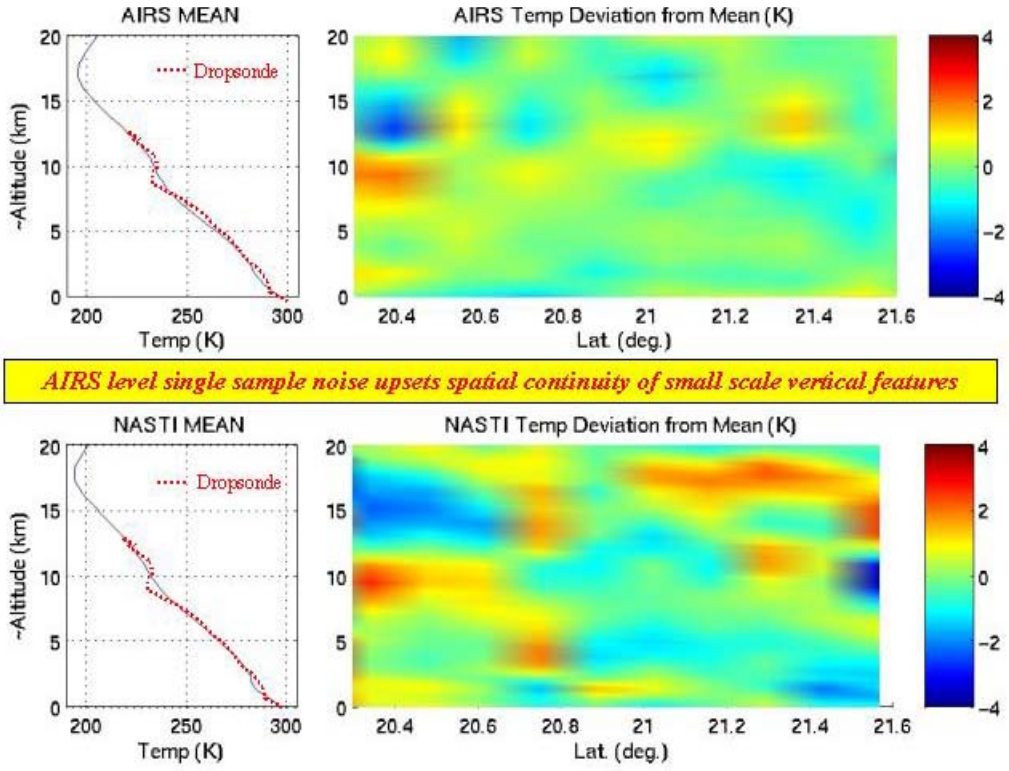

Figure 8. Cross-section of the full spatial resolution AIRS soundings and those retrieved from NAST-I radiances after AIRS level instrument noise was artificially added to the full resolution NAST-I radiance measurements.

Spatial averaging of the data can reduce AIRS random instrument noise. Thus, 3 x 3 averaging of the AIRS radiances were performed to produce a factor of 3 decrease in the noise level of the AIRS radiances used for the sounding retrievals. Figure 9 shows the AIRS retrieval result in comparison to retrievals from the NAST-I radiance measurements spatially averaged to the spatial resolution of the 3 x 3 averaged AIRS data. Also shown is the cross-section constructed with the three dropsondes along the flight track. Here the AIRS and NAST-I data above the NOAA G-4 aircraft level is blanked out for the purpose of the dropsonde intercomparison. As can be seen the spatially averaged AIRS retrievals now produce spatially coherent fine scale vertical structure which is in general agreement with that retrieved from NAST-I radiance measurements and observed with the dropsonde measurements. The residual difference in vertical sensitivity between the AIRS and the NAST-I results may be attributed to the higher spectral resolution of the NAST-I data. Both the AIRS and NAST-I retrieval cross-sections show the same features illustrated in the dropsonde cross-section, but at significantly lower vertical resolution. Whereas the dropsonde vertical resolution is on the order of several meters, the retrieved sounding resolution in the free troposphere varies from 1-2 kilometers, decreasing with increasing altitude.

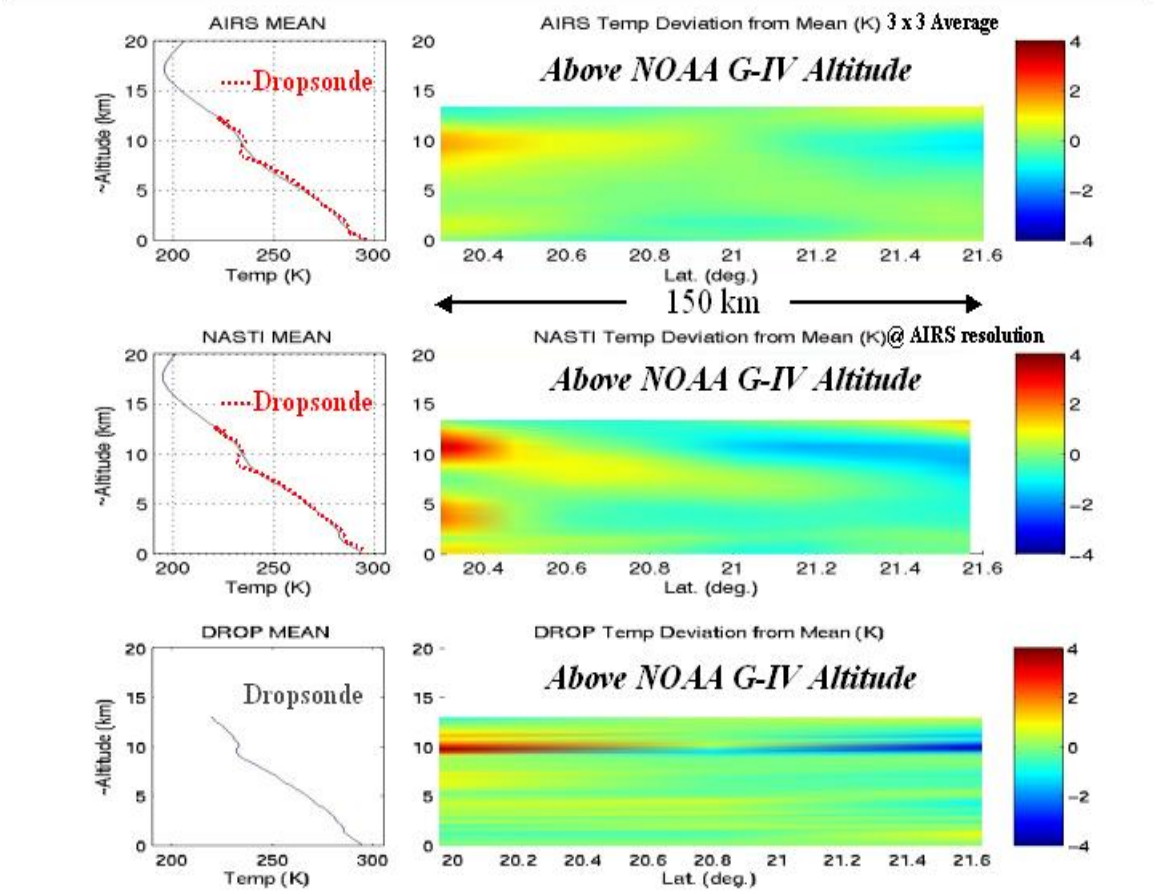

Figure 9. Comparisons of cross-sections of retrievals from AIRS and NAST-I radiance data for 3 x 3 spatially averaged AIRS radiance measurements. The NAST data was also averaged to the 3 x 3 average spatial resolution of the AIRS data. A cross-section constructed from G-4 dropsonde data is also shown for validating the AIRS and NAST-I retrieval results.

5. Summary and Implications for Future Satellite Sounding Capability

Initial results of comparing AIRS temperature sounding retrievals to much higher spatial resolution aircraft NAST-I retrieved soundings and dropsondes, clearly show the value of airborne satellite product validation campaigns. It is shown that high vertical resolution soundings can be achieved by transformation of the amplitudes of a relatively small set of eigenvectors (~ 30-40, depending on atmospheric condition) of large samples (~ 2000 – 5000 spectral points, depending upon the instrument) of spectrally independent atmospheric radiances, as the predictors of the atmospheric profiles. The eigenvector decomposition produces very high signal to noise radiance information input to the vertical sounding retrieval process. High signal to noise radiance input is important for resolving fine scale vertical features because the retrieval process is one of deconvolution of the spectral structure of the radiance measurements.

In the example shown here, AIRS measurements can provided high vertical resolution sounding information when the noise was reduced to one third of the single sample noise level. This reduction can be performed by 3 x 3 averaging of the AIRS data, however, this averaging will degrades the horizontal resolution of the AIRS products and introduce significantly more cloud contamination of the radiance used to obtain the retrieved products. The vertical structure of the retrieved atmospheric soundings appear to be consistent with the 1-2 kilometer vertical resolution expected from upwelling spectral radiances.

The physically based statistical retrieval method used here was trained to produce accurate soundings down to cloud top level. The above cloud top vertical extent limitation will soon be alleviated by training the algorithm to produce soundings below semi-transparent and/or broken cloud conditions. Also, it has been shown that simultaneous multi-spectral imaging spectrometer data provided by the Aqua MODIS instrument can be used to cloud clear the AIRS data to enable soundings to be obtained below a single layer of scattered to broken clouds[18].

The implications for future satellite sounding instruments (i.e., IASI, CrIS, and GIFTS) is that their effective noise level, and therefore vertical profile resolution, should be comparable, and in most cases better, than that achieved with the AIRS. In the case of the IASI, the detector noise performance should be comparable to AIRS, however the IASI possess 2-5 times higher spectral resolution, depending on the spectral region. The CrIS will have a spectral resolution comparable to AIRS, but its detector noise is expected to be considerably smaller than that associated with AIRS, at least for the longer wavelength region of the spectrum. The GIFTS will have a detector noise level comparable to AIRS, a somewhat higher spectral resolution in the water vapor band, but much higher (4 km vs. 15 km linear) spatial resolution. Thus, the effective sounding retrieval noise level of the future sounders should be smaller than the experimental AIRS instrument leading to generally higher vertical resolution atmospheric profile retrievals.

Acknowledgements
We gratefully acknowledge the support of the Integrated Project Office (IPO) for support of NAST-I instrument maintenance, field deployment, and analysis of field deployment data.

6. References

1. Henry E. Revercomb, David C. Tobin, Robert O. Knuteson, Fred A. Best, William L. Smith*, Paul van Delst, Daniel D. LaPorte, Scott D. Ellington, Mark W.Werner, Ralph G. Dedecker, Ray K. Garcia, Nick N. Ciganovich, H.Benjamin Howell,

Steven Dutcher, and Joe K. Taylor, Validation of Atmospheric InfraRed Sounder (AIRS) Spectral Radiances with the Scanning High-resolution Interferometer Sounder (S-HIS) aircraft instrument In: Proceedings of the International TOVS Study Conference 13, 29 October to 4 November, 2003, Montreal Canada.

2. Smith, W. L., H. B. Howell, and H. M. Woolf, 1979: The use of interferometric radiance measurements for sounding the atmosphere. J. Atmos. Sci., 36, 566-575.

3. Smith, W. L., 1991: Atmospheric soundings from satellites - false expectation or the key to improved weather prediction? Royal Meteorological Society, Symons Memorial Lecture, London, UK, May 16, 1990. J. Roy. Meteor. Soc., 117, 267-297.

4. Smith, W. L., H.E. Revercomb, and G. Bingham, 2000: Geostationary Fourier Transform Spectrometer (GIFTS) – The New Millennium Earth Observing-3 Mission. *Current Problems in Atmospheric Radiation*, A. Deepak Publishing, Hampton, Virginia.

5. Revercomb, H.E., H. Buijs, H.B. Howell, R.O. Knuteson, D.D. LaPorte, W.L. Smith, L.A. Sromovsky, and H.W. Woolf, 1989: Radiometric Calibration of IR Interferometers: Experience from the High-resolution Interferometer Sounder (HIS) Aircraft Instrument. RSRM '87:Advances in Remote Sensing Retrieval Methods, A. Deepak, H. Fleming, J. Theon (Eds.). A. Deepak Publishing, Hampton, Virginia

6. Revercomb, H.E., D.D. LaPorte, W.L. Smith, H. Buijs, D.G. Murcray, F.J. Murcray, and L.A. Sromovsky, 1988a: High-Altitude Aircraft Measurements of Upwelling IR Radiance: Prelude to FTIR from Geosynchronous Satellite. Mikrochimica Acta [Wien], II, 439-444.

7. Aumann, H.H., Chahine, M.T., C. Gautier, M.D. Goldberg, E. Kalnay, L.M. McMillan, H. Revercomb, P.W. Rosenkranz, W.L. Smith, D.H. Staelin, L.L. Strow, and J. Susskind, 2003: AIRS/AMSU/HSB on the Aqua Mission: Design, Science Objectives, Data Products, and Processing Systems. IEEE Transactions on Geoscience and Remote Sensing, 41, p 253-264.

8. Strow, Larabee, L. Strow, S. Hannon, S. Machado, H. Motteler, and D. Tobin, An Overview of the AIRS Radiative Transfer Model, IEEE Transactions on Geoscience and Remote Sensing, Vol. 41, No. 2, Pgs. 303-313, (2003).

9. Xu Liu, "Application of Optimal Spectral Sampling (OSS) Radiative Transfer Model to High Resolution FTIR Measured Radiances", *24th AFRL Transmission Meeting*, 6-8 June 2001.

10. D. Cousins, and W. L. Smith, "National Polar-Orbiting Operational Environmental Satellite System (NPOESS) Airborne Sounder Testbed-Interferometer (NAST-I)", in *Proceedings, SPIE Application of Lidar to Current Atmospheric Topics II*, A. J. Sedlacek, and K. W. Fischer, Eds., **3127**, 323–331, 1997.

11. W. L. Smith, A. M. Larar, D. K. Zhou, C. A. Sisko, J. Li, B. Huang, H. B. Howell, H. E. Revercomb, D. Cousins, M. J. Gazarik, D. Mooney., "NAST-I: results from revolutionary aircraft sounding spectrometer", in *Proceedings, SPIE Optical Spectroscopic Techniques and Instrumentation for Atmospheric and Space Research III*, A. M. Larar, Ed., **3756**, 2–8, 1999

12. W. L. Smith and H. M. Woolf, "The use of eigenvectors of statistical co-variance matrices for interpreting satellite sounding radiometer observations," *J. Atmos. Sci.*, **33**, 1,127–1,140 (1976).

13. D. K, Zhou, W. L. Smith, J. Li, H. B. Howell, G. W. Cantwell, A. M. Larar, R. O. Knuteson, D. C. Tobin, H. E. Revercomb, and S. A. Mango, "Thermodynamic product retrieval methodology for NAST-I and validation," *Applied Optics*, **41**, 6,957–6,967, 2002.

14. J. W. Salisbury, and D. M. D'Aria, "Emissivity of terrestrial material in the 8–14 μm atmospheric window," *Remote Sens. Environ*., **42**, 83–106, (1992).

15. D. K. Zhou, W. L. Smith, and A. M. Larar, "Tropospheric ozone near-nadir-viewing IR spectral sensitivity and ozone measurements from NAST-I," in *Proceedings, SPIE Hyperspectral Remote Sensing of the Land and Atmosphere*, W. L. Smith, and Y. Yasuoka, Eds., **4151**, 277–284 (2001).

16. D. K. Zhou, W. L. Smith, and A. M. Larar, "Surface temperature and emissivity from airborne measurements of IR radiance spectra," *Eos Trans. AGU*, **82**(47) (2001).

17. W. L. Smith, A. M. Larar, S. A. Mango, E. Revercomb., and D.K. Zhou, "The NPOESS Aircraft Sounder Testbed-Interferometer", to be submitted to the Bulletin of the AMS, October, 2002

18. W.L. Smith, G. E. Bingham, G. W. Cantwell, M. J. Gordon, D. K. Zhou, and H-L. Huang, "AIRS Cloud-clearing Using Multi-spectral MODIS Imagery", Available from bill.l.smith@larc.nasa.gov

Effects of GPS/RO refractivities on IR/MW retrievals

Éva Borbás [1], W. Paul Menzel [2], Jun Li [1], and Harold M. Woolf [1]

[1]Cooperative Institute for Meteorological Satellite Studies, University of Wisconsin/Madison
[2]NOAA/NESDIS Office of Research and Applications, Madison, Wisconsin

Abstract

The ability of Global Positioning System Radio Occultation (GPS/RO) to improve tropospheric profile retrievals was examined. Retrievals were performed using IR and MW radiometric measurements from the ATOVS (Advanced TIROS Operational Vertical Sounder) on current NOAA polar orbiting satellites and simulated high spectral resolution infrared measurements from the Cross-track Infrared Sounder (CrIS) planned for the future NPOESS. First a simulation study will be presented wherein a statistical regression is used to get temperature and moisture retrievals from the combination of the ATOVS/CrIS brightness temperatures (BTs) and GPS/RO refractivity data. Retrievals from the ATOVS/CrIS and GPS/RO combination is found to yield tropospheric profiles in better agreement with those from radiosondes than profiles inferred from either system alone. Second, the associated study with real GPS/RO (CHAMP and SAC-C satellite measurements) and sounder (NOAA16/ATOVS) data is also shown.

Introduction

For weather prediction and climate research, accurate observations of the atmospheric moisture and temperature with good temporal and spatial coverage are required. The existing operational meteorological satellites rely primarily on passive radiometric techniques that provide good information on lower tropospheric temperature and upper tropspheric moisture and little information around the tropopause. On the other hand the GPS/RO measurements using active limb sounding technique have been shown to provide accurate information of the upper level temperature and lower tropospheric moisture. While ATOVS IR/MW measurements have good horizontal but limited vertical resolution, the GPS/RO has high vertical resolution (better than 500m for 0-18 km) but limited horizontal resolution (150-300 km). This study examines whether the combination of these two complementary systems are able to provide better quality temperature and moisture profile retrievals around the tropopause region of the atmosphere.

Simulation study - method

The NOAA88 radiosonde (RAOB) dataset containing 7547 temperature and moisture profiles is used to simulate IR and MW BTs representing the NOAA/ATOVS and NPOESS/CrIS measurements, GPS refractivities and surface observations. All 39 channels for ATOVS measurements and a subset of 393 (optimal) channels (from 1403) for CrIS measurements are simulated for this study.

A fast and accurate transmittance model called PFAAST (Pressure–layer Fast Algorithm for Atmospheric Transmittances) (Hannon et al. 1996) is used to simulate ATOVS and CrIS data. Nominal instrument noise plus 0.2 K forward model error is randomly added to the BTs calculated in the simulation. The GPS/RO refractivity profiles are simulated with 1 km vertical resolution between 6 and 28 km from the NOAA88 temperature and moisture profiles using an algorithm provided by the Met Office in the United Kingdom (Healy and Eyre, 2000). Vertically correlated noise is added to the simulated refractivity profiles using the method of Healy and Eyre (2000) and the error estimation of Kurskinski et al. (1997). The surface temperature and moisture observation is inferred from the values at the lowest level of the radiosonde profiles. Errors of 0.5 K and 10 % are assumed for the surface temperature and moisture (mixing ratio) respectively.

A statistical regression approach is used for retrieving temperature and humidity profiles. Both linear and quadratic terms for BTs, GPS/RO refractivities, and surface observations are included in the regression relationship. Regression coefficients are derived from 90 % of all profiles; the remaining 10 % are used for validation. Bias and RMS differences are computed between the retrievals and the true (NOAA88 RAOB) profiles in 1 km vertical layers for temperature profiles and 2 km vertical layers for moisture profiles. The moisture differences are normalized by the true value of the mixing ratio to derive a percentage difference.

Simulation study - results

Retrievals are calculated using different combinations of measurements (ATOVS, CrIS, GPS/RO and surface data): and RMS and bias differences are determined with respect to RAOB profiles (Figure 1). Large RMS values in the retrievals using only GPS/RO data above and below the tropopause region occur because only a vertical subset (between about 400 hPa and 20 hPa) of GPS/RO profiles is used. However, it can be seen that the GPS/RO data plays an important role between 300 hPa and 100 hPa for temperature retrievals and has little effect on moisture retrievals since GPS/RO profiles are used above the 400 hPa, where the water vapor content is small. GPS/RO improves CrIS + AMSU temperature profile retrievals around the tropopause level by 0.4 K and ATOVS temperature retrievals by 0.8 K. More detailed comparisons can be found in the work of Borbas et al. (2003).

There are no differences between ATOVS + GPS/RO and CrIS + GPS/RO temperature retrievals around the tropopause; the GPS/RO provides the main information around the tropopause region, but the differences above and below the tropopause indicate that CrIS measurements improve the profiles between 10 hPa and 700 hPa. Using CrIS data in the moisture retrievals is crucial. A comparison of the ATOVS and CrIS moisture retrievals (the vertical subset of GPS/RO profiles used in this study has no effect on moisture) shows an improvement of more than 10 % leading to an RMS difference between CrIS retrievals and RAOB profiles less than 10 % in every layer of the atmospheric column. The use of surface observations is significant in both the temperature and moisture retrievals (right panels in Fig. 1.).

The impact of various levels of GPS/RO refractivity noise is also studied (Borbas et al., 2003). Even with triple refractivity observation noise, GPS/RO improves ATOVS temperature retrievals by 0.5 K between 85 and 350 hPa pressure levels.

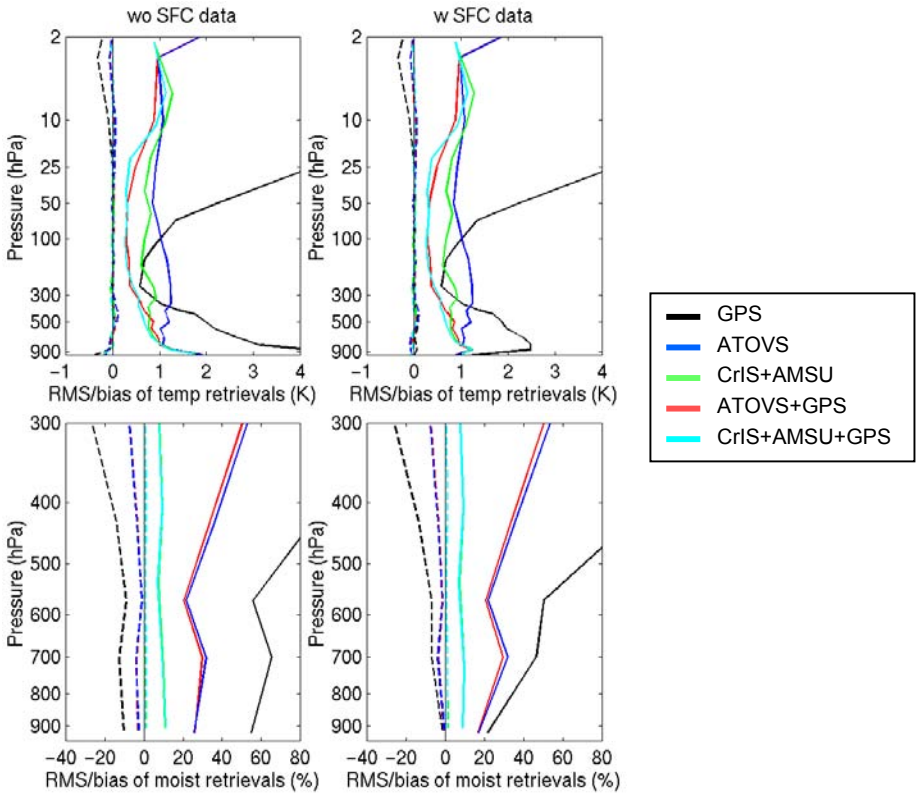

Fig. 1: RMS (solid lines) and bias (dashed lines) differences of the temperature (Kelvin) (top panels) and moisture (percentage difference of derived mixing ratio) (bottom panels) retrievals derived from only GPS (black), only ATOVS (blue), from CrIS + AMSU (green), ATOVS and GPS/RO data together (red), and CrIS + AMSU + GPS data altogether (cyan) with respect to the RAOB profiles. On the right panel surface (SFC) data are also added to all kind of retrievals.

Study with real data – data collection and evaluation

To expand this retrieval study to real data, NOAA16/ATOVS radiance observations are collocated with GPS/RO data measured from the German CHAMP and Argentinean SAC-C satellites. NOAA-16 ATOVS radiances are converted to BTs using the ATOVS and AVHRR Processing Package (AAPP) (Klaes and Schraidt, 1999) and the International ATOVS Processing Package (IAPP) (Li et al., 2000). For each HIRS FOV, a cloud detection algorithm (Li et al. 2000) is applied. In overcast conditions, only AMSU channels are used. GPS/RO and ATOVS collocations are found within 3 hours and 300 km. In cases of multiple collocations, the collocation with more clear pixels or better temporal collocation is chosen. ATOVS BTs are the average of the clear pixel values or the average of all 9 cloudy pixel values in overcast conditions. A simple quality control is performed on the data as follows: data in polar regions (higher than 70 latitude) are excluded from the study and differences exceeding 10 % between GPS/RO and RAOB and GPS/RO and NWP derived refractivity profiles are rejected.

The number of occultations between July 2001 and July 2002 for each GPS satellite is over 25000 separately. The highest density of the GPS observations is around the sub-polar and polar region (one-third of the total number) providing help in this890 data sparse polar region. Validation of GPS/RO refractivity profiles is made with calculated refractivities from interpolated RAOB (for four selected months representing the four seasons) and AVN/NCEP analyses (for the whole year) temperature and moisture profiles. Validation is done separately over the seasons and for different regions of the Earth. Both results (see Fig. 2 and 3) show that the quality of CHAMP data is better (more obvious in the NWP validation, on Fig. 2) than SAC-C. Both CHAMP and SAC-C datasets have large biases in the tropical and mid-latitude areas. Overall, the quality of SAC-C and CHAMP refractivity data is within 1% (the estimated error of the refractivity profiles was 0.3 %).

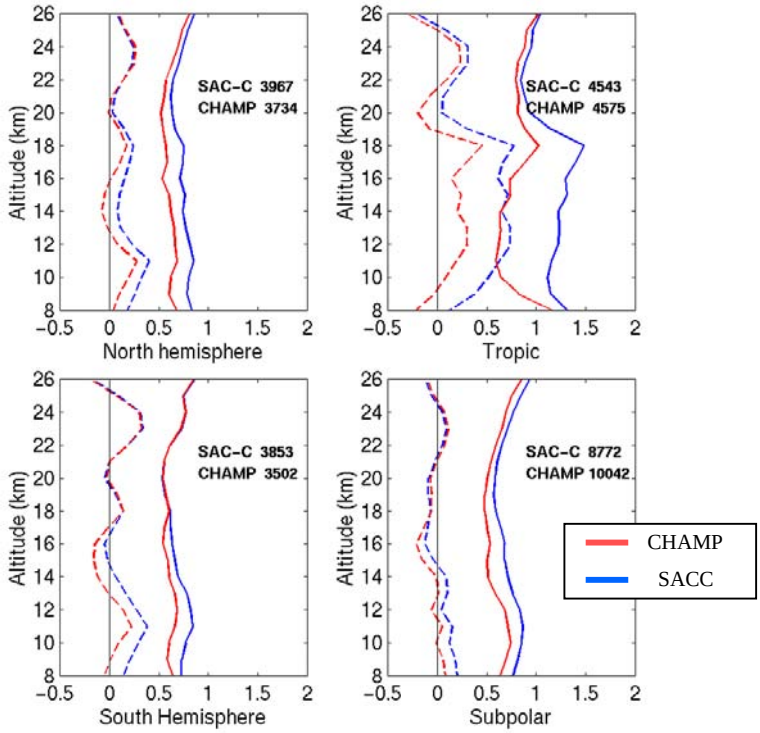

Fig. 2: Validation of CHAMP (red lines) and SAC-C (blue) refractivities profiles (in percentage of refractivity units) with computed profiles from the NCEP analyses between July 2001 and May 2002. The collocations are separated for four regions: Tropical (between 0° and ±25° latitude), North and South mid-latitude (between 25° and 50° latitude in the northern and southern hemisphere) and sub polar (between 50° and 70° in both northern and southern hemisphere) region. Solid lines indicate the RMS and dashed lines indicate the bias differences. The number of collocations is also shown.

Study with real data – validation of temperature retrievals

Collocated ATOVS BTs and CHAMP and SAC-C refractivities are regressed against NWP (AVN/NCEP) profiles to generate algorithm coefficients. ATOVS and CHAMP/SAC-C data collocated with RAOBs are used for validation and are excluded from the regression calculations.

CHAMP refractivities at 23 levels (between 8 and 30 km with 1 km vertical resolution), 16 HIRS BTs (excluding channels 17-19, the short wave infrared), 12 AMSU-A BTs (excluding channels 1,2 and 15), and 4 AMSU-B BTs (excluding channel 1) are used in the regression to determine temperature profiles.

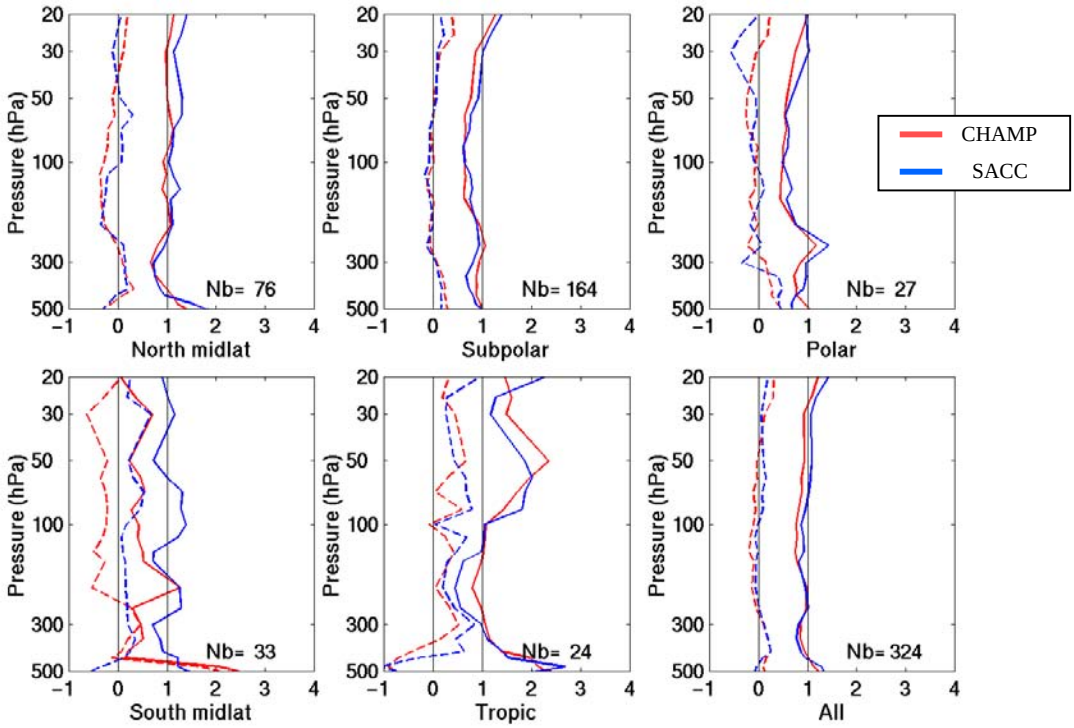

Fig. 3: Validation of CHAMP (red lines) and SAC-C (blue) refractivities profiles (in percentage of refractivity unit) with computed profiles from RAOB temperature and moisture profiles for April 2002 between 20 hPa and 500 hPa pressure levels. The collocations are separated for the same regions as Figure 2, but polar region (latitude higher than ±70°) and all cases (right bottom panel) is also added. Solid lines indicate the RMS and dashed lines indicate the bias differences. The number of the collocation is also shown.

Figure 4 shows temperature retrievals using only ATOVS and ATOVS + GPS/RO data compared to collocated RAOB data for four months (Oct 2001, Jan, Apr, and Jul 2002). The validation is done for cloudy and clear skies separately. The preliminary study with real data shows that the GPS/RO data has a positive impact on the ATOVS temperature retrievals from 670 hPa up to 25 hPa. GPS/RO (both CHAMP and SAC-C) data improves the radiometric (ATOVS) temperature retrievals around the tropopause by 0.5 K. In cloudy conditions the impact is larger than in clear skies.

Conclusions and Future Plans

The effect of GPS/RO measurements around the tropopause region on radiometric (infrared and microwave) tropospheric profile retrievals was studied.

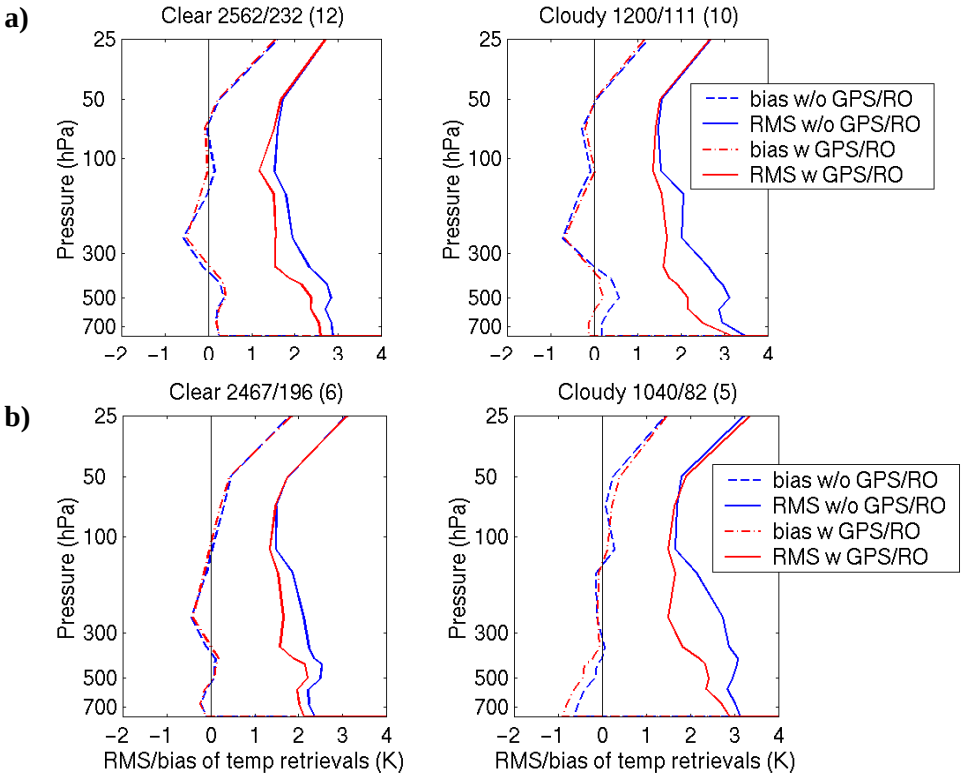

Fig. 4: RAOB validation of ATOVS temperature retrievals with (blue lines) and without (red) GPS/RO CHAMP (a) and SAC-C (b) data for four months (Oct 2001, Jan, Apr, and Jul 2002) separated into clear and cloudy situations. For each panel, the first number in the title indicates the number of training cases (using AVN NWP analyses), the second is the number of the test cases (with collocated RAOB profiles), and the third (in brackets) is the number of rejected (filtered) profiles. Dashed lines indicate the bias and solid lines indicate the RMS differences between the retrievals and the RAOB profiles.

A simulation study and a study using real data were presented wherein a statistical regression was used to generate temperature and moisture retrievals from the combination of passive (IR and MW sounders) and active (GPS/RO) systems. The simulation study shows that the combined systems produce improved tropospheric temperature profiles in comparison with radiosonde profiles over those inferred from either system alone. GPS/RO improves the ATOVS temperature profile retrievals by 0.8 K and the advanced IR sounder (CrIS) temperature retrievals by 0.4 K around the tropopause.

CHAMP and SAC-C refractivity measurements were compared with radiosonde and NWP analyses derived values. The measured and calculated refractivities have good agreement with RMS differences less than 1%.

The study of temperature profiles regressed from CHAMP/SAC-C and ATOVS data for four selected months representing the four seasons reveal that CHAMP/SAC-C refractivity measurements improve the ATOVS retrieval comparisons to radiosonde determinations. Near the

tropopause at least 0.5 K improvement is found in clear conditions; the improvement over the cloudy skies is even larger.

Future work will be to increase the number of collocations, to use a larger vertical subset of GPS/RO refractivity profiles closer to the surface with more information about the moisture content of the lower troposphere, and to study combined retrievals with real CHAMP/SAC-C, AIRS (Atmospheric Infrared Sounder) plus AMSU data.

Acknowledgments

We thank GeoForschungsZentrum and the Jet Propulsion Laboratory for providing CHAMP and SAC-C data. The authors also acknowledge the Met Office for providing the forward model of GPS/RO refractivity. This work was supported in part by NOAA Cooperative Agreement NAO7EC0676.

References

Borbas, E., Menzel, W.P., Li, J. and Woolf, H.M. 2003: Combining radio occultation refractivities and IR/MW radiances to derive temperature and moisture profiles: a simulation study plus early results using CHAMP and ATOVS. J. Geophys. Res., 108(D21), 4676, doi:10.1029/2003JD003386, pp. ACL 9,1-15.

Healy, S.B. and Eyre, J.R. 2000. Retrieving temperature, water vapour and surface pressure information from refractivity-index profiles derived by radio occultation: A simulation study. Q. J. R. Meteorol. Soc., 126, 1661-1683.

Hannon, S., Strow and McMillan, W.W. 1996. Atmospheric infrared fast transmittance models. A comparison of two approaches. in Proceedings of SPIE, 2830, 94-105.

Klaes, K.D. and Schraidt, R. 1999. The European ATOVS and AVHRR Processing Package (AAPP) development. in Technical Proceedings of the Tenth International ATOVS Study Conference, Boulder, Colorado, 288-294.

Kursinski, E.R., Hajj ,G.A., Schofield, J.T., Linfields, R.P. and Hardy, K.R. 1997. Observing Earth's atmosphere with radio occultation measurement using the Global Positioning System, J Geophys Res., 102, 23,429-23,465.

Li, J., Wolf, W., Menzel, W.P., Zhang, W., Huang, H-L. and Achtor, T.H. 2000. Global Sounding of the Atmosphere from ATOVS Measurements: The Algorithm and Validation, J. Appl. Meteor., 39, 1248-1268.

Characterization of troposphere and land surface properties from CMIS

Presenter: Alan Lipton

Jean-Luc Moncet and Alan Lipton
AER Inc.

The NPOESS Conically-scanning Microwave Imager/Sounder (CMIS) will provide polarimetric measurements in the range 6-183 GHz. CMIS will combine capabilities of AMSR, WindSat and SSMIS, in that it will enable the retrieval of soil moisture, ocean surface wind direction, and mesospheric temperature, in addition to the more traditional microwave land/surface environmental variables. The combination of sounding and imaging channels on the CMIS instrument will be exploited to enhance both surface and lower atmosphere characterization and maintain physical consistency between the atmosphere and surface variables. In particular, the presence of vertically and horizontally polarized channels near 23 GHz and in window regions, together with the presence of sounding channels, will open the door to significant advances in assimilation or retrieval of lower atmosphere data over land. In addition, there are plans to quantify the impact of incorporating the information provided by VIIRS and CrIS, on the same platform, on the system performance over land and on the EDR quality control.

Progress on the New Generation of Chinese Meteorological Satellites and Some Applications

DONG Chaohua*, ZHANG Wenjian

National Satellite Meteorological Center of CMA,
46, Zhong GuanCun Nan Dajie, Beijing 100081, CHINA

Abstract

This paper concentrates on the recent research progress, such as the applications in dust storm, cloud thermodynamic phase analysis and numerical weather prediction, as well as the new generation of Chinese meteorological satellite programs.

Keyword: Meteorological satellite, new generation, dust storm, radiance

1. Introduction

The National Satellite Meteorological Center (NSMC) was established within the Chinese Meteorological Administration (CMA) in 1970. The responsibility of NSMC is to operate, manage, and improve the Nation's operational meteorological satellite system; to make requirements for new satellites; to archive and disseminate satellite data/ products to meet the need of users in public, decision making, private, and scientific research programs.

China has Launched six meteorological satellites, four of them are sun-synchronous, two of them are geostationary satellites, and will continue its two types of meteorological satellite programs. Characteristics of the Chinese new generation payload for polar orbit are described specifically in this paper. The new generation for Chinese geostationary Meteorological satellite is only in a proposal stage. This paper just briefly introduces the current progress on meteorological satellite application research and new generation of Chinese Meteorological satellite programs.

2. New Generation of Chinese Meteorological Satellites

2.1 Polar orbiting meteorological satellite

FY-3 series, the second generation of Chinese polar orbiting meteorological satellites is now under construction. The first satellite will be launched in 2006. The main mission objectives of FY-3 are:

- To provide global sounding of 3-dimensional atmospheric thermal and moisture structures, cloud and precipitation parameters to support global numerical weather prediction.
- To provide global images to monitor large scale meteorological and/or hydrological disasters and biosphere environment anomalies.
- To provide important geophysical parameters to support study on global change and climate prediction.
- To perform data collection.

To achieve the above objectives, the FY-3 system satellites will have a meteorological and

* Dchua@nsmc.cma.gov.cn; Phone (86-10)68406237; fax (86-10)62172724

environmental payload as follows:

- The Imaging Mission:
  - VIRR Visible and InfRared Radiometer
  - MERSI Medium Resolution Spectral Imager
  - MWRI Microwave Radiation Imager

- The Sounding Mission
  - IRAS InfraRed Atmospheric Sounder
  - ASI Atmospheric Sounding Interferometer
  - MWTS MicroWave Temperature Sounder
  - MWHS MicroWave Humidity Sounder
  - SBUV Solar Backscatter Ultraviolet Sounder
  - TOU Total Ozone Unit

- The Complementary Mission
  - SIM Solar Irradiation Monitor
  - ERM Earth Radiation Measurement
  - SEM Space Environment Monitor

FY-3 will have a sun-synchronous orbit at 836km, crossing the Equator in a southward direction at 1010 Local time. The spacecraft will weigh a total of 2200kg.The number of channels, scan spots and spatial resolution for each instrument are listed in Table 2.1.

Table 2.1 Basic Information for each Instrument

Name of Instrument	Number of Channels	Field of Views /line	Spatial Resolution at Sub point
VIRR	10	2048	1.1
IRAS	26	56	17
MWTS	4	15	50/75
MWHS	5	90	15
MERSI	20	2048/8192	1.1/250
SBUS	12	240	70/10
TOU	6	31	50
MWRI	6	240	15-70
ASI	TBD		

The characteristics of VIRR, IRAS, WWTS, WMHS, MERSI, SBUS, TOU are shown in Tables 2.2-2.9, respectively.

Table 2.2 Visible and Infrared Radionmeter (VIRR) Channel Characteristics

Channel No.	Wavelength (μm)	Dynamic range	Detecting Sensitivity
1	0.58~0.68	ρ : 0~90%	S/N≥3(ρ =0.5%)
2	0.84~0.89	ρ : 0~90%	S/N≥3(ρ =0.5%)
3	3.55~3.95	190~340K	NE Δ T≤0.4K(300K)
4	10.3~11.3	190~330K	NE Δ T≤0.22K(300K)
5	11.5~12.5	190~330K	NE Δ T≤0.22K(300K)
6	1.58~1.64	ρ :0~80%	S/N≥3(ρ =0.5%)
7	0.43~0.48	ρ :0~50%	S/N≥3(ρ =0.5%)
8	0.48~0.53	ρ :0~50%	S/N≥3(ρ =0.5%)
9	0.53~0.58	ρ :0~50%	S/N≥3(ρ =0.5%)
10	0.900~0.965	ρ :0~90%	S/N≥3(ρ =0.5%)

Table 2.3 IRAS Channel Characteristics

Channel No.	Channel Central		Half-Power Band Width (cm^{-1})	Main Absorber	Max.Scene Temperature (K)	NE△N (mW/m^2-sr-cm^{-1})
	(ch^{-1})	(μm)				
1	669	14.95	3	CO_2	280	4.00
2	680	14.75	10	CO_2	265	0.80
3	690	14.49	12	CO_2	250	0.60
4	703	14.22	16	CO_2	260	0.35
5	716	13.97	16	CO_2	275	0.32
6	733	13.84	16	CO_2/H_2O	290	0.36
7	749	13.35	16	CO_2/H_2O	300	0.30
8	802	12.47	30	Window	330	0.20
9	900	11.11	35	Window	330	0.15
10	1030	9.71	25	O_3	280	0.20
11	1345	7.43	50	H_2O	330	0.23
12	1365	7.33	40	H_2O	285	0.30
13	1533	6.52	55	H_2O	275	0.30
14	2188	4.57	23	N_2O	310	0.009
15	2210	4.52	23	N_2O	290	0.004
16	2235	4.47	23	CO_2/N_2O	280	0.006
17	2245	4.45	23	CO_2/N_2O	266	0.006
18	2388	4.19	25	CO_2	320	0.003
19	2515	3.98	35	Window	340	0.003
20	2660	3.76	100	Window	340	0.002
21	14500	0.69	1000	Window	100%A	0.10%A
22	11299	0.885	385	Window	100%A	0.10%A
23	10638	0.94	550	H_2O	100%A	0.10%A
24	10638	0.94	200	H_2O	100%A	0.10%A
25	8065	1.24	650	H_2O	100%A	0.10%A
26	6098	1.64	450	H_2O	100%A	0.10%A

Table 2.4 MWTS Channel Characteristics

Channel No.	Central Frequency (CHz)	Main Absorber	Band Width (MHz)	NE△T (k)	Antenna Beam Efficiency (%)	Dynamic Range (K)
1	50.30	Window	180	0.5	>90	3-340
2	53.596±0.115	O_2	2X170	0.4	>90	3-340
3	54.94	O_2	400	0.4	>90	3-340
4	57.290344	O_2	330	0.4	>90	3-340

Table 2.5 MWHS Channel Characteristics

Channel No.	Central Frequency (CHz)	Main Absorber	Band Width (MHz)	NE△T (k)	Antenna Beam Efficiency (%)	Dynamic Range (K)
1	150(V)	Window	2000	0.9	⩾95%	3-340
2	150(H)	Window	2000	0.9	⩾95%	3-340
3	183.31±1	H2O	500	1.1	⩾95%	3-340
4	183.31±3	H2O	1000	0.9	⩾95%	3-340
5	183.31±7	H2O	2000	0.9	⩾95%	3-340

Table 2.6 Moderate Medium Spectral Imager (MERSI) Channel Characteristics

Channel No.	Central Wavelength (μm)	Band Width (μm)	Sub-point Resolution (m)	NEΔT ρ (%) K (300K)	Dynamic Range(ρ),(K)
1	0.470	0.05	250	0.45	100%
2	0.550	0.05	250	0.4	100%
3	0.650	0.05	250	0.3	100%
4	0.865	0.05	250	0.3	100%
5	11.25	2.5	250	0.4K	330K
6	0.412	0.02	1000	0.1	80%
7	0.443	0.02	1000	0.1	80%
8	0.490	0.02	1000	0.05	80%
9	0.520	0.02	1000	0.05	80%
10	0.565	0.02	1000	0.05	80%
11	0.650	0.02	1000	0.05	80%
12	0.685	0.02	1000	0.05	80%
13	0.765	0.02	1000	0.05	80%
14	0.865	0.02	1000	0.05	80%
15	0.905	0.02	1000	0.10	90%
16	0.940	0.02	1000	0.10	90%
17	0.980	0.02	1000	0.10	90%
18	1.030	0.02	1000	0.10	90%
19	1.640	0.05	1000	0.05	90%
20	2.130	0.05	1000	0.05	90%

Table 2.7 Solar Backscatter Ultraviolet Sounder(SBUS) Channel Characteristics

Channel No.	Central Wavelength (nm)	Band Width (nm)
1	252.00±0.05	1+0.2, -0
2	273.62±0.05	1+0.2, -0
3	283.10±0.05	1+0.2, -0
4	287.70±0.05	1+0.2, -0
5	292.29±0.05	1+0.2, -0
6	297.59±0.05	1+0.2, -0
7	301.97±0.05	1+0.2, -0
8	305.87±0.05	1+0.2, -0
9	312.57±0.05	1+0.2, -0
10	317.56±0.05	1+0.2, -0
11	331.26±0.05	1+0.2, -0
12	339.89±0.05	1+0.2, -0
Cloud Cover Radiometer	379.00±1.00	3+0.3

Table 2.8 Total Ozone Unit (TOU)
Channel Spectrum Characteristics

Channel No.	Central Wavelength (nm)	Band Width (nm)
1	308.68±0.15	1+0.3, -0
2	312.59±0.15	1+0.3, -0
3	317.61±0.15	1+0.3, -0
4	322.40±0.15	1+0.3, -0
5	331.31±0.15	1+0.3, -0
6	360.11±0.25	1+0.3, -0

Table 2.9 Microwave Radiation Imager (MWRI) Channel Spectrum Characteristics

Channel No.	Central Frequency (GHz)	Polarization	Main Absorber	Band Width (MHz)	NE△T (K)	Antenna Beam Efficiency	Dynamic Range (K)
1	10.65	V.H	Window	180	0.5	≥90%	3-340
2	18.7	V.H	Window	200	0.5	≥90%	3-340
3	23.8	V.H	H2O	400	0.8	≥90%	3-340
4	36.5	V.H	Window	900	0.5	≥90%	3-340
5	89	V.H	Window	4600	1.0	≥90%	3-340
6	150	V.H	Window	3000	1.3	≥90%	3-340

2.2 Geostationary meteorological satellites

Geostationary meteorological satellite FY-4 series, the second generation of Chinese geostationary meteorological satellites is now in the concept design phase. Considerations for the FY-4 system are as follows:

- Three-Axis stabilization
- More powerful imager
- Sounding capability
- Lightning detection
- Data collection
- Powerful ground control capability
- Application and services system

FY-4 is expected to be launched beyond 2010.

3. Progress on Satellite Applications

3.1 Real time monitor and quantitative prediction of Northeast Asian dust storms

From spring to early summer, dust storms frequently occur in Northeast Asian (in some places throughout the year). Northern China was seriously affected by a dust storm and dust weather system in spring. These dust storms and dust weather systems are generally generated in the drought and part drought areas at middle latitudes, which just have a sparse vegetation coverage, as strong winds entrain large quantities of dust particles into the atmosphere and carry them over large distances downstream. These dust storms have a severe impact upon the air quality in regions downwind of the dust sources. The real-time monitoring and prediction of dust storms therefore are highly desirable as a meteorological service to the public.

The payload of meteorological satellites has several spectral regions located at visible, near infrared, infrared and microwave bands so the satellite sensors can receive reflection, emission and absorption from the observed targets, such as aerosol, clouds, and earth's surface. Based on different spectral signatures, the geophysical parameters can be obtained.

As the meteorological satellites have a wide monitoring scale, good time frequency and spatial resolution and high precision, it is the most effective way for monitoring dust storms (Zheng et al., 2002). A 24 hour operational dust storm monitoring system by using both geostationary and polar orbiting satellite data was established in NSMC/CMA on March 1, 2001. With this system, we can dynamically monitor dust storms, analyze dust storm sources and transport paths, as well as calculate dust storm range of influence and aerosol strength.

A detailed analysis has been done on the influence of dust storms reaching Beijing. We find that there are two major sources of dust storm, one is in Mongolia, the other is in the Inner Mongolia Autonomous Region and northern part of Hebei province in 2002. Affected by the Mongolian cyclone and cold front systems in spring, the dust storm occurred in Mongolia and continuously strengthened on the way, it would affect a wide area and had a high strength.

The dust storm influencing Beijing has three paths based on the meteorological satellite observations, during the spring time of 2002. A. from Mongolia to Beijing via Hunsandake Desert in the Inner Mongolia Autonomous Region and Hei-he in Hebei province; B. from Zhurihe to Beijing via Zhangjiakou in Hebei province; C. from north Shanxi province to Beijing via Shanggan-he in Hebei province.

The form of dust storm is a very complicated physical process, such as atmospheric movement, type of land surface, dust emission etc. The prediction model of dust activities must involve the key processes of dust emission, dust transport and dust deposition. It requires the coupling of the dust emission scheme with an atmospheric model, supported by other modules and adequate land-surface parameter, i.e., the establishment of an integrated modeling system. The theory and model framework can be found in several publications (Shao 2001; Shao et al., 2002).

In order to test the integrated modeling system, a joint working group in which the scientists are from different institutes, such as the CMA, the Chinese Academy of Science and City University of Hong Kong, China, did 24, 48 and 72hr forecasts of Northeast Asian dust events for March and April, 2002. The results are validated with synoptic records from the meteorological network and dust concentration measurements at 12 stations in China, Japan and Korea. The predicted spatial patterns and temporal evolution of dust events and the predicted near-surface dust concentrations are found to agree well with the observations (see Figure 3.1). In Figure 3.2, successive forecasts of near surface dust concentration for the 10-day period between 15 and 24 March 2002 are compared with observations. The figure demonstrates that the modeling system well predicted the spatial distributions and temporal evolutions of all dust events in this period of time (Shao et al., 2003).

We have determined the total dust emission, total dust deposition and total dust load for the

entire domain of simulation and have found that the total dust emission is on average 11.5 $x10^6$ tn day^{-1} (maximum 65.7 $x10^6$ tn day^{-1}); total dust deposition is 10.8 $x10^6$ tn day^{-1} ((maximum 51.4 $x10^6$ tn day^{-1}) and total dust load is 5.5 $x10^6$ tn with a maximum of 15.9 $x10^6$ tn.

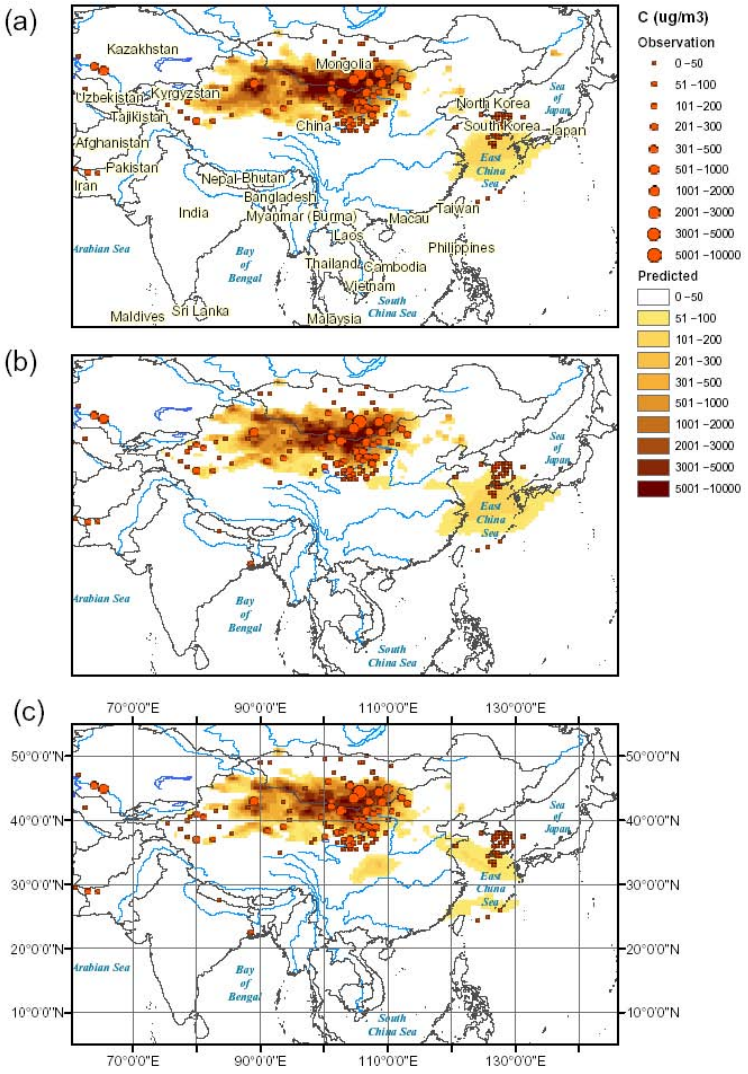

Figure 3.1: Comparisons of the predicted and observed near surface dust concentration for March 19. (a) the 24hr forecast; (b) the 48hr forecast; and (c) the 72hr forecast. Full dots represent the stations where dust activities were observed and the size of dots represents the magnitude of dust concentration.

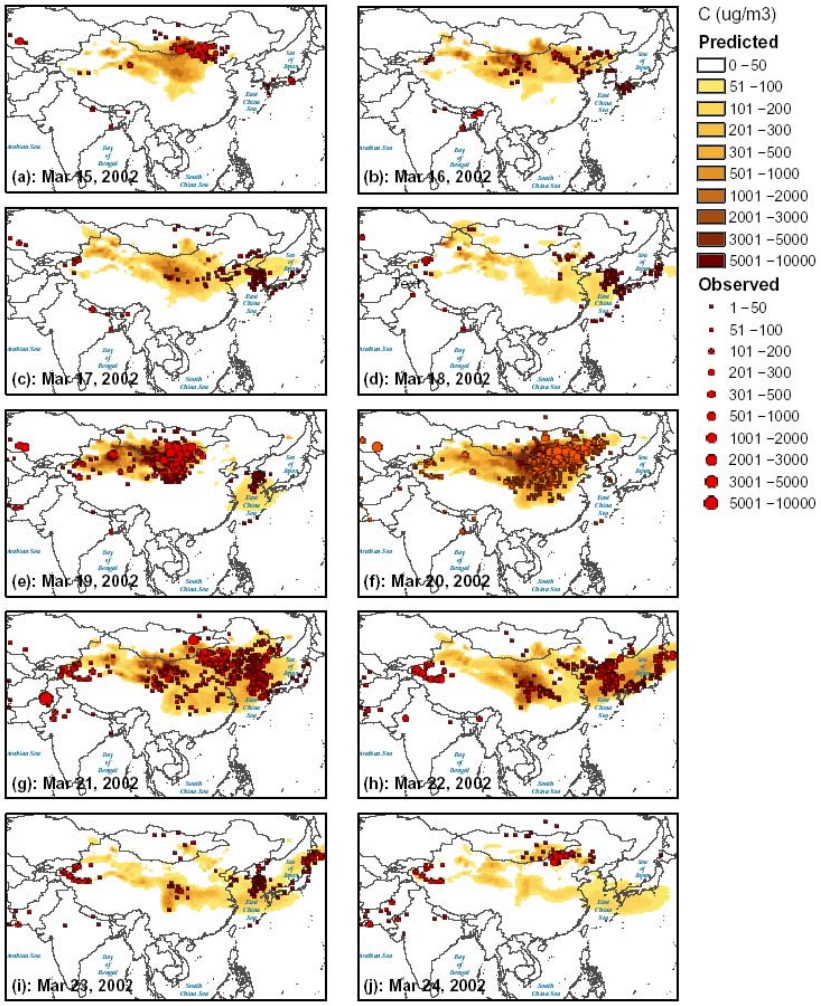

Figure 3.2: Comparisons of the predicted and observed near surface dust concentration for 10 successive days from 15 to 24 March 2002. The model results are the 24hr forecasts.

3.2 Thermodynamic phase analysis of cloud particles with FY-1C satellite data

There are many studies determining cloud particle thermodynamic phase. The underlying principle that these techniques are based on is the fact that water and ice have different absorption at 1.6μm. The ice has larger absorption at 1.6μm, so it has a lower reflectance and water has the contrary properties. Thus reflectance at 1.6μm is sensitive to the thermodynamic phase of cloud. The FY-1C polar orbiting meteorological satellite, which was launched on May 10 1999, has ten spectral channels that cover the visible, near infrared and infrared spectral bands. These data are very useful for the research of cloud particle thermodynamic phase.

According to the model calculations, one can infer that optical thickness affects the reflectance at 0.65μm greatly, the thicker optical thickness, the larger the reflectance. There is almost a linear relationship between the reflectance and optical thickness at 0.65μm. The reflectance increases monotonically at 0.65μm as a function of cloud optical thickness. The reflectance at 1.6μm is affected greatly by the effective radius of particles, the larger effective radius the smaller the reflectance. So it is known that there is a larger difference of the

reflectance between 0.65μm and 1.6μm and the reflectance at 1.6μm is smaller than that at 0.65μm when the cloud particle effective radius becomes larger. Thus ice cloud can be distinguished from water cloud by using the reflectance difference.

Case studies indicate that FY-1C multi-channel data can be efficiently used for detecting clouds and thermodynamic phase of cloud particles (Liu et al., 2002). It is helpful to improve the accuracy of geophysical parameters retrieval from meteorological satellite data. Figure 3.3 illustrates the cloud analysis results.

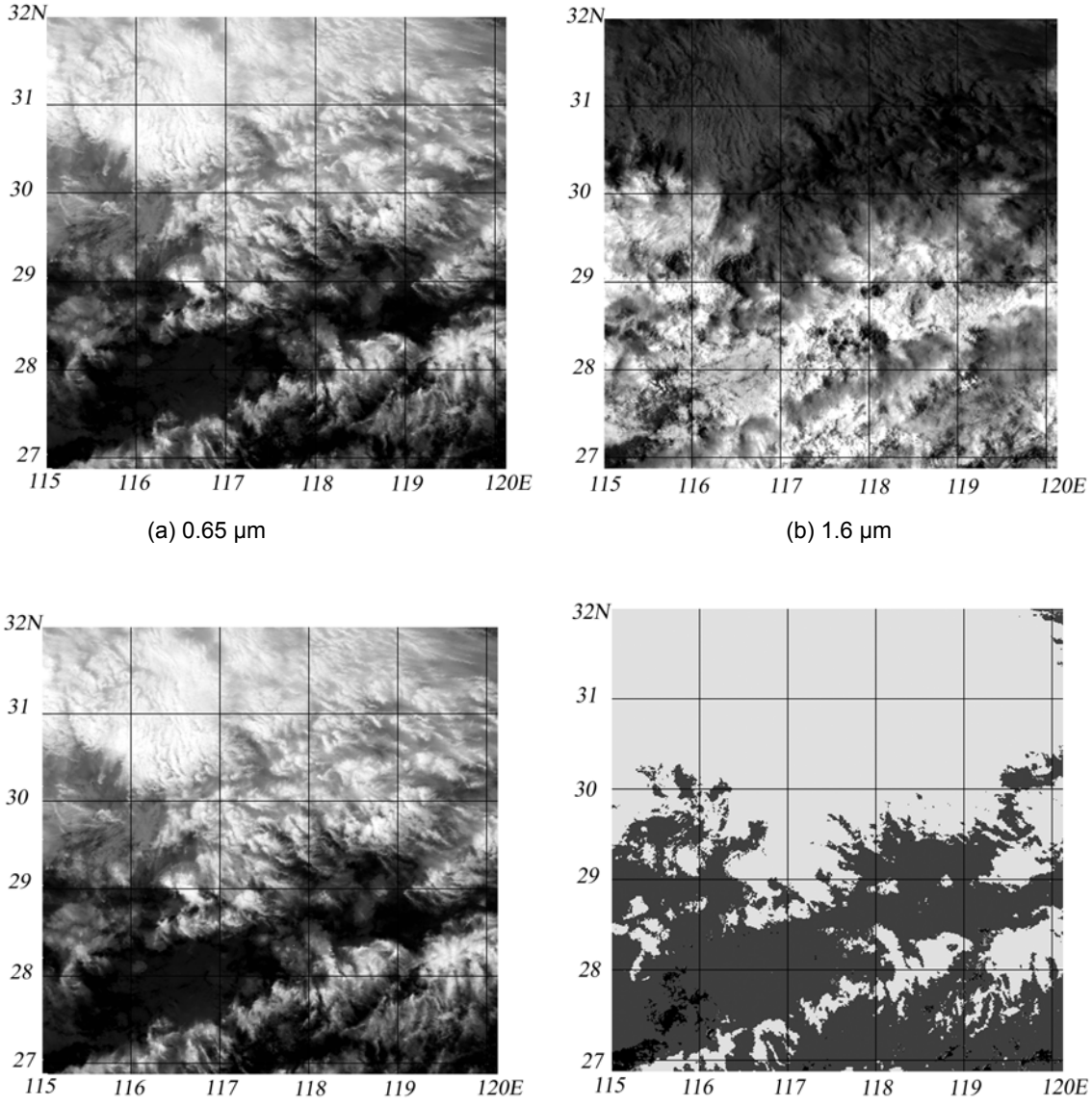

(a) 0.65 μm (b) 1.6 μm

(c) 11 μm (d) result

Figure 3.3: (a) - (c) are the 0.65 μm, 1.6 μm and 11 μm images, (d) is cloud particle thermodynamic phase results: White is ice cloud, Grey is water cloud, Black is clear

3.3 Study on 3D-VAR direct assimilation of ATOVS radiance data in NWP

Two comparison experiments, named NOAMSUA and AMSUA respectively, are carried out to simulate a very heavy rainstorm which occurred in Wuhan City and the region to the east in

July 21-22, 1998 with the incremental form of three-dimensional variational method (3D-Var) being used as the data assimilation method, and MM5 mesoscale numerical model as the assimilating and forecast model. NOAMSUA experiment assimilates radiosonde observations only, whereas AMSUA assimilates simultaneously radiosonde observations and channel brightness temperatures detected by AMSU-A which is carried on NOAA-15. The forward integration of MM5 prediction model in two comparison experiments are both conducted with assimilation analyses as model initial conditions (Pan et al., 2003).

The comparison results show that assimilating AMSU-A brightness temperature adjusts the temperature background of the middle and upper atmosphere more distinctly and the prediction of basic elements such as temperature is mostly better in the AMSU-A experiment than in the NOAMSUA experiment, which means that directly assimilating AMSU-A data has a positive impact on MM5 model prediction as a whole. It is also found in each comparison experiment that the different simulations not only influence the system of the rainstorm, southwest vortex and shear at low level but also the precipitation area. A strong precipitation phase is preferable, and the prediction of precipitation intensity almost achieves actual intensity level although prediction of 6-hours-precipitation amount is much less than actual value. Due to using AMSU-A radiances which mainly contains information of vertical air temperature distribution, assimilating AMSU-A data acts less on adjusting background of water vapor mixing ratio, which results in simulation of precipitation in AMSUA experiment not being improved too much over that in NOAMSUA experiment.

4. Summary

Meteorological satellite observations include rich information, which requires us to make great contributions to retrieval theory and algorithms. Starting from the FY-3, Chinese Meteorological satellites have a sounding capability. The FY series, with the combination of GEO/LEO satellites, will make contributions to the regional and global weather forecasting, climate and environment monitoring.

References

1. Zheng xinjiang, j. Luo, W. lu, and S. Sun, Research on Monitoring Dust Storm Using Meteorological Satellite Data, J. of Natural Disasters, 11, 210-216 (in Chinese), 2002.
2. Shao yaping, A Model for Mineral Dust Emission, J. Geophys. Res. 106, 20239-20254, 2001.
3. Shao yaping, Jung, E. J., and Leslie, L. M., Numerical Prediction of Northeast Asian Dust Storms Using an Integrated Wind Erosion Modeling System, J. Geophys. Res, 107, 4814-4824, 2002.
4. Shao, et al., Real-time Numerical Prediction of Northeast Asian Dust Storms Using an Integrated Modeling System, J. Geophys. Res (in press), 2003.
5. Liu-jian, C. Dong, and X. zhu, Thermodynamic Phase Analysis of Cloud Particles with FY-1C Data, Meteorol. Atmos. Phys. 80, 65-71, 2002.
6. Pan Ning, C. Dong, and W. Zhang, The Experiments on Direct Assimilationg ATOVS Radiance, ACTA Meteorological Sinica, 61, 226-236(in Chinese), 2003.

CURRENT AND FUTURE SATELLITE PROGRAMS AND SYSTEMS IN INDIA

Devendra Singh and R.C.Bhatia
India Meteorological Department,
Lodhi Road, New Delhi-110003, India
Email: dschahar@hotmail.com

ABSTRACT

This paper describes the technical details and status of currently operational satellites of INSAT series. The last satellite of INSAT-1 series (INSAT-1D) was deactivated on 14 May 2002 after providing useful services for about 12 years. A new dedicated meteorological satellite (KALPANA-I) has been successfully commissioned recently. The last satellite of INSAT-2 series (INSAT-2E) has also been providing useful cloud imagery data in 3-channels of CCD - payload at 1 km resolution. **.** Another Indian Geostationary multipurpose satellite, INSAT-3A, with VHRR, CCD and DRT payloads has become operational since April 2003**.** The other communication based operational services being derived from INSAT series of satellites are also described in this paper, along with the activities of India Meteorological Department related to application of satellite products in day-to-day operational use. Details of bilateral collaboration program with USA for exchange of INSAT data are also given.

Introduction

INSAT is an operational multipurpose satellite system catering to the needs of three different services - Television & Radio Broadcasting, Communications and Meteorology. The INSAT project is a joint venture of the Department of Telecommunications (DOT), the India Meteorological Department (IMD), Doordarshan and All India Radio (AIR). The responsibility for overall management and coordination of the INSAT system among the user agencies rests with the INSAT co-ordination committee (ICC).

The first satellite INSAT-1A of the INSAT-1 series was launched in April 1982 and it ceased to function totally from 6 September 1982 as a result of major anomaly on the satellite. The second satellite (INSAT-1B) was launched on 30 August 1983 and it became operational on 15 October 1983. It was the main operational satellite all through the 1980s and provided very good services during its entire mission life. It was deorbited in July 93. The third satellite of the series (INSAT-1C) was launched on 22 July 1988. Due to some technical problem it lost control on 22nd November 1989 after which it was not available for operational services. The last satellite of INSAT-1 series (INSAT-1D) was launched on 12 June 1990 and became operational on 17 July 1990. After having provided services for nearly 12 years, INSAT-1D reached its end of life on 13th May 2002.

The 2nd generations of INSAT satellites (INSAT-2 series) were started from July 1992 with the successful launch of the first satellite of the series (INSAT-2A) on 10th July 92. The 2nd satellite of INSAT-2 program (INSAT-2B) was also launched successfully on 22 July 1993. All INSAT satellites are three-axis body stabilized spacecrafts. The last satellite of INSAT-2 series i.e., INSAT-2E was launched successfully on 3 April 1999. It is operational from May 1999. It has a new payload, called Charged Coupled Device (CCD) capable of taking 1 km resolution images in 3 bands. The meteorological imaging capability has also been upgraded on this satellite, as compared to its predecessors, by providing a water vapor channel with 8 km resolution in the VHRR, the imaging instrument of the satellite. However, on account of some limitations, the VHRR data is of limited use. A new satellite KALPANA-I has been launched on 12th Sept. 2002 and has been declared operational with effect from 25th Sept. 2002. This satellite has VHRR (Vis, IR & Water vapor) and Data Relay Transponder (DRT) on board

and is exclusively dedicated to Meteorological services of the country. Recently INSAT-3A was launched in April 2003 that is having identical payloads as INSAT-2E.

1.1 Current operational status

The imaging mission is working satisfactorily with KALPANA-I satellite and it continues to be used operationally from 74^{o}E longitude position. High resolution (1km) images in 3 channels are also available operationally from CCD camera onboard INSAT-2E. The activities like image processing, derivation of meteorological products, data archival and dissemination of products to field stations for operational use are being done on an operational routine basis.

VHRR images are normally received at three- hourly intervals. More frequent images are taken for monitoring the development of special weather phenomena such as tropical cyclones and adverse weather conditions as and when the situation demands. CCD images from 2E are also being taken every three hours for operational use during daytime. More frequent images are also taken if situation demands. However, due to some anomaly in scan mechanism VHRR onboard INSAT-2E is not currently available for operational use and INSAT-3A that was launched in April 2003 is expected to takeover the INSAT-2E operational jobs after the validation of the products is completed. For the derivation of CMVs half hourly triplets at 00 UTC is also received from KALPANA-I and data processed operationally. The KALPANA-I derived CMVs are available on GTS. The details of present and past satellites of INSAT-1 and INSAT-2 series are given in Table 2 and 3.

1.2 Characteristics of VHRR payload

THE VHRR onboard KALPANA-I includes:

A visible channel operating in the spectral wavelength of 0.55-0.75 microns.
Infrared (IR) channel operating in 10.5-12.5 microns.
Water Vapor channel operating at 6.7 microns.

Main differences between INSAT-1, INSAT-2 and KALPANA-I are in VHRR resolution; scan time, data rate and frequency of transmission that are given in Table-1.

INSAT-2E is located at 83 deg E longitude and provides imaging capability at 1 km resolution in 3 channels of visible, Near IR and Short-wave infrared. INSAT data are being processed at IMD facility “INSAT Meteorological Data Processing System (IMDPS)” located in IMD’s campus at Lodi Road, New Delhi.

The processing system is configured around eight VAX Computers in a clustered network, with a number of other peripheral devices attached. The processed data and products are stored for database. Users can access the database in real-time through four workstations connected to the system. Imagery data of main synoptic hours are being archived as hard copies. Processed 8 bit imagery data are also archived on magnetic tapes at 6250 BPI for later use in R&D related works. Quantitative products such as OLR, QPE and SSTs are also archived on magnetic tapes. Photographic recorders of three different types are also connected to the system for generation of B& W and color photographic pictures in real- time for the users.

1.3 METEOROLOGICAL DATA DISSEMINATION (MDD)

The processing system is also being used for generating analogue type of cloud imagery data which are transmitted through INSAT-2C to field stations using S-band broadcast capability of the satellite along with other conventional meteorological data and FAX charts. This scheme is called Meteorological Data Dissemination (MDD).

There are about 90 MDD receiving stations in the country being operated by different agencies. Two MDD receiving stations are also operating in neighboring countries at Sri Lanka and Male under bi-lateral agreement. In general, the processed images are sent to these stations every three hours and every hour during cyclone

periods. These stations are receiving direct broadcasts of cloud imagery, weather facsimile charts and meteorological data on an operational basis.

The frequency of transmission from ground to satellite (Uplink) is 5899.225 MHz and downlink is at 2599.225 MHz.

1.4 DATA COLLECTION PLATFROM (DCP)

The Data Relay transponder (DRT) on board INSAT is being used for collection of meteorological, hydrological and oceanographic data from remote and inaccessible areas. The DCP data are received through KALPANA-I. IMD has installed 100 Data Collection Platforms (DCPs). Other agencies have also installed about 70 DCP stations, which are operational with KALPANA-I.

Characteristics of DCPs.

Frequency of transmission	402.75 MHz (uplink)
Downlink frequency	4504.1 MHz
Bit rate	4.8 kbps
EIRP (uplink)	16.5 dbw
Mode of transmission	Burst mode
Burst length	87 milliseconds
Number of sensor	10 (7 analog & 3 digital)
Number of bits in one frame	422 bits

1.5 CYCLONE WARNING DISSEMINATION SYSTEM (CWDS)

For quick dissemination of warnings against impending disaster from approaching cyclones, IMD has installed specially designed receivers within the vulnerable coastal areas for direct transmission of warnings to the officials and people in general using broadcast capability of INSAT satellite. IMD's Area Cyclone Warning Centers (ACWC) generates these special warning bulletins and transmits them every hour in local languages to the affected areas. IMD in the field areas has installed 250 such receivers in the field areas. CWDS has proved very effective system of warning people during the cyclone affecting the coastal areas. For this service the frequency of transmission from ground to satellite (uplink) is 5859.225 MHZ and Downlink is at 2559.225 MHz. Recently this technology has been upgraded to include digital transmission instead of analogue. Initially 100 numbers of new Digital Cyclone Warning Dissemination Systems (DCWDS) have been deployed in the coastal areas of Andhra Pradesh for reception of cyclone warnings.

1.6 RECEPTION OF NOAA SATELLITE DATA

The data from NOAA series of polar orbiting satellites are received and processed by IMD at Delhi and Chennai. Both AVHRR and TOVS data are processed in real time and the weather forecasters are utilizing cloud imagery and derived products operationally. The derived products are archived for distribution on demand basis to the scientists for use in research work. Based on a limited study done by IMD, the vertical temperature and moisture profiles derived from the NOAA satellite have shown positive impact on forecasts generated with numerical models. The old HRPT receiving station at New Delhi has been replaced with a new system, which is also capable of receiving data from new generation of NOAA satellites (K, L, M and N series).

1.7 PDUS for METEOSAT-5 data reception

A PDUS receiving station had been installed in early 2000 at IMD, New Delhi for reception of high resolution imagery data from METEOSAT-5 satellite located at 63 deg E over the Indian Ocean. This system continues to be used operationally for providing cloud imagery data to the forecasters.

1.8 INDO–US data Exchange Centre

Under the bilateral programme of co-operation with USA, an INDO-US data Exchange Centre has been established at IMD, New Delhi in Nov. 99 for exchange of satellite data with USA. Processed INSAT imagery data is being transmitted every three hours to the USA. GOES imagery data is also being received from USA. Data exchange takes place through dedicated communication links.

2. Future Indian Satellite missions

Future missions planned to meet the requirements of the Indian Meteorology/Oceanography community are given in Table.4. The INSAT-3D, to be launched during the year 2006 will carry an improved 6-channel imager and a 19-channel sounder for temperature/humidity profiles. The Megha-Tropiques mission slated for 2006 is a joint effort of ISRO, India and CNES, France for study of the water cycle and deep convection in the tropical region. The unique payloads of the Megha-Tropiques are MADRAS (5 channel multi-frequency microwave radiometer – including 157 GHz), ScaRaB (radiation budget - for both short and long wavelengths) and SAPHIR (humidity sounder). The mission will operate in an inclined equatorial orbit of 20^0 for repetitive coverage of tropical ocean areas.

Table –1: Main differences between INSAT-1, INSAT-2 and KALPANA-I

	INSAT-1D		INSAT-2B		KALPANA-I		
Parameter	Visible	IR	Visible	IR	Visible	IR	WV
Spatial Resolution in Km	2.75	11	2.0	8.0	2.0	8.0	8.0
Scanning lines	4548	1137	6240	1560	6240	1560	1560
Quantization level	1024	1024	1024	1024	1024	1024	1024
Field of view (μr)	76.8	307	56	224	56	224	224
Detectors	Silicon photodiodes	HgCdTe	Si	HgCdTe	Si	HgCdTe	HgCdTe
Location	Deorbited		111.5 Deg E		74 deg E		
Modes of Operation	Full Frame 20 X 20 Sector Scan 20 E-W X 5 N		FF 20 X 20 Normal Scan 20 EW X 14 NS Sector Scan 20 EW X 4.5 NS		FF 20 X 20 Normal Scan 20 EW X 14 NS Sector Scan 20 EW X 4.5 NS		

Table –2: INSAT-1 Geostationary Satellite Series

Satellite	**Launch Date**	**Met. Payload with Wavelength Bands**	**Major Applications**	**Active / Inactive**
INSAT-1A	April10, 1982	Very High Resolution Radiometer (VHRR) Visible 0.55- 0.75μm IR 10.5 - 12.5μm	• Monitoring cyclones & monsoon • CMV Winds • OLR • Rainfall Estimation	Inactive
INSAT-1B	August 30, 1983	-do-	-do-	-do-
INSAT-1C	July 22, 1988	-do-	-do-	-do-
INSAT-1D	June12, 1990	- do-	-do-	-do-

Table –3: INSAT-2 and 3 Geostationary Satellite Series

Satellite	Launch Date	Met. Payload with Wavelength Bands	Major Applications	Active/ Inactive
INSAT- 2A	July10, 1992	Very High Resolution Radiometer (VHRR) Bands: 0.55 - 0.75μm 10.5 - 12.5μm	• Monitoring cyclones & monsoon • CMV Winds • OLR • Rainfall Estimation • Mesoscale features • Flood/intense precipitation advisory • Snow detection	Inactive
INSAT-2B	July23, 1993	Very High Resolution Radiometer (VHRR) Bands: 0.55 - 0.75μm 10.5 - 12.5μm	-do-	Inactive
INSAT-2E	April, 1999	1. VHRR: As above + WV Band: 5 - 7.1μm 2. CCD Payload Bands: 063 - 0.79μm 0.77 - 0.86μm 1.55 - 1.70μm	-do-	Active
KALPANA-I	12 Sept.2002	Very High Resolution Radiometer (VHRR) Bands: 0.55 - 0.75μm 10.5 - 12.5μm WV Band: 5.7 -7.1μm	• Monitoring cyclones & monsoon • CMV Winds • OLR • Rainfall Estimation	Active
INSAT-3A	10 April, 2003	Same as INSAT-2E above	Same as INSAT-2E above	Active

Table –4: FUTURE SATELLTE PROGRAM

Satellite	Launch Date	Met. Payload with Wavelength Bands	Major Applications	Active/Inactive
INSAT- 3D	Around 2006	1. 6 channel Imager Band: 0.55 – 0.75μm (Vis- 1 km), 1.55 – 1.70μm (IR- 1km), 3.70-3.95μm(Mid Wave IR- 4 km), 6.5- 7.10 μm (Thermal IR- 4 km), 10.3-11.3μm (T IR- 4 km), 11.3-12.5μm(WV- 5 km) 2. Sounder Bands: 19 channels between 0.69-4.71 μm	Monitoring cyclones & monsoon CMV Winds OLR Rainfall Estimation Temperature and Humidity profiles in the atmosphere.	----
Megha-Tropiques (A joint project by ISRO and CNES, France with the objective of studying the water cycle and energy exchanges in the tropics)	Around 2006	1.SAPHIR 6 bands around 183 GHz (10 km Res.) 2. SCARAB Radiation instrument in short & long wave (40 km Res.) MADRAS 89 & 157 GHz radiometer 10, 18 & 37 GHz radiometer (10 km Res.)	Water vapor profile up to 12 km Radiation budget Ice particles in cloud tops, cloud liquid water and precipitation; sea surface wind speed. 23 GHz: Integrated water vapor	----

EUMETSAT Plans

K. Dieter Klaes
EUMETSAT
Am Kavalleriesand 31
D-64295 Darmstadt
Germany

Abstract

This paper provides a summary on EUMETSAT current and planned programmes. EUMETSAT is currently developing, jointly with ESA the EUMETSAT Polar System (EPS) and commissioning the Meteosat Second Generation (MSG). The launch of the first Metop satellite is planned for 2005. MSG-1 has been successfully launched in 2002 and will start to provide validated observations from the Earth/Atmosphere system early 2004 (MSG-1). The ATOVS Retransmission service became operational and provides observations from six stations. With Jason-2 EUMETSAT goes towards its first optional programme, which will provide operational altimetry services.

Introduction

The European Organisation for the Exploitation of Meteorological Satellites (EUMETSAT), contributes to the World Weather Watch system with a number of operational meteorological satellite programmes. These programmes include the continuation and improvement of the current European geostationary meteorological satellite system and also the EUMETSAT Polar System (EPS), as a contribution to the low earth orbiting, quasi sun synchronous weather satellites system. User and Data Services are provided together with these systems.

Programmatic Aspects

EUMETSAT Polar System (EPS)

The EUMETSAT Polar System (see Fig. 1) will complement the US provided system and together with the latter continue the present NOAA polar orbiting satellite system in the frame of the Initial Joint

Polar System (IJPS) (Figure 1). The future EUMETSAT satellites of this new polar system are the METOP (METeorological OPerational Satellite) satellites, jointly developed with ESA. They will provide high-resolution sounding and also high-resolution imagery in global coverage. The EPS Programme activities have started in September 1998, while full approval to the programme was given in June 1999. The first two of the METOP satellites will be operated in the frame of the Initial Joint Polar System (IJPS) together with the present NOAA system of the United States. These METOP-1 and METOP-2 spacecraft are foreseen for a sun synchronous orbit in the 9:30 AM equator crossing (descending node). They will provide polar data from 2005 onwards. With the third

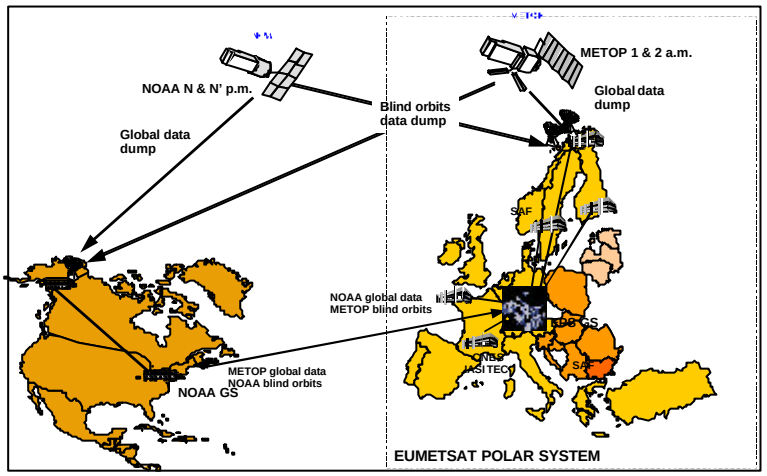

Figure 1: EPS as part of the Initial Joint Polar System.

spacecraft the converged military and civilian US-Systems NPOESS will form together with METOP-3 the Joint Polar System (JPS). METOP-3 is planned to be a recurrent copy of METOP-1 and 2. No HIRS/4 will be flown on METOP-3. Payload options for the imager and the microwave sounding instruments are VIRI-M and ATMS in case AVHRR and AMSU were not available and are currently being investigated. The EPS programme is planned to cover 14 years of operation. For mission objectives and expected capabilities see Klaes et al., 2001.

Geostationary Systems

Meteosat-7 assured since 1997 the continuity of meteorological geostationary satellite data coverage until the end of the commissioning phase of the new generation of the Meteosat Second Generation (MSG) Spacecraft. Meteosat-7 has the same capabilities as its predecessors. Together with MOP and then after 2003, together with MSG, MTP will be operated as part of a redundant two satellite system. The first spacecraft of the MSG was successfully launched in August 2002 and will become

operational in early 2004. It has an improved observation capability and a lifetime of seven years. Two further spacecraft, MSG-2 and MSG-3 are foreseen, and a fourth MSG is in the approval process.

The Meteosat—5, -6 and -7 satellites represent the current operational geostationary satellites. Meteosat-5 is supporting the INDOEX experiment and is currently situated at 63°E over the Indian Ocean. The Indian Ocean Coverage is authorised to be continued until end 2005. Meteosat-6 is the hot stand-by satellite and provides the rapid scan service, which is operational since 2001. Meteosat-7 is in the nominal operational position at 0° longitude providing half-hourly full disk images.

Optional Programmes

The Optional Jason-2 programme on altimetry entered into force on 27 June 2003, after sufficient member states have subscribed to the programme.

The Jason-2 altimetry programme is the first EUMETSAT optional programme to implement EUMETSAT's amended Convention from November 2000. This Convention expands the mandate given to EUMETSAT by its Member States in operational climate monitoring and the detection of global climatic changes. EUMETSAT will contribute to the operations of the overall system and to the generation of the data stream, using a European Earth Terminal and a real time processing chain.

The programme is EUMETSAT's contribution to a joint undertaking with the French Centre National d'Etudes Spatiales (CNES), the US National Oceanic and Atmospheric Administration (NOAA) and the US National Aeronautics and Space Administration (NASA), known as the Ocean Surface Topography Mission (OSTM). It is an important element in the overall altimetry data system and will bring high precision altimetry to a full operational status, as a result of a balanced co-operation between Europe and the USA.

SPACECRAFT AND INSTRUMENTS

EUMETSAT Polar System

The METOP satellites of the EUMETSAT Polar System (EPS) will be launched into a sun synchronous, near polar orbit with an equator crossing time of 09:30 AM (descending node), i.e. the so called morning orbit in 2005. The main mission objectives for the system are Operational Meteorology and Climate Monitoring. In addition the Search and Rescue Instruments and also the Space Environment Monitor are embarked. To achieve these objectives the appropriate payload will be embarked on METOP, with a number of sounding instruments. The HIRS/4 (High Resolution Infrared Radiation Sounder) instrument, the AMSU-A (Advanced Microwave Sounding Unit - A) and the MHS

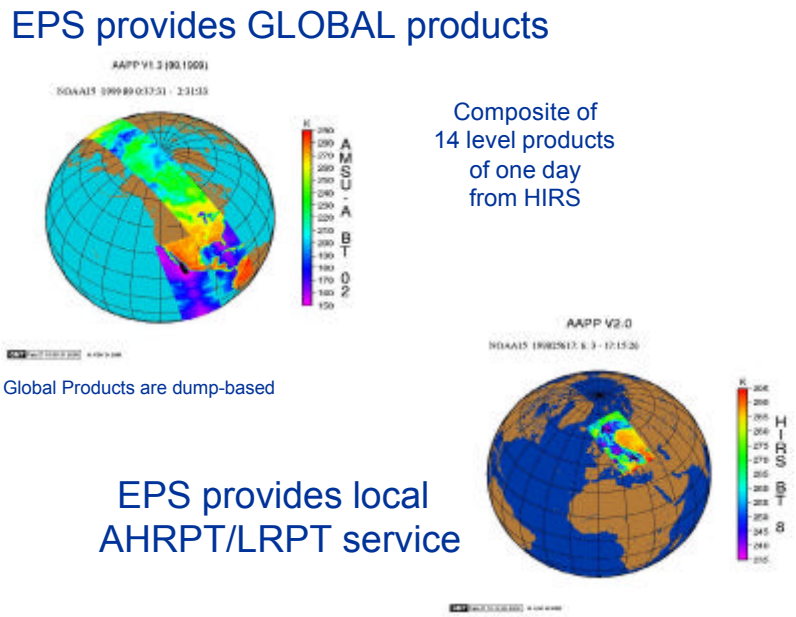

Figure 2. EPS services: Examples of global and local service.

(Microwave Humidity Sounder) instrument as successor instrument of AMSU-B (MHS was developed by EUMETSAT), will provide the continuity to the current polar sounding capabilities onboard the NOAA-15, NOAA-16 and NOAA-17 spacecraft. Highly improved sounding capability will be provided by the IASI (Infrared Atmospheric Sounding Interferometer) instrument, both in accuracy and also vertical and horizontal resolution. The sounding payload is complemented by the AVHRR/3 (Advanced Very High-Resolution Radiometer) multi-spectral imager, which will provide global visible and infrared imagery at high horizontal resolution. EPS products comprise centrally processed level 1 products from

all instruments and level 2 sounding products from ATOVS and IASI and a large number of level 2 and higher products from the distributed Satellite Application Facilities (see Figure 2 for examples).

The GOME-2 instrument for Ozone profiling and trace gas retrieval will provide additional sounding capabilities. Further sounding capabilities will be provided by the GRAS (GPS Radio-Occultation Atmospheric Sounder) system, which will make use of the information on the atmosphere and ionosphere contained in the GPS navigation satellite signals through the radio-occultation technique. This will be the first operational radio-occultation mission.

An Advanced Scatterometer (ASCAT) will provide improved capability to retrieve wind vectors at the ocean surface.

Geostationary Satellites

Meteosat Transition Programme

The Meteosat Operational System and the equivalent Meteosat Transition Programme Satellite (Meteosat-7) have as payload a three-channel imager with broad band channels in the visible, infrared and water vapour region of the spectrum. The spacecraft is spin stabilised with 100 rotations per minute. The imager yields a full disk image every 30 minutes. The sampling distance at the sub satellite point is 2.5 km for the visible, 5 km for the infrared and water vapour channels. There are 5000 x 5000 pixel of visible and 2500 x 2500 pixel of infrared and water vapour channel data per full disk image. The products include satellite-tracked winds, cloud products, upper level tropospheric humidity and others.

Meteosat Second Generation

The Meteosat Second Generation spacecraft is also a spin-stabilised satellite. Its payload comprises

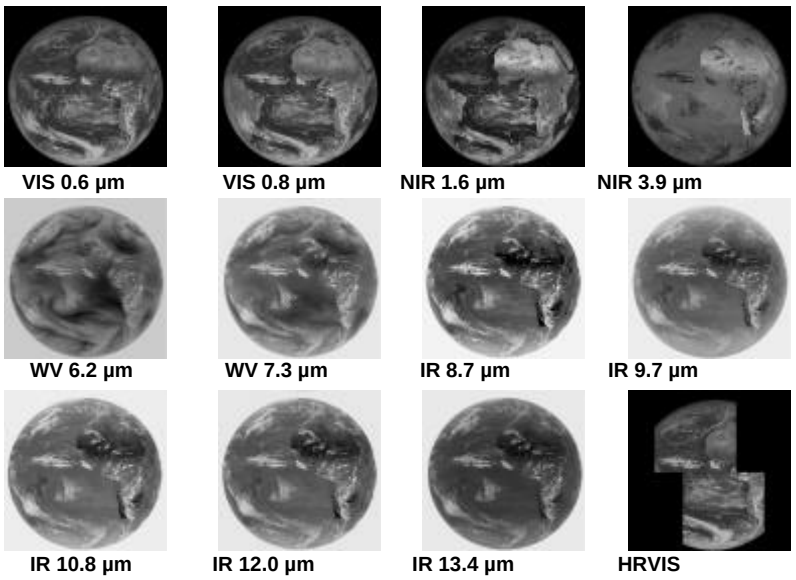

Figure 3: MSG capabilities: Example images from 12 SEVIRI Channels.

the Spinning Enhanced Visible and Infrared Imager - SEVIRI) with 12 different spectral channels (see

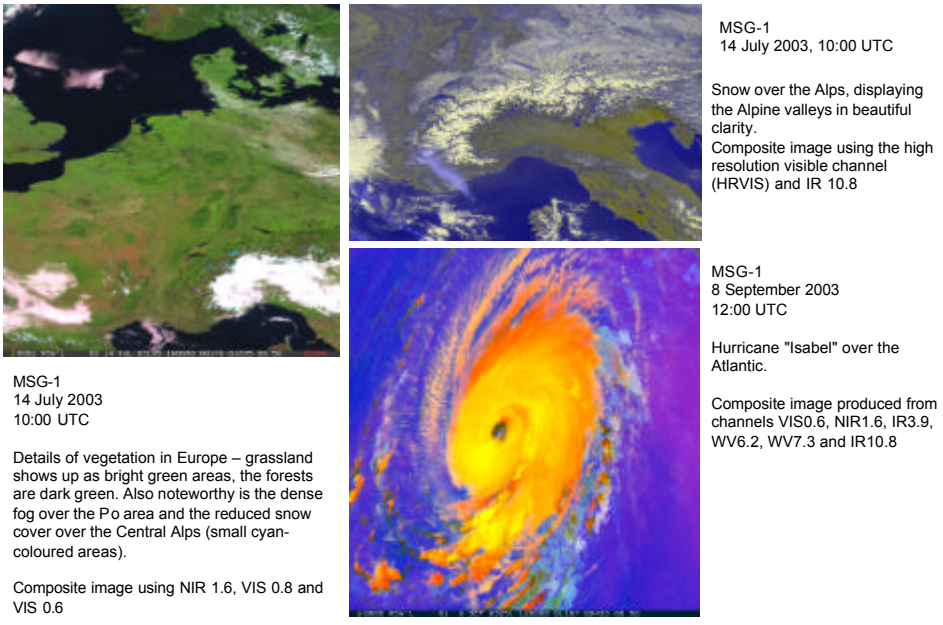

Figure 4: MSG-1 Example Images

Figure 3) in the visible and infrared region of the spectrum (see example images in Figure 4) and the GERB (Geostationary Earth Radiation Budget) instrument, intended to make accurate measurements of the Earth Radiation Budget from geostationary orbit. Stability parameters can be derived from pseudo-sounding (e.g. lifted index). Humidity fields can be derived in the upper and mid-troposphere. Total ozone fields can be estimated. The sampling of the image data at the sub-satellite point are 3 km with exception of the High Resolution Visible channel (HRV), where the resolution is planned to be 1 km. The full disk image is composed of 3750 x 3750 pixels (except for HRV). It is planned to provide one full disk image every 15 minutes, but alternative repeat cycles up to 3 minutes are also possible. In HRV mode the scan area can be selected among predetermined rectangular blocks. Products are generated in the central facility and in the distributed part of the EUMETSAT application ground segment, the SAF. For details see Schmetz et al., 2002.

.

ATOVS RETRANSMISSION SERVICE

The members of the HIRLAM Group (Denmark, Finland, Ireland, The Netherlands, Norway, Spain, Sweden and Iceland) approached EUMETSAT in November 2000 to assess the feasibility of a fast delivery service of HRPT based ATOVS data for the Northern Atlantic and European Area. The

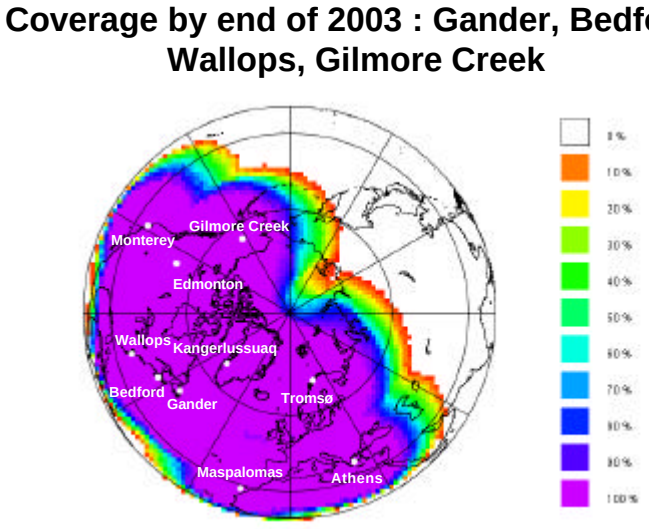

Figure 5: EARS data coverage.

service provides ATOVS level 1a and level 1c data with a timeliness of 30 minutes to cover the needs of EUMETSAT Member States regional and local Numerical Weather Prediction requirements for sounder data. The service within the pilot project started in October 2002. By end of 2003 the data of ten HRPT stations are distributed (see Fig. 5). The initial operational phase is approved until end 2004.

Details can be seen on EUMETSAT's web page (see http://www.eumetsat.de, on the EARS (EUMETSAT ATOVS Retransmission Service) home page.)

Conclusions

The above-presented systems represent the EUMETSAT contribution to the global system of satellite observation within the World Weather Watch and the Global Observation System. Considerably improved sounding capabilities are expected to provide a major contribution towards the improvement of operational meteorological services, in particular Numerical Weather Prediction. An important contribution to climate monitoring will arise from the coming programmes and satellites. Further contributions from EUMETSAT include optional programmes like the Jason-2 data processing and distribution.

References

Klaes, D., J. Schmetz, M.Cohen, Y. Buhler, J. Figa, J.-P. Luntama, R. Munro, P. Schlüssel, J. Kerkmann and A. Ratier, 2001: The EUMETSAT Polar System within the Initial Joint Polar System: Mission objectives, expected capabilities and products. 1st Post EPS User Consultation Workshop, AEG Reference Documentation, 48 pp.

Schmetz, J., P. Pili, S.Tjemkes, D. Just, J.Kerkmann, S. Rota and A.Ratier, 2002: An Introduction to Metetosat Second Generation (MSG). Bull. Amer. Meteorol. Soc., 83, Number 7, 977 – 992.

Update about Frequency Protection: Results of WRC 2003 and SFCG 23… What to do now?

Guy Rochard
Meteo-France

This paper will report on results from the WRC 2003 and SFCG 23 meetings. Additional information about frequency protection can be found on these web sites:

http://cimss.ssec.wisc.edu/itwg/groups/frequency/
and
http://guy.rochard.free.fr/meteo/

NESDIS ATOVS Operational Sounding Products Processing and Distribution

A. K. Sharma
NOAA/NESDIS
Washington DC 20233

Since 1979 the National Oceanic and Atmospheric Administration National Environmental Satellite, Data, and Information Service (NOAA/NESDIS) has been providing the operational sounding products from the polar orbiting satellites continuously with a suite of infrared and microwave radiation sounder measurements, and derived temperature and moisture sounding products on a global scale. NOAA's primary mission for sounding data products represents a unique source of global, atmospheric, weather information, with a demonstrated positive impact on Numerical Weather Prediction (NWP) forecasts. Current polar orbiting satellites provide measurements from the HIRS/3, AMSU-A and AMSU-B sounder instruments on board NOAA-15, NOAA-16 and NOAA-17. Advanced TIROS (Television and Infrared Observation Satellite) Operational Vertical Sounding (ATOVS) sounding products from NOAA-15 were operationally implemented by NESDIS in April 1999 and AMSU-B processing was delayed until May 2000. NOAA-16 and NOAA-17 were made operational in March 2001 and October 2002 respectively. There are over 500,000 soundings made every day from the ATOVS on aboard NOAA-15, 16 and 17 series of Polar Orbiting Environmental Satellites (POES). Monitoring sounding data products generation systems on a 24 hours basis is important. A web-based user interface has been developed and implemented for monitoring the products generation systems. Quality of the data products and timeliness for processing and distribution are extremely important factors in designing the operational systems at the NESDIS. This presentation will include the discussion on the improvements on the quality and timeliness and the operational changes required by the systems to accommodate the future instruments data processing such as pipeline processing for granules instead of orbits. The processing changes required for the upcoming launches of the NOAA satellites NOAA-N and NOAA-N' and the European Organization for the Exploitation of Meteorological (EUMETSAT) satellites, Meteorological Operational Satellite (MetOp)-1 and MetOp-2 will be discussed. Re-hosting of operational systems from a slower processor CRAY machine to a faster processor IBM machine will also be discussed.

NOAA OPERATIONAL SOUNDING PRODUCTS FOR ADVANCED-TOVS

Anthony L. Reale
NOAA/NESDIS
Washington D.C.

INTRODUCTION

The National Oceanic and Atmospheric Administration, National Environmental Satellite Data and Information Service (NESDIS) operates a fleet of civilian, polar orbiting environmental satellites which provide users and researchers with a suite of atmospheric and surface measurements, and derived products on a global scale. On May 13, 1998, the Advanced TIROS Operational Vertical Sounder (ATOVS) radiometer configuration onboard NOAA-15 was successfully deployed into a morning orbit, replacing TOVS, followed by NOAA-16 into an afternoon orbit, on September 21, 2000, and NOAA-17 on June 22, 2002, which was launched into a mid morning orbit half way between NOAA-16 and NOAA-17. The ATOVS featured the Advanced Microwave Sounding Unit which replaced the MSU and SSU, along with the 20-channel HIRS/3 and a 6-channel Advanced Very High Resolution Radiometer (AVHRR/3) similar to its predecessors. The following report summarizes the processing systems for deriving the NESDIS operational ATOVS sounding products and provides a review of the derived weather products and evaluation results for the current 3-satellite configuration of ATOVS operational satellites.

ORBITAL PROCESSING

A brief summary of the scientific algorithms comprising the orbital processing system is provided, for further details see Reale (2001 and 2002).

The **Orbital** processing system provides:

- Pre-processing,
- Contamination detection,
- First guess and retrieval for soundings, and
- Cloud, Radiation, and Total Ozone products.

Pre-processing steps include instrument calibration, quality control (QC) of the sounder measurements, attachment of ancillary data such as terrain designation, Sea Surface Temperature, and numerical weather prediction (NWP) forecasts, the spatial interpolation of the AMSU-A measurements to the HIRS/3 fields-of-view, and measurement adjustment to the nadir view (Allegrino *et al.* 1999).

Contamination detection consists of the identification of effects due to precipitation on the AMSU measurements, and due to clouds for the HIRS/3 measurements. Global cloud detection (Ferguson and Reale 2000) and the resulting cloud-mask constrain the use of HIRS in subsequent retrieval steps.

The **first guess** is uniquely determined for each sounding using a library search technique (Goldberg *et al.* 1988). The libraries consist of segregated samples of collocated radiosonde and satellite measurements (Tilley *et al.* 2000) which are updated on a daily basis and which are directly accessed during orbital processing.

The first guess is obtained by minimizing an equation equivalent to (1):

$$D = (R - R_k)^t \, B^{-1} \, (R - R_k) \qquad (1)$$

where the superscript *t* indicates the matrix transpose, -1 the inverse, and

D : scalar closeness parameter,
B : sounding channel radiance covariance matrix; dimension (35 x 35),
R : adjusted, observed radiance temperature vector; dimension ($N_{A,i}$), and
R_k : adjusted, library radiance temperature vector; dimension ($N_{A,i}$).

The B-matrix is computed consistent with the collocation library searched for a given sounding, and is updated daily. The dimension "35" for the B matrix in denotes the total number of sounder channels available from ATOVS; not all are used. The dimension ($N_{A,i}$) denotes the specific channel combination used to compute D, and the subscript "k" denotes the collocations searched. The channel combination for a given sounding varies depending on whether the sounding type is clear or cloudy, and sea or non-sea. The actual first guess temperature, moisture and radiance temperature profiles for a given sounding are computed by averaging the 10 closest collocations with smallest D.

The **retrieval** is done using a Minimum Variance Simultaneous solution (Fleming *et al.* 1986), which is given by equation (2):

$$T - T_g = S A^t \, (A S A^t + N)^{-1} \, (R - R_g) \qquad (2)$$

where the subscript *t* indicates the matrix transpose, -1 the inverse, and:

T: final soundings products vector, (133),
T_g: first guess products vector, (133)
S: first guess covariance matrix, (133 x 133),
A: sounder channel weighting matrix, (35 x 133),
N: measurement uncertainty matrix, (35 x 35),
R: observed radiance temperature vector, ($M_{A,j}$), and
R_g : first guess radiance temperature vector, ($M_{A,j}$).

The internal product vector (T) includes one-hundred (100) levels of atmospheric temperature (1000mb to .1mb), thirty-two (32) levels of moisture (1000mb to 200mb), and the surface temperature. The dimension thirty-five (35) for the A and N matrices denotes the available ATOVS channels; not all are used. The dimension ($M_{A,j}$) denotes the specific channel combination used for retrieval depending on the sounding type.

The S, A and N matrices of Equation-2, along with the B-matrix of Equation-1 are computed based on the latest collocations of radiosonde and satellite data, and updated weekly (Tillet *et al.* 2000). There are four (4) separate B-matrices for clear and cloudy collocations over sea and non-sea terrains, four (4) corresponding "S " matrices, and nine (9) sets of associated "A" and "N" matrices stratified by latitude and terrain, one set each for clear and cloudy soundings. A total of 28 unique retrieval operators are available, the one used depends upon the latitude, cloud and terrain designation of the satellite sounding.

RESULTS

The following sections illustrate the value of satellite derived products in the analysis of global and regional weather, and is divided into three parts. Part-1 provides a classic illustration of the **information content** of derived sounding products **in the context of NWP** forecasts which assimilate radiance, for a meteorologically active case in the remote, data devoid South Indian Ocean. Part-2 provide a series of **global analysis** illustrating the consistency and meteorological representativeness of (NESDIS) derived sounding products from the current fleet of (three) NOAA operational satellites, followed by a **regional analysis** illustrating consecutive passes of satellite observations and their use in tracking an approaching storm system off the US West Coast. Part-3 provides examples of **vertical statistics** which estimate the accuracy of the satellite derived soundings based on global (ensemble) samples of collocated radiosonde and satellite observations.

Information in the Context of Numerical Weather Prediction (NWP)

The panels in Figure 1 illustrate the information content of the NOAA operational sounding products from ATOVS in the context of NOAA, Environmental Modeling Center (EMC) NWP data (Kalnay *et al.* 1990). The upper two panels show difference fields for **SAT**ellite (NOAA-16) operational soundings minus **NWP** [1] for the 500mb to 300mb layer mean virtual temperature, with the SAT-NWP time differences constrained to be within 2 hours. The middle two panels display analyzed EMC 400mb wind fields (m/s) corresponding to the two upper panels, and the lower two panels are the corresponding AMSU-A channel 5 radiance temperature measurements (K), which are sensitive to middle tropospheric temperature. The region is the remote South Indian Ocean (see EMC panels for latitude and longitude boundaries), on March 23, 2002 (left) and 48 hours later on March 25 (right).

As can be seen, there is a very high correlation among the SAT-NWP difference patterns, the location of the 400mb maximum wind (jet-stream) in the EMC analyzed wind fields, and the satellite measurement data in denoting the frontal zone. This correlation and its persistence over time illustrates the additional information content that derived soundings provide in the context of NWP forecasts, information which may be compromised in current NWP systems which assimilate radiance based on a NWP first guess (McNally et.al., 2000). Unlike NWP which tends to become less reliable in remote frontal zones, the reliability of the derived satellite soundings is not affected by remoteness or ambient weather[2].

[1] Available 6 and 12-hour forecasts from the operational Aviation cycle.

[2] The relatively sharp and dynamic nature of the atmospheric structures in frontal zones can enhance the sensitivity of derived products.

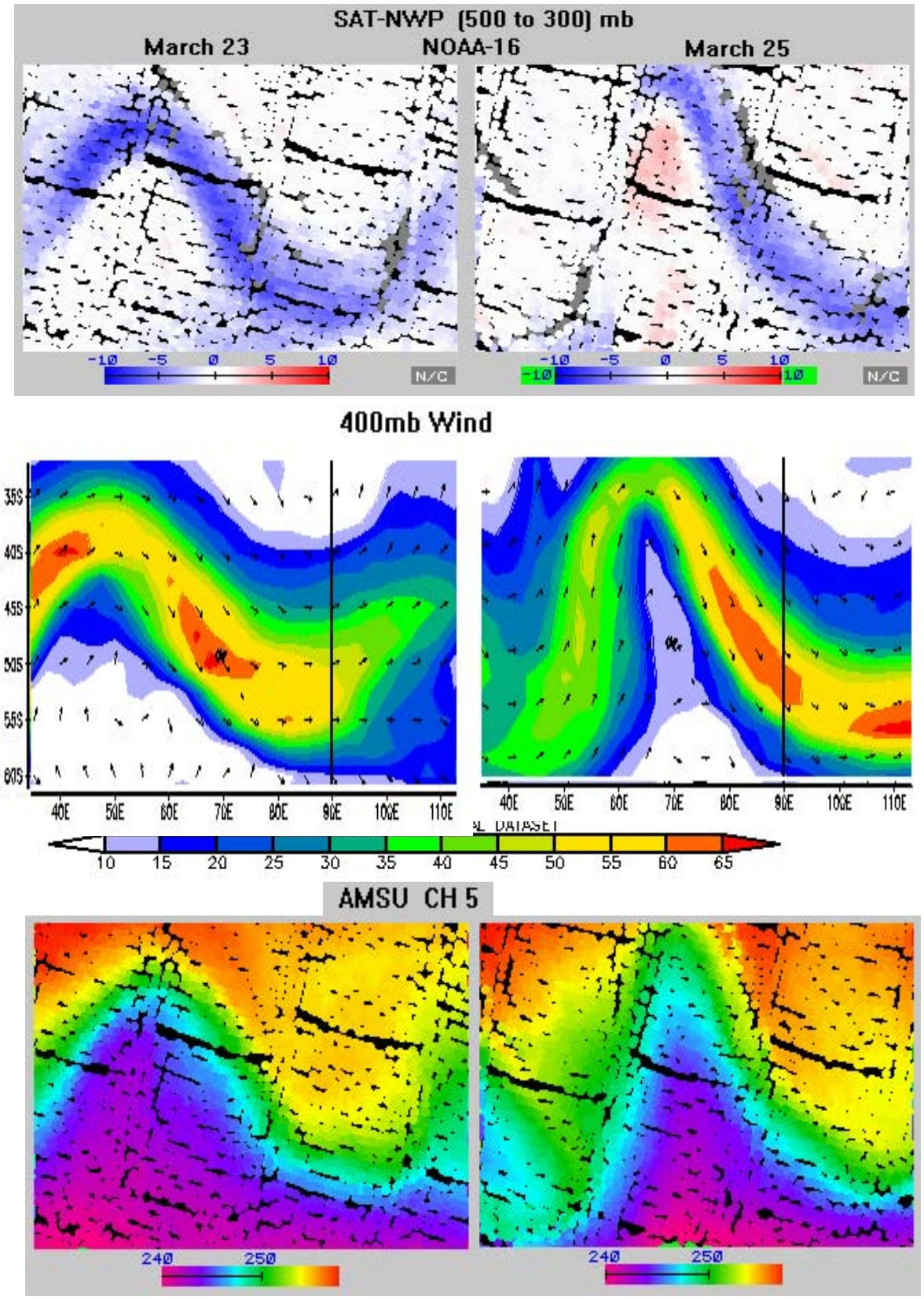

Figure 1: **(SAT-NWP) differences (K) for the 500 to 300mb layer (upper), NOAA/NWP Wind (m/s) Analysis at 400mb (middle), and AMSU-A channel 5 (K) data (lower) over the Indian Ocean on March 23, 2002 (left) and 48 hours later on March 25 (right).**

Patterns such as those shown in Figure 1are not isolated occurrences, but have been observed on a regular basis since the early 1990's (Reale 1995) in conjunction with the initial experiments with the assimilation of NWP-based "interactive" retrievals (Daniels et.al., 1988), and persist today (Reale, 2001 and 2002) in conjunction with current NWP-based "radiance" assimilation (McNally et.al., 2000). The existence of such patterns warrant further study to better understand their importance as a diagnostic tool, and to assist forecasters in identification and prediction of developing storm systems.

Global (and Regional) Analysis

Figures 2 through 7 show a series of color-enhanced, horizontal fields which display NESDIS operational satellite products. Each figure contains a set of four panels, and each panel a global time-composite of the satellite data for selected parameters and satellites. Each of the panels cover the same 12-hour period [3], consisting of approximately seven orbits displayed in a rectangular-Cartesian projection along with the corresponding color scale and data range. Together, the combined fields illustrate the internal consistency and meteorological representation of NESDIS derived weather products through the atmosphere.

Figure 2 shows **SAT**ellite minus **NWP** differences for the 1000mb to 700mb layer mean virtual temperature. The time difference for the SATellite and NWP data vary over +/- 3 hours, and similar to Figure 1 the 6-hour NWP forecasts used are from the Aviation forecast cycle. Differences are shown (clockwise beginning upper left) for the NOAA operational soundings from NOAA-15, NOAA-16, NOAA-17, and for Defense Meteorological Satellite Program (DMSP) operational soundings (Reale *et al.* 1995) from the F-15 satellite. Similar to Figure 1, the difference patterns tend to trace frontal zones, but in this lower layer positive differences (Red) tend to correlate with warm advection and negative differences (Blue) with cold advection zones; in neutral zones or warm/cold cores differences tend to zero (white) (Reale 1995).

Figure 3 illustrates **SAT**ellite minus **NWP** differences (similar to Figure 2) for the 500mb to 300mb layer mean virtual temperature. Once again, very good consistency is observed among the difference patterns for the four independently operated satellite systems. Compared to Figure 2, the differences for this layer are smaller in magnitude, with noticeably more structure in the southern hemisphere and a more definable cold bias. Since the 500mb to 300mb layer represents one of the most reliable regions of the atmosphere with respect to satellite observations and derived products, the importance of these differences in the context of NWP is enhanced particularly in this remote ocean region. The value and consistency of the signature difference patterns illustrated in Figures 1, 2 and 3 for monitoring NOAA operational weather data systems cannot be overstated.

Figure 4 illustrates global time-composite fields of satellite derived cloud mask data (blue is clear, white is cloudy), clockwise beginning in the upper left, for NOAA-15, NOAA-16, and NOAA-17. The cloud mask is important as it determines whether infrared (HIRS) measurements can be used to generate soundings, and as can be seen the consistency among the three operational satellites is very good. The lower left quadrant shows a concurrent image of the AVHRR infrared measurements for

[3] Each satellite measures a different location of the earth at a given time depending on its local equator crossover time.

channel 4 from NOAA-16. AVHRR data are highly sensitive to clouds which contaminate these data resulting in lower values, and are used along with the HIRS to provide the ATOVS cloud mask (Ferguson and Reale 2000). As can be seen, there is good agreement among the global cloud masks for each satellite, and between the colder, contaminated AVHRR data and cloudy regions for NOAA-16.

Figure 5 illustrates global analysis for the satellite derived 850mb water vapor mixing ratio, clockwise beginning in the upper left, from ATOVS for NOAA-15, AMSU-B for NOAA-17, and ATOVS from NOAA-17 and NOAA-16 respectively. Moisture products from AMSU-B are independently derived using a statistical regression approach (Chalfant *et al.* 1999 and Reale 2001)[4]. In general, good consistency among the global moisture patterns are observed, however, areas of difference particularly compared to the AMSU-B products are seen, for example, over northern Africa, and in moisture laden tropical areas where the AMSU-B products show a dry bias of up to 1.5 g/kg. Given the inherent difficulty of validating global moisture given its relatively high spatial/temporal variability, the degree of consistency among these products is encouraging. The problem of deriving global moisture profiles using satellite observations represents one of the foremost challenges for satellite meteorologists.

Figure 6 illustrates 200mb temperature for (clockwise beginning upper left) NOAA 15, NOAA-16 and NOAA-17, with the lower left panel illustrating the corresponding EMC analysis field valid at 00Z (the center point of the 12 hour satellite time-composites). In general, the global 200mb temperature is one of the most difficult parameters to retrieve as it represents the mean location of the tropopause, a region of the atmosphere where associated temperature lapse rate structures can reduce the sensitivity of the satellite sounders. The excellent agreement among the satellites and against the EMC analysis underscores the reliability of the NESDIS scientific approach to provide consistent data even as the information from the sounder is reduced. This can be attributed to the apriori guess, and also the vertical statistical correlation constraints imposed in the retrieval solution through the first guess error correlation "S" matrix of Equation 2.

Figure 7 illustrates upper stratospheric composite fields of 10mb temperature for the four (4) NESDIS operational satellite product systems. The 10mb level is typically above the highest report levels of most conventional radiosonde observations and NWP forecast models, rendering the satellites as a primary source of contiguous global measurements at such levels. Once again, excellent agreement is observed among the four independent satellite derived product Operations.

Figures 8 and 9 integrate selected horizontal field and vertical profile data in a series of single-orbit observations from each satellite over an approximately 7-hour time period, to track an advancing weather front as it approaches the northwest US coast. Such studies simulate a realistic scenario in which forecasters may utilize the information provided by polar satellites in a real-time environment.

[4] NESDIS plans to simultaneously process AMSU-B with HIRS and AMSU-A during the Year 2004, see Section 5.

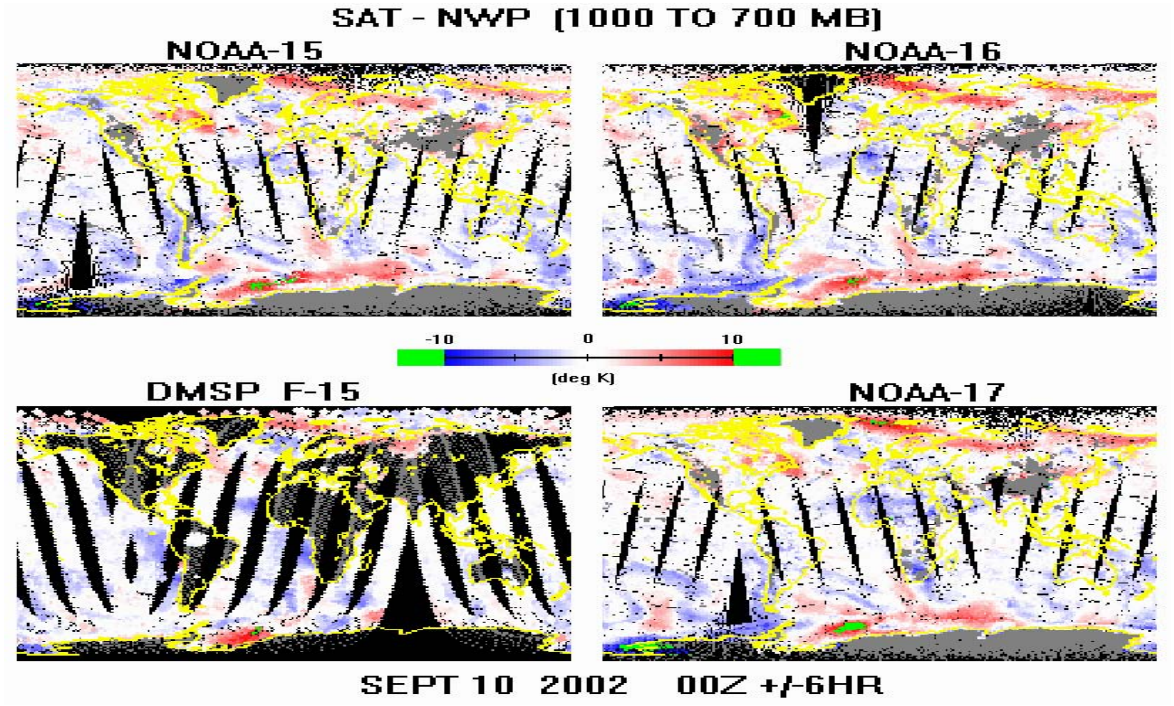

Figure 2: **Satellite sounding minus NWP difference patterns for the 1000mb to 700mb layer mean virtual temperature for the four (4) NESDIS operational sounding systems, composited over the 12 hour period.**

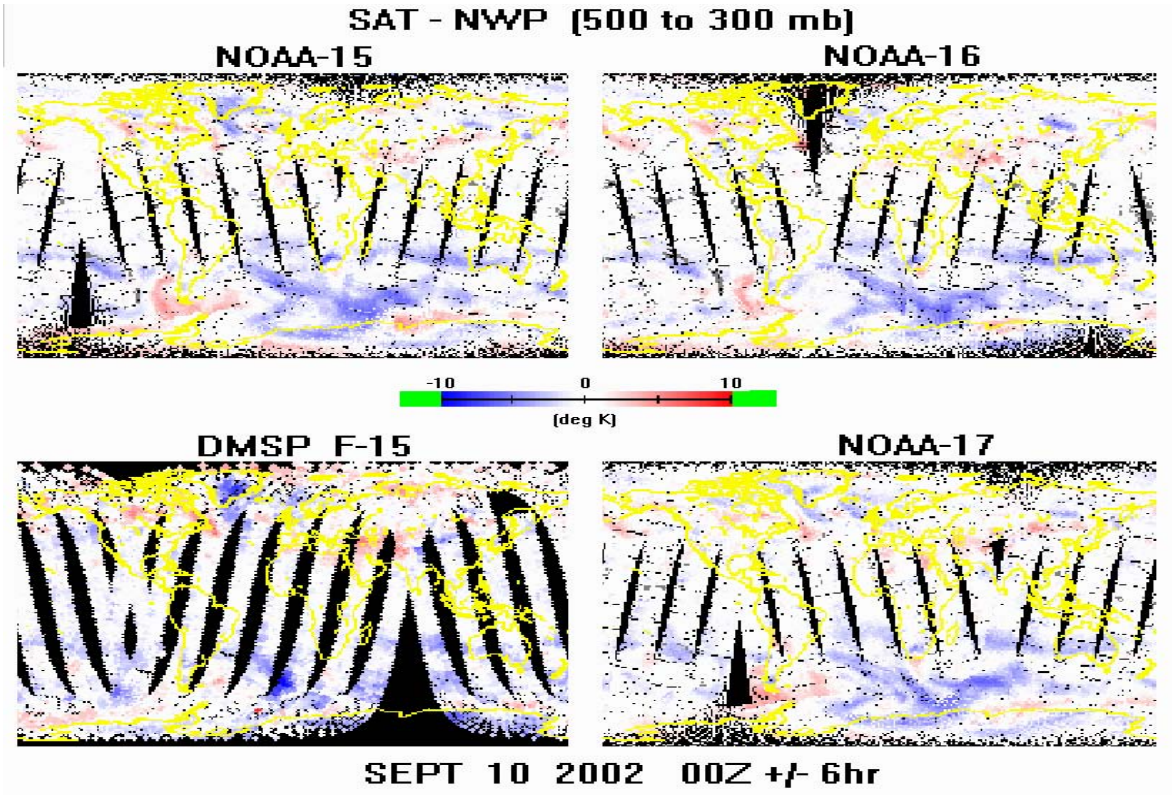

Figure 3: **Satellite sounding minus NWP difference patterns for the 500mb to 300mb layer mean virtual temperature for the four (4) NESDIS operational sounding systems, composited over the 12 hour period.**

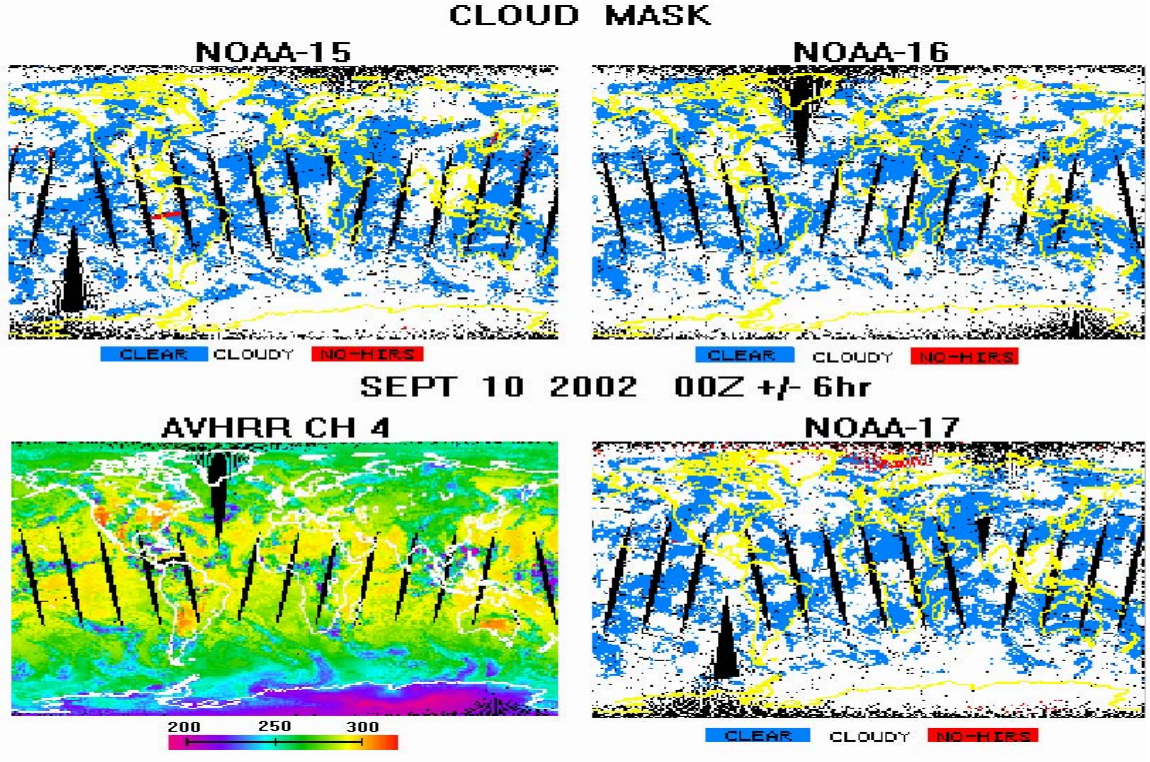

Figure 4: **Satellite derived cloud mask for NOAA-15, 16 and 17 and the corresponding AVHRR channel 4 observations from NOAA-16, composited over the 12 hour period.**

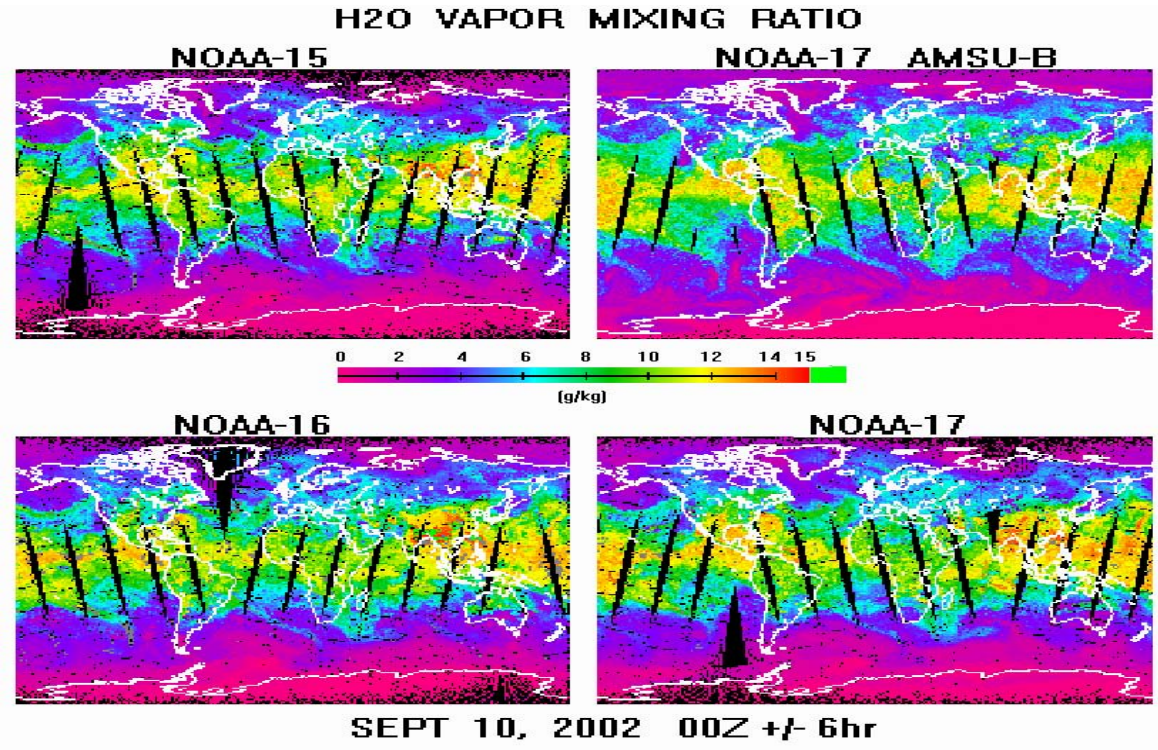

Figure 5: **Satellite derived water vapor mixing ratio (g/kg) for ATOVS from NOAA-15 (upper left), NOAA-17 (lower right) and NOAA-16 (lower left), and for NOAA-17 using AMSU-B only (upper right), composited over the 12 hour period.**

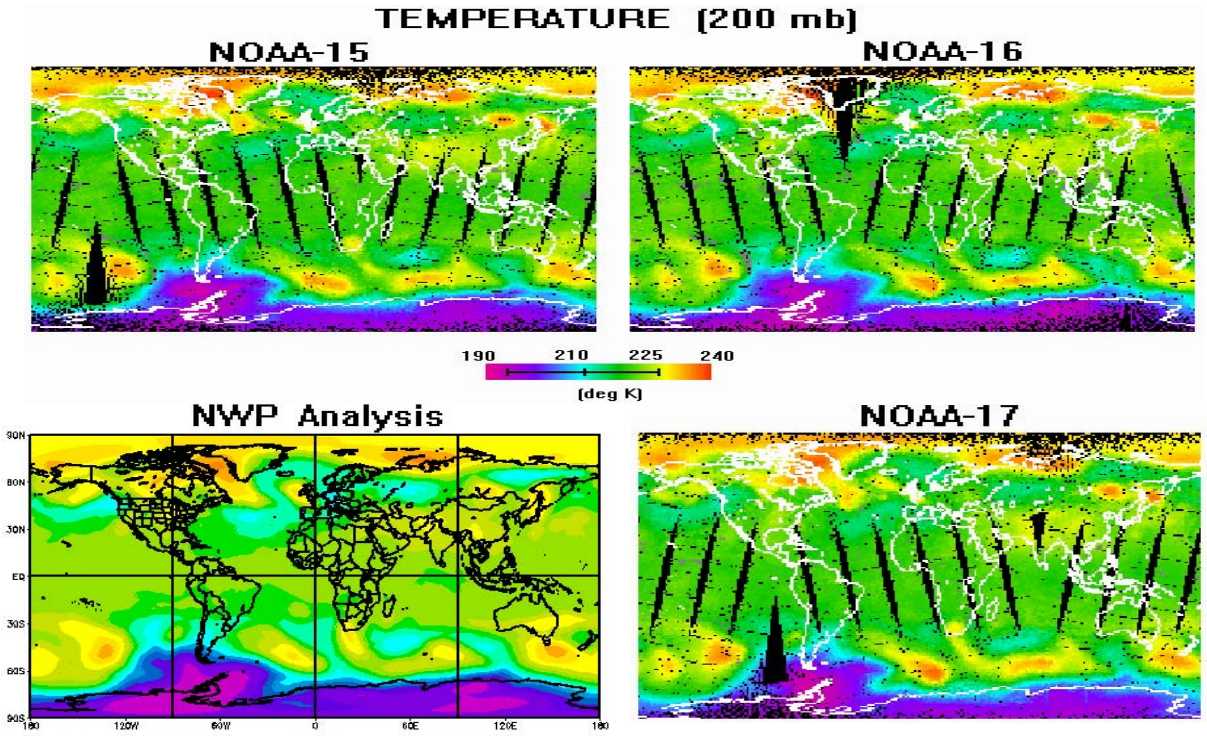

Figure 6: **Satellite derived 200mb temperature (K) from NOAA-15 (upper left), NOAA-16 (upper right) and NOAA-17 (lower right), each composited over the 12 hour period from 18Z Sept.9 thru 6Z Sept. 10, and for the corresponding EMC-NWP Analysis (lower left) valid at 00Z on September 10, 2002.**

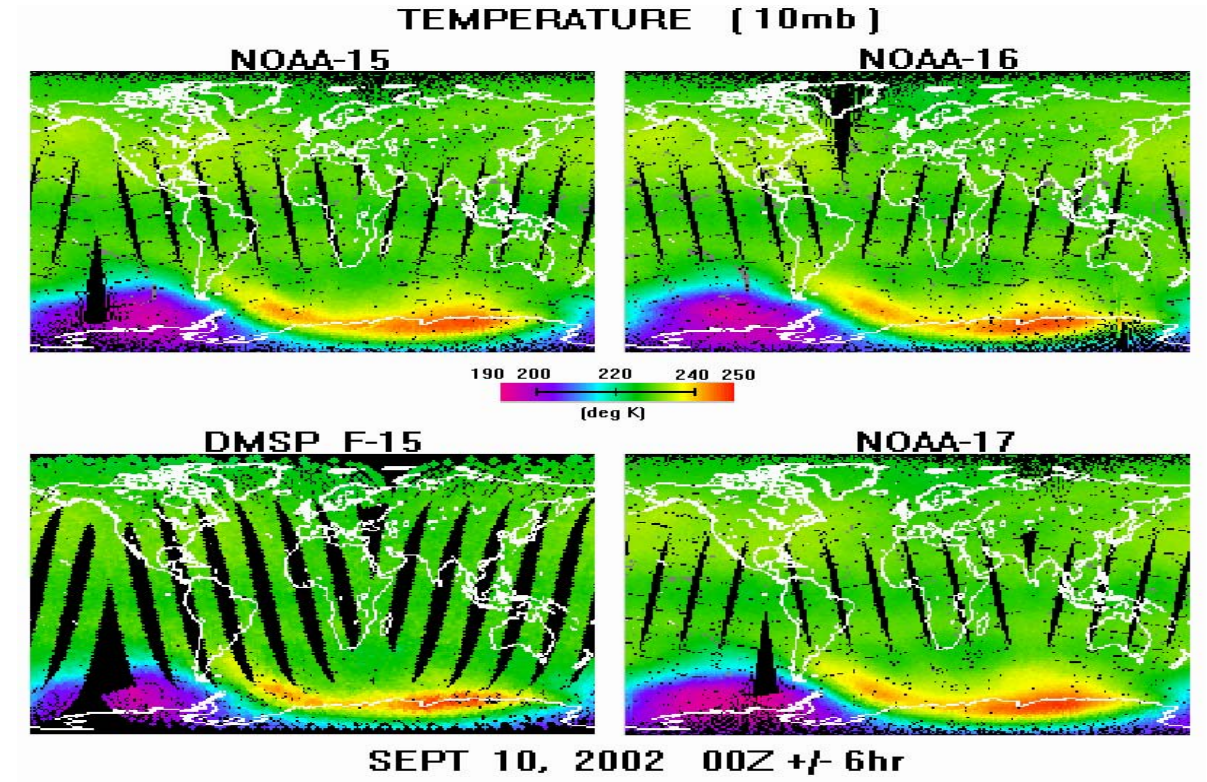

Figure 7: **Satellite derived temperatures at 10mb for the four (4) NESDIS operational sounding systems, composited over the 12 hour period.**

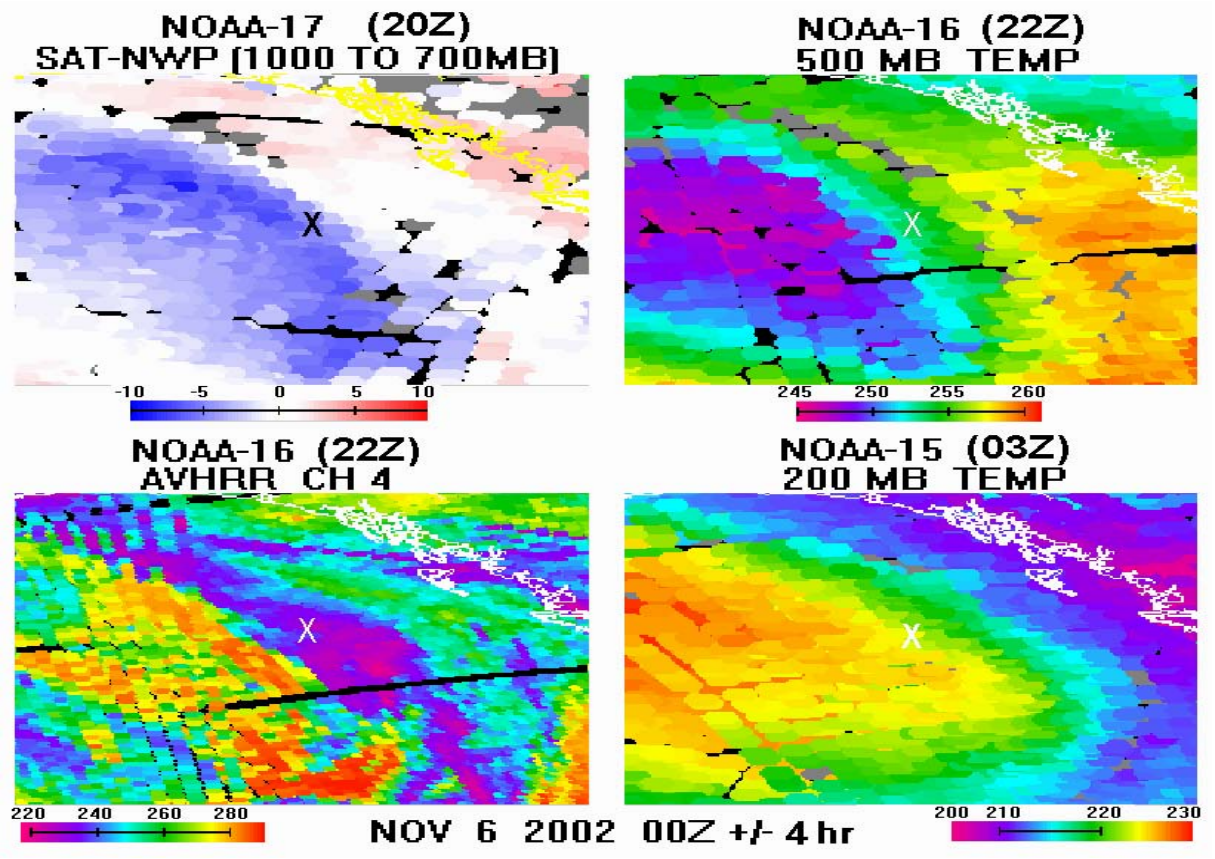

Figure 8: **NOAA-17 satellite minus NWP temperature difference patterns for the 1000mb to 700mb layer (upper left), NOAA-16 retrieved temperature at 500mb (upper right), NOAA-16 AVHRR measurements for channel 4 (lower left), and NOAA-15 retrieved temperatures at 200mb (lower right) for successive passes over a 7-hour period in conjunction with an advancing weather front off the northwest US coast.**

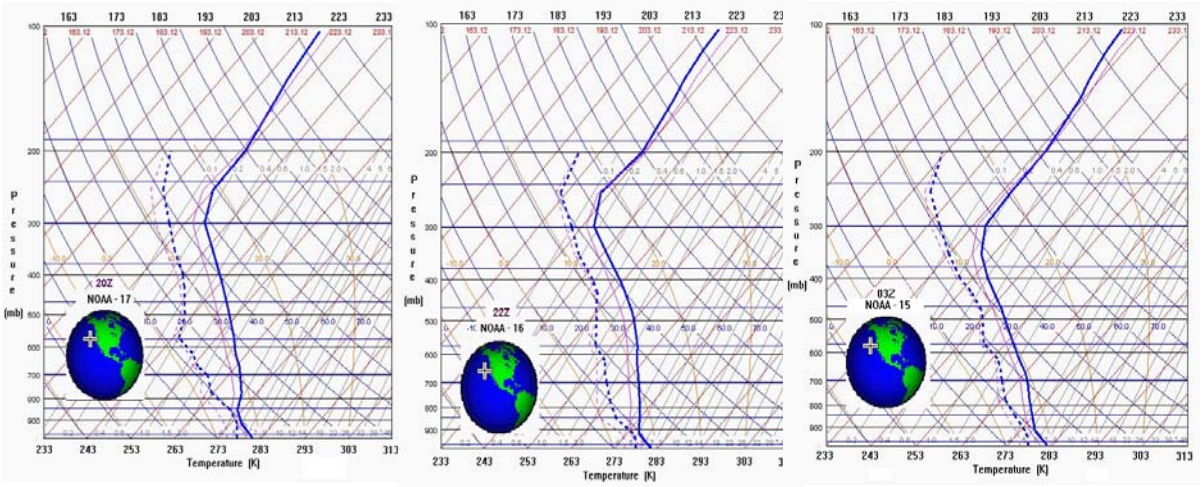

Figure 9: **Satellite sounding temperature (solid) and moisture (dashed) profiles for consecutive passes of NOAA-17 (top) at 20Z, NOAA-16 (middle) at 22Z, and NOAA-15 at 03Z at the location "X" in Figure 8; the associated red curves indicate first guess profiles.**

The two upper panels of Figure 8 illustrate horizontal fields from consecutive passes of NOAA-17(left) and NOAA-16 (right) at approximately 20Z and 22Z, respectively. The NOAA-17 data are the **SAT**ellite minus EMC 6-hour **NWP** differences for the 1000mb to 700mb layer (similar to Figure 2) , and the NOAA-16 data are for 500mb temperature. The two lower panels show corresponding AVHRR data for NOAA-16 (at 22Z) indicating clouds, and 200mb temperature fields from NOAA-15 at approximately 03Z the following day.

The three vertical profiles illustrated in Figure 9 correspond to derived temperature and moisture sounding from the consecutive passes (left to right) of NOAA-17 (20Z), NOAA-16 (22Z), and NOAA-15 (03Z), at the location of the"X"indicated in each of the panels of Figure 8.

The combination of data shown in Figures 8 and 9 show how satellite derived products can assist forecasters in making forecasts particularly in data sparse regions. For example, the panels of Figure 8 show a sharp demarcation of relatively small and decidedly negative differences between the **SAT**ellite data for NOAA-17 and the **NWP,** which line up slightly to the west of the advancing cold front boundary as indicated two hours later in the 500mb temperature and cloud analysis fields from NOAA-16. Some 5 hours later, the 200mb temperature fields from NOAA-15 clearly indicate the sharp stratospheric infusion (lowering tropopause) indicative of subsiding air directly behind the front as it continues to intensify and approach the coast.

The analysis of the series of vertical temperature profiles for each satellite over the seven hour period as shown in Figure 9 is a little more subtle. At first glance there appears to be little difference in the respective profiles, but closer inspection reveals characteristics consistent with cold air advection behind the front, for example, middle tropospheric cooling and the lowering tropopause (stratospheric infusion) height in the latest (03Z) temperature profile from NOAA-15.

Vertical Statistics

The final evaluation strategy concerning satellite derived sounding products are the vertical accuracy statistics based on collocated radiosonde and satellite sounding differences. Such statistics are useful as an overall indicator, but are limited given the spatial and temporal windows for making collocations, subsequent bias in the global sampling bias per satellite (see Part 2), and radiosonde report uncertainties.

Figure 10 provides estimates of the vertical accuracy of the ATOVS temperature soundings for the NOAA-17, 16 and 15. Mean and standard deviation differences are shown for the first guess (light) and final sounding (dark) profiles, with pressure along the x-axis and sample size on the right. The time period is a 7-day period during September, 2002, for combined clear and cloudy soundings from the 60N to 60S latitude belt. As can be seen, mean bias and standard deviation values for the final soundings are typically close to zero and 2.0K respectively, with maximum values near the surface and tropopause, and minimum values in the middle troposphere. Differences for the final soundings are less than those for the first guess throughout the profile for all three satellites, indicating the consistent convergent nature of the final retrieval solution relative to the guess.

Figure 11 show similar statistics but for the ATOVS moisture soundings, showing results (from left to right) for ATOVS from NOAA-17, ATOVS for NOAA-16), AMSU-B for NOAA-17 (Chalfant et.al., 1999), and ATOVS for NOAA-15.

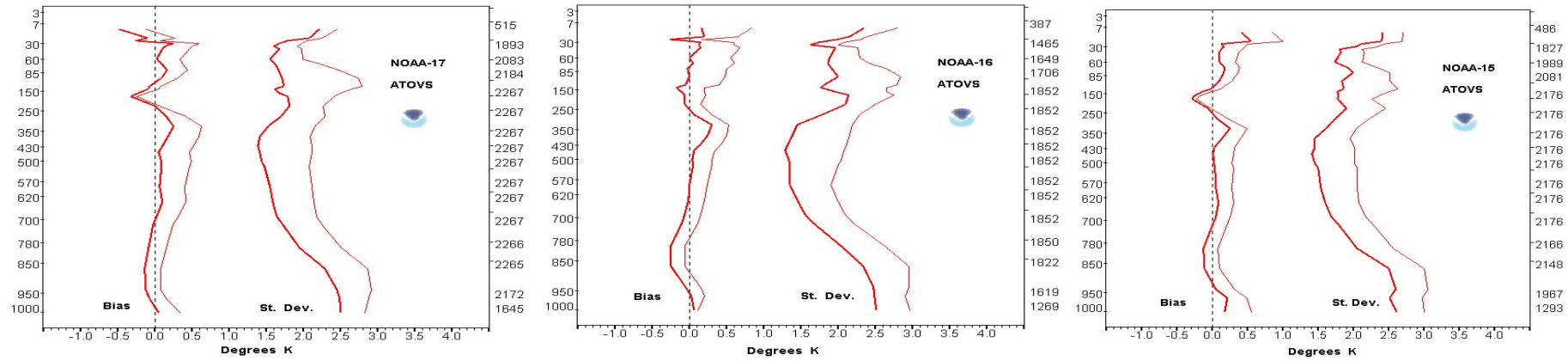

Figure 10: **Vertical statistics of atmospheric temperature (Deg K) differences for derived soundings minus radiosondes from ATOVS NOAA-17 (left), NOAA-16 (middle) and NOAA-15 (right) from the 60N to 60S for the period Sept 2-8, 2002; the atmospheric pressure (mb) and sample size per level are shown along the left and right axis, with heavy curves showing final derived sounding and lighter curves the first guess differences from radiosondes, respectively.**

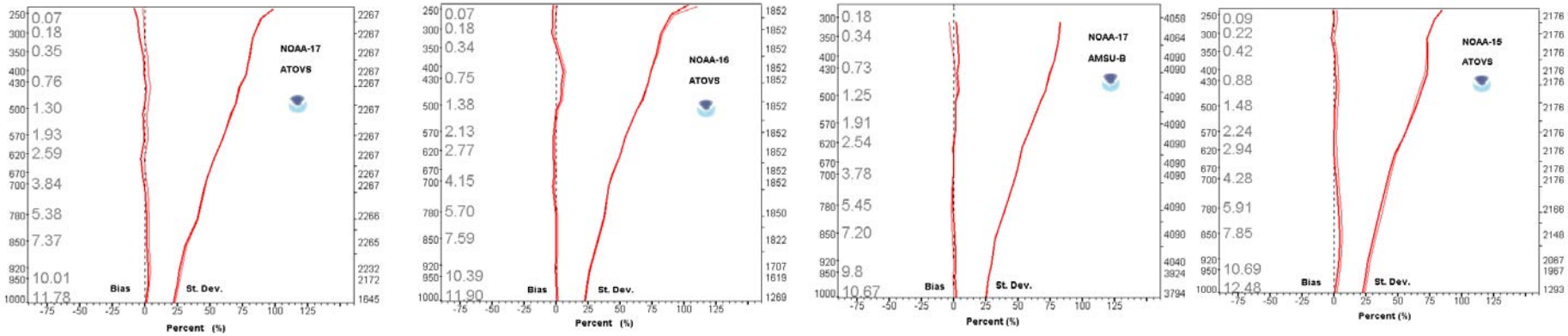

Figure 11: **Satellite minus radiosonde differences in percent (%) water vapor mixing ratio (g/kg) for (left to right) ATOVS from NOAA-17, ATOVS from NOAA-16, AMSU-B from NOAA-17, and ATOVS from NOAA-15, covering the 60N to 60S region over the period Sept 2-7, 2002; the atmospheric pressure and sample size per level are shown along the outside of each vertical axis, with the mean mixing ratio values used to compute percentages inside each left axis.**

The moisture curves represent difference in percent (%) of satellite minus radiosonde moisture at each level based on the mean moisture profiles indicated on the inside of the leftmost axis of each plot (which explains why the values increase with height). A high degree of consistency is observed among the ATOVS moisture soundings from the three operational satellites, and against the AMSU-B products, with estimated accuracies ranging from about 25% [5] near the surface (about 1.2 g/kg) to about 75% (less than .1 g/kg) aloft.

FUTURE PLANS

A new series of science changes for NESDIS derived sounding products are currently under development for ATOVS. Referred to as System-2004, the motivation for these upgrades is to satisfy the greatest common denominator of the total user need, as well as to provide a benchmark capability which is compatible with planned next generation of NPOESS systems (Aumann *et al.* 2003). System-2004 will provide a dual set of "derived" products, first, a more stable and clearly traceable data set of measurements and products suitable for climate, embedded within and serving as the apriori estimates for the more dynamic and traditional second set of real-time weather products for NWP, but one which is well-behaved with respect to the background error problem, explicitly satisfies the measurements within some known uncertainty interval, and is independent of any particular NWP model.

The **scientific upgrades** planned by NESDIS for ATOVS System 2004 derived sounding products include:

- inclusion of AMSU-B measurements in the simultaneous retrieval of temperature and moisture soundings,
- replacement of the library search technique for computing the first guess with an AMSU based statistical regression approach (Goldberg 1999),
- radiative transfer bias adjustment of sounder measurements, and
- more explicit use of radiative transfer (McMillin *et al.* 1995) model to retrieve soundings.

In addition, **peripheral upgrades** to improve ancillary data and products validation in conjunction with the System-2004 modifications will include:

- more stabilized limb adjustment procedures,
- convergence with techniques resident in the NESDIS operational Microwave Surface and Precipitation Products System,
- expanded validation to compare collocated satellite, NWP, and radiosonde data including observed versus calculated radiances, and
- grid satellite parameters.

These upgrades are targeted for a phased operational implementation beginning the Summer of 2004.

[5] Values are inflated given the inherent uncertainty in radiosonde moisture measurements and the high spatial and temporal variability of moisture (compared to temperature).

REFERENCES

Allegrino, A., A.L. Reale, M.W. Chalfant and D.Q.Wark, 1999: Application of limb adjustment techniques for polar orbiting sounding data. *Technical Proceedings of the 10th International TOVS Study Conference*, Jan 26- Feb 2, Boulder, Colorado, USA., 1-10.

Aumann, H.H., M.T. Chahine, C. Gautier, M.D. Goldberg, E. Kalnay, L.M. McMillin, H. Revercomb, P.W. Rosencranz, W.L. Smith, D.H. Staelin, L.L. Strow, and J. Susskind, 2003: AIRS/AMSU/HSB on the AQUA mission: design, science objectives, data product, and processing systems. *IEEE Trans. Geosci. Remote Sensing*, Vol 41, pp253-264.

Chalfant, M.W., A. Reale and F. Tilley, 1999: Status of NOAA advanced microwave sounding unit-B products. *Technical Proceedings of the 10th International TOVS Study Conference*, Jan 26-Feb 2, Boulder Co., USA, pp. 60-71.

Daniels, J.M., M.D. Goldberg, H.E. Fleming, B. Katz, W.E. Baker, and D.G. Deaven, 1988: A satellite retrieval/forecast model interactive assimilation system. *12th Conference on Weather Analysis and Forecasting*, AMS, Monterey, Ca..

Ferguson, M.P., and A.L. Reale, 2000: Cloud detection techniques in NESDIS Advanced-TOVS sounding products systems. *10th Conf. on Satellite Meteorology and Oceanography*, 9-14 January, Long Beach, CA

Fleming, H.E., D.S. Crosby, and A.C. Neuendorffer, 1986: Correction of satellite temperature retrieval errors due to errors in atmospheric transmittances. *Journal of Climate and Applied Meteorology*, Vol 25, No. 6, 869-882.

Goldberg, M, J. Daniels and H. Fleming, 1988: A method for obtaining an improved initial approximation for the temperature/moisture retrieval problem. *Preprints, 3rd Conference on satellite Meteorology and Oceanography*, Anaheim, Ca, 16-19.

Kalnay, E., M. Kanamitsu, and W.E. Baker, 1990: Global numerical weather prediction at the National Meteorological Center. *Bull. Amer. Meteor. Soc.*, Vol 71, pp. 1410-1428.

McMillin, L.M., L. Crone and T.J. Kleespies, 1995: Atmospheric transmittances of an absorbing gas. 5. Improvements to the OPTRAN approach. *J. Appl. Opt.*, 34, 8396-8399.

McNally, A.P., J.C. Derber, W.S. Wu, and B.B. Katz, 2000: The use of TOVS level-1B radiances in the NCEP SSI analysis system. *Q.J.R. Meteorol Soc.*, Vol 126, pp. 689-724.

Reale, A.L., 2001: NOAA operational sounding products from advanced-TOVS polar orbiting environmental satellites. *NOAA Technical Report NESDIS 102*, U.S. Dept. of Commerce, Washington D.C., 61 pp.

Reale, A.L., 2002: NOAA operational sounding products for advanced-TOVS: 2002. *NOAA Technical Report NESDIS 107*, U.S. Dept. of Commerce, Washington D.C., 29 pp.

Reale, A.L. 1995: Departures between derived satellite soundings and numerical weather forecasts: present and future. *Tech. proceeding of the 8th International TOVS Study Conf.*, Queenstown, New Zealand, 395-404.

Tilley, F.H., M.E. Pettey, M.P. Ferguson, and A.L. Reale, 2000: Use of radiosondes in NESDIS advanced-TOVS (ATOVS) sounding products. *10th Conference on Satellite Meteorology and Oceanography*, 9-14 January, Long Beach, CA.

Further development of the ATOVS and AVHRR Processing Package (AAPP), including an initial assessment of EARS radiances

Nigel C Atkinson and Keith W Whyte

Met Office, Exeter, UK

Introduction

AAPP is a retrieval and analysis package for ATOVS and AVHRR. The package is maintained by the EUMETSAT Satellite Application Facility for Numerical Weather Prediction (NWP SAF). The host centre for the NWP SAF is the Met Office, with partners ECMWF, KNMI and Météo-France (see http://www.metoffice.com/research/interproj/nwpsaf/index.html).

This paper describes the latest updates to AAPP which are incorporated into the newly-released version 4.0. It also describes the changes being implemented for future releases, firstly to allow for processing of data from the NOAA-N and N′ satellites and secondly for the METOP era.

A recent development in the acquisition of ATOVS data is the establishment of the EUMETSAT ATOVS Retransmission Service (EARS), in which data from a network of HRPT receiving stations are collected by EUMETSAT and re-transmitted to users in a timely manner suited to the needs of European operational short-range NWP (see http://www.eumetsat.de/en/dps/atovs.html). EARS data from up to 8 receiving stations are currently being received and processed routinely at the Met Office using AAPP, in order to assess the data quality, with any anomalies being automatically reported to EUMETSAT. The paper includes some examples of comparisons between global (NESDIS) and EARS data, and discusses the potential contribution of EARS data in the context of NWP.

AAPP Version 4

Version 4.0 of AAPP is scheduled for release in October 2003. It includes the following enhancements compared with Version 3:

1. Rationalised documentation. The following documents are now included:
   - Scientific description
   - Software description
   - Data formats document
   - AAPP overview
   - Installation guide (html)
2. Compatible with both Fortran 90 and FORTRAN 77 compilers.
3. Correction for the presence of the moon in the AMSU-A space view. When the moon passes through the AMSU-A space view the space-view brightness temperature increases by typically 2K, causing errors in the calibrated scene radiances. The predicted position of the moon is computed using standard astronomical formulae, and a correction is applied for those scans for which the moon is within 3.5° of the space view, by interpolating the calibration gain from the neighbouring uncontaminated scans. The correction forms part of the AAPP pre-processing stage (atovin) and therefore applies to both global and local data. The method has been in operational use in the Met Office implementation of AAPP since 2002.

   Note that NESDIS are planning to introduce a moon correction at 1b level based on antenna patterns, i.e. the space-view brightness temperature error is estimated and subtracted prior to computing the calibration coefficients (Kigawa and Mo, 2002). Both methods are expected to be effective in reducing the errors to below 0.1K.

4. Allow different antenna efficiencies for different satellites (in subroutine *infdf*). Previously only one set of antenna efficiencies could be used. The antenna efficiencies are used in the pre-processing to correct for contamination of the AMSU Earth views by cold space.
5. Correct 'bug' in subroutine *surfelev*. Use of real variable in DO loop caused different results for F90 and F77.

Developments for NOAA-N and N'

AAPP version 5 will include the ability to process data from NOAA-N and N'. It is intended that version 5 will be released shortly after the NOAA-N launch, currently scheduled for summer 2004. The NOAA-N satellite includes two new instruments:

- Microwave Humidity Sounder (MHS) replaces AMSU-B
- HIRS/4 replaces HIRS/3

The differences between MHS and AMSU-B include the following:

1. Channel 20 is a single band centred on 190.31 GHz; AMSU-B has bands at 183.31±7 GHz.
2. Channel 17 is moved to 157 GHz; AMSU-B uses 150 GHz.
3. Channels 18-19 have horizontal polarization at nadir; AMSU-B has vertical polarization
4. MHS has spare local oscillators, referred to as LO-A and LO-B. The nonlinearity coefficients are characterized separately
5. MHS has spare processing electronics (PIE-A and PIE-B)
6. The method of computing the internal target temperature is different, involving the use of three precision resistors for MHS.
7. The MHS instrument itself outputs data in 'packet' format, as required by METOP. The NOAA satellites use an on-board MHS Interface Unit (MIU) to convert the packet data to a form that the satellite can handle. For the HRPT transmission, the MIU writes the MHS data into the same data slots as are currently used for AMSU-B.

The changes needed in AAPP to process MHS are as follows:

- Updated decommutation program, to read the new MHS data format within the HRPT stream
- New level 1b format (*mhs1b.h*)
- New calibration and navigation program, *mhscl*
- Updated pre-processing to allow conversion of MHS level 1b into a level 1c format that is common to MHS and AMSU-B (i.e. *amb1c.h* is unchanged)

The differences between HIRS/3 and HIRS/4 are relatively minor, but do require a new level 1b format.

Other enhancements planned for AAPP version 4 include:

- Capability of using the new HIRS calibration algorithm (version 4.0 – Changyong Cao, pers. comm.)
- Correction for moon contamination in AMSU-B/MHS space views, as part of *amsubcl* and *mhscl*. Currently the affected scan lines are rejected by quality control. The positions of the 4 space view samples will computed and compared with the predicted position of the moon. Any samples that are too close to the moon will be rejected – up to 3 samples may be rejected by this method, but the calibration will still be valid, albeit slightly noisier than normal. NESDIS currently allow for moon contamination by rejecting space-view samples with significantly elevated counts (i.e. a diagnostic method), but are planning for MHS to implement the prognostic method described above.
- Navigation updates, including capability of using 2-line orbital elements, with SGP4 propagation model.

Developments for METOP

The NWP SAF is currently working with EUMETSAT in order to develop AAPP for the METOP era. It is anticipated that developments for METOP will form part of AAPP version 6. Receiving stations and software for the direct broadcast HRPT signal will be supplied by EUMETSAT, with the output data being interfaced to AAPP at EUMETSAT level 0 (which is equivalent to NOAA level 1a). Developments required for AAPP will include:

- Reading in the level 0 data
- New orbital prediction and attitude prediction software. Note that METOP will normally operate in yaw-steering mode, in which the satellite attitude is controlled such that it is always pointing towards the local normal to the Earth's surface (as compared with NOAA satellites which point at the centre of the Earth).
- Use of 'Admin' messages to provide navigation information, and also to provide warnings of imminent spacecraft manoeuvres. In-plane manoeuvres have only a small impact as far as the data are concerned, but out-of-plane manoeuvres require the satellite to be rotated through 90º, with consequent loss of data for a period of a few hours.

The NWP SAF are responsible for providing near-real-time data from AMSU-A, MHS, AVHRR, HIRS and IASI. For IASI, the pre-processing code is being developed by CNES and will be kept separate from AAPP where possible.

Use of EARS data in the Met Office

AAPP is used operationally in the Met Office for the pre-processing of ATOVS data from the following sources:

1. Global data from NOAA/NESDIS, received via the Global Telecommunications Service network (GTS)
2. HRPT direct from the NOAA satellites, received at West Freugh (Scotland)
3. EARS data transmitted via the EUMETCast service. Both levels 1a and 1c are currently received, though 1c is not routinely processed.

The EARS data are potentially useful for both global and local forecasting because the service provides data over a wide area, with much shorter delays than is the case for global data. EARS data are typically available within 30 minutes of the start of the satellite over-pass – as compared with 3 to 6 hours for global data. However, before they can be used in NWP it is necessary to ensure that the data are reliable and that the radiances are consistent with the global radiances. Therefore a system of monitoring has been implemented based on AAPP, as shown in Fig. 1.

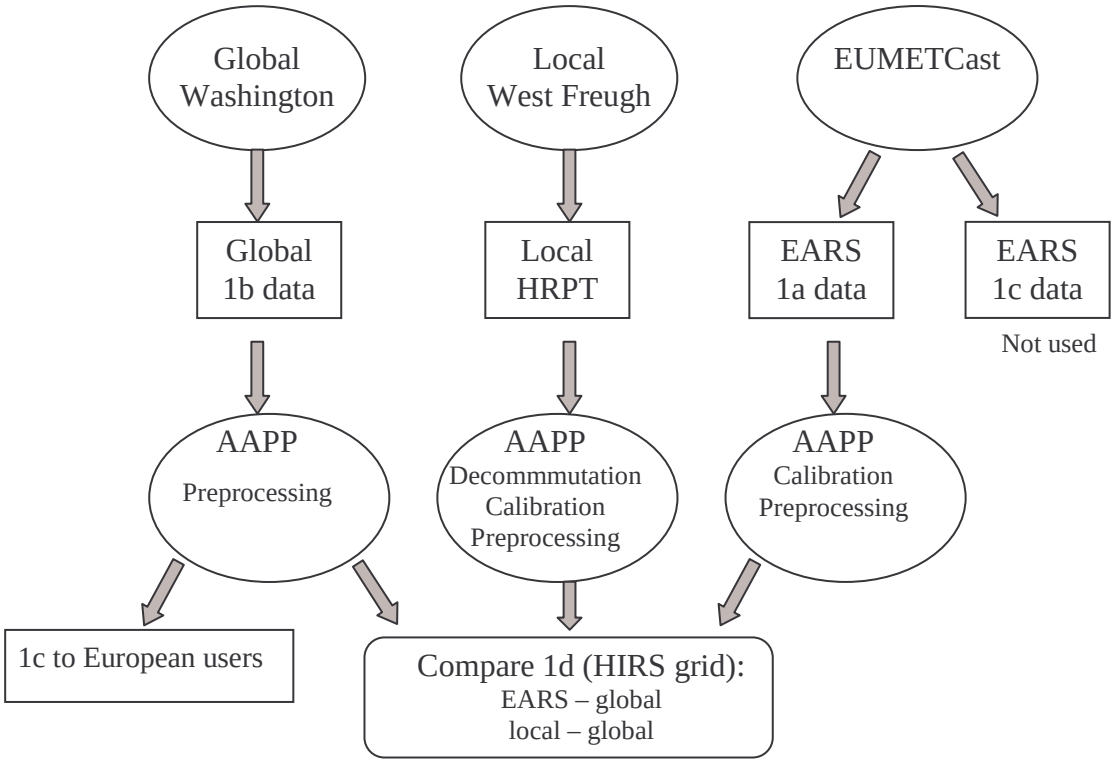

Fig. 1: Use of AAPP in the Met Office for processing global, local and EARS ATOVS data.

Data are received and processed routinely from the following stations in the EARS network:

- Tromsø (Norway)
- Kangerlussuaq (Greenland)
- Maspalomas (Canaries)
- Edmonton (Canada)
- Athens (Greece)

Data are also received from Bedford (Canada), Gander (Newfoundland) and Monterey (California), but not processed routinely.

Figs 2 to 5 show examples of comparisons between global data, local data and EARS data from Tromsø. Fig. 2 compares the geolocation of the HIRS footprints for global data and EARS. There are differences of about 10% of the cross-track sampling distance, for reasons that will be explained below. Fig. 3 and Fig. 4 compare the brightness temperatures of AMSU channel 15 (89GHz), for Tromsø and local data respectively. Note that this comparison is at level 1d, i.e. after mapping to the HIRS grid.

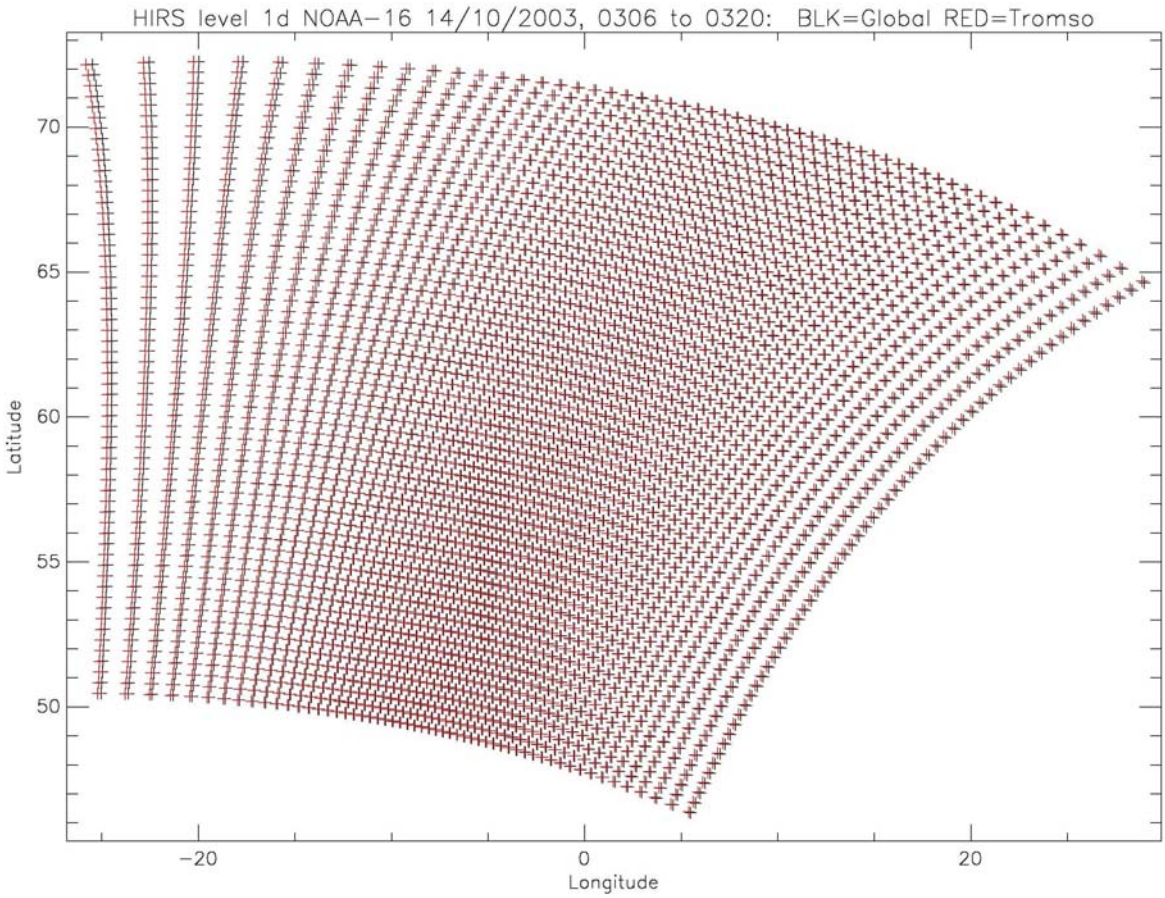

Fig. 2: HIRS Geolocation for Tromsø EARS data processed to level 1d, compared with global data.

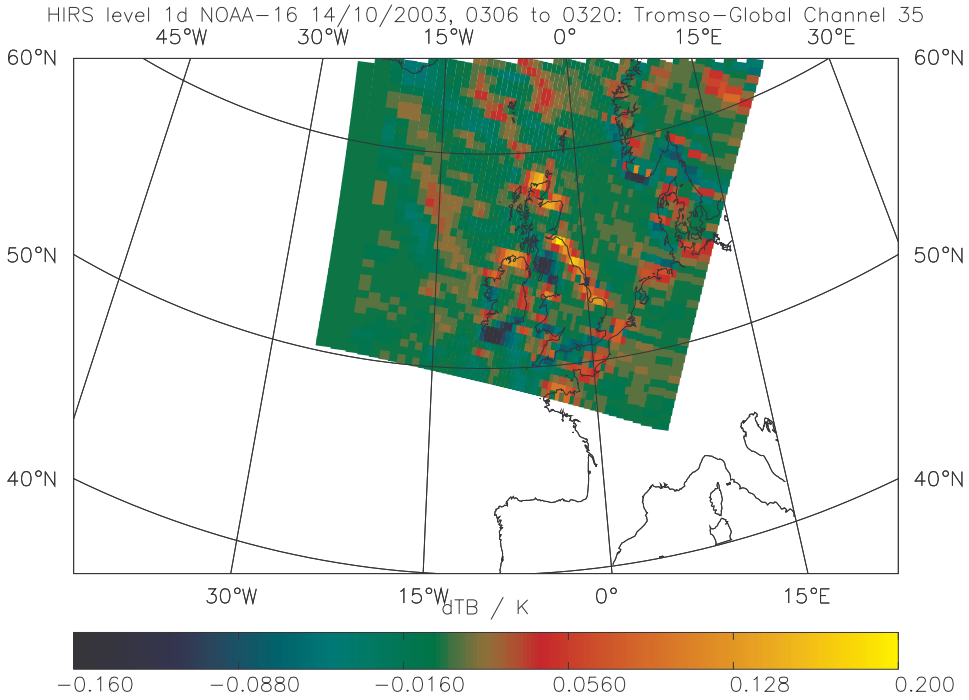

Fig. 3: Brightness temperature for AMSU channel 15 (89GHz):EARS Tromsø compared with global, at level 1d.

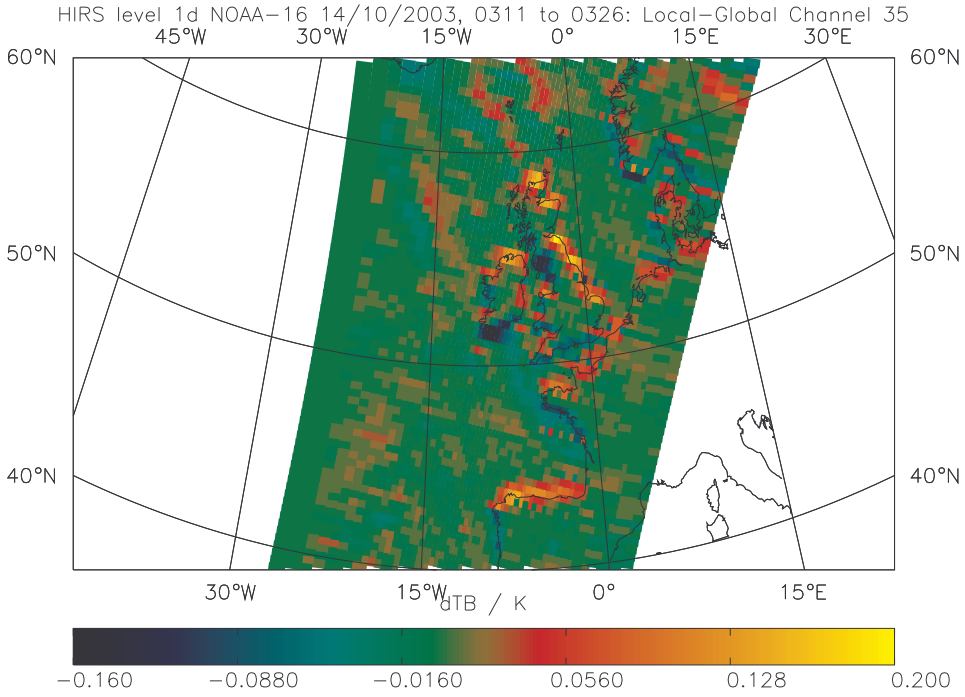

Fig. 4: Brightness temperature for AMSU channel 15 (89GHz):local compared with global, at level 1d.

For mapping, differences between global and EARS (or local) data can be caused by the following:

1. Orbit and attitude prediction method. The Met Office implementation of AAPP uses TBUS bulletins from NOAA which are updated daily via the GTS. For global data, NOAA uses a more sophisticated method which is not available to users. Finally, EARS data processed to level 1c by EUMETSAT use TBUS bulletins obtained from the NOAA web site. For more information on TBUS bulletins, see http://noaasis.noaa.gov/NOAASIS/ml/navigation.html.
2. Re-mapping to the HIRS grid. The HIRS instruments on NOAA-16 and NOAA-17 have a cross-track pointing error of approximately one sample. For global data, NOAA assume a fixed offset of 1.8° compared with nominal; AAPP currently assumes offsets of 2.0° for NOAA-16 and 1.7° for NOAA-17, these values having been determined from comparisons with AVHRR (see `include/timang.h` in the aapp code)

Brightness temperature differences can be caused by the following:

1. Re-mapping to HIRS grid (as above)
2. Differences in the calibration coefficients.

For the microwave radiometers (AMSU-A, AMSU-B) the calibration has been found to be consistent between global and local data to ~0.01K (i.e. at level 1c), so the global-local differences in Figs 3 and 4 are due almost entirely to the HIRS misalignment in the re-mapping process. The differences shown (up to 0.2K) are generally acceptable, and would be expected to be reduced for the higher sounding channels that are not sensitive to surface features.

For HIRS itself, a calibration is only performed every 256 seconds, so significant calibration differences can result for those parts of the local over-pass that are not bounded by calibrations. This is a drawback with the use of locally-received HIRS data.

Potential impact of EARS data in NWP

The timeliness of EARS data makes it valuable in the context of operational NWP. In the Met Office, the main 12Z global forecast run is performed at approximately 1400 GMT, accepting observations valid between 0900 and 1500 GMT. Fig. 5 shows an example of the global ATOVS observations that have been received and pre-processed by that time, over Europe and the northern Atlantic. We see that not only is there a large data void between 30°W and 10°E, but no NOAA-17 data are available in the displayed area.

By contrast, Fig. 6 shows the EARS observations that are available, completely filling the data void and providing several passes of NOAA-17 data.

It is planned to start assimilation trials using EARS during autumn 2003.

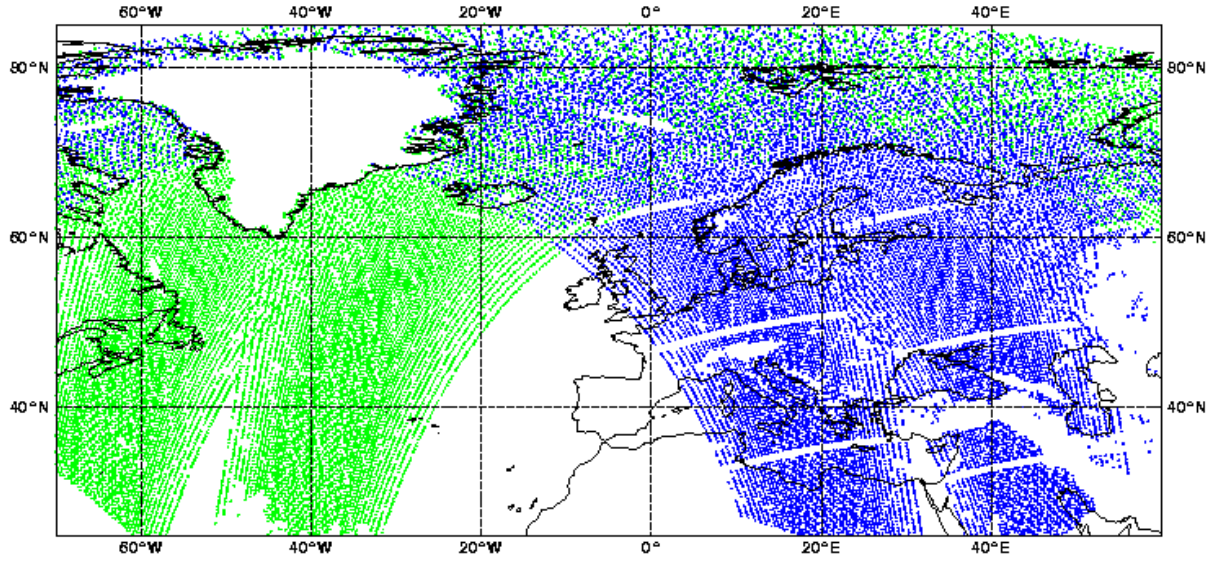

Fig. 5: ATOVS observations available for forecast run at 14:00, accepting observations between 09:00 and 15:00 GMT. Green: NOAA-15; blue: NOAA-16.

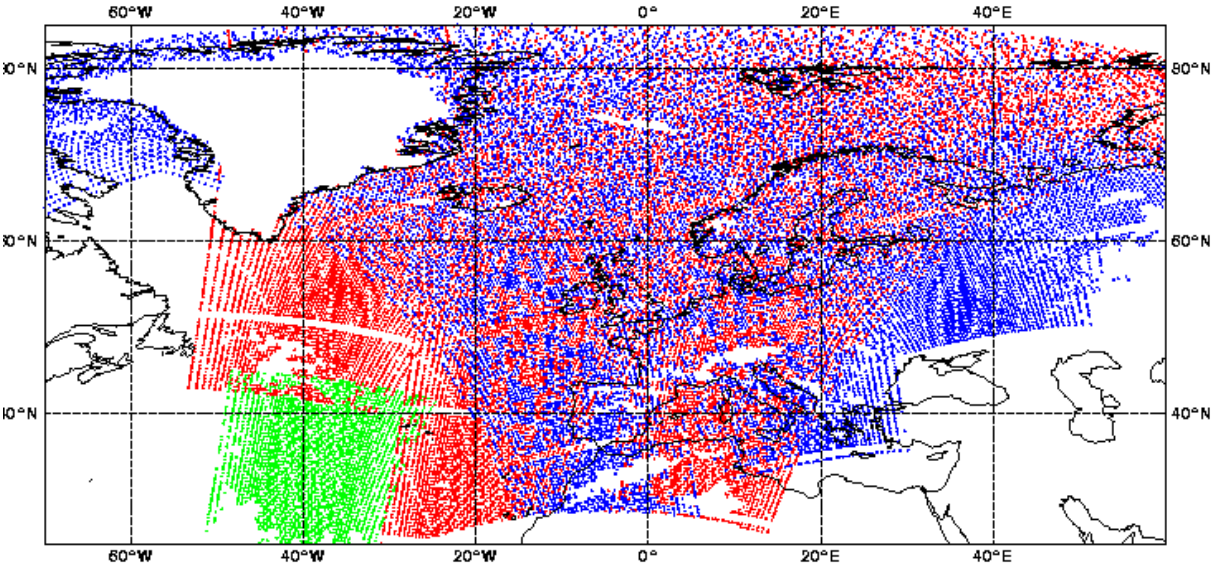

Fig. 6: EARS observations available for forecast run at 14:00, accepting observations between 09:00 and 15:00 GMT. Green: NOAA-15; blue: NOAA-16; red: NOAA-17.

Conclusions

AAPP version 4 includes a number of enhancements compared with version 3, including Fortran 90 compatibility, improved documentation and a correction for lunar contamination in AMSU-A. Version 4 is being released by EUMETSAT in October 2003.

Preparations are underway for the launch of NOAA-N in 2004. AAPP version 5 will include the ability to process the NOAA-N instruments, as well as enhanced navigation modules. The NWP SAF is working with EUMETSAT in order to ensure continuation of a direct reception capability in the METOP era.

Data from the EUMETSAT EARS system are being received routinely at the Met Office, and monitored for data quality. The consistency between global NESDIS data and EARS data processed via AAPP is generally good, and the excellent timeliness of EARS means that it should have a useful impact in NWP. Trials are expected to start in autumn 2003 in order to quantify the impact.

Acknowledgements

Thanks are due to Pascal Brunel and Tiphaine Labrot (Meteo-France) for their contributions to AAPP via the NWP SAF, and also to Rainer Schraidt at EUMETSAT.

Thanks also to Brett Candy and Una O'Keeffe (Met Office) for their work in analysing and monitoring the EARS data.

References

Kigawa, S. and Mo, T. 2002. An algorithm for correction of lunar contamination in AMSU-A data. *NOAA Technical Report NESDIS 111*.

The National Polar-orbiting Operational Environmental Satellite System: Future U.S. Operational Earth Observation System

Hal J. Bloom and Peter Wilczynski

Over the last decade, the tri-agency Integrated Program Office (IPO), comprised of the National Oceanic and Atmospheric Administration (NOAA), the Department of Defense (DoD), and the National Aeronautics and Space Administration (NASA), has been managing the development of the National Polar-orbiting Operational Environmental Satellite System (NPOESS). NPOESS will replace the current military and civilian polar-orbiting environmental satellites. The IPO, through its Acquisition and Operations (A&O) contractor, Northrop Grumman, will begin in 2009 to launch NPOESS spacecraft into three orbital planes to provide a single, national system capable of satisfying both civil and national security requirements for space-based, remotely sensed environmental data.

In 1997, the IPO initiated a robust sensor risk reduction effort that was focused on early development of the critical sensor suites and algorithms necessary to support NPOESS. In 2001, preliminary design efforts were completed for the last of five critical imaging/sounding instruments for NPOESS. Three of these sensors are scheduled to fly on the joint NASA/IPO NPOESS Preparatory Project (NPP) mission in 2006. Early flight-testing of instruments will reduce development risk and demonstrate and validate global imaging and sounding instruments, algorithms, and pre-operational ground processing systems prior to delivery of the first NPOESS spacecraft.

To meet user-validated requirements for 55 geophysical parameters, NPOESS will deliver global Stored Mission Data (SMD) to four U.S. centers for processing and distribution, with 95% of the data being delivered in less than 28 minutes from the time of collection. Global SMD will be down-linked to 15 globally distributed ground stations at Ka-band frequencies and will be the complete, full resolution data set containing all sensor data and auxiliary data necessary to generate all NPOESS Environmental Data Records. NPOESS spacecraft will also simultaneously broadcast two types of real-time data to suitably equipped ground stations. The NPOESS High Rate Data broadcast (X-band frequencies) will be a complete, full resolution data set and is intended to support users at regional hubs. The NPOESS Low Rate Data broadcast (L-band frequencies) will be a subset of the full data set and is intended for U.S. and worldwide users of remote/mobile field terminals.

The advanced technology visible, infrared, and microwave imagers and sounders that will fly on NPOESS will deliver higher spatial and temporal resolution atmospheric, oceanic, terrestrial, climatic, and solar-geophysical data, enabling more accurate short-term weather forecasts and severe storm warnings, as well as serving the data continuity requirements for improved global climate change assessment and prediction.

PREPARATIONS FOR THE GEOSYNCHRONOUS IMAGING FOURIER TRANSFORM SPECTROMETER

J.F. Le Marshall[1], W.L. Smith[2], R.G. Seecamp[1], A. Rea[1], L.M. Leslie[3], M. Dunn[4] and B. Choi[5]

[1] Bureau of Meteorology, Melbourne, Australia, [2] NASA Langley Research Center, Hampton, VA, 23681, USA, [3] University of Oklahoma, Norman, Oklahoma, USA, [4] Latrobe University, Melbourne, Australia, [5] Latrobe University, Bendigo, Australia

INTRODUCTION

The Geosynchronous Imaging Fourier Transform Spectrometer (GIFTS) will be completed in late 2005, to support a 2006 or later launch. The GIFTS will be orbited as part of NASA's New Millennium Program Earth Observing-3 (EO-3) Mission and will serve as a prototype of sounding systems to fly on future operational geostationary satellites.

The first year of operation of GIFTS will support the infusion of new technologies and data processing techniques into future geostationary operational satellite systems and ensure their timely exploitation in numerical weather prediction (NWP). The mission will validate the GIFTS measurement concept for altitude-resolved (water vapour observation based) winds. The GIFTS will result in high temporal and spatial resolution soundings of the atmosphere for temperature and absorbing species such as water vapour and ozone, and demonstrate new technologies for future research and operational systems.

We note some of the development activity in support the application of GIFTS data over continental USA and also note preparation for the collection and utilisation of this data when the GIFTS is stationed over its permanent position which is dependent upon the satellite mission of which GIFTS is part. The development activity includes preparation for providing; radiance products for NWP, altitude resolved, error characterised winds, temperature and moisture profiles, product imagery (stability fields, water vapour fields, etc.), sea and land surface temperatures with attendant emissivities, ozone and CO amounts and cloud properties. The development activity has included use of aircraft ultra spectral observations, AIRS (Advanced Infrared Sounder) data, and also synthetic GIFTS data. Overall, it is clear that the program indicates significant potential benefit from the high temporal, spectral and spatial resolution ultra spectral observations provided by this instrument and supports further preparation for their exploitation.

2. BACKGROUND

The GIFTS (Smith et al. 2001) was selected for NASA's New Millennium Program (NMP) Earth Observing-3 (EO-3) mission in 2000. The GIFTS combines emerging sensor and data processing technologies to make geophysical measurements that will contribute to earth system science and lead to significant improvements in meteorological observation and forecasting. The mission will demonstrate revolutionary technologies for future research and operational systems and will validate the measurement concept of water vapour observation based altitude-resolved winds. The use of GIFTS technologies in operational instrumentation

is vital for optimizing the next generation of geostationary weather and climate observing systems.

The first year of operation of GIFTS is particularly important for supporting the infusion of GIFTS technology and data processing techniques into the future operational GOES-R system. After a validation and demonstration phase over continental USA, it is planned to transfer the GIFTS operation to a permanent location dependent upon the specific satellite mission selected for the GIFTS. The intent is to use the GIFTS data for Earth Observing System (EOS) scientific research and also for operational weather forecasting as a component of the Global Observing System (GOS).

3. THE GIFTS EO-3 MISSION

The GIFTS New Millennium Program Earth Observing-3 (EO-3) satellite mission will allow advanced technologies to observe surface thermal properties, and atmospheric weather and chemistry variables in four dimensions. Focal plane detector arrays, combined with a Fourier Transform Spectrometer will enable atmospheric radiance spectra from many fields of view to be observed simultaneously at the detector elements, thereby providing high horizontal, vertical and temporal resolution temperature and moisture sounding information. The temporal resolution will be provided by the geosynchronous satellite platform, which allows near continuous imaging of the atmosphere's three-dimensional structure.

The GIFTS instrument will be completed, tested, and launch ready by the end of 2005. There is currently considerable effort being devoted to identifying a spacecraft opportunity for a 2006-2009 launch, possibly through the US Air Force space test program. After the validation and demonstration phase over continental USA, the GIFTS will be moved to its permanent location, dependent upon the specific space mission chosen for the GIFTS, to continue its Earth Observing System role as part of the GOS. The GIFTS permanent location may be over the Indian Ocean, as originally planned, or for example the western Pacific Ocean. The Australian Bureau of Meteorology has already undertaken planning and development activity to support GIFTS data acquisition, processing, distribution, application and archival for such an eastern hemisphere satellite position.

4. THE INSTRUMENT AND MEASUREMENTS

All of the new GIFTS technologies are now developed, being tested and meeting or exceeding requirements. The GIFTS uses large area format focal plane array (LFPA) infrared (IR) detectors (128 × 128) in a Fourier Transform Spectrometer (FTS) mounted on a geosynchronous satellite to gather high-spectral resolution (0.6 cm^{-1}) and high-spatial resolution (4-km footprint) infrared radiance spectra over a large geographical area (512 km × 512 km) of the Earth in a 10-second time interval. Extended Earth coverage is achieved by step scanning the instrument viewing area in a contiguous fashion. The radiance spectra observed at each time step (see Fig. 1) can be used to infer high vertical

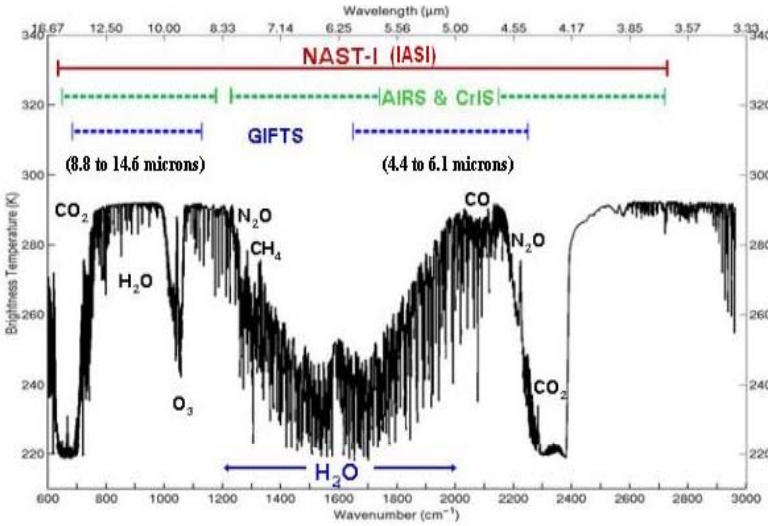

Figure 1. The NAST-I spectral coverage compared to that of advanced satellite sounders.

resolution (1 - 2 km) temperature and water vapour mixing ratio profiles. These profiles are obtained on a 4-km grid and may be converted to relative humidity profiles. Images of the horizontal distribution of relative humidity for atmospheric levels, vertically separated by approximately 2 km, can be constructed for each spatial scan. Successive images of clouds and the relative humidity for each atmospheric level can then be used to reveal the motion of small-scale thermodynamic features of the atmosphere, providing a measure of the wind velocity distribution as a function of altitude. The net result is a dense grid of temperature, moisture, and wind profiles which can be used for atmospheric analyses and operational weather prediction. Ozone (O_3) and carbon monoxide (CO) features observed through their spectral radiance signatures provide a measure of the transport of these pollutant and greenhouse gases.

5. PRODUCTS

Programs are now well underway to develop products for the validation, demonstration and extended operational phases of the GIFTS EO-3 mission. The products include :

- Radiance products (selected channels, superchannels, eigenvectors),
- Altitude-resolved winds
- Water vapour (soundings, fluxes, winds),
- Temperature (soundings, stability),
- Carbon monoxide concentration (2 Layers),
- Ozone concentration (4 Layers),
- Surface Temperature and emissivity,
- Clouds (altitude, optical depth, microphysical properties, winds),
- Mineral Dust / Aerosol Concentration and Visibility.

These applications are under test, supported by well-advanced development programs.

6. A PRODUCT EXAMPLE – ALTITUDE-RESOLVED WINDS

A key measurement concept associated with GIFTS is high spatial and temporal resolution altitude resolved winds. These winds represent an important product to be produced by the GIFTS. Work to date on this application has used both synthetic data and airborne interferometer observations. Here, we note recent work based on airborne interferometer data taken in association with THORPEX (THe Observing system Research and Predictability EXperiment). The data was collected by the NAST-I (National Polar-orbiting Operational Environmental Satellite System (NPOESS) Airborne Sounding Testbed-Interferometer) instrument flown aboard a NASA ER-2 aircraft. The NAST-I is described below.

6.1 The NAST-I Instrument

The NAST-I (Smith et al. 1999) was developed by the NPOESS Integrated Program Office (IPO) to be flown on high altitude aircraft and provide the experimental observations needed for finalizing specifications and testing proposed designs and data processing algorithms for the Cross-track Infrared Sounder (CrIS) and for the GIFTS. The NAST-I has a spectral range of 3.6–16.1 μm, without gaps (See Fig. 1) and covers the spectral ranges and resolutions of current and planned advanced high spectral resolution infrared spectrometers to fly on polar orbiting and geostationary weather satellites. These include the EOS-AIRS (Advanced Infrared Sounder), METOP-IASI (Infrared Atmospheric Sounding Interferometer), the NPP (NPOESS Preparatory Project)/NPOESS-CrIS (Cross-track Infrared Sounder), and the EO-3/GIFTS. The NAST-I spectral resolution is equal to, in the case of IASI, or higher than all current and planned advanced sounding instruments. Hence, the NAST-I data can be used to simulate the radiometric observations to be achieved from these advanced sounding instruments. Moreover, the forward radiative transfer models and product retrieval algorithms planned for these satellite systems can be validated prior to launch. The NAST-I can also be used for the vital purpose of post-launch calibration and validation of sensors and data products for the advanced satellite sounding systems.

The NAST-I spatially scans the Earth and atmosphere from an aircraft, such as the high-altitude NASA ER-2 research aircraft. From an altitude of 20 km, 2.6 km spatial resolution and a 46 km swath width can be achieved, thereby providing three-dimensional hyperspectral images of radiance (x, y, υ) and derived geophysical products. Sequential aircraft over flights can provide a fourth dimension, time.

6.2 Altitude-resolved Winds

In February 2003, the THORPEX field experiment west of the California coast was instrumental in providing data to allow generation and validation of water vapour tracer wind profiles generated from consecutive NAST-I multi-frequency images. The data was from a NASA ER-2 flight on 11 February 2003 and the method used for determination of the atmospheric water vapour concentration was the eigenvector method of Smith and Wolf (1976), (Zhou et al. (2002)). The winds were subsequently generated from consecutive single pressure level relative humidity images using an automatic tracking program, developed at the University of Wisconsin. The winds at 950 and 850 hPa are shown in Fig. 2.

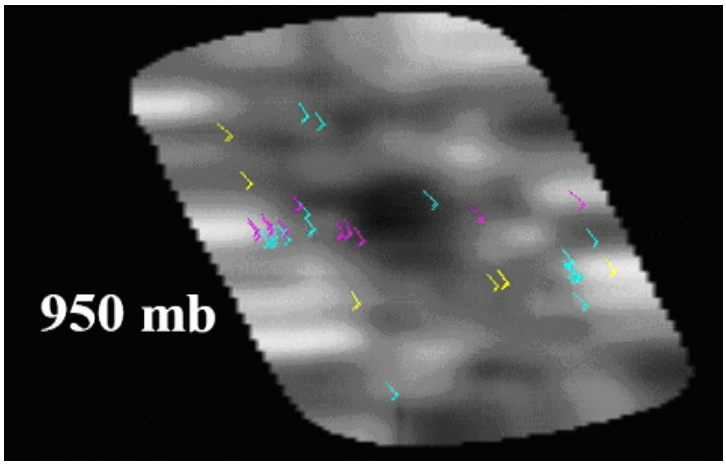

Fig. 2 (a) Automated NAST Water Vapour Profile Tracer Winds at 950 mb

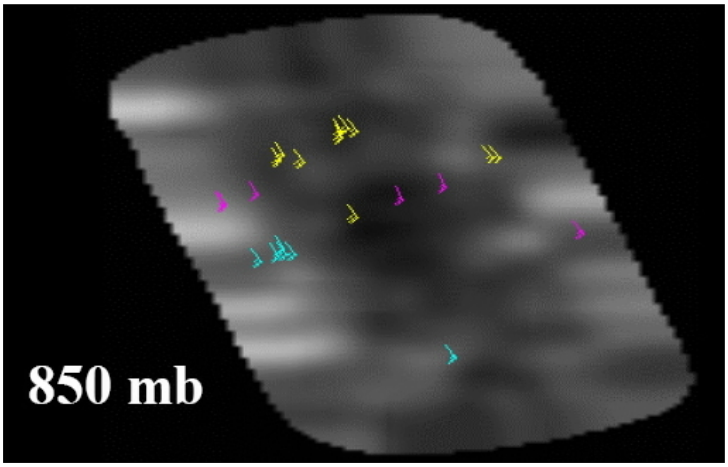

Fig. 2 (b) As in Fig. 2 (a) but at 850 mb

The automated NAST-I water vapour profile tracer winds showed good time and space continuity. A comparison of the NAST-I winds with those measured by Twin Otter Doppler LIDAR is shown in Fig. 3. The profiles indicated differences generally less than 3 m/s.

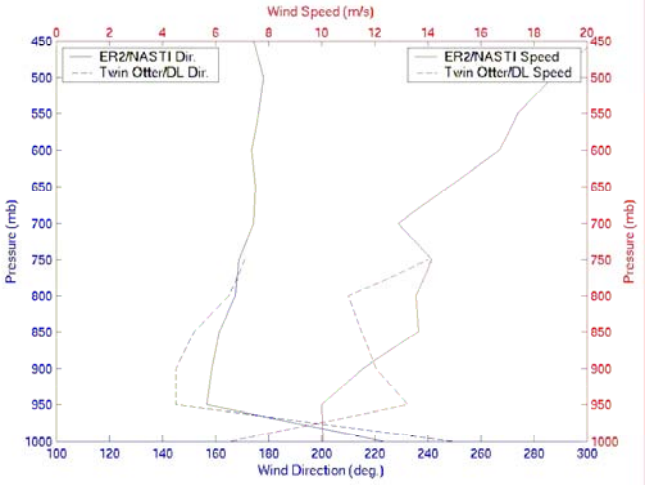

Fig. 3 A comparison of collocated, contemporaneous winds from NAST-I water vapour observations and NOAA measurements near 35° N, 121° W on 11 February 2003

This study has also been complemented by earlier work using airborne advanced sounder observations taken during the CAMEX experiment in September 1998. In that study, sequential NAST-I based water vapour and temperature retrievals were used with 4D-VAR (Bennett et al. 1996) in a study to demonstrate the influence of these data on the assimilated wind field (Leslie et al. 2002, Le Marshall et al. 2003).

The application of winds generated directly from multi-frequency imagery to NWP has also been investigated. The error characterisation of atmospheric motion vectors, including the estimation of their expected error, and their application to NWP, is reported in Le Marshall et al. (2004a, 2004b). The accurate error characterisation of GIFTS based AMVs is considered an important part of this development activity.

7. SUMMARY

All the new technologies required for GIFTS are developed and under test. They are meeting or exceeding mission requirements. The instrument is expected to be completed, tested and launch-ready by the end of 2005. A spacecraft opportunity for a 2006 – 2009 launch is currently being identified. Development work supporting the effective exploitation of GIFTS data is well advanced and shows the significant potential benefit from the instrument.

The validation phase over the first eighteen months involves data delivery to NASA, NOAA, the US Navy and the UW CIMSS for operational utility demonstration and a comprehensive validation process. Movement of the GIFTS to a permanent location for the extended operations phase of the mission could benefit greatly from reception, data processing and product generation at a ground station in the Eastern Hemisphere region such as Australia. Planning for such an involvement has been undertaken in the Australian Bureau of Meteorology and development work related to product generation is already underway.

8. ACKNOWLEDGEMENTS.

Many thanks are due to Terry Adair for his assistance in preparing the manuscript and Terry Skinner for helpful suggestions.

9. REFERENCES

Bennett, A.F., Chua, B.S. and Leslie L.M. 1996. Generalized inversion of a global numerical weather prediction model. *Meteor. Atmos. Phys.*, **60**, 165–178.

Le Marshall, J., W.L. Smith, F. W. Harrison, G. E. Bingham, R. Huppi, H.E. Revercomb, R. Seecamp, B. Choi and M. Dunn. 2003. GIFTS-IOMI High Spectral, Temporal and Spatial Resolution Data Assimilation. *Tech. Proc. Twelfth International TOVS Study Conference, Lorne, Australia, 27 Feb. – 5 Mar. 2003.* 166 – 169.

Le Marshall, J., A. Rea, L. Leslie, R.Seecamp and M. Dunn. 2004a. Error Characterization of Atmospheric Motion Vectors. Accepted for publication in *Aust. Meteor. Mag.* June 2004.

Le Marshall, J., R. Seecamp, J. Daniels, C. Velden, K. Puri, R. Bowen, A. Rea and M. Dunn 2004b. The Contribution of GOES-9 to Operational NWP Forecast Skill in the Australian Region. Submitted for publication in *Aust. Meteor. Mag.*

Leslie, L.M., J. Le Marshall and W.L. Smith, 2002. Mesoscale Initialisation using Advanced Sounder Data. *Adv. Space Res.* **11**, 2479 – 2484.

Smith, W.L. and H.M. Woolf. 1976. The use of eigenvectors of statistical covariance matrices for interpreting satellite sounding radiometer obse4rvations. *J. Atmos. Sci.* **33**, 1127 – 1140.

Smith, W. L., A. M. Larar, D. K. Zhou, C. A. Sisko, J. Li, B. Huang, H. B. Howell, H. E. Revercomb, D. Cousins, M. J. Gazarik, D. Mooney. 1999. NAST-I: results from revolutionary aircraft sounding spectrometer, *SPIE Optical Spectroscopic Techniques and Instrumentation for Atmospheric and Space Research III*, A. M. Larar, Ed., 3756, 2 – 8.

Smith, W. L., H. E. Revercomb, and G. E. Bingham. 2001. Geostationary Fourier Transform Spectrometer (GIFTS) – The New Millennium Earth Observing-3 Mission, *Proc. of IRS 2000: Current Problems in Atmospheric Radiation*, A Deepak Publishing, Hampton, Virginia, 2001.

Zhou, W. D. K., L. Smith, J. Li, H. B. Howell, G. W. Cantwell, A. M. Larar, R. O. Knuteson, D. C. Tobin, H. E. Revercomb, and S. A. Mango, 2002. Thermodynamic product retrieval methodology for NAST-I and validation. *Applied Optics*, **41**, 6,957–6,967.

Retrieving Infrared Land Surface Emissivity With AIRS Simulation Data

Xuebao Wu[1], **Jun LI**[2], **Yuanjing Zhu**[1], **Paul Menzel**[2] **and Wenjian Zhang**[3]

[1] *Department of Atmospheric Science, Peking University, Beijing, China*
[2] *CIMSS/SSEC/UW-Madison, USA*
[3] *National Satellite Meteorological Center, Beijing, China*

Abstract

This report reviews briefly the characteristics of high spectral resolution satellite infrared remote sensing. The paper also describes the use of EOS-Aqua AIRS measurements to characterize the surface properties important for IR thermal emission. Infrared rapid transmittance model is used for the sensitivity study of surface parameters and the atmospheric parameters from lower troposphere. Six standard model atmospheres are utilized to generate the simulated AIRS radiances. An experiment is carried out to retrieve the land surface emissivity with the AIRS simulation data. The MLEV (**M**inimum **L**ocal **E**missivity **V**ariance) retrieval method is implemented for this simulation study.

Introduction

The Atmospheric InfraRed Sounder (AIRS) is the first of a new generation of high spectral resolution atmospheric sounders. AIRS is the infrared instrument onboard the NASA Earth Observing System Aqua satellite launched on May 4, 2002. It is a grating spectrometer designed to measure the upwelling radiances from the Earth and its atmosphere with 2378 spectral channels between 650-2670 cm-1 with a spectral resolving power on the order of 1200. Details on the AIRS instrument and performance are given in Aumann et al. (2003). AIRS is a multi-purpose instruments used for measuring global atmospheric temperature, water vapor, trace gas concentration, surface temperature, surface emissivity, aerosols, as well as cloud parameters and cloud properties. AIRS observation should lead to significant advances on the weather prediction and the better understanding of the climate (Goldberg, 2003).

In this paper, MLEV technique is utilized for its particular advantage of the continuous sampling of

long-wave infrared radiances available with high spectral resolution instruments, simultaneously determining land surface temperature and land surface emissivity spectrum. The optimal land surface temperature and land surface emissivity spectrum solution derived from MLEV is that which yields the smallest local spectral variation of the derived emissivity spectrum from synthetic AIRS data.

Sensitivity Study for Land Surface Emissivity

SARTA (Stand-Alone Radiative Transfer Algorithm) is a fast forward model developed by AIRS team (Strow et al. 2003). SARTA could generate very quickly a simulated AIRS radiances and transmittance spectrum for any plausible atmosphere profile. It has 100 layers with pressures from 1100hPa at the bottom to 0.005hPa at the top of atmosphere. We used the SARTA fast model to calculate simulated radiances for the ECMWF profiles within an AIRS granule on Sept. 6, 2002. The difference between the SARTA simulation and the real AIRS observation provides an estimate of the accuracy of the parameterizations and approximations introduced in SARTA model. Figure 1 shows the mean brightness temperatures and standard deviation errors of SARTA model for all clear fields of view within AIRS granule 182. For long-wave AIRS band, the mean biases are about –1K to 1K, while the standard deviations are around 1K for most channels within this band.

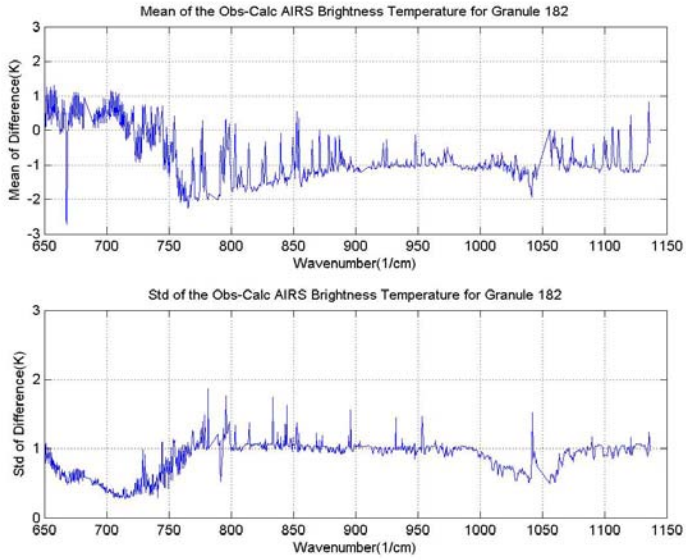

Fig.1: The mean and standard deviation between the calculated and observed AIRS brightness temperature for all clear fields of view within granule 182 of Sept.6, 2002

The emissivity spectral distributions are determined as a function of assumed surface emissivity increment for six standard model atmospheres (1976 U.S. standard, tropic, mid-latitude winter, mid-latitude summer, subarctic summer, subarctic winter) to demonstrate the information content of the simulation radiances. The results are shown in Figure 2 through 4. Figure 2 displays the change of synthetic radiances

(in brightness temperature) with the assumed surface emissivity increment of 0.01 for two different standard atmospheres. The upper panel is for 1976 U.S standard, and the lower one is for tropic atmosphere. For AIRS long-wave band, the brightness temperature is increased to 0.7K for most channels. Only some channels have been affected in the water vapor band. For shortwave band, the brightness temperature is increased much less, about 0.2K. Figure 3 is similar to figure 2 except for mid-latitude winter atmosphere and mid-latitude summer atmosphere. Figure 4 is the similar result for subarctic summer and subarctic winter atmospheres.

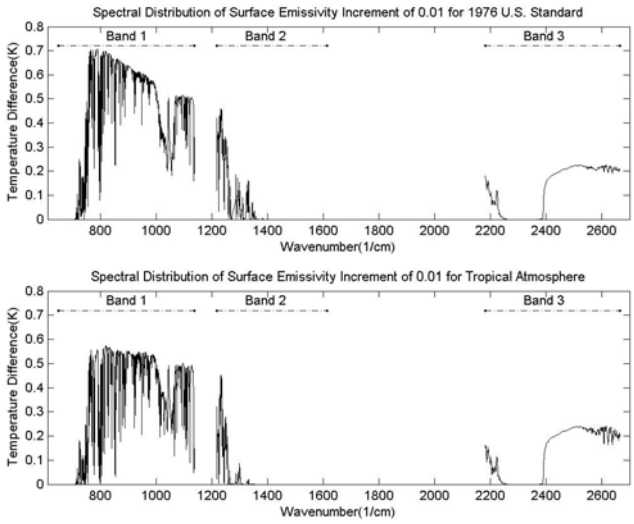

Fig.2: Spectral distribution of surface emissivity increment of 0.01 for 1976 U.S. and tropic atmospheres

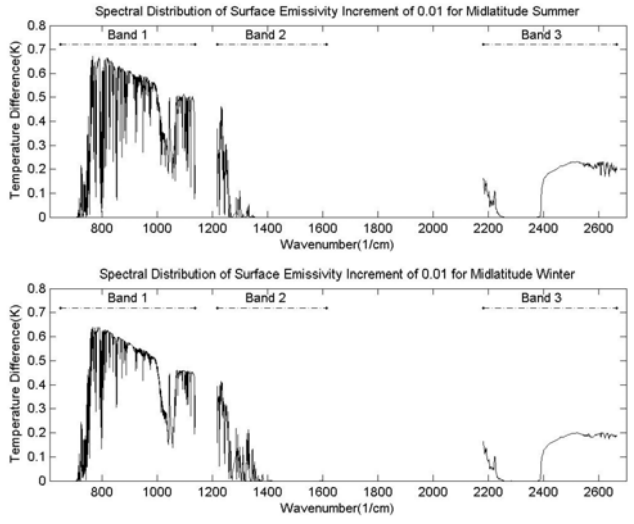

Fig.3: Spectral distribution of surface emissivity increment of 0.01 for midlatitude summer and midlatitude winter atmospheres

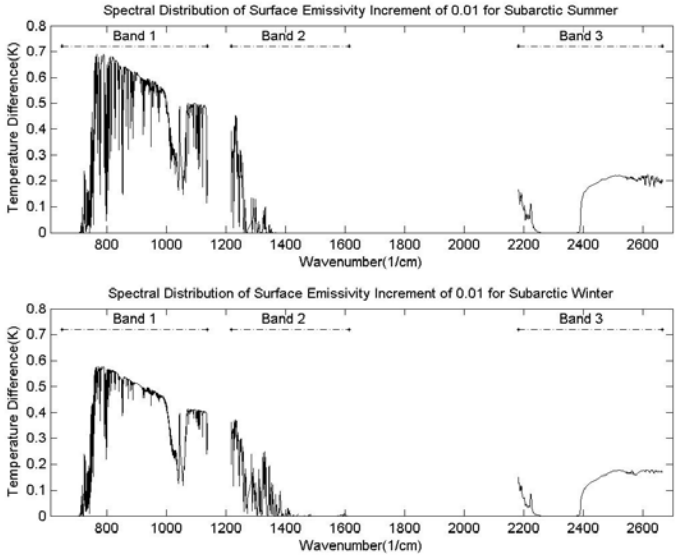

Fig.4: Spectral distribution of surface emissivity increment of 0.01 for subarctic summer and subarctic winter atmospheres

Sensitivity Study for Atmospheric and Surface Parameters

Similar sensitivity study was carried out for atmospheric and surface parameter variation as in the previous session, SARTA fast forward model was used as again to generate synthetic radiances for 1976 U.S. standard atmosphere. The results are shown in Figure 5 through 6. Figure 5 displays the change of synthetic radiances (in brightness temperature) with the assumed temperature increment of 1K. The upper panel is for surface temperature increase, and the lower one is for low troposphere temperature increase. For AIRS long-wave band, the brightness temperature is increased to 1K for most channels, only part of water vapor band has been affected. For shortwave band, the brightness temperature is increased by 1K with the exception for transparent window channels. Figure 6 displays the change of synthetic brightness temperature with variation of low troposphere humidity and ozone profile. The upper panel is for humidity decrease of 15%. Note that the temperature difference exists nearly everywhere in the entire infrared region. It is caused by the attenuation due to water vapor absorption, which has an impact on AIRS radiances in the whole region. The lower panel is for ozone decrease of 10%. In contrast with water vapor absorption, ozone only has a significant impact on AIRS radiances in localized spectral regions.

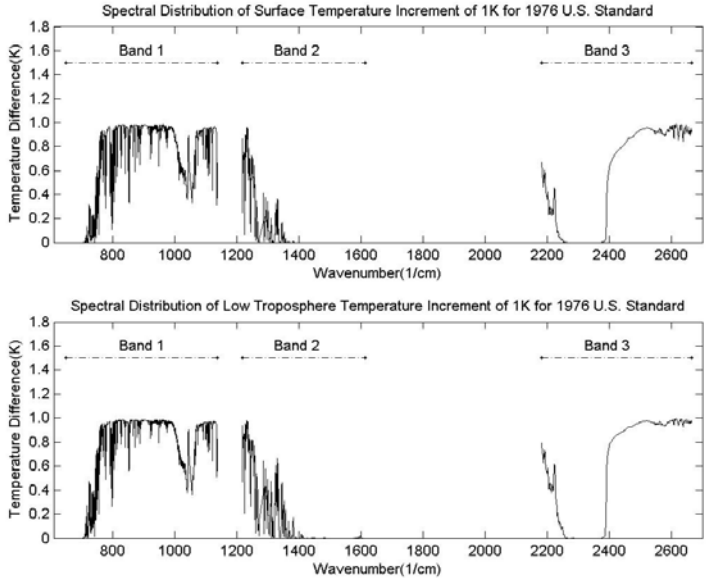

Fig.5: Spectral distribution of surface temperature and low troposphere temperature increment of 1K for 1976 U.S. standard atmosphere.

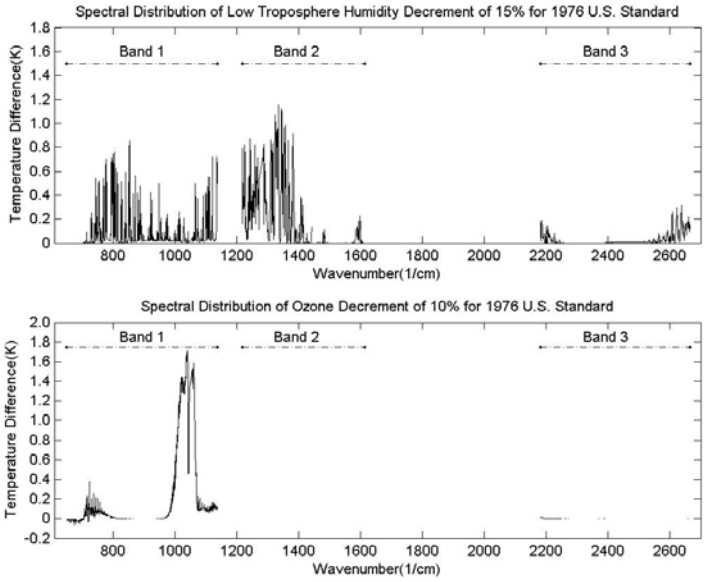

Fig.6: Spectral distribution of low troposphere humidity decrease of 15% and ozone decrease of 10% for 1976 U.S. standard atmosphere

Retrieving LSE With Simulation AIRS Data

To achieve the objectives of obtaining accurate atmospheric profiles over land, the land surface

temperature (LST) has to be known to a target accuracy better than 0.5K and land surface emissivity (LSE) to an accuracy better than 0.01. High spectral resolution measurements have the potential to allow the separation of LST and LSE (Knuteson et al. 2003). Figure 7 is a diagram for MLEV technique.

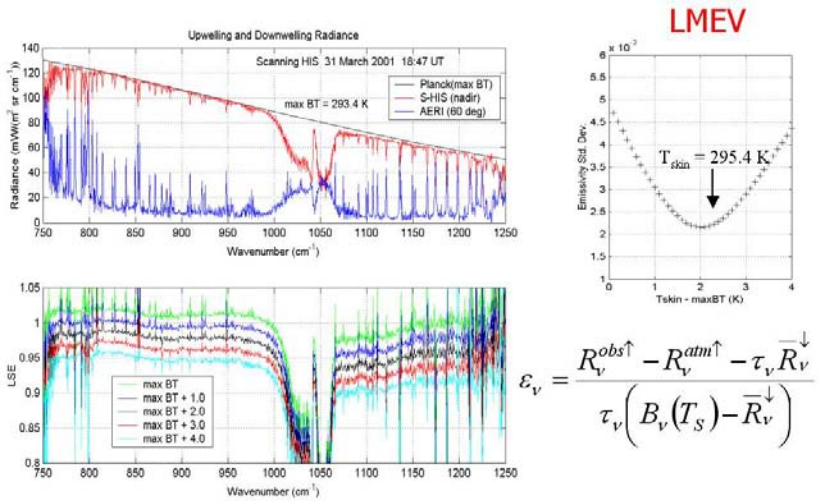

Fig7: The S_HIS and AERI observations used in the MLEV technique are shown in the upper panel. The lower panel shows a range of surface skin temperature values. The best fit is the one which minimizes the spectral line variations of the derived emissivity. (Courtesy of Robert Knuteson).

The MLEV land surface temperature and land surface emissivity retrieval principle is demonstrated by comparing the land surface emissivity and its local variance determined as a function of assumed land surface temperure. The land surface emissivity spectrum and land surface temperature are selected for that land surface temperature for which the derived land surface emissivity exhibits minimal local spectral variation and a structure that is uncorrelated with the local variations in radiances produced by absorption lines. MLEV algorithm is named after the principle that the optimal land surface emissivity spectrum should have the feature of “minimum local emissivity variance” among the retrieved emissivity spectra associated with different land surface temperatures.

Figure 8 shows the determined surface emissivity with variation of surface temperature estimate. Of the three estimates shown in this figure. The optimum surface temperature is the one calculated emissivity has a maximum smoothness. Error occurs with an over- or under-estimation of the surface skin temperature.

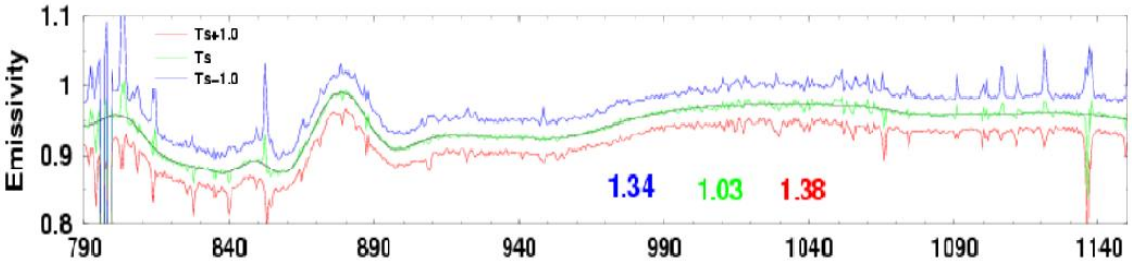

Fig8: The emissivity spectra derived with the wrong/correct surface temperature. Error occurs with an over- or under-estimation of the surface skin temperature

Discussions and Future Plans

SARTA model is used for the sensitivity study of surface parameters and the atmospheric parameters from lower troposphere. Six standard model atmospheres are utilized to generate the simulated AIRS radiances. MLEV is a relatively simple technique that takes advantage of the continuous sampling of long-wave infrared radiance measurements, simultaneously determining land surface temperature and land surface emissivity spectrum. The optimal land surface temperature and land surface emissivity spectrum solution derived from MLEV is that which yields the smallest local spectral variation of the derived emissivity spectrum. A near future study will involve the implementation of MLEV technique for the real hyperspectral AIRS measurements, in conjunction with its validation.

References

Aumann, H. H., Chahine, M.T., et al. 2003. AIRS/AMSU/HSB on the Aqua Mission: Design, Science Objectives, Data Products, and Processing Systems, *IEEE Trans. Geosci. Remote Sensing*, **41**, No.2, 253-264.

Goldberg, M. D., Qu,Y. and McMillin L. M. et al. 2003. AIRS Near–Real-Time Products and Algorithms in Support of Operational Numerical Weather Predication, *IEEE Trans. Geosci. Remote Sensing,* **41**, No.2, 379-389.

Strow, L. L., Hannon, S. E. et al. 2003. An Overview of the AIRS Radiative Transfer Model, *IEEE Trans. Geosci. Remote Sensing,* **41**, No.2, 303-313.

Knuteson, R., Dedecker, R., Feltz, W., Osborne, B., Revercomb, H., Tobin D. 2003. Infrared

Land Surface Emissivity in the Vicinity of the ARM SGP Central Facility *Proceedings of the Thirteenth ARM Science Team Meeting,* 31 March – 4 April, 2003, Broomfield, CO

Surface effects in hyperspectral infrared measurements from the AIRS instrument on the Aqua satellite

Youri Plokhenko[1] and W. Paul Menzel[2]

[1] CIMSS, University of Wisconsin – Madison , 1225 W. Dayton St., Madison WI 53706 (608) 262 7287 , (608) 262-5974 (FAX) , YouriP@ssec.wisc.edu
[2] Office of Research and Applications, NOAA / NESDIS, 1225 W. Dayton St., Madison WI 53706

Abstract Surface emissivity (SE) variations cause measurable changes in infrared radiances. To improve the accuracy of vertical temperature-moisture profiles retrieved from AIRS sounder infrared measurements, the surface emissivity must be accounted for in the solution of the inverse problem. The accuracy of atmospheric parameters retrieved depends on the measurement accuracy and accurate definition of measurement model. The associated inverse problem based upon the numerical solution of the radiative transfer equation (RTE) is ill posed. Disregarding the spectral-spatial variations of SE in the RTE magnifies the errors. Different types of surface cover, with different surface optical properties and extremely high spatial and temporal variations, restrict the use of a priori estimates of SE. The direct evaluation of SE is an effective alternative. The RTE solution includes the surface emissivity, the surface temperature, and the temperature-moisture profile. The RTE equation is solved using the method of least squares in coordinate descent based on the Gauss-Newton numerical schema. Results of SE estimation are demonstrated. The SE estimates over land show significant spectral-spatial variability. Accounting for the emissivity positively affects the atmospheric temperature-moisture profile estimates.

Introduction To estimate the atmospheric temperature-humidity vertical distributions from the multi-spectral infrared measurements requires a numerical solution of the radiative transfer equation (RTE). Accounting for emissions from both the earth surface and the atmosphere is critical since even small SE variations cause measurable changes in the infrared radiances. The spectral-spatial variations of SE in RTE, if ignored, can drastically reduce the accuracy of the solution. An algorithm is described in Plokhenko and Menzel (2000 and 2003). Results of data analysis and experimental processing of AIRS nighttime spectral measurements from the granule 016 of September 6, 2002 are presented.

Data analysis and physical interpretation The Atmospheric Infrared Sounder (AIRS) spectral channels along with their intended purposes are given in Aumann and Miller 1995. The measurements demonstrate the following properties: (a) surface reflection is substantially larger in shortwave (SW) bands than in longwave (LW) bands, (b) radiation absorption by cloud ice particles is substantially larger in LW than in SW bands, and (c) SW bands are less affected by variations of atmospheric moisture than LW bands. In processing the AIRS measurements, the solution of the inverse problem includes the surface emissivity, the surface temperature, and the vertical temperature-humidity profile. Only spectral measurements at cloud free pixels are processed. The RTE for the cloud free atmosphere is:

$$\tilde{J}^{\uparrow}(\theta)=\varepsilon_s(\theta)\tau^{\uparrow}(p_s,\theta)B[T_s] + \int_{\tau^{\uparrow}(p_s,\theta)}^{1} B[T(p)]\, d\tau^{\uparrow}(p,\theta) + (1-\varepsilon(\theta))\tau^{\uparrow}(p_S,\theta) \int_{1}^{\tau^{\uparrow}(p_s,\vartheta)} B[T(p)]\, d\tau^{\downarrow}(p,\vartheta) + \xi$$

where: $\tilde{J}^{\uparrow}(\theta)$ is the radiance measured at the angle of incidence θ; $\varepsilon_s(\theta)$ is the effective hemispherical directional SE at the angle θ; φ is the effective angle of incidence of the downwelling radiance; $\tau^{\uparrow}(p,\theta)$, $\tau^{\downarrow}(p,\vartheta)$ are the atmospheric upwelling and downwelling transmittances, *T(p)* and *Q(p)* are temperature and moisture profiles; T_s is the surface temperature; ξ is an error of the measurement. In the RTE, the optical surface effects are described by $\varepsilon_s(\theta)$, ϑ.

As a first guess of emissivity spectrum, the constant 0.94 is assumes. ECWMF forecasts of temperature-moisture profiles are used as a first guess (FG). The retrievals are successful if they improve upon the accuracy of the background FG. Because the FG is already quite good, there is the problem that model uncertainties are comparable to the amplitude of signal variations. An estimate of the emissivity spectrum is expected to reduce the measurement modeling uncertainties.

SE and vertical moisture-temperature profiles are estimated in parametric form. The emissivity spectrum variation is represented by 11 basis functions, the moisture vertical profile variation by 17 basis functions, the temperature vertical profile variation by 31 basis functions. The moisture basis functions are chosen so that they can describe both the solution and the underintegral kernel: the moisture profile is exponentially decreasing with altitude; the spectrum sensitivity to the moisture profile variation (functional derivative) is the exponentially increasing (in some sense) with altitude. Including the surface temperature estimate, a solution for 60 parameters is sought for (see Fig. 1). The non-linear Fredholm equation of the first kind is solved using a method of least squares in coordinate descent based on a Gauss-Newton numerical schema; 2378 channels are analyzed. Noisy measurements are rejected. Measurements in 2100 channels are used on average per retrieval at a pixel.

a

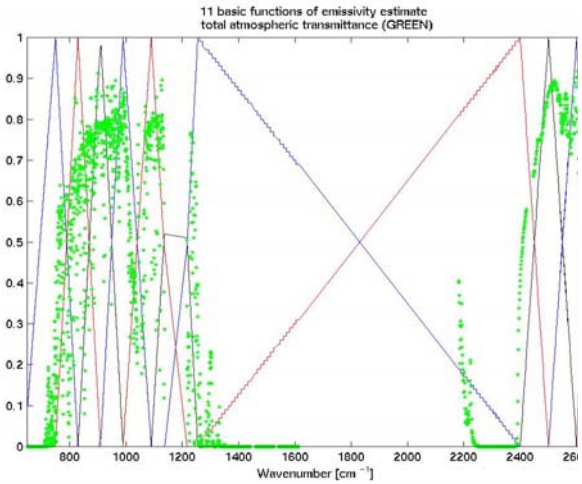

b

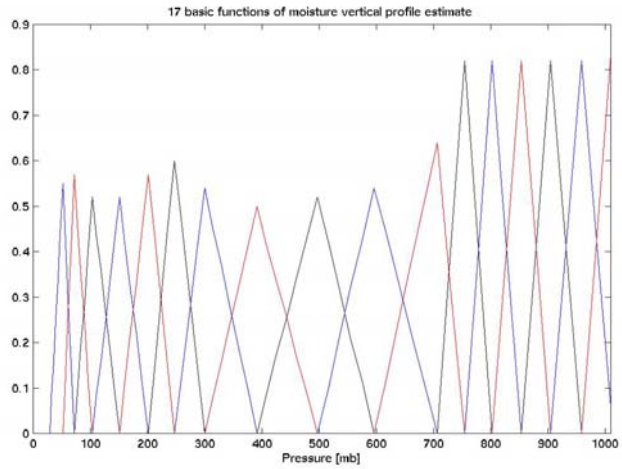

Figure 1. Solution components basis functions, (a) – emissivity spectrum (GREEN shows total atmospheric transmittance), (b) – atmospheric moisture.

Data analysis The AIRS spectral measurements from the granule (total pixels number is 135 scan lines by 90 scan elements) 016 of September 6, 2002 are analyzed. It is nighttime data at 1h 40' GMT. The spectral information is stable, reliable and well calibrated. Surface elevation and meteorological conditions are shown in Figs 2(a,b,c,d). The spectral measurements cover a portion of Western Europe, Mediterranean Region and North Africa. Figure 2(a) shows complicated terrain, characterized by large variability of surface types (part of Sahara desert extreme right part of images) with significant differences in the surface optical properties. Figures 2(b,d) shows the spectral images [K] in SW (2555[1/cm]) and LW (944.1 [1/cm]) atmospheric windows, Fig.2(c) shows their spectral difference [K]. Areas in Fig 2(b,d) with low temperatures correspond to cloud atmosphere; areas with high temperatures correspond to the warm sea surface. There are distinctive differences in the spectral-spatial patterns corresponding to different surface types: small variability over water surface and noticeably larger over desert area. Fig 2(c) (spectral difference of the measurements from (b)– (d)) shows spectral peculiarities of atmospheric effects (related to clouds and water vapor areas) and surface optics effects (water surface and different types of land cover). Differences in the spectral absorption of cloud particles (size, phase) explain large spectral variability in the measurements: large positive differences correspond to high altitude clouds (low temperatures), negative differences occur for lower level clouds. Cloud free measurements over sea surface are characterized by high temperatures associated with the spatial-spectral uniformity (the small spectral variability of the reflection of the water surface). The measurement spatial

variability in LW window over water surface can be explained by the atmospheric water vapor absorption. The Mediterranean coastline of North Africa is clearly visible, indicating mostly cloud free atmospheric conditions at that region (some lower level clouds are visible at the upper right corner)

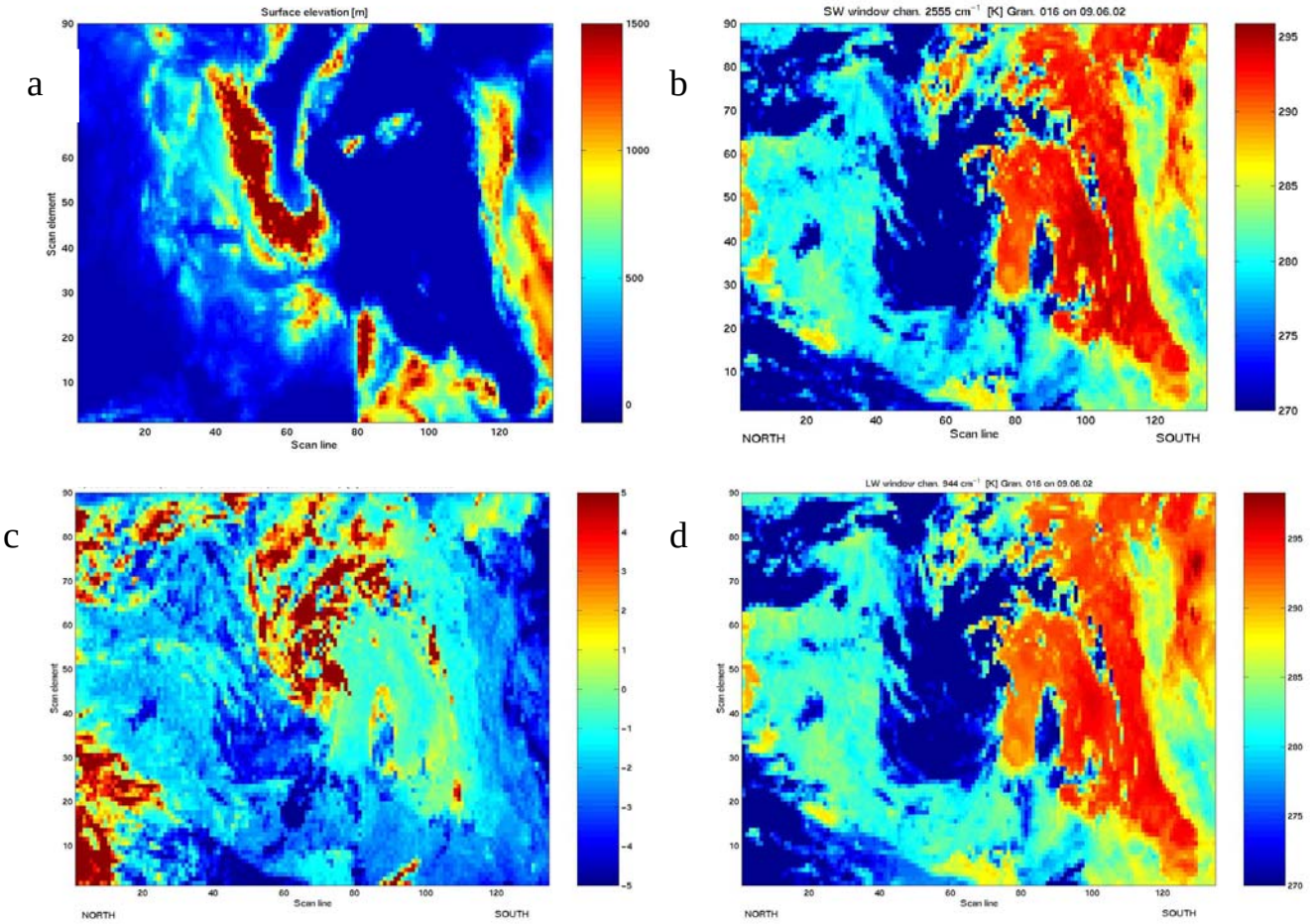

Figure 2 Surface elevation [m] (below 1500m) at sounding pixels (a); Spatial distribution of measurements [K] at atmospheric windows (b) 2555[1/cm] and (d) 944.1 [1/cm]; (c) spectral difference [K] of measurements from (b – d)

The spatial-spectral analysis and spatial filtering of the measurements are effective tools in the meteorological analysis. It is important to reduce measurement uncertainties to reveal meteorologically meaningful signal. Spatial filtering reduces the influence of instrument noise. It is expected that the filtered measurements will have a nominal accuracy better than 0.2 K in all channels (see at Plokhenko and Menzel, 2001). Figures 3(a-d) show measurement error spectral distributions (a) and the effect of the spatial filtering in the lower stratospheric channel 7 at 651.05 1/cm (b,c,d). The spatial distribution of the original measurements in channel 7 (panel b) corresponds to measurement error 0.7 K, derived from onboard black body measurements. The spatial filter (averaging moving rectangular box) is 13 scan lines by 7 scan elements (for channel 7). Panel (c) shows measurement noise (difference (b) - (d)). The expected measurement error of filtered data from panel (c) is 0.07K. The improvement of signal to noise is significant.

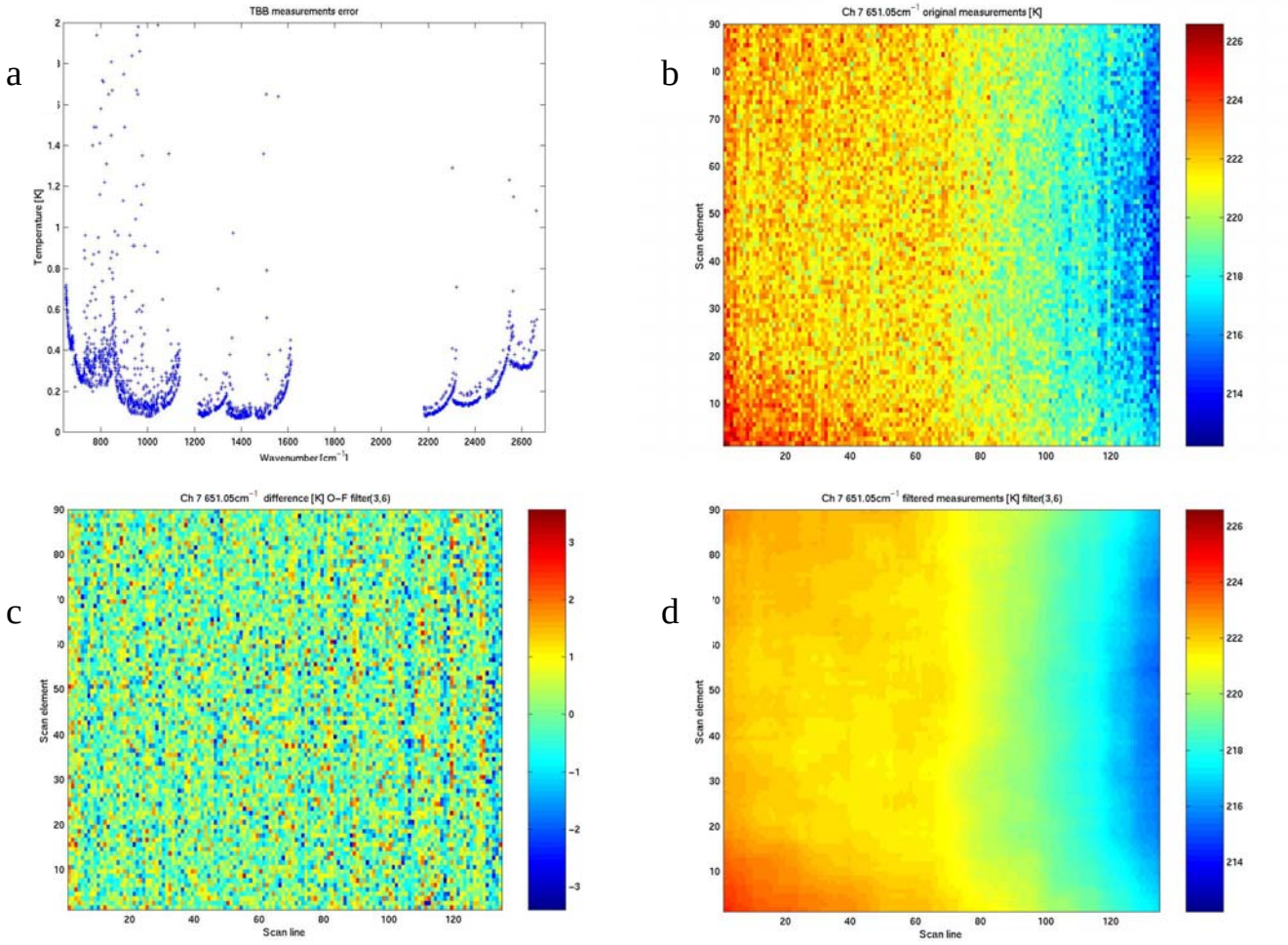

Figure 3 Measurements accuracy characteristics: (a) spectrum of standard deviation of measurement noise derived from black body measurements; (b,c,d) spatial distribution of measurements in channel 7 at 651.05 1/cm: (b) original measurements, (c) after spatial filtering, (d) difference (b-c).

Results from Figs 3(a-d) show that spatial filtering significantly improves the measurements in upper tropospheric – lower stratospheric spectral channels. The spectral sensitivity to a variation +1K of the vertical temperature profile below 500hPa is shown in Fig 4(a). Panel (b) shows the spectral response to 0.02 increases in the surface emissivity (0.94 –0.96). Measurements in corresponding spectral channels are used for estimation surface of the emissivity spectrum and surface temperature.

a

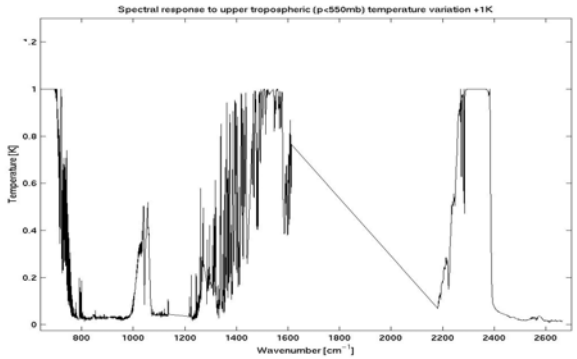

b

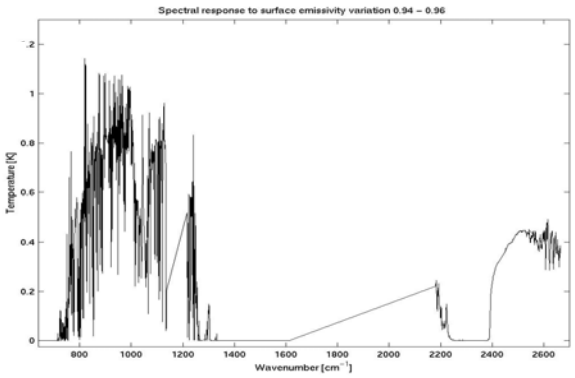

Figure 4(a,b) Measurements spectral characteristics: modeling measurements spectral response to: (a) - the 1K variation of the atmospheric temperature vertical profile below 500hPa and (b) – 0.02 variation of the surface emissivity (0.94 –0.96).

Expected spectral-spatial variability of the surface emissivity and its impact on modeling accuracy are shown in Figures 5(a,b). Panel (a) shows the laboratory measurements [%] of the sand surface reflection, it shows 25% variation. Panel (b) shows the radiance spectral response [%] to 2% emissivity variation.

a

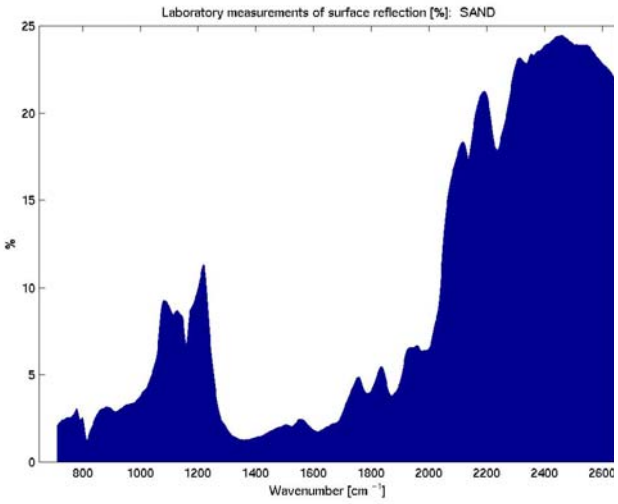

b

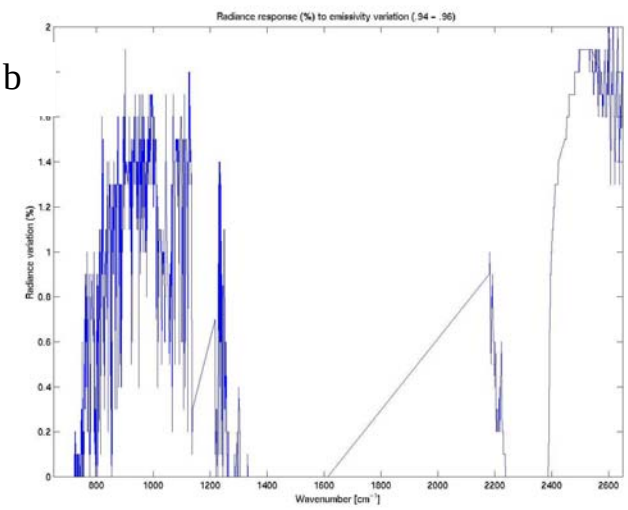

Figure 5 (a,b). The laboratory measurements [%] of the spectrum of the sand surface reflection (a); the radiance spectral response [%] to 2% emissivity variation

It follows from 5(a,b) that emissivity modeling error will substantially vary spatially and spectrally, especially affecting MW and SW measurements. Approximately 1% emissivity error will contribute 0.5% modeling error of measurement.

An example of spectral-spatial distribution of emissivity estimates derived from the AIRS nighttime measurements is shown in Fig 6(a-d). Figure 6a shows the spatial (latitudinal) crossection of emissivity estimates over North Africa (Sahara). It indicates two distinctive minima in the emissivity spectrum (compare with reflectivity in Fig 5a).

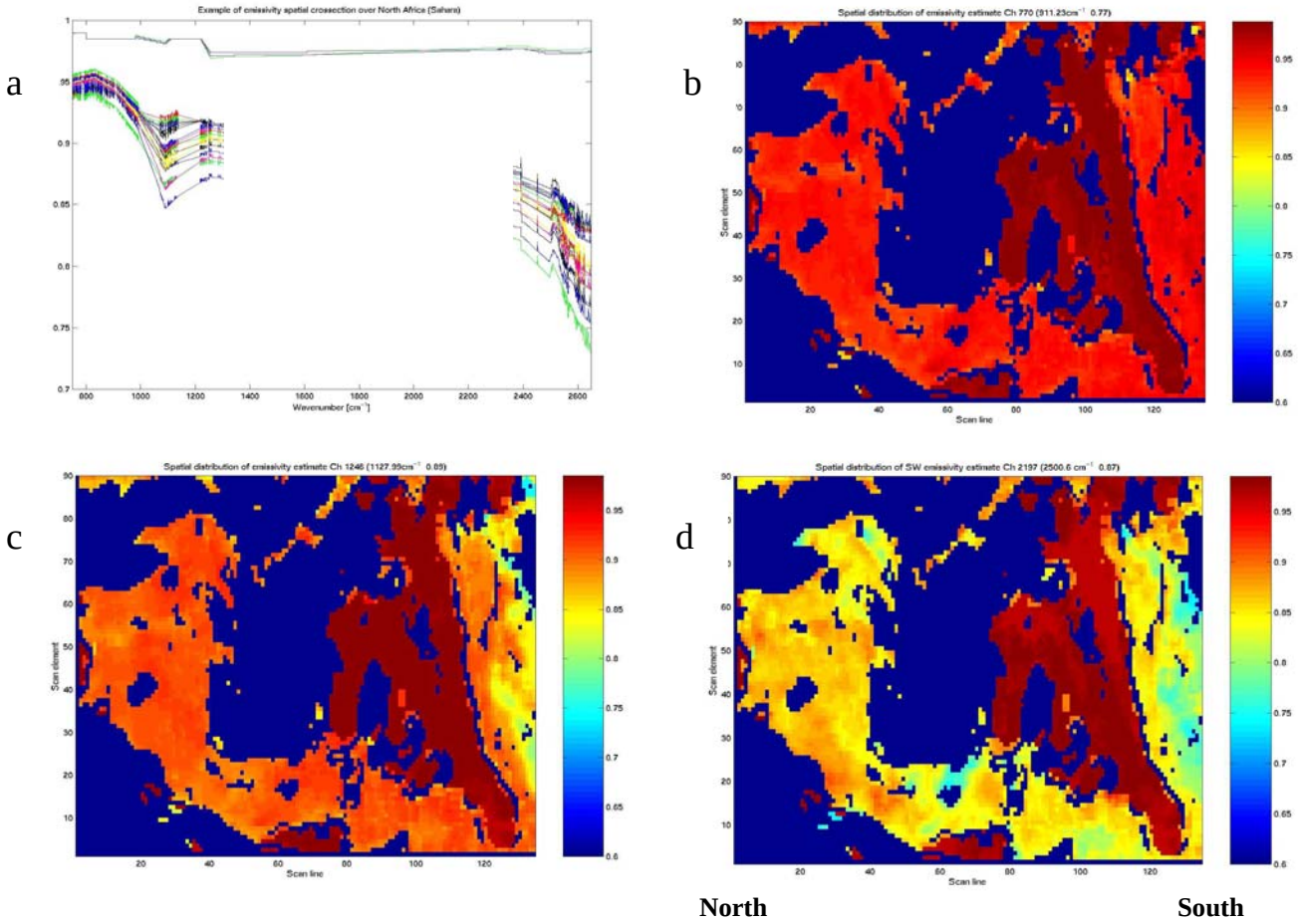

Figure 6 (a-d) Examples of spectral-spatial distributions of the emissivity estimates: (a) example of spatial (latitudinal) crossection of emissivity estimates over North Africa (Sahara); spatial distribution of emissivity estimates in Ch 977 at 990.34 [1/cm] (b), Ch 1246 at 1127.99 [1/cm] (c), Ch 2197 at 2500.6 [1/cm] (d) (dark blue areas correspond to missing data: clouds or solution low convergence at pixel). Dark red (high emissivity values) areas indicates water surface: Mediterranean Sea and North Africa shoreline are visible at the right parts of images. Sahara desert area is characterized by low emissivity at 9 and 4 μ bands.

The emissivity estimates vary from 0.7 to 0.96. Figures 6(b-d) show spatial distribution of the emissivity estimates at 11, 9 and 4μ. They show significant differences in spectral patterns of different surface types: there are distinctive differences between spatial-spectral patterns of Europe and North Africa. European areas are quite smooth (some variations relate to mount areas and cloud identification errors). North African areas vary at a noticeably larger scale.

Figures 7(a-f) demonstrate the spatial distribution and variability of the lower tropospheric moisture estimate at the pressure levels 950, 900 and 850hPa (figures 7(a-b)); the first guess fields are presented in figures 7(d-f) (units [%] in the data transformation $W_{s,f}(p)=100*(w_{s,f}(p)-\bar{w}_f(p))/\bar{w}_f(p)$, where mixing ratio profiles [g/kg] $w_{s,f}(p)$, $\bar{w}_f(p)$ (s-solution, f – first guess), the letter is average moisture profile for granule). Fig 7 (a-c) show solution fields at the cloud free pixels (see Figs. 6(b-d), FG is shown at cloud pixels). Figures 7(a-f) show that moisture

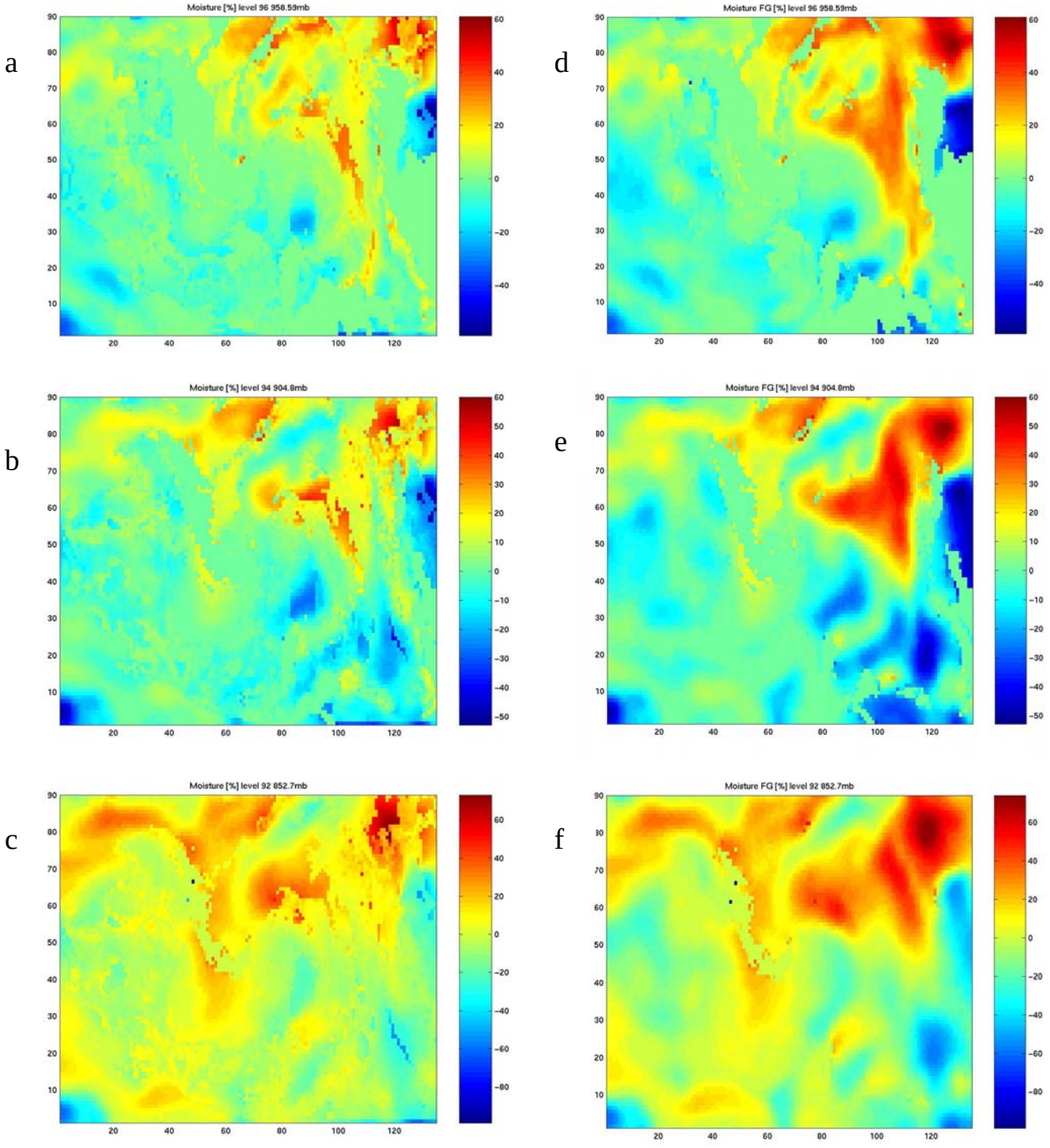

Figures 7 (a-f). The spatial distribution of the lower tropospheric moisture estimate at the pressure levels 950, 900 and 850mb: (a-b) –estimate [%], (d-f) – first guess [%] (from the ECMWF forecast) (units [%] in the data transformation $W_{s,f}(p)=100*(w_{s,f}(p)-\bar{w}_f(p))/\bar{w}_f(p)$, where mixing ratio profiles [g/kg] $w_{s,f}(p)$, $\bar{w}_f(p)$ (s-solution, f – first guess), the letter is average moisture profile for granule). The solution fields were imposed on the corresponding first guess fields from the (d-f) at the cloud free pixels (see Figs. 6(b-d))

Estimates in the lower troposphere are successfully retrieved from spectral measurements using non-linear model that includes the surface emissivity in the inverse problem solution. The solution is spatially consistent, major first guess spatial peculiarities are reshaped. The solution is retrieving new spatial features and noticeably modifying some dry / wet air pools. The solution amplitude is significant to 40%.

Conclusion Analysis of nighttime hyperspectral measurements from the AIRS instrument shows that SE significantly affects the infrared measurements. The spectral-spatial SE distributions at the AIRS spectral bands were estimated for the data from the granule 016 of September 6, 2002. An algorithm for solving the non-linear inverse problem to retrieve effective SE and temperature plus atmospheric moisture-temperature profiles was developed. Results show a strong spatial-spectral dependence in the surface variability. The spatial distribution of the SE estimates is coherent with the ecosystem characteristics. Direct evaluation of the SE in the inverse solution of the radiative transfer equation is an effective approach for accounting for surface optics. The vertical-spatial distributions of the estimates of atmospheric temperature and moisture are more components of the solutions.

References

Aumann, H.H., and Miller, Chris, "Atmospheric Infrared Sounder (AIRS) on the Earth Observing System", SPIE Vol.2583, 32-343, 1995.

Plokhenko, Y. and W. P. Menzel, 2000: The effects of surface reflection on estimating the vertical temperature-humidity distribution from spectral infrared measurements. Jour Appl. Meteor. **39**, 3-14.

Plokhenko, Y. and W. P. Menzel, 2001: Mathematical aspects in meteorological processing of infrared spectral measurements from the GOES sounder. Part I: Constructing the measurement estimates using spatial smoothing. Jour. Appl. Meteor, **40**, 556-567.

Plokhenko, Youri; Menzel; Bayler, Gail and Schmit, Timothy J. Mathematical Aspects in Meteorological Processing of Infrared Spectral Measurements from the GOES Sounder. Part II: Analysis of Spatial and Temporal Continuity of Spectral Measurements from the GOES-8 Sounder. Journal of Applied Meteorology: Vol. 42, No. 6, 2003, pp. 671–685.

Plokhenko, Youri and Menzel, W. Paul. Mathematical Aspects of the Meteorological Processing of Infrared Spectral Measurements from the GOES Sounder. Part III: Emissivity Estimation in Solving the Inverse Problem of Atmospheric Remote Sensing. Journal of Applied Meteorology: Vol. 42, No. 11, 2003, pp.1533-1546.

Advanced TOVS (ATOVS) Cloud Products Using HIRS/3 and AMSU-A Measurements

Michael W. Chalfant
Office of Research and Applications / NESDIS / NOAA, Washington DC

Franklin H. Tilley
ITSS Division / Raytheon Corporation, Lanham MD

The National Oceanic and Atmospheric Administration (NOAA) , National Environmental Satellite Data and Information Service (NESDIS) currently produces a suite of operational quality cloud products from the Advanced TIROS Operational Vertical Sounder (ATOVS) system using the High-resolution Infrared Radiometer Sounder (HIRS/3) and Advanced-Microwave Sounding Unit (AMSU-A) instruments onboard the NOAA polar orbiting satellites. These global products include Cloud Top Temperature, Cloud Top Pressure and Cloud Amount, in support of NESDIS commitment to improve Short Term Warnings and Forecasts. The ATOVS cloud products are dependent upon the generation of accurate temperature and moisture retrievals for both the generation of a correction for the attenuation of radiances above the cloud tops as well as the determination of cloud top pressure.

The ATOVS cloud products are generated using the CO_2 Slicing technique, at each HIRS/3 Field-of-View (FOV). These products are also output to 1 X 1 degree gridded fields, for ascending and descending orbital passes and separated into Total, High, Medium and Low pressure layers, where the parameters are calculated as a function of the Effective Cloud Fraction. The ATOVS cloud products, at the sounding location are being archived and distributed via AWIPS, to NWS field forecast offices. Two cloud product statistical tables are generated globally and updated daily on the NESDIS web site, for comparison with other cloud product systems as well as assessing the performance of the ATOVS cloud product system.

The ATOVS cloud products have been undergoing extensive evaluation by NESDIS and National Weather Service (NWS) personnel for possible use in regional and global Numerical Weather Prediction (NWP) forecasts. Comparisons of the ATOVS Cloud products with several other cloud product generation systems such as the ATOVS temperature retrieval Cloud Mask; the AVHRR/3 based CLAVR-x and UK Meteorological Office's Clear Fraction; GOES and the USAF RTNEPH, have resulted in substantial improvement in the coverage of retrieved marine stratus plus providing for an independent quantative verification of the ATOVS cloud parameter values. This paper describes the algorithms for deriving these cloud products as well as the scientific and system upgrades which have resulted in significant increases in both cloud product accuracy and coverage.

Cloud parameters from a combination of infrared and microwave measurements

F. Romano* , V. Cuomo* and R. Rizzi°

*Istituto di Metodologie Avanzate di Analisi Ambientale, IMAAA/CNR, Potenza, Italy
° ADGB - Dip. Fisica, viale Berti Pichat 6/2, Bologna, Italy

INTRODUCTION

Clouds are both absorbers of outgoing longwave radiation and reflectors of incoming solar radiation. Due to their crucial role, the knowledge of the horizontal and vertical distribution and the optical properties of globally distributed clouds are of fundamental importance to the understanding of the radiation and heat balance, weather and climate of the earth and the atmosphere. Measurements of radiation from space can play a big role in helping us to understand how radiation depends on cloud properties. They can also help us to identify which are the most critical cloud properties to measure. The goodness of satellite-based measurements is that they offer the only practical way of making cloud measurements over the entire global. The improvement of spatial resolution and spectral characterisations allow us to apply sophisticated retrieval procedures, which will provide new cloud products with enhanced accuracy. Since clouds are practically opaque in the infrared sounding frequencies and since the majority of the clouds are transparent in the microwave regions, it would appear that a proper combination of infrared and microwave measurements could be useful and significant data to determine the cloud coverage, the vertical cloud structure and the composition in all weather conditions. First of all the paper explores the performance of a cloud detection scheme for the Atmospheric Infrared Sounder (AIRS) data, then the improvements in retrieval cloud parameters, using high spectral resolution AIRS sounder data. together with the Advanced Microwave Sounding Unit (AMSU-A) and the Humidity Sounder for Brazil (HSB) on the Aqua mission, represents the most advanced sounding system ever deployed in space. AIRS measures simultaneously in more than 2300 spectral channels in the range of 0.4 to 1.7 μm and 3.4 to 15.4 μm. AIRS measurements are at 13.5 km resolution in infrared bands and at 2.3 km in four visible and near-infrared bands. AMSU has 42 km FOVs and is a temperature sounder (15 channels in the range of 50 to 89 GHz). HSB has 15 km FOVs and is a moisture sounder (4 channels in the range of 150 to 183MHz). AMSU and HSB are co-aligned with AIRS.

AIRS CLOUD DETECTION VALIDATION

Cloud detection depends on the contrast between cloud and the cloud free pixels. The contrast depends on wavelength, so that a multispectral approach gives reliable results. Cloud free and fully cloudy pixels differ considerably in their spectral properties and allow simple threshold techniques. Partially cloudy pixels vary from cloud free to fully cloudy and always require a decision about their cloud coverage. In the microwave region clouds have a negligible effect on the radiances. For this reason using some information coming from AMSU data can be useful to improve a cloud detection algorithm. The threshold tests, based on AIRS/AMSU inter-channel regressions, allow us to detect all the overcast FOVs. Thin clouds, cirrus and partially cloudy FOVs are detected using IR thresholds test on window channel differences. Using the line-by-line Hartcode (F. Miskolczi et al, 1989), RTTOV (J. Eyre , 1991) and RT3 (Evans et al, 1991, Amorati et al, 2002) forward models, spectral clear radiances and spectral cloudy radiances are calculated for different cloud types in order to compute the dynamic thresholds. The dynamic thresholds are a function of observing geometry and they are selected on the basis of AMSU brightness temperature, of

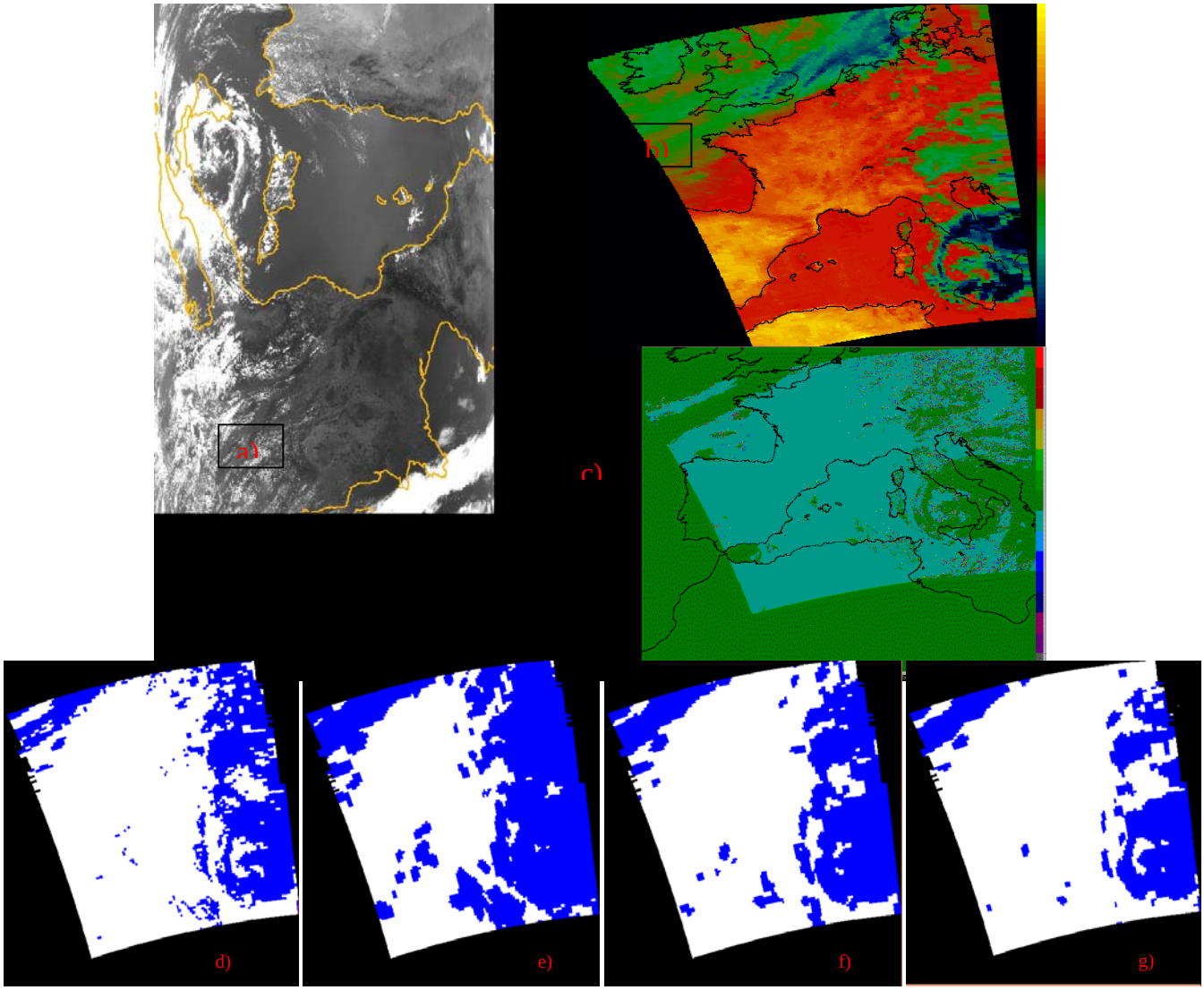

Fig.1 a) MODIS band 3, b) AIRS window channel at 909.09 cm, c) MODIS cloud mask, d) Airs cloud mask, e) MODIS cloud mask at AIRS resolution 100% clear, f) MODIS cloud mask at AIRS resolution 90% clear and g) MODIS cloud mask at AIRS resolution 70% clear. Blue pixel are cloudy, white are clear. Data from 1 August 2003.

water vapour, derived from AMSU, and on the basis of the highest AIRS brightness temperature value in the AIRS granule. In order to validate the AIRS cloud detection, the MODIS (Moderate-Resolution Imaging Spectroradiometer) cloud mask is collocated within the AIRS footprint. MODIS measures Earth radiances in two visible bands at 250m resolution, in five other visible bands at 500 m resolution and the remaining bands at 1 km resolution. The cloud detection is performed at 1 km resolution for all scenes and also at 250 m in daytime only (Ackerman et al, 1998). The AIRS cloud mask has been compared with the results derived from MODIS data. The AIRS FOVs is declared clear if a fixed percentage (70%, 90% and 100%) of MODIS pixels within AIRS IR FOV have been determined to be confident clear or probably clear. The three different cloud masks obtained in this way have been compared with the cloud mask derived from AIRS cloud detection algorithm. Figure 1 and 2 show for two different granules a MODIS channel, a window AIRS channel, the MODIS cloud mask, the AIRS cloud mask and the cloud mask derived from collocated MODIS cloud mask at different percentage. The table 1 show the comparison for 30 granules; the granules have been selected for different areas and months. When MODIS is used to validate an AIRS cloud detection scheme, it is very important to take into consideration the different spatial resolutions of sensors. The MODIS cloud-tests generates a cloud mask on the MODIS grid, and the it must be "translated" into the AIRS grid; only the clear (i.e. detected as clear) MODIS FOVs contribute to determine the percentage clear on AIRS grid. When the are many partially cloudy MODIS FOVs, it results that the AIRS is assumed to

have an high fraction of cloud coverage even if this does not necessarily imply that the AIRS radiances are strongly affected by clouds. MODIS often overestimates cloud fraction on AIRS grid, then the percentages reported in Table 1 overestimate the number of failures.

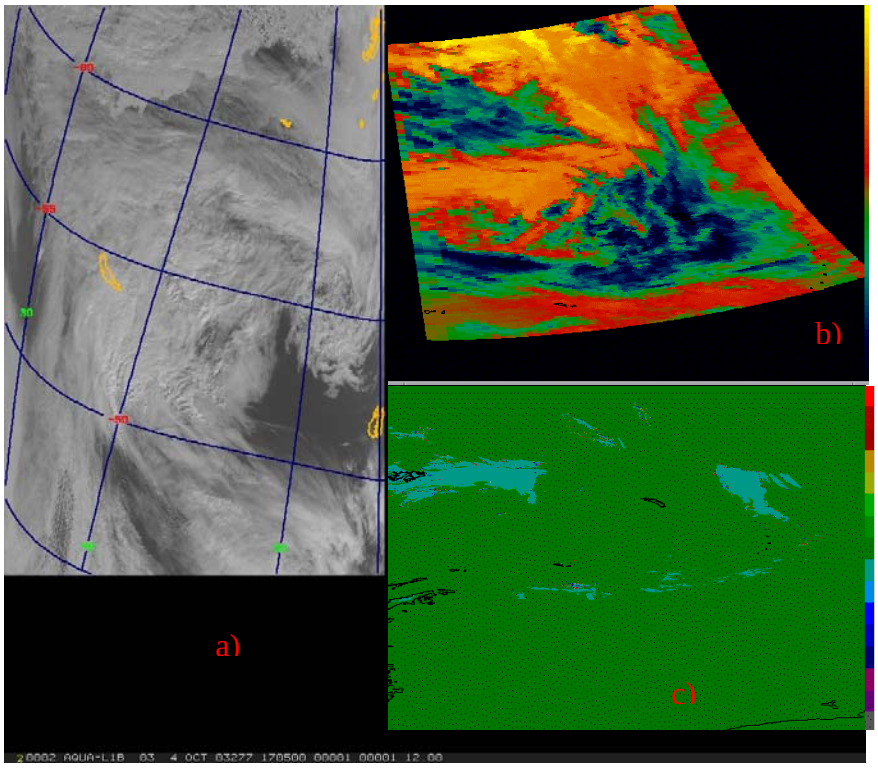

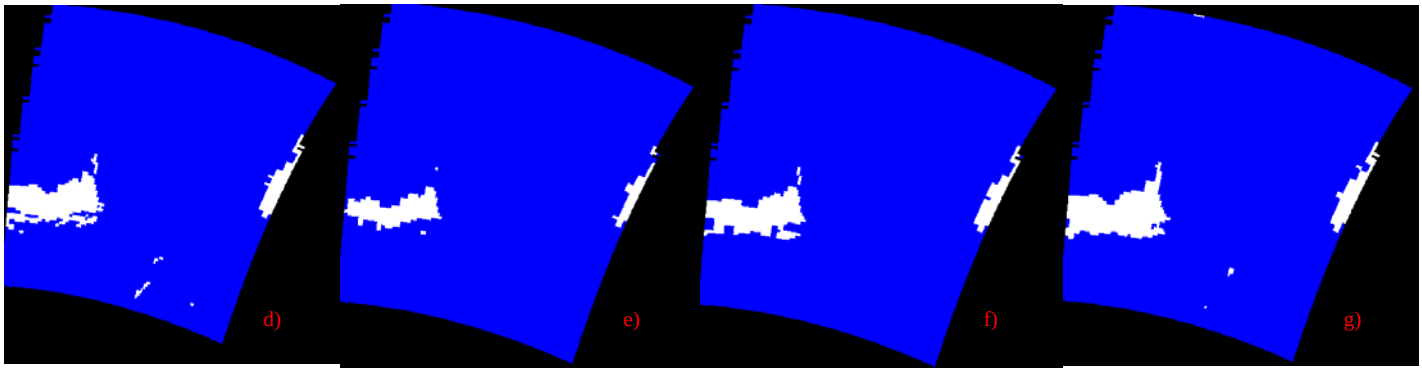

Fig.2 a) MODIS band 3, b) AIRS window channel at 909.09 cm, c) MODIS cloud mask, d) Airs cloud mask, e) MODIS cloud mask at AIRS resolution 100% clear, f) MODIS cloud mask at AIRS resolution 90% clear and g) MODIS cloud mask at AIRS resolution 70% clear. Blue pixel are cloudy, white are clear. Data from 4 October 2003.

.

30 granules	FOVs detected exactly
70%	82.7%
90%	95.8%
100%	92.3%

Tab.1 Comparison between AIRS and MODIS at AIRS resolution cloud masks.

CLOUD TOP HEIGHT: SINGLE CLOUD LAYER

CO_2 slicing (Wylie/Menzel, 1989, 1991) has been extensively used to retrieve cloud top pressure and cloud effective emissivity using High Resolution Infrared Radiation Sounder (HIRS) and MODIS data. Clouds at various levels of the atmosphere can be detected using radiances around the broad CO_2 absorption band at 15 μm. Radiances near the centre of the absorption band are only sensitive to upper levels, while the radiances from the wings of the band are sensitive to lower levels of the atmosphere. Based on radiative transfer principles, this technique is independent of intrinsic cloud properties and knowledge of the fraction of cloud cover is not required. It also allows both the calculation of the cloud top altitude and the cloud emissivity from a temperature profile and the profiles of atmospheric transmittance for two spectral channels sufficiently close. The accuracy of the cloud height estimation can be greatly improved through application to high resolution spectra. Difficulties arise when the differences between the clear and cloudy radiances for a spectral band are smaller than the instrument noise.
The radiance from a partially cloudy air column region can be written as:

$$R_\lambda = \alpha R_\lambda^{cloud} + (1-\alpha) R_\lambda^{clear}$$

where α is the fractional cloud cover; R_λ^{clear} and R_λ^{cloud} are respectively the clear and the cloudy radiance for a given spectral channel λ.
The cloud radiance is given by:

$$R_\lambda^{cloud} = \varepsilon_\lambda R_\lambda^{bc} + (1-\varepsilon_\lambda) R_\lambda^{clear}$$

where ε_λ is the emissivity of the cloud, and R_λ^{bc} is the radiance from a completely opaque cloud. Using the Radiative Transfer Equation it is possible to write:

$$R_\lambda^{clear} = B_\lambda(T(p_s))\tau_\lambda(p_s) + \int_{p_s}^{0} B_\lambda(T(p))d\tau_\lambda$$

and

$$R_\lambda^{bc} = B_\lambda(T(p_c))\tau_\lambda(p_c) + \int_{p_c}^{0} B_\lambda(T(p))d\tau_\lambda$$

where p_c is the cloud top pressure. Integrating by part and subtracting the two terms to obtain the following relation:

$$R_\lambda - R_\lambda^{clear} = \alpha \varepsilon_\lambda \int_{p_s}^{p_c} \tau_\lambda(p) dB_\lambda$$

Following the work of Chahine (1974) to assign a cloud top pressure to a given cloud element, the ratio of the deviations in observed radiances, R_λ and the corresponding clear air radiances, R_λ^{clear} , for two spectral channels of frequency λ_1 and λ_2 viewing the same FOV can be written as

$$\frac{R_{\lambda_1} - R_{\lambda_1}^{clear}}{R_{\lambda_2} - R_{\lambda_2}^{clear}} = \frac{\varepsilon_{\lambda_1} \int_{p_s}^{p_c} \tau_{\lambda_1}(p) dB_{\lambda_1}}{\varepsilon_{\lambda_2} \int_{p_s}^{p_c} \tau_{\lambda_2}(p) dB_{\lambda_2}}$$

If the frequencies are close enough, then $\varepsilon_{\lambda_1} \approx \varepsilon_{\lambda_2}$ and the cloud top pressure can be determined minimising the difference between the left and the right side. The left side (cloud radiative forcing) of the Equation is determined from the satellite observed radiances in a given FOV and the cleared radiance. The right side is calculated from a temperature profile and the profiles of atmospheric transmittance for the spectral frequency as a function of p_c, the cloud top pressure. CO_2 cloud top pressure is estimated when the cloud forcing (clear minus cloud radiance) is greater than five time the instrument noise level.

In order to apply the CO_2 slicing technique to AIRS data, it is necessary to select the best pairs of frequency to be used in the cloud top retrieval. The used method selects all the channels in the CO_2 absorption band whose weighting functions peak between 200 mb and 900 mb. It uses all the possible combinations of these channels, with the first channel of the pair always associated with the lower wavenumber one. Then the CO_2 slicing technique is applied to retrieve the cloud top heights, using all the selected channel pairs. Finally it selects the number of pairs that best satisfy the radiative transfer equation for all the spectral channels. For each FOV the different solutions found are used to evaluate a cost function:

$$\chi = \sum_1^N \varphi_{\lambda i}^2$$

where N is the total pairs of channels and the φ_{λ_i} is defined in this way:

$$\varphi_{\lambda_i} = \left(R_{\lambda_i} - R_{\lambda_i}^{clear}\right) - \alpha \varepsilon_i \int_{p_s}^{p_c} \tau_{\lambda_i}(p) dB_{\lambda_i}$$

The solutions associated to the smallest values of χ are averaged to determine the cloud top height. Increasing the number of used channels pairs in average causes an improvement in the accuracy of the cloud top height retrieval. At the end the algorithm selects 36 pairs of channels.

The cleared AIRS brightness temperature have been estimated using the Kriging cloud scheme (Cuomo et al. 1999). In order to improve the number of AIRS FOVs cleared, MODIS data have been introduced in the scheme. The root mean square error of the Kriging clear brightness temperatures estimates is well below 0.5 °K for any AIRS channels and the bias is about to ±0.1 °K.

Figure 3a shows cloud top pressure estimate using MODIS data, figure 3b using AIRS data. Figure 4a shows the comparison between the cloud top pressure estimate by MODIS and that estimates by AIRS. The MODIS collocated points are also used to determine the scene homogeneity within the AIRS footprint; only homogeneous AIRS FOVs have been used in this comparison. Figure 4b show the comparison with ground based measurements (radar and lidar for different side); only homogeneous AIRS FOVs have been used.

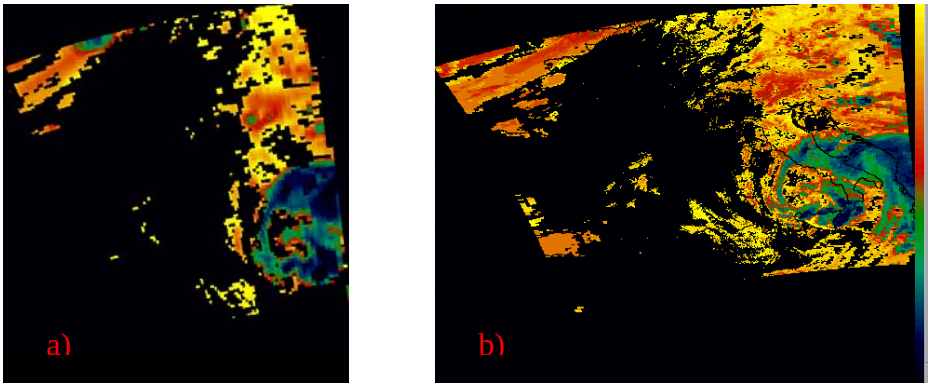

Fig.3 a) AIRS top cloud pressure , b) MODIS top cloud pressure. Data from 1 August 2003.

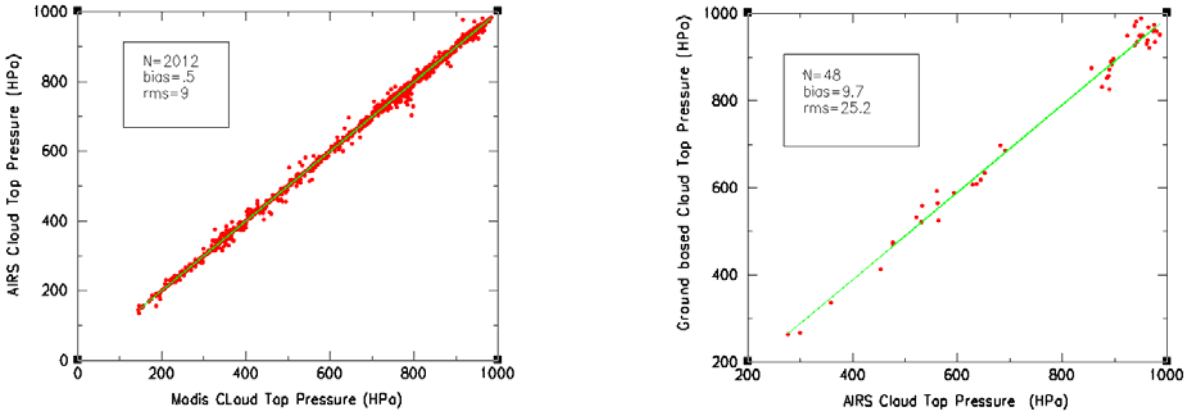

Fig.4 a) Comparison between the cloud top pressure estimate by MODIS and that estimates by AIRS, b) comparison with ground based measurements.

CLOUD TOP HEIGHT: TWO CLOUD LAYERS

When you consider two levels cloud (upper and lower cloud) , the cloud forcing can be expressed as:

$$R_\lambda - R_\lambda^{clear} = \alpha_l \varepsilon_l (1 - \alpha_h \varepsilon_h) \int_{p_s}^{p_{cl}} \tau_\lambda(p) dB_\lambda + \alpha_{h\varepsilon_h} \int_{p_s}^{p_{ch}} \tau_\lambda(p) dB_\lambda$$

where α_l is the fractional cloud cover and ε_l the emissivity of the lower cloud, α_h is the fractional cloud cover and ε_h the emissivity of upper cloud; p_{cl} is the lower cloud top height and p_{ch} is the upper cloud top height. in this case there are four unknown variables: $\alpha_l \varepsilon_l$, $\alpha_h \varepsilon_h$, p_{cl} and p_{ch}. For each spectrally close pairs of CO_2 absorption band (700 – 753 cm-1), all possible $\alpha_l \varepsilon_l$ and $\alpha_h \varepsilon_h$ values are calculated as a function of cloud top height, p_{cl} and p_{ch} by means of the following expression:

$$\alpha\varepsilon = \frac{R_w - R_w^{clear}}{B_w(T(p_c)) - R_w^{clear}}$$

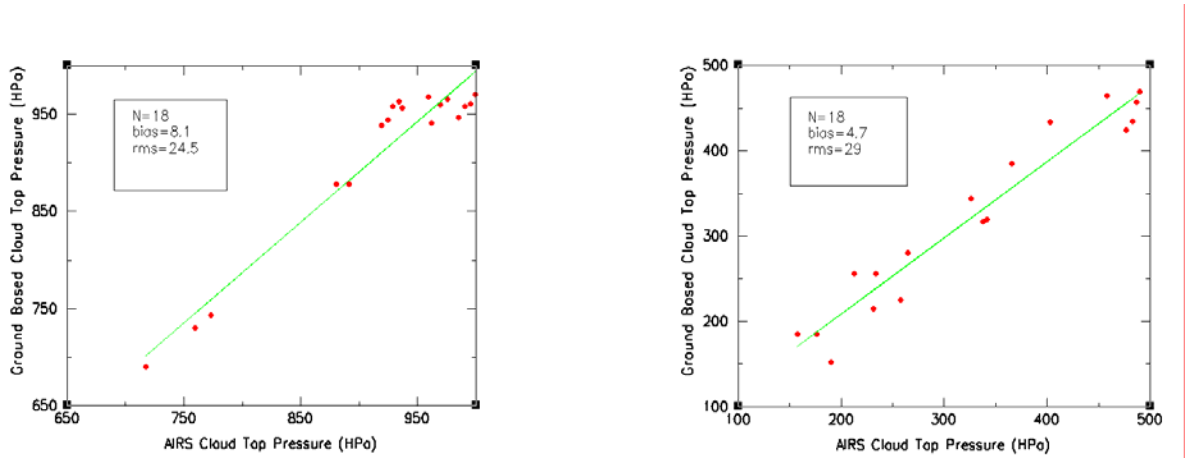

Fig.5 Comparison between the cloud top pressure estimate by AIRS and that estimate by ground based instruments for two cloud level.

from all the solutions we select the best ones that satisfy the radiative transfer equation for all spectral channels. In the same way. we define a cost function in the same way as we did for the single cloud layer and the solutions associated to the smallest values of χ are averaged to determine the upper and lower cloud top height. Increasing the number of used channel pairs in average causes a improvement in the accuracy of the cloud top height retrieval. At the end the algorithm selects 44 pairs of channels. Figure 5 shows the comparison with ground based measurements, only homogeneous AIRS FOVs have been used. The MODIS collocated points are also used to determine the scene homogeneity within the AIRS footprint.

CLOUD THICKNESS

In order to estimate the cloud thickness, cloud water content (CWC, liquid or ice) from AMSU measurements has been estimated using a neural network based algorithm A large set of vertically inhomogeneous clouds based on radiosonde profiles has been applied to the infrared and microwave transfer code RT3. The neural network algorithm uses the radiances at AMSU-B (HSB) frequencies. Water and temperature profiles from AIRS/AMSU or ECMWF have been used. Surface emissivity is adjusted according to the surface type. Simulated brightness temperature are compared to the observed AIRS and AMSU data. If the difference between the observed and the estimated reach a minimum, the retrieval process finished. Figure 6a show cloud thickness for a single cloud level and figure 6b e 6c for two cloud level.

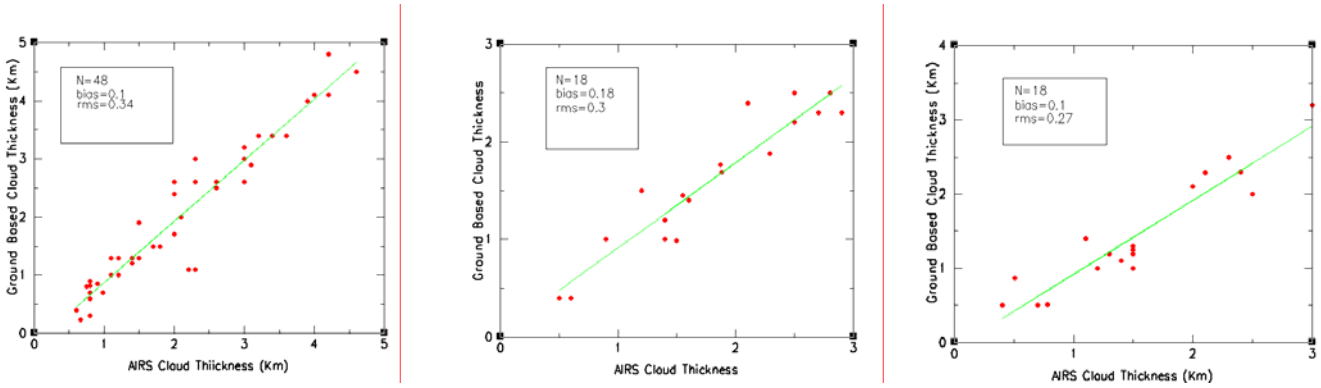

Fig.6 a) Cloud thickness for a single cloud level and b) and c) for two cloud level .

CONCLUSION AND FUTURE WORK

Since clouds are practically opaque in the infrared sounding frequencies and since the majority of the clouds are transparent in the microwave regions, it would appear that a proper combination of infrared and microwave measurements could be useful and significant data to determine the cloud coverage, the vertical cloud structure and composition in all weather conditions. The paper examines the combination of AMSU and AIRS data in the horizontal and in the vertical cloud structure retrieval. The results have been compared for homogenous AIRS pixels with ground based measurements. In the future cloud mask validation based on MSG (SEVIRI) data will be carried out, SEVIRI is a very useful tool for the clouds investigation. Validation, based on ground based measurements, will be extend to a large data set.

REFERENCES

Ackerman, S. A., K. I. Strabala, W. P. Menzel, R. A. Frey, C. C. Moeller, and L. I. Gumley, 1998: Discriminating clear-sky from clouds with MODIS. J. Geophys. Res., 103, D24 , 32141-32158.

Amorati, R and R. Rizzi, 2002, Radiances simulated in the presence of clouds by use of a fast radiative transfer model and a multiple-scattering scheme, Applied Optics,41, n.9.

Chahine M.T., 1974, Remote sounding of cloudy atmospheres. I. The single cloud layer. J. Atmos. Sci ,31, 233-243.

Cuomo V., Lanorte V., Pergola, N., Pietrapertosa, C., Rizzi, R., Romano, F., Serio, C., 1999, A new cloud-clearing scheme for infrared sounder measurements by using Kriging technique, International TOVS Study Conference. Boulder , CO, USA

Evans, K. F. and G. L. Stephens, 1991, J. Quant. Spectros. Radiat.Transfer,46,412-423.

Eyre, J. R. and P. D. Watts, (1987) A sequential estimation approach to cloud-clearing for satellite temperature sounding, Q. J. R. Meteorol. Soc. 113, 1349-1376.

Miskolczi, F, R. Rizzi, R. Guzzi, M. Bonzagni, in IRS'88, 1989: Current Problems in Atmospheric Radiation, A. Deepak Publishing, pp. 388-391

Rizzi, R., Serio, C., Kelly, G., Tramutoli, V., McNally, A., Cuomo, V., 1994, Cloud Clearing of Infrared Radiances, Journal of Applied Meteorology, 33, 2, 179-194.

Wylie, D. P. and W. P. Menzel, 1989, Two Years of cloud cover statistics using VAS. J. Clim., 2, 230-392.

Wylie, D. P. and W. P. Menzel, 1991, Two Years of global cirrus cloud statistics using HIRS. Technical Proceedings of the Sixth International TOVS Study Conference held 1-6 May 1991 in Airlie, Va, 344-353.

Correlations between microphysical properties of large-scale semi-transparent cirrus from TOVS and the state of the atmosphere from ECMWF ERA-40 reanalyses

G. Rädel, C. J. Stubenrauch, F. Eddounia

C. N. R. S. / IPSL Laboratoire de Météorologie Dynamique, Ecole Polytechnique, 91128 Palaiseau cédex, France

Introduction

Cirrus clouds (semi-transparent ice clouds) cover about 30% of the globe (e. g., Wylie and Menzel, 1999). Their radiative effect due to changes of their microphysical properties can vary significantly (e.g., Kristjansson et al., 2000). In General Circulation Models these microphysical properties, such as dominating ice crystal shape and sizes, must be predicted from available macrophysical quantities, such as temperature, ice water path and winds (e. g. McFarlane et al., 1992; Donner et al., 1997; Kristjansson et al., 1999). Most utilised relationships have been established only for a few places on earth and for very limited time periods (e. g. Heymsfield and Platt, 1984; McFarquar and Heymsfield, 1996; Korolev et al., 2001). The use of satellite observations allows one to obtain a more coherent image of the validity of these correlations found in regional field campaigns.

Since 1979, the TIROS-N Operational Vertical Sounder (TOVS) instruments (Smith et al., 1979) aboard the NOAA Polar Orbiting Environmental Satellites have measured radiation emitted and scattered from different levels of the atmosphere, and therefore are an important tool for a continuous survey of the state of the atmosphere over the whole globe. Their relatively high spectral resolution yields reliable cirrus properties, day and night (e.g., Wylie et al., 1994, Stubenrauch et al., 1999a). Mean effective ice crystal diameters, D_e, of cirrus clouds are retrieved by taking advantage of the fact that spectral cirrus emissivity differences between 11and 8 μm depend on this parameter (Stubenrauch et al., 1999b; Rädel et al., 2003). This method is sensitive to diameters up to 80 μm, and is applied to large-scale semi-transparent cirrus (visible optical thickness between 0.7 and 3.8). Ice water path (IWP) is then determined from the cirrus emissivity at 11 μm and the retrieved D_e. The averages of these quantities over the globe from 60°N to 60°S are 55 μm and 30 gm^{-2}, respectively.

In this article we study seasonal and regional variations of these quantities as well as correlations with atmospheric properties. Therefore, atmospheric humidity and dynamical properties of the atmosphere, such as horizontal and vertical winds, have been extracted from the ERA-40 reanalyses of the European Centre for Medium Range Weather Forecasts (ECMWF).

Cloud properties from TOVS Path-B

The TOVS system consists, in particular, of two sounders: the High resolution Infrared Radiation Sounder (HIRS/2) with 19 infrared (IR) spectral channels between 3.7 and 15 μm and one visible (VIS) channel (0.7 μm) and the Microwave Sounding Unit (MSU) with four microwave channels around 5 mm. In order to convert these measured radiances into atmospheric properties, complex

inversion algorithms are necessary. At present, the TOVS Path-B dataset (Scott et al., 1999) provides eight years of atmospheric temperature profiles (in 9 layers) and water vapour profiles (in 4 layers) as well as cloud and surface properties at a spatial resolution of 1° latitude x 1° longitude. A fast line-by-line radiative transfer model (4A, Scott and Chédin, 1981) and a huge collection of radiosonde measurements of temperature, humidity and pressure that are grouped by atmospheric conditions are used to generate the Thermodynamic Initial Guess Retrieval (TIGR) database for the initial guess of the atmospheric temperature profile retrieval (Chédin et al., 1985; Chevallier et al., 1998).

Clouds are detected at HIRS spatial resolution (17 km at nadir) by a succession of threshold tests, which depend on the simultaneous MSU radiance measurements that probe through the clouds. To insure more coherence with the MSU spatial resolution (~100 km at nadir), the HIRS radiances are averaged separately over clear pixels and over cloudy pixels within 100 km x 100 km regions. Average cloud-top pressure and effective cloud emissivity over cloudy pixels are obtained from four radiances in the 15 μm CO_2 absorption band (with peak responses from 400 to 900 hPa levels in the atmosphere) and one in the 11 μm IR atmospheric window by minimizing a weighted χ^2 (Stubenrauch et al., 1999c). The method is based on the coherence of the effective cloud emissivity, obtained from the five wavelengths at the pressure level of the real cloud. The cloud-top temperature, T_{cld}, is determined from p_{cld} by using the retrieved atmospheric temperature profile.

Retrieval of mean effective ice crystal size and ice water path of large-scale semi-transparent cirrus and their regional and seasonal variation

The mean effective diameter, D_e, can be considered as an effective photon path of the ice crystal size distribution and is defined by (Mitchell, 2002):

$$D_e = \frac{3}{2}\frac{IWC_s + IWC_l}{\rho_i (P_s + P_l)} \qquad (1)$$

where ρ_i is the bulk density of ice and is assumed to have the value of 0.92 g cm^{-3}, IWC_s and IWC_l are the ice water contents, and P_s and P_l are the projected areas, corresponding to number densities of small and large particle modes, respectively.

The retrieval of mean effective ice crystal diameters, D_e, of cirrus as well as sensitivity studies have been described in detail by Rädel et al. (2003). The cirrus emissivity at 8 μm should be smaller than or equal to the one at 11 μm, depending on D_e. The emissivity difference is largest for small ice crystals (about 0.3 for D_e = 5 μm). It becomes negligible for ice crystal diameters of about 80 μm. Since the retrieval in the IR is mainly based on spectral absorption difference, it performs only for semi-transparent cirrus clouds (IR effective emissivity between 0.3 and 0.85 or visible optical thickness between 0.7 and 3.8).

Cirrus emissivities, ε, at 8.3 and 11.1 μm are computed from the measured brightness temperatures T_B^m, cloud-top temperature T_{cld} and surface temperature T_{surf}. To transform the retrieved cirrus emissivities into D_e, we compare them to look-up tables. These have been constructed from radiative transfer computations (Key and Schweiger, 1998) for a homogeneous ice cloud of 1 km thickness, with a top at 10 km, containing planar polycrystals distributed according a bimodal Γ-size distribution. The lapse rate is assumed as 6.5°C/km. Since the TOVS Path-B dataset provides simultaneous information on cloud properties and atmospheric profiles, we compute the cirrus emissivities by taking out atmospheric water vapour contributions from the measured radiances. Therefore, we can compare the cirrus emissivity difference between 8 and 11 μm to simulations not taking into account the atmosphere, contrary to approaches which use brightness temperature differences. The latter have to

be compared to simulations under a certain assumption of the underlying atmosphere.
To reduce the contribution of partly covered pixels, the ice crystal size retrieval is only performed for overcast high clouds (p_{cld} < 440 hPa), with all HIRS pixels cloudy over an area of 1° latitude x 1° longitude. The frequencies of these large-scale high clouds lie about 10 % below those of all high clouds. The D_e retrieval is influenced by the increase of pixel size and path of the emitted radiation received by the HIRS radiometer with viewing zenith angle. Therefore, we limit the D_e retrieval to cirrus clouds identified under a viewing zenith angle up to 25°.

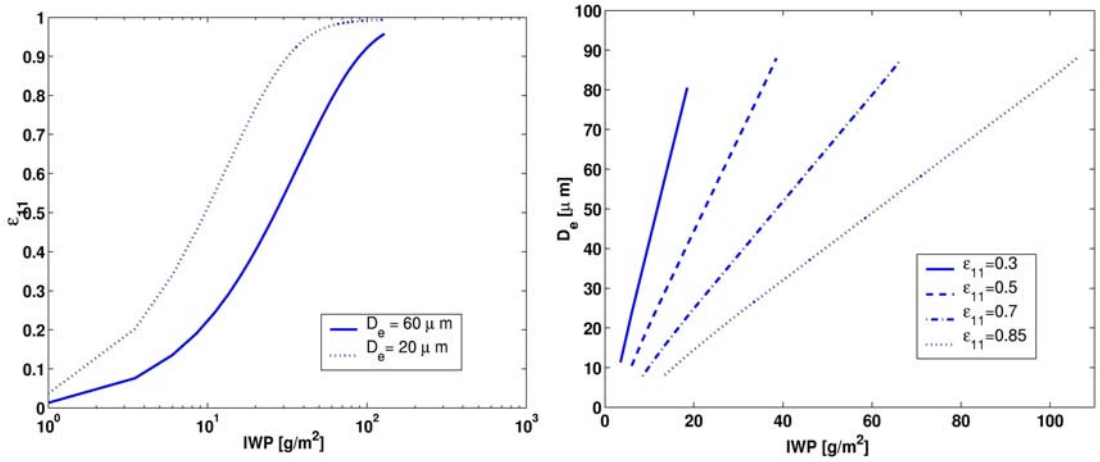

Fig. 1: a) Simulated cirrus emissivity at 11 μm, ε_{11}, as a function of ice water path, IWP, for two different mean effective ice crystal diameters D_e, and b) possible values of D_e and IWP for four distinct simulated cirrus emissivities.

Once D_e is retrieved from the cirrus emissivity difference between 8.3 and 11.1 μm, the ice water path (IWP) can be obtained from D_e and ε(11μm), because the emissivity is a function of IWP and D_e. Therefore, another set of look-up tables has been created from these simulations. Fig. 1a presents the cirrus emissivity at 11μm as a function of IWP, simulated for two mean effective ice crystal diameters. From this figure we deduce that the same cirrus emissivity (for example 0.6) can be reached by small D_e (20 μm) and IWP (10 gm^{-2}) or by large D_e (60 μm) and IWP (30 gm^{-2}). Fig. 1b shows which ranges of D_e and IWP can produce a given cirrus emissivity, using the same simulation. In the case of optically thin cirrus, D_e varies stronger within a small IWP range whereas in the case of optically thicker cirrus, D_e varies within a larger IWP range.

At present we have determined the mean effective ice crystal diameters and IWP of large-scale cirrus clouds NOAA10 TOVS observations. The cover the period from July 1987 until August 1991, with local observation times at 7h30 and 19h30.

Fig. 2 presents the seasonal variation of cirrus emissivity, cloud-top temperature, IWP and D_e, separately for ocean and land of the three latitude bands NH midlatitudes (30°N-60°N), tropics (20°N-20°S) and SH midlatitudes (30°S-60°S). IWP and D_e are on average the largest in the tropical region.

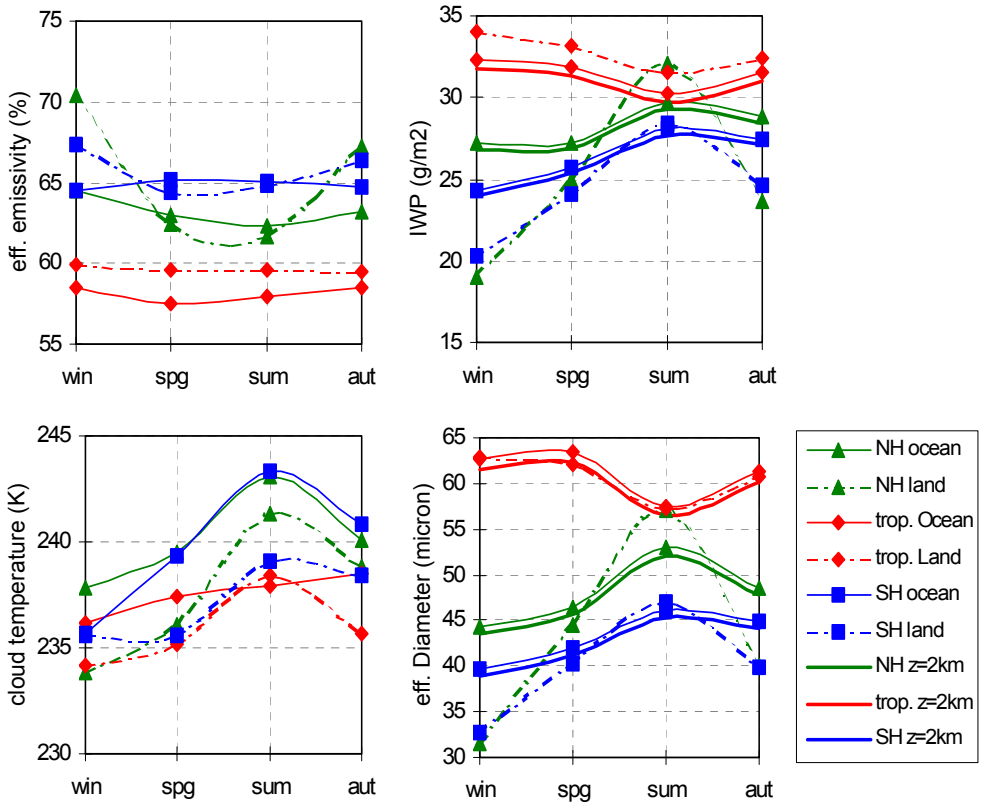

Fig. 2: Average cirrus emissivity (right), mean ice crystal diameter (middle) and IWP (left) of large-scale semi-transparent cirrus as function of season. Three-year averages over three latitude bands (Northern hemisphere midlatitude, tropics and Southern hemisphere midlatitude) are shown separately for land and ocean. Data were averaged using NOAA-10 TOVS observations from June 1987 until Mai 1990

From this figure we conclude the following:

- Large-scale semi-transparent cirrus have on average a smaller effective emissivity (0.57 over ocean and 0.60 over land) in the tropics than in the midlatitudes. However, their average IWP is larger (33 gm^{-2}) than the average IWP in the midlatitudes (28 gm^{-2} except summer). Their mean effective ice crystal diameter (60 µm) is then also larger than the average D_e in the midlatitudes (except during summer over NH land).

- Differences in cirrus emissivity between tropical ocean and land mainly result from differences in IWP.

- Large-scale semi-transparent cirrus in the tropics have no remarkable seasonal cycle in cirrus emissivity, IWP and D_e.

- Large-scale semi-transparent cirrus in the midlatitudes reveal a seasonal cycle, with larger IWP and D_e in Large-scale semi-transparent cirrus have on average a smaller effective emissivity (0.57 summer than in winter. The seasonal cycle of IWP and D_e is also stronger over land than over ocean. Cloud-top temperature in the midlatitudes is also higher in summer than in winter.

- Over ocean during all seasons, IWP and D_e are slightly larger in the Northern Hemisphere than in the Southern Hemisphere.

Since retrieved D_e and IWP can have biases linked to different assumptions (see Table 1 in Rädel et al. 2003), we have investigated the effect of doubling the cloud thickness (from 1 km to 2 km), by recalculating new look-up tables. These results, shown in addition in Fig. 2 for ocean, are very similar.

Correlations between D_e, IWP and T_{cld}

In many climate models D_e, and IWP are parameterised as functions of the cloud-top temperature $T_{cld.}$ Until now, these parameterisations were developed from restricted in-situ data. Fig. 3 presents the average D_e and IWP of all large-scale cirrus clouds between 60°N and 60°S as a function of T_{cld}.

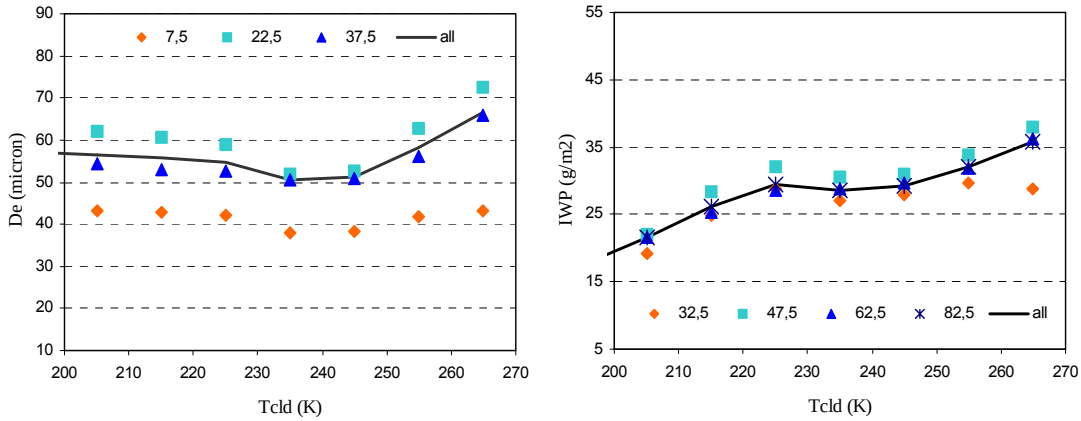

Fig. 3: Average mean ice crystal diameter D_e (left) and IWP (right) of large-scale semi-transparent cirrus as function of cloud temperature. The full line represent three-year averages over the globe from 60°N to 60°S. In addition, D_e averages are shown separately for three IWP intervals and IWP averages for four D_e intervals.

Whereas IWP increases steadily over the whole temperature range (from 200 K to 270 K) from 20 gm^{-2} to 35 gm^{-2}, the behaviour of D_e with cloud temperature is less clear. For cold temperatures (T_{cld} < 235 K), there is no dependence, while for warmer temperatures D_e increases slightly from 50 to 62 µm. The IWP also seems to change its slope slightly around T_{cld} of 235 K. This can be linked either to different processes of cloud formation (the probability of homogeneous freezing increases with decreasing temperature (e. g., Khain et al., 2000) or to the fact that at higher temperatures more water droplets are included in the cloud (e. g., Cober et al., 2001). The inclusion of water droplets would lead to a slight overestimation of D_e (Rädel et al., 2003; Yang et al., 2003).

We refine our analysis by studying separately three different IWP intervals and four different D_e .

The dependence of D_e and IWP on T_{cld} for the respective intervals is again shown in Fig. 3. One observes only a small scatter of IWP due to different D_e (about 5 gm^{-2}), whereas the scatter of D_e due to different IWP is large (up to 30 µm) and is certainly larger than the dependence on T_{cld}.

Figs. 4 show the dependence of D_e and IWP on T_{cld} for midlatitude summer and tropics. Midlatitude winter is not shown but shows similar behaviour as midlatitude winter. From these figures we conclude:

- D_e of large-scale semi-transparent cirrus varies in all regions more with IWP than with T_{cld}

- IWP of these cirrus increases steadily with T_{cld} in the midlatitudes , whereas in the tropics this behaviour is valid only for T_{cld} < 235K and the increase is faster for smaller D_e

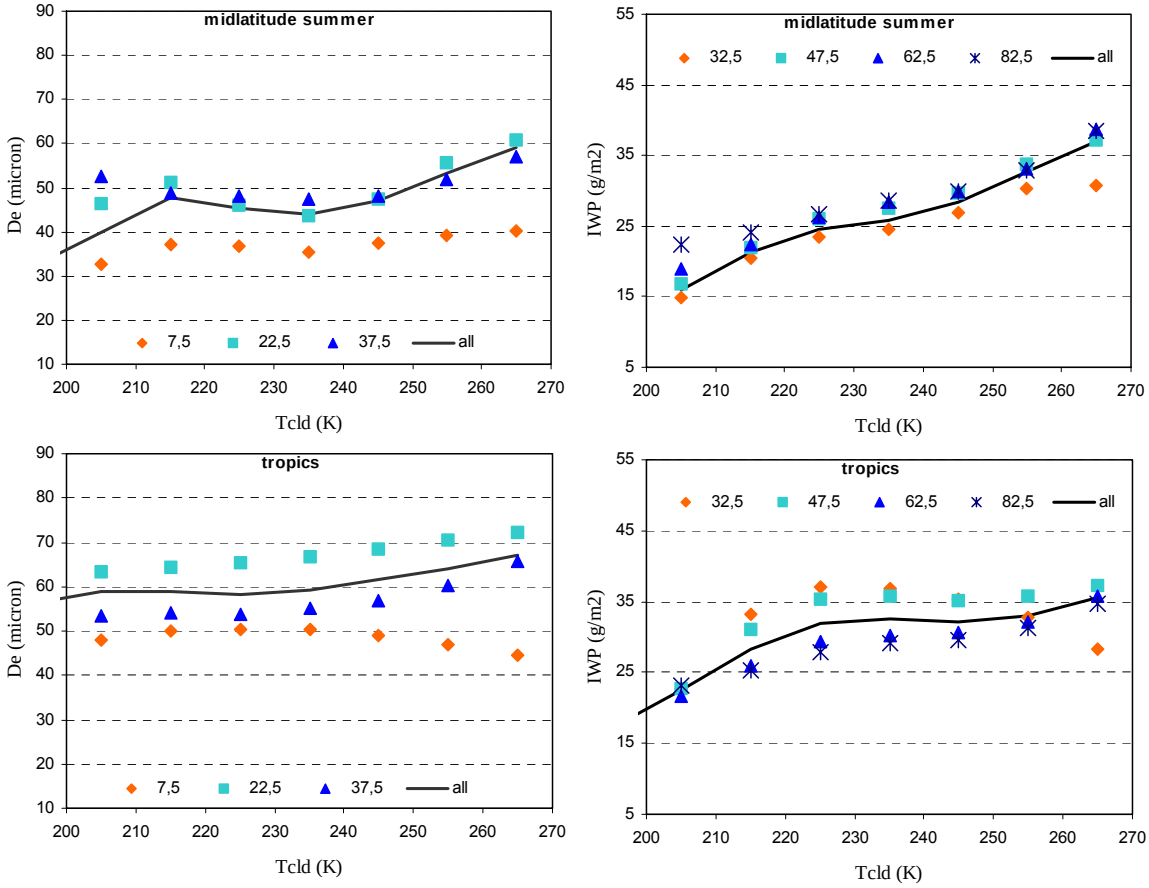

Fig. 4: Average D_e (left) and IWP (right) of large-scale semi-transparent cirrus as function of cloud temperature, separately for midlatitude summer and tropics. The full lines represent three-year averages. In addition, D_e averages are shown separately for three IWP intervals and IWP averages for four D_e intervals.

Field campaigns often measure microphysical properties of specific types of cirrus. Therefore we separated the large-scale cirrus into those with a relatively small effective emissivity ($0.30<\varepsilon(11\mu m)<0.55$) and those with a relatively large effective emissivity ($0.55<\varepsilon(11\mu m)<0.80$). As can be expected from Figs. 1a and 1b, we observe on average lower IWP values in the case of optically thin clouds than in the case of optically thicker clouds. It is interesting to note that D_e of optically thin cirrus is on average larger than D_e of optically thick clouds. The spread of D_e and IWP due to different IWP (and D_e) is slightly larger for optically thin cirrus than for optically thicker cirrus (40 µm (10 gm^{-2}) and 30 µm (7 gm^{-2}), respectively). For both types of cirrus, there is no dependence of D_e on T_{cld} for cold temperatures. For large-scale cirrus with $\varepsilon_{cld} > 0.55$ the spread of D_e and IWP due to different IWP (and D_e) is much smaller in the tropics than in the midlatitudes. This will be investigated further in the next section, by introducing dynamical parameters of the atmosphere.

Atmospheric properties related to large-scale semi-transparent cirrus

The ECMWF reanalysis ERA-40 (e.g. Courtier et al., 1998; Andersson et al., 1998) is based on the Integrated Forecast System and makes use of historical ground-based observations (components of the

Word Weather Watch by the World Meteorological Organization) as well as of multi-channel satellite radiances (from TOVS) through a three dimensional variational assimilation. It also includes a one dimensional variational assimilation of total column water content and surface wind speed using the Special Sensor Microwave / Imager (SSM/I) data. Cloud motion winds are integrated from geostationary satellite observations. At the end of the processing, the period covered should be about 40 years, from mid-1957 to 2002. The ERA-40 reanalysis provides, among other parameters, temperature, humidity, vertical and horizontal winds within grids of 1.125° latitude x 1.125° longitude. Vertical Pressure levels are given at intervals of 75 hPa between 1000 and 700 hPa, of 100 hPa between 700 and 300 hPa and of 50 hPa between 300 and 100 hPa. The temporal resolution is six hours, with data at the same universal time.

To study correlations between cirrus bulk microphysical properties of large-scale semi-transparent cirrus and the humidity and dynamics of the atmosphere in which they are embedded, we couple the TOVS Path-B cirrus data with the most coincident ERA-40 data (less than 6 hours before and less than 50 km apart). The vertical (w) and horizontal winds (u,v) are chosen to be in the closest vertical pressure level underneath the cirrus. The horizontal wind has been computed from the South-North (v) and West-East components (u) as $uv = \sqrt{(u^2+v^2)}$. For the following analysis, we have coupled ERA-40 data with TOVS Path-B data for summer (June to August) and winter (December to February) of 1989 and 1990.

Average atmospheric properties related to large-scale semi-transparent cirrus in NH midlatitudes, tropics and SH midlatitudes.

	Water vapour (cm)		Horizontal wind (m/s)		Frequency of situations with		
	mean	RMS	mean	RMS	updraft	no wind	downdraft
NHmidlatitude summer	3.0	1.2	14.5	10.9	9%	38%	3%
NH midlatitude winter	1.4	0.8	26.1	15.8	13%	29%	7%
tropics	5.0	0.9	7.6	6.0	7%	44%	0.1%
SH midlatitude summer	2.3	1.0	23.4	13.8	6%	42%	4%
SH midlatitude winter	1.5	0.8	22.3	15.2	10%	34%	4%

Table 1 gives an overview of atmospheric properties in the three latitude bands NH midlatitudes, tropics and SH midlatitudes, when large-scale cirrus are present. For the midlatitudes, average properties are shown for summer and winter separately. As expected, total atmospheric water vapour is highest in the tropics and lowest in midlatitude winter. Horizontal wind at cloud level is on average weakest in the tropics and strongest in NH midlatitude winter. In the southern hemisphere, horizontal winds are strong in winter and in summer. Vertical wind can appear as updraft or as downdraft. To investigate vertical wind, we therefore compute frequencies of occurrence of situations with strong large-scale updraft ($w < -0.2$ Pa/s), very weak vertical wind ($|w| < 0.05$ Pa/s), and strong large-scale downdraft ($w > 0.2$ Pa/s), all averaged over 1.125° latitude x 1.125° longitude. At this spatial resolution, the vertical wind in the tropics is often weak, in 7% of the large-scale cirrus situations there is a strong updraft, there are nearly no downdraft situations. In the midlatitudes, there are more situations with a large updraft in winter than in summer.

Correlations between D_e, IWP, atmospheric humidity and winds

To understand the dependence of D_e and IWP of large-scale cirrus on all these atmospheric

properties, we study mean D_e and IWP as function of atmospheric humidity, in the case of four different dynamic situations: no winds (|w| < 0.05 Pa/s and uv < 20 m/s), strong vertical updraft (w < -0.2 Pa/s and uv < 20 m/s) only, strong horizontal wind only (|w| < 0.05 Pa/s and uv > 35 m/s), and strong vertical updraft and horizontal wind (w < -0.2 Pa/s and uv > 35 m/s), as presented in Figs. 5 for cold large-scale cirrus (T_{cld} < 233 K) over the globe (60°N-60°S).

On global average IWP, as well as D_e of these cold, large-scale cirrus are larger in a humid than in a dry atmosphere. In humid situations, IWP is about 10 gm^{-2} larger in regions with strong large-scale vertical updraft than in regions with strong horizontal winds. The latter possibly increase the horizontal cirrus extent and therefore decrease on average the IWP.

Also the mean effective ice crystal size seems to depend on the large-scale dynamical situation, especially in humid air: D_e is about 10 μm larger in case of no large-scale winds than in case of strong large-scale winds. Vertical updraft seems to play a slightly bigger role in the decrease of D_e than horizontal wind.

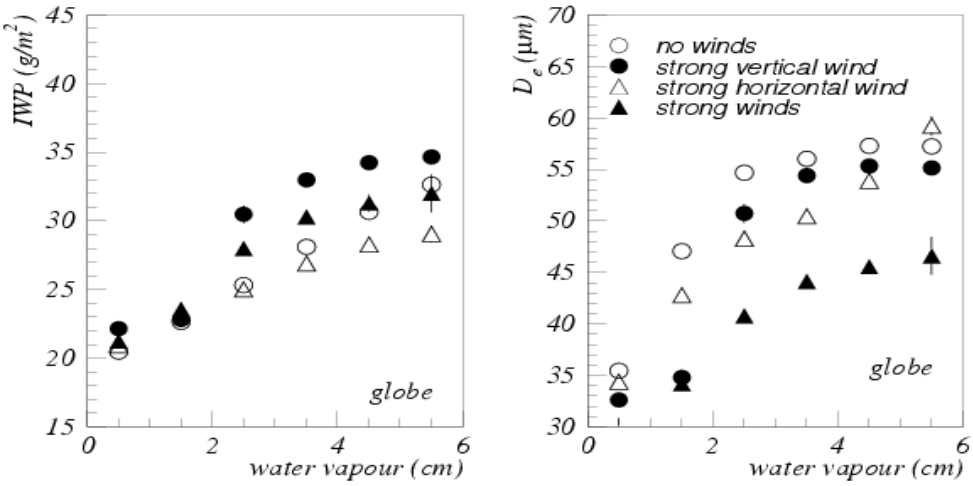

Fig. 5: Global average ice water path IWP (left) and mean ice crystal size D_e (right) of all cold, large-scale semi-transparent cirrus as function of atmospheric humidity, for four different dynamic situations: no winds (o), strong vertical updraft only (•), strong horizontal wind only (△), and strong horizontal wind and vertical updraft (▲)

Our large-scale observations show that in addition to temperature also atmospheric water vapour and winds play a role in the distribution of bulk microphysical properties of cirrus.

It is difficult to compare these results to in-situ data, because the horizontal wind has not been measured or analysed and only ice crystal concentrations (and not IWP) have been analysed in studies which have connected cirrus bulk microphysical properties to vertical updraft (Stith et al., 2002; Kärcher and Ström, 2003).

Conclusions and outlook

In addition to cirrus physical properties, such as cloud-top temperature and effective cloud emissivity, the TOVS instruments also allow to retrieve their mean effective ice crystal diameters, integrated over the cloud depth, and then their IWP. Since the D_e retrieval method is essentially based on the spectral difference in absorption, it can only be applied to semi-transparent cirrus (ε_{IR} < 0.85 or τ_{VIS} < 3.8). The method is sensitive to diameters up to 80 μm, and to avoid too much horizontal heterogeneity and too much influence from the atmosphere below, it is applied to large-scale (covering at least 1° latitude x 1° longitude) semi-transparent cirrus with ε_{IR} > 0.3 or τ_{VIS} > 0.7. The global

averages (from 60°N to 60°S) of D_e and IWP of these clouds are 55 µm and 30 gm^{-2}, respectively. IWP and D_e are on average larger in the tropics than in the midlatitudes, where they are larger during summer than during winter.

Correlations between average D_e, IWP and cloud-top temperature of semi-transparent cirrus over the globe have been investigated. IWP was found to increase steadily over the whole temperature range (from 200 K to 270 K) from 20 gm^{-2} to 35 gm^{-2}. However, the behaviour of D_e, with cloud-top temperature is not so clear. For cold temperatures (T_{cld} < 235 K), there is no dependence, whereas for warmer temperatures mean D_e increases slightly. On the other hand, the scatter of D_e due to different IWP is large (up to 30 µm) and is certainly larger than the dependence on T_{cld}. In addition correlations are different for optically thicker or thinner cirrus, and depending on the latitude.

By making use of TOVS Path-B satellite retrievals and ECMWF reanalyses, we could analyze for the first time correlations between bulk microphysical properties of large-scale semitransparent cirrus and thermodynamic and dynamic properties of the surrounding atmosphere.

On global average, IWP as well as D_e of cold large-scale cirrus are larger in a humid than in a dry atmosphere. In humid situations, IWP is about 10 gm^{-2} larger in regions with strong large-scale vertical updraft than in regions with strong horizontal winds. The latter possibly increase the horizontal cirrus extent and therefore decrease on average the IWP.

Also the mean effective ice crystal size seems to depend on the large-scale dynamical situation, especially in humid air: D_e is about 10 µm larger in case of no large-scale winds than in case of strong large-scale winds. Differences between midlatitudes and tropics suggest that dynamical and thermodynamical parameters of the atmosphere are very important for the resulting bulk microphysical properties of cirrus, in addition to formation process. In the tropics, most large-scale semitransparent cirrus are part of anvils of tropical convection, whereas in the midlatitudes these clouds are related to jet streams and weather fronts.

This study was performed in the framework of the European project CIRAMOSA (http://www.lmd.polytechnique.fr/CIRAMOSA/Welcome.html) and will be published in more detail in Stubenrauch et al. 2004.

In a next step, we will try to find parameterizations of IWP as a function of water vapour, vertical updraft, horizontal wind and T_{cld} as well as D_e as a function of water vapour, vertical updraft, horizontal wind and IWP. These parameterizations could be used in climate models for the computation of radiative fluxes of cirrus clouds, until cloud resolving models find more sophisticated parameterizations

References

Andersson, E., Haseler, J., Unden, P., Courtier, P., Kelly, G., Vasiljevic, D., Brankovic, C., Cardinali, C., Gaffard, C., Hollingsworth, A., Jakob, C., Janssen, P., Klinker, E., Lanzinger, A., Miller, M., Rabier, F., Simmons, A., Straus, B., Thépaut, J.-.N., Viterbo, P., 1998. The ECMWF implementation of three-dimensional variational assimilation (3D VAR). III: Experimental results. *J. Roy. Meteor. Soc.*, **124**, 1831-1860.

Chédin, A., Scott, N. A., Wahiche, C., Moulinier, P., 1985. The Improved Initialized Inversion method: A high resolution physical method for temperature retrievals from the TOVS-N series. *J. Climate Appl. Meteor.*, **24**, 128-143.

Chevallier, F., Chéruy, F., Scott, N. A., Chédin, A., 1998. A neural network approach for a fast and accurate computation of a longwave radiative budget. J. Appl. Meteor. 37, 1385-1397.

Cober, S.G., Isaac, G.A., Korolov, A.V., Strapp, J. W., 2001. Assessing Cloud-Phase Conditions. *J. Appl. Meteor.* , **40**, 1967-1983.

Courtier, P., Andersson, E., Heckley, W., Pailleux, J., Vasiljevic, D., Hamrud, M., Hollingsworth, A., Rabier, F., Fisher, M., 1998. The ECMWF implementation of three-dimensional variational assimilation (3D-

VAR). I: Formulation. *Quart. J. Roy. Meteor. Soc*., **124**, 1783-1807.

Donner, L. J., C. J. Seman, B. J. Soden, R. S. Hemler, J. C. Warren, J. Ström, and K.-N. Liou, 1997: Large-scale ice clouds in the GFDL SKYHI general circulation model. *J. Geophys. Res.*, **102**, 21745-21768.

Heymsfield, A. J., 1977. Precipitation development in stratiform ice clouds: A microphysical and dynamical study. *J. Atmos. Sci.* , **34**, 367-381.

Heymsfield, A. J., Platt, C. M. R., 1984. A parameterization of the particle size spectrum of ice clouds in terms of the ambient temperature and the ice water content. *J. Atmos. Sci.*, **41**, 846-855.

Kärcher, B., Ström, J., 2003. The roles of dynamical variability and aerosols in cirrus cloud formation. *Atmos. Chem. Phys. Discuss.*, **3**, 1415-1451.

Key, J., Schweiger, A., 1998. Tools for atmospheric radiative transfer: Streamer and FluxNet. *Computer & Geosciences*, **24**, 443-451.

Khain, A., Ovtchinnikov, M., Pinsky, M., Pokrovsky, A., Krugliak, H., 2000: Notes on the state-of-the-art numerical modelling of cloud microphysics. *Atmos. Res.*, **55**, 159-224.

Korolev, A. V., Isaac, G. A., Mazin, I. P., Barker, H. W., 2001. Microphysical properties of continental clouds from in-situ measurements. *Quart. J. Roy. Meteor. Soc*. ,**127**, 2117- 2151.

Kristjansson, J. E., Edwards, J. M., Mitchell, D. L., 1999. A new parameterization scheme for the optical properties of ice crystals for use in general circulation models of the atmosphere. *Phys. Chem. Earth* **B 24**, 231-236.

Kristjansson, J. E., Edwards, J. M., Mitchell, D. L., 2000. Impact of a new scheme for optical properties of ice crystals on climates of two CGM's. *J. Geophys. Res.*, **105**, 10063-10079.

McFarlane, N. A., Boer, G. J., Blanchet, J. P., Lazare, M., 1992. The Canadian Climate Centre second-generation general circulation model and its equilibrium climate. J. Climate 5, 1013-1044.

McFarquhar, G. M., Heymsfield, A. J., 1996. Microphysical Characteristics of three Anvils sampled during the Central Equatorial Pacific Experiment (CEPEX). *J. Atmos. Sci.* , **53**, 2401-2423.

Mitchell, D. L., 2002. Effective diameter in radiative transfer: Definition, applications and limitations. *J. Atmos. Sci.*, **59**, 2330-2346.

Rädel, G., Stubenrauch, C. J., Holz, R., Mitchell, D. L., 2003. Retrieval of Effective Ice Crystal Size in the Infrared : Sensitivity Study and Global Measurements from the TIROS-N Operational Vertical Sounder. *J. Geophys. Res.*, **108**, D9 4281-4292..

Smith, W. L., Woolf, H. M., Hayden, M. C., Wark, D. Q., McMillin, L. M., 1979. The TIROS-N Operational Vertical Sounder. *Bull. Amer. Meteor. Soc.* , **60**, 1177-1187.

Scott, N. A., Chédin, A., 1981. A fast line by line method for atmospheric absorption computations: the Automized Atmospheric Absorption Atlas. *J. Appl. Meteor.*, **20**, 802-812.

Scott, N. A., Chédin, A., Armante, R., Francis, J., Stubenrauch, C. J., Chaboureau, J.-P., Chevallier, F., Claud, C., Chéruy, F., 1999. Characteristics of the TOVS Pathfinder Path-B Dataset. *Bull. Amer. Meteor. Soc.*, **80**, 2679-2701.

Stith, J. L., Dye, J. E. Bansemer, A., Heymsfield, A. J., Grainger, C. A., Petersen, W. A. , Cifelli, R., 2002. Microphysical observations of tropical clouds. *J. Appl. Meteor*., **41**, 97-117.

Stubenrauch, C. J., Rossow, W. B., Scott, N. A., Chédin, A., 1999a. Clouds as seen by Infrared Sounders (3I) and Imagers (ISCCP): Part III) Combining 3I and ISCCP Cloud Parameters for better Understanding of Cloud Radiative Effects. *J. Climate*, **12**, 3419-3442.

Stubenrauch, C. J., Holz, R., Chédin, A., Mitchell, D. L., Baran, A. J., 1999b. Retrieval of Cirrus Ice Crystal Sizes from 8.3 and 11.1 μm Emissivities Determined by the Improved Initialization Inversion of TIROS-N Operational Vertical Sounder Observations. *J. Geophys. Res*., **104**, 31793-31808.

Stubenrauch, C. J., A. Chédin, R. Armante, and N. A. Scott, 1999c: Clouds as seen by Infrared Sounders (3I) and Imagers (ISCCP): Part II) A New Approach for Cloud Parameter Determination in the 3I Algorithms. *J. Climate*, **12**, 2214-2223.

Stubenrauch, C. J., Eddounia, F., Rädel, G., 2004. Correlations between microphysical properties of large-scale semi-transparent cirrus and the state of the atmosphere. To appear in *Atmos Res.*.

Wylie, D. P., Menzel, W. P., Woolf, H. M., Strabala, ,K. I., 1994. Four Years of Global Cirrus Cloud Statistics using HIRS. J. Climate 7, 1972-1986.

Wylie, D.P., Menzel, W.P., 1999. Eight Years of High Cloud Statistics Using HIRS. J. Climate 12, 170-184.

Yang, P., Wei, H.-L., Baum, B., Huang, H.-L., Heymsfield, A. J., Hu, Y. X., Gao, B.-C., Turner, D. D., 2003. The spectral signature of mixed-phase clouds composed of non-spherical ice crystals and spherical liquid droplets in the terrestrial window region. J. Quant. Spectros. Rad. Trans. 79-80, 117.

Synergistic Cloud Clearing and Cloud Property Retrieval Using Aqua Sounding and Imaging Infrared Measurements

Hung-Lung Huang[1], Kevin Baggett[1], Elisabeth Weisz[1], Jun Li[1], and William L. Smith[2]
[1]Cooperative Institute of Meteorological Satellite Studies,
University of Wisconsin – Madison
[2]Langley Research Center, NASA

High spectral resolution (~0.5 cm-1) infrared sounding and high spatial resolution (~1 km) infrared imaging measurements on board the NASA EOS Aqua satellite provide an unprecedented opportunity to characterize the full clear and cloudy sounding and cloud property retrieval capability that no single instrument has been able to achieve, up to now.

The Atmospheric Infrared Sounder (AIRS) has single field of view resolution at sub satellite point (i.e. nadir) of about 14 km. The clear sounding sampling probability is less than 10%. It requires the use of infrared measurements from multiple AIRS field of views and co-located microwave measurements to improve the yield of high performance clear sounding retrieval. Unfortunately, this procedure reduces the spatial resolution (from one single to 3 by 3 field of views, for example) and is also limited by the inhomogeneity (different types, phases, and heights) and contrast (difference of cloud fraction within each field of view) of the clouds within the processing footprint.

As part of International MODIS and AIRS Processing Package (IMAPP), AIRS sounding and cloud property retrieval will be demonstrated by the fusion of 1-km MODIS infrared radiances with the derived cloud mask and phase products. We will present the details of this synergistic procedure, performance of the cloud cleared radiances and the associated sounding and cloud property retrievals.

Characteristics of the Cloudy Atmosphere Observed the Atmospheric Infrared Sounder (AIRS)

Evan Fishbein, Luke Chen and Sung-Yung Lee
[1]Jet Propulsion Laboratory, California Institute of Technology

The Atmospheric Infrared Sounder (AIRS) derives surface and profiles quantities under partial cloudy conditions by estimating the clear sky component of the observed radiances. The procedure uses microwave and infrared radiances to provide independent estimates of the clear component. It also assumes variability at scales less than 50 km occurs only in the cloudy component. We are validating both the assumptions and results of the procedure. We compare clear sky radiances produced from forecasts with those from our algorithms. We compute the spatial coherency of the cloudy component and are examining its daily and seasonal variability.

Synergistic use of high spatial resolution imager and high spectral resolution sounder for cloud retrieval

Jun Li*, Timothy, J. Schmit@, Fengying Sun*, W. Paul Menzel@

*Cooperative Institute for Meteorological Satellite Studies (CIMSS)University of Wiscon-Madison
Madison, WI 53706, U.S.A.
@NOAA/NESDIS, Office of Research and Applications
Madison, WI 53706, U.S.A.

Jun.Li@ssec.wisc.edu

Abstract

The Moderate-Resolution Imaging Spectroradiometer (MODIS) and the Atmospheric Infrared Sounder (AIRS) measurements from the Earth Observing System's (EOS) Aqua satellite enable global monitoring of the distribution of clouds. The MODIS is able to provide at high spatial resolution (1 ~ 5km) a cloud mask, surface and cloud types, cloud phase, cloud-top pressure (CTP), effective cloud amount (ECA), cloud particle size (CPS), and cloud optical thickness (COT). The AIRS is able to provide CTP, ECA, CPS, and COT at coarser spatial resolution (~ 14 at nadir) but with much better accuracy using its high spectral resolution measurements. The combined MODIS/AIRS system offers the opportunity for cloud products improved over those possible from either system alone. A variational (1DVAR) methodology is used to retrieve the CTP, ECA, CPS and COT from AIRS longwave (650 – 1130cm^{-1} or 15.38 – 8.85μm) cloudy radiance measurements. Operational CTP, ECA, CPS and COT products from the high spatial resolution MODIS serve as background and first guess information in the AIRS 1DVAR cloud retrieval process. The atmospheric temperature profile, moisture profile and surface skin temperature from the forecast model analysis are used in the AIRS radiance calculation in the cloud retrieval processing. The AIRS 1DVAR cloud properties show significant improvement over the MODIS CO_2-slicing cloud properties in a simulation study. The 1DVAR approach is applied to process the AIRS longwave cloudy radiance measurements; results are compared with MODIS and Geostationary Operational Environmental Satellite (GOES) sounder cloud products. The use of a high-spatial resolution imager, along with information from a high-spectral resolution sounder is analogous to instruments planned for the next generation geostationary operational instruments. Data from ground-based instrumentation at the Atmospheric Radiation Measurement (ARM) Program Cloud and Radiation Test Bed (CART) in Oklahoma are used for validation; results show that AIRS improves the MODIS CTP especially in low-level clouds.

Keywords: Synergism, MODIS, AIRS, CO_2-slicing, 1DVAR

1. Introduction

The Atmospheric Infrared Sounder (AIRS) (http://www-airs.jpl.nasa.gov) (Aumann et al. 2003) on NASA's Earth Observing System (EOS) Aqua satellite is a high spectral resolution ($\nu/\Delta\nu$ = 1200) infrared sounder with 2378 channels, measuring in the infrared region 3.74 – 15.4 μm, that obtains the vertical profiles of atmospheric temperature and water profiles from the Earth's surface to an altitude of 40km. AIRS provides infrared information at a 13.5 km horizontal resolution at nadir. Taking advantage of high spectral resolution AIRS longwave cloudy radiance measurements, CTP and ECA can be retrieved with better accuracy than with MODIS. A scheme called Minimum Local Emissivity Variance (MLEV) (Huang et al. 2003a) has been tested for retrieving the CTP and ECA from high spectral resolution sounder radiances; the scheme seeks the CTP solution with minimum local cloud emissivity variance. However, MLEV is not appropriate for operational processing due to its considerable computational requirements; overcast radiance calculations are needed from upper- to low-level clouds for each longwave channel in order to seek the minimum. The CO_2-slicing algorithm can also be applied to retrieve CTP and ECA from AIRS radiances; however, it is difficult to select pairs from high spectral resolution sounder channels and give proper weight to each pair (Antonelli 2001; Smith and Frey 1990). 1DVAR, using an iterative approach to find the solution, provides an efficient way for cloud retrieval using high spectral resolution sounder longwave cloudy radiance measurements. Since an AIRS independent background and first guess are needed in the 1DVAR approach, the 5km MODIS cloud product is an obvious choice.

MODIS (http://modis.gsfc.nasa.gov/about/specs.html) is a key instrument on the EOS Terra and Aqua satellites for conducting global change research. It provides global observations of Earth's land, oceans, and atmosphere in 36 visible (VIS), near infrared (NIR) and IR regions of the spectrum from 0.4 to 14.5 μm. MODIS cloud products (http:/modis.gsfc.nasa.gov/data/dataproducts.html) include, but are not limited to, the cloud mask (Ackerman et al. 1998) which provides each MODIS 1km pixel with a clear index (confident clear, probably clear, confident cloudy, probably cloudy), cloud phase with 1km resolution which provides each MODIS 1km pixel a phase index (water clouds, ice clouds, mixed phase, etc.), CTP and ECA from MODIS CO_2 band measurements with 5km spatial resolution, along with CPS and COT with 1km spatial resolution (King et al. 2003; Platnick et al. 2003).

The 1DVAR algorithm simultaneously accounts for the instrument noise, uncertainties of the radiative transfer model, atmospheric temperature and moisture effects, and the satellite cloudy measurements. Since all longwave CO_2 spectral cloudy radiances are (a) inversely weighted by their instrument noise along with the assumed forward model error and (b) used simultaneously in the 1DVAR retrieval processing, noticeable improvements in 1DVAR cloud retrievals were found over the CO_2-slicing cloud parameters (Li et al. 2001). A fast and accurate radiative transfer model called Stand alone AIRS Radiative Transfer Algorithm (SARTA) (Hannon et al. 1996; Strow et

al. 2003; http://asl.umbc.edu/pub/rta/sarta/) was used for AIRS clear sky atmospheric transmittance calculation.

In order to account for the scattering and absorption effects of ice clouds and water clouds in radiances, a fast radiative transfer cloudy model for hyperspectral IR sounder is being developed through the joint efforts of University of Wisconsin-Madison and Texas A&M University. In the fast cloudy radiative transfer model, a single scattering of ice cloud under the assumption of hexagonal for large particles and droxtals for small particles is used (Yang et al. 2001; 2003). For water clouds, spherical water droplets are assumed, the Lorenz-Mie theory is used to calculate the single-scattering properties. The cloud microphysical properties are described in terms of cloud particle size (CPS) or effective cloud particle radius and visible cloud optical thickness (COT). Given the visible COT and CPS, the IR COT, single-scattering albedo, and asymmetry factor can be parameterized for radiative effects of ice clouds and water clouds. The cloudy radiance for a given AIRS channel can be calculated by combining the clear sky optical thickness from SARTA and the cloud effects by adding a COT, single-scattering albedo, and scattering phase function. Studies show that the slope of an IR cloudy BT spectrum between 790 (12.6 μm) and 960 cm^{-1} (10.4 μm) is sensitive to the CPS, while the cloudy radiances are sensitive to COT in the region of 1050 (9.5 μm) – 1250 cm^{-1} (8 μm) for ice clouds (Huang et al 2003b).

Synergistic use of high spatial resolution MODIS cloud products and AIRS longwave cloudy radiance measurements, described in this paper, can be applied to process EOS direct broadcast MODIS/AIRS data. These techniques will be relevant to data from the Visible Infrared Imaging Radiometer Suite (VIIRS) and Cross-track Infrared Sounder (CrIS) - VIIRS / CrIS on the National Polar Orbiting Environmental Satellite System (NPOESS), and relevant to data from the Advanced Baseline Imager (ABI) (Schmit et al. 2002) and Hyperspectral Environmental Suite (HES) system – ABI / HES on the GOES-R (Gurka and Schmit 2002).

2. The 1DVAR retrieval scheme

The 1DVAR algorithm for AIRS CTP, ECA retrievals uses the MODIS CO_2-slicing derived CTP, ECA, CPS and COT as background and first guess information to calculate the nonlinear optimal solution of cloud parameters from the AIRS longwave spectral band cloudy radiance measurements. AIRS channels with wavenumbers between 700 and 790 cm^{-1} are used in the CTP and ECA retrieval, while those channels with wavenumbers between 790 and 1130 cm^{-1} are used for CPS and COT retrieval. Given the AIRS observed cloudy radiance, R, for each channel, then $R = R(T, q, T_s, \varepsilon_s, p_c, N\varepsilon_c, D_e, O_T)$ (the fast cloudy radiative transfer calculation) which has the form

$$Y = F(X), \qquad (1)$$

where the vector X contains the CTP, ECA, CPS and COT (the atmospheric temperature profile, moisture profile, surface skin temperature and infrared surface emissivity are assumed to be known or obtained from the forecast model analysis), and Y contains N satellite observed cloudy radiances. The linear form of Eq. (1) is

$$\delta Y = F' \cdot \delta X \,, \qquad (2)$$

where F' is the linear or tangent model of the fast cloudy forward model F.

The 1DVAR approach is to minimize a penalty function $J(X)$, which measures how well the radiance measurements fit the background information, and possibly to other physical constraints. A general form of the 1DVAR solution (Rodgers 1976; Eyre 1989) is given by

$$J(X) = [Y^m - Y(X)]^T E^{-1} [Y^m - Y(X)] + [X - X_B]^T B^{-1} [X - X_B] \,, \qquad (3)$$

where the vector X contains the CTP, ECA, CPS and COT that need to be solved. Since ECA is spectrally dependent, ECAs at ten wavenumbers (710, 720, 730, 740, 750, 760, 770, 780, 790, 800 cm^{-1}) are retrieved, and ECA for a given channel will be obtained by linear interpolation from these ten ECAs. X_B is the background information inferred from the MODIS operational products, Y^m is the vector of the AIRS measured cloudy radiances used in the retrieval process, $Y(X)$ is a vector of cloudy radiances calculated from the cloud state X, E is the observation error covariance matrix which includes instrument noise plus the assumed forward model error, and B is the assumed background error covariance matrix which constrains the solution. To solve Eq. (3), a Newtonian iteration is used

$$X_{n+1} = X_n + J''(X_n)^{-1} \cdot J'(X_n) \,, \qquad (4)$$

and the following quasi-nonlinear iterative form (Eyre, 1989) is obtained

$$\delta X_{n+1} = (F_n'^T \cdot E^{-1} \cdot F_n' + B^{-1}) \cdot F_n'^T \cdot E^{-1} \cdot (\delta Y_n + F_n' \cdot \delta X_n) \,, \qquad (5)$$

where $\delta X_n = X_n - X_B$, $\delta Y_n = Y^m - Y(X_n)$. The AIRS channels with wavenumbers between 700 and 790 cm^{-1} are used for CTP and ECA retrieval while the IR longwave window channels with wavenumbers between 790 and 1130 cm^{-1} are used for cloud microphysical property (CPS and COT) retrieval.

The measurement error covariance matrix, E, is a fixed diagonal matrix, where each diagonal element is the square of the AIRS instrument noise plus an assumed forward model error of 0.2 K for each longwave channel. The first guess X_0, or the starting point of the iteration in Eq.(5), are also the MODIS CTP and ECA products.

3. Retrieval results

A granule of AIRS data was studied. Figure 1 shows the AIRS longwave window ($906cm^{-1}$) brightness temperature (BT) images at 19:17 UTC 6 September 2002, the red color indicates warm scene or clear skies, while the blue color represents cold scene or cloudy skies. Collocated MODIS data were used for the AIRS CTP and ECA retrieval study. Radiances from 14 MODIS spectral bands are used to estimate whether a given view of the Earth surface is affected by clouds, aerosol, or shadow (Ackerman et al. 1998). The AIRS footprint is determined to be cloudy for cloud retrieval only when the percentage of the clear MODIS pixels within the AIRS footprint is less than 10%. The atmospheric temperature and moisture profiles as well as the surface skin temperature are taken from the European Center for Medium-range Weather Forecasting (ECMWF) forecast model analysis in the 1DVAR retrieval.

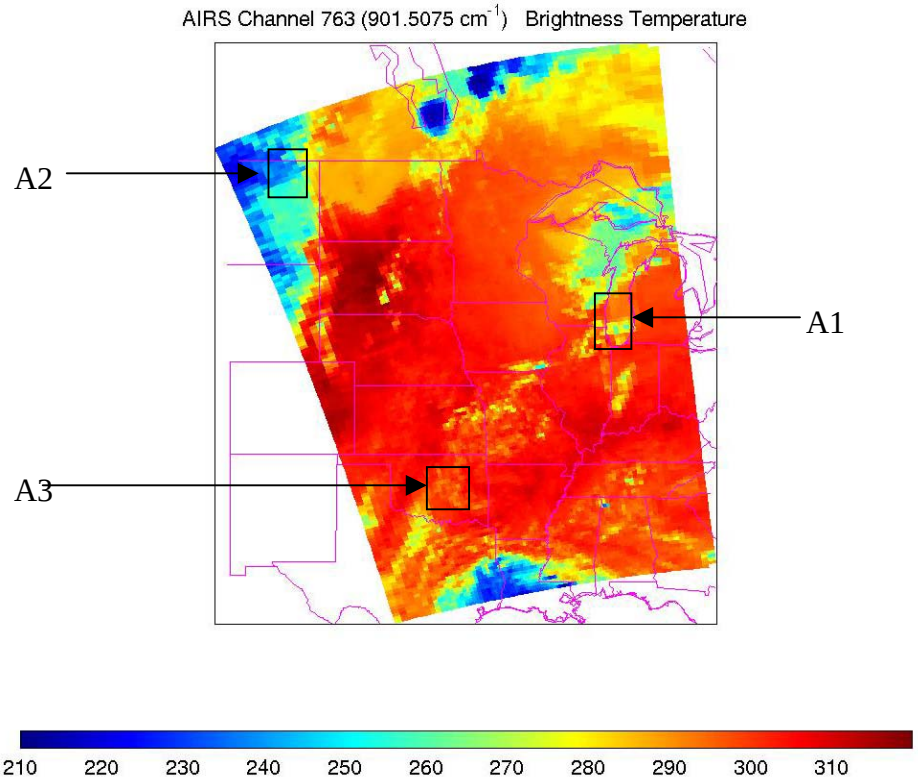

Figure 1. The AIRS longwave window channel (906cm^{-1}) BT image at 19:17 UTC 6 September 2002 (AIRS granule 193).

In each iteration, the CTP is limited to 115 hPa for the highest and 1000 hPa for the lowest, while the ECA must be between 1.0 and zero. Only AIRS longwave channels with observed minus calculated brightness temperatures (BT) greater than 3 times the instrument noise are used in the 1DVAR; 1DVAR will not be attempted if less than 5 AIRS channels are found.

Each AIRS granule has 135 scan lines and each scan line has 90 footprints. In the selected granule, 6332 AIRS footprints were detected to be cloudy. 5232 had successful cloud retrievals (83%). For the remaining 1100, the residual between measured and calculated (from the MODIS CTP and ECA background information) brightness temperatures was too small (8%) or the cloud retrieval failed to converge (9%); non-convergence occurred primarily in multi-layer cloud conditions as estimated by the MODIS classification (Li et al. 2003a).

Figure 2 shows the study area A1 (Lake Michigan area, see Figure 1 for the location of the study area A1). Footprints F1 and F2 view ice clouds in partly cloudy conditions. Figure 3 shows the AIRS longwave clear BT calculation from the ECMWF forecast model analysis (yellow line), cloudy BT calculation with the MODIS CTP and ECA (green line), the BT calculation with the AIRS retrieved CTP and ECA (blue line), and the BT calculation with the AIRS retrieved CTP, CPS and COT (red line), as well as the cloudy BT observation (black line) spectra for AIRS footprint F1 (upper panel). Again,

the MODIS cloud products are used as the background and first guess information in the AIRS retrieval. The lower panel shows the corresponding BT difference between the observation and the calculation (Obs – Cal). Figure 3 indicates that AIRS produces only slight changes in the MODIS CTP in this very thin cloud case of footprint F1; however, AIRS changes the MODIS ECA by 0.05 which results in a significant BT differences. Although the calculation with AIRS retrieved CTP and ECA fits the observation very well in the CO_2 region (650 – 790 cm^{-1}), there is still a discrepancy between the calculation and observation in the longwave IR window region (900 – 1130 cm^{-1}, or 8.8 – 11 μm) due to the scattering of ice clouds.

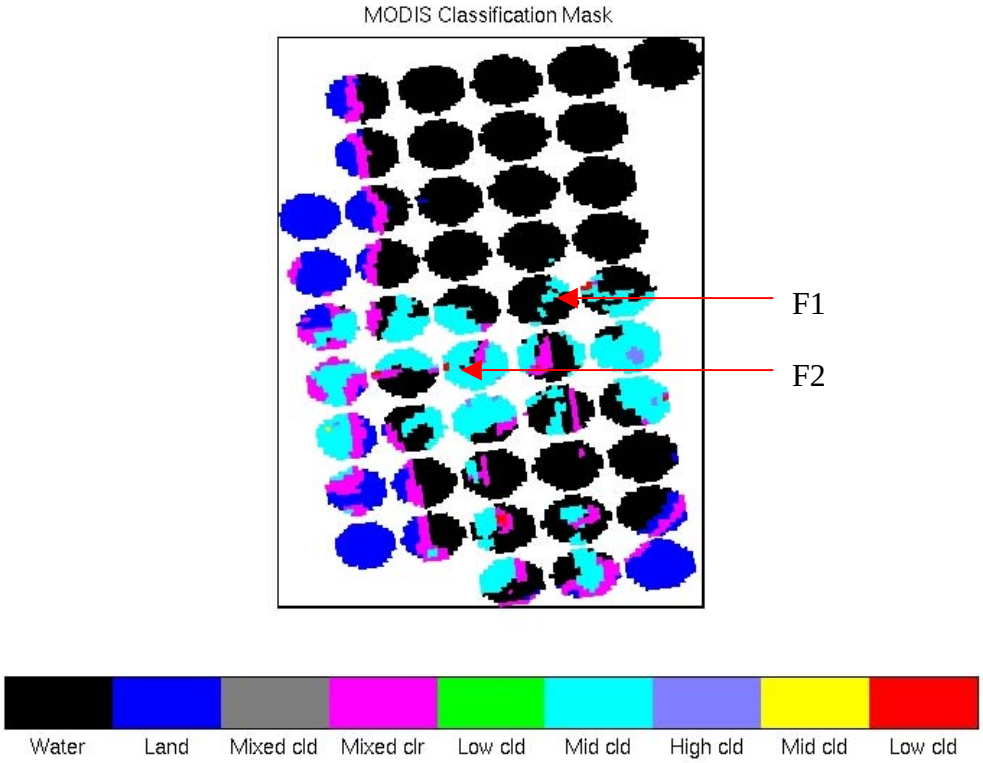

Figure 2. The study area A1 (Lake Michigan area, see Figure 2 for the location of the study area A1) of the MODIS classification mask collocated to the AIRS footprints.

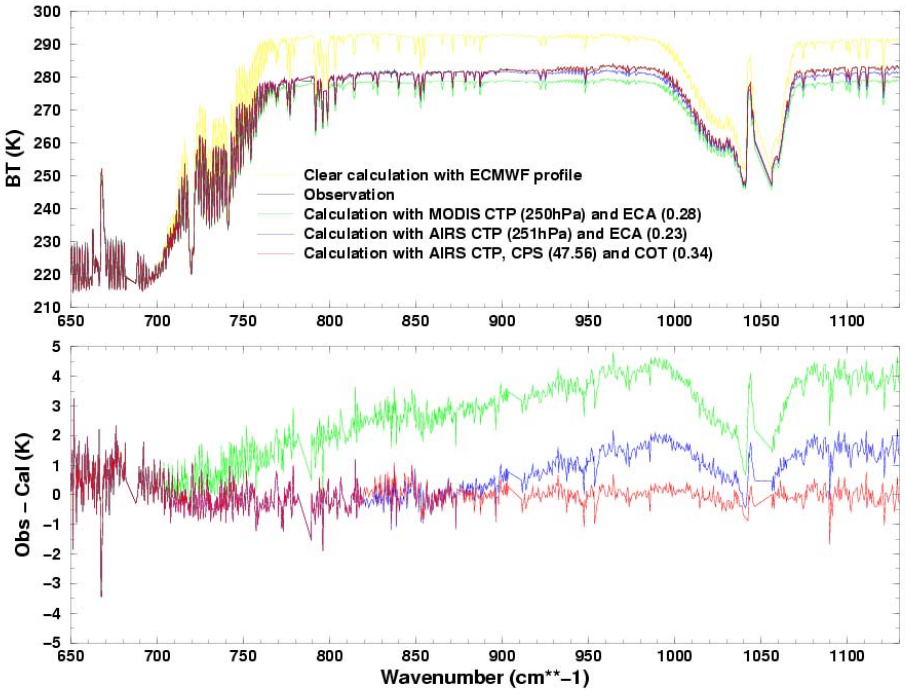

Figure 3. The AIRS longwave clear BT calculation from the ECMWF forecast analysis (yellow line), cloudy BT calculation with the MODIS CTP and ECA (green line), the BT calculation with the AIRS retrieved CTP and ECA (blue line), and the BT calculation with the AIRS retrieved CTP, CPS and COT (red line), as well as the cloudy BT observation (black line) spectra for AIRS footprint F1 (upper panel). The lower panel shows the corresponding BT difference between the observation and the calculation (Obs – Cal).

With determined CTP, the CPS and COT can be retrieved simultaneously from 800 (12.5 μm) – 1130 cm^{-1} (8.8 μm) with also the variational approach. Again, the MODIS CPS and COT products serve as the background and first guess information. Calculations that include the AIRS estimates of CPS and COT fit well to the observations for all AIRS longwave channels (see the red line in Figure 3). Figure 4 is the same as Figure 3 but for footprint F2 that has more ice cloud cover. The AIRS radiance measurements raise the MODIS CTP by 17 hPa, while they decrease the MODIS ECA by approximately 0.05; the calculation fits the observation better after this CTP and ECA adjustment from the AIRS radiance measurements. Again, there is a significant difference between the calculation and the observation in the window region by the opaque cloud assumption; this discrepancy is almost removed by accounting for the effects of the cloud particle size and the BT calculation with CPS and COT also fits the slope of the observation.

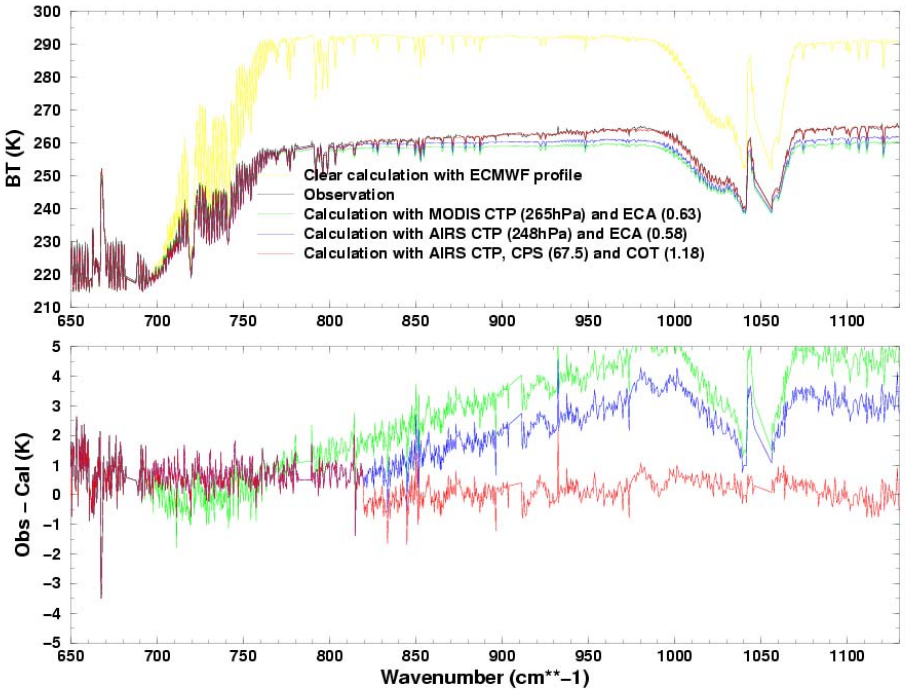

Figure 4. The AIRS longwave clear BT calculation from the ECMWF forecast analysis (yellow line), the cloudy BT calculation with the MODIS CTP and ECA (green line), the BT calculation with the AIRS retrieved CTP and ECA (blue line), and the BT calculation with the AIRS retrieved CTP, CPS and COT (red line), as well as the cloudy BT observation (black line) spectra for AIRS footprint F2 (upper panel). The lower panel shows the corresponding BT difference between the observation and the calculation (Obs – Cal).

Figure 5 shows the study area A2 (see Figure 1 for the location of the study area A2) of the MODIS classification mask collocated to AIRS footprints. Footprint F3 represents mid-level ice clouds according to the MODIS classification mask and the MODIS cloud phase mask. Figure 6 shows that there is a large difference between calculation with the MODIS cloud products and observation in the CO_2 region. However, the difference in the CO_2 region is almost removed by the calculation with the AIRS retrieved CPT and ECA; AIRS adjusted the MODIS CTP by 68 hPa. The slope of the BT in the spectral window region for F3 is significantly larger than that found in F1 and F2 suggesting smaller CPS. With AIRS retrieved CPS and COT for this footprint, the calculation (red line in this figure) fits the slope very well, indicating that the cloud microphysical properties can be retrieved effectively by the AIRS radiance measurements.

Figure 7 shows the 6 September 2003 retrieved MODIS 5km CTP (a) and AIRS 14km CTP (b) for 1917 UTC as well as the GOES sounder 10km CTP (c) for 1846UTC. The GOES sounder CTP retrieval uses the National Center for Environmental Prediction (NCEP) forecast model analysis, the MODIS CTP retrieval uses NCEP's Global Data Analysis System (GDAS) analysis, while the AIRS CTP retrieval uses the ECMWF

forecast model analysis. Different forecast analyses should not result in significantly different CTP retrievals according to Menzel et al. 1992.

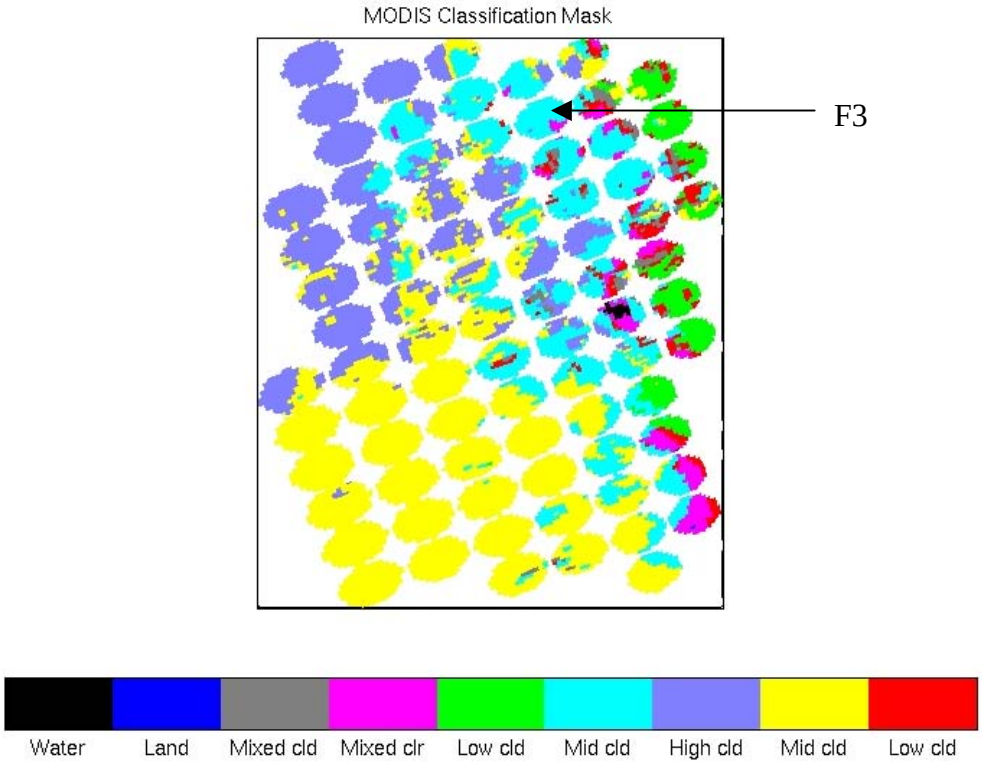

Figure 5. The study area A2 (see Figure 1 for the location of the study area A2) of the MODIS classification mask collocated to AIRS footprints.

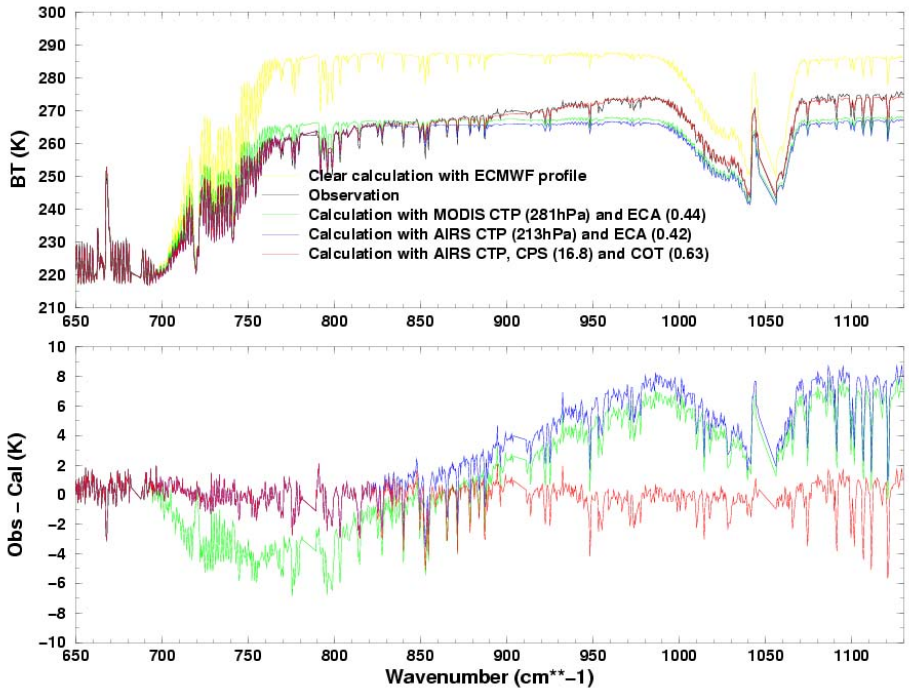

Figure 6. The AIRS longwave clear BT calculation from the ECMWF forecast analysis (yellow line), the cloudy BT calculation with the MODIS CTP and ECA (green line), the BT calculation with the AIRS retrieved CTP and ECA (blue line), and the BT calculation with the AIRS retrieved CTP, CPS and COT (red line), as well as the cloudy BT observation (black line) spectra for AIRS footprint F3 (upper panel). The lower panel shows the corresponding BT difference between the observation and the calculation (Obs – Cal).

For validation, AIRS cloud-top heights (CTHs) at the ARM-CART site in Purcell, Oklahoma were compared with the ground-based VCEIL cloud-base height (CBH) measurements. Four nearest AIRS footprints (F4, F5, F6 and F7) surrounding the ARM-CART site at Purcell in the small area A3 (see Figure 2 for the location of the study area A4) were selected for comparison. The MODIS true color image (not shown) indicates thin and very low-level clouds exist in this area, the MODIS classification mask also indicates very thin and low clouds within the four AIRS footprints. The CTHs retrieved by AIRS and MODIS measurements for the four footprints are listed in Table 1. AIRS and MODIS have similar CTHs for footprint F4 and F5, both are close to the VCEIL CBH. However, AIRS significantly lowers the CHTs from the MODIS CTHs for F6 and F7, and the AIRS CTHs are closer to the VCEIL CBH than the MODIS for these two AIRS footprints.

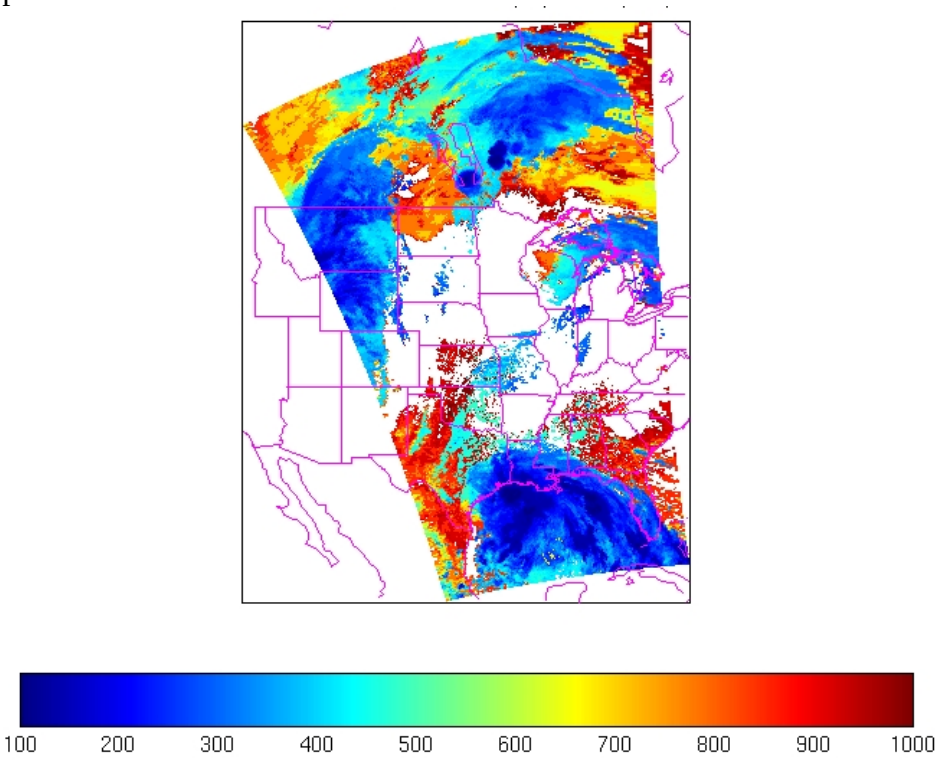

(a)

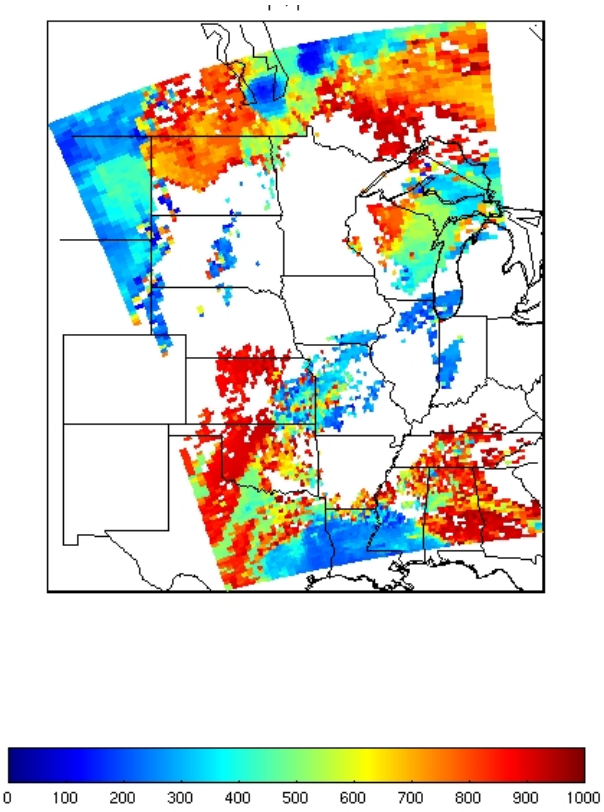
0
100
200
300
400
500
600
700
800
900
1000

(b)

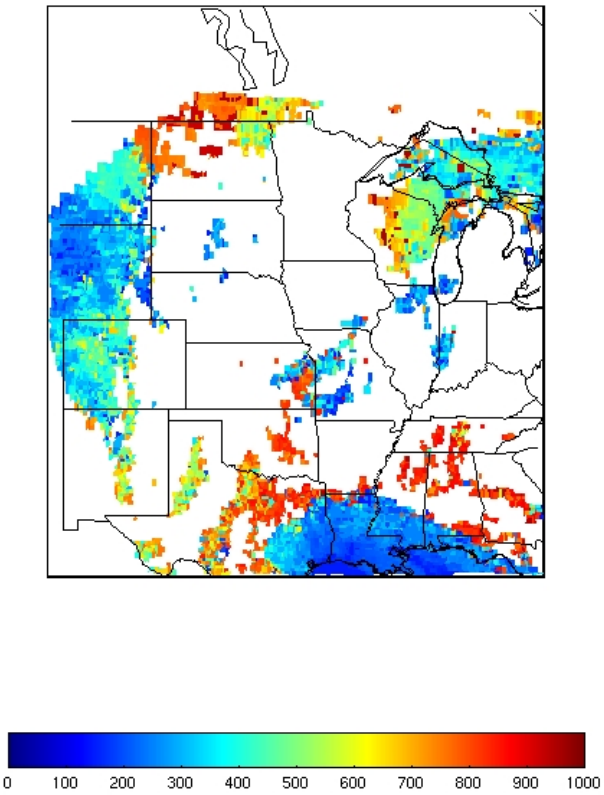
0
100
200
300
400
500
600
700
800
900
1000

(c)

Figure 7. The operational MODIS CTP product with 5km resolution (a), the AIRS retrieved CTP with 14km resolution (b), and the GOES sounder CTP product with 10km resolution (c) images on 06 September 2002.

Table 1. The cloud-top heights retrieved by AIRS and MODIS measurements for the four nearest AIRS footprints surrounding the ARM_CART site at Purcell, Oklahoma.

Instruments	F4	F5	F6	F7
MODIS CTH (km)	1.475	1.475	2.760	2.510
AIRS CTH (km)	1.468	1.452	1.730	1.483
VCEIL CBH (km)	1.100	1.100	1.100	1.100
AIRS COT	0.278	0.185	0.070	0.065

4. Conclusions

An approach for synergistic use of MODIS cloud product estimates and AIRS radiance measurements to retrieve cloud properties is described in this paper. CTP, ECA, CPS and COT derived from the MODIS operational algorithm are used as background and first guess information in the AIRS 1DVAR retrieval processing. Results presented suggest that the AIRS plus MODIS retrievals compare better with other cloud measurements (radiosonde and ceilometer). In addition, spectra calculated from AIRS/MODIS cloud properties agree quite well with actual AIRS measurements. Specifically the following can be concluded.

1) AIRS/MODIS CTPs and GOES sounder CTPs show similar overall cloud patterns.
2) Forward calculations using AIRS 1DVAR retrieved CTP and ECA fit the AIRS observations very well in the CO_2 region, however scattering and absorption effects have to be accounted for in the calculations to fit the AIRS observation in the longwave window region.
3) Validation efforts in a small number of comparisons over the ARM-CART site show that AIRS improves cloud property retrievals in low and thin clouds.

Further validation is necessary using other sources of cloud measurements such as lidar and ground observations. Retrievals in multi-layer clouds still require more work; a large portion of AIRS observations appear to be in multi-layer clouds and a retrieval scheme using AIRS radiance measurements needs to be developed. Nonetheless, this preliminary work presents a strong case for the assertion that AIRS plus MODIS cloud property retrievals will produce improved results over those achieved by either system alone. In addition, simultaneous retrieval of atmospheric profile and cloud property using combined MODIS/AIRS data will also be attempted.

Acknowledgement

The authors would like to thank Anthony J. Schreiner for producing the 10km GOES sounder CTP products. Thanks to Richard A. Frey for numerous discussions on the MODIS CTP cloud product. The AIRS group at the University of Maryland – Baltimore County developed and provided SARTA for the AIRS radiance calculation.

This research was supported HES/ABI program by NOAA Grant NA07 EC00676, and the MODIS science program by NASA grant NAS5-31367.

References

Ackerman, S. A., K. I. Strabala, W. P. Menzel, R. A. Frey, C. C. Moeller, and L. E. Gumley, 1998: Determinating clear sky from clouds with MODIS, J. *Geophys. Res.*, 103, No. D24, 32141-32157.

Antonelli, P., 2001: Principal Component Analysis: a tool for processing hyperspectral infrared data, Ph.D thesis, University of Wisconsin-Madison,1225 West Dayton Street, Madison, WI.

Aumann, H. H., M. T. Chahine, C. Gautier, M. D. Goldberg, E. Kalnay, L. M. McMillin, H. Revercomb, P. W. Rosenkranz, W. L. Smith, D. H. Staelin, L. L. Strow, and J. Susskind, J., 2003: AIRS/AMSU/HSB on the Aqua mission: design, science objectives, data products, and processing systems. *IEEE Trans on Geosci. and Remote Sensing*, NO. 2, 41, 253- 264.

Eyre, J. R., 1989: Inversion of cloudy satellite sounding radiances by nonlinear optimal estimation I: Theory and simulation. *Q. J. R. Meteorol. Soc.*, 115, 1001-1026.

Frey, R. A., B. A. Baum, W. P. Menzel, S. A. Ackerman, C. C. Moeller, and J. D. Spinhirne, 1999: A comparison of cloud top heights computed from airborne lidar and MAS radiance data using CO2 slicing. *J. Geophys. Res.*, 104, 24547-24555.

Gurka, J. J., and T. J. Schmit, 2002: Recommendations on the GOES-R series from the GOES users' conferences. SPIE proceeding 4895, *Applications with Weather Satellites*, Oct. 23 – 27, 2002, Hangzhou, China, 95 - 102.

Hannon, S., L. L. Strow, and W. W. McMillan, 1996: Atmospheric infrared fast transmittance models: A comparison of two approaches. *Proceedings of SPIE*, 2830, 94-105.

Huang, H. L., W. L. Smith, J. Li, P. Antonelli, X. Wu, R. O. Knuteson, B. Huang, and B. J. Osborne, 2003a: Minimum local emissivity variance retrieval of cloud altitude and effective spectral emissivity simulation and initial verification, *J. Appl. Meteorol.* (in press)

Huang, H. L., P. Yang, H. Wei, B. A. Baum, Y. Hu, P. Antonelli, S. A. Ackerman, 2003b: Inference of ice cloud properties from high spectral resolution infrared observations. *IEEE Transactions on Geoscience aad Remote Sensing* (submitted)

King, M.D., W. P. Menzel, Y. J. Kaufman, D. Tanre, B. Gao, S. Platnick, S. A. Ackerman, L. A. Remer, R. Pincus, and P. A. Hubanks, 2003: Cloud and aerosol properties, precipitable water, and profiles of temperature and water vapor from MODIS. *IEEE Transactions on Geoscience nad Remote Sensing*, 41, No. 2, 442-458.

Li, J., W. P. Menzel, Z. Yang, R. A. Frey, and S. A. Ackerman, 2003a: High spatial resolution surface and cloud type classification from MODIS multi-spectral band measurements, , *J. Appl. Meteorol.*, 42, 204 – 226.

Li, J., Menzel, W. P., and A. J. Schreiner, 2001: Variational retrieval of cloud parameters from GOES sounder longwave cloudy radiance measurements. *J. Appl. Meteorol.* 40, 312-330.

Li, J., W. P. Menzel, F. Sun, T. J. Schmit, and J. Gurka, 2003b: AIRS sub-pixel cloud

characterization using MODIS cloud products, *J. Appl. Meteorol.* (submitted)

Li. J., P. Yang, et al. 2003: Retrieval of cloud microphysical properties by synergistically using MODIS and AIRS data, *J. Appl. Meteorol.* (manuscript under preparation)

Lonnqvist, L. 1995: Experiences with a Novel Single-lens Cloud Height Lidar. Preprints, *Ninth Symposium on Meteorological Observations and Instrumentation,* 27-31 March 1995, Charlotte, NC, Amer. Meteorol. Soc., Boston, MA, pp. 106-109

Platnick, S.; M. D. King, S. A. Ackerman, W. P. Menzel, B. A. Baum, J. C. Riedi, and R. A. Frey, 2003: The MODIS cloud products: algorithms and examples from Terra. *IEEE Transactions on Geoscience nad Remote Sensing,* 41, No.2, 459- 473.

Rodgers, C. D., 1976: Retrieval of atmospheric temperature and composition from remote measurements of thermal radiation. *Rev. Geophys. Space Phys*., 14, 609-624.

Schmit, T. J., J. Li, and W. P. Menzel, 2002: Advanced Baseline Imager (ABI) for future Geostationary Operational Environmental Satellites (GOES-R and beyond), SPIE proceeding 4895, *Applications with Weather Satellites*, Oct. 23 – 27, 2002, Hangzhou, China, 111 – 122.

Smith, W. L., and R. A. Frey, 1990: On cloud altitude determinations from high resolution interferometer sounder (HIS) observations. *J. Appl. Meteorol*., 29, 658-662.

Strow, L. L., S. E. Hannon, S. DeSouza-Machado, H. Motteler, and D. Tobin, An overview of the AIRS radiative transfer model, *IEEE Transactions on Geoscience nad Remote Sensing,* Vol. 41, No. 2, 303-313, 2003.

Yang P., B. C. Gao, B. A. Baum, Y. X. Hu, W. J. Wiscombe, S. C. Tsay, D. M. Winker, and S. L. Nasiri, 2001: Radiative properties of cirrus clouds in the infrared (8–13 μm) spectral region, *J. Quant. Spectrosc. Radiat. Transfer, 70,* 473–504.

Yang P., B. A. Baum, A. J. Heymsfield, Y. X. Hu, H.-L. Huang, S.-Chee Tsay, and S. Ackerman, 2003: Single-scattering properties of droxtals, *J. Quant. Spectrosc. Radiat. Transfer. 79–80,* 1159–1169.

Estimates of the Dynamics of Volcano Eruption Column Using Real-time AVHRR Data

Ignacio Galindo

Centro Universitario de Investigaciones en Ciencias del Ambiente (CUICA)
UNIVERSIDAD DE COLIMA,
Colima, México
galindo@ucol.mx

Abstract

Using real-time AVHRR infrared data, it is shown a quantitative model capable to estimate plume dynamic parameters such as emplacement temperatures related with the total energy of the column, gas weight fraction, bulk density of the mixture, cloud rise velocity, etc. The model opens new possibilities to generate in real-time important dynamic parameters of volcano eruption columns.

Introduction

Volcanic plumes are one of the most spectacular of natural phenomena. Fundamentally they represent convective transfer of substantial amounts of heat, from the Earth´s interior in a very short period of time. They also transfer particles, gases, and aerosols to the surface environments of the Earth. The focused convective flows that constitute volcanic plumes involve a rich variety of dynamical processes that are both fascinating and challenging to study (Sparks et al, 1997).

Volcanic activity at Popocatépetl (19.02 N, 98.62 W, 5426 m) during March-July 2003 was comprised principally of multiple exhalations (some with significant ash), volcano tectonic earthquakes and explosions. Daily exhalations averaged 50 events during July. The largest explosive events in July were recorded on 1,15, 19 and 25. The event of 19 July caused light ash fall as far as the southern metropolitan area of Mexico City (Smithsonian Institution, 2003).

The short-lived Vulcanian-style explosion of 19 July occurred at 9:21 local time (see Fig. 1) which was fortuitously captured by AVHRR 1 km LAC (local area coverage) multispectral scenes during the NOAA-17 satellite pass received at our ground NOAA satellite receiving station in real-time (Galindo and Domínguez, 2003)

In Volcanology satellite images have been used to estimate volcanic eruption column height and plume top temperature (Sparks et al, 1997). On the other hand, theoretical work based on turbulent gravitational convection forms the basis of the investigation of plume behavior (Sparks, 1986), however, field determinations of the physical parameters from volcanic explosion clouds are made using high sampling photographic records (1 frame per second) (Rose et al, 1978, Wilson and Self, 1980).

Fig 1. Explosion eruption of Popocatépetl volcano at 09:15 a.m. local time. July 19, 2003

In this paper an attempt is made to estimate plume dynamic parameters such as emplacement temperatures related with the total energy of the eruption column gas weight fraction, bulk density of the mixture, cloud rise velocity, etc., from the real-time AVHRR middle and thermal infrared data.

Estimates of eruption column height

AVHRR digital images of the 9:15 a.m. (local time) NOAA-16 satellite pass have been used to estimate eruption column height. The shadow method (Glaze et al 1989) was applied to one of the images with known control references. Using basic geometry it was estimated the column height by measuring the length of the shadow cast (≈ 13 km) on the Earth´s surface. The sun angle (h = 29.2°) was determined as usual as a function of solar declination, latitude, and local hour angle, Then the cast shadow of the highest point of the cloud was determined, H = 7.3 km.

Temperature and irradiance distribution of the explosion cloud

The temperature of the plume was determined as brightness temperature $\Delta T_{34} = T_3 - T_4$ from the AVHRR channel-3 and channel-4 temperatures. Channel-4 temperature, T_4 represents the ambient temperature (Harris et al, 1995 , Galindo and Dominguez, 2003). The irradiance of the plume was obtained with the aid of the inverted Planck´s equation.

Figure 2 shows the irradiance distribution of the volcanic cloud. It is observed that there are three nuclei of maximum irradiance. The largest one is located at the western part of the summit, it continues to the second nuclei located outside of the summit at the southeast. The smallest nuclei but the most intense is seen outside the summit at the northwest direction. The latter nuclei it is also seen in the visible and near infrared channels -1 and –2 indicating, besides reflected sunlight, energy emission in the 0.725 to 1.10 μm waveband. Following Planck´s law, thermal emittance at these wavelengths indicates the presence of an extremely hot surface together with. ash emission in very discrete amounts was also detected at the southeast side of the summit (Figure 3).

The model of a discrete volcanic explosion cloud

In what follows an attempt is made to estimate several dynamic parameters of volcanic explosion clouds from the satellite irradiance data.

To test the validity of the approach and results here presented we shall follow the model of Wilson and Self (1980) who analyzed photographic records of 10 volcanic eruption clouds during the 1978 eruption of Fuego Volcano in Guatemala.

The motion of a discrete explosion cloud as it emerges from the vent can be studied if the following simple approximations are made:

(1) the cloud decompresses to atmospheric pressure quickly,
(2) the cloud is treated as a rigid, incompressible vertical cylinder

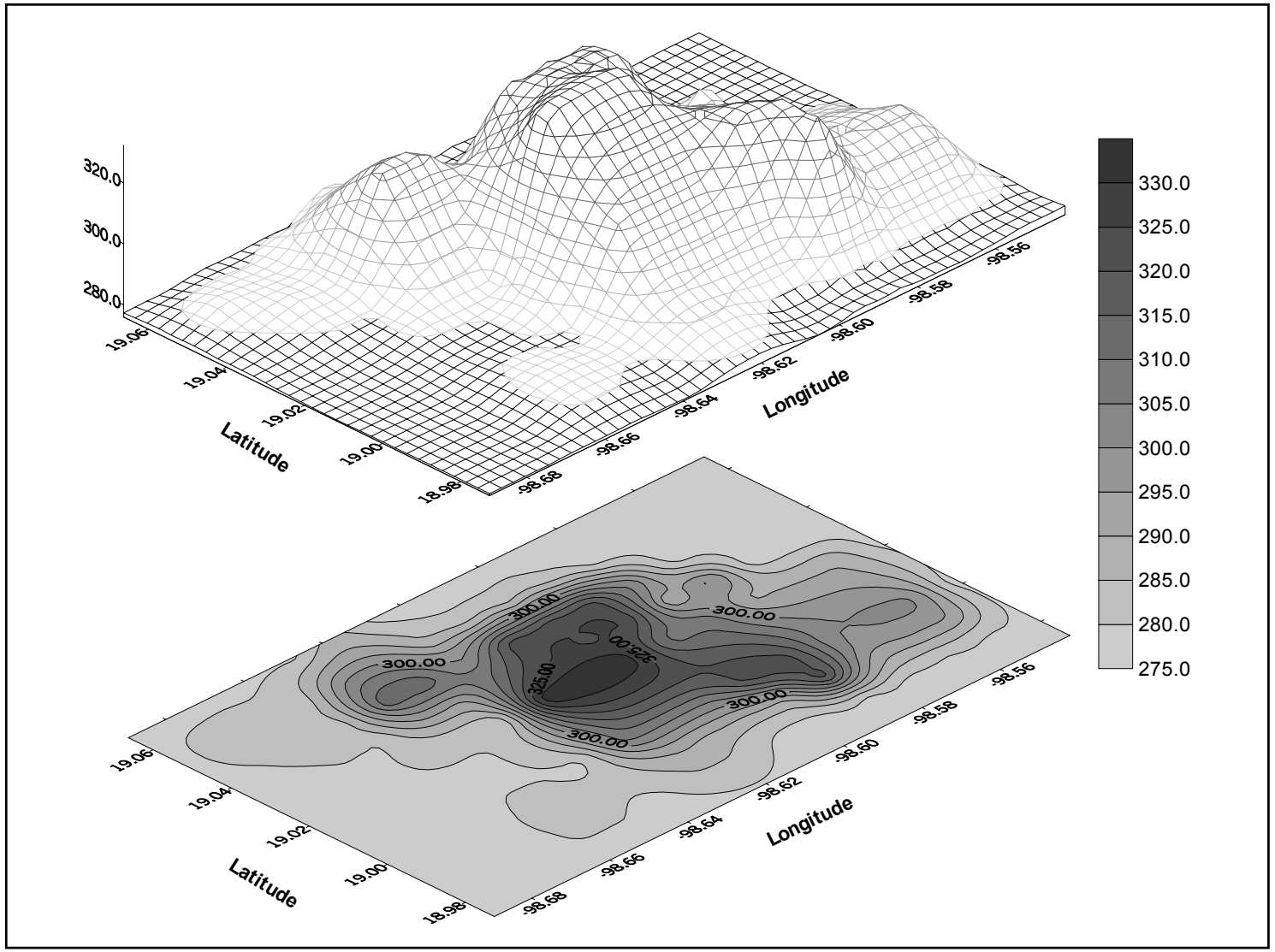

Fig. 2. Effective infrared brightness temperature [K] distribution of the explosion plume as it was detected by NOAA-15 satellite pass at 9:15 local time

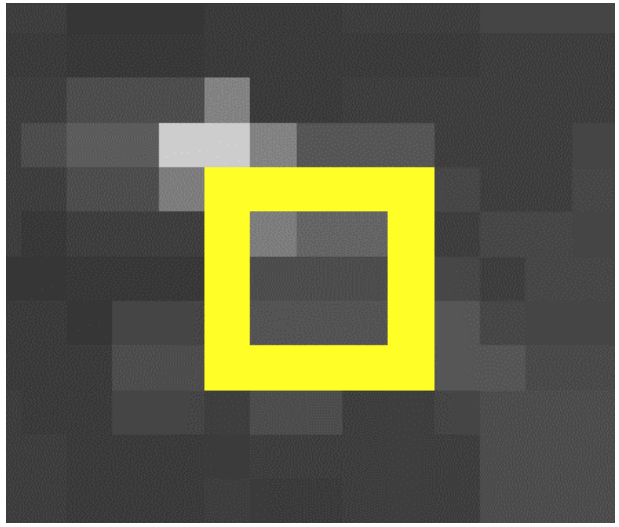

Channel-1. Visible

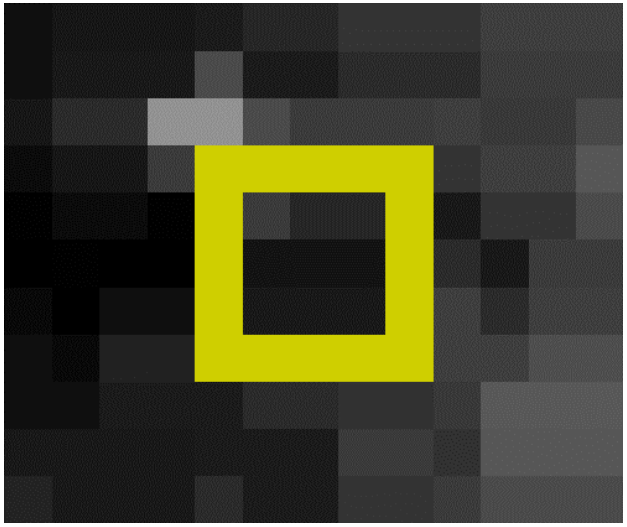

Channel-2. Near infrared

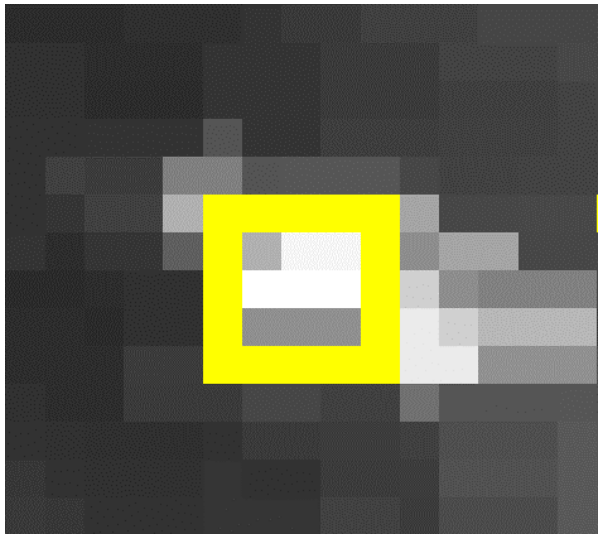

Channel-3. Middle infrared

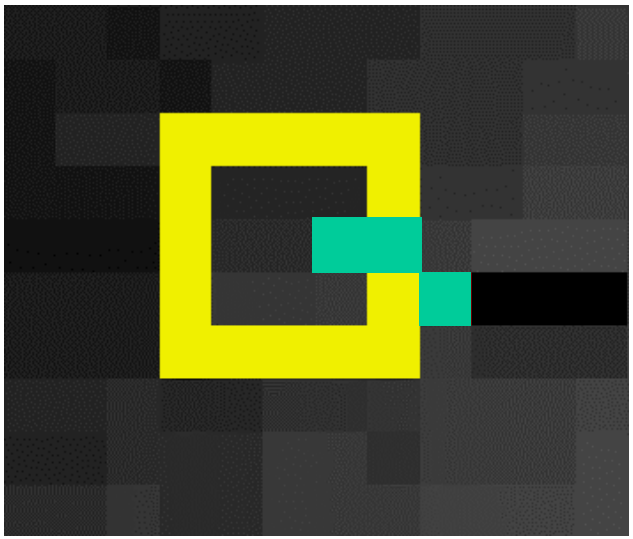

Fig. 3. Explosion eruption of Popocatépetl volcano as detected by AVHRR NOAA-15 at 09:15 a.m. local time. July 19, 2003

{the latter approximation is valid if velocities are well below the speed of sound but becomes increasingly inadequate with time after emergence as spatial gradients develop in pyroclastic number density, particle size, water vapor content, and temperature (Wilson and Self, 1980)}.

The equations of motion for the vertical cylinder are found by equating the product of mass and acceleration to the total forces acting on the cloud: atmospheric drag, gravity, and buoyancy.

After some parameterizations of the basic equations, Wilson and Self (1980) have obtained expressions in terms of the quotient β/α. Where β is the bulk density of the mixture (kgm^{-3}) and α (kgm^{-3}) represents the density on environment.

For a vertical cylinder the equivalent equation is

$$\beta/\alpha = (g - 3\ C_c\ W^2/2H)/(g + du/dt) \qquad (1)$$

Here the upward acceleration of the cloud is du/dt (negative if the cloud is decelerating), and the dimensionless drag coefficient C_c for a cylinder is about 1.0, W is the relative velocity of the leading edge of the cloud and the air, and u the velocity of the cloud center. H = 7.3 km is the cylinder height, i.e., the obtained estimate of eruption column height

The relation of β/α to other parameters can be investigated by considering the behavior of temperature within the eruption clouds.

After few seconds of rise, a cloud consists essentially of incorporated air plus those particles that have not fallen out of the cloud. As the air temperature rises from an ambient temperature θ_a to a new value θ, the air density will decrease from α to $(\alpha\theta_a/\theta)$.

If the gas weight fraction of the cloud is n, the particle weight fraction is (1- n) and the bulk density β is given by

$$1/\beta = (n/\alpha(\theta_a/\theta)) + (1 - n)/\rho \qquad (2)$$

where ρ is the density of the gas (kgm^{-3}), i.e.,

$$\alpha/\beta = n(\theta_a/\theta) + \alpha(1 - n)/\rho \qquad (3)$$

i.e.,

$$1/\beta = n/\alpha(\theta_a/\theta) + (1 - n)/\rho \qquad (4)$$

If the clasts removed from the cloud an any stage contribute negligible heat to the cloud. Then θ is obtained by equating the heat loss by clasts

$$[(1 - n)\ S_s\ (\theta_s - \theta)]$$

to the heat gained by air

$$[n\, S_a\, (\theta - \theta_a)],$$

$$\theta/\theta_a = [n\, S_a/S_s + (1- n)\, \theta_s/\theta_a]/[1 + n\, (S_a/S_s - 1)] \quad (5)$$

where S_a and S_s are the specific heats at constant pressure of air and rock, the adopted values being 0.24 and 0.20 cal/g/K, respectively.

A simplification can be made to (3) because all values of β/α encountered in the cases analyzed by Wilson and Self (1980) are greater than 0.5 and mostly close to 1; at the height of the summit of Fuego, but ρ is about 2 g cm^{-3}, so α/ρ is < 0.001; hence $(1 - n)\, \alpha/\rho$ is always << α/β and can be neglected, giving

$$\alpha/\beta = n\, \theta/\theta_a, \quad (6)$$

At the height of the summit of Popocatépetl volcano α is about 8.194 x 10^{-4} g cm^{-3}. At the umbrella region of the volcanic cloud α is about
5.25 x 10^{-4} g cm^{-3}.

Air temperature at the summit of Popocatépetl volcano was estimated using channel-4 temperature, T_4 outside of the volcanic cloud, i.e., $T_4 = \theta_a =$.
Whereas θ_s = 337 K is the temperature of the rocks, i.e., the maximum temperature detected at the main nuclei of Figure 3, i.e., at the gas thrust region and the minimum temperature of the plume is taken as the new reference temperature θ = 291 K measured within the convective region.

Having done that, the algorithm runs and calculates n, from equation 4. Given a range of value for n, equations 4-6 can be used to estimate successive values of β/α from brightness temperatures of θ/θ_a.

Wilson and Self (1980) assumed "in situ" values for θ_s/θ_a, i.e., if θ_s = 1373 K (1100 °C) and θ_a = 273 K (0 °C), then θ_s/θ_a = 5.0, if θ_s is as low as 1123 K (850 °C) and θ_a is as large as 288 K (15 °C).These two values probably bracket the range of reasonable possibilities.

Results

A comparison of β/α for the explosions of Fuego volcano (Wilson and Self, 1980). and Popocatépetl volcano is shown in Table 1. Since the agreement is quite good, then one can use the cloud rise velocity u calculated for Fuego.

The middle infrared irradiance emitted from the volcanic cloud and detected by the AVHRR channel-3 is proportional to the total energy that the cloud is emitting into the atmosphere, then the detected brightness temperatures θ_s/θ_a should be proportional to those "in situ" values considered by

Theoretical

θs/θa = 4

n	θ / θa	β / α
0.01	3.98	25.156
0.05	3.87	5.162
0.10	3.75	2.669
0.30	3.21	1.037
0.50	2.64	0.758
0.70	2.02	0.707
0.80	1.69	0.738
0.90	1.35	0.820
0.95	1.18	0.893
0.99	1.04	0.975
1.00	1.00	1.000

θs/θa = 4.5

n	θ / θa	β / α
0.01	4.47	22.367
0.05	4.35	4.594
0.10	4.20	2.378
0.30	3.58	0.931
0.50	2.91	0.687
0.70	2.19	0.652
0.80	1.81	0.691
0.90	1.41	0.786
0.95	1.21	0.871
0.99	1.04	0.969
1.00	1.00	1.000

Our results

θs/θa = 4

n	θ / θa	β / α
0.02	3.93	13.603
0.06	3.80	4.676
0.09	3.67	2.888
0.19	3.33	1.559
0.29	3.00	1.133
0.40	2.67	0.937
0.51	2.33	0.840
0.63	2.00	0.800
0.74	1.67	0.806
0.87	1.33	0.862
1.00	1.00	1.000

θs/θa = 4.5

n	θ / θa	β / α
0.01	3.98	35.651
0.05	3.83	5.315
0.90	3.68	2.956
0.11	3.60	2.442
0.22	3.23	1.378
0.34	2.85	1.028
0.46	2.48	0.873
0.59	2.10	0.807
0.72	1.73	0.801
0.86	1.35	0.858
1.00	1.00	1.002

Table 1. Comparison of theoretical eruption cloud data (Wilson & Self, 1980) against data obtained from measurements of infrared brightness temperature

Wilson and Self (1980). A comparison of our results with the theoretical eruption cloud parameters. shows a very good agreement..

Conclusions

Besides the estimates of volcanic eruption column height and plume top temperature, satellite brightness temperatures can be used to estimate some parameters related with the plume dynamics, such as thermal energy, gas weight fraction, bulk density of the mixture and cloud rise velocity.

Brightness temperature of the volcanic cloud is proportional to the total emitted energy from the volcanic cloud. Therefore, upwelling middle infrared radiation data at the gas thrust region can be "calibrated" to estimate total emitted energy and related dynamic parameters of a explosion cloud

References

Galindo, I:, and T. Domínguez: Real-time AVHRR Thermal Monitoring and Ash Detection: the Case of Colima, Volcano (Mexico). A. Robock and C. Oppenheimer, Eds. *¨Volcanism and the Earth's Atmosphere"*, Geophysical Monograph 139, American Geophysical Union, pp. 133-150, 2003.

Glaze et al

Harris, A.J.l., S.E.J. Swabey, and J. Higgins, Automated thresholding of active lavas using AVHRR data . *Int. J. Remote Sensing*, **16**, 3681-3686. 1995.

Smithsonian Institution, *Bulletin of the Global Volcanism Network* **28**, 9, 2003.

Sparks, R.S. J. The dimensions and dynamics of volcanic eruption columns. *Bull. Volcanol.* **48**, 3-15, 1986.

Sparks, R.S. J., M.I. Bursik, S.N. Carey, J.S. Gilbert, L.S.Glaze, H. Sigurdsson and A. W. Woods, *Volcanic Plumes*, John Wiley Sons, Chichester, U.K., 1997, 574 pp.

Rose, W. I., R.D. Cadle, A.L., Lazrus, L. E. Heidt, B. J. Huebert, R.E. Stoiber, S. Self, G.Bratton, R.L. Chuan, D.C. Woods, I. Friedman, and L. Wilson, 1978 Volcanic eruption cloud sampling project. *Geo.. Soc. Amer. Abstr. Programe* **10** (7), 480, 1978.

Wilson, L. and S. Self, Volcanic explosion clouds: density, temperature, and particle content estimates from cloud motion. *J. Geophys. Res.*, **85**, 2567-2572, 1980.

Diagnosing the Global Energy-Water Cycle with Satellite Observations

William B. Rossow

As part of the World Climate Research Program, the Global Energy and Water Experiment (GEWEX) is, as its name suggests, attempting to diagnose the atmospheric energy-water cycle and its variations. Note that this cycle is central to determining the climate's sensitivity (feedbacks) to forced changes and plays a role in determining unforced climate variations by connecting all of the other components of the climate system. To achieve this, the GEWEX Radiation Panel (GRP) is working to assemble a complete diagnostic dataset that describes the main components of the energy-water cycle and its weather-scale variations over a period of a few decades to support research on these topics. Some of these datasets are ready now and appear to be of useful accuracy, some exist but their accuracy is not well known and some do not exist at all. The rationale for assembling this data collection and a summary of the current status will be presented. Since these data are now being used for climate research, the GRP is proposing that a careful assessment of their quality be carried out to: (1) set the stage for re-processing (if needed) to improve quality, (2) provide a better understanding of these data when used for analyses of the energy-water cycle and (3) to support the next IPCC assessment, which will focus on water. Given the expertise in the ITWG, GRP proposes to partner with ITWG for the assessment of satellite-based tropospheric water vapor data products. It might make sense for this task to be combined with a complete assessment of tropospheric and surface temperature measurements from satellites as well.

Climate variability and change of tropical tropospheric humidity as observed by HIRS

Mark McCarthy[1] & Ralf Toumi[2]
[1]Hadley Centre of Climate Prediction and Research, Met Office, UK
[2]Imperial College, London, UK

We review some of our results from analysing the Upper Tropospheric Relative Humidity (UTRH) product of J.Bates et al. (2001) from the High Resolution Infra-Red Sensor (HIRS) for the period 1979-98

The only mode of interannual variability that can be identified in the HIRS record are UTRH variations following patterns of anomalous convection associated with El Nino and the Southern Oscillation (ENSO). We describe the seasonal pattern of this variability and show that extremes in UTRH during the northern hemisphere winter of an ENSO event are dominated by regional changes in tropospheric temperatures. Atmosphere-ocean dynamics coupled with the seasonal cycle in UTRH can result in regional UTRH anomalies during the following summer season. We further discuss the importance of being able to simultaneously diagnose temperature and humidity products in climate research, and radiosonde data are used to highlight differences in temperature-humidity relationships over a range of space and time scales.

The HIRS dataset contains significant regional trends characterised by increasing humidity over Africa, the West Indian ocean and the Amazon, and decreasing humidity over the southern hemisphere convergence zones and subtropics. We show that changes in ENSO, or a simple intensification of the Hadley circulation are inadequate to describe these observations, a number of alternative scenarios are discussed, including the suitability of the current version of the HIRS dataset for trend analysis.

The results are presented with comparison to those produced by the atmosphere only model HadAM3 forced with observed SSTs for the same period.

Use of radiances data in ERA-40

Graeme Kelly
ECMWF, United Kingdom

At ECMWF a re-analysis has been completed using all available satellite and conventional data from 1967 to 2002. A reduced resolution version of the ECMWF operational IFS system (3D-VAR at 60 levels and horizontal resolution of TL 159 (120 km) was used for the data assimilation system. The use of satellite radiances started with VTPR radiances in 1973 and radiances were used directly in the assimilation from VTPR, HIRS, MSU, SSU, and AMSU. SSMI radiances where input to a pre-processing 1D-VAR and the retrieved products of total precipitable water and wind speed were then assimilated in the 3D-VAR analysis. Some of the difficulties that arose with the satellite data during the re-analysis discussed. The re-analysis was highly successfully but it is clear that further re-analyses could be further improved with the knowledge obtained from ERA40 about the performance of the satellite sensors.

The use of MSU in climate change studies

Peter Thorne, Simon Tett, & David Parker
Hadley Centre for Climate Prediction and Research, Met Office, UK

We briefly summarize our recent research using two independently produced MSU climate timeseries.

We illustrate the use of MSU products in attempts to resolve the observed discrepancy between a significant surface warming and little tropospheric temperature change within the tropics over the satellite period. This is contrary to climate model predictions of increasing warming aloft under anthropogenic forcings. We use MSU data both to inform and to test our hypothesis that this disagreement occurs because tropical tropospheric temperature evolution on climate timescales is a two-boundary problem with both surface and stratospheric constraints.

We also show how MSU data can be usefully used to inform us as to the potential causes of recent climate change. Space-time global optimal detection studies using a climate-model yield significant both natural and anthropogenic climate change signals within tropospheric MSU timeseries. This result is shown to be insensitive to the choice of MSU dataset within the mid to upper troposphere. For stratospheric temperatures our analyses imply that the model significantly overestimates the response - most likely because it has too much ozone reduction in comparison to recent observations.

Satellite Upper Air Network

Tony Reale
NOAA/NESDIS
Washington DC

INTRODUCTION

The following report proposes a network of about 40 upper-air sites (and available ships) that would routinely launch reference radiosondes coincident with polar satellite overpass, referred to as the Satellite Upper Air Network (SUAN). The candidate SUAN sites are presented, along with the potential mutual benefits of SUAN on satellite data systems, climate, numerical weather prediction (NWP), radiative transfer (RT) models, future advanced sounders, and the radiosondes, and the growing support for SUAN as an important step toward insuring that past mistakes are not repeated.

BENEFITS OF SUAN:

Satellite Data and Products

Operational polar satellite measurements and derived products utilize collocations of satellite data and radiosondes for validation and also for direct product tuning during retrieval (Reale, 2002). Troubling degrees of inconsistency among the global distributions of collocations available per satellite, and the need for broad time windows to achieve large enough global samples has raised questions concerning their suitability for these purposes. Typical global distributions of collocations for NOAA-15 (top) and NOAA-16 (middle) operational Advanced-TOVS satellites (Tilley et.al., 2000) are shown in the 2 panels of Figure 1. The two panels of Figures 2 show corresponding vertical accuracy statistics per satellite for the 30N to 30S land regions, respectfully. As can be seen the accuracy curves show significant differences particularly for bias, but these are much more indicative of systematic uncertainties due to sampling inconsistencies than actual satellite dependent product structures.

A projection of the problem in "radiance" space is illustrated in the two panels of Figure 3, which show examples of RT bias adjustments derived for the AMSU-B channel 3 (183 +/-1 GHz) from NOAA-16 (top), and NOAA-15 (bottom). It can be seen that although correlated, there are satellite dependent differences in the magnitudes of the adjustments, in some cases exceeding 5K. Since the samples of data used to compute "bias-adjustment" coefficients are the collocation data-sets as shown in Figures 5, it is uncertain whether the differences per satellite are indicative of actual radiometer sensitivity or sampling difference. These are discussed further in Section 2.4.

Figures 4 shows collocations for N-16 using a 1-hour time window. As can be seen the coverage and sample size is certainly too small and isolated to be meaningful for purposes as shown in Figures 2 and 3. Sampling characteristics of collocations within 1 hour of NOAA-15 (as well as NOAA-17) reveal similar problems, along with their being mutually exclusive per satellite.

The resolution of global sampling problems described in Figures 1 through 4 would have positive impacts for not just satellite products, but all scientific areas as addressed in the following sections.

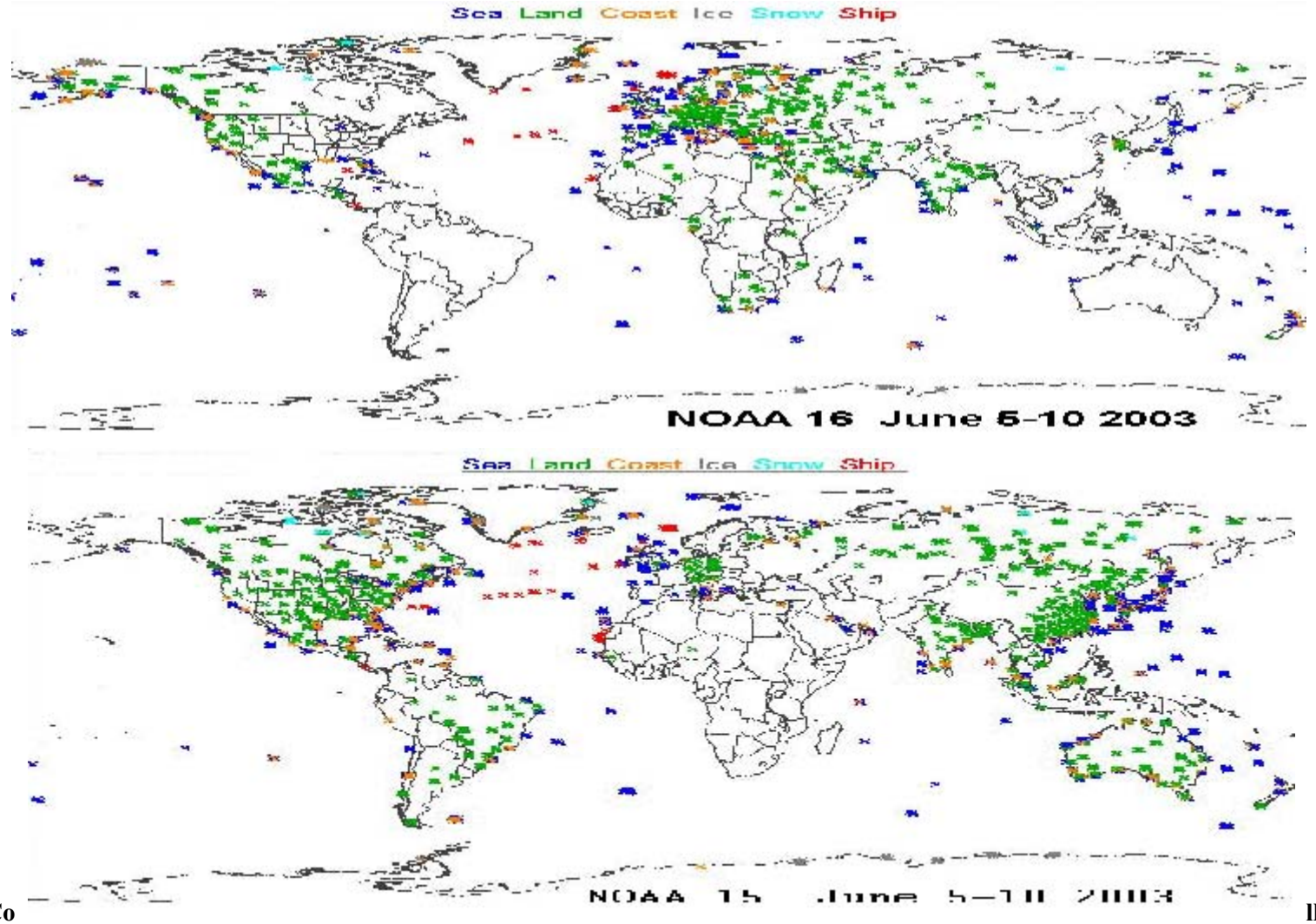

Figure 1: Co llocated radiosonde and satellite observation samples compiled by NESDIS for NOAA-16 (upper) and NOAA-15 (lower) using 3-hour (land) and 5-hour (sea) time windows.; Sea, Land, Coast, Ice, Snow and Ship.

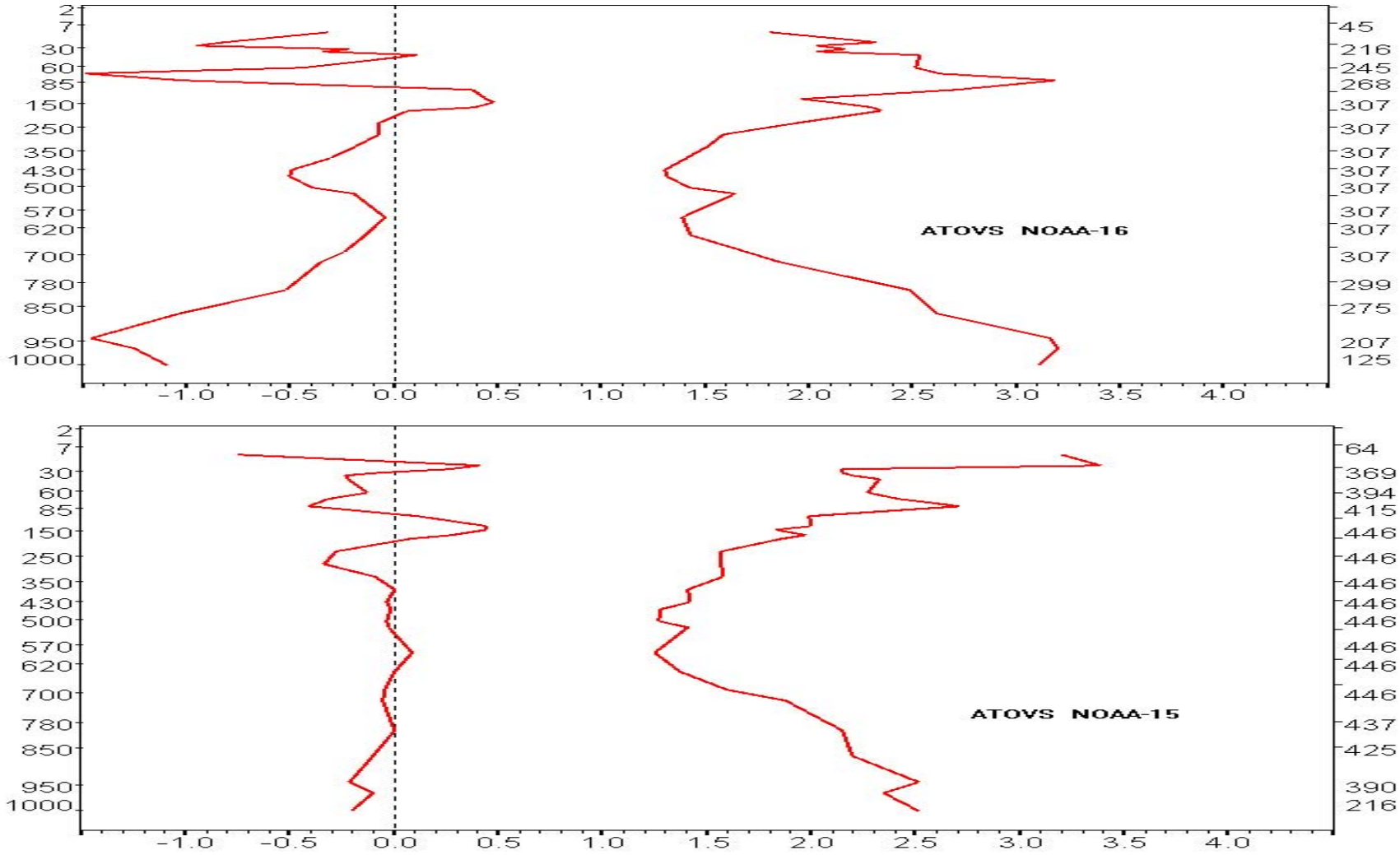

Figure 2: **Vertical accuracy statistics of mean (left) and standard deviation (right) satellite minus radiosonde differences for NOAA-16 (top) and NOAA-15 (bottom) using samples corresponding to Figure 5.**

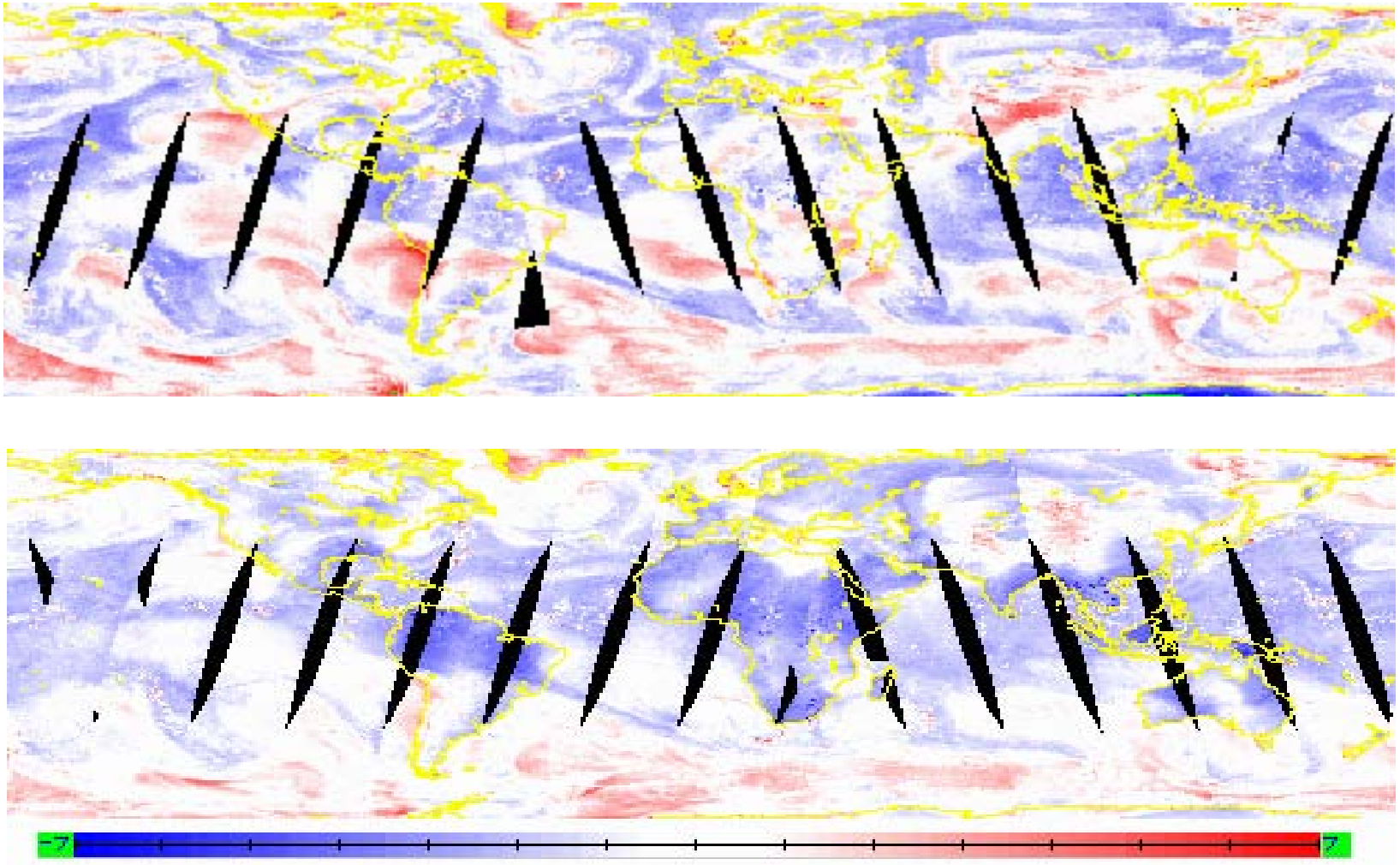

Figure 3: **RT bias adjustments for NOAA-16 (top) and NOAA-15 (bottom) for AMSU-B Channel-1 (183 +/- 1 GHz) on October 13, 2003.**

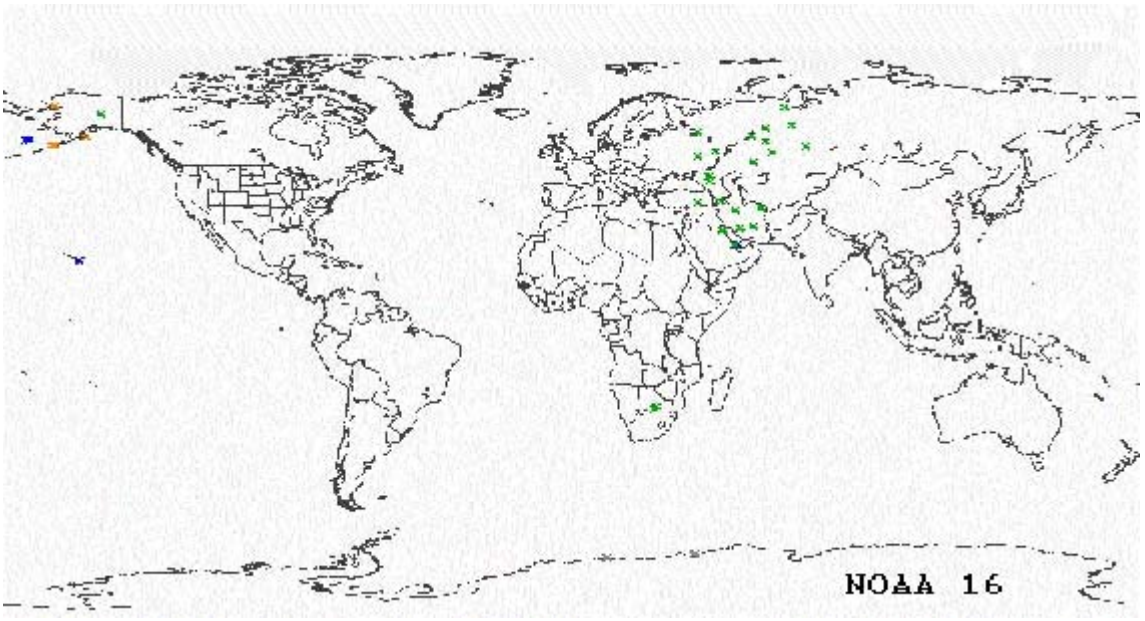

Figure 4: **Collocated radiosonde and satellite Observations for NOAA-16 using a minus 1 hour time window; Sea, Land, Coast, Ice, Snow and Ship.**

Climate

The problems of detecting global climate change from operational satellites and radiosonde observations has been addressed by a number of researchers with often conflicting results or a conclusion that the data available are not suitable for detecting the extremely small climate signals. Examples can be found, for example, of several attempts to use the 20+ years of historical TOVS-MSU data and radiosondes to detect climate changes with several publications citing results with little overlap. The bottom line is that recent constructions of a number of tropospheric temperature climate data-sets has nominally served only to increase our uncertainty in the true multi-decadal trends (Seidel et.al., 2004).

Examples of these kinds of problems are illustrated in the two panels of Figure 5 using the relatively short term data set of AMSU-B measurements from NOAA-15. The top panel shows AMSU-B, 183 +/-1 GHz measurements and associated RT bias adjustments for NOAA-15 from September 2000. Comparing the lower panels of Figure 5 and Figure 3 indicates an apparent drift in this channel, however, it is uncertain whether this drift is real or a manifestation of sampling differences and/or radiosonde instrument changes over that time.

A potentially significant portion of such uncertainty could disappear in the presence of a sufficiently robust and consistent transfer standards, most critical for example for free-troposphere variables such as those observed by the radiosondes and satellites. Any transfer standard would optimally need to be a two-point calibration system. For one of the points, the potential of using SUAN sites is quite high, and perhaps sufficient under ideal circumstances. As needed, a second calibration point could be derived from a future middle earth orbit (MEO) satellite (operating between polar orbiting and geostationary altitudes) as a transfer standards for polar orbiting retrievals and synoptic radiosondes.

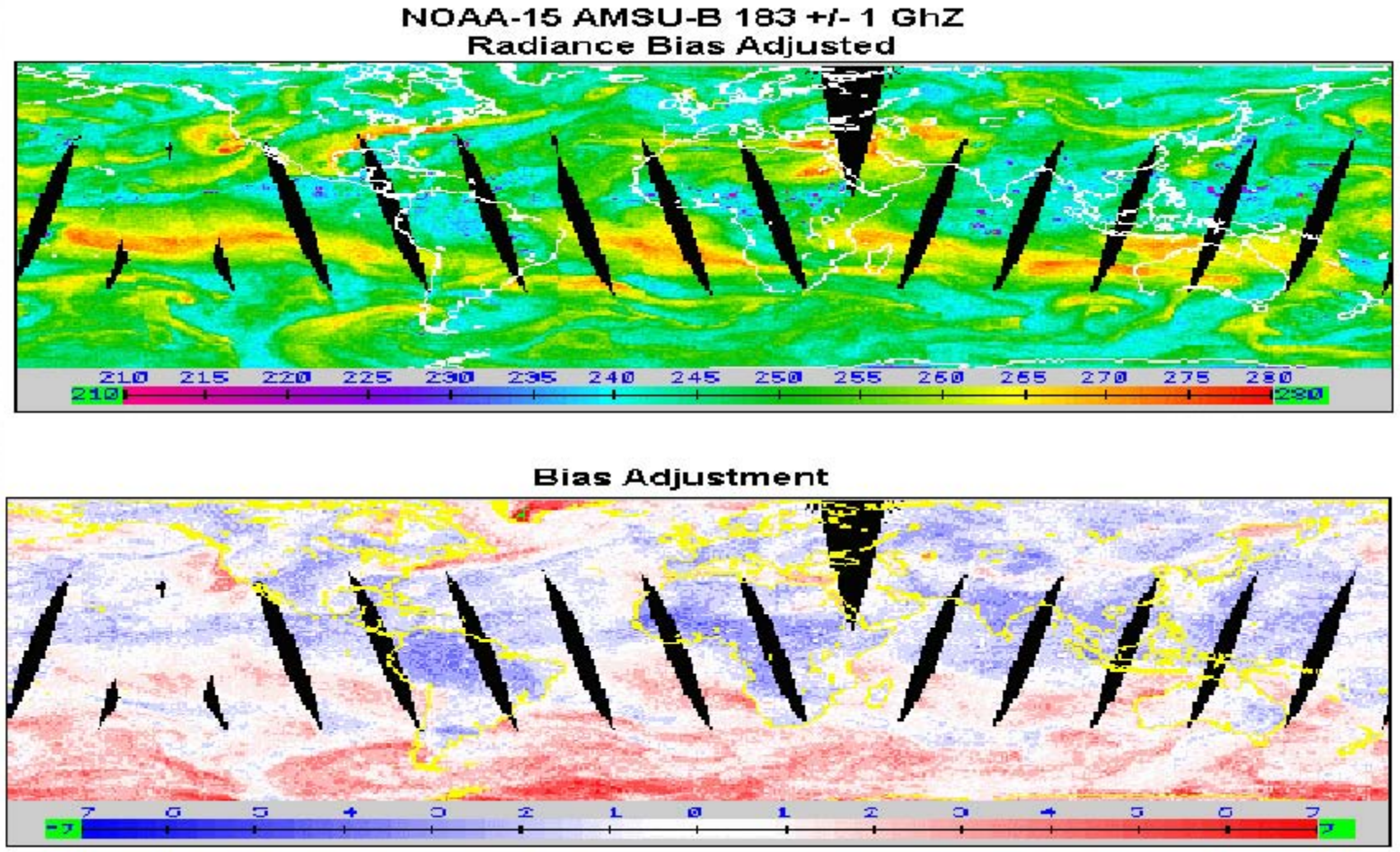

Figure 5: **AMSU-B measurements (upper) and associated RT bias adjustments (lower) for NOAA-15 from September, 2000.**

Numerical Weather Prediction (NWP)

Scientist from the NWP community have cautiously supported the potential for positive impacts using SUAN, recognizing that the radiosondes are very important to the effective use of satellite sounding data in NWP and that a well-distributed network of radiosonde stations providing high quality data coincident with satellite overpass could play a valuable role in improving these processes and ultimately the impact of satellite data on NWP. Under ideal circumstances, SUAN could provide a data platform to segregate the residual NWP error from the RT bias. However, this could also resurrect the difficult background error problem for NWP, which became somewhat more manageable when using the NWP to compute the observational data adjustments (McNally et.al., 2000). It becomes a (nasty) question of tradeoffs and whether it would be worth the effort?

Figures 6 provides some insights through analysis of derived satellite (SAT) sounding (tuned using radiosondes) minus NWP ("cooked" as described above) forecast fields. The two upper right panels of each Figure illustrate such differences for 500mb to 300mb (upper) and 1000 to 700mb (middle) layer mean virtual temperatures (T*), respectively. A red, white and blue color scale is used to denote differences, with red indicating that the satellite (SAT) was warmer; white indicating that differences were between +/- 1K, and blue indicating that the satellite was colder. To the left of each panel are the corresponding AMSU-A channels 6 and 4, shown in spectral color scales, which have sensitivity in these layers. The bottom two panels of Figure 10 show corresponding AVHRR channel 4 measurements denoting clouds, and NWP 12-hour forecast minus verifying Analysis differences scaled identical to the SAT-NWP differences. The region shown is a large portion of the remote (and data devoid) Pacific Ocean off the northwest US coast on January 15, 2004.

Figure 6 demonstrates that differences between the SAT and NWP data serve as good tracers of frontal zones, precisely where NWP is most prone to error. Outside these zones, for example in the warm and cold core sectors, differences tend to zero. It can also be seen that the signature of the differences in the lower layer tend to be correlated with the advection, with the satellite soundings typically colder in cold advection zones and warmer in warm advection zones. The relationship in the upper layer shows more of a tendency for the satellite data to be colder than the NWP when differences occur. Together, these suggest a more destabilizing pattern for the satellite soundings in the warm air and a more stabilizing pattern in the cold air relative to the NWP, in each case a more dynamic pattern. The bottom right panel shows that the initializing 12-hr NWP forecast and verifying Analysis agree quite closely, with little or no impact from the assimilated satellite data in the frontal regions, where one would expect to see changes.

Radiative Transfer (RT) Models

RT models represent a scientific area shared among satellite, climate, NWP, and radiosonde data platforms, and is the critical process for achieving absolute accuracy. Unfortunately, combined/unresolved errors in the satellite, meteorological and/or RT model itself makes absolute validation nearly impossible; catch-22. However, a carefully designed SUAN data-set which minimizes unresolved errors in the collocated spectral and meteorological (radiosonde) data would provide the robust and reliable information for validating RT models, the key for ascertaining and maintaining the "absolute" accuracy of the operational satellite and radiosonde data.

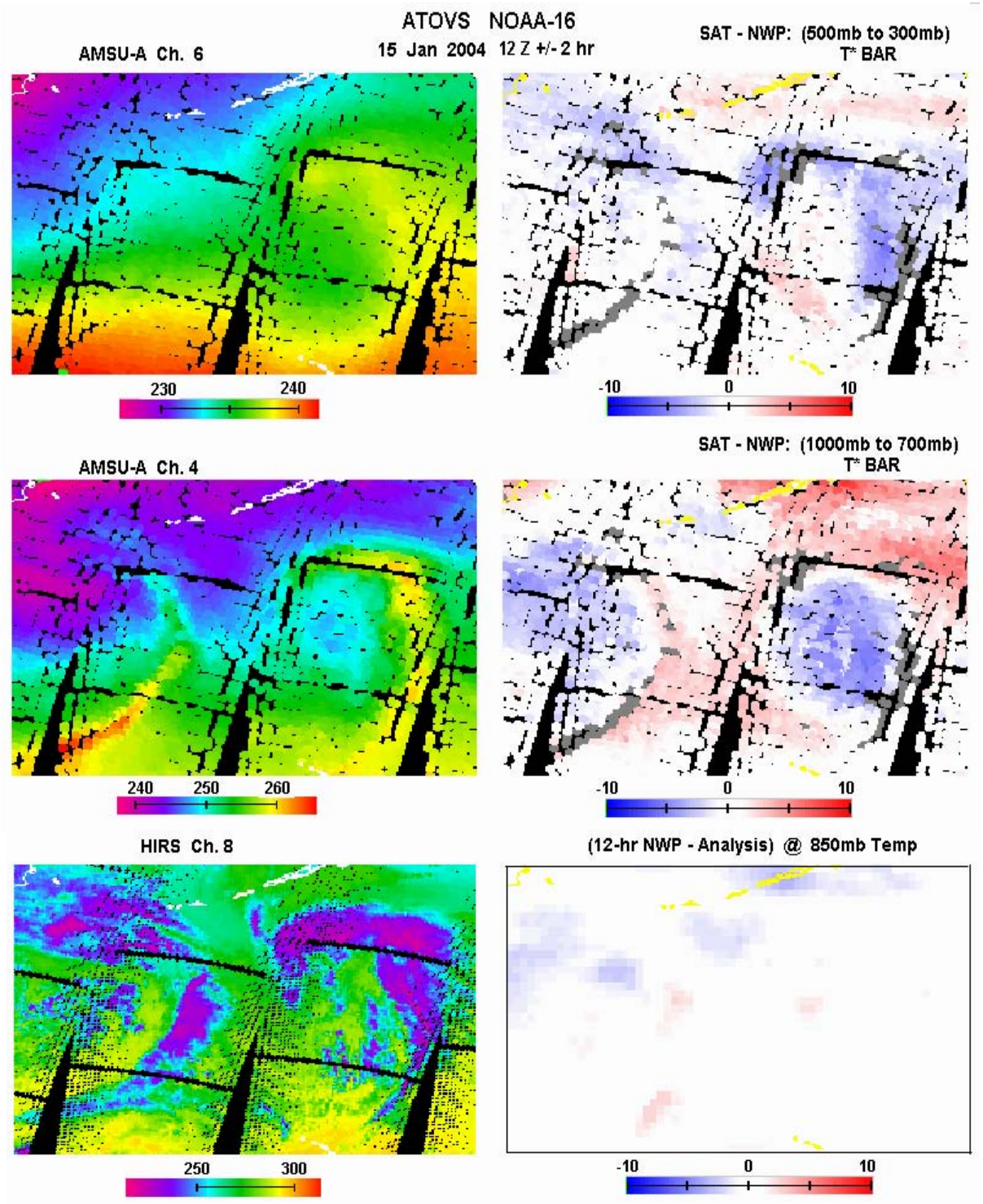

Figure 6: **NOAA-16 (SAT) minus NWP difference fields for 500mb to 300mb and 1000mb to 700mb layer mean temperatures (T*), associated AMSU-A Channel 4 and 6 measurements, HIRS Channel 8 measurements (Clouds), and 12-hr NWP minus verifying Analysis differences**

SUAN would provide a great data-set in support of RT development and validation exercises supporting the continued evolution of satellite and radiosonde instruments. SUAN would be useful to resolve problems as shown in Figure 3, in which the spectral adjustments (for the AMSU-B 183+/- 1 GHz data sensitive to upper level moisture) are far greater than one would expect given the expected accuracy of these measurements. SUAN would also support associated surface and atmospheric emissivity algorithms and the generation of global atlas data (ie, for surface temperature and emissivity) of the earth from polar satellites.

Future Advanced Sounders

Having a SUAN in place several years prior to next generation satellites (NPOESS), would represent an enormous advantage to future users of these data. SUAN sites would provide attractive locations in support of ongoing CALVAL activities currently underway in support of the next generation advanced instruments (ie, EOS/ AQUA) and would ultimately accelerate their operational deployment, as well as insuring the continuation of ongoing records, for example the AMTS with AMSU-A and MSU (Aumann et.al., 2003).

The WG on Advanced Sounders of the **ITSC-13** has documented the need for high quality global in-situ measurements concurrent with next generation sounder data, and support the Satellite Upper Air Network (SUAN) initiative as a mechanism for achieving this.

Radiosonde Monitoring

The problem of global radiosonde measurement errors is an underlying problem across the satellite, climate, NWP and RT model landscapes since they are often used directly or indirectly for scientific tuning/cooking and/or validation. Such errors typically occur as either systematic, for example, due to a specific radiosonde type or correction procedure, or in a less predictable random manner due to the need for better measurement technologies. A component of this problem can also be traced to bookkeeping type errors, for example, uncertainties concerning the radiosonde types flown, launching protocols, corrections applied and other deficiencies concerning available meta-data records from long-term archive centers.

The deployment of SUAN would provide a manageable program for monitoring radiosondes, not only SUAN radiosondes but also the greater radiosonde network, as well as providing a very good network for radiosonde instrument testing, new technology research and development. For example, SUAN sites located in the vicinity of existing synoptic sites would offer ample opportunities for a variety of studies ranging from straightforward inter-comparisons of the radiosonde measurements to the modeling of localized effects such as frontal passage, local weather features, terrain, and balloon drift. Appropriately planned multi-instrument launches at satellite overpass would provide useful information for testing radiosonde instrument bias, and attractive locations for long-term studies of instrument performance, data corrections, new technologies (ie, drift-sondes) and integrated ground based spectral measurements. Finally, and perhaps most important, deploying SUAN could ultimately provide information for determining absolute radiosonde accuracies by using the satellite observations as a transfer standard for radiosonde corrections (McMillin et.al., 1988).

THE SUAN NETWORK

Candidate Sites

The current candidate stations for SUAN consist of the 43 radiosonde sites illustrated in Figures 7. The stations were selected so as not to interfere with ongoing, long-term climate records. Climate record scores (provided by Dr Peter Thorne) rank each site according to its' contribution to the long-term Climate record. A score or 1 or 0 indicates that the site has no climate record, a score of 2 or 3 indicate an insignificant climate record, and a score of 4 or more indicates a potentially significant climate record; the maximum possible score for a site is 11.

Figure 7 shows the global distribution of the 43 candidate SUAN sites color coded:

- Green are sites with no climate record and acceptable radiosonde type (24)
- Yellow are sites with little or no climate record and acceptable radiosonde type (11),
- Red are sites with a climate record and acceptable radiosonde type (4), and
- Blue are sites with little or no climate record but unacceptable radiosonde type (4).

Other factors considered in the establishment of the candidate network included the radiosonde instrument type, global distribution, and a desire to avoid sites at coastal and high terrain locations, for example, no site exceeds 456m. There are a total of 20 Land, 20 Sea, and 3 Sea-Ice locations.

Global Robust Network: How Much is Enough?

The premise is that if each station would provide at least one launch per day, and that this would be enough to adequately monitor a two satellite operational configuration. An obvious question is whether these target numbers are enough? The answer to a large extent depends on the quality of the "standardized" measurements. Assuming good quality, then a simplified look at the number of observations from the proposed SUAN network can provide some insight. If each of the 43 stations provide one launch per day, and assuming a two-polar satellite configuration, then a 4-day cycle of observations per site that coincident with each satellite and orbital node would occur (two satellites times two orbital nodes). Over the course of one month (30 days), this would provide approximately fifteen collocations per satellite and site, equally distributed among the ascending and descending orbital nodes. Globally, this would provide over 600 observations per month per satellite (equally divided among the ascending and descending nodes), and over 7000 satellite dependent observations per year. This would appear to be enough.

Endorsements

The following are summary listings lists of endorsements:

- Workshop to Improve Usefulness of Operational Radiosondes (Durre et.al., 2003)
- ITSC-13, with specific endorsements from following WG:
  - Satellite Sounder Science and Products
  - TOVS/ATOVS Data in Climate
  - Advanced Sounders
  - International Affairs

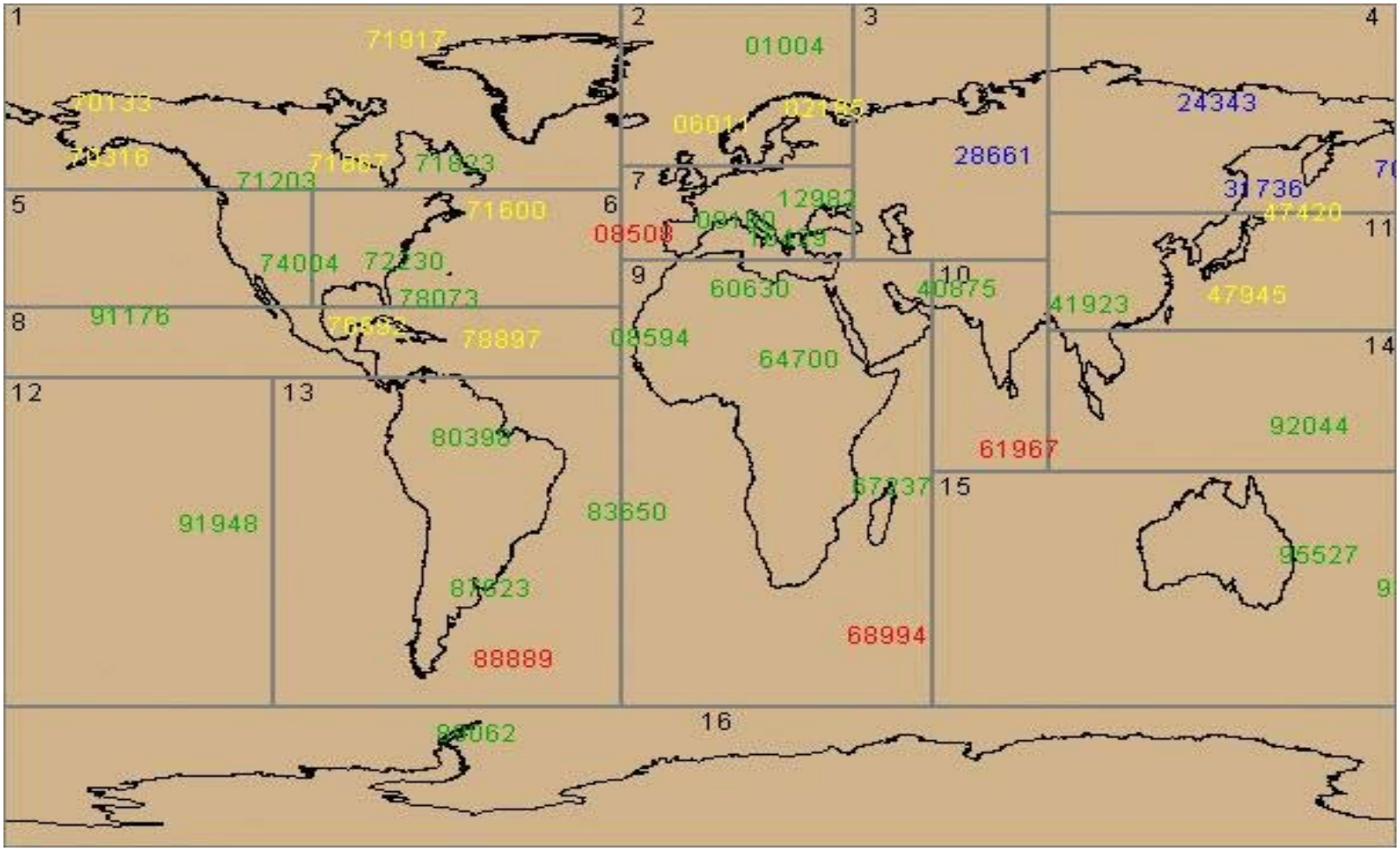

Acceptable Raob Types: *Mesei RS2-91* *VIZ MARK II and B2;* *Vaisala RS80/90*

Figure 7: **Candidate SUAN sites listed according to their geographic Box location (1 thru 16) and color coded: *Green* are sites with no climate record, *Yellow* are sites with little or no climate record, *Red* are sites with a significant climate record, and *Blue* are sites with an un-acceptable radiosonde type.**

Additional support for SUAN can be found in recommendations specified in

- *The White Paper on Climate Data Records from NOAA Operational Satellites* (Goldberg and Bates, 2003), and
- *NOAA Council on Long-term Climate Modeling* (January, 2003).

WMO Report

The World Meteorological Organization (WMO) must play a pivotal role in the deployment of SUAN. A report to the WMO describing SUAN, and associated resources, protocols and perceived benefits to users and researchers of global environmental data is planned by early 2004.

REFERENCES

Aumann, Hartmut H., Moustafa T. Chahine, Catherine Gautier, Mitchell D. Goldberg, Eugenia Kalnay, Larry M. McMillin, Hank Revercomb, Philip W. Rosenkranz, William L. Smith, David H. Staelin, L. Larrabee Strow, and Joel Susskind, 2003: AIRS/AMSU/HSB on the AQUA mission: design, science objectives, data products, and processing systems. *IEEE Transactions on Geoscience and Remote Sensing*, Vol. 41, #2, p 253-441.

Durre, Imke, T. Reale, D. Carlson, J. Christy, M. Uddstrom, M. Gelman and P. Thorne, 2003: Report from the workshop to improve the usefulness of operational radiosonde data. *Bull. Amer. Meteor. Soc.*, submitted for publication.

Goldberg, M, and J. Bates, 2003: Creating climate data records from NOAA operational satellites. *White Paper*, NOAA/ NESDIS, Washington DC, August, 53 pp.

McMillin, L.M., M.E. Gelman, A. Sanyal and M. Sylva, 1988: A method for the use of satellite retrievals as a transfer standard to determine systematic radiosonde errors. *Mon. Wea. Rev.*, 116,1091-1102.

McNally, A.P., J.C. Derber, W.S. Wu, and B.B. Katz, 2000: The use of TOVS level-1B radiances in the NCEP SSI analysis system. *Q.J.R. Meteorol Soc.*, Vol 126, pp. 689-724.

Reale, A.L., 2002: NOAA operational sounding products for advanced-TOVS: 2002. *NOAA Technical Report NESDIS 107*, U.S. Dept. of Commerce, Washington D.C., 29 pp.

Tilley, F.H., M.E. Pettey, M.P. Ferguson, and A.L. Reale, 2000: Use of radiosondes in NESDIS advanced-TOVS (ATOVS) sounding products. *10th Conference on Satellite Meteorology and Oceanography*, 9-14 January, Long Beach, CA.

Seidel, D.J., J.K. Angell, J. Christy, M. Free, S.A. Klein, J.R. Lanzante, C. Mears, D. Parker, M. Schabel, R. Spencer, A. Sterin, P. Thorne, and F.Wentz, 2004: Uncertainty in signals of large-scale climate variations in radiosonde and satellite upper-air temperature data sets. *J. Climate*, 17, in press.

GeoSTAR - A New Approach for a Geostationary Microwave Sounder

Bjorn Lambrigtsen
Jet Propulsion Laboratory
4800 Oak Grove Drive
Pasadena, CA 91109, USA

Abstract

The Geostationary Synthetic Thinned Aperture Radiometer (GeoSTAR) is a microwave atmospheric sounder, with capabilities similar to those of the AMSU-A/B system, and is intended for deployment in geostationary orbit – where it will complement future infrared sounders to enable all-weather temperature and humidity soundings. It also has the capability of mapping rain rates, and it can be deployed in medium earth orbits as well. GeoSTAR is based on spatial-interferometric principles and uses a stationary array of a large number of individual receivers to synthesize a large aperture and achieve the required spatial resolution, an approach that has significant advantages over conventional real-aperture systems – such as full-disk scanning with no moving parts. GeoSTAR will implement the same tropospheric sounding channels as AMSU-A (temperature) and AMSU-B (humidity) and will achieve an initial spatial resolution of 25-50 km. Future versions will have significantly higher spatial resolution. The required technology is currently being developed at the Jet Propulsion Laboratory and other collaborating organizations, under NASA's Instrument Incubator Program, and a ground based demo system will be ready in 2005.

Introduction

The National Oceanic and Atmospheric Administration (NOAA) has for many years operated two weather satellite systems, the Polar-orbiting Operational Environmental Satellite system (POES), using low-earth orbiting (LEO) satellites, and the Geostationary Operational Environmental Satellite system (GOES), using geostationary earth orbiting (GEO) satellites. Similar systems are also operated by other nations. The POES satellites have been equipped with both infrared (IR) and microwave (MW) atmospheric sounders, which together make it possible to determine the vertical distribution of temperature and humidity in the troposphere even under cloudy conditions. Such satellite observations have had a significant impact on weather forecasting accuracy, especially in regions where in situ observations are sparse, such as in the southern oceans. In contrast, the GOES satellites have only been equipped with IR sounders, since it has not been feasible to build the large aperture system required to achieve sufficient spatial resolution for a MW sounder in GEO. As a result, and since clouds are almost completely opaque at infrared wavelengths, GOES soundings can only be obtained in cloud free areas and in the less important upper atmosphere, above the cloud tops. This has hindered the effective use of GOES data in numerical weather prediction. Full sounding capabilities with the GOES system are highly desirable because of the advantageous spatial and temporal coverage that is possible from GEO. While POES satellites provide coverage in relatively narrow swaths, and with a revisit time of 12-24 hours or more, GOES satellites can provide continuous hemispheric or regional coverage, making it possible to monitor highly dynamic phenomena such as hurricanes. Such observations are also important for climate and atmospheric process studies.

In response to a 2002 NASA Research Announcement calling for proposals to develop technology to enable new observational capabilities from geostationary orbits, the Geostationary Synthetic Thinned Aperture Radiometer (GeoSTAR) was proposed as a solution to the GOES microwave sounder problem. GeoSTAR synthesizes a large aperture to measure the atmospheric

parameters at MW frequencies with high spatial resolution from GEO without requiring the very large and massive dish antenna of a real-aperture system – a major advantage of this approach. There are a number of other advantages as well. Sponsored by the NASA Instrument Incubator Program, an effort is currently under way at the Jet Propulsion Laboratory to develop the required technology and demonstrate the feasibility of the synthetic aperture approach – in the form of a small ground based prototype. When this risk reduction effort is completed in 2005, a space based GeoSTAR program can be initiated, which will for the first time provide microwave temperature and water vapor soundings as well as rain mapping from GEO, with the same measurement accuracy and spatial resolution as is now available from LEO – i.e. 50 km or better for temperature and 25 km or better for water vapor and rain.

Physical Basis for Measurements

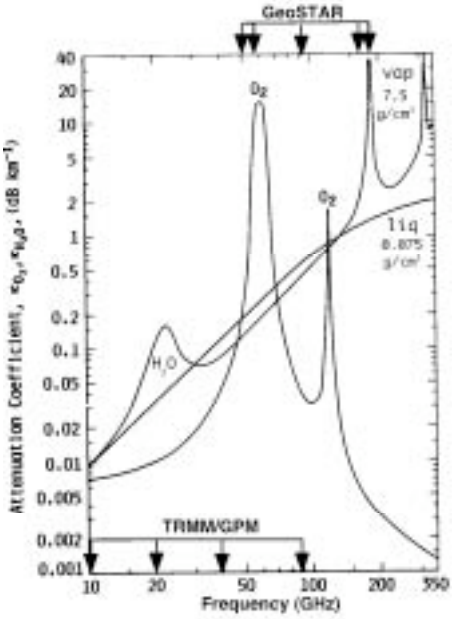

Fig. 1. Microwave atmospheric absorption spectra

GeoSTAR is an atmospheric sounder with rain mapping capabilities. It operates primarily in two millimeter-wave bands. For tropospheric temperature sounding it will have a small number of channels near 50 GHz. For water vapor sounding it will use a set of 183-GHz channels, which are also used for rain mapping, as well as an intermediate "window" channel near 90 GHz. The atmospheric absorption spectra and the GeoSTAR channels are illustrated in Fig. 1, where the spectral channels of GeoSTAR are marked at the top of the figure. GeoSTAR will utilize the same approach as is used with the Advanced Microwave Sounding Unit (AMSU-A/B) system currently operated by NOAA as part of its POES weather satellites as well as by NASA for its Aqua research satellite, an approach that is now well established. These measurements will provide information to 'cloud clear' the observations from the GEO IR sounders, just as is currently being done in the LEO sounding systems. The cloud-cleared radiances are either directly assimilated into a weather forecasting system or are used to retrieve atmospheric profiles. This is done everywhere, not just in clear areas.

To enable full IR-based soundings under cloudy conditions, the ability to provide microwave soundings all the way to the surface, at incidence angles up to 60°, is critical. For temperature sounding, which uses oxygen absorption features, this necessitates using the 50-60 GHz oxygen band and precludes the use of the oxygen line at 118 GHz. The latter would have the highly desirable advantage of permitting a much smaller aperture for a given spatial resolution, but as Fig. 2 (Grody 1993) shows, the atmosphere is often so opaque, due to water vapor and clouds, as to make such a sounder useless under many common weather conditions. For example, the 118-GHz transmittance in a tropical cloudy atmosphere and at high incidence angles is so low that the crucial planetary boundary layer (i.e. the lowest 2 km) will be invisible.

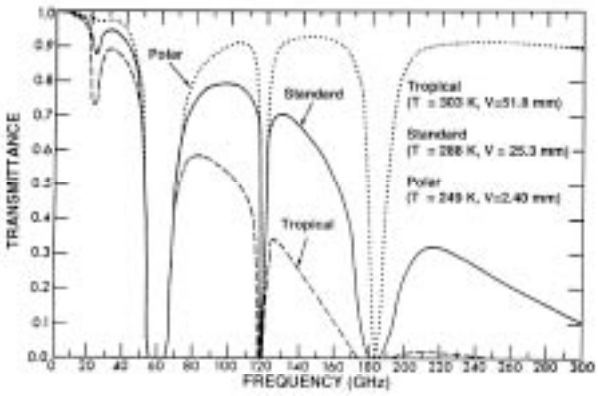

Fig. 2. Atmospheric transmittance

GeoSTAR will also use the 183-GHz water vapor sounding channels for precipitation measurements. While the approach used with LEO rain radiometers, such as the currently operating Tropical Rain Mapping Mission (TRMM) and the planned Global Precipitation

Mission (GPM), is primarily based on measuring the absorption effects of rain at lower frequencies, between 10 and 37 GHz (marked on Fig. 1), the GeoSTAR approach is primarily based on measuring the scattering effects associated with precipitation. The greatest advantage of the high frequency GeoSTAR approach is that high spatial resolution is easily achieved. This is because the antenna size required to achieve a certain spatial resolution is inversely proportional to the frequency. For a given spatial resolution, the aperture of a 200-GHz radiometer is 20 times smaller than that of a 10-GHz radiometer. That is what makes it feasible to deploy GeoSTAR as a rain mapper in GEO, where the great advantage of continuous spatio-temporal coverage is also realized. Because of size and weight and torque effects, it is very difficult and high-risk to implement the conventional scanning antenna approach in GEO. GeoSTAR for the first time makes it feasible to directly measure rain from GEO.

The GeoSTAR scattering approach derives from observations made in recent years with 183-GHz radiometers operated on high altitude aircraft. When passing over rain cells, a pronounced apparent cooling due to scattering is observed. This cooling can exceed 100 K over intense convective cells, a very large signal that can be used to detect and track hurricanes and other severe storms without the need for high radiometric sensitivity (i.e. dwell time). Since these radiometers are sounders, they have channels with a varying degree of opacity (so that they can sound different depths of the atmosphere). Some are so opaque that the surface is normally invisible. When rain is observed through an opaque channel, the scattering, which dominates over absorption at these frequencies, causes a severe apparent cooling over a background that represents the underlying atmospheric state (i.e. its temperature, water vapor, and cloud liquid water). This background is easily measured with a sounder. A new method has recently been developed by Staelin and Chen (2000) to retrieve rain rates from such high frequency observations and is now used with the NASA Aqua satellite launched in 2002. It is expected that the retrieval accuracy will be substantially improved during the Aqua mission.

Instrument Concept

GeoSTAR uses a two-dimensional sparse array of receiving elements to synthesize a large aperture. The array is rigid and stationary, and is rigidly attached to the spacecraft. The array is pointed toward the Earth and has a constant full view of the visible Earth disk. This yields continuous high spatial resolution and wide coverage. GeoSTAR is a 2-D spatial interferometric system, which measures the complex cross-correlations between the output signals of all pairs that can be formed from a large number of millimeter wave radiometers arrayed in a "Y" shaped configuration[1], as shown in Fig. 3. The symmetric Y configuration results in a symmetric hexagonal sampling grid in UV-space (i.e. in the receiver plane, measured in wavelength units), also shown in Fig. 3. The smallest pair spacing (called a baseline), i.e. the spacing between neighboring receiving elements, determines the overall field of regard. For GEO, where the required field of regard is about 17.5° - the size of the Earth disk as seen from GEO, the receiver spacing is therefore approximately 3.5 wavelengths (about 2 cm at 50 GHz and about 6 mm at 183 GHz). The longest baseline determines the smallest spatial scale that can be resolved. To achieve a 50 km spatial resolution at 50 GHz, an aperture diameter in excess of 4 meters is required. That corresponds to approximately 100 receiving elements per array arm, or a total of about 300 elements. This in turn results in 45,000 unique baselines and 90,000 uv sampling points.

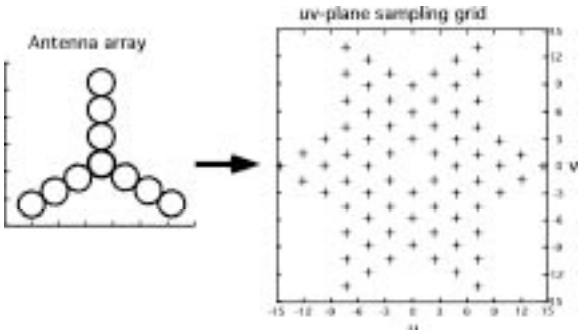

Fig. 3. Antenna array and UV samples

An innovative calibration system is used to

[1] Other configurations are also possible, such as a square, a U-shape, a T-shape or a circle

constantly monitor the phase relationships between the array elements. That eliminates the need for precise control of the alignment between the antenna elements. This is what makes the aperture synthesis approach superior to the real aperture approach – no ultra precise surface accuracy, alignment or mechanical scanning are required. Phase knowledge takes the place of mechanical control, and the field of view is inherently matched to the Earth.

The measurements are divided into relatively brief measurement cycles of a few tens of seconds in duration. During each cycle the cross-correlations are accumulated simultaneously at each uv-grid point. Interleaved with these are calibration measurements of phase and offset. At the end of each measurement cycle, all observations from that cycle are summed and saved for later transmission to the ground, along with engineering data. In the meantime, the next measurement cycle gets under way. The radiometers are sequentially tuned to different frequencies to measure the separate channels across the frequency band. The measurements are called visibilities and represent samples at the uv-grid points of the so-called visibility function.

The measurement cycle described above is relatively brief (~20 seconds) to make it possible to compensate for possible instrument phase changes, which could be caused by thermal strains in the receiver array as well as system pointing changes and other effects. The first processing task on the ground is therefore to apply phase calibration measurements and other equivalent information to the visibilities formed in the measurement cycle. The objective is to produce a set of adjusted visibility images that are aligned in terms of phase. They can then be co-added to form a single visibility image for each channel, which represents the much longer time span needed to achieve the required radiometric accuracy – typically, on the order of 5-15 minutes for each spectral channel. These visibility images have much lower noise than the individual measurement-cycle images.

Once the visibility image has been determined, the interferometric equation

$$V_{ij} = \iint \frac{T_B(\xi,\eta)}{\sqrt{1-\xi^2-\eta^2}} F_i(\xi,\eta) F_j^*(\xi,\eta) \tilde{r}_{ij}\left(\tau - \frac{u_{ij}\xi + v_{ij}\eta}{f_0}\right) e^{-i2\pi(u_{ij}\xi + v_{ij}\eta)} d\xi d\eta$$

is inverted to form the radiometric field T_B. Here V_{ij} is the visibility (i.e. the complex cross-correlation) measured between receivers i and j (i.e. at uv location u_{ij}, v_{ij}), f_0 is the center frequency, $F_i(\xi,\eta)$ is the normalized antenna pattern for receiver i, ξ and η are the direction cosines to the radiometric source field, and

$$\tilde{r}_{ij}(t) = e^{-i2\pi f_0 t} \int_0^{\cdot} H_i(f) H_j^*(f) e^{i2\pi f t} df$$

is the so-called fringe wash function. $H_i(f)$ is the normalized frequency response of receiver i. For the GeoSTAR prototype, various methods to invert the visibility equation will be explored, including the so-called G-matrix method and an iterative method called the CLEAN technique. The latter is used in interferometric radio astronomy, but the technique has been modified for extended source fields. A major element of this technique is a Fourier transform, and an FFT procedure adapted for hexagonal grids by Camps et al. (1997) will be used. To reduce grid-cell sidelobes, it may also be necessary to incorporate a spatial sampling window - a so-called taper - into the inversion process. A number of different taper functions will be examined as part of the prototyping effort. During routine operation, the inversion process will also be tuned by using "ground truth" data.

Calibration Approach

Unlike for conventional radiometers, where radiometric calibration is the most important, for interferometric radiometers it is phase calibration that is most important. The image synthesis process requires accurate knowledge of the interferometric fringes associated with each visibility measurement. Such calibration data will be established and validated through pre-flight measure-

ments, multiple on-board (internal) calibration circuits, and external references available from GEO.

The pre-flight measurements will include

- receiver frequency response
- elemental antenna patterns
- antenna element mutual coupling
- antenna range measurements of the interferometer as a system

These measurements are used to validate models of the system's spatial response, which form the basis for image synthesis.

The on-board calibration subsystem will be used to stabilize the system response so that pre-flight measurements and models can be transferred to orbit. These circuits include a correlated noise source, which is distributed from a central source and injected behind each antenna in an array "arm" with equal phase to provide an accurate amplitude and phase reference. The phase between each arm can be controlled separately, which makes it possible to rotate the calibration measurements in phase space. Independent noise sources in each receiver front-end will be used to measure null-offsets in the correlators.

It will also be possible to use external calibration sources to validate the calibration on-orbit. These fall into four categories:

- ground beacon
- the Earth's limb
- radiometric references
- the Sun

The ground beacon is a noise source that periodically transmits a brief noise signal in a narrow beam. Since the location of the transmitter is known, this allows absolute phase calibration. The Earth limb also acts as an absolute reference, since the space background temperature of 2.7 K is known. Other radiometric references will be available from time to time from other simultaneous radiometric remote sensing observations from LEO orbiters and aircraft. These can be used to provide absolute radiometric calibration of GeoSTAR. Finally, when the Sun transits near the Earth, it will be aliased into the field of view in a fully predictable manner. That will be used to provide an additional phase calibration.

Two self-consistency techniques will also be applied to the calibration. The first, closure, traces errors in the visibility plane to the amplitude and phase response of each receiver through a network analysis approach. This method makes it possible to extend a partial calibration to the entire uv-plane. The second method, self-calibration, developed by the radio astronomy community – where no absolute calibration references are available, consists of starting with a trial image and then solving for all unknown system parameters until the reconstructed image converges.

The uv-plane sampling grid illustrated in Fig. 3 lacks a sampling point at the origin, the so-called zero-baseline. This point corresponds to the constant in a Fourier expansion and represents the spatial mean value of the brightness temperature field that is being observed. A single, separate receiver is dedicated to provide that measurement, since it cannot be provided by a correlation system. This receiver is operated as a conventional Dicke switched radiometer and is otherwise identical to the array receivers. All receivers, including the zero-baseline one, have the same field of view to encompass the entire Earth disk – about 17.5° from GEO. The zero-baseline receiver therefore measures the average brightness temperature of the Earth disk, as required.

Coincident AMSU observations from underpassing POES satellites will give additional absolute radiometric reference points, since the GeoSTAR channel frequencies will be identical to those used for AMSU.

Prototyping Effort

An effort, funded by NASA, is currently under way at the Jet Propulsion Laboratory to develop a small ground based prototype unit. This is being done jointly with collaborators at the NASA Goddard Space Flight Center and the University of Michigan. The objectives are to reduce technology risk for future space implementations as well as to demonstrate the measurement concept, test performance, evaluate the calibration approach, and assess measurement accuracy. The prototype will be used for laboratory and antenna range measurements. A limited set of field observations will also be made to demonstrate the ability to derive geophysical parameters with commonly used retrieval algorithms.

To minimize cost and time to completion, the prototype consists of a small array of 24 elements operating with 4 channels between 50 and 54 GHz. This makes it feasible to address the most important and difficult system issues relevant to an operational 2-D system and to use mature MMIC receiver technology and components. The physical configuration will be a Y shape, with 8 elements in an arm with about 3.5-wavelength element spacing (2.0 cm) as required for a GEO system. The system will incorporate similar calibration and LO subsystems and distribution schemes as the operational instrument. The prototype correlator is being developed at the University of Michigan based on current related work with other synthetic aperture systems. A standard personal computer (PC) will be used for the data collection and instrument control. A sketch of the system is shown in Fig. 4 and a block diagram is shown in Fig. 5.

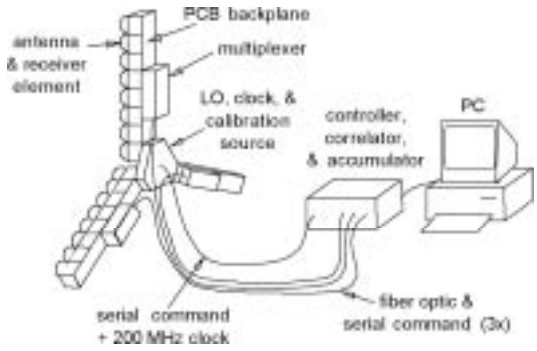

Fig 4. Prototype GeoSTAR configuration

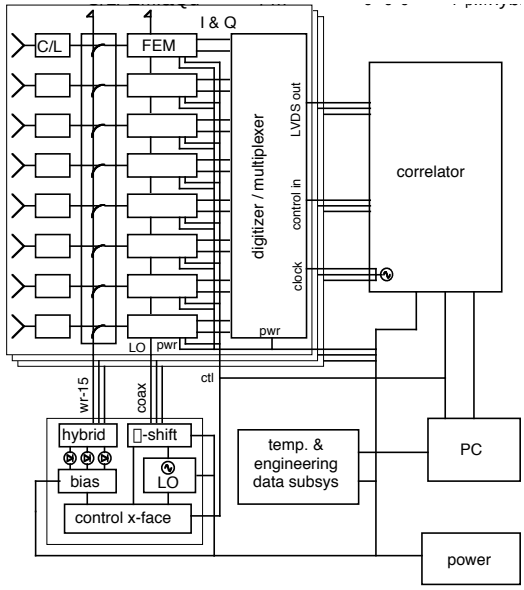

Fig. 5. Receiver system block diagram

The 24 receiving elements are arranged in the Y-formation described above. Each arm is a single physical module containing a linear array of 8 receiving elements combined with a signal multiplexer. It is envisioned that larger arrays will be formed by combining a number of such modules end to end. Fig. 6 shows the antenna array and illustrates an innovative staggered arrangement that makes it possible to transfer phase measurements between the arms.

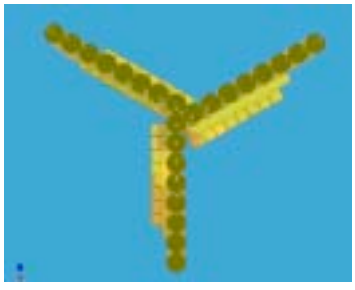

Fig. 6. Antenna array

Each element receives RF energy through a feedhorn, and Fig. 7 illustrates a Potter horn design that is being considered. Other designs are also being evaluated. The receivers are miniature I/Q

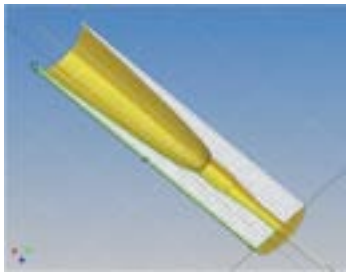

Fig 7. Drawing of Potter horn

mixer designs using low noise amplifiers as a first stage and utilizing MMIC technology. The physical layout of a prototype 50-GHz receiver is illustrated in the photos in Fig. 8.

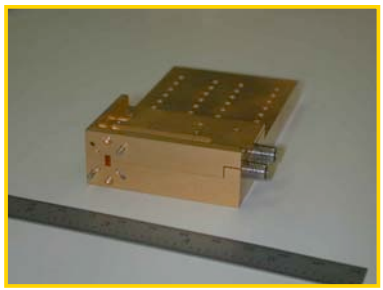

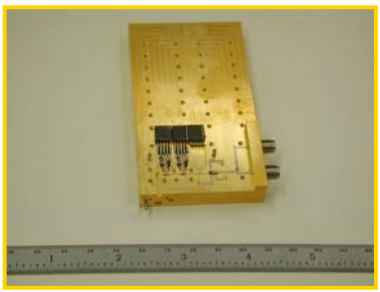

Fig. 8. Prototype 50-GHz receiver

Perhaps the most important subsystem is the correlator, which must perform multiplications of all 100-MHz signal pairs in real time. For an operational system with 100 elements per arm, as discussed above, that requires on the order of 20 trillion multiplications per second. (The prototype system requires substantial lower bandwidth, however.) To achieve such a high processing rate with a reasonable power consumption, the correlators are implemented as 1-bit digital multiply-and-add circuits, using a design developed for the University of Michigan. For the GeoSTAR prototype, where low cost is more important than low power consumption, this design will be implemented in FPGAs, while an operational system will use low-power application specific integrated circuits (ASICs).

Conclusions

The technology elements required for an operational GeoSTAR are relatively mature. For example, MMIC chips required for 50-GHz miniature low-power receivers are available commercially off the shelf. Low noise amplifiers up to 200 GHz are also maturing rapidly. The same is the case for correlator integrated circuits, where technology developed for miniature low-power consumer and communications electronics can be leveraged. 1-bit multipliers operating at 100 MHz have been demonstrated that consume about 0.5 mW each, and that is expected to decline to less than 0.1 mW within 3-5 years. At that level, the corelator subsystem for the 100 elements per arm example discussed above would consume only about 20 W – an almost trivial amount for today's satellite systems. The current challenge, where the GeoSTAR prototype is intended as a risk reduction effort, is in terms of system development and integration. Although several efforts have been under way for some time to develop 2-dimensional aperture synthesis systems, none has been demonstrated to date.

The advantages of an aperture synthesis system over a real aperture system are significant. The most important ones are summarized in Table 1. In particular, error budget calculations based on simulations, summarized in Table 2, indicate that a synthetic aperture system can be expanded in size without unduly stressing the phase stability requirements. It is therefore well suited to meet future needs as the spatial resolution of numerical weather prediction models increase.

Table 1. GeoSTAR vs. real-aperture systems

Feature	GeoSTAR	Real-Aperture
Aperture size	**Any size**	**Limited**
Scanning	**No scanning**	**Mech. scanning**
Spatial coverage	**Full disk**	**Limited**
Spectral coverage	**One array: one band**	**One antenna: all bands**
Accommodation	Easy	**Difficult**
Power consumption	**'03: high; '08: low**	**Moderate**
Platform disturbance	None	**High**

Table 2. Error budget

Array size	delta-T = $T_{sys}/\sqrt{B\tau}$ additive noise	delta-G =gain error in each correlator	delta-P =phase error at each correlator	phase error scaled by spacing (at max spacing)	antenna pattern error
50x50	0.0076 K	0.32 %	0.19°	1.7°	0.17 %
200x200	0.0019 K	0.32 %	0.19°	3.5°	0.17 %

References

Grody, N. 1993. “Atmospheric Remote Sensing by Microwave Radiometry” (M. Janssen ed.), Wiley

Staelin, D. and Chen, F. 2000. Precipitation observations near 54 and 183 GHz using the NOAA-15 satellite, *IEEE Trans. Geosci. Rem. Sens*., **38**, 2322-32

Camps, A. et al. 1997. The processing of hexagonally sampled signals with standard rectangular techniques: Application to 2-D large aperture synthesis interferometric radiometers, *IEEE Trans. Geosci. Remote Sens*., **35**, 183-190

Acknowledgments

This work was carried out at the Jet Propulsion Laboratory, California Institute of Technology under a contract with the National Aeronautics and Space Administration.

International TOVS Study Conference-XIII Proceedings

VIIRS Sensor Performance

Carl Schueler , J. Ed Clement, Russ Ravella, Jeffery J. Puschell
Raytheon Santa Barbara Remote Sensing, Goleta CA 93117

Lane Darnton
Northrop Grumman Space Technologies, Redondo Beach CA 90278

Frank DeLuccia
The Aerospace Corporation, Los Angeles, CA 90245

Captain Tanya Scalione USAF and Hal Bloom
NPOESS Integrated Program Office, Silver Spring, MD 20910

Hilmer Swenson
The Aerospace Corporation, Silver Spring, MD 20910

***Abstract*-This paper summarizes the anticipated performance of the National Polar-orbiting Operational Environmental Satellite System (NPOESS) Visible Infrared Imaging Radiometer Suite (VIIRS) sensor. Predictions are generated from models and demonstration hardware based on the design described in a companion paper [1]. VIIRS risk-reduction will continue as the Engineering Development Unit (EDU) is assembled and tested over the next year facilitating performance verification and lowering flight unit development risk.**

I. INTRODUCTION

The Visible Infrared Imaging Radiometer Suite (VIIRS) sensor has been designed to provide the performance necessary to meet the Environmental Data Record (EDR) requirements defined by the National Polar-orbiting Environmental Satellite System (NPOESS) Integrated Program Office (IPO) in the NPOESS Integrated Operational Requirements Document-II (IORD-II) and the VIIRS Sensor Requirements Document (SRD) [2,3]. VIIRS successfully completed its Critical Design Review (CDR) in Spring 2002. Previous reports document the design prior to CDR [4-7], at CDR, and a companion paper documents refinements since CDR [7]. The next stage of development is completion of an Engineering Development Unit (EDU) in 2004. This EDU will allow verification of VIIRS Sensor performance prior to completion in 2005 of the first flight model which is scheduled for launch in 2006 on the NPOESS Preparatory Project (NPP) spacecraft.

Fig. 1 presents a mechanical view of the VIIRS design; a functional block diagram is provided in Fig. 2. At the preliminary design review (PDR), sensor performance was predicted using models developed by Raytheon SBRS. These models were the basis of the performance predictions previously reported for the initial sensor design. System-level simulations allowed Raytheon to conduct the sensor design and algorithm trades necessary to select the best balance of sensor performance, cost, design, and risk vs. system-level EDR performance.

In September 2002, the Raytheon VIIRS contract was transferred to TRW, now Northrup-Grumman Space Technologies (NGST), following TRW's receipt of an IPO contract to manage NPOESS and build the spacecraft. During the associated contract negotiation, responsibility for VIIRS EDR performance was transferred to NGST, limiting Raytheon SBRS' responsibility to production of VIIRS sensors in accordance with the sensor specification.

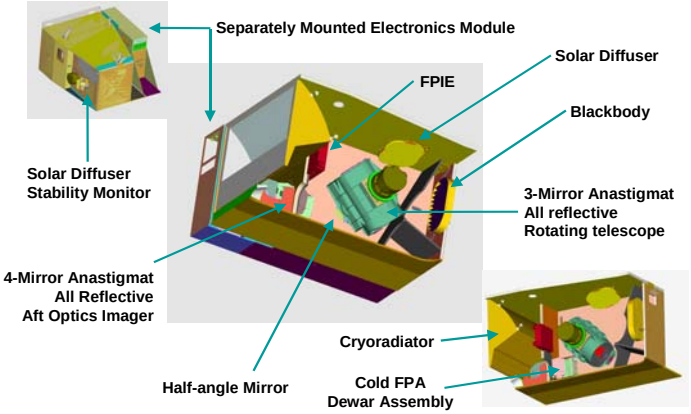

Figure 1. Single sensor design contains substantial flight hardware heritage.

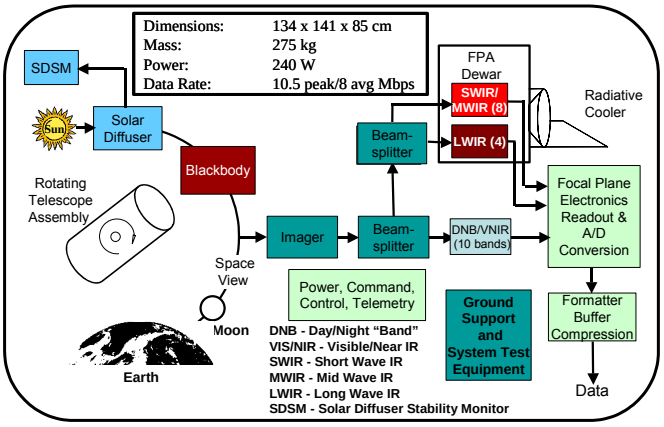

Figure 2: VIIRS block diagram traces photons from the Earth scene or internal calibration mechanisms to the focal plane arrays (FPA) and data output.

This paper presents sensor performance predictions for the updated design. These predictions are not only based on math models and simulations, but also take into account performance measured on recently completed engineering development hardware. These measurement results have both verified the accuracy of the models initially used to predict performance of these sensor subsystems and also increased confidence in updated predictions of sensor-level performance.

II. VIIRS PERFORMANCE MODELING

VIIRS sensor performance is predicted using models referenced in Fig. 3 and Table I. Some are VIIRS-specific, such as the Microsoft Excel SNR and dynamic-range model and the reflective and emissive band absolute radiometric error Mathcad models. Inputs to these models are derived from other modeling and simulation programs such as the optical transmission, modulation transfer function (MTF), forward and reverse ray tracing, and polarization models in Code V, ASAP, Excel, and the Sinda thermal model.

III. VIIRS PERFORMANCE

SNR, spectral radiance dynamic range, spatial MTF, polarization, radiometric accuracy, and structural and thermal performance under operational environments represent the primary sensor performance parameters that determine VIIRS overall EDR performance success.

Table II lists predicted horizontal sample intervals (HSI), MTF at the Nyquist frequency (0.5 HSI^{-1} cycles/km), and radiance dynamic range and SNR in each VIIRS spectral band. Specified and predicted SNR margins are shown on the far right. Note HSI is not the same as horizontal spatial resolution (HSR), although for most spectral bands the two are very close in value. HSR is defined as half the inverse of the spatial frequency at which the MTF equals 0.5.

The imagery EDR's fine HSR requirements were met with balanced optical and focal plane MTFs. The detector field stops in the moderate resolution (radiometry) bands were sized to provide improved HSI for coarser horizontal cell size (HCS) non-imagery EDRs, which also improves detector yield and lowers detector noise. VIIRS offers HSI <1.3 km nearly to edge-of-scan (EOS) in all bands, though required only to 43.6 degrees off-nadir. VIIRS offers finer nadir HSI than the Polar-orbiting Operational Environmental Satellite (POES) Advanced Very High Resolution Radiometer (AVHRR) and Terra/Aqua satellites MODerate resolution Imaging Spectroradiometer (MODIS), and with better nadir SNR via 3:1 aggregation following a patented design approach [9]. At EOS, the HSI is 4:1 finer in the cross-track dimension compared to AVHRR and MODIS, yet with comparable SNR, better than the Defense Meteorological Satellite Program (DMSP) Operational Line Scanner (OLS). Diverse Civil and DoD requirements therefore support one another through an integrated single-sensor design that balances improved imagery and spectro-radiometry.

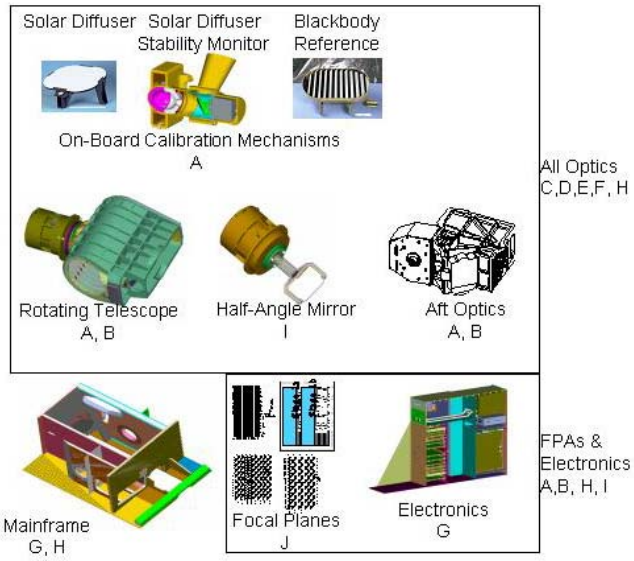

Figure 3: Simulations permit end-to-end sensor performance predictions.

Table I. Models used to predict VIIRS sensor performance.

Fig. 3 legend	Model Description
A	Signal to Noise Ratio (SNR)
B	Modulation Transfer Function (MTF)
C	Polarization Performance
D	Sequential Ray Trace
E	Non-sequential Ray Trace
F	Thin Films Design and Performance
G	Structural Design and Performance
H	Thermal Design and Performance
I	Electronics Simulation
J	Focal Plane Array (FPA) Performance

Table II shows two radiance ranges in "dual-gain" bands. In seven bands the saturation radiance and SNR requirements at low radiance made it impractical to meet both the dynamic range and sensitivity requirements with a single detector-channel gain setting. In these cases, Raytheon could have designed two separate detector arrays to meet the EDRs, one with high gain and excellent low radiance sensitivity, and another with lower gain and high saturation radiance. MODIS uses this approach for several spectral bands because when MODIS was designed in 1990, similar conflicting dynamic range and sensitivity requirements could not be met with one detector array. Raytheon since developed a readout integrated circuit (ROIC) capacitive transimpedance amplifier (CTIA) unit-cell with automatic gain control to cover the dynamic range, called "dual-gain." This allows the data necessary for the wide range of VIIRS EDRs to be accommodated with fewer detector arrays, reducing cost, data rate, and electronics mass, power, and volume.

The predicted SNR for all bands nadir to EOS for both single and dual-gain bands have margin of better than 97%. The Day/Night Band (DNB) CCD array provides a minimum SNR greater than 6 at EOS under its minimum radiance condition.

Table II. VIIRS Requirements and Predicted Performance by Spectral Band

		Band No.	Wave-length (μm)	Horiz Sample Interval (km Downtrack x Crosstrack)		Driving EDRs	Radi-ance Range	Ltyp or Ttyp	Signal to Noise Ratio (dimensionless) or NEΔT (Kelvins)		
				Nadir	End of Scan				Required	Predicted	Margin
VIS/NIR FPA	Silicon PIN Diodes	M1	0.412	0.742 x 0.259	1.60 x 1.58	Ocean Color	Low	44.9	352	483	37%
						Aerosols	High	155	316	827	162%
		M2	0.445	0.742 x 0.259	1.60 x 1.58	Ocean Color	Low	40	380	501	32%
						Aerosols	High	146	409	774	89%
		M3	0.488	0.742 x 0.259	1.60 x 1.58	Ocean Color	Low	32	416	573	38%
						Aerosols	High	123	414	747	80%
		M4	0.555	0.742 x 0.259	1.60 x 1.58	Ocean Color	Low	21	362	482	33%
						Aerosols	High	90	315	586	86%
		I1	0.640	0.371 x 0.387	0.80 x 0.789	Imagery	Single	22	119	135	13%
		M5	0.672	0.742 x 0.259	1.60 x 1.58	Ocean Color	Low	10	242	306	26%
						Aerosols	High	68	360	450	25%
		M6	0.746	0.742 x 0.776	1.60 x 1.58	Atmospheric Corr'n	Single	9.6	199	279	40%
		I2	0.865	0.371 x 0.387	0.80 x 0.789	NDVI	Single	25	150	212	41%
		M7	0.865	0.742 x 0.259	1.60 x 1.58	Ocean Color	Low	6.4	215	467	117%
						Aerosols	High	33.4	340	467	37%
CCD		DNB	0.7	0.742 x 0.742	0.742 x 0.742	Imagery	Var.	6.70E-05	6	6.2	3%
S/MWIR	PV HgCdTe (HCT)	M8	1.24	0.742 x 0.776	1.60 x 1.58	Cloud Particle Size	Single	5.4	74	109	47%
		M9	1.378	0.742 x 0.776	1.60 x 1.58	Cirrus/Cloud Cover	Single	6	83	156	88%
		I3	1.61	0.371 x 0.387	0.80 x 0.789	Binary Snow Map	Single	7.3	6.0	71	1084%
		M10	1.61	0.742 x 0.776	1.60 x 1.58	Snow Fraction	Single	7.3	342	461	35%
		M11	2.25	0.742 x 0.776	1.60 x 1.58	Clouds	Single	0.12	10	14	44%
		I4	3.74	0.371 x 0.387	0.80 x 0.789	Imagery Clouds	Single	270 K	2.500	0.236	68%
		M12	3.70	0.742 x 0.776	1.60 x 1.58	SST	Single	270 K	0.396	1.039	141%
		M13	4.05	0.742 x 0.259	1.60 x 1.58	SST	Low	300 K	0.107	0.051	111%
						Fires	High	380 K	0.423	0.353	20%
LWIR	PV HCT	M14	8.55	0.742 x 0.776	1.60 x 1.58	Cloud Top Properties	Single	270 K	0.091	0.057	60%
		M15	10.763	0.742 x 0.776	1.60 x 1.58	SST	Single	300 K	0.070	0.034	105%
		I5	11.450	0.371 x 0.387	0.80 x 0.789	Cloud Imagery	Single	210 K	1.500	1.004	49%
		M16	12.013	0.742 x 0.776	1.60 x 1.58	SST	Single	300 K	0.072	0.059	23%

The models used to predict SNR have been updated to take into account the most recent estimates of optical transmission based on recently completed tests of silver mirror witness samples, measured dichroic and spectral filter performance, and a reduction in optical aperture resulting in an f/6.2 system. Data from on-orbit MODIS and Enhanced Thematic Mapper (ETM) instruments has been used to more accurately predict end-of-life optical transmission that will result from degradation due to long term exposure to Earth-reflected ultraviolet radiation. Additionally, measured Noise Equivalent Irradiance (NEI) data from recently completed and in-process EDU focal planes indicates that the associated noise allocations in the SNR model will generally be achievable and with significant margin for many bands.

As discussed in the companion paper on VIIRS design changes since CDR[1], the sensor optical aperture stop has been repositioned from the primary mirror in the telescope (where it resides in MODIS) to a position immediately following the half angle mirror (HAM) derotator. Detailed optical analyses indicated that this was necessary to eliminate modulated instrument background (MIB) resulting from the VIIRS rotating telescope [1]. The emissive band radiometric error model was updated to include a more accurate representation of rotating optics emissions.

In parallel, the sensor thermal model was updated to provide higher fidelity predictions of internal sensor surface temperatures as a function of time in orbit (representative thermal data is shown in Fig. 4). These updated thermal predictions were used in the emissive band radiometric uncertainty model to verify that this modification to the optical design will achieve the excellent emissive band radiometric performance (Table III) predicted at CDR.

As part of this design update, a modest band-to-band registration improvement was possible. This was done by optimizing the location of the S/MWIR and LWIR detector field stops so that their locations better compensate residual pin cushion distortion in the overall sensor optical system. The updated band-to-band registration model predicts that the areas associated with spatially overlapping instantaneous fields of view (IFOVs) of specified moderate resolution S/MWIR and LWIR bands will be matched to better than 82%.

Table IV shows ASAP model predicted mirror coating and dichroic VNIR polarization. The 555 nm band is conservatively representative of 445-746 nm bands polarization, all specified at 2.5%.

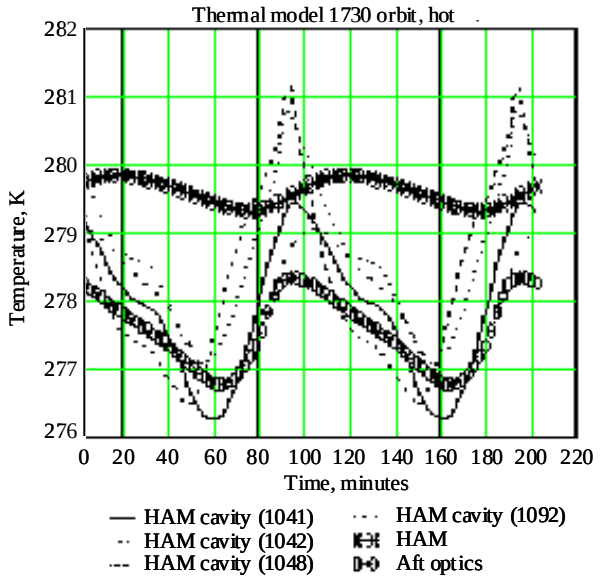

Figure 4. Updated VIIRS thermal modeling provides details of internal time-varying temperatures.

Table III. VIIRS provides excellent emissive band radiometric performance.

Parameter	VIIRS Center Wavelength (μm)				
	3.70	4.05	8.55	10.76	12.01
T typical (K)	270	300	270	300	300
Temp. Knowledge Effect (%)	0.32	0.24	0.14	0.09	0.08
Wavelength Knowledge Effect (%)	0.20	0.20	0.04	0.03	0.04
Integrated OOB Effect (%)	0.30	0.30	0.20	0.10	0.10
RVS Knowledge (%)	0.20	0.20	0.60	0.20	0.20
RVS Pedestal Knowledge	0.20	0.20	0.60	0.20	0.20
Emittance Knowledge (%)	0.20	0.20	0.20	0.20	0.20
Electronic Crosstalk (%)	0.20	0.20	0.20	0.20	0.20
Ghosting (%)	0.24	0.24	0.24	0.24	0.24
Polarization Knowledge Effect (%)	0.01	0.01	0.10	0.10	0.10
Earthshine Effect (%) (Tearth=343K)	0.029	0.025	0.009	0.008	0.007
AlSD Screen Emission (%) (Tinst=285K)	0.0293	0.0245	0.0091	0.0076	0.0071
SD Sunlight Scatter (%)	0.128	0.110	0.047	0.041	0.038
BB Skin Temp Effect (%) (Tinst=275K)	0.014	0.003	0.0	0.0	0.0
Surround Correction Effect (%) (Tinst=285K)	-0.031	-0.028	-0.013	-0.011	-0.01
Rad. Cal'n Model Stand. Dev. (%)	0.68	0.62	0.55	0.35	0.35
Allocation Reqmt (%)	0.7	0.7	0.6	0.4	0.4

Table IV. ASAP model predicts margin against polarization specification

Band name	Bandcenter (nm)	Specification (%)	-45 degrees	Zero degrees	+45 degrees
M1	412	3.0	1.30	2.00	2.90
M4	555	2.5	0.50	0.30	0.60
I2 & M7	865	3.0	0.70	0.04	0.02

IV. SUMMARY

The NPOESS VIIRS is a 22-band sensor employing a cross-track rotating telescope. The scene is imaged onto three focal planes separating VNIR, S/MWIR, and LWIR energy. The VNIR FPA has nine spectral bands, the S/MWIR FPA has eight spectral bands, and the LWIR FPA four spectral bands. The integral DNB capability provides a very large dynamic range low-light capability in all VIIRS orbits. VIIRS has been modeled via an extensive set of commercial ray tracing and structural and thermal design programs, as well as VIIRS specific radiometric models developed by Raytheon and validated against flight hardware measurements on earlier programs and on preliminary VIIRS engineering development hardware. The predicted performance based on these models shows margin against the sensor specification. The next major step in hardware performance assessment will be achieved with the completion and test of the VIIRS Engineering Development Unit (EDU) in 2004. EDU performance measurements will be used to verify the design, and to identify remaining design adjustments required to ensure that the flight models perform as required.

ACKNOWLEDGEMENTS

Phase I work was supported under NPOESS contract number F04701-97-C-0028 and partially by Raytheon funding, while post-PDR efforts are supported by NPOESS contract number F04701-01-C-0500. VIIRS sensor development is continuing under NGST contract 63549DGE2S to Raytheon SBRS. The authors wish to thank the excellent Raytheon, NGST, IPO and Aerospace Corporation design and review teams whose dedication and professionalism have made the results reported here possible.

REFERENCES

[1] T. Scalione, H. Swenson, F. De Luccia, N. Baker, C. Schueler, J. Clement, and L. Darnton, "Design Evolution of the NPOESS VIIRS Instrument Since CDR," International Geoscience and Remote Sensing Symposium (IGARSS) Proceedings, 25-30 July 2003.

[2] NPOESS IPO, Integrated Operational Requirements Document I (IORD II), version 6, 2002.

[3] NPOESS IPO, VIIRS Sensor Requirements Document, version 2b, 4 November 99.

[4] C. Welsch, H. Swenson, S. A. Cota, F. DeLuccia, J. M. Haas, C. Schueler, R. M. Durham, J. E. Clement, and P. E. Ardanuy, "VIIRS (Visible Infrared Imager Radiometer Suite): A Next-Generation Operational Environmental Sensor for NPOESS," International Geoscience and Remote Sensing Symposium (IGARSS) Proceedings, 8-14 July 2001.

[5] P. Ardanuy, C. Schueler, S. Miller, P. Kealy, S. Cota, J.M. Haas, and C. Welsch, "NPOESS VIIRS Design Process," SPIE 2001 4483-03

[6] C. Schueler, J. Clement, C. Welsch, F. DeLuccia, and H. Swenson, "NPOESS VIIRS Sensor Design Overview," SPIE 2001 4483-02

[7] C. Schueler, P. Ardanuy, P. Kealy, S.W. Miller, H. Swenson, J. M. Haas, F. DeLuccia, and S.Cota, "Remote Sensing System Optimization," IEEE Aerospace 2001

[8] C.Schueler and W.L. Barnes, "Next-Generation MODIS for Polar Operational Environmental Satellites," Journal of Atmospheric and Oceanic Technology, Vol. 15, No. 2, April 1998, pp. 430-439.

[9] R. Murphy, W. Barnes, A. Lyapustin, J. Privette, C. Welsch, F. DeLuccia, H. Swenson, C. Schueler, P. Ardanuy, and P. Kealy, "Using VIIRS to provide Data Continuity with MODIS," International Geoscience and Remote Sensing Symposium (IGARSS) Proceedings, 8-14 July 2001.

[10] C. Schueler, "Dual-use Sensor Design for Enhanced Spatioradiometric Performance," US patent 5,682,034; October 1997.

Overview of the CrIMSS (CrIS/ATMS) retrieval algorithm

Xu Liu and Jean-Luc Moncet,
AER, Inc

AER is the retrieval algorithm developer for the Cross Track Infrared and Microwave Sounder Suite (CrIMSS), which will fly onboard of NPP and NPOESS platforms. The infrared component of the CrIMSS is an interferometer-based Cross-Track Infrared Sounder (CrIS). The microwave component is an Advance Technology Microwave Sounder (ATMS). The radiative transfer forward model uses an innovative parameterization, which models both radiances and weighting functions accurately and efficiently. The inversion algorithm uses a physical retrieval method to retrieve atmospheric and surface properties from both microwave and infrared sensors. Different strategies for dealing with clouds will be discussed. Some results of applying the CrIMSS algorithm to real data will be presented.

IASI on Metop : an Advanced Sounder for Operational Meteorology and Climate studies.

T.Phulpin, G. Chalon and D. Blumstein
Centre National d'Etudes Spatiales

IASI is a new generation infrared vertical sounder developed jointly by CNES and EUMETSAT that will be embarked on METOP 1 to 3. It has been designed for operational meteorological soundings with a very high level of accuracy (Specifications on Temperature accuracy : 1K for 1 km and 10 % for humidity) and also for estimating and monitoring trace gases on a global scale. The IASI system includes the 3 instruments, a data processing software integrated in the EPS ground segment and a technical expertise centre (TEC) implemented in CNES Toulouse.
The instrument is composed of a Fourier transform spectrometer and an associated infrared imager. The optical configuration is based on a Michelson interferometer and the interferograms are processed by an on-board digital processing subsystem, which performs the inverse Fourier transforms and the radiometric calibration. The infrared imager co-registers the IASI soundings with AVHRR imager (AVHRR is another instrument on the Metop satellite).The first flight model has just been delivered by the prime Alcatel to be integrated in the next months on METOP 1. Its radiometric performances are compared to its specifications.

The operational software for level 1 and level 2 is currently under development respectively under CNES and Eumetsat responsibility. The Level 1 processing is devoted to deliver to end users very well calibrated and located radiance spectra. Its functions and parameters will be established , monitored and updated by the TEC. A calibration/validation plan to ascertain level 1 data quality has been defined.
Based on actual current instrument performances, simulations performed in the framework of preparatory studies by the IASI sounding study working group (ISSWG) show that with the current assimilation or inversion techniques, mission requirements are met.

IASI on Metop: The Operational Level 2 Processor

Peter Schlüssel

EUMETSAT
Am Kavalleriesand 31, 64295 Darmstadt, Germany

Abstract

The operational IASI level 2 processor will be part of the EPS Core Ground Segment. Starting with IASI level 1c data the level 2 processor generates vertical profiles of temperature and humidity, ozone columns of deep layers, and columnar amounts of carbon monoxide, methane, nitrous oxide, and carbon dioxide, along with surface temperature, surface emissivity, cloud amount, cloud-top height, and cloud phase. The processor not only makes use of IASI data but also utilises information from the companion instruments AVHRR, AMSU-A, MHS, as well as level 2 products from the ATOVS instrument suite.

Introduction

The Infrared Atmospheric Sounding Interferometer (IASI) will be flown on the Metop satellites as part of the EUMETSAT Polar System (EPS). The main purpose of IASI is to deliver temperature and water vapour profiles for the numerical weather prediction (NWP) at accuracies of 1K or 5%, respectively, at high vertical resolution. Cloud parameters to be derived from IASI include cloud fraction, cloud top temperature, cloud height, and cloud phase. Surface skin temperature over land and ocean are to be derived from IASI along with a surface emissivity characterisation over land. Trace gases that will be derived from IASI are ozone profiles and columnar amounts of carbon monoxide (CO), carbon dioxide (CO_2), nitrous oxide (N_2O), and methane (CH_4).

The IASI Level 2 Product Processing Facility (PPF) is being built by industry in the frame of the EPS Core Ground Segment development, according to specifications given by EUMETSAT. The specifications have been written according to current scientific knowledge as expressed in literature, results from scientific studies, heritage of AIRS (Atmospheric Infra-Red Sounder flown on Aqua), and from research results of the IASI Sounding Science Working Group (ISSWG).

Properties of the IASI Level 2 Processor

For a best use of IASI measurements the level 2 processing can combine IASI data with concurrent measurements of the Advanced Very High resolution radiometer (AVHRR), the Advanced Microwave Sounding Unit A (AMSU-A), and the Microwave Humidity Sounder (MHS), which are flown together with IASI on Metop. Also, the Level 2 products of the Advanced TIROS Operational Vertical Sounder (ATOVS, a combination of AMSU-A, MHS, and the High-resolution Infrared Radiation Sounder, HIRS) are used to support the IASI Level 2 processing. They are mainly used in aiding cloud detection and the initialisation of the geophysical-parameters retrieval, but also for inclusion in the latter. Consequently, the processing chains show complex interdependencies (Figure 1).

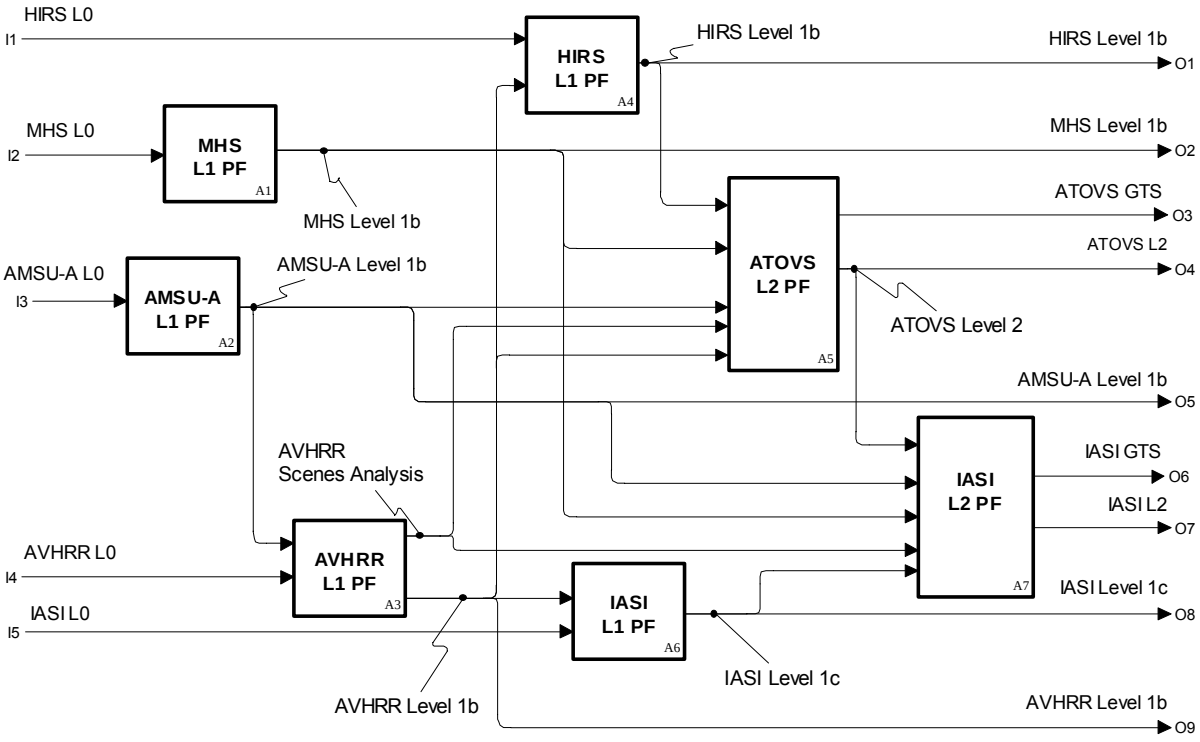

Fig. 1: Processing chain interdependencies

IASI stand-alone processing is possible if other measurements are not available, or if the PPF is explicitly configured to exclude other instruments. NWP forecast is included to provide surface pressure as reference for the temperature and humidity profiles to be retrieved and NWP supplied surface wind speed over sea is used for the calculation of surface emissivity. Optionally, the NWP forecast profiles of temperature, water vapour and ozone can be used to initialise or constrain the retrieval.

The processing is steered by configuration settings, the specification of 80 configurable auxiliary data sets, including data such as threshold values, radiative transfer coefficients, error covariances, processing choices etc., allows for the optimisation of PPF before and during commissioning. As soon as physical knowledge changes the corresponding auxiliary data sets can be updated to improve on the level 2 processing.

An online quality control supports the choice of the best processing options in case of partly unavailable IASI data or in cases of missing or corrupt side information (e.g. data from other instruments or NWP forecast). Part of the online quality control is the generation of 40 flags. These steer the processor according to configuration, data availability and data quality. The flags are part of the level 2 product.

The IASI measurements are represented as spectra, resolving the domain between 645 and 2760 cm^{-1} at 0.35 to 0.5 cm^{-1}. The spectra are sampled at 0.25 cm^{-1}, so that 8461 IASI "channels" can be identified. The spectra are divided in three bands, due to the use of different detectors (Figure 2). If available, all IASI channels are used in the retrieval to maximise the extracted information. However, besides the nominal instrument mode the PPF also supports the processing of data from degraded modes, for example, reduced number of spectral bands in case of failed detectors.

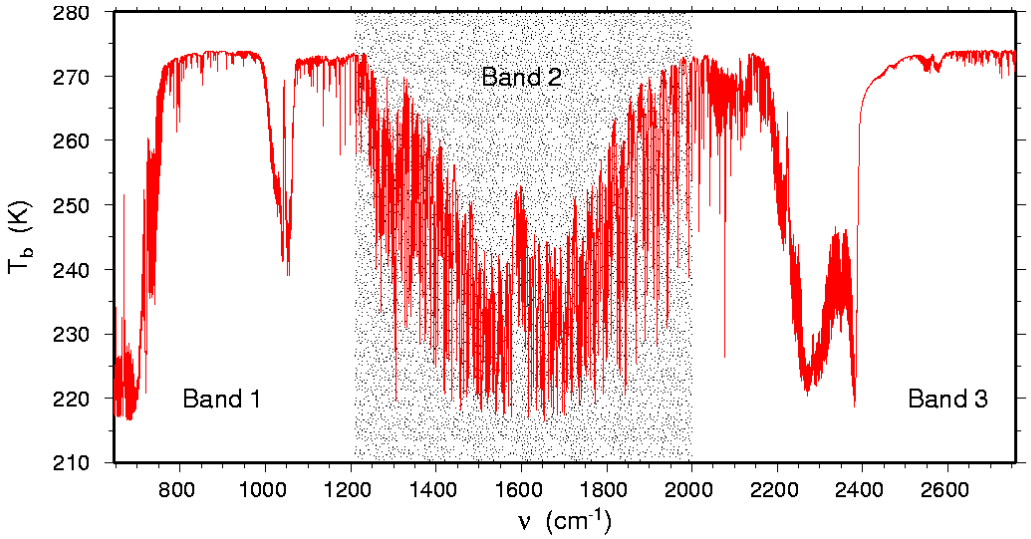

Fig. 2: Example of a (synthetic) brightness temperature spectrum as measured by IASI

A bias tuning is foreseen by configuration setting to allow for the adjustment of the radiative transfer model, included in the final iterative retrieval, to the real atmospheric transfer.

The IASI Level 2 Product contains the following information per sounding

- State vector
- Covariance matrix (compressed)
- Flag Collection
- Pointer to configuration setting
- Location and time information
- Scan geometry

The level 2 product is disseminated to the users within 3 hours after the measurements via Near Real Time (NRT) Terminals. All level 2 products will be archived in the Unified Meteorological Archiving Facility (UMARF) at EUMETSAT HQ, from where they can be obtained for off-line use.

The IASI level 2 processing can be roughly broken down in a pre-processing step, the cloud detection and cloud-parameters determination, and the geophysical-parameters retrieval.

Pre-processing

The pre-processing starts with the acceptance and validation of data. All input data will be checked against valid bounds and invalid or missing data will be flagged. Further processing depends on availability of data, the processing will proceed if possible with available data, and even if incomplete (e.g. IASI stand-alone processing is foreseen). Redundant information is used in case of IASI, for example, highly correlated channels can be used, where available, as proxy if measurements of single channels are invalid or missing.

Tuning coefficients will be applied to the measurements for removal of bias between calculated and measured radiances.

Other data are mapped to IASI:

- Auxiliary data, such as land mask, topography, land surface type, are extracted from data bases and mapped to the IASI IFOV (Instantaneous Field Of View).

- Land/sea fractions are calculated, weighted with the Instrument Point Spread Function (IPSF).
- An IPSF-weighted surface height is calculated.
- The degree of surface height variability within an IFOV is determined.
- The radiances of the secondary instruments AMSU-A and MHS are interpolated to the IASI IFOV.
- The ATOVS level 2 product is interpolated to the IASI IFOV.
- The AVHRR scenes analysis is mapped to the IASI IFOV and IPSF-weighted cloud fraction, surface temperature, and cloud-top temperature are calculated.

The AVHRR scenes analysis is matched with the AVHRR radiance analysis (part of IASI L1c product) to locate cloud and surface formations in IASI IFOV. This is used to correct IASI radiances with respect to ISRF changes due to non-homogeneity in IASI IFOV.

An initial choice of setting for cloud processing and retrieval procedures depends on configuration, environmental conditions (cloud amount, surface type, elevation), data availability, and data quality

Cloud Processing

The cloud processing includes the cloud detection, and the determination of cloud parameters. The latter can be refined by the final, iterative retrieval step.

Cloud Detection

No single cloud detection method is able to detect clouds properly in all situations, so that a number of cloud detection methods are used concurrently. The variety of method also takes account of the possibility that IASI can be processed in a stand-alone mode or in combination with the ATOVS and AVHRR instruments.

AVHRR Based Cloud Detection

The AVHRR scenes analysis results mapped to the IASI IFOV gives a direct estimate of the cloud coverage within the IASI IFOV. Additionally, the cloud-top temperature as derived from AVHRR, together with the temperature profile from the ATOVS level 2 product gives the cloud-top pressure.

Window Channel Tests

Clouds usually assume different temperatures than the underlying surfaces due to varying temperature in the atmosphere. The IASI brightness temperatures in window channels near 3.7, 4.0, 8.7, 11, and 12 μm are checked against pre-defined thresholds for the cloud detection. The exact selection of channels and the threshold values are configurable. The thresholds typically vary with surface condition, latitude, and season.

IASI Inter-Channel Regression Tests

Three empirically derived multi-channel regression methods using IASI channels in transparent and opaque spectral regions near 3.95, 4.40, 4.46, 6.28, 6.30, 7.53, 7.70, 10.35, 12.80, and 14.70 μm are derived to detect clouds. Different linear combinations of the brightness temperatures in those channels are checked against pre-defined threshold values. The latter are dependent on latitude, season, surface type and surface elevation.

IASI-AMSU Inter-Channel Regression Tests

Two empirically derived multi-channel regression methods using IASI channels near 4.00, 4.40, 4.50, 4.55, and 11.10 μm are used together with AMSU-A channels 1, 4, 5, 6, 7, 8, 9, 10, and 15 are derived to detect clouds. Different linear combinations of the brightness temperatures in those channels are checked against pre-defined thresholds. The thresholds depend on latitude, season, surface type, and surface elevation.

Horizontal Coherency Test

Usually, the surface temperature is horizontally more homogeneous than the cloud-top temperature, in particular for convective clouds. The brightness temperature in a channel near 3.7 µm is checked against a pre-defined threshold to detect clouds. The threshold value is configurable and depends on the surface condition.

Thresholds on IASI EOF Residuals

A limited number of pre-calculated principal component scores of measured spectra are used to re-construct clear-sky spectra. The difference between measured and re-constructed spectra is checked against a pre-defined threshold to detect clouds. The pre-calculated eigenvectors of the clear-sky spectra and the threshold values are configurable.

Window Cross-Correlation Test

The atmospheric window regions cover many atmospheric absorption lines, which make up a unique spectral signature in clear situations. This signature partly disappears in cloudy cases. A cross-correlation between clear-sky reference spectrum and measured spectrum is tested against a pre-defined threshold to detect cloudy spectra. The threshold value and the reference spectrum are configurable and depend on surface type and elevation, season, and latitude.

Test for Clouds over Elevated Polar Regions

Strong surface inversions of the temperature profile over elevated polar regions in winter lead to higher radiation emission in water vapour bands than in window channels. In cloudy situations the emission in window channels, apart from absorption lines, increases, leading to changed brightness temperature differences between 11 and 12 µm. This difference is checked against a pre-defined threshold to detect clouds. The threshold value is configurable.

Detection of Dust Storms

Increasing dust optical depth increases the difference in brightness temperatures at 11 and 12 µm due to higher reflectivity of dust at 12 µm (Ackerman, 1997) . Over desert areas this difference is checked against pre-defined thresholds to detect dust clouds. The threshold value and the area covered by this test are configurable.

Thin Cirrus Detection

This test utilises the lower emissivity of ice particles at 11 µm. If the brightness temperature at 11 µm is below a pre-defined threshold then the brightness temperature difference between 11 and 12 µm is checked against another threshold to detect thin cirrus clouds. The selection of the channels and the threshold values are configurable.

Cloud Parameters Retrieval

If a cloud has been identified in the IASI IFOV a number of cloud parameters is determined, namely the cloud-top pressure, the cloud amount and the cloud phase.

Cloud-Top Pressure and Cloud Amount

The cloud-top pressure and the cloud amount are determined by the CO_2 Slicing Method, adapted for hyper-spectral sounding (Smith and Frey, 1990). If clouds are detected this method is used to calculate cloud-top pressure and cloud amount in single IASI IFOVs, using a sub-set of 500 IASI channels. The measured radiances of each channel and a reference channel are used together with synthetic radiances calculated for the clear-sky and overcast situations with the same temperature and water vapour profiles. For each channel/reference-channel pair a cloud-top pressure is obtained, which enters the calculation of a weighted mean, where the weight is the temperature weighting function.

Once the cloud-top pressure is known the cloud fraction can be calculated from the measured radiance and the synthetic radiances for the clear-sky and overcast situations. The calculation requires a temperature profile, which is taken from the ATOVS level 2 product or from NWP forecast, depending on configuration.

3.2 Cloud Phase

The emission spectrum of the atmosphere between 11 and 12 µm shows a steeper slope for liquid water than for ice clouds (Figure 3). This spectral behaviour is used to discriminate between ice clouds, mixed phases, and liquid-water clouds. The sum of brightness temperature differences between 12 and 11 µm and that between 8 and 11 µm are tested against pre-defined thresholds for the cloud-phase determination.

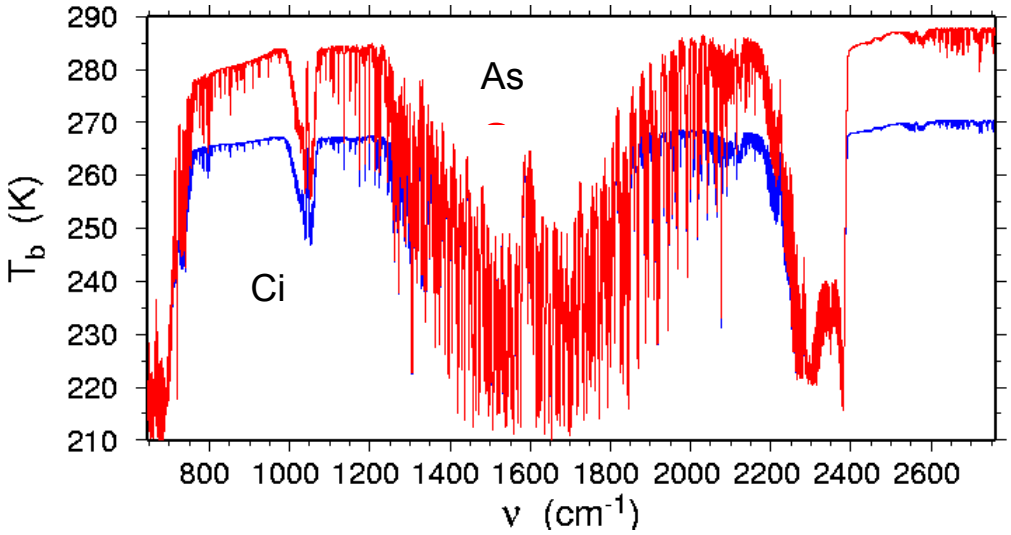

Fig. 3. IASI brightness temperature spectra (simulated) fora liquid-water cloud (As: alto stratus) and a cirrus cloud (Ci)

Geophysical Parameters Retrieval

Once the cloud detection and cloud parameters retrieval have been completed further geophysical parameters are derived. The number of variables retrieved from the measurements depends on the cloud conditions, which also determine the set-up of the retrieval scheme. Depending on configuration, data availability, surface and cloud conditions different retrieval types are foreseen.

State Vector

The state vector to be retrieved consists of the following parameters:

- Temperature profile at a minimum of 40 levels
- Water vapour profile at a minimum of 20 levels
- Ozone columns in deep layers (0-6km, 0-12 km, 0-16 km, total column)
- land or sea surface temperature
- surface emissivity at 12 spectral positions
- Columnar amounts of N_2O, CO, CH_4, CO_2
- Cloud amount (up to three cloud formations)
- Cloud top temperature (up to three cloud formations)
- Cloud phase

In case of clouds and elevated surfaces the state vector has to be modified to reflect the actual situation.

First Retrieval

The first retrieval consists of statistical methods, based on a linear EOF regression (Schlüssel and Goldberg, 2002) or a non-linear artificial neural network (ANN). For temperature and water-vapour profiles, ozone columns of deep layers, surface temperature, and surface emissivity the entire IASI spectrum is used to calculated principal component scores, which enter the linear regression retrieval. Likewise, the principal component scores can be entered into a feed-forward ANN to retrieve temperature and water-vapour profiles. Up to 100 principal component scores are used in the regression or the ANN retrievals. The retrieval of trace-gas columns is done using an ANN with a set of selected IASI radiances (Hadji-Lazaro et al., 1999), sensitive to the particular trace gases, together with the previously derived temperature profile. The selection between linear regression and ANN, the number of principal component scores, as well as all weights and regression coefficients are configurable.

The results from the first retrieval may constitute the final product or may serve as input to the final, iterative retrieval; the choice depends on configuration setting and on quality of the first retrieval results.

Final, Iterative Retrieval

The final retrieval is a simultaneous iterative retrieval, seeking the maximum a-posterior probability solution for the minimisation of a cost function seeking by the Marquardt-Levenberg method (e.g. Rodgers, 2000). The cost function aims at minimising the difference between measured and simulated radiance vectors, subject to a constraint given either by climatology, the ATOVS level 2 product, or NWP forecast. The chosen constraint can be tightened or removed, depending on configuration. As the iterative retrieval involves radiative transfer calculations of radiances and Jacobians it is too costly to include all IASI channels. A selection of up to 500 channels or super-channel clusters is made via configuration. The super-channel clusters consist of channels with highly correlated radiances, which are represented by a weighted mean of the measured radiances and by a selected lead channel in the radiative transfer calculations. The advantage of using super channels is the reduced radiometric noise of the average measured radiance. However, super channels are not available to replace all IASI channels, of which some carry unique information. Therefore, super channels and single channels are used concurrently in the same iterative retrieval.

The iterative retrieval is initialised with results from first retrieval. Other choices of initialisation may be selected, depending on configuration setting and availability (e.g. NWP forecast, climatology, or ATOVS Level 2 product).

The composition of the state vector to be iterated depends on cloud conditions and configuration setting. In case of very small cloud amounts (< 2%) the sounding can be considered as cloud-free and a corresponding retrieval is made for the atmospheric and surface parameters. At higher cloud amounts the cloud amount and the cloud-top pressure for up to three cloud formations are explicitly included in the state vector. At cloud amounts exceeding a second threshold the retrieval of parameters below the cloud top is no longer possible on a single IFOV basis. Under the assumption of homogeneity within four adjacent IFOVs, except for the cloud amount, a variational cloud clearing (Joiner and Rokke, 2000) is done, deriving a mean state vector for the IFOV quadruples. If the cloud amount exceeds a third threshold no information from below the cloud top is available and the atmospheric parameters will be derived only above the cloud top.

Radiative transfer calculations are parameterised according to the fast model RTIASI (Matricardi and Saunders, 1999). It is a semi-empirical model that supplies radiances and analytical Jacobians at the top of the atmosphere. Radiation included comes from the upwelling atmospheric emission, the downwelling atmospheric emission reflected at the surface and transmitted to the satellite, the surface emission transmitted to the top of the atmosphere, and the solar radiation transmitted to the surface and reflected to space.

Together with the iterated state vector an error covariance matrix is calculated, which is part of the level 2 product. The final product is composed of the results from the geophysical parameters retrieval

and from the cloud processing. Besides the full product, which is generated for every IFOV, a vertically and horizontally sub-sampled product is prepared for GTS (Global Telecommunications System for the exchange of meteorological data among the WMO members) distribution.

Online Quality Control

The online quality control plays an important role, as only the knowledge of the product quality lets the user judge whether and how to use the data. The main quality indicator is the error covariance of the product, giving the errors of the single state vector variables, together with their inter-dependencies. Besides this 40 flags are part of the product, informing the user about details of the processing and any deficiencies, processing options, data corruption or unavailability, surface conditions, cloud conditions and how they were identified, completeness of the product, and overall quality of the product.

Performance

As there are no IASI data available yet, the performance analyses made so far are given are based on synthetic data, created by different radiative transfer models. Some validation with real data has been done by adaptation of the methodologies to other instruments like IMG (Interferometric Monitor for Greenhouse Gases), AIRS (Atmospheric Infra-red Sounder), and NAST-I (NPOESS Airborne Simulator Test-bed-Infrared).

The temperature and humidity retrievals reach an accuracy of 1K and 15%, respectively, in the lower atmosphere. The land surface emissivity is derived with a relative accuracy between 1.8% and 2.4%, depending on the spectral region. Trace gas columnar amounts are retrieved with an accuracy of 5 to 6% (Turquety et al., 2002), the deep ozone columns with an accuracy between 15 and 22%.

References

Ackerman, S.A. (1997) Remote sensing aerosols from satellite infrared observations, J. Geophy. Res., **102**, 17069-17079.

Hadji-Lazaro, J., Clerbaux, C., Thiria, S. (1999) An inversion algorithm using neural networks to retrieve atmospheric CO total columns from high resolution nadir radiances, J. Geophys. Res., **104**, 23841-23854.

Joiner, J. and Rokke, L. (2000) Variational cloud-clearing with TOVS data, Q. J. Roy. Met. Soc., **126**, 725-748.

Matricardi, M. and Saunders, R.W., (1999) Fast radiative transfer model for simulation of infrared atmospheric sounding Interferometer radiances, Appl. Optics, **38**, 5679-5691.

Rodgers, C.D. (2000) Inverse methods for atmospheric sounding - theory and practice, World Scientific, Singapore, 238 pp.

Schlüssel, P. and Goldberg, M. (2002) Retrieval of atmospheric temperature and water vapour from IASI measurements in partly cloudy situations, Adv. Space Res., **29**, 11, 1703-1706.

Smith, W.L. and Frey, R. (1990) On cloud altitude determination from high resolution interferometer sounder (HIS) observations, J. Appl. Meteorol., **29**, 658-662.

Turquety, S., Hadji-Lazaro, J., Clerbaux, C. (2002) First satellite ozone distribution retrieved from nadir high -resolution infrared spectra, Geoph. Res. Let., **29**, 2198,doi:10.1029/2002GL016431.

Joint Temperature, Humidity, and Sea Surface Temperature Retrieval from IASI Sensor Data

Marc Schwaerz and Gottfried Kirchengast

Institute for Geophysics, Astrophysics, and Meteorology (IGAM), University of Graz, Graz, Austria

Abstract

We discuss a joint retrieval algorithm of temperature, humidity, ozone, and sea surface temperature (SST; more precisely, this is the surface skin temperature of the ocean) for the IASI (Infrared Atmospheric Sounding Interferometer) instrument. The algorithm is based on optimal estimation methodology and was carefully tested under realistic conditions (using high resolution ECMWF analysis fields). The algorithm contains in a first step an effective and fast channel selection method based on information content theory, which leads to a reduction of the total number of IASI channels ($>$8400) to about 3 % only ($\sim$250), which are subsequently used in the retrieval processing. We show that this reduction is possible without significant decrease in performance compared to using many more (order 2000) channels. The clearly improved performance of the joint algorithm compared to more specific retrieval setups is exemplified as well. Finally, the application of the algorithm to AIRS (Advanced Infrared Sounder) data, a next step planned, is addressed.

Introduction

The IASI (Infrared Atmospheric Sounding Interferometer) instrument will be part of the core payload of the METOP series of polar-orbiting operational meteorological satellites currently prepared for EUMETSAT (first satellite to be launched in 2005). IASI is a Michelson type fourier transform interferometer which samples a part of the infrared spectrum contiguously from 645 cm^{-1} to 2760 cm^{-1} ($\sim$3.6 μm - 15.5 μm) with an unapodized spectral resolution of 0.25 cm^{-1}. Compared to existing operational satellite radiometers, this high spectral resolution instrument allows significantly improved accuracy and vertical resolution of retrieved temperature and humidity profiles, and also delivers ozone profiles and sea surface temperature (SST). The intsrument is also designed for detection of additional trace gases and improved cloud characterization.

In this study, simulated IASI measurements are used to estimate temperature and humidity profiles and the surface skin temperature. We used the fast radiative transfer model RTIASI for forward modeling and simulating the IASI measurements (see subsection *Forward Modeling*). Due to performance and numerical reasons a fast channel selection method based on information content theory, which leads to a reduction of the total number of IASI channels ($>$8400) to about 3 % only ($\sim$250), is introduced in the subsection *Channel reduction procedure*. The retrieval of the atmospheric variables is prepared by following the Bayesian approach for an optimal combination of *a priori* data and new measurements using a fast converging iterative optimal estimation algorithm (Rogers, 2000) (see subsection *Retrieval Algorithm*). The retrieval algorithm is applied to a quasi realistic METOP/IASI orbit track for September 15, 1999. Results for this case study are presented in the section *Results*. A summary of the work presented here as well as suggested improvements and future steps on the IASI retrieval problem are given in the section *Summary and Outlook*.

Data Simulation and Retrieval Methodology

We briefly describe our retrieval scheme in this section, the forward modeling involved, main aspects of the retrieval algorithm itself, and the important procedure of information content based channel reduction. The description follows (Lerner et al., 2002), and (Weisz et al., 2003) and more details can be found there. Those earlier studies used the same methodology as applied here but were linked to the development of single parameter (temperature-only and humidity-only) retrieval schemes.

Forward Modeling

For a successful retrieval of atmospheric parameters within the framework of an optimal estimation approach as adopted here, the underlying physics of the measurement needs to be properly modeled by a forward model solving the radiative transfer equation. At the same time, a proper modeling of the "Jacobian matrix" (also termed "weighting function matrix", i.e., the derivative of the forward model with respect to the state vector) is quite important, especially with regard to computational efficiency, since non-linearities in the problem of interest demand an iterative state estimation. The general forward model equation mapping the atmospheric state into the measurement space (satellite-measured radiance spectrum) has the form (Rogers, 2000):

$$\mathbf{y} = \mathbf{F}(\mathbf{x}) + \epsilon, \tag{1}$$

where $\mathbf{y}$ is the measurement vector, $\mathbf{F}(\mathbf{x})$ is the forward model operator for a given state $\mathbf{x}$, and ϵ is the measurement error. The measurement error characteristics should be known in terms of systematic biases and random instrument noise. The measurements $\mathbf{y}$ should in fact be corrected for biases before using them in the retrieval to characterize ϵ statistically well by a measurement error covariance matrix. Inserting reasonable test profiles for temperature and humidiy, equation (1) was used to confirm that the present retrieval problem is moderately non-linear only, i.e., we can apply equation (1) in a linearized form by replacing:

$$\mathbf{y} = \mathbf{F}(\mathbf{x}) \qquad \Longrightarrow \qquad (\mathbf{y} - \mathbf{y}_0) = \mathbf{K}_0(\mathbf{x} - \mathbf{x}_0), \tag{2}$$

where $\mathbf{K}_0 = \partial\mathbf{F}(\mathbf{x})/\partial\mathbf{x}\,|_{\mathbf{x}=\mathbf{x}_0}$ is the Jacobian Matrix (evaluated at state $\mathbf{x}_0$) and $\mathbf{x}_0$ is a suitable reference state (Rogers, 2000).

For simulating the measurement vector and calculating $\mathbf{F}(\mathbf{x}) = \mathbf{T}_B$ ($\mathbf{T}_B$: brightness temperature) and the Jacobians $\mathbf{K}_0$, the fast radiative transfer model RTIASI (Matricardi and Saunders, 1999) was used, which uses temperature, humidity, and ozone profiles and some surface parameters (e.g., surface skin temperature, surface air temperature, etc.) as input and then furnishes simulated IASI brightness temperature measurements and Jacobians of the input atmospheric species for any desired subset of IASI channels. This model calculates level-to-space transmittances on 43 fixed pressure levels spanning from 0.1 hPa (∼65 km height) to surface. We used these same levels, the so called "ATOVS pressure level grid", also as our retrieval grid (all 43 levels for temperature, the lowest 28 levels for humidity).

Retrieval Algorithm

We approach the inverse problem associated with equation (2), i.e. the retrieval of temperature and humidity profiles and of SST $\mathbf{x}$, from brightness temperature measurements, $\mathbf{y}$, by the concept of Bayesian optimal estimation described in detail by (Rogers, 2000). With the assumption of Gaussian probability distributions and a linearized forward model, we choose a fast converging iterative optimal estimation algorithm (Rogers, 2000):

$$\mathbf{x}_{i+1} = \mathbf{x}_{ap} + \mathbf{S}_i\mathbf{K}_i^T\mathbf{S}_\epsilon^{-1}\left[(\mathbf{y} - \mathbf{y}_i) + \mathbf{K}_i(\mathbf{x}_i - \mathbf{x}_{ap})\right], \tag{3}$$

where the subscript *i* is the iteration index. $\mathbf{x}_{i/i+1}$ and $\mathbf{x}_{ap}$ are the iterated and *a priori* state vectors, respectively ($\mathbf{T}$, $\ln\mathbf{q}$, and SST combined in one state vector), and $\mathbf{S}_i$ is the retrieval error covariance matrix, defined by:

$$\mathbf{S}_i = \left[\mathbf{S}_{ap}^{-1} + \mathbf{K}_i^T\mathbf{S}_\epsilon^{-1}\mathbf{K}_i\right]^{-1}. \tag{4}$$

Here $\mathbf{S}_{ap}$ is the *a priori* error covariance matrix. The optimization scheme expressed by equation (3) is usually termed the Gauss-Newton method and provides a reliable maximum *a posteriori* estimate for

"small residual" inverse problems as the one dealt with here (Rogers, 2000). In applying equation (3), the iteration was initialized with $\mathbf{x}_0 = \mathbf{x}_a$ and state estimate $\mathbf{x}_i$, measurement estimate $\mathbf{y}_i = \mathbf{F}(\mathbf{x}_i)$, weighting function matrix $\mathbf{K}_i = \partial\mathbf{F}(\mathbf{x})/\partial\mathbf{x}\,|_{\mathbf{x}=\mathbf{x}_i}$, and retrieval error covariance estimate $\mathbf{S}_i$, were updated at each iteration step *i* until the convergence criteria were reached.

Dependent on the quality of the *a priori* profile, the first or the first two steps may need special aid with convergence due to linearization errors, which is often dealt with in extending the Gauss-Newton scheme to the Levenberg-Marquardt scheme (Rogers, 2000; Rieder and Kirchengast, 1999). We utilized the more simpe but for the present purpose equivalently effective extension introduced by (Liu et al., 2000) termed the "D-rad" method. This method leaves equation (3) unchanged, just $\mathbf{S}_\epsilon$ is modified in its diagonal according to:

$$\mathbf{S}_\epsilon(n,n) = max\left[\frac{(\mathbf{y}(n) - \mathbf{y}_i(n))^2}{\alpha}, \sigma_i^2(n)\right] \tag{5}$$

where *i* is the iteration index, $\mathbf{y}(n)$ is the measurement value of channel n, $\mathbf{y}_i(n) = F_n(\mathbf{x}_i)$ is the forward model measurement, α is a (free) control parameter set to 4 for this study, and $\sigma_i^2(n)$ is the variance of the measurement noise for channel n (the original $\mathbf{S}_\epsilon(n,n)$ values). (Liu et al., 2000) found the "D-rad" extended Gauss-Newton algorithm to perfom equally well or better than the Levenberg-Marquardt algorithm in aiding convergence when a poor initial guess profile was given.

A Priori error Covariance Matrix

For the elements of $\mathbf{S}_{ap}$ we used an auto-regressive model variant and adopted $\mathbf{S}_{ap}$ to be non-diagonal such that there exists inter-level correlation and the non-diagonal components fall off exponentially from the diagonal, i.e.:

$$\mathbf{S}_{ap}(i,j) = \sigma_i\sigma_j \exp\left[-\frac{|z_i - z_j|}{L}\right], \tag{6}$$

where σ_i and σ_j are the standard deviations at height (log pressure) levels z_i and z_j, respectively, and L is the correlation length. For temperature $L = 6$ km was set and the standard deviation settings were devided into 3 latitude regions – 0° to 30°, 30° to 60°, and 60° to 90° – with the specifications given in table 1. For humidity we have $L = 3$ km and the standard deviation values grow from 20% at surface to 100 % at 500 hPa, then they are staying constant until 300 hPa and decrease to 50 % at 100 hPa (the shape of the curve was set in this way to approximately satisfy the ECMWF standard deviations for humidity).

pressure [hPa]	temperature errors [K]		
	0° - 30°	30° - 60°	60° - 90°
1.00	6.0	8.0	9.0
50.00	1.5	2.0	2.5
1013.25	1.5	2.0	2.5

Table 1: Standard deviation values for the temperature *a priori* error covariance matrix.

Measurement Error Covariance Matrix

In order to create an appropriate (and consistent) measurement error covariance matrix $\mathbf{S}_\epsilon$, we assumed the squared IASI 1c noise values (obtained from Peter Schluessel, EUMETSAT, personal communications, 2000) to be our diagonal elements. Since they are specified at a reference temperature $T_r = 280$ K the values are modified according to the actual brightness temperture, based on the Planck law. The temperature factor to be multiplied by the noise values is evaluated in form of (z_1/z_2) with:

$$z_1 = T_B^2 \exp\left[\frac{c_2\nu}{T_r}\right] \exp\left[\frac{2c_2\nu}{T_B}\right], \tag{7}$$

$$z_2 = T_r^2 \exp\left[\frac{2c_2\nu}{T_r}\right] \exp\left[\frac{c_2\nu}{T_B}\right], \tag{8}$$

where ν is the wavenumber and $c_2 = hc/k$ is the second radiation constant. Finally the temperature modified 1c noise values are superposed with an 0.2 K forward model error value to roughly account for errors in the forward model ((Collard, 1998), (J. Eyre, The Met. Office, personal communications 2000)). The impact of the RTIASI forward model error on the IASI retrieval accuracy is described in (Sherlock, 2000). Figure 1, bottom, shows the raw IASI 1c noise values and the modified values, according to a brightness temperature calculated for the U.S. standard mid-latitude summer profile.

For the off-diagonal elements we assume a correlation c_{ij} between the three nearest neighboring channels of 0.71, 0.25, and 0.04, according to $S_{ij} = c_{ij}\sqrt{S_{ii}S_{jj}}$, which we also have to account for in $\mathbf{S}_\epsilon$. This produces a covariance matrix with a rather steep descent from the main diagonal (Peter Schluessel, EUMETSAT, personal communications, 2000).

Simulation of the measurement vector

Since we do not have true measurements, we add a random noise factor $\Delta\mathbf{y}$ to the simulated measurements in order to generate quasi realistic data. For the noise modeling (receipt obtained from Peter Schluessel, personal communications, 2000) we first create normally distributed random numbers with standard deviation values according to the diagonal elements of the measurement error covariance matrix. Since RTIASI calculates apodized radiances and brightness temperatures, respectively, we apodize this noise with a Gaussian function of a full width at half maximum of 0.5 cm^{-1} ($\sigma = 0.212$ cm^{-1}). The resulting values are shown in Figure 1,top.

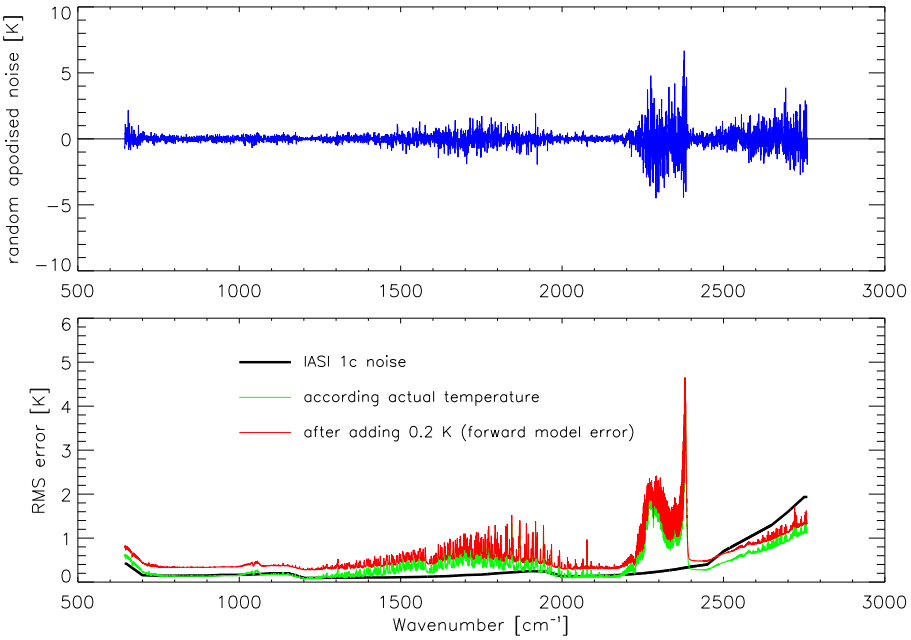

Figure 1: Top: Random apodized noise values versus wavenumber. Bottom: Square roots of the diagonal elements of the measurement error covariance matrix $\mathbf{S}_\epsilon$.

Channel Reduction Procedure

Since the full IASI spectra contain 8461 channels it is essential to reduce this number and somehow remove redundant information for computational and performance reasons. Hence, our task is to find a subset of channels which is sufficiently sensitive to the retrieved variables. Therefore we remove the channels above 2500 cm^{-1} (spectral range $< 4\ \mu m$ – here residual solar contribution becomes important) and those channels whose "foreign" gas emissions contribute significantly to the measured brightness temperature (i.e., 975.0 cm^{-1} - 1100 cm^{-1}, 1220 cm^{-1} - 1370 cm^{-1}, and 2085 cm^{-1} - 2200 cm^{-1}). At this point we have still about 5700 channels, which is still too much for our purpose.

Therefore we perform a further reduction of the number of channels by utilizing two different methods: the information contnent theory and the maximum sensitivity approach.

In information content theory one seeks to know how much information is contained in a possible outcome by knowing it. If we select the channels sequentially by retaining the channels with highest information content (H) and removing them from subsequent calculations, we may write:

$$H_i = \frac{1}{2} \log_2 \left| \mathbf{S}_{i-1} \mathbf{S}_i^{-1} \right|, \tag{9}$$

where $\mathbf{S}_{i/i-1}$ is the retrieval error covariance matrix. For $\mathbf{S}_0$ the *a priori* error covariance matrix $\mathbf{S}_{ap}$ was used.

As a simplified and faster alternative of using information content theory we can also use an approach, which is solely based on the weighting function matrix scaled by the measurement errors. It is desireable to selectively choose those channels whose instrument noise is small or the measurement sensitivity to temperture an humidity perturbation is high. This is achieved by using the following channel selection criterion which maximizes the sensitivity-to-error ratio, a matrix denoted by $\mathbf{H}$:

$$\mathbf{H} = \mathbf{S}_\epsilon^{-\frac{1}{2}} \mathbf{K}, \tag{10}$$

where $\mathbf{S}_\epsilon$ is again the measurement error covariance matrix (with dropping the non-diagonal elements for this purpose) and $\mathbf{K}$ is the Jacobian Matrix.

Results

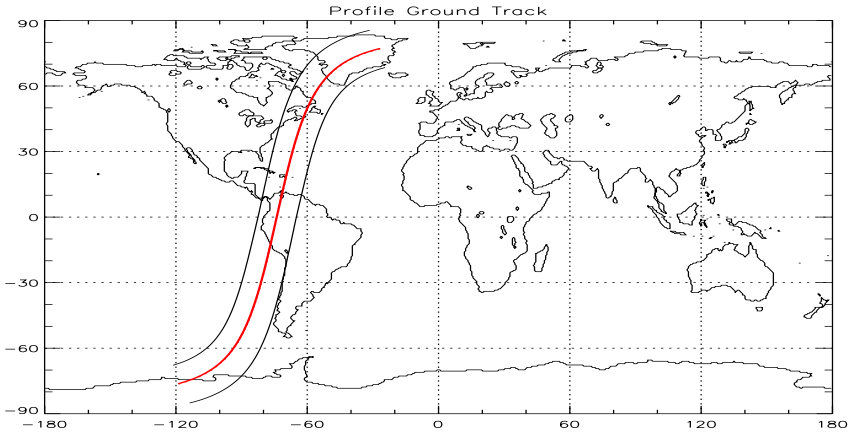

Figure 2: Simulated quasi-realistic swath of the IASI instrument. The red line delineates the suborbital track for which retrieval performance examples are shown.

The algorithm was tested for a quasi-realistic orbit arc of metop with a full swath of the IASI instrument (more than 10000 profiles) with an ECMWF analysis field of September 15, 1999, 12 UTC, as ”true” field (see left plots of Figure 3 for temperture, Figure 5 for humidity, and Figure 7 for SST), and the 24h forecast of this analysis as first guess (see right plots of Figure 3 for temperture, Figure 5 for humidity, and Figure 7 for SST – these are the *a priori*-minus-true plots). The simulation region (Figure 2) covers the western Atlantic Ozean and is also situated over the Humboldt stream. Parts of Greenland and of the Americas are covered as well. The red line shows the ground track of the quasi-nadir profiles which are shown as exemplary results of our simulation study.

The simulation study was done under clear air conditions. We emphasize on showing the significantly improved performance of the joint retrieval algorithm compared to the more specific temperature, humidity, and SST only retrievals (see Figure 4, Figure 6, Figure 8).

Another aspect highlighted is that there is no significant loss in the retrieval performance if one chooses fairly few channels (about 250) compared to many channels (about 2000).

Temperature Results

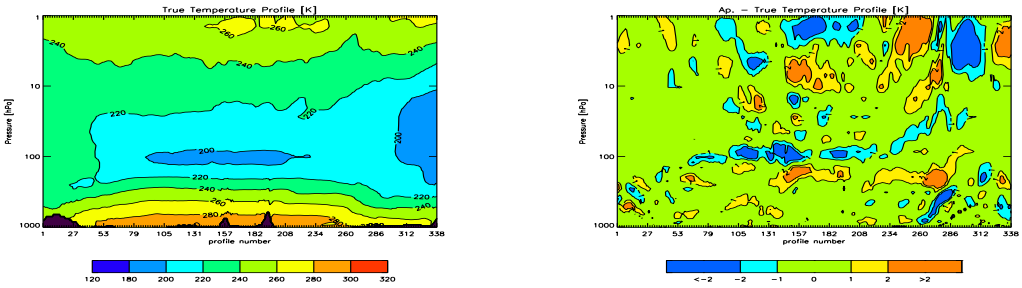

Figure 3: Left: ”True” temperature profiles. Right: *A priori*-minus-true temperature profiles.

Figure 4, top left, shows the estimated temperature where IC (information content theory approach) with about 250 channels was used for channel selection. Comparing it with Figure 4, top right, where MS (maximum sensitivity approach) with few channels (also about 250 channels) was used, we can see that there is almost no difference between them. The MS approach is simpler and slightly faster than the IC approach but there is essentially no difference in performance, so if concerned about efficiency one might choose the simpler MS approach.

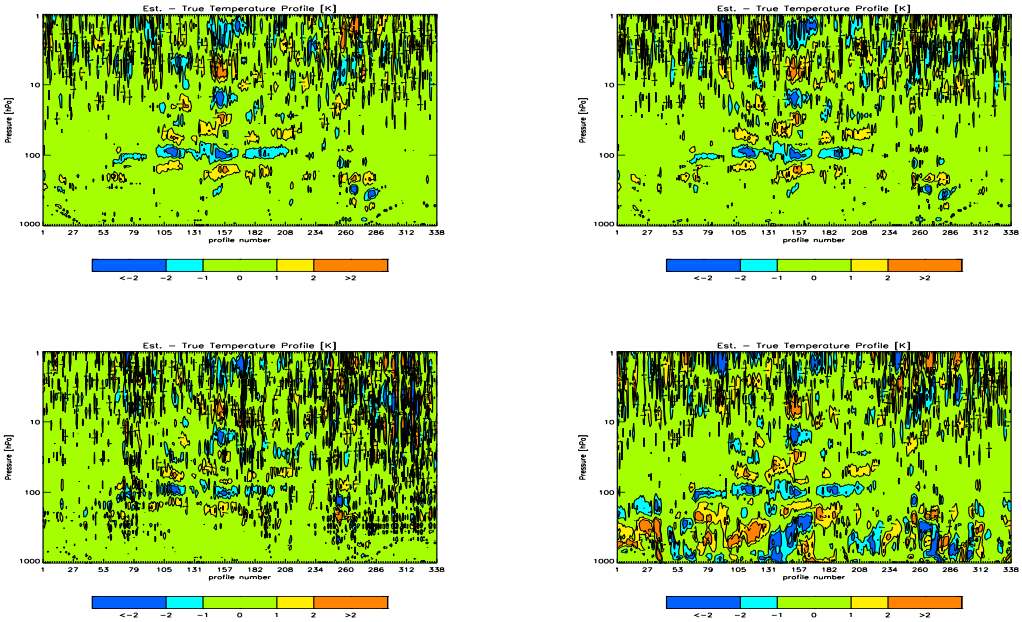

Figure 4: Estimated-minus-true temperature profiles. Top left: IC with few channels, top right: MS with few channels, bottom left: IC with many channels, bottom right: temperature-only retrieval.

Figure 4, bottom left, shows the estimated temperature for IC with many channels ($\sim$2000). One can see that using few channels in the retrieval results in no significant loss of information. Figure 4,

bottom right, shows the results for a temperature only retrieval. Here we recognize that the absence of the humidity retrieval produces a highly negative impact in the retrieval performace.

Humidity Results

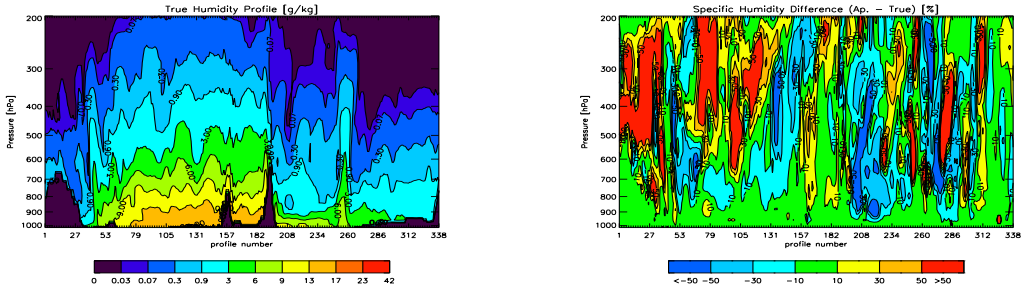

Figure 5: Left: ”True” humidity profiles. Right: *A priori*-minus-true humidity profiles.

For the results of the different humidity retrievals nearly the same things as for the temperature retrievals can be said (see Figure 6). The not-so-bad result for the humidity-only retrieval is caused by a good choice in the temperature *a priori* profiles.

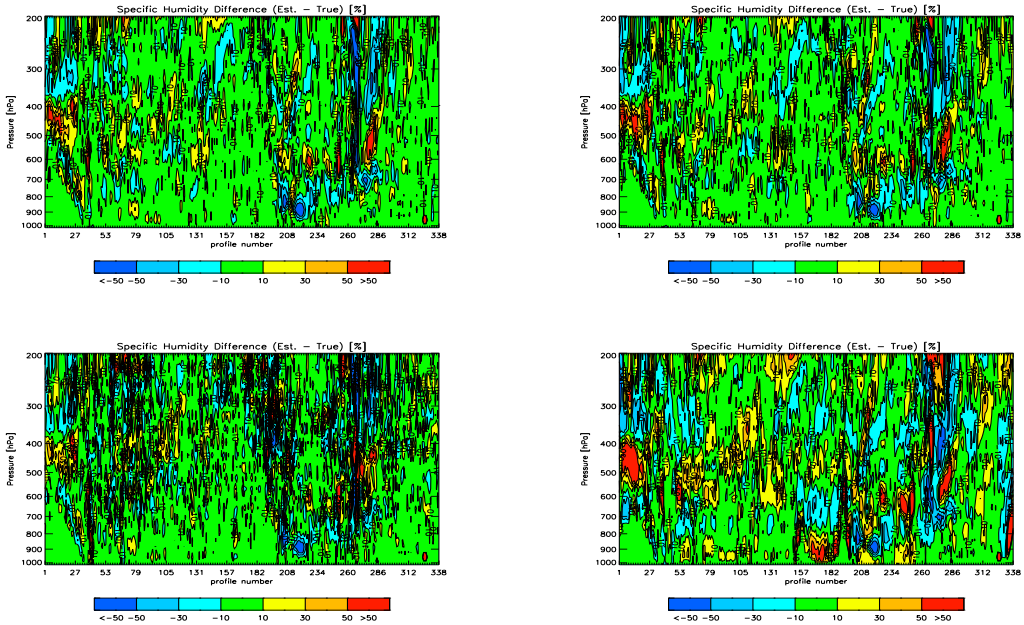

Figure 6: Estimated-minus-true humidity profiles. Top left: IC with few channels, top right: MS with few channels, bottom left: IC with many channels, bottom right: humidity-only retrieval.

We tested also a joint temperature-humidity profile retrieval between 200 hPa and 500 hPa, a region of special interest to us, in order to check wether the estimated humidity becomes better and significantly faster because of a more limited to channel selection for this region. It turned out, however, that this upper-troposphere-focused approach was only very moderately faster and, in particular, the retrieval performance degraded.

Sea Surface Temperature Results

To get a reasonably ”bad” first guess for the SST (sea surface temperature) we perturbed the true SST with 3 K to demonstrate the performance of our retrieval algorithm for SST since generally the 24 hour forecast is clearly very close to the analyzed SST.

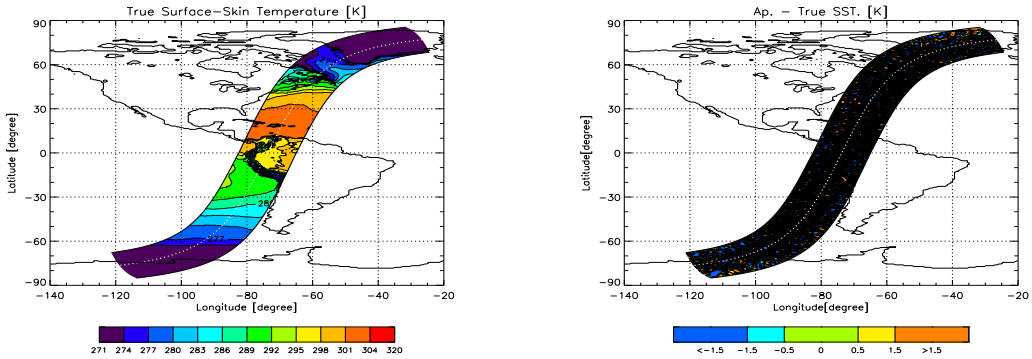

Figure 7: Left: ”True” sea surface temperature. Right: *A priori*-minus-true sea surface temperature.

Figure 8, left, illustrates the quite improved performance of the joint algorithm compared to an SST-only retrieval (Figure 8, right). A further confirmation of this can be seen in the comparison of the average error bar plots for the joint and SST only retrieval (Figure 9, top left and right). The error bars of the SST-only retrieval show quite big rms errors and have also marked biases, which do not occure in the case of the joint retrieval. The comparison of the error bars between IC with few channels (Figure 9, top left) and IC with many channels (Figure 9, bottom) reflects that there is only very moderately accuracy gain in the use of many channels in the joint retrieval to get a good result for the SST retrieval given the very significant increase in computational cost for $\sim$2000 channels relative to $\sim$ 250 channels.

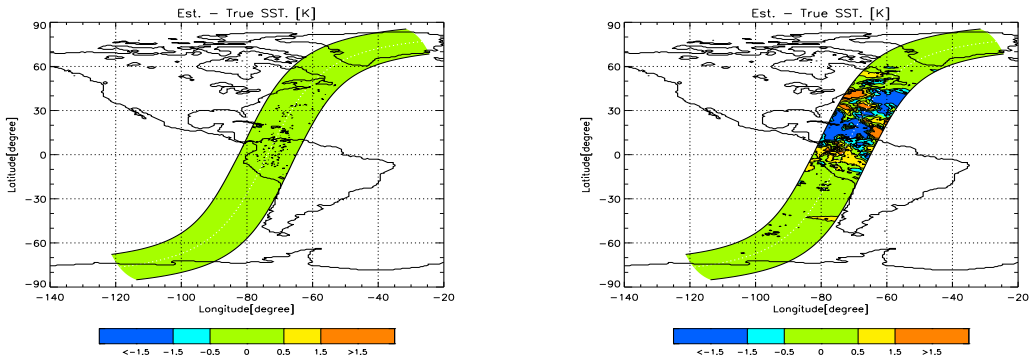

Figure 8: Estimated-minus-true sea surface temperature. Left: Joint $\mathbf{T}$, $\mathbf{q}$, and SST retrieval. Right: SST-only retieval.

Summary and Outlook

We presented a retrieval algorithm for determining temperature, humidity and SST from radiance measurements made by the IASI instrument, scheduled for launch onboard of the METOP weather satellite series (first satellite to be launched in 2005). Main features are a sensible channel reduction procedure followed by an iterative optimal estimation retrieval. The channel reduction algorithm based on the information content theory makes the retrieval efficient – the procedure results in a reduction of the number of channels from more than 8400 to about 3% only ($\sim$250 channels). The retrieval performance does

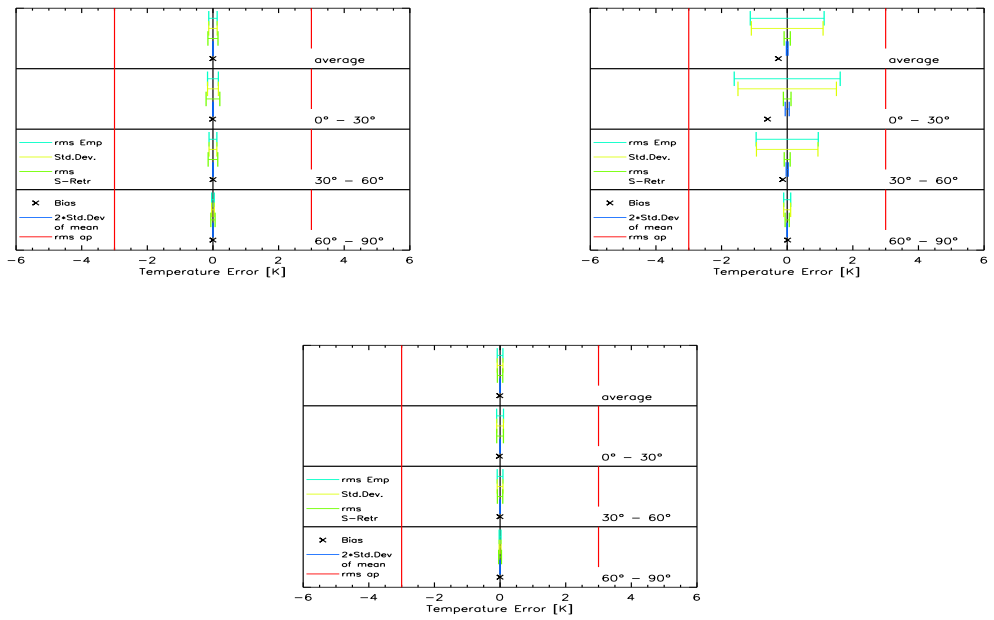

Figure 9: Top Left: SST error analysis for joint retrieval – IC, few channels. Top Right: Error analysis for SST-onl Retieval. Bottom: SST error analysis for joint retrieval – IC, many channels.

not significantly degrade due to this reduction. We also showed that the joint algorithm leads to a clearly improved perfomance compared to more specific retrieval setups, such as temperature-only or SST-only retrievals.

We obtain a retrieval accuracy of about 1 K in temperature and 15% in humidity with a vertical resolution of 1 km to 3 km in the troposphere. For the stratosphere we found that *a priori* data exhibit important influence. Some challenging areas arose in the mid-latitude regions and at heights with weak sensitivity of the weighting functions (e.g., the tropopause).

The results of this study provide guidance for further advancements. Our current and future work plan includes improvements of the *a priori* covariance matrices for temperature and humidity (e.g., usage of the the relevant ECMWF *a priori* covariance matrices) and cross-testing the algorithm with another ground track region and alalysis. Furthermore we work to complete the joint algorithm by including as well the retrieval of ozone profiles.

As a future step towards real data, the completed temperature, humidity, ozone, and SST algorithm will then be applied to AIRS (Advanced Infrared Radiation Sounder) data, where our domain of particular interest is the upper troposphere and its climatic variability in humidity and temperature.

Acknowledgments

We thank E. Weisz (SSEC, Univ. of Wisconsin, Madison, WI, U.S.A.) for valuable discussions on retrieval methodology and U. Foelsche (IGAM, Univ. of Graz, Austria) for support with acquisition and preprocessing of ECMWF fields. The work of M. S. was financed by the START research award of G. K., financed by the Austrian Ministry for Education, Science, and Culture and managed under Program No. Y103-N03 of the Austrian Science Fund.

References

Collard, A. D. (1998). Notes on IASI Performance. *Forecasting Research Technical Report No. 256*.

Lerner, J. A., Weisz, E., and Kirchengast, G. (2002). Temperature and humidity retrieval from simulated Infrared Atmospheric Sounding Interferometer (IASI) measurements. *Journal of Geophysical Research*, 107(10.1029/2001JD900254).

Liu, X., Zaccheo, T. S., and Moncet, J.-L. (2000). Comparision of Different Non-Linear Inversion Methods for Atmospheric Profiles. In *Proceedings of the* 10^{th} *Conference of Satellite Meteorology*, pages 293–295.

Matricardi, M. and Saunders, R. (1999). A fast radative transfer model for simulation of Infrared Atmospheric Sounding Interferometer radiances. *J. Appl. Optics*, 38:5679–5691.

Rieder, M. and Kirchengast, G. (1999). Physical-statistical retrieval of water vapor profiles using SSM/T-2 sounder data. *Geophys. Res. Lett.*, 26:1397–1400.

Rogers, C. D. (2000). *Inverse Methods for Atmospheric Sounding: Theory and Practice*. World Scientific Publ.

Sherlock, V. J. (2000). Results from the first U.K.MO IASI Radiative Transfer Model Intercomparison. *Forecasting Research Technical Report No. 287*.

Weisz, E., Kirchengast, G., Schwaerz, M., and Lerner, J. A. (2003). An efficient channel selection method for Infrared Atmospheric Sounding Interferometer data and characteristics of retrieved temperature profiles. *Wissenschaftl. Ber. No. 15*, page 32pp.

SIRAS-G, The Spaceborne Infrared Atmospheric Sounder: The Potential for High-Resolution IR Imaging Spectrometry From Geosynchronous Orbit

Thomas U. Kampe
Ball Aerospace & Technologies Corp.
1600 Commerce St.
Boulder, Colorado USA

Abstract
The Spaceborne Atmospheric Infrared Sounder for Geosynchronous Earth Orbit (SIRAS-G) represents a new approach to infrared atmospheric sounding of the Earth from geosynchronous orbit. SIRAS-G, one of nine proposals selected for development under NASA's 2002 Instrument Incubator Program, is an instrument development effort for an instrument of less mass and power than heritage sounding instruments that offers enhanced capabilities for the measurement of atmospheric temperature, water vapor profiles, and trace gas column abundances. The SIRAS-G flight instrument concept is designed to measure infrared radiation in 2048 spectral channels with a nominal spectral resolution ($\Delta\lambda/\lambda$) of 1100. Combined with large area 2-D focal planes, this system simultaneously provides both high-resolution spectral and spatial imaging. In 1999, the SIRAS team built and tested the LWIR (12.0 – 15.4μm) SIRAS spectrometer under NASA's Instrument Incubator Program (IIP-1999). SIRAS-G builds on this experience with a goal of producing and demonstrating a laboratory prototype instrument. In this paper, we describe planned development activities and potential future scientific instrument applications for this instrument concept.

Introduction
The Spaceborne Infrared Atmospheric Sounder for Geosynchronous Earth Orbit (SIRAS-G) is an instrument concept designed to provide highly accurate atmospheric temperature and water vapor profile measurements from geosynchronous orbit (GEO) to facilitate weather forecasting, severe storm tracking, and scientific research. The flight instrument concept measures infrared radiation in 2048 channels extending from 3.7μm to 14.8μm with a spectral resolution ($\lambda/\Delta\lambda$) of 700 to 1100. As currently envisioned, large format 512 x 512 (spatial by spectral), focal plane arrays (FPAs) will provide the maximum information collection given the current state of technology. SIRAS-G employs a wide field-of-view (WFOV) hyperspectral infrared optical system that splits the incoming radiation into four separate grating spectrometer channels. This allows for slow scanning of the scene, increasing dwell time, and improved radiometric sensitivity. Unlike competing technologies, such as Fourier Transform Spectrometers (FTS), the SIRAS-G grating spectrometers employ no moving parts or metrology lasers, leading to improved reliability over mission lifetime. SIRAS-G follows the successful completion of the 1999 NASA-sponsored SIRAS (Spaceborne Infrared Atmospheric Sounder) Instrument Incubator Program (Kampe and Pagano, 2002) which focused on the development of a compact LWIR spectrometer module as a potential follow-on to the Atmospheric Infrared Sounder (AIRS) instrument (Aumann et al., 2001).

NASA Instrument Incubator Program
SIRAS-G, one of nine, but the only industry-led proposal, selected for the third IIP solicitation in 2002 and is being managed by Ball Aerospace & Technologies Corp. (Ball). The NASA Instrument Incubator Program was established as a mechanism for the development of innovative technology concepts suitable for future space-borne Earth Science Enterprise (ESE) programs and as a means to demonstrate and assess the performance of these instrument concepts in ground, airborne, and engineering model demonstrations. IIP is funded through NASA's Office of Earth Sciences Technology Office (ESTO). The goals set forth for an IIP

program are to (1) develop and demonstrate mission development in less than thirty-six months; (2) develop the technology such that it is suitable for integration in an operational space instrument within eighteen months following the 3-year IIP development; (3) the instrument concepts developed under IIP must reduce instrument and measurement concept risk to allow the concept to be competitive in an Earth Science Enterprise Announcement of Opportunity; and finally, (4) the concepts shall enable new science and/or reduce instrument cost, size, mass and resource use. More information on the Instrument Incubator Program can be found at *http://esto.gsfc.nasa.gov/programs/iip/*.

SIRAS-G Overview

The SIRAS-G IIP effort will focus on advancing the SIRAS instrument concept for insertion into future Earth Science missions and on developing an engineering demonstration instrument. While the SIRAS-G hardware demonstration instrument is primarily intended as a laboratory demonstration, it will be built sufficiently robust to be upgradeable to an airborne instrument. As part of this program, a series of engineering studies will be conducted to demonstrate the applicability of SIRAS-G to a variety of critical earth remote sensing needs.

SIRAS-G builds on the success of the earlier SIRAS-1999 IIP effort. Here we successfully demonstrated a compact long wavelength infrared (12-15.4μm) grating spectrometer with a spectral resolution ($\lambda/\Delta\lambda$) of 900 to 1200. In SIRAS-G, we will improve on the SIRAS-1999 spectrometer by increasing the spatial FOV to provide true hyperspectral imaging capability. One of the key benefits offered by SIRAS-G is in its ability to improve the spatial resolution of future sounders while simultaneously providing high spectral resolution. This allows more opportunities for clear sky measurements in the absence of a microwave instrument; a crucial factor in improving the yield of retrieved cloud-free scenes that can be assimilated into Numerical Weather Prediction (NWP) models. As an example, for the current state of the art instrument flying, the Atmospheric Infrared Sounder, currently on NASA's Earth Observing System (EOS) Aqua satellite, Goldberg et al. (2003) found that only 4.5% of fields observed over oceans exhibited less than 0.6% cloud contamination. This is largely attributable to the relatively large footprint (13.5-km) of AIRS, which is flying in Low Earth Orbit (LEO). SIRAS-G, on the other-hand, is being designed for a 4-km footprint from GEO, and a LEO version of the same instrument concept would yield a 0.5-km footprint.

SIRAS-1999 Results

In 1999, the NASA JPL-lead SIRAS team undertook the development of an advanced instrument concept as a potential replacement for AIRS. This instrument concept is referred to as SIRAS-1999. The original SIRAS-1999 instrument concept was designed to meet the requirements of AIRS, but in a smaller package and with improved spatial resolution (0.5-km vs. AIRS 13.5-km). This effort focused on the development the SIRAS flight instrument concept suitable for LEO and the development of a hardware demonstration of the SIRAS LLWIR (12-15.4 μm) spectrometer (Spectrometer No. 4 in Table 1). A high-resolution infrared imaging spectrometer was built and tested at cryogenic temperatures in a laboratory environment. A detailed study of the size, mass, and power of a SIRAS-L (Low Earth Orbit) instrument configuration was also performed. Finally, it was demonstrated that the same spectrometer could meet the requirements of a GEO sounder. A system concept was developed that included scanning, passive and active cooling systems, the infrared spectrometers, fore-optics and the focal plane arrays offering a system of comparable performance, yet with considerable size, mass, and power savings. Reductions in subsystem complexity through modular design, the use of standard format FPAs and low-order gratings results in significant cost reductions when compared to AIRS.

The flight instrument concept developed in SIRAS-1999 has four spectrometer modules that cover the 3.4 to 15.4 μm spectral region with the spectral bands broken out as shown in Table 1. A barrel scan mirror provides the ground coverage, and an all-reflective fore optic serves to focus the scene energy onto the slit. Scene energy was then split into four separate spectrometer modules via beamsplitters. The requirement for low background required that the spectrometer modules be cryogenically cooled to 140 K, and the focal planes to 60 K. Active cooling of the detectors was proposed for the flight instrument configuration using a split-Stirling pulse-tube cooler.

Table 1. Preliminary Design Parameters for SIRAS

Parameter		Spectrometer Number			
		1	2	3	4
λ_{min}	(μm)	3.7	6.2	8.8	12
λ_{max}	(μm)	4.61	8.22	12	15.4
$\lambda/\Delta\lambda$ Avg. Sampling		2200	2200	2200	2200
$\lambda/\Delta\lambda$ Avg. Resolution		1100	1100	1100	1100
Ruling	(μm)	8	14	10	13
Order	(-)	2	2	1	1
λ_{blaze}	(μm)	8.31	14.42	10.40	13.70
Incidence Angle	(deg)	45	45	45	45
Avg. Disp	(rad/μm)	0.2677	0.1534	0.1082	0.0832
Field of View	(deg)	13.957	17.752	19.844	16.201
Detector IFOV	(mr)	0.500	0.500	0.500	0.500
Slit IFOV	(mr)	1.000	1.000	1.000	1.000
EFL	(cm)	5.00	5.00	5.00	5.00
F-Number	(-)	1.70	1.70	1.70	1.70
Aperture Size	(cm)	2.94	2.94	2.94	2.94
Resolution	(mr)	0.1723	0.2991	0.4314	0.5683
Detector Size	(μm)	25	25	25	25
No. Channels	(-)	487	620	693	566
Transmission	(-)	0.5	0.5	0.5	0.5
FPA-Length	(cm)	1.22	1.55	1.73	1.41

The laboratory spectrometer developed on this program is shown in Figure 1. The spectrometer measures 10 x 10 x 14 cm and weighs only 2.03 kg. For the purposes of laboratory measurements, a PV HgCdTe multiplexed detector array was provided on loan from the AIRS program. All hardware development and testing was performed at BALL. The most challenging optical system was the camera. This fast (F/1.7) optical system required near diffraction-limited performance over a wide field-of-view.

Key results from the SIRAS-1999 program included demonstration of the performance of the SIRAS spectrometer concept, including:

1. Demonstrated optical quality and spectral resolution consistent with the required resolving power ($\lambda/\Delta\lambda$) between 900 and 1400.
2. Demonstrated that the optical transfer function (spatial performance) required to perform as an accurate radiometer in the presence of high scene contrast (referred to as the Cij requirement on AIRS) was achieved.
3. Demonstrated that the high optical throughput required meeting the NEdT requirement could be achieved.
4. Demonstrated a spectrometer system of significantly reduced size, weight, and volume but of comparable performance to that of AIRS.

The entry point for SIRAS-1999 IIP was TRL 3. The TRL level of the SIRAS-1999 spectrometer on completion was 5.

Spectrometer-level testing was performed in a thermal vacuum chamber operating at cryogenic temperatures. Thermal sources were viewed through a zinc selenide window and included a collimator and source assembly for spatial performance tests, and a blackbody for radiometric performance testing. Spectral measurements

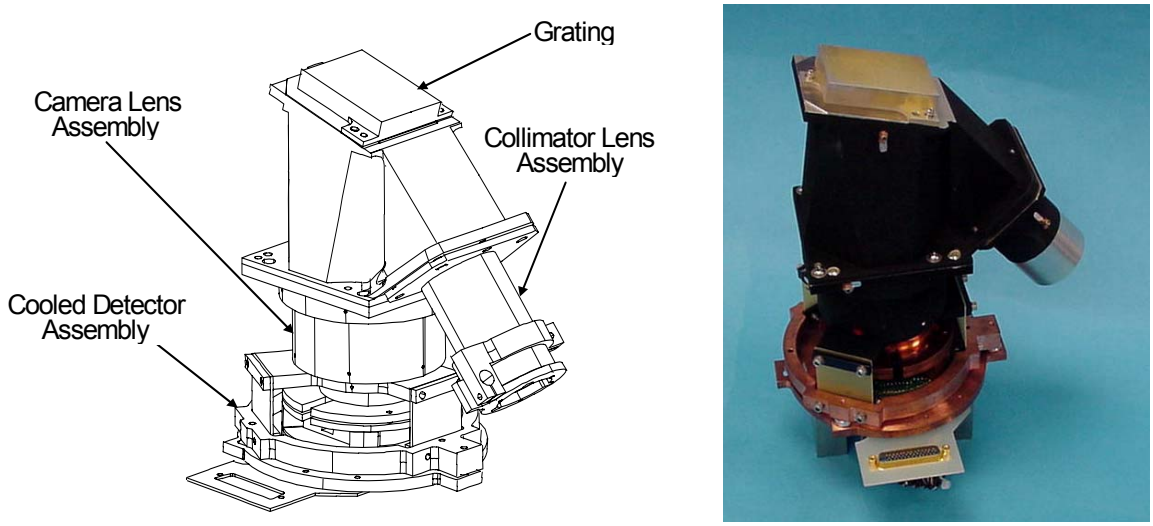

Figure 1. SIRAS-1999 IIP spectrometer design (left) and as-built configuration (right).

were made by adjusting the air path length between the test thermal/vacuum chamber and the blackbody, and then measuring the CO_2 absorption features.

Figure 2 shows the results of the air path test. The data were analyzed for spectral resolution by comparing them to theoretical atmospheric transmission spectra for a 3-meter path length with varying spectral response widths. The response widths were varied until the resulting convolved modeled spectra matched the measured spectra. The results show that the SIRAS-1999 spectral resolution is 1200 ± 300.

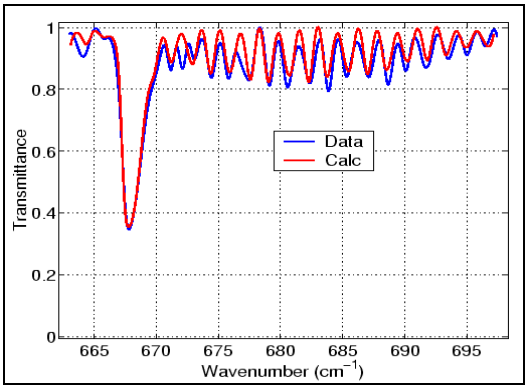

Figure 2. SIRAS-1999 measurements of laboratory air confirmed that spectral resolution was achieved.

SIRAS-G IIP Program Objectives

The SIRAS-G spaceborne instrument is being developed to address several high priority research topics identified in NASA's ESE Research Strategy for 2000-2010. The high spectral resolution and compact size of SIRAS-G make it broadly applicable to a wide range of future missions. Key ESE research topics that SIRAS-G is targeted toward include:

How are global precipitation, evaporation, and the cycling of water changing?

SIRAS-G will make measurements similar to those currently being made by AIRS but from GEO. It will provide measurements of atmospheric temperature and water vapor, cloud properties, and land and ocean skin temperatures, with the accuracy and spectral resolution required for numerical weather prediction models. The goal is for SIRAS-G to provide significantly more rapid revisit time (6 minutes regional) and higher spatial resolution (4-km compared to 13.5-km for AIRS). These are well suited to addressing weather forcing factors on shorter time scales. Without synergistic microwave instruments, SIRAS-G will require ancillary data from the National Center for Environmental Prediction (NCEP), the European Center for Medium Range Weather Prediction (ECMWF) or other surface analysis data to retrieve cloud properties. Such retrieval methods have been developed by the AIRS Science Team as contingency algorithms to be

used in case of ASMU failure. SIRAS-G offers a pathway to providing a continuous long-term data set complementary to that currently being provided by AIRS.

What are the effects of regional pollution on the global atmosphere, and the effects of global chemical and climate changes on regional air quality?

The ability of SIRAS-G to provide simultaneous observations of the Earth's atmospheric temperature, ocean surface temperature, and land surface temperature, as well as humidity, clouds, and the distribution of atmospheric trace gases enables SIRAS-G to provide a single data set that can be used to understand the horizontal and temporal changes in column abundances of important minor atmospheric gases such as CO_2, CO, CH_4, and N_2O. This capability is potentially greatly enhanced by combining SIRAS-G with a high spectral resolution ($0.05 – 0.1$ cm^{-1}) instrument such as the Imaging Multi-Order Fabry-Perot Spectrometer (IMOFPS) described in Johnson, et al (2003).

What are the consequences of climate and sea level changes and increased human activities on coastal regions?

SIRAS-G provides high spectral resolution in the atmospheric window regions in the infrared, and will be able to observe the surface temperature in these regions with minimum atmospheric absorption. This can prove to be particularly useful in coastal regions where higher atmospheric water vapor amounts may be present. With the higher spatial resolution offered by SIRAS-G, there is a higher probability of finding cloud-free regions near the coastline than with larger footprints instruments such as AIRS or the NPOESS Cross-track Infrared Sounder (CrIS).

The flight system requirements established for SIRAS-G at the proposal stage were largely based on the requirements outlined for the NOAA GOES Hyperspectral Environmental Sounder (HES) at the time of the IIP proposal submission. These requirements have evolved over time and, in fact, are now compatible with grating spectrometer instrument architecture. The systems studies that are a part of the SIRAS-G effort will continue to explore the feasibility of SIRAS-G for technology insertion into the HES program. In addition, we continue to explore other mission opportunities for which the SIRAS-G technology is suitable.

Technology Demonstration Objectives

SIRAS-G will increase the capability of the SIRAS hardware to accommodate a wide field of view (WFOV) and demonstrate the high level of performance required in a system configuration. This will be achieved by building a demonstration instrument consisting of a WFOV reflective collimator, a spectral separation subassembly, and a single grating spectrometer module. The complete SIRAS-G demonstration instrument will also incorporate an active cooler, a 256 x 256 element FPA, a low heat-load dewar, and electronics. A non-flight, laboratory grade telescope of the proper aperture and F/# will be mated to the Spectrometer Assembly for system level performance measurements including a measurement of the night sky. An unobscured reflective telescope is our baseline for the flight instrument configuration, but due to cost considerations, an obscured on-axis Ritchey-Chretrien telescope will be used for the technology demonstration instrument. We aim to build and test a nearly complete SIRAS-G instrument, including as least one spectrometer channel, moving the Technical Readiness Level (TRL) of SIRAS-G to TRL-5 or 6.

There are several challenges that will be addressed on SIRAS-G before implementation of a flight system. These include the following:

- **Spatial & Spectral Errors in Spectral Response Function (SRF):** In an imaging spectrometer such as SIRAS-G, the slit is dispersed and imaged onto an area array of detectors. This is shown conceptually in Figure 3. The introduction of distortion (keystone and smile) and variation in point-spread function (PSF) width by the optical system can cause different spectral response profiles to be obtained at each pixel. This must be controlled by constraining the allowable distortion and balancing the requirements on image

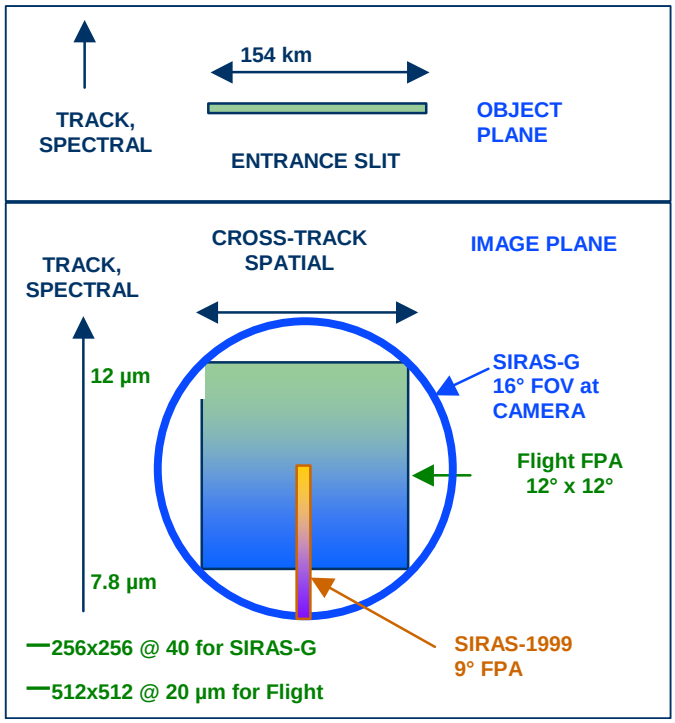

Figure 3. SIRAS-G, unlike SIRAS-1999, provides imaging over an appreciable cross-track FOV

quality, spatial and spectral distortion (Mouroulis et al. 2000). Similar control must be maintained during integration to ensure that the "as-built" instrument achieves the predicted level of performance.

- **Dewar Thermal Loads**: The increased number of cold shields (due to the use of 4 dewars and FPAs) increases parasitic cryocooler heat loads. Mitigation includes a full thermo-optical study of the loads at the dewars and the development of the dewar module for SIRAS-G. The tested and characterized dewar subsystem will be integrated into the SIRAS-G hardware demonstration instrument and tested.
- **Background thermal noise suppression**: The reduction of background flux at the detectors is key for a high performance IR system. Rigorous radiometric modeling is employed in the design process with careful attention to reducing background photon flux and controlling in-field stray light (Kampe and Waluschka 1994).
- **Co-registration of 4 Spectrometers**: Four physically separate spectrometer modules complicate the co-registration amongst channels. This concern is mitigated by using a common entrance slit and collimator and by employing temporal phase delay as done on the Moderate Resolution Imaging Spectroradiometer (Barnes et al. 1998) to allow on-orbit adjustment of residual alignment errors in the aft optics.

SIRAS-G Hardware Demonstration

A Major aspect of the SIRAS-G IIP effort will be the design, fabrication and testing of a hardware demonstration instrument. The key components of the SIRAS-G hardware demonstrator include the optical assembly (full aperture telescope, WFOV reflective collimator, spectral separation subassembly, and a single WFOV grating spectrometer module), the scan mirror assembly, an active cooler, an IR FPA, a low heat-load dewar, and associated electronics. The optical design, tolerancing and analysis for this system will be undertaken at Ball, as will all mechanical, cryogenic, focal plane and electronics engineering. .

A two-stage Ball Model BS-232 Sterling Cycle cooler, the specifications for which are listed in Figure 4, will be used on this program. A 256x256 format engineering-grade FPA with 40 µm pixel pitch will be utilized for the laboratory demonstrator. The selected device provides sufficient well depth and readout rate to support the SIRAS-G instrument requirements. A set of electronics will be supplied which provide all necessary clocks, biases and signals necessary for the operation of the FPA. The electronics will provide analog to digital conversion (14bit) for each output channel of the FPA. The electronics are programmable from a host computer. It is anticipated that a custom format FPA will be required to provide the ideal spectral sampling in the flight implementation.

SB235 Cryocooler Parameters

- **3rd Generation Multi-stage 35 K Cooler**
- **Performance: 0.5 W @ 40 K & 3.5 W @ 100 K for 90 W motor**
- **99% reliability at 10 years**
- **10.5 kg mass**
- **Verified non-contacting operation over wide temperature range (-60 to +80 ^{0}C)**
- **Active vibration isolation to below 0.10 N**
- **Fixed-regeneration cold finger capable of withstanding high side loads**
- **Inherently insensitive to 1-g orientation**
- **Proven and verified EM control features**
- **Flight-qualified 2-stage SB235**

Figure 4. Ball Aerospace & Technologies Model SB235 Cryocooler

System Configuration Studies

One of the primary objectives of the IIP is to determine the potential benefits of the technology to future ESE programs. SIRAS-G is widely applicable to a number of Earth Science Enterprise needs. As such, we have identified several key ESTO measurement parameters for which SIRAS-G is well suited. These include:

- Atmospheric temperature and water vapor profiles from GEO
- Total ozone column and precursors, cloud structure and winds, and trace gas sources from GEO
- Sea surface temperature from LEO (in addition to temperature, water vapor profiles, and cloud properties)
- Storm cell properties from an airborne platform (UAV)

In the following paragraphs, we identify several candidate future missions would benefit from the technology developed under this IIP. In many instances, SIRAS is in direct competition with interferometer-based Fourier Transform Spectrometers (FTS). Although FTS instruments exhibit very high spectral resolution over a broad spectral range, they tend to be large expensive instruments with very demanding optomechanical requirements on precision and stability, and the grating technology used by SIRAS offers an approach with potentially greater flexibility, wider field of view and smaller, lower cost sensors.

Hyperspectral Environmental Sounder. The grating technology used on SIRAS-G is well suited to the Hyperspectral Environmental Sounder (HES), the next-generation geosynchronous operational IR atmospheric sounder. With the spectrometer 1-milliradian IFOV for SIRAS-G, we currently estimate a ground footprint of ≤ 5 km would be achieved from GEO with an 8" aperture. Unlike competing technologies, SIRAS grating spectrometers have no moving parts, requires no transforms to obtain spectra, and use proven AIRS data processing algorithms.

AIRS Follow-on (SIRAS-L). Initially, SIRAS was considered as the follow-on for AIRS. The concept developed, shown schematically in Figure 5, offers the high spatial resolution of MODIS and the high spectral resolution of AIRS. SIRAS-L offers a ground footprint of less than 0.6 km (as compared to AIRS at 13.5 km) and is used in "pushbroom" mode to maximize integration time. Further studies will be undertaken in this IIP to explore the utilization of this instrument concept atmospheric sounding from LEO.

Geostationary Atmospheric Chemistry Mission. Key measurement objectives for a GEO Tropospheric Chemistry Mission include observations of ozone, aerosols, and important atmospheric trace gases

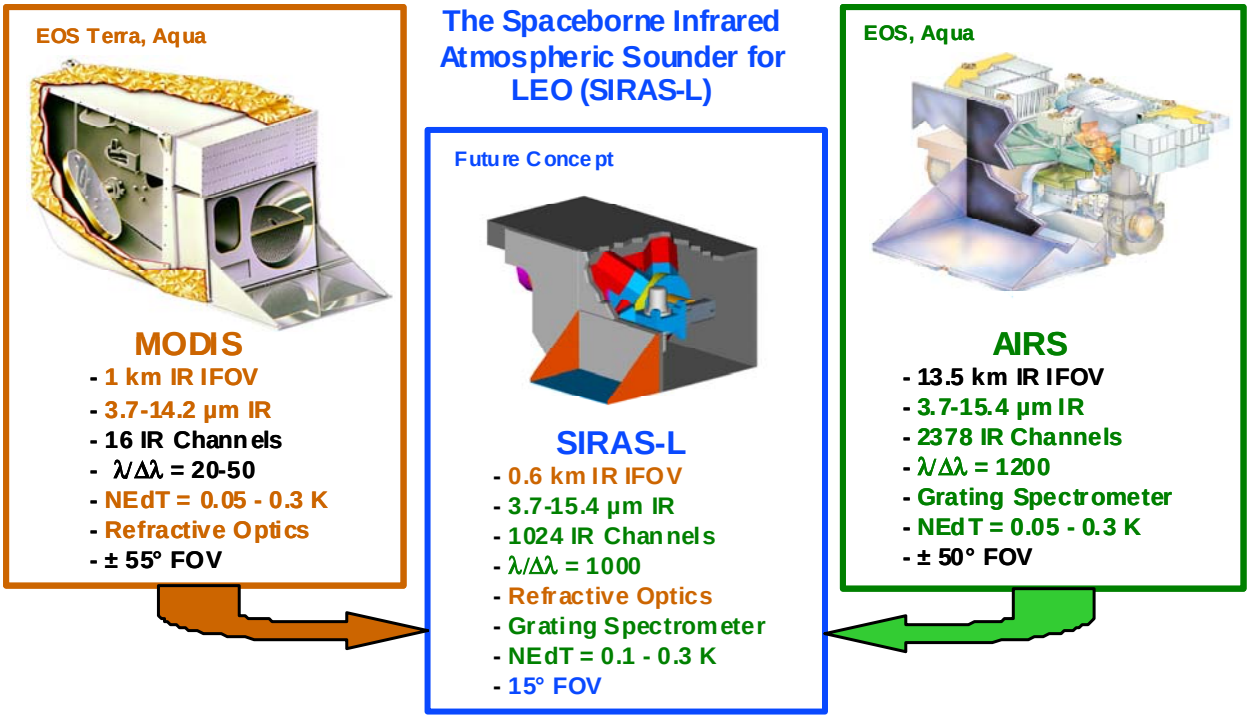

Figure 5. SIRAS-L can also meet the majority of requirements of AIRS and MODIS infrared channels with a significant size, mass and power reduction compared to either instrument

such as CO, CH_4 and NO_x. The combination of a SIRAS-G derivative and a multi-channel high-resolution spectrometer, such as the IMOFPS, can provide these measurements in a compact, solid-state instrument suite. The IMOFPS instrument concept, shown in Figure 6, consists of three co-boresighted correlation spectrometers for measuring vertical profiles of CO and column amounts of CO_2 and CH_4. The addition of a fourth spectrometer channel for measuring NO_x would provide a tracer of motion and cloud detection. A two-channel version of SIRAS-G, one channel extending from 12.3-µm to 15-µm and a second centered at the 9.6-µm ozone band, with spectral resolution "tuned" appropriately in both channels, would provide temperature and water vapor sounding and ozone column.

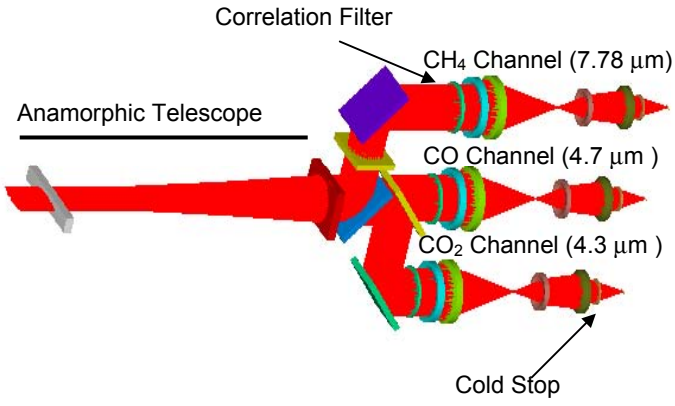

Figure 6. 3-Channel IMOFPS Sensor Concept

Summary And Conclusions

NASA's support of independent technology development for future Earth science needs is a positive step forward. It offers promising benefits in terms of early identification of appropriate technologies and retiring technical risks. This will lead to mission development cycle time from inception to completion and reduce overall cost, and ultimately, lead to more frequent science missions at lower overall cost. SIRAS-G exemplifies this approach and represents an advance in high-resolution IR atmospheric

sounding from geosynchronous orbit. The grating instrument architecture on which SIRAS-G is based is well suited to a wide variety of high priority NASA ESE missions, both from GEO and LEO platforms, and is an instrument architecture suitable for next-generation missions aimed at providing continued atmospheric data for long-term climate change research. The combination of SIRAS-G with other innovative instrument concepts such as IMOFPS offers the path to smaller, more capable instruments well suited to future NASA earth science missions. The Instrument Incubator Program, funded out of NASA, provides the mechanism to move SIRAS-G from concept to hardware demonstration, improving its technology readiness to where it will be ready for insertion into future spaceborne missions. Key to this is the successful completion and testing of the hardware demonstration instrument.

Acknowledgements

The authors would like to thank the NASA Earth Science Technology Office for supporting this effort. We would also like to thank Harmut H. Aumann of JPL for his science leadership, and Thomas Pagano and Steven Broberg of JPL for their systems engineering and analysis support on the SIRAS-1999 effort. The SIRAS-G effort is supported by a NASA ESTO IIP contract. The IMOFPS development was supported by Ball Aerospace & Technologies Corp. internal research and development funds.

References

T. U. Kampe, T. S. Pagano. 2002. SIRAS, The Spaceborne Infrared Atmospheric Sounder: an approach to next-generation infrared spectrometers for Earth remote sensing. *SPIE Proceedings,* **4485**, Optical Spectroscopic Techniques, Remote Sensing, and Instrumentation for Atmospheric and Space Research IV, A. M. Larar & M. G. Mlynczak: Eds, 60–68.

H. H. Aumann, T. S. Pagano, L. L. Strow. 2001. Atmospheric Infrared Sounder (AIRS) on the Earth Observing System. *SPIE Proceedings,* **4151**, 115-125.

M. D. Goldberg, Y. Qu, L. M. McMillan, W. Wolf, L. Zhou, and M. Divakarla. 2003. AIRS near-real-time products and algorithms in support of numerical weather predictions. *IEEE Trans. Geosci. Remote Sensing,* **41**, 379-389.

B. R. Johnson, T. U. Kampe, W. B. Cook, G. Miecznik, P. C. Novelli, H. E. Snell, J. Turner-Valle. 2003. Imaging Multi-Order Fabry-Perot Spectrometer (IMOFPS) for Spaceborne Measurements of CO. *SPIE Proceedings,* **5157**, Optical Spectroscopic Techniques and Instrumentation for Atmospheric and Space Research V, A. M. Larar and J. A. Shaw: Eds, 165-177.

P. Mouroulis, R. O. Green, T, G, Chrien. 2000. Design of pushbroom imaging spectrometers for optimum recovery of spectroscopic and spatial information. *Appl. Opt.,* **39**, 2210-2220.

T. U. Kampe, E. Waluschka. 1994. Near-Field Stray Light Rejection Techniques for the Moderate Resolution Imaging Spectroradiometer. *OSA Proceedings of the International Optical Design Conference, 1994,* G.W. Forbes, ed., Optical Society of America, 273-279.

W. L. Barnes, T. S. Pagano, and V.V. Salomonson. 1998. Prelaunch characteristics of the Moderate Resolution Imaging Spectroradiometer (MODIS) on EOS-AM1. *IEEE Trans. Geosci. Remote Sensing,* **36**, 1088-1100.

Introduction of the Hyperspectral Environmental Suite (HES) on GOES-R and beyond

[1]Timothy J. Schmit, [2]Jun Li, [3]James Gurka

[1]NOAA/NESDIS, Office of Research and Applications, Advanced Satellite Products Team (ASPT)
[2]Cooperative Institute for Meteorological Satellite Studies (CIMSS), University of Wisconsin-Madison
Madison, WI 53706
[3] NOAA/NESDIS, Office of Systems Development, Silver Spring, Maryland

Presented at the International (A)TOVS Science Conference (ITSC-13) in Sainte Adele, Quebec, Canada October 18 – November 4, 2003. Corresponding author's e-mail: Tim.J.Schmit@noaa.gov

Abstract

The Hyperspectral Environmental Suite (HES), scheduled for implementation on the Geostationary Operational Environmental Satellite (GOES)-R, will be launched in approximately 2013. This is the next generation operational geostationary sounder. Presently in formulation phase, it will replace the filter-wheel sounder that flies on the current GOES satellites. The HES will provide dramatic improvements over current sounder data and products, including better spectral resolution, faster geographic coverage rate, and improved spatial resolution.

Introduction

The Hyperspectral Environmental Suite (HES) on-board GOES-R (beginning in approximately 2013) will perform a number of functions with the data obtained in the infrared (Gurka and Dittberner 2001, Gurka and Schmit 2002). The two main tasks are to provide high-spectral resolution radiances for Numerical Weather Prediction (NWP) applications (Bayler et al 2001) and to provide temperature and moisture soundings (and various derived parameters) for a host of applications dealing with near or short-term predictions. Derived products include, but are not limited to: cloud-top information, winds, ozone, surface emissivity, and satellite-to-satellite inter-calibrations (Goerss et al 1998, Chung et al 2000, Li et al 2001a). There are actually two HES sub-tasks or modes. One mode is the HES - Disk Sounding (HES-DS) and the other is HES - Severe Weather / Mesoscale (HES-SW/M). The threshold spectral resolutions of these two tasks are 10 and 4 km, respectively. The coverage rate for the HES-DS is to cover the full "sounding disk" (less than 62 degrees view angle) is one hour, while the HES-SW/M will cover a 1,000 km x 1,000 km area in less than 4.4 minutes. This means the HES-DS will have a coverage rate approximately five times faster than the current GOES Sounder. The spectral coverage of the infrared portion of the HES will be 650 –1200 cm^{-1}, 1650 -2150 cm^{-1} or 1210 –1740 for the water vapor continuum and 2150 –2250 cm^{-1}.

The infrared data from the HES instrument on-board GOES-R will complete a decade long march to both high-spectral and high-temporal operational sounding data. There have been many important steps along the way (Figure 1). This includes, but is not limited to, the first theoretical works, the pioneering low-earth orbiting sounders, the experimental, multi-spectral resolution geostationary VISSR Atmospheric Sounder (VAS) instrument (Smith 1983; Hayden 1988; Hayden et al 1996), the experimental high-spectral resolution low-earth orbiting sounders, the operational, low-spectral resolution GOES sounders (Menzel and Purdom 1994, Schmit et al

2002a) and finally the operational high-spectral resolution low-earth orbiting sounders. The HES on GOES-R will be the first operational, high-spectral resolution instrument in geostationary orbit (Li et al 2001b, Li et al 2002). Of course the geostationary orbit offers high temporal resolution to monitor a host of parameters.

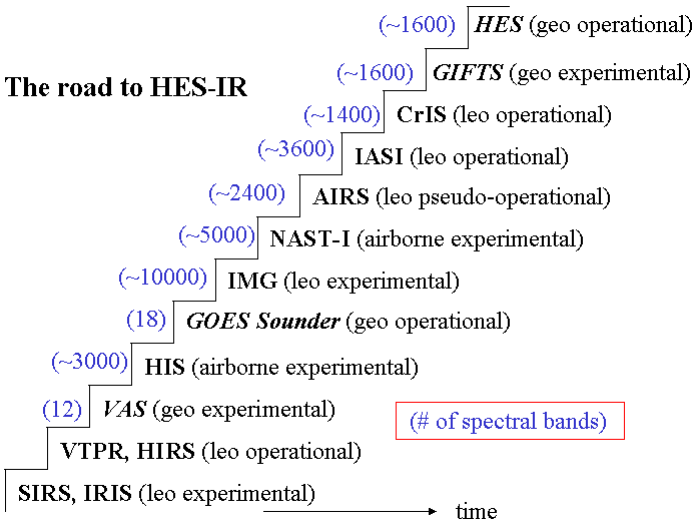

Figure 1: The path to the HES. The instruments in geostationary orbit are in italic.

The HES instrument will improve on the four key remote sensing areas. These are spatial resolutions, spectral coverage and resolution, temporal resolution and radiometric accuracy.

Results for HES studies

Water vapor information

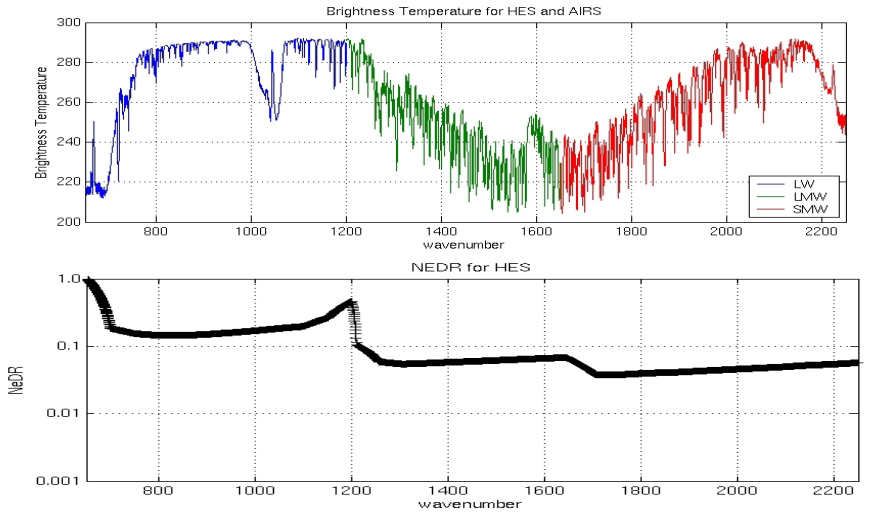

Figure 2: Example of BT spectral for HES LW, LMW, SMW (upper panel) and the noise in NEDR (lower panel).

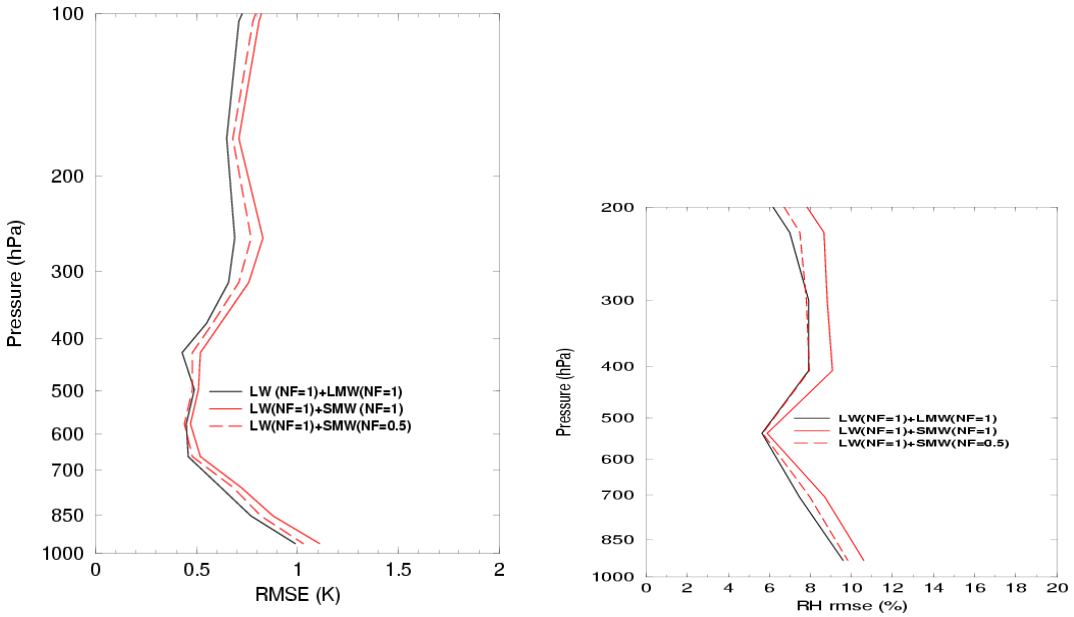

Figure 3: The temperature retrieval rmse at 1km vertical resolution and water vapor RH retrieval rmse at 2km vertical resolution LW + LMW, LW + SMW, and LW + SMW with the SMW noise reduced by half.

One important issue for the HES instrument is to select the water vapor spectral coverage. Usually the longwave coverage (LW, approximately 650 – 1200cm^{-1}) is selected for temperature, ozone and surface property retrievals. For the water vapor region, one can use either longer middlewave (LMW, approximately 1200 – 1650cm^{-1}) or shorter middlewave (SMW, approximately 1650 – 2250cm^{-1}). For example, AIRS uses the LMW while Geosynchronous Imaging Fourier Transform Spectrometer (GIFTS) uses the SMW region. Selection of both water vapor sides might be a better option in terms of information. For example, having both sides of the water vapor continuum would allow better trace gas measurements, and improved ABI back-up mode, better continuity for climate applications and improved retrievals. However, data volume will be increased. To compare the water vapor information from LMW versus SMW, a simulation study was carried out to simulate the retrieval performance for HES LW + LMW versus LW + SMW. Eigenvector regression followed by physical retrieval algorithm was used in the simulation (Li et al. 2003a); the spectral resolution for all spectral band channels is 0.625 cm^{-1}. 523 global independent profiles were used in retrieval performance study, and 1 km temperature root mean square error (rmse) and 2 km relative humidity (RH) rmse were calculated to evaluate the retrieval difference between LW + LMW and LW + SMW. The 14bit HES instrument noise from the Technical Requirement Document (TRD) was used in simulating the HES radiances. Figure 2 shows an example of HES BT spectrum for LW (blue line), LMW (green line) and SMW (red line) (upper panel), the HES instrument noise in NEDR for LW, LMW and SMW is also shown in the lower panel. Figure 3 shows temperature retrieval rmse at 1km vertical resolution for LW + LMW, LW + SMW, and LW + SMW with SMW noise reduced by half (NF=0.5) (left panel), and the water vapor RH retrieval rmse at 2km vertical resolution (right panel). In general, the temperature retrieval difference between LW+LMW and LW+SMW is about 0.1K, while the water vapor retrieval difference is about 1%. With SMW noise reduced by half, both temperature and water vapor retrieval differences between LW+LMW and LW+SMW are reduced. Considering other factors for LMW (for example, lower spectral resolution than SMW, more trace gas other than water vapor, etc.), the temperature and moisture retrieval differences between LW + LMW and LW + SMW are very small.

Spatial resolution study using MODIS data

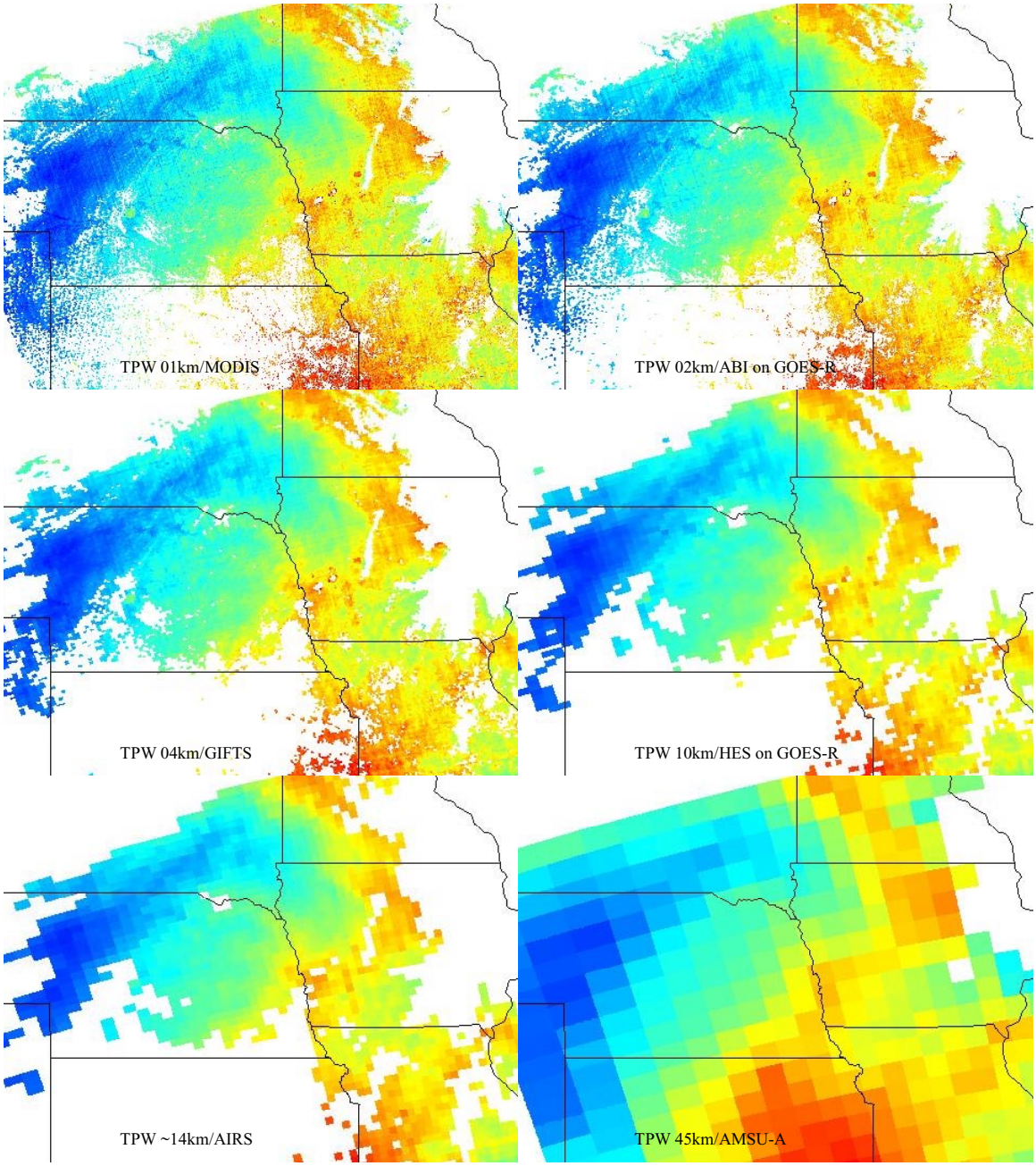

Figure 4: The 1km MODIS TPW (upper left panel) at 1900UTC on July 20, 2002 from the AQUA satellite, the simulated ABI resolution at 2km resolution (upper right panel), simulated GIFTS resolution at 4km spatial resolution (middle left panel), simulated HES resolution at 10km spatial resolution (middle right panel), simulated AIRS resolution at 14km spatial resolution (lower left panel), and simulated AMSU resolution at 45km spatial resolution (lower right panel), respectively, from the MODIS 1km TPW.

The spatial resolution for HES is very important because "hole hunting" will be the effective method to find clear pixels for atmospheric sounding without microwave sounding capability on the geostationary satellite. Fine spatial resolution allows a higher possibility of finding clear

pixels and maintaining spatial gradients. This is very important because (a) fine spatial resolution HES measurements will meet the mesoscale forecast requirement, and (b) fine spatial resolution enable to find more homogeneous fields-of-view (FOV) scenes for the cloud-clearing process.

Figure 4 shows the 1km MODIS TPW at 1900UTC on July 20, 2002 from EOS' AQUA satellite, and a number of reduced spatial resolutions for IR sounders. It can be seen that coarser spatial resolution results in smoothed TPW gradients and less clear coverage. The goal spatial resolutions of HES are 2 km.

Spectral resolution study for non-sounding applications

A study has been carried to demonstrate that in the IR longwave window region, a spectral resolution of 1cm^{-1} or better is necessary for accurately retrieving the non-sounding products such as IR surface emissivity and surface skin temperature by using the minimum local emissivity variance (MLEV) algorithm. Figure 5 shows the calculated LW BT spectrum at 0.625cm^{-1} with two different IR surface emissivity spectra (one is from the constant emissivity of 0.98 and the other is from an observed rock emissivity spectrum). The BT difference between the two spectrum in the figure results solely from the different emissivity spectrum in the calculations. Figure 6 shows from upper to lower panels the BT spectrum with rock emissivity, true emissivity spectrum (black line), retrieved emissivity spectra with true surface skin temperature (green line) and surface skin temperature deviated by 1K (green and red lines). The noise factor indicates the noise added (e.g., 0.5 means half noise). The mean local emissivity variance is indicated. Both half noise and nominal noise will create emissivity variance contrasts between true skin temperature and wrong skin temperature, indicating that both surface skin temperature and IR emissivity spectrum can be retrieved. However, the emissivity variance contrasts are very small with doubled noise, indicating that the skin temperature and surface emissivity retrieval will be difficult with doubled noise. Figure 7 is the same as Figure 6 but with a spectral resolution of 1.25 cm^{-1}, in this case, only half noise will create good emissivity variance contrasts in a lower spectral resolution.

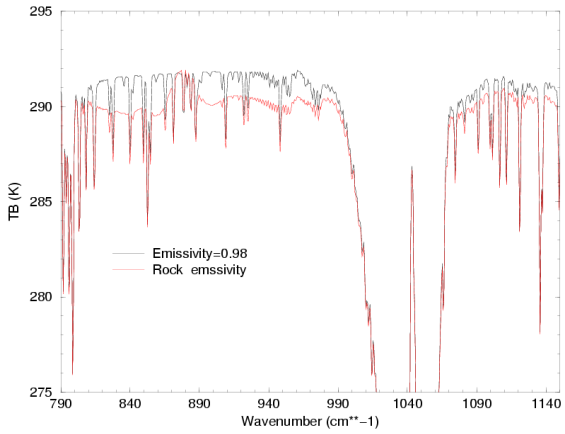

Figure 5. The calculated LW BT spectrum at 0.625cm^{-1} with two different IR surface emissivity spectrum (black line shows the BT with a constant emissivity of 0.98 and the red line shows the BT with rock emissivity spectrum from observation).

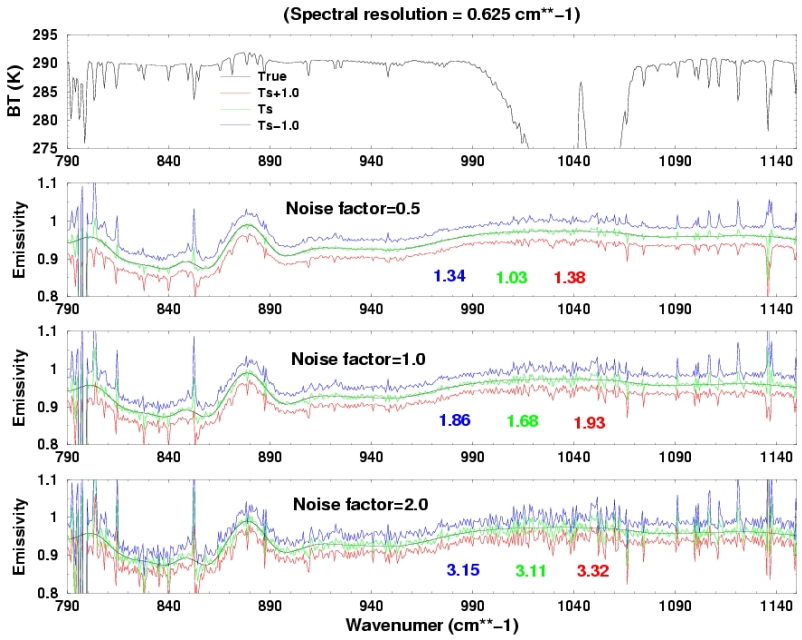

Figure 6. The BT spectrum with an observed rock emissivity spectrum, true emissivity (black line), retrieved emissivity spectra with true surface skin temperature (green line) and surface skin temperature deviated by 1K (green and red lines). The noise factor indicates the noise added in the simulation (e.g., 0.5 means half noise). The mean retrieved local emissivity variance is also indicated in each panel.

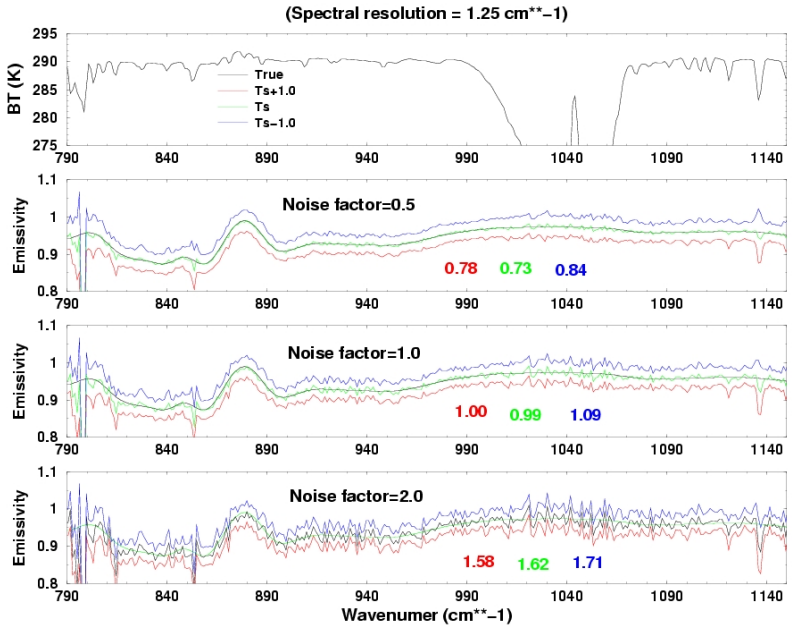

Figure 7. The same as Figure 6 but with a spectral resolution of 1.25cm^{-1}.

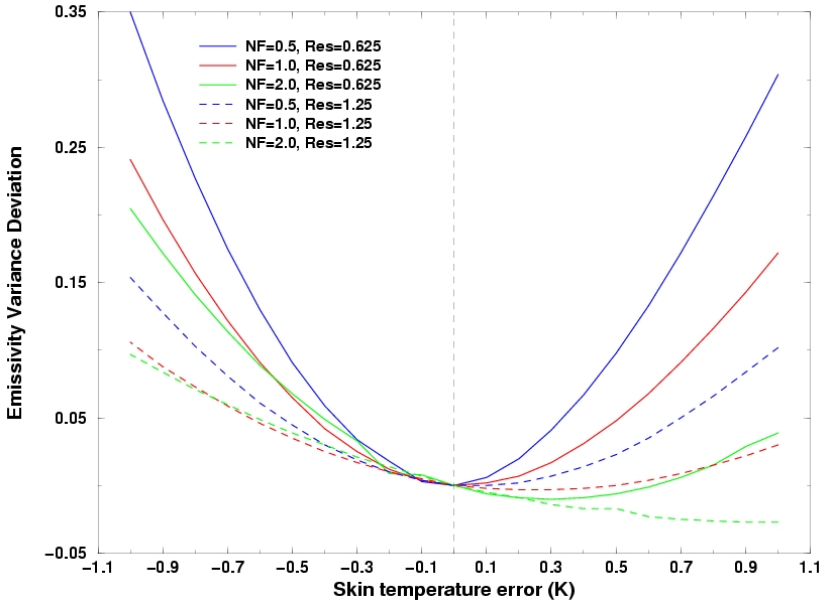

Figure 8. The emissivity variance difference between wrong skin temperature and true skin temperature as a function of skin temperature error, different lines correspond to various spectral resolutions and noise factors.

Figure 8 shows the emissivity variance differences between the wrong skin temperature and the true skin temperature as a function of skin temperature error, different lines correspond to various spectral resolutions and noise factors. It clearly indicates that a spectral resolution of 0.625 cm^{-1} with half noise and nominal noise will create an accurate emissivity and skin temperature retrievals, while only half noise will create good surface property retrieval with lower spectral resolution (e.g., 1.25 cm^{-1}). Note that this effect is not the only error source in estimating surface emissivity and skin temperature.

Summary

The GOES-R HES will be launched in approximately 2013. This is the next generation operational geostationary sounder that is currently in the formulation phase and will replace the currently used filter-wheel instrument. The HES data and derived products will improve over the current operational instruments in many areas. These include more spectral bands, faster geographical coverage rate and potentially improved spatial resolutions. Of course the GOES-R HES instruments will not be acting alone, but should use nearly time co-incident measurements from the high spatial resolution ABI to improve GOES-R products (Li et al 2003a, Li et al 2003b, Schmit et al 2002b, Schmit et al 2004).

Acknowledgments

The authors would like to thank the host of CIMSS, NOAA NESDIS and other scientists that contributed to this research.

References

Bayler, G. M., R. M. Aune, and W. H. Raymond, 2001: NWP cloud initialization using GOES sounder data and improved modeling of non-precipitating clouds. *Mon. Wea. Rev*., 128, 3911-3920.

Chung S., S. Ackerman, P. F. van Delst, and W. Paul Menzel, 2000: Model calculations and interferometer measurements of ice-cloud characteristics. *J. Appl. Met*., 39, 634-644.

Hayden, C. M., 1988: GOES-VAS simultaneous temperature-moisture retrieval algorithm. *J. Appl. Meteor*., **27**, 705-733.

Hayden, C. M., G. S. Wade, and T. J. Schmit, 1996: Derived product imagery from GOES-8. *J. Appl. Meteor*., 35, 153-162.

Li, J.**,** W. P. Menzel, F. Sun, T. J. Schmit, and J. Gurka, 2003a: AIRS sub-pixel cloud characterization using MODIS cloud products*, J. Appl. Meteorol.* (submitted)

Li, J., W. P. Menzel, W. Zhang, F. Sun, T. J. Schmit, J. Gurka, and E. Weisz, 2003b: Synergistic use of MODIS and AIRS in a variational retrieval of cloud parameters, *J. Appl. Meteorol,* (submitted).

Li, J., T. J. Schmit, and W. P. Menzel, 2002: Advanced Baseline Sounder (ABS) for future Geostationary Operational Environmental Satellites (GOES-R and beyond), SPIE proceeding, *Applications with Weather Satellites,* Oct.23 – 27, 2002, Hangzhou, China.

Li, J., Menzel, W. P., and A. J. Schreiner, 2001a: Variational retrieval of cloud parameters from GOES sounder longwave cloudy radiance measurements. *J. Appl. Meteorol.* 40, 312-330.

Li, J., T. J. Schmit, H. L. Huang, and H. M. Woolf, 2001b: Retrieval of atmospheric inversions using geostationary high-spectral-resolution sounder radiance information. *11th Conference on Satellite Meteorology and Oceanography,* 15 – 18 October 2001, Madison, WI.

Goerss, J. S., C. S. Velden, and J. D. Hawkins, 1998: The impact of multispectral GOES-8 wind information on Atlantic Tropical Cyclone track forecasts in 1995. Part II: NOGAPS Forecasts. *Mon. Wea. Rev*, 126, 1219–1227.

Gurka J. J., and G. J. Dittberner, 2001: The next generation GOES instruments: status and potential impact". Preprint Volume. *5th Symposium on Integrated Observing Systems*. 14-18 January, 2001, Albuquerque, NM., Amer. Meteor. Soc., Boston.

Gurka, J. J, and T. J. Schmit, 2002: Recommendations on the GOES-R series from GOES users' conferences, *SPIE Proceeding 4895,* 95 - 102.

Menzel, W. P., and J. F. W. Purdom, 1994: Introducing GOES-I: The first of a new generation of geostationary operational environmental satellites, *Bull. Amer. Meteor. Soc.*, 75, 757-781.

Schmit, T. J., et al., 2004: Study of ABI on GOES-R and beyond, *Proceeding of 20th International Conference on Interactive Information and Processing System (IIPS) for Meteorology, Oceanography, and Hydrology,* American Meteorological Society, Jan. 10 – 14, 2004, Seattle, WA, AMS

Schmit T. J., W. F. Feltz, W. P. Menzel, J. Jung, A. P. Noel, J. N. Heil, J. P. Nelson III, G. S. Wade, 2002a: Validation and use of GOES sounder moisture information. *Wea. Forecasting*, **17**, 139-154.

Schmit, T. J., J. Li, W. P. Menzel, 2002b: ABI for future GOES-R and beyond, *SPIE Proceeding 4895,* 111-122.

Smith, W. L., 1983: The retrieval of atmospheric profiles from VAS geostationary radiance observations. *J. Atmos. Sci*., **40**, 2025-2035.

PAPERS FROM POSTERS

Meteorological Products Generation Using Combined Analysis of NOAA AVHRR and ATOVS Data.

Izabela Dyras, Danuta Serafin-Rek, Zofia Adamczyk

Institute of Meteorology and Water Management,

P. Borowego 14, 30-215 Kraków, Poland

Abstract

The satellite observations in different spectral ranges provide the important information on the state of the atmosphere that is used for weather analysis and forecast. Combining these data into one system encounters problems due to the data various range as well as temporal and spatial resolution. The Geographical Information System (GIS) methods can be a useful tool for the data analysis and presentation.

The paper presents the progress in the cloud analysis on NOAA AVHRR images as well as in algorithms allowing the retrieval of various parameters from NOAA AMSU data in the Satellite Research Department, Institute of Meteorology and Water Management in Poland.

The meteorological products prepared for the Polish meteorological service include several thematic layers such as precipitation intensity and range, convective clouds' detection, and total precipitable water estimation. The combined analysis maps are created and then disseminated via Intranet to the regional forecasting offices. Such satellite maps enhance the ability to diagnose the precipitation using satellite imagery.

The GIS technology is used for preparation and visualisation of the products derived from various sources including additional overlays such as geographical data and administrative boundaries.

The AMSU data have been processed using the Advanced ATOVS Processing Package (AAPP ver.3.7) and visualized using ER Mapper 6.3 software.

Introduction

The satellite observations, ground measurements and numerical weather prediction (NWP) models provide continuous information on the state of the atmosphere that are used for weather analysis and forecast. Combining these data into one system encounters problems due to the data various range as well as temporal and spatial resolution, however, GIS can provide the useful tool for the data analysis and presentation.

Since their launch the satellites NOAA-15, 16 and 17 are equipped with microwave radiometers (AMSU) that are very useful for atmosphere sounding i.e. evaluation of precipitable water and ice crystal distribution. There has been significant progress in developing methods using microwave information over the sea and oceans. However, the methods of sounding from the microwave spectrum over land are still inadequate and these problems are researched in several centres in the world.

Data and software

A summary of the data used in this work is presented in the Table 1, which demonstrates the potential problems caused by different spatial resolution, frequency, temporal resolution and scale. SYNOP data provided information concerning temperature, dew temperature at the surface, as well as present and past weather, cloud cover and cloud type. Precipitation data was used from SYNOP at 12.00 GMT (precipitation sum for the last 6 hours). Vertical profiles of temperature, dew point and geopotential height from TEMP data were used to calculate air relative humidity and cloud water content. Water vapour mixing ratio, relative humidity and liquid water contents and consequently - cloud liquid water path (LWP) were calculated at the standard pressure levels.

Data Type	Range	Resolution	Frequency	Scale
SYNOP	Europe	synoptic/	1 h	regional
KLIMAT	Poland	climatic stations	3 h 6 h/12 h/24 h	regional
AEROLOGICAL SOUNDING	Poland/Europe	aerological stations	1x -4x /day	global
NOAA AVHRR	Central Europe	1.1 km	6/day	regional
NOAA AMSU		17/40 km		regional
NOAA HIRS		10 km		regional
SAFIR	Poland	1 km	1 min	regional
NUMERICAL WEATHER PREDICTION MODEL	Central Europe	13 km	6/12 h	mezoscale

Table 1: Meteorological and climatological data.

Satellite data was introduced into the present system come from the polar orbiting NOAA satellite system. The Advanced Very High Resolution Radiometer (AVHRR/3) is a multipurpose imaging instrument used for global measurement providing the characteristics of cloud cover, sea surface temperature, ice, snow and vegetation cover. AVHRR has 6 channels in the visible and infra-red between 0.63 and 12.0 micrometers, with a resolution of 1.1 km at the sub-satellite point [NESDIS, 1998]. The Advanced Microwave Sounding (AMSU) sounder consists of 3 radiometers. The first two radiometers AMSU-A1and AMSU-A2 provide measurements in 15 channels with 40 km resolution in sub-satellite point, in the range of 23.8 GHz to 89 GHz. The third - AMSU-B provides data in 5 channels; in frequencies 89GHz, 150 GHz and 183 GHz with 16 km resolution. Passive microwave instruments provide information about precipitation, since precipitation directly influences the radiation field. The drawback of passive microwave instruments is their low spatial resolution.

Figure 1 shows a good example of combining different information. In the background there is a False Colour Composite (FCC-channels 321) from the AVHRR/3 radiometer on board the polar orbiting meteorological satellite - NOAA 16. The clouds appear in white to blue colours, sea in black and land in shades of green and brown. Several different thematic layers are laid on top of the FCC; the locations of the SYNOP stations in Europe and Poland are shown as blue and yellow dots, respectively. Yellow dots show the marked SYNOP stations with the

recorded precipitation over 1 mm. The labels show the recorded precipitation. The recorded lightning from Safir system is shown in red.

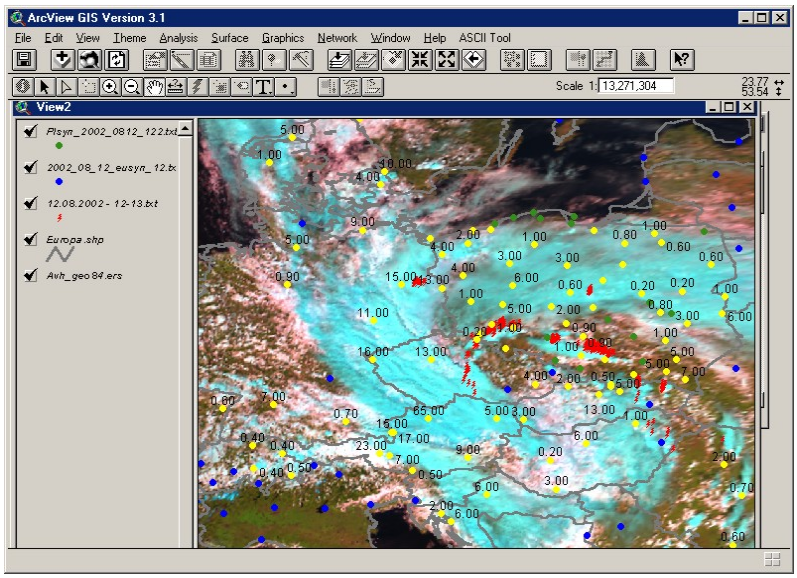

Fig. 1: Satellite data with the SYNOP stations overlay, 12.08.2002 (ArcView).

Several specialized software packages are used in order to process different types of data. Initially, the satellite data are processed using the Advanced ATOVS Processing Package (AAPP) created and distributed by the EUMETSAT [AAPP, 1997; AAPP Documentation, 1999a, 1999b; Renshaw and English, 1998]. Received AVHRR and ATOVS data are transformed to the AAPP level 1d format i.e. all necessary decommutation, calibration, geo-referencing and identification of cloud contamination are performed by the package. Specially designed routines allow the automatic control of the AAPP package for the current satellite pass of NOAA 15, 16 and 17. The output data sets are in the form of an ASCII (x,y,z), where x – longitude, y – latitude and z – albedo or brightness temperature. The separate files are created for AVHRR and AMSU data with some auxiliary information such as logistic Crosby test, precipitation probability, satellite and sun angles, land cover type, etc.

ER Mapper is the commercial software package used for the raster images processing and visualization. It also allows presenting raster data with the vector layers. ArcView 3.1 and ARCGIS 8.3 packages are used in order to combine the ground data with the satellite-derived parameters.

Products generation

Precipitation is a highly variable parameter with time and space therefore the use of satellite data allows obtaining the global information. The measurements in microwave channels are a particularly interesting source of information concerning the humidity of the atmosphere [Muller, 1994].

The microwave humidity products are made available as Microwave Sounding Service and TOVS Sounding Service. They are based on the regression algorithms described in previous works [Dyras I. and D. Serafin-Rek, 2001a, 2001b, 2002a, 2002b].

Rain Rate

The maps of precipitation intensity - Rain Rate (RR) are created for the current satellite pass of the polar orbiting satellites NOAA 15, 16 and 17. Fig. 2 shows the three classes of light, moderate and high precipitation intensity. The Rain Rate was calculated according to the regression algorithm 1.

RR = 47,75 - 0,096*TB(50)+0,123*TB(89)-0,158*TB(150)-0,037*TB(183.7)) [mm//h] **(1)**

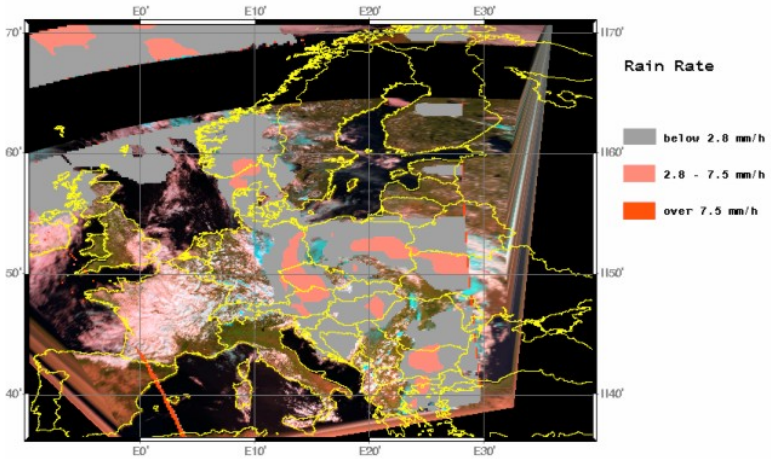

Fig. 2: Precipitation Intensity map from AMSU data; NOAA 16, 12.08.2002, 12:24 GMT. Intensity is broken into 3 classes – light, moderate and high.

Scattering Index

Microwave data NOAA/AMSU is valuable for the recognition of extreme situations such as convective cloud systems or extended storm clouds. The results of testing and verification of the precipitation detection versus ground measurements for the summer-autumn season in 2002 is shown in Table 2. It was observed that he majority of precipitation occurred when the value of $SI_{\_land}$ was greater that 3.

SATELLITE SYNOP	PRECIPITATION $SI_{\_land}$ >=3	NO PRECIPITATION $SI_{\_land}$ <3
PRECIPITATION	338	2
NO PRECIPITATION	27	4

Table 2: The results of precipitation detection using scattering index – comparison of the results obtained from AMSU data vs. SYNOP for the summer-autumn season in 2002 (371 cases).

$SI_{\_land}$ = 42.72+TB(89)-TB(150) **(2)**

Scattering Index (SI), used for convective clouds detection ($SI_{\_land}$), is calculated according to the regression algorithm 2. It is assumed that the precipitation occurs if $SI_{\_land}$>=3.The horizontal size of the cloud is important – big systems are recognised better than small that sometimes are ignored. Fig. 3 shows the detected convective systems over the Central Europe.

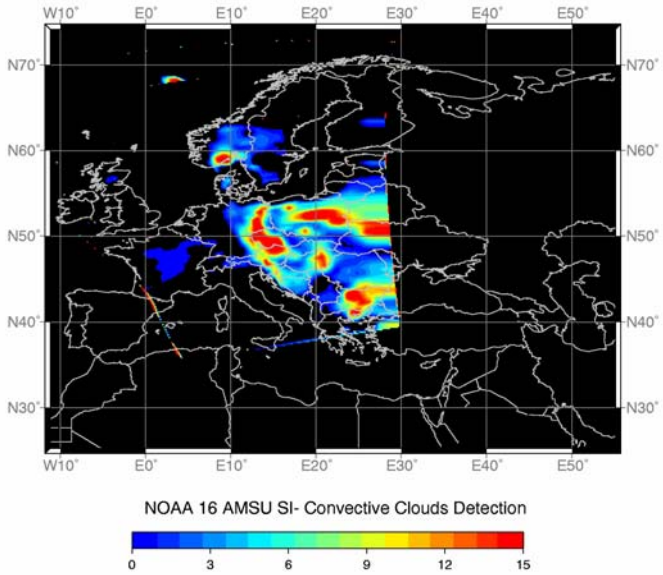

Fig. 3: Scattering Index over land map – areas of detected convection from AMSU, NOAA 16, 12.08.2002, 12:24 GMT.

Total Precipitable Water

Total Precipitable Water (TPW) as described by formula (3) allows estimating the water vapour content in the air over the land. The obtained regression fitting index R^2 = 0.59 with standard deviation ±4.6 mm, for 618 cases. Table 3 contains the results of regression analysis.

TPW = -26,94+ 0,32*TB(50) + 1,0198*TB(89) - 0,404*TB(150) - 0,789*TB(183±7)) [mm] **(3)**

STATISTICA MULTIPLE REGRESSION	Regression Summary for Dependent Variable: **TPW** R= 0,76699883 **R^2 = 0,58828720** Adjusted R^2 = 0,58560066 F(4,613)=218,98 p<0,0000 **Std. Error of estimate: 4,5781**					
N=618	BETA	St. Err. of BETA	**B**	St. Err. of B	t(613)	p-level
Intercpt			**-26,9441**	13,23545	-2,03576	0,042204
T50_3	0,238232	0,096127	**0,3202**	0,12921	2,47831	0,013469
T89_0	0,918632	0,165788	**1,0198**	0,18404	5,54101	0,000000
T150	-0,444990	0,140871	**-0,4043**	0,12798	-3,15886	0,001662
T183_7	-0,667865	0,067999	**-0,7887**	0,08030	-9,82171	0,000000

Table 3: The results of the regression analysis obtained for Total Precipitable Water (STATISTICA).

The case of very intense rain causing flooding in the Czech Republic in August 2002 was chosen to visualize the usefulness of microwave TPW sounding. The map on Fig. 4 shows the example of TPW product created for the NOAA16 pass on 12.08.2002 and it shows the high TPW content over Central Europe. The highest TPW values are shown in red. Fig. 5 presents the spread between TPW values from radiosonde data (on axis Y) and TPW values determined from the combination of brightness temperatures of AMSU channels (on axis X) as calculated by a STATISTICA program.

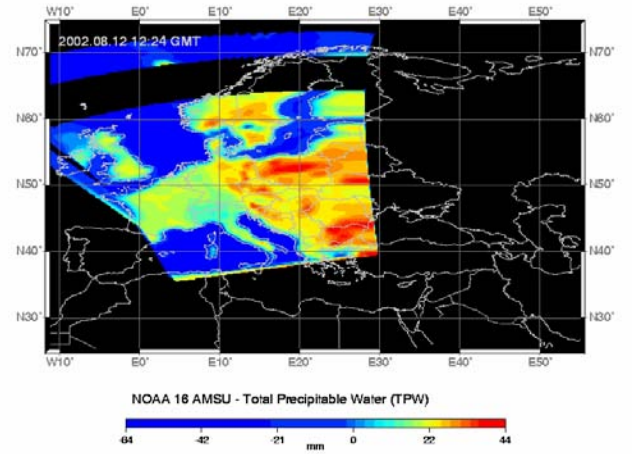

Fig. 4: Total Precipitable Water (kg/m^2), calculated from microwave AMSU data, NOAA 16 12.08.2002; 12:24 GMT.

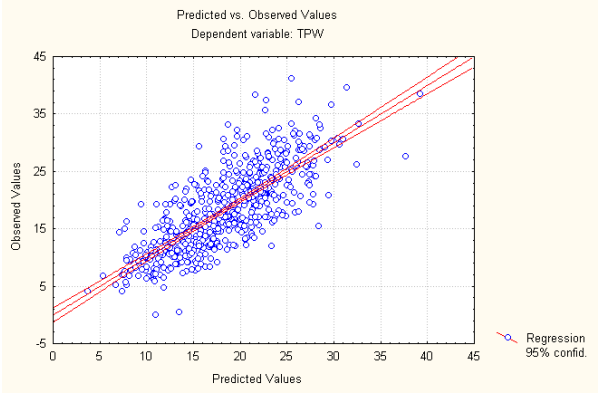

Fig. 5: The spread between TPW values calculated from radiosonde data – axis Y and TPW values determined from combination of brightness temperature of AMSU channels– axis X.

The location of the low and system of fronts shown on the surface analysis map (Fig. 6) has a good representation on the satellite image. The microwave algorithms adequately define the areas of the high humidity values, rain rate intensities as well as ranges.

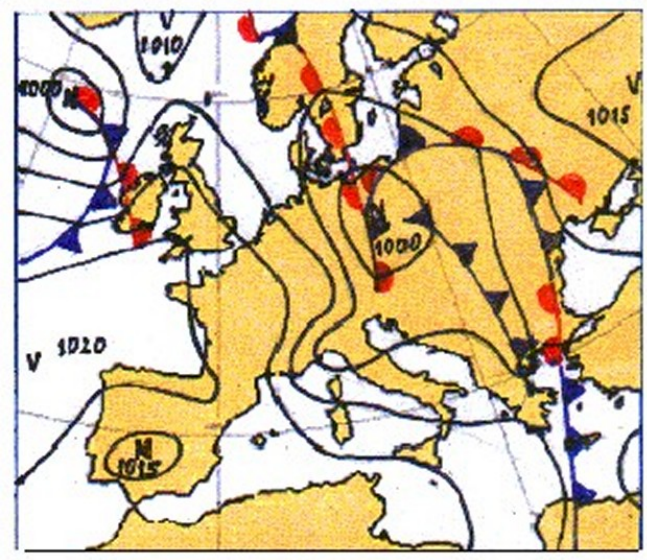

Fig. 6: Meteorological situation on 12.08.2002, analysis at the surface. (source:http://www.chmi.cz/hydro/pov02/flood.htm)

Composite Images

Creating a False Colour Composite (FCC) is very simple technique for cloud cover enhancement (Fig. 8). It simultaneously combines satellite images from three channels of AVHRR data into one colour image product. Discrimination between low clouds and fog, thin and thick cirrus, cloud free land ocean, and thick non-precipitating clouds from nimbostratus can be performed more successfully and more confidently when using multi-spectral infrared and visible colour imagery in conjunction in one another. Convective clouds are in blue, low clouds in pink. More advanced techniques – supervised or unsupervised classification can also applied as shown on the Fig. 9.

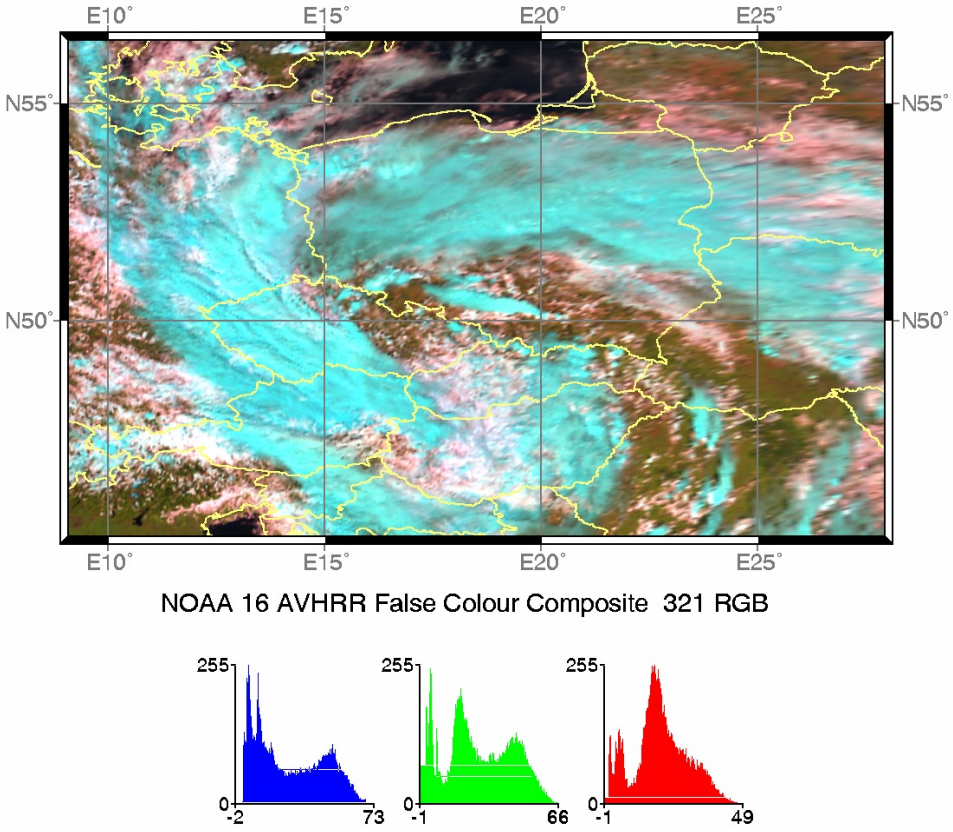

Fig. 8: False Colour Composite (NOAA / AVHRR - RGB) - of channels 3_A21; NOAA16, 12.08.2002; 12:24 GMT.

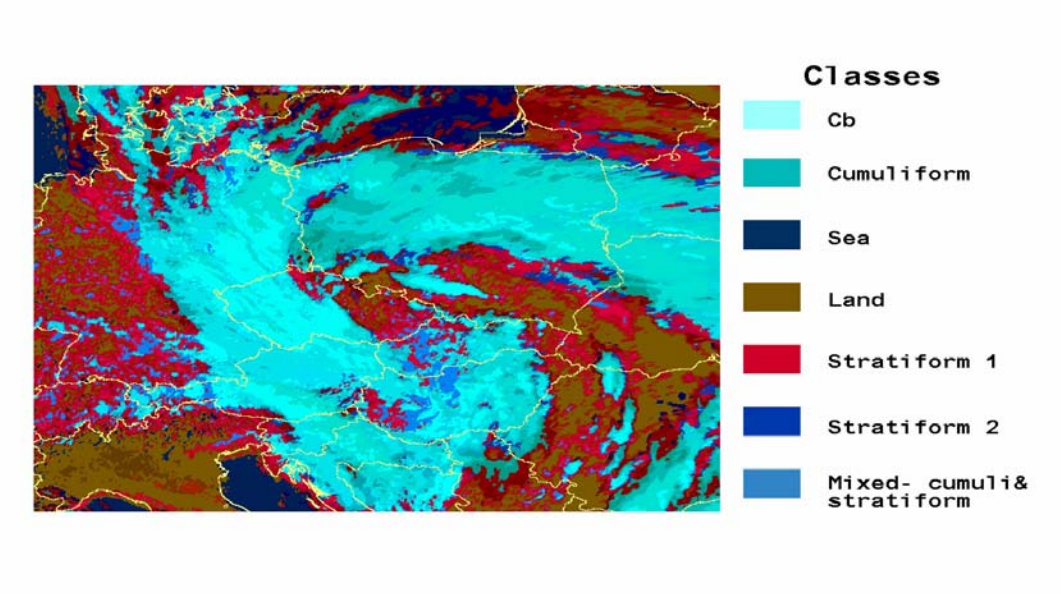

Fig. 9: Satellite cloud cover classification based on NOAA/AVHRR data.

Numerical Weather Prediction Model Fields

Temperature and precipitation forecast fields imported in order to create the thematic layers are shown in Fig. 10 and in Fig. 11, respectively.. Temperature at 7 pressure levels (surface, 925, 850, 700, 550, 450, 300 hPa) and the forecasted precipitation at +03h and +06h (stratiform, convective) were rasterised using a gridding procedure and rectified by triangulation using ER Mapper 6.3 software.

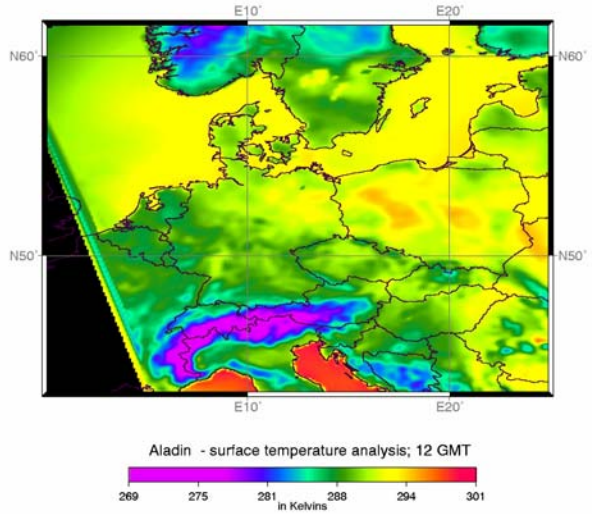

Fig. 10: Temperature field at the surface– from numerical model Aladin.

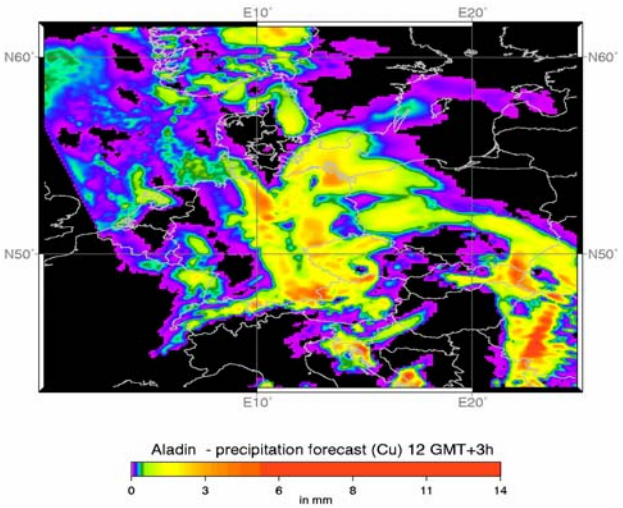

Fig. 11: Convective precipitation forecast (Aladin) on 12.08.2002, 12.00 GMT + 3 h.

Conclusions

Geographical Information System (GIS) methods and tools proved very useful for joint analysis and presentation of satellite as well as meteorological data.
GIS used for the joint analysis and presentation of satellite and meteorological data allow the preparation of:

- Maps of the integrated information from all satellite sensors (AVHRR, HIRS and AMSU) such as TPW, RR, SI.
- Classification and visualisation of the multi-spectral data with the vector overlays (i.e. geographic or administrative boundaries)
- Development, testing and verification of the suitable algorithms for various meteorological parameters;

GIS methods allow presenting the integrated information from NOAA satellite sensors (AVHRR and AMSU) transformed to a suitable projection; creating composite images using different spectral channels and overlaying with the vector data (geographic and administrative boundaries); developing the suitable algorithms for various meteorological parameters calculation, testing and verification. Finally, these methods allow combining different data (raster and vector) into one thematic layer for their Internet distribution. The Intranet service for NOAA Microwave sounding products was created. It consisted of maps for convective clouds detection, precipitation probability, Liquid Water Path, Total Precipitable Water and Rain Rate respectively prepared for the NOAA passes.

Acknowledgments

The work was partially supported by the Polish Committee for Scientific Research (KBN) under the Grant No. 618/E-217/ SPUB-M/COST/P-04/DZ 245/2001-2003.

References

AAPP Module Design, 1997, AAPP Data Set Definition, Documentation EUMETSAT –Vol.1, Vol. 2;

AAPP Documentation, 1999a, SCIENTIFIC PART Réf.: CMS/R&D/AAPP/SA Ver. 1.0;

AAPP Documentation, 1999b, General specifications for the AAPP preprocessing package related to NOAA polar orbiting weather satellites, Software Description, Météo France Document;

Dyras I. and D. Serafin-Rek, 2001a: The use of NOAA-15 satellite data for meteorological products generation and visualisation., in *IRS 2000: Current Problems in Atmospheric Radiation*, W. L. Smith and Yu. M. Timofeyev (Eds.). A. Deepak Publishing, Hampton, Virginia, 17-20;

Dyras I. and D. Serafin-Rek, 2001b, The Use of Microwave NOAA/AMSU Data for Precipitation Estimation, *Proceedings RSPS2001*, London, UK, 136-144;

Dyras I.and Serafin-Rek D., 2002a,The Use of AMSU Data from NOAA-KLMN Satellites for Precipitation Intensity Estimation,*Proceedings,EUMETSAT – IMWM Training Course Proceedings --,,From MTP to MSG – where are We and where are We going*??",18-20.06.2001 Kraków,IMGW Kraków 2002,65-74;

Dyras I., Serafin-Rek D., 2002b,"The use of AMSU data from NOAA-15 satellite for meteorological products generation *",Advances in Space Research,*Vol. **30/11**,2461-2466*;*

Muller B.M., H.E.Fuelberg and Xuwu Xiang, 1994: Simulations of the effects of water vapor, cloud liquid water, and ice on AMSU moisture channel brightness temperatures. *J.Appl.Meteorol.* **33**, 1133 – 1154;

NESDIS, 1998, Polar-Orbiting Operational Satellite (POES)Program,78th Annual Meeting of the American Meteorological Society,*14th International Conference on Interactive Information and Processing Systems (IIPS) For Meteorology,Oceanography and Hydrology*, Phoenix, Arizona, January 11-16,1998, pp.7-12;

Renshaw R.,S.English – 1998, Scientific Documentation for ATOVPP, ATOVS Processing Package APP1041;

http://www.chmi.cz/hydro/pov02/flood.htm

Comparison of AMSU-B Brightness Temperature with Simulated Brightness Temperature using Global Radiosonde Data

V.O. John, S.A. Buehler, and M. Kuvatov

Institute of Environmental Physics, University of Bremen, Otto-Hahn Alle 1, 28359 Bremen, Germany, vojohn@uni-bremen.de

Abstract

We present a comparison of brightness temperature measured by AMSU to radiative transfer model calculations based on radiosonde data. The forward model used is the stable version of the Atmospheric Radiative Transfer Simulator(ARTS), a general purpose radiative transfer model which can handle many different remote sensing instruments in the millimeter to infrared spectral region. The atmospheric profiles used are the Met Office - Global Radiosonde Data taken from the British Atmospheric Data Center (BADC). As a first step, the comparison is done for Lingenberg, Germany which uses Vaisala RS80 radiosondes and Kem, Russia which uses Goldbeater's skin radiosondes.

As the forward model ARTS has already been validated against AMSU brightness temperatures using high resolution radiosonde data from Lindenberg which is a reference station for German Weather service(DWD), the main aim of this comparison is to check the quality of the radiosonde data from the different stations.

Introduction

Upper tropospheric humidity (UTH) is a crucial parameter for meteorology and climate research. There are two global and continuous data sets for this parameter, one from polar orbiting meteorological sensors, the other from synoptic meteorological radiosondes. The basic idea of the study is to compare satellite and radiosonde data. The atmospheric radiative transfer simulator - ARTS [1] is used to generate simulated AMSU measurement from the radiosonde data.

The aims of the study are, to develop a robust methodology for such a comparison and to pave the way for a systematic comparison of all stations in the global radiosonde network to satellite data. This will allow an intercomparison and quality control of the different radiosonde stations, assuming that the satellite instrument's properties are stable during a few orbits. In this article a comparison between two mostly used radiosonde instruments namely Vaisala RS80 and Goldbeater's skin radiosondes is demonstrated.

Data Used

Radiosonde data

To develop the methodology for the comparison we used radiosonde data from Lindenberg (52.22°N, 14.12°E) which is a reference station of the German Weather Service, DWD. This station uses RS-80 Vaisala radiosondes for routine operations. The reason for selecting this particular station is that the data are subjected to a number of corrections as

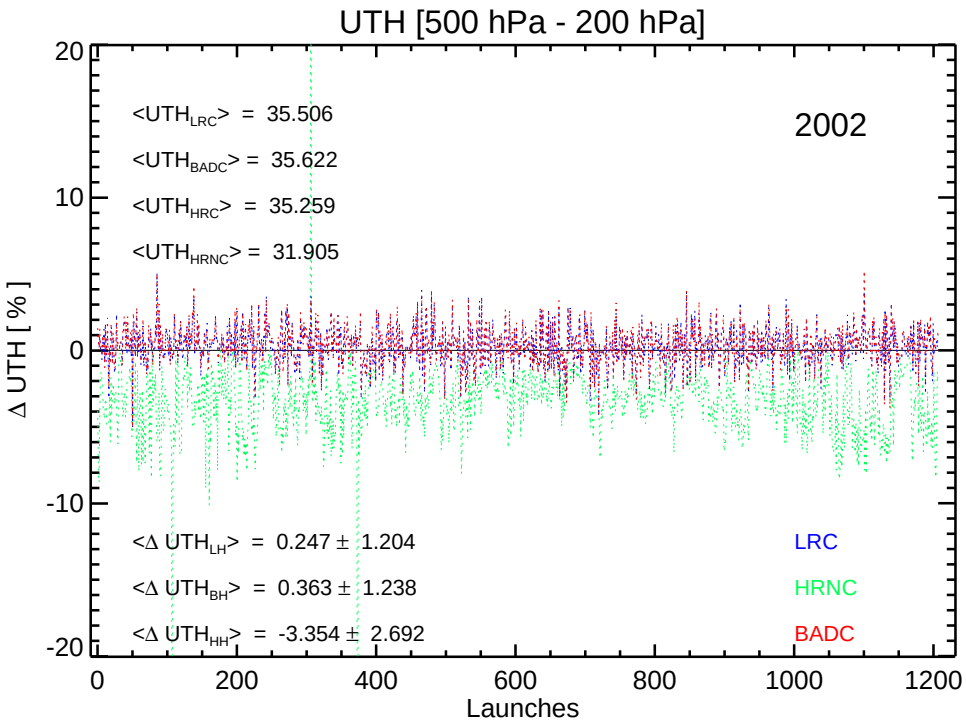

Figure 1: ΔUTH for different versions of the Lindenberg radiosonde data for the year 2002 with HRC as the reference.

described in [3]. Three versions of the data have been received: a) High Resolution Not Corrected (HRNC), High Resolution Corrected (HRC), and Low Resolution Corrected (LRC). Another version of the data set can be obtained from British Atmospheric Data Center (BADC). Figure 1 shows a comparison of upper tropospheric humiditiy (UTH) of the different versions of the data.

The uncorrected version of the data shows a significant dry bias [6] in UTH but the other two versions (LRC and BADC) do not show any significant difference in UTH.

AMSU data

Advanced Microwave Sounding Unit - B (AMSU-B) is a cross track scanning microwave humidity sounder [4]. The footprint size is $20\times16\,\mathrm{km}^2$ for the innermost scan positions, but increases to $64\times52\,\mathrm{km}^2$ for the outermost positions. Figure 2 shows an example of AMSU data from Channel 20. This is an overpass over the station Lindenberg. The circle represents a 50 km area around the station and the pixels in this area are used for the comparison. If there is a cloud over the station, there will be a large inhomogeneity among the pixels as shown in the figure 2.

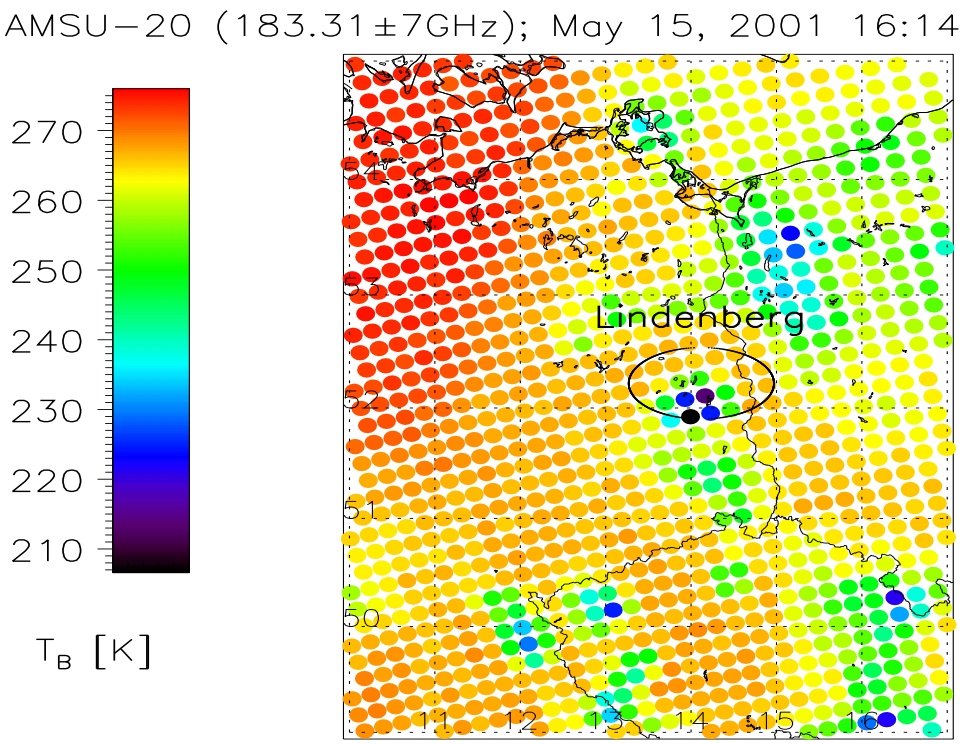

Figure 2: An AMSU overpass over station Lindenberg. The circle drawn around the station has a radius of 50 km.

Results and Discussion

The methodology of our comparison, the validation of the RT model, and the intercomparison between different satellites can be seen in [2]. Figure 3 shows the comparison for the two stations Lindenberg, Germany and Kem (64.95°N, 34.65°E), Russia for the year 2001. There are significant differences in channels 18 and 19, the two channels which are sensitive to the upper tropospheric humidity. The bias, slope and offset were calculated as explained in [2].

There is a slope in the channel 18 for Lindenberg. The possible explanation for the slope is that the correction of the data is not sufficient enough in extremely dry conditions. Therefore the modeled brightness temperatures are higher than the measured ones because the weighting functions peak lower in a drier atmosphere.

A large bias exists in the case of Kem for channels 18 and 19. The modeled brightness temperatures overestimate the measured ones because there is a wet bias in the radiosonde humidity measurements using Goldbeater's skin radiosondes [5].

In order to translate the bias in brightness temperature to bias in relative humidity we made a sensitivity chart. This is shown in Figure 4. It can be seen that a bias of about 7 K in channel 18 is equivalent to that of 10–12 % in RH. This result is consistent with the results of Soden and Lanzante [5].

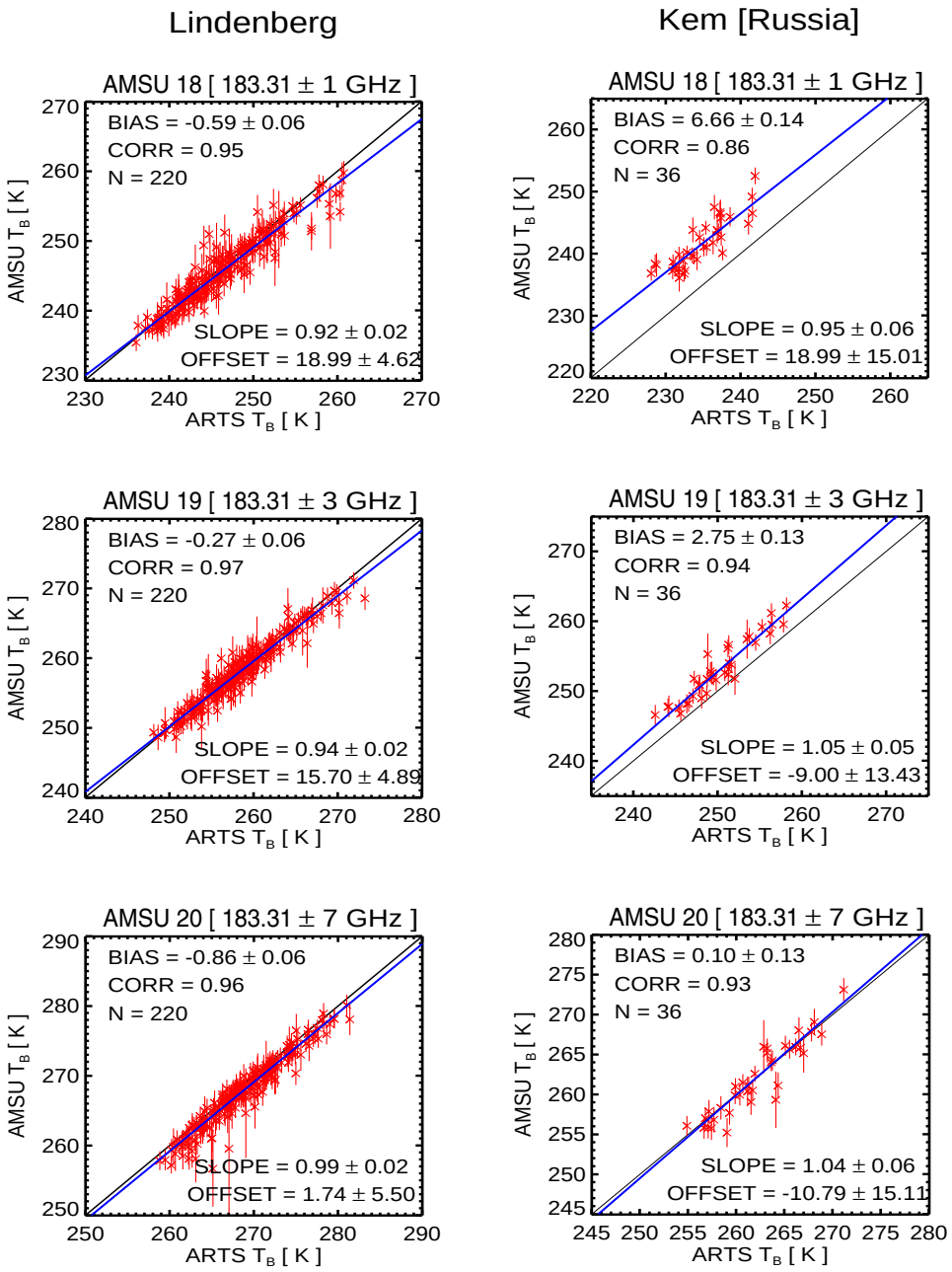

Figure 3: Comparison between modeled and measured radiance for Lindenberg and Kem. Year: 2001, Satellite: NOAA-16. The blue curve shows a linear fit of modeled and measured radiance.

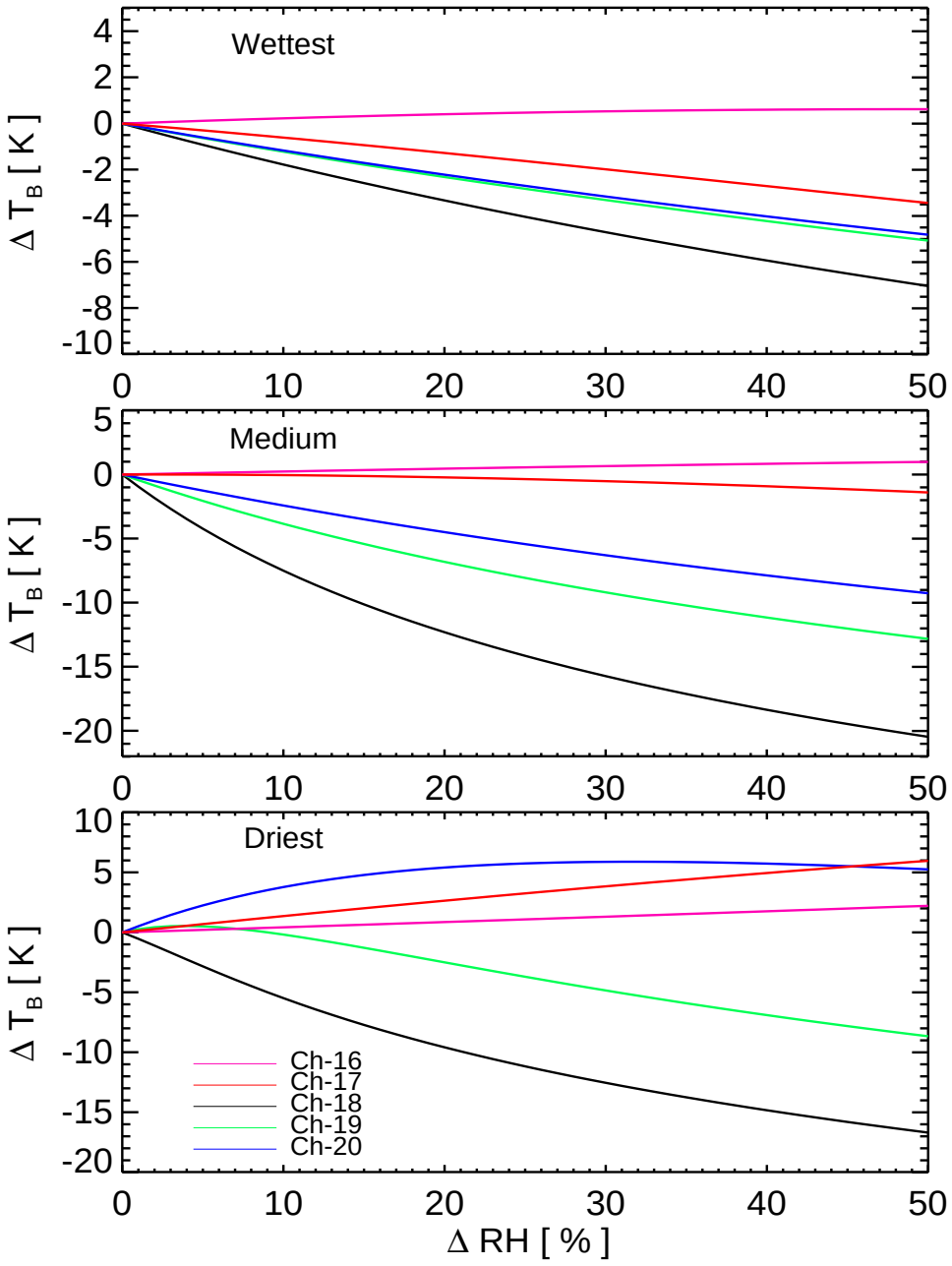

Figure 4: Sensitivity of ΔT_B to ΔRH for the AMSU-B channels. There profiles were selected based on the total water vapor content labelled as wettest, medium, and the driest.

Summary and Future Work

A robust methodology is developed for the comparison of satellite microwave humidity data with radiosonde data. This method is sensitive to the dry and wet biases in the radiosonde humidity measurements taking the satellite measurement as reference.

We plan to apply this method for other stations and types of radiosonde sensors to find the possible biases in data set.

Acknowledgments

We thank Lisa Neclos, CLASS, NOAA, for providing AMSU data, Ulrich Leiterer and Horst Dier of Lindenberg weather station, for providing the radiosonde data. Furthermore, we wish to acknowledge funding through the German AFO 2000 research project UTH-MOS (GFS 07ATC04). It is a contribution to COST Action 723 'Data Exploitation and Modeling for the Upper Troposphere and Lower Stratosphere'.

References

[1] S. A. Buehler, P. Eriksson, T. Kuhn, A. von Engeln, and C. Verdes. ARTS, the Atmospheric Radiative Transfer Simulator. *JQSRT*, submitted 2003. Preprint at: http://www.sat.uni-bremen.de.

[2] S. A. Buehler, M. Kuvatov, V. O. John, U. Leiterer, and H. Dier. Comparison of Microwave Satellite Humidity Data and Radiosonde Profiles: A Case Study. *JGR*, Submitted 2004. Preprint at: http://www.sat.uni-bremen.de.

[3] U. Leiterer, H. Dier, and T. Naebert. Improvements in radiosonde humidity profiles using RS80/RS90 radiosondes of Vaisala. 70(4):319–336, 1997.

[4] R. W. Saunders, T. J. Hewison, S. J. Stringer, and N. C. Atkinson. The radiometric characterization of AMSU-B. 43(4):760–771, 1995.

[5] B. J. Soden and J. R. Lanzante. An Assessment of Satellite and Radiosonde Climatologies of Upper-Tropospheric Water Vapor. *J. Climate.*, 9:1235–1250, 1995.

[6] J. Wang, H. L. Cole, D. J. Carlson, E. R. Miller, and K. Beierle. Correction of Humidity Measurement Errors from the Vaisala RS80 Radiosonde - Application to TOGA COARE Data. *J. Atm. Ocean. Tech.*, 19:981–1002, 2002.

International MODIS and AIRS Processing Package (IMAPP) – Package Status and Features

Hung-Lung Huang, Liam E. Gumley, Kathy Strabala, Jun Li, Elisabeth Weisz, Thomas Rink, Kevin C. Baggett, James E. Davies, and Tom Achtor
Cooperative Institute for Meteorological Satellite Studies,
University of Wisconsin-Madison, Madison, Wisconsin

1. Introduction

The National Aeronautics & Space Administration (NASA) Earth Observing System (EOS) spacecrafts Terra and Aqua are providing a new generation of sensor observations of planet Earth. The instruments onboard these platforms provide a wealth of information on ocean, atmosphere, and land processes that are of global environmental importance. A critical component of the data distribution system for Terra and Aqua is the direct broadcast service on the spacecraft. The International MODIS/AIRS Processing Package (IMAPP) (Huang et al. 2004) provides researchers, governmental, educational, and commercial sector users with the capability of receiving and processing raw data in real-time (i.e., as observations are acquired) and creating environmental products which provide immediate information in areas as diverse as severe weather monitoring, forest fire detection, fisheries management, weather forecasting, aviation safety, and ice forecasts, to name a few.

In anticipation of these activities, NASA funded IMAPP in 2000, to provide freely distributed science production software that will transform Level 0 MODIS/AIRS data into calibrated and geolocated radiances and reflectances (level 1B) as well as a limited set of environmental products (level 2). Both Terra (MODIS am) and Aqua (MODIS pm and AIRS) platforms have a direct broadcast X-band downlink that allows data to be received in real time by sites having the proper reception hardware. IMAPP is derived from the operational processing software developed by NASA, and is modified to be compatible with direct broadcast data.

2. Software Package

Distribution of IMAPP to the user community means that the production software must be easy to install and use. With this in mind, the software was developed with these requirements:

- IMAPP must be portable to a wide range of UNIX/PC platforms.
- The number of required toolkits must be kept to a minimum.
- Ancillary data sets must be easily accessible.
- Software must be able to process overpasses of any size.
- Downlinked spacecraft ephemeris and attitude data may be used for real-time geolocation.
- Distributed products must be similar to those produced at the Goddard Space Flight Center (GSFC) Distributed Active Archive Center (DAAC).
- The code must be efficient.

2.1 *MODIS*

Following the requirements outlined above, MODIS IMAPP v1.1 geolocation and calibration L1B software modules were developed and first released in May 2000 and included the following functionality for Terra MODIS:

- Reformatting from time-ordered CCSDS Level-0 packets to Level-1A.
- Geolocation for every 1000 m pixels.
- Calibration for every pixel in bands 1-2, 1-7, and 1-36 at 250, 500 and 1000 m resolution respectively.

The first international user was the University of Dundee, where IMAPP was used to process the first Terra MODIS pass collected by the institution on May 8th, 2000 (Dundee served as a beta test site for IMAPP v1.0).

To date, SSEC has released IMAPP versions for MODIS level 1 geolocation (Barbieri 1997) and a selection of MODIS level 2 geophysical products. Versions 1.1, 1.2, 1.3, and 1.4 of IMAPP MODIS level 1 were released in November 2000, April 2001, December 2001, and September 2003, respectively. These updates allowed EOS direct broadcast users to keep pace with improvements to the calibration for Terra and Aqua MODIS in a systematic fashion. IMAPP MODIS level 2 version 1.1 was released to the community in May 2002 (version 1.0 was not released to the public). The first products released were the cloud mask (Ackerman, et al 1998) and cloud top properties (King et al 1992, and Menzel et al 2002) and cloud phase (Baum et al 2000) algorithms. Version 1.2 followed in October 2002, and included the MODIS atmospheric profile algorithm, and version 1.3 was released in February 2003 and contained Aqua compatible versions of the aforementioned algorithms. Most recently, Version 1.4 was released in September 2003 containing scientific updates to the atmospheric profiles algorithm.

All IMAPP released software has been ported and tested on the following UNIX/PC platforms:

- SGI MIPS, IRIX 6.5
- Sun Ultra, SunOS 5.7
- IBM RS/6000, AIX 4.3
- HP PA-RISC, HP-UX B.10.20
- Intel Pentium, Red Hat Linux 7.2 (2.4.7-10) (with gcc/g77 2.96)
- Intel Pentium, Solaris8 x86 5.8 (with gcc/g77 2.95.2)

All IMAPP source code and test data are freely available for download from http://cimss.ssec.wisc.edu/~gumley/IMAPP/. Top level README files provide detailed installation instructions. Implementation of the software involves execution of simple scripts and only the National Center for Supercomputing Applications (NCSA) Hierarchical Data Format 4 (HDF4) toolkit is required. The processing environment has been greatly simplified from the DAAC environment and overpasses of any size may be processed. The software runs efficiently taking ~45 minutes to process a 10 minute MODIS overpass through level 1B on an Intel Pentium, Solaris x86.

2.1.1 *File Formats*

The format of the IMAPP MODIS level 1B output files is very similar, but not identical, to the format of the GSFC DAAC (B output files. In particular, IMAPP output

files are written using HDF only (not HDF-EOS), and IMAPP output files store metadata in separate global attributes. The difference can best be seen by comparing an alphabetized listing of the HDF SDS and Vdata objects in an IMAPP Level 1B 1000 meter file and the corresponding DAAC file. Similarly, the format of the geolocation files produced by IMAPP is very similar, but not identical to, the GSFC DAAC format, as seen in the alphabetized listing of the HDF SDS objects in an IMAPP geolocation file and the corresponding DAAC file.

The level 2 product file formats are not HDF. For simplicity, a straight binary file format and ascii header file that is compatible with ENVI and freelook, a freely distributed visualization tool, were selected as the output file format. For those desiring HDF, simple IDL routines to convert from binary to HDF are included with each MODIS level 2 software release.

2.1.2 Ancillary Data

External data sets are required as input in order to successfully run the MODIS IMAPP level 2 product software. All required ancillary data sets are staged together in real-time on an anonymous ftp site: (ftp://aqua.ssec.wisc.edu/pub/aqua/ancillary) which contains the current and previous 4 days of ancillary data. This facilitates the use of MODIS product software by providing a one-stop shop for all the ancillary data needed to run the algorithms. The files included at the site are:

(1) Near Real-Time SSM/I EASE-Grid Daily Global Ice Concentration and Snow Extent (NISE) file from the National Snow and Ice Data Center (NSIDC) in Colorado, USA for providing help in identifying cloud mask snow backgrounds.

(2) Daily SSMI sea ice concentration from the National Center for Environmental Prediction (NCEP). This provides help in identifying cloud mask sea ice backgrounds.

(3) 6 hourly Global Data Assimilation System T126 resolution profiles of temperature and moisture analyses from NCEP. These profiles are required in order to run the CO_2 slicing portion of the cloud top properties and cloud phase algorithm as well as perform retrievals of atmospheric temperature and moisture profiles.

2.2. *AIRS*

Working in conjunction with the AIRS Team at NASA Jet Propulsion Laboratory (JPL) (Aumann et al 1999, and Hofstadter et al 1999), SSEC received the first post-launch delivery of the AIRS/AMSU/HSB level 1 software package in September 2002. In January 2003, SSEC demonstrated the ability to transform locally acquired direct broadcast AIRS Level 0 data to Level 1. Due to the complexity of the calibration software for the more than 2300 spectral bands of the AIRS instrument, NASA agreed upon a strategy for level 1 IMAPP release whereby JPL would create the software and SSEC would test and distribute the binaries. SSEC is currently finalizing the beta testing of this package; the first version of AIRS/AMSU/HSB level 1 software is released on 5 November 2003.

3 Imagery and Products

IMAPP software has been successfully downloaded and installed by users all over the world. Correspondence from IMAPP users indicates that the software is in use in the USA, UK, Germany, Italy, Norway, Japan, China, Russia, South Korea, Singapore, Thailand, Vietnam, Brazil, South Africa, Australia and Mexico. In addition, the released operational automated products that are generated at SSEC in real-time (MODIS level 1 through all level 2 products), are placed on an ftp site for open access (ftp://aqua.ssec.wisc.edu/pub/). Quick look images are automatically generated for each captured overpass and placed on a web page in real-time: http://eosdb.ssec.wisc.edu/modisdirect/. The total end-to-end processing time between ingest and placement of MODIS level 1 to level 2 product files on the ftp site for distribution is ~ 1 1/2 - 2 hours on a Sun Intel Pentium, Solarisx86 2.5.1. An example of the CIMSS IMAPP automated product suite for MODIS Terra is shown in figure 1.

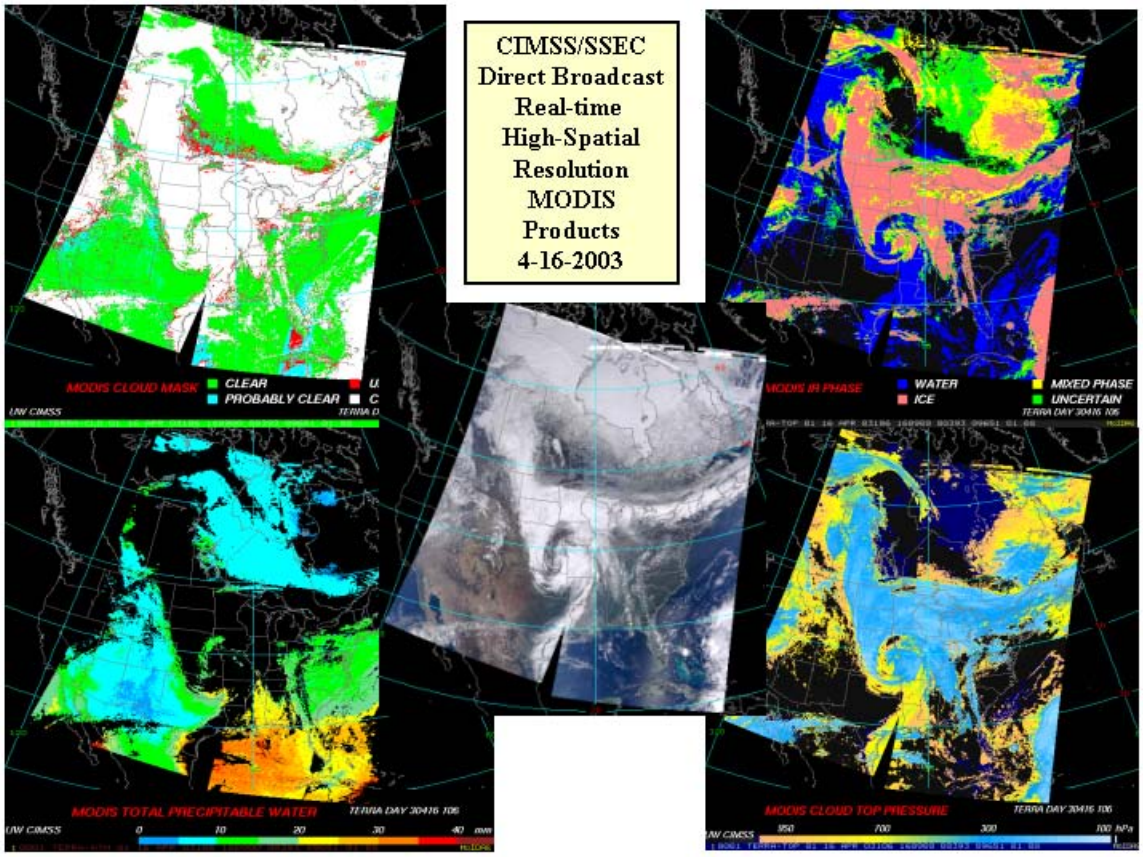

Figure 1. IMAPP products from Terra MODIS, 16 April 2003. Middle panel: true color image, upper left: cloud mask, upper right: cloud phase, lower left: total precipitable water, lower right: cloud top pressure.

Retrieval algorithms for AIRS level 2 products have been developed using a focus data set provided by the JPL AIRS science team. Figure 2 shows a sample of the AIRS/AMSU and HSB level 1 imagery from the focus data. AIRS color composite image and cloud phase are shown in figure 3.

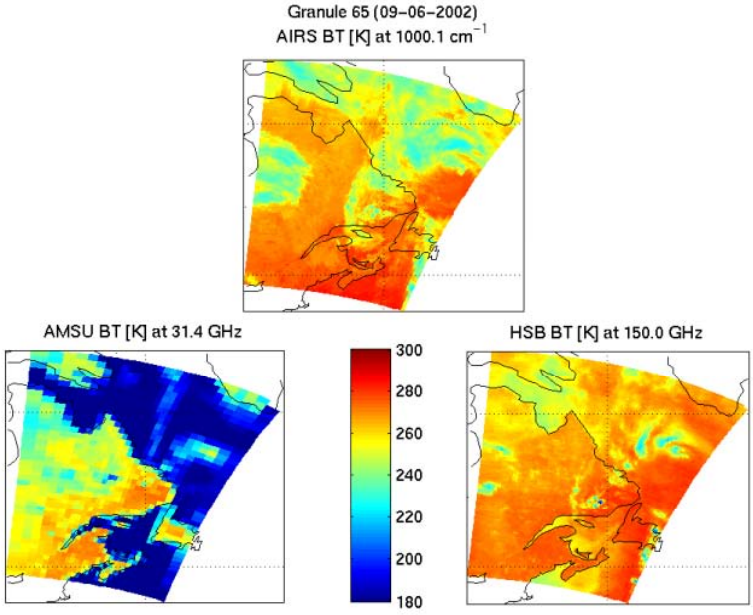

Figure 2. AIRS, AMSU and HSB level 1 brightness temperatures as produced by IMAPP software over North America on 20 July 2002.

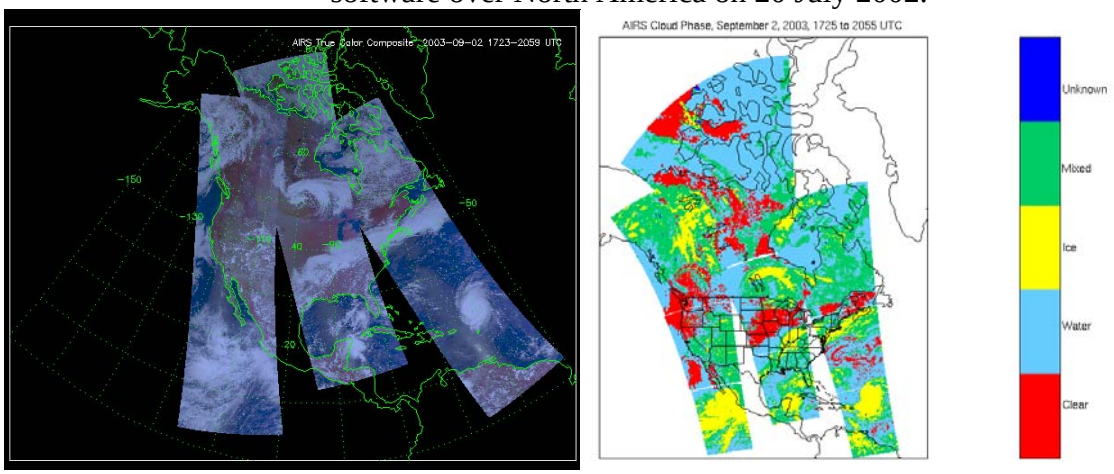

Figure 3. AIRS level 1B color composite and cloud mask derived from MODIS single filed of view (spatial resolution of ~ 1km at nadir) cloud mask pixels.

Figure 4 displays level temperature and water vapor retrievals derived from AIRS, MODIS and GOES, respectively. The retrieval differences are due to factors such as spectral and spatial measurement information content, data signal to noise ratio, and temporal discrepancy. All retrieval products are currently undergone validation. Retrieval algorithm refinement is expected once products validation suggests the need of product performance improvement.

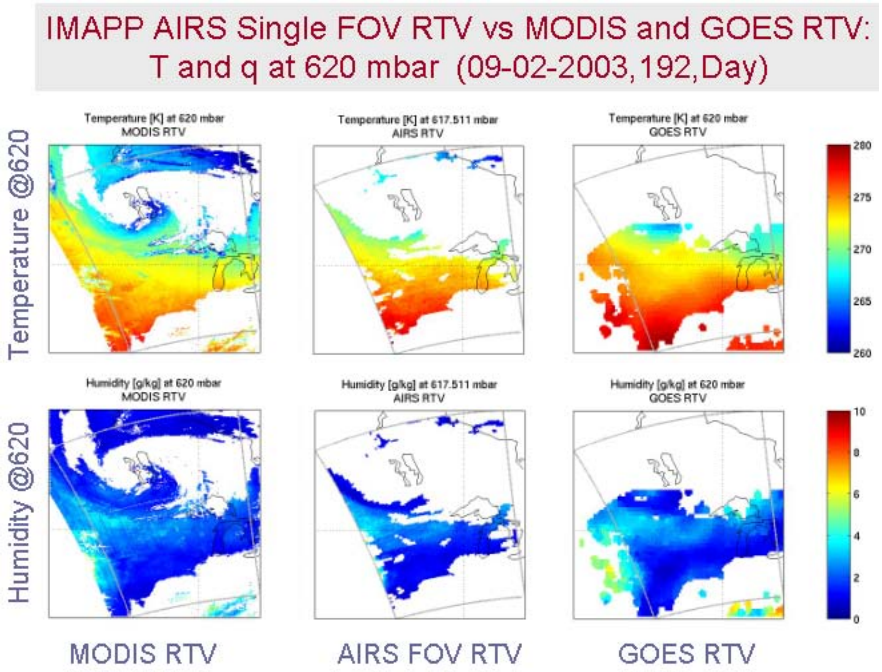

Figure 4. IMAPP AIRS single FOV, MODIS and GOES retrieval of temperature and water vapor of 620 mb on 2 September 2003.

CIMSS is using the real time products for many purposes. These include validation of MODIS products, testing new MODIS algorithms and changes to existing production software. Real-time data collection and processing allow us to routinely sample the data sets over pre-determined regions for investigations. For instance, MODIS water vapor retrievals from the direct broadcast atmospheric profiles product, along with MODIS radiances are being extracted and saved for all overflights of the Oklahoma, USA, Cloud and Radiation Testbed (CART) site. These are used for comparisons with other instrument retrievals made at the site (Seeman et al., 2003). Data is also being routinely extracted and shared with other collaborators such as Dr. Simon Hook of NASA's Jet Propulsion Laboratory (JPL), who is using the data for MODIS calibration and product validation over Lake Tahoe, Nevada, USA (Hook et al., 2001).

Real-time IMAPP products are also supporting the US National Weather Service as a forecasting tool under the NASA supported Short-term Prediction Research and Transition (SPORT) program. Other users of MODIS data acquired and processed by IMAPP at SSEC include:

- Naval Research Laboratory, Monterey
- Satellite Services Division, NOAA/NESDIS
- Atmospheric and Environmental Research, Inc, Lexington MA
- Upper Midwest Aerospace Consortium, University of North Dakota
- National Center for Environmental Prediction (NCEP), NOAA
- MODIS Snow and Sea Ice Global Mapping Project, NASA/GSFC

IMAPP is also used globally to generate real-time products of local interest. As an example, Plymouth Marine Laboratory's Remote Sensing Data Analysis Service (RSDAS) in the UK posts real-time IMAPP MODIS products on their web site for use in the CLOUDMAP2 European program. One of the goals of CLOUDMAP2 is "to produce and exploit value-added remote sensing data products on macroscopic (e.g. cloud-top height) and microscopic (e.g. cloud droplet radius) properties and water vapor distributions to characterize sub-grid scale processes within Numerical Weather Prediction Models (NWP) through validation and data assimilation".

4 Future Work

Table 1 briefly summarizes the current IMAPP product algorithms, along with those planned for production during the three-year continuation phase. MODIS algorithms released for Terra and Aqua have received the most attention during the initial phase.

Table 1. Summary of current and upcoming IMAPP MODIS and AIRS product algorithms.

	MODIS	**AIRS/AMSU/HSB**
Current	Geo-location/Navigation Cloud mask Cloud Phase Cloud top Property Clear T/Q Sounding Total Precipitable Water	Geo-location/Navigation
Planned	Cloud Particle Size Cloud Optical Thickness Aerosol Optical Thickness Surface Reflectance Sea Surface Temperature Snow Detection Sea Ice Detection Scene Classification (Clouds and Land Surface)	Clear/Cloudy T/Q Sounding Cloud Detection Cloud Clearing Cloud Height/Emissivity Surface Skin Temperature Cloud Liquid Water AMSU Precipitation estimate
	MODIS/AIRS Collocation	

5. Summary

The International MODIS/AIRS Processing Package has been successful in providing a portable, relatively easy to install and use software package for converting direct broadcast EOS Terra and Aqua data into valuable environmental products. The number of products within IMAPP continues to grow. The list now includes MODIS calibrated/navigated radiances, cloud mask, cloud top properties and cloud phase, and retrievals of atmospheric profiles (temperature, moisture) and total precipitable water. AIRS products are in beta test mode and will be added to the IMAPP suite in early 2004. All IMAPP released products have been verified against the NASA production counterparts.

IMAPP is going to evolve to adopt, adapt and develop new processing algorithms to meet global users' demands for regional real time multi-disciplinary applications. Most of all, with open source architecture and rigorous documentation standards, IMAPP can be easily implemented on almost any computing platform. In the near future, the International NPP/NPOESS Processing Package (INPP) as the next generation of IMAPP can continue to optimize the global utilization of earth observation data to improve our ability to monitor and understand the natural environment.

Acknowlegements

The Research Division, Office of Earth Science, NASA Headquarters Washington, DC funded this research as part of EOS Direct Broadcast program.

References

ACKERMAN, S. A., STRABALA, K. I., MENZEL, W. P., FREY, R. A., MOELLER, C. C., and GUMLEY, L. E., 1998, Discriminating clear sky from clouds with MODIS. *Journal of Geophysical Research*, **103**, 32141–32157.

AUMANN, H., GAISER, S., TING, D., and MANNING, E., 1999, AIRS Algorithm Theoretical Basis Document Level 1B Part 1: Infrared spectrometer. EOS Project Science Office, NASA Goddard Space Flight Center.

BARBIERI, R., 1997, MODIS Level 1B Algorithm Theoretical Basis Document. EOS Project Science Office, NASA Goddard Space Flight Center, 70 pp.

BAUM, B. A., P. F. Soulen, K. I. Strabala, M. D. King, S. A. Ackerman, W. P. Menzel, and P. Yang, 2000: Remote sensing of cloud properties using MODIS Airborne Simulator imagery during SUCCESS. II. Cloud thermodynamic phase. *J. Geophys. Res.*, **105**, 11,781-11,792.

HOFSTADTER, M., AUMANN, H., MANNING, E., GAISER, S., GAUTIER, C., and YANG, S., 1999, AIRS Algorithm Theoretical Basis Document Level 1B Part 2: Visible/Near-Infrared Channels. EOS Project Science Office, NASA Goddard Space Flight Center.

HOOK, S. J, PRATA, F. J., and SCHLADOW, G. S., 2001, Validation of Thermal Infrared Data and Products from MODIS and ASTER over Land. NASA progress report. See http://eospso.gsfc.nasa.gov/ftp_docs/validation/Hook.01.report.pdf .

HUANG, H.L., L.E. Gumley, K. Strabala, J. Li, E. Weisz, T. Rink, K.C. Baggett, J. E. Davies, W.L. Smith, J. C. Dodge, 2004: International MODIS and AIRS Processing Package (IMAPP) – A Direct Broadcast Software Package for the NASA Earth Observing System. American Meteorological Society Bulletin, February 2004, 17-19.

KING, M. D., KAUFMAN, Y. J., MENZEL, W. P., and TANRE, D. 1992, Remote sensing of cloud, aerosol, and water vapor properties from the Moderate Resolution Imaging Spectrometer (MODIS). *IEEE Transactions on Geoscience and Remote Sensing*, **30**, 2-27.

MENZEL, W. P. SEEMAN, S. W., LI, J., and GUMLEY, L. E., 2002, MODIS Atmospheric Profile Retrieval Algorithm Theoretical Basis Document. EOS Project Science Office, NASA Goddard Space Flight Center, 39 pp.

SEEMAN, S. W., LI, J., MENZEL, W. P., and GUMLEY, L. E., 2003, Operational retrieval of atmospheric temperature, moisture , and ozone from MODIS infrared radiances. *Journal of Applied Meteorology*, **42**, 1072-1091.

First comparison of radiances measured by AIRS/AQUA and HIRS/NOAA-16&-17

Pubu Ciren
QSS Group Inc. Lanham, Maryland, U.S.A

Changyong Cao
NOAA/NESDIS/ORA/STAR, Camp Springs, Maryland, U.S.A

Introduction

Cross sensor comparison of the measured radiances has become increasingly important, as it is not only highly significant for the validation of instrument performance, but also is crucial for inter-satellite calibration to achieve consistency and tractability required for long-term climate studies. The High Resolution Infrared Radiation Sounder (HIRS) has flown on National Oceanic and Atmospheric Administration (NOAA)'s polar-orbiting satellites for over two decades. Data from the HIRS instruments are used, in conjunction with other instruments, to calculate the atmosphere's vertical temperature profile, Outgoing Long-wave Radiation (OLR), and upper tropospheric humidity. AIRS (Atmospheric Infrared Radiation Sounder) is a relatively new hyperspectral thermal sensor onboard AQUA with spectral overlaps to most of the HIRS channels (see Table 1). Comparing the radiances measured by these two instruments allows us to check their calibration to ensure consistency. In addition, the hyperspectral nature of AIRS may allow us to evaluate the spectral response functions of HIRS, which has uncertainties due to lack of stringent specification. In this paper, we present the method and results of the comparison between HIRS/NOAA-16&-17 radiances with the convolved AIRS radiance.

Satellite data

The data used in this comparison are level-1b radiance data from HIRS/NOAA-16&17 and that from AIRS/AQUA. AIRS is a high spectral resolution spectrometer with coverage in nearly 2400 bands in the infrared and visible ranges: 3.7 - 15 μm and 0.4 - 1.0 μm. It views the earth through a cross track rotary scan mirror which provides a viewing angle of ±49.5° and with a spatial resolution of 13.5km in the infrared and Vis/NIR spatial resolution of 2.3km, respectively. AIRS has been flowing onboard AQUA - NASA EOS PM (1:30 pm Equatorial Crossing Time) polar orbiting platform since April 2002. HIRS is onboard NOAA polar orbiting satellites. Similar to AIRS, HIRS observes the earth through a scanning mirror with a viewing angle of ±49.5°, and a spatial resolution of around 20 km, slightly larger than AIRS. It consists of 19 broadband IR channels (7 channels in the wavelength rang from 3.7 to 4.6 μm and 12 channels in the wavelength range from 6.5 to 15.0 μm). The spectral overlap between AIRS and HIRS IR channels can be seen in Figure 1, which shows that all the HIRS channels have some spectral overlaps with AIRS. However, only 7 HIRS channels are fully overlapped by AIRS. To minimize the uncertainty associated with the spectral differences, comparisons shown in this study are only for the 7 fully spectrally overlapped channels.

The time period of the collocated AIRS and HIRS data in this study covers from March 11, 2003, the first day when AIRS becomes publicly available, to October 15, 2003. AIRS level-1b data before September 1 are obtained from the NASA DAAC, hereafter the corresponding data are provided

operationally by the NESDIS AIRS team. The HIRS level1b data are acquired from the NOAA Satellite Active Archive.

Table 1. Specification of AIRS/Aqua and HIRS/NOAA

	AIRS/Aqua	HIRS/NOAA
Spectral Coverage	3.74~4.61μm 6.20~8.22μm 8.88~15.4μm	7 channels:3.70~4.60μm 12 channels:6.5~15.0μm
Scan angle	±49.5 from nadir	±49.5 from nadir
IFOV	1.1º	SWIR: 1.4 º LW IR: 1.3 º
Earth view Coverage	13.5 km at Nadir	20.3 km at Nadir SWIR 18.9 km at Nadir LWIR

Collocating, remapping and convolving

Based on predictions using orbital perturbation models (Cao, et al., 2003), it is found that simultaneous nadir overpasses between Aqua and NOAA-16 & -17 occur every 2-3 days. After collecting AIRS granules and HIRS orbits which contains potential intersections, simultaneous nadir observations (SNO) between AIRS and HIRS are selected based on two criteria, i.e., distance between nadir pixels < half the size of the HIRS pixels (~10 km), and time difference between nadir pixels < 30 seconds. As a result, a total number of 50 and 70 intersections are found for Aqua vs. NOAA-16 and Aqua vs. NOAA-17 respectively, during the time period from March 11 to October 15 2003. The locations of these intersections are given in Figure 2. It is seen that nearly all intersections occur in polar regions. The distance between pixels of two satellites (*D*) is defined as:

$$D = R/[\cos(\sin l_1 \sin l_2 + \cos l_1 \cos l_2 \cos(m_2 - m_1)] \qquad (1)$$

here R is the mean Earth radius, given as 6378km. l_1 and l_2 is pixel latitude, respectively of the AIRS and HIRS. m_1 and m_2 is the corresponding pixel longitude.

After finding the SNOs, HIRS observations are remapped to AIRS pixels around SNOs by using the same criteria as mentioned above. However, in order to compare with the HIRS radiances in 7 fully spectrally overlapped broadband channels, AIRS hyperspectral measurements must be convolved with the HIRS spectral response function. This is carried out in two steps. First of all, since every measurement at AIRS channel is a convolved result of its neighboring 471 channels (+235), spectral response function of HIRS (SRF_{HIRS}) at AIRS channel λ_1 is first convolved with AIRS spectral response function (SRF_{AIRS}) as shown in equation 3. Secondly, AIRS radiance is further convolved with the consequent spectral response function values ($w(\lambda_1)$), as shown in equation 2, producing the radiance equivalent to HIRS measurements with the same spectral coverage.

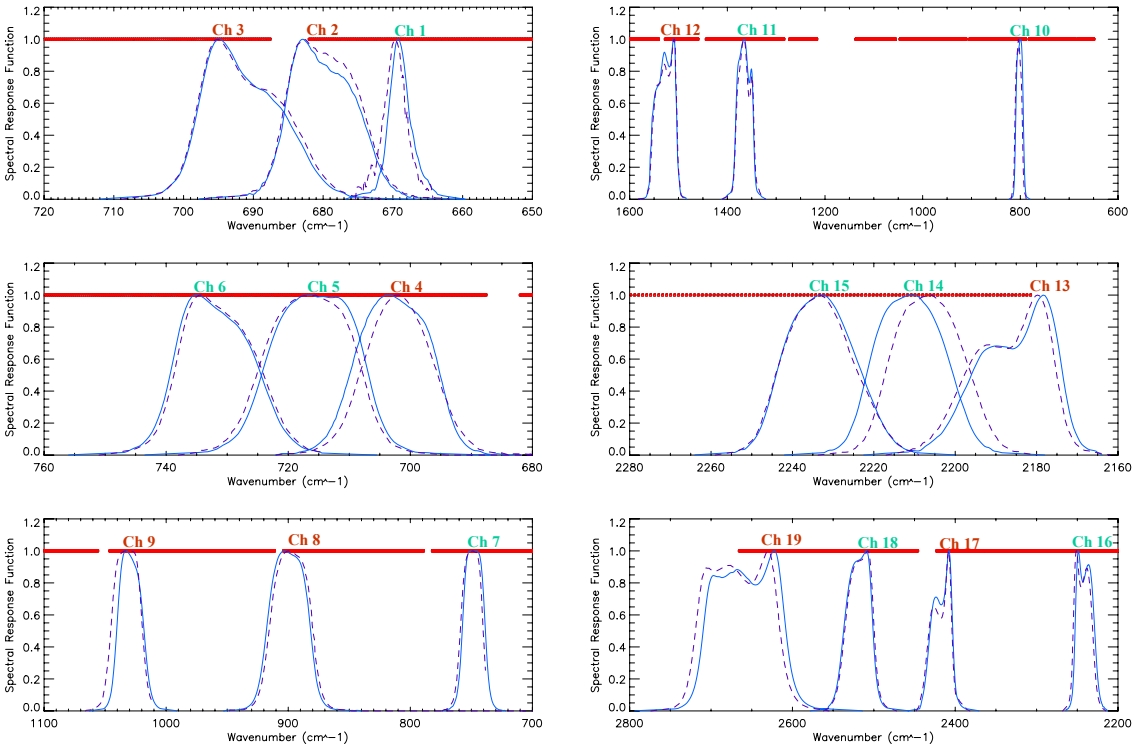

Figure 1. HIRS spectral response functions for the 19 IR channels (solid line for NOAA-16; dashed line for NOAA-17). Red lines show the corresponding AIRS spectral channel coverage. Only 9 HIRS IR channels are fully spectrally overlapped by AIRS, shown as green color.

$$R_{COV} = \frac{\int_{\lambda_1}^{\lambda_2} R_{AIRS}(\lambda) \bullet w(\lambda) \bullet d\lambda}{\int_{\lambda_1}^{\lambda_2} w(\lambda) \bullet d\lambda} \qquad (2)$$

$$w(\lambda_1) = \frac{\int_{\lambda_1-\Delta\lambda}^{\lambda_1+\Delta\lambda} SRF_{HIRS}(\lambda_1) \bullet SRF_{AIRS}(\lambda) \bullet d\lambda}{\int_{\lambda_1-\Delta\lambda}^{\lambda_1+\Delta\lambda} SRF_{AIRS}(\lambda) \bullet d\lambda} \qquad (3)$$

Results

Difference between the collocated measurements from two different satellites may originate from several sources. The purpose of the comparisons in this study is to evaluate the calibration differences since uncertainties due to differences in observation geometry, spectral coverage, and time have been reduced to a level that is negligible in this study by using simultaneous nadir observations. The contribution from the difference in viewing geometry and small differences in the spatial resolution are further reduced by only using the averaged radiance in a box with 4 by 5 pixels around the SNO pixel in this study.

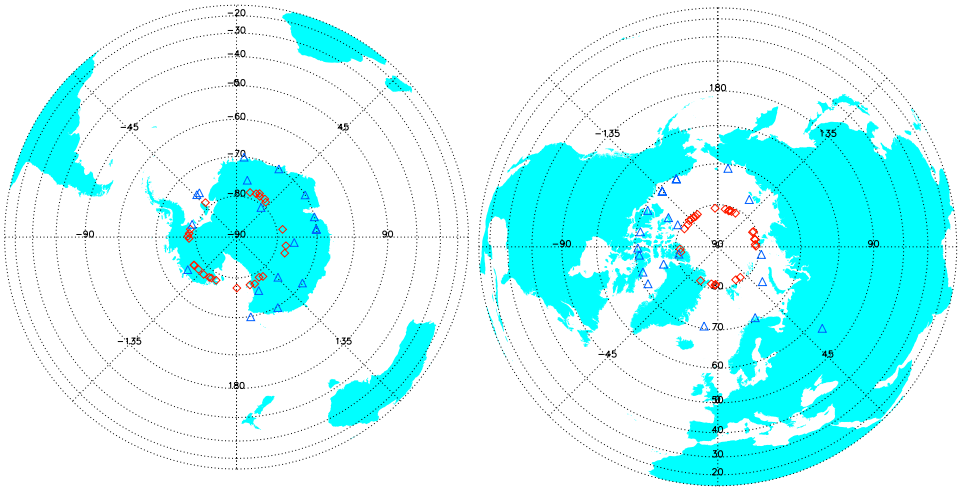

□ —— Aqua&NOAA-16 Δ —— Aqua&NOAA-17

Figure 2. Collocated intersections between AIRS/AQUA and HIRS/NOAA-16 (or NOAA-17)

An example is given in Figure 3 which shows simultaneous nadir observations between AIRS/Aqua and HIRS/NOAA-16 on July 22, 2003. It is seen that, for all 7 spectrally fully overlapped channels, similar pattern are shown in both the remapped HIRS radiance and the convolved AIRS radiance. However, there is a significant discrepancy (as much as 3~4 K) in the HIRS channel 1, and the spread is relatively large. This may indicate a problematic calibration in this HIRS channel, which has a number of known calibration problems. For other channels, both HIRS observations and the convolved AIRS measurements have much smaller differences. In addition, the difference between the mean HIRS and AIRS radiance inside the nadir window box at the SNO pixel is less than 1 K (see Figure 3), which indicates a good agreement between AIRS and HIRS.

To investigate thoroughly the agreement between HIRS and AIRS observations, the mean and standard deviation of measured radiances in the window described above are calculated for all the intersections and for both NOAA-16 and NOAA-17. In addition, to evaluate a newly developed HIRS calibration algorithm (Cao and Pubu, 2003), i.e. Version 4.0, HIRS radiance is calculated with both the current operational calibration algorithm (i.e., Version 3.0) and the new one. The results are shown in Figure 4a and b, which presents the mean radiance difference between the convolved AIRS radiance and HIRS radiance as a function of Julian day, for NOAA-16 and NOAA-17 respectively. The corresponding statistics of the resulting difference in brightness temperature is given in Table 2. It is seen that, except for channel 1, the agreement between the observed HIRS and AIRS is generally good. The difference in brightness is generally smaller than ±1K. In addition, it appears that the deviations are considerably smaller in

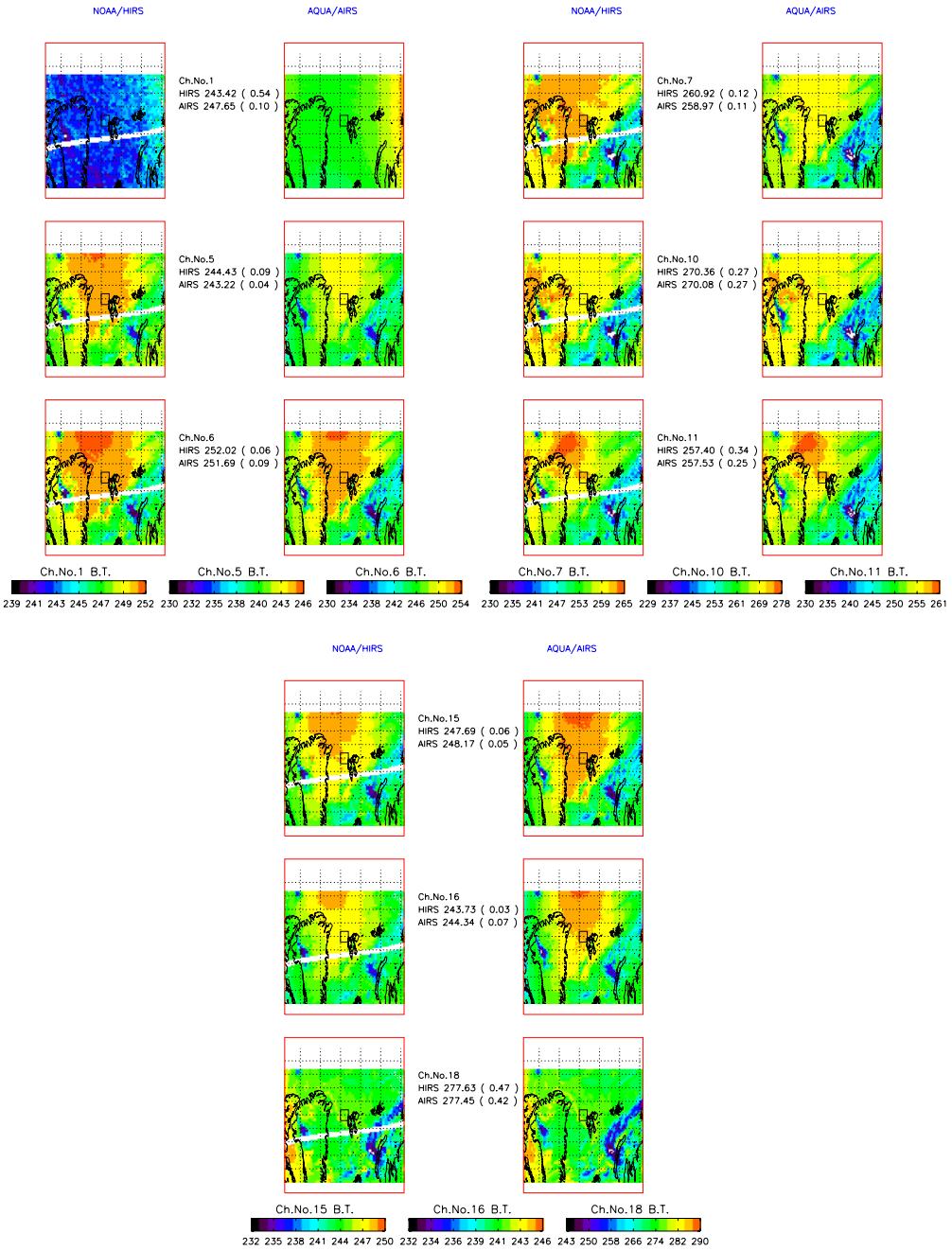

Figure 3. Example data set shows simultaneous nadir observations between AIRS/Aqua and HIRS/NOAA-16 on July 22, 2003. AIRS data are spectrally convolved with HIRS spectral response functions, and HIRS pixels are remapped to AIRS pixels. The black box in the center represents the 4 by 5 pixels window near the nadir intersection of these two satellites, for which the brightness temperature differences (mean and standard deviation) are given in the parenthesis.

the longwave channels than in the shortwave channels. For example, the brightness temperature difference in channel 5 is about -0.8 K, while it decreased to less than 0.1 K for channel 16. There is no significant difference between NOAA-16 and NOAA-17 in terms of the mean bias

for most channels, however, the standard deviation of the difference is noticeably smaller in NOAA-16/HIRS than those for NOAA-17/HIRS (see Table 2). On the other hand, it is also found that the application of the newly developed calibration algorithm does not have significant effect on the systematic bias in the comparisons shown in this study. This is probably due to the fact that the HIRS orbits used in this study do not have the problems of rapid filter temperature change, which was the problem that the new algorithm is designed to solves [Cao and Pubu , 2003].

Concluding remarks

Comparisons of HIRS with AIRS radiance is carried out by comparing the simultaneous nadir observations at intersections of these two satellites. The AIRS spectral radiances are convolved with the HIRS spectral response functions to generate HIRS equivalent channels based on AIRS spectral radiance data. The comparisons are carried out for both NOAA-16/HIRS and NOAA-17/HIRS.

a. NOAA-16

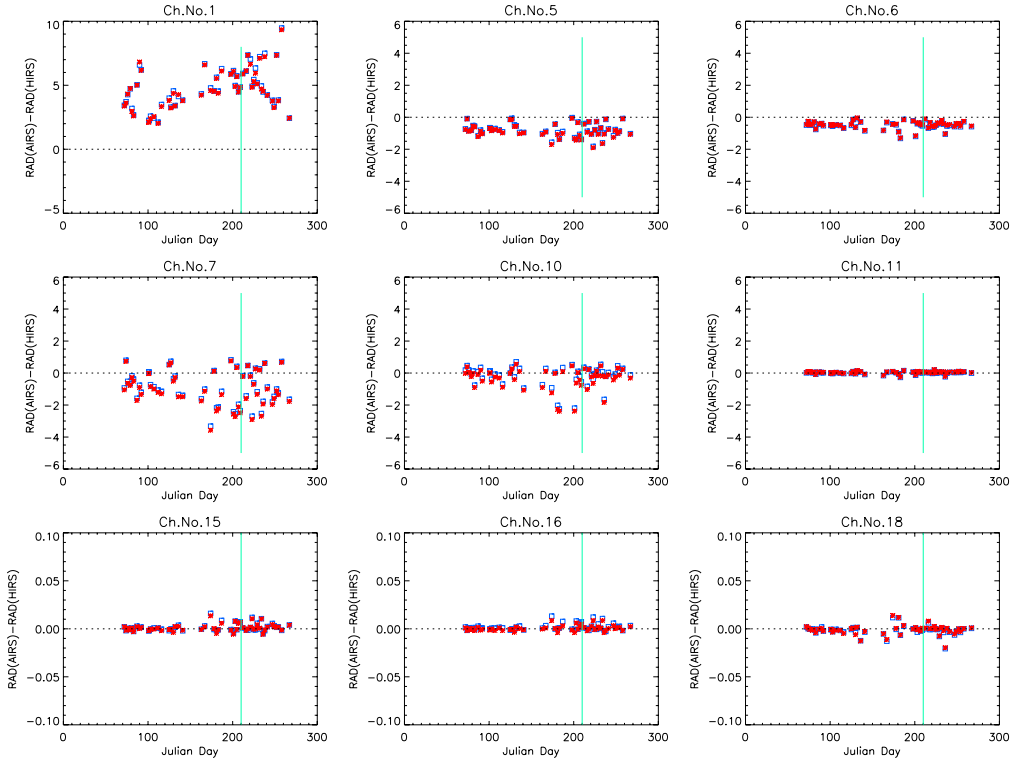

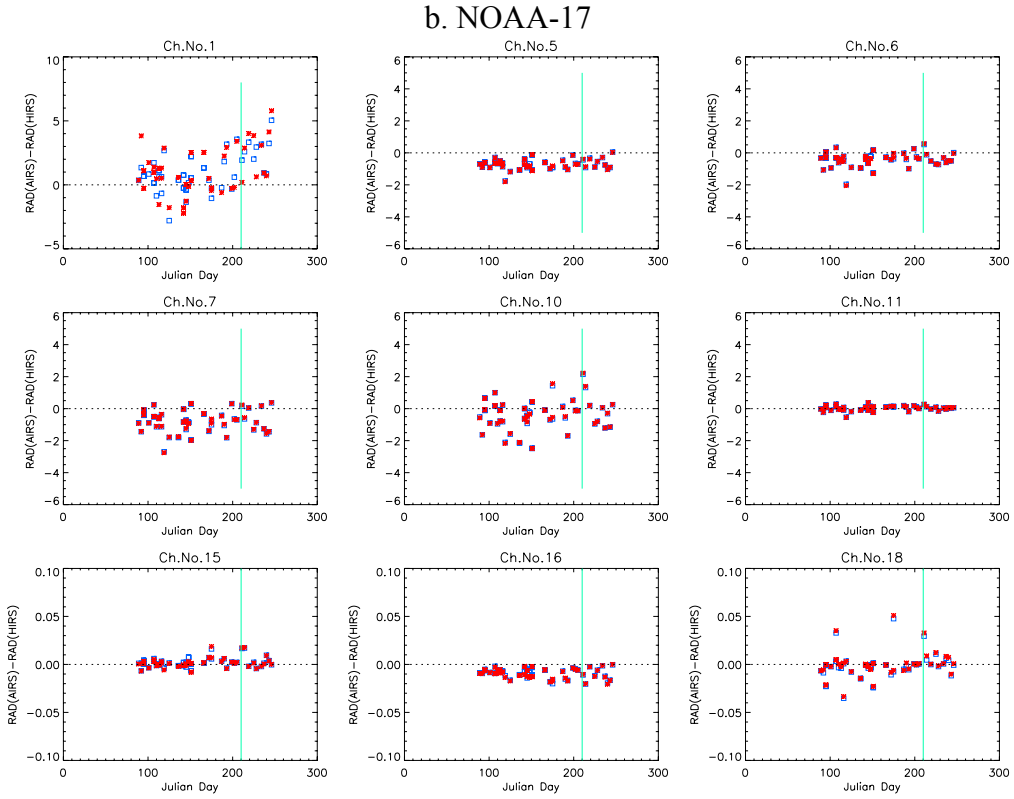

Figure 4. Difference between AIRS (spectrally convolved to match HIRS) and HIRS are given in radiance (a and b), and brightness temperature (c and d). The green line indicates the date when AIRS L1B data changed from version V. 2.7 to V. 3.05. □ ─ HIRS calibration algorithm 3; * ─ HIRS calibration algorithm 4

Table 2. Brightness temperature comparison summary. ΔBT1 and ΔBT2 represent the difference (AIRS – HIRS) for HIRS calibration algorithm 3 and 4 respectively.

AIRS-HIRS			Ch. 1	Ch. 5	Ch. 6	Ch. 7	Ch. 10	Ch. 11	Ch. 15	Ch .16	Ch. 18
NOAA-16	ΔBT1	mean	5.1	-0.8	-0.5	-0.7	-0.1	0.04	0.02	0.1	-0.4
		Std	2.1	0.4	0.2	0.9	0.6	0.3	0.4	0.4	0.8
	ΔBT2	mean	5.0	-0.8	-0.5	-0.8	-0.3	0.1	0.02	-0.01	-0.2
		std	2.0	0.4	0.2	0.9	0.6	0.3	0.3	0.3	0.8
NOAA-17	ΔBT1	mean	1.0	-0.7	-0.4	-0.7	-0.3	0.07	0.08	-1.0	-0.3
		std	1.6	0.3	0.4	0.6	0.8	0.5	0.5	0.3	0.9
	ΔBT2	mean	1.0	-0.7	-0.4	-0.7	-0.3	0.07	0.05	-1.0	-0.1
		std	1.9	0.3	0.4	0.6	0.8	0.5	0.5	0.4	0.9

It was found that observations by HIRS and AIRS generally agree well with each other for most channels. The agreement is better than 0.5 K for HIRS Channel 6, 10,11,15,16 and 18. Slightly larger (about 1K) discrepancy is observed for channel 5 and 7. For channe1 1, considerably large difference exists. No significant difference between NOAA-16/HIRS vs. AIRS and NOAA-17/HIRS vs. AIRS comparisons. However, NOAA-17 appears to give a larger standard deviation. Finally, comparisons made in this study are based on 68 (or 57) intersections for NOAA-16 vs. AIRS (or NOAA-17 vs. AIRS) during a 6 months period. More data is needed to better characterize the agreement between HIRS and AIRS to account for any possible seasonal variations.

Acknowledgements

Many thanks to Mr. Walter Wolf of QSS group Inc., who greatly facilitated the AIRS level 1b data acquisition for this study. Comments and suggestions from Dr. Chris Barnet are also appreciated.

References

Cao, C., M. Weinreb, and H. Xu, 2003, Predicting simultaneous nadir overpasses among polar-orbiting meteorological satellites for the inter-satellite calibration of radiometers, Journal of Atmospheric and Oceanic Technology, in press.

Cao, C., P. Ciren, 2003, Operational high resolution infrared radiation sounder(HIRS) calibration algorithms and their effects on calibration accuracy, Proceeding of 13th International TOVS Study Conference, Sainte-Adele, Canada, 29 October – 4 November 2003.

Japanese Advanced Meteorological Imager (JAMI): Design, Characterization and Expected On-Orbit Performance

Jeffery J. Puschell*, Howard A. Lowe, James Jeter, Steven Kus, Roderic Osgood,
W. Todd Hurt, David Gilman, David Rogers, Roger Hoelter
Raytheon Space and Airborne Systems, Santa Barbara Remote Sensing

Ahmed Kamel
Space Systems/Loral

ABSTRACT

The Japanese Advanced Meteorological Imager (JAMI) was developed by Raytheon and delivered to Space Systems/Loral as the Imager Subsystem for the Japanese MTSAT-1R system. Detailed characterization tests show JAMI meets all MTSAT-1R requirements with margin. JAMI introduces the next generation of operational weather imagers in geosynchronous Earth orbit (GEO) and provides much improved spatial sampling, radiometric sensitivity, Earth coverage and 24-hour observation capability compared with current GEO imagers.

Keywords: remote sensing, advanced technology, meteorological imaging, geosynchronous orbit

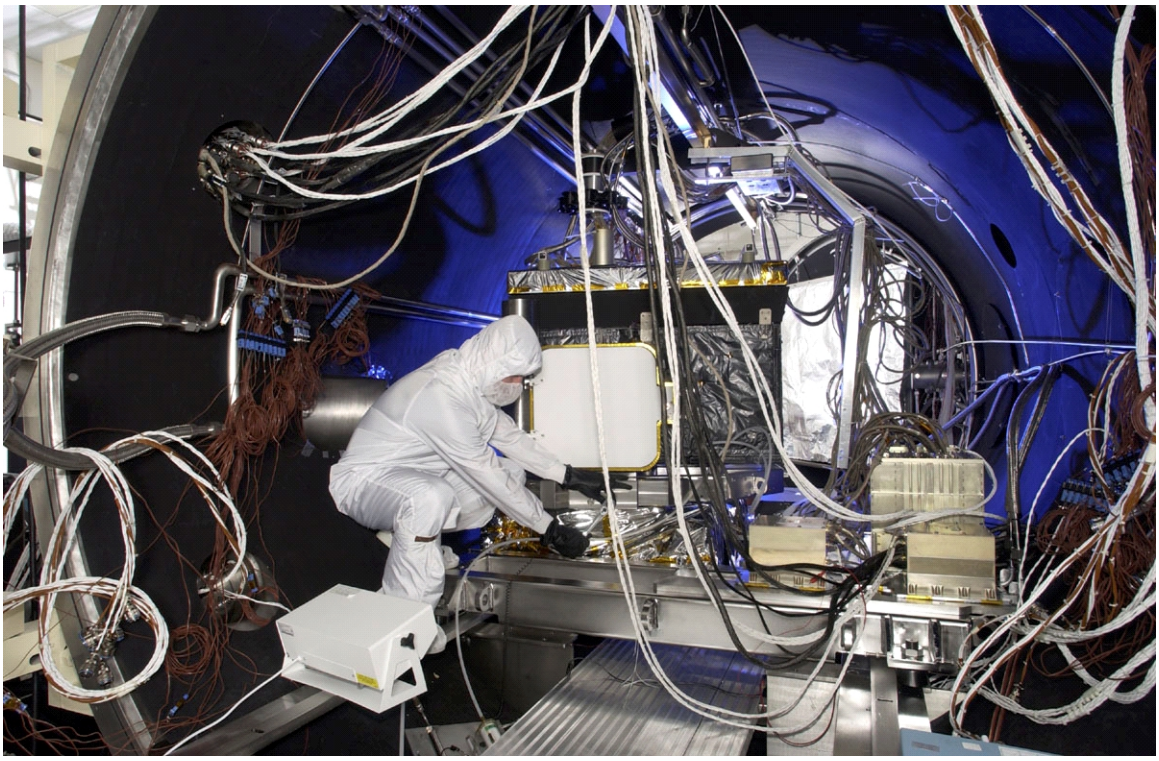

Figure 1. JAMI is prepared for thermal-vacuum and calibration testing, in advance of its delivery on 2003 June 17.

* Correspondence: Jeffery J. Puschell, Raytheon Space and Airborne Systems, Santa Barbara Remote Sensing, 75 Coromar Drive, B32/15, Goleta, CA 93117 USA; e-mail: jjpuschell@raytheon.com.

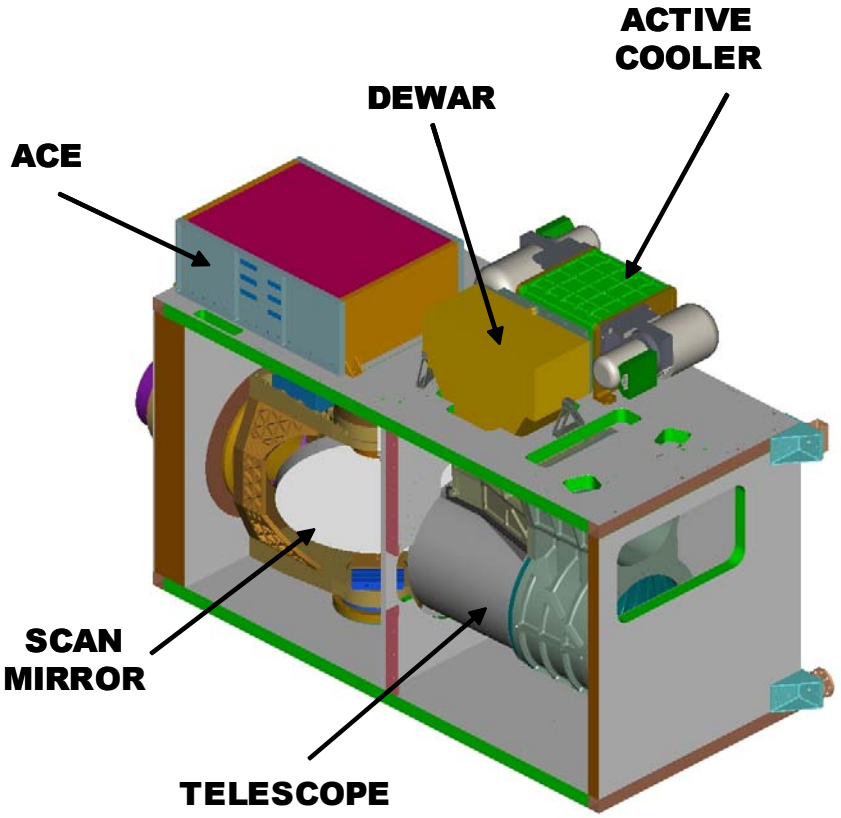

Figure 2. JAMI provides data with unprecedented detail and fidelity by means of recently proven new technology such as active cooling that was implemented successfully in a compact, efficient design architecture.

1. INTRODUCTION

Raytheon Santa Barbara Remote Sensing built the Japanese Advanced Meteorological Imager (JAMI) for Space Systems/Loral as the Imager Subsystem for Japan's MTSAT-1R multifunctional satellite system. MTSAT fulfills a meteorological mission by providing timely, high quality full-disk multispectral imagery for operational weather needs in Japan, East Asia and Australia along with a civil aviation mission by relaying digitized voice data and other data for aircraft along with radio navigation signals. MTSAT-1R is a replacement satellite for MTSAT-1, which was destroyed at launch on 1999 November 15. Due to Japan's urgent need to replace MTSAT-1, JAMI was developed on a challenging schedule that began with the Japanese request for proposal on 2000 January 11 and resulted in instrument delivery on 2003 June 17, roughly three and half years later. Raytheon's success in responding to the needs of MTSAT-1R and delivering an excellent operational GEO imager was enabled by an elegant instrument architecture and use of newer but proven technology that simplified design, assembly and test of the Imager while simultaneously supplying superior performance. A dedicated and talented management and test team (cf. Figure 1) characterized performance of this innovative, advanced technology design with unmatched efficiency. As shown below, JAMI breaks through limitations of earlier three-axis stabilized GEO instruments with significant improvements in many areas, including spatial sampling, radiometric sensitivity, calibration and performance around local midnight.

2. DESIGN

Puschell et al.[1] described many of the design characteristics of JAMI. Figure 2 illustrates an isometric view of the imager. Table 1 compares general design and measured performance characteristics of JAMI with MTSAT-1R requirements.

Table 1. JAMI's measured performance meets MTSAT-1R requirements with significant margin.

Parameter	MTSAT-1R Requirement	JAMI Performance
Spectral Channels	Visible: 0.55 μm to 0.75 - 0.90 μm IR1: 10.3 μm to 11.3 μm IR2: 11.5 μm to 12.5 μm IR3: 6.5 μm to 7.0 μm IR4: 3.5 - 3.8 μm to 4.0 μm	Visible: 0.55 μm to 0.90 μm IR1: 10.3 μm to 11.3 μm IR2: 11.5 μm to 12.5 μm IR3: 6.5 μm to 7.0 μm IR4: 3.5 μm to 4.0 μm
Detector Sample Resolution at Nadir	Design Dependent	0.5 km (visible), 2 km (infrared)
HiRID Data Ground Resolution	1.25 km (visible), 5.0 km (infrared)	1.0 km (visible), 4.0 km (infrared)
HRIT Data Ground Resolution	1.0 km (visible), 4.0 km (infrared)	1.0 (visible), 4.0 km (infrared)
MTF(IR2) at 4473 rad-1(Observation Data)	>0.25	>0.44
Field of View	Design Dependent	0.269 deg per swath
Image Frame	17.6 deg (N-S) by 17.6 deg (E-W)	21.4 deg (N-S) by 23.6 deg (E-W)
Detector Array Lengths	Design Dependent	336 (visible), 84 (infrared)
Detector Operating Temperatures	Design Dependent	Ambient (visible), 75 K (IR)
Full Disk Coverage Time	<30 min	<24 min
Calibration Accuracy (One Observation) *Analysis in progress on 2003 August 1*	2.5% (visible) 0.21 K (IR at 300 K) 0.10 (IR at 220 K)	2.5% (visible) 0.08 - 0.16 K (IR at 300 K) 0.08 - 0.10 K (IR at 220 K)

Design features. JAMI covers the 0.55 μm to 12.5 μm spectral region using the required 4 infrared bands and 1 visible wavelength band that are listed in Table 1. JAMI's thermal IR bands have fully redundant 84 element 1-d arrays that sample Earth with 2 km ground-projected instantaneous field of view (IFOV) at nadir. The visible band has 336 element 1-d arrays that sample Earth with 0.5 km ground-projected IFOV at nadir. These large format arrays enable faster full disk coverage rate with slower scan rate than current systems. Benefits of slower scan rate include better radiometric sensitivity, a longer life scanner and less impact on the spacecraft. JAMI covers the full Earth disk, including all required pointing verification and calibration scans, in ~24 minutes. An onboard calibration system for all bands is built into the imager.

The imager provides a 21.4 deg (N-S) by 23.6 deg (E-W) full frame scan area that is centered at the projection of spacecraft nadir on Earth (Figure 3). After launch in 2004, JAMI will be stationed at the 140 E longitude orbital slot that has traditionally been reserved for operational weather imaging for Japan, East Asia and Australia. JAMI's full frame includes a complete view of Earth as well as views of cold space for calibration and star sensing.

Raytheon's JAMI design is based on advanced imager technologies that have already been space-qualified and flown in research systems such as MODIS and MTI. The design addresses and mitigates limitations of existing operational GEO imagers with respect to performance around local midnight, spatial sampling, radiometric sensitivity, calibration and image navigation and registration. The heart of the design is a wide field-of-view, off axis telescope that enables an elegant two focal plane architecture while intrinsically mitigating effects of sunlight shining directly into the instrument aperture around local midnight, the single most challenging design issue for a GEO imager. The two focal plane design offers significant advantages with respect to other design approaches. These include separation of visible and infrared arrays to improve cooling performance of the infrared arrays, better throughput and a much simpler and easier to build optical layout than previous operational imagers. The off axis telescope offers better MTF performance and reacts less to solar heating than current system designs because no central secondary mirror with support spider is present to be heated by the Sun and distort optical performance, as in current operational imagers.

This advanced MTSAT imager represents the best balance between heritage and newer space-qualified technology. Use of proven second-generation focal plane technology from MODIS, MTI and other Raytheon programs improves radiometric and calibration performance eliminates 1/f noise striping problems of current operational imagers while simplifying instrument integration and test. JAMI's active cooler enables exceptional radiometric sensitivity performance over a long life using an approach flight

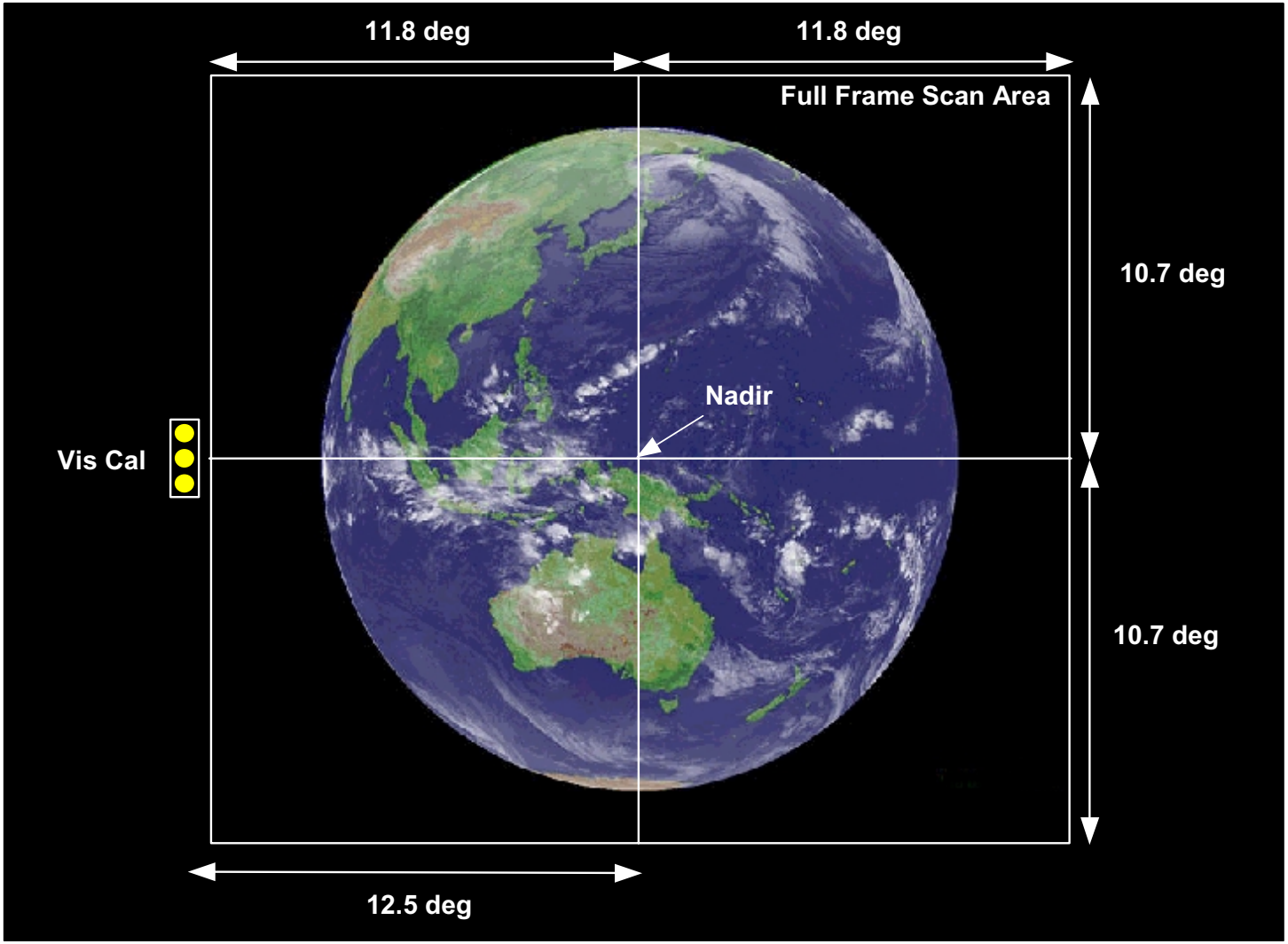

Figure 3. JAMI's full frame scan area accommodates full disk imaging, calibration and star sensing and exceeds MTSAT-1R requirements.

tested most recently in MTI and AIRS. The combination of focal plane technology, optical configuration and scan approach designed into JAMI provides spatial resolution, MTF and radiometric sensitivity performance that is superior to current operational GEO imagers, while also eliminating the "keep-out zones" and instrument down times caused by solar intrusion effects on current systems. Built-in modularity simplified imager system integration and facilitated selection and insertion of alternative subassemblies or component elements as dictated by cost, performance and schedule issues. JAMI embodies first use of all PV detector arrays for the infrared bands in an operational meteorological instrument, first use of second-generation focal plane technology in an operational meteorological instrument, first use of active cryogenic cooling of infrared focal plane arrays in an operational meteorological instrument and in GEO and first deliberate use of Nyquist sampling of pixels in an operational meteorological instrument.

Design description. A gimbaled two-axis scan mirror relays input scene radiance to an off axis focal telescope. The scanner can be commanded to point outside this full frame scan area and provide views of onboard blackbody and albedo monitoring sources. The scan function for this imager is completely flexible. For example, regions of any size within the imager frame may be scanned. Scan mirror pointing can be adjusted during each scan by commands from the spacecraft that correct for pointing errors resulting from spacecraft attitude variations. Full disk coverage time for this imager, including all pointing verification and calibration source observations, is about 24 minutes. Half disk coverage time including verification and calibration measurements is about 13 minutes.

A focal three-mirror off axis reflective telescope (cf. Figure 4) collects and focuses input radiance onto two focal planes which spatially sample Earth at the Nyquist rate for pixels with 4 km IR ground resolution and 1 km visible ground resolution. The re-imaged focal three-mirror anastigmat (TMA) telescope delivers diffraction-limited performance over a wide flat field, with superior stray light rejection to improve performance in all spectral bands, especially in the visible and IR4 (3.75-μm) bands. JAMI's Nyquist spatial sampling improves radiometric accuracy of resampled and registered data compared with current operational systems that undersample the Earth scene. Furthermore, its higher spatial sampling rate enables improved image navigation and registration by providing better daytime and nighttime landmarking and better capability to determine non-static visible-infrared co-registration errors by viewing landmarks at high resolution.

Detector arrays in both focal planes are completely redundant and contain monolithic detector arrays that use materials optimized to their spectral regions. As shown in Figure 5, two columns of detectors are fabricated for each infrared band. This provides a primary and an alternative detector element, individually selectable during focal plane subsystem integration and testing and even during flight operations in GEO to improve producibility of 100% operable arrays and provide an additional degree of redundancy to support long-life operation. Characterization testing showed that all of JAMI's arrays are 100% operable, without making use of alternative detector selections. This second-generation Raytheon technology provides excellent sensitivity, low noise, very low power and simple electrical and mechanical interfaces.

Each focal plane contains one set of arrays for each spectral band in that plane with individualized spectral filters over the arrays. The visible array is uncooled and uses technology already proven in a number of Raytheon programs, including EO-1. The infrared bands are contained in two sensor chip assemblies (SCAs), a design approach already proven on TRMM/VIRS, MODIS and MTI. The infrared focal plane operates at a temperature of 75 K.

The manufacturing alignment tolerances of these arrays built with semiconductor device lithographic techniques provide deviations in relative detector sample locations that are far superior to misalignments associated with manual assembly processes. The combination of this advanced focal plane technology with the Nyquist sampling approach used by JAMI and the resampling of detector samples on the ground to create pixels enables unsurpassed band-to-band pixel registration.

Signal processing electronics convert the Nyquist-sampled focal plane output to digital form, process and format the raw data for transmission to the JAMI Ground Processor. JAMI delivers 12-bit dynamic range data, which enables low light level visible band measurements that improve image navigation performance

at night and provide forecasters with better data to discern fog and severe weather outflow boundaries earlier in the morning as well as later at night.

JAMI transmits 2-km infrared data in normal operating modes and can provide 0.5-km visible band data on demand. Higher spatial resolution data improves cloud edge detection and tracking, which results in more accurate wind drift information, better capability to describe and forecast behavior of rapidly evolving weather systems and better typhoon tracking. Furthermore, JAMI will enable identification of smaller scale phenomena such as fog, cloud-top thermal gradients and outflow boundaries that are unresolved by current systems.

The JAMI Ground Processor transforms JAMI data from its Tapered Elevation Scan (Figures 6 and 7) native format into a GOES-like fixed grid in scan angle space, calibrates and then transmits that data to the MTSAT Image Data Acquisition and Control System (IDACS). The better spatial sampling provided by JAMI improves data quality compared with existing systems.

Calibration is provided through several mechanisms that are designed to work together to supply accurate, stable performance: space view and V-groove blackbody source (already flight-proven on TRMM/VIRS and MODIS) for the infrared bands and a reflective solar albedo monitor for the visible band. The albedo monitor design is derived from heritage approaches developed over decades of onboard visible wavelength calibration work with Landsat, TRMM/VIRS, SeaWiFS and MODIS.

3. CHARACTERIZATION

JAMI performance was characterized during a comprehensive series of subsystem and system-level tests. JAMI entered the thermal-vacuum chamber twice. The first test series was a 31-day run that was stopped just a few hours before planned completion by an electrical short in the redundant winding of the north-south scan motor. The final test series was a 17-day run that occurred shortly before instrument delivery.

All aspects of required JAMI performance were tested and verified. For instance, measured Line of Sight (LOS) stability was measured to be 3-μrad versus the 6-μrad requirement. This higher level of performance enables much improved Image Navigation and Registration (INR) with respect to previous systems. LOS stability was not affected by the active cooler.

This paper summarizes results from a few of the more important tests and associated analyses including:

1. End-to-end performance verification
2. Radiometric sensitivity (signal-to-noise ratio and NEDT)
3. Spectral response
4. Line spread function and MTF
5. Performance around local midnight.

End-to-end performance verification. One of the earliest system-level tests verified JAMI's end-to-end function and Earth coverage performance. Frames of JAMI data like that shown in Figure 8 were collected by scanning the instrument in full disk observation mode across a projected GOES-12 image. The projector, which was originally part of an airborne reconnaissance system, functioned as a very large format, wide field of view collimator for this application. The physical extent of the projected Earth image corresponds to the view from GEO. The end-to-end tests showed that JAMI meets requirements in a number of important performance areas including full disk coverage time, line-of-sight repeatability, pixel-to-pixel simultaneity and data latency.

Radiometric sensitivity. JAMI's radiometric sensitivity was measured in all spectral bands with both primary and secondary detector arrays. As shown in Table 2, measured JAMI performance meets sensitivity requirements with comfortable margin in all bands. Margin ranges from roughly a factor of three in the 12.0-μm band (IR2) up to about a factor of eight in the visible, IR1 and IR4 bands. Figure 9 shows that detector response to a uniform scene in the visible is very consistent across both arrays, especially for the primary (or A) array. SNR for one detector on the B side fell far below the others

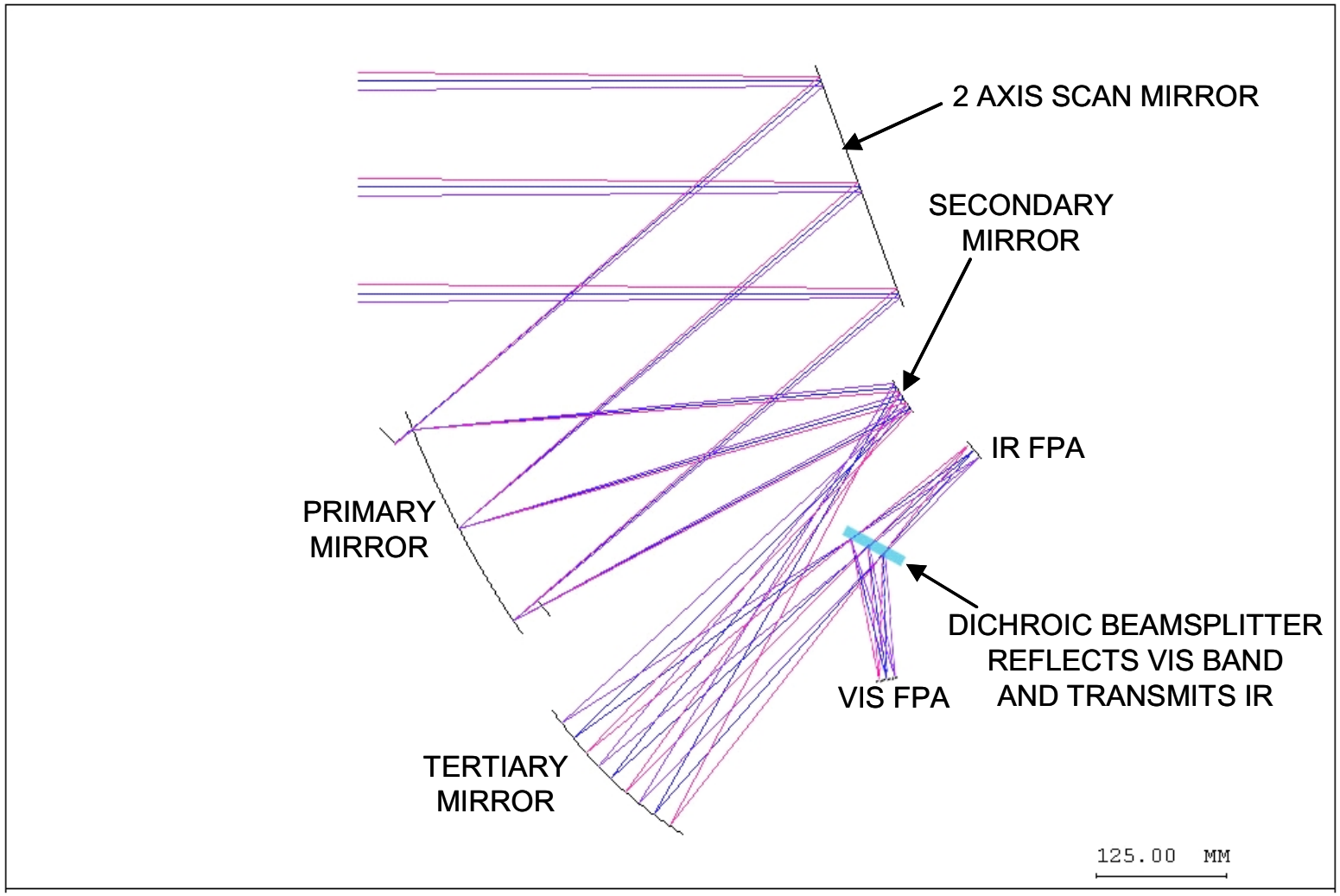

Figure 4. JAMI's straightforward optical layout is at the heart of this advanced technology instrument.

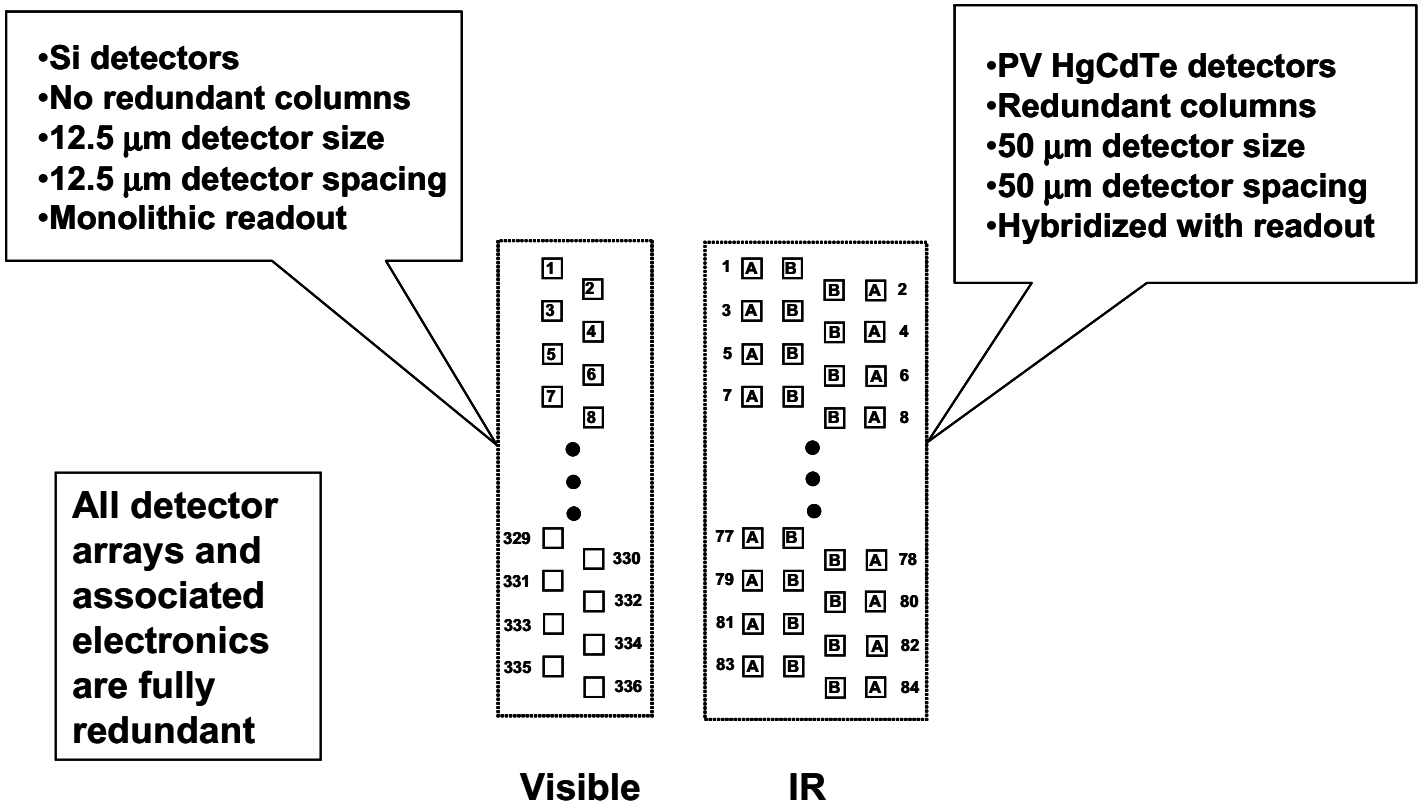

Figure 5. JAMI's detector arrays provide an additional degree of redundancy for the infrared bands.

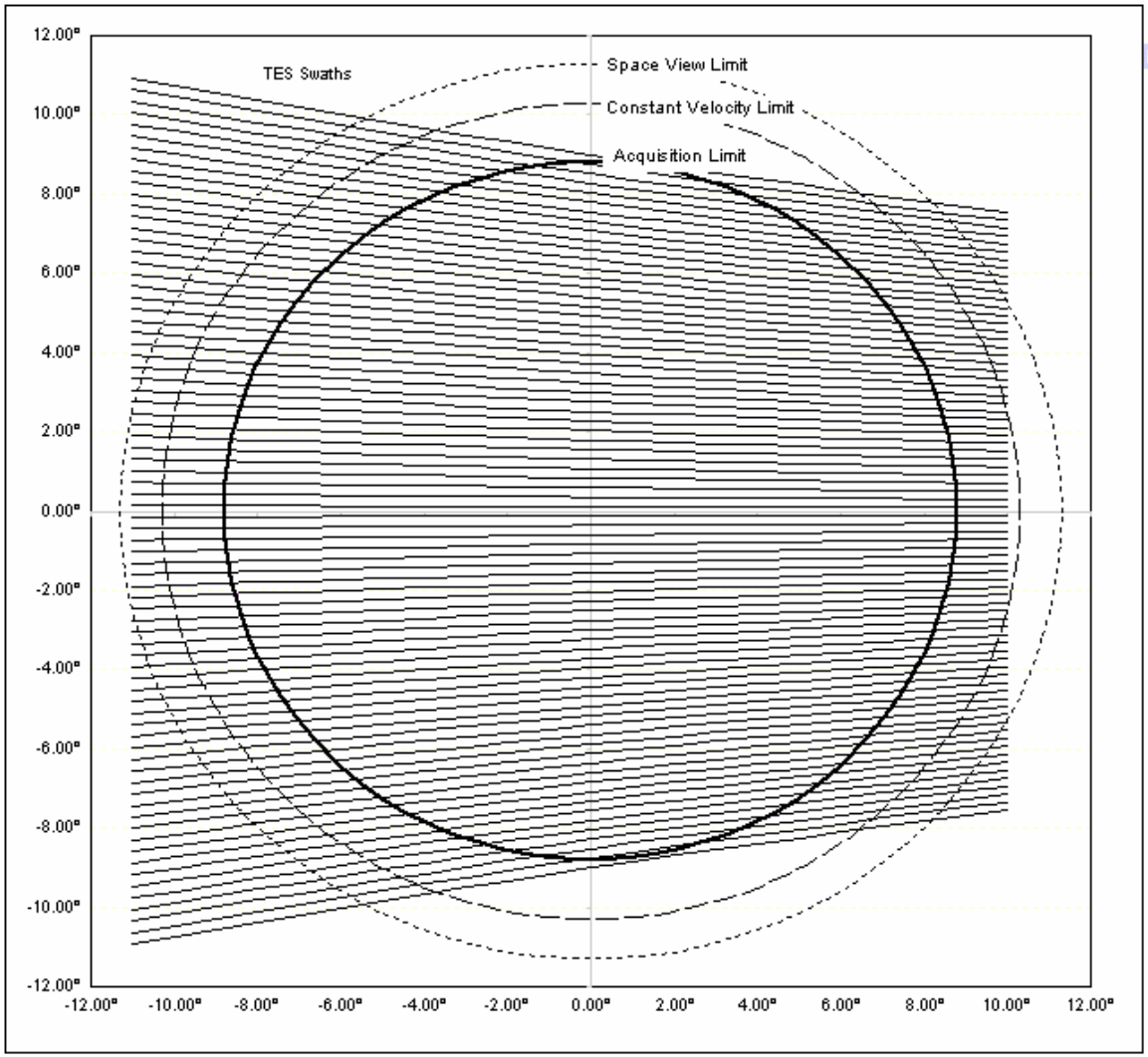

Figure 6. JAMI scans the Earth with swaths whose elevation angle changes with East-West location.

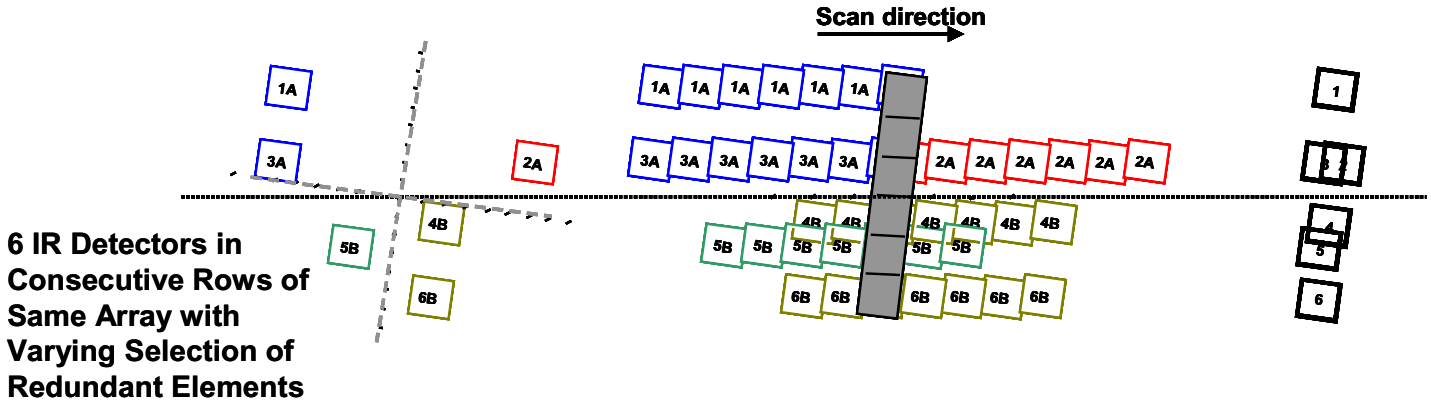

Figure 7. JAMI's tapered elevation scan approach avoids coverage gaps and provides band-to-band detector sample registration by scanning swaths perpendicular to projected detector array orientations. Rotation angle for the projected detector arrays is equal to the scanner elevation angle.

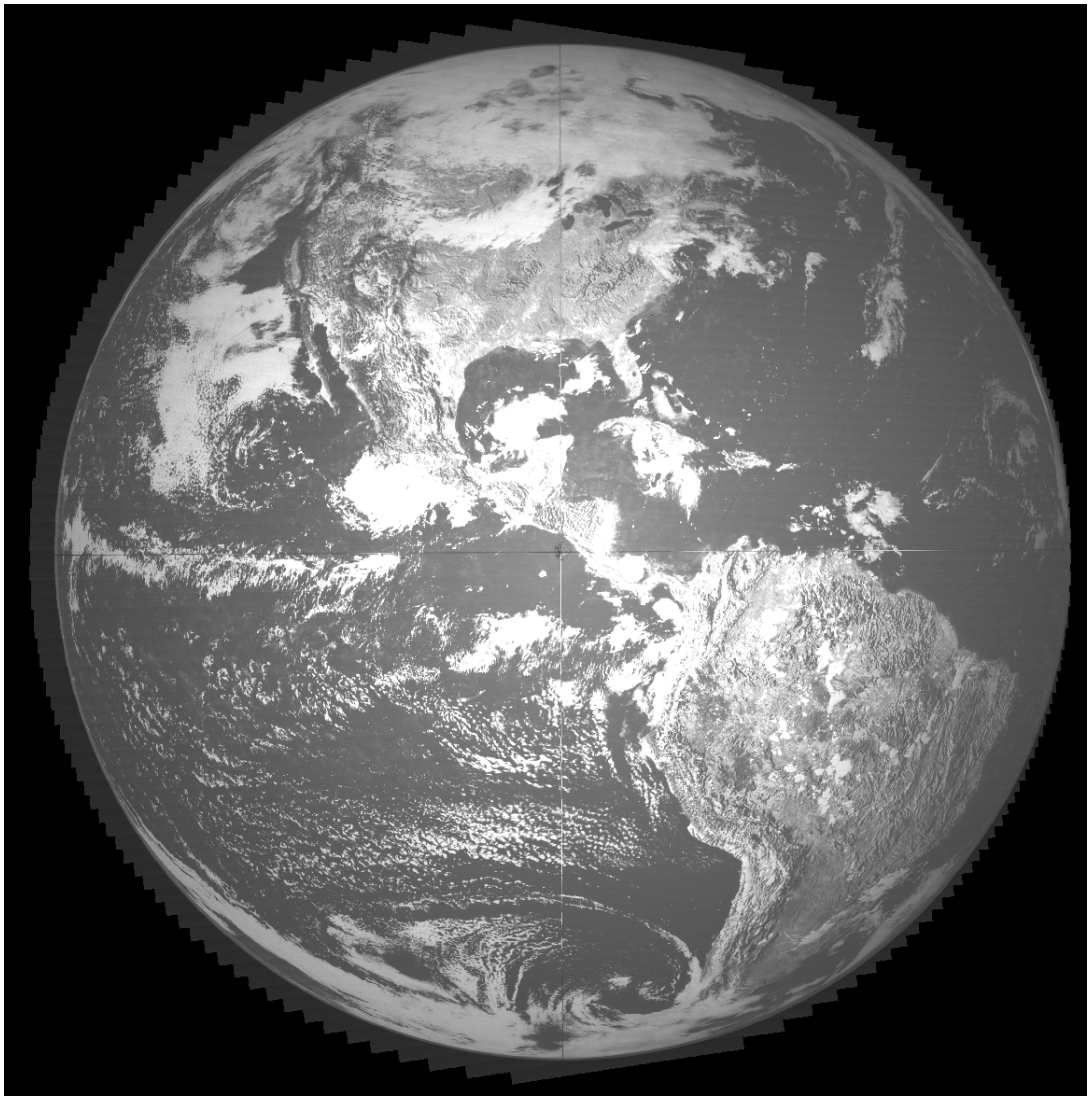

Figure 8. End-to-End JAMI system operation was verified by this observation of a Full Disk Earth Image projected into the Imager.

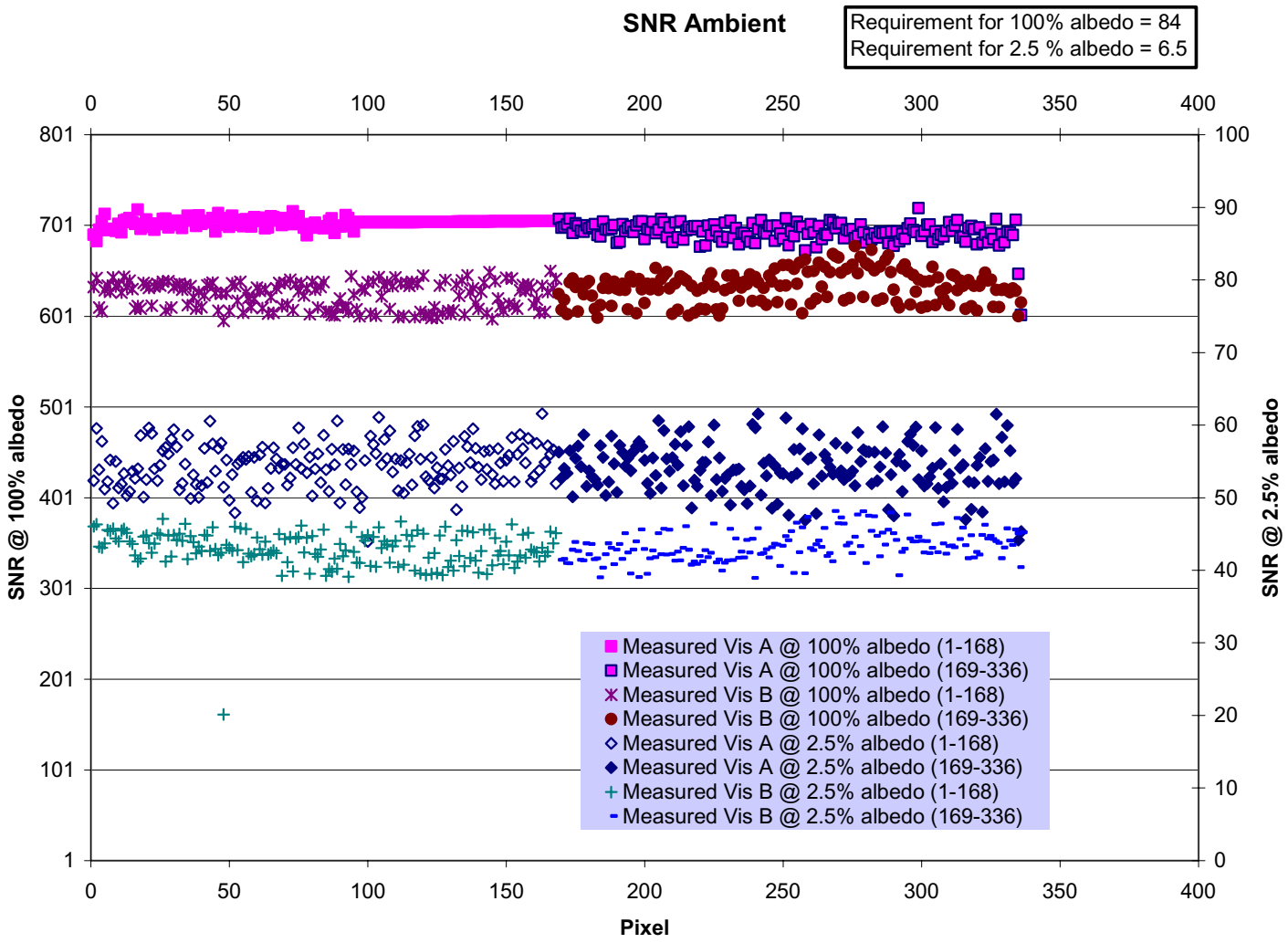

Figure 9. JAMI's visible band SNR meets requirements with ~8x margin.

Table 2. Measured JAMI performance meets sensitivity requirements with considerable margin.

Spectral Band	Visible	IR1	IR2	IR3	IR4
Central Wavelength	0.725-μm	10.8-μm	12.0-μm	6.75-μm	3.75-μm
Scene1: SNR or NEdT	54	0.05	0.14	0.11	0.35
Scene2: SNR or NEdT	690	0.02	0.06	0.02	0.03
Spec: Scene1	6.5	0.45	0.45	0.75	4.2
Spec: Scene2	84	0.15	0.15	0.15	0.15
Ratio Scene1	8.3	9.0	3.2	6.8	12
Ratio Scene2	8.2	7.5	2.5	7.5	5.0

(Ratio > 1 means measured performance is better than specification.)

Scene1: Scene Temperature = 220 K ; Albedo = 2.5%
Scene2: Scene Temperature = 300 K ; Albedo = 100%

for the test results shown here. Even so, the SNR for this one B side detector still meets MTSAT-1R SNR requirements by about a factor of three.

Spectral response. Figure 10 shows that JAMI's spectral response in the infrared bands meets all requirements. Visible band spectral response is even closer to the center of the MTSAT-1R response envelope than for the infrared bands. The clean spectral response provided by JAMI in the infrared bands should enable improved measurements of sea surface temperature and other geophysical data products with respect to GMS-5.

Line spread function (LSF) and modulation transfer function (MTF). Measured performance of JAMI exceeds all LSF and MTF requirements both at the detector sample and pixel (output of ground processor) levels. Figure 11 shows LSF and MTF measurements for the IR2 (12.0-μm) band at the output of the JAMI Ground Processor. JAMI outperforms current operational GEO imagers in MTF, despite its relatively small 20-cm aperture, because of its Nyquist sampling approach, off-axis telescope design and excellent implementation.

Performance around local midnight. A vitally important performance area for a GEO imager aboard a three-axis stabilized platform is performance around local midnight. JAMI performance around local midnight was characterized using a combination of laboratory measurements and performance modeling. As shown in Figure 12, visible band MTF meets MTSAT-1R requirements even in the worst case for solar intrusion, which is when the Sun transits across the south limb of the Earth. JAMI MTF performance in the IR is almost unaffected by solar intrusion. In addition, other analysis not presented here shows that JAMI meets all star sensing requirements near local midnight. However, SNR in the visible and IR4 bands decreases noticeably within ~2 hr of local midnight; but, unlike some current operational GEO imagers, JAMI does not require "keep out" zones or down time near local midnight.

4. PROJECT STATUS

JAMI was delivered to Space Systems/Loral on 2003 June 17. It was installed and aligned on the spacecraft within 5 days of arrival. As of early 2003 August, detailed integration and testing of MTSAT-1R is ongoing and analysis of JAMI test results continues in a few areas, including radiometric calibration.

5. SUMMARY

JAMI introduces the next generation of GEO meteorological imager and provides much improved spatial sampling, radiometric sensitivity, Earth coverage and 24-hour observation capability compared with current operational GEO imagers. JAMI was delivered to Space Systems/Loral on 2003 June 17 for integration into the MTSAT-1R system. The instrument was installed and aligned on the spacecraft within 5 days. JAMI reduces risk for future GEO imagers by early implementation of advanced instrument technologies in GEO.

REFERENCES

1. Jeffery J. Puschell, Howard A. Lowe, James W. Jeter, Steven M. Kus, W. Todd Hurt, David Gilman, David L. Rogers, Roger L. Hoelter and Russ Ravella, "Japanese Advanced Meteorological Imager: a next generation GEO imager for MTSAT-1R," *SPIE Proceedings* **4814**, pp. 152-161, 2002.

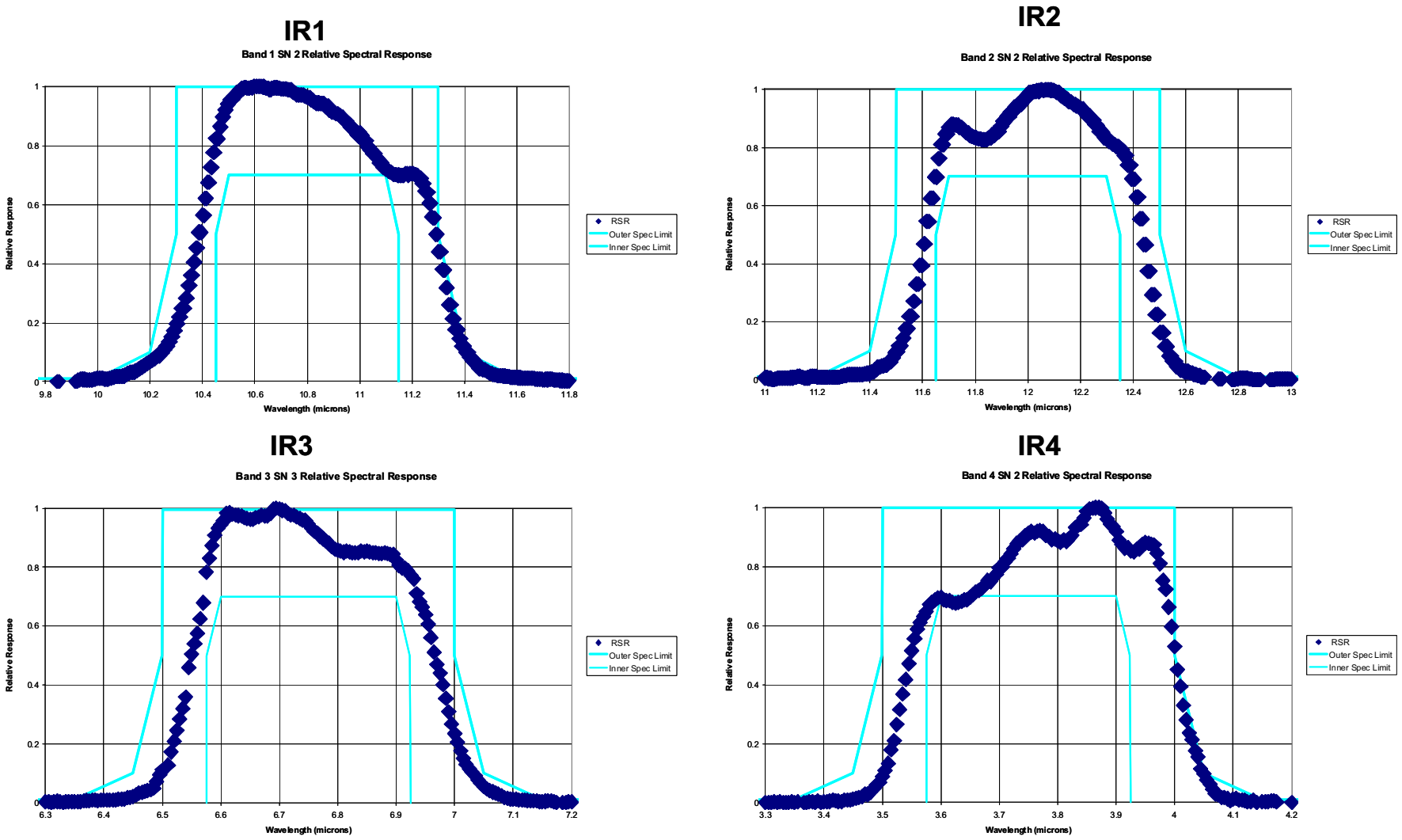

Figure 10. JAMI's measured spectral response in the IR bands fall within the MTSAT-1R envelope. .

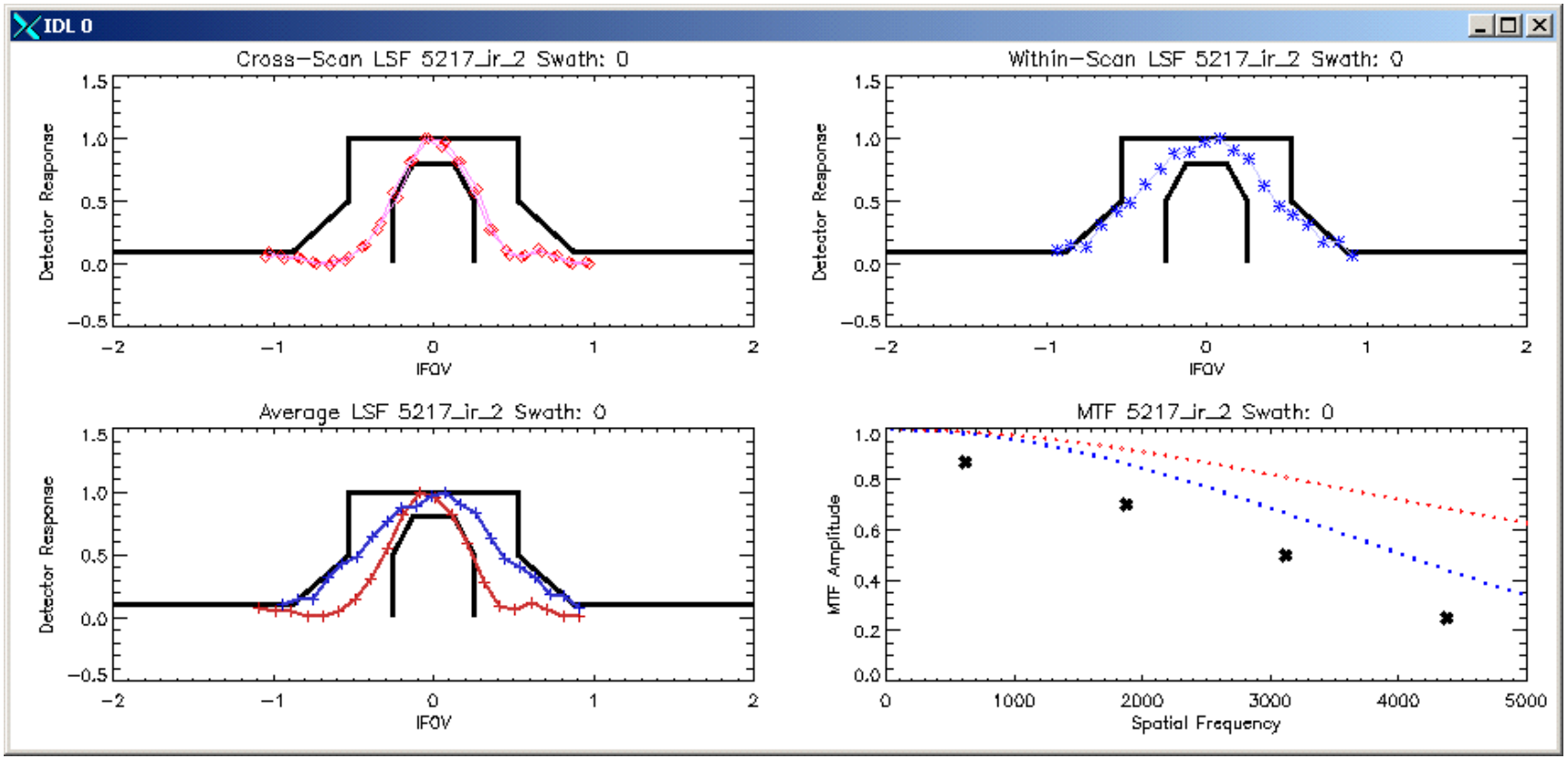

Figure 11. Measured LSF and MTF performance for JAMI meets all MTSAT-1R requirements in all bands, including the IR2 band shown here.

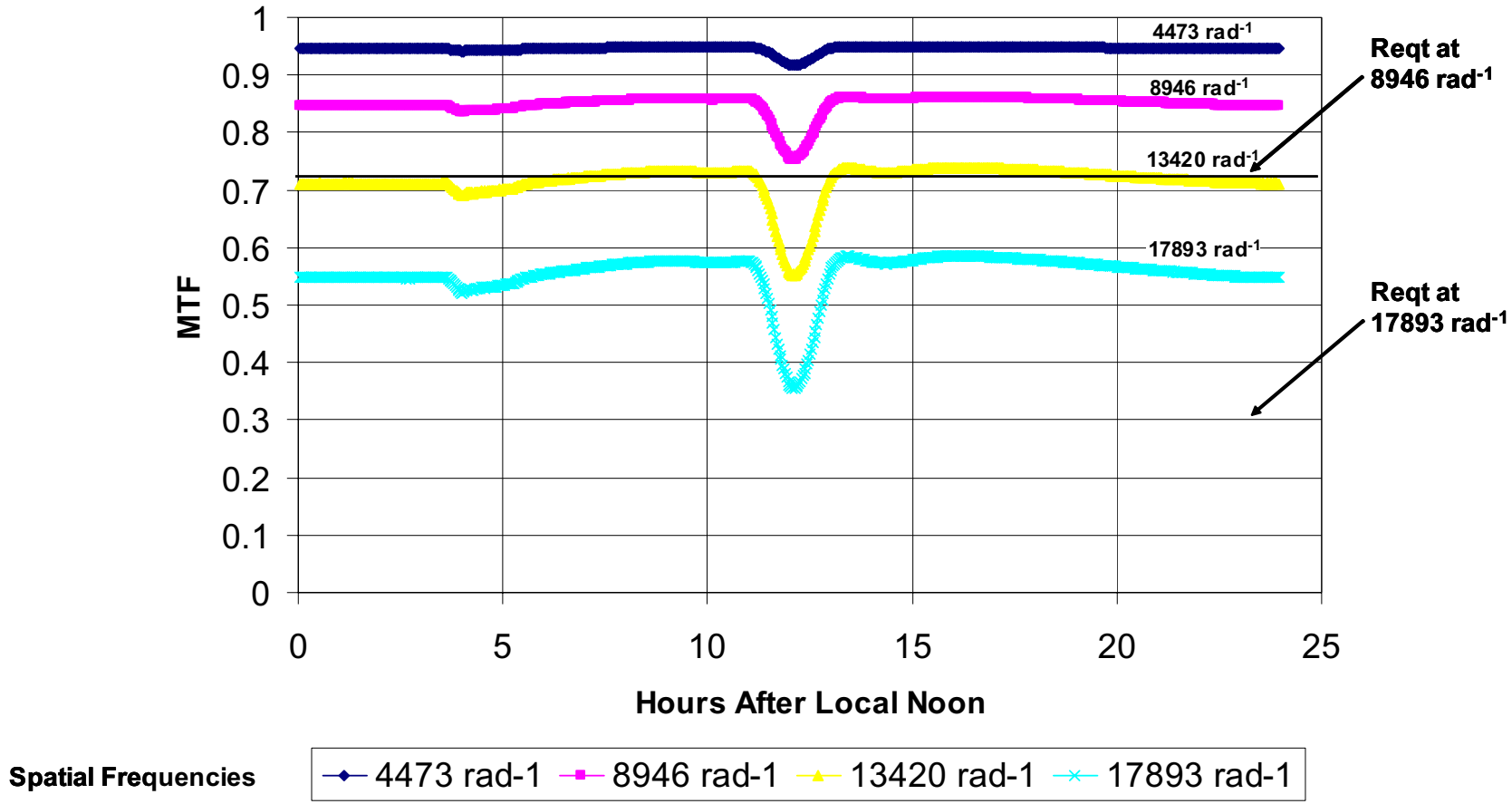

Figure 12. JAMI meets MTSAT-1R visible MTF requirements with margin even around local midnight for the worst case (shown here) of the Sun transiting across the south limb of the Earth.

Ongoing and Planned Activities Concerning Assimilation of ATOVS Data At SMHI Sweden

Per Dahlgren
E-mail: Per.Dahlgren@smhi.se
Swedish Meteorological and Hydrological Institute
Folkborgsvagen 1, 601 76 Norrkoping

Abstract

AMSU-A radiances are soon to be operationally assimilated at SMHI. The effects of how careful data are selected for bias correction are therefore important to study. We will present some experiments where the effects of screening out data not in the vicinity of soundings have been studied. A further development in the use of AMSU-A data is to assimilate radiances over ice and land. Due to the importance of the non linear properties of surface skin temperature and surface emissivity, we will perform tests where these variables are included in the control vector. We also plan to assimilate AMSU-B, first only over oceans but then do research on how to use it over ice.

The HIRLAM model and ATOVS at SMHI

At SMHI the HIRLAM model is used for operational forecasts up to +48h four times a day. Two domains are used, one large with 44km resolution and one smaller domain with 22km resolution, figure 1. A 3DVAR system is used for the analysis with a 2h cut of time. The large domain uses ECMWF forecasts as boundaries, and the small (22km) area uses HIRLAM44.

ATOVS in HIRLAM at SMHI

In order to gain as much as possible from AMSU-A data we need, due to the short cut of time, fast access to AMSU data from the Atlantic where conventional observations are sparse. Therefore it was not until the EARS (EumetsAt Retransmission Service) became operational that we could really benefit from ATOVS data in the Swedish HIRLAM. We are collecting AMSU-A data from noaa15 and noaa16 and run them in passive mode for producing statistics for bias correction. The coverage of received EARS data during one day (2:nd of October 2003) are shown in figure 2. From there it can be seen that we get a good amount of data from the Atlantic but also that the data sample varies a lot from forecast to forecast.

Bias correction of AMSU-A radiances

We use the bias correction scheme presented in (B.A Harris,) with 7 predictors:

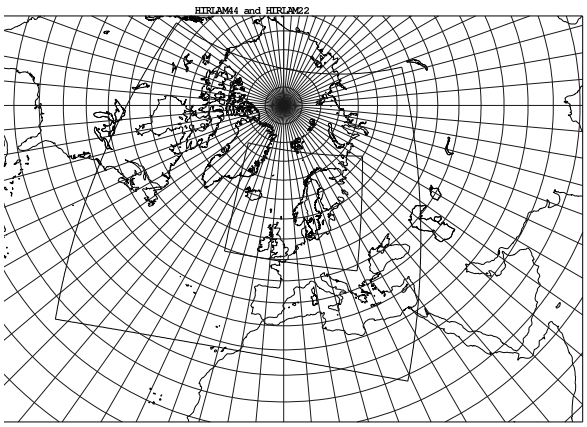

Figure 1: Operational HIRLAM domains at SMHI

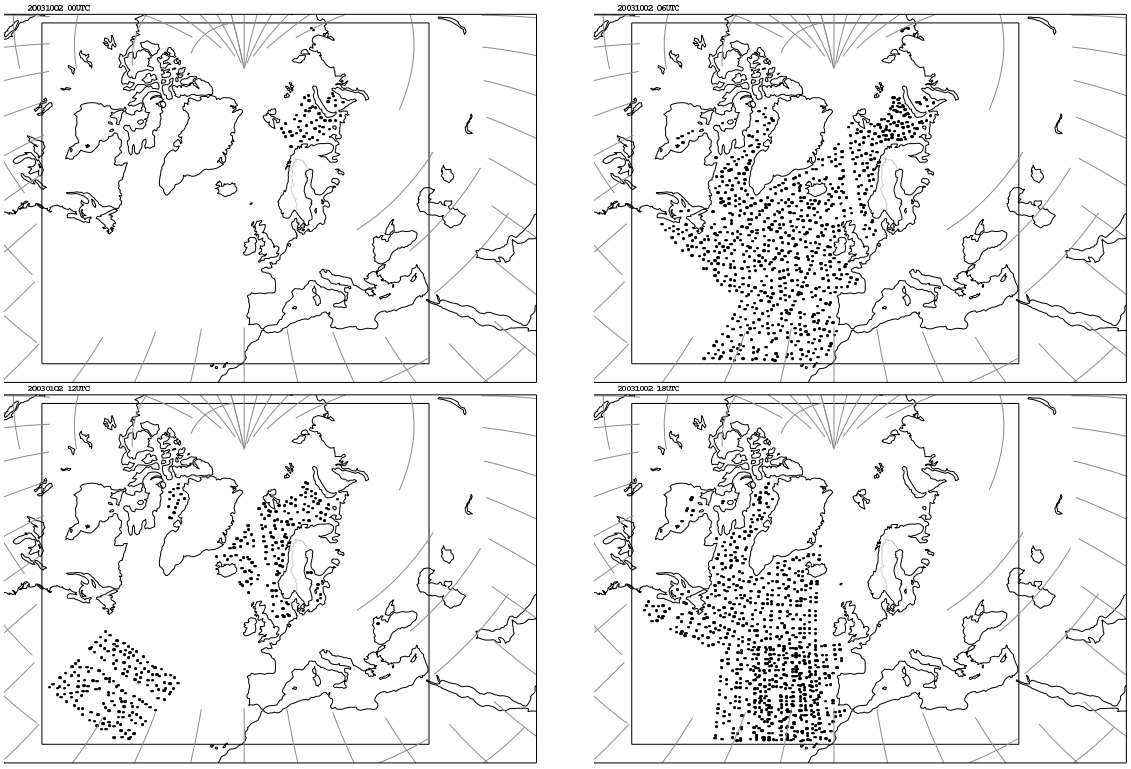

Figure 2: Available AMSU-A data from noaa15 and noaa16 for different HIRLAM forecasts on the 2:nd of October 2003. The figures show data available for minimization, i.e cloud cleared, land/ice contaminated obs screened out and thinned data

1. A constant displacement
2. A measure of the mean forecast temperature between the 1000hPa and 300 hPa pressure levels
3. A measure of the mean temperature between 200 hPa and 50 hPa
4. The surface temperature (here analyzed sea surface temperature values)
5. The integrated water vapor content per area from the surface up to the top of the atmosphere
6. The square of the observation zenith angle
7. The observation zenith angle

When using the model for bias correction as we are doing here it is important not to include model biases in the calculation of the regression coefficients. We have done some experiments where the data samples used for calculation of the coefficients have been selected in different ways. Figures 3 - 5 shows time series of daily bias (obs-first guess) and (corrected obs - first guess), i.e a 24 hour mean.

1. A dataset of 2 months where land/ice and cloud contaminated obs have been screened out. Figure 3
2. For every day, update the coefficients with a 30 day data set with land/ice and cloud contaminated obs screened out. Figure 4
3. A dataset of 2 months with land/ice and cloud contaminated obs screened out. Only data in the vicinity of soundings are used. Figure 5

From figures 3 - 5 it seems like screening out data not in the vicinity of soundings reduces most of the bias in the observations. For now, we will use those coefficients as long as they produce reasonable statistics. Bias correction in limited area models still remains an open issue though.

Research

In order to improve the analysis over the Arctic region, we participate in project called IOMASA. The purpose of the NWP part of this project (met.no and SMHI) is to assimilate radiances from AMSU-A and AMSU-B over ice. In that case the surface skin temperature T_{skin} and surface emissivity ϵ_{surf} become important. If T_{skin} and ϵ_{surf} are not allowed to vary during the minimization it may be difficult to achieve convergence towards the optimal solution. We will therefore perform tests where these variables are included in the control vector x, in the J_o term in equation 3, and adjusted by the minimization procedure.

We will only use AMSU-B where we have AMSU-A information to help us with quality control, cloud clearing etc. We therefore need some tool to map the AMSU-B footprint onto AMSU-A.

$$x = \begin{pmatrix} u \\ v \\ T \\ q \\ lnp_s \end{pmatrix} \longrightarrow J_b = (x - x_b)B^{-1}(x - x_b) \tag{1}$$

$$x = \begin{pmatrix} u \\ v \\ T \\ q \\ lnp_s \\ T_{skin} \\ \epsilon_{surf} \end{pmatrix} \longrightarrow J_o = (y - Hx)O^{-1}(y - Hx) \tag{2}$$

$$J = J_b + J_o \tag{3}$$

References

B.A Harris, G. K. A satellite bias correction scheme for data assimilation. *Quaterly Journal of the Royal Meteorological Society*, 127:1453–1468.

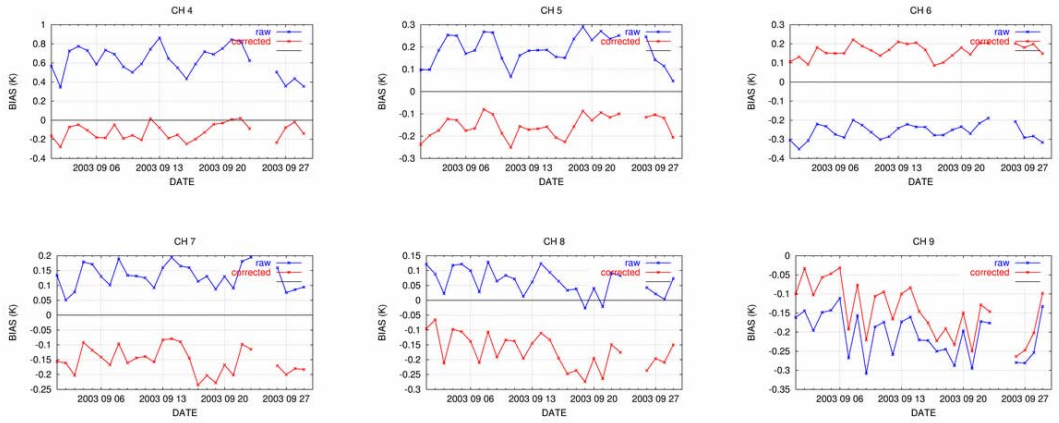

Figure 3: Red curve: bias corrected observations. Blue curve: raw data. All obs used for calculation of the coefficients

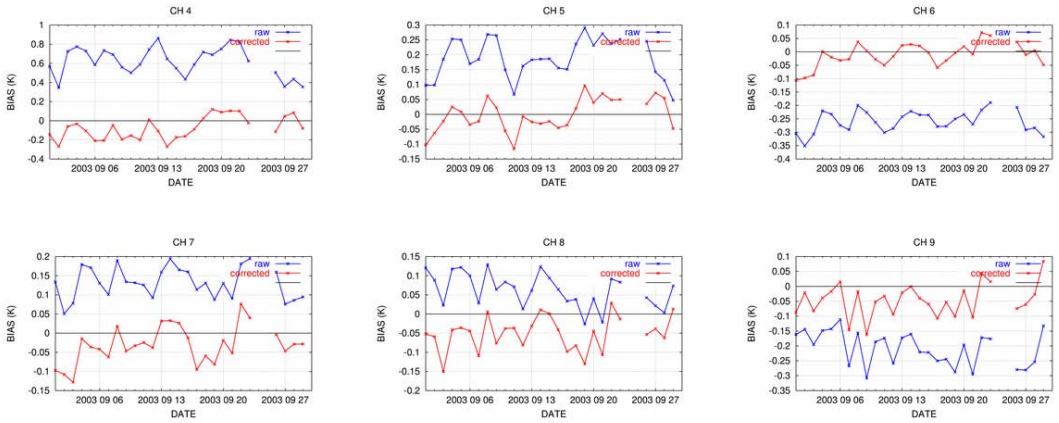

Figure 4: Red curve: bias corrected observations. Blue curve: raw data. Coefficients updated every day

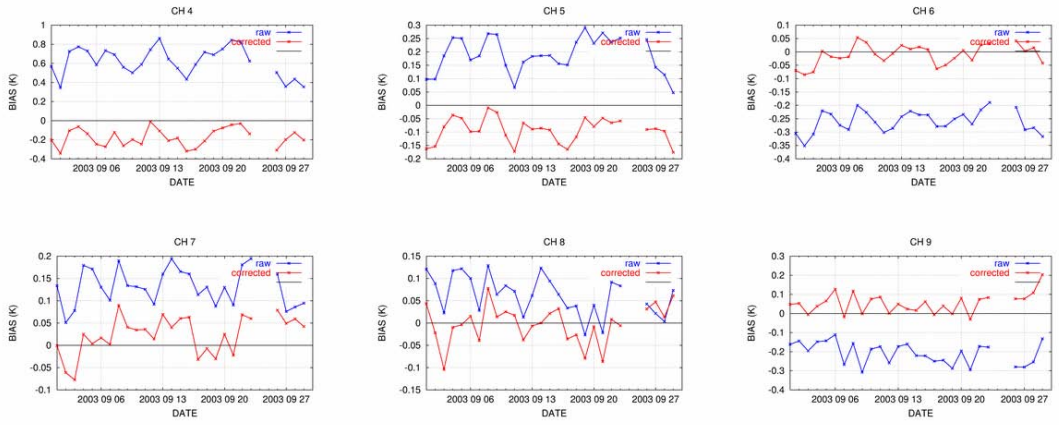

Figure 5: Red curve: bias corrected observations. Blue curve: raw data. Only data in the vicinity of soundings are used for calculation of the coefficients.

Use and impact of ATOVS in the DMI-HIRLAM regional weather model

J. Grove-Rasmussen B. Amstrup and K.S. Mogensen
E-mail: jgr@dmi.dk, bja@dmi.dk and ksm@dmi.dk
Danish Meteorological Institute
Lyngbyvej 100, DK-2100 Copenhagen, Denmark

Abstract

Until recently (A)TOVS[1] data have mainly been (operationally) assimilated into global numerical weather models, but the study of their impact on a regional model is of great relevance for many weather services, especially if data can be made available with sufficiently short delay for operational use.

A study of the impact of adding NOAA16 and NOAA17 ATOVS AMSU[2]-A radiances to the DMI-HIRLAM[3] system is carried out. The analysis is performed with both locally received data from the two stations Smidsbjerg (Denmark) and Sdr. Strømfjord/Kangerlussuaq (Greenland), and with data from EARS[4]. The data used are from the temperature sounding channels (channels 4-10) from the AMSU-A instrument. A positive impact is observed in the winter time when using the satellite data, whereas the conclusion on summertime use of the data is less certain.

As a result of the assimilation experiments the satellite observations have been used operational at DMI since December 2002.

DMI-HIRLAM

At DMI a local version of the HIRLAM is being used (Sass et al., 2002; Amstrup et al., 2003). The model is regional and nested with four different regions (see figure 1 for an illustration and table of the position and resolution for the various models). The largest model (DMI-HIRLAM-G) has lateral boundaries from ECMWF[5], whereas the inner models have lateral boundaries from their surrounding HIRLAM model. The DMI-HIRLAM analysis and forecasting system consists of a 3 dimensional variational data analysis system (Gustafsson et al., 2001; Lindskog et al., 2001) with an assimilation window of 3 hours, and a forecast model with 40 levels reaching the 10 hPa pressure level - above this a climatological model is applied for data needed in the radiative transfer model. The HIRLAM partners are Denmark, Finland, Iceland, Ireland, Netherlands, Norway, Spain and Sweden.

[1] (Advanced) TIROS Operational Vertical Sounder
[2] Advanced Microwave Sounding Unit
[3] Danish Meteorological Institute - HIgh Resolution Limited Area Model
[4] EUMETSAT ATOVS Retransmission Service
[5] European Centre for Medium-Range Weather Forecasts

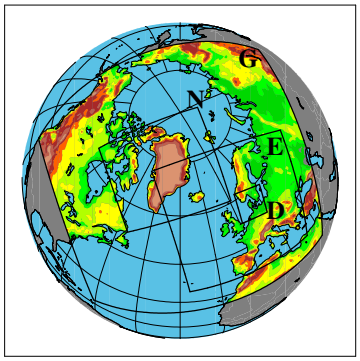

Model Identification	G	N	E	D
grid points (mlon)	202	194	272	182
grid points (mlat)	190	210	282	170
No. of vertical levels	40	40	40	40
horizontal resolution	0.45°	0.15°	0.15°	0.05°
time step (dynamics)	150 s	60 s	60 s	25 s
time step (physics)	450 s	360 s	360 s	150 s

Figure 1: The DMI-HIRLAM regions, geographical coverage and resolution specifications.

Data sources

Initially two sources of ATOVS AMSU-A data were available: the global dump from NOAA/NESDIS[6] and the locally received. Each data set has advantages and disadvantages. The global dumps have global coverage but arrive late (hours) after data recording, whereas the locally received data only have low coverage, but arrive within half an hour of data recording. In between the two sources one with high coverage and low time delay would be useful. This has been made available through EARS which uses the best of the two systems: locally received data from several stations are transmitted to EUMETSAT[7] from where they are retransmitted through an ordinary digital broadcasting channel to all end-users, ready to be received by relatively simple and cheap equipment. The total time from data recording to reception by the end-users is specified to be less than half an hour.

At DMI two stations for locally reception are available, one in Kangerlussuaq/Sdr. Strømfjord (Greenland) and one at Smidsbjerg. They provide a good coverage for DMI-HIRLAM, but still more data could be used. With the EARS the coverage by the originally proposed 6 stations (of which one is the DMI station at Kangerlussuaq) is as seen in figure 2. The position of the receiver stations are such that a large fraction of DMI-HIRLAM is covered.

EARS has a structure which makes addition of further stations rather easy, and new stations have already been added. This would increase the geographical coverage without having to restructure the system unless the data volume increase above the present system limits.

Data flow

Data are received via HRPT[8] and pre-processed through the AAPP[9] to level 1c which is geolocated and calibrated to radiances and brightness temperatures. The level 1c data is received

[6] National Oceanic and Atmospheric Administration/National Environmental Satellite, Data, and Information Service

[7] EUropean organisation for the exploitation of METeorological SATellites

[8] High-Rate Picture Transmission

[9] ATOVS and AVHRR Processing Package, provided by EUMETSAT

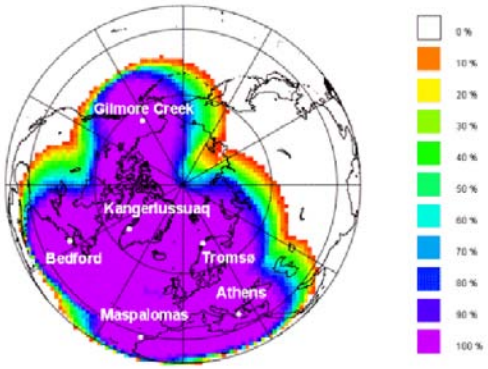

Figure 2: Percentage of observed data at a specific position being retransmitted through EARS. From `http://www.eumetsat.de/en/dps/atovs.html`.

either via local equipment or via EARS, and is encoded into BUFR[10] for the use in the DMI assimilation system.

Forward model and data usage

The forward model presently used at DMI to calculate model derived brightness temperatures for ATOVS data is RTTOV7[11] developed in the Numerical Weather Prediction SAF[12] project setup by EUMETSAT. As DMI-HIRLAM reach only 10 hPa the radiative transfer equation integration is using a climatological model above this height.

Data is presently rejected over land and ice, and a cloud clearing based on the total cloud liquid water content is made since the effect of precipitable particles is not modelled in the radiative transfer model. The data are subsequently thinned to 0.9° for NOAA16 and NOAA17 data separately.

Bias correction and error statistics

For bias-correction a Harris-Kelly (Harris and Kelly, 2001) scheme with 7 predictors from the background model (model first guess) is used: **1)** a constant displacement, **2)** thickness between 1000 hPa and 300 hPa, **3)** thickness between 200 hPa and 50 hPa, **4)** the surface temperature, **5)** the integrated water vapor content per area from the surface up to the top of the atmosphere, **6)** the square of the observation zenith angle and **7)** the observation zenith angle. The examination that was done for NOAA16 data (Schyberg et al., 2003) showed that the scatter of the difference between observed and modelled brightness temperature varied significantly as a function of latitude. Accordingly, there are separate bias-correction coefficients for three latitude bands: **1)** up to 50°N, **2)** between 50°N and 65°N, and **3)** north of 65°N. The bias-correction coefficients used operationally at DMI for the NOAA17 data were originally based on passive runs from October 19th to November 12th 2002. For NOAA16 data the bias-correction coefficients were based on data from the full month of April 2002. New bias estimates are based on 7.5 months of data from 2003. This has decreased the bias slightly.

[10] Binary Universal Form for Representation, defined by World Meteorological Organization.
[11] Radiative Transfer model for TOVS, release 7
[12] Satellite Application Facility

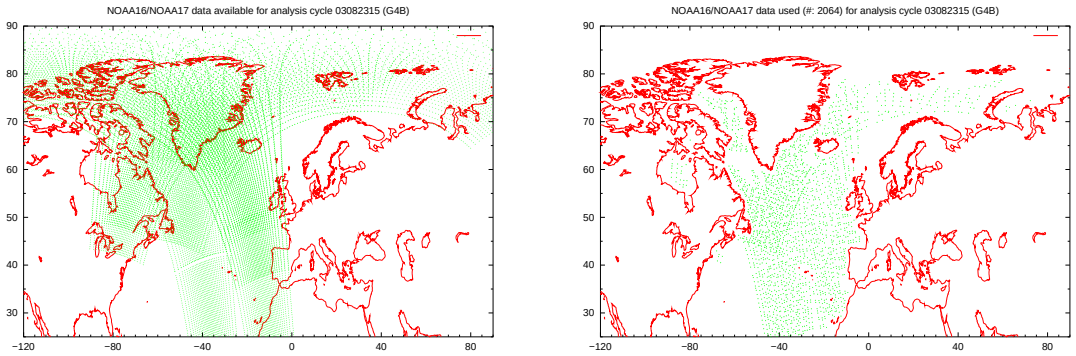

Figure 3: ATOVS AMSU-A data before (left) and after (right) removal and thinning of data points for August 23rd 2003, 15:00 UTC.

The observation error covariance matrix has been chosen diagonal with the same values for NOAA16 and NOAA17. The values for channels 1-3 ("surface channels") are so large that effectively only channels 4-10 are used (see table 1). An example of the effect of bias correction for NOAA16 in the operational DMI-HIRLAM-G model is found in figure 6

Table 1: The values in the diagonal of the observation error covariance matric. All off-diagonal elements are 0.

channel	1	2	3	4	5	6	7	8	9	10
error (K^2)	900	900	900	90	0.35	0.35	0.35	0.35	0.70	1.40

Results

An assimilation experiment has been made in the DMI-HIRLAM system to visualize the impact of the added data.
Figure 3 shows the amount of data before and after screening for land, ice and cloud contamination, and thinning for August 23rd 2003, 15:00 UTC. Due to summer data are used far to the north. More data (especially in the south-western Atlantic) could be used in case of better ground station coverage.

Figure 4 shows results from observation verification using an EWGLAM[13] station list for an OSE[14] experiment in September 2003. The rms-scores are slightly better for most variables for the run including AMSU-A data and the impact from using AMSU-A data is positive. See (Amstrup, 2003) for further results from an OSE impact study for January and February 2003. Similar experiments in the winter season gives a more consistent positive impact.

[13] European Working Group on Limited Area Model
[14] Observing System Experiment

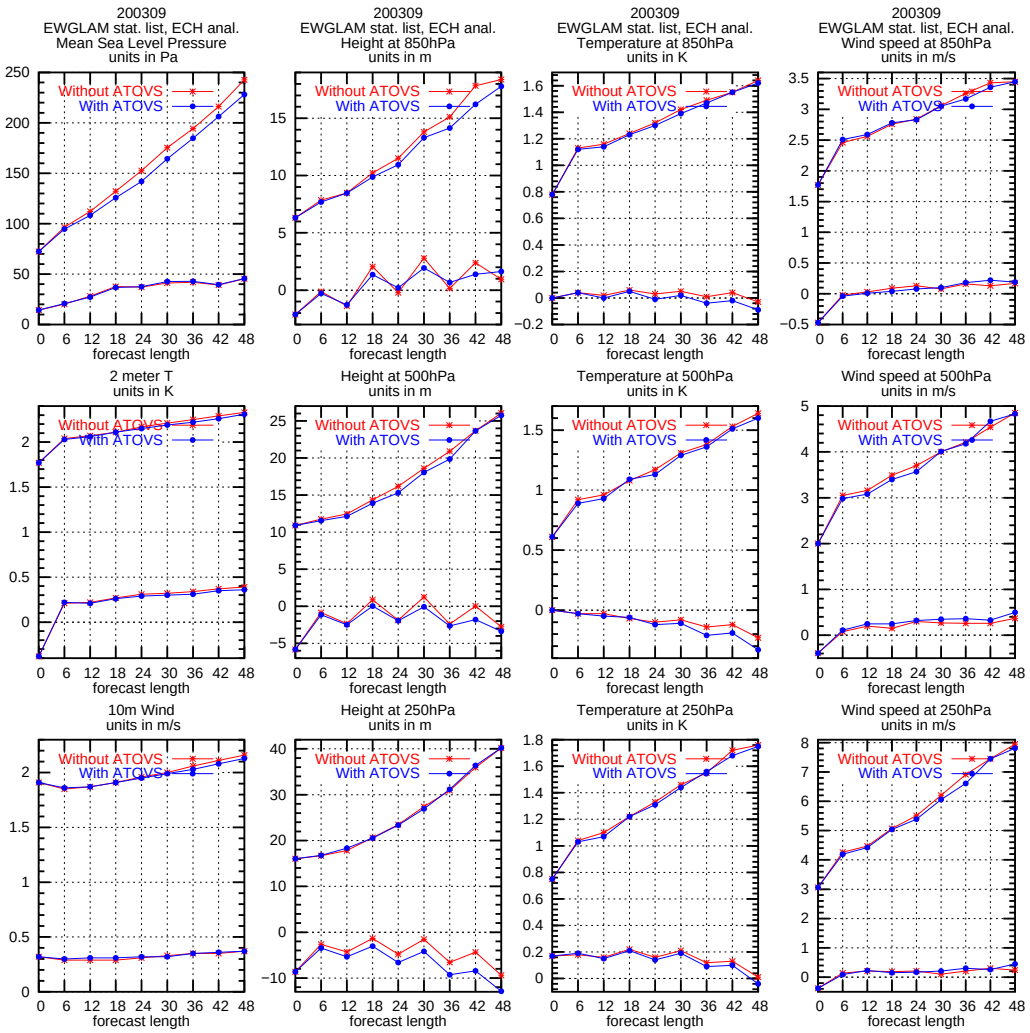

Figure 4: Observation verification (bias and rms, EWGLAM station list) results for September 2003 of surface parameters and geopotential height, temperature and wind for pressure levels specified in the plot. The OSE experiment was done with the DMI-HIRLAM-G model (see figure 1). The upper curves are rms and lower curves bias, red without ATOVS and blue with ATOVS.

Conclusion and future work

ATOVS AMSU-A data have been assimilated into the regional DMI-HIRLAM model, with data from the two local receiver stations and from the EUMETSAT Retransmission Service.

Use of NOAA16 and NOAA17 ATOVS AMSU-A data has a positive impact in the DMI-HIRLAM limited area models based on standard observation verification scores, in particular in the winter season. In the summer season, the impact is largest on mslp scores (not shown).

New bias estimators have not improved the forecasts dramatically, but a slight improvement is found in mean sea level pressure scores for a testrun in a June/July period 2002 using only NOAA16 data.

Plans are in the future to make use of data points also over ice (especially relevant for the Greenland region) and land, either by applying an emissivity scheme or by using only channels not reaching the surface. Furthermore the upper boundary for DMI-HIRLAM should be changed from the present climatological model to data from ECMWF, and the processing should be prepared for AMSU-B and other available sounder instruments.

After ITSC13

After the unfortunate breakdown of AMSU-A on NOAA17 we were encouraged to implement use of NOAA15 data in the DMI-HIRLAM system. The NOAA15 data are received rather sparse at DMI, and hence the effort on their implementation has previously not been large. The implementation including preparation of new bias estimators was done by the end of November 2003. Subsequently, an impact study was done with the DMI-HIRLAM-G version for five weeks from the end of October to the end of November 2003. Three runs were made: one without use of NOAA AMSU-A data, one including NOAA16 AMSU-A data and finally a run including both NOAA15 and NOAA16 AMSU-A data. The results from an observation verification using the EWGLAM station list is shown in figure 5. For these measure, there is in general a clear positive impact from using the AMSU-A data. The impact from additional NOAA15 AMSU-A data compared to using only NOAA16 AMSU-A data is rather small except for somewhat better root mean square scores for mean sea level pressure, which appears to be the most sensitive parameter to adding AMSU-A data to the data assimilation system.

The bias and RMS for NOAA16 AMSU-A channels 2 to 10 for mid November to mid December 2003 are plotted in figure 6. The bias and RMS of most of the channels is significantly decreased, the bias to close to 0 K.

The bias estimate is based on 5 months of data from June to November 2003, made available to DMI from SMHI[15].

Acknowledgments

This work is partly financed through a EUMETSAT research fellowship on ATOVS AMSU assimilation in regional NWPs. We are gratefull for the NOAA15 data provided by Per Dahlgren, SMHI.

[15]Swedish Meteorological and Hydrological Institute

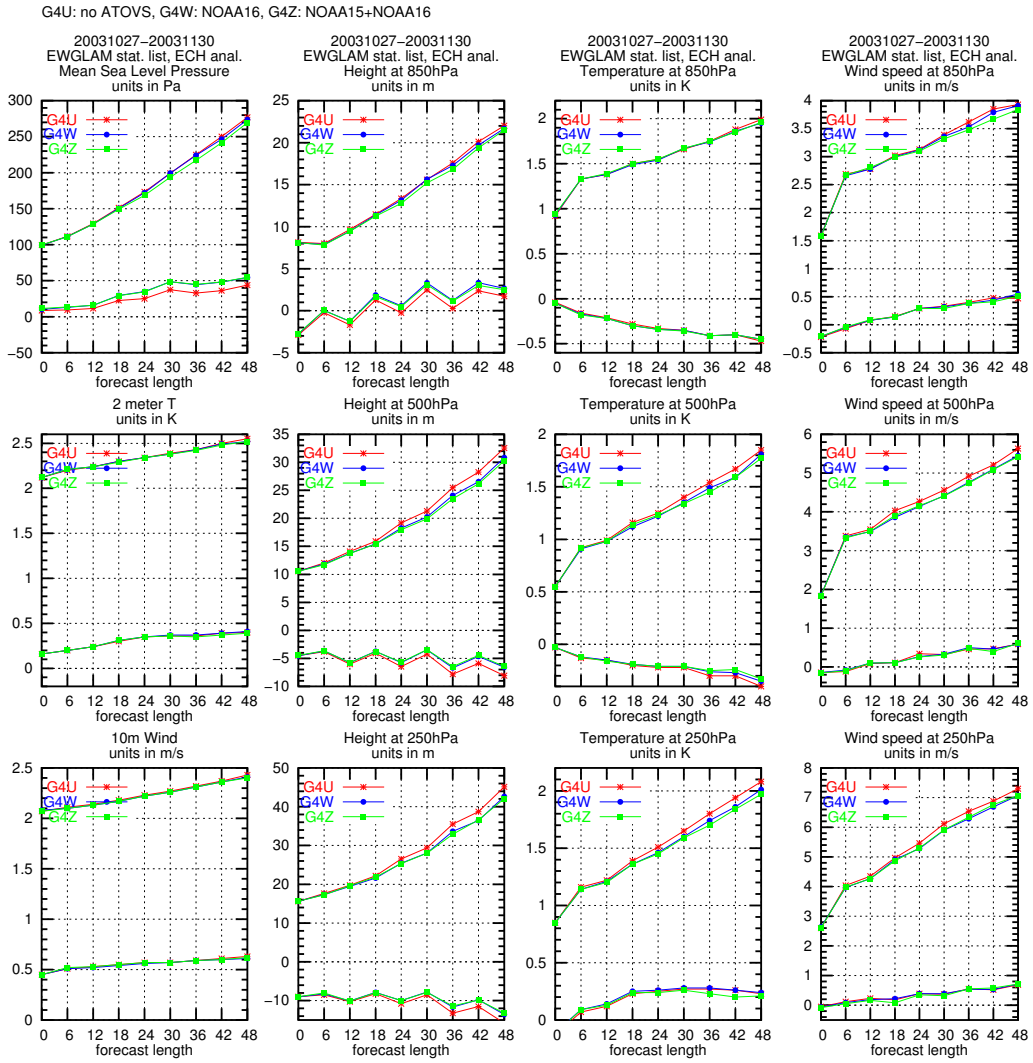

Figure 5: Impact of adding NOAA15 ATOVS AMSU-A to NOAA16 ATOVS AMSU-A. The red curves with crosses are without any ATOVS, blue curves with filled circles with only NOAA16 ATOVS AMSU-A, and the green curces with filled squares with both NOAA15 and NOAA16 ATOVS AMSU-A. The curves are based on data from October 27th to November 30th 2003.

References

Amstrup, B. (2003). Impact of NOAA16 and NOAA17 ATOVS AMSU-A radiance data in the DMI-HIRLAM 3D-VAR analysis and forecast system - January and February 2003. Scientific Report 03-06, Danish Meteorological Institute. `http://www.dmi.dk/f+u/publikation/vidrap/2003/Sr03-06.pdf`.

Amstrup, B., Mogensen, K. S., Nielsen, N. W., Huess, V., and Nielsen, J. W. (2003). Results from DMI-HIRLAM pre-operational tests prior to the upgrade in December 2002. Technical Report 03-20, Danish Meteorological Institute. `http://www.dmi.dk/f+u/publikation/tekrap/2003/Tr03-20.pdf`.

Gustafsson, N., Berre, L., Hörnquist, S., Huang, X.-Y., Lindskog, M., Navascués, B., Mogensen,

K. S., and Thorsteinsson, S. (2001). Three-dimensional variational data assimilation for a limited area model. Part I: General formulation and the background error constraint. *Tellus*, 53A:425–446.

Harris, B. and Kelly, G. (2001). A satellite radiance-bias correction scheme for data assimilation. *Q.J.R. Meteorol. Soc.*, 127:1453–1468.

Lindskog, M., Gustafsson, N., Navascués, B., Mogensen, K. S., Huang, X.-Y., Yang, X., Andræ, U., Berre, L., Thorsteinsson, S., and Rantakokko, J. (2001). Three-dimensional variational data assimilation for a limited area model. Part II: Observation handling and assimilation experiments. *Tellus*, 53A:447–468.

Sass, B. H., Nielsen, N. W., Jørgensen, J. U., Amstrup, B., Kmit, M., and Mogensen, K. S. (2002). The Operational DMI-HIRLAM System - 2002 version. Technical Report 02-5, Danish Meteorological Institute. `http://www.dmi.dk/f+u/publikation/tekrap/2002/Tr02-05.pdf`.

Schyberg, H., Landelius, T., Thorsteinsson, S., Tveter, F., Vignes, O., Amstrup, B., Gustafsson, N., Järvinen, H., and Lindskog, M. (2003). Assimilation of ATOVS data in the HIRLAM 3D-VAR System. Technical Report 60, HIRLAM. `http://hirlam.knmi.nl/open/publications/TechReports/TR60.pdf`.

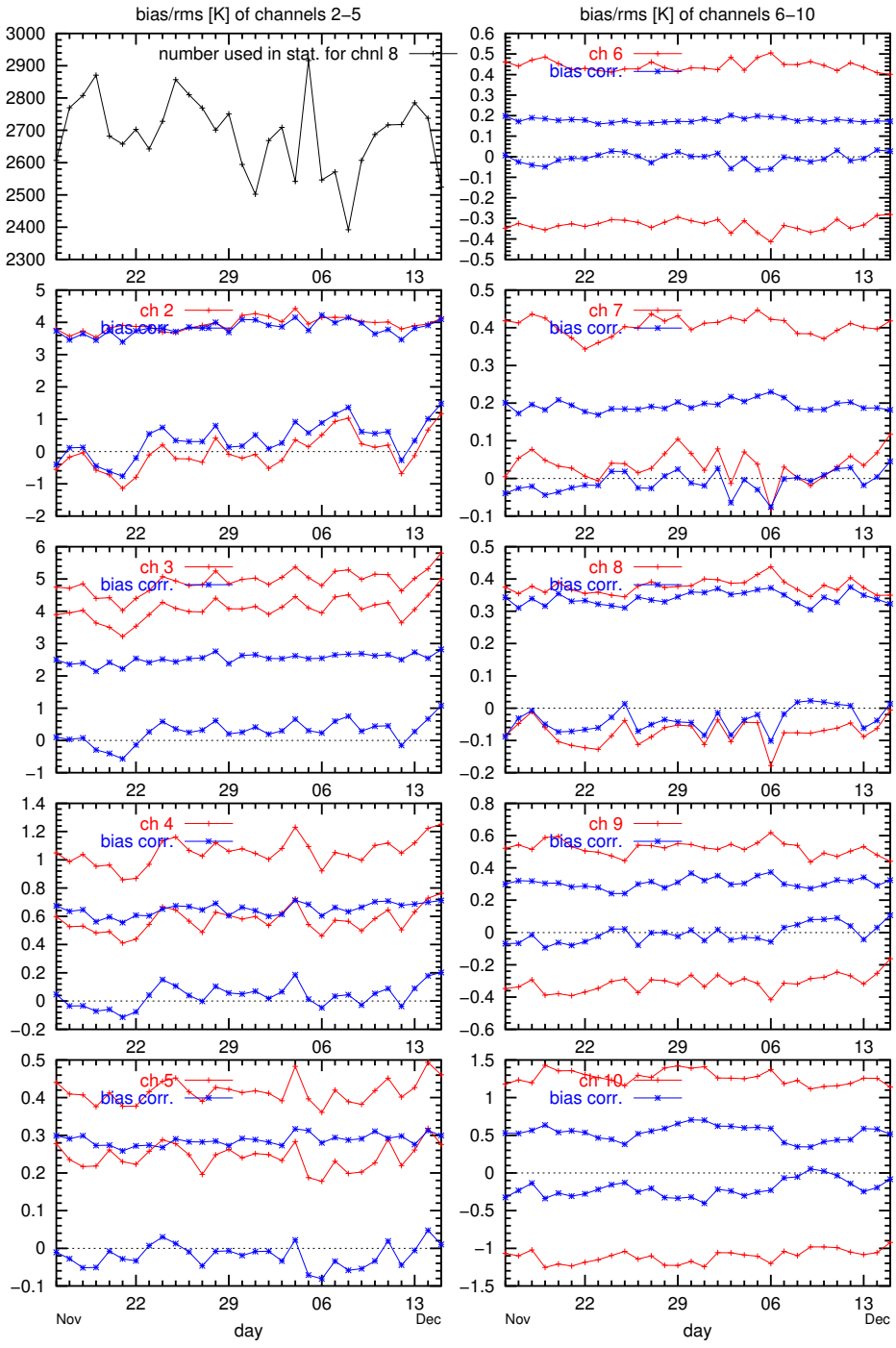

Figure 6: Bias and RMS (in brightness temperature Kelvin) for NOAA16 for November 15th to December 15th 2003 for channels 2 to 10. Uncorrected data in red and bias corrected in blue for the DMI-HIRLAM-G analysis. In the the top right panel the number of datapoints used is plotted. Notice the changing scale on the bias and RMS axis.

Cloud Overlap Detection from HIRS and AVHRR

Michael J. Pavolonis[1] and Andrew K. Heidinger[2]

[1]Cooperative Institute for Meteorological Satellite Studies,

University of Wisconsin, Madison, WI

[2]Office of Research and Applications, NOAA/NESDIS, Madison, WI

Abstract

An algorithm for detecting multi-layered cloud systems with satellite data is presented. The algorithm was designed to be applicable to data in the 0.63 μm, 10.8 μm, and 12 μm regions of the spectrum that are available on the Advanced Very High Resolution Radiometer (AVHRR). The cloud overlap algorithm has been validated and is currently used operationally in the Extended Clouds from AVHRR (CLAVR-x) processing system. In this study, the unmodified AVHRR cloud overlap detection scheme is applied to the 0.69 μm, 11.11 μm, and 12.47 μm channels on the High Resolution Infrared Radiation Sounder (HIRS). The results from 60°N to 60°S were compared with results from the AVHRR. It was found that the AVHRR algorithm could be effective at detecting cloud overlap with HIRS. Regions of cloud overlap were compared to the HIRS operational CO_2 slicing-based cloud top pressure product. The results indicate that the retrieved cloud top pressure is generally consistent with the location of the top cloud layer.

Introduction

Surface observations have shown that multi-layered cloud systems occur in most parts of the world (Warren et al., 1985). Such systems are especially common in the tropics where anvils associated with convective systems can spread out over large horizontal distances and with mid-latitude cyclones (Hahn et al., 1982, 1984: Tian and Curry, 1989). In addition, satellite cloud property retrievals are generally performed under the assumption that only a single cloud layer is present in a given pixel. Because of this assumption, the quality of cloud optical depth, particle size, and cloud height retrievals may suffer when more than one cloud layer is actually present.

Detecting multi-layered cloud systems from space is often difficult since the higher clouds may be optically thick and obscure the presence of a lower cloud layer. Conversely, higher level clouds may be too thin to be detected in the presence of a thicker lower cloud from current passive remote sensing observations. Two cloud layers may also have an insufficient vertical separation, making it difficult to distinguish the multi-layer cloud system from a single layer cloud using thermal emission signatures. Nevertheless, a technique for detecting cloud overlap is presented. This technique is partially based on the work of Ou et al. (1996) and was designed to work on data from the Advanced Very High Resolution Radiometer (AVHRR) which is on board the National Oceanic and Atmospheric Administration (NOAA) polar orbiting satellites. This algorithm is used operationally in the Extended Clouds from AVHRR (CLAVR-x) processing system The utility of this method will be demonstrated with AVHRR data and the algorithm will then be applied to data

from the High Resolution Infrared Radiation Sounder (HIRS), which is also on the NOAA polar orbiting satellites. The results will be compared to results using AVHRR data and the HIRS cloud top pressure product will be qualitatively analyzed in regions where cloud overlap is indicated by the AVHRR cloud overlap algorithm.

Cloud Overlap Algorithm Description

The AVHRR algorithm utilizes 0.63 μm reflectance and brightness temperatures from the infrared window region of the spectrum (10.8 μm and 12 μm). The premise of the algorithm is that for a single layer cloud, the 0.63 μm reflectance and the 10.8 - 12 μm brightness temperature difference (split window brightness temperature difference) should behave as predicted by plane-parallel radiative transfer simulations. In general, as a single layer cloud becomes optically thick, its reflectance increases and its split window brightness temperature decreases (Inoue, 1985). In the case of a semi-transparent cirrus cloud overlying a lower water cloud, the vertical separation has little effect on its reflectance but a large effect on the split window brightness temperature difference. Given a sufficient temperature difference between the cirrus and the lower water cloud, the difference in transmission through the cirrus cloud at 10.8 μm and 12 μm will generally result in a split window brightness temperature difference that is much larger than that predicted by plane parallel theory for a single-layer cloud with a similar reflectance. A radiative transfer model was used to perform single-layer (water and ice) simulations and simulations with an ice cloud overlapping a water cloud with the optical depth of both clouds and the atmospheric profiles being varied. Thresholds of 10.8 - 12 μm brightness temperature difference were determined as a function of 0.63 μm reflectance for various viewing and solar zenith angles. When the actual 10.8 - 12 μm brightness temperature difference exceeds the threshold value and the 10.8 μm brightness temperature is less than 270 K and the 0.63 μm reflectance is greater than 30%, cloud overlap is said to be present. For additional details concerning this algorithm refer to Pavolonis and Heidinger (2003).

Results

To qualitatively illustrate the effectiveness of the AVHRR cloud overlap detection scheme, an AVHRR scene is analyzed. Fig. 1a shows a Red Green Blue (RGB) multi-spectral AVHRR Global Area Coverage (GAC) image from July 2, 2001 over the Eastern Pacific Ocean. AVHRR channel 1 (0.63 μm) reflectance, channel 3a (1.65 μm) reflectance, and channel 4 (10.8 μm) brightness temperature are displayed on the red, green, and blue color guns respectively. In this image, ice clouds will have a pink hue, low water clouds will appear yellow, and mid-level cloud will appear to be white/off-white. From Fig. 1a, it is clear that there are regions in this scene where cloud overlap is present. Fig. 1b shows the results of the AVHRR cloud overlap algorithm. The results from the complete AVHRR cloud typing algorithm used in CLAVR-x are also shown in Fig. 1b. It is evident that the algorithm is able to correctly identify regions where cloud overlap is present, more specifically, on the left and top sides of the image. The AVHRR cloud overlap algorithm has also

been validated against cloud radar data. The validation technique and results are detailed in (Pavolonis and Heidinger, 2003).

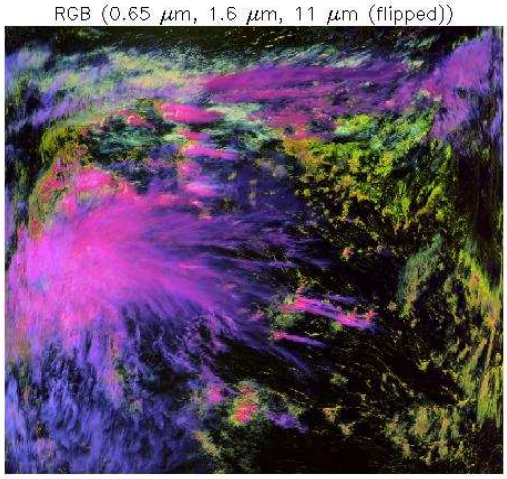

Fig. 1a: An RGB (0.63 μm, 1.65 μm, 10.8 μm) image of an AVHRR GAC scene over the Eastern Pacific Ocean on July 2, 2001.

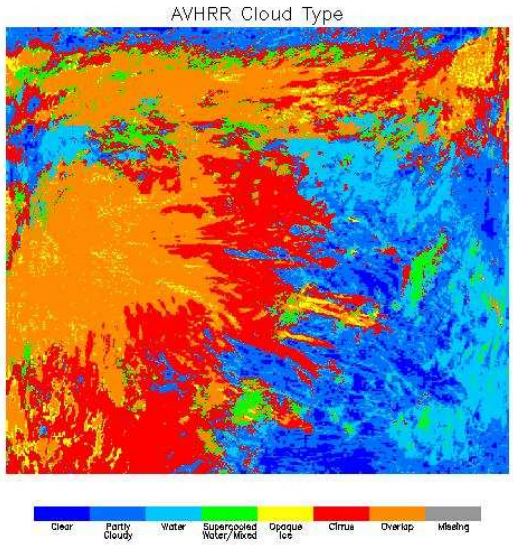

Fig. 1b: AVHRR cloud typing results for the scene shown in Fig. 1a.

The complete AVHRR cloud typing algorithm was applied to AVHRR data for the ascending node of NOAA-16 on October 13, 2003. Fig. 2 shows the dominant cloud type within 0.5 degree equal area grid cells from 60°S to 60°N. The regions where cloud overlap is dominant are displayed in orange. As would be expected, most of the cloud overlap is present in the tropics and the mid-latitude storm tracks. The AVHRR cloud overlap algorithm was applied to HIRS channel 20 (0.69 μm), channel 8 (11.11 μm), and channel 7 (12.47 μm) cloudy field-of-views (FOVS). No adjustments were made to the algorithm. A cloud overlap mask for the HIRS data is shown in Fig. 3. These preliminary results indicate that the AVHRR cloud overlap scheme can be effective on HIRS data, which has a much courser spatial resolution (~19 km compared to ~4 km) and the channels used have slightly different spectral characteristics compared to AVHRR GAC data. Many areas of cloud overlap indicated by the AVHRR data are present in the HIRS analysis, although some clear differences exist, especially in the tropics. However, the AVHRR algorithm was not modified, it is likely that some modification is needed to optimize the algorithm to be used with HIRS data. Thus the results presented here can likely be improved, assuming the AVHRR results are accurate.

HIRS-derived cloud top pressures for the same orbits shown in Figs. 2 and 3 were mapped to 0.5 degree equal area grid and are shown in Fig. 4. The HIRS cloud top pressures were obtained from an Advanced TIROS (Television Infrared Observation Satellites) Operational Vertical Sounder (ATOVS) rotating 1T file and were retrieved using a CO_2 slicing technique. In regions where cloud overlap is present, the retrieved cloud top pressures are predominantly consistent with the presence of high clouds. Most of the overlap retrieved with the AVHRR algorithm is characterized by high ice clouds that overlap lower clouds. Thus, the CO_2 slicing technique seems to

be largely insensitive to lower cloud layers when multiple cloud layers are present.

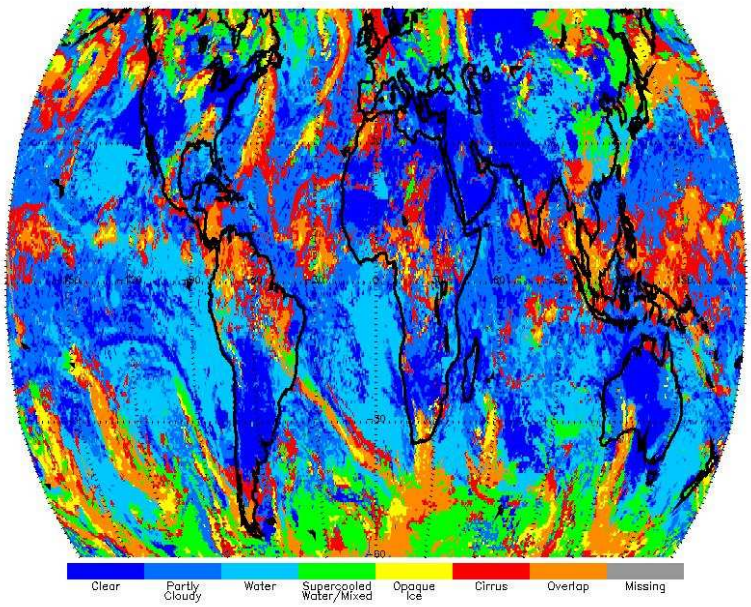

Fig. 2: AVHRR cloud typing results for the ascending node of NOAA-16 on October 13, 2003. The dominant cloud type within a 0.5 degree equal area grid cells is shown.

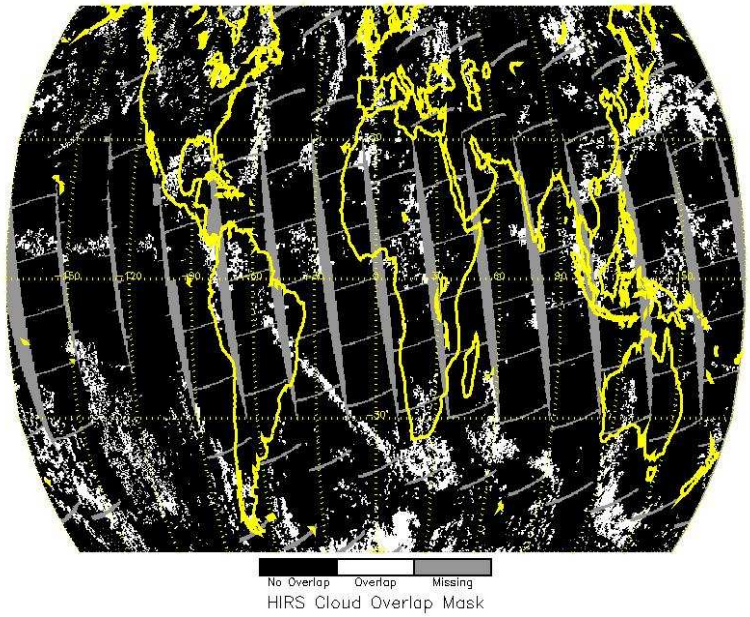

Fig. 3: Results from the AVHRR cloud overlap algorithm when applied to HIRS data for the scene shown in Fig. 2.

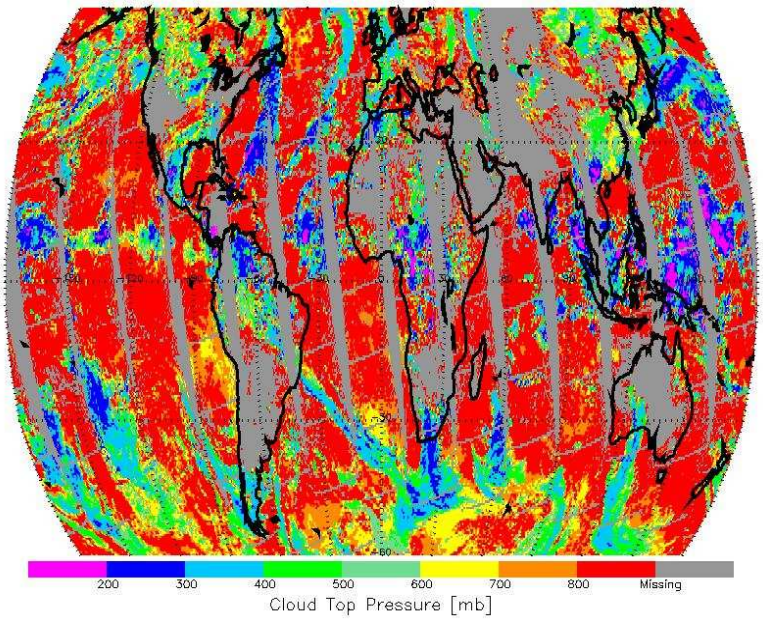

Fig. 4: HIRS-derived cloud top pressures (mb) mapped to a 0.5 degree equal area grid for the same orbits shown in Fig. 2.

Conclusions

Multi-layered cloud systems are commonly observed in many regions of the world. In this work, a multi-spectral algorithm was presented for identifying cloud overlap. The algorithm was designed to be applicable to AVHRR data and utilizes information from the 0.63 μm, 10.8 μm, and 12 μm regions of the spectrum. The AVHRR cloud overlap detection scheme has been validated and is currently used operationally in the Extended Clouds from AVHRR (CLAVR-x) processing system. Further, the utility of the algorithm was demonstrated through a qualitative analysis 4 km AVHRR data.

The AVHRR cloud overlap algorithm was applied to HIRS channel 20 (0.69 μm), channel 8 (11.11 μm), and channel 7 (12.47 μm) cloudy field-of-views (FOVS), with no adjustments. Comparisons with results using AVHRR data show that the algorithm has the potential to be effective with HIRS data. Regions of cloud overlap were then compared to the HIRS operational CO_2 slicing-based cloud top pressure product. The results indicate that the retrieved cloud top pressure is generally consistent with the location of the top cloud layer.

References

Hahn, C. J., Warren, S. G., London, J., Chervin, R. M., and Jenne, R. 1982. *Atlas of Simultaneous Occurrence of Different Cloud Types over the Ocean*. NCAR Tech. Note TN-201 + STR, 212 pp. [NTIS PB83-152074].

Hahn, C. J., Warren, S. G., London, J., Chervin, R. M., and Jenne, R. 1984. *Atlas of Simultaneous Occurrence of Different Cloud Types over Land*. NCAR Tech. Note TN-241 + STR, 214 pp.

Inoue, T. 1985. On the temperature and effective emissivity determination of semi-transparent cirrus

clouds by bi-spectral measurements in the 10 μm window region. *J. Meteor. Soc. Japan*. **64**, 88-99.

Ou, S. C., Liou, K. N., and Baum, B. A. 1996. Detection of multilayer cirrus cloud systems using AVHRR data: Verification based on FIRE II IFO composite measurements. *J. Appl. Meteor*., **35**, 178-91.

Pavolonis, M. J. and Heidinger, A. K. 2003. Daytime cloud overlap detection from AVHRR and VIIRS. *J. Appl. Meteor*. (accepted December, 2003).

Tian, L. and Curry, J. A. 1989. Cloud overlap statistics. *J Geophys. Res*., **94**, 9925-35.

Warren, S. G., Hahn, C. J., and London, J., 1985. Simultaneous occurrence of different cloud types. *J. Climate and Appl. Meteor*., **24**, 658-67.

Operational Assimilation of GOES Imager Water Vapor Channel at MSC

Nicolas Wagneur and Louis Garand
Meteorological Service of Canada, Dorval, Québec, Canada

Abstract

The assimilation of GOES imager radiance data at 6.7 micron (channel 3) was made operational in the Canadian Meteorological Center (CMC) global 3Dvar analysis system June 19th 2003. GOES imager channel 3 is sensible to moisture in the atmosphere at 500 to 250 mb. The MSCFAST physical radiative transfer model is used as forward operator (Garand et al. 1999). This implementation of GOES water vapor radiances was made in the same time as ATOVS AMSU B radiance data were added in the assimilation system. Impact on water vapor fields of these two data sets assimilated separately is quite similar for overlapping areas in the 500 to 250 mb layer. The improvement of adding independently GOES imager channel 3 on moisture analysis and forecasts is shown. Positive impact on the quality of forecasted moisture fields is present up to 48 hours. Quantitative precipitation forecasts improvement over North America is also noted. The monitoring suite of data treatment shows stable innovations statistics. Furthermore geographical maps of monthly averages of innovations show no viewing angle bias problems yet significant local monthly mean corrections. These data are to be implemented in the regional system as the new main frame computer becomes operational. GOES radiance data are readily available for the CMC's regional system despite a short cutoff time. This is not necessarily the case for AMSU B data where large data voids are noted.

Similarity of impacts of GOES imager water vapor and AMSU B radiances

In order to evaluate the effect of a new data type on the quality of the assimilation system an experimental cycle is launched with the addition of this data. Here two experiments were run with each the addition of GOES channel or ATOVS AMSU B data only. Maps of 6 weeks averaged differences to the control of dew point depression (T-Td) analysis are shown for both experiments (see Fig. 1). Theses averaged "corrections" to the control are remarkably similar. This is a strong validation of both data sets as they show almost the same behavior when tested independently.

Impact on analysis and forecast quality

An objective evaluation of both cycles was done. The improvements noted were mainly on moisture fields, but mass fields were also somewhat better. Figure 2 shows objective scores of the forecast issued from the cycle with added GOES data using radiosonde measurements from South America as reference observations. Even if the analysis does not agree as well with radiosondes, the 6 hour forecasted moisture is greatly improved over the control run and is still somewhat present up to 48 hours. The scores are more neutral over North America. However a significant gain over that area is noted in precipitation scores when goes radiances are added (see Fig. 3).

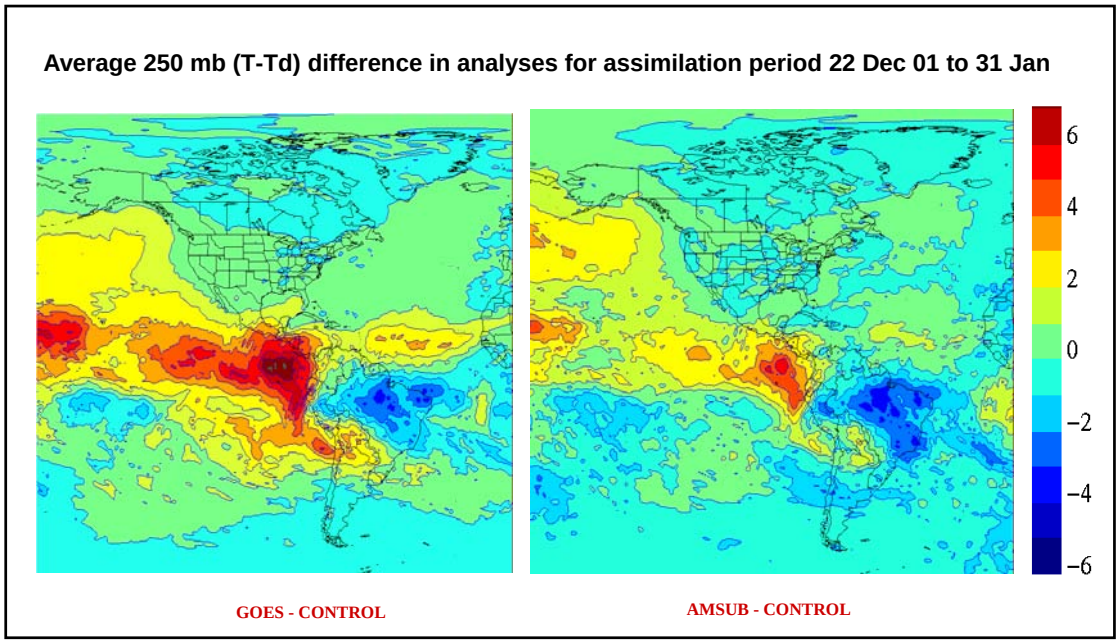

Fig. 1: Comparison of mean dew point depression changes induced by adding of GOES Imager channel 3 and AMSUB radiances derived from a 41 day analysis cycle.

The bias are marginally affected (top panels of Fig. 3) but the threat scores are better for every precipitation class (bottom panels), and this is true for the first and second day of the forecast (left and right panels). This may be attributed to the added information in upstream moisture captured by GOES west over the Pacific Ocean.

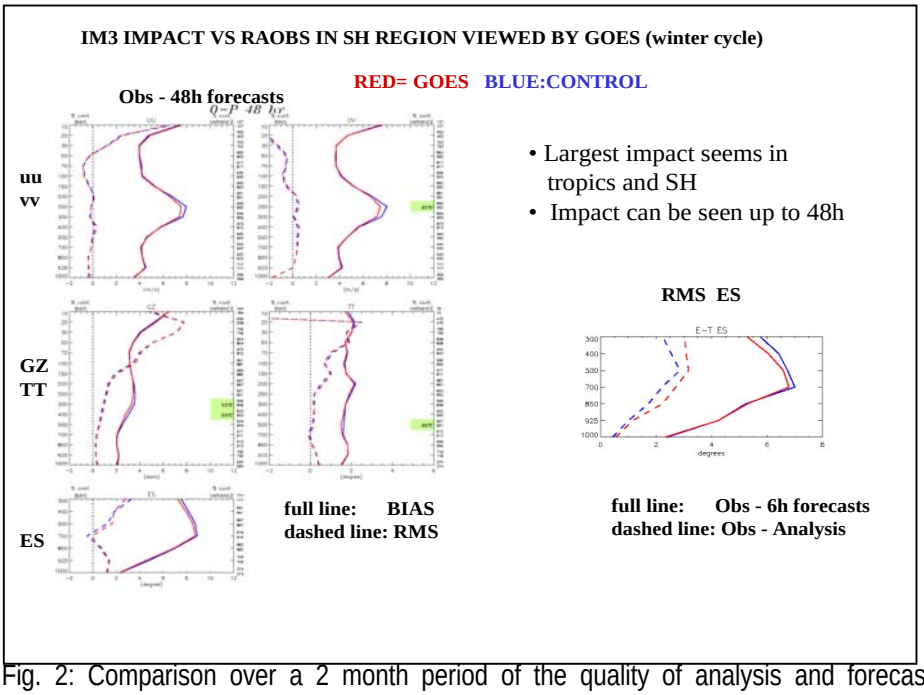

Fig. 2: Comparison over a 2 month period of the quality of analysis and forecasts against South American radiosonde data between a control cycle (blue) and a test cycle that included GOES imager 3 data (red).

The cycle with AMSU B data only has greater positive impact on scores (not shown). Results from a similar cycle with both AMSU B and GOES radiance included shows substantial improvement over the southern hemisphere and good improvement over the northern hemisphere, with gains lasting up to 96 hours (see Chouinard and Hallé, this volume).

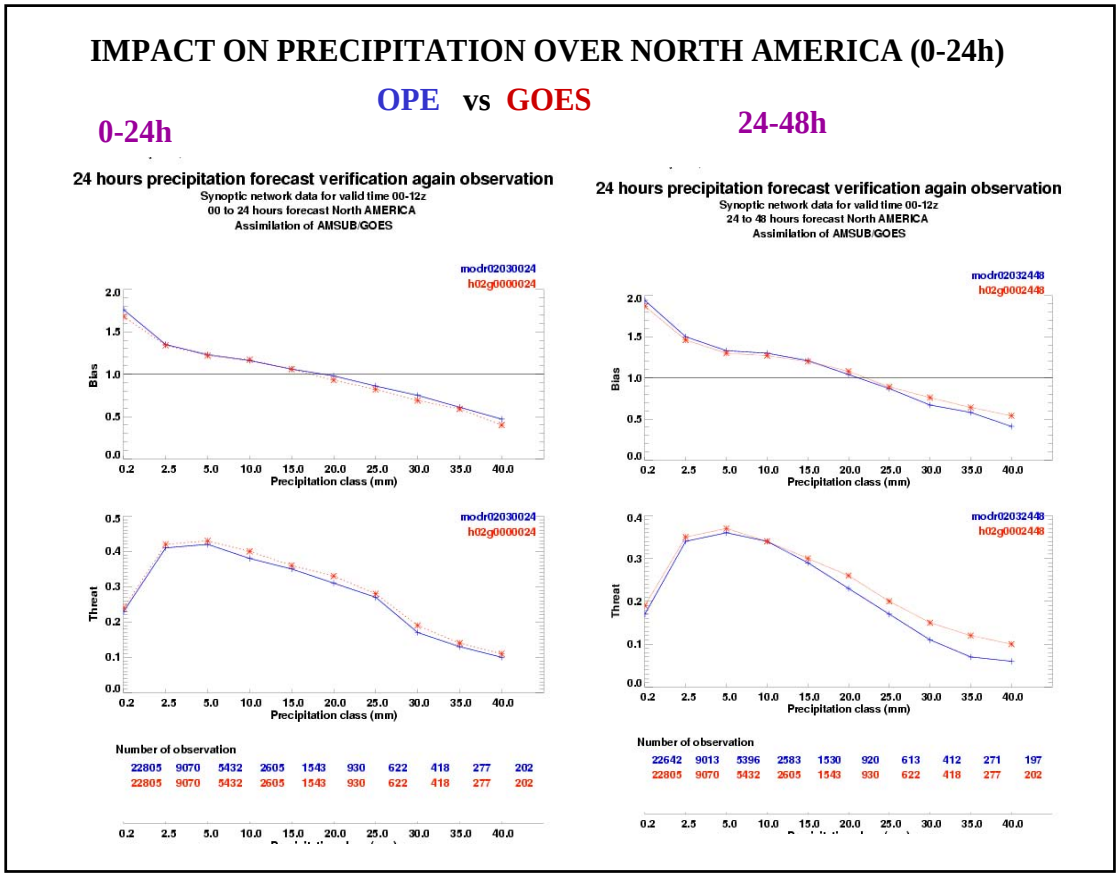

Fig. 3: Evaluation over a 2 month period of the quality of 24 hour accumulated forecast precipitation against North American synoptic rain gages for the control cycle (blue) and a test cycle that included GOES imager 3 data (red). Bias and threat scores are shown with the number of observations per rainfall category.

Monitoring diagnosis

When assimilating large amounts of satellite data it is essential to routinely check the quality of the data. A time series trough every analysis time of the average and standard deviation of the innovations (observation – 6 hour forecast) allows for identification of any sudden drop in data quality. For GOES data, the stability of the bias correction and standard deviation can be verified on Figure 4: no derivation in time of the statistics is noted. The bias correction used here is a simple linear fit with brightness temperature (Garand, 2003). The coefficients found are kept constant until the need of readjustment is revealed from the monitoring. Figure 4 also shows the residuals (observation – analysis) time series. Note the standard deviation reduction from red to blue confirming a good fit of the analysis to these observations.

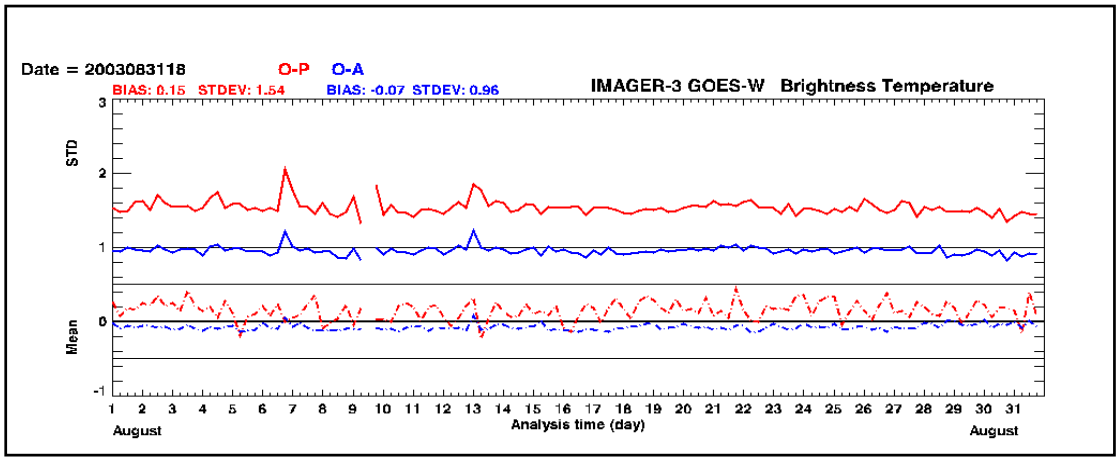

Fig. 4: A monthly time series of imager 3 brightness temperatures innovations (Observation minus 6 hours Forecast, in red) in CMC's current operational analysis system. A significant variance reduction is obtained after assimilation represented by brightness temperature residuals (Observation – Analysis, in blue). The solid lines show the standard deviation and the dotted lines the bias.

Another way of evaluating the behavior of this type of data in an assimilation system is to map mean brightness temperatures. Figure 5 shows such a map where pixels are averaged over a month of innovations located within a 2 degree box. This plot indicates no presence of obvious bias with viewing angle. Furthermore the plot shows areas of substantial correction to the model's climatology. Here positives innovations imply drying of the atmosphere.

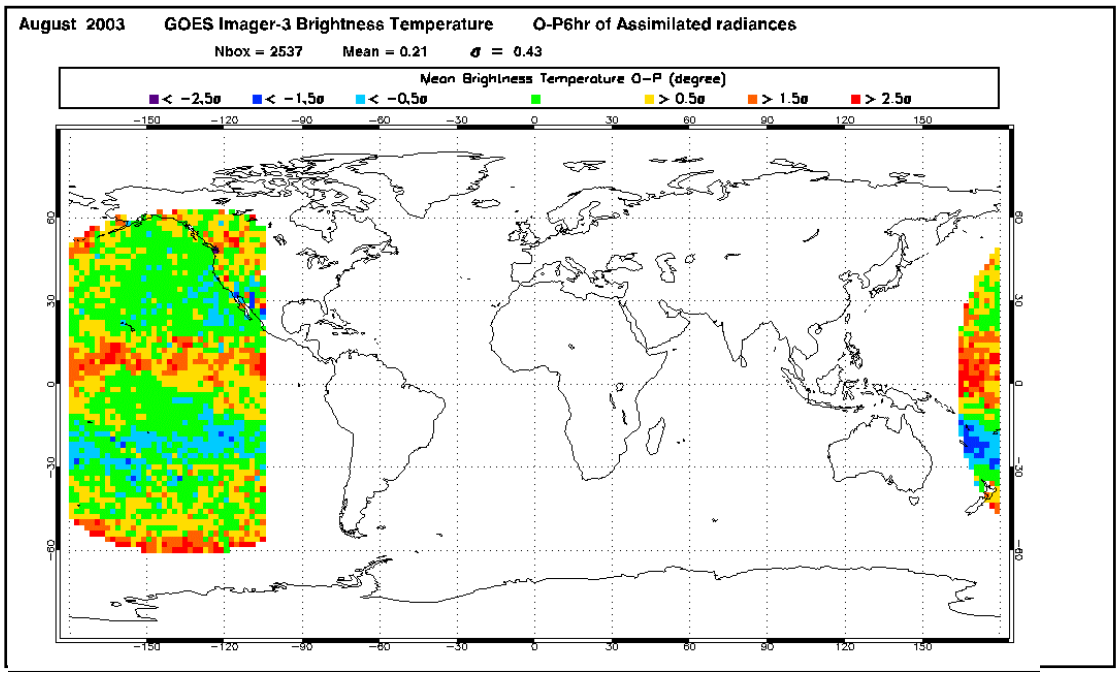

Fig. 4: A monthly average of brightness temperatures innovations (observation minus 6 hours forecast) over 2 degree boxes in CMC's current operational analysis system. The color scale is in units of the overall standard deviation (σ = 0.43 K).

Data availability

An important consideration for the operational use of satellite measurements is the timeliness of the availability of the data. This is especially true when a model has to be launched with a relatively short cutoff time. At the Canadian Meteorological Center, the regional model (with higher resolution over North America) has a 1 hour and 40 minutes cutoff time. As one can see on figure 6, the late arrival of the NOAA17 data makes for large gaps in the coverage at the regional cutoff time. Depending on time of day, the available swaths can miss regions of interest for the regional model. However the GOES coverage is precisely over the area of interest and is available within 15 minutes of the analysis time (see Figure 7). This is an important additional justification for including also GOES channel 3 data in the operational assimilation system even if moisture information seems redundant when AMSU B data from the NOAA satellites are present.

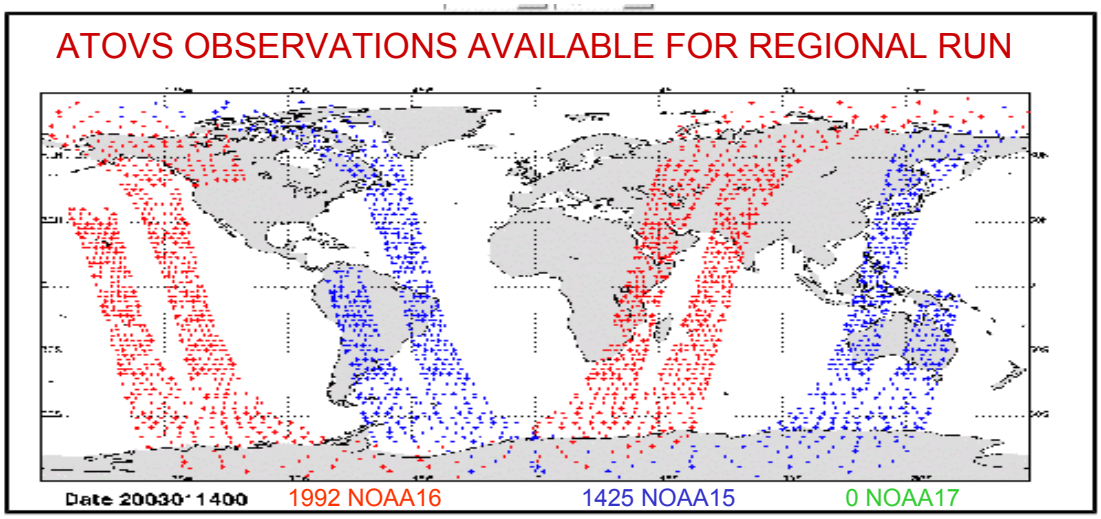

Fig. 6: An example of NOAA ATOVS coverage available at CMC for regional model (after thinning).

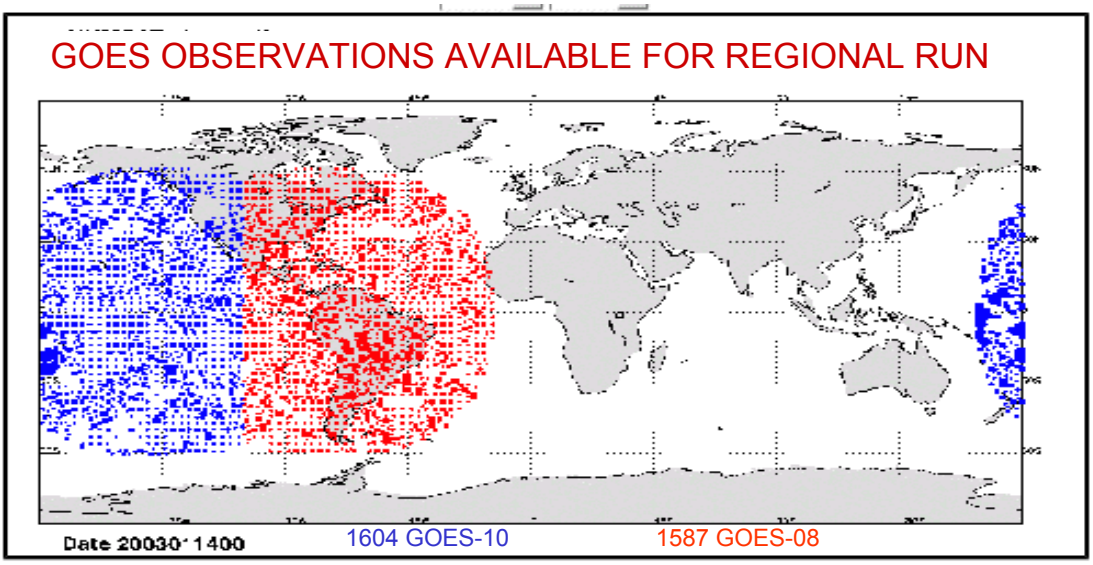

Fig. 7: An example of GOES imager data coverage available at CMC for regional model (after thinning).

Conclusions

GOES water vapor channel has a positive impact on analyses and forecasts, especially over South America. A good synergy with AMSU B data is noted. The availability within 15 minutes of GOES data makes possible its use in CMC's regional model (centered over North America) despite its short cutoff time. Work is under way to include radiances from the recently activated GOES-12 satellite. Assimilation at higher temporal frequency is foreseen with implementation of 4Dvar (2004). Surface channels imager 4 and 5 are also monitored and available for eventual assimilation (see Garand et al., this volume). Applying a similar procedure to geostationary satellites MSG and MTSAT water vapor channels is planned in order to cover the whole globe in the tropics and mid-latitudes.

References

Garand. L., D.S. Turner, C. Chouinard and J. Hallé 1999. A physical formulation of atmospheric transmittance for the massive assimilation of satellite infrared radiances. *J. Appl. Meteor.*, **38**, 541-554.

Garand. L., 2003. Toward an Integrated Land-Ocean Surface Skin Temperature Analysis from the Variational Assimilation of Infrared Radiances *J. Appl. Meteor.*, **42**, 570-583.

An Improved OPTRAN Algorithm

Yong Han[1], Xiaozhen Xiong[2], Paul van Delst[3],
Yoshihiko Tahara[4], Larry M. McMillin[1], Thomas J. Kleespies[1]

1. *Office of Research and Application, National Environmental Satellite, Data, and Information Service, NOAA, Camp Springs, MD*
2. *QSS Group Inc, Lanham, MD*
3. *CIMSS, University of Wisconsin*
4. *Japan Meteorology Agency, Japan*

Abstract

Presented here is an improved algorithm for the fast and accurate transmittance-calculation procedure, optical path transmittance (OPTRAN). This algorithm combines two techniques developed separately at the NOAA NESDIS and NCEP and implemented in OPTRAN version 7 and 8, respectively. The first technique applies a correction factor to account for the differences between the total transmittances averaged over spectral response function (SRF) and the transmittances that are the product of the SRF-averaged transmittances of individual gases. The correction factor is estimated from a given atmospheric state in a similar way as that to predict transmittances for each gas. The motivation for developing the technique is to eliminate the use of the effective transmittances, a technique difficult to apply in situations when transmittances are estimated for four or more gases. The second technique is developed in order to reduce the number of regression coefficients used to predict the transmittances. It is especially useful for hyper-spectral sensors, such as AIRS, for which the number of coefficients is reduced to 183,106 from 4,280,400 in the previous versions. The technique applies a polynomial function with the gas amount as a dependent variable to estimate the vertical variations of the coefficients, rather than having a separate set of regression coefficients for each vertical layer. We will also present results in improving the computational efficiency for OPTRAN version 8.

1. Introduction

Over the past two decades, the National Environmental Satellite, Data, and Information Service (NESDIS) and National Centers for Environmental Prediction (NCEP) of the Oceanic and Atmospheric Administration (NOAA) have jointly developed an accurate and fast radiative transfer (RT) model (McMillin et al., 1995; Kleespies et al., 2003). The model is an essential component in the NCEP satellite data assimilation system. Its core is a regression-based fast radiative transmittance model, called Optical Path TRANsmittance (OPTRAN). One of its unique features is that the radiative transmittances of an absorbing gas are computed at fixed levels of integrated amount of the gas along the optical path, rather than at fixed pressure levels. OPTRAN has so far eight versions. OPTRAN-V6 (Kleespies et al., 2003) is the current version used in the Global Data Assimilation System (GDAS) at NCEP. Recently, two new versions, OPTRAN-V7 (Xiong et al., 2003) and OPTRAN-V8, have been developed simultaneously at NESDIS and NCEP, respectively. The latter is currently being evaluated, improved and implemented in GDAS.

Both OPTRAN-V7 and -V8 are developed from OPTRAN-V6, which applies the effective-transmittance technique to account for the instrumental band averaging effect and a fixed multi-layer structure to estimate transmittances at fixed layers. OPTRAN-V7 has replaced the effective-transmittance technique with the correction-factor technique. This change makes OPTRAN more efficient and easier to be extended to include more variable gases. However, it requires the same 300-layer structure as that used in OPTRAN-V6, which needs 300 regression equations and 1800 regression coefficients to estimate transmittances per gas and channel. The large number of regression coefficients, however, is a problem for the current NCEP analysis system to assimilate data from hyper-sensors such as AIRS, due to the limitation of the computer memory capacity. OPTRAN-V8 was initiated to solve the problem. It introduces a polynomial function to fit the absorption coefficients along optical paths and thus does not require the multi-layer structure. As a result, the number of regression coefficients is reduced by a factor of 23. However, OPTRAN-V8 still uses the same effective transmittance technique as that used in OPTRAN-V6, and consequently is difficult to be extended to include more variable gases.

In this paper we report the work to integrate OPTRAN-V7 and –V8 by implementing the correction-factor technique into OPTRAN-V8. We also present results from the work to improve OPTRAN-V8 efficiency. We start with a brief description of OPTRAN-V7 and –V8, and then present the methods and preliminary results, followed by a summary.

2. Description of OPTRAN-V7 and –V8

2.1 OPTRAN-V7

In OPTRAN-V7, the atmosphere is divided vertically into 300 layers along the optical path in the so-called absorber space. The absorber space is a set of discrete integrated gas amount $\{A_i, i=0, 300\}$ with A_0 being the minimum value at the top of the atmosphere and A_{300} the maximum value at the surface. Since three gas types are included in OPTRAN-V7, three absorber spaces are required. The distribution of the levels in the absorber space has large impact on the accuracy of the transmittance estimation (Xiong et al., 2003). Once determined, the absorber space is fixed and applied for any cases. OPTRAN estimates gas transmittances, but they are not predicted directly. The absorption coefficients is predicted directly using the following 5-predictor regression equation,

$$k_i = c_{i,0} + \sum_{j=1}^{5} c_{i,j} X_{i,j} \qquad (1),$$

where k_i is the absorption coefficient at layer i , and $\{c_{i,j}\}$ and $\{X_{i,j}\}$ are regression coefficients and the predictors, respectively. Then, k_i is converted to layer transmittance τ_i using

$$\tau_i = \exp(-k_i (A_i - A_{i-1})) \qquad (2).$$

Note that τ_i is the transmittance averaged over the frequency band with the instrument spectral response function (SRF). The regression coefficient set $\{c_{i,j}\}$ in (1) is obtained from a statistical atmospheric profile ensemble, in which both the dependent variable k_i or τ_i and independent variable $X_{i,j}$ are calculated from the ensemble, with τ_i computed using a line-by-line model and the SRFs. The predictor set $\{X_{i,j}, j=1,5\}$ is selected from a pool of 18 pre-defined predictors. The total transmittance

$\tau_{tot,i}$ is a product of three gas transmittances, multiplied by a correction factor τ_c as (for simplicity the layer index *i* is dropped),

$$\tau_{tot} = \tau_{dry}\tau_{H2O}\tau_{O3}\tau_c \qquad (3),$$

where τ_{H2O} and τ_{O3} are the water vapor and ozone transmittances, respectively, and τ_{dry} is the so-called dry gas transmittance, which includes the contributions from other absorbing gases such CO_2 and CH_4. The function of τ_c is to correct the difference between the SRF-averaged total transmittance and the product of individual SRF-averaged gas transmittances. Examples of the correction factors are shown in Fig. 1.

The correction factor τ_c is estimated in the same way as that for the gas transmittances, by using (1) and (2). The process also requires an absorber space. It is found that the water vapor absorber space is a good choice for τ_c, although more complicated procedures may be adopted (Xiong et al., 2003).

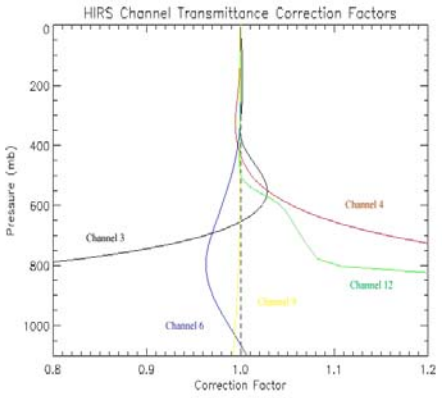

Fig. 1 Correction factors for selected HIRS channels computed using LBLRTM (Clough et al. 1992)

2.2 OPTRAN-V8

In OPTRAN-V8, the multi-layer structure is no longer used. Instead, a single regression equation is applied to predict transmittance at any level as

$$\ln(k(A)) = c_0(A) + \sum_{j=1}^{6} c_j(A) X_j(A), \qquad (4)$$

where *A* is the absorber amount of the gas whose transmittances are estimated and $c_j(A)$ is given by a polynomial function as

$$c_j(A) = \sum_{m=0}^{10} a_{j,m} A^m, \; j = 0,6$$

where $\{a_{j,m}\}$is a set of constants. OPTRAN-V8 uses 6 predictors selected from a pool of 17 pre-defined predictors and a 10^{th} order polynomial function. There are total 77 regression coefficients in (4), which is a much smaller number compared with the 2400 coefficients, required by OPTRAN-V7. In practice, instead of using the absorber amount *A* directly in (4), *A* is replaced by the following variable,

$$Z = \frac{1}{\alpha}\ln(\frac{A-b_2}{b_1}), 0 \le Z \le 1 \qquad (5),$$

where α is a constant determined by trial, and b_1 and b_2 are also constants determined by the minimum and maximum values of the absorber amount A. The absorption coefficient k_c in (4) is related to transmittance by the same formula given by (2), but the transmittance is the effective transmittance, defined in the following,

$$\tau_{tot} = \tau_{dry}^{*}\tau_{H2O}^{*}\tau_{O3}^{*}, \qquad (6),$$

where τ_{H2O}^{*}, τ_{O3}^{*} and τ_{dry}^{*} are the effective transmittances of dry gas, water vapor and ozone, respectively, given by

$$\tau_{dry}^{*} = \tau_{tot} / \tau_{H2O+O3},$$

$$\tau_{H2O}^{*} = \tau_{H2O},$$

and

$$\tau_{O3}^{*} = \tau_{H2O+O3} / \tau_{H2O}.$$

The main drawback of the effective-transmittance technique is that it is difficult to be applied for the case in which there are more than three variable gases. In the following section we describe methods to replace the effective-transmittance technique with the correction-factor technique.

3. Implementation of Correction-factor Technique into OPTRAN-V8

The correction-factor technique is first implemented in OPTRAN-V7. As mentioned in the previous section, OPTRAN-V7 treats τ_c as a pseudo transmittance and predicts it in the same way as for the gas transmittances. This treatment simplifies the computing process. With OPTRAN-V8, however, the same treatment does not apply for the following reasons. First, since OPTRAN-V8 predicts ln(k), not k, it is not valid to treat τ_c as a pseudo transmittance. Secondly, it is found that not all the polynomial modes $\{A^m, m=1,10\}$ in the regression equation have significant contributions for predicting τ_c. The insignificant modes should be dropped to benefit the computational stability. After many experiments, the following regression equation is formulated,

$$\ln(\tau_c) = c_0 + \sum_{j=1}^{n} c_j X_j \qquad (6),$$

where $\{c_i, j=0, n\}$ is a set of constants and $\{X_j, j=1,n\}$ a subset of the 12 predictors listed in Table 1. The accuracy of (6) has been evaluated and the results are shown in Fig. 2 and 3. In these figures, the RMS accuracies are obtained by comparing the OPTRAN-based RT model with a line-by-line model. Fig 2 shows the RMS brightness temperature differences for a subset of AIRS channels computed from both the dependent (blue line) and independent (red line) databases, with the correction-factors estimated using (6) and the gas transmittances calculated exactly. Fig. 3 shows the RMS differences at the HIRS channels from the dependent (Fig. 3a) and independent (Fig. 3b) databases, with both the correction factors and gas transmittances estimated. We see that errors in general are below the 0.1 K level except a few ozone channels.

i	1	2	3	4	5	6	7	8	9	10	11	12
X_i	A_{H2O}	A_{H2O}^2	A_{H2O}^3	A_{H2O}^4	A_{O3}	A_{O3}^2	A_{O3}^3	A_{O3}^4	$P^{1/4}$	PT	$A_{H2O}PT$	$A_{O3}PT$

Table 1. The set of predictors, from which a subset is selected for estimating the correction factors. *A*: integrated space-to-layer absorber amount; *P*: pressure; *T*: temperature.

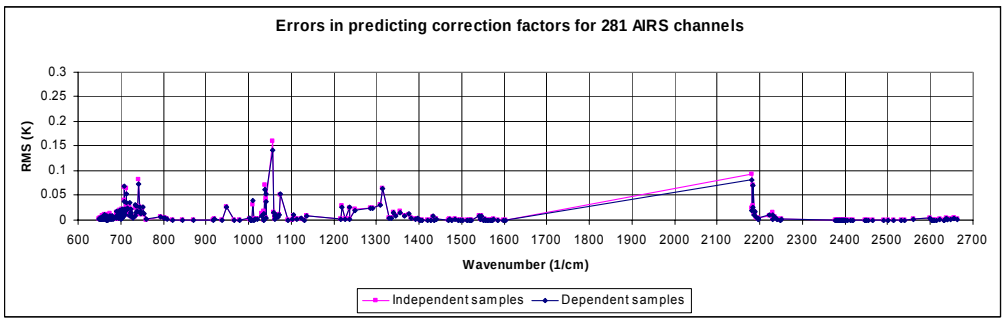

Fig. 2 RMS brightness temperature differences between the OPTRAN-V8 based RT model and the line-by-line mode LBLRTM at the selected 281 AIRS channels. The OPTRAN-V8 model has been modified to include the correction-factor technique. These are the errors from the correction factor only. The gas transmittances are computed exactly using LBLRTM. The independent (red) and dependent (blue) sample sets are based on the CIMSS 32 and UMBC 48 profiles, respectively

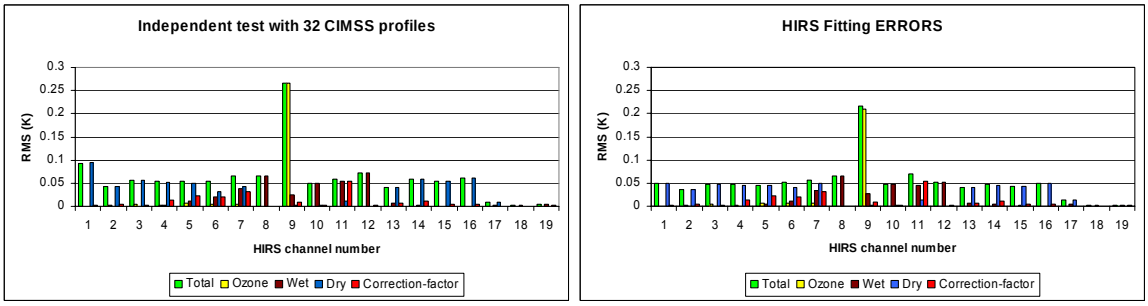

Fig. 3 RMS brightness temperature differences between the OPTRAN-V8 based RT model and the LBLRTM model at the HIRS channels. The OPTRAN-V8 model has been modified to include the correction-factor technique. Fig 3a: the independent data set from the CIMSS 32 profiles; Fig 3b: the dependent data set from the UMBC 48 profiles. Yellow – errors from ozone transmittances; brown – water vapor; blue – dry gas; red – correction factor; green – total transmittances.

4. Efficiency Improvement

Although OPTRAN-V8 uses fewer regression coefficients than OPTRAN-V7, it requires more computational time due to the need to evaluate various polynomial modes. One of the solutions to improve its efficiency is to reduce the order of the polynomial functions under the condition not to decrease the targeted accuracy. Experiment showed that not all transmittance calculations require a 10^{th} order polynomial. For example, for the subset of AIRS channels, only less than 5% of the transmittance calculations need the 10^{th} order polynomial for a targeted fitting error of less than 0.05

K as shown in Fig. 6. Most of the calculations reach this accuracy with a third or second order polynomial function. By varying the order of polynomial functions, we can improve the computational efficiency substantially, as demonstrated in Table 2, which shows a comparison of the time needed to compute the forward RT model and the temperature, water vapor and ozone Jacobians between the fixed 10th order and the varying order polynomial algorithms.

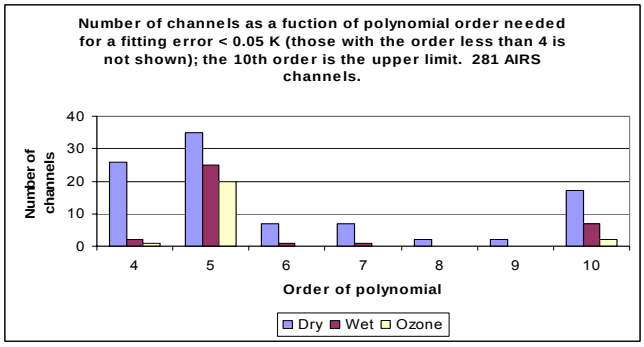

Fig. 4 Number of channels as a function of polynomial order required for estimating raidative transmittances based on a total 281 AIRS channels for a targeted fitting error 0.05 K. Blue - dry gas, red - water vapor, yellow – ozone. The channel distributions for a polynomial order smaller than 4 are not shown in the figure due to their large magnitudes.

	Varied order	Fixed 10th order
Forward model	26 sec	10 min 30 sec
Jacobian	2 min 43 sec	37 min 29 sec

Table 2 Comparisons of time needed for computing forward model and the dry gas, water vapor and ozone Jacobians for 281 AIRS channels between the varying order and fixed 10th order algorithms.

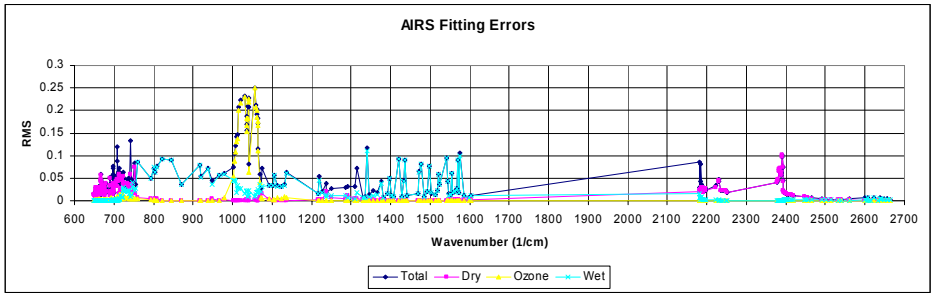

Fig. 5 RMS brightness temperature differences between OPTRAN-V8 based RT model and a line-by-line model at the 281 AIRS channels. The OPTRAN model has been modified to include the varying order algorithm.

5. Summary

We have developed methods to implement the correction-factor technique applied in OPTRAN-V7 into OPTRAN-V8 to account for the difference between the SRF-averaged total transmittances and

the product of the SRF-averaged transmittance components. Our preliminary results show that with these methods the correction factors can be rapidly estimated with an accuracy of better than 0.1 K. We also have done work to improve computational efficiency for OPTRAN-V8. By varying the order of the polynomial function, the computational efficiency can be substantially increased without reducing OPTRAN accuracy.

References

McMillin, L. M. Crone, L. J. and Kleespies, T. J. 1995. Atmospheric transmittance of an absorbing gas. 5. Improvements to the OPTRAN approach. Appl. Opt. 34, 8396 – 8399.

Kleespies, T. J. Delst, P. V. McMillin, L. M. and Derber, J. 2003. Atmospheric transmittance of an absorbing gas. 6. An OPTRAN status report and introduction to the NESDIS/NCEP community radiative transfer model. Submitted to Appl. Opt..

Xiong, X. , McMillin, L. M. and Kleespies, T. J. 2003. Atmospheric transmittance of an absorbing gas 7. Further improvements to the OPTRAN approach. Submitted to Appl. Opt..

Clough, S. A., Iacono, M. J. and Moncet, J. L. 1992. Line-by-line calculations of atmospheric fluxes and cooling rates: Application to water vapor. J. Geophys. Res., **97,** 15761-15785.

Cloud characteristics and channel selection for IASI radiances in meteorologically sensitive areas

Nadia Fourrié and Florence Rabier
CNRM/GMAP METEO FRANCE, Toulouse, France

Introduction

Advanced infrared sounders, such as the Atmospheric InfraRed Sounder (AIRS, launched on board the Aqua satellite in May 2002) and the Infrared Atmospheric Sounding Interferometer (IASI) scheduled to be on board the first operational European polar-orbiting satellite Metop, measure or will measure radiation in many thousands of channels. They have the potential to provide atmospheric temperature and composition information at a much higher vertical resolution and accuracy that can be achieved with the previous generation of satellite instruments such as the High resolution Infrared Radiation Sounder. As it is neither feasible nor efficient to assimilate all the channels in a Numerical Weather Prediction (NWP) system, channel selection policies have been designed in the NWP context. Previous studies have proposed methods in order to reduce the number of channels to keep only the ones, which bring the most useful information. In particular Rabier et al. (2002) and Fourrié and Thépaut (2003) have used a method based on the information content following Rodgers (1996) for clear sky conditions.

If such advanced sounders have to lead to a very significant impact on the forecast quality, one should address in details the question of retaining the most information possible in the sensitive areas. Previous studies such as those of Prunet et al. (1998) and Collard (1998) have suggested that IASI could resolve some of the small scale baroclinic structures that have been identified by the sensitivity studies as being crucial to forecast error development (Rabier et al. 1996). Nevertheless, the main obstacle to use observation from advanced sounders is the presence of cloud, which can severely limit the information from infrared sounders. In this context, McNally (2002) previously investigated the occurrence of clouds in the sensitive areas with cloud fields from the European Centre for Medium-range Weather Forecasts model and showed with an “observable” sensitivity variable that there was a high correlation between the meteorologically sensitive areas and the cloud cover produced by the ECMWF model.

The first objective of this study is also to study the cloud cover and the cloud top level, but from the satellite imager AVHRR (Advanced Very High Resolution Radiometer) in simulated IASI pixels. This is done over the North Atlantic Ocean for cases of FASTEX (Front and Atlantic Storm-Track Experiment, Joly et al. 1999), and more particularly in the sensitive areas for the forecasts of storms of 8 Intensive Observing Periods (IOP). Once the cloud characteristics of the sensitive areas will be established, the robustness of the iterative channel selection method used by Rabier et al. (2002) (hereafter R02) and Fourrié and Thépaut (2003) will be addressed for these regions. This method will be compared with two channel selection methods using a criterion based on the adjoint sensitivity. These last two methods were developed in the context of the targeting problem, which consists in optimally selecting observations in the sensitive areas in order to reduce the error in the initial state of the forecast.

The next section presents the study of the cloudiness in the meteorological sensitive areas for the 8 FASTEX IOPs. The description of the channel selection framework and results obtained in a simple context of perfect observations for profiles with cloud top level at 1000 hPa from the FASTEX IOP sensitive areas are then discussed in section 3. The channel

selection methods are then applied in a more general context, always for these particular synoptic situations and a constant set is studied respectively in a new section. Finally, results are summarized and conclusions are given.

Study of the cloudiness in the meteorological sensitive areas

In this study, the cloud parameters (cloud cover and cloud top pressure in the simulated IASI pixels) have been retrieved from the AVHRR imager using the MAIA (Mask AVHRR for Inversion ATOVS) method, which was originally developed at the Centre de Météorologie Spatiale (CMS) in the frame of the AVHRR and ATOVS Processing Package (Lavanant et al, 1999).

The MAIA method has then been adapted to the IASI observations (Lavanant, personal communication). It processes the AVHRR observations mapped inside the simulated IASI pixel and determines the mean clear percentage cover in the IASI spot. With a succession of threshold tests applied to the AVHRR channels inside the simulated IASI pixel, it is possible to determine some cloud parameters. The cloud cover is evaluated from the percentage of clear AVHRR pixels in each simulated IASI ellipse shape. A minimum threshold of 90% of clear AVHRR spots has been arbitrarily chosen in order to consider this IASI pixel as clear. In addition, for the cloudy pixels, the cloud top temperature (if the cloud can be considered as a black body) among other parameters is available as outputs of the MAIA algorithm. The cloud top pressure level is deduced from the cloud top temperature with a series of differences between the cloud top temperature from the MAIA method and a temperature profile interpolated onto the simulated observation location. The temperature fields are available at every 50 hPa in the vertical and are provided by the FASTEX 4D-Var reanalysis (Desroziers et al. 2003) including additional observations from the field experiment. The cloud top pressure level is found when the difference between the cloud top temperature and the atmospheric profile temperature is the smallest. It is worthwhile to note that only pixels over sea and for which a cloud top temperature could be retrieved have been considered in this study. Indeed, the MAIA method having been mainly tested over ocean owing to the CMS reception area, there is a lack of confidence in the method over iced land surfaces in the Halifax reception area.

Determination of the sensitive areas

The short-term forecast errors are mainly due to errors in the initial state of the forecast. In order to determine the regions where small errors in the initial state may increase and lead to major forecast errors, the gradient of a diagnostic function of the final state with respect to the initial conditions can be used (e.g. Rabier et al. 1996). Sensitive areas can be defined with scaled gradients resulting from these adjoint calculations. In this study, the gradient is based on the diagnostic function of the study from Hello et al.(2000). It is computed from the forecast of the mean sea level pressure over the area of the considered FASTEX weather systems. Eight dates on February 1997 have been studied. This period corresponds to a zonal weather regime, which is favourable to the development of cyclonic systems over western Europe (Joly et al. 1999 and Baehr et al. 1999). The temperature fields of the gradient at 900, 800, 700, 600 and 500 hPa levels have been squared and summed at each geographical location in order to obtain a single horizontal sensitivity field. Once the sensitivity field has been computed, a threshold arbitrarily fixed at 30% of the sensitivity field maximum is applied to this field in order to obtain a horizontal mask for the observations located in the sensitive area for which the cloud cover and the cloud top height will be studied. It should be noted that the extent of the derived sensitive area slightly depends on this threshold.

Averaged results

A brief description of the 8 FASTEX IOPs synoptic cases corresponding to some cases studied by Hello and Bouttier (2001) and Hello (2002) is given in Fourrié and Rabier (2002). The sensitive direction is computed with the forecast trajectory of the cyclones following the definition target and verification times, as described in Bergot (1999). The overall forecast range is mostly 36 hours and the verification area situated offshore of western Europe is centred on the location of the cyclones at the time of the verification. For six cases out of eight, the sensitivity maximum is located below or at the 700 hPa level.

The IASI pixels have been simulated in the same area as the AVHHR observations, which are available from the Halifax reception station. These observations are representative of a mid-latitude region.

The averaged results of the distribution of the cloud top pressure for the sensitive areas and the whole dataset are presented in Fig. 1. For the sensitive areas, two maxima in the distribution of the cloud top level are identified for the atmospheric layers located between 1000 and 900 hPa (low-level clouds) and 400-300 hPa (high-level clouds). Nonetheless, this synthetic table does not illustrate the case-to-case variability of the cloud top pressure in the sensitive area. In contrast, for the whole IASI dataset, almost 60% of the cloud tops of the observations are situated below 600 hPa. Furthermore, the cloud top pressure of observations of the mid-latitude area seems almost constant in time, mainly with low-level cloud. The sensitive areas are often located in the southern entrance area of an upper level jet-streak. Their horizontal extension depends also on the weather system. For almost all cases, the northern part of the sensitive area corresponds to low-level cloud and the southern one to high-level clouds. This particular shape of the cloud cover strongly limits an adequate sampling of the sensitive areas, the maximum of which is located at or below 700 hPa. These results corroborate the study of McNally (2002) who found a high degree of correlation between high cloud and sensitive areas during the winter.

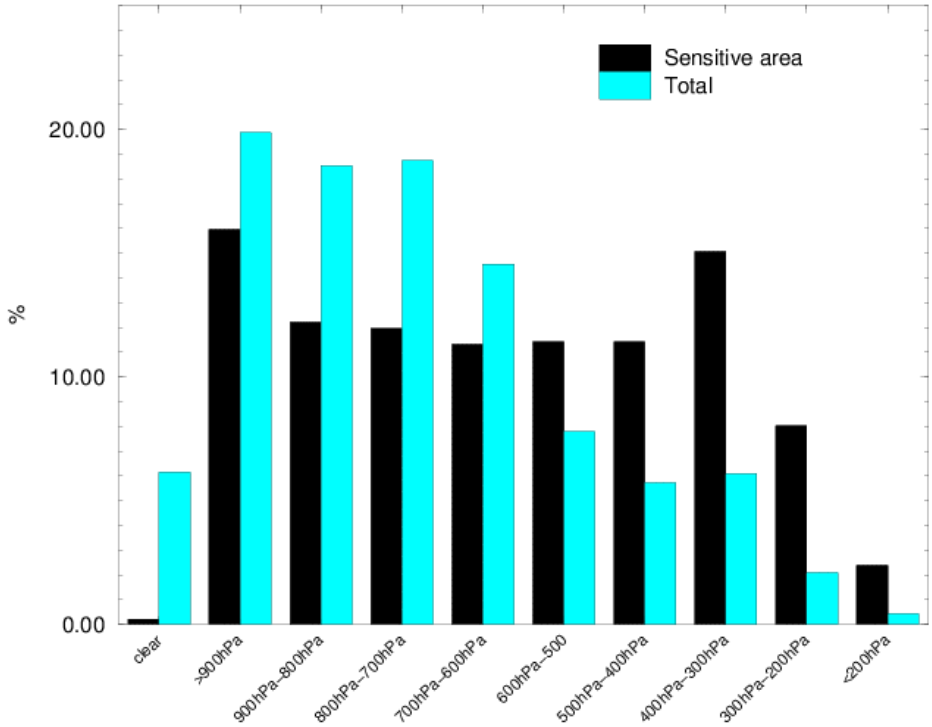

Fig. 1: Averaged distribution of the cloud top pressure as seen by the AVHRR imager in the IASI pixels for the sensitive areas (black bars) and for the whole set of pixels located in the mid-latitude area (blue bars).

In conclusion, we have shown that a part of the simulated IASI pixels located in the sensitive areas were covered by low-level clouds and by high-level clouds. We will now more particularly tackle the question of the channel selection for these low-level cloud observation conditions (noting that the high-level cloud conditions are not likely to provide useful information from the infrared sounders).

Description of the channel selections

The general framework of this study is the linear optimal estimation theory in the context of NWP. The atmospheric profile in temperature, humidity and ozone at a given location is represented by a vector x and the satellite observations by a vector **y**. The observations are linked to the atmospheric state by the radiative transfer equation:

$$\mathbf{y}=\mathcal{H}(x)+\varepsilon_{\mathbf{O}}+\varepsilon_{\mathbf{F}} \quad (1)$$

where the measurement and the forward model errors $\varepsilon_{\mathbf{O}}$ and $\varepsilon_{\mathbf{F}}$ are assumed to be gaussian noises with error covariance matrices **O** and **F**. We will denote **R** = **O**+**F** the resulting observation error covariance matrix. The background state vector $\mathbf{x}_b$ has an error covariance matrix denoted **B**. The radiative transfer equation is assumed to be weakly non-linear, making the tangent linear assumption valid in the vicinity of the background state:

$$\mathcal{H}(\mathbf{x})=\mathcal{H}(\mathbf{x}_b)+\mathbf{H}(\mathbf{x}-\mathbf{x}_b) \quad (2)$$

where **H** is the tangent linear model of the radiative transfer model $\mathcal{H}$ (also called the jacobian matrix).

The optimal analysed state $\mathbf{x}_a$ is given by $\mathbf{x}_a = \mathbf{x}_b + \mathbf{K}(\mathbf{y}-\mathbf{y}_b)$ with $\mathbf{K}=\mathbf{AHR}^{-1}$ and

$$\mathbf{A}=\mathbf{B}^{-1}+\mathbf{H}\,\mathbf{R}^{-1}\,\mathbf{H}^{-1} \quad (3)$$

K is the Kalman gain matrix and **A** is the analysis error covariance matrix.

The parameter space is the temperature on the 43 pressure levels of the fast radiative-transfer model RTIASI (Matricardi and Saunders, 1999). The IASI data have been simulated from atmospheric profiles (temperature, humidity and surface temperature) for nadir views and noise has been added to the simulated data using the **O** covariance matrix provided by CNES in 2001. As in the R02 study, a constant error of 0.2K coming from the RT model noise is added to the measurement errors. The correlations existing between adjacent channels are ignored in the observation error matrix.

Only low-level clouds were tackled here. We have studied atmospheric profiles with a cloud top level at 1000 hPa because the MAIA method found a maximum of low-level cloud top for this level. We assume cloud tops at the 1000 hPa level with a surface emissivity of 1. As our RT model is not assumed to be very accurate for the cloudy brightness temperature simulation and because there is an uncertainty on the cloud information coming from the accuracy of the MAIA algorithm, the channels sensitive to the cloud effects have been removed before the channel selection. The choice criterion is the jacobian: the test used for the determination of the cloud contamination is the ratio between the total jacobian surface and the jacobian surface below the cloud top level. If this ratio shows that more than 2% of the jacobian surface below cloud level, which corresponds to the 2 lowest levels of RTIASI for a cloud at 1000 hPa, the channel is considered to be too sensitive to the cloud to be kept in the channel selection. This allows the channels sensitive to the two last levels below 1000 hPa to be removed from the channel selection and the number of channels is decreased from 8461 to 2300 channels. This number would be reduced to about 1600 channels if one considered cloud top level at 950 hPa. This prior channel selection is intended to keep the simulations as realistic as possible, assuming that the channel contaminated by cloud effects will be more difficult to use for the day-1 assimilation of IASI.

The problem of dynamical channel selection is tackled here. The iterative channel selection of R02 is compared to two methods developed in the framework of the targeting problem, which

consists in determining where to select optimally some observations in order to reduce the forecast error variance.

Entropy reduction

This iterative method for channel selection, as proposed by Rodgers (1996) and used in R02, consists in performing successive analyses, each one using only channel at a time. The channel selection in our case is based on maximizing the Entropy Reduction (ER, Rodgers, 2000):

$$ER=-1/2 \log_2 \det(\mathbf{AB}^{-1}) \quad (4)$$

The analysis error covariance matrix **A** is updated accordingly and is used at the next step as the background error covariance matrix. This ensures that all the information brought by previous channels is taken into account for the selection of the new channel. It will be called in the following the "ER method".

Sensitivity to observations

The sensitivity to observations (Baker and Daley, 2000 and Doerenbecher and Bergot, 2001) has been developed in the context of adaptive observation and these authors have suggested that the sensitivity with respect to observations could be an efficient tool for defining the location of targeted observations. An advantage of this kind of sensitivity is that it takes into account the way in which the observations will be assimilated through the multiplication of the gradient by the **A** matrix. Another advantage is that the sensitivity to observations is significantly reduced in regions already sampled by existing observations. This method will be applied to our problem of channel selection. Following the philosophy of the method, the channel y_i selected is the one, which maximizes the sensitivity to observation:

$$\nabla_{\mathbf{y}o} J = r_i \, \mathbf{h'}_i^{\,T} \, \mathbf{A_i} \, \nabla_{\mathbf{x}a} J \quad (5)$$

where r_i is the corresponding observation error value, $\mathbf{h}'_i$ is the vector corresponding to a line of the Jacobian matrix, $\nabla_{\mathbf{x}a} J$ is the sensitivity to the initial conditions and $\mathbf{A}_i$ is computed from Eq. 3 for the corresponding channel $\mathbf{y}_i$. As previously, this matrix is used at the next step as the background matrix in order to take into account the information brought by the already selected channels.

Kalman Filter Sensitivity

This Kalman Filter Sensitivity method was proposed by Bergot and Doerenbecher (2002) in order to find the optimal deployment of targeted observations. This method is based on the maximum decrease of the variance of the error on a given scalar function of forecast. The reduction in the variance of the error on a given scalar function of the forecast, due to the inclusion of one channel y_i is given by:

$$(\delta\sigma_i)^2 = \nabla_{\mathbf{x}a} J \, \mathbf{B}_{i-1} \, \mathbf{h'}_i \, (r_i + \mathbf{h'}_i^{\,T} \, \mathbf{B}_{i-1} \, \mathbf{h'}_i)^{-1} \, \mathbf{h'}_i^{\,T} \, \mathbf{B}_{i-1} \, \nabla_{\mathbf{x}a} J \quad (6)$$

where $\mathbf{B}_{i-1}$ corresponds to the analysis error covariance matrix obtained at the previous step. As for the ER method, the **A** matrix is updated and is used as the **B** matrix for the next step. This method is the so-called "KFS method".

Key analysis errors matrix

One month of "Key Analysis Errors" (KAE, as described in Klinker et al. 1998) has been computed at a resolution of T159 (120 km): these "errors" represent perturbations that, if added to the ECMWF operational analysis, reduce the 48-hour forecast error (defined as the global difference between the 48-hour forecast and the verifying analysis). Up to now, humidity perturbations are not considered in the sensitivity computations, therefore only temperature is included in the sensitivity study described here. These structures generally are of small amplitude (meaning that a small atmospheric perturbation in this area can have a very large impact on the forecast quality) and can be fairly sharp both in the horizontal and in

the vertical. The associated covariance matrix (averaged over one month) is sharper in the vertical and horizontal than the operational background covariance error. In addition, the error standard deviations are proportionally large in the troposphere in comparison with the ones of the stratosphere: the error maximum in the troposphere at about 300 hPa is of the same order than in the stratosphere, when the error maximum in the troposphere for the "climatological" B matrix is two times smaller than the stratospheric maximum. This KAE covariance matrix has been chosen as the B matrix because our study is focussed on the channel selection in the sensitive areas.

Results obtained with perfect observations

In this first study, the truth is a "corrected state" which is a 3D-Var analysis modified with a scaled gradient perturbation. The coefficient applied to the perturbation was found by Hello (2002) in order to guarantee that inside the sensitive area the distance between the corrected state and the observations is minimal (Hello et al. 2000). Different observation sets can be used and the coefficient for which the forecast score based on verifying observations from the corrected state is the best, is chosen. The IASI measurements are simulated from this "corrected state". In order to better understand the manner in which the 3 channel selection methods work, no noise has been added to the observations. The background profile comes from the 3D-Var analysis ("uncorrected" by the gradient) and one tries to retrieve the sensitive perturbation with perfect observations of the reality. The **B** matrix used in the computation comes from the KAE matrix. We assume that KAE represent well perturbations from the gradient perturbations. As in the R02 study, 300 channels have been selected.

In order to study more precisely the channels selected by the three methods, attention has been paid to a single profile with a cloud top level of 1000 hPa and close to the centre of the sensitive area. The results in term of background and analysis errors are shown in Fig. 2. The background error represents the difference between the original 3D-Var and the "corrected" analysis. It is larger in the 400-900 hPa atmospheric layer and its maximum is located at about 550 hPa. Another relative maximum is present at 700 hPa. The three methods largely decrease the analysis error in comparison to the background one, although they slightly degrade the analysis in the 650-750 hPa atmospheric layer. In addition, the analysis error is slightly smaller for the two methods based on the adjoint gradient than for the ER method around the mean error peak while the ER method gives better results near the surface and in the high troposphere.

Impact of a constant channel set

Here, one wants to study the impact of a non-optimal channel set. As in R02, a constant channel set has been built from the ER method. The "constant" selection is computed as an average selection based on a set of representative mid-latitude situations. This set is part of the ECMWF atmospheric database (Chevallier et al. 2000) and forms a set of 170 vertical profiles of temperature, humidity, ozone together with values of surface pressure and surface temperature. The KAE matrix has been used as the **B** matrix during the channel selection process and a noise derived from the KAE matrix has been added in order to obtain the background state. This channel set has been used for the analysis of the 142 profiles located in the sensitive areas.

Before using the channels in the assimilation, it has been checked that these channels were not contaminated by clouds and the number of channels of the constant set actually used is close to 220 but depends on the profile. Figure 3 shows the results obtained with these two constant sets for the KAE matrix. A slight degradation is obtained in the troposphere in comparison with an optimal channel set. Moreover, the constant sets provide larger DFS or ER than the KFS set and a smaller rms ratio than the KFS set. These results suggest that an optimal channel set is not necessarily required for the analysis and that a constant set is a good compromise between the CPU cost and the quality of the analysis.

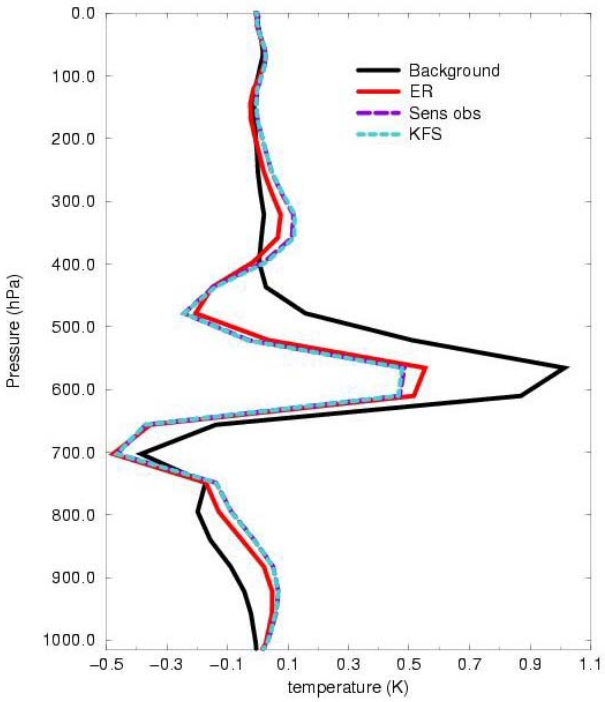

Fig. 2: Deviations from the true temperature for one particular representative profile for the background and the 3 different analyses. “Background” refers to the background error, “ER" to the analysis error obtained with the Entropy Reduction method, “Sens obs" to the analysis error given by the sensitivity to observation method and “KFS” to the analysis error produced by the Kalman filter Sensitivity method.

Conclusions

In this paper, the issue of reducing the number of IASI channels to be used in data assimilation has been specifically addressed in the context of the sensitive areas and for low-level clouds. In a first section, the cloud top level in simulated IASI pixels for FASTEX sensitive areas has been studied from the MAIA method using the AVHRR imager observations. It is found that the sensitive areas are usually covered by low-level clouds in their northern parts and by high-level clouds in their southern ones. These results corroborate the study of McNally (2002) who established a high correlation between the meteorologically sensitive areas and the cloud cover produced by the ECMWF model.

As a result of this first study, the channel selection has then been tackled in the context of low-level clouds (1000 hPa) for the 8 FASTEX IOPs in order to retrieve information from the sensitive areas. The so-called iterative method of R02, based on the ER, has been compared to two methods derived from the targeting strategy that consists in adding optimal observations in the sensitive areas in order to reduce the error in the analysis, which can lead to a large forecast error. These methods are the sensitivity to observations and the Kalman Filter Sensitivity. In a first step, these three methods have been compared for the retrieval of one sensitive perturbation with perfect observations and it is shown that they provide similar results even though the ER selection and the other ones share few channels.

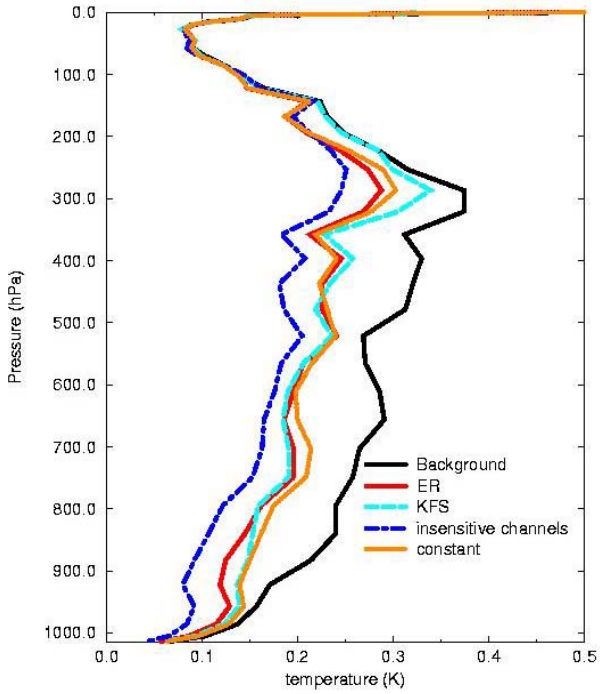

Fig. 3: Root mean square errors for 4 channel selection methods averaged over 142 profiles corresponding to a cloud top level of 1000 hPa. “Insensitive channels” corresponds to the assimilation of all the channels not contaminated by low-level clouds. “Constant” corresponds to an analysis computed with a constant channel set for clear sky conditions but the channels contaminated by cloud effect have been removed (about 220 channels depending on each profile)

As the sensitivity to observation channel selection method is very expensive in term of CPU cost, only the ER and KFS methods have then been compared from a statistical point of view over profiles from the FASTEX IOPs with low-level clouds. The ER method seems robust, even if the profiles are located within the sensitive areas. The use of a constant channel set computed from an independent set of atmospheric profiles still leads to a significant improvement of the analysis compared to the background even if this analysis error is slightly larger than the one obtained with an optimal channel set. More details about this study can be found in Fourrié and Rabier (2004).

Our main conclusions are: the ER channel selection method is quite robust, even for the studied highly sensitive profiles. In addition, the constant channel set deduced from this optimal channel selection can be computed from an independent atmospheric database, if it is representative of the profile air-mass. The ER channel selection method is very promising as previous results had not been focussed on such a characteristic set of profiles, especially crucial for the NWP. However, the first part of this study suggests that clouds are an important issue and that a radiative transfer model taking into account the cloud effect is required to go further in the channel selection studies in this context. One limitation of our work is that it took place out of the context of the operational NWP assimilation scheme and that the results of cloud level study in the sensitive areas are only valid for the limited number of the 8 FASTEX IOP synoptic situations and may have no general applicability to other situations and seasons. A future work could be the assimilation of the IASI radiances in a NWP assimilation scheme. This will provide the opportunity to test the real impact of the different channel selections on the forecast score, for which the gradient based channel selections are optimised.

Acknowledgment

The study was partly supported by CNES trough post-doctorate fellowship of Nadia Fourrié. The authors wish to thank Gwenaëlle Hello (CNRM) who ran the computation of the gradient for the determination of the sensitive area. Tiphaine Labrot and Lydie Lavanant (CMS) are also acknowledged for having provided the cloud determination with the AVHRR observations interpolated onto IASI pixels for the Halifax area.

References

Baehr C., Pouponneau, B., Ayrault, F. and Joly, A. 1999. Dynamical characterization of the FASTEX cyclogenesis cases. *Quart. J. R. Met. Soc.,* **125**, 3469-3494.

Baker N. L. and Daley, R. 2000. Observation and background adjoint sensitivity in the adaptive observation targeting problem. *Quart. J. R. Met. Soc.*,**126**, 1431-1454.

Bergot T.1999. Adaptive observations during FASTEX: A systematic survey of upstream flights. *Quart. J. R. Met. Soc.*, **125**, 3271-3298.

Bergot T. and Doerenbecher, A. 2002. Study on the optimisation of the deployment of targeted observations using adjoint-based methods. *Quart. J. R. Met. Soc* , **128**, 1689-1712.

Cammas J.-P., Pouponneau, B., Desroziers, G., Santurette, P., Joly, A., Arbogast, P., Mallet I., Cagnaux, G. and Mascart, P. 1999. FASTEX IOP 17 cyclone: Introductory synoptic study with field data. *Quart. J. R. Met. Soc.* , **125**, 3393-3314.

Chevallier F. , Chédin A., Chéruy F. and Morcrette J.-J. 2000. TIGR-like atmospheric profile databases for accurate radiative flux computation. *Quart. J. R. Met. Soc.* ,**126**, 777-785.

Collard A. D., 1998. Notes on IASI performance, NWP Technical Report No. 253, Met Office, Bracknell, UK.

Desroziers, G., Hello, G. and Thépaut J.-N., 2003. A 4D-VAR Re-analysis of the FASTEX experiment, *Quart. J. R. Met. Soc*., **129**. 1301-1315.

Doerenbecher, A. and Bergot, T. 2001. Sensitivity to observations applied to FASTEX cases. *Nonlinear Processes in Geophysics*, **8**(6), 467-481.

Fourrié N. and Rabier F. 2002. Use of advanced infrared sounders in cloudy conditions. *Proceedings of the Twelfth International TOVS Study Conference.*

Fourrié N. and Rabier F. 2004. Cloud characteristics and channel selection for IASI radiances in meteorologically sensitive areas. *Quart. J. R. Met. Soc*., in revision, 18 p.

Fourrié, N. and Thépaut, J.-N., 2003. Evaluation of the AIRS Near Real Time channel selection for application to numerical weather prediction. *Quart. J. R. Met. Soc.,* **128**, 2425-2439.

Hello G., Lalaurette F. and Thépaut J.-N. 2000. Combined use of sensitivity information and observations to improve meteorological forecasts: A feasibility study applied to the 'Christmas Storm' case. , *Quart. J. R. Met. Soc.,* **126**, 621-647.

Hello, G., and Bouttier, F. 2001. Using adjoint sensitivity as a local structure function in variational assimilation. *Nonlinear Processes in Geophysics.* **8**(6), 347-355.

Hello, G. 2002. Prise en compte de la dynamique associée aux dépressions des latitudes moyenne dans la détermination des conditions initiales des modèles météorologiques. PhD Thesis, Université Paul Sabatier, Toulouse III. 231 pp.

Joly, A. Browning K. A., Bessemoulin P., Cammas J.-P., Caniaux G., Chalon J.-P., Clough S. A., Dirks R., Emanuel K. A., Eymard L., Gall R., Hewson T. D., Hildebrand P. H., Jorgensen D., Lalaurette F., Langland R. H., Lemaitre Y., Mascart P., Moore J. A., Persson P. O., Roux F., Shapiro M. A., Snyder C., Toth Z. and Wakimoto R. M. 1999. Overview of the field phase of the Fronts and Atlantic Storm-Track EXperiment (FASTEX) project. *Quart. J. R. Met. Soc.* **125** 877-946.

Klinker, E., Rabier, F. and Gelaro, R. 1998. Estimation of the key-analysis errors using the adjoint technique. *Quart. J. R. Met. Soc.* 124, 1909-1933.

Lavanant, L., Legléau, H., Derrien, M., Levasseur S., Monnier G., Ardouin L., Brunel P. and Bellec B. 1999. AVHRR Cloud Mask for Sounding Applications, *Proceedings of the Tenth International TOVS Study Conference.*

Matricardi M. and Saunders, R., 1999. A fast radiative transfer model for Infrared Atmospheric Sounding Interferometer radiances. *Journal of Applied Optics*. **38**, 5679-5691.

McNally, 2002. A note on the occurrence of cloud in meteorologically sensitive areas and the implications for advanced infrared sounders. *Quart. J. R. Met. Soc*. **128**, 2551-2556.

Prunet P., Thépaut J.-N. and Cassé V. 1998. The information content of clear-sky IASI radiances and their potential for numerical weather prediction., *Quart. J. R. Met. Soc*. **124**, 211-241.

Rabier, F., Klinker, E., Courtier, P. and Hollingsworth, A. 1996. Sensitivity of forecast errors to initial conditions. *Quart. J. R. Met. Soc*. **122**, 121-150.

Rabier, F., Fourrié, N., Chafaï D. and P. Prunet 2002. Channel selection methods for infrared atmospheric sounding interferometer radiances. *Quart. J. R. Met. Soc*. **128** 1011-1027.

Rodgers, C. D. 1996. Information content and optimisation of high spectral resolution measurements. *Optical Spectroscopic Techniques and Instrumentation for Atmospheric and Space Research II*, **SPIE Volume 2830**, 136-147.

Rodgers, C. D. 2000. Inverse methods for atmospheres: Theories and practice. *World Scientific Publ., Singapore*, 238pp.

Estimation of AMSU –A radiance error statistics, using an optimality criterion

B.Chapnik*, G.Desroziers*, F.Rabier* and O.Talagrand*
* Météo France, CNRM **CNRS, LMD

Definition of the tuning

Denoting $\boldsymbol{\varepsilon}_b$ and $\boldsymbol{\varepsilon}_o$ the background and observational errors, let $\mathbf{B}$ be the background error covariance matrix specified in an operational data assimilation system and let $\mathbf{B_t} = E(\boldsymbol{\varepsilon}_b.\boldsymbol{\varepsilon}_b^T)$ be the "true" matrix (E is the mathematical expectation operator). In the same way let us define $\mathbf{R}$ and $\mathbf{R_t}$ « true » $= E(\boldsymbol{\varepsilon}_O.\boldsymbol{\varepsilon}_O^T)$ as the specified and true observational error covariance matrices, and $\mathbf{R_k}$, $\mathbf{R_{tk}}$ and $\mathbf{B_l}$, $\mathbf{B_{tl}}$ the specified and true matrices related to the k^{th} type of observations and to the l^{th} independent subpart of the control vector.
Assuming that one can write

$$\mathbf{B}_t = s_b\,\mathbf{B},\ \mathbf{R}_t = s_o\,\mathbf{R}$$

or

$$\mathbf{R_{tk}} = s_{ok}\,\mathbf{R_k},\ \mathbf{B_{tl}} = s_{bl}\,\mathbf{B_l},$$

the aim of this work is to answer the question:how to evaluate the tuning coefficients: s_o and s_b (s_{ok} and s_{bl})?
Desroziers and Ivanov (2001) proposed to use an optimality criterion found by Talagrand (1999). The tuning coefficients are those for which this criterion if fulfilled.

Desroziers and Ivanov's method (2001)

Let $\boldsymbol{J=\Sigma J_{ok} + \Sigma J_{bl}}$ be the suboptimal cost function used in an operational system; let $\boldsymbol{J_t=\Sigma J_{ok}/s_{ok} + \Sigma J_{bl}/s_{bl}}$ be the optimal cost function using « true » matrices.
If $\boldsymbol{x_a}$ is the minimizer of J_t then, following Talagrand (1999), the expectations of the subparts of the cost function at the minimum are:

$$\mathbf{E(2J_{ok}(x_a)/s_{ok}) = Tr\,[\pi_k(I_p - HK)\pi_k^T]}$$
$$\mathbf{E(2J_{bl}(x_a)/s_{bl}) = Tr\,(\pi_l KH\pi_l^T)}.$$

Where **K** is the Kalman gain matrix, **H** is the observation operator, and $\boldsymbol{\pi_k}$ and $\boldsymbol{\pi_l}$ are respectively the projections onto the k^{th} type of observations and to the l^{th} independent subpart of the control vector. The latter equations may be written

$$s_{ok} = 2J_{ok}(\boldsymbol{x_a})/\,\mathrm{Tr}\,[\pi_k(\mathbf{I}_p - \mathbf{HK})\pi_k^T]$$
$$s_{bl} = 2J_{bl}(\boldsymbol{x_a})/\,\mathrm{Tr}\,(\pi_l\mathbf{KH}\pi_l^T).$$

In this case **K** can be written as a function of s_{ok} and s_{bl}. This is therefore a fixed-point relation. We will use a fixed-point algorithm to compute the tuning coefficients, going from step *i* to step *i+1* using the following relations:

$$s^{(i+1)}{}_{ok} = 2J_{ok}(\boldsymbol{x_a}(\mathbf{s}^{(i)}))/\,\mathrm{Tr}\,[\pi_k(\mathbf{I}_p - \mathbf{HK}^{(i)})\pi_k^T],\ \forall k$$
$$s^{(i+1)}{}_{bl} = 2J_{bl}(\boldsymbol{x_a}(\mathbf{s}^{(i)}))/\,\mathrm{Tr}\,(\pi_l\mathbf{K}^{(i)}\mathbf{H}\pi_l^T),\ \forall l.$$

It is to be noticed that no matrix is explicitly stored in the system. In order to compute Tr (HK) one can use a randomized trace estimation technique, several of them exist. For example, Desroziers and Ivanov adapted a method proposed by Girard (1987).

Some properties of the method

Chapnik *et al*. (2003) have shown that:

- the method is equivalent to a Maximum likelihood tuning of the variances. Maximum likelihood is a general method to tune parameterized probability densities with respect to observed data; its application in data assimilation is discussed in Dee and da Silva (1998);
- the quality of the estimates depend on the number of observations;
- tuning independently the guess errors and the observation errors or two statistically independent observation error variances has little or no effect on the coefficients;
- Observations with spatially correlated errors, analyzed with a prescribed diagonal R matrix may have their variance (possibly grossly) under estimated by the method;
- the computed values are temporally stable (up to four years); on the contrary they react quickly and increase when the quality of observations is degraded: they behave like variances are supposed to.

Moreover, as already stated by Desroziers and Ivanov, the first iteration of the fixed-point algorithm is a good approximation of the final result. It is possible to show that it is a biased estimate of the tuning coefficients, the more observations there are, the smaller the bias is.

Another implementation of the method

Following Sadiki and Fischer (2003), the fixed-point algorithm was used with one iteration only, and to increase the accuracy of the estimate, several situations were "concatenated":

If $J_{ok}^{i}(x_a)$ is the minimum of the subpart of the cost function related to observation type *k* on day *i* and Tr $[\pi_k(\mathbf{I}_p - \mathbf{H}^i\mathbf{K}^i)\pi_k^T]$ is its expected value if it were optimal, then the tuning coefficients are computed as

$$s_{ok}=\left(\sum_i \mathbf{J}_{ok}^{i}(x_a)\right) / \left(\sum_i \mathrm{Tr}\,[\pi_k(\mathbf{I}_{pi} - \mathbf{H}^i\mathbf{K}^i)\pi_k^T]\right).$$

As suggested by Sadiki and Fischer, the different dates used in the computation are separated by at least 5 days in order to prevent time correlation.

Results

Results with simulated satellite radiances

Figure 1 shows the ability of the method to retrieve optimal variances in a simulated case. In this case the true standard deviations are the operational values and the mis-specified standard deviations are equal to the square root of the operational values; six dates, separated by more than five days, between 03/15/2003 and 05/19/2003 were used. Another computation was carried out with more thinning of the data in order to check the impact of a smaller number of observations. The standard deviations were computed for each of the three satellites NOAA15, NOAA16 and NOAA17, and a difference was made between sea and land observations. In all cases the computed deviations are fairly close to the expected ones.

Results with true observations

Estimation of TEMP temperature and wind speed vertical profile of standard deviations

The method was first tried with real observations, the standard deviations of which are supposed to be well documented: TEMP observations. Figure 2 shows the prescribed profile and the computed profile of standard deviations for wind speed. Figure 3 shows the same for temperature.
Those profiles were computed, cumulating the observations of 15 dates separated by five days between 03/15/2003 and 05/24//2003. The two figures clearly show that the computed deviations remain close to the prescribed ones, which was expected. In this case the estimates are realistic.

Estimation of AMSU A channels standard deviations.

With the same conventions as for Fig. 1, Fig. 4 shows the standard deviations computed for true data from 12 dates between 03/15/2003 and 05/24//2003. Some features appear: roughly, all the standard deviations are over estimated by a factor of 2. It can be seen that, according to this tuning, AMSU –A channel 5 has a larger standard deviation for land observations than for sea observations. Satellite NOAA16 instrument seems to have a larger standard deviation for channel 8 than the other satellites. The standard deviations computed with a twice larger thinning interval are almost always larger than those computed with the operational thinning. Such a difference did not appear in the simulated case. This may be due to spatial correlation or maybe inter-channel correlation which are known to lead to underestimating the evaluates.

Conclusions and future directions.

The first iteration of Desroziers and Ivanov's algorithm, cumulating the observations over several dates, has been shown to be able to produce reliable estimates in a simulated case. The estimates seem reasonable in the case of true TEMP messages, its application to ATOVS radiances show several possibly useful and unexpected features but the role of possible correlations has to be clarified.
Future work will extend to the tuning of all observation types and a level by level tuning of B in order to evaluate the impact of this tuning on the analysis and on the forecasts.

References

B. Chapnik, G. Desroziers, F.Rabier and O.Talagrand. 2003,
Properties and first applications of an error statistic tuning method in variationnal assimilation. Submitted to Q.J.R.M.S

G. Desroziers and S. Ivanov. 2001,
Diagnosis and adaptive tuning of information error parameters in a variational assimilation.
Quart. J. Roy. Meteor. Soc., 127, 1433--1452

D. Dee and A. da Silva. 1998,
Maximumlikelihood estimation of forecast and observation error covariance parameters. part I: Methodology.
Mon. Wea. Rev., 124:1822--1834.

D. Girard. 1987,
A fast Monte Carlo cross-validation procedure for large leastsquares problems with noisy data.
Technical Report 687-M,IMAG, Grenoble, France.

W. Sadiki and C.Fischer. 2003,
A posteriori validation of real data assimilation system.
To be submitted.

O. Talagrand. 1999;
A posteriori verification of analysis and assimilation algorithms.
In Proceedings of the ECMWF Workshop on Diagnosis of Data Assimilation Systems, 24 November pages 17--28, Reading

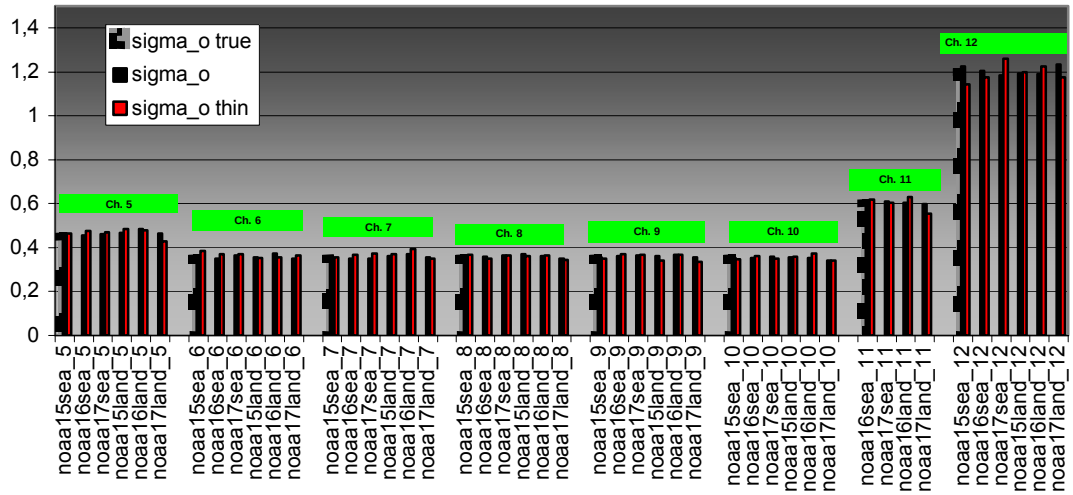

Figure. 1: Standard deviations of AMSU A channels obtained by the method in a simulated case. The black bars are computed with the operational thinning between obs. and the red bars with a twice larger thinning interval. A different deviation is computed for each satellite , a difference is also made between sea and land observations. The grey bars with dots show the simulated « true » standard deviations.

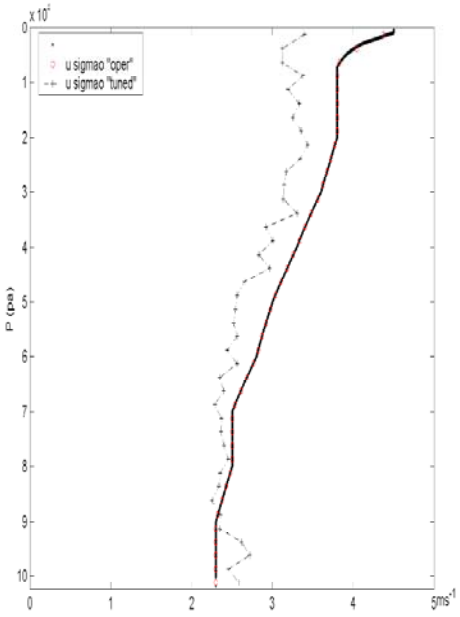

Figure 2: Vertical profiles of TEMP wind speed error standard deviations. The black line with red circle markers is the prescribed profile, the dashed line with "+" markers is the computed profile

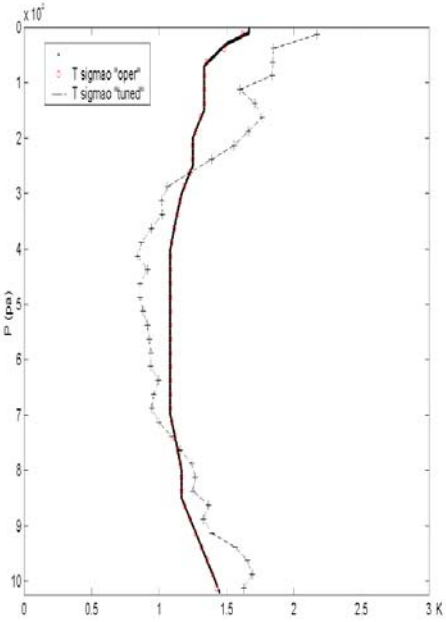

Figure 3: As in Fig. 2 but for TEMP temperature error standard deviation profile.

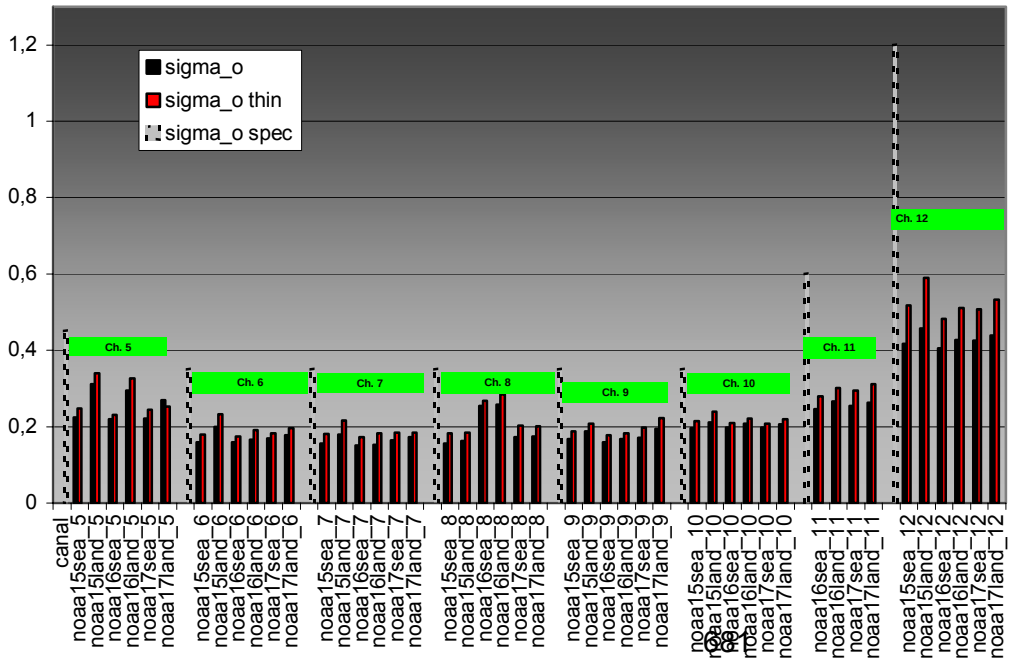

Figure 4: Standard deviations of AMSU A channels obtained by the method in a true case. Plotting conventions are the same as in Fig. 1 but this time the grey bars with black dots are the prescribed standard deviations

Can a statistical regression be a valuable tool for the inversion of advanced IR sounders data?

A.B.Uspensky*, S.V.Romanov, A.N.Trotsenko****

**Scientific and Research Center "Planeta",Roshydromet, Moscow, Russia*
*** Russian Research Center Kurchatov Institute, Moscow, Russia*

Abstract

The paper summarizes the performance characteristics of linear statistical regression approach to the inversion of advanced IR-sounders data and retrieval of atmospheric temperature, humidity and ozone concentration profiles. The retrieval experiments with synthetic IASI data demonstrate the ability of proposed techniques to derive rather accurate sounding products at a reasonable cost.

Introduction

The new-generation IR-sounders on board future operational satellites (IASI/MetOp, CrIS/NPOESS, IRFS/Meteor) will provide high resolving power (0.25 – 0.6 cm^{-1}) spectral radiance measurements of continuous or quasi-continuous coverage from 3.7 (5.0) to 15.5 μm. Because of highly increased satellite data volume, large number of sought variables and data intrinsic properties the application of traditional inversion methodology ("physical" inversion, statistical regression) may cause significant problems. In particular, the major disatvantages of linear regression techniques application are as follows (Crone et al. 1996; Fleming et al. 1986; Rodgers 2000):

(i) Neglecting the non-linearity of original inverse problem;
(ii) Systematic biases in regression estimates caused by random errors in predictor variables;
(iii) Gross error covariances of individual predictands induced by data multicollinearity (radiances in a number of channels are nearly linear dependent);
(iv) Sampling effects.

In our study several refinements and modifications of standard regression technique have been developed and examined to alleviate negative effects (i), (iii), (iv) and to provide reasonably accurate retrieval of atmospheric temperature (T), water vapor (q) and ozone concentration (Q) profiles from IASI measurements (Chalon et al. 2001). The first approach is based on the Principal Component Analysis (PCA) technique. The known retrieval algorithms (Empirical Orthogonal Function or EOF regression) have been refined through the introduction of generalized empirical orthogonal functions both in measurement and state spaces.

The alternate (and sometimes complementary to PCA) approach to reduce the dimension of original inverse problem and thus to alleviate negative effects (iii), (iv) has also been investigated. It is based on the methods of selecting the most informative variables. Under many situations the critical issue for efficient regression performance is the choice of relevant predictors and predictands. For this reason, we have reexamined the use of physically valid predictors and predictands to account for non-linearity and interfering factors effect in original inverse problem. Along with this the problem of compilation the representative training datasets with minimal sample size is discussed.

A simulation study has been performed to demonstrate the capabilities of proposed techniques in the retrievals of T-, Q-, q- profiles from synthetic IASI measurements. The application of developed algorithms is shown to enable reasonable accuracy levels for T-, Q- profile retrievals close to those specified in IASI mission objectives (Chalon et al. 2001).

Methodology

We start with brief description of PCA and refined EOF regression algorithms, see for more details (Huang and Antonelly 2001; Uspensky et al. 2003b). Than the issues will be discussed relating to selection of the most informative variables as well as to the statement of relevant predictors in linear regression scheme. Finally, the technique to reduce the size of training datasets is described.

PCA technique

Each measured spectrum $\mathbf{R_j}$ subject to analysis (either compression or "inversion") is treated as n-dimensional random vector with known mean $\overline{\mathbf{R}}$ and covariance matrix S. The orthogonal basis in PCA is formed using normalized eigenvectors (e.v.) $\{\mathbf{u}_\kappa\}$ of covariance matrix S:

$$S\mathbf{u}_\kappa = \lambda_\kappa \mathbf{u}_\kappa,\ \kappa = 1, \ldots, n \quad \text{or} \quad SU = U\Lambda. \qquad (1)$$

Here U is (n x n) matrix composed from n column-vectors $\mathbf{u}_\kappa$, and Λ is (n x n) diagonal matrix with eigenvalues $\lambda_1, \ldots, \lambda_n$ at principal diagonal.

If matrix S is not known , one can calculate the sample covariance matrix S_R, using spectral radiance measurements:

$$\mathbf{R}_j = \mathbf{R}_{jt} + \mathbf{e}_j,\ j = 1, \ldots, N. \qquad (2)$$

Here N is a sample size, $\mathbf{R}_{j.t}$ are spectral radiance "true" values, and $\mathbf{e}_j$ is (nx1) vector of measurement errors with zero mean and known covariance matrix S_e.

Thus for each individual spectra $\mathbf{R}_j$ we have matrices S_R and S_e characterizing respectively the population variability and original data uncertainties. To account for the uncertainties in the data, the orthonormal basis $\{\mathbf{u}_\kappa\}$ from (1) is substituted by the new basis $\{\mathbf{v}_\kappa\}$ derived via solving the eigenproblem for so called "information operator" $G = S_R S_e^{-1}$ (Kozlov 1978; Thaker 1996):

$$GV = V\Lambda \ (\text{or } S_e^{-1}\mathbf{v}_k = \lambda_k S_R^{-1}\mathbf{v}_k,\ k = 1, \ldots n). \qquad (3)$$

To facilitate the solving of problem (3) with possibly asymmetric matrix G, one can introduce new variables $\mathbf{r_j} = S_e^{-1/2}\mathbf{R_j}$, where $S_e^{1/2}$ is the matrix S_e square root (Rodgers 2000). Solving the new eigenproblem for symmetric matrix $G' = S_r = S_e^{-1/2} S_R S_e^{-1/2}$

$$G'V = V\Lambda \ (\text{или } G'\mathbf{v}_k = \lambda_k \mathbf{v}_k,\ k = 1, 2, \ldots, n) \qquad (4)$$

results in the set of orthonormal e. v. $\{v_\kappa\}$, hereinafter referred to as generalized EOF's or GEOF's.

The compression or in other words the development of approximate model for the measurements (2) is performed using GEOF's as orthonormal basis. Each variation $\delta r_j = r_j - \bar{r}$ is fitted using least square estimation: $\delta r_{jtr} = V_{tr}\widetilde{\Theta}_j$, $\widetilde{\Theta}_j = V^T_{tr}\delta r_j$, where ($n_c$ x n) matrix V_{tr} is composed from $n_c < n$ leading e.v. and Θ_j is (n_cx1) vector of principal components (PC's) or metric-based PC's (Thaker 1996). The $\Theta_{\kappa j}$ values represent decorrelated and orthogonal linear combinations of the original variables with decreasing variances λ_k.

The approximation or reconstruction root-mean-square error (r.m.s.e.) is defined as

$$\rho^2 = n^{-1} \cdot E\left[(\delta r_j - \delta r_{j.tr})^T (\delta r_j - \delta r_{j.tr})\right] = n^{-1} \sum_{n_c+1}^{n} \lambda_k.$$

Evident constraint $\rho^2 \le 1$ allows to define the minimum dimension n_c, that guarantees the required rmse level.

EOF and GEOF regression

The linearized problem of data (2) inversion and vector **x** retrieval is stated as follows:

$$\delta R = A\delta\mathbf{x} + \mathbf{e}, \qquad (5)$$

where (n x m) matrix A is Jacobian matrix and $\delta\mathbf{x} = \mathbf{x} - \overline{\mathbf{x}}$, $\overline{\mathbf{x}}$ is a mean vector.

The special orthogonal basis is formed by e.v. of information operator $G = S_{o.x} \cdot S_x^{-1}$, where $S_{o.x}$ is covariance matrix for the ensemble $\{\mathbf{x_j}\}$ and $S_x = M^{-1}$, $M = A^T S_e^{-1} A$ is Fisher information matrix.. Corresponding eigenproblem, analogous to (3), is written as

$$GW = W\Lambda \text{ or } Mw_k = \lambda_k S_{o.x} w_k,\ k = 1,\ldots,m. \quad (6)$$

The following modification of G regards to substitution of original normalized (noise scaled) spectra δr_j by compressed ones $\delta r_{j.tr}$. As a result, matrix M is replaced by matrix $M' = A^T S_e^{-1/2} V_{tr} V_{tr}^T S_e^{-1/2} A$ and matrix G is replaced by matrix $G' = S_{o.x} M'$.

Since matrices G, G' can be asymmetric, it is rational beforehand to transform original variables as follows:

$$\mathbf{r} = S_e^{-1/2} R, \quad \mathbf{h} = S_{o.x}^{-1/2} \mathbf{x}.$$

The eigenproblem (6) becomes the problem with symmetric matrix $G'' = S_{o.x}^{1/2} M' S_{o.x}^{1/2}$:

$$G''W = W\Lambda. \quad (7)$$

Derivation of the eigenvalues $\{\lambda_a\}$ provides the specification of dimension $m_c < m$ for the GEOF basis W_{tr} consisting of $m_c = \max\{a: \lambda_a \geq 1\}$ leading e.v. $\{w_k\}$.

The decompositions $\delta h_{j.tr} = W_{tr} \Theta_{j.h}$ and $\delta r_{j.tr} = V_{tr} \Theta_{j.r}$ can be used in the GEOF regression algorithm:

$$\Theta_{jh} = C\Theta_{jr},\ \delta h_j = W_{tr}\Theta_{j.h} = W_{tr} C V_{tr}^T \delta r_j, \quad (8)$$

where C is (m_c x n_c) matrix of regression coefficients (Smith and Woolf 1976; Uspensky et al. 2003b). The major advantage of (8) is that dimensions m_c, n_c are consistent to the informativity of original data (2) with respect to **x**.

Selection of the most informative variables

There exist at least two approaches to reduce the number of predictors: the transformation of original variables (like above PCA technique) and the selection of the most informative variables (channels), see e.g.(Aires et al. 2002; Rodgers 1996; Rabier et al. 2002; Uspensky et al. 2003a).The PCA methods may lead to the selection of a few linear combinations, which perfectly predict the variables of interest; but along with this the PC's depend upon all R_j components and their introduction doesn't provide real reduction in the number of measured quantities. The efficient reduction of the inverse problem dimension can be provided via application the methodology of the selection the most informative variables (channels). The recurrent algorithms of direct selection of informative variables (Rodgers 1996; Rabier et al. 2002) or exchange-type procedures of searching optimal channels (similar to technique applied in experimental design theory) may be utilized.

Starting from our experience, it seems reasonable to apply less formalized but more "physically-grounded" methodology. The proposed algorithm of optimal channels subset selection consequently analyses the information content (sensitivity of various channels to sought parameters), the altitude dependence of weighting function maximums, as well as level of the main interfering factors contribution to the measured radiance in each initially selected IASI channel (Trotsenko et al. 2003). The example of channel subsets selection (using described technique) is given below.

The choice of relevant variables in regression procedures

As mentioned in the Introduction, the specification of relevant predictor/ predictand variables helps under many situations to overcome (at least, partially) the non-linearity of original inversion problem and to account for the effect of interfering factors. Because listed features are mounting in case of Q-, and q- profile retrievals, the standard linear regression approach as well as EOF regression could become inefficient. To reduce the impact of surface temperature T_s and T- profiles variations (as key interfering factors) on the measured radiances the refined regression scheme should consider a priori

knowledge for these factors at the level of 0.5K and 1.5 K/km, respectively. Basing on these assumptions, the expression for the radiance in particular channel could be linearized respecting the reference state vector (X_0) as follows:

$$R = \mathbf{B}^T j_0 + \mathbf{B}^T dj, \qquad (9)$$

where R signifies the measured radiance correspondent to target state vector **x**; **B** is a vector composed of the Planck functions for the T_s (the first element) and the T-profile correspondent to state **x**; j_0 is a vector containing full atmosphere transmittance as the first element and accordingly normalized transmittance derivatives respecting altitude coordinates correspondent to reference state vector $\mathbf{x_0}$, and dj is the deviation of vector φ respecting j_0. In line with (9) the vector of predictors is composed of the values of $\Delta R = R - \mathbf{B}^T j_0$ specified for each channel and expressed in units of equivalent brightness temperature. Namely vector **B** is composed on the basis of preceding retrievals for the T_s and the T-profile whereas vector j_0 is produced (individually for each channel) by correspondent averaging of the pre-calculated transmittances and their derivatives over the learning sample. In turn the vector of predictands initially contains the values of $\ln(x_i / x_i^0)$, i = 0, 1,… L, where L is the number of atmosphere levels in the profile, and elements x_i denote the ozone (or water vapor) column integrated contents and relevant mixing ratios at i = 0 and i > 0, respectively. Note that just introduced predictor/predictand variables are, of course, not unique. In the next section the example will be given of q-profile regression retrieval with other predictor variables. Besides, the option to apply EOF decomposition for introduced predictor/ predictand variables is proved to be acceptable.

How to reduce the size of training samples?

The accuracy of regression estimates depends crucially on the quality of training samples. In order to decrease sampling effects the special approach may be applied based on the ideas of quasi-statistical modeling and design theory.

Suppose the goal is to generate the representative sample $\{\mathbf{R_j}\}$ using known first and second moments $\overline{\mathbf{R}} = 0$ and S. Standard approach consists of usage well known formulae

$R_j = V_{tr} \Lambda_{tr}^{1/2} V_{tr}^T \xi_j$, j=1,…,N,

where ξ_j is a random n-dimensional vector, Gaussian- distributed with zero mean and identity covariance matrix.

In order to reduce radically the sample size N it is proposed to build the new sample $R^* = \{\mathbf{R_j}\}$, j=1,…,N*, $N^* = n_c + 1 << N$ as follows:

$R^* = V_{tr} \Lambda_{tr}^{1/2} V_{tr}^T H$,

where H is N*xN* Hadamard matrix composed of +1 and -1; moreover N* should be multiple to 4, for example, N* =20 or N* =40.

Simulation study results

Proposed algorithms have been evaluated in the series of retrieval experiments with synthetic IASI data incorporated into two special global datasets. The first dataset (named RIE) that has been complied by Eumetsat, comprises of about 2000 collocated pairs of “observed” (synthetic)spectra $\mathbf{R_j}$ and respective state vectors $\mathbf{x_j}$. The original dataset has been subdivided into statistically homogeneous ensembles relating to various latitude zones and sounding time, namely, SAS (SubArctic Summer), SAW (SubArctic Winter), MLS (Mid Latitude Summer), TRP (Tropics).

Dataset II incorporates about 20000 state vectors $\mathbf{x_i}$ extracted from well- recognized data catalogue NOAA 88/89 and ECMWF 60-level sampled database as well as respective “pieces”of synthetic spectra $\mathbf{R_j}$. Beforehand the clear-sky atmospheric models have been identified within mentioned

ensembles, using the analysis of the temperature and water vapor spatial derivatives behavior. The resulted ensemble of clear sky atmospheric models incorporates about 10000 implementations. The values $\mathbf{R}_j$ have been calculated using specially developed fast radiative transfer model, see (Trotsenko et al. 2001).

The retrieval experiments have been performed separately on the base of RIE dataset (EOF and GEOF regressions) and dataset II (linear regression with selection of informative variables and statement of relevant predictors/predictands). Moreover, the results are discussed, for the most part not reported in our preceding publications (Uspensky et al. 2003 a, b; Trotsenko et al. 2003).

RIE dataset

Q-profile retrievals

The radiance spectra within R3 band (1000-1070 cm^{-1}) and within R1 band (650-770 cm^{-1}) were used as predictors for the retrieval of atmospheric ozone profiles Q(z).

Experiment #1 Standard EOF regression algorithm; the PC's are introduced both in measurement and state spaces; the original predictor variables are from R3 band.

Experiment #2 The same as experiment #1, but original predictor variables from R3 band are supplemented by 40 radiances measured in informative channels from RI band.

Experiment #3 GEOF regression using GEOF's both in measurement and state spaces; the original predictor variables are from R3 band (the same, as in experiment # 1).

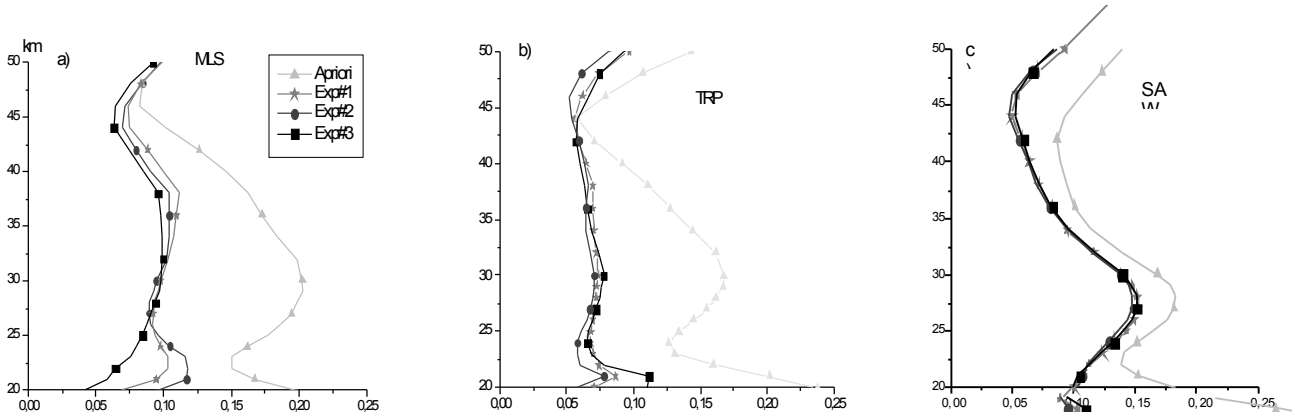

Fig.1 Ozone profile retrieval error statistics in Experiments #1-3

Fig. 1 (a, b, c) demonstrate error statistics for retrieval experiments #1-3 and control samples extracted from MLS (N=145), TRP (N=276), SAW (N=300) ensembles. Each fig contains three rmse profiles together with natural variability curve (square root of $S_{o.x}$ diagonal elements) that are plotted for the atmospheric layer within 20-50 km. It is not succeeded to achieve admissible level of retrieval accuracy (about 10 %) for SAW.Application of GEOF regression enables to improve the accuracy of ozone profile estimation only for MLS, while for the TRP ensemble the best results are provided by increasing the number of predictor variables (experiment # 2). Nevertheless in the majority of cases considered the use of developed technique enables to achieve the 10% accuracy levels of Q-profile retrievals.

T-profile retrievals

Retrieval experiments have been performed using the data from R1 band (481 IASI channels).

Experiment #1 Standard EOF regression; the PC's are introduced in both measurement and state spaces; the original predictor variables are from R1 band.

Experiment #2. The same as experiment #1, but the GEOF regression is applied.

As follows from the assessment of the layer mean r.m.s.e. values (defined via averaging over 3 layers: 0-10, 10-20, 20-30 km), the application of GEOF regression algorithm enables to improve slightly (<0.3K) the retrieval accuracy for the troposphere layers. Moreover, for all cases considered the developed algorithm ensures the retrieval of T-profiles with mean accuracy (mean r.m.s.e. about 1.3K within the layer 0-20 km.

q-profile retrievals

The retrieval technique, subject to testing, presents EOF regression algorithm with specially stated predictors/predictands. In contrast to above text dew point temperatures (DPT) were chosen as predictand variables, while the atmospheric brightness temperature (T_{AB}) were used as predictors. The T_{AB} values are derived as follows :$B_i(T_{AB}) = [R_i - B_i(T_s)\ \tau_{s,i}]/(1-\tau_{s,i})$, where $B_i(\ )$and R_i are the Planck function and radiance in the i-th IASI channel; $\tau_{s,i}$ is the total atmospheric transmittance. The error statistics of the DPT regression estimation (T_{AB} in spectral region 1260-1360 cm^{-1} were replaced by 20 PC's and DPT profiles-by 15 PC's) is shown at fig.2a along with the a priori DPT variability for MLS atmosphere. The accuracy of the relative humidity (RH) profile retrieval is shown at fig.2b.

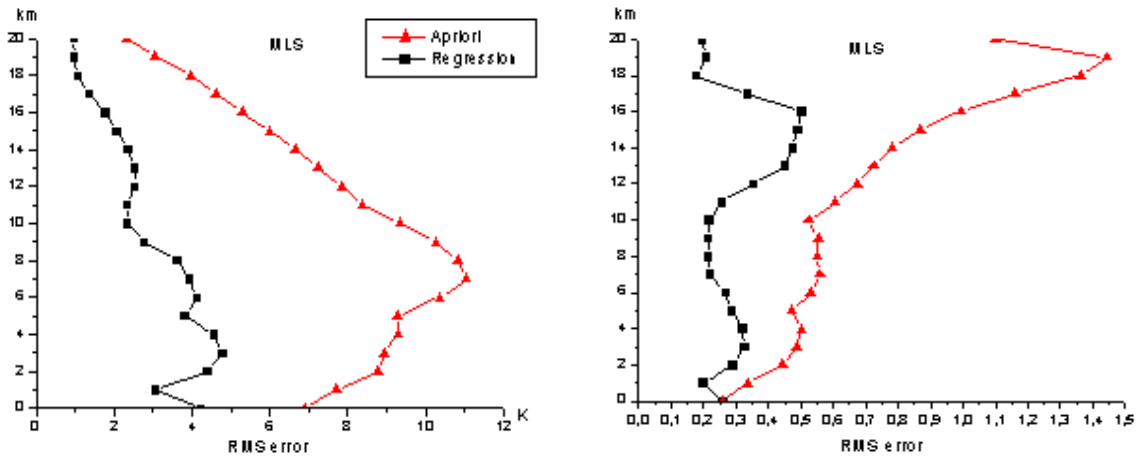

Fig. 2. The retrieval accuracy and a priori variability for DPT- and RH-profiles

As follows from fig.2, the accuracy of RH-profile retrievals is not high; therefore further refinements of retrieval technique are needed.

Verification experiments with dataset II

T- profile retrieval

The regression procedure for T-profile retrieval is based upon the use of IASI data in 55 selected channels (within band 652-743 cm^{-1}), see fig.3 below, illustrating the behavior of weighting functions in these channels. The use of optimal" channels subset permits to exclude the main interfering factors (the water vapor, the ozone, and the surface temperature). The retrieval tests show that the achieved rmse within 2 – 30 km altitude range is about or even better than 1 K. In turn the accuracy within the 0-1 km layer is not greater than 1.8 - 2 K. As illustration, the following fig.4 demonstrates the altitude dependence of the r.m.s.e. resulted from the retrieval test included 1213 independent implementations (70S-70N; 10W-45E).

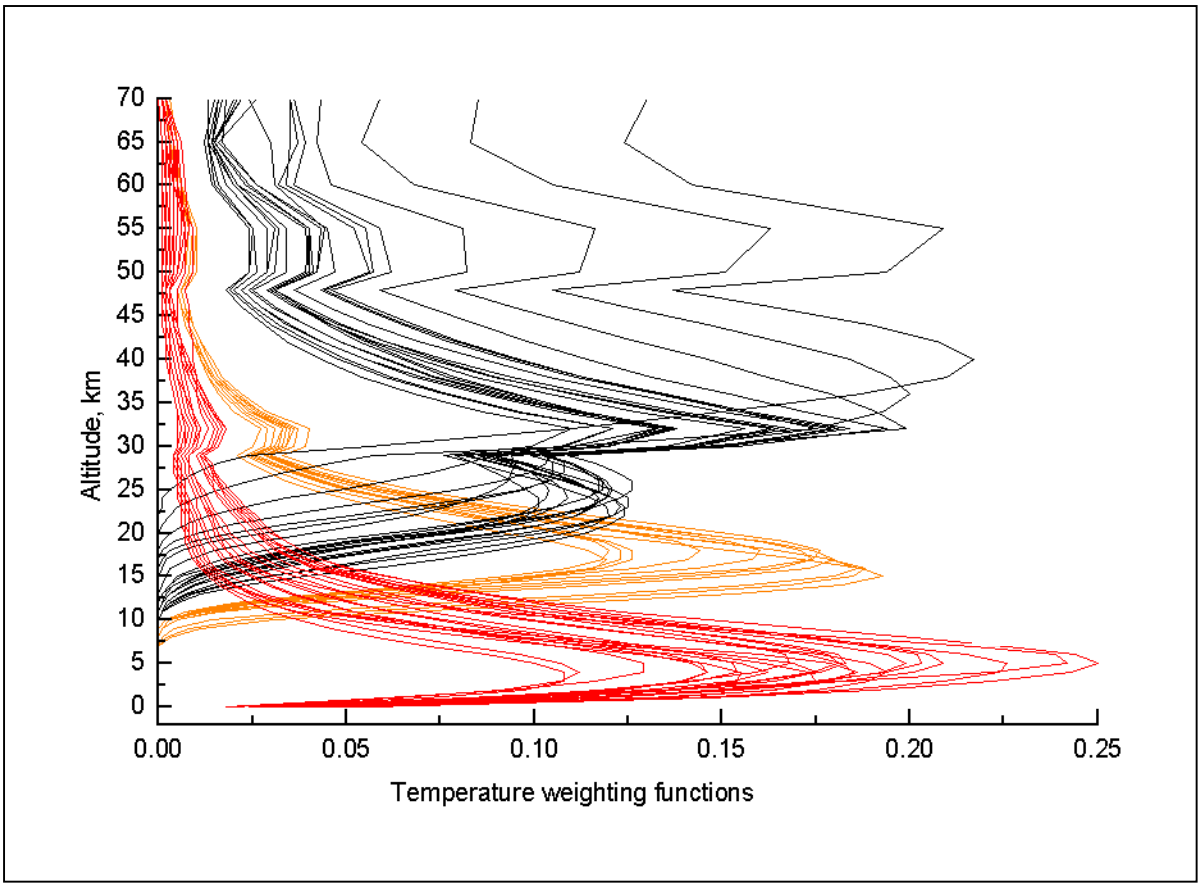

Fig.3 Temperature weighting functions for 55 selected channels

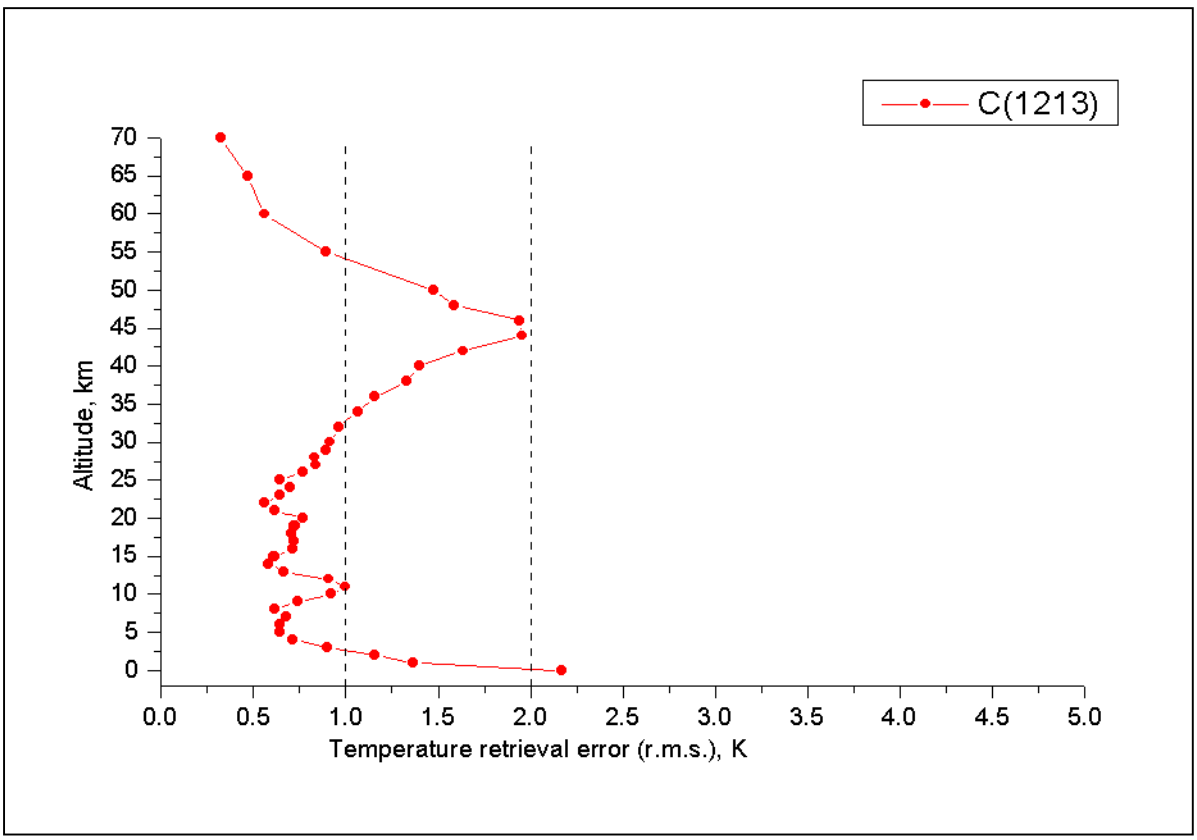

Fig. 4. Error statistics for T-profile retrieval

Q-profile retrieval

The developed regression procedure utilizes the data in the dedicated channel subset as well as specially chosen predictor/predicatand variables (described above). The selection of the dedicated channel subset (universal for all atmospheric conditions) has resulted in the specification of 58 IASI channels centered withinR3 band. The composing of the training samples has been carried out according to prescribed sub-ranges of the ozone column amount. The altitude dependence of Q-profile retrieval accuracy (in terms of rmse) is shown at fig.5 (left panel) together with natural variability curves (right panel) for 6 samples relating to various atmosphere model ensembles. As it is illustrated on fig.5, the achieved retrieval accuracy within 20-50 km altitude range is about or even better than 10 %. Note that the comparison fig.5 with fig.1 manifests evident benefits of using dedicated subset of channels and relevant predictor/predictand variables.

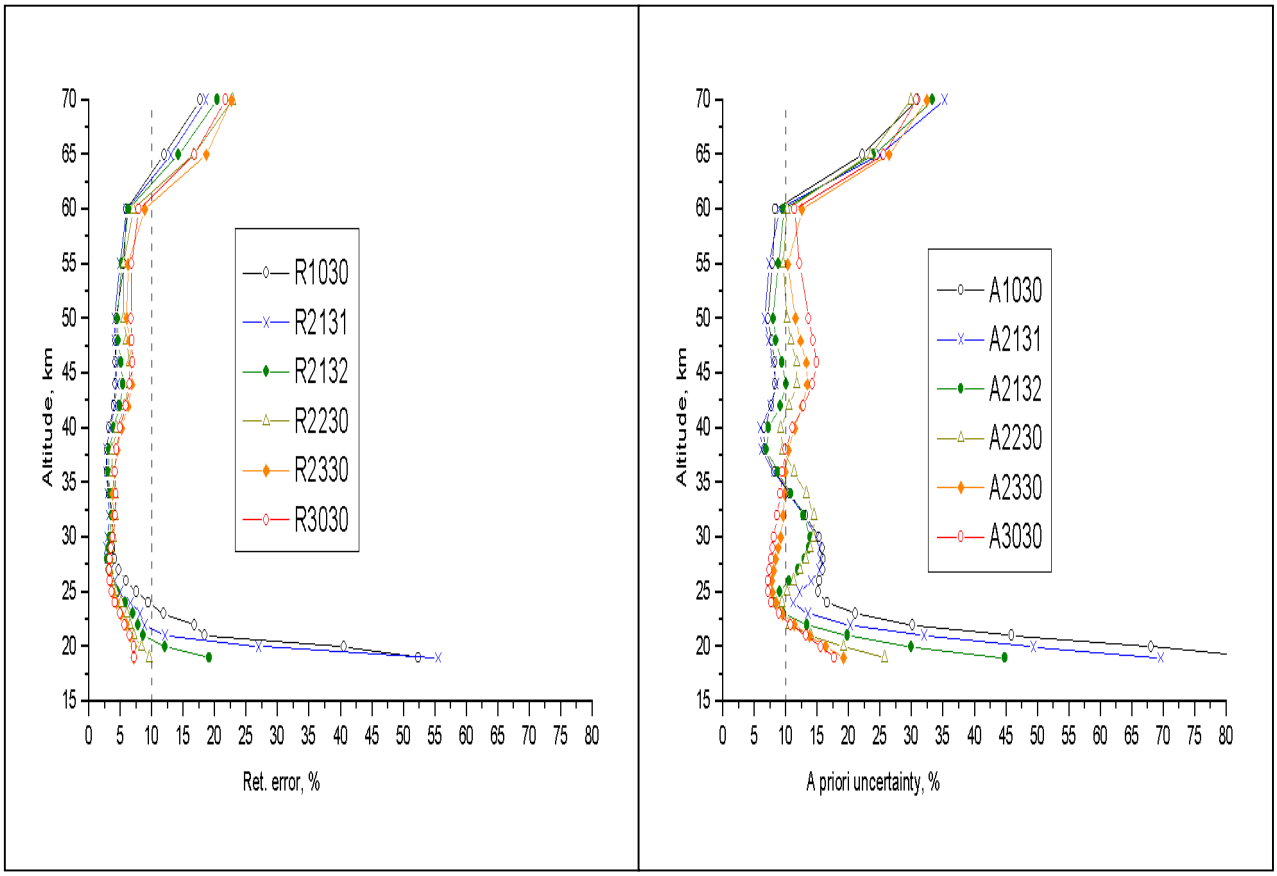

Fig.5 The retrieval accuracy and a priori variability for ozone profile

q –profile retrieval

The developed regression procedure is quite similar to Q-profile regression retrieval. Namely, it uses the data in the dedicated subset of 60 channels within 1206-1485 cm^{-1} band as well as predictor/predictands variables formally coinciding with those adopted for Q-profile retrieval scheme. At it has been shown by correspondent tests, the developed version provides rather good accuracy characteristics at least in the lower troposphere. This is illustrated by fig.6, where the r.m.s.e. altitude dependence (left panel) together with natural variability (right panel) are presented for 7 different samples. Comparison fig.6 with fig.2 demonstrates the advantages of proposed approach.

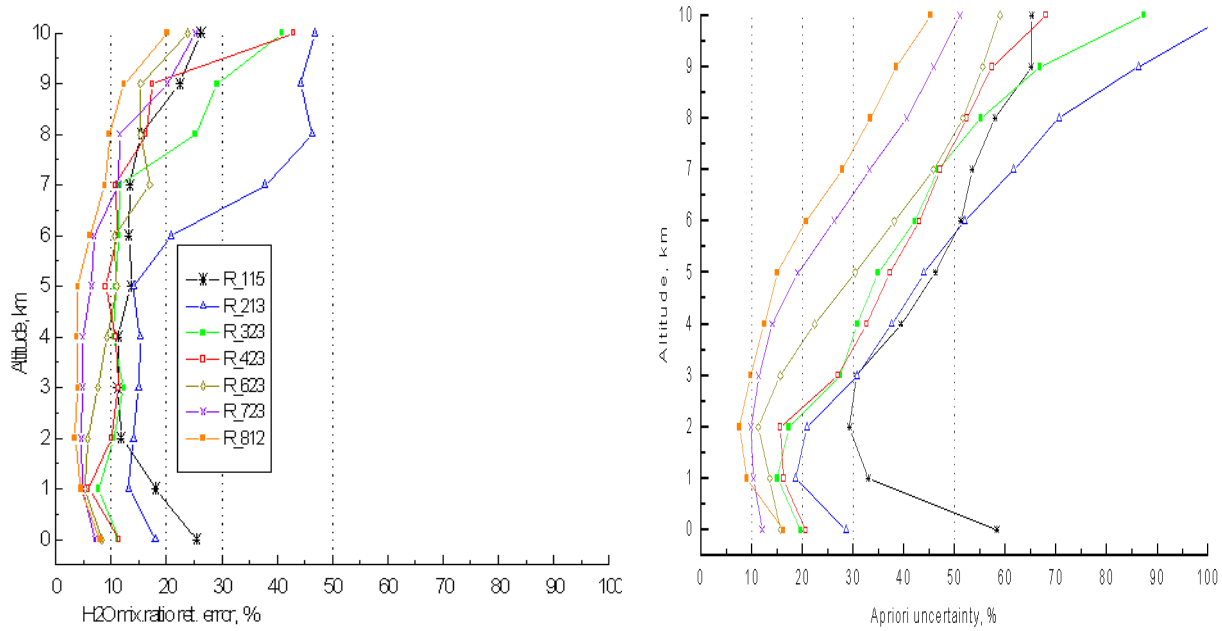

Fig.6 The retrieval accuracy and a priori variability for water vapor mixing ratio profile

Summary and conclusions

1.Statistical regression algorithms can definitely be a valuable tool for the inversion of advanced IR sounders data and retrieval of T-, q-, Q- profiles, if:

-to reduce significantly the number of original predictor variables as well as data multi-collinearity via introduction of PC's (EOF's, GEOF's) or selection of the most informative channels;

-to suppress (at least partially) the non-linearity effects through physically valid choice of predictors and predictands as well as through detailed classification of training samples;

-to reduce sampling effects through careful compiling of training samples, in particular, removing cases that are "cloudy"(especially for q- retrievals).

2. The simulation study with synthetic LASI spectra demonstrate the benefits of using the procedure of the most informative channels subset selection at the first stage of data inversion: the accuracies of output regression retrievals are better than those provided by "pure" EOF regression algorithms.

Acknowledgements

We thank EUMETSAT for supporting this research

References

Aires F., Chedin A., Scott N.A., Rossow W.B. 2002. A regularized neural net approach for retrieval of atmospheric and surface temperatures with IASI instrument. J. Appl. Meteorol., 41, 144-159.

Chalon G., Cayla F., Diebel D. 2001. IASI. An advanced sounder for operational meteorology. CNES Rep., 9 p.

Crone L.J., MeMillin L.M., Crosby D.S. 1996. Constrained regression in satellite meteorology. J. Appl. Meteorol., 35, 2023-2-35.

Fleming H.E., Crosby D.S., Neuenderffer A.C. 1986. Correction of satellite temperature retrieval errors due to errors in atmospheric transmittances. J. Clim. Appl. Meteorol. v. 25, 6, 869-882.

Huang H.-L., Antonelly P. 2001. Application of principal component analysis to high-resolution infrared measurement compression and retrieval. Journ. Appl. Meteor., v.40, 365-388.

Kozlov V.P. 1978. Mathematical aspects of radiance measurements inversion. In "Abel inversion and its generalizations" Ed. Preobrazhensky N.G., Novosibirsk, Nauka, 68-95 (in Russian).

Rabier F.et al. 2002. Channel selection methods for IASI. Q. J. R. Meteorol. Soc., 128, 1011-1027.

Rodgers C.D. 1996. Information content and optimization of high spectral resolution measurements. In Optical Spectroscopy Technique and Instrumentation for Atmospheric and Space Research.II.SPIE, 23,136-147.

Rodgers C.D. 2000. Inverse methods for atmospheric sounding: theory and practice. World Sci. Publishing Co. 2000. 238 p.

Smith W.L., Woolf H.M. 1976. The use of eigenvectors of statistical covariance matrices for interpreting satellite sounding radiometer observations. J.Atm.Sci., v.33, 7, 1127-1140.

Thaker W.C. 1996. Metric-based principal components: data uncertainties. Tellus, 48A, 584-592.

Trotsenko A.N. et al. 2001. Efficient forward model to simulate IASI/METOP measurement and its validation against high-resolution field observations. In: IRS' 2000: Current Problems in Atmospheric Radiation, W.L.Smith, Ju.M.Timofeev (eds.), A.Deepak Publishing, Hampton,Virginia, USA, 401-404.

Trotsenko A.N. et al. 2003. Modular prototype processor for geophysical parameters retrieval from IASI: pilot version. The 2003 EUMETSAT Meteorol. Sat. Conf. Weimar, Germany, 29 Sept.-03 Oct. 2003 (In press).

Uspensky A.B., Romanov S.V., Trotsenko A.N. 2003a. Modeling of the atmospheric ozone vertical distribution remote measurements by the IR satellite sounders of high spectral resolution. J. Earth Research from space. Russian Acad. Sci., 1, 49-57 (in Russian).

Uspensky A.B., Romanov S.V., Trotsenko A.N. 2003b. Use of principal components technique for the analysis of advanced IR-sounders data. J. Earth Res. from space. Russian Acad. Sci., N 3, 26-33 (in Russian).

AUTHOR INDEX

Author Index